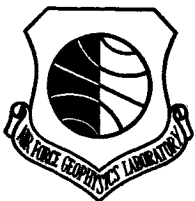


*NASA Conference Publication 2182*  
*AFGL-TR-81-0270*

# **Spacecraft Charging Technology 1980**

*A conference held at  
U.S. Air Force Academy  
Colorado Springs, Colorado  
November 12-14, 1980*



*NASA Conference Publication 2182  
AFGL-TR-81-0270*

# **Spacecraft Charging Technology 1980**

*A conference sponsored by  
U.S. Air Force Geophysics  
Laboratory, Hanscom AFB,  
Massachusetts, and NASA Lewis  
Research Center, Cleveland,  
Ohio, and held at U.S. Air  
Force Academy, Colorado  
Springs, Colorado,  
November 12-14, 1980*



**National Aeronautics  
and Space Administration**

**Scientific and Technical  
Information Office**

**1981**



## PREFACE

The third Spacecraft Charging Technology Conference was held at the U.S. Air Force Academy from November 12-14, 1980, continuing the trend of having such meetings every two years. The objectives of this conference series are to summarize the status of environmental interaction technology and to present information for use by satellite designers.

This conference was planned as an overview of both space flight and ground technology studies directed toward controlling satellite interactions with the space environment. Flight data from P78-2, SCATHA, satellite instruments were stressed since, for the first time, simultaneous measurements of the environment and satellite system response were made. These data can meld with the ongoing analytical modeling and ground simulation studies both in this country and Europe to validate concepts. The investigation is not yet complete: There are still serious questions to be resolved, not the least of which is the question of how stringent a standard should be imposed on the industry for design and testing of future satellites. The panel discussion on this topic allowed a forum for various opinions to be expressed.

The spacecraft charging technology investigation is in its final phases and a new Air Force-NASA cooperative program to investigate environmental interactions with future large satellites operating in all orbits has been established. This program was outlined at the conference and a brief summary of current work presented.

This proceedings includes all 66 papers presented, along with a scheduled paper that was not given. The panel discussion was recorded, transcribed, and edited for inclusion. The proceedings follows the conference session format.

Col. Thomas R. Ferguson, Assistant Director of Science and Technology, Headquarters, Air Force Systems Command, and Walter Olstad, Acting Associate Administrator for Aeronautics and Space Technology, NASA, approved and endorsed the conference. Col. James E. Baker, Commander of the Air Force Geophysics Laboratory, USAF Systems Command, and Dr. John F. McCarthy, Jr., Director of the NASA Lewis Research Center encouraged and supported the conference. Lt. Gen. K. L. Tallman, Superintendent of the Air Force Academy approved our use of the Academy. Ms. Janet Shea, Directorate of Plans and Programs, Air Force Academy, provided outstanding support at the conference including arrangements for accommodations, transportation, meals, and facilities. The members of the Conference Program Committee were Dr. A. R. Frederickson, Dr. W. L. Lehn, C. K. Purvis, Major J. L. Roberts, and R. Broussard.

N. John Stevens  
NASA Lewis Research Center

Charles P. Pike  
Air Force Geophysics  
Laboratory

## CONTENTS

	Page
KEYNOTE ADDRESS	
Dell P. Williams III . . . . .	1
SESSION 1 - MATERIAL RESPONSES	
DIELECTRIC DISCHARGE CHARACTERISTICS IN A TWO-ELECTRON SIMULATION ENVIRONMENT	
M. Treadaway, R. Leadon, C. Mallon, T. Flanagan, R. Denson, and E. Wenaas . . . . .	4
ELECTRON-BEAM-CHARGED DIELECTRICS - INTERNAL CHARGE DISTRIBUTION	
Brian L. Beers and V. W. Pine. . . . .	17
BULK CHARGING AND BREAKDOWN IN ELECTRON-IRRADIATED POLYMERS	
A. R. Frederickson . . . . .	33
CHARGING AND DISCHARGING TEFLON	
B. C. Passenheim and V. A. J. van Lint . . . . .	52
EXPERIMENTAL VALIDATION OF A NUMERICAL MODEL PREDICTING THE CHARGING CHARACTERISTICS OF TEFLON AND KAPTON UNDER ELECTRON BEAM IRRADIATION	
R. C. Hazelton, E. J. Yadlowsky, R. J. Churchill, L. W. Parker, and B. Sellers . . . . .	65
ROLE OF ENERGETIC PARTICLES IN CHARGING/DISCHARGING OF SPACECRAFT DIELECTRICS	
J. B. Reagan, R. W. Nightingale, E. E. Gaines, R. E. Meyerott, and W. L. Imhof. . . . .	74
ELECTRON PENETRATION OF SPACECRAFT THERMAL INSULATION	
Walter L. Powers, Barbara F. Adams, and George T. Inouye . . . . .	86
ELECTROSTATIC DISCHARGING BEHAVIOUR OF KAPTON IRRADIATED WITH ELECTRONS	
Derek Verdin . . . . .	96
DIELECTRIC SURFACE DISCHARGES: EFFECTS OF COMBINED LOW-ENERGY AND HIGH-ENERGY INCIDENT ELECTRONS	
K. G. Balmain and W. Hirt. . . . .	115
PRELIMINARY COMPARISON OF MATERIAL CHARGING PROPERTIES USING SINGLE- ENERGY AND MULTIENERGY ELECTRON BEAMS	
R. C. Adamo and J. E. Nanevich . . . . .	129
BRUSHFIRE ARC DISCHARGE MODEL	
G. T. Inouye . . . . .	133

## SESSION 2 - MATERIAL CHARACTERIZATION

### EFFECTS OF SECONDARY ELECTRON EMISSION ON CHARGING

Martin S. Leung, Michael B. Tueling, and Edwin R. Schnauss . . . . . 163

### SECONDARY ELECTRON EMISSION YIELDS

I. Krainsky, W. Lundin, W. L. Gordon, and R. W. Hoffman. . . . . 179

### OBLIQUE-INCIDENCE SECONDARY EMISSION FROM CHARGED DIELECTRICS

James W. Robinson and Paul A. Budd . . . . . 198

### TANK TESTING OF A 2500-cm<sup>2</sup> SOLAR PANEL

Renate S. Bever and John Staskus . . . . . 211

### CHARGING AND DISCHARGING CHARACTERISTICS OF A RIGID SOLAR ARRAY

George F. Brady, Jr., David A. Vance, and Stanley A. Greenberg . . . . 228

### MATERIALS CHARACTERIZATION STUDY OF CONDUCTIVE FLEXIBLE SECOND SURFACE MIRRORS

F. Levadou, S. J. Bosma, and A. Paillous . . . . . 237

### DESIGN OF AN ARC-FREE THERMAL BLANKET

Christakis N. Fellas . . . . . 261

### CHARGING CONTROL TECHNIQUES

R. E. Schmidt. . . . . 267

### CHARGING CHARACTERISTICS OF SILICA FABRICS

Léon Levy and Alain Paillous . . . . . 287

### ELECTROSTATIC CHARGING CHARACTERISTICS OF THERMAL CONTROL PAINTS AS FUNCTION OF TEMPERATURE

Paul A. Robinson, Jr., and A. C. Whittlesey. . . . . 309

### EVALUATION OF CHARGE CONTROL TECHNIQUES ON SPACECRAFT THERMAL SURFACES (ELECTROSTATIC DISCHARGE STUDY)

P. A. Robinson, Jr., E. M. Brown, S. M. Conan, C. R. Dulgeroff,  
W. R. Elkman, G. J. Holm, L. C. Lawton, G. J. Pack,  
and D. L. Shannon. . . . . 320

### CONDUCTION THROUGH PUNCTURES IN METAL-BACKED DIELECTRICS

A. Meulenberg and P. A. Robinson, Jr. . . . . 342

### ACCELERATED ALPHA-S DETERIORATION IN A GEOSTATIONARY ORBIT

Otto K. Husmann. . . . . 353

## SESSION 3 - SCATHA FLIGHT DATA

### OPERATIONAL STATUS OF THE SPACE TEST PROGRAM P78-2 SPACECRAFT AND PAYLOADS

1Lt. Richard N. Osgood . . . . . 365

ELECTRON ANGULAR DISTRIBUTIONS DURING CHARGING EVENTS J. F. Fennell, D. R. Croley, Jr., P. F. Mizera, and J. D. Richardson . . . . .	370
OPERATION OF SC5 RAPID SCAN PARTICLE SPECTROMETER ON SCATHA SATELLITE Frederick A. Hanser, Bach Sellers, David A. Hardy, H. A. Cohen, J. Feynman, and M. S. Gussenhoven. . . . .	386
REVIEW OF HOT PLASMA COMPOSITION NEAR GEOSYNCHRONOUS ALTITUDE Richard G. Johnson . . . . .	412
SCATHA OBSERVATIONS OF SPACE PLASMA COMPOSITION DURING A SPACECRAFT CHARGING EVENT R. G. Johnson, R. Strangeway, S. Kaye, R. Sharp, and E. Shelley. . . .	433
P78-2 ENGINEERING OVERVIEW A. L. Vampola. . . . .	439
SATELLITE SURFACE POTENTIAL SURVEY Paul F. Mizera and G. M. Boyd. . . . .	461
PRELIMINARY ANALYSIS OF DATA FROM SRI INTERNATIONAL TRANSIENT PULSE MONITOR ON BOARD P78-2 SCATHA SATELLITE S. A. Damron, R. C. Adamo, and J. E. Nanevicz. . . . .	470
ASPECT DEPENDENCE AND FREQUENCY SPECTRUM OF ELECTRICAL DISCHARGES ON THE P78-2 (SCATHA) SATELLITE Harry C. Koons . . . . .	478
FLIGHT EVIDENCE OF SPACECRAFT SURFACE CONTAMINATION RATE ENHANCEMENT BY SPACECRAFT CHARGING OBTAINED WITH A QUARTZ CRYSTAL MICROBALANCE D. M. Clark and David F. Hall. . . . .	493
P78-2 SATELLITE AND PAYLOAD RESPONSES TO ELECTRON BEAM OPERATIONS ON MARCH 30, 1979 H. A. Cohen, R. C. Adamo, T. Aggson, A. L. Chesley, D. M. Clark, S. A. Damron, D. E. Delorey, J. F. Fennell, M. S. Gussenhoven, F. A. Hanser, D. Hall, D. A. Hardy, W. B. Huber, I. Katz, H. C. Koons, S. T. Lai, B. Ledley, P. F. Mizera, E. G. Mullen, J. E. Nanevicz, R. C. Olsen, A. G. Rubin, G. W. Schnuelle, N. A. Saflekos, M. F. Tautz, and E. C. Whipple. . . . .	509
SESSION 4 - ANALYTICAL MODELING	
REPRESENTATION AND MATERIAL CHARGING RESPONSE OF GEO PLASMA ENVIRONMENTS P. R. Stannard, G. W. Schnuelle, I. Katz, and M. J. Mandell. . . . .	560
SIMULATION OF CHARGING RESPONSE OF SCATHA (P78-2) SATELLITE G. W. Schnuelle, P. R. Stannard, I. Katz, and M. J. Mandell. . . . .	580

SCATHA SSPM CHARGING RESPONSE: NASCAP PREDICTIONS COMPARED WITH DATA Carolyn K. Purvis and John V. Staskus . . . . .	592
THREE-DIMENSIONAL ANALYSIS OF CHARGING EVENTS ON DAYS 87 and 114, 1979, FROM SCATHA N. A. Saflekos, M. F. Tautz, A. G. Rubin, D. A. Hardy, P. F. Mizera, and J. Feynman . . . . .	608
COMPUTER SIMULATION OF SPACECRAFT CHARGING ON SCATHA A. G. Rubin, H. A. Cohen, D. A. Hardy, M. F. Tautz, and N. A. Saflekos . . . . .	632
ANALYSIS OF AMBIENT AND BEAM PARTICLE CHARACTERISTICS DURING THE EJECTION OF AN ELECTRON BEAM FROM A SATELLITE IN NEAR-GEOSYNCHRONOUS ORBIT ON MARCH 30, 1979 M. S. Gussenhoven, H. A. Cohen, D. A. Hardy, W. J. Burke, and A. Chesley . . . . .	642
COMPARISON OF NASCAP MODELING RESULTS WITH LUMPED-CIRCUIT ANALYSIS David B. Stang and Carolyn K. Purvis . . . . .	665
NASCAP CHARGING CALCULATIONS FOR A SYNCHRONOUS ORBIT SATELLITE N. L. Sanders and G. T. Inouye . . . . .	684
RESULTS FROM A TWO-DIMENSIONAL SPACECRAFT-CHARGING SIMULATION AND COMPARISON WITH A SURFACE PHOTOCURRENT MODEL J. G. Laframboise, S. M. L. Prokopenko, M. Kamitsuma, and R. Godard. . . . .	709
ANALYTICAL MODELING OF SATELLITES IN GEOSYNCHRONOUS ENVIRONMENT N. John Stevens. . . . .	717
CALCULATION OF SURFACE CURRENT RESPONSE TO SURFACE FLASHOVER OF A LARGE SAMPLE UNDER GROUNDED AND FLOATING CONDITIONS M. J. Mandell, I. Katz, and G. W. Schnuelle. . . . .	730
MODEL OF COUPLING OF DISCHARGES INTO SPACECRAFT STRUCTURES A. J. Woods, M. J. Treadaway, R. Grismore, R. E. Leadon, T. M. Flanagan, and E. P. Wenaas . . . . .	745
DISAPPEARANCE AND REAPPEARANCE OF PARTICLES OF ENERGIES >50 KEV AS SEEN BY P78-2 (SCATHA) AT NEAR GEOSYNCHRONOUS ORBIT J. Feynman, N. A. Saflekos, H. G. Garrett, D. A. Hardy, and E. G. Mullen . . . . .	755
SESSION 5 - SYSTEMS DESIGN AND TEST	
MILITARY STANDARDS AND SCATHA PROGRAM UPDATE OF MIL-STD-1541 D. T. Frankos. . . . .	768

MILITARY STANDARD FOR SPACECRAFT CHARGING STATUS REPORT	
Alan B. Holman . . . . .	772
USE OF CHARGING CONTROL GUIDELINES FOR GEOSYNCHRONOUS SATELLITE DESIGN STUDIES	
N. John Stevens. . . . .	789
P78-2 SCATHA ENVIRONMENTAL DATA ATLAS	
E. Gary Mullen, David A. Hardy, Henry B. Garrett, and Elden C. Whipple . . . . .	802
METEOSAT SPACECRAFT CHARGING INVESTIGATION	
Dierk G. Hoge. . . . .	814
ELECTRON IRRADIATION TESTS ON EUROPEAN METEOROLOGICAL SATELLITE	
J. Reddy . . . . .	835
SPACECRAFT CHARGING TECHNOLOGY IN THE SATELLITE X-RAY TEST FACILITY	
Troy J. Sponaugle. . . . .	856
SIMULATION OF SPACECRAFT CHARGING ENVIRONMENTS BY MONOENERGETIC BEAMS	
Ward Halverson . . . . .	866
IMPORTANCE OF DIFFERENTIAL CHARGING FOR CONTROLLING BOTH NATURAL AND INDUCED VEHICLE POTENTIALS ON ATS-5 AND ATS-6	
E. C. Whipple and R. C. Olsen. . . . .	887
A COMPARISON OF THREE TECHNIQUES OF DISCHARGING SATELLITES	
H. A. Cohen, A. L. Chesley, T. Aggson, M. S. Gussenhoven, R. C. Olsen, and E. Whipple. . . . .	888
ELECTROMAGNETIC FIELDS PRODUCED BY SIMULATED SPACECRAFT DISCHARGES	
J. E. Nanevich, R. C. Adamo, B. L. Beers, and T. N. Delmer . . . . .	894
SESSION 6 - ENVIRONMENTAL INTERACTIONS	
AGREEMENT FOR NASA/OAST-USAF/AFSC SPACE INTERDEPENDENCY ON SPACECRAFT- ENVIRONMENT INTERACTION	
C. P. Pike and N. J. Stevens . . . . .	912
PLASMA INTERACTIONS WITH SOLAR ARRAYS AT HIGH VOLTAGES	
Norman T. Grier, Craig Smith, and Lisa M. Johnson. . . . .	922
EXPERIMENTAL PLASMA LEAKAGE CURRENTS TO INSULATED AND UNINSULATED 10 m <sup>2</sup> HIGH-VOLTAGE PANELS	
J. E. McCoy and D. T. Martucci . . . . .	931
NUMERICAL SIMULATION OF PLASMA-INSULATOR INTERACTIONS IN SPACE	
PART I: THE SELF-CONSISTENT CALCULATION	
J. H. Nonnast, R. C. Chaky, T. P. Armstrong, J. Enoch, and G. G. Wiseman. . . . .	932

NUMERICAL SIMULATION OF PLASMA-INSULATOR INTERACTIONS IN SPACE

PART II: DIELECTRIC EFFECTS

R. C. Chaky, J. H. Nonnast, T. P. Armstrong, J. Enoch, and G. G. Wiseman. . . . .	946
THREE-DIMENSIONAL SPACE CHARGE MODEL FOR LARGE HIGH-VOLTAGE SATELLITES	
David Cooke, Lee W. Parker, and James E. McCoy . . . . .	957
CHARGING OF A LARGE OBJECT IN LOW POLAR EARTH ORBIT	
D. E. Parks and I. Katz. . . . .	979
PANEL DISCUSSION . . . . .	990

## KEYNOTE ADDRESS

**Dell P. Williams III**  
**NASA Headquarters**

Ladies and gentlemen, I would like to add to the welcome offered by the conference organizers to all attendees to this, the Third Spacecraft Charging Technology Conference. Many of you here, I am sure, participated in the conferences held in 1976 and 1978. These next 3 days will dramatically demonstrate the progress that has been made since the last conference with the launch and operation of SCATHA and the related ground technology.

Today, I would like to review the events that have led us to this point because this area of technology has been a showcase for NASA-Air Force coordination in general technological development. Expanding on this, I personally believe that it has been, is now, and will continue to be very important for the civilian and Air Force space programs to undertake cooperative or interdependent technology programs. As you all know, the manpower and budget resources for research and technology are always the last to be increased in good times and the first to be reduced in bad times. While we all read about the proposed buildup in the defense budget, we can anticipate that it might be some time before this buildup is felt by the technology program offices. To accomplish the many good things we need to do, we, NASA and the Air Force, simply must make the most efficient use of joint resources to solve joint problems.

I am aware, however, how difficult it really is to get beyond the philosophical presumption of such a need, through the reality of the problems involved in reaching such an objective, to a finally implemented joint program. Such a joint program can never be accomplished just because of the desires or dictates of Headquarters managers. Through the NASA-AFSC Interdependency Program, many joint activities have been initiated, but many of these have been failures, or at best, limited successes. This has not been the case with the Spacecraft Charging Program. This program has been a large success. Those of you who have had to work on day-to-day problems associated with the joint program should feel a great sense of pride in your accomplishments.

The Spacecraft Charging Program was initiated in late 1975 under joint NASA-AFSC sponsorship because of an awareness of the possible harmful effects of charged-particle interactions with geosynchronous spacecraft. The first elements of this program were designed to establish the nature of the plasma environment and the charging phenomenon. The available instrument data from the NASA Advanced Technology Satellite (ATS) program were analyzed, and the charging program funded additional studies with these same instruments. This work established a positive connection between spacecraft electrical charging events and geomagnetic substorm activity. Additional ATS and laboratory data proved that spacecraft could become charged to large negative potentials and that discharge events on insulating



surfaces could result in dangerous electromagnetic contamination. Such contamination could affect telemetry or control systems, causing pseudocommands and noise. Additionally, these studies produced the concept of differentially charged satellite surfaces, the demonstration of thermal control coating degradation, and the realization of the importance of this phenomenon in attempts to measure scientifically interesting, low-energy phenomena.

This joint NASA-AFSC program was built on these studies to expand both experimental and analytical investigations and to conduct a specially designed space test program to fully characterize the phenomena. The experimental program characterized materials and charge neutralization techniques. Additionally, materials and coatings were developed to control charge buildup. A military standard, a design standards monograph, and a charging analyzer computer program (NASCAP) were designed to predict and minimize charge buildup. Finally, the Space Test Program (STP) P78-2 spacecraft (SCATHA), incorporating a variety of engineering and scientific experiments, was designed and developed and was launched in January 1979.

During this conference you will have a chance to hear the results of all this activity, including many of the results of the SCATHA space flight. We are all, I am sure, eagerly awaiting the opportunity to discuss these findings. However, even while we have been systematically investigating these reasonably well understood phenomena, new charging phenomena have been identified and experienced.

Today, NASA's Voyager spacecraft is broadcasting live its observations of its historic encounter with Saturn. However, on an earlier encounter of the same spacecraft with Jupiter, numerous small anomalies occurred that were probably associated with charging. Luckily, our joint NASA-AFSC program had made its results known, and the spacecraft had been reworked at a late stage to minimize the potential charging effects. These experiences, as well as the latest results from SCATHA, will be used to ensure incorporation of charging control techniques into the design of the follow-on Galileo spacecraft.

Assuming continued success at the same rate as we have come to expect from this program, we will have completed our original objectives in 2 years. Only one small problem exists, and that is for the sponsoring organizations to provide sufficient funding to completely analyze the acquired data. However, beyond this the advanced systems which can be anticipated in the Shuttle era will present new challenges. These challenges will have the form of a different type of environmental interaction that could profitably use investigating in the same type of joint NASA-AFSC technology programs that have been pioneered in the Spacecraft Charging Program.

Both NASA and the Air Force are likely to require much larger spacecraft in this Shuttle era, involving larger power systems operating at significantly higher voltages. These spacecraft power systems may well have capacities 10 to 100 times higher than any operated to date and will be composed of complex structures made up of metals, insulators, and

composites. At these power levels the line voltages must be increased to hundreds of volts, resulting in perhaps a whole new set of environmental possibilities which must be evaluated and addressed.

To answer this new challenge, Col. Tom Ferguson of AFSC and I have recently approved a new interdependency investigation structured in the same way as the charging program. This program is anticipated to run for 9 years and to have a larger basis for support than its predecessor. Details of this investigative program will be provided in the last session of this conference, and, if history is an accurate predictor of the future, this program should be of enormous value to both NASA and the Air Force and should be an efficient expenditure of our valuable R&D resources.

I would like to again thank the conference organizers for inviting me to address you and to participate. I look forward to hearing the technical progress which has occurred since the last meeting.

## **DIELECTRIC DISCHARGE CHARACTERISTICS IN A TWO-ELECTRON SIMULATION ENVIRONMENT\***

**M. Treadaway, R. Leadon, C. Mallon,  
T. Flanagan, R. Denson, and E. Wenaas  
JAYCOR**

### **INTRODUCTION**

In the space environment, electrons are present with energies from a few eV to several MeV. Most studies of the charging of spacecraft dielectrics have focused on charging by the low-energy (5 to 20 keV) portion of the space electron spectrum. As part of the Air Force Weapons Laboratory (AFWL)-sponsored electron-caused electromagnetic pulse (ECEMP) program, the effect of the high-energy portion of the electron spectrum on the charging of spacecraft dielectrics was investigated. Results of an initial series of experiments performed at accelerated fluxes indicated that the charging and discharging characteristics of spacecraft dielectrics are significantly altered by the presence of high-energy electrons (refs. 1,2,3). In this paper, the results of a second series of experiments, in which flux levels more representative of the space electron environment were used, are presented and compared to the results of the high flux tests. The simulation approach was to partition the space electron spectrum into two parts, those electrons which do not penetrate a material and therefore contribute to charging and those which completely penetrate the material. The non-penetrating electrons were simulated using 25-keV electrons and the penetrating electrons by 350-keV electrons.

The materials included in this investigation were Kapton, optical solar reflectors (OSRs), and a ground test satellite surface potential monitor which contained Kapton, Astroquartz, OSRs and Teflon.

### **EXPERIMENTAL DETAILS**

The low flux experiments were performed in the AFWL 4-m-diameter, 6-m-long vacuum chamber shown in figure 1. During these tests, the chamber pressure was maintained between  $5$  and  $8 \times 10^{-6}$  torr. A Kimball Physics electron flood gun was used as a source of 6 to 25 keV electrons and a High Voltage Engineering Van de Graaff as a source of 350 to 450 keV electrons. Both electron beams were collimated and rastered. The current densities of the low energy (6 to 25 keV) and high energy (350 to 400 keV) electrons could be varied from 5 to 350 pA/cm<sup>2</sup> and 1.0 to 60 pA/cm<sup>2</sup>, respectively (measured at the sample location). Current densities were measured using 195 cm<sup>2</sup> aluminum stopping blocks which were connected to a current meter.

---

\*Work sponsored by AFWL under Computer Sciences Corporation Subcontract S-220.

The test samples included a 400 cm<sup>2</sup> array of twenty 8 mil OSRs, a 25 cm diameter sample of 2 mil aluminized Kapton, and four samples (3 mil Teflon, 5 mil aluminized Kapton, 8 mil OSRs and Astroquartz) mounted in a ground test version of the SCATHA Satellite Surface Potential Monitor (SSPM).

The 8 mil OSRs and 2 mil Kapton samples were placed on aluminum mounting plates. The mounting plates were each connected to ground through a one-ohm resistor across which discharge-induced voltages were measured with an oscilloscope. The samples were mounted in a sample carousel and a shielding plate in front of the carousel could be removed remotely to allow irradiation of the samples. Measurements of the surface potential of these samples were performed using a scanning capacitive divider electrostatic voltmeter (ESV). The ESV was fabricated by JAYCOR and was calibrated prior to and during the experimental sequence by biasing the sample mounting plates to potentials from -1 to -10 kV.

The SSPM was mounted directly above the sample carousel. The SSPM electronics were used to monitor the surface potential and leakage currents of the SSPM samples.

#### ENVIRONMENT AND SIMULATION

Figure 2 shows two electron spectra measured at geosynchronous altitudes. As a first approximation for simulation, these spectra were partitioned into non-penetrating and penetrating electrons. The non-penetrating electrons were simulated using a monoenergetic low energy electron beam (6 to 25 keV) and the penetrating electrons were simulated using a monoenergetic high energy electron beam (350 to 400 keV)\*. Using this simulation philosophy the spectra shown in figure 2 would be simulated by the fluxes listed in table 1. These fluxes were determined from consideration of the practical range of electrons in the test materials which is material dependent. Also listed in table 1 are the ranges of fluxes available during the tests described in this paper.

For a planar sample in a steady-state charging condition, charge conservation requires that

$$J_B - J_S - J_L - J_P = 0 \quad (1)$$

where  $J_B$  is the current density of electrons that stop in the sample,  $J_S$  is the secondary electron emission current density,  $J_L$  is the leakage current density and  $J_P$  is the photoemission current density.

---

\*The practical range of a 350 keV electron in SiO<sub>2</sub> is roughly 0.053 cm (≈21 mils) and the thickest sample tested was the 8 mil OSRs.

The secondary electron current is a function,  $\delta$ , of the energy,  $E_B$ , of the electron beam, the incident electron current density, and the sample surface potential,  $V$ .  $J_S$  can be written as

$$J_S = J_B \delta(E_B - V) \quad (2)$$

If the penetration depth of the incident low energy electrons is small compared to the thickness,  $L$ , of the dielectric sample and if the conductivity,  $\sigma$ , of the dielectric is uniform, then the leakage current density can be written as

$$J_L = \frac{V}{L} \sigma$$

The conductivity of the bulk dielectric is the sum of the ambient and radiation-enhanced conductivities,  $\sigma_A$  and  $\sigma_R$ , respectively. The radiation induced conductivity can be written as

$$\sigma_{\text{rad}} = K \dot{\gamma}^\Delta = K J_{\text{Pen}}^\Delta$$

where  $K$  and  $K$  are material dependent constants,  $\dot{\gamma}$  is the radiation dose rate of the penetrating electrons,  $J_{\text{Pen}}$  is the current density of penetrating electrons and  $\Delta$  is a material dependent constant which has values between 0.8 to 1.0 for most materials. Thus, the total conductivity can be written as

$$\sigma = \sigma_A + K \dot{\gamma}^\Delta \quad (4)$$

If the sample is in the dark, the photoemission current can be considered to be negligible.

Manipulation of equations (1), (2), and (3) yields the surface potential as a function of the incident electron current density in the form

$$V = \frac{J_B L}{\sigma} [1 - \delta(E_B - V)] \quad (5)$$

For exposure to non-penetrating electrons only, at beam energies significantly larger than the secondary electron second crossover energy,  $V_S$ , the function  $\delta$  in equation (5), will be small compared to unity and the potential will increase linearly from zero as a function of  $J_B/\sigma$ . At larger values of the surface potential,  $\delta$  will no longer be negligible and the potential will asymptotically approach a value  $V_m$  given by

$$V_m = E_B - V_S \quad (6)$$

assuming that the dielectric does not break down first. Obviously from equation (6) the asymptotic value of the surface potential is different for different beam energies. Figure 3 shows plots of  $V$  versus  $J_B/\sigma$  for 2 mil and 5 mil ( $L = 0.005$  and  $0.0127$  cm, respectively) samples, where a value for  $V_S$  of 1.5 kV has been assumed, which is approximately the value for the secondary emission crossover of Kapton. The shape of the transition region from the linearly increasing curve to the horizontal asymptote was estimated using the secondary emission curve for Kapton given in reference 6.

If a Kapton sample is simultaneously exposed to non-penetrating, e.g., 10 keV, and totally penetrating electrons, then several limiting cases can be considered. If the flux of penetrating electrons is small such that the rate of energy deposition due to the penetrating electrons produces only a negligible increase in the conductivity of the Kapton, then the surface potential will be dominated by the ambient conductivity and can achieve a maximum value of  $\approx 8.5$  kV. If, however, the flux of penetrating electrons is sufficiently large so as to increase the conductivity well above the ambient conductivity, i.e.,  $\sigma_R \gg \sigma_A$ , then the surface potential will be given by

$$V = \frac{J_B L}{K J_P \Delta} [1 - \delta(E_B - V)] \quad (7)$$

As can be seen in Figure 3, the equilibrium surface potential will be less than 8.5 kV as the conductivity increases, assuming the flux of non-penetrating electrons remains the same. Thus, it can be seen that the effect of the penetrating electrons on the equilibrium surface potential is a function of the flux of non-penetrating electrons and penetrating electrons as well as the secondary electron emission properties, the ambient conductivity and the radiation-induced conductivity coefficient of the exposed material.

Equation (7) predicts that for some conditions the potential to which a material will charge upon exposure to non-penetrating and penetrating electrons will be independent of the absolute magnitudes of the electron current densities and will be dependent only on the ratio of the fluxes of the non-penetrating and penetrating electrons.

## EXPERIMENTAL RESULTS

### OSR's

When the OSRs were exposed to low energy (25 keV) electrons alone, discharge currents on the order of 28 to 35 A were measured. Table 2 lists a comparison of the discharge characteristics data obtained during the low flux tests and the previously reported high flux tests (refs. 1,2). In general, one can conclude that there is at most only a small dependence of the discharge characteristics upon the exposure flux in the range of 0.19 to 5 nA/cm<sup>2</sup>.

When the OSRs were exposed to high- and low-energy electrons simultaneously, discharges occurred only when the ratio of the low- to high-energy electron flux was greater than 63 to 76. Figure 4 shows a comparison of the discharge pulses observed for low energy electron exposure and combined low- and high-energy electron exposure. Note that the peak discharge current observed during the combined energy electron exposure is only 1.3 A which is roughly 1/25 the peak current observed during the low-energy electron exposures. When the ratio of the low energy and high energy electron fluxes was less than 63 to 76 no discharges were observed and measurements of the equilibrium surface potential after these exposures showed the surface potential to be less than 5 kV.

Table 3 shows a comparison of OSR discharge characteristics obtained during the low and high flux tests. The results are effectively the same with the exception of the discharge threshold data, which indicates that the discharge threshold in the combined energy electron exposures was lower in the high flux test than in the low flux tests. Since the high flux tests (refs. 1,2) were originally performed in a different facility than the low flux tests, a series of additional high flux tests were performed in the low flux test chamber to discriminate between actual flux effects and possible facility effects. This second series of high flux tests indicated a threshold potential for discharge for the OSRs of 5 to 6 kV which is in agreement with the low flux test results. No explanation for the relatively low discharge threshold potential determined in the original high flux tests has been proposed at this time.

#### KAPTON

When the 2 mil Kapton sample was exposed to low energy (25 keV) electrons alone at fluxes greater than 1 or 2 nA/cm<sup>2</sup>, the sample charged up to 13 kV at which time discharges occurred (Ref. 1). When the sample was exposed to a combined high- and low-energy electron environment, no discharges occurred and the surface potential remained well below the 13 kV discharge threshold. Figure 5 shows the Kapton surface potential measured after exposure of the sample to combined high- and low-energy electron environments with various relative fluxes. The relative fluxes are given as the ratio of the low energy electron current density to the dose rate of the high energy electrons [where a conversion factor of 560 (rad/s)/(nA/cm<sup>2</sup>) has been used]. The data labeled Phase II was obtained in the high flux tests which were performed at rates roughly 5 to 100 times those for which the low flux (Phase III) data was obtained. The data indicates a linear dependence of the surface potential on the ratio of the low to high energy electron fluxes. This linear dependence is predicted by equation (7) when  $\delta(E_B - V)$  is either small or a constant. Equation (7), however, predicts a zero intercept for the surface potential, whereas the data indicates an intercept of roughly 1.1 kV. It is interesting to note that for a two-energy simulation of the electron distributions shown in figure 2, the ratio of the non-penetrating to the penetrating electron fluxes can be determined from table 1 to be  $2 \times 10^{-3}$  and 0.57 (rad/s)/(nA/cm<sup>2</sup>) for the "AE4" and "SCATHA" environments, respectively. From figure 5 this would imply that the 2-mil Kapton would charge to 1.1 and 8.1 kV respectively in these environments.

From the data shown in figure 5 and the curves shown in figure 3, values for the radiation-induced conductivity coefficient, K, can be determined. In figure 5, an equilibrium surface potential of 2 kV is associated with a flux ratio of 0.07 (nA/cm<sup>2</sup>)/(rad/s). From figure 3 an equilibrium surface potential of 2 kV is associated with a value of J<sub>B</sub>/σ of 0.37 x 10<sup>6</sup> V/cm. Since

$$\frac{J_B}{\sigma} = \frac{J_B}{\dot{\gamma}K}$$

if  $V_B \gg V_S$  and  $\sigma_{rad} \gg \sigma_A$  then a value of the radiation-induced conductivity coefficient can be determined by

$$K = \left( \frac{J_B}{\dot{\gamma}} \right) \cdot \left( \frac{\sigma}{J_B} \right) = 1.9 \times 10^{-16} \text{ (ohm-cm)/(rad/s)}$$

This value is roughly an order of magnitude or more larger than published values (ref. 7). It is important to note, however, that the method of measuring radiation-induced conductivities often involves placing a bias across a dielectric by means of electrodes and measuring the currents that flow upon either pulsed or continuous radiation exposures. It is conceivable that the conductivity measured by this technique, while applicable to many radiation problems, results in a lower value of the radiation-induced conductivity than would be measured by monitoring the conduction of embedded electrons.

#### SSPM

Upon exposure to low energy (6 to 10 keV) electrons alone, the SSPM 5 mil Kapton sample charged to potentials roughly equal to the beam energy minus the secondary emission second cross over potential. When the SSPM was exposed to a combined low (10 keV) and high (450 keV) energy electron environments the equilibrium surface potential was only about 1000 volts less than that observed during the low energy electron exposures as shown in table 4. This result was surprising in light of the results presented above. Using the value for K of  $1.6 \times 10^{-16}$  ohm/cm/(rad-s) determined above, the radiation-induced conductivity during the combined energy electron exposures would have been on the order of  $5.6 \times 10^{-16}$  ohm-cm. Thus, for the combined 10 keV and 450 keV electron exposure

$$\frac{J_B}{\sigma} = \frac{200 \times 10^{-12}}{5.6 \times 10^{-16}} = 3.4 \times 10^5 \text{ V/cm}$$

Referring to figure 3 for a 5-mil Kapton sample, one would expect the equilibrium surface potential to be on the order of 3.8 kV as opposed to the 6.99 kV that was measured by the SSPM.

In subsequent tests the SSPM Kapton sample was charged to roughly 8 kV using only a 10 keV electron beam. The 10 keV beam was turned off and the surface potential of the sample was monitored while the sample was exposed to 350 keV electrons only. Figure 6 shows the surface potential measured during



this experiment as a function of exposure time. When the 350 keV electron beam current was increased from 1 to 5 pA/cm<sup>2</sup>, the decay of the surface potential did not accelerate and thus the decay of the surface potential is apparently due primarily to the basic conductivity of the sample. Measurements of the leakage current through the sample via the SSPM instrumentation, however, indicated as much as a factor of 40 increase in the leakage current when high energy electrons were incident on the sample as compared to the leakage current measured when only low energy electrons were incident on the sample. This observation indicates that the conductivity of the SSPM 5 mil Kapton sample is greatly enhanced by the presence of the high energy electrons. These apparently contradictory results led us to question the method by which the SSPM measures surface potential. As shown in figure 7 the SSPM measures surface potential at the rear of the sample at a point from which the vacuum deposited aluminum has been removed. The diameter of the hole in the metalization is large compared to the thickness of the material (diameter/thickness  $\approx 20$ ). The 6 to 25 keV electrons which stop near the surface of the material in the center of the hole and subsequently flow to the nearest ground plane must move a much larger distance than those trapped in the Kapton over areas where the metalization is intact. Thus, in the region of the hole the effective thickness of the material for conductivity calculations is larger than the thickness of the material. The ratio of the average distance that the trapped electrons must travel in the hole region to reach the ground plane ( $\sim 0.5 \times$  hole radius) to the sample thickness is about 10. If one ratioed the predicted 3800 volts for a fully metalized 5-mil sample by this factor, to determine the potential in the hole region, the potential would be greater than the beam voltage. Thus, it would not be unexpected that the potential as measured in the hole region would be larger than that predicted for a fully metalized 5-mil sample and would approach the measured SSPM surface potential for low-energy electron exposure (8250 volts).

The data for the other SSPM samples has not been reduced at this time.

## CONCLUSIONS

From a comparison of the low and high flux data as well as comparison of the data from low energy monoenergetic electron exposures and combined low and high energy electron exposures, one can conclude:

1. The presence of high energy electrons can significantly affect the charging and discharging characteristics of spacecraft dielectrics,
2. Discharge currents in combined-energy electron simulation environments can be considerably lower than those in low energy electron simulation environments,
3. Equilibrium surface potentials will often be held below discharge threshold potentials due to enhanced conductivity caused by the high energy electrons,
4. Over a wide range of simulation current densities, accelerated rate testing appears not to affect the test results as long as the ratio

of low energy to high energy electron fluxes is preserved, and

5. In space environments where high energy electrons are present, the surface potential at the SSPM measurement area may be higher than the surface potential over the remainder of the SSPM sample area.

The primary implication of these conclusions is that charging and discharging characterization data obtained from low energy electron simulations of space environments will lead one to expect much larger discharge currents and more frequent discharges than may occur in space environments.

#### REFERENCES

1. Treadaway, M. J., et al.: The Effects of High Energy Electrons on the Charging of Spacecraft Dielectrics. IEEE Trans. Nucl. Sci., NS-26, no. 6, Dec. 1979.
2. Treadaway, M. J., et al.: Effects of Laboratory Simulation Parameters on Spacecraft Dielectric Discharges. JAYCOR report no. 200-79-155, July 1979.
3. Treadaway, M. J., et al.: ECEMP Phase III Low Flux Tests. JAYCOR report no. 200-80-235/2176, July 1980.
4. Panlikas, G. A.: Electron Irradiation in Synchronous Orbit. Aerospace Tech. Memo 7616260-201-3, Aug. 3, 1976.
5. Mizera, Paul, Aerospace Corp., March 1980, private communication.
6. Katz, I., et al.: A Three Dimensional Dynamic Study of Electrostatic Charging in Materials. NASA CR-135356, Aug. 1977.
7. Ahrens, T. F., and Wooten, F.: Electrical Conductivity Induced in Insulators by Pulsed Radiation. IEEE Trans. Nucl. Sci., NS-12, June 1976.

TABLE 1. ENVIRONMENTAL SIMULATION FLUXES

MATERIAL	AE4 ENVIRONMENT		SCATHA ENVIRONMENT	
	25 keV (pA/cm <sup>2</sup> )	350 keV (pA/cm <sup>2</sup> )	25 keV (pA/cm <sup>2</sup> )	350 keV (pA/cm <sup>2</sup> )
KAPTON (2 mil)	7.4	6.2	96	0.3
KAPTON (5 mil)	9.6	3.2	96	0.2
OSR ARRAY	10	1.7	96	0.05

## FLUX RANGES ACHIEVABLE

25 keV:  $5 < J < 350 \text{ pA/cm}^2$   
 350 keV:  $1 < J < 60 \text{ pA/cm}^2$

TABLE 2. COMPARISON OF OSR DISCHARGE CHARACTERISTICS IN 25 keV ELECTRON ENVIRONMENT AT LOW AND HIGH FLUXES

	PHASE III RESULTS	PHASE II RESULTS
DISCHARGE THRESHOLD (kV)	5-6	~ 2
RETURN CHARGE ( $\mu\text{C}$ )	0.2 (25 keV, 0.29 nA/cm <sup>2</sup> ) (350 keV, 0.003 nA/cm <sup>2</sup> )	0.5-1.0 (25 keV, 13 nA/cm <sup>2</sup> ) 350 (keV, 0.17 nA/cm <sup>2</sup> )
FLUX AT WHICH DISCHARGES BEGIN( $J_{\text{low}}/J_{\text{high}}$ )	~ 63	~ 76

TABLE 3. COMPARISON OF OSR DISCHARGE CHARACTERISTICS IN COMBINED ENERGY ELECTRON ENVIRONMENTS AT LOW AND HIGH FLUXES

	PHASE III (0.19 nA/cm <sup>2</sup> )	PHASES I AND II (1-5 nA/cm <sup>2</sup> )
DISCHARGE THRESHOLD (kV)	6.5-7.5	6-7
PEAK CURRENT (amps)	28	35
RETURN CHARGE ( $\mu\text{C}$ )	16	28-24
PULSE WIDTH, $Q/I_p$ ( $\mu\text{sec}$ )	0.57	0.68 - 0.8
FREQUENCY OF DISCHARGE (#/min)	0.08	0.1 <sup>a</sup>

<sup>a</sup> EXTRAPOLATED LINEARLY TO 0.19 nA/cm<sup>2</sup>

TABLE 4. SSPM KAPTON SURFACE POTENTIAL VS EXPOSURE CONDITIONS

LOW ENERGY ELECTRON BEAM ENERGY (Flux)	EQUILIBRIUM SURFACE POTENTIAL (kV)		
	LOW ENERGY ELECTRONS ONLY (Measured)	COMBINED ENVIRONMENT (450 keV, 5 pA/cm <sup>2</sup> )	
		MEASURED BY SSPM	PREDICTED
6 keV(200pA/cm <sup>2</sup> )	3350	---	---
8 keV(200pA/cm <sup>2</sup> )	6430	5450	---
10 keV(200pA/cm <sup>2</sup> )	8250	> 6990	3800

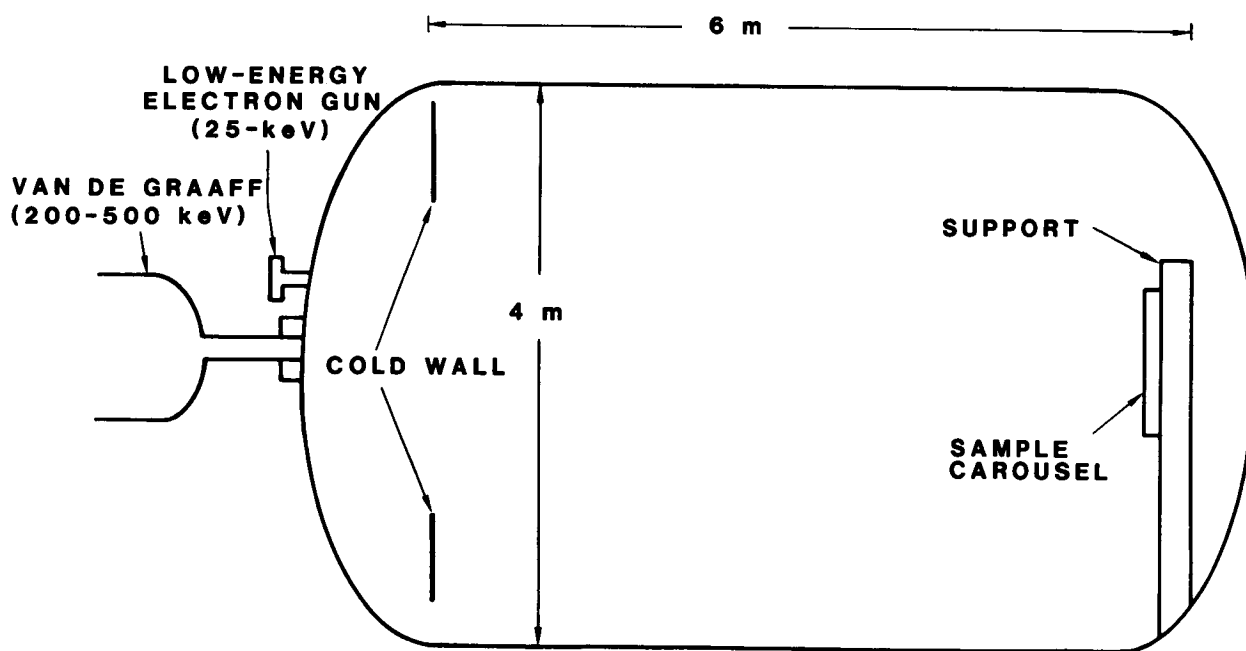


FIGURE 1. OVERVIEW OF THE LOW FLUX TEST FACILITY

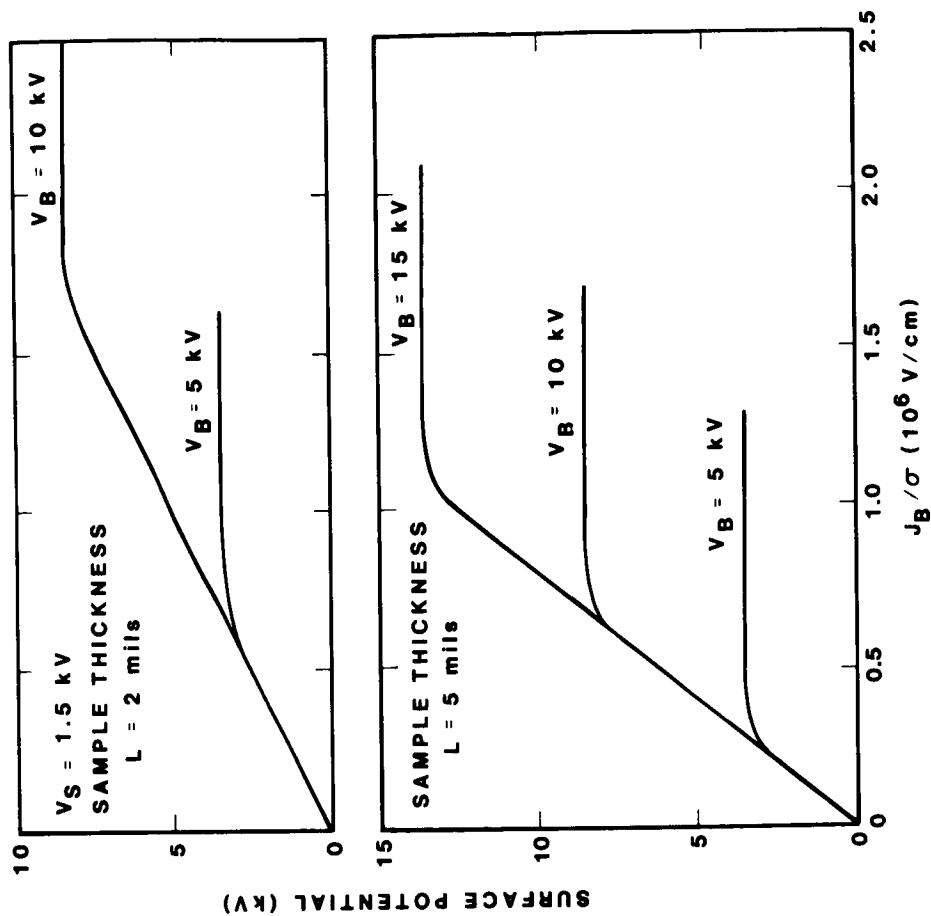


FIGURE 3. VARIATION OF SURFACE POTENTIAL,  $V$ , WITH LOW-ENERGY BEAM CURRENT,  $J_B$ , AND BULK CONDUCTIVITY,  $\sigma$

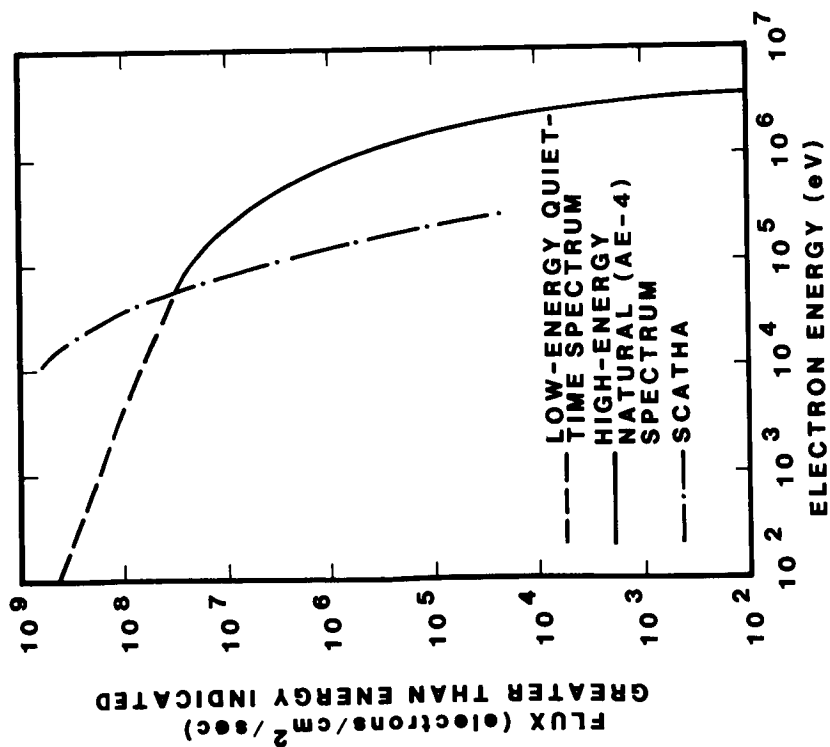


FIGURE 2. TWO ELECTRON ENERGY DISTRIBUTIONS AT SYNCHRONOUS ALTITUDE

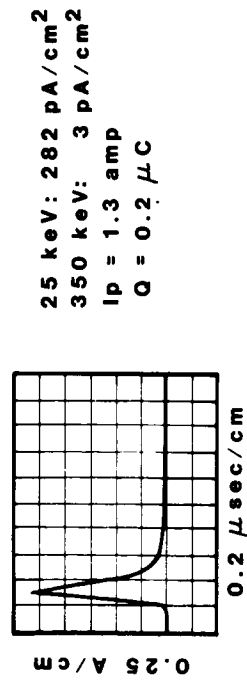
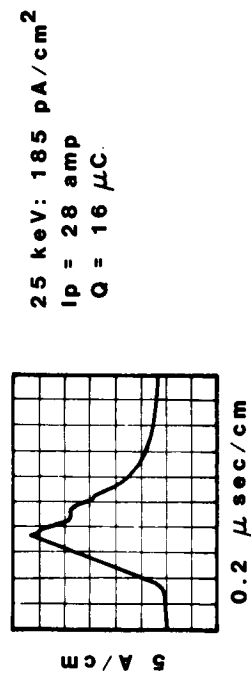


FIGURE 4. COMPARISON OF OSR DISCHARGES IN:  
 LOW ENERGY AND COMBINED LOW AND HIGH  
 ENERGY ELECTRON ENVIRONMENTS

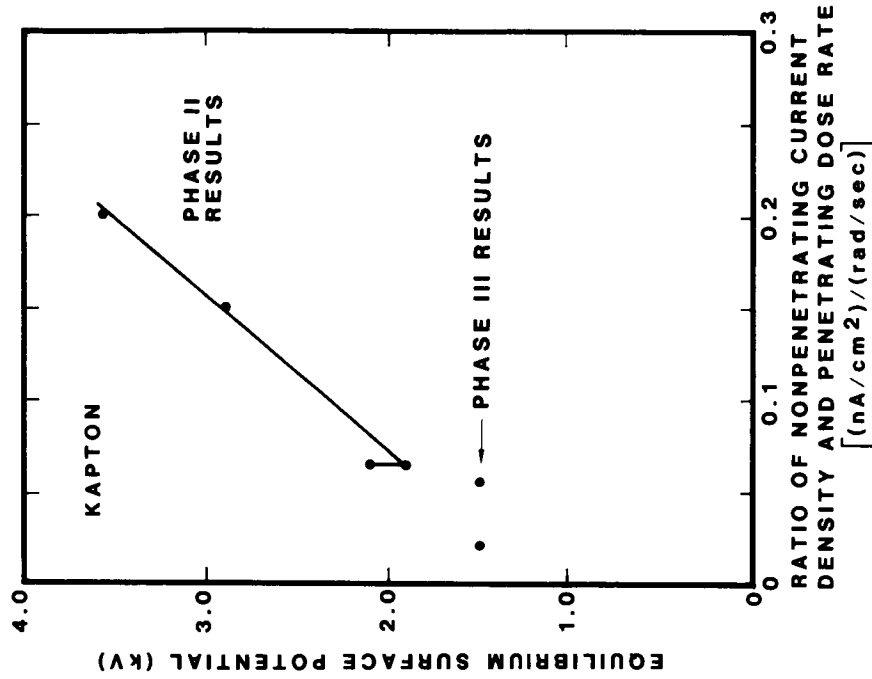


FIGURE 5. EQUILIBRIUM SURFACE POTENTIAL  
 OF 2 mil KAPTON FOR VARIOUS COMBINED  
 LOW AND HIGH ENERGY ELECTRON  
 FLUX CONDITIONS

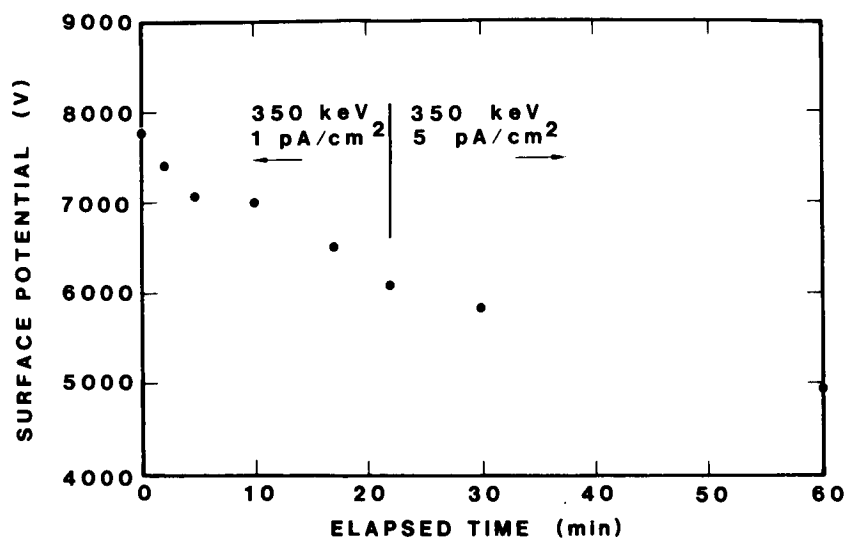


FIGURE 6. SSPM KAPTON SURFACE POTENTIAL VS TIME FOR HIGH-ENERGY ELECTRON EXPOSURE

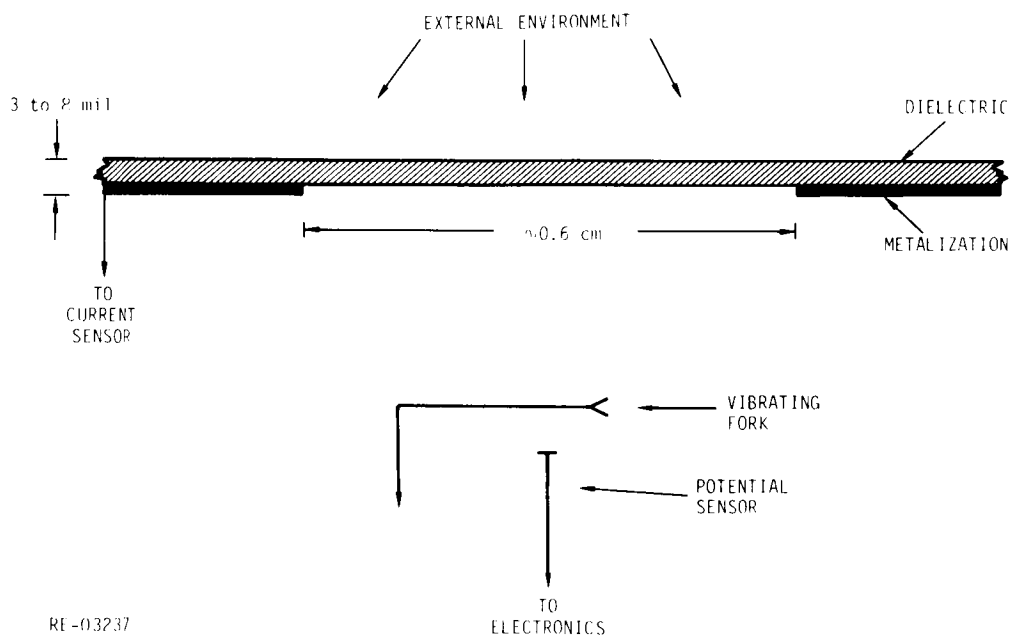


FIGURE 7. DIAGRAMATIC REPRESENTATION OF SSPM POTENTIAL AND CURRENT MONITORS

## **ELECTRON-BEAM-CHARGED DIELECTRICS— INTERNAL CHARGE DISTRIBUTION\***

**Brian L. Beers and V. W. Pine  
Beers Associates, Inc.**

### **SUMMARY**

An electron transport model of the charging of dielectrics due to electron bombardment has previously been given.<sup>1</sup> In this paper, we present a comparison of theoretical calculations based upon this model to measurements of internal charge distributions which have previously been performed.<sup>3</sup> The emphasis is on the distribution of Teflon. Several interesting features of the results are noted. First, the position of the charge centroid as a function of time is not monotonic. Instead, it first moves deeper into the material and then moves back near to the surface. Second, in most time regimes of interest, the charge distribution is not unimodal, but instead has two peaks. Third, the location of the centroid near saturation is a function of the incident current density as has previously been measured.<sup>11</sup> While the qualitative comparison of theory and experiment are reasonable, quantitative comparison shows discrepancies of as much as a factor of two.

### **I. INTRODUCTION**

In the 1978 meeting of this conference two papers<sup>1,2</sup> were presented which provided models for the charging of dielectrics by electron sources. These models included a description of processes occurring internal to the dielectric, and thus permitted the computation of internal charge densities and electric fields. In particular, several computations for internal charge distributions and fields were presented in Reference 1 for the conditions which have become common in laboratory spacecraft dielectric irradiations, monoenergetic kilovolt electrons incident on a free floating dielectric surface. No comparison between the computations and experimental data was presented at that time.

It is the purpose of this paper to compare computations of the internal charge distribution with experimental data for the same quantity which has been reported in the literature.<sup>3</sup> The irradiation conditions correspond to

---

\*Supported in part by United States Air Force Space Division under subcontract to SRI, International.



those discussed above. It should also be noted that Frederickson is providing a comparison of other quantities, for a metallized front surface in another presentation at this conference.<sup>4</sup> This information, together with two recently published discussions<sup>5,6</sup> of the same subject, will provide a reasonably complete picture of the state-of-the-art of the understanding of this important subject. It is anticipated that the reader will come to the conclusion that a great deal remains to be learned as quantitative agreement is not particularly good.

As noted in Reference 1, for conditions in which the mean electron range is small compared to the dielectric thickness, the external charging characteristics (surface voltage) are effectively decoupled from the details of the internal charge rearrangement in the material. Because these conditions almost universally prevail for the environments of interest (if the Van Allen electrons are ignored), it might be asked why the spacecraft community should care about the fine details represented in these models. Implicit in this question is the assumption that the only parameter of importance is the surface differential potential relative to spacecraft ground. In a presentation by Stevens<sup>7</sup> at this conference, a very strong case is developed which suggests that this is not the case for orbiting spacecraft. In particular, transient pulses associated with breakdown appear to be occurring even when differential voltages are substantially below those required in the laboratory to induce breakdown. The conclusion is that the differential voltage is not the only diagnostic required to understand discharges which occur in space — other more subtle processes may be involved. It was pointed out in Reference 1 that substantial electric fields can exist inside the dielectric even when the external differential voltage is small. This observation provides one speculation about the source of low voltage breakdowns. It is also not difficult to imagine theories of breakdown which depend on a critical trapped charge density.<sup>8,9</sup> Thus, the study of internal charge distributions and fields is probably not some esoteric backwash in spacecraft research, but is rather an essential ingredient in developing an understanding of discharges in space. It is the intent of this paper to provide sufficient data to assess how well this important subject is understood. Conditions in the laboratory are investigated exclusively. The implication for the exoatmospheric environment are left for future investigations.

In Section II, a technical modification to the model is discussed. The modification permits the incorporation of the delayed conductivity in the model. Section III presents the major results of the paper. A discussion of these results is given in Section IV.

## II. DELAYED CONDUCTIVITY MODEL

When a free-floating front surface of a dielectric is irradiated with electrons, it is raised to a negative potential relative to the system ground. Electrons arriving later at the sample surface are retarded and consequently penetrate less deeply into the material. This range shortening results in regions of dielectric which are initially irradiated becoming non-irradiated.

Within the numerics of a code model of the process, this leads to regions of dielectric which go from being rather strongly conducting because of the radiation-induced conductivity to the weakly conducting state associated with the dark dielectric. This transition can occur rather abruptly in a Monte Carlo simulation and is distinctly non-physical. This situation can be ameliorated by using improved numerical techniques or by adequately modeling the decay of the conductivity in these regions. We choose the later approach here. The specifics of the approach have previously been given by other researchers.<sup>10</sup>

When dielectrics are subjected to ionizing radiation, charge carriers are liberated giving rise to a radiation-induced conductivity. Since the carriers do not instantaneously recombine when the ionizing radiation ceases, there persists a delayed component of the radiation-induced conductivity. The decay of the delayed conductivity is given by:

$$\sigma = \frac{\sigma'}{1 + bt} \quad (1)$$

where:

$$\sigma' = \sigma_0/F;$$

$$\sigma_0 = \text{conductivity at the end of irradiation};$$

$$F = \text{factor by which the conductivity drops in a short } (\mu\text{sec}) \text{ time } \approx 3;$$

$$t = \text{time in sec; and}$$

$$b = \text{parameter of order unity.}$$

The above model has been incorporated into the code in the following manner. At each grid point in the dielectric, the newly calculated prompt conductivity,  $\sigma_p$ , is compared to  $\sigma'$  if  $\sigma_p < \sigma'$ , then the conductivity is obtained from 1), otherwise, the conductivity is set to  $\sigma_p$ .

### III. INTERNAL CHARGE DISTRIBUTION

Researchers at Bell Laboratories have developed significant experimental techniques for investigating various features of the internal charge distribution in dielectrics.<sup>3,10,11</sup> These techniques rely inherently on the interpretation of measurements made using electron beam irradiations (so-called split Faraday cup techniques). While other techniques which do not rely on beams have been reported in the literature,<sup>12</sup> to our knowledge these techniques have not been applied to beam charged dielectrics. In this paper, we will rely exclusively on the results of these researchers for providing comparisons.

The material used in all the reported experiments has been FEP Teflon. For the purposes of the primary electron transport, Teflon may be treated as a uniform material with an atomic composition of  $\text{CF}_2$  and a density of  $2.2 \text{ gm/cm}^3$ . Several of the features of the primary transport have already

been published,<sup>1</sup> and will not be reproduced here. It may be recalled that the primary electrons deposit in a region rather broadly distributed about the mean, and that the computational algorithm provides the charge deposition profile  $Y(x)$  and the energy dose deposition profile  $D(x)$  as a function of the penetration  $x$ . The backscatter yield is automatically computed as part of the primary transport. The secondary yield is taken to be proportional to the surface dose in accordance with the model of Burke, Wall, and Frederickson<sup>13</sup> appropriately normalized to fit the monoenergetic data.<sup>14</sup>

The bulk conductivity in Teflon was taken from the data of Adamo, Nanevich, and Grier.<sup>15</sup> The model assumes that the prompt conductivity is proportional to the local dose rate in the material. The relaxation of this enhanced conductivity to the ambient was discussed in Section II above. The prompt conductivity coefficient  $K_p$  is normally taken to have a value of  $5 \times 10^{-15}$  mho/m/rad/sec<sup>14</sup>, although this parameter has been varied in some of the calculations reported herein. The value chosen for a particular calculation is indicated with the computed results.

The easiest quantity to obtain experimentally using a split Faraday cup arrangement is the charge centroid  $\langle x \rangle$  which is defined by:

$$\langle x \rangle = \frac{\int_0^d x \rho(x) dx}{\int_0^d \rho(x) dx} \quad (2)$$

where  $d$  is the sample thickness, and  $\rho(x)$  is the charge density. The quantity  $\langle x \rangle$  represents the mean location of the excess charge in the medium. This quantity has been measured for a variety of charging conditions.<sup>11</sup>

Shown in Figure 1 is a computation of the location of the centroid of charge  $\langle x \rangle$  as a function of time. The charging conditions are for normally incident monoenergetic electrons of energy 20 keV at a current density of  $3.3 \text{ nA/cm}^2$  incident on a 1 mil sample of Teflon. The transient conductivity coefficient  $K_p$  was taken to be  $5 \times 10^{-15}$  mho/m/rad/sec.<sup>13</sup> The addition of the delayed conductivity does not make a significant difference in the temporal behavior of this quantity. Note, in particular, that this quantity initially increases as the deposited electrons are redistributed to the end of the transient conductivity region by conduction processes, and then begins to decrease in longer times as the external potential builds up and slows down the incident electrons. Qualitatively, both models (with and without delayed conductivity) give rise to this same phenomenon. Only the quantitative features are changed by the model change. In any case, the addition of the delayed conductivity more nearly represents the true physics, and is included in all other calculations reported herein.

Shown in Figure 2 is a reproduction of Figure 3 of Reference 11 showing measured values of the charge centroid in Teflon. The charging conditions are for normally incident electrons of varying energies at a current density of

3.3 nA/cm<sup>2</sup> incident on 1 mil Teflon. Three values of  $\langle x \rangle$  are reported, one very near the beginning of the charging, one at the end of the charging time ( $\sim 15$  sec), and one five minutes after the beam has been turned off. It is clear that the delayed conductivity model is extremely important in modeling this final measurement. Shown in Figure 3 are the time histories of two simulations of the charging conditions of Figure 2 for a 20 keV beam. The two simulations correspond to two choices of the value of the prompt conductivity coefficient  $K_p$ . Note that the larger value of  $K_p$  gives rise to a more rapid increase in  $\langle x \rangle$  as expected. Generally, the larger value of  $K_p$  gives results which are more nearly consistent with the data. The best computed values of  $\langle x \rangle$  at the measured times are indicated on Figure 2. Generally, the computations have the correct qualitative behavior compared to the data (see also Figure 4 of Reference 11), but the computed results show a uniformly smaller penetration. This difference is not understood.

Shown in Figure 4 are the computed time histories of the location of charge centroid for a variety of conditions corresponding to normal laboratory charging operation. Note that the lower energy beams have uniformly smaller value of  $\langle x \rangle$ . Shown in Figure 5 is a scatter plot of the computed values of  $\langle x \rangle$  near saturation for a variety of charging conditions.

An examination of the plots of Figures 4 and 5 indicates that the computed charge centroid location is roughly independent of the incident current density and depends only on the total charge deposited.

This behavior is not in agreement with reported results. As explained in Reference 1 the prompt conductivity is normally taken to be proportional to some power of the local dose rate. The model reported here uses an exponent smaller than unity, the computational results become strongly dependent on the value of the incident current density. Shown in Figure 6 is a reproduction of Figure 6 of Reference 11, which presents data on the dependence of  $\langle x \rangle$  versus beam current density. The decrease in  $\langle x \rangle$  for larger values of the current density strongly suggests a nonlinear dependence of the prompt conductivity on dose rate. The present model can adequately represent this behavior. Because sufficient independent data on this nonlinearity does not appear to be available, no attempt was made to generally incorporate this behavior in the model. Reproducing Figure 6 is merely an exercise in fitting.

The researchers at Bell Laboratories have carried their techniques further, enabling them to ascertain the internal charge distribution with the aid of external measurements.<sup>3</sup> Shown in Figure 7 is the computed charge density in Teflon for a 20 keV beam with a current density of 0.5 nA/cm<sup>2</sup> incident on 1 mil Teflon for 20 secs. Note the double peaked distribution of charge due to the ohmic relaxation of the initial deposited charge. Measured values of this charge density as taken from Reference 3 are shown on the same plot. It is seen that the qualitative behavior is certainly similar. Qualitatively, the calculated charge density profile is seen to be compressed in range compared to the experimental profile. Note the strong dissimilarity between this distribution and the primary deposition profile given in Reference 1.

A computation showing the evolution of the charge density to the bimodal type of distribution is shown in Figure 8 for the case of a 15 keV beam of current density of 5 mA/cm<sup>2</sup>. The dependence of the computations on the assumed problem current density, and the assumed value of  $K_p$  is displayed in Figure 9. This figure gives the saturation charge distribution in the medium for a 15 keV beam having the indicated current density. Note the extremely strong dependence on  $K_p$ , and the essentially non-existent dependence on the current density.

#### IV. DISCUSSION

It may generally be said that the results presented above appear to be in agreement with experiments in a qualitative fashion, and that the quantitative agreement is approximately a factor of two. Because it might have been hoped before making this comparison that the agreement would be significantly better, some discussion of apparent sources of discrepancies is in order.

The most telling information is presented in Figure 2. The computed penetrations of the charge centroid are substantially below the measured penetrations. This suggests that either a systematic calibration error exists in the experiments or that the method of computing the primary deposition is fundamentally incorrect. We have no comment to make on the former possibility. Taking the data at face value, however, one begins to think more carefully about the primary deposition algorithm. As is evidenced on the figure, the disagreement becomes more severe for lower incident beam energies. It is well-known that the assumptions of the continuous-slowing-down-approximation<sup>16</sup> (CSDA) become less and less correct as the electron energy decreases. The present Monte Carlo algorithm follows the electrons to energies of 1 keV, and then deposits the electron in the final spatial bin. It might be imagined that the electrons below this energy travel somewhat further before being trapped. A test of this hypothesis requires that a non-Monte Carlo method be used for modeling the primary transport. This is possible within the state-of-the-art using the methodology developed at Oak Ridge National Laboratory for computing the differential inverse mean-free-path, and using the method of Strickland<sup>18</sup> to solve the resulting Boltzmann equation.

The above procedure could be used as a test of the CSDA procedure for the initial deposition profile. Note on the figure, however, that the initial location is within acceptable limits of the CSDA ranges. These discrepancies do not appear overly serious. Indeed, for a relatively low-energy beam, it is quite likely that the CSDA approximation is not sufficiently accurate. The discrepancies after the beam are on for a short time are more serious, as they show significant penetration of the beam well beyond the maximum CSDA range. This may be understood if straggling at the end of the range permits transport beyond the maximum CSDA range. Physically, this certainly happens. The abrupt drop-off in deposition which is computed with the Monte Carlo method using the CSDA leads to a significant discontinuity in the conductivity at the maximum range. The computational results are extremely sensitive to the behavior of the charge deposition and dose profiles in this region, because the internal

electric field pushes the electrons to precisely this location. It is likely that the Monte Carlo method is inadequate for handling the behavior in this region. A direct solution of the Boltzmann equation, as suggested above, should alleviate this difficulty. Should this procedure be adequate for explaining the deeper penetration of the electrons, the discrepancies shown in Figure 7 could equally well be understood. The computation is qualitatively correct, again showing significantly smaller penetration than the data.

The other major area of concern in the model is the handling of the radiation-induced conductivity (RIC) in the electron deposition region, and the transition to bulk conduction and charge transport. The behavior shown in Figure 6 cannot be explained in the present model using a conductivity which is linearly dependent on dose rate. This behavior might very well be extremely important. One can easily envision models of the discharge process in which the depth of the charge is an important parameter in determining the blow-off current. A correlation between this behavior of  $\langle x \rangle$  as a function of beam current and the current density dependence of discharges which has been observed<sup>19</sup> might then be expected.

As explained above, the behavior shown in Figure 6 may be reproduced in the model by choosing a sublinear dependence of the RIC on dose rate. While this procedure is certainly justified based upon present understanding of RIC, it is desirable to have an independent confirmation of the parameters required to provide the data fit. This is particularly true because a recent paper by the Bell Laboratories' group<sup>20</sup> calls into question the simplicity of the above assumption about the proportionality of the conductivity with some power of the dose rate. Indeed, this paper suggests that the conductivity varies during the time of the irradiation. This type of behavior can be understood in terms of trap-filling in the deposition region. Requiring such an explanation, however, implies that a simple phenomenological description of the conduction process in the irradiated region is inadequate and that a more fundamental kinetic description is required. It is very likely that this situation prevails. Unfortunately, a more fundamental model will require many more fundamental parameters for its implementation. Many of these are unavailable for the materials of interest. It may be expected that the requirement for understanding low voltage discharges in spacecraft dielectrics will spawn serious attempts to quantify thermal transport processes in dielectrics.

#### REFERENCES

1. B. L. Beers, H. C. Hwang, D. L. Lin, and V. W. Pine, "Electron Transport Model of Dielectric Charging", in Spacecraft Charging Technology - 1978, AFGL-TR-79-0082, page 209 (1979).
2. A. R. Frederickson, "Electric Fields in Irradiated Dielectrics", Reference 1, idem., page 554.

3. G. M. Sessler, J. E. West, and D. A. Berkley, "Determination of Spatial Distribution of Charges in Thin Dielectrics", *Phys. Rev. Letters* 38, 368 (1977).
4. A. R. Frederickson, "Bulk Charging and Discharges Characteristics of Several Polymers", this volume.
5. B. Gross, J. E. West, H. von Seggern, and D. Berkley, "Generalized Box Model for Electron Irradiated Teflon Foils", Conference on Electrical Insulation and Dielectric Phenomena, 1980 Annual Report, page 313 (1980).
6. K. Labonte, "Charge Buildup During Electron Irradiation", Reference 5, *idem.*, page 321.
7. N. J. Stevens, "Utilization of Charging Control Guidelines in Geosynchronous Satellite Design Studies", this volume.
8. J. J. O'Dwyer, "The Theory of Electrical Conduction and Breakdown in Solid Dielectrics", Clarendon Press, Oxford (1973).
9. M. A. Lampert and P. Mark, "Current Injection in Solids", Academic Press, New York (1970).
10. B. Gross, G. M. Sessler, and J. E. West, "Charge Dynamics for Electron-Irradiated Polymer Foil Electrets", *J. Appl. Phys.* 45, 2841 (1974).
11. B. Gross, G. M. Sessler, and J. E. West, "Location of Charge Centroid in Electron-Beam Charged Polymer Films", *J. Appl. Phys.* 48, 4303 (1977).
12. See, for example, R. E. Collins, "Use of Thermal Pulsing Technique to Obtain Information About the Distribution of Charges in Polymers", Conference on Electrical Insulation and Dielectric Phenomena, 1979 Annual Report, page 307 (1979); A. Migliorio, "A Non-Destructive Acoustic Electric Field Probe", *idem.*, page 315; P. I. Kuindersma and R. M. van der Hey, "Dynamic Methods for the Determination of the Charge Density on Unipolar Electrets", *idem.*, page 325.
13. E. A. Burke, J. A. Wall, and A. R. Frederickson, "Radiation-Induced Low Energy Electron Emission from Metals", *IEEE Trans. Nuc. Sci.*, NS-19, 193 (1972).
14. J. A. Wall, E. A. Burke, and A. R. Frederickson, "Results of a Literature Search on Dielectric Properties and Electron Interaction Phenomena Related to Spacecraft Charging", in Proceedings of the Spacecraft Charging Technology Conference, C. P. Pike and R. R. Lovell, eds., AFGL-TR-77-0051, page 569 (1977).
15. R. C. Adamo, J. E. Nanevich, and N. Grier, "Conductivity Effects in High-Voltage Spacecraft Insulating Materials", Reference 14, *idem.*, page 669.

16. M. J. Berger, "Monte Carlo Calculation of the Penetration and Diffusion of Fast Charged Particles", in Methods in Computational Physics, Vol. 1, Academic Press, New York (1963).
17. J. C. Ashley, "Inelastic Interactions of Low-Energy Electrons with Organic Solids: Simple Formulae for Mean Free Paths and Stopping Powers", IEEE Trans. Nuc. Sci., Vol. NS-27, No. 6, to be published.
18. D. J. Strickland and D. L. Lin, "Electron Transport Properties for Soft Electron Sources Incident on Conducting and Insulating Materials", IEEE Trans. Nuc. Sci., Vol. NS-26, No. 6, page 4879 (1979).
19. K. G. Balmain and W. Hirt, "Dielectric Surface Discharges: Dependence on Incident Electron Flux", IEEE Trans. Nuc. Sci., Vol. NS-27, to be published.
20. B. Gross, J. E. West, H. von Seggern, and D. A. Berkley, "Time-dependent Radiation-Induced Conductivity in Electron-Irradiated Teflon Foils", J. Appl. Phys. 51, page 4875 (1980).

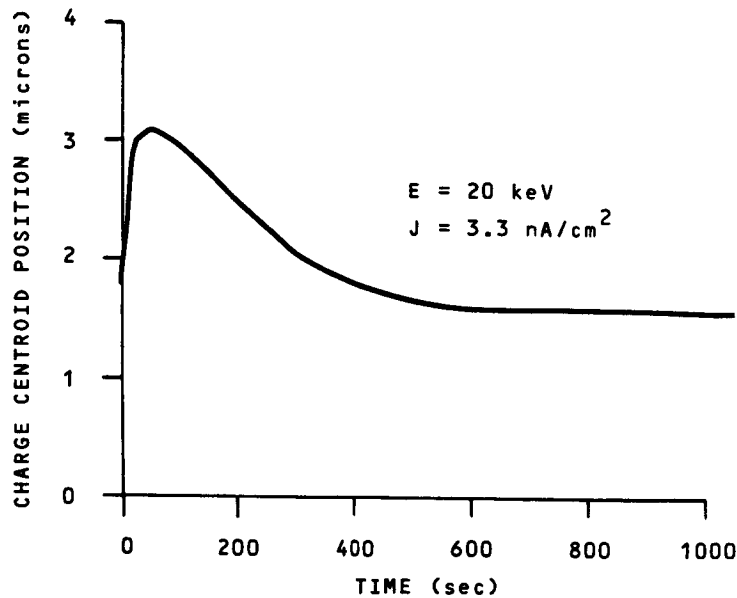


Figure 1. - Location of charge centroid as a function of time for 1 mil Teflon.



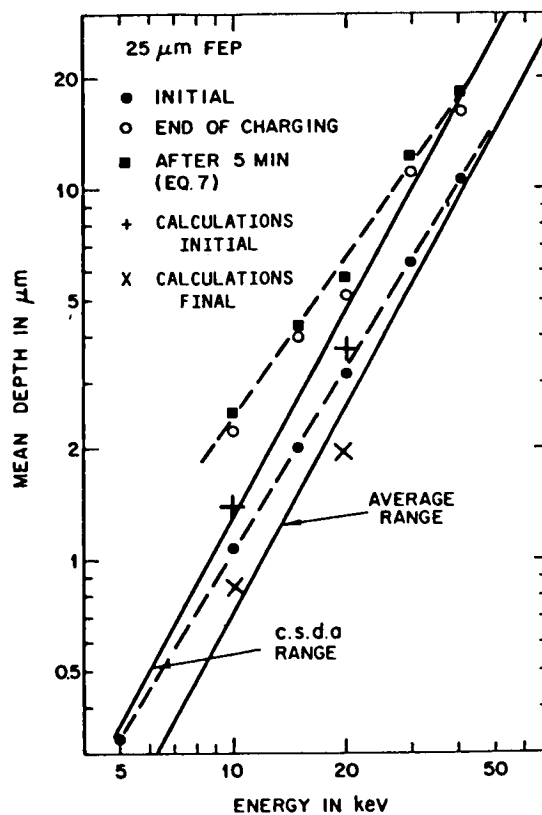


Figure 2. - Comparison of measured charge depth in Teflon with average and CSDA ranges (reproduced from ref. 11; computed results are superimposed).

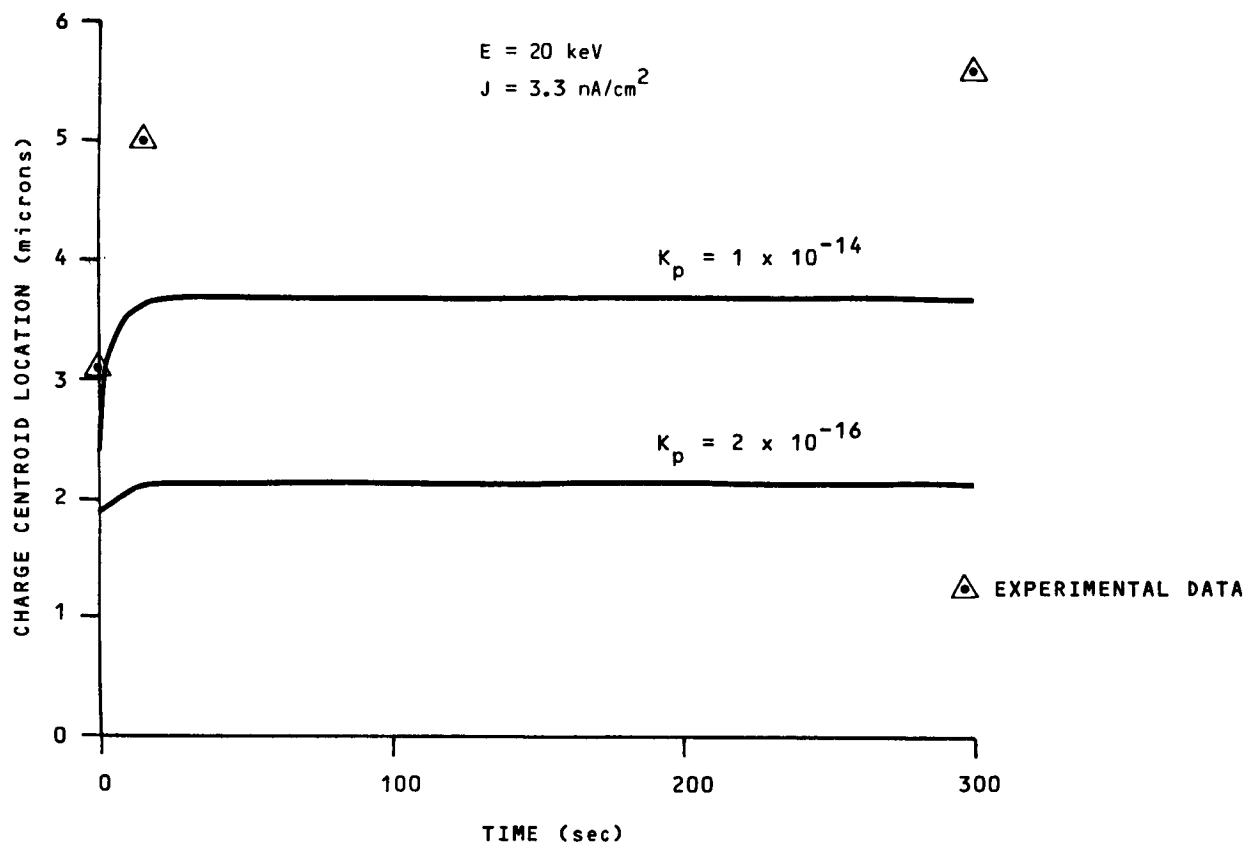


Figure 3. - Location of charge centroid as a function of time for 1 mil Teflon.

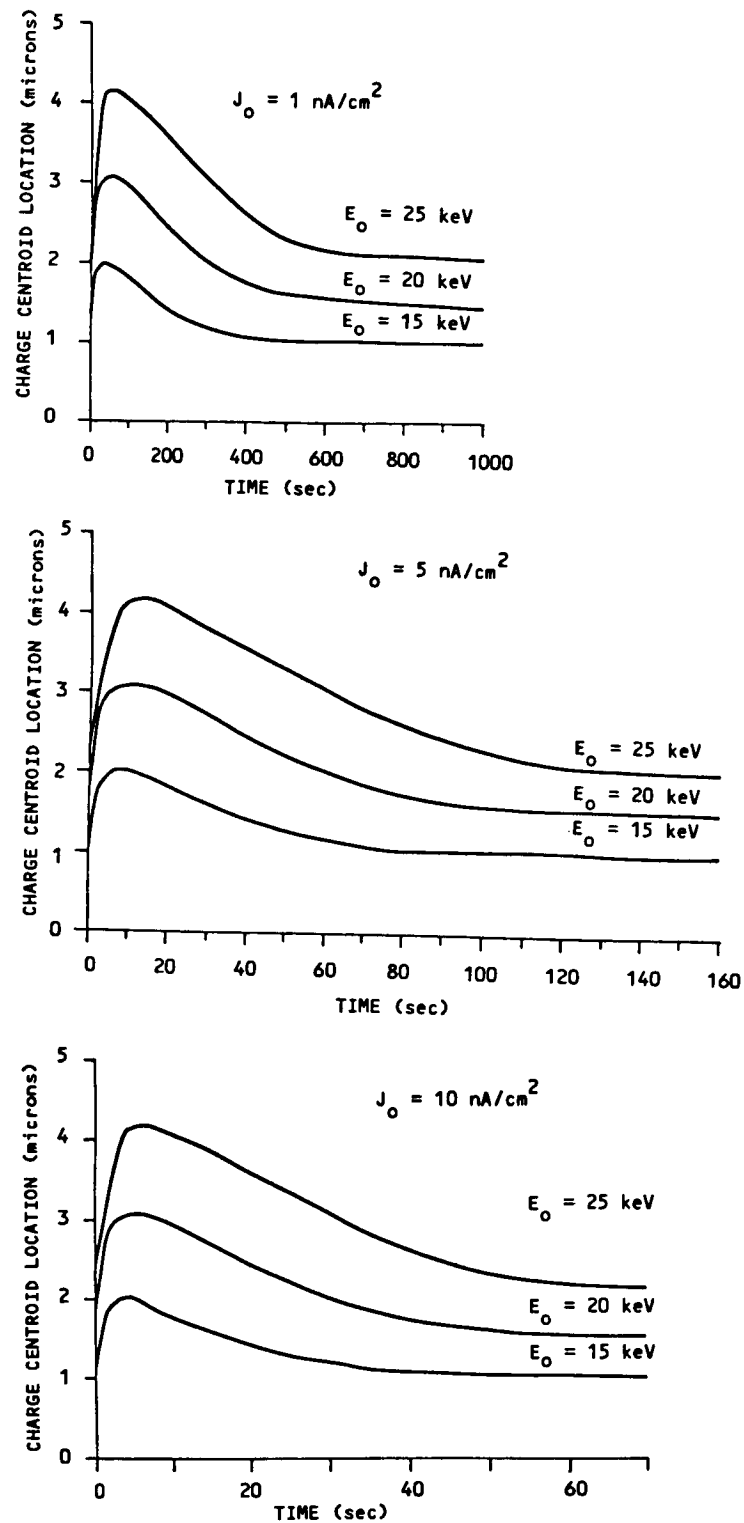


Figure 4. - Location of charge centroid as a function of time for 1 mil Teflon - various charging conditions.

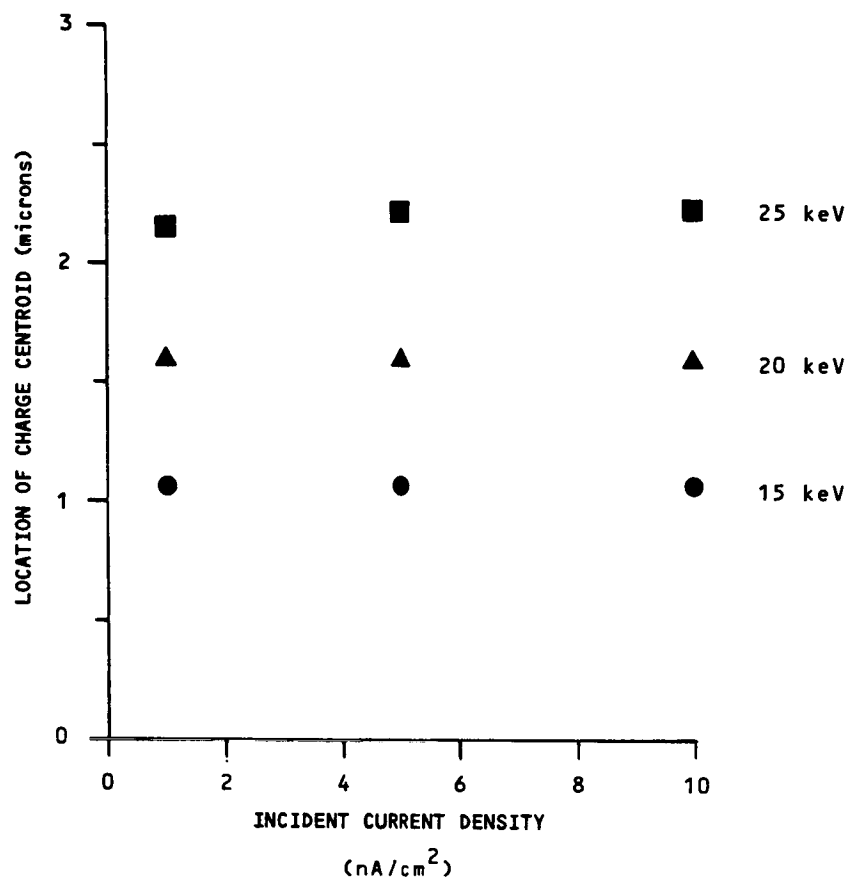


Figure 5. - Location of charge centroid for 1 mil Teflon near saturation.

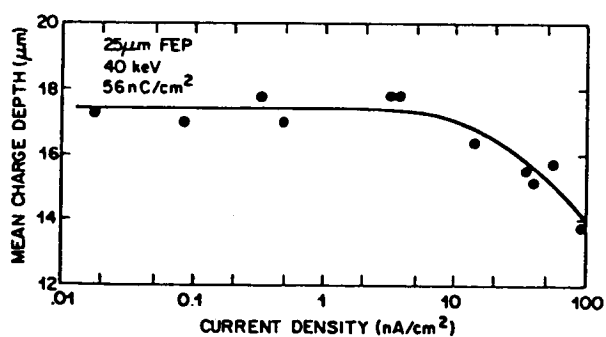


Figure 6. - Charge centroid as a function of injected current density (reproduced from ref. 11).

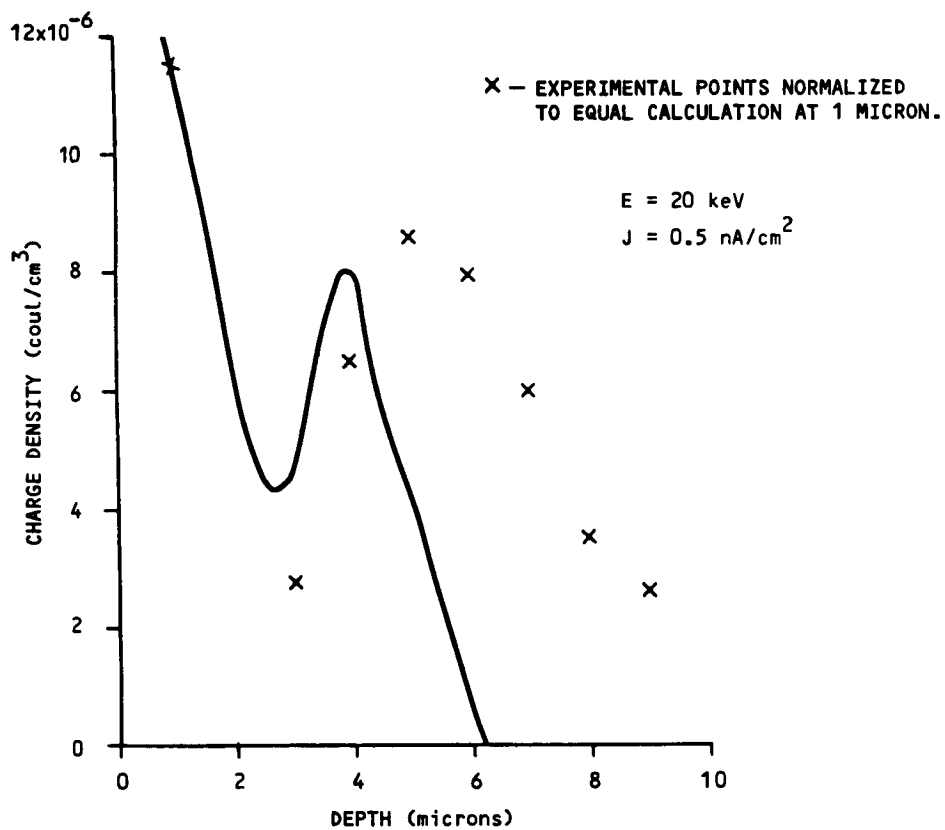


Figure 7. - Charge deposition profile for  
1 mil Teflon.

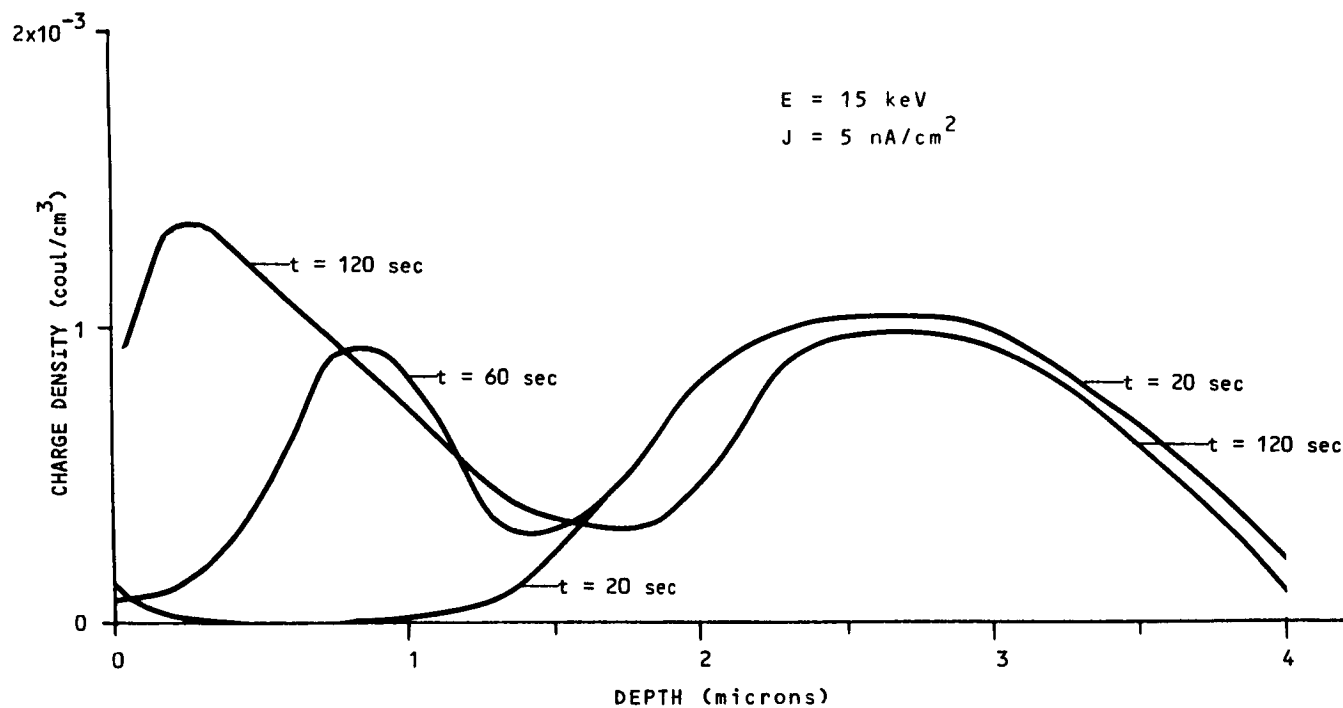


Figure 8. - Evolution of charge density of 1 mil Teflon.

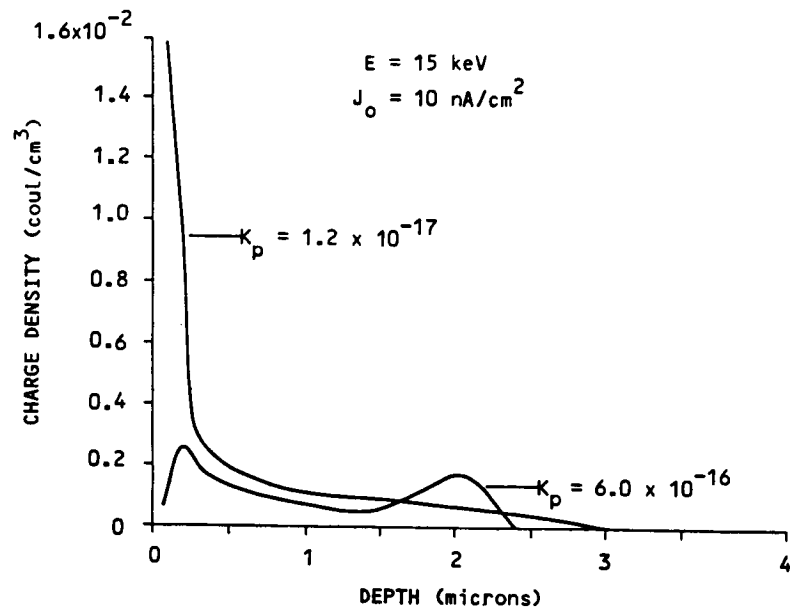
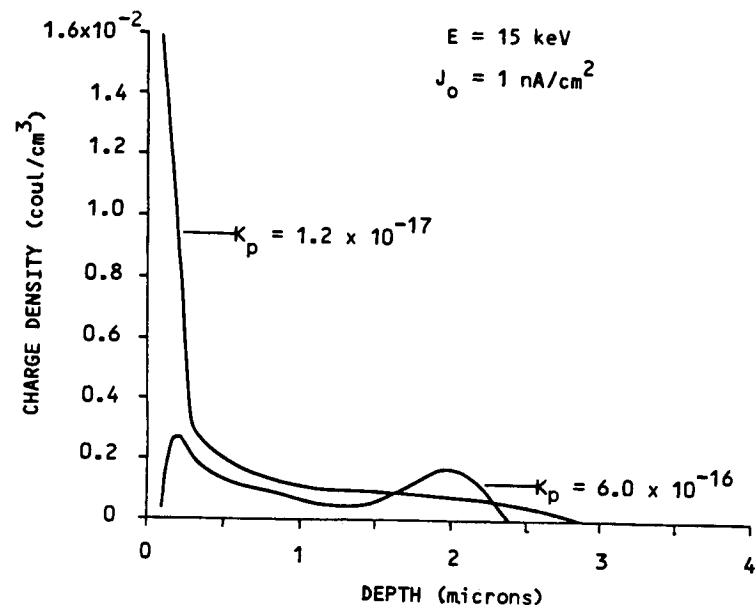


Figure 9. - Saturation  $\rho$  for various charging conditions in Teflon.

## **BULK CHARGING AND BREAKDOWN IN ELECTRON-IRRADIATED POLYMERS**

**A. R. Frederickson  
Rome Air Development Center**

High energy electron irradiations were performed in an experimental and theoretical study of ten common polymers. Breakdowns were monitored by measuring currents between the electrodes on each side of the planar samples. Sample currents as a function of time during irradiation are compared with theory. Breakdowns are correlated with space charge electric field strength and polarity. Major findings include:

- a. All polymers tested broke down.
- b. Breakdowns remove negligible bulk charge.
- c. No breakdowns are seen below  $2 \times 10^7$  V/m.

A model of surface plasma blowoff is proposed to explain how these results are compatible with other published findings.

### **I. INTRODUCTION**

We have performed an experimental study of radiation induced dielectric breakdowns on several common polymers under electron irradiation. The statistics of the breakdown probabilities can be directly related to the radiation induced electric field strengths and indirectly related to material parameters such as conductivity and radiation damage. More than 100 samples have been investigated and several consistent patterns have emerged. The patterns will be discussed in reference to typical sample responses. At this point in time it looks like each material may have its own breakdown signature and that virtually any good insulating polymer dielectric ( $\rho > 10^{15}$  ohm cm) can be made to break down under synchronous orbit irradiation intensities.

Many breakdown processes are conceivable but in this study we constrain ourselves to look for breakdowns occurring in the bulk of the polymer due to electric fields originating only from radiation induced bulk space charge. Other types of breakdowns such as those caused by micrometeorite impact, externally applied voltage, internal thermal effects, or electromagnetic pulses from adjacent space are not addressed.

Over the past several years, a model (refs 1, 2) has been developed to predict electric fields, currents and space charge densities internal to



irradiated dielectrics. The major points in the model will be only briefly described here since they are fully described elsewhere (ref. 2, 3, 4, 5). The radiation driven currents in the polymer are based on data in the literature. The space charge resulting from these currents and from conduction currents is obtained from the equation of continuity. The conduction currents produced by the spacecharge fields include all conduction effects available but to date we find that it is sufficient to include only dark conductivity and radiation induced conductivity. The equations are solved numerically with a computer. Space charge densities, electric field strength and total current are each calculated as a function of depth and time. I feel that this conceptual framework is the best presently available to describe the dielectric response in the above parameters to electron and x-ray irradiation at intensities below the thermal effects threshold and where the electrostatic approximation to Maxwell's equations is valid. Space radiation intensities are at least five orders of magnitude below this threshold. We use the model to describe the time evolution of the radiation induced electric fields and currents resulting from the laboratory or space irradiation of polymer samples.

While the sample is being irradiated we continuously monitor the current flowing between the electrodes which are on each side of the planar samples. The model is very successful at predicting the experimentally observed currents and by implication is probably predicting the internal fields as well. Using a transient pulse monitor during the irradiation we find that breakdowns do not occur unless the model predicts that internal fields exceed  $2 \times 10^7$  V/m. The polarity of the breakdowns is in agreement with model predictions. Since the parameters of the model are well substantiated data based on "fundamental concepts" we can use the model to predict the probable onset of breakdowns (i.e. fields exceeding  $2 \times 10^7$  V/m) for any\* irradiation by x-rays or electrons with any known energy distribution above 1 keV.

It might be argued by some that the use of such high energy irradiations does not correspond to space spectra and therefore does not model results in space. I believe such an argument is very weak. "All" of the important physical processes occurring at 10 or 50 keV also occur at 500 keV and vice versa\*\*. These results are not in disagreement with those of Gross, et. al. at 10 to 50 keV (ref. 1, 15). The only change due to the high energy electrons involves the depth of penetration of the irradiation and thus the extent of material involved. The electric field strengths produced in each case will be similar and have similar time dependences. The concepts presented here are immediately applicable to any electron or x-ray irradiation from 1 keV to 10 MeV.

---

\* Below 1 keV I have unsubstantiated doubts concerning the models validity since the relation between radiation induced conductivity and dose becomes more complex.

\*\* Except for atomic displacements which occur at 500 keV but are rare.

## II. THE EXPERIMENT

### A. The Apparatus and Samples

The samples are circular discs approximately ten centimeters in diameter. A carbon electrode is painted over the entire face of the sample through which the electron beam penetrates into the dielectric. A carbon coated aluminum electrode (with guard ring) is spring loaded against the back of the sample; this rear electrode is approximately 7.7 centimeters in diameter. Figure 1 sketches the electrode arrangement.

The sample is housed in a gold coated aluminum vacuum chamber at typically  $3 \times 10^{-6}$  Torr and at room temperature, nominally 20°C. The electron beam exits the accelerator in a 1 cm diameter spot and passes through a titanium foil of .01 cm thickness. The beam loses an average of 70 keV in penetrating the foil and is scattered into a broad beam. The sample lies approximately 40 cm beyond the scattering foil where the beam intensity is uniform to within 20% over the surface of the sample. A metal ring surrounding the sample monitors the beam current intensity. Sample current as measured by meter A in figure 1, and the beam current are monitored by Kiethley model 410 electrometers and chart recorders.

The guard ring arrangement eliminates edge effects and defines the region of current collection in the sample. The experiment closely approximates the one dimensional analysis of the model. The samples are reasonably thick so that surface effects at the electrode-polymer interfaces contribute negligibly to the current monitored by the meter, A.

### B. Interpretation of the Results

At the beginning of an irradiation the sample has little or no internal space charge. It appears that the electrostatic fields often associated with nonelectroded polymers are due primarily to surface charge and such charge is bled-off upon application of the electrodes. The beam is turned on and rises within a fraction of a second to a preset level and then its intensity remains constant during the irradiation. Information in the radiation (ref. 2) transport literature is used to assess the distribution in depth to which the primary electrons penetrate and become trapped space charge. We also include space charge introduced by the conduction currents.

Figure 2 shows typical computer predicted electric fields for samples thin compared to the incident electron range. As time progresses, the trapped space charge builds-up and large electric fields develop. Thicker samples result in larger electric fields (ref. 2). It is important to note that the field is bipolar: positive in the left region of the sample and negative in the right region.

Currents caused by the electric fields such as dielectric breakdown currents occurring in the left region of the sample in figure 2 would be positive as measured by the meter A. Similarly caused currents occurring in the right region would be negative. Notice that the peak negative electric field reaches

any given absolute magnitude sooner than the peak positive electric field.

Suppose that discharges will occur when the electric field exceeds  $2 \times 10^7$  V/m. In the case of Fig. 2, we would expect to see negative discharge pulses in meter A first (beginning at about 400 seconds) and positive discharges later (at about 900 seconds). This effect is dramatically seen in our results below.

Meter A also measures the integral over space of the total current flowing in the dielectric. Using the model we predict the measured current at all times and obtain good agreement with experiment. This good agreement lends support to our predicted space charge densities and electric field distributions.

### III. RESULTS

It is impossible to completely list all results for the over 100 samples tested. However very obvious trends have developed and indicative results will be used to describe the basic trends. We will begin with the simplest examples and progress to the most interesting cases at the end.

#### A) .338 cm Polystyrene, $3.64 \mu\text{A}/\text{m}^2$ , 1 MeV

Figure 3 shows the experimental and theoretical measured currents, A, as a function of time. The excellent agreement after 2000 seconds is very gratifying. The discrepancy at early time is not understood but appears unimportant for our purposes; it may be due to a small amount of initial space charge or polarization.

At first look the result in fig. 3 appears uninteresting. However the theory indicates that large electric fields occurred reaching magnitudes of  $+2.7 \times 10^7$  V/m and  $-3.5 \times 10^7$  V/m at the front and rear surfaces respectively. From the time constant of the curve we can predict the coefficient of radiation induced conductivity to be  $k = 7 \times 10^{-16}$  sec/ohm-m-rad (ref. 6). The time constants\* of the theoretical and experimental curves are similar and in agreement with other irradiations. Based on the theory very large conduction currents were occurring inside the dielectric at late times of magnitude similar to the incident beam current. In terms of their effect on the measured currents the conduction currents cancelled each other to a large extent producing little change in the measured current. The theory quite accurately predicts the cancellation; this is a pleasant confirmation of the theory.

Note that on this particular sample and run no breakdown pulses were seen. Other polystyrene samples exhibited breakdowns similar to results discussed later.

#### B) .345 cm Polypropylene, $3.77 \mu\text{A}/\text{m}^2$ , 0.43 MeV

---

\* The actual data contained sufficient accuracy to measure a time constant even though it appears in only the second and third significant figure.

The irradiation shown in figure 4 differs from the prior polystyrene irradiation primarily by the fact that in this case incident electrons are not energetic enough to penetrate into the rear quarter of the dielectric. Thus the conductivity in the rear quarter of the dielectric is not significantly enhanced by radiation induced conduction and extremely large electric fields may be created after long times (ref. 7).

The 10% discrepancy between theory and experiment is not important and is probably due to an error in calibration. The decay time provides an estimate of the coefficient of radiation induced conductivity,  $k = 2.2 \times 10^{-16}$  sec/ohm-m-rad.

The theoretical model provides an estimate for the electric field strength during the irradiation. It is felt that the reasonably good agreement between measured and theoretical currents supports the theory's predictions. The front surface field reached  $2 \times 10^8$  V/m while the rear surface attained  $0.8 \times 10^8$  V/m at 2850 seconds. It is surprising that no breakdown was seen.

Approximately a dozen polypropylene samples did not breakdown while another dozen showed multiple breakdowns. One sample, during its third irradiation in a week showed clock-like regular breakdowns spaced a minute apart. Some samples showed breakdowns during one irradiation and no breakdowns during prior but similar irradiations. We will see that breakdowns cannot be predicted on the basis of high field strength alone.

C) .168 cm Polypropylene, 0.6 MeV,  $3.18 \mu\text{A}/\text{m}^2$

Figure 5 describes the results of this irradiation where the sample is about 1/2 of an electron range thick. The rise and fall of the current at the beginning of the run has been observed in about 25% of the polypropylene samples, has been seen to occur at later times on a few other samples (ref. 2) and is akin to some results under  $^{60}\text{Co}$  gamma irradiation (ref. 6). Its cause is unknown.

More importantly, this sample exhibits typical breakdown pulses. The first pulse occurred when the field attained  $4 \times 10^7$  V/m, and based on the polarity of the pulse, it occurred near the front surface. Notice that even though the fields continued to increase with time to  $6 \times 10^7$  V/m the discharge pulse rate decreased! The fields at the front and rear surfaces are always approximately equal in this irradiation yet only one pulse is seen to occur in the rear region.

D) .166 cm Polypropylene, 0.43 MeV,  $3.46 \mu\text{A}/\text{m}^2$

Figure 6 describes the results for this sample, similar to the previous sample irradiated at lower energy. Notice again the unexplained early rise and fall in the measured current. The "large" discrepancy between experiment and theory is probably caused by our inability to accurately calculate dose at depths near the end of the electron range. In this case a factor of three error in dose at the rear surface or 10% error in energy or sample thickness could explain the discrepancy; and such errors are probable. Because

the sample is very close to an electron range thick, it is very sensitive to some of these complex effects; thicker and thinner samples are not at all so sensitive when the theory predicts rear surface fields of  $1.6 \times 10^8$  V/m and front surface fields of  $1.0 \times 10^8$  V/m. The front surface reached  $1.1 \times 10^8$  V/m at 4000 seconds after which breakdowns there became more probable. The magnitudes of these fields is only indicative, not absolutely correct. But it is encouraging to see that the theory predicts correctly which polarity breakdown occurs first.

E) .612 cm Polycarbonate  $4.47 \mu\text{A}/\text{m}^2$ , 1 MeV

Figure 7 describes the results for this sample of polycarbonate which is approximately 30% thicker than the range of 1 MeV electrons. The small discrepancy between theory and experiment at zero seconds is probably due to incident intensity calibration errors. Again we have predicted the polarity of the initial breakdown correctly. At the first breakdown (which occurred near the front) the predicted front surface field is  $6 \times 10^7$  V/m while the rear surface field is  $3 \times 10^7$  V/m. At approximately 1000 seconds the rear surface began arcing at  $6 \times 10^7$  V/m at which time the front surface field is predicted to be  $1 \times 10^8$  V/m.

The coefficient of radiation induced conductivity,  $k$ , (ref. 6, 1) controls the slope of the current vs. time curve. For polycarbonate there is no choice of  $k$  which could provide a perfect fit because at early times the response shows first a slow decrease in the current followed by a more rapid decrease. The theory which assumes a constant value for  $k$  predicts that the rate of decrease in current is maximum immediately after the irradiation begins. One probable answer is that field enhanced conduction plays a large role, perhaps doubling the conductivity after 400 seconds. All materials show this effect to some extent to date but thick polycarbonate seems to have the largest apparent field enhanced conduction of those materials tested.

This is an excellent time to describe a major finding. Note the breakdown pulses: they never change the slope or value of the meter current except briefly during the pulse ( $<0.1$  sec). If any significant current had flowed during the pulse charge would have been removed, the meter would have gone off-scale and the measured current would then return somewhat closer to the initial (time zero) current. We have probably seen tens of thousands of pulses but they have never\* displaced the measured current except for the brief period of the pulse. Breakdowns do not remove much bulk charge, even at irradiation intensities ten times as large as shown in these figures. From the data presented so far breakdowns remove not more than one percent of the charge; later we see that they remove virtually no charge.

Lichtenberg patterns are produced by breakdowns. We have looked for the patterns in fewer than ten samples and have seen extensive patterns in one polycarbonate and one polystyrene sample. The irradiation history of these samples is not well documented and the number of meter pulses was not recorded

---

\* "never" means: not even once!

so we don't know how large a lichtenberg pattern results from only one or a few pulses. The entire diameter of the samples contained the pattern; thus large patterns result from small total current flows.

This major finding also describes why many experimenters see almost continuous light pulsing after a dielectric has been irradiated to the breakdown "threshold". Virtually no bulk charge is removed by each breakdown pulse and the large internal fields remain to cause further pulses.

F) Decay of the bulk space charge.

Figures 8 and 9 describe the bleeding off of space charge in polypropylene after the irradiation ends. No theoretical work has been done yet on this problem. The meter current in figure 8 was not monitored continuously, each dot represents one reading. On some samples currents were still non-zero a day later.

Several samples were re-irradiated a number of times under similar conditions. The initial current in the initial irradiation is indicative of a sample response with no internal space charge. Figure 9 shows that a polypropylene sample which has rested 4 or 5 days will "lose" some of its charge, returning to within 10% of its initial  $t = 0$  value. This doesn't mean that the sample lost 90% of its irradiation space charge but it does imply that the charge was at least severely redistributed.

G) .620 cm, Polyvinylchloride,  $4.63 \mu\text{A}/\text{m}^2$ , 1 MeV.

Figure 10 is typical of PVC but includes shifts in the irradiation energy at late times. At early times we again see the apparent field dependent conduction effect. The initial breakdowns are in the front surface as predicted by the model and occur at  $4 \times 10^7$  V/m. The rear surface breakdowns begin later as predicted but the first one occurred at  $2 \times 10^7$  V/m. Other samples have broken-down at this level but this is the lowest field at which we have ever seen a breakdown. The theoretical slope is due to a value  $k = 2.3 \times 10^{-16}$  sec/ohm-m-rad, typical of such polymers.

The interesting point here is the results for small incident energy changes. At 3600 seconds the energy was lowered to 0.93 MeV while maintaining constant incident current. A seven percent change in energy changes the range of incident electrons only 7% so that if this change had occurred at  $t = 0$  only a small ( $\approx 7\%$ ) measured current change would have occurred. However, at late times there are various bulk currents all partially canceling each other and a small change in one can severely alter the net measured current as we see here at 3600 seconds.

It has been predicted (ref. 2) that a change in irradiation spectrum could cause breakdowns. Such spectral changes are certainly seen in space routinely. The prediction is dramatically reinforced in fig. 10. However it occurred only by lowering the energy. At 4220 seconds the beam energy was raised to 1.06 MeV but not without some excursions to other energies over a two minute period. For a small change in energy we again saw a large change in

current but we saw no breakdowns. It would be nice to try to predict these results using the theory but we haven't done so to date.

In this irradiation we also dramatically see the cessation of breakdowns even though high fields exist. Most samples show a tendency to decreasing frequency of breakdowns under continued irradiation. However, some samples, having not shown any breakdowns in a first irradiation, show many breakdowns in a similar irradiation repeated days later. Obviously we do not understand the breakdown process and its causes. We are simply developing a large statistical sample.

H) .607 cm, Polyphenylene Sulfide (glass filled)\* 5.0  $\mu\text{A}/\text{m}^2$  at 0.6 MeV.

Figure 11 describes the results of the breakdown champion of the samples tested to date. This data could not be redrawn in ink so the original chart recording is used directly. All four samples showed similar results.

The theoretical prediction is in excellent agreement with the measured current. For this sample  $k = 1.7 \times 10^{-16}$  sec/ohm-m-rad. Even with all those breakdowns having occurred, virtually no charge was lost in the breakdown process. However, the polarity of the first many breakdowns is not as predicted.

Only the first third of the sample is penetrated by the primary radiation and thus the fields at the front surface must usually be larger than at the back surface. Yet the rear surface breakdowns occur earlier and at lower fields. Front surface breakdowns hardly occur at all, only after 2000 seconds and after field build-up to  $2 \times 10^8$  V/m.

Perhaps the glass fibres and/or the many small voids are playing a dominant role here. In the irradiated front part of the sample the glass fibres are held in good electrical contact with the polymer molecules by the super hot conduction electrons (and holes) created by the radiation. This radiation induced conductivity may prevent fields of breakdown strength from occurring at the glass-polymer interface in the irradiated region. In the unirradiated region or in the transition zone between irradiated and unirradiated regions many small breakdowns may occur at glass-polymer interfaces. This is all conjecture and it would be nice to really understand these results.

As with the other samples, there is a definite tendency for breakdowns to become less probable as the irradiation continued. In this case the breakdown rate decreased at least a factor of four and the meter stopped going off scale after 2000 seconds. However, this material is different in one significant way: after the irradiation ends, breakdowns continue to occur for more than one day. Breakdowns become smaller and less probable as the hours pass but nevertheless this is a surprising result. Several polyphenylene sulfide samples have been tested and all show the same effects.

This particular sample provided a clue to solving the surface blowoff

---

\* Phillips Chemical Co. "RYTON" trademark.

problem. All samples have had electrodes painted on the front surface but this sample's electrode had a hole (by accident) of roughly 20 $\mu$  diameter. After 2000 seconds some arcing was occurring in the front surface region and we were surprised to see current pulses on the beam current monitor ring. Electrons were being emitted in pulses from the front surface, presumably from the hole, into the vacuum space. Sometimes these were accompanied by a current pulse in the rear electrode meter, sometimes not. In any case, even though all breakdown pulses are small, surface blowoff currents are to be seen (ref. 15) associated with these small internal discharges. We will return to the blowoff problem later.

I) .318 cm polytetrafluoroethylene (PTFE), 1.2 MeV, 6.15  $\mu$ A/m<sup>2</sup>

PTFE is severely different from all the other polymers tested\*. Three differences dominate:

(a) The coefficient of radiation induced conductivity  $k \approx 5 \times 10^{-15}$  sec/ohm-m-rad is typically twenty times larger than the other polymers.

(b) This material structurally degrades at irradiation doses of less than  $10^6$  rads (equivalent to only a few thousand seconds in these typical runs).

(c) Significant conductivity is added by a radiation induced damage process at only  $10^5$  or less rads dose.

I was not so clearly aware of (a) and (c) until 1979, so it was unfortunate that ref. 7 improperly assigns typical polymer parameter values to a dielectric called "teflon". Apparently others are finding similar results (ref.8). Values for  $k$  available in the literature vary widely (probably due to experimental error more than to sample differences) and improved values are only now becoming available.

Figure 12 describes typical results for PTFE when the electrons do not penetrate to any great extent. The initial current decay rate is indicative of the large value of  $k$  ( $5 \times 10^{-15}$  sec/ohm-m-rad). Field enhanced conductivity can be seen but is not significant. What is significant is the measured current reversal after roughly ten minutes. This reversal is probably due to enhanced conduction produced by the high dose rate over the first 70% of the primary electron range. This enhanced conduction allows the space charge to relax back to the front surface. We can test for this enhanced conduction days later by repeating the irradiation and noticing the initial measured current decay is very fast indicating a vastly increased conduction relative to the earlier irradiation. We have repeated this test several times and find that the enhanced conduction lasts at least a week. I guess that the enhanced conduction is related to the known chemical degradation of PTFE under this level of irradiation.

---

\* As well as the polymers reported above we tested nylon, delrin, polymethylmethacrylate and polyethylene.



Breakdowns have been seen in PTFE but only a few and they are slow, lasting nearly two seconds\*. Such breakdowns may not cause problems like faster breakdowns do. I believe we have recorded only one probable fast breakdown in about 8 teflon sample runs. See ref. 15 for data on pressure actuated breakdowns.

We have attempted to fit the teflon data with a conduction term due to total dose (not delayed conductivity but instead permanent dose related conduction) as shown by the dots. The prediction uses the theory (ref. 2) with values for conductivity given by:

$$\sigma(x,t) = \sigma_{\text{dark}} + kD(x,t) + k_1 D(x,t)t \text{ where } D \text{ is}$$

dose rate in rads/second

$$k = 5 \times 10^{-15} \text{ sec/ohm-m-rad}$$

$$k_1 = 5 \times 10^{-16} (\text{ohm-m-rad})^{-1}$$

$$t = \text{irradiation time in seconds.}$$

By this simple theory we have not yet been able to reproduce the change in current polarity experimentally observed because the computer algorithm blows up at the zero crossing.

Teflon is substantially different than the other samples but how much different? These samples were only irradiated to  $10^6$  rads. What if we went to  $10^9$  rads to simulate more time in space? We don't know what we would see! Maybe the annealing effect would go away and breakdowns would reoccur with renewed vigor; related effects have been seen with 10 to 40 keV electrons (ref. 15).

#### IV. Proposal for Blowoff Currents

Combining the findings of this paper with reports from the 1978 conference and references 9-14, and with vague notions concerning breakdown propagation, let me propose the following model for blowoff currents.

We now know that very little net charge moves in a breakdown tunnel or streamer but that a lichtenberg pattern results. We know that light is emitted so there probably is a plasma. The material is not heated severely or melted locally outside the channel so the plasma must travel as a wave front rather than a repeating process or continuous wave. The lichtenberg channels exit a surface in many cases.

So I propose that a nearly net neutral plasma bursts from the surface at the channel-surface intersection as shown in figure 13. If the net charge

---

\* In private discussions J. West, Bell Laboratories, disclosed that he sees the fast type breakdown pulses in his FEP teflon samples (Dec 1980).

in the dielectric is negative, the plasma will partially separate: electrons will rapidly move away from the dielectric and positive ions will return to the dielectric surface partially neutralizing the trapped charge fields external to the dielectric. The process is dynamic containing force terms due to E-M cavity oscillations,  $\partial B/\partial t$  terms, and self shielding in the plasma region. Thus full neutralization of the dielectric space charge fields external to the dielectric will not usually occur, just 50% or 80% neutralization. The amount of net current flow from the plasma will depend on the total dielectric trapped charge along with the time dependent vacuum chamber cavity fields -- thus we would have the so called "surface area scaling laws". But the trapped dielectric charge remains in the bulk so that further breakdowns are likely to reoccur soon in rapid succession even though the surface potential appears mostly neutralized; light pulses would continue to occur. And I predict a new observable -- the net neutral plasma will produce microwave bursts when it exits the surface in the classical plasma oscillation character. From the radio frequency of these bursts we can obtain the plasma density, or vice-versa. Of course the density and the total charge are decaying rapidly so the R.F. bursts are both amplitude and frequency modulated.

## V. CONCLUSIONS

The results discussed above are quite extensive and have been reported as briefly as possible. These results are boiled down from many experiments and represent the major patterns. New patterns would probably emerge as more samples and longer irradiations are performed. The following is a list of the major findings or concepts. Please return to the text for discussion of these points.

### MAJOR FINDINGS.

1. High field strength does not guarantee breakdowns.
2. No breakdowns seen below  $2 \times 10^7$  V/m.
3. Teflon less likely to break down and extended irradiation severely increases dark conductivity.
4. Breakdown pulses last less than 100 ms except in Teflon where they can last 2 seconds.
5. Field enhanced conduction occurs but is not important for mitigating breakdowns
6. Breakdowns do not remove any bulk space charge.
7. Lichtenberg patterns occur, even at these very low intensities.
8. Decay of bulk charge requires at least a week, if not years.

9. Most materials radiation anneal to decrease breakdowns under continued irradiation; this is due to some effect other than increased conductivity.

10. Spectral changes reintroduce breakdowns.

11. Glass filled polyphenylene sulphide (and perhaps other filled polymers) shows enhanced breakdowns.

12. Penetrating radiations also cause breakdowns so that broad spectra will not significantly reduce breakdown probabilities.

13. I propose a net neutral plasma pulse as driving function for blowoff currents. such a model can explain the results seen here as well as other results published elsewhere.

## REFERENCES

1. Gross, B., Topics in Applied Physics 33, Electrets; G. M. Sessler Editor, p.217-84. Springer Verlag, Berlin, 1979. This is a thorough review of the analytic modeling and basic concepts complete with an extensive set of references.
2. Frederickson, A. R., AIAA Progress in Astronautics and Aeronautics 71, "Space Systems and Their Interactions with Earth's Space Environment", p. 386-412. This is a review of a relatively precise numerical solution including only a minimum of material parameters.
3. Frederickson, A. R., IEEE Trans. Nuc. Sci., NS-22, 2556-61, (Dec. 1975).
4. Matsuoka, S., et. al., IEEE Trans. Nuc. Sci., NS-23, 1447-52, (Oct. 1976).
5. Berkley, D. A., J. A. P. 50, 3447-53, (May 1979).
6. Frederickson, A. R., IEEE Trans. Nuc. Sci., NS-24, 2532-39, (Dec. 1977).
7. Frederickson, A. R., "Electric Fields in Irradiated Dielectrics", NASA Publication 2071 (AFGL-TR-79-0082) Spacecraft Charging Technology 1978, p. 554-69.
8. Gross, B., West, J. E., von Seggern, H., Berkley, D. A., J. A. P. 51, p. 4875 (Sep. 1980). *ibid*: private communication, Dec 1979.
9. Treadaway, M. J., et. al., IEEE Trans. Nuc. Sci., NS-26, 5102 (Dec. 1979).
10. Keyser, R. C., and Wilkenfeld, J. M., *ibid*, 5121.
11. Beers, B. L., et. al., *ibid*, 5127.
12. Flanagan, T. M., et. al., *ibid*, 5134.
13. Hazelton, R. C., et. al., *ibid*, 5141.
14. Balmain, K. G., and Dubois, G. R., *ibid*, 5146.
15. Gross, B., Sessler, G. M. and West, J. E., Applied Physics Letters 24, No. 8, 351 (1974). *ibid*: private communication, 1980.

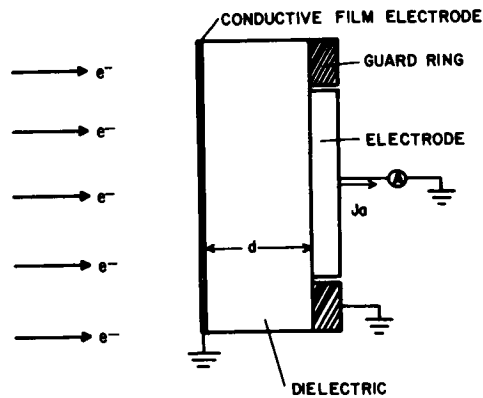


Figure 1 Typical Dielectric Irradiation Geometry.

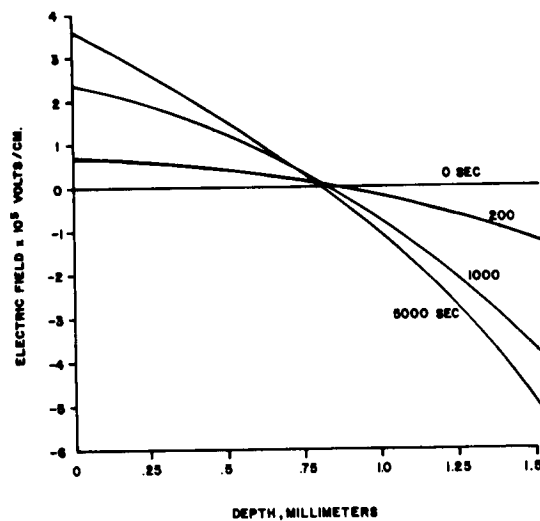


Figure 2 Electric fields as a function of depth at various times after initiation of a constant 1 MeV electron irradiation of intensity  $3.9 \times 10^{-6}$  A/m<sup>2</sup> in polyvinylchloride 1.5mm thick. No further changes in field occur after 5000 seconds. Note the electric field is bipolar. These calculations are based on the model described in reference 2.

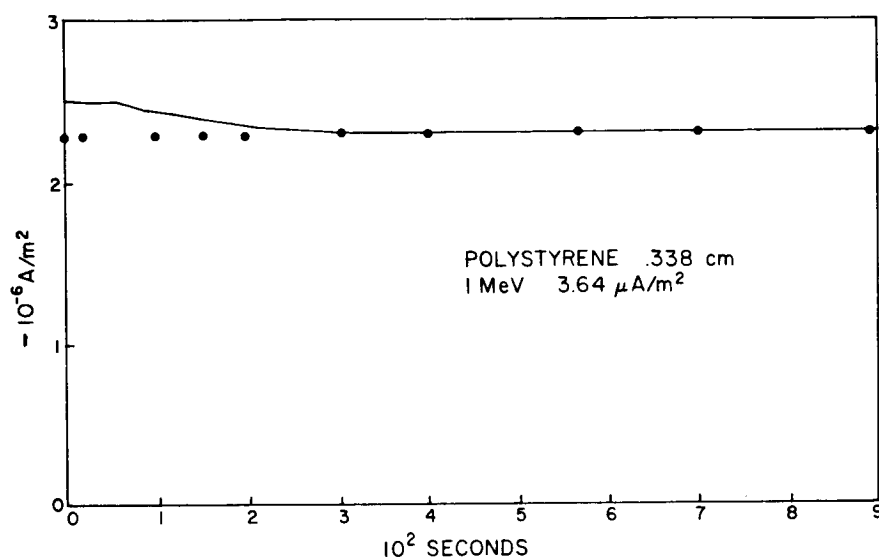


Figure 3 Measured current density by meter A vs. time in .338cm thick Polystyrene, irradiated by 1 MeV electrons at  $3.64 \mu\text{A}/\text{m}^2$ . Solid line is the experiment, dots are the theoretical prediction.

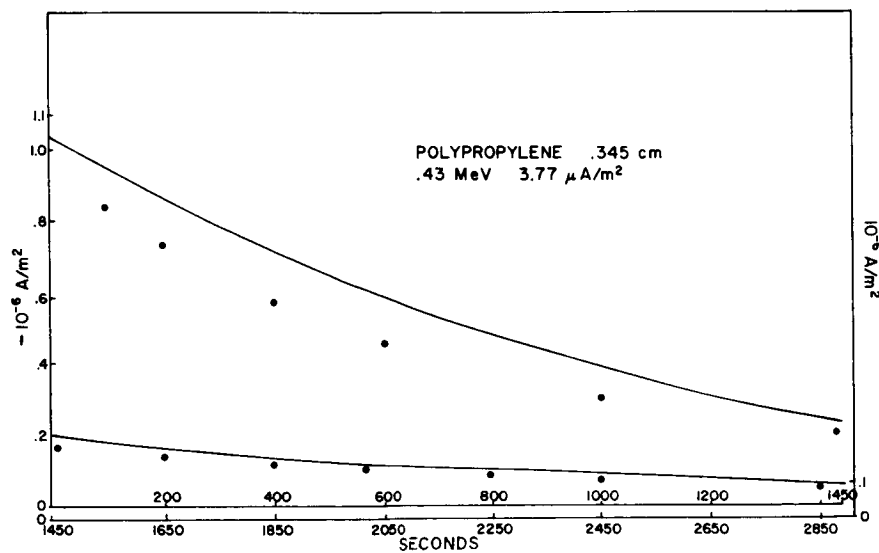


Figure 4 Measured current density by meter A vs. time in .345cm Polypropylene irradiated by 0.43 MeV electrons at  $3.77 \mu\text{A}/\text{m}^2$ . The lower curve is the continuation of the upper curve with displaced axes. The dots are theoretical predictions.

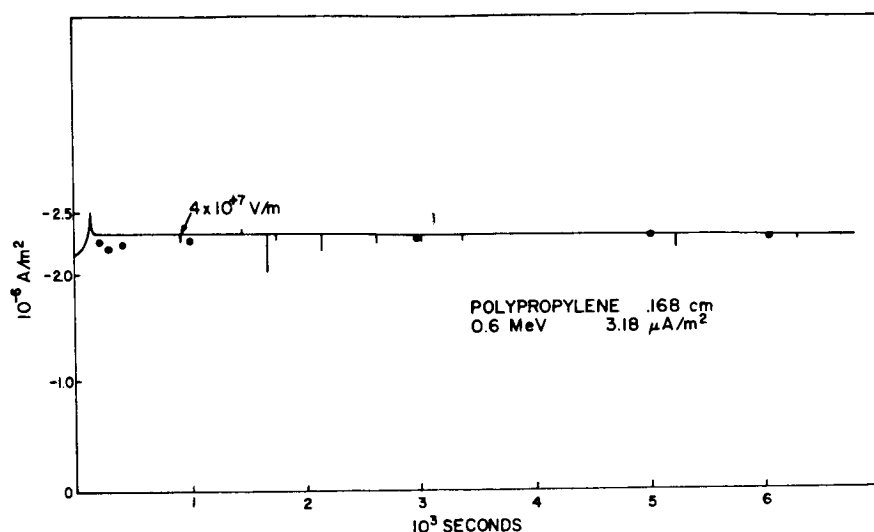


Figure 5 Measured current density by meter A vs. time in 0.168cm Polypropylene irradiated by .6 MeV electrons at  $3.18 \mu\text{A}/\text{m}^2$ . Dots are theoretical predictions. The first breakdown pulse occurred at nearly 1000 seconds and the polarity indicates it occurred near the left (front) electrode (inspect figs. 1 and 2). The early rise and fall is not a breakdown pulse, it took tens of seconds to occur. At 1000 seconds the electric field adjacent to the front electrode was theoretically estimated to be  $4 \times 10^4 \text{ V/m}$ .

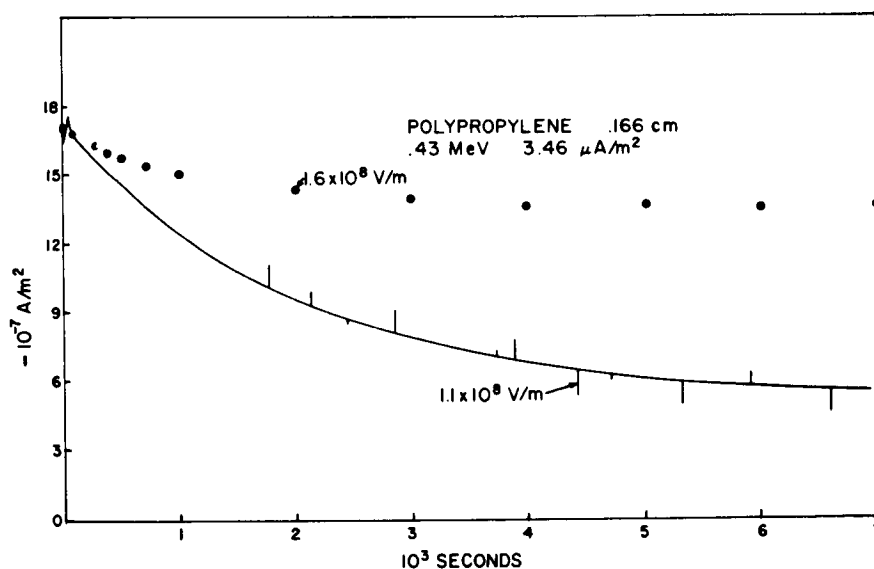


Figure 6 Measured current density by meter A vs. time in 0.166cm Polypropylene irradiated by  $3.46 \mu\text{A}/\text{m}^2$  electrons at 0.43 MeV. Dots are theoretical predictions. At nearly 1800 seconds we see the first breakdown pulse. Qualitative inspection of figure 2 and the polarity of this first pulse indicate that this breakdown occurred in the right portion of the sample where the field was negative. At 2000 seconds the theory estimated the electric field adjacent to the rear electrode to be  $1.6 \times 10^8 \text{ V/m}$ . At 4400 seconds the field adjacent to the front electrode was roughly  $1.1 \times 10^8 \text{ V/m}$ .

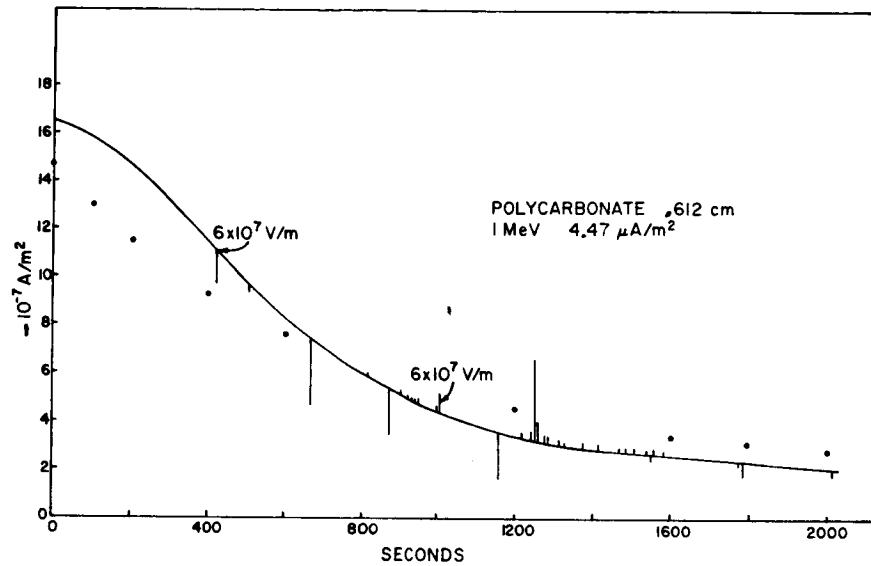


Figure 7 Measured current density by meter A vs. time in 0.612cm thick Polycarbonate irradiated by  $4.47 \mu\text{A}/\text{m}^2$  of 1 MeV electrons. Dots are theoretical predictions.

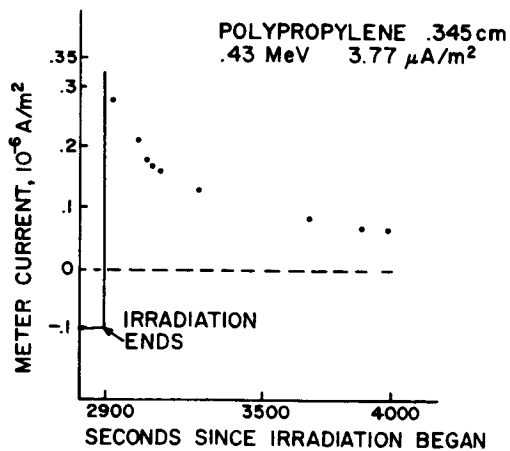


Figure 8 Space charge decay meter current after end of irradiation.

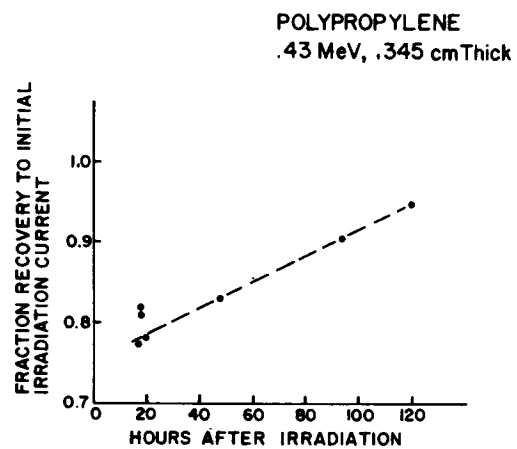


Figure 9 Sample recovery days after irradiation.



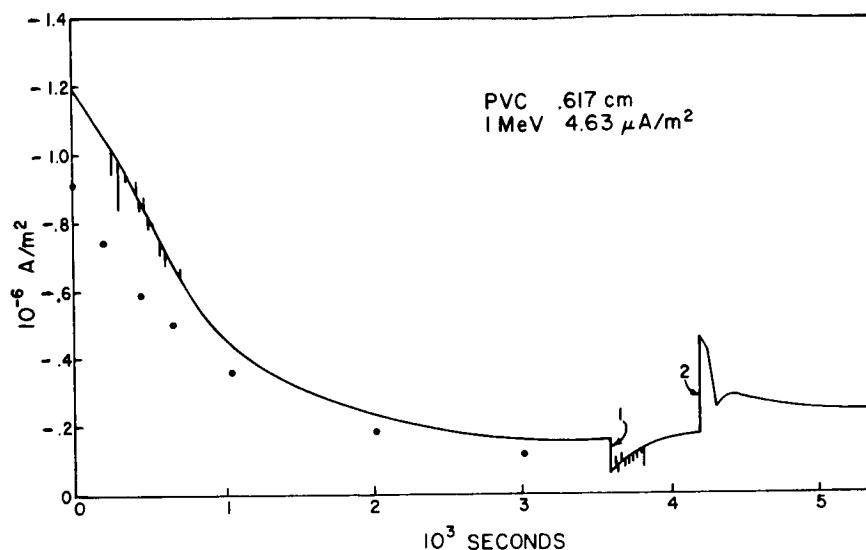


Figure 10 Measured current density by meter A vs. time in .617cm Polyvinylchloride irradiated by  $4.63 \mu\text{A}/\text{m}^2$  of 1 MeV electrons. Dots are the theoretical predictions. Incident energy was changed after 3600 seconds. At 3600 seconds, step 1, the energy was quickly lowered to 0.93 MeV and remained constant until step 2 at 4220 seconds when the energy was raised. Note that the initial breakdowns ceased after 700 seconds but reoccurred after step 1 and then later ceased again.

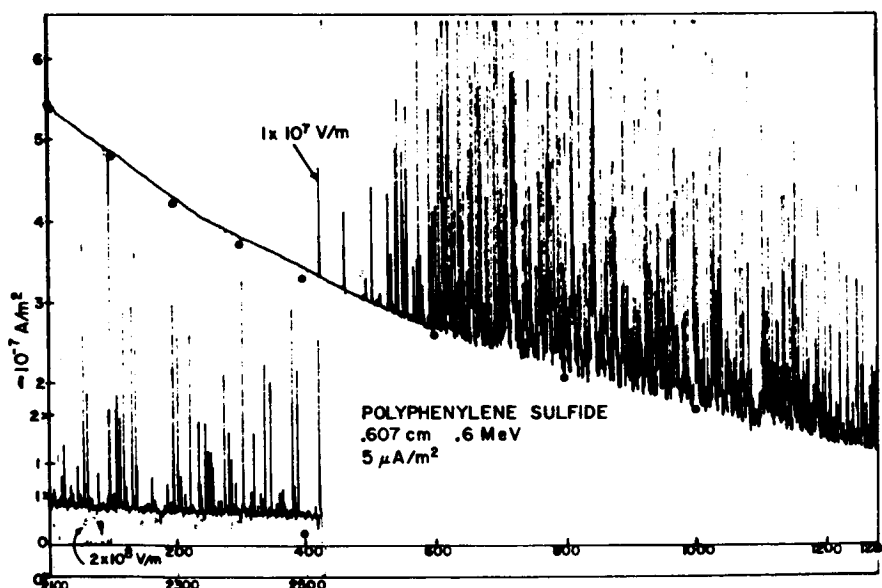


Figure 11 Results for Polyphenylene Sulfide, glass filled. Dots are theoretical predictions. It is not obvious from the chart recording but at 2200 seconds small breakdowns of positive polarity (downward) began when the field adjacent to the front surface was estimated to be  $2 \times 10^8 \text{ V/m}$ . At this time blowoff current pulses began to be monitored by an electrode mounted in front of the sample (but not blocking the incident beam).

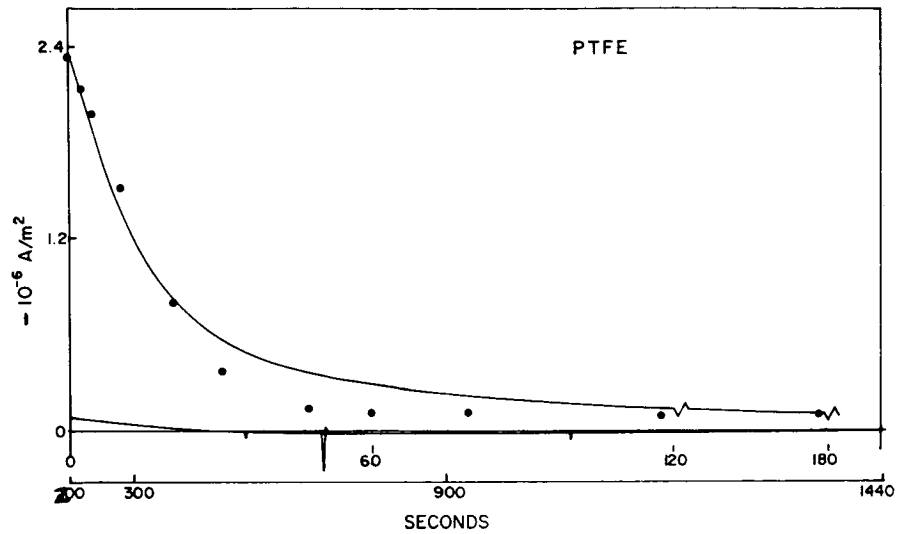


Figure 12 Typical results for Polytetrafluoroethylene. Dots are theoretical predictions including radiation damage induced conduction. Note the breaks in the time scale at 180 and 120 seconds, and the slow pulse at 700 sec.

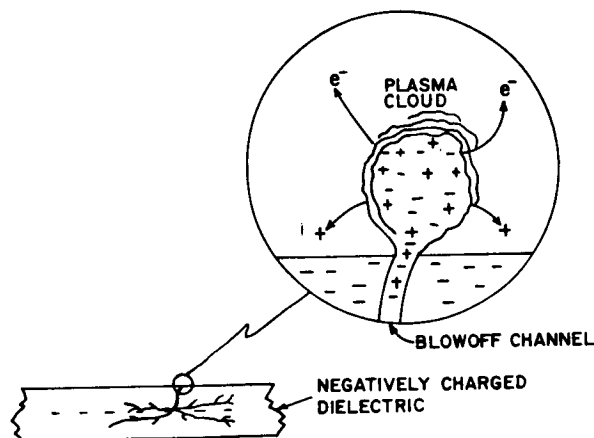


Figure 13 Proposed surface blowoff current source function -- a net neutral plasma.

## **CHARGING AND DISCHARGING TEFLON\***

**B. C. Passenheim and V. A. J. van Lint**  
**Mission Research Corporation**

### **1. INTRODUCTION**

In this paper we present some results selected from a program designed to measure the charging and discharging characteristics of several common satellite materials exposed to 0-30KV electrons. SGEMP related aspects of this experiment are described in Reference 1. We have chosen to discuss teflon in this paper because the charging characteristics are radically altered immediately after a spontaneous discharge.

In Section 2 we discuss the experimental configuration, in Section 3 we present experimental observations, and in Section 4 we offer a hypothesis to explain the observations.

### **2. EXPERIMENTAL DETAILS**

The exterior geometry of the test structure is indicated in Figure 1. In all cases dielectric samples were 82 cm in diameter mounted on the front of a 120 cm diameter cylinder supported on an 85 cm, 0.95 cm thick plexiglass disc. Dielectric materials investigated were: back surface aluminized Kapton, back surface silvered Teflon, Silicon Alkyd white thermal control paint, and 50 cm by 50 cm array of 0.030 cm thick  $MgF_2$  coated fused silica solar cell cover slips.

Spontaneous discharges and SGEMP emissions were measured with EG&G CMLX3B surface current probes and CT-2 current transformers. Fast transient data was transmitted to the recording instrumentation through HDL/DNA 400 MHz fiber optic data links, recorded on Tektronix 7912 transient digitizers and processed on a PDP/1140 computer.

---

\*Experimental observations were obtained under Defense Nuclear Agency contract DNA001-78-C-0269. Data reduction was performed under AFWL contract F29601-78-C-0012.

The test cylinder was connected to instrumentation ground through a 50 K $\Omega$  resistor chain. This provided a cylinder potential of less than 0.5 volts during charge, at measured current densities of approximately  $10^{-9}$  A/cm<sup>2</sup>. However, the RC time constant of this resistor string and cylinder capacitance to the tank was about 8 microseconds, so the test structure was effectively isolated during spontaneous discharges and exploding wire photon pulses. As indicated in Figure 1 the front of the cylindrical test object was surrounded by a square frame which supported small motors, pulleys and belts, (not shown) to drive a traverse carrying the probe of a TREK noncontacting electrostatic voltmeter, a Faraday cup, and an E sensor over the surface of the sample. The spatial resolution of the electrostatic voltmeter is estimated to be  $\pm 3$  mm, the Faraday cup was approximately 1 cm<sup>2</sup> and the E probe was used as an oscilloscope trigger in spontaneous discharge studies. Both the traverse frame and the aluminum rings surrounding the dielectrics were coated with colloidal graphite to inhibit dielectric charging and minimize photoelectric emission from the aluminum. The tank was lined with 2 cylindrical layers of 200  $\Omega$ /square carbon coated cloth to suppress tank wall photoemission and damp tank EM resonances. The test cylinder was suspended with nylon ropes from a rotary feed through near the center of the 10 foot diameter and 12 foot long vacuum tank.

The chamber was evacuated with a liquid nitrogen trapped, silicon oil diffusion pump and a mechanical roughing pump. In addition there was a liquid nitrogen cold wall in the tank. The tank pressure normally ranged about  $2 - 5 \times 10^{-6}$  torr. Rapid discharge (approximately  $10^3$  volts/sec) of all charged insulators was observed at  $\sim 2 \times 10^{-4}$  torr. This discharge was accompanied by a flash of light and a temporary reduction in pressure.

Samples were handled with gloves with more-than-normal care, but were unavoidably exposed to laboratory atmosphere for several weeks prior to testing. Close, careful visual examination of the reflecting kapton samples after several days of tests revealed traces of vacuum pump oil. Subsequently, all samples were washed with reagent grade ethyl alcohol after installation and before pumpdown.

Two electron guns were employed. Faraday measurements indicated that the DNA electron flood gun provided illumination which differed by less than a factor of two from the center to the edge of the sample. Acceleration potential was established by floating the gun filament to a negative potential with respect to a grounded fine wire grid. Gun current was regulated with a feed-back circuit which sensed emission current and modulated the filament power. We also employed an electrostatically focused and deflected cathode ray tube gun, focused to provide to a 2 cm diameter spot on the sample. For equal total gun current the beam current density was approximately 1600 times larger in the focused beam. Comparable potential distributions were produced with comparable total electron fluences from either gun. This indicates the charge build-up is not particularly sensitive to beam current densities over a range from approximately  $10^{-10}$  to about  $10^{-6}$  A/cm<sup>2</sup>.

Figure 2 represents the electrical equivalent circuit of this experiment, where node 1 is the trapped electron charge layer, node 2 is the metal film on the back of the teflon, node 3 is the test cylinder and node 4 is the vacuum chamber. Current generator  $I_{12}$  represents a "punch-through" current,  $I_{14}$

represents "blow off" from the dielectric to the tank wall.  $I_{34}$  represents charge emission from the test cylinder to the tank wall, and  $I_{13}$  represents charge transfer from the dielectric to the test object.  $I_{23}$  is the current actually measured with a Tektronix CT-2 sensor and is influenced by blow-off, edge and punch through currents.  $V_{out}$ , the body voltage, is proportional only to blow-off current. The indicated capacitances are self-explanatory. For teflon they are estimated to be  $C_{12} \sim 70$  pf,  $C_{13} \sim 40$  pf,  $C_{14} \sim 100$  pf,  $C_{34} \sim 60$  pf.

### 3. EXPERIMENTAL OBSERVATIONS

The average surface potential of teflon charged with 15 kV electrons was  $9.2 \pm 1.0$  kV, the average potential of teflon charged with 25 kV electrons was  $9.6 \pm 0.8$  kV. We attribute the asymptotic behavior to leakage currents through the bulk dielectric to the metal substrate.

Unlike kapton, which exhibited the tendency to produce fewer and fewer spontaneous discharges under extended irradiation, teflon continued to exhibit spontaneous discharges at nearly constant rate. By repeatedly measuring the surface potential after radiation ceased, we obtained indications that the charge leak rate of teflon, charged to approximately 10 kV, diminished from about 0.6%/min in the first minute after irradiation to approximately 0.03%/min after 40 minutes.

During the course of this investigation we observed a wide variety of responses, and individual charge transfer of up to 500  $\mu$ C. It should be noted that for this geometry, at most approximately 800 nC could be discharged to infinity (blown off) because the removal of that amount of charge would raise the body potential to such an extent that no further charge could be expelled. Therefore, on very large discharges, the bulk of the charge must be returned to the test object itself (we call these edge currents). Figure 3 (a-b-c) represent substrate current  $I_{23}$  for three successive discharge events. The integral of the substrate current ( $Q_{23}$ ) is the sum of "blow-off" charge and "edge" charge. The (transient) increase in the test object potential is proportional to the blow-off divided by the capacitance of the object to the tank. For the first event, in Figure 3, the integral of the substrate current and the body voltage (not shown) indicate a charge release of approximately  $9 \pm 1$  nC. In the second event the charge release was  $0.4 \pm 0.4$  nC and the third event approximately  $3 \pm 1$  nC. For these three specific events virtually all the charge was blown off to the tank walls. Notice that all three of these events exhibit an early time high-frequency ring which is determined by the LC product of the inductance of the wire connecting the substrate to the body (to measure  $I_{23}$ ) and the capacitance between the dielectric and the body. The net charge released in the high frequency portion of these signals is nearly zero. According to these records, the charge actually blown off starts to leave the body at approximately 0.4  $\mu$ s and persists for approximately 0.5 to 1.0  $\mu$ s. We will soon suggest that the blow-off pulse width is determined by propagation rate of an ion wave front.

In addition to these transient measurements we periodically measured the surface charge state of the dielectric with the TREK electrostatic voltmeter. Sweeping the sensor across the surface of the sample in a tic-tac-toe pattern, Figures 4 a-h show one series of measurements in which the teflon sheet was charged in steps, by 15 kV electrons, at a current density of approximately 8 nA/cm<sup>2</sup>. Figure 5a indicates the degree of nonuniformity of the incident electron beam. The surface potential approached an asymptotic value of approximately 9 kV (Figure 5d and 5e). This sample was then intentionally discharged by admitting gas, raising the pressure to approximately  $8 \times 10^{-4}$  torr. The discharge was accompanied by a flash visible light which covered the entire exposed surface. The light visually resembled the glow of a gas flame. We note that spontaneously discharging samples exhibited both these flame-like flashes as well as dendritic sparks. The TREK probe was located at x,y coordinates of 24 cm and 20 cm during the discharge. As indicated in Figure 4f the discharge was incomplete in the vicinity of the electrostatic probe because the external electric field was near zero at that location. Figures 4g and 4h show that it took much longer to recharge the teflon surface after it had been intentionally discharge than it initially had. Figure 5 shows the average surface potential as a function of exposure time indicating that the sample originally approached 90% of the asymptotic limit in approximately seven seconds while after discharge the same charging process took about 7 minutes.

Figure 6a - 6f is another series of potential profiles. Figure 6a shows a sample which had been charged with 3 nA/cm<sup>2</sup> of normally incident 25 kilovolt electrons. Figure 6b shows a traverse measured immediately after a spontaneous charge transfer of approximately 400  $\mu$ C (inferred from  $C\Delta V$  and size of the discharged area). Figures 6c, d, e indicate that, as with the gas discharged sample, the spontaneously discharged area was difficult to recharge. The chamber pressure at the time of the spontaneous discharge was approximately  $4 \times 10^{-6}$  torr, which is much too low for gas induced discharge.

#### 4. HYPOTHESIS

We note two similarities between the spontaneous discharge and the one produced by the presence of gas, the first is the visual appearance of the discharge, the second is the diminished tendency to accept recharge. In the gas discharge case, we know that the charged dielectric surface was neutralized by ionized gas molecules. The surface was bombarded with approximately  $6 \times 10^{11}$  ions/cm<sup>2</sup> accelerated to approximately 10 kilovolts. Only the first few microns of the surface participate in this discharge process. Therefore any changes in the material response must be attributed to changes in the sample surface rather than the bulk dielectric. The spontaneously discharged dielectric exhibited similar characteristics, even though the ambient pressure was too low to be attributed to gas discharge. Consequently we speculate that the reduced recharge rate is because the secondary emission coefficient of a freshly ion bombarded surface is substantially greater than for an aged or dirty surface and the spontaneous discharge involves the generation and propagation of a wave front of ions of the dielectric itself. Thus the propagation velocity of the dielectric ions in the pre-existing electric field of the charged dielectric determines the

rate of the spontaneous discharge. This accounts for the comparatively slow emission of blow off charge noted in Figure 3. This model is also supported by the calculations presented in reference 2.

Acknowledgements: The authors thank Billie Carr and Jim Riddell for data compilation and manipulation.

## 5. REFERENCES

1. van Lint, V.A.J., et. al.: The Effect of Electron Precharging on SGEMP Response of Insulators. IEEE Trans Nuclear Science, Vol. NS-26, No. 6, December 1979, pp. 5024-5029.
2. Mandell, M.J., Katz, I., Schnuelle, G.W., "Calculation of Surface Flashover of a Large Sample Under Grounded and Floating Conditions", Spacecraft Charging Technology Conference, November 14, 1980 (this conference)

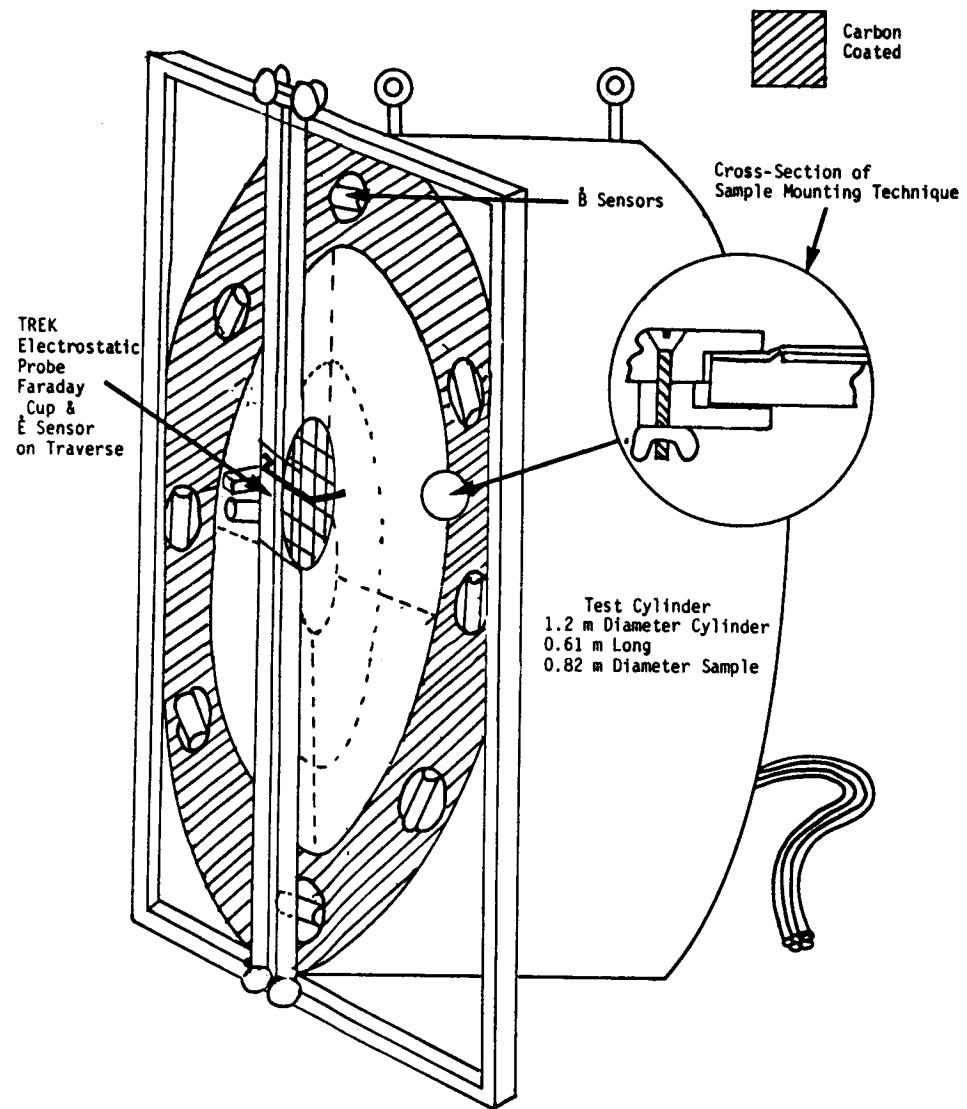


Figure 1. Picture of the test body showing traverse, sample and  $\dot{B}$  sensors. Insert shows the way the sample was attached to the test body.



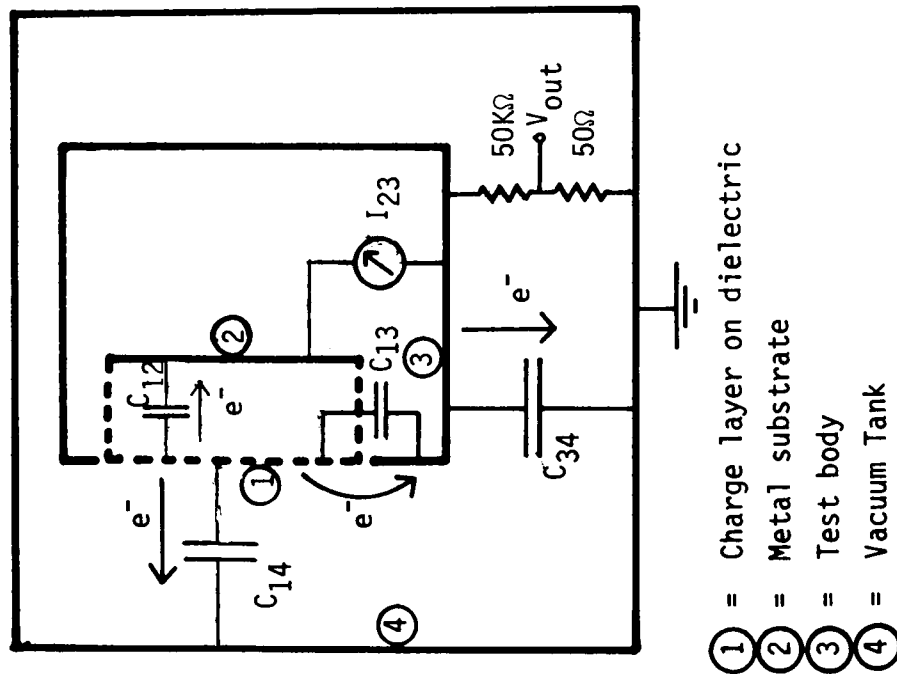


Figure 2. Schematic and electrical equivalent circuit of a dielectric disk on the end of a cylinder in a vacuum chamber.

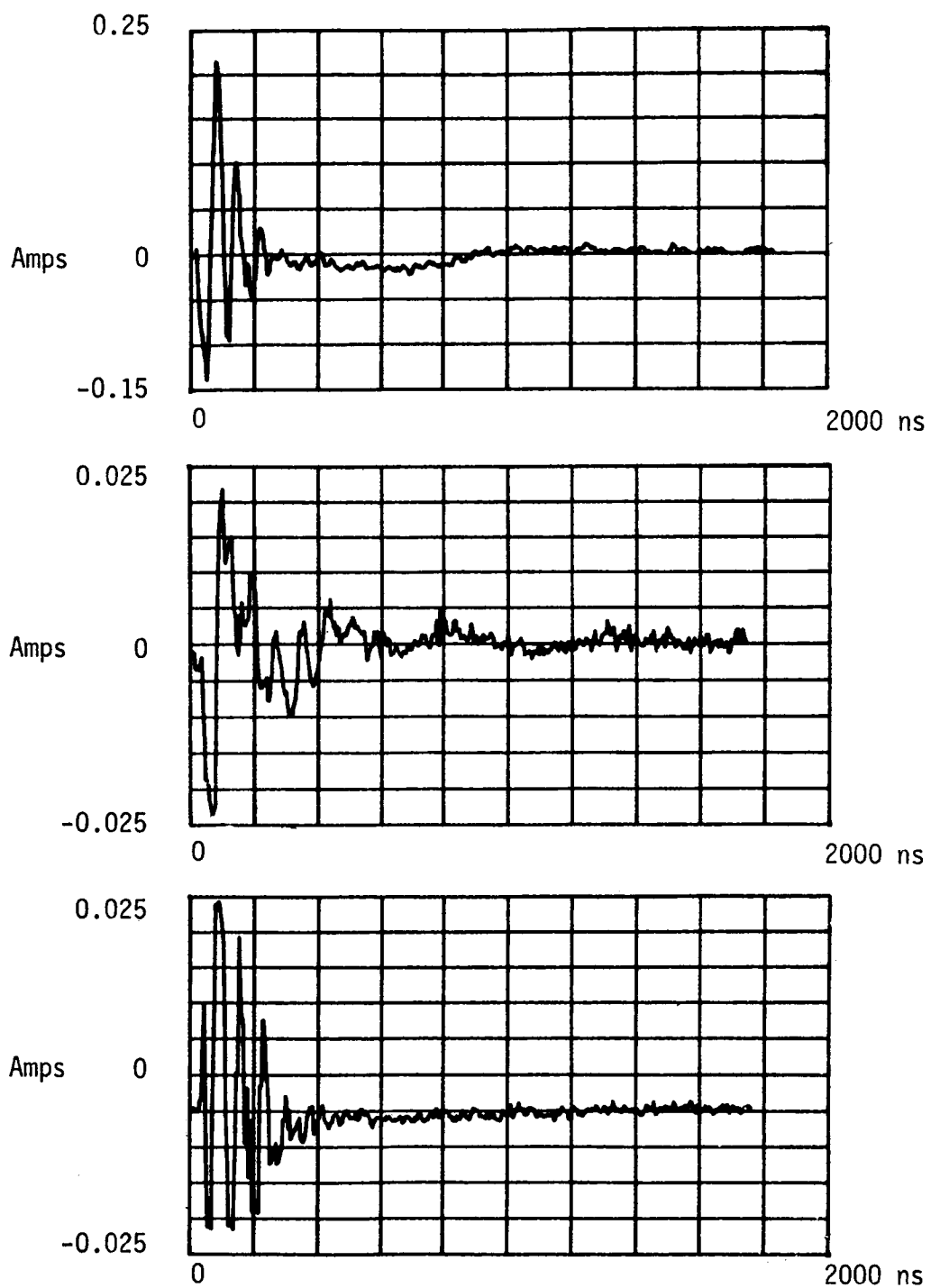


Figure 3. Substrate-to-body current record ( $I_{23}$ ) for three spontaneous discharge events.

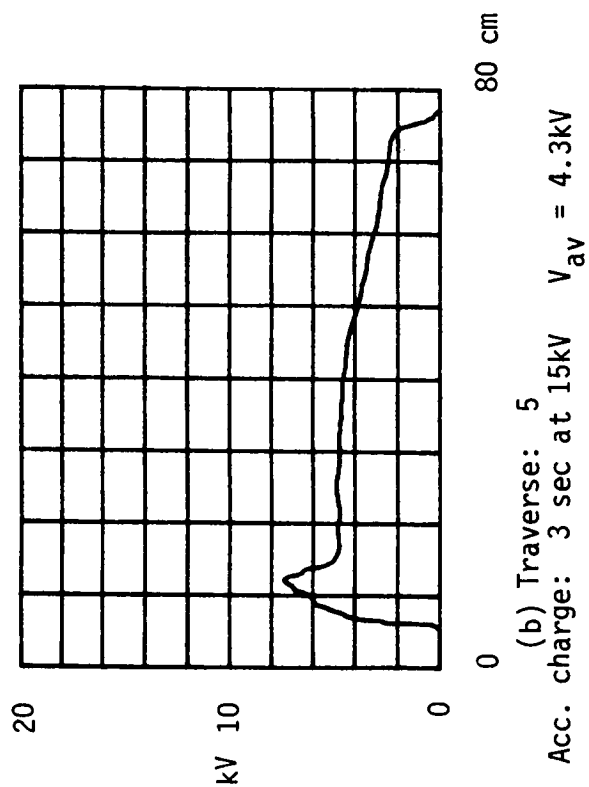
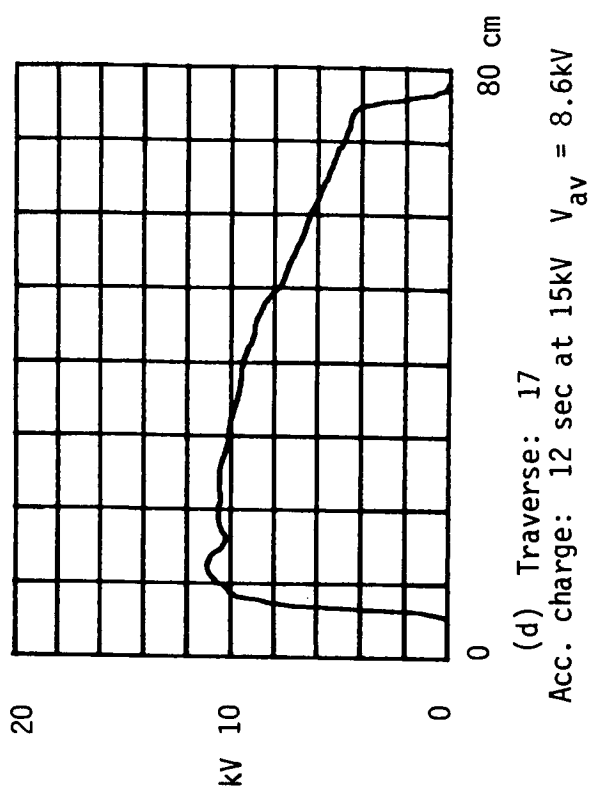
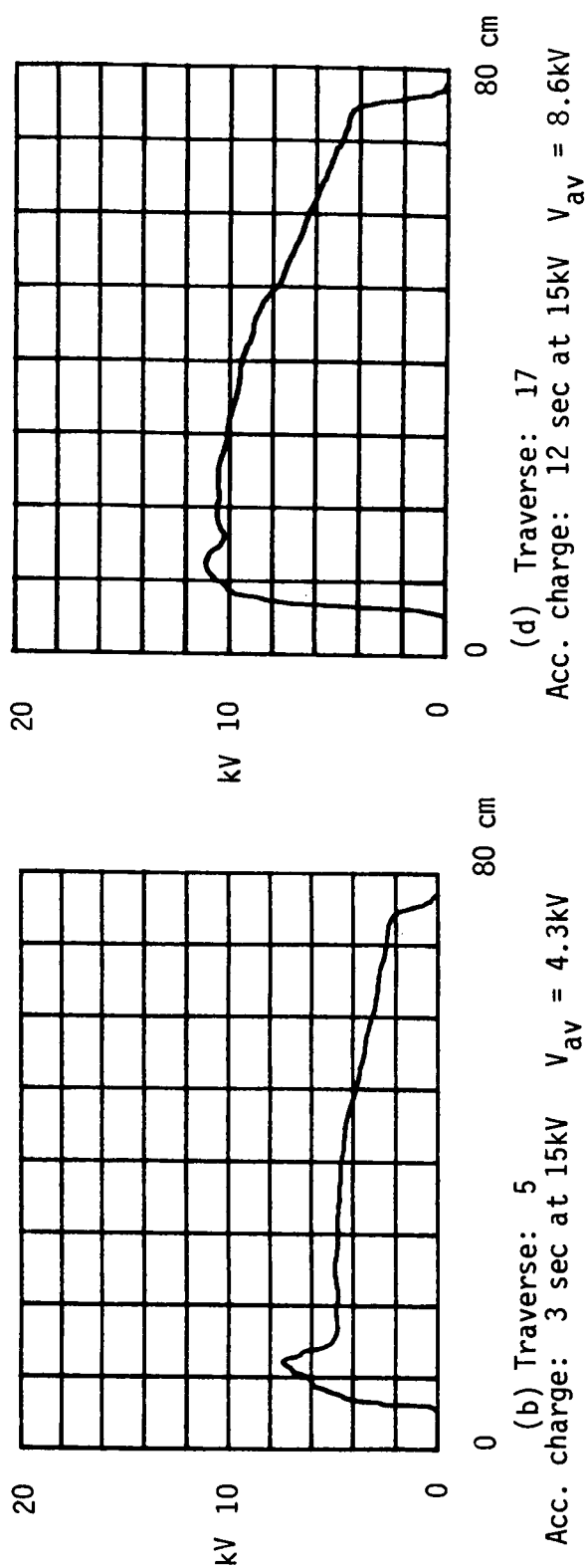
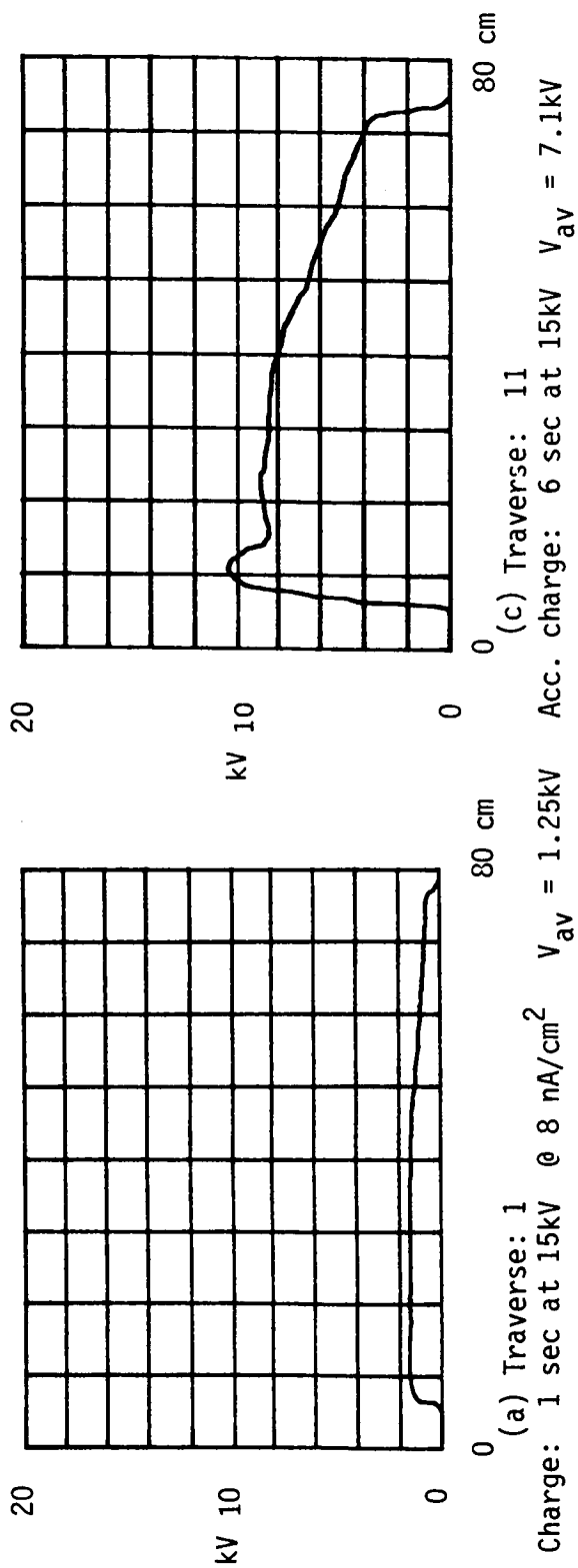


Figure 4. TEFLON - Charging at 15 kV -  $V(x)$  traverses  $x$  at  $y = 20$  cm.

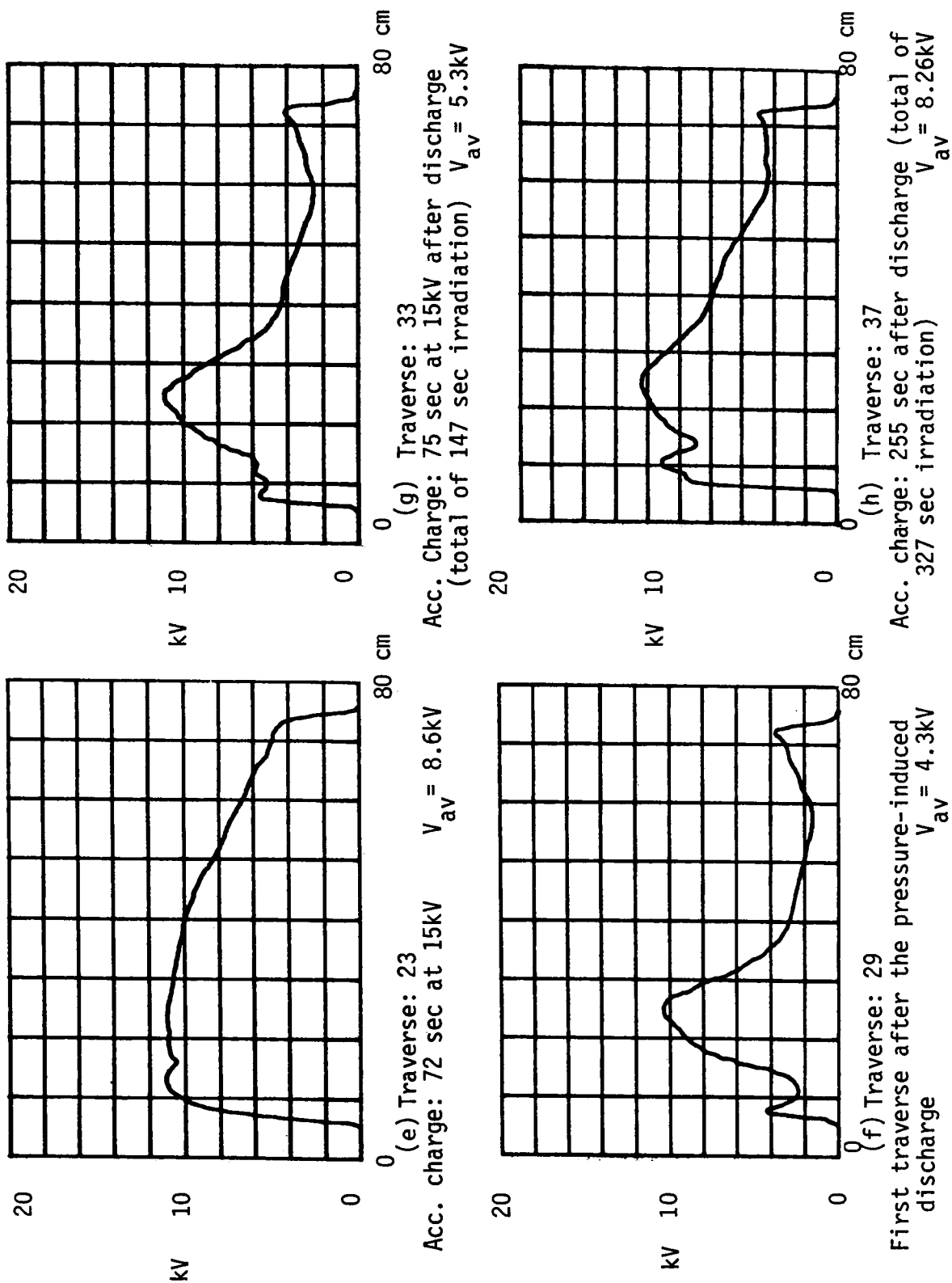


Figure.4. (cont.). TEFLON - Charging at 15 kV -  $V(x)$  traverses along x at y = 20 cm

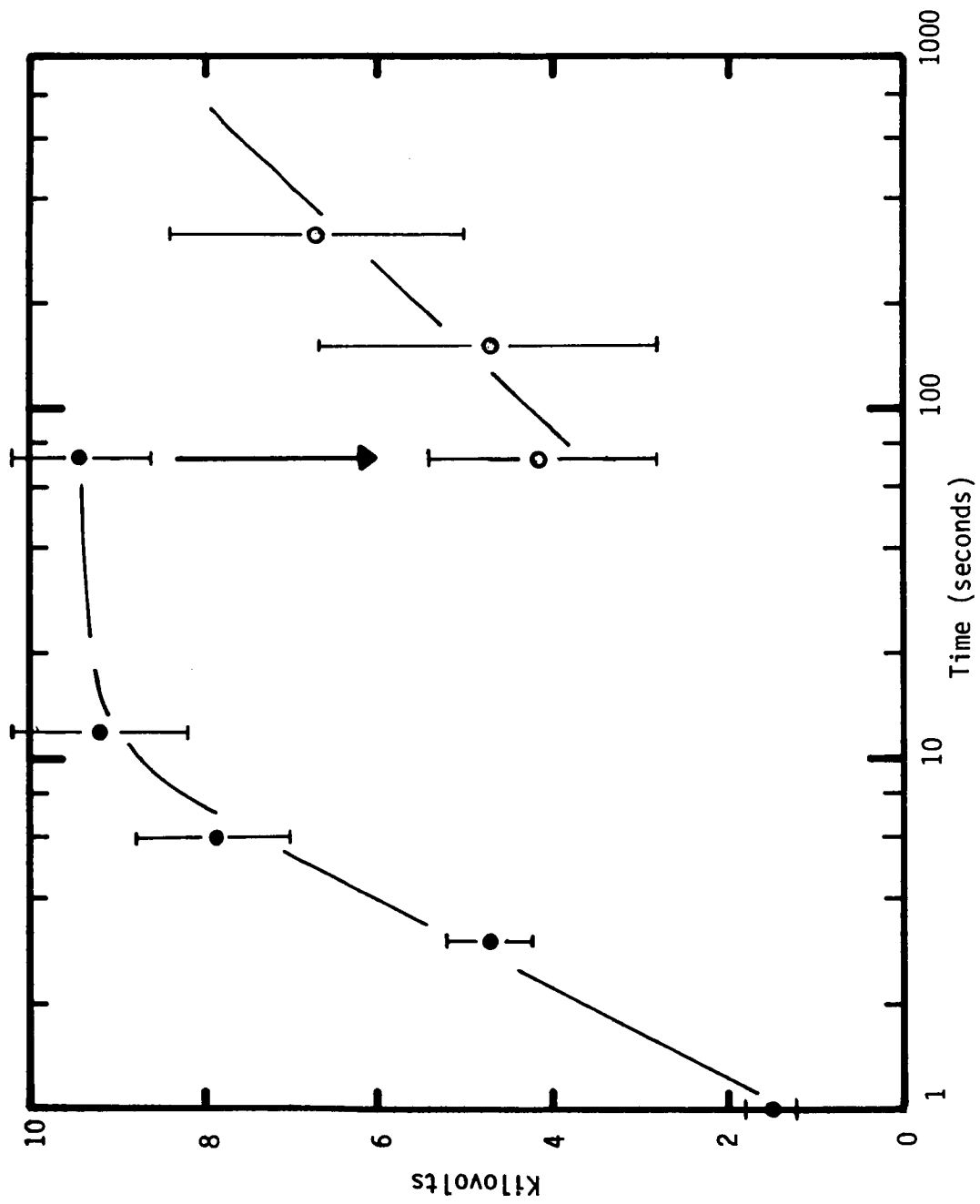


Figure 5. Surface potential of teflon as a function of charging time before and after a gas-induced discharge.

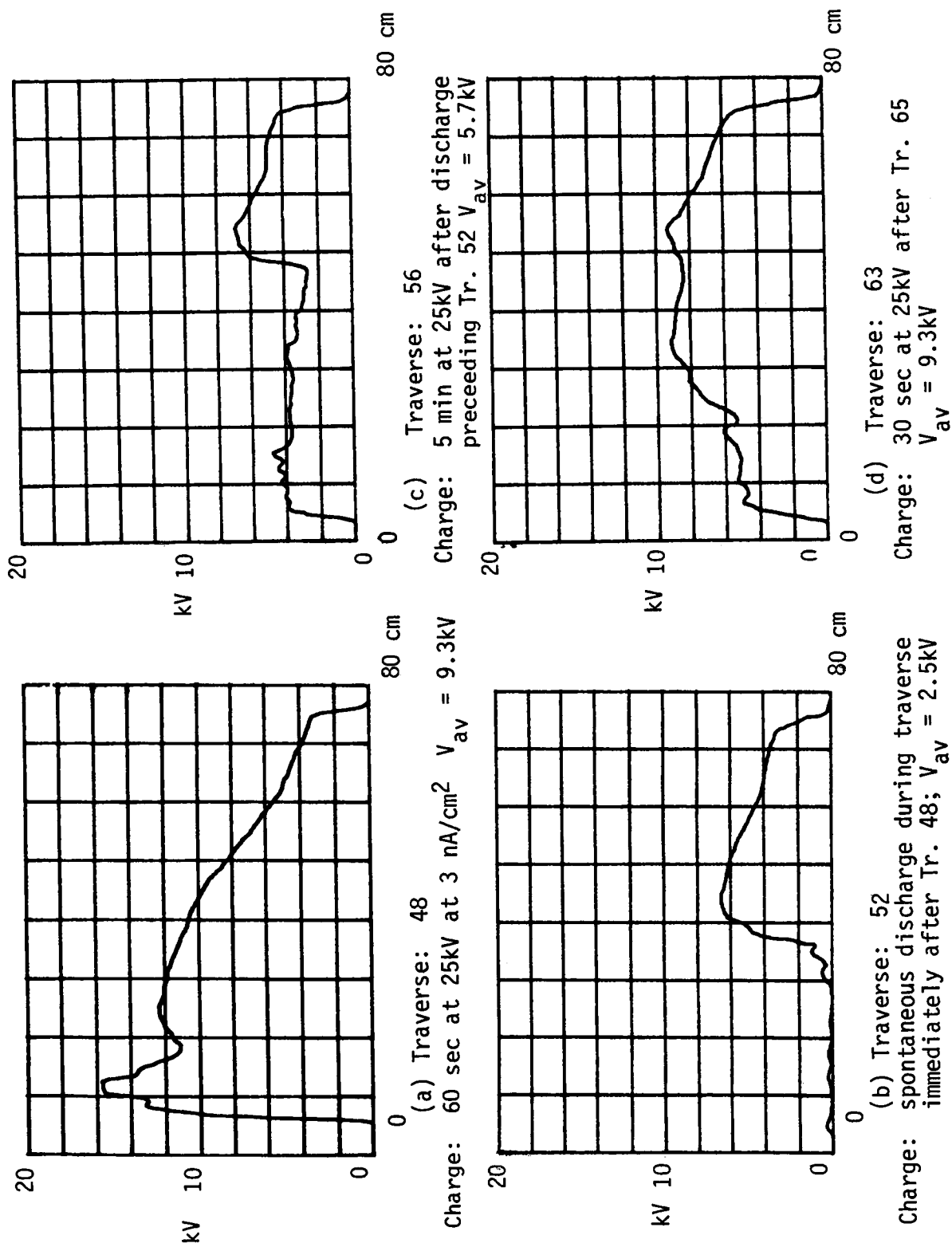


Figure 6. TEFLON - 25kV charging after spontaneous discharge in high vacuum.  $V(x)$  traverses along x at  $y = 20$  cm.

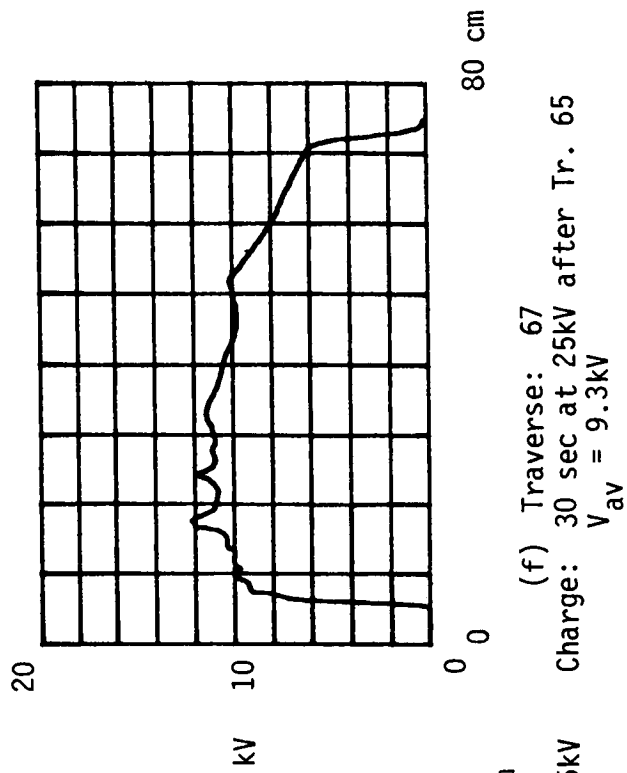
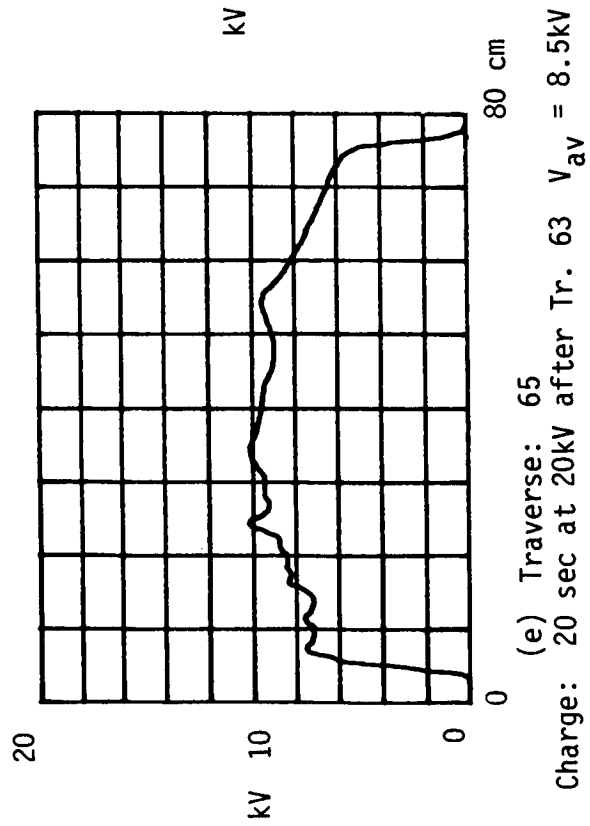


Figure 6. (cont.) TEFLON - 25kV Charging after spontaneous discharge in high vacuum.  $V(x)$  Traverses along x at  $y = 20$  cm.

**EXPERIMENTAL VALIDATION OF A NUMERICAL MODEL PREDICTING THE  
CHARGING CHARACTERISTICS OF TEFLON AND KAPTON UNDER  
ELECTRON BEAM IRRADIATION\***

**R. C. Hazelton, E. J. Yadlowsky, and R. J. Churchill  
Inland Research and Development Center**

**L. W. Parker  
Lee W. Parker, Inc.,**

**B. Sellers  
Panametrics, Inc.**

**SUMMARY**

In order to assess the effect of differential charging of spacecraft thermal control surfaces the dynamics of the charging process must be understood. To that end a program to experimentally validate a computer model of the charging process has been established.

Time resolved measurements of the surface potential have been obtained for samples of Kapton and Teflon irradiated with a mono-energetic electron beam. Results indicate that the computer model and experimental measurements agree well and that for Teflon secondary emission is the governing factor. Experimental data indicate that bulk conductivities play a significant role in the charging of Kapton.

**INTRODUCTION**

The effects of dielectric breakdown observed on board spacecraft and in the laboratory have demonstrated the need for a charging model capable of predicting surface voltages and internal electric fields for dielectric surfaces subject to the spacecraft environment. A joint theoretical and experimental program has been initiated to both improve and validate such a model using an iterative procedure. Concurrent development of the computer code and experimental measurements will allow modifications of both programs to produce an optimum correlation.

The model is a modification of one developed for Communications Research Centre (ref. 1) which takes into account subsurface charge dynamics, energy deposition ranges, secondary electron emission, radiation induced conductivities and bulk resistivity. The program predicts the temporal evolution of the

---

\*This work is sponsored by the International Telecommunications Satellite Organization (INTELSAT). Any views expressed are not necessarily those of INTELSAT.



surface voltage, charging currents, charge deposition profiles and internal electric fields for a given incident particle spectra and material parameters.

The model is being evaluated using data from an experimental program developed to measure the material parameters pertinent to the problem as well as the charging characteristics of the dielectric sample.

The work described here deals with the charging characteristics of Teflon and Kapton samples irradiated with a monoenergetic beam of electrons having an energy of up to 16 keV. The surface voltage is determined from the energy spectrum of secondary electrons measured with a curved plate electrostatic surface emission analyzer (ESEA). Particular attention has been directed toward avoiding fringing fields and surface leakage effects near the sample edges, obtaining a uniform irradiating beam density with minimum beam divergence effects, and adequately resolving the surface voltage during the charging processes.

Measurements on Teflon are in good agreement with the numerical model predictions. The results indicate that the equilibrium surface voltage is determined by secondary emission and that bulk resistivity and radiation induced conductivity are unimportant. The data points can be adequately predicted by an ideal one dimensional capacitor model. Measurements on Kapton have not been compared with numerical calculations. The results indicate that the bulk resistivity is important and that a leaky capacitor (i.e. a capacitor in parallel with a resistor) is required to approximate the charging characteristics. The results establish the practicality of using the ESEA for measuring the surface voltage during charging.

In the remainder of the paper, the experimental system is discussed briefly. This is followed by a presentation of the experimental techniques and the measurements obtained. A discussion of results and a conclusion section complete the paper.

#### EXPERIMENTAL SYSTEM

In order to carry out the required measurements the system shown in figure 1 has been assembled. The electron flood gun provides a source of energetic electrons (0-30 kV, 0-10 nA/cm<sup>2</sup>) to irradiate the dielectric samples. The flux density of the beam is uniform to  $\pm 15\%$  over the surface of the dielectric. The total electron flux is continuously monitored.

The measurement system is enclosed in a multi-port glass vacuum chamber which is pumped by a turbomolecular pump. This pumping system was chosen to reduce surface contamination by pump oils which can affect secondary emission yields and surface conductivity.

The sample mount was designed principally to establish a one-dimensional geometry which conforms as closely as possible to the one-dimensional geometry assumed for the computer code. For this purpose the samples are mounted upon

a split ring assembly so that fringing fields at the edge of the guard ring have no effect upon the dielectric in the region of the central disc. The dielectric is mounted to the split ring assembly by first removing an annular region of the metallic backing with sodium hydroxide. This region corresponds to the spacing between the guard ring and central disc. When the samples are affixed to sample mount using a conductive epoxy (Eccobond V-91), the guard ring and central disc are electrically isolated. With this configuration the equilibrium current measured with the central disc reflects only the bulk conduction currents through the dielectric. On the other hand, the current measured with the guard ring includes both bulk conduction current and surface leakage current. To provide further one-dimensionality a grounded grid has been placed 1 cm in front of the sample. This provides a uniform, parallel electric field normal to the sample surface. In this way electron beam divergence due to the fields produced as the dielectric charges is minimized.

The sample mount and grid are tilted at  $14^\circ$  to relative to the beam in order to facilitate the measurement of secondary electrons which are ejected normally from the sample surface. After the secondary electrons pass the grid, they traverse a field free region and are detected by a curved-plate electrostatic surface emission analyzer (ESEA) which resolves the energy spectrum of the secondary and back-scattered electrons. The ESEA, developed by Panametrics, Inc. has an energy resolution of 5% of full scale and a time resolution of 4 sec. Picoammeters record the currents collected by the central disc, guard ring and beam current monitor.

## MEASUREMENT TECHNIQUES AND RESULTS

In order to do the initial iteration of fitting experimental data with output of the computer model the time evolution of surface potential, charging current and secondary emission were measured.

The surface potential was determined from a set of time resolved secondary electron spectra obtained with the ESEA. This can be accomplished because the electron spectra secondary electrons are produced at the dielectric surface with a small kinetic energy ( $<100\text{eV}$ ). The kinetic energy gained as these electrons fall from the dielectric surface potential to ground potential is a measure of the surface potential. By taking successive spectra of the secondary electrons and noting the maximum energy a set of time-resolved surface potentials can be obtained. This method was tested and calibrated by replacing the dielectric sample with a gold plate. The irradiated plate was biased at a number of potentials and the secondary electron energy measured with the ESEA. A linear relation was obtained between the applied bias and the energies of the emitted electrons establishing the calibration.

Figure 2 illustrates a set of four time-resolved spectra each of which has two distinct peaks. The first peak is the secondary electron peak which increases both in energy and magnitude with time. The magnitude provides a measure of secondary electron yield. The second peak corresponds to backscatter

electrons whose energy remains essentially constant in time.

The split ring sample mount assembly is instrumented with picoammeters to measure individually the substrate currents flowing to the central disc and guard ring during charging. These currents along with the beam monitor current are recorded using a Bascom-Turner data acquisition system and are stored on magnetic disc. This data can then be recalled and analyzed.

In a typical charging run a new sample is installed and the surface potential and charging currents measured. Figures 3 and 4 exhibit the central disc currents measured and a normalized secondary yield for 125  $\mu\text{m}$  thick samples of Teflon and Kapton under similar irradiation conditions (beam energy = 11.7 keV and electron flux  $\sim 1 \text{ nA/cm}^2$ ). It should be noted that due to geometrical factors that the secondary yield is not an absolute calibration and further experimental analysis is required.

In figures 5 and 6 the solid circles represent the temporally resolved surface potentials measured with the ESEA for the 125  $\mu\text{m}$  Kapton and Teflon samples. At the end of a run the samples are discharged by back filling the vacuum chamber to 200 Torr with dry nitrogen. Subsequent charging runs indicate that the surface is almost completely discharged by this process.

A computer run was made for a Teflon sample for irradiation conditions that correspond to the experimental conditions (beam energy = 11.7 keV and electron flux =  $0.96 \text{ nA/cm}^2$ ). A one-dimensional parallel plate geometry was used to calculate the surface to substrate capacitance ( $0.74 \times 10^{-9}\text{F}$ ). The backscatter yield was calculated to be a constant value equal to ten percent of the incident electron flux. The secondary yield was chosen to conform to data of Wall et al (ref. 3). The time-resolved surface potentials generated by the computer code are represented by the dashed curve in figure 5.

#### DISCUSSION OF RESULTS

The comparison of experimentally measured surface voltages with the theoretically predicted values in figure 5 reveals good agreement. The observation that the equilibrium voltage is approximately  $1800 \pm 125 \text{ V}$  less than the beam voltage is consistent with the measurements of others and is also consistent with the explanation that the charging ceases when the secondary emission coefficient is unity (at the second cross-over point). Although the equilibrium current is buried in the noise and cannot be readily measured with the present technique the upper limit on the conductivity approaches the bulk conductivity value presented in the literature (ref. 4). The surface voltage measurements on Kapton (figure 6) reveals a larger equilibrium current and hence larger conductivity. In both the Teflon and Kapton measurements, the initial slope of the charging voltage curves (figure 5 and 6) are proportional to the ratio of the initial charging current to the calculated capacitance ( $i_c/C$ ).

The experimental results were compared with simple one-dimensional

capacitor models to evaluate the relative importance of various material characteristics on the charging results. For Teflon, the bulk conductivity was ignored and the surface voltage was calculated from the relation

$$v(t) = \frac{1}{C} \int_0^t i_c dt$$

where the charging current,  $i_c$ , was taken to be the central disc current. The results are shown as the curve in figure 5. The good agreement with the measured results demonstrates that bulk conductivity and radiation induced conductivity are relatively unimportant in the non-penetrating beam situation presented here. The measurements further establish the ESEA as a suitable non-perturbing method of measuring time dependent surface voltages for relatively slowly varying conditions. For Kapton, a leaky capacitor model was used to compute the surface voltage from the relation

$$v(t) = \frac{1}{C} \int_0^t \left[ i_c(t') - \frac{1}{RC} \int_0^{t'} (i_c(t'') - \frac{v(t'')}{R}) dt'' \right] dt'$$

where the sample resistance was experimentally determined from the equilibrium charging current and surface voltage. The results obtained by approximating  $v(t'')/R$  by the equilibrium value are presented in figure 6 along with the experimental points. The relative good agreement shown there demonstrates the importance of dielectric conductivity on the charging characteristics of Kapton.

## CONCLUSIONS

Measurements of charging voltage and charging currents have been made on dielectric samples irradiated by a monoenergetic electron beam. A guard ring sample mounted together with a transparent grid in front of the sample surface has been utilized to reduce the fringing fields, edge leakage currents and beam divergence effects to insure a one dimensional geometry. Comparison of experimental results with the prediction of a numerical model which takes secondary emission and subsurface charge dynamics into account reveals good agreement for 125  $\mu\text{m}$  Teflon samples irradiated by  $\sim 1 \text{ nA/cm}^2$  11.7 keV electron beam. Secondary electron emission is the important factor determining the surface voltage with bulk resistivity and radiation induced conductivity relatively unimportant. A one-dimensional capacitor model appears to represent the charging characteristics very well.

Measurements on Kapton samples are in relatively good agreement with a one-dimensional leaky capacitor model. The results reveal the more important effect that bulk conductivity has on the charging characteristics of Kapton. Calculations for Kapton using the numerical model are underway.

The good agreement between the theoretical calculation and experimental measurements establish the ESEA as a satisfactory instrument for measuring time dependent surface voltages at irradiation levels of  $\sim 1 \text{ nA/cm}^2$ . The agreement also indicates that leakage currents and fringing field effects at sample edges have been minimized.

#### REFERENCES

1. Gore, J. V., Communications Research Center, Ottawa, Ontario, Canada.
2. Meulenberg, A., Jr., Private Communication.
3. Wall, J. A., Burke, E. A. and Frederickson, A. R., "Results of Literature Search on Dielectric Properties and Electron Interaction Phenomena Related to Spacecraft Charging," Proceedings of the Spacecraft Charging Technology Conference, C. P. Pike and R. R. Lovell, AFGL-TR-77-0051/ NASA TMX-73537 (1977), Pg. 569.
4. DuPont Technical Information Bulletin T-4D.

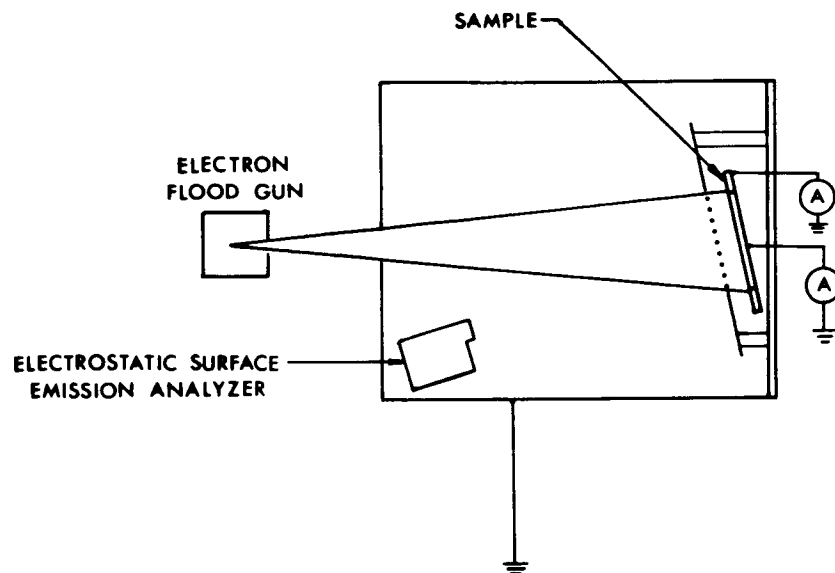


FIG. 1. EXPERIMENTAL SYSTEM

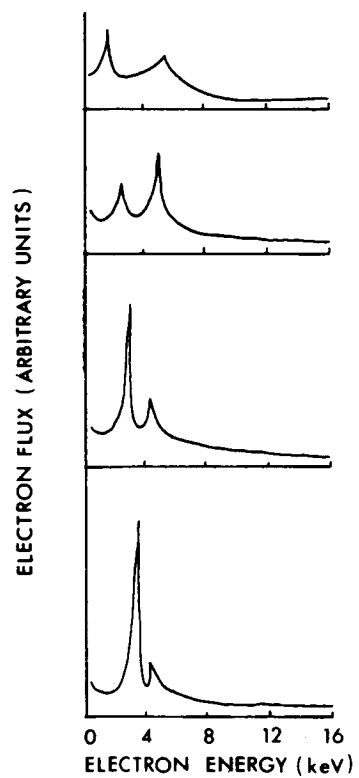


FIG. 2. ELECTRON ENERGY SPECTRA AT DIFFERENT TIMES DURING CHARGING.

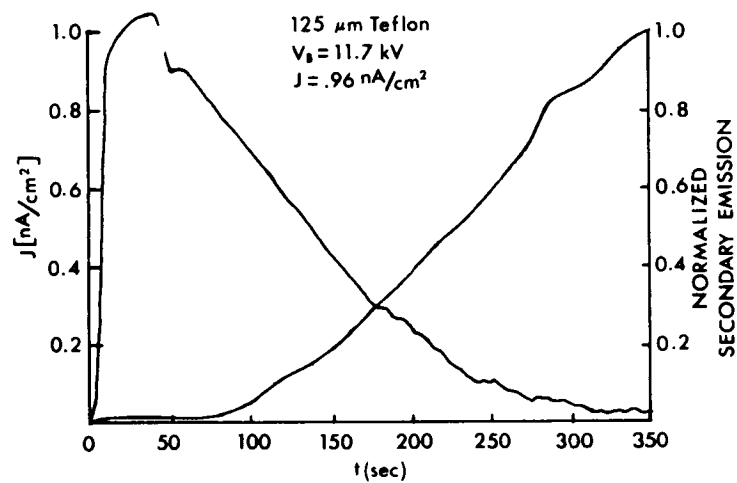


FIG. 3. CURRENT TO CENTRAL DISC AND SECONDARY ELECTRON EMISSION ON IRRADIATED TEFLON.

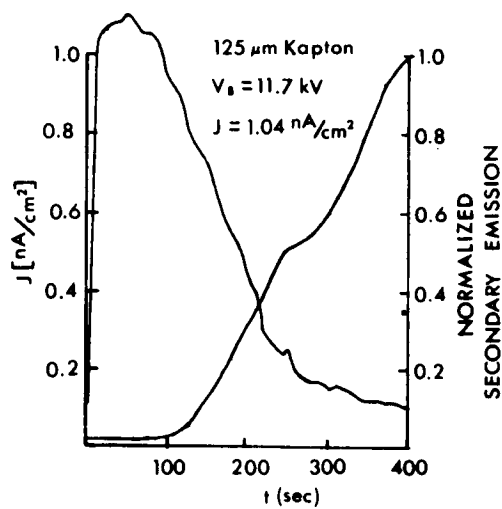


FIG. 4. CURRENT TO CENTRAL DISC AND SECONDARY ELECTRON EMISSION ON IRRADIATED KAPTON.

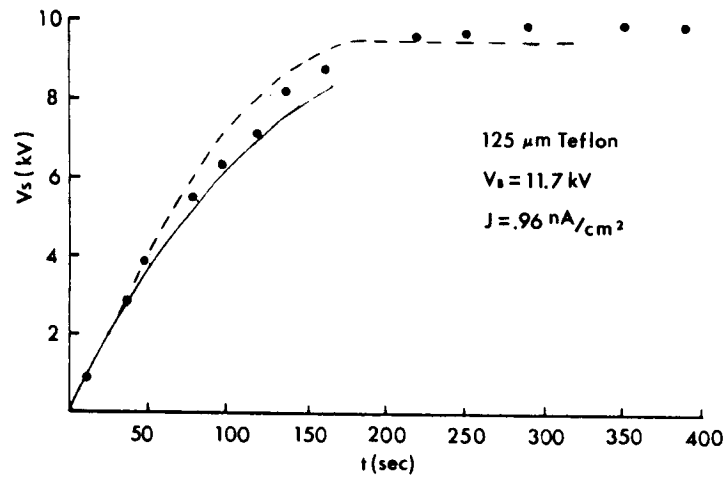


FIG. 5. SURFACE VOLTAGE ON IRRADIATED TEFLON WITH EXPERIMENTAL POINTS DENOTED BY DOTS, NUMERICAL MODEL CALCULATIONS BY DASHED CURVE, AND CAPACITOR MODEL CALCULATIONS BY SOLID CURVE.

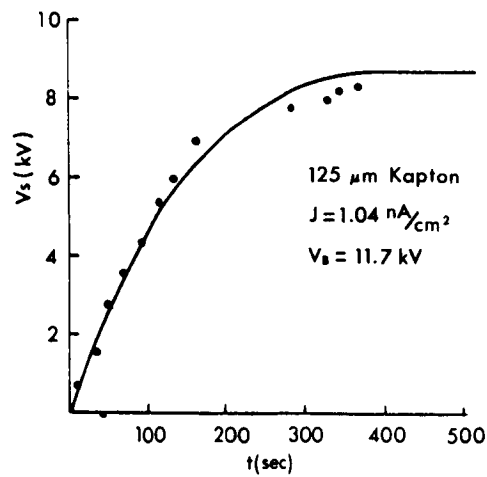


FIG. 6. SURFACE VOLTAGE ON IRRADIATED KAPTON WITH EXPERIMENTAL POINTS DENOTED BY DOTS AND CAPACITOR MODEL CALCULATIONS BY SOLID CURVE.



## ROLE OF ENERGETIC PARTICLES IN CHARGING/DISCHARGING OF SPACECRAFT DIELECTRICS\*

J. B. Reagan, R. W. Nightingale, E. E. Gaines,  
R. E. Meyerott, and W. L. Imhof  
Lockheed Palo Alto Research Laboratory

### SUMMARY

The role that energetic particles in the substorm plasma have on the charging and discharging of typical dielectric layers used on spacecraft has been investigated using spectra and pitch angle distributions measured in situ on the SCATHA spacecraft prior to and during a few kilovolt differential charging event in eclipse conditions on 28 March 1979. The particle spectra have been input to deposition codes that determine the dose rate as a function of depth in kapton and teflon layers used in the SSPM experiment on SCATHA. The calculated ambient dose rates of a few rads/sec throughout the bulk of the sample are sufficiently high that radiation damage levels can be reached on the time scale of 1 year. Surface dose is a factor of 100 higher. Bulk conductivity profiles have been obtained from the dose rates using empirical relationships available in the literature. The radiation-induced bulk conductivities calculated at the peak charging time are found to be smaller than the intrinsic dark conductivity range of solar-conditioned kapton but higher than the corresponding value for teflon. The radiation-induced surface conductivities in both materials are significantly higher than their intrinsic values. It is concluded that in this event the surface potentials of both materials were determined primarily by the current density carried by the electrons in the energy range  $< 30$  keV and that radiation-induced bulk conductivity changes were not important for kapton but may be for teflon. It is further concluded that surface charging occurred when the spectrum hardened and a corresponding larger fraction of the charging current density was carried by higher energy electrons. The measured charging spectrum in this event is within a factor of 5 of the maximum allowable trapping limit according to experimental verifications of the Kennel-Petschek theory. It is proposed that the charging current density at this limit, in conjunction with material properties, will directly determine the maximum possible surface potential in eclipse conditions. Based on the measured potential across the SSPM kapton sample in this event, the maximum likely surface potential to be encountered in a substorm having similar spectral characteristics has been estimated.

### INTRODUCTION

The purpose of this paper is to assess the role that the energetic portion of the substorm plasma has on the charging/discharging of spacecraft dielectric materials such as kapton and teflon. It is a well established fact that the most severe charging of spacecraft operating at high altitudes occurs in the magnetic midnight-to-dawn time sector where substorms are highly prevalent and

---

\* Work performed under ONR contract N00014-76-C-0444.

where spacecraft at times can be eclipsed from solar illumination. At these times the electron plasma is characterized by a harder and more intense than normal spectrum, i.e., the number density of energetic electrons ( $\geq 1$  keV) is increased over ambient conditions. The role that these energetic electrons play in dielectric surface charging through enhancement of bulk conductivities or to the generation of internal electrical discharges through charge buildup and subsequent dielectric breakdown are important issues that have not been adequately addressed for the actual substorm environment. A large body of data exists in the literature on this subject (see Ref. 1) but at electron irradiation levels that are typically several orders of magnitude higher than the substorm environment. Hence the results obtained in those cases are not directly applicable to the substorm case.

Recently Wall et al. (Ref. 2) performed an excellent parameterization of dielectric properties and electron interaction phenomena related to spacecraft charging. Frederickson (Ref. 3) and Summerfield (Ref. 4) have also reported recent work in this area. The measured plasma characteristics and the parameterization of Wall et al. have been used in this paper to evaluate the radiation-induced conductivity in an actual eclipse charging event experienced on 28 March 1979 by the Satellite-Surface-Potential-Monitor (SSPM) on the SCATHA (P78-2) spacecraft as reported by Mizera (Ref. 5). The electron and proton spectra before and during this charging event were measured on SCATHA with a variety of plasma instruments. These spectra have been input to computer deposition codes that determine the ionization rate and hence dose rate profiles in 127 micron (5 mil) thick samples of kapton and teflon that are used in the SSPM. The radiation-enhanced conductivity levels were then determined using available empirical relationships between dose rate and conductivity. These values have been compared to typical intrinsic dark conductivities for kapton and teflon as measured in the laboratory and, in the case of kapton, in orbit with the SSPM experiment.

From the measured electron spectra, the current densities have also been determined as a function of particle energy and evaluated in light of the measured charging potentials on the SSPM samples. It will be shown that the measured electron flux at the peak of this event was within a factor of 5 of the maximum trapping limit set by experimental verification (Ref. 6 and 7) of the Kennel-Petschek theory (Ref. 8). It is proposed that this self-limiting process will determine the maximum charging current density and hence, in conjunction with the material properties, the magnitude of the charging potential that a dielectric can experience in the space environment. The maximum potential to which the SSPM kapton sample would ever likely charge in eclipse conditions during a substorm having an electron population with similar spectral parameters but at an intensity determined by the measured Kennel-Petschek stable-trapping limit (Ref. 6) has been estimated. Knowledge of these limits and measurements of the spectral hardness parameter in the substorm environment can therefore be used to guide laboratory testing and computer modeling of the spacecraft charging phenomena.

#### EXPERIMENTAL DATA

The SCATHA (P78-2) spacecraft, which is in a near-equatorial 24-hour orbit having an apogee of 43,192 km and a perigee of 27,517 km, contains a variety of

plasma diagnostic and engineering experiments to study the spacecraft charging phenomena. A complete description of the P78-2 mission is provided in Reference 9. At 1637 UT on 28 March 1979, after the SCATHA spacecraft had been in eclipse for some 19 minutes, the kapton, quartz fabric and teflon samples in the SSPM experiment experienced charging to -2100, -1000 and -2000 volts, respectively, below spacecraft ground (Ref. 5). The charging characteristics of the kapton sample located on the bellyband of the spinning spacecraft (~1 RPM period) are shown in the top panel of Figure 1. The behavior of the energetic electron environment before and during this charging event is shown in the lower panels of Figure 1. The electron data were obtained with the Lockheed SC-3 experiment which measures electrons in several energy channels between 47 and 4970 keV. The SC-3 experiment is described in detail in References 9 and 10. The higher energy electrons measured in this experiment provide excellent tracers of the geomagnetic field behavior before and during substorms.

The time interval marked "A" centered at 1510 UT in Figure 1 represents the ambient flux levels prior to the sequence of the occurrence of the substorm, eclipse and the charging of the samples. It should be noted that the spacecraft at this time was in the pre-magnetic-midnight time period (22 MLT) at a magnetic L-shell of 6.7 and below the magnetic equator by 18 degrees. At 1520 UT the energetic electrons at all energies began to decrease precipitously by almost three orders of magnitude prior to the substorm. The period marked "B" in Figure 1 centered at 1615 UT represents a depressed flux situation in which the corresponding plasma current density is inadequate to charge the spacecraft despite its entry into eclipse at 1618 UT as indicated. That is, the current density incident on the spacecraft at this time was sufficiently low that it could be adequately compensated by the current density being emitted from the spacecraft through backscattering and secondary emission and significant charging was not required to maintain overall current balance.

At 1600 UT the Boulder index lists the occurrence of a substorm according to ground-based magnetometer records but the flux increase indicating the onset of the substorm effect at the SCATHA satellite did not occur until 1630 UT. Note that at this time the spacecraft is on the magnetic shell  $L = 7.2$  at 2340 MLT and had been in eclipse for 12 minutes. The occurrence of eclipse and the timing of the substorm is coincidental. As the energetic electron flux increased rapidly at all energies up to a few MeV, the kapton sample on the spacecraft bellyband began to charge above ambient at 1637 UT and reached a maximum value of -2100 volts with respect to the spacecraft body by 1641 UT, a charging period of 4 minutes. The period marked "C" in Figure 1 represents the plasma conditions at this peak time of the charging event. The plasma intensity stayed high during the remainder of the eclipse period. As the spacecraft returned to sunlit conditions at 1716 UT the surface voltage on the SSPM discharged to the ambient state. Note the temporary reduction of the energetic electrons at the umbral exit and the subsequent return to the maximum levels. Whether this is a temporal coincidence or the result of the redistribution of the entire plasma environment around the spacecraft at the time of solar illumination is not known.

## PARTICLE SPECTRA

The electron and proton spectra during the three periods identified in Figure 1 were measured over a broad energy range with a variety of instruments on SCATHA. For this study the lower and higher energy portions of the electron spectrum were obtained from the SC-2 experiment (courtesy of Dr. J. F. Fennell, The Aerospace Corporation) and from the Lockheed SC-3 experiment, respectively. Both experiments are located on the body of the spinning spacecraft. The pitch angle distributions measured with the SC-3 instrument at these times indicate a near-isotropic situation with the exception of a narrow but relatively empty loss cone. For treatment of the dielectric samples on the spinning portion of the spacecraft, spin-averaged flux intensities are the most relevant and have been used in this study. Figure 2 shows the resultant electron spectra obtained between 20 eV and 3000 keV, a dynamic range of 5 decades in energy and 11 decades in intensity. The ambient condition "A" exhibits a high intensity of low energy electrons. During the substorm precursor period "B" the lower energy fluxes decrease but the striking feature is the precipitous decrease of some 3 orders of magnitude in the flux at energies  $> 1$  keV. At the time of sample charging, "C", the lower energy portion of the spectrum is decreased over an order of magnitude as a result of the negative barrier potential on the spacecraft body and dielectrics during this time. The energetic portion of the spectrum ( $> 5$  keV) becomes more intense than that under ambient conditions. Thus, the electron plasma can be characterized as hotter than normal.

The proton spectra at the three corresponding times are also shown in Figure 2. The lower and higher energy portions were obtained from the Lockheed SC-8 experiment (courtesy of Dr. S. K. Kaye) and the SC-2 experiment (courtesy of Dr. J. Fennell, The Aerospace Corporation), respectively. The protons also exhibit a marked decrease during the substorm precursor period "B". It should be noted that overall proton flux is one to two orders of magnitude less than the electron flux at energies  $< 10$  keV.

## DOSE RATES

The electron and proton spectra shown in Figure 2 were input to two deposition programs available at Lockheed. The ion-pair production rate due to electron deposition in a simulated SSPM sample consisting of a 127 micron (5 mil) layer of kapton ( $C_{22}H_{10}N_2O_4$ )<sub>n</sub> followed by a 76 micron (3 mil) layer of silver epoxy and a 51 micron (2 mil) layer of copper, was obtained with a computer code called AURORA which solves the Fokker-Planck steady-state diffusion equation (Ref. 11). With this code the scattering and diffusion of electrons through the various layers are properly tracked and the energy loss rate (dose rate) and current density crossing each layer in the material are calculated. A similar calculation was performed for a teflon layer ( $C_2F_2$ )<sub>n</sub> of the same thickness. The ion-production rates in kapton corresponding to the three electron spectra are shown in Figure 3 based on the assumption that 30 eV of energy loss is required to create each ion-pair. The ionization rates are very high in the first 5 to 10 microns of the material near the surface. The bulk ionization throughout the remainder of the sample is relatively uniform and about 2 orders of magnitude lower than near the surface. The peak substorm flux, case "C", results in the highest ionization rates throughout the material.

The proton spectra were input to a code called PROTON (Ref. 12) which determined the ionization losses due to coulomb collisions in the kapton. The results of this code for the three cases are also shown in Figure 3. Except for the first few microns near the surface and in the pre-substorm case "B", the electron induced ionization dominates over the proton induced ionization by approximately two orders of magnitude and hence is potentially more important in altering the bulk conductivity properties of the material.

The dose rates corresponding to the calculated ionization rates are also shown in Figure 3. Near the surface the dose rates are in excess of 100 rads/sec. If period "A" is representative of ambient conditions over a year in the orbit, then this rate corresponds to an accumulated annual surface dose of over 3000 megarads. Such radiation levels are extremely damaging to dielectric materials such as teflon and hence the surface properties of these samples should be degraded after a year or so in orbit. The bulk material dose rate of a few rads/sec results in an annual dose of 63 megarads, a level that is also of some concern to the bulk properties of such materials as teflon.

#### BULK CONDUCTIVITIES

The dose rates shown in Figure 3 have been used with the formalism reported in References 2 and 13 to obtain the radiation-induced conductivities. Basically, the radiation-induced conductivity,  $\sigma_R$ , can be quantitatively related to the dose rate,  $\dot{D}$ , by two material dependent parameters, as follows:

$$\sigma_R = k \dot{D}^N \quad (1)$$

where  $k$  is called the coefficient of radiation-induced conductivity and  $N$  is a value that lies between 0.5 and 1.0. For this study  $N$  has been chosen to be 1.0 and hence represents the maximum possible conductivity value. The values of  $k$  for both teflon and kapton vary widely and hence we have used the range of values cited in Reference 2 in our calculations.

Figure 4 shows the radiation-induced conductivity profiles derived in this manner for the "B" and "C" time periods as a function of the kapton and teflon thickness. The electron and proton dose rates have been summed in obtaining Figure 4. The ambient "A" period was not plotted because it significantly overlapped the "C" data. The intrinsic dark conductivity ranges for both kapton and teflon are also shown against which the radiation-induced conductivity can be compared. An intrinsic bulk dark conductivity in a dielectric is a difficult parameter to define. Virgin kapton when exposed to solar illumination exhibits as much as a four order of magnitude increase in its bulk conductivity and even retains up to a three order of magnitude higher conductivity after being returned to the dark for several hours (Ref. 14). The actual bulk conductivity of  $4.5 \times 10^{-16}$  Siemen (S)-cm<sup>-1</sup> measured on SCATHA with the SSPM kapton sample at the time of peak charging in this event (Ref. 5 and personal communication, P. F. Mizera, 1980) is shown as Item 1 in Figure 4. Also shown are the intrinsic bulk dark conductivities for kapton taken from References 15 (Item 2) and 14 (Item 3). For teflon, which has a much lower bulk dark conductivity than kapton, the intrinsic values were obtained from References 1 (Item 4) and 14 (Items 5 and 6). Adamo and Nanevich (Ref. 14) report a value

of  $2.2 \times 10^{-18} \text{ S-cm}^{-1}$  for a 127 micron (5 mil) sample of FEP teflon at a surface potential of -1700 volts. Van Lint et al. (Ref. 1) gives a value of  $3 \times 10^{-18} \text{ S-cm}^{-1}$  for a teflon sample exposed to a dose rate of 1 rad/sec at 25°C temperature.

The depressed fluxes during the "B" period clearly do not influence the intrinsic bulk dark conductivities of either kapton or teflon except within the first few microns of the surface. Even during the charging period "C", the radiation-induced conductivity in kapton is approximately one- to two-orders of magnitude smaller than the intrinsic bulk dark conductivity, except near the surface. The very high enhanced conductivity within the first few microns of the surface may, however, be important to surface leakage and surface discharge effects in dielectrics. Hence it can be reasonably concluded that in either the ambient or substorm environment the radiation-induced conductivity through the bulk of the kapton sample is significantly less than the intrinsic bulk dark conductivity. The case of teflon is less clear. At the time of peak charging the radiation-induced conductivity is comparable with the intrinsic dark conductivity but the uncertainties in both conductivity values are large. It is fair to conclude that radiation-induced conductivity in teflon is more important than in kapton and may have an effect on the surface charging potential depending upon the detailed history of the sample.

#### CHARGING CURRENTS

Since enhancement of the bulk conductivities of kapton and teflon does not appear to be the dominant factor in determining the magnitude of the surface charging potential in this event, another key parameter, the charging current density, has been examined. From Figure 2 it is evident that the dominant charging current is carried by the electrons. In Figure 5 the integral electron current density greater than energy E is shown as a function of E for the three periods during this event.

During the ambient period "A" the charging current density of ~50-60 picoamps/cm<sup>2</sup> is carried principally by electrons with energy < 1 keV. At these energies the secondary emission coefficient of teflon is > 1 (Ref. 2) and the surface can adequately balance the incident current without charging to any significant voltage, even in eclipse. During the depressed period "B" the current density is again carried by low energy electrons and because the magnitude is low, the dielectric surface can easily balance the incident current through secondary emission.

During the main portion of the substorm, the current density begins to be carried by higher energy electrons in the several kilovolt range. The relatively flat curve of current density vs. electron energy up to a few kilovolts is probably due to the fact that the entire spacecraft body at this time in eclipse is charged negatively to several kilovolts. The spacecraft therefore acts as a retarding potential barrier to incident electrons up to several kilovolts. At this time the kapton and teflon samples charged to -2000 volts with respect to this negatively charged spacecraft. At 2 keV energy the current density is ~40 picoamps/cm<sup>2</sup> and higher than the corresponding density in the ambient case "A" at this energy. At 2 keV the secondary emission coefficient of teflon is unity, that is, an electron is

emitted from the surface for every incident electron (Ref. 2). Thus, the incident current is effectively self-balanced by secondary emission from the surface up to an energy of 2 keV in the incident spectrum.

As the incident electron energy increases above 2 keV the secondary emission coefficient drops below unity and charging will have to occur. With the onset of surface charging, a current will be conducted through the sample to the spacecraft. The magnitude of this steady-state conduction current,  $i$ , will be equal to  $\sigma V/d$  where  $\sigma$  is the bulk conductivity,  $V$  is the charging potential and  $d$  is the sample thickness. The bulk conductivity is a fairly strong function of the electric field above a few kilovolts (Ref. 2) as well as a function of other environmental factors such as temperature, solar illumination and particle radiation.

The steady-state surface charging potential with respect to the spacecraft will be determined by the position along the "C" curve in Figure 5 where the current density incident on the surface is just equal to the sum of the secondary emission and backscattered current leaving the surface and the conduction current through the sample. For teflon, the conduction current should be approximately equal to the integral current density given in Figure 5 greater than an energy of  $V + 2$  keV. Below this potential the current density is balanced by secondary emission. The magnitude of  $V$  can be determined approximately from

$$V = \frac{d}{\sigma} i_{V+2 \text{ keV}} \quad (2)$$

Thus, the magnitude of the surface potential is directly related to the shape of the incident electron spectrum. As the spectrum becomes harder in the crucial 2 to 30 keV region, the surface potential must become more negative to retard the incident current density to the point where it just equals the bulk conduction current plus the secondary emission. There is a compensating feature in that as  $V$  increases linearly, the bulk conductivity increases faster than linear at potentials above 2000 volts (Ref. 2). The surface potential will therefore not need to rise linearly with increasing current density in order to satisfy Equation 2.

Of interest is the maximum potential to which a dielectric surface can charge in eclipse conditions. Dielectric breakdown of the material may well be the practical limit but the magnitude of the available charging current is the fundamental limit. It is proposed that there is a natural self-limit to this charging current in the magnetospheric substorm. According to the Kennel-Petschek theory (Ref. 8) the trapped electron flux on a magnetic field line can increase to a limit at which instabilities set in. Whistler waves which grow as a result of the instability interact with the trapped electrons resulting in the alteration of their pitch angle motion such that precipitation into the atmospheric loss cone occurs. Baker et al. (Ref. 6) established this limit for the geosynchronous orbit ( $L = 6.6$ ) at a flux of  $5 \times 10^7$  electrons/cm<sup>2</sup>-sec-sr<sup>-1</sup> for energies  $> 30$  keV. In case "C" on 28 March 1979 the integral flux  $> 30$  keV is  $\sim 1 \times 10^7$  electrons/cm<sup>2</sup>-sec-sr<sup>-1</sup>. Hence, the substorm conditions on this day were probably within a factor of 5 of the maximum possible current density. If we assume a substorm condition having this maximum intensity and the same spectral characteristics as period "C", the limiting curve shown in Figure 5 is

obtained. This curve will not be highly valid at energies below  $\sim 2$  keV but should be more valid above that energy. Thus, for modeling and laboratory testing purposes charging current densities of 20 to 100 picoamps/cm<sup>2</sup> at energies near 10 keV would represent the range to be expected in the substorm environment.

The SSPM kapton sample charged to a differential potential of -2100 volts in the 28 March 1979 substorm. In the most intense substorm set by the trapping limit and under similar eclipse conditions, the sample would charge to -10,500 volts according to Equation (2), i.e. five times the value in case "C" on the assumption that the conductivity did not change with the impressed electric field. In fact, however, the conductivity of kapton at room temperature would increase by a factor of 30 between a potential of -2100 and -10,500 volts (Ref. 2). The actual surface potential would therefore be significantly less than -10,500 volts because of the increased conductivity and the fact that the integral electron current density to be conducted at -10,500 volts is less than at -2100 volts by approximately a factor of 2. In the case of teflon, the radiation-induced conductivity may be quite important. As the storm intensity increases, the teflon bulk conductivity would also increase in a linear and compensating manner such that the final surface voltage in the limit would be significantly less than -10,500 volts. Therefore, energetic particles can play an important role in determining the surface charging potential of dielectric materials in the geomagnetic substorm environment.

#### REFERENCES

1. Van Lint, V. A.; Flanagan, T. M.; Leadon, R. E.; Naber, J. A.; and Rogers, V. C.: Mechanisms of Radiation Effects in Electron Materials, vol. 1. Published by J. Wiley and Sons, New York, New York, 1980.
2. Wall, J. A.; Burke, E. A.; and Frederickson, A. R.: Results of Literature Search on Dielectric Properties and Electron Interaction Phenomena Related to Spacecraft Charging. In Proceedings of Spacecraft Charging Technology Conference, editors C. P. Pike and R. R. Lovell, report AFGL-TR-77-0051, 24 February 1977.
3. Frederickson, A. R.: Electric Fields in Irradiated Dielectrics. Spacecraft Charging Technology--1978. Proceedings of a conference held at Colorado Springs, 31 October to 2 November 1978, edited by R. C. Finke and C. P. Pike, NASA Conference Publication 2071/AFGL-TR-79-0082, 1979.
4. Summerfield, M.: Space Systems and Their Interactions with Earth's Space Environment. In Progress in Astronautics and Aeronautics, vol. 71, 1980, pp. 386-412.
5. Mizera, P. F.: Natural and Artificial Charging: Results From the Satellite Surface Potential Monitor Flown on P78-2. AIAA-80-0334. Paper presented at the AIAA 18th Aerospace Sciences Meeting, Pasadena, California, 14-16 January 1980.



6. Baker, D. N.; Stauning, P.; Hones, Jr., E. W.; Higbie, P. R.; and Belian, R. D.: Strong Electron Pitch Angle Diffusion Observed at Geostationary Orbit. *Geophys. Res. Lett.*, 6, 205, 1979.
7. Davidson, G. T.; and Sears, R. D.: Pulsating Aurorae: Evidence for Flux Limiting. *Geophys. Res. Lett.*, 7, 185, 1980.
8. Kennel, C. F.; and Petschek, H. E.: Limit on Stably Trapped Particle Fluxes. *Jour. Geophys. Res.*, 71, 1, 1966.
9. Stevens, J. R.; and Vampola, A. L.: Description of the Space Test Program P78-2 Spacecraft and Payloads. SAMS0 TR-78-24, The Aerospace Corporation, El Segundo, California, 31 October 1978.
10. Reagan, J. B.; Nightingale, R. W.; Gaines, E. E.; and Imhof, W. L.: Outer Zone Energetic Electron Spectral Measurements. AIAA-80-0390. Paper presented at the AIAA 18th Aerospace Sciences Meeting, Pasadena, California, 14-16 January 1980.
11. Walt, M.; McDonald, W. M.; and Francis, W. E.: Penetration of Auroral Electrons into the Atmosphere. In *Physics of the Magnetosphere*, editors R. Carovillano and J. F. McClay, Reinhold Publishing Co., New York, New York, 534, 1968.
12. Francis, W. E.; and Bradbury, J. N.: PROTON--A Code for Generating Ionization Production Rates in the Atmosphere Due to Solar Protons and Alpha Particles. Lockheed Report D409467, January 1975.
13. Frederickson, A. R.: Radiation Induced Currents and Conductivity in Dielectrics. *IEEE Trans. on Nuclear Science*, vol. NS-24, No. 6, 1977, p. 2532.
14. Adamo, R. C.; and Nanevich, J. E.: Effects of Illumination on the Conductivity Properties of Spacecraft Insulating Materials. NASA Report CR-135201 by Stanford Research Institute, July 1977.
15. Stevens, N. J.; Staskus, J. V.; Roche, J. C.; and Mizera, P. F.: Initial Comparison of SSPM Ground Test Results and Flight Data to NASCAP Simulations. NASA Report TM-81394. Paper presented at the AIAA 18th Aerospace Sciences Meeting, Pasadena, California, 14-16 January 1980.

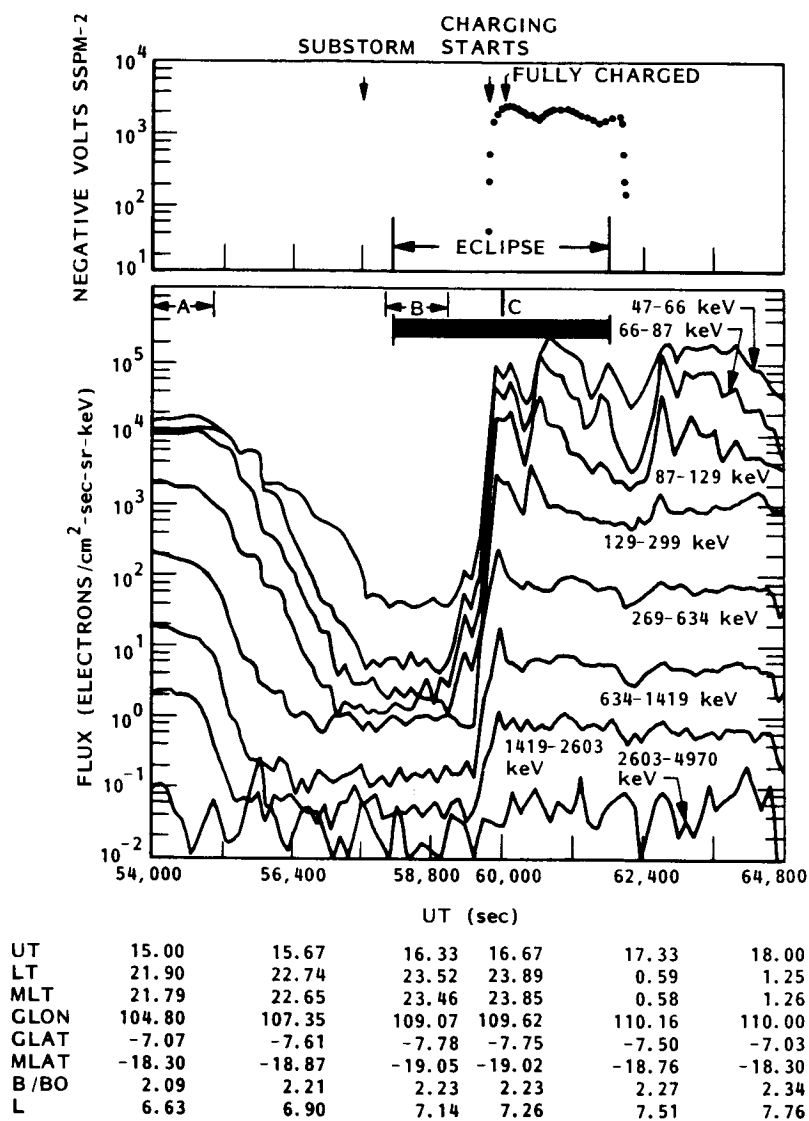


Figure 1. Top Panel. Charging voltage characteristics of the SSPM-2 kapton sample on the SCATHA satellite during eclipse on 28 March 1979. Bottom Panel. Characteristics of the energetic electron environment prior to, during and after the eclipse and charging event as measured with the Lockheed SC-3 experiment on SCATHA.

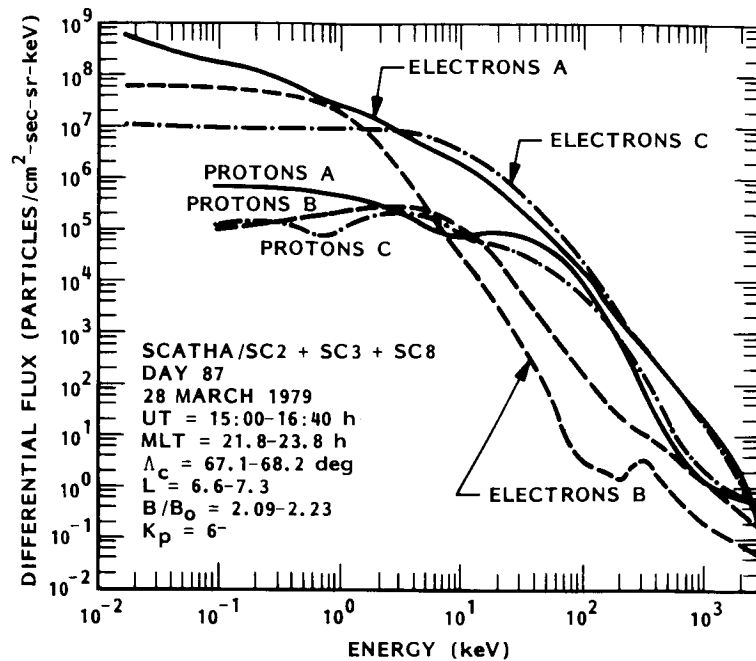


Figure 2. The electron and proton spectra measured on the SCATHA satellite during the three intervals indicated in Figure 1.

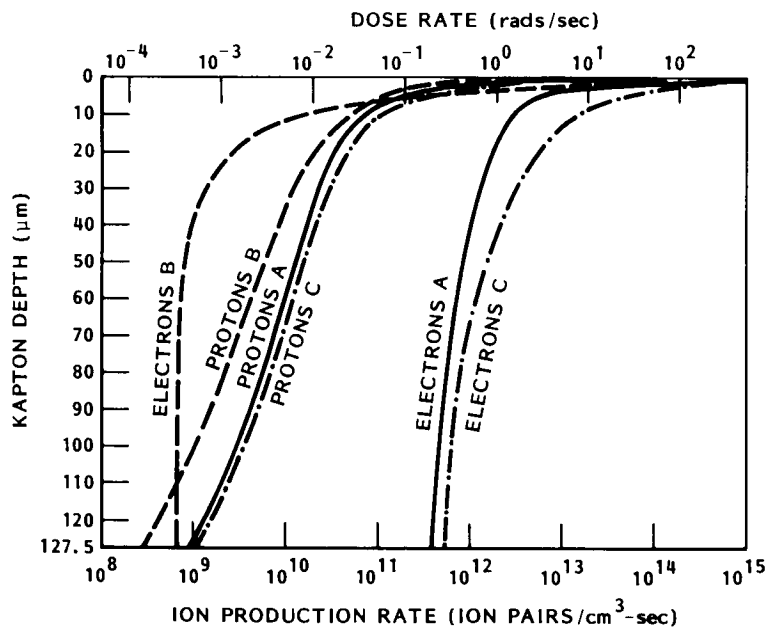


Figure 3. The ion production rate (bottom scale) and the dose rates (top scale) as a function of depth in the SSPM kapton sample resulting from the electron and proton spectra shown in Figure 2.

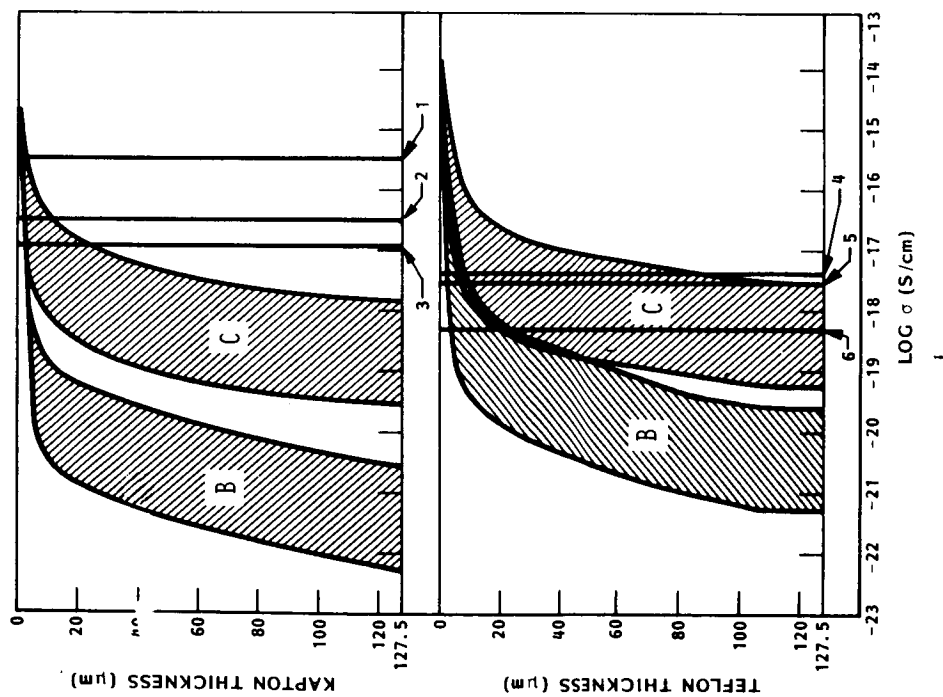


Figure 4. Radiation-induced conductivity as a function of kapton and teflon thickness corresponding to the combined electron and proton ionization created at the two time periods shown. Also shown as vertical lines are several different values of the intrinsic dark bulk conductivity of kapton and teflon cited in the text.

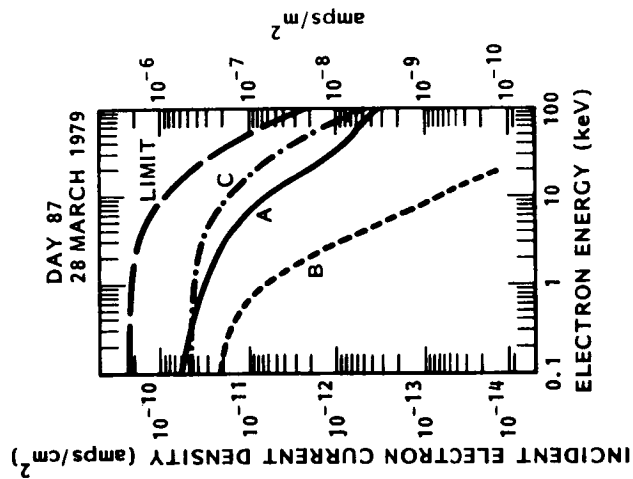


Figure 5. Integral electron current density greater than energy  $E$  as a function of  $E$  for the three spectra cited in the text. Also shown is the expected maximum limit to the substorm charging current density based on experimental verification of the Kennel-Petschek theory.

## **ELECTRON PENETRATION OF SPACECRAFT THERMAL INSULATION\***

**Walter L. Powers, Barbara F. Adams, and George T. Inouye**  
**TRW Defense and Space Systems Group**

### **ABSTRACT**

The International Solar Polar Mission spacecraft is designed to use Jupiter's large mass to project it into an orbit perpendicular to the ecliptic plane to enable its onboard scientific experiments to collect data over the north and south poles of our sun. The spacecraft will approach as close as 5 or 6 Jupiter radii during the critical day of maximum orbit change and must be designed to survive the high electron flux surrounding the planet.

Most of the electrons striking the spacecraft will be stopped within the various materials and produce an increasing negative potential and possibly hazardous electric fields, except for a few electrons of extremely high energy which pass on through and those which are sputtered off as secondaries and those which are repelled by the increasing negative potential. If the electrons deposited in insulators produce electric fields which exceed the dielectric strengths, i.e., fields of the order of  $10^6$  volts/cm, then undesired internal discharging can occur. When energetic electrons penetrate or are stopped in a nonconductor they reduce its bulk electrical resistivity by increasing the number of electron-hole carriers rendering it more of a semiconductor, a phenomena known as radiation induced conductivity. This then permits more of the electrons to flow through the dielectric toward nearby conductors and away from the regions of high deposited electron density, thereby reducing the accompanying electric field and perhaps avoiding any troublesome arcing and flashovers.

In this study we have taken the external thermal blanket to be 13 mils of polyethylene which has known range and stopping power as a function of electron energy, applied the most recent omnidirectional peak Jovian electron flux at 5 Jupiter radii, calculated the electron current penetrating the thermal blanket and allowed this to impinge on a typical 20 mil polyethylene insulator surrounding a wire. The radiation dose rate to the insulator is then calculated and the new electrical conductivity found. The results demonstrate that the increased electronic mobility is sufficient to keep the maximum induced electric field two orders of magnitude below the critical breakdown strength.

### **CALCULATIONS**

A thermal blanket 13 mils thick consisting of 22 layers of Sheldahl, kapton, mylar, teflon, and vacuum deposited aluminum is approximated in this study by a 13 mil layer of polyethylene. The polyethylene parameters used in this calculation are: a dielectric constant of 2.3, a density of 0.92

---

\*This work supported in part under NASA Contract No. 955500.

gram/cm<sup>2</sup>, a volume resistivity of 10<sup>17</sup> ohm-cm, and a dielectric strength of 0.5 x 10<sup>6</sup> volts/cm.

Figure 1 displays the electron range in polyethylene as a function of electron energy plotted from data in Reference 1. For a 13 mil or 0.033 cm. thickness we find that electrons with energies below 0.16 Mev are stopped within the thermal blanket. In this study we are concerned with the electrons which penetrate this blanket and reach a typical insulated wire within the spacecraft; the insulation around this wire is taken to be polyethylene with a thickness of 20 mils or 0.051 cm. We find from Figure 1 that electrons with energies greater than 0.29 Mev pass on through this 0.051 cm. of insulation.

Figure 2 illustrates the total stopping power in polyethylene as a function of electron energy plotted from data in Reference 1. The electrons with energies between 0.16 Mev and 0.29 Mev which are deposited in our 20 mil insulator of interest lose an average of 2.6 Mev/cm.; therefore, they impart an energy to this dielectric equal to their initial energy minus the energy they lost while traversing the 13 mils of thermal blanket. This average 0.22 Mev electron loses an average of 2.6 Mev/cm. times 0.033 cm. or 0.086 Mev traversing the thermal blanket, and has remaining 0.22 Mev minus 0.086 Mev yielding 0.134 Mev for deposit in our inner insulator. The electrons having energies greater than 0.29 Mev which pass through our inner dielectric lose approximately 2.2 Mev/cm.; therefore, they impart 2.2 Mev/cm. times 0.051 cm. for 0.112 Mev per electron to the polyethylene.

Figure 3 gives the Jovian electron omnidirectional integral peak flux as a function of energy at a distance of 5 Jupiter radii plotted from data in Reference 2. This omnidirectional flux needs to be divided by 4 to obtain the correct number crossing unit surface per second according to Reference 3. Values from Figure 3 are 2.8 x 10<sup>8</sup> electrons/cm<sup>2</sup>-sec at 0.16 Mev and 1.7 x 10<sup>8</sup> electrons/cm<sup>2</sup>-sec at 0.29 Mev. After appropriately dividing by the necessary 4, these fluxes become 7.0 x 10<sup>7</sup> electrons/cm<sup>2</sup>-sec at 0.16 Mev and 4.2 x 10<sup>7</sup> electrons/cm<sup>2</sup>-sec at 0.29 Mev.

The rate of electron density deposited in the inner insulator is (7.0 - 4.2) x 10<sup>7</sup> e-/cm<sup>2</sup>-sec = 2.8 x 10<sup>7</sup> e-/cm<sup>2</sup>-sec. This is multiplied by the electronic charge of 1.6 x 10<sup>-19</sup> coulomb to yield a current density of 4.5 x 10<sup>-12</sup> amp/cm<sup>2</sup>. These 2.8 x 10<sup>7</sup> e-/cm<sup>2</sup>-sec which stay in the insulator impart an average energy of 0.134 Mev per electron for a product of 3.75 x 10<sup>6</sup> Mev/cm<sup>2</sup>-sec. The 4.2 x 10<sup>7</sup> e-/cm<sup>2</sup>-sec of higher energy electrons which penetrate the inner insulator lose an energy of 0.112 Mev per electron for a product of 4.7 x 10<sup>6</sup> Mev/cm<sup>2</sup>-sec. This total of 8.4 x 10<sup>6</sup> Mev/cm<sup>2</sup>-sec is converted to a dose rate by using the identity 1 rad ≡ 6.25 x 10<sup>7</sup> Mev/gram to give:

$$(8.4 \times 10^6 \text{ Mev/cm}^2\text{-sec})(1 \text{ rad-gm}/6.25 \times 10^7 \text{ Mev}) \\ \times (1 \text{ cm}^3/0.92 \text{ gm})(1/0.051 \text{ cm}) = 2.9 \text{ rad/sec}$$

The radiation induced conductivity is calculated using

$$\Delta\sigma = qK_T\mu\dot{D} = 5 \times 10^{-17} \dot{D}$$

from Reference 4, where  $q$  is the electronic charge of  $1.6 \times 10^{-19}$  coulomb,  $K$  is the density function for electron-hole pairs of  $3 \times 10^{13}$  pairs/cm<sup>3</sup>-rad,  $\tau$  is the state lifetime of  $10^{-11}$  sec,  $\mu$  is the mobility of  $1 \text{ cm}^2/\text{volt-sec}$ , and  $\dot{D}$  is the dose rate in rad/sec. Our typical inner polyethylene insulator has its conductivity changed near Jupiter by the amount

$$\Delta\sigma = 5 \times 10^{-17} \text{ sec/rad-ohm-cm (2.9 rad/sec)} = 14 \times 10^{-17} \text{ ohm}^{-1}\text{-cm}^{-1}$$

The new conductivity is expressed as the sum of the initial and the change yielding

$$\sigma = \sigma_0 + \Delta\sigma = 1 \times 10^{-17} + 14 \times 10^{-17} = 15 \times 10^{-17} \text{ ohm}^{-1}\text{-cm}^{-1}$$

An electrical model is now constructed for the charge density deposited in the insulator and for the equivalent circuit. It turns out that the assumed shape of the charge density doesn't really matter, i.e., it may be an isosceles triangle distribution with the apex at the center of the insulator, or a sinusoidal distribution with the maximum in the center, or a delta function with all charge deposited right at the center. The maximum value of the electric field produced in the insulator is found from Poisson's equation

$$\frac{d^2V}{dx^2} = \frac{dE}{dx} = -\frac{\rho}{\epsilon}$$

to be  $E_{\max}(x,t) = \pm s \rho_{\max}(t)/\epsilon$ , where  $s$  is the insulator thickness and  $\epsilon$  is the insulator permittivity. The equivalent electrical circuit is taken to be an insulator having both capacitance and resistance in parallel, grounded on each side, with half the deposited electron current flowing in each direction as shown in Figure 4. This model becomes

$$J_e/2 = J_R + J_C$$

The resistive current density is given by Ohm's equation

$$J_R(x,t) = \sigma(t)E(x,t) = \sigma s \rho_m(t)/\epsilon$$

The capacitive or displacement current density is given by

$$J_C = dQ/dt \text{ where } Q = \int \rho_m(t)\delta(x-0)dx = s \rho_m(t)$$

This yields

$$J_e/2 = \sigma s \rho_m(t)/\epsilon + s d\rho_m(t)/dt$$

which has the solution

$$\rho_m(t) = \frac{\epsilon J_e}{2\sigma s} (1 - e^{-\sigma t/\epsilon})$$

This is expressed in terms of the maximum electric field as

$$E_m(t) = \frac{J_e}{2\sigma} (1 - e^{-\sigma t/\epsilon})$$

The charging time constant is found by

$$\begin{aligned} \epsilon/\sigma = K\epsilon_0/\sigma &= 2.3(8.85 \times 10^{-12} \text{ coul/volt-m})/(15 \times 10^{-17} \text{ ohm}^{-1}\text{-cm}^{-1}) \\ &\times (1 \text{ m}/100 \text{ cm}) = 1360 \text{ sec} \end{aligned}$$

The maximum obtainable electric field is given by

$$\begin{aligned} E_{\max} &= J_e/2\sigma = (4.5 \times 10^{-12} \text{ amp/cm}^2)/2(15 \times 10^{-17} \text{ ohm}^{-1}\text{-cm}^{-1}) \\ &= 1.5 \times 10^4 \text{ volts/cm} \end{aligned}$$

The equation for the electric field becomes

$$E_m(t) = 1.5 \times 10^4 \text{ volts/cm} (1 - e^{-t/1360 \text{ sec}})$$

This maximum electric field of  $1.5 \times 10^4$  volts/cm is between one and two orders of magnitude less than  $5 \times 10^5$  volts/cm, the dielectric strength of polyethylene; therefore, no electric discharges are expected to occur within the insulation surrounding wires beneath the spacecraft's thermal blanket.

An interesting graph, Figure 5, is produced by plotting the equation for the charging time versus the absorbed current for various values of resistivity

$$t = \frac{\epsilon}{\sigma} \ln (J_e/(J_e - 2\sigma E_m))$$



One can locate the appropriate curve for the new radiation induced conductivity or resistivity, locate the deposited current density and therefore find the time to breakdown which for our particular values gives a time of infinity.

One final interesting conclusion is found by inspecting the maximum electric field that would be produced if there were no radiation induced conductivity, i.e., by using the initial conductivity of  $10^{-17}$  ohm<sup>-1</sup>-cm<sup>-1</sup>

$$E_{\max} = Je/2\sigma = 4.5 \times 10^{-12}/2 (1 \times 10^{-17}) = 2.25 \times 10^5 \text{ volts/cm}$$

This is still less than polyethylene's breakdown strength of  $5 \times 10^5$  volts/cm; therefore, no breakdown would be expected even without the dielectric degradation. Of course, this applies only to insulation beneath the thermal blanket.

#### REFERENCES

1. Berger, Martin J., and Seltzer, Stephen M., Tables of Energy-Losses and Ranges of Electrons and Positrons, National Academy of Sciences, National Research Council Publication 1133, Nuclear Science Series Report No. 39, Studies in Penetration of Charged Particles in Matter, Article 10, 1964, Page 205.
2. Ragsdale, George G., Environmental Design Requirements for the NASA Spacecraft, International Solar Polar Mission, (Draft), Jet Propulsion Laboratory, Pasadena, CA, Appendix B, Nov. 15, 1979.
3. Loeb, Leonard B., The Kinetic Theory of Gasses, Dover Publications, Inc., New York, NY, 1927, Page 42.
4. DASA 1420, Tree (Transient Radiation Effects on Electronics) Handbook, Prepared for Defense Atomic Support Agency by Battelle Memorial Institute, Sept. 1969, Page E-40.

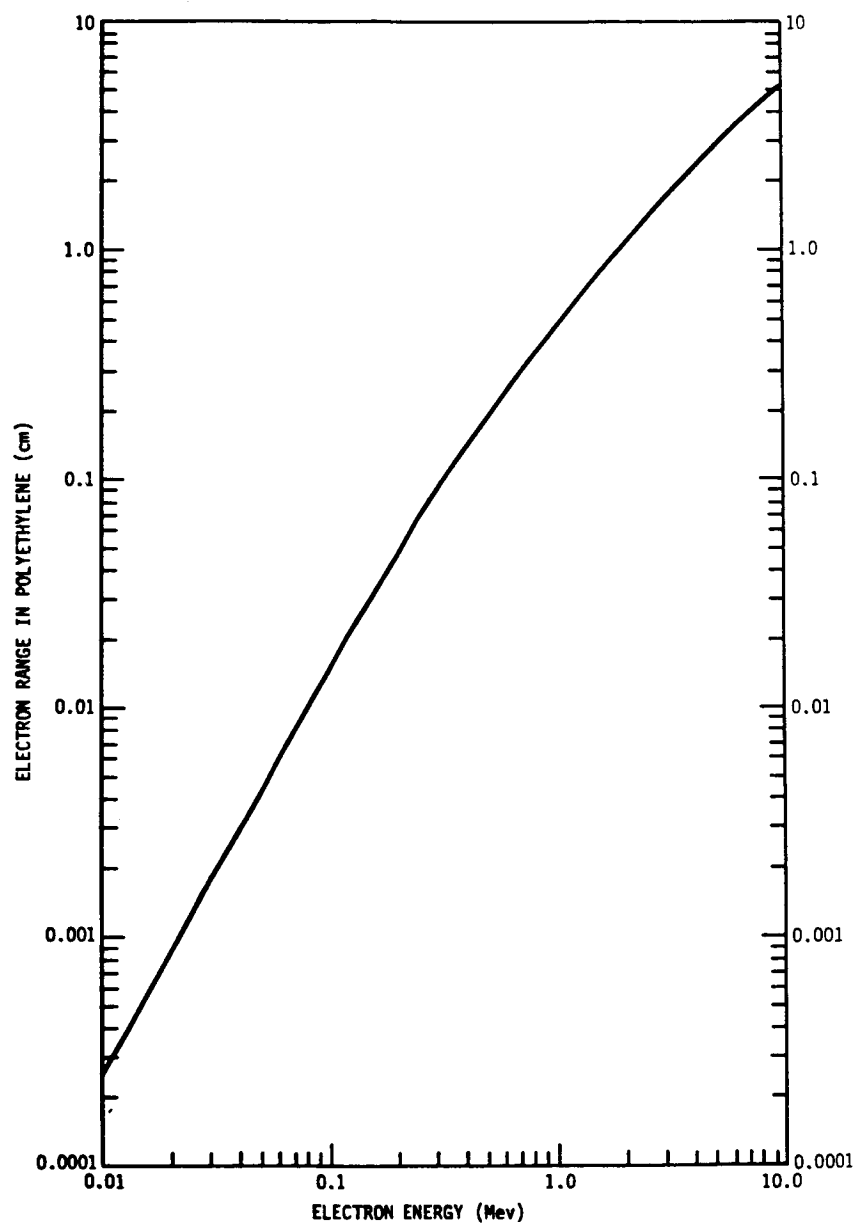


FIGURE 1.

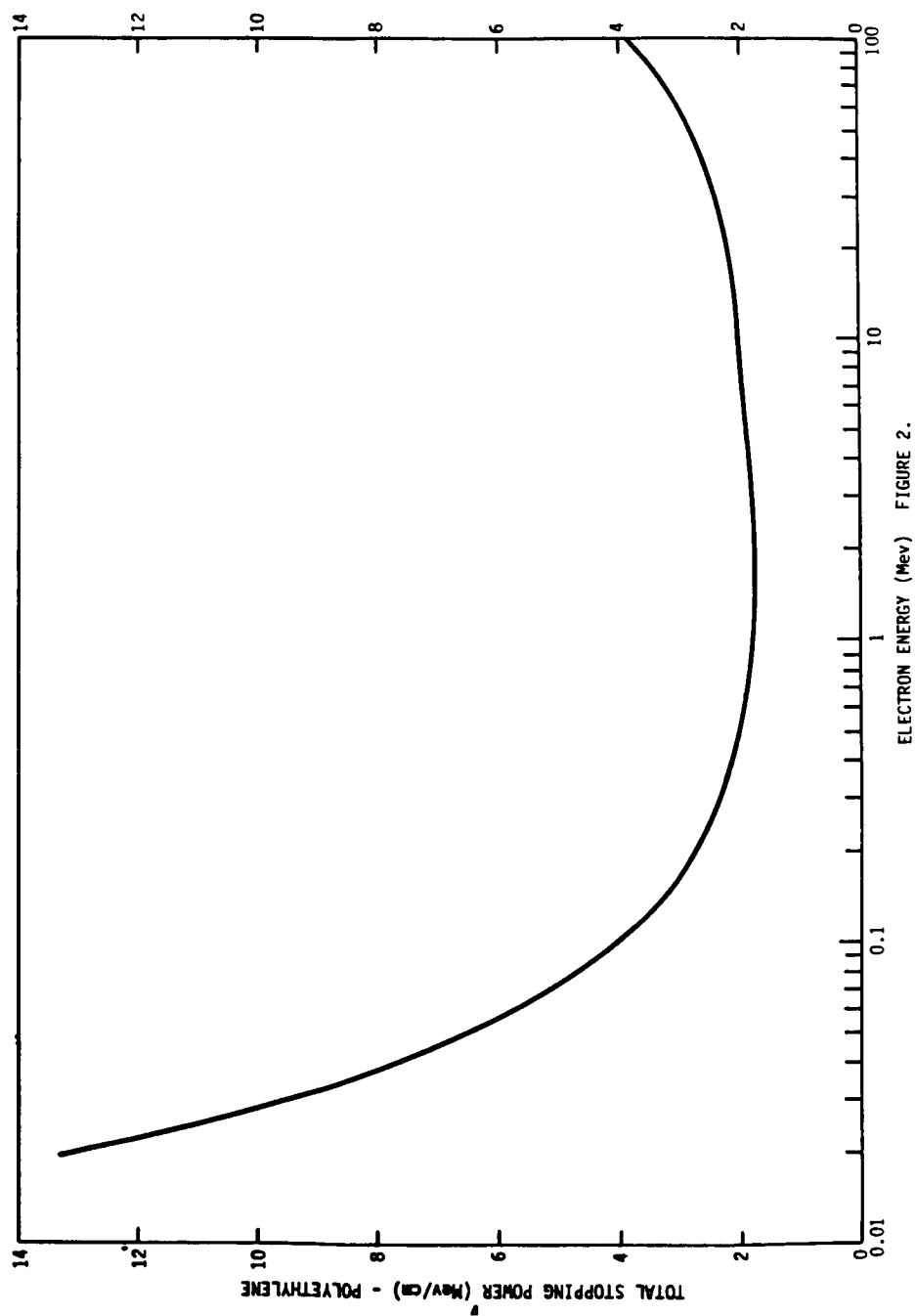
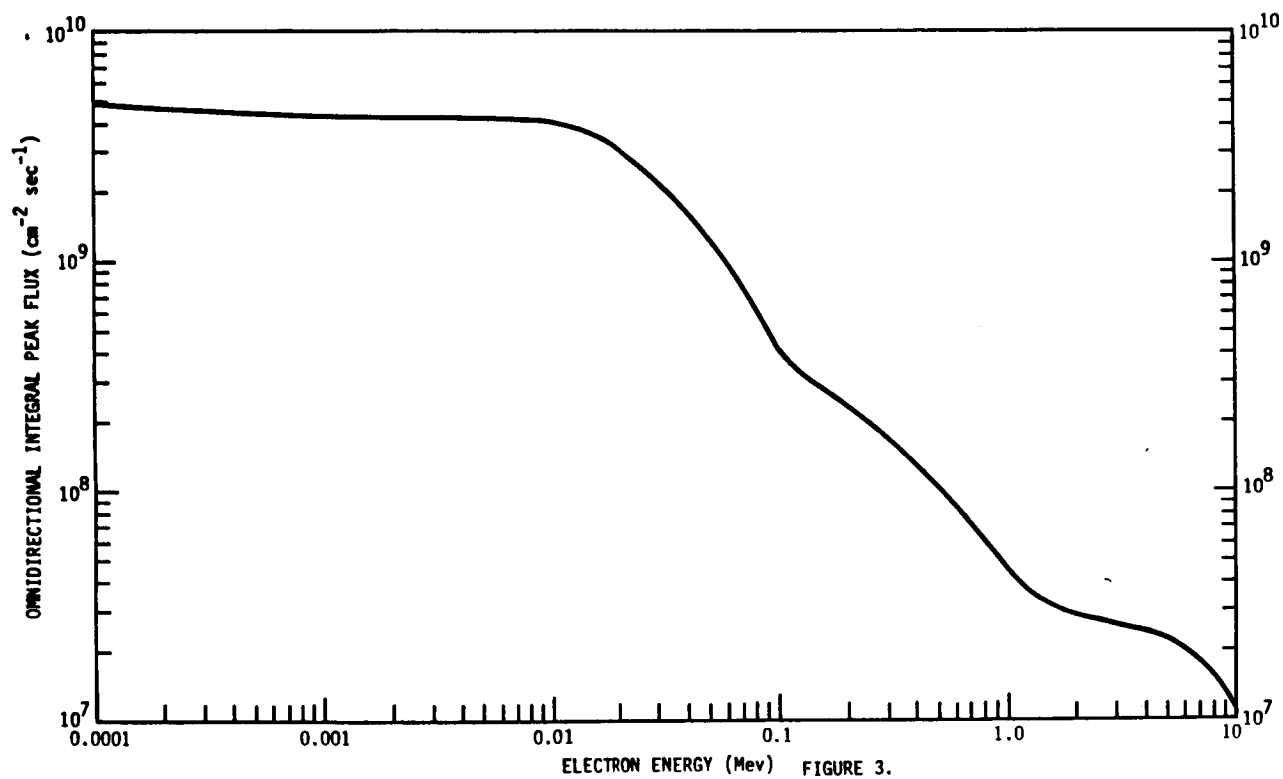
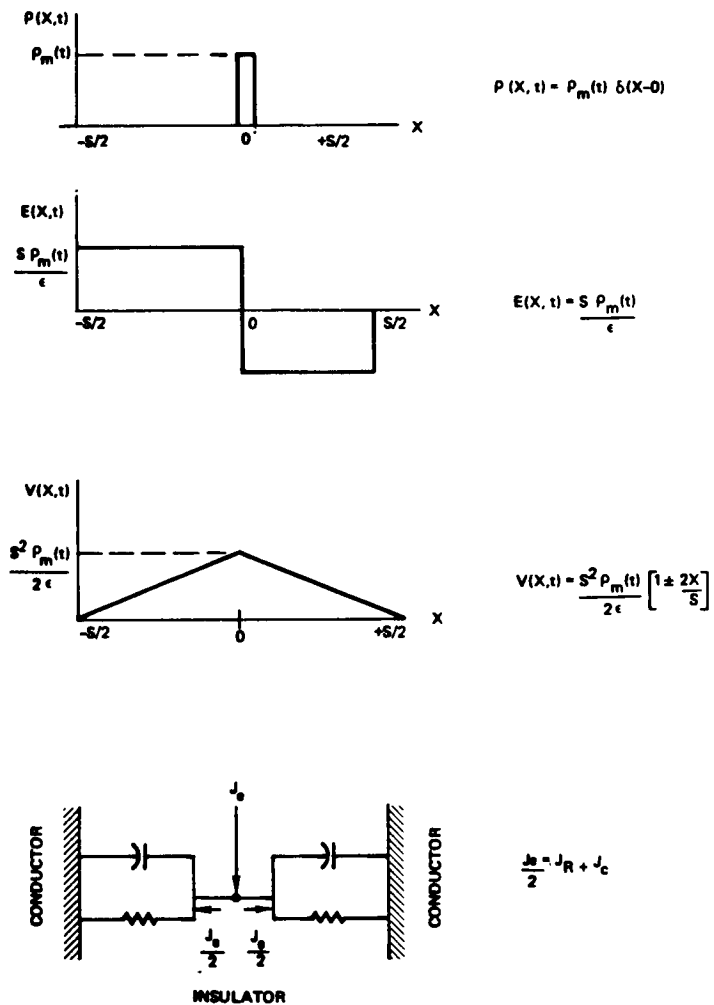


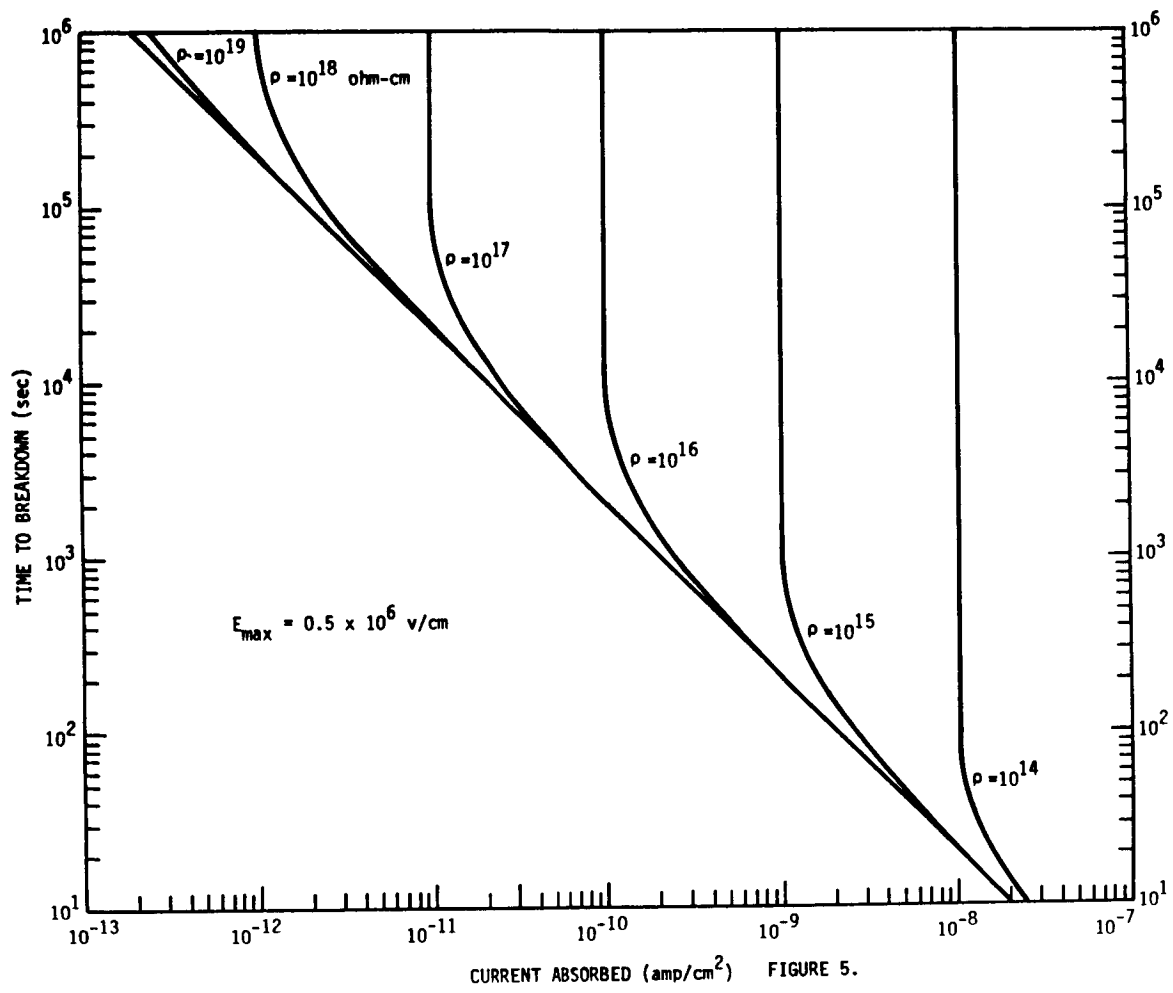
FIGURE 2.





Models for Electron Distribution and Electrical Circuit

FIGURE 4.



# **ELECTROSTATIC DISCHARGING BEHAVIOUR OF KAPTON IRRADIATED WITH ELECTRONS\***

**Derek Verdin  
U.K. Atomic Energy Authority, Harwell**

## **SUMMARY**

The electrostatic charging and discharging of Kapton when irradiated with mono-energetic electrons of 5 to 30 keV energy has been studied. The leakage currents and rates of discharging always increased with the incident electron energy and flux, whereas the surface voltage showed a more complex behaviour depending on the thickness of the material: for the thinner films it exhibited a maximum and then fell at higher energies. The surface voltage, the rate of discharging, and the peak current and total charge flow during a discharge were enhanced as the temperature was decreased from +70°C to -180°C, and were accompanied by a decreasing leakage current. Visible light or the presence of an aluminium coating on the irradiated surface caused reductions in the surface voltage and changes in the discharging characteristics. The results of these investigations are discussed in terms of the leakage currents and the secondary emission of electrons. Photomicrographs taken after irradiation, and photographs of samples during irradiation, have shown good correlations between the positions of light flashes and of pinholes produced by the discharge arcs.

## **INTRODUCTION**

Kapton film is widely used on geostationary satellites as the outer layer of passive thermal control systems, and as a substrate for flexible solar arrays, in which the solar cells are mounted on a single sheet of the polyimide film having an area of several square metres (ref. 1). Since the exposed dielectric can be of large area, is relatively thin, and usually has a conductive backing, large capacitances exist, which under the conditions prevailing in geosynchronous orbit and in the absence of sunlight, can become electrostatically charged during geomagnetic substorms and result in arc discharges.

Many aspects of the charging and discharging of various dielectrics have been reported (ref. 2), but there is a sparsity of data obtained by varying a wide range of irradiation parameters under identical experimental conditions. Such data has been obtained for Kapton as part of a materials characterisation programme, and is reported here to provide additional information for testing the validity of models for the mechanism of dielectric discharging. Very few observations exist of the effect of temperature on the surface voltage and

---

\* This work was sponsored by the Space Department, Royal Aircraft Establishment, Farnborough under Contract A52a/188

discharging activity of Kapton, and this parameter has therefore been studied in some detail. The surface potential of a dielectric material exposed to solar radiation may be largely determined by photoemission of electrons (ref.3) and by thermal effects, however, visible light may make a contribution and the significance of this has been demonstrated in the absence of the other two factors. Conductive coatings such as indium-tin oxide can eliminate the discharging problem with dielectrics (ref.4), and observations of the effect of a conductive (aluminium) coating on the surface voltage and leakage currents in irradiated Kapton have therefore been included in the present study.

## EXPERIMENTAL TECHNIQUE

The equipment used for this work (fig.1) was based on a 0.5 m diameter vacuum chamber, operating at a pressure of  $\sim 2 \times 10^{-7}$  torr, in which samples could be irradiated with mono-energetic electrons at temperatures from 25°C to 75°C, or at about -180°C. The electron energies were in the range 3 to 30 keV, and the beam flux was from 0.02 to 35 nA.cm<sup>-2</sup>. The samples usually consisted of 140 mm diameter circles of Kapton type H film having projections for electrical connections (fig.2). A central current collector (101 mm dia. in "standard" samples) and a concentric guard ring of aluminium were vapour deposited on the lower surface, and subsequently sprayed with an insulating coating. To facilitate heat transfer the samples were secured on the sample holder with a silicone encapsulant (Dow Corning 93-500) used as a low bond strength adhesive. The electron beam uniformity over the irradiated zone of 111 mm diameter was  $\pm 30\%$ .

During irradiation the leakage current from the central collector to earth was measured with an electrometer (Keithley, model 610C), the output of which was displayed on a chart recorder to show the frequency of discharges. The pulse characteristics were monitored with a fast current probe (Tektronix, type P6303) inductively coupled to the lead from the sample to the electrometer. The output of the probe amplifier was displayed on a 100 MHz storage oscilloscope (Tektronix, type 466) so that pulses could be photographed for measurement of peak current, pulse duration, and the area beneath the trace, which gives the total charge flowing during a discharge.

The surface voltage profile of the top surface of the samples was measured during irradiation by a non-contacting electrostatic voltmeter (Trek, model 340HV) equipped with a probe (type 4031S) having a voltage sensing aperture of 0.5 mm diameter. This was swept, about 3 mm above the sample surface, across a diameter of the sample in 12 seconds, and operated at the potential it was measuring, thus avoiding distortion of the surface voltage and the risk of discharges between the probe and the sample. The output of the probe was not affected by the electron beam.

The electromagnetic radiation associated with the current discharges was monitored with a circular loop antenna mounted in the vacuum chamber. The voltage induced in this loop by discharges was displayed on a second identical oscilloscope. For the particular components employed this system gave relative measurements of the electromagnetic signal at 20 MHz.



Visual and photographic observation of samples during irradiation was made through a port in the vacuum chamber.

## IRRADIATION OF KAPTON - RESULTS AND DISCUSSION

### Surface Voltage and Leakage Current

Measurement of voltage profiles across the surface of Kapton during irradiation showed that it required several minutes to attain an equilibrium level at a flux of  $5 \text{ nA.cm}^{-2}$ , and figure 3 shows how the profile changed for 5 keV electrons incident on a sample having a small diameter collector. The equilibrium level was  $\sim 1 \text{ kV}$  below the energy of the incident electrons, and this was also true of the maximum levels attained over the unaluminised areas of the sample with higher energy electrons (fig.3). The surface voltage profiles also show that earthed aluminium on the rear surface of the Kapton lowered the potential of the irradiated surface. The maximum surface voltages attained on unaluminised Kapton and those measured at the centre of standard samples are presented in figure 4 as a function of the incident electron energy and the thickness of the Kapton, for irradiations performed at  $-180^\circ\text{C}$  with a beam flux of  $5 \text{ nA.cm}^{-2}$ . The plots all extrapolate to an intercept which indicates that under certain conditions the surface tends to attain a voltage which is  $1.3 \text{ kV}$  below the energy of the incident electrons.

The leakage current through Kapton to the aluminium collector during irradiation was proportional to the area of this collector from  $8.0$  to  $80.1 \text{ cm}^2$ , and to the incident electron flux up to at least  $35 \text{ nA.cm}^{-2}$ . The surface voltage and the leakage current were reproducible from sample to sample, being reflections of a bulk property of the polymer film. The leakage current was also a function of the energy of the electrons, and it is seen from the data in figure 5 for  $5 \mu$  thick Kapton irradiated at two temperatures that at  $25^\circ\text{C}$  it accounts for essentially all of the incident flux at the highest energy.

The above observations are consistent with a charging mechanism for dielectrics in which the surface voltage attained represents a balance between the incident flux and the loss of electrons by conduction and by secondary emission and backscattering. When there is no aluminium collector present on the lower surface, or for very thick films, conduction is low, and in the absence of light secondary emission plays a decisive role (ref.5). For a surface to attain equilibrium under these conditions with electrons of a given incident energy  $E$ , the secondary emission coefficient  $\delta$  must be unity i.e. one electron leaves for each one arriving at the surface. If  $\delta$  were always  $>1$  or always  $<1$  the surface would charge positively or negatively respectively and could never attain equilibrium.  $\delta$  is a function of the incident electron energy (ref.6) such that it is greater than unity in the range  $\sim 1 \text{ eV} < E < \sim 1 \text{ keV}$ , so that when irradiation of a surface commences with electrons of energy  $E \gg 1 \text{ keV}$  very little secondary emission occurs. However, as the incident electrons are trapped (assuming the dielectric is thick enough) the resulting potential of the surface retards the electrons subsequently arriving and the surface will charge up negatively until its potential reaches a level at which it retards the incoming electrons to an energy for which their secondary emission coefficient is unity.

Davies (ref. 5) showed this energy was 0.9 keV for Kapton at 25°C, and the present results indicate there is very little effect of temperature on the upper threshold for secondary emission, since at -180°C the Kapton surface acquires a voltage which is 1.3 kV lower than the energy of the incident electrons.

The lower resistance of the thinner samples permits higher leakage currents to flow through the polymer, thus providing a second route for electron loss when the lower surface is conductive. Equilibrium is therefore maintained by a decrease in secondary emission,  $\delta$  falls below unity, and equilibrium is established with incident electrons of higher energy. There is therefore less retardation of the incident electrons so that the surface is at a lower potential. However, the variation of resistance with thickness alone cannot account for the differences between the plots in figure 4. The greater penetration of the more energetic electrons during the charging process will presumably result in a radiation-induced contribution to the conductivity which extends to a greater fraction of the thickness of the film at the higher electron energies, thus raising the leakage current (fig.5). The range of 30 keV electrons in Kapton is estimated from electron range data (ref.7) to be 12.3 $\mu$  which represents a penetration of half of the thickness of the 25 $\mu$  film but only 1/10 of that of the thickest film. When the penetration is a significant fraction of the thickness the enhanced conductivity results in even lower secondary emission to maintain equilibrium and so the surface voltage falls at the highest energies.

In the case of the thinnest film (6.9 $\mu$ ) studied, the range of 22 keV electrons is equal to the thickness of the film, and therefore above this energy the surface voltage would be expected to be very low, as was indeed found (fig. 4). These low voltages were accompanied by high leakage currents. With a flux of 5 nA.cm<sup>-2</sup> of 5 keV electrons incident on the film the leakage current at -180°C was 0.3 $\mu$ A, and it reached a level of 0.49 $\mu$ A for electrons having energies of 20 keV or higher. The leakage current therefore rises much more rapidly than in the case of 51 $\mu$  thick Kapton (fig.5), presumably as a consequence of the greater radiation-induced conductivity associated with the higher penetration of the electrons in the thin film.

For low energy (<5 keV) electrons impinging on the thinner films the above conduction effects are negligible since the penetration is low and secondary emission is still the decisive factor; all of the plots in figure 4 therefore approach that for unaluminised Kapton.

On the basis of the above considerations it would appear that the use of the thinnest Kapton films available as the outer component of thermal blankets would facilitate the removal of even the lower energy incident electrons, and result in very low surface voltages with a consequent reduction in susceptibility to dielectric breakdown by arc discharge. This conclusion has recently been reached independently on theoretical grounds by Fellas (ref.8)

## Discharging Behaviour

Electrical discharges were observed when Kapton was irradiated with electrons having an energy exceeding a threshold value. This was about 15keV for 51 $\mu$  thick Kapton at 25°C. The discharges were not of constant size, nor did they occur at regular intervals, so that there were short term variations in the rate of discharging, which fell progressively as irradiation continued (fig.6). A second irradiation of the same sample after 24 hours in vacuum showed continuation of the process i.e. no 'recovery' occurred, and the discharging eventually ceased, presumably as a result of the production of permanent low resistance routes to earth due to repeated dielectric breakdown. This must be at points where discharges have occurred, but it did not cause any significant increase in the leakage current, which remained constant throughout the irradiation, since the electron transport in discharge pulses was only a few percent of the continuous loss by bulk conduction. It is evident from figure 6 that pre-irradiation with electrons of the same (and presumably different) energy can lead to lower discharge rates.

The rate of discharging varied in a non-linear manner with the beam flux (fig.7), presumably because apart from the rate of arrival of electrons at the sample surface other factors control the initiation of discharges and the amount of charge removed in a single event, e.g. variation of the radiation-induced component of the surface conductivity with the incident flux. This figure shows a smooth change in behaviour for a particular sample, but comparison of data from different samples, even when taken from adjacent areas on a roll of film showed discharge rates varying by factors of 2 or 3. This is common for observations on the dielectric breakdown of organic polymers, and is attributed to the fact that the point of breakdown is believed to be an impurity or defect site in the structure (ref.6). The concentration of these defects varies widely across a film, giving local variations in dielectric strength, and consequent variations in discharge rates between samples.

The majority of discharges observed were of the form shown in figure 8. The current rose within about 0.5  $\mu$ sec to a peak which was as high as 20A and then decayed to the level of the leakage current in a period of several  $\mu$ sec. The charge associated with the pulse is given by the area under the curve, and in the example shown (A) it is  $7.6 \times 10^{-6}$  coulomb. Since the corresponding voltage profiles indicated a fall in potential of about 11kV, then the energy associated with this discharge was about 40mJ, which was a typical value for 51 $\mu$  thick Kapton irradiated with 25 keV electrons at -180°C. Many of the current pulses were more complex and exhibited smaller secondary pulses superimposed on the decay of the initial pulse, presumably due to secondary dielectric failure within the area from which the first discharge was collecting electrons. An example of such a discharge is included in figure 8 together with the associated signal induced in the antenna by the electromagnetic radiation. The latter demonstrates the usual decay of the RF signal in about 1  $\mu$ sec, and also that the small subsidiary current pulse shown in figure 8B generated a significant RF signal.

The surface voltage profiles provided an indication of the extent in terms of area and voltage level to which a surface was discharged in a single event.

The scans reproduced in figure 9 were recorded during the irradiation at  $-180^{\circ}\text{C}$  of a standard  $51\mu$  thick Kapton sample with 30 keV electrons at a beam flux of  $5\text{ nA.cm}^{-2}$ . The first scan shows that when the surface was at only about 11.5 kV a discharge occurred which reduced the voltage to zero. Immediate reversal of the probe traverse revealed in the second scan that the whole width of the sample had discharged, and if account is taken of the partial recharging of the surface by the electron beam during the sweep, which was estimated by comparison of these two scans to be at a rate of about 170 V/sec, then the whole sample must have fallen very close to zero volts. The third scan, commenced immediately after a discharge, illustrates the fact that in other cases the full width of the sample discharged, but the surface did not fall below 5kV. The fourth scan shows the result of another common type of discharge which was very localised and reduced the voltage over only a fraction of the Kapton surface. This was towards the edge of the sample which is the region of maximum voltage gradient and where initiation of discharges would be expected. These wide variations in the changes in surface voltage caused by discharges are consistent with the differences which exist between the amounts of charge associated with the individual discharges occurring in a sample under steady irradiation conditions.

The behaviour of the  $25\mu$  thick Kapton differed from that of the thicker films in that the discharge which occurred had almost no influence on the surface voltage, in spite of involving significant amounts of charge. Furthermore the charge associated with the largest pulse observed for each incident electron energy decreased with increase in this parameter, being 29.8, 17.1 and  $3.8 \times 10^{-7}$  C for 20, 25 and 30 keV electrons respectively. It is suggested that these effects result from the greater penetration of higher energy electrons in the thin film due to its lower surface voltage (fig.4), with the consequence that a higher proportion of the electrons become trapped at distances approaching the range of electrons possessing the incident energy. Thus, 30 keV electrons penetrate nearly to the centre of the  $25\mu$  film, and dielectric breakdown in this case will involve only half of the thickness of the Kapton. This will presumably remove fewer electrons as the incident energy is increased since they will be trapped more diffusely in the upper part of the film at the higher energies, and probably only those electrons from the zone near the maximum range will be involved in a discharge. Removal of electrons primarily from the deeper trapping zones would also account for the small changes in surface voltage caused by discharges from the  $25\mu$  film. Moreover, since the breakdown voltage involved would be that of about half of the thickness of the Kapton, then the occurrence of discharges does not contradict the reported dielectric strength of  $\sim 9\text{ kV}$  for  $25\mu$  thick Kapton at  $-180^{\circ}\text{C}$  (ref.9).

With the  $6.9\mu$  thick film the normal type of discharges were observed only with 10 and 15 keV electrons, and they were very small, the charge associated with the largest pulses being 6.9 and  $2.5 \times 10^{-8}$  C respectively. The discharges had no effect on the surface voltage, and presumably occurred at the edge of the central collector, but in the unaluminised annulus, where the voltage was up to 2 kV higher than in the centre of the sample. At higher energies the electrometer recorded no discharges of this type but did show small negative displacements, indicating a change in behaviour when the incident electrons had sufficient energy to penetrate the film completely.

## Influence of Temperature

The temperature at which Kapton is irradiated has a significant influence on its behaviour. When irradiated with 30 keV electrons at a flux of  $5 \text{ nA.cm}^{-2}$  some standard  $51\mu$  thick samples showed no discharges at  $80^{\circ}\text{C}$ , and others gave a maximum rate of only 1 per hour. At  $25^{\circ}\text{C}$ , however, the rate was initially about 2 per minute, while at  $-180^{\circ}\text{C}$  the initial rate had risen to about 4 per minute. Moreover, the charge associated with each pulse was on average several fold greater at  $-180^{\circ}\text{C}$  than at  $25^{\circ}\text{C}$ , and as the irradiation proceeded there was a much slower fall in the rate of discharging at the lower temperature. This is significant since  $-180^{\circ}\text{C}$  is more representative than  $25^{\circ}\text{C}$  in terms of the temperature at which discharging occurs in satellite solar arrays during eclipses.

The volume resistivity of Kapton is greater at lower temperatures (ref.9), and this would be expected to lead to reductions in the leakage currents and increases in the surface voltages as the temperature is reduced. The data in table 1 show that the voltages at the side (unaluminised region) and in the centre of standard  $51\mu$  thick Kapton samples do indeed increase as the temperature is reduced, and at the same time the leakage current falls. However, the decrease in the latter is much smaller than would be predicted from the volume resistivity, which decreases nearly 10-fold between  $25^{\circ}$  and  $70^{\circ}\text{C}$  (ref.9), so that presumably radiation-induced conductivity makes a much greater contribution than ohmic conductivity. Nevertheless the latter probably determines the effect of temperature, since the radiation-induced effect would not be expected to vary with the temperature. The data given in table 1 were measured under conditions where little or no discharging occurred so that the voltages represent equilibrium values rather than the breakdown voltages of the sample.

## Photoconduction Effects

The influence of visible light on the electrostatic behaviour of Kapton was examined by exposing samples to a 15W filament lamp mounted so as to illuminate the whole area of the sample. The glass envelope of the bulb limited the wavelengths of the light emitted to above about 350 nm, and separate tests showed that illumination caused no change in the temperature of the Kapton film, so that there was no thermal contribution to the effects observed.

When unaluminised Kapton which was being irradiated with 20 keV electrons was exposed to visible light there was no change in the surface voltage, which is consistent with the fact that light of these wavelengths causes no photo-emission. However, when Kapton aluminised on the lower surface was illuminated under similar conditions the surface voltage dropped by several kV, and the leakage current was enhanced, the behaviour being illustrated by the data given in table 2. No further changes occurred when the light intensity was increased. On illuminating Kapton the changes in surface voltage and leakage current occurred quite rapidly, within about 1 minute, but although the data shows that the effects were almost completely reversible the recovery when the light was

switched off was much slower, taking up to 20 minutes. These effects presumably result from photoconduction of electrons to the metal layer.

Illumination caused no changes in the rates at which discharges occurred in Kapton samples. However the peak currents in the pulses and the amount of charge associated with each pulse was reduced by a factor of about 2, and this resulted in the surface voltage being quite stable during the period when the light was on. Nevertheless, this voltage was still quite high, at about 9 kV. Moreover, the photoconduction had a progressively smaller effect on the leakage current as its value increased at the higher electron energies.

The observations made in the present work are in accord with the changes in bulk conductivity which Coffey et al (ref.10) found when exposing Kapton to much higher light intensities (2.3 solar constants) from a xenon lamp. They found up to five orders of magnitude increase in the conductivity, caused primarily by radiation having wavelengths from 380 to 680 nm. They also noted that the photoconductivity persisted after the light was extinguished, and attributed this to the fact that the trapping of charge carriers at imperfections is a slow process.

#### Physical Damage Resulting from Discharges

The discharge arcs produced pinholes in the Kapton film, but the first pinhole formed was not the site for all subsequent discharges even over a small area, i.e. when an arc has occurred at a particular point it may leave that area of the polymer with a higher dielectric breakdown strength than an adjacent zone containing some inherent defects in the polymer structure. The discharges were accompanied by visible light flashes, and photographs showed that they occurred exactly at points where pinholes were found and that one or several pinholes may be involved in a particular discharge. Repeated discharging may take place at a given pinhole but not necessarily successively at the same hole. For all of the samples examined the pinholes and other damage occurred within the unaluminised zone or at the adjacent edge of the aluminium collector, indicating that discharges are initiated in those regions where the voltage stress is greatest.

Figure 10 shows details of a pinhole with charring of the polymer and a surrounding network of discharge tracks. More extensive damage arose when discharges occurred in aluminised areas, and figure 11 shows a hole caused by complete vaporisation of Kapton and aluminium due to an arc just within the aluminised collector. The damage seen in these pictures has resulted from discharges of an area of at most  $100 \text{ cm}^2$  and involving  $<0.1 \text{ J}$  of energy. Since the area of dielectric surface on a satellite thermal control blanket can be  $\sim 1 \text{ m}^2$  and on solar arrays several  $\text{m}^2$ , and scaling experiments have shown (ref. 11) that the maximum energy in discharges is proportional to the function (area of dielectric) $^{1.5}$  then it is apparent that discharges of tens of Joules of energy can occur and cause considerable damage to the satellite in addition to giving rise to electrical interference.

## Influence of a Conductive Coating on Kapton

The presence of an earthed aluminium coating on the irradiated surface of 25 or 51 $\mu$  thick standard Kapton samples at  $-180^{\circ}\text{C}$  held the surface potential of the central zone at (or very close to) zero for incident electrons of all energies. The conductive surface layer also completely changed the behaviour in respect of the leakage currents since as the electron energy was increased the total leakage current to the two conductors on 51 $\mu$  thick samples decreased to a limiting value which accounted for about 50% of the incident flux (fig.12). In the case of 25 $\mu$  thick Kapton with aluminium on the upper surface the leakage current was essentially independent of the incident electron energy. These observations are in complete contrast to the progressive increase in leakage current with electron energy for Kapton of either thickness having aluminium on the lower surface only.

With the aluminised top surface near zero potential the impinging electrons are not retarded as they approach it, and they will therefore penetrate further into the film than when the top surface is unaluminised. Nevertheless, for the thinner (25 $\mu$ ) film conduction removes almost all of the incident electrons for all energies, presumably because as the penetration increases with energy the probability of conduction via the lower aluminium coating increases in proportion to the fall in conduction via the top aluminium layer. Thus, 30 keV electrons, having a range in Kapton of 12.3 $\mu$ , will penetrate to the centre of the film and will have similar probabilities of escape to either surface. For lower energy electrons incident on the 51 $\mu$  thick film the penetration will be small and a high proportion of the incident flux can be removed by conduction. However, as the energy, and therefore the penetration, increases the electrons become trapped further from the top aluminium layer and so less conduction to it occurs, and for this thicker film there will be little change in the probability of reaching the lower surface. This qualitative interpretation is in accord with the fact that the leakage current for 30 keV electrons from the 25 $\mu$  thick film is about twice that for the 51 $\mu$  film. At the highest electron energies the leakage current from 'standard' samples of the thicker film exceeds that from samples having an upper aluminium layer, presumably due to the differences in the secondary emission and backscattering from the aluminised and plain Kapton surfaces. Thus, although a metallic layer on the exposed surface of a 25 $\mu$  thick Kapton film can remove most of the incident electrons it is seen that for thicker films it becomes progressively less effective as the incident electron energy is increased.

## CONCLUSIONS

The charging and discharging characteristics of different thicknesses of aluminised Kapton indicate the importance of the degree of penetration of the incident electrons into the film, and the interaction between this factor and the potential acquired by the irradiated surface. The results demonstrate that for Kapton having a conductive coating on the rear surface, films of less than 25 $\mu$  thickness exhibit the minimum susceptibility to electrostatic charging and discharging when exposed to electrons of up to 30 keV energy.

## REFERENCES

1. Treble, F.: The RAE Lightweight Solar Array, RAE Tech.Rep. 73172 (1974).
2. Stevens, N.J.; et al.: Testing of Typical Spacecraft Materials in a Simulated Substorm Environment. Proc. Spacecraft Charging Technol. Conf., AFGL-TR-77-0051, NASA TM X-73537, 1977, pp. 431-457.
3. Rosen, A.: Large Discharges and Arcs on Spacecraft. Astronautics and Aeronautics, June 1975. pp 36-44.
4. Bosma, J.; and Levadou, F.: Electrostatic Charging and Space Materials. Proc. ESA Symposium "Spacecraft Materials in Space Environment", ESA SP-145, 1979, pp. 189-207.
5. Davies, D.K.: Charges and Vacuum Flashover. Nature 262, 1976, p.279.
6. Davies, D.K.: The Charging and Discharging of Spacecraft Dielectrics. Proc. ESA Symposium "Spacecraft Materials in Space Environment", ESA SP-145, 1979, pp. 217-221.
7. Spencer, L.V.: Energy Dissipation by Fast Electrons. N.B.S. Monograph No.1, 1959.
8. Fellas, C.N.: An Arc-Free Thermal Blanket for Spacecraft Use. IEEE 1980 Conf. on Nucl. and Space Radiation Effects. Paper H.9.
9. Technical Information Bulletin H-4. Film Department, Electrical Insulation Products Division. Du Pont de Nemours Inc.
10. Coffey, H.T.; et al.: Photoconductivity of High-Voltage Space Insulating Materials. (Stanford Research Inst., NASA Contract NAS3-18912). NASA CR-134995, 1975.
11. Balmain, K.G.: Scaling Laws and Edge Effects for Polymer Surface Discharges. Proc. Spacecraft Charging Technol. Conf. AFGL-TR-79-0082, 1979. pp. 646-656.



TABLE 1 - EFFECT OF TEMPERATURE ON SURFACE VOLTAGE OF IRRADIATED KAPTON

Electron Energy keV (Beam Flux $5\text{nA}\cdot\text{cm}^{-2}$ )	80°C			25°C			-180°C		
	Voltage at sample edge kV	Voltage at sample centre kV	Leakage current $\text{A} \times 10^{-7}$	Voltage at sample edge kV	Voltage at sample centre kV	Leakage current $\text{A} \times 10^{-7}$	Voltage at sample edge kV	Voltage at sample centre kV	Leakage current $\text{A} \times 10^{-7}$
15	10.3	8.7	2.9	11.1	9.3	2.5	12.5	11.8	1.5
20	9.7	8.2	3.5	11.3	9.1	3.0	14.0	12.4	1.9
25	-	-	-	-	-	-	$\geq 13.4$	$\geq 11.8$	3.0

TABLE 2 - EFFECT OF ILLUMINATION ON IRRADIATION OF KAPTON SAMPLES AT -180°C

Electron energy (Beam flux $5\text{nA}\cdot\text{cm}^{-2}$ )	Unilluminated		Illuminated		Unilluminated		Discharge rate per min.
	Surface voltages* in kV $V_{\text{max}} : V_{\text{min}}$	Leakage current A	Surface voltage in kV	Leakage current A	Surface voltages $V_{\text{max}} : V_{\text{min}}$	Leakage current A	
5	3.7	$5.0 \times 10^{-10}$	3.4	$1.0 \times 10^{-9}$	3.5	$5.0 \times 10^{-10}$	-
10	9.0, 8.2:9.0	$3.0 \times 10^{-8}$	8.3	$1.3 \times 10^{-7}$	9.0, 8.2: 9.0	$3.0 \times 10^{-8}$	
15	11.6, 10.8:10.2	$2.0 \times 10^{-7}$	8.9	$2.6 \times 10^{-7}$	11.6, 10.8:10.2	$1.7 \times 10^{-7}$	0.65
20	12.2, 11.6:10.1	$3.1 \times 10^{-7}$	10.0	$3.5 \times 10^{-7}$	12.3, 11.6:10.1	$2.9 \times 10^{-7}$	1.40
25	11.2, 11.2:9.6	$3.3 \times 10^{-7}$	9.1	$3.9 \times 10^{-7}$	<10.8	$3.5 \times 10^{-7}$	1.44

\* When surface voltage profile is not flat  $V_{\text{max}}$  values are voltages at opposite edges of sample and  $V_{\text{min}}$  is voltage at centre of sample.

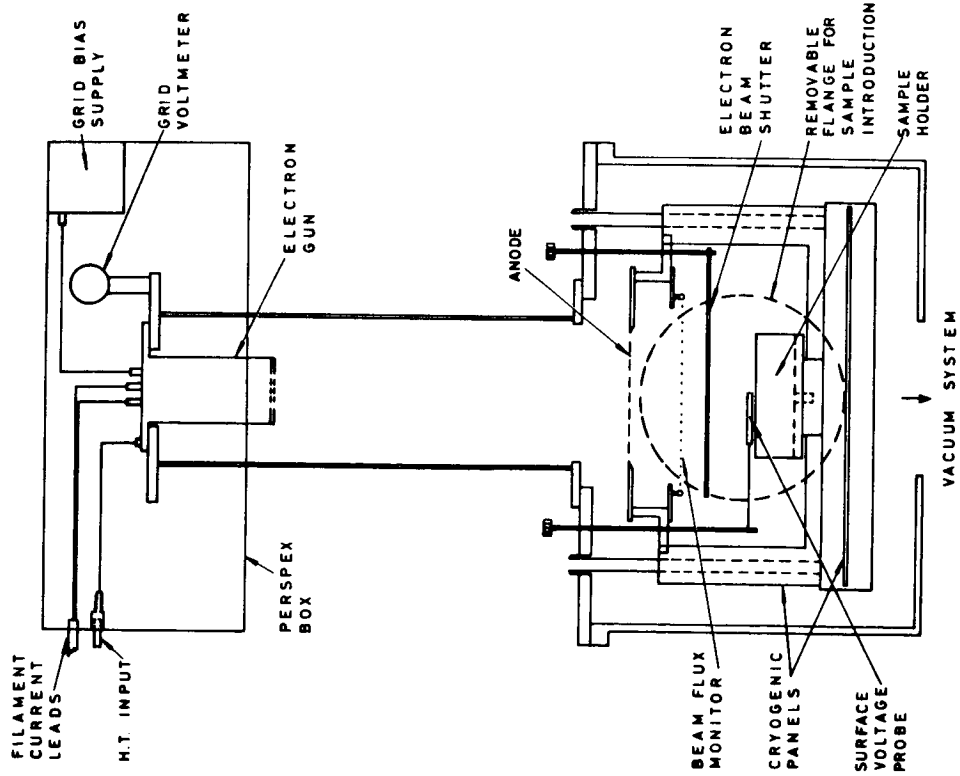


FIGURE 1. IRRADIATION CHAMBER AND ELECTRON GUN ASSEMBLY

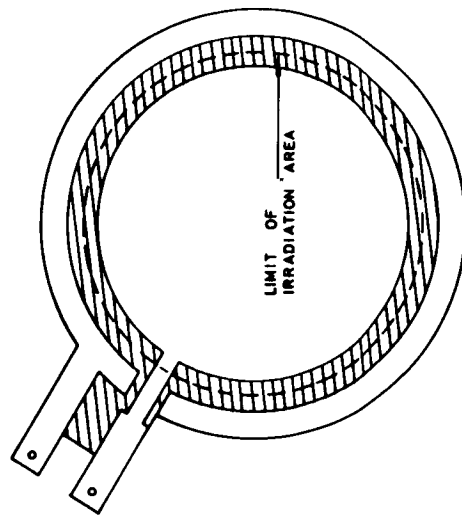
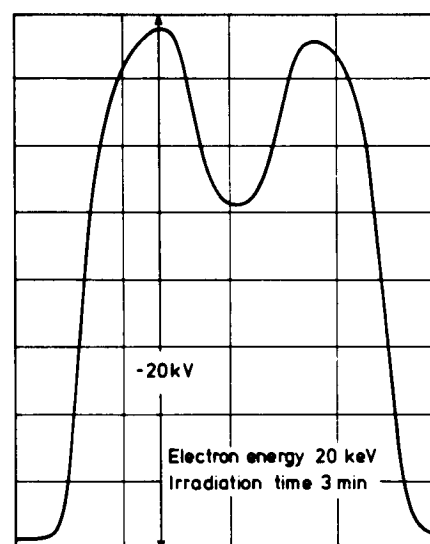
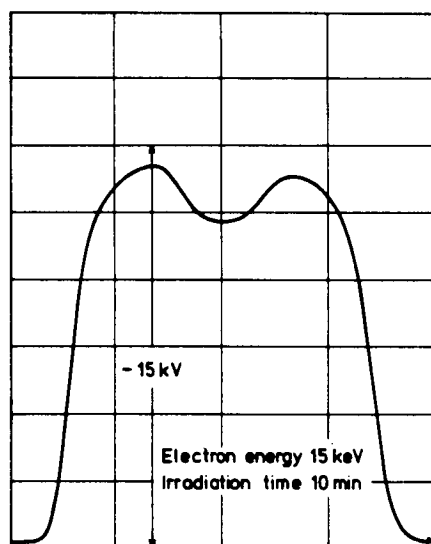
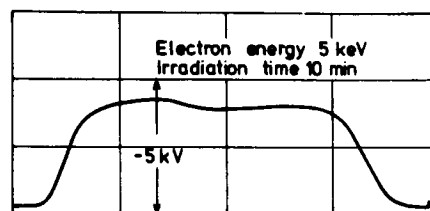
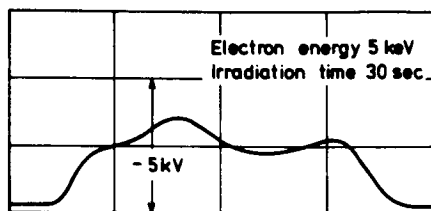


FIGURE 2. "STANDARD" ALUMINISED KAPTON SAMPLE



Kapton thickness  $50\mu$   
Beam flux  $5\text{ nA cm}^{-2}$   
Diameter of irradiated zone 111mm.  
Current collector diameter 32mm

FIGURE 3. SURFACE VOLTAGE PROFILES FOR  
ELECTRON IRRADIATION OF KAPTON.

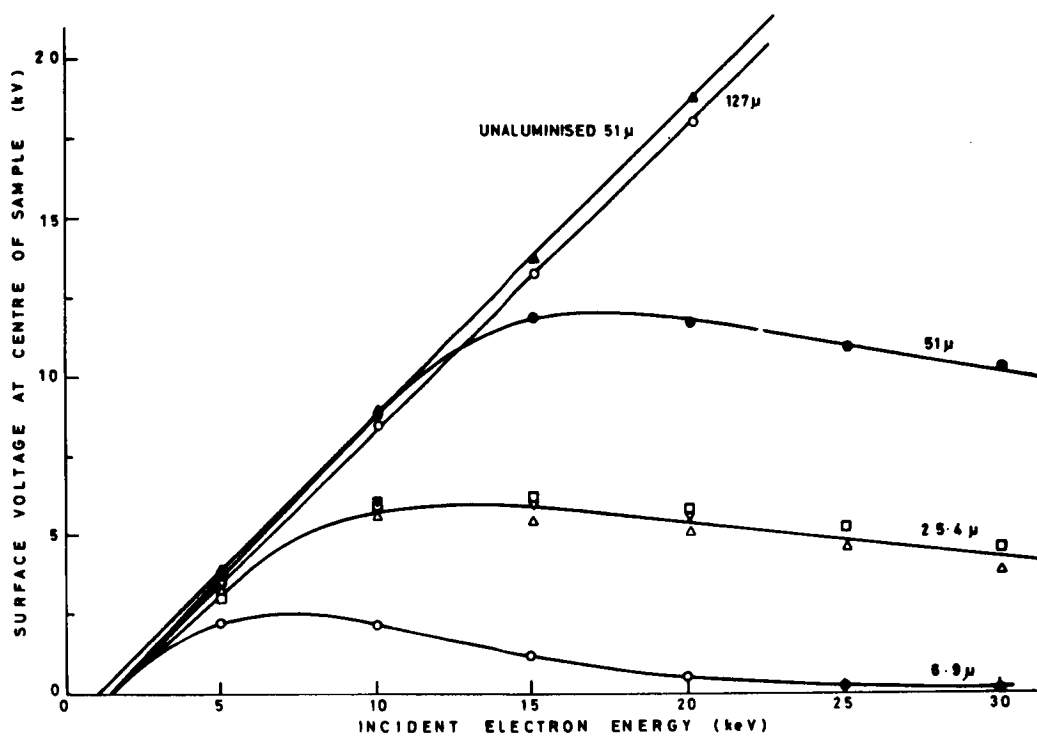


FIGURE 4. SURFACE VOLTAGE AS A FUNCTION OF INCIDENT ELECTRON ENERGY FOR DIFFERENT THICKNESSES OF KAPTON IRRADIATED AT  $-180^{\circ}\text{C}$

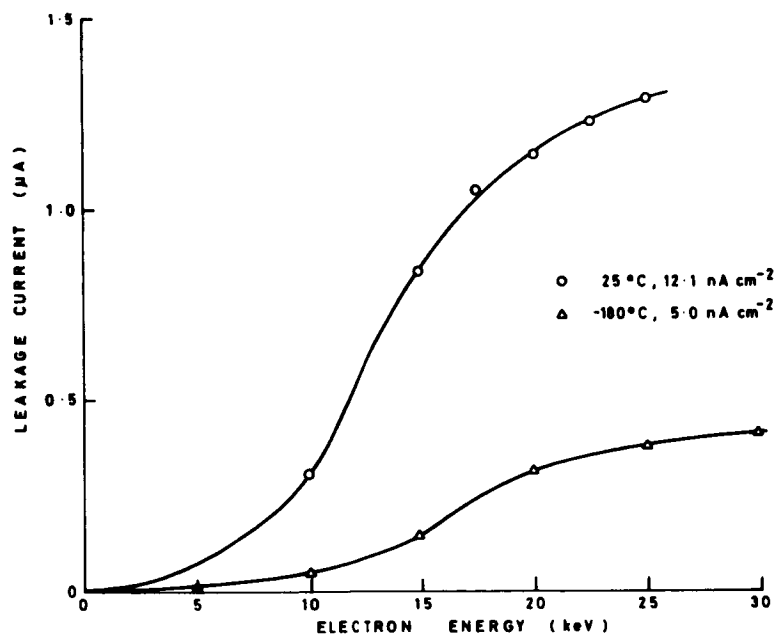


FIGURE 5. VARIATION OF LEAKAGE CURRENT WITH ELECTRON ENERGY FOR  $51\mu$  THICK KAPTON

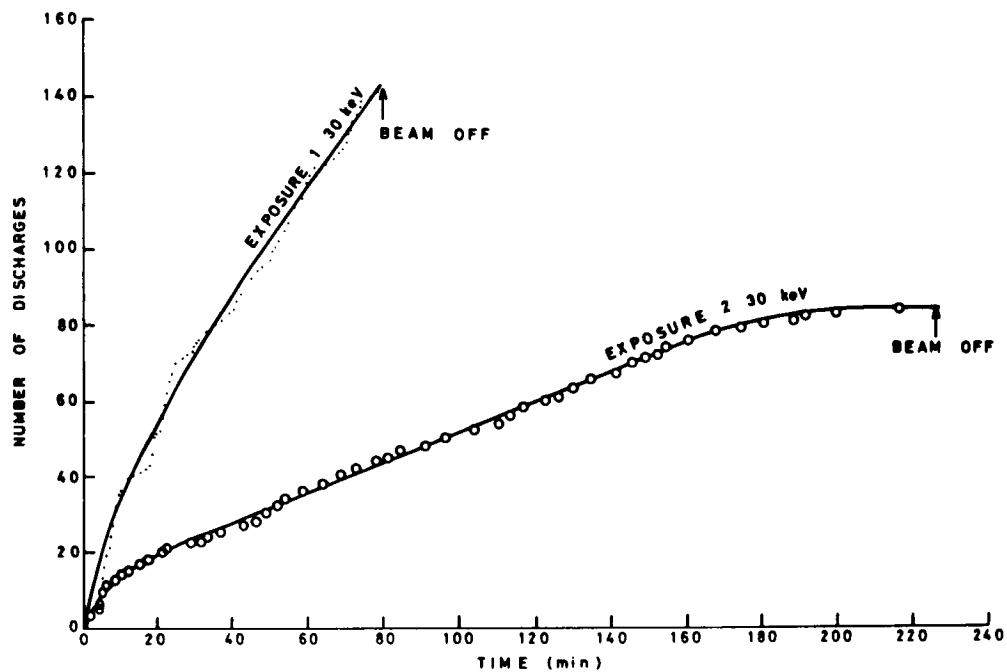


FIGURE 6  $51 \mu$  KAPTON IRRADIATED AT  $25^{\circ}\text{C}$ ; BEAM FLUX  $12.1 \text{ nA cm}^{-2}$

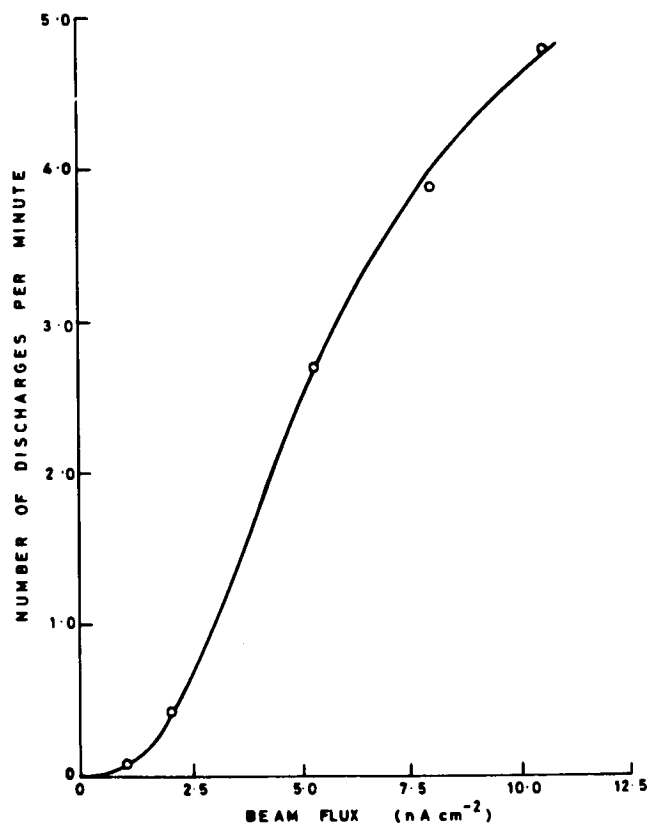
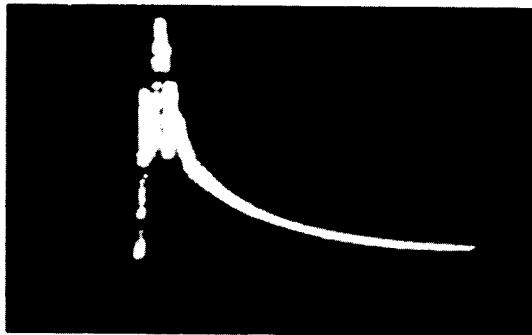
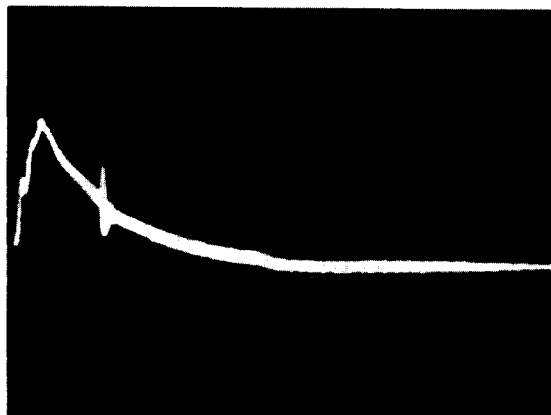


FIGURE 7. VARIATION OF DISCHARGE RATE WITH BEAM FLUX FOR  $51 \mu$  THICK KAPTON AT  $25^{\circ}\text{C}$

A  
Single current pulse  
1.0 A/small division  
0.5  $\mu$ sec/small division



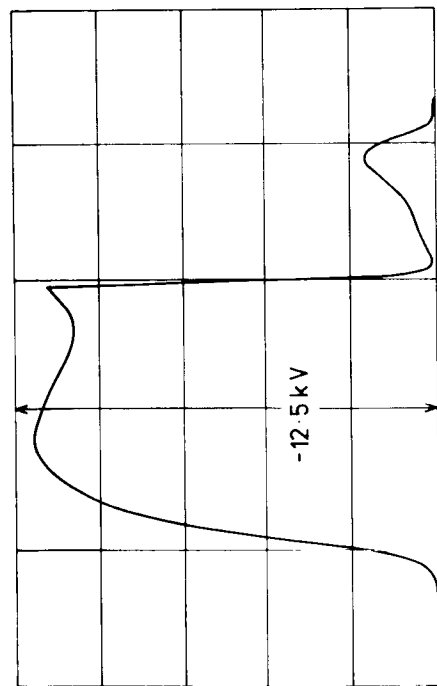
B  
Multiple current pulse  
0.5 A/division  
1  $\mu$ sec/division



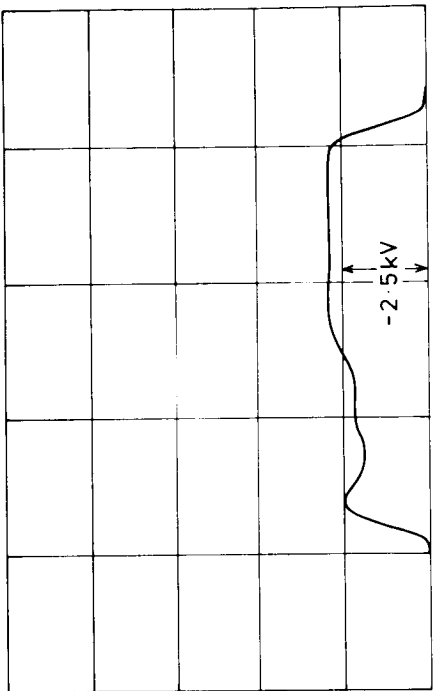
C  
RF pulse  
0.2 V/small division  
0.2  $\mu$ sec/small division



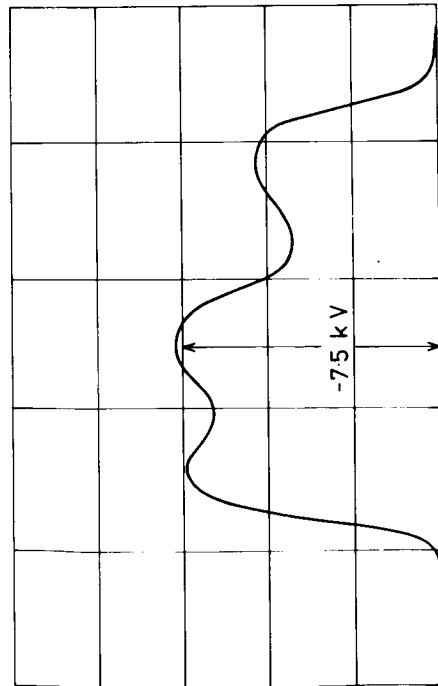
FIGURE 8. CHARACTERISTICS OF DISCHARGES FROM KAPTON



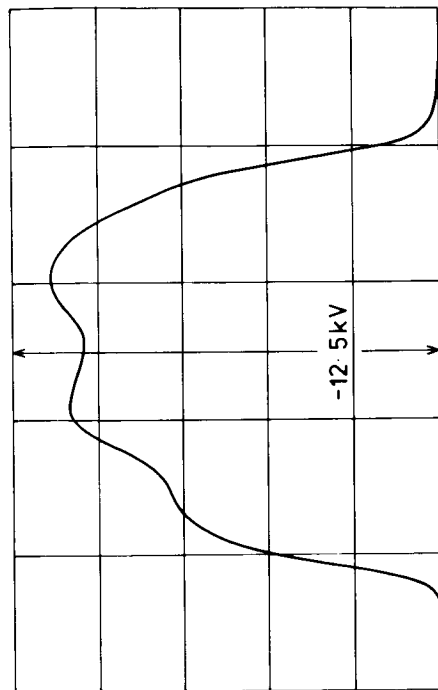
Discharge during a scan



Total discharge of sample



Discharge immediately before scan



Localised discharge

FIGURE 9 EFFECT OF DISCHARGES ON SURFACE VOLTAGE PROFILES OF KAPTON

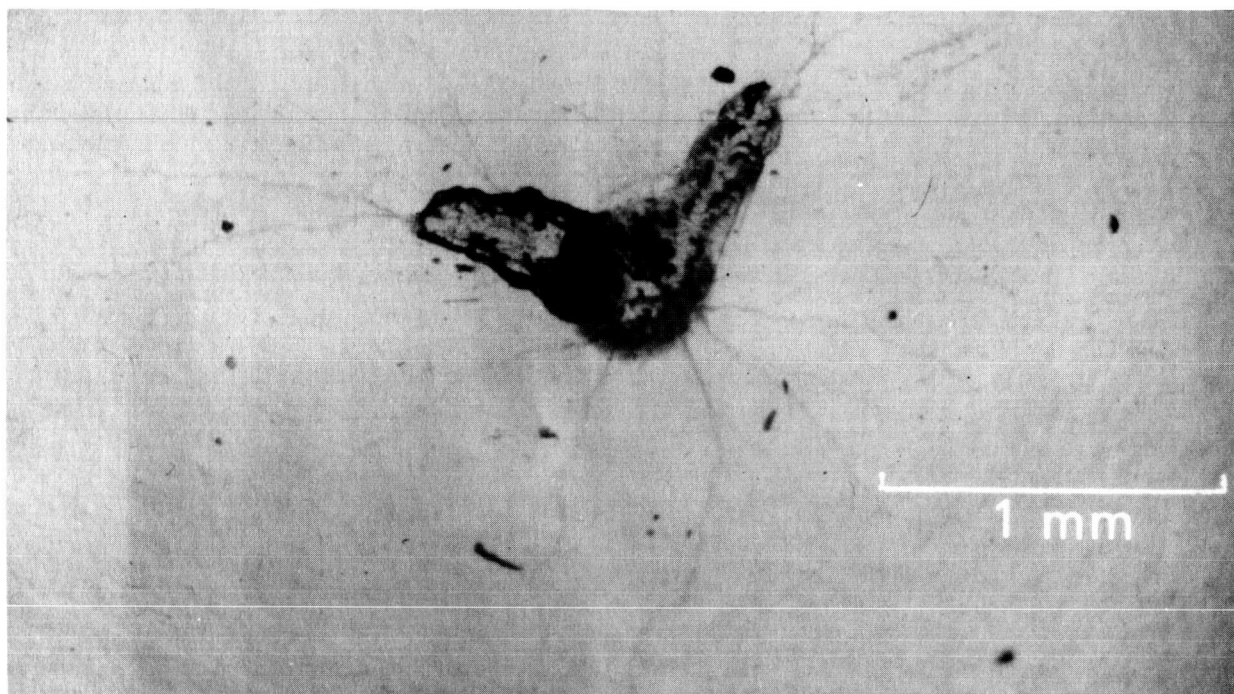


FIGURE 10. PINHOLE AND TRACKING DUE TO DISCHARGE IN ELECTRON-IRRADIATED KAPTON. ELECTRON ENERGY, 30 keV; BEAM FLUX,  $12 \text{ nA cm}^{-2}$ ; MAGNIFICATION,  $\times 12$ .

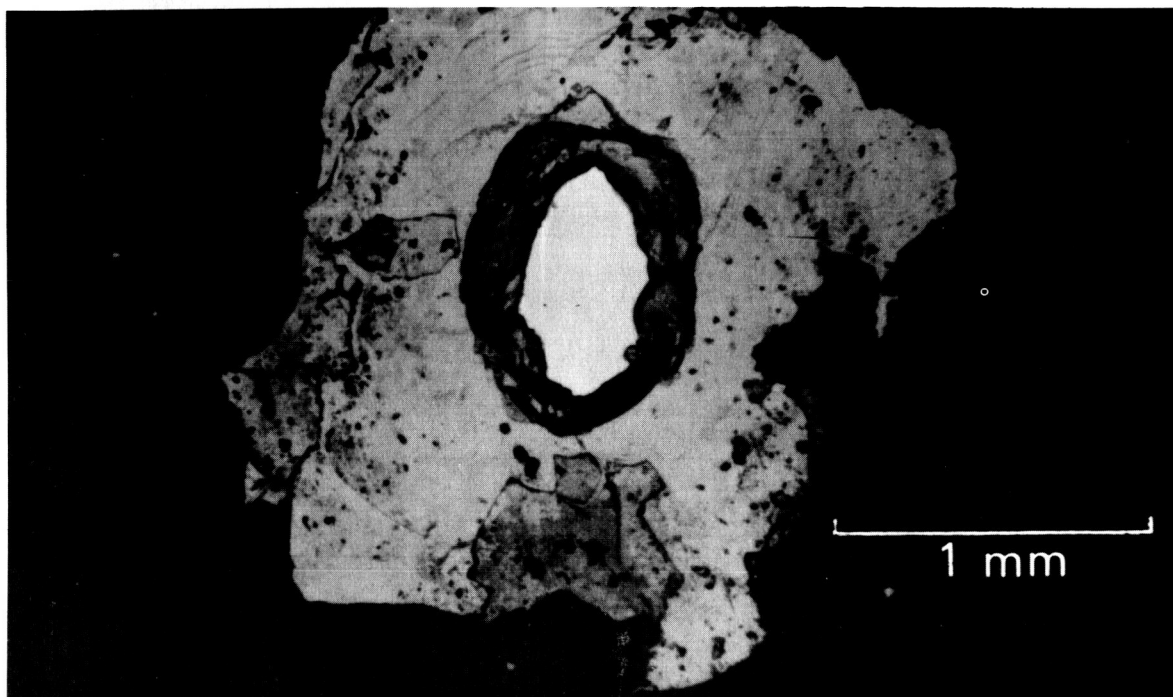


FIGURE 11. EVAPORATION OF POLYMER AND METAL DUE TO DISCHARGE IN ELECTRON-IRRADIATED ALUMINIZED KAPTON. ELECTRON ENERGY, 30 keV; BEAM FLUX,  $12 \text{ nA cm}^{-2}$ ; MAGNIFICATION,  $\times 12$ .



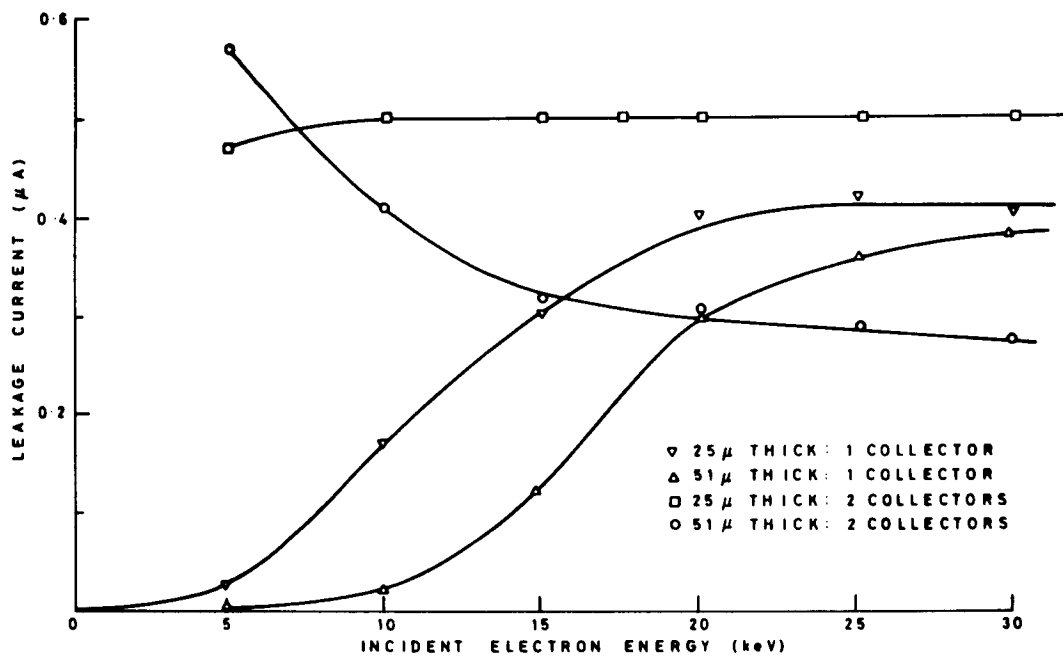


FIGURE 12. THE EFFECT ON THE LEAKAGE CURRENT OF ALUMINISING THE IRRADIATED SURFACE OF KAPTON

# **DIELECTRIC SURFACE DISCHARGES: EFFECTS OF COMBINED LOW-ENERGY AND HIGH-ENERGY INCIDENT ELECTRONS\***

**K. G. Balmain and W. Hirt  
University of Toronto**

## **SUMMARY**

A study has been made of the effect on dielectric surface discharges of adding high energy electrons at  $5 \text{ pA/cm}^2$  to a primary 20 keV,  $10 \text{ nA/cm}^2$  electron beam, the high-energy broad-spectrum particles coming from the  $\beta$ -decay of Strontium -90. Kapton exhibits the most surprising effect, which is significantly increased discharge strength, increased waiting time between discharges, and a decreased number of discharges per specimen before discharge cessation. Mylar exhibits similar but less pronounced effects, while Teflon is relatively unaffected. There is evidence that with Kapton and Mylar the high energy electrons act in some way to delay the instant of discharge ignition so that more charge can be accumulated and hence released during discharge.

## **INTRODUCTION**

Spacecraft in synchronous orbit are exposed to a natural energetic electron flux with a continuous energy spectrum extending into the MeV range. It has been estimated that this energetic flux could penetrate the outer skin of a spacecraft and cause arc discharges to occur in interior dielectrics (ref.1). It has also been estimated that nuclear  $\beta$ -decay electrons could augment the naturally occurring high-energy electron flux by one to two orders of magnitude, thereby contributing to stronger charging or discharging phenomena (ref.2).

Most laboratory simulations of spacecraft charging have been carried out using metal-backed dielectric sheets exposed to monoenergetic electron beams in the relatively low energy range of 15-25 keV, but recently evidence has been introduced indicating that a monoenergetic electron beam in the relatively high energy range of 200-500 keV can by itself cause discharges to occur (ref.3) or can modify discharges caused by a simultaneously applied low-energy beam (ref.4). In particular it was found (ref.4) that the addition of 200 keV electrons at  $100 \text{ pA/cm}^2$  completely prevented the occurrence of

---

\*Research supported by U.S. Air Force Weapons Laboratory and by NASA under NASA Grant NSG-7647.

discharges due to a 25 keV beam, even when this low energy beam's current density was as high as 13 nA/cm<sup>2</sup>. The further investigation of this latter effect of combined high and low energy beams is the objective of the research reported here, with the primary innovation being the use of a broad-spectrum Strontium - 90 high-energy  $\beta$ -particle source.

#### EXPERIMENTAL CONDITIONS

In the planning stage it became clear that the experiments would be extremely time-consuming, so that the number and ranges of the parameters selected would have to be limited. Therefore it was decided to select only one set of fluxes, with the high energy flux lying very roughly between the expected natural and nuclear-enhanced values as evaluated in the literature (ref. 4), and the low energy flux large enough to permit completion of the experiments in a reasonable time. Thus the selected current densities were 10 nA/cm<sup>2</sup> for monoenergetic 20 keV electrons and 5 pA/cm<sup>2</sup> for the broad-spectrum emission from <sup>90</sup>Sr. Theoretical estimation of the emission from a 100 mCi <sup>90</sup>Sr source indicated that a current density of 5 nA/cm<sup>2</sup> would exist at a distance of 3 cm from the source and Faraday cup measurements in a vacuum confirmed this estimate.

It was decided to test three materials, FEP Teflon 50  $\mu$ m thick, Kapton H 50  $\mu$ m thick and Mylar 75  $\mu$ m thick. One reason for this choice was the existence of extensive discharge data on these three materials with respect to exposed-area scaling (ref. 5) and with respect to incident-flux scaling of the discharge peak current, released charge, energy dissipated and pulse duration (ref. 6). Also, Kapton was selected because of its use in previous high-energy tests, and Teflon and Mylar were chosen to reveal differences among polymers. The specimen area was kept constant at 11.7 cm<sup>2</sup>.

It has been mentioned that discharge tests can be time-consuming. One reason for this is specimen fatigue which means that on a particular specimen discharging can suddenly stop and not recommence, or the properties of the discharges can change as the discharges continue. This means that a complete discharge history for each specimen must be recorded and the specimens changed frequently. Furthermore specimen fatigue is a property which is as important as discharge pulse strength in assessing the effects of high-energy electron exposure.

The experimental arrangement is shown in figure 1. The radioisotope source was positioned so as to produce minimum blockage of the low energy beam when the low and high energy electrons were incident simultaneously. For low energy incidence alone, the radioisotope source was removed. Also shown in figure 1 is the emission spectrum of the high-energy source, a spectrum which exhibits a lower-energy peak due to the  $\beta$ -decay of <sup>90</sup>Sr to <sup>90</sup>Y, and a higher-energy peak due to the  $\beta$ -decay of <sup>90</sup>Y to stable <sup>90</sup>Zr.

## SPECIMEN DISCHARGE HISTORY EXAMPLES

Each specimen was found to exhibit a particular kind and degree of fatigue as discharges recurred, and so for each specimen the discharges were assigned serial numbers. The progression of some discharge properties with serial number is shown in figure 2 for a single Teflon specimen and low-energy electron incidence. The substrate and mask peak currents both decrease slowly for the first nine discharges, during which the waiting time between discharges increases erratically. Then there is a sudden change to lower peak currents and shorter waiting times. This type of sudden change correlates with the formation of a "punchthrough" or "pinhole" in the specimen and the subsequent arcs tend to concentrate on the punchthrough. It would appear probable that subsequent discharge arcs are initiated at the punchthrough and then propagate away from it.

The specimen time histories were organized according to serial number and the discharge properties averaged for each type of material. The example of Kapton exposed to low-energy electrons is shown in figure 3, in which the average peak current actually rises slightly as the discharges proceed, a process which is clearly the opposite to fatigue. The vertical bars in figure 3 indicate the ranges for all values measured.

As shown in figure 3 the waiting time exhibits a great deal of variability, indicating that the slight downward trend in the average may not be significant. It is worth noting that the longest waiting time before a discharge in this sequence was  $1\frac{1}{2}$  hours while the shortest was 20 seconds. Any specimen which did not discharge over a period of  $1\frac{1}{2}$  to 2 hours was deemed to have ceased discharging and was replaced with an unexposed specimen; some specimens did not discharge at all. In this set of experiments Kapton did not develop punchthroughs although in previous experiments on the same type and thickness of material, occasional punchthroughs did occur.

## DISCHARGE OCCURRENCE

The periods of discharge occurrence and the points of discharge cessation are charted for the individual specimens as horizontal lines in figure 4. For Teflon, punchthrough-type discharge occurrence is designated by dashed lines. In the figure the vertical bar following each 6th discharge is a reminder that the computed averages of the discharge properties include only the first six discharges, and furthermore these averages exclude punchthrough-type discharges.

For Teflon the effect of adding high-energy broad spectrum electrons was to increase by 50% the number of instances of punchthrough occurrence; however the number of normal discharges per specimen remained essentially constant at about 6. For Kapton the number of discharges per specimen declined from 10 to 4.5 upon addition of the high energy electrons. For Mylar the corresponding change was from 4 to 3 discharges per specimen. Clearly Kapton was the only one of the three materials to exhibit increased fatigue in the form of

significantly fewer discharges per specimen upon addition of high energy electrons from the  $^{90}\text{Sr}$  source.

#### AVERAGE DISCHARGE PROPERTIES

The discharge current pulse properties were averaged over the first six normal discharges and the results depicted as bar graphs in figures 5, 6, 7 and 8. As for the discharge strength, figure 5 shows that on Teflon the addition of high energy electrons causes the peak current and released charge to decrease slightly, but has the opposite and much stronger effect on Kapton and Mylar. Indeed for Kapton the released charge is tripled and the energy dissipated (shown in figure 6) is multiplied by a factor of seven. The pulse durations shown in figure 6 are relatively unaffected by the high energy electrons.

#### AVERAGE WAITING TIME

The increased discharge strength for Kapton and Mylar as referred to above correlates fairly well with the increased waiting time shown in figure 7. This correlation is better for the released charge than for the other discharge properties as can be seen in the table below.

Ratio of High + Low to Low Energy Average Discharge Properties

	$I_s$	$Q_s$	$E_s$	$T_s$	$T_w$
Kapton	2.6	3.0	7.1	1.2	4.1
Mylar	1.6	1.8	2.6	1.2	1.9

Presumably the added high energy electrons act in some way to permit charge to build up for a longer period before discharge occurs. It is conceivable that the beam-induced conductivity allows enough charge redistribution to prevent early formation of charge concentrations and resultant breakdown-level fields. Whatever the reason may be, the factor of four increase in waiting time is particularly significant because it allows time for a much larger charge to accumulate. The longer waiting time also greatly extends the time required to perform the experiments.

The average mask-to-substrate ratios of figure 8 indicate that the addition of high-energy electrons has little effect. Because these ratios and also the pulse durations are so little affected, it seems reasonable to conclude that the addition of high-energy incident electrons does not affect discharge dynamics.

## TRENDS DURING FIRST SIX DISCHARGES

It is reasonable to ask whether or not the averages presented as bar graphs in figures 5 through 8 mask any significant variations during the first six discharges. The average discharge histories plotted in figure 9 address this question by showing that the peak current does not change greatly with discharge serial number, and even increases slightly in the case of Kapton for both the low energy and the combined high and low energy exposure. For specific serial numbers, the peak currents varied typically over a 2:1 range. The other discharge properties (released charge, energy, pulse duration) exhibited similar variations, indicating that the average discharge properties are indeed representative of all the discharges.

The waiting times as shown in figure 9 vary appreciably, with the rapid increase for Teflon exposed to low energy electrons being especially noticeable. These waiting times for Teflon for a given serial number varied typically over only a 4:1 range while the averages varied over a 10:1 range, which tends to support the significance of the 10:1 variation. However no explanation is apparent. For Mylar the variation with serial number is less pronounced and probably not significant in view of the 4:1 range at a given serial number. For Kapton the situation is quite different because the variations at a given serial number were typically over a 15:1 range. In addition for the high-energy case the 6th Kapton discharge waiting time was derived from only two specimens, so consideration of all these factors suggests that the Kapton waiting time variations (decreases) over the first six discharges probably are not significant.

## CONCLUSIONS

It is necessary to consider a detailed discharge history for each specimen tested in order to characterize properly each material with respect to both fatigue and average discharge properties. Such discharge histories show, for example, that the formation of a punchthrough is characterized by an abrupt change to weaker and more frequent discharges.

The addition of high-energy, broad-spectrum electrons to a  $10 \text{ nA/cm}^2$ , 20 keV electron beam has the following effects:

1. For Kapton the number of discharges per specimen is cut in half.
2. For Kapton and Mylar, the discharges that do occur are much stronger.
3. The waiting time between discharges for Kapton and Mylar increases greatly, in approximate proportion to the charge released during discharge.
4. The pulse durations and mask-to-substrate ratios remain essentially unchanged for Teflon, Kapton and Mylar.

5. For Teflon the steadily increasing waiting times for low-energy electrons become appreciably smaller and constant upon addition of high-energy electrons.

Thus for Kapton in particular, and to a lesser degree for Mylar, the effect of adding broad-spectrum high-energy incident electrons is to cause discharges which are stronger but fewer in number and less frequent. However the fact that the pulse durations and mask-to-substrate ratios are unchanged suggests that the physics of the discharge process is unaffected by the high-energy electrons. The correlation between the waiting-time and released charge suggests that the high energy electrons influence strongly the charge accumulation process. It is postulated that additional beam-induced and nonlinear conductivity during the charge-up process acts to delay the formation of charge concentrations and resultant high-field regions which are strong enough to trigger discharges.

The low-energy flux levels employed are somewhat higher than the values expected in synchronous orbit, and the ratio of low-energy to high-energy fluxes is 2000 which is also high with respect to synchronous orbit. Nevertheless conditions have been found such that discharges are made stronger by the addition of energetic electrons rather than being eliminated completely as found in earlier work done at lower low-energy fluxes (ref. 4). Although further study is required, it is clear at this stage that the spacecraft charging threat to satellites cannot be dismissed easily because of the presence of high-energy electrons in synchronous orbit.

#### REFERENCES

1. Wenaas, E. P.: Spacecraft Charging Effects by the High-Energy Natural Environment. IEEE Trans. Nucl. Sci., Vol. NS-24, No. 6, Dec. 1977, pp. 2281-2284.
2. De Plomb, E. P.; and Rich, W.F.: Charging of Spacecraft by Nuclear Electrons. IEEE Trans. Nucl. Sci., Vol. No. NS-24, No. 6, Dec. 1977, pp. 2298-2304.
3. Wenaas, E. P.; Treadaway, M. J.; Flanagan, T. M.; Mallon, C. E.; and Denson, R.: High-Energy Electron-Induced Discharges in Printed Circuit Boards. IEEE Trans. Nucl. Sci. Vol. NS-26, No. 6, Dec. 1979, pp. 5152-5155.
4. Treadaway, M. J.; Mallon, C.E.; Flanagan, T. M.; Denson, R.; and Wenaas, E. P.: The Effects of High-Energy Electrons on the Charging of Spacecraft Dielectrics. IEEE Trans. Nucl. Sci. Vol. NS-26, No. 6, Dec. 1979, pp. 5102-5106.
5. Balmain, K. G.; and Dubois, G. R.: Surface Discharges on Teflon, Mylar and Kapton. IEEE Trans. Nucl. Sci., Vol. NS-26, No. 6, Dec. 1979, pp. 5146-5151.

6. Balmain, K. G.; and Hirt, W.: Dielectric Surface Discharges: Dependence on Incident Electron Flux. To be published in the IEEE Trans. Nucl. Sci., Vol. NS-27, No. 6, Dec. 1980.

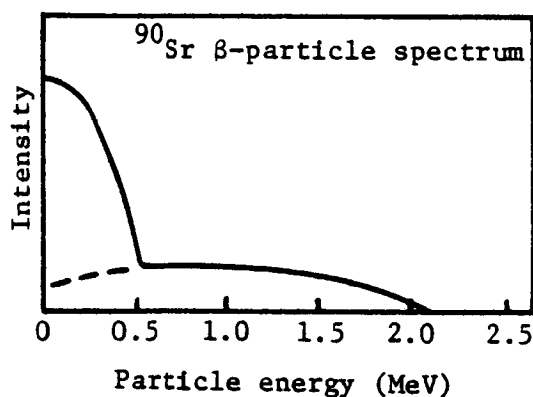
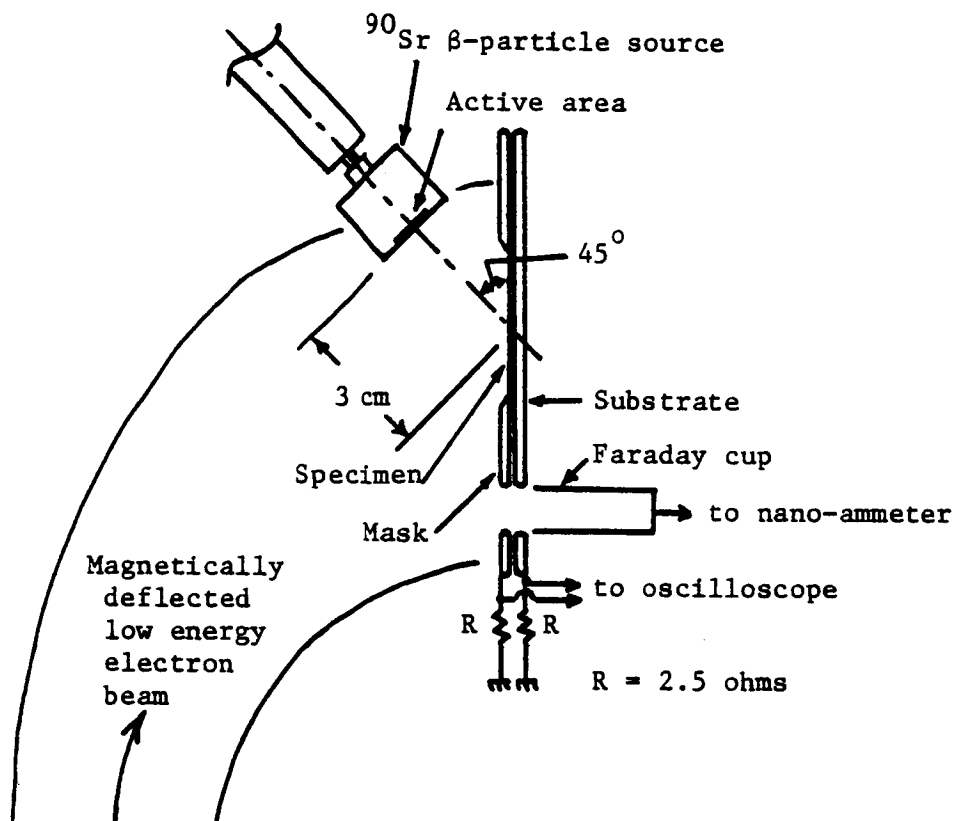


Fig.1 Experiment arrangement (a), and Strontium-90  $\beta$ -particle spectrum (b). The spectrum is taken from the CRC Handbook of Radiation Measurement and Protection, p.354.



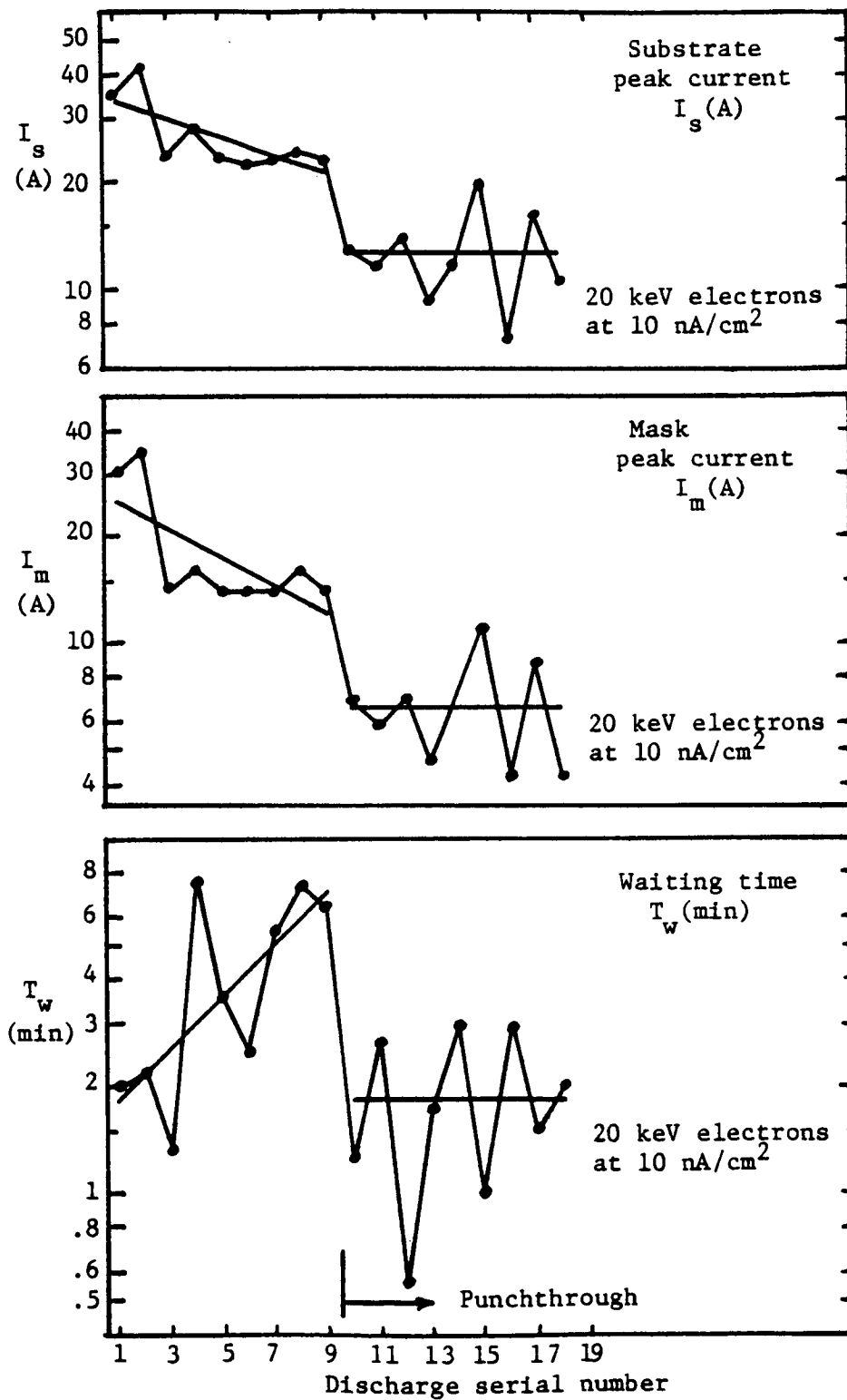


Fig.2 Discharge history of a single Teflon specimen, illustrating effects of punchthrough formation.

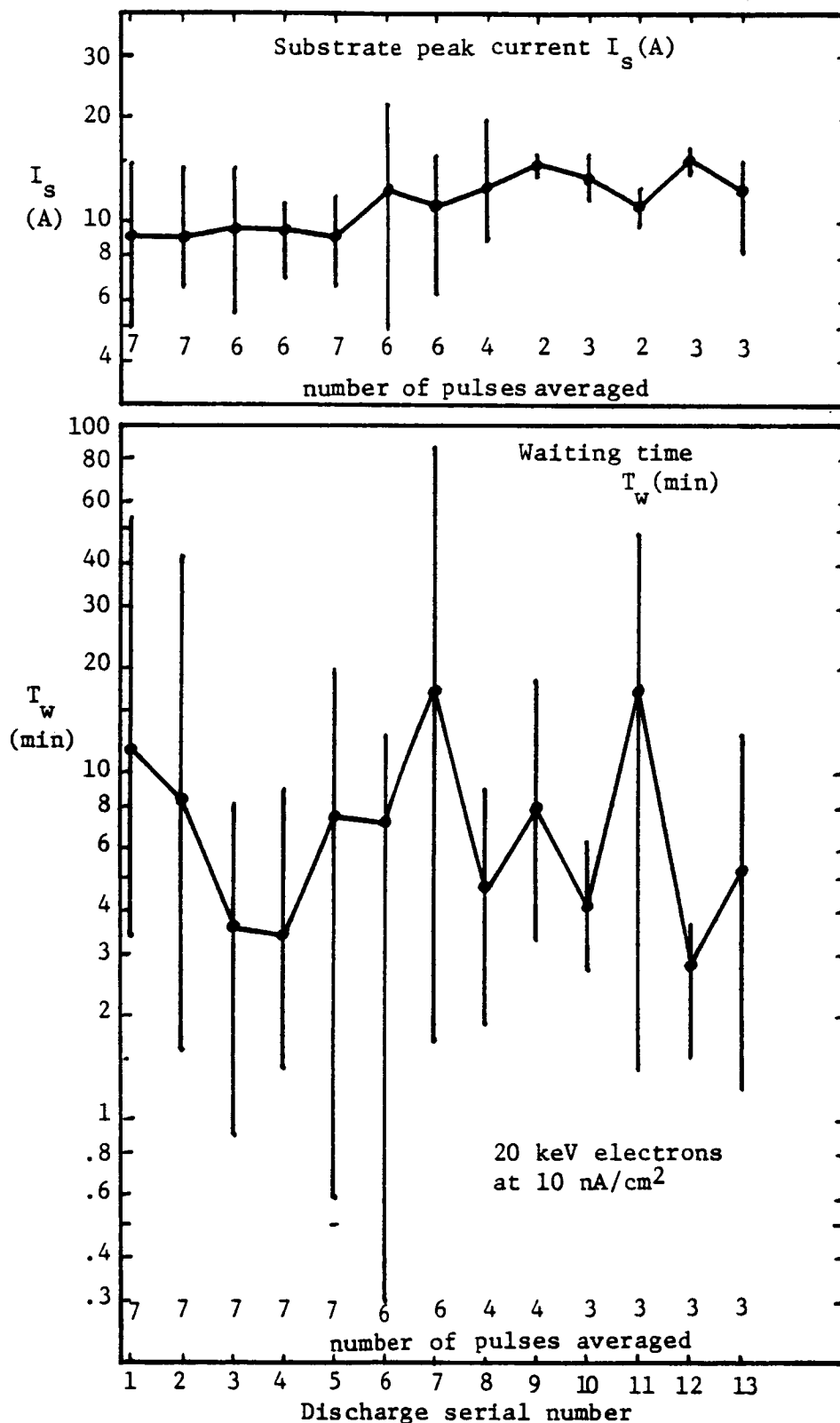


Fig.3 Average discharge history for seven Kapton specimens.

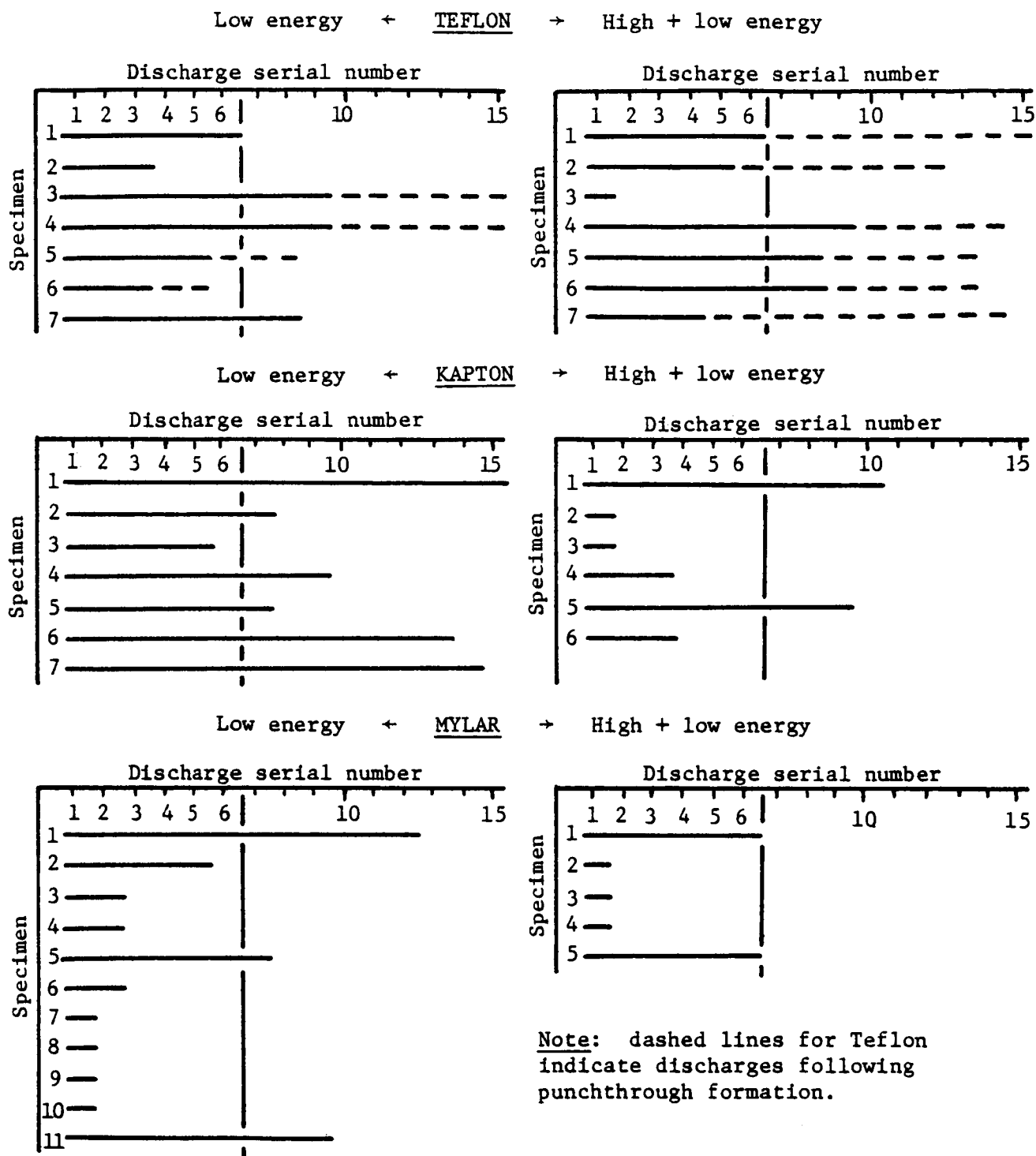


Fig.4 Discharge occurrence on individual specimens, showing effects of adding high energy electrons from strontium - 90 to a monoenergetic 20 keV beam.

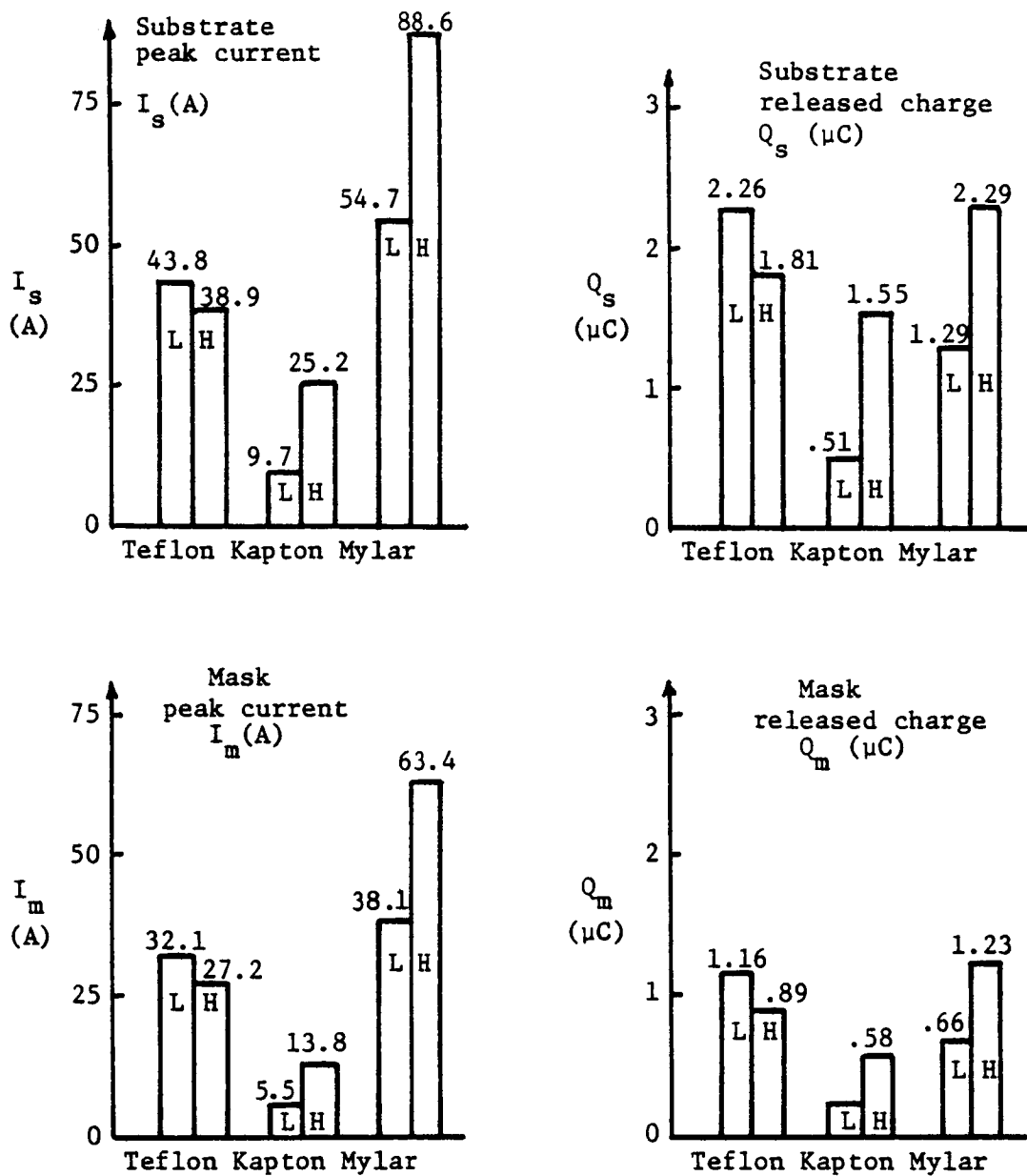


Fig.5 Average peak current and average released charge for substrate and mask as measured over first 6 discharges. L denotes low energy electron exposure and H denotes combined high and low energy exposure.

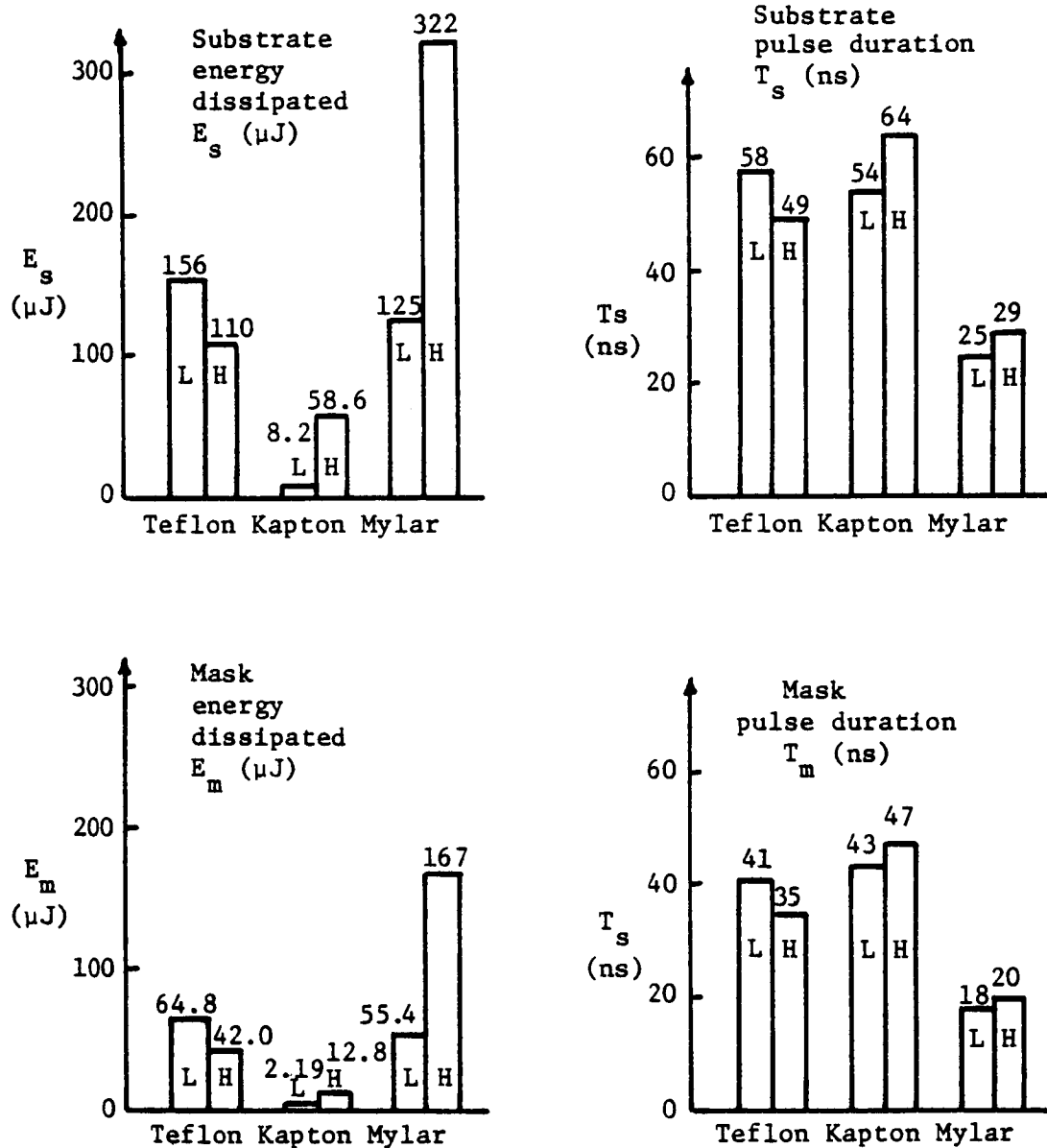


Fig.6 Average energy dissipated in a 2.5 ohm load resistor and average pulse duration for both substrate and mask as measured over first 6 discharges. L denotes low energy electron exposure and H denotes combined high and low energy electron exposure.

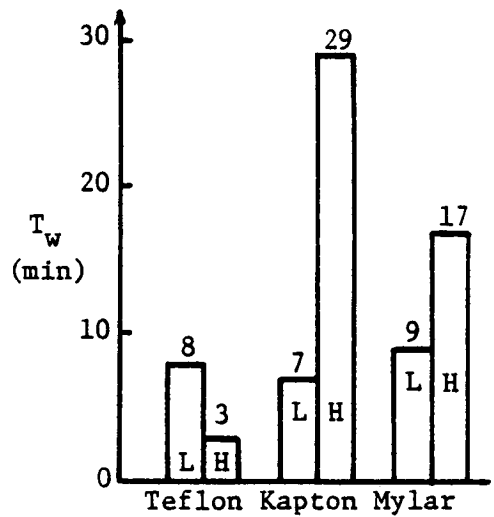


Fig.7

Average waiting time between discharges as measured over first 6 discharges. L and H denote low and combined high and low energy incident electrons.

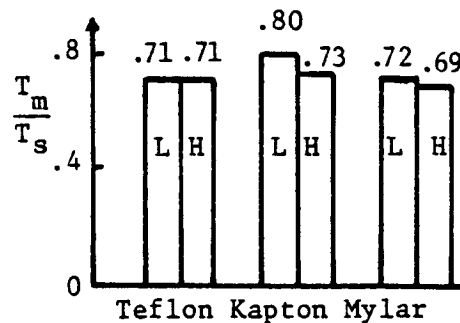
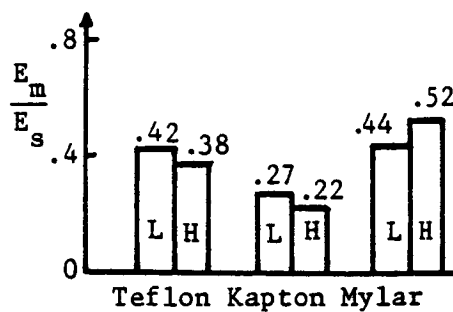
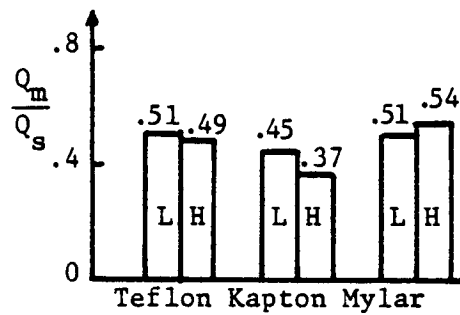
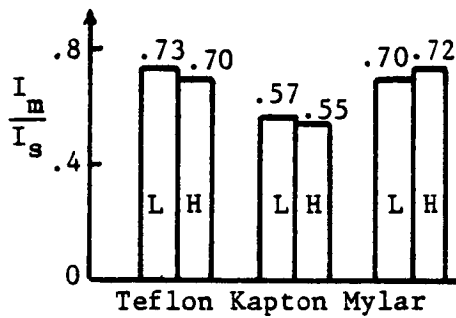


Fig.8 Average mask-to-substrate ratios over first 6 discharges for peak current, released charge, energy dissipated in a 2.5 ohm load resistor, and pulse duration.

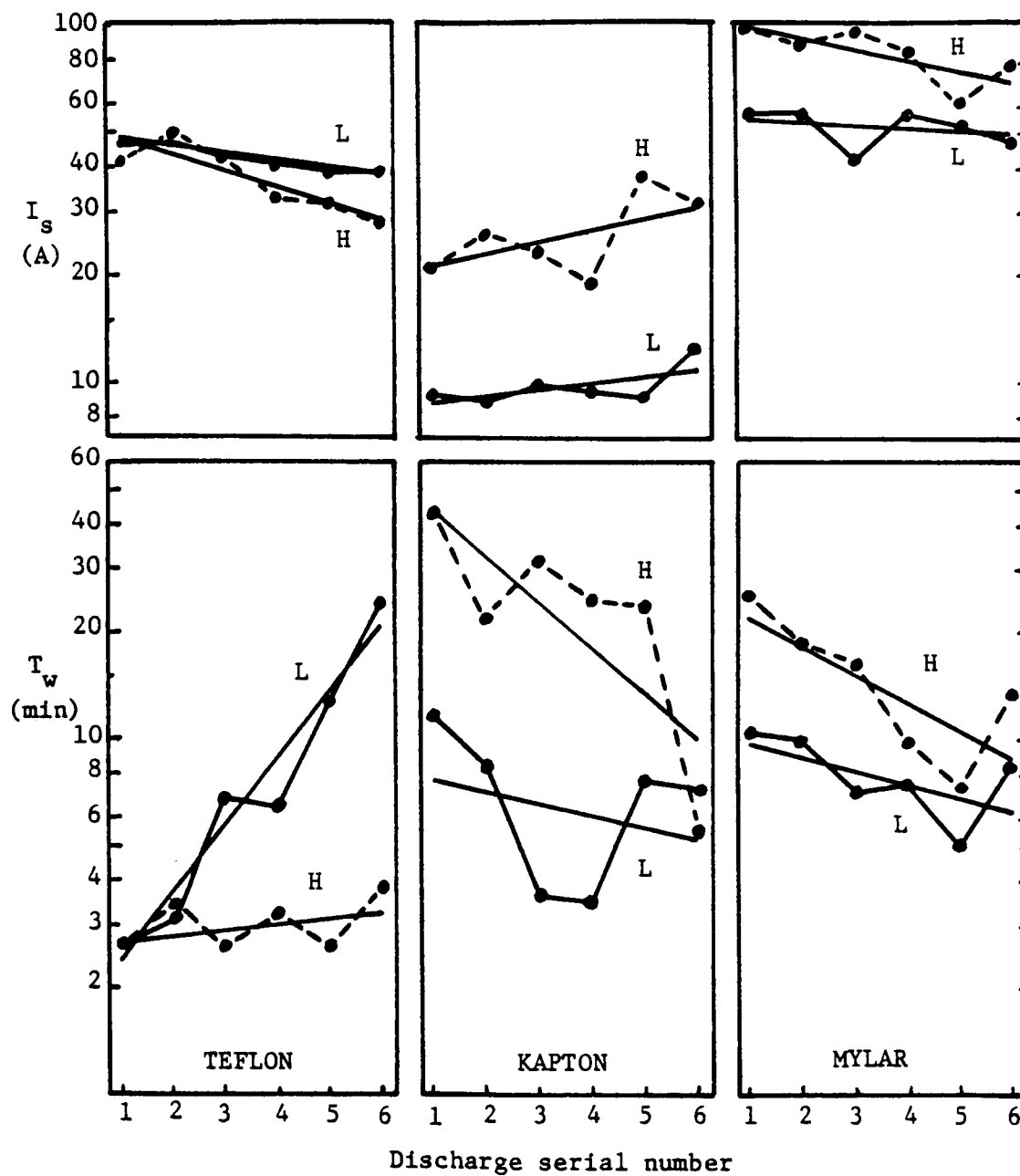


Fig.9. Average discharge histories for all specimens tested for the first 6 discharges. L and H denote low and combined high and low energy incident electrons.

## PRELIMINARY COMPARISON OF MATERIAL CHARGING PROPERTIES USING SINGLE-ENERGY AND MULTIENERGY ELECTRON BEAMS

R. C. Adamo and J. E. Nanevich  
SRI International

### BACKGROUND

Although it has long been recognized that the electron injections occurring during a magnetic substorm have a continuous energy distribution,<sup>1,2</sup> monoenergetic beams have been used for laboratory simulations of spacecraft charging starting with the early experiments at SRI<sup>3-5</sup> and continuing for several years.<sup>6-8</sup> The use of monoenergetic beams for laboratory experiments and simulations continued largely because they were easy to assemble. It was recognized, however, that the results observed with a monoenergetic simulator might not duplicate those that would occur in space. Accordingly, when the prototype of an electron source capable of producing a continuous energy distribution became available at SRI, it was applied immediately in a set of coarse experiments to compare the charging properties of a spacecraft material under a monoenergetic beam and under a continuously distributed beam.

### EXPERIMENTAL SETUP

The test setup used in these preliminary experiments is shown in Figure 1. The electron source was mounted in the top of a cylindrical vacuum chamber. A sheet of 5-mil-thick Kapton was placed on an insulated metal substrate placed on the bottom of the vacuum chamber. Provisions were made to measure the dc current arriving on the substrate. A field meter located off the edge of the test sample provided a means for measuring the potential of the test sample. A retarding potential analyzer was used to measure the energy spectrum of the incident electron beam.

The energy spectra of the electron beams used in the experiments are shown in Figure 2. These included a 15-keV monoenergetic spectrum shown in Figure 2(a), and two continuous spectra with the characteristics shown in Figures 2(b) and 2(c). The total beam current density in each case was adjusted to be 10 nA/cm<sup>2</sup>. It should be noted that, in these experiments, no effort was made to duplicate the spectra occurring in space. The tests were intended simply to compare material charging properties using monoenergetic and continuous multi-energy beams. Although the spectra in Figures 2(b) and 2(c) are shown stepped, they were actually continuous. The steps in the figure are simply an artifact of the energy-measurement technique employed.

### TEST RESULTS

The results of the tests on the 5-mil Kapton sample are shown in Table 1. With the monoenergetic beam, the sample charged to 12 kV and electrical discharges occurred. With the multi-energy spectra the samples charged to only 6 kV and 4 kV, and no discharges were observed.



Although only the most rudimentary experiments have been conducted thus far using the SRI multi-energy electron gun, the results of these experiments and other work reported at this conference indicate the need for accurate simulation of the space environment if we are to be able to relate the simulation results to in-orbit behavior of satellites.

#### REFERENCES

1. Garrett, H. B., "Modeling of the Geosynchronous Plasma Environment," Spacecraft Charging Technology - 1978, NASA Conference Publication 2071, AFGL-TR-79-0082.
2. Su, S.-Y. and Konradi, A., "Average Plasma Environment at Geosynchronous Orbit," Spacecraft Charging Technology - 1978, NASA Conference Publication 2071, AFGL-TR-0082.
3. Nanevicz, J. E., Adamo, R. C., Scharfman, W. E., "Satellite-Lifetime Monitoring," Final Report, Contract F04701-71-C-0130, SRI Project 2611, Stanford Research Institute, Menlo Park, California (March 1974).
4. Adamo, R. C. and Nanevicz, J. E., "Spacecraft-Charging Studies of Voltage Breakdown Processes on Spacecraft Thermal Control Mirrors," Spacecraft Charging by Magnetospheric Plasmas, Vol. 47, Progress in Astronautics and Aeronautics, Martin Summerfield, Series Editor-in-Chief, Princeton University, Princeton, New Jersey (June 1975).
5. Nanevicz, J. E. and Adamo, R. C., "Transient Response Measurements on a Satellite System," Proceedings of the Spacecraft Charging Technology Conference, NASA TMX-73537, AFGL-TR-0051, Air Force Surveys in Geophysics, No. 364 (February 1977).
6. Berkopce, F. D., Stevens, N. J., and Sturman, J. C., "The Lewis Research Center Geomagnetic Substorm Simulation/Facility," Proceedings of the Spacecraft Charging Technology Conference, NASA TMX-73537, AFGL-TR-77-0051, Air Force Surveys in Geophysics, No. 364 (February 1977).
7. Stevens, N. J. et al., "Testing of Typical Spacecraft Materials in a Simulated Substorm Environment," Proceedings of the Spacecraft Charging Technology Conference, NASA TMX-73537, AFGL-TR-77-0051, Air Force Surveys in Geophysics, No. 364 (February 1977).
8. Nanevicz, J. E., and Adamo, R. C., "A Rugged Electron/Ion Source for Spacecraft Charging Experiments," Proceedings of the Spacecraft Charging Technology Conference, NASA TMX-73537, AFGL-TR-77-0051, Air Force Surveys in Geophysics, No. 364 (February 1977).
9. Leung, M. S., Tueling, M. B., and Schnauss, E. R., "Effects of Secondary Emission on Charging," Proceedings of USAF/NASA Spacecraft Charging Technology Conference III, U. S. Air Force Academy, Colorado (12-14 November 1967).

Table 1  
Test Results on 5-mil Kapton Sample

Spectrum ( $10 \text{ nA/cm}^2$ )	Equilibrium Potential	Equilibrium Bulk-Current
15-keV Mono-energetic	12 kV (at breakdown)	$2 \text{ nA/cm}^2$ (at breakdown)
#1 Multi-energy	6 kV (no breakdown)	$0.2 \text{ nA/cm}^2$
#2 Multi-energy	4 kV (no breakdown)	$0.15 \text{ nA/cm}^2$

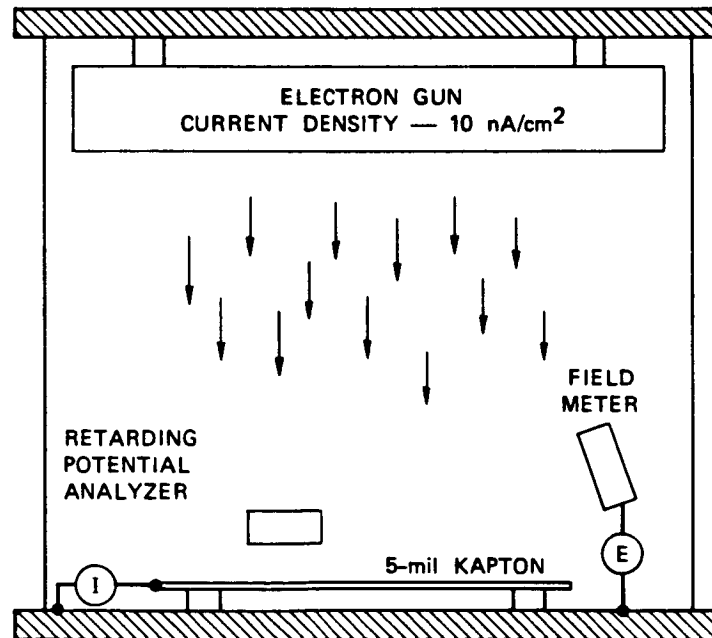


FIGURE 1 TEST SETUP

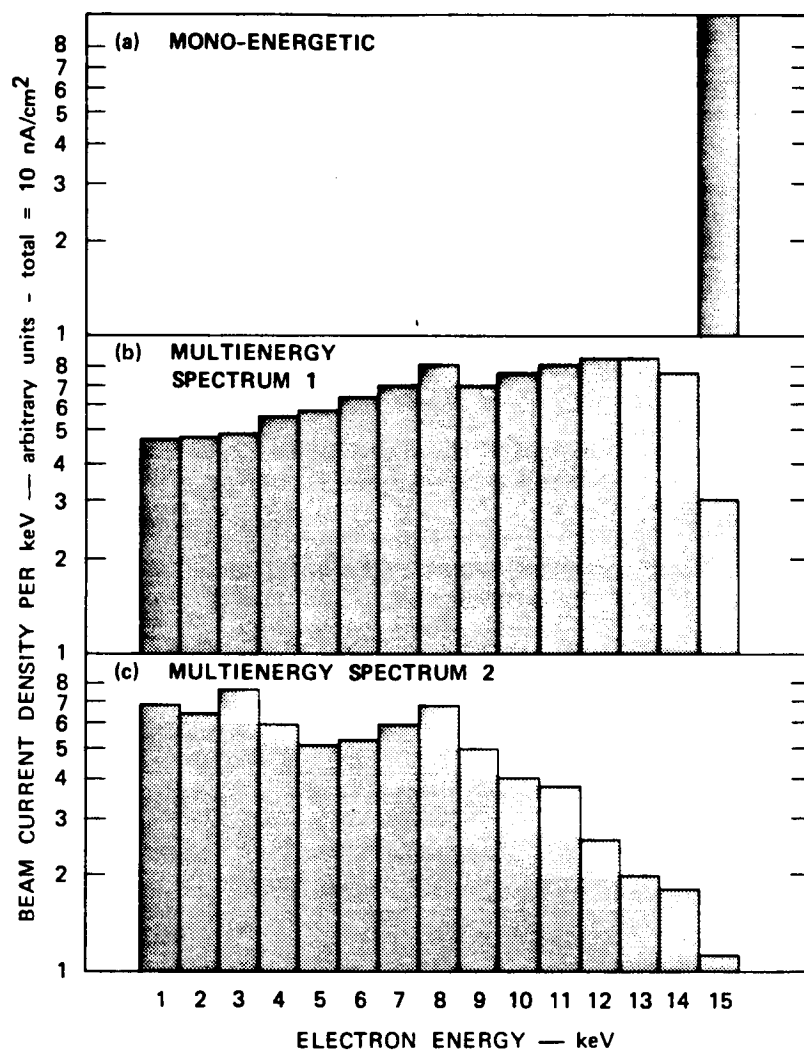


FIGURE 2 ELECTRON BEAM ENERGY SPECTRA

## **BRUSHFIRE ARC DISCHARGE MODEL\***

**G. T. Inouye**  
**TRW Defense and Space Systems Group**

### **SUMMARY**

A 1-dimensional arc discharge model incorporating a brushfire-type propagation of a discharge wavefront has been investigated. A set of equations somewhat similar to those leading to the diffusion equation have been developed which include electrical, thermal, and plasma parameters. The solutions of these equations are shown, under simplifying assumptions, to be consistent with a propagating brushfire wavefront. Voltage, current, plasma density, temperature, and resistivity profiles are obtained.

Mechanical forces, magnetic and electrostatic, are considered in evaluating the flashover to blowout current ratio,  $G'$ , for arc discharges with the brushfire parameters developed in the model. This ratio is an important factor in determining the electromagnetic interference (EMI) impact of arc discharges on spacecraft electrical subsystems. The conclusion of the analysis is that electrostatic forces are much more important than magnetic forces. The magnitude of the  $G'$  factor obtained, 58.5 percent, is within the range of those obtained by experimental means. Improvements in the analytical model as well as in the experimental approach are recommended.

### **INTRODUCTION**

The problem of characterizing dielectric surface arc discharges due to spacecraft charging has been approached mainly by experimental means in the past because of the lack of an analytical model. A number of recent papers have presented analytical approaches to the problem.<sup>(1,2)</sup> The work presented here is a continued development of the concept of a brushfire propagation model developed by J. M. Sellen Jr. and the author.<sup>(3,4)</sup>

From the viewpoint of the implications of arc discharges on the immunity of spacecraft to the EMI generated, the question of where the arc discharge currents flow is a critical factor. This problem has been formulated by defining a factor,  $G'$ , which is defined as the ratio of the blowout to flashover currents. The flashover component is viewed as that which flows essentially from the dielectric surface through a breakdown region, perhaps an edge with high electric fields, directly back to the metallized backing of the dielectric surface. Flashover currents, because their geometrical extent is limited, are not expected to be a major source of spacecraft EMI. Blowout currents, on the other hand, may have a large impact on electrical subsystems because they result in replacement currents flowing through the spacecraft structure which must be of a magnitude equal to the blown off electron current. The density of replacement current flowing in the spacecraft

---

\*This work was supported under NASA Contract NAS3-21961.

structure is highly dependent on the location of the arcing source and on the particular configuration of the spacecraft. An arc on a boom mounted object, for example, may result in boom currents which couple very well into cabling along the boom. A spacecraft body-mounted source, on the other hand, may be so well grounded and shielded that only currents very close to the source are of sufficient magnitude to be of concern. Thus, the determination of a representative value of  $G'$  and its dependence on the size of the arcing source and any other parameters is of prime concern for spacecraft design. Any analytical arc discharge model should provide results that are consistent with experimental data. In addition, however, the work presented here predicts facets of the experimental approach, such as the spatial distribution of blowout currents and the dependence of  $G'$  on the sample grounding impedance, which were not adequately considered previously.

### ARC DISCHARGE OVERVIEW

The brushfire propagation model addresses only the latter portion of the evolutionary processes involved in an arc discharge. The scenario would be as follows:

1. Differential chargeup by the environmental plasma and solar ultra-violet radiation
2. Edge breakdown at a weak point
3. Surface breakdown
  - o High field emission
  - o Avalanching processes
4. Brushfire propagation
  - o Blowout and flashover currents,  $G'$
  - o Dependence on spacecraft potential
  - o Limiting mechanisms on propagation

The question of how external dielectric surfaces charge up differentially with respect to the grounded underlying vacuum deposited aluminum (VDA) or to structural metal is a complex problem which is not addressed here. Generally, the most hazardous situation exists when a dielectric surface is charged negatively with respect to the underlying metals by an excess of impinging electrons over positive ions. This is because with a reverse polarity, i.e., when the metals are negative and the dielectric surface is more positive because of photoemission or secondary emission, a field emission/secondary electron avalanche process tends to limit the magnitude of the differential potential to below 1000 V.

For the purpose at hand of developing an arc discharge model, the chargeup process is important in that negative chargeup potentials of 5 kV to

20 kV have been measured experimentally. The other important feature of chargeup for our present purpose is that theory and experimental evidence(5) indicate that significant densities of electrons may be buried at depths of the order of 1 micron below the surface at the time of the discharge. This feature of buried electronic charge should also exist on dielectric surfaces which have no net surface charge because of photoemission or secondary emission. In fact, the buried charge should be somewhat deeper and more dense since retarding potentials are not present.

Dielectric breakdown due to high differential voltage stresses generally occurs for electric fields in the range of  $10^5$  to  $10^6$  V/cm at the edges of thin (~50 microns or 0.005 cm) insulating sheets. Punch-through far from the edges occurs with fields of the order of  $10^7$  V/cm. In practice, even punch-throughs probably occur at weak points where slight imperfections or irregularities exist in the material. Edges consist of exaggerated irregularities because they are created by slicing with a knife edge or by punching with stitching needles, and thus, are subject to high field emission and avalanche breakdown in a manner similar to that which will be discussed for surface breakdown. The similarity to surface breakdowns probably goes even further in that this type of breakdown is associated with surface and off-surface processes rather than those within the bulk of the material.

The net effect of an edge breakdown is that the potential of the surface near the edge goes to nearly 0 V, assuming that the thin dielectric is over a conducting plate which is at voltage reference, 0 V. Taking a single ionized particle of atomic weight 16 (oxygen) as being typical, the velocity associated with a 10 kV voltage drop is  $3.5 \cdot 10^5$  m/s. Starting at zero velocity, the time for such an ion to traverse the 2 mils or 50 micron thickness of the dielectric is 0.3 ns. This order of magnitude time span, a fraction of a ns, is much shorter than the tens to hundreds of ns duration of vacuum dielectric surface arcs.

Assuming that a 2-mil thick sheet of Kapton,  $\epsilon_r = 3$ , breaks down at 10 kV over a semicircular area with a radius equal to its thickness, the capacitance is 52 pf/cm<sup>2</sup> or  $2 \cdot 10^{-3}$  pf, and the charge stored is  $2 \cdot 10^{-11}$  Coulomb. Assuming that all of this charge is dissipated in 0.3 ns, the corresponding current would be 0.068 A. Thus, the current, charge, time span, and energy ( $\sim 10^{-7}$  joule) involved in the initial edge breakdown are quite small and negligible compared to those in the events that follow. The main effect of the initial edge breakdown is to create a plasma cloud and a surface electric field which initiates a subsequent surface discharge.

Dielectric surface breakdown has been reported to occur more readily, at  $10^4$  to  $10^5$  V/cm surface electric fields, than breakdown in the bulk of dielectric materials. The surface breakdown fields are expected to be highly dependent on surface conditions such as cleanliness, smoothness and absorbed gases.

#### BRUSHFIRE PROPAGATION MODEL

The experimentally observed "wipeoff" of charge over many hundreds of cm<sup>2</sup>, and possibly greater areas of dielectric surface, requires either some

mechanism for propagation of an initial surface breakdown in a brushfire mode or that somehow all of the participating charge release occurs simultaneously over a large area. The propagation mode seems more plausible and is discussed further here. The source of discharging energy, the stored charge per unit area, is depleted, and the discharge must be fed by a forward propagation of the brushfire periphery into the still-charged regions of the dielectric. To discuss the brushfire propagation process, some of the basic equations are presented first. Then, a simplistic piecemeal solution of various aspects of the problem is presented to provide an insight into the quantitative aspects of the problem. Even the basic relations such as those for ablation and ionization are not developed from first principles, but rather, are taken from existing experimental data and theoretical work found in the literature. Figure 1 provides an overview of the brushfire propagation analysis.

The basic equations to be satisfied for the brushfire propagation problem are:

$$\frac{\partial V}{\partial t} = -\frac{1}{C} \frac{\partial J_s}{\partial x} \quad \text{and} \quad J_s = -\frac{1}{\rho_s} \frac{\partial V}{\partial x} \quad (1,2)$$

where the potential,  $V$ , and surface current density,  $J_s$ , are functions of horizontal distance,  $x$ , and time,  $t$ . The two other parameters of this 1-dimensional formulation are the capacitance per unit area,  $C$ , which is 52 pf/cm<sup>2</sup> for a 2-mil thick dielectric with a dielectric constant of 3, and the surface resistivity,  $\rho_s$  (ohms-per-square), of the plasma sheet that conducts the arc discharge current,  $J_s$ . The geometry of the problem is shown in Figure 2. The initial voltage, -5 kV, was selected to give a 10<sup>6</sup> V/cm electric field bulk breakdown for the 2-mil dielectric thickness. A final voltage of -2.5 kV was assumed on the basis that about 50 percent of the initial voltage has been observed experimentally to remain after the discharge. As an initial guess, the voltage is assumed to decrease linearly with distance providing an electric field of 10<sup>4</sup> V/cm. The voltage gradient region is therefore 0.25 cm long. Combining equations (1) and (2) to eliminate  $J_s$  gives

$$\frac{\partial V}{\partial t} = \frac{1}{C\rho_s} \frac{\partial^2 V}{\partial x^2} \quad (3)$$

This would be the diffusion equation with the diffusion coefficient,  $D$ :

$$\frac{\partial V}{\partial t} = D \frac{\partial^2 V}{\partial x^2} \quad \text{where } D = \frac{1}{C\rho_s}$$

except that  $\rho_s$  is not a constant in our problem. This is fortunate because the diffusion equation does not lead to a propagating mode with a constant velocity.

The plasma resistivity,  $\rho$ , and surface resistivity,  $\rho_s$ , are functions of the temperature,  $T$ :<sup>(6)</sup>

$$\rho = \frac{K}{T^{3/2}} \text{ ohm - cm, where } K = 0.03 \text{ ohm-cm-ev}^{3/2} \quad (4a)$$

$$\rho_s = \rho/d = \frac{K}{d} T^{-3/2} \text{ ohms} \quad (4b)$$

where  $d$  is the thickness of the plasma sheet. It is of interest to note that  $\rho$  is independent of the density of the plasma particles.

$T$  is governed by a set of equations similar to those for  $V$ :

$$\frac{\partial T}{\partial t} = - \frac{1}{cM} \frac{\partial H}{\partial x}, \quad H = - \frac{1}{R} \frac{\partial T}{\partial x} \quad (5,6)$$

where  $H$  is the heat flux,  $c$  is the specific heat,  $M$  is the mass density, and  $R$  is the thermal resistivity. For our problem here we neglect thermal conductivity, because of the short time spans involved, and assume that  $R$  is infinite. The rate of heat energy deposition in an incremental distance,  $dx$ , in equation (5) is the power density,  $P_s$ :

$$- \frac{\partial H}{\partial x} = P_s = -J_s \frac{\partial V}{\partial x} \text{ watts/cm}^2 \quad (7)$$

The specific heat,  $c$ , is obtained using the gas constant,  $R$ , by assuming that the plasma consists of neutrals, ions and electrons, each with 3 degrees of freedom.

$$c_m = \frac{1}{2} \cdot 9R = 4.5R = 4.5 \cdot 8.314 = 37.41 \text{ joule/(deg-mole)} \quad (8a)$$

Assuming the dielectric material has a molecular weight,  $G_m$ , of 16,  $c$  is given by:

$$c = c_m/G_m = 2.34 \text{ joule/(deg-gram)} = 2.71 \cdot 10^4 \text{ joule/(ev-gram)} \quad (8b)$$

where  $c_m$  is defined as the specific heat per mole and  $G_m$  is defined as the mass density per mole.

The mass density,  $M$ , to be used in equation (5) is composed of two components,  $M_a$ , due to ablation because of the power dissipation,  $P_s$ , and  $M_0$  which is due to the initial field emission electrons:



$$M = M_a + M_0 \text{ grams/cm}^2 \quad (9)$$

The ablated mass density,  $M_a$ , is assumed to be proportional to the time-integrated power density,  $P_s$ :

$$M_a = \int g P_s dt \text{ grams/cm}^2 \quad (10)$$

The proportionality constant,  $g$ , is taken from the pulsed plasma thruster technology data.<sup>(7)</sup>

$$g = 8.32 \cdot 10^{-6} \text{ grams/joule}$$

We view ablation as being due to "pounding" of the surface by ions which are accelerated by the electric field due to the electrons which have been stored (buried) by the basic spacecraft charging process.

$M_0$  is not due to heating in the thermal sense but rather is due to collisions between the initial electrons, that are emitted or "pulled-out" by high field emission at localized regions of high electric field, and the dielectric surface atoms. The high field emission current density,  $J$ , is described in terms of the electric field,  $E$ , by:<sup>(8)</sup>

$$J = 6.5 \cdot 10^7 E^2 e^{-6.5 \cdot 10^9}$$

According to this equation,  $J$  has a nearly step-function increase at

$$E = 6.5 \cdot 10^9 \text{ volt/meter} = 6.5 \cdot 10^7 \text{ V/cm}$$

Experimentally observed threshold electric field intensity of  $10^4 \text{ V/cm}$ , nearly four orders of magnitude less, must be due to the fact that localized regions of high electric fields exist on a sufficiently small microscopic scale.

$M_0$  may be evaluated by equating the energy gained by these field-emitted electrons to an initial temperature,  $T_i$ :

$$k \Delta T_i = e \Delta V = e E_b \Delta \lambda$$

where  $k$  is the Boltzmann constant and  $e$  is the electronic charge. We take the characteristic distance,  $\lambda$ , to be the Debye shielding distance:

$$\lambda = 6.9 \sqrt{\frac{T_i}{n}}$$

where  $T_i$  is the temperature in  $^{\circ}\text{K}$ , and  $n$  is the plasma density in number/cc.  $E_b$  is the surface breakdown electric field of  $10^4$  V/cm. These equations may be integrated to give:

$$T_i = \frac{A^2}{n+n_0} \text{ } ^{\circ}\text{K}, \text{ where } A^2 = \left( \frac{6.9eE_b}{2k} \right)^2 = 1.602 \cdot 10^{17}$$

$$T_i = \frac{1.381 \cdot 10^{13}}{n + n_0} \text{ ev where } n \text{ and } n_0 \text{ are in particles/cm}^3 \quad (11)$$

The constant of integration,  $n_0$ , has been introduced approximately in the form of additional number density where  $T_i$  varies inversely as the total density, by taking  $T_i$  as 2500 ev when  $n$  is zero. Recall, that  $n$  is the number density due to ablation.

This density,  $n$ , is evaluated from the ablated mass density,  $M_a$ , by

$$n = 6.02 \cdot 10^{23} \frac{\text{molecules}}{\text{mole}} \left( \frac{1 \text{ mole}}{16 \text{ grams}} \right) M_a \frac{\text{grams}}{\text{cm}^2} \cdot d \frac{1}{\text{cm}} =$$

$$3.76 \cdot 10^{22} \frac{M_a}{d} \frac{\text{molecules}}{\text{cm}^3}$$

The parameter,  $d$ , is the thickness of the plasma film or sheet and is assumed to be 1 percent of the voltage gradient region of 0.0025 cm. The number density,  $n_0$ , is

$$n_0 = \frac{1.38 \cdot 10^{13}}{2500} = 5.523 \cdot 10^9 \text{ particles/cm}^3 \quad (12a)$$

The corresponding mass density,  $M_0$ , is:

$$M_0 = n_0 d \cdot \frac{16}{6.02 \cdot 10^{23}} = 3.67 \cdot 10^{-16} \text{ grams/cm}^2 \quad (12b)$$

#### SIMPLIFIED ANALYSIS

The simultaneous solution of all of the equations presented up to now is rather complex and requires a computerized solution.

Here, some quantitative feeling for the results is obtained by a piecemeal approach with simplifying assumptions.

The first assumption is that there is a solution in which a constant brushfire propagation velocity,  $v_b$ , is appropriate. With this assumption, time variables may be replaced with space variables:

$$x = v_b t; \quad \frac{\partial f}{\partial t} = v_b \frac{\partial f}{\partial x} \quad (13)$$

Equations (1) and (2) may then be integrated to give:

$$J_s = C v_b (V_m - V), \text{ and} \quad (14)$$

$$V = V_m (1 - e^{-f(x)}), \text{ where } f(x) = C v_b \int_x^{\ell} \rho_s dx \quad (15)$$

where  $V_m$  is the maximum voltage change (2500 volts), and  $V$  is the voltage at any point  $x$  in the voltage gradient region. For this part of the analysis the zero reference voltage is taken to be the potential at the bottom of the voltage falloff region; i.e., the  $V = 0$  at  $x = \ell$ .

A further simplification of the problem is obtained by assuming that the voltage profile is known, a linear dropoff to a  $V_{\text{final}}$  of zero as shown in Figure 2. Temperatures, resistivities, particle densities, current densities as well as a new voltage profile can then be calculated. Consistency of the new voltage profile with the assumed profile will put constraints on the possible values of the parameters involved.

The assumed voltage profile is given by

$$V = V_m (1 - \frac{x}{\ell}) = V_m - E_b x$$

The breakdown value of the surface electric field,  $E_b$ , is assumed to be  $10^4$  V/cm.

The plasma parameters for the voltage gradient region may be calculated and are shown in table I. The parameter,  $h$ , is included in the equation for  $T_h$  to account for the fact that not all of  $P_s$  goes into heating of the plasma, and raising the temperature. A heat absorption calculation shows that the heat loss into the dielectric surface constitutes a major sink for the energy in the plasma. The plasma thickness,  $d$ , was assumed to be 0.0025 cm, or 1 percent of the length of the voltage gradient region,  $\ell$ .  $M_a$  and  $T_h$  do not depend on  $d$ , but  $n$  and  $\rho_s$  do. It should also be noted that all four of these parameters are independent of the brushfire velocity,  $v_b$ . This is because they all depend on the time-integrated power density,  $P_s$ , i.e., the

energy, which is independent of velocity. The temperature,  $T$ , in the equation for surface resistivity,  $\rho_s$ , is a composite of the initial field emission/low collisional plasma temperature,  $T_i$ , and the temperature due to heating,  $T_h$ . These two temperature profiles have been combined in the root-sum-square sense:

$$T = (T_i^2 + T_h^2)^{0.5}$$

Since only the  $T_h$  component of  $T$  depends on  $h$  and the  $T_i$  component does not,  $h$  was selected to give the most reasonable voltage profile,  $V(x)$  (see Figure 3a), when computed using equation (15). The value selected was

$$\frac{h}{cg} = 8.71 \cdot 10^{-4}, \quad h = 1.964 \cdot 10^{-4}, \quad \text{where } c = 2.71 \cdot 10^4 \text{ joules/(ev-gram), and}$$

$$g = 8.32 \cdot 10^{-6} \text{ grams/joule}$$

As noted previously,  $h$  is a very small fractional number. The term in the expression for  $f(x)$  in equation (15):

$$12 \left( \frac{cg}{h} \right)^{3/2} C v_b$$

must be a constant.

This means that the individual parameters may change as long as the value of the above combination remains constant. For example, if the per unit area capacitance  $C$  is doubled, the propagation velocity,  $v_b$ , is halved. There is no reason to expect  $c$ ,  $g$ , or  $h$  to change when  $C$  is doubled by halving its thickness. It is possible, however, that  $c$ ,  $g$ , or  $h$  may have values different from those assumed here, but their combination,  $cg/h$  must remain at the same value.

For all of the computations and parametric curves which will be presented next, the brushfire propagation velocity,  $v_b$ , was selected to correspond to that of an ion of mass 16 (oxygen) accelerated through the breakdown voltage,  $V_b$ , or a 2-mil sheet of Kapton. The bulk breakdown electric field is assumed to be  $10^6$  V/cm:

$$v_b = \sqrt{2eV_b/m} = 2.45 \cdot 10^7 \text{ cm/sec for } V_b = 5000 \text{ V}$$

Figure 3a shows the assumed voltage profile,  $V(x)$ , which is moving to the left at a velocity,  $v_b$ , equal to  $2.45 \cdot 10^7$  cm/sec.  $V$  drops linearly from 2500 V at  $x = 0$  to zero at  $x = l$  where  $l$  was chosen to be 0.25 cm in order to give the surface breakdown electric field of  $10^4$  V/cm. Figure 3a also shows the current density,  $J_s$ , which increases linearly from zero at  $x = 0$  to 3.18

A/cm at  $x = l$ . Figure 3b shows the power density,  $P_s$ , which increases linearly from zero at  $x = 0$  to  $3.18 \cdot 10^4$  W/cm<sup>2</sup> at  $x = l$ . The plasma ion and electron density,  $n_i$ , is also shown in Figure 3b. It varies parabolically from zero at  $x = 0$  to  $2.03 \cdot 10^{15}$  particles/cm<sup>3</sup> at  $x = l$ . The ionization is assumed to be 10 percent of the total and therefore the neutral particle density is  $1.83 \cdot 10^{16}$  particles/cc at  $x = l$ .

Figure 4a shows the temperature,  $T$ , and surface resistivity,  $\rho_s$ , as a function of  $x/l$ .

Figure 4b shows the originally assumed linearly falling voltage profile and the voltage profile computed by using the  $\rho_s$  integral in equation (15). It can be noted that  $V(0)$  is only 90 percent of  $V_m$  at  $x = 0$ . However, the voltage gradient is greater than the surface breakdown electric field of  $10^4$  V/cm when  $x/l$  is greater than about 0.5. The temperature in Figure 4a is extremely "hot" for small  $x/l$  values but cools down quickly as the plasma density increases. A minimum is reached at  $x/l$  equal to about 0.4 where the heating effect takes over, and the temperature rises slowly as  $x/l$  increases beyond this point. The surface resistivity profile in Figure 4a varies as the inverse three-halves power of  $T$ .

In order for the computed voltage to be identical to the assumed voltage profile, the surface resistivity would have to be an inverse function of  $x$ :

$$\rho_s = \frac{1}{C V_b x}, \quad C V_b \int_x^l \rho_s dx = \ln \frac{l}{x}, \quad \text{where } e^{-f(x)} = \frac{x}{l}$$

The physics of the problem requires initially a very hot plasma and therefore a very small resistivity, rather than the initially very large surface resistivity required by the assumed linear voltage profile. What this says is that the linear voltage profile was not a good assumption. The computed profile of Figure 4b is presumably a better approximation to the "real" propagating brushfire voltage profile. In principle, iteration of the computations performed here with the computed voltage should provide a better solution. This is not done here, and a more thorough analysis using a computer is recommended.

#### BLOWOUT AND FLASHOVER CURRENTS, $G'$

The ratio of blowout to flashover currents,  $G'$ , is a very important parameter in defining the EMI margin of immunity of a spacecraft to arc discharges. The current density,  $J_s$ , of 3.18 A/cm calculated in the previous section is that which flows to the point of arc discharge initiation in a plasma sheet and thence directly to the conductive substrate below. This is what has been termed the flashover current. Because of the localized nature of this component, the electric and magnetic fields effects are also expected to be localized. Previously, the only long range effect considered was that due to the displacement current,  $C dV/dt$ , where  $C$  is effectively the capacitance to space of the arcing element and  $dV/dt$  is the time rate of change of the surface voltage. Because  $C$  is very small ( $\sim$ pf/cm<sup>2</sup>) the

corresponding currents are very small, and the voltages induced into cable harnesses were very small and at nonhazardous levels. Blowout currents are additional to the displacement currents discussed above. If they are of appreciable magnitude, they could be a serious source of hazard to spacecraft electrical subsystems.

In this section the results of the previous section on brushfire propagation are used to estimate the blowout current. Both magnetic and electrostatic forces were examined, and the conclusion was reached that only the latter is of consequence. Electric fields normal to the dielectric surface will force electrons to move away in the z direction. The overwhelming majority of electric field lines emanating from the electrons collected from environmental charging land on positive charges induced on the substrate. A few field lines, however, must go off to space to account for the voltage fall-off (or rise) from the dielectric surface potential to the space plasma potential (zero). Thus, it is already clear that the dielectric surface potential, through its associated electric field, plays an important role in determining the blowout to flashover arc discharge current ratio, G'. The magnitude of the electric field for a conducting sphere is

$$E_{\text{radial}} = \frac{Q}{4 \pi \epsilon_0 a^2} = \frac{V_s}{a} \text{ (MKS units)}$$

where a is the radius of the sphere and  $V_s$  is the surface potential and Q is the charge. For an arcing dielectric surface on a real spacecraft, a is not an easily defined parameter and requires a time-dependent NASCAP type of 3-dimensional Laplace's equation solution in an arc whose discharge charge time is measured in nanoseconds.

We know that a is not as large as the spacecraft dimension and not as small as the dielectric thickness. For our purposes here, we assume that it is comparable to the size of a typical spacecraft box (or 20 cm), but keeping in mind that  $E_{\text{radial}}$  varies inversely as a.

The fact that edge or punch-through breakdown occurs at -5 kV, but -2.5 kV remains after the discharge, has been ignored up to now except to take the 2.5 kV differential as the voltage which "drives" the brushfire.

Thus:

$$V_s = V_0 + V_r + V_m \left(1 - \frac{x_l}{l}\right)$$

where  $V_0$  is the spacecraft ground potential,  $V_r$  is the remaining voltage after the discharge (2500 V) and  $V_m$  is the maximum brushfire driving potential (2500 V). The proper signs have to be used to account for the fact that we are considering forces which drive electrons off of the surface. Ions are pulled harder against the surface. For the time being  $V_0$  will be assumed to be zero.

The velocity and displacement in the off-surface z-direction for an electron released at  $z = 0$  and  $t = 0$  are given by

$$F_z = eE_z = e V_s/a = m \frac{dv_z}{dt}$$

Incorporating, as before, the space-time equivalence via the brushfire propagation velocity  $v_b$ :

$$v_z(x) = \int_0^x \frac{2eV_m}{mav_b} \left(1 - \frac{x}{2l}\right) dx = \frac{2eV_m}{mav_b} x \left(1 - \frac{x}{4l}\right)$$

$$z(x) = \frac{2eV_m}{mav_b^2} \int_0^x \left(x - \frac{x^2}{4l}\right) dx = \frac{eV_m}{mav_b^2} x^2 \left(1 - \frac{x}{6l}\right)$$

The above equations apply in the MKS system of units. If  $a$ ,  $v_b$ , and  $x$  are in cgs units,  $v_z$  and  $z$  may be obtained in cgs units by multiplying both of the above equations by  $10^4$ .

Figure 5 shows  $v_z$  and  $z$  plotted as functions of  $x/l$ . At  $x = l$ ,  $v_z$  is  $3.37 \cdot 10^9$  cm/sec and  $z$  is 19.1 cm. These values for electrostatic deflection are about eight orders of magnitude greater than the comparable values caused by magnetic forces on the plasma current.

To calculate the off-surface surface current density,  $J_{sz}$ , an integration over  $x$  has to be performed:

$$J_{sz}(x_1) = \int_0^{x_1} e n(x) v_z(x_1 - x) dx$$

$$\text{where } v_z(x_1 - x) = \frac{2eV_m}{mav_b} (x_1 - x) \left(1 - \frac{x_1 - x}{4l}\right) \cdot 10^4 \text{ cm/sec}$$

$$n(x) = Ax^2 \text{ electrons/cm}^3 \text{ (x in cm)}$$

$$A = 0.1 \cdot 3.76 \cdot 10^{21} \text{ gCE}_b^2 / 2d = 3.25 \cdot 10^{16}$$

$J_{sz}(x_1)$  is plotted in Figure 8 for  $0 < x < 0.05l$ .

$$J_{sz}(x_1) = 3.04 \cdot 10^4 \left(\frac{x_1}{l}\right)^4 \left(1 - \frac{2x_1}{5l}\right) \text{ amp/cm}$$

At  $x_1 = \ell = 0.25$  cm,  $J_{sz}$  would be 18,240 A/cm, which is much too large in view of the 3.18 A/cm value for  $J_s$  (in the x-direction) in the plasma sheet at  $x = \ell$ . There is, however, a mechanism whereby  $J_{sz}$  is cut off at a much smaller value. The situation is that at the same time as the off-surface charge is being evaluated by electrostatic forces, the charge finds itself above a plasma whose Debye length is shorter than its height above the surface of the dielectric. At some height,  $\bar{z}$ , and Debye length,  $\lambda$ , the electric field due to the charges below becomes completely blocked off, and the effective electric field becomes zero. We assume that this height,  $\bar{z}$ , is equal to  $4.6\lambda$ ; i.e., when the electric field is shielded by 99 percent.

The effective height  $\bar{z}(x)$  is calculated by averaging the z-distance travelled by all of the particles released from  $x = 0$  to  $x = x_1$ .

$$\bar{z}(x_1) = \frac{1}{\int_0^{x_1} n(x) dx} \int_0^{x_1} n(x) z(x_1 - x) dx$$

$$\text{where } z(x_1 - x) = \frac{2eV_m}{mav_b^2} (x_1 - x)^2 \left(1 - \frac{x_1 - x}{6\ell}\right) \cdot 10^4 \text{ cm}$$

$$\bar{z}(x_1) = \frac{eV_m \ell^2}{mav_b^2} \left(\frac{x_1}{\ell}\right)^2 \left(1 - \frac{x_1}{12\ell}\right) \cdot 10^3 = 2.29 \left(\frac{x_1}{\ell}\right)^2 \left(1 - \frac{x_1}{12\ell}\right) \text{ cm}$$

The Debye length is given by

$$\lambda = 6.9 (T/n)^{0.5} \text{ cm}$$

where  $T$  is the temperature in  $^{\circ}\text{K}$  and  $n$  is in electrons/cm<sup>3</sup>. Figure 6 shows  $\bar{z}$  and  $\lambda$  plotted for  $0 < x < \ell$  (where  $\ell = 0.25$  cm). It can be seen that  $\bar{z}$  is much greater than  $\lambda$  for most of the range of  $x/\ell$  except near  $x = 0$ . At  $x = \ell$ ,  $\bar{z}$  is about 2 cm, which is about 10 percent of the value for  $\bar{z}$ , the height of a single electron released at  $x = 0$ . Since the temperature for small values of  $x$  is nearly completely dominated by the initial high-field-emitted electrons which are cooling off:

$$T \approx T_i = \frac{1.381 \cdot 10^{13}}{n + n_0} \text{ ev} \approx \frac{1.60 \cdot 10^{17}}{n} \text{ } ^{\circ}\text{K}$$

$$\text{and } \lambda = \frac{6.9 \cdot 4.00 \cdot 10^8}{n} = \frac{2.76 \cdot 10^9}{3.25 \cdot 10^{16} x^2} = \frac{8.49 \cdot 10^{-8}}{x^2} = \frac{1.36 \cdot 10^{-6}}{(x/\ell)^2} \text{ cm}$$



Equating  $z$  to  $4.6\lambda$ :

$$(x_1/\ell)^4 = 2.73 \cdot 10^{-6}, \quad x_1/\ell = 0.0407, \quad x_1 = 0.0102 \text{ cm}$$

Putting this value for  $x_1$  into the equation for  $J_{SZ}(x_1)$ :

$$J_{SZ}(x_1) = 3.04 \cdot 10^4 \cdot 2.73 \cdot 10^{-6} = 0.083 \text{ A/cm}$$

The blowout to flashover current ratio,  $G'$ , taken to be the ratio of  $J_{SZ}(x_1)$  to the maximum value of the plasma sheet current,  $J_S$ , (at  $x = \ell$ ) is then  $G' = J_{SZ}(x_1)/J_S(\ell) = 0.083/3.18 = 0.026$  or 2.6 percent. Figure 7 shows  $z$  and  $4.6\lambda$  plotted versus  $x/\ell$  and their intersection at  $x/\ell = 0.041$ .

A more nearly correct calculation for  $J_{SZ}$  involves inserting the Debye shielding effect into the expression for  $v_z$ . We consider the shielding to apply to the external electric field by multiplying the potential by the exponential factor so that the corrected off-surface velocity,  $v_z^*$  is given by:

$$v_z^*(x_1) = \int_x^{x_1} \frac{2 e V_m (1 - \frac{x}{\ell})}{m a v_b} e^{-\bar{z}/\lambda} dx$$

Since the  $x$  values of consequence are very small ( $x/\ell < 0.05$ ), the above expression may be simplified to

$$v_z^* \approx \frac{2 e V_m}{m a v_b} \int_x^{x_1} e^{-\bar{z}/\lambda} dx$$

From the previous analysis,

$$\bar{z}/\lambda = 2.29 (x/\ell)^2 / (1.36 \cdot 10^{-6} x^2 / \ell^2) = 1.68 \cdot 10^6 (x/\ell)^4$$

Figure 8 shows  $v_z^*$  computed numerically and plotted as a function of  $x/\ell$ . It starts at about  $10^8$  cm/sec at  $x = 0$  and drops to nearly zero by the time that  $x/\ell = 0.04$ . The expression for  $J_{SZ}$  now is

$$J_{SZ}(x_1) = \int_0^{x_1} e n(x) v_z^*(x) dx = \frac{2 e^2 V_m A}{m a v_b} \int_0^{x_1} x^2 dx \int_x^{x_1} e^{-1.68 \cdot 10^6 (x/\ell)^4} dx$$

independent of the upper limit of the integral,  $x_1$ , for values of  $x/\ell$  greater than about 0.04. This value is

$$J_{sz} = 0.0126 \text{ A/cm}$$

and the ratio of blowout to flashover currents,  $G'$ , is

$$G' = J_{sz}/J_z = 0.0126/3.18 = 0.40\%$$

Comparing Figures 7 and 8, it is clear that cutting off  $J_{sz}$  at  $z = 4.6\lambda$  gives too large a value of  $x/\ell$  and hence too large a value for  $J_{sz}$  and  $G'$ . From Figure 8, the "correct" values of the parameters for Figure 7 should have been:

$$x_1/\ell = 0.0254, \lambda = 2.11 \cdot 10^{-3} \text{ cm}, z = 1.47 \cdot 10^{-3} \text{ cm}$$

$$z/\lambda = 1.43, \text{ and } e^{-z/\lambda} = 0.24$$

The Debye shielding effect has reduced  $J_{sz}$  from an excessively large value, 18,240 A/cm, to a value of 0.0216 A/cm. This latter value leads to a  $G'$  of 0.40 percent, which is much smaller than those that have been previously reported by us as well as by others. Another "correction" that should be applied is the fact that Debye shielding does cut off the electrons that are leaving the plasma sheet due to electric fields. However, the potential of the plasma remains unchanged, and thus the electric fields beyond the plasma remain unchanged. Therefore the "escaped" electrons continue to be accelerated by the surface potential even though their number is fixed. Since cutoff occurs at a very small  $x$  value ( $x/\ell = 0.0254$ ,  $\ell = 0.25 \text{ cm}$ ), the accelerating potential is very nearly:

$$V_m + V_r = 2500 + 2500 = 5000 \text{ volts}$$

where  $V_m$  is the maximum voltage change, and  $V_r$  is the remaining voltage after the discharge.

The surface current density,  $J_{sz}$ , by the time the escaped electrons have traversed the whole arcing source then is given by:

$$J_{sz} = Nev_z \text{ where } v_z = \left[ \frac{2e(V_m + V_r)}{m} \right]^{0.5} = 4.19 \cdot 10^9 \text{ cm/sec}$$

$N$  is the number of released electrons per  $\text{cm}^2$  and is obtained from  $n(x)$  by integration from  $x = 0$  to  $x = x_1$  or  $x/\ell = 0.0254$ :

$$n(x) = 3.25 \cdot 10^{16} x^2 \text{ electrons/cm}^3$$

$$N = \int_0^{x_1} n(x) dx = 2.774 \cdot 10^9 \text{ electrons/cm}^2$$

Therefore

$$J_{sz} = Nev_z = 1.86 \text{ A/cm, and } G' = J_{sz}/J_x = 1.86/3.18 = 58.5\%$$

Since the electrons, in increasing their kinetic energy by 5 keV, have been accelerated in the x-direction as well as the z-direction, the use of the full 5 keV in calculating  $J_{sz}$  is not valid. A particle pushing trajectory calculation for the electrons in the presence of existing electric fields is required. Figure 9 is the author's conception of how the equipotential and electric field lines should appear. The escaping electrons do accelerate through the full 5 keV but the current, properly, should not be termed  $J_{sz}$ . From the "guessed" field configuration it appears that the blowout currents should be travelling at about a 45 degree angle to the surface in the direction of the ignition point.

#### EFFECT OF SPACECRAFT POTENTIAL ON $G'$

The importance of external electric fields in determining the blowout to flashover current ratio,  $G'$ , has been discussed in the previous section. In the analysis, the change in the surface electric field due to the arc discharge was taken into account by the space and time dependence of the surface potential,  $V_s$ . However, the reference voltage, the spacecraft potential,  $V_0$ , was assumed to be constant at zero volts. In orbit, the blowout of the arc discharge electrons must be compensated by the recollection of an equal number of electrons if the spacecraft potential is to be unchanged. Any inequality between blowout currents and return currents must be "made up" by displacements currents in the following charge balance equation:

$$C_s \Delta(V_s + V_0) + \int_0^t I_z dt = C_0 \Delta V_0 + \int_0^t I_r dt$$

In the above equation  $C_s$  is the capacitance of the arcing element to the remainder of the spacecraft (or to space), and  $C_0$  is the capacitance of the spacecraft to space.  $I_z$  is the blowout current from the arcing element, and  $I_r$  is the replacement current to the remainder of the spacecraft. Taking the derivative of the equation gives the current balance equation which must be satisfied during the arc discharge:

$$C_s \frac{d}{dt} (V_s + V_o) + I_z = C_o \cdot \frac{d}{dt} V_o + I_r$$

$I_z$  is the blowout current density,  $J_{sz}$ , computed in the preceding section, multiplied by an appropriate width dimension.  $I_r$  is the integral of all of the replacement current densities collected over the entire exposed surface of the spacecraft. As  $I_r$  is collected, it returns to the arcing element via various structural paths on the spacecraft. Obviously, the structural current density is low at remote portions of the spacecraft, and becomes greater as the current flow paths converge towards the arcing element. For this reason, it is to be expected that the potential victims of EMI closest to the arcing source would be the most susceptible.

The point here is that  $V_o$  adjusts itself in a time dependent manner to assure that the current continuity equation is satisfied. Since electrons are leaving,  $V_o$  will go more positive. If, as assumed,  $V_o$  is initially near zero,  $V_o$  will become absolutely positive and attract electrons from the environment surrounding it, and repel ions. How far positive it becomes is a function of the surface area of the whole spacecraft, and the accessibility of replacement electrons. The problem is similar to that of computing the spacecraft charging potentials, but on a much shorter time scale—tens of ns rather than minutes.

The availability of electrons in the ambient plasma may be estimated as follows: Assume that electrons may take as long as  $1 \mu s$  to reach the spacecraft, a sphere of radius,  $R$ , of one meter at a potential,  $V_o$ , of 1 kV. The radius,  $r$ , from which electrons can arrive at the surface in  $1 \mu s$  is given by:

$$\frac{dr}{dt} = v(r) = \left[ \frac{2e}{m} V(r) \right]^{0.5} = \left[ \frac{2e}{m} \cdot \frac{Q}{4\pi\epsilon_0 r} \right]^{0.5}$$

$$\frac{2}{3}(r^{1.5} - R^{1.5}) = \frac{2e}{m} \cdot \frac{Q}{4\pi\epsilon_0} t = \frac{2e}{m} V_o R^{0.5} t$$

$$r = \left\{ \frac{3}{2} \left[ \frac{2e}{m} V_o R \right]^{0.5} t + R^{1.5} \right\}^{2/3} = 9.47 \text{ meters for } t = 1 \mu s$$

For  $t = 100 \text{ ns}$ ,  $r$  is 2.44 meters. Assuming that the electron density is  $1/\text{cm}^3$ , a spherical volume, for  $1 \mu s$ , contains  $3.20 \cdot 10^{10}$  electrons or a charge of  $5.12 \cdot 10^{-9}$  coulombs. By comparison, a 20 cm wide arcing source, grounded, would have a current  $I_z$  of 19 A, and would emit, in  $1 \mu s$ , a charge of  $1.9 \cdot 10^{-5}$  coulombs. This is more than three orders of magnitude more charge than is available.

Another calculation which indicates that the current available is insufficient to "clamp"  $V_0$  utilizes the Langmuir - Mott Smith equation for the attraction of electrons at a Maxwellian temperature,  $T$ , to a conducting sphere of radius  $R$ :

$$I = 4\pi R^2 J_0 \left(1 + \frac{V_0}{T}\right) = 22.5 \cdot 10^{-4} \text{ A}$$

$$\text{for } R = 1, V_0 = T = 1 \text{ kV, and } J_0 = 1 \text{ na/cm}^2 = 10^{-5} \text{ A/m}^2$$

$$\text{a "resistance," } R_0, \text{ may be calculated from } R_0 = \frac{V}{I} = 4 \cdot 10^6 \text{ ohms}$$

The solution for the blowout current,  $I_z$ , in the presence of a variable time dependent  $V_0$  may be obtained from the following

$$I_z = J_{sz} w; J_{sz} = N e v_z; v_z = \sqrt{\frac{2eV_s}{m}}; V_s = V_r - V_0$$

$$V_0 = I_r R_0; V_0 = \frac{1}{C_0} \int I_c dt$$

In the above equations,  $w$  is the width of the arcing source,  $N$  is the number of electrons that have been ejected before the Debye shielding cutoff,  $V_s$  is the surface potential,  $V_r$  is the remaining voltage after the discharge (2500 V),  $I_r$  is the resistive replacement current flowing in  $R_0$ , and  $I_c$  is the displacement current flowing in the capacitance of the spacecraft to space,  $C_0$ . The electrical circuit is shown in Figure 10.

The above equations lead to the following result:

$$\frac{t}{\tau} = \frac{1}{p-q} \ln\left(\frac{x-p}{x-q} \cdot \frac{1-q}{1-p}\right) - \ln\left(\frac{x^2 + Bx - 1}{B}\right)$$

where  $p$  and  $q$  are roots of  $x^2 + Bx - 1 = 0$ ,

$$\tau = R_0 C_0, x = I_z / I_{z0}, I_{z0} = A / V_r^{0.5} = 1.316 \cdot w(\text{cm}) \text{ A,}$$

$$A = Ne(2e/m)^{0.5} \cdot 100 w = 0.0236 w, B = R_0 I_{z0} / V_r = w \cdot R_0 / 1900.$$

Figures 11 and 12 show  $I_z(t)$  and  $V_0(t)$  for  $w = 10 \text{ cm.}$  and various values of  $R_0$ . The time constant,  $\tau = R_0 C_0$ , varies from 1 ns to 1  $\mu$ s on the assumption that the  $C_0$  is 100 pf. For  $R_0$  large,  $V_0$  approaches  $V_r$  and  $I_z$  decreases because  $V_s$  becomes small. For  $R_0$  small, as in many vacuum tank experiments,  $V_0$  never gets very large, and  $I_z$  remains near  $I_{z0}$ . Figure 13 shows the steady state  $I_z$  and  $V_0$  plotted as a function of  $R_0$ .

The preceding discussion about  $R_0$  indicates that it is quite large. For the approximation that  $I_r \ll I_c$ , the solutions for  $I_z$  and  $V_0$  are:

$$I_z = I_{z0} [1 - t/(2\tau_0)], \quad V_0 = V_r [1 - (1 - \frac{t}{2\tau_0})^2]$$

$I_z$  decreases linearly to zero in a time  $2\tau_0 = 2C_0V_r/I_{z0} = 3.8 \cdot 10^{-7}/w$  seconds or 38 ns for  $w = 10$  cm.  $V_0$  rises parabolically to  $V_r$  in the same time period. For a 10 cm square sample, then the brushfire propagates according to our model in a time,  $t$ , of:

$$t = \frac{10 \text{ cm}}{2.45 \cdot 10^7 \text{ cm/sec}} = 408 \text{ ns}$$

$I_z$ , however, lasts for only 38 ns or about 10 percent of the discharge time with an "average"  $G'$  of 29 percent rather than the peak value of 58 percent. Thus, the in-orbit  $G'$  is of shorter duration and of lower average magnitude as compared to a laboratory determination with  $R_0$  shorted to ground. A proper laboratory experiment should incorporate a high  $R_0$  but should also include an appropriate  $C_0$ .

#### LIMITING MECHANISMS ON BRUSHFIRE PROPAGATION

The question arises as to whether some processes exist whereby the brushfire propagation might be limited. The paper by Aron and Staskus<sup>(9)</sup> seems to indicate that propagation continues for samples as large as 5058 cm<sup>2</sup>. Their samples (4 mil teflon) were laid on an aluminum plate that was 0.313 cm thick. This seems to indicate that the plasma sheet resistance, the part behind the voltage gradient region, is not a problem.

In some applications, the dielectric sheet with the vacuum deposited aluminum (VDA) is not over a good conducting ground plane. In these cases the surface resistivity of the VDA film becomes important. Typical values are in the order of 1 ohm-per-square, but this may be exceeded by more than a factor of 10 after handling and during the installation process. A 100 cm long sample then will develop more than 1 kV with a 1 A/cm arc discharge surface current density,  $J_s$ . If one considers then that arc discharge surface currents are really not 1-dimensional, but rather flow from the whole surface towards a single breakdown point, the surface current density increases greatly and therefore the voltage drop may become comparable to the voltage across the dielectric before breakdown. Although the brushfire propagation as developed depends only on the electric field at breakdown,  $E_b$ , rather than the voltage,  $V_b$ , a dependence on the latter may develop in a more critical analysis.

Figure 14 shows an example of a set of surface voltage measurements before and after an arc discharge. The discharge clearly did not wipe off the stored charge uniformly. The charge seems to have flowed towards the edge at which breakdown occurred, but was slowed down as the distance from that

location increased. This particular sample was mounted on an aluminum substrate. However, the VDA was sandwiched with a Kapton sheet between the VDA and the aluminum substrate. Thus, resistive currents were forced to flow through the VDA rather than through the substrate.

#### SUMMARY AND CONCLUSIONS FROM THE BRUSHFIRE ARC DISCHARGE MODEL ANALYSIS

Summarizing the analytical development of the arc discharge brushfire propagation model should begin with noting the many deficiencies. The first is that the analysis is 1-dimensional while most arcing configurations are 2-dimensional. Thus, no account is taken of the "sideways" propagation effect both as it affects the brushfire wavefront steepness requirements, and the greater concentration of plasma sheet currents as they converge towards the arc initiation point. There are many assumptions which may or may not be justified such as the ignoring of thermal conductance, and the assumption that the plasma thruster data,  $8.32 \cdot 10^{-6}$  gram per joule of material ablated, was applicable. The assumption of a plasma sheet thickness, 1 percent of the length of the voltage gradient region, was not derived from physical principles, but rather, from an idea of what a "sheet" should be. The gram-molecular-weight of the dielectric material, 16, also was a guess, and the specific heat depends on this number. The plasma properties which would clearly identify the time dependent roles of electrons, ions and neutrals have not been carefully treated. In particular, the inertial/collisional role of ions in determining the brushfire velocity should be included in the basic equations so that the velocity is consistent with the other physical processes involved. The areas of improvements that are needed in the present analysis are summarized below. As stated previously, there are many improvements that can be made in the analytical model as presented here, and it is hoped that this work will provide some insight into how a more nearly correct model should be formulated.

- o Many assumptions need to be examined
  - Thermal conductivity, mass ablated, plasma sheet thickness, etc.
- o More physical processes need to be included
  - Role of ions in determining brushfire velocity; ablation, ionization and radiation processes
  - "Mechanical" processes of particle acceleration and collisions
- o Self-consistent solutions are needed
  - Computerized approach
- o Model should be expanded to include the 2-dimensional problem

The analysis has provided a first-cut solution to voltage, current, plasma density, temperature and resistivity profiles associated with the

plasma sheet of a propagating brushfire wavefront. The flashover surface current density associated with the discharge rises linearly with distance away from the head of the wavefront as

$$J_{sx} = C v_b V_m x / l$$

At the bottom of the voltage falloff region  $J_s$  reaches a maximum value:

$$J_{sx} = C v_b V_m = 3.18 \text{ A/cm, for } V_m = 2500 \text{ V}$$

which is proportional to the breakdown voltage  $V_m$ . The duration of the arc discharge is simply the sample size (linear dimension) divided by the brushfire propagation velocity,  $v_b$ . To the extent that the theory is applicable to the 2-dimensional case, the duration should be proportional to the square root of the area. The following combination of parameters for a given dielectric material must be a constant:

$$\left( \frac{cg}{h} \right)^{3/2} C v_b$$

where  $c$  is the specific heat,  $g$  is the mass ablated per joule,  $h$  is the fraction of the power expended in raising the plasma temperature,  $C$  is the dielectric capacitance per unit area and  $v_b$  is the brushfire propagation velocity. The above combination of parameters must be a constant for a given dielectric material except that  $C$  also depends on the thickness. Thus, increasing the thickness decreases  $C$ , and hence  $v_b$  should decrease correspondingly.

Another result of the analysis is that magnetic  $V \times B$  forces are much less effective in producing blowout currents than electric field forces. Debye shielding of electric fields limits the blowout electrons to the very tip of the brushfire wavefront. An analogy for the blowout current would be the smoke puffing out of the smokestack of the locomotive of a train as it moves forward -- not the whole train burns. The blowout electrons are accelerated by the chargeup potentials and the ratio of blowout to flashover currents,  $G'$ , has been calculated to be

$$G' = 58.5\%$$

This value of  $G'$  takes into account the experimentally observed fact that about one-half of the stored charge (1/4 of the stored energy) remains after the discharge. If the fraction of remaining charge were lower, the flashover current would be proportionately larger, but the blowout current would be about the same since the number of electrons remains nearly the same and the total accelerating potential also remains the same. Thus  $G'$  would decrease, but only by a factor of about two. From the results of the above analysis,  $G'$  is independent of the size of the arcing source. The surface voltage at breakdown affects  $G'$  as its square-root.



The dependence of the blowout current, and therefore  $G'$ , on the spacecraft potential is rather drastic, and depends on the capability of the spacecraft to collect return currents, either from the surrounding plasma or from the blowout current itself. The spacecraft potential rises in order to compensate for the blown off charges and to collect the required number of electrons, or to make up the deficiency via displacement currents. Because the spacecraft capacitance to space,  $D_0$ , is small ( $\sim 100$  pf), the accelerating potential for the blowout electrons is quickly cancelled -- in 38 ns out of a total of 408 ns for the whole brushfire process to take place -- in our example of a 10 cm square arcing source. Most laboratory experiments in the past have grounded the arcing source to the vacuum system ground through a low resistance of a few ohms. A more proper simulation of in-orbit conditions for arc discharges would be to increase the grounding resistance to greater than 10,000 ohms, and add a parallel capacitance of about 100 pf. The conclusions resulting from the brushfire model analysis are summarized below:

- o The flashover surface current density,  $J_{SX}$ , (3.18 A/cm), is proportional to  $V_m$ .
- o  $(h/cg)^{3/2} \cdot C v_b$  is a constant (see text for definition of parameters).
- o The discharge duration is proportional to the length of a 1-dimensional source.
  - And is proportional to the square-root of the area of a 2-dimensional source.
- o The blowout surface current density,  $J_{SZ}$ , (1.86 A/cm), is proportional to the square-root of the surface potential at breakdown.
- o  $G'$  (58.5 percent) is independent of the area of the arcing source.
  - Depends on electric field forces; magnetic forces are negligible.
- o  $G'$  is grossly affected by how the spacecraft potential varies during the discharge.
  - $J_{SZ}$  is cut off by positive spacecraft potentials (smaller net potentials) during the discharge.
- o Laboratory measurements of  $G'$  should take into account conditions on orbit.

The author acknowledges the contributions of two colleagues to the present analysis of the arc discharge brushfire propagation model. J. M. Sellen, Jr. coined the term, "brushfire," and formulated the initial concepts on the steepness requirements for a propagating wavefront. R. L. Wax critiqued many aspects of the model. In particular, his insight into the plasma physical processes was invaluable.

## REFERENCES

- (1) R. Leadon and J. Wilkenfeld, "Model for Breakdown Process in Dielectric Discharges," Spacecraft Charging Technology - 1978. NASA Conference Publication 2071, AFGL-TR-79-0082.
- (2) I. Katz, M. J. Mandell, D. E. Parks and G.W. Schnuelle, "A Theory of Dielectric Surface Discharges," 1980 IEEE Annual Conference on Nuclear and Space Radiation Effects, July 1980.
- (3) A. Rosen, N. L. Sanders, J. M. Sellen, Jr., and G. T. Inouye, "Final Report - Effects of Arcing Due to Spacecraft Charging on Spacecraft Survival," NASA/LeRC Report No. CR-159593, November 14, 1978.
- (4) G. T. Inouye and J. M. Sellen, Jr., "A Proposed Mechanism for the Initiation and Propagation of Dielectric Surface Discharges," Proc. 1978 Symposium on Effects of the Ionosphere on Space and Terrestrial Systems.
- (5) K. G. Balmain, "Scaling Laws and Edge Effects for Polymer Surface Discharges," Spacecraft Charging Technology - 1978, NASA Conference Publication 2071, AFGL-TR-79-0082.
- (6) L. Spitzer, Jr., "Physics of Fully Ionized Gases," Interscience Publishers, Ltd., 1956, pp. 82-86.
- (7) R. J. Vondra, K. Thomasson and A. Solbes, "Analysis of Solid Teflon Pulsed Plasma Thruster," J. Spacecraft and Rockets, Volume 7, No. 12, December 1970.
- (8) J. Millman and S. Seeley, "Electronics," Second Edition McGraw-Hill Book Co., Inc., 1951, pp. 111-112.
- (9) P. R. Aron and J. V. Staskus, "Area Scaling Investigations of Charging Phenomena," Spacecraft Charging Technology - 1978, NASA Conference Publication 2071, AFGL-TR-79-0082.

Table 1. Plasma Parameter Resulting from a Linear Voltage Gradient

---

$J_s = C v_b V_m x / l = C v_b E_b x$	$\rho_s = \frac{k}{d} T^{3/2} = 12 \left( \frac{cg}{h} \right)^{3/2} \left[ \ln \left( 1 + \frac{x^2}{A} \right) \right]^{-3/2}$
$P_s = J_s \frac{\partial V}{\partial x} = J_s E_b = C v_b E_b^2 x$	$T_h = - \frac{h}{c_m} \int P_s dt = \frac{h}{cg} (1 + x^2/A)$
$M_a = \int g P_s dt = g C E_b^2 x^2 / 2$	where $A = 2 M_0 / (g C E_{bb}^2) = 1.70 \cdot 10^{-8} \text{ cm}^2$
$n = 3.76 \cdot 10^{22} g C E_b^2 x^2 / (2d)$	and $T_h$ is the temperature due to heating.

---

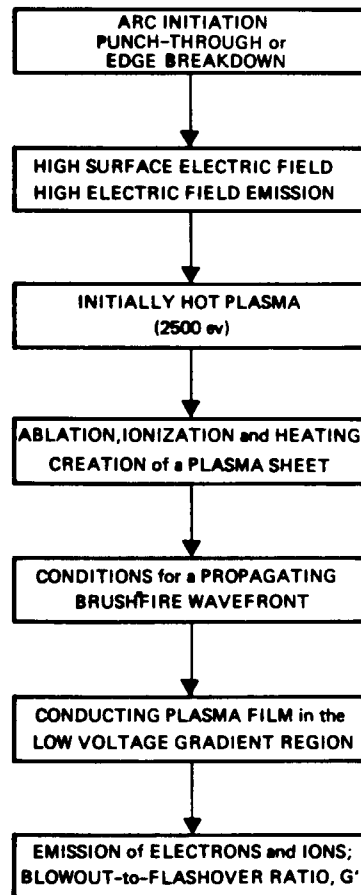


Figure 1. Overview of the Brushfire Propagation Analysis

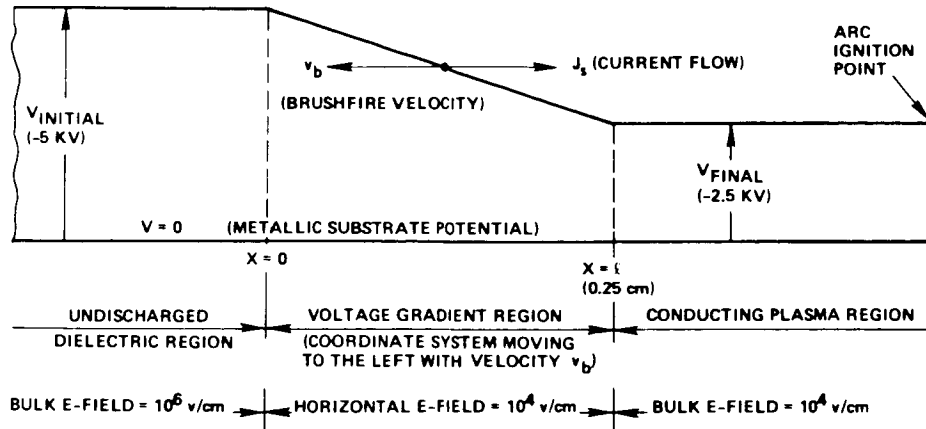


Figure 2. Voltage Profile of a Propagating Brushfire Wave Front

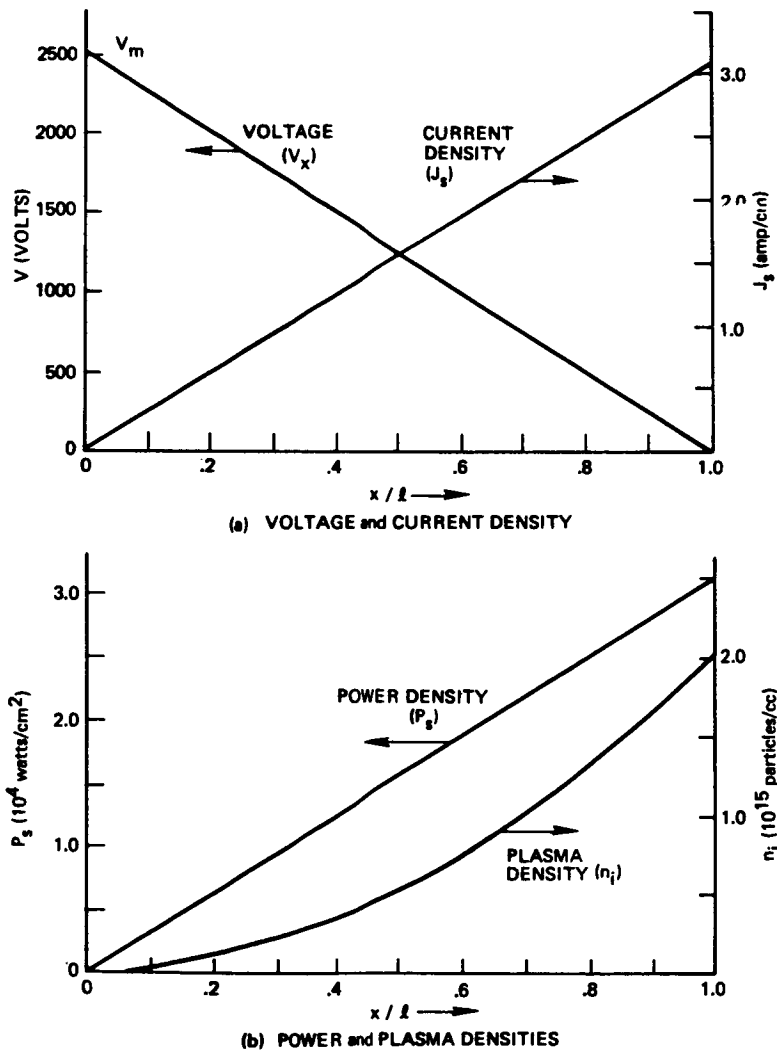
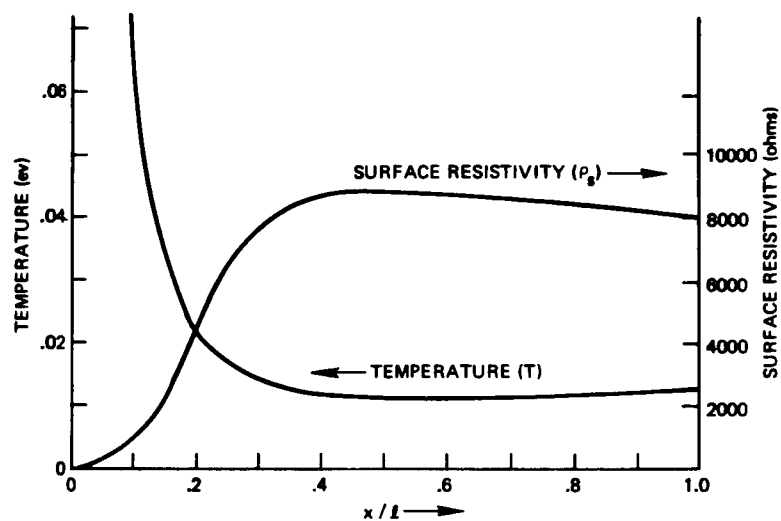
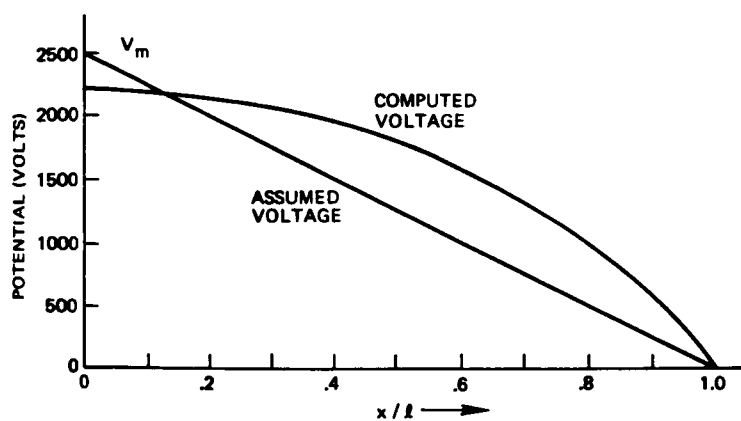


Figure 3. Plasma Parameters Resulting from an Assumed Linear Voltage Profile



(a) TEMPERATURE and SURFACE RESISTIVITY PROFILES



(b) ASSUMED and COMPUTED VOLTAGE PROFILES

Figure 4. Additional Plasma Parameters Resulting from a Assumed Linear Voltage Profile

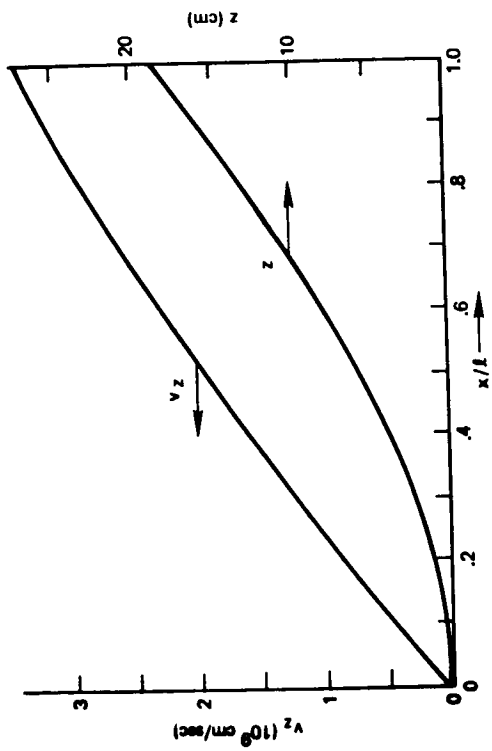


Figure 5.  $v_z$  and  $z$  for Electron at  $x = 0$   
(No Plasma Shielding)

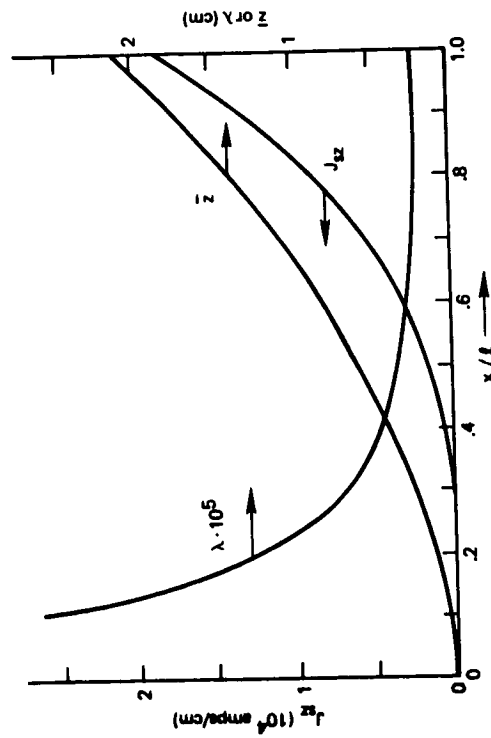


Figure 6. Debye Length ( $\lambda$ ),  $J_{sz}$  and  $z$   
(No Plasma Shielding)

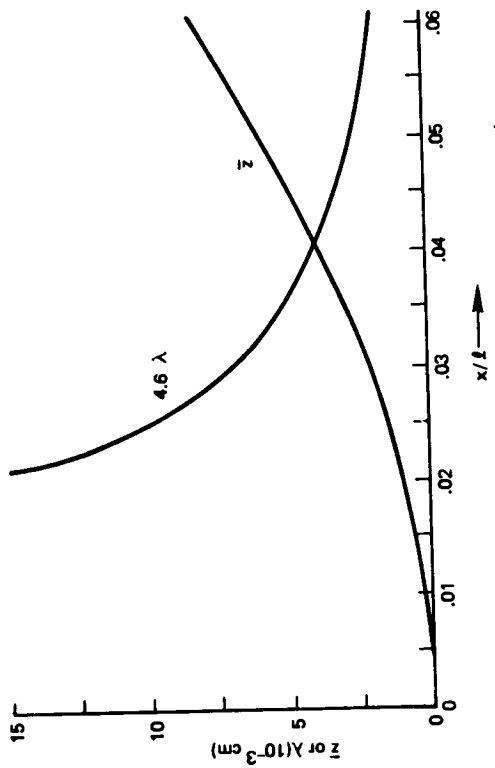


Figure 7.  $4.6\lambda$  and  $z$  versus  $x/\lambda$

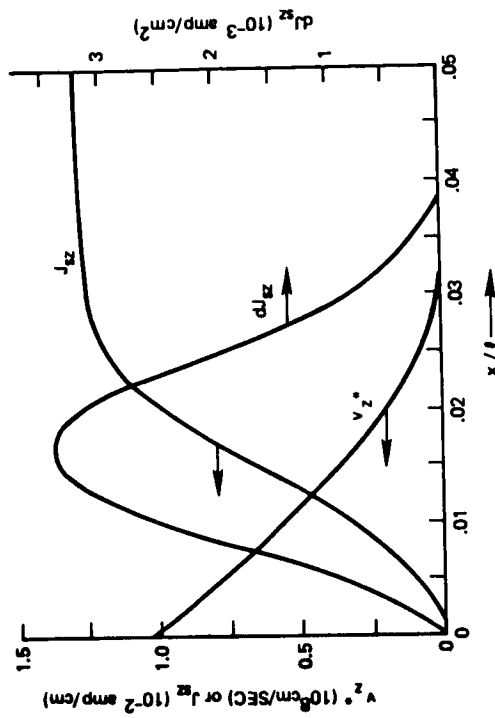


Figure 8.  $v_z^*$ ,  $dJ_{sz}$  and  $J_{sz}$  Versus  $x/\lambda$   
(Shielding by Plasma)

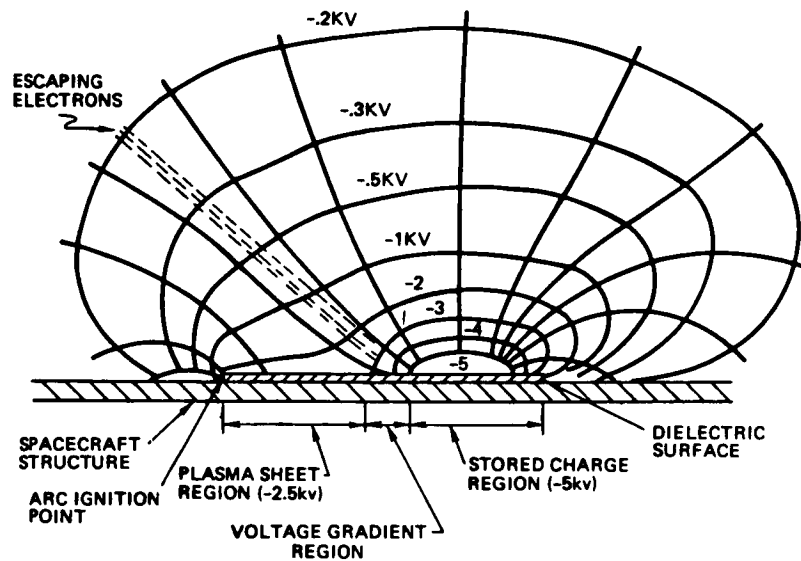


Figure 9. Brushfire Equipotential and E-field Lines

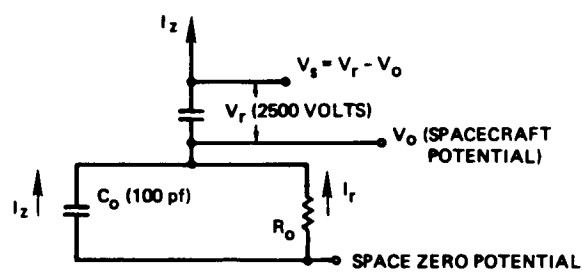


Figure 10. Electrical Circuit Defining  $I_z$  and  $V_0Ct$

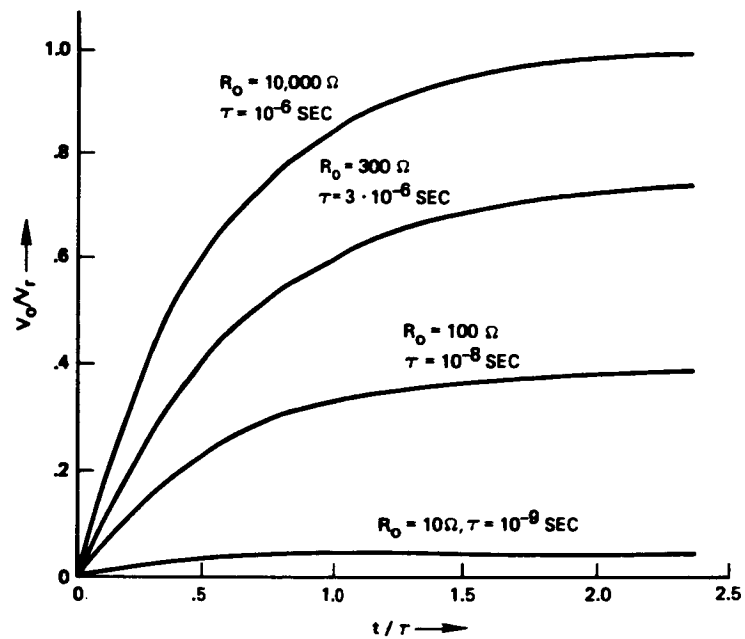


Figure 11.  $V_O/V_r$  as a Function of  $t/\tau$

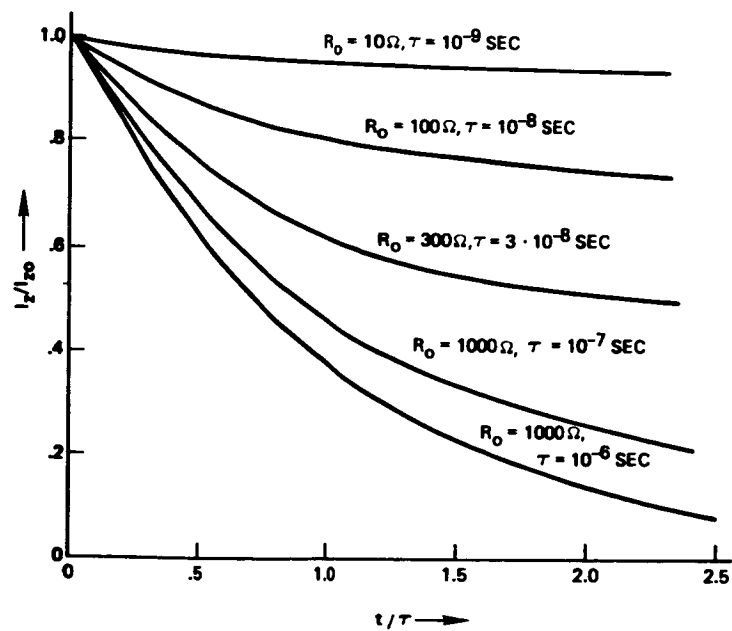


Figure 12.  $I_z/I_{z0}$  as a Function of  $t/\tau$



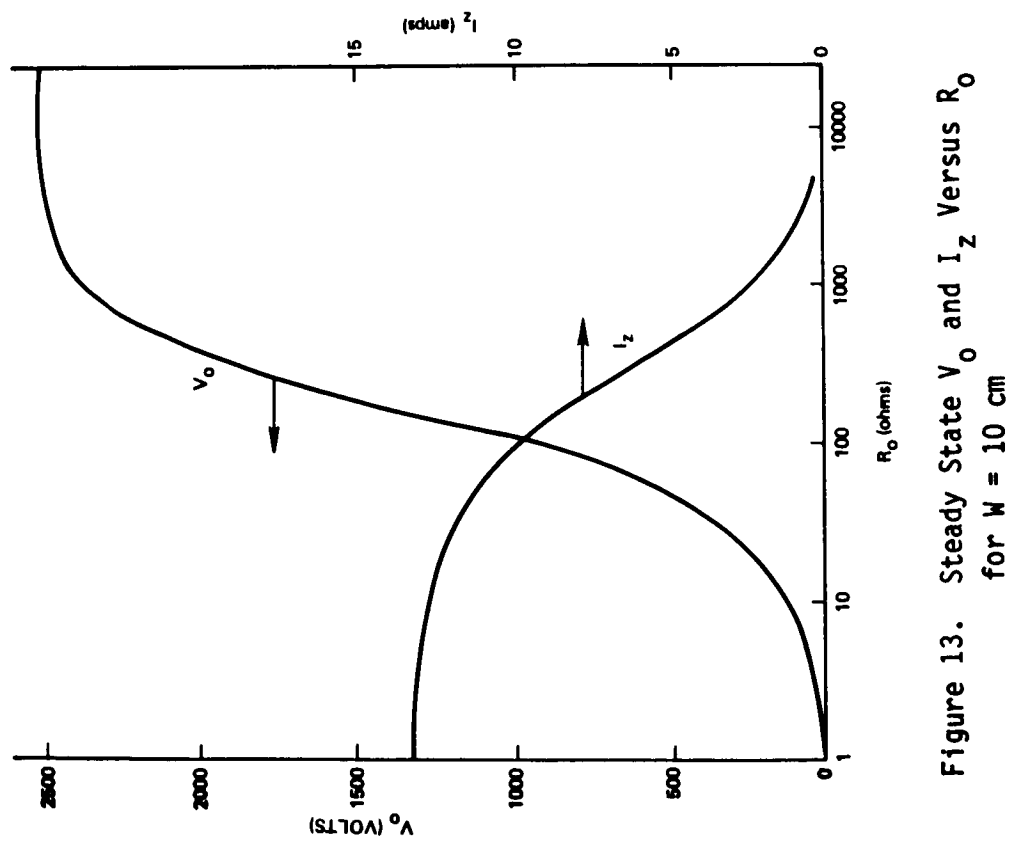


Figure 13. Steady State  $V_o$  and  $I_z$  Versus  $R_o$  for  $W = 10$  cm

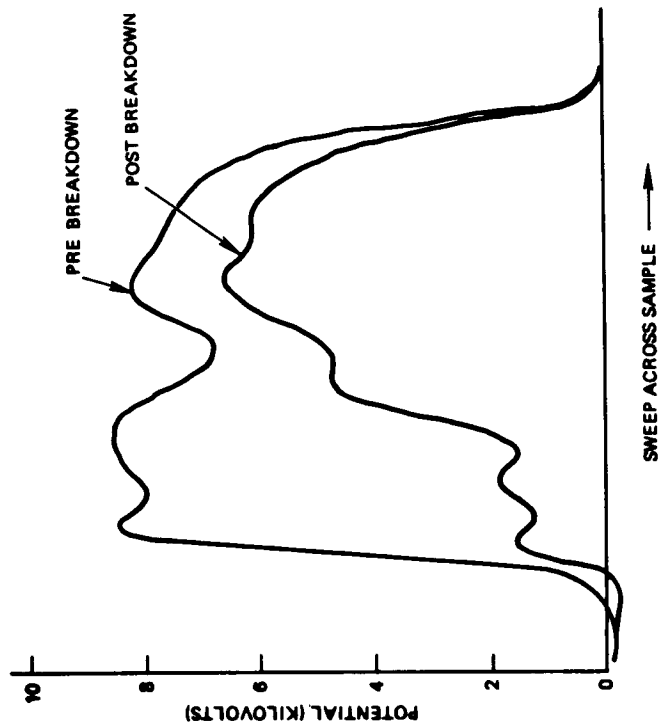


Figure 14. A Potential Profile of 6 x 6 inch Kapton Laminate Sample Before and After a "Relatively" Low Voltage Breakdown Near Edge of Sample

## EFFECTS OF SECONDARY ELECTRON EMISSION ON CHARGING\*

Martin S. Leung, Michael B. Tueling, and Edwin R. Schnauss  
The Aerospace Corporation

### ABSTRACT

A detailed description of the secondary electron emission characteristics is essential to the understanding of the charging behaviors of various dielectrics. Laboratory charging studies using two electron sources with different energies show that the charging behaviors of typical spacecraft thermal control dielectric surfaces are extremely sensitive to the shape of their secondary emission curves. The results also suggest that the electron spectrum in a natural charging environment can be separated into three distinct regions (noninteracting, discharging, and charging) depending on the kinetic energy of the incident electron relative to the charged surface, and on the secondary emission characteristics of the material. To a first order approximation, the relative number of electrons in these different regions determines the potential of the charged surface. In this paper, we report detailed measurements of the secondary electron emission characteristics of Kapton, and also discuss the effects of bulk conductivity and secondary emission on surface charging of these materials.

### INTRODUCTION

The understanding of material charging requires a detailed knowledge of both the charging environment (ref. 1) and certain electronic properties of the material (ref. 2). Under electron irradiation and in the absence of photoillumination, the equilibrium surface potential is determined by two basic material properties: its conductivity, and secondary electron emission. The relative importance of these two properties depends on the magnitude of the incident current compared to the bulk leakage current. In conductors and semiconductors, the leakage current is high and the material behaves as a simple ohmic element, i.e., the surface voltage is directly proportional to the incident current density. In the case of low-conductivity materials, the incoming current is not necessarily dissipated by the leakage current, resulting in a charge buildup in the material. Such a buildup retards the incident current and modifies the kinetic energy of the electrons such that there is an increase in the number of secondary electrons emitted from the surface. Eventually, the surface will charge to an equilibrium potential, at which point, the incoming primaries will be balanced by the outgoing secondaries. In this limit, the equilibrium surface potential is controlled by the secondary electron emission behavior of the target material. The purpose of this paper is to discuss the effects of secondary emission on material charging under single and dual energy electron irradiation, and to present novel techniques for measuring secondary emission parameters in the laboratory. We would also like to

---

\*This work was supported by the U.S. Air Force Space Division under Contract F04701-80-C-0081.

point out how these parameters can be used to add to the understanding of material charging in an environment where the electrons are distributed both in energy and space.

## BACKGROUND

When a solid is bombarded with energetic electrons in the keV range, a large number of low energy secondary electrons are generated in the solid within a certain distance from the surface. The secondaries which have the appropriate trajectories and sufficient energy to overcome the work function of the surface can escape from the solid. A number of authors (ref. 3) have written on the theoretical as well as the experimental aspects of the basic phenomenon. In general, it is found that the number of secondary electrons emitted depends critically on the kinetic energy of the primary electrons. In addition, it is also observed that the yield curve describing the production of the secondaries as a function of the primary electron energy can be reduced to fit a universal shape. A "typical" secondary yield curve for an insulator is shown in figure 1. The curve is a plot of  $\delta$ , the number of secondaries emitted per incident primary, as a function of the kinetic energy of the primary electrons at the surface. At low incident kinetic energy, the electrons striking the surface do not have sufficient energy to generate large numbers of secondaries and hence  $\delta$  is less than unity. As the kinetic energy increases, although the incident electrons penetrate deeper into the material, more secondaries are being created and allowed to escape giving rise to a  $\delta$  which can be significantly greater than unity. Thus,  $\delta$  will continue to increase rapidly until the penetration depth most favorable for the production of secondaries is reached. At this point,  $\delta$  reaches a maximum ( $\delta_{\max}$ ) at energy  $E_{\max}$ . Beyond this point, the number of electrons emitted decreases because the bulk of the internal secondaries are generated increasingly deeper in the solid reducing the probability of escape. This results in  $\delta < 1$  at high incident electron energies. Depending on the material and its structure, the values of  $\delta_{\max}$  and  $E_{\max}$  can differ widely. For most insulating materials, such as metal oxides and organic polymers,  $\delta_{\max}$  is usually greater than unity. In these materials, two other energies in the secondary yield curve are important for describing material charging. They are the first and second crossover points,  $E_I$  and  $E_{II}$ , where  $\delta = 1$ . In particular,  $E_{II}$  is especially important to material charging due to electron bombardment.

In terms of theoretical treatment of secondary emission, the formulation given by Sternglass (ref. 4) has been found to be in fairly close agreement with experimental measurements. This formulation assumes that all the secondary electrons are generated at a mean depth,  $\lambda_m$ , where the average forward momentum of the primaries vanishes. Secondly, the model assumes that the fraction of the secondaries escaping from the surface decreases exponentially with the depth of generation. Further considerations show that  $\lambda_m$  is proportional to the square root of the primary energy,  $E$ . Therefore, the fraction of secondary electrons emitted is proportional to  $\exp(-\beta E^{1/2})$ , where  $\beta$  is a constant related to the escape depth of the material. The total secondary yield is then given by

$$\delta(E) = AE \cdot \exp(-\beta E^{1/2}) \quad (1)$$

where A is material dependent parameter, characteristic of the efficiency of secondary electron emission and backscattering. For a particular material,  $\delta(E)$  is fixed by two points,  $\delta(E_{II}) = 1$  and

$$\left. \frac{d\delta(E)}{dE} \right|_{E_{\max}} = 0$$

Hence, equations (1) can be rewritten as

$$\delta(E) = \frac{E}{E_{II}} \cdot \exp \left[ -\frac{2}{E_{\max}^{1/2}} \left( E^{1/2} - E_{II}^{1/2} \right) \right] \quad (2)$$

$E_{\max}$  and  $E_{II}$  in equation (2) control the shape of the secondary yield curve. In the following, we shall describe how these parameters are determined in the laboratory and how they can affect material charging in space.

## EXPERIMENT

Our technique to study secondary emission was based on measuring the back surface electric field of a sample film while the front surface was irradiated with either one or two monoenergetic electron beams. The back field measurement method was the same as the one used in the Satellite Surface Potential Monitor (SSPM) for determining material charging aboard the P78-2 SCATHA satellite (ref.5). The crucial part of the instrument consists of an electrostatic field meter placed at a fixed distance behind the dielectric film sample which was mounted rigidly on a holder with conductive epoxy. The samples used in the measurement were common external spacecraft thermal control surfaces, in many cases they were polymers with their back surfaces metalized. Therefore, a small portion of the metalization had to be removed to enable the electric field due to the charge build-up to terminate at the sensor. The removal of metalization lowers the capacitance of the film in the region where the measurement is made, causing that portion of the film to charge much more rapidly than the rest of the sample. However, at equilibrium, independent measurement of the front surface potential profile showed that the potentials of the metalized and the unmetalized portions of the film are equal. Moreover, the back and the front surface measurements were sufficiently well correlated that the back surface field can be calibrated to infer the front surface potential accurately. In addition, the back metalization acts as a collector for the current passing through the bulk of the film. Hence, this configuration provides the measurement of both the surface potential as well as the leakage current at equilibrium simultaneously.

In the laboratory, the front surface of the sample was irradiated with one or two monoenergetic electron flood guns in a vacuum chamber at a pressure of  $10^{-7}$  Torr. To avoid undue damage to the sample by arc discharges, the incident electron energy was kept below 6 keV. Both the surface potential and the bulk leakage current were monitored continuously. The samples used in the actual measurements were made from 5 mil aluminized Kapton obtained from the same batch used for making the SSPM flight samples. The samples were assem-

bled by the Air Force Material Laboratory and the aluminized Kapton film was supplied by Sheldahl, Northfield, Minnesota.

## RESULTS AND DISCUSSION

### Charging under Monoenergetic Irradiation

In this set of experiments, the surface potential of Kapton was monitored while being irradiated with a single electron beam at normal incidence. The energy of the primary beam was varied from several hundred volts to several kilovolts. The results show that the equilibrium surface potential of a low conductivity material, such as Kapton, is clearly dominated by secondary emission. A plot of the measured surface voltage as a function of the primary beam energy is given in figure 2. For beam energies below  $E_{II}$ , where  $\delta > 1$  (shown in the upper trace), the surface tends to charge up positively instead of negatively. Within this  $\delta > 1$  range, the equilibrium surface potential is insensitive to the incident beam energy; a large change in the primary electron beam energy causes only a small change in the surface voltage. However, for incident beam energies near  $E_{II}$ , the surface potential drops rapidly as it crosses the zero line. Beyond this point, the surface charges up negatively and the measured potential is directly proportional to the primary beam voltage with a slope of unity. This behavior can be understood by the following explanation.

At low incident beam energy, the kinetic energy of the electron arriving at the surface causes more secondary electrons to be emitted per primary electron,  $\delta > 1$ . The surface experiences a net depletion of electrons, giving rise to a positive surface voltage. In principle, the magnitude of the positive potential will continue to increase and accelerate the primaries towards the surface until the kinetic energy of the primaries striking the surface is equal to  $E_{II}$  where  $\delta = 1$ . However, the surface is prevented from becoming too positive due to the abundance of low energy electrons around. The re-attraction of these low energy electrons pins the surface voltage low and makes it rather insensitive to changes in the incident beam energy. When the beam energy is equal to  $E_{II}$ , the number of incoming primaries is exactly balanced by the number of outgoing secondaries. There is no net gain or loss of electrons at the surface and thus the surface becomes uncharged. In figure 2, this corresponds to the point at which the measured surface voltage goes to zero. At this point,  $E_{II}$ , the second crossover energy, can be measured directly from the beam voltage. Beyond this point, the beam energy moves into a region where  $\delta < 1$ . There will be a net absorption of electrons at the surface. The accumulation of these incoming electrons gives rise to a negative potential at surface. This negative potential slows down the incoming primaries and causes  $\delta$  to increase towards unity. At equilibrium, the surface will charge to a potential such that the electrons arriving at surface will have a kinetic energy equal to  $E_{II}$  and a  $\delta = 1$ . As a result, the surface charges up to a potential equal to beam energy minus  $E_{II}$ . Experimental observation agrees quite well with this analysis. At beam energy higher than  $E_{II}$ , the surface potential tracks the beam energy linearly and

$$-eV_S = E_B - E_{II} \quad (3)$$

where  $V_S$  and  $E_B$  are the surface potential and the beam energy, respectively. In addition, the linear relationship between  $V_S$  and  $E_B$  extends over several kilovolts. This result points out the fact that the secondary emission yield is not sensitive to the surface potential acquired on the material. This is important because the bulk of the secondary emission data reported in the literature were obtained by conventional methods which required the material surface to be at or near ground potential. This finding removes some of the uncertainty concerning the validity of using the data obtained by the conventional methods and applying them to situations where the material is charged to several kilovolts.

### Two-Electron Beam Charging

In this section, the charging behavior of a dielectric in a multienergetic electron environment will be discussed. The discussion will be based on the results of a set of charging experiments using two electron guns at different energies. The angle of incidence for each gun was offset about 3 degrees from the sample normal. Based on the data presented in the next section, the effects of this minor offset are negligible and will be ignored in the following discussion.

The significance of secondary emission in a distributed environment can be understood by the following analysis. First consider an insulator being irradiated by a single electron beam. As a result, the surface potential developed is controlled by the energy of the beam,  $E_{B1}$ , via secondary emission. As we have shown in the previous section, for beam energy greater than  $E_{II}$  of the material, the surface charges up negatively, and, at equilibrium,  $-eV_S = E_{B1} - E_{II}$ . When the second beam is turned on, the surface potential created by the first beam retards the electrons in the second beam. At the same time, the origin of the secondary electron yield curve is also shifted from zero for an uncharged surface to  $-eV_S$  when the surface is charged, as shown on an absolute energy scale in figure 3. In this representation, it is clear that the electrons from the second beam fall into three distinct categories, namely noninteracting, discharging, and charging, depending on the beam energy.

Based purely on an energy argument, electrons with energy lower than the surface potential will be reflected and will not interact with the surface at all. As we increase the energy of the second beam, it is equivalent to moving the arrow for  $E_{B2}$  in figure 3 to the right. We note that there is a region between  $-eV_S$  and  $-eV_S + E_I$  (the first crossover) where the electrons are weakly charging. However, since this region is narrow ( $\sim 50$  V for Kapton) and the effect small, we can safely ignore its contribution. Therefore, electrons from the second beam with energy less than  $-eV_S + E_I$  can be considered noninteracting.

In the second category, at higher beam energies, the electrons with  $E_{B2}$  between  $-eV_S + E_I$  and  $-eV_S + E_{II}$  will have the appropriate kinetic energy to impact the surface with a secondary yield greater than one. The net increase in the secondary emission due to the second beam causes the surface to discharge. Consequently, the surface voltage will shift to a lower value  $V_S'$  in order to re-establish current balance. At equilibrium, the number of

electrons emitted due to the second beam has to be balanced by the number of electrons absorbed from the first beam, or,

$$\delta(E_{B2} + eV_S)J_{B2} + \delta(E_{B1} + eV_S)J_{B1} = J_{B2} + J_{B1} \quad (4)$$

where  $J_{B1}$  and  $J_{B2}$  are the current densities of the first and the second beam at the surface, respectively. The relation described in equation (4) provides a way of sweeping out the shape of the secondary emission yield curve by varying the current densities and the beam energies. However, this way of determining  $\delta$  is tedious experimentally and requires a great deal of curve fitting and optimization. Fortunately, a faster and more convenient method has been developed for determining the secondary emission yield curve by measuring  $E_{\max}$  and  $E_{II}$  for a particular material.

In this method, the dielectric is irradiated simultaneously with two electron beams. The energy of one beam is fixed while a second, the probe beam, whose intensity is modulated scans continuously over a wide range of energy. The current of the probe beam is deliberately kept low in order not to disturb the equilibrium surface voltage established by the first beam. In this measurement, the surface voltage is monitored continuously and the small AC component in surface voltage induced by the modulated probe beam is measured by synchronous detection. The amplitude and phase of the AC component are determined by the number of electrons emitted or absorbed by the surface due to the probe beam. Hence, a plot of the synchronous change in surface voltage as a function of the energy of the probe beam is directly related to the secondary emission yield curve of the material. Such a plot and the experimental conditions used are shown in figure 4 from which we can extract  $E_{\max}$  and  $E_{II}$  directly. For Kapton, we found that  $E_{\max} = 250$  V and  $E_{II} = 1000$  V. These values agree with those determined previously in our laboratory. Figure 5 shows the secondary yield curve for Kapton obtained from equation (2) using the values given above. These results show that the modulated probe beam method offers a convenient and accurate way for determining the secondary emission properties of various film-type dielectric materials.

Once the shape of the secondary emission curve is determined, the charging response of a material to a multienergetic electron flux,  $F(E)$ , can be understood. As discussed earlier, the spectrum of these electrons can be divided into three critical regions, as shown in figure 6. Electrons with energy below  $-eV_S + E_I$  are noninteracting and can be eliminated right away. Between  $-eV_S + E_I$  and  $-eV_S + E_{II}$ , electrons have a  $\delta > 1$  and a tendency to discharge the surface. Above  $-eV_S + E_{II}$ , because  $\delta < 1$ , electrons in this region tend to cause the surface to charge negatively. In order to maintain current balance for a material with zero leakage, the total number of electrons emitted ( $\delta > 1$ ) must be balanced the electrons absorbed ( $\delta < 1$ ). Hence,

$$\int_{-eV_S}^{E_U} [\delta(E + eV_S) - 1] F(E) dE = 0 \quad (5)$$

where  $E_U$  is the highest energy of the nonpenetrating electrons and  $F(E)$  is the incident electron flux at normal incidence. When equation (5) is not

satisfied,  $V_S$  will shift to a new surface potential  $V_S'$  until current balance is reestablished. Similarly, a change in the electron distribution will result in a change in the surface voltage. Therefore, conceptually, this analysis provides a physical link between the properties of the material and the electron distribution of the environment in determining its surface potential. It should be noted that, in the absence of photoillumination (causing photoemission and photoconductivity), secondary emission is the most important factor in controlling surface charging of low-conductivity materials. However, a number of other effects, such as electron induced conductivity and ion induced secondary emissions, have to be considered in the order to make the analysis more applicable to actual substorm charging in space.

### Angular Dependence

In the preceding discussion, it has been assumed that the primary electrons strike the material surface at normal incidence. However, it is well known that oblique incidence produces more secondaries than normal incidence. This is due to the fact that the secondary electrons are generated closer to the surface and have a greater probability of escaping from the solid. As a result, both  $E_{\max}$  and  $E_{II}$  in equation (2) will increase as the angle of incidence increases. Hence, the dependence of these parameters on incident beam angle is critical to understanding the charging behavior of materials in space where the incident electrons may strike from all directions.

Recent analyses indicate that the electron angular distributions in near geosynchronous orbits are highly anisotropic during geomagnetically disturbed times. An estimate indicates that the electron current normal to the earth's magnetic field line is roughly three times larger than the current parallel to the field line (fig. 7). The data presented in the figure were obtained from a natural charging event on Satellite P78-2 on February 12, 1979. The angular distribution of the electron current was obtained by integrating the electron flux between 3.4 and 19.4 keV provided by the SC-2 particle counter on board P78-2. In figure 7, the angularly resolved current was plotted as a function of magnetic angle and universal time (UT) in seconds for three consecutive satellite spin cycles. Each spin cycle is about 60 seconds long. Due to symmetry along the magnetic axis, the current-angle profile is approximately the same in each half cycle. Since this charging event was occurring in the sun and the direction of the solar radiation was approximately parallel to that of the current maximum, charging of the SSPM samples could only take place in the dark half cycle of each satellite rotation. Since the SC-2 particle counter and the SSPM are located at different parts on the spacecraft, there is a time delay between the two measurements. The crosses in figure 7 mark the onsets of the dark half cycles from which the SSPM charging data presented in figure 8 were obtained. The solid lines in figure 7 represent, given the time delay, approximately the current profiles that would impinge on the SSPM in the dark half cycles marked by the crosses respectively. Notice in figure 8 that, during the first dark half cycle (UT = 18292), the Kapton surface did not show any sign of charging until the sample rotated to within 30 degrees  $[120^\circ]$  from the current maximum  $[90^\circ]$ . The angles quoted in brackets are the magnetic angles given in figure 8. In the next dark half cycle (UT = 18346), the electron distribution in the plasma sheet hardened and the peak current in figure 7 went up. During this time, the Kapton sample began to charge earlier



(about 55 degrees [145°] from the maximum) and subsequently charged to a higher potential. In the last half cycle, the electron distribution softened slightly and the Kapton charging profile is intermediate between the profiles in the first and second half dark half cycles, it did not begin to charge immediately. Instead, charging occurred only when the angle of incidence of the peak current approached normal incidence. In addition, the onset and the magnitude of charging are highly correlated to the intensity of the peak current. These results show that charging is quite sensitive to the anisotropy of the electrons in the plasma sheet. Hence, there is a need to understand how the angle of incidence influences the charging behavior of dielectrics.

In the laboratory, a monoenergetic charging beam was used to examine the effects of varying the angle of incidence on charging. The equilibrium surface voltage was found to decrease with increasing angle of incidence as expected from higher secondary emission. Figure 9 shows a family of charging curves for Kapton at different angles of incidence. When the threshold beam voltages for surface charging and the slopes of the charging curves of figure 9 are plotted against the angle of incidence,  $\theta$ , they are found to follow  $\cos^2\theta$  (fig. 10). From these results, we found that the angular dependence of the equilibrium surface potential is given by

$$-eV_S(\theta) = \cos^2\theta E_B - E_{II}^0 \quad (6)$$

where  $E_{II}^0$  is the second crossover energy of the material at normal incidence and  $E_B$  the primary electron energy. Consequently, the angular dependence of the second crossover,  $E_{II}(\theta)$ , for Kapton can be determined by setting  $-eV_S(\theta) = 0$ , and,  $E_{II}(\theta) = E_B$ ,

$$E_{II}(\theta) = \frac{E_{II}^0}{\cos^2\theta} \quad (7)$$

The same angular dependence can be obtained by applying Sternglass' theory. These results indicate that, for a particular material, the momentum-loss mean free path controls the production of the secondaries and hence the charging characteristics of the material. They further suggest that the secondary emission yield should increase as  $(\cos^2\theta)^{-1}$  with increasing angle of incidence. However, more work is needed to confirm the validity of this dependence.

#### SUMMARY

In the absence of light and high energy particles, the surface potential of Kapton is found to be controlled by secondary emission. Under monoenergetic electron irradiation, the surface voltage varies linearly with the beam voltage. In a multienergetic environment, the surface voltage is determined by the convolution of the electron distribution and the secondary electron yield of the material. Using single and dual electron beam charging techniques, we have devised methods for measuring the critical secondary emission yield parameters as well as the angular dependence of these parameters for Kapton. This information is not only essential to the understanding of mate-

rial charging in space but also valuable as input to the NASCAP spacecraft charging modeling code.

#### REFERENCES

1. Space Systems and Their Interaction with Earth's Space Environment, edited by H. B. Garrett and C. P. Pike, Progress in Astronautics and Aeronautics, Vol. 71, American Institute of Aeronautics and Astronautics, New York, N.Y.
2. Purvis, C. P.: Status of Material Characterization Studies, Proceedings of Spacecraft Charging Technology Conference, R. C. Finke and C. P. Pike, eds., AFGL-TR-79-0082, NASA Conference Publication 2071, pp. 437-456.
3. Dekker, A. J.: Secondary Electron Emission, Solid State Phys., Vol. 6, 1958, pp. 215-311.
4. Sternglass, E. J.: Secondary Electron Emission and Atomic Shell Structure, Phys. Rev., Vol. 80, 1950, p. 925.
5. Stevens, J. R.: Description of Space Test Program P78-2 Spacecraft and Payloads, SAMSO TR-78-4, 1978.

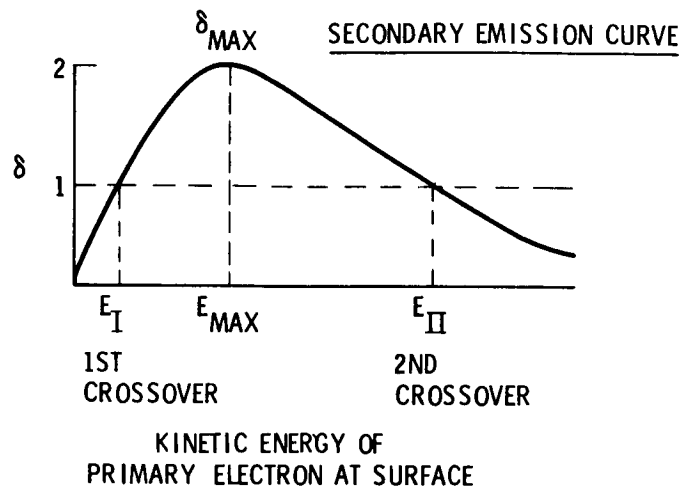


Figure 1. - A "typical" secondary emission yield curve of an insulator.

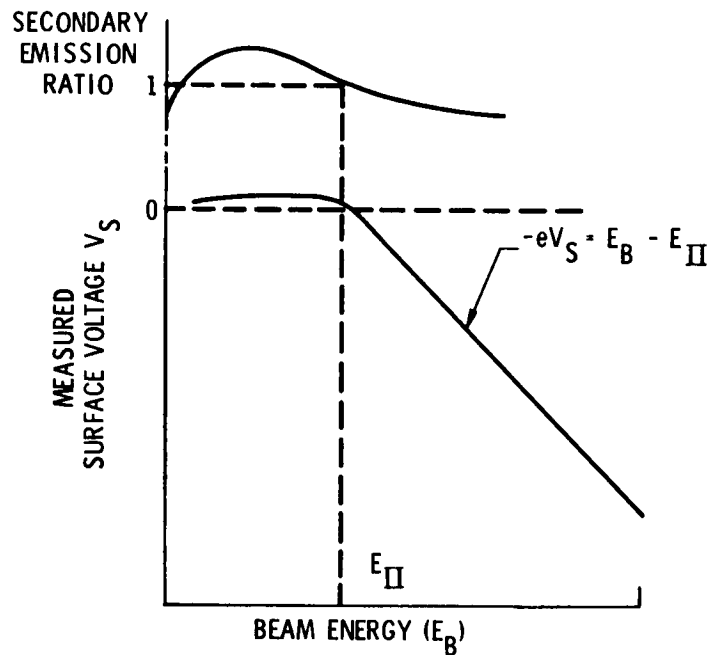


Figure 2. - Charging behavior of a low-conductivity material under monoenergetic electron irradiation. The top trace is the secondary emission yield curve and the bottom trace is the measured surface voltage vs beam energy.

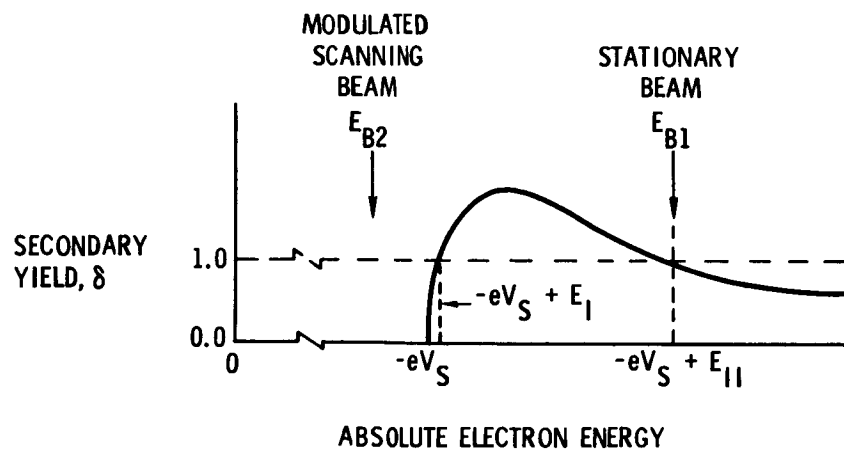


Figure 3. - For a charged surface, the origin of the secondary electron yield curve is shifted to  $-eV_S$  on an absolute energy scale. The arrows indicate the energies of the stationary and scanning electron beams.

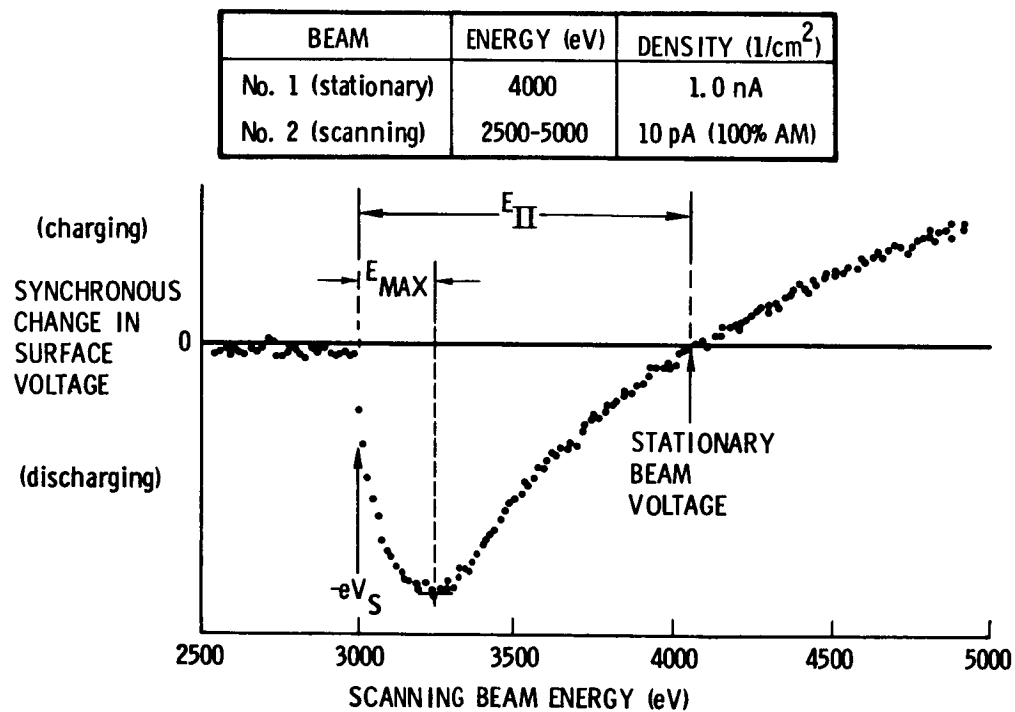


Figure 4. - Results of the modulated two-beam charging experiment.  $E_{max}$  and  $E_{II}$  can be obtained directly from this plot.

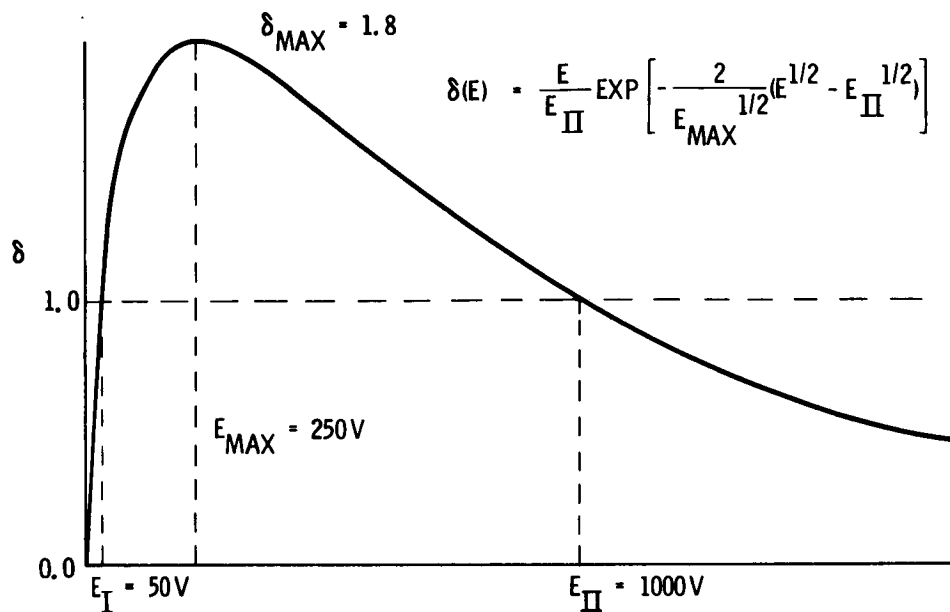


Figure 5. - Secondary yield curve for Kapton obtained from equation (2) by using the values determined by the modulated beam method.

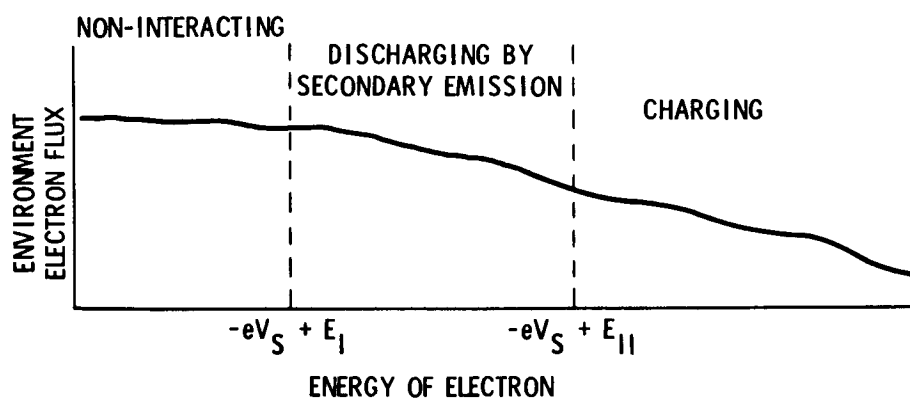


Figure 6. - Electron distribution separated into three distinct regions: noninteracting, discharging ( $\delta > 1$ ), and charging ( $\delta < 1$ ).

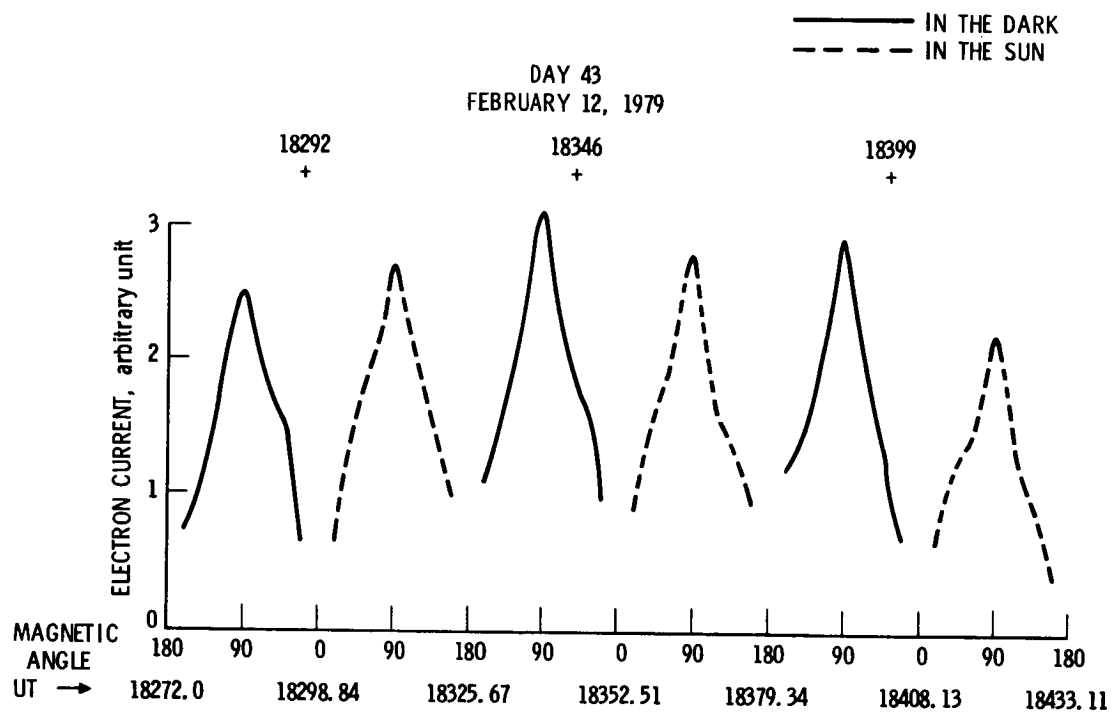


Figure 7. - Anisotropy in electron angular distribution during a "typical" charging event. Current-angle profiles are shown for three consecutive satellite rotations.

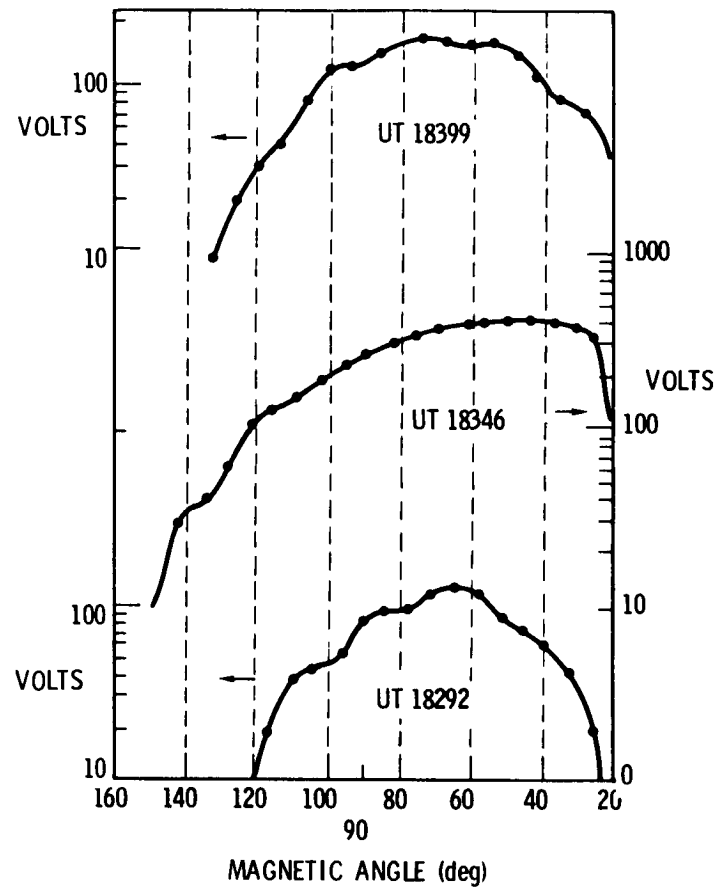


Figure 8. - Charging response of SSPM Kapton to the anisotropic electron environment described in figure 7.

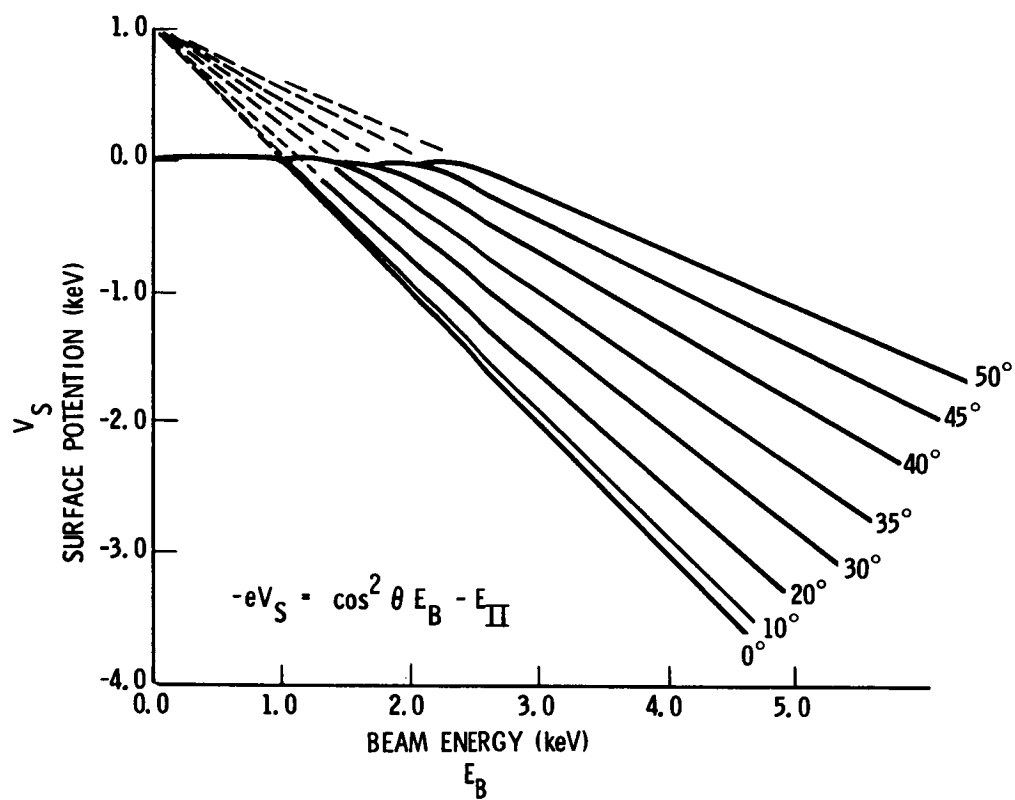


Figure 9. - Monoenergetic charging curves of Kapton at different angles of incidence.



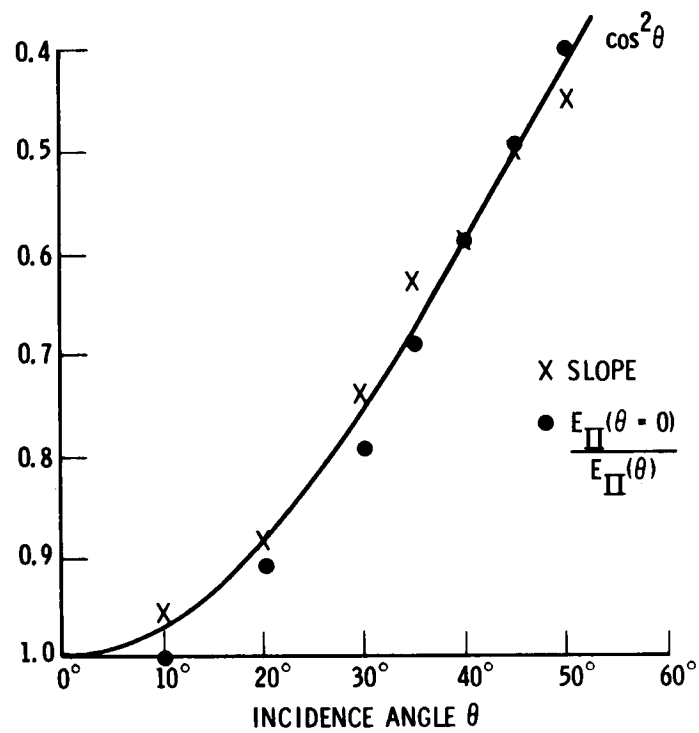


Figure 10. - Variation of threshold beam voltage and charging slope as a function of angle of incidence.

## SECONDARY ELECTRON EMISSION YIELDS\*

I. Krainsky, W. Lundin, W. L. Gordon, and R. W. Hoffman  
Case Western Reserve University

### SUMMARY

The secondary electron emission characteristics for a variety of spacecraft materials have been determined under UHV conditions using a commercial double pass CMA which permits sequential Auger electron spectroscopic analysis of the surface. We have examined the transparent conductive coating indium tin oxide (ITO) on Kapton and borosilicate glass and indium oxide (IO) on FEP Teflon. Total yields vary slightly with samples and with substrates. The total SEE coefficient,  $\sigma_{\max}^+$ , ranges from 2.5 to 2.6 on as-received surfaces and from 1.5 to 1.6 on  $\text{Ar}^+$  sputtered surfaces with  $< 5$  nm removed.

For these measurements a cylindrical sample carousel provides normal incidence of the primary beam as well as a multiple Faraday cup measurement of the  $\sim$  nA beam currents. Total and true secondary yields are obtained from target current measurements with biasing of the carousel. A primary beam pulsed mode to reduce electron beam dosage and minimize charging of insulating coatings has been applied to  $\text{MgF}_2$  coated solar cell covers.

Electron beam effects on ITO were found quite important at the current densities necessary to do Auger studies ( $0.6 \mu\text{A}$  minimum or  $\sim 1 \times 10^{-4} \text{ A/cm}^2$ ) but relatively unimportant at the 10 nA levels used in short exposure methods or pulsed methods (150 nA peak, 2  $\mu\text{s}$ ) for obtaining SEE coefficients. Angle of incidence dependence for IO on FEP Teflon has been obtained for  $0.5 < \text{EP} < 5.0 \text{ keV}$ .

### INTRODUCTION

One result of the current interest in spacecraft charging phenomena has been the development in 1978 by NASA of a computer code - NASCAP - capable of providing a detailed picture of the charging process for realistic three-dimensional models of spacecraft (ref. 1). A major impediment to the use of NASCAP is the paucity of data for the secondary electron emission characteristics of actual spacecraft materials. Methods for obtaining these data from well-characterized surfaces using a commercial cylindrical mirror analyzer (CMA) were developed, tested on clean Ag and Cu surfaces, and applied to aluminum alloys with varying surface treatments typical of those used on spacecraft (ref. 2). Target current measurements gave electron yield data as a function of primary energy, EP. The CMA provided both the surface composition and the secondary electron energy distributions,  $N(E)$ , for a given EP from integration of the CMA output, operating in the standard derivative mode.

To overcome severe charging effects experienced with a thick insulating coating such as anodized samples we have developed a pulsed beam technique using sufficiently low dosage to permit measurements on thin insulating layers.

\*Work performed under NASA Grant No. NSG-3197

This method, together with that of short DC exposures to the primary beam, has been used to obtain secondary yields from thin ( $\sim 20$  nm) transparent conducting coatings, indium-tin oxide (ITO), on three insulating substrates: borosilicate glass, Kapton, FEP Teflon, and  $\text{MgF}_2$  on quartz. The influence of electron beam dosage effects has been explored in order to extrapolate the results back to typical current densities at the spacecraft surfaces. The effect of mild Ar ion sputtering of as-received surfaces has also been observed as a guide to changes in yield which may occur under prolonged plasma exposure in space. Secondary electron yields for  $0.5 \text{ keV} < EP < 5 \text{ keV}$  have been measured at varying angles of incidence.

## EXPERIMENTAL TECHNIQUES AND MODIFICATIONS

The electrons below 50 eV are usually termed "true secondaries" and the electrons above 50 eV termed "backscattered" (ref. 3). Thus, the true SEE coefficient  $\delta$  is just the number of true secondaries emitted per primary electron. Typically, measurements of conducting surfaces involve determination of the target current under two conditions:  $I_+$ , where backscattered electrons are rejected (biasing the target at +50 V relative to the grounded surroundings) and  $I_-$ , where all outgoing electrons are rejected (biasing the target at -50 V). The primary current,  $I_p$ , is found by displacing the carousel so that the beam enters the Faraday cup. As noted in reference 2,  $\delta = (I_+ - I_-)/I_p$  to a good approximation while the total SEE coefficient  $\sigma = 1 - I_-/I_p$  and includes elastically and inelastically backscattered electrons in addition to the true secondaries.

With thick insulating layers on the target surface, charging will take place, where the sign of the charge depends on whether  $\sigma$  is  $\lesssim 1$ . For our geometry, the CMA entrance grid subtends an angle of  $1.5 \pi$  steradians and is always grounded. Thus electric fields are developed as the target surface becomes charged.

### Pulsed Beam Techniques

To minimize charging effects on insulating layers as described above, we have introduced a pulsed beam technique together with a low energy electron flood gun to restore the surface to an uncharged state. If a single square current pulse of length  $\tau$  is incident on the insulator layer mounted on the target and the target is biased negatively to repel all secondaries then, referring to the equivalent circuit (figure 1(a)), the charge accumulated on the target is

$$q = \int_0^\tau I_- dt = \tau I_- \text{ and the potential drop across the input capacitor}$$

$C_1$  is  $V_- = q/C_1 = \tau I_-/C_1$ . Hence, as defined earlier, the total SEE coefficient  $\sigma = 1 - I_-/I_p = 1 - V_-/V_p$ . By observing  $V_-$  for a series of pulses at fixed EP, the presence of charging effects can be observed as a monotonic change in its value. Exposure of the surface of the insulating layer to low energy electrons from a flood gun will then restore the surface to a nearly uncharged state. Pulse measurements with +50 V applied to the target provide  $I_+$  so that  $\eta$  might be determined as well.

Beam pulses were produced through pulsing a beam blanking circuit. The process is illustrated schematically in figure 1(b). Single pulses from the pulse generator drive the blanking circuit which in turn controls the electron gun extractor potential. Target current pulses are typically 2  $\mu$ s duration with a 0.2  $\mu$ s rise time. They are registered by a sample-and-hold circuit for measurements by a DVM. The original pulses are stretched in time by a high input impedance follower, amplified by a factor of 100, and then enter the sample-and-hold circuit.

#### Methods used for Secondary Yield Measurements

##### A - Short exposure to the primary beam

In measurements of secondary yield from conducting surfaces, DC exposure to the primary beam is a standard practice. To avoid over-exposure to the beam, particularly in the case of transparent conducting coatings, we have been careful to limit exposure time to a minimum, consistent with the observation of adequate signals. Thus we have used the beam blanking circuit in a manual operation mode to limit the time on the sample to 1 to 2 seconds. After completing beam alignment and focus of the primary beam,  $I_p$  is measured using the Faraday cup. The beam is then cut off and the carousel translated so that the beam will strike the sample at the new desired location. With the target biased at +50 V,  $I_+$  is found by disengaging the beam blanking circuit for  $\sim 2$  sec. The ammeter response time is  $\sim 1$  sec. The target is then biased to -50 V and  $I_-$  is found in another 2 to 3 sec. interval. Finally, the carousel is translated to bring the beam into the Faraday cup and again disengaging the blanking circuit to permit a second measurement of  $I_p$ . This procedure is repeated for each required value of EP.

From this series of measurements we obtain both  $\sigma$  and  $\delta$  as defined earlier. Also, by scanning across the Faraday cup we determine that the beam diameter is  $\sim 2$  mm. Typical primary currents ranged from 1 to 10 nA.

##### B - Pulsed beam measurements

A manually pulsed beam is employed, as described earlier, for the study of insulating surfaces and to avoid beam damage with conducting surfaces. The value of  $I_p$  is determined with the Faraday cup in place. During this time the beam is operated in a chopped mode to allow centering on the cup. A typical maximum value of the current pulses is  $\sim 50$  nA. After blanking, the carousel is shifted so that beam will strike the desired location on the sample. Then, with the target biased at -50 V relative to ground a 2  $\mu$ sec pulse is delivered and the value of  $I_-$  on the sample-and-hold circuit read from the DVM. Repetition of a single pulse in the region where  $\sigma > 1$  provides a quick test for charging, since  $\sigma_{obs}$  will drop monotonically if charging is present. In the presence of charging, use of the low energy flood gun between pulses assures that the sample surface is restored to its uncharged state, but does not guarantee the absence of charging during an individual pulse nor avoid field gradients in the sample near-surface region. Testing for charging in this latter case can be done by reducing pulse height and width and comparing the  $\sigma$

values obtained. At present, noise in the sample-and-hold circuit limits us to a pulse height of  $\sim 12$  nA in  $I_p$ .

Generally, only  $I_-$  was measured in this mode so the backscatter coefficient,  $\eta$ , was not obtained. Since  $\eta$  is not a large fraction of  $\sigma$  for insulators of low atomic number and is relatively constant in energy above a few hundred volts, an estimated value can be assigned without introducing serious Z-dependent uncertainties.

#### MATERIALS EXAMINED

Samples of three insulating materials, Kapton, FEP Teflon, and borosilicate glass coated with indium tin oxide (ITO) by the General Electric Company were provided to W. L. Lehn of the Air Force Materials Lab, Wright Patterson Air Force Base. Reactive sputtering techniques (ref. 4) were employed using a magnetron sputter gun, In/Sn targets and an oxygen + argon atmosphere. The compositions are nominally 90%  $\text{In}_2\text{O}_3$  and 10%  $\text{SnO}_2$  but the stoichiometries are uncertain. ITO film conductivity generally increases with the density of oxygen defects (ref. 5).

Table I gives a summary of the types of samples studied with nominal ITO thickness and back surface coating listed. We found that the ITO coating on the FEP sample had a very high-to-infinite resistance and showed sufficient charging that we could not make an Auger determination of In, Sn, or O present on the surface. An indium oxide (IO) coating, found by GE to be more compatible with FEP Teflon (ref. 6) was obtained. It had been prepared in essentially the same manner as the ITO coating. Samples are  $\sim 1$  cm x 1 cm, cut from 10 cm x 10 cm sheets of ITO on Kapton or IO on FEP Teflon and from 2.5 cm x 2.5 cm tiles of ITO on borosilicate glass with individual samples identified. All samples were inserted into the UHV system without prior surface cleaning except for blow-dusting with Freon gas.

The relative amount of In, Sn, and O in ITO, as well as other contaminants were obtained by AES methods. A surface contamination layer was present which increased the secondary yield compared to samples from which the contamination layer had been removed by Ar ion sputtering.

As a comparison with commercially available transparent conducting coatings (TCC) films, samples were obtained from Sheldahl. No nominal composition was supplied but our Auger analysis indicated the major components of TCC on Kapton were In, Sn, and O plus contamination.

$\text{MgF}_2$  coatings on quartz substrates were obtained from OCLI, and data obtained from both the coated and uncoated surfaces of the solar cell substrates.

#### RESULTS AND DISCUSSION

The results will focus on yield data and include figures of  $\sigma(E)$  and/or  $\delta(E)$  for various coatings. Results of a study of the influence of the electron beam and sputtering of samples are included.

## Indium Tin Oxide Coatings

These data, in contrast with later pulsed results, have the advantage of containing both the total SEE coefficient,  $\sigma$  and true SEE coefficient  $\delta$  so are presented first, although they do represent a greater net exposure to the electron beam than do our pulse measurements. Furthermore, we note that earlier data obtained in this system for the SEE backscatter coefficient,  $\eta$ , of Ag ran (ref. 2) about 35% below the accepted value.<sup>†</sup> The reason for this discrepancy has not been determined but may be related to field distortions between the carousel and its surroundings during  $I_+$  measurements. Thus, we place greater emphasis on the  $\sigma$  values obtained here.

Typical results for as-received surfaces of ITO on Kapton and borosilicate glass and IO on FEP Teflon are presented in figures 2, 3, and 4. Primary beam currents and current densities are provided with each figure and SEE parameters tabulated. Particular samples cut from the sheet initially provided to us are identified for future reference. The current density values are only approximate since the beam profile is not rectangular. The data are remarkably similar considering the range of samples. Figure 5 presents the normalized  $\delta$  curves.

Differences between measurements on nominally similar specimens introduce the general question of reproducibility. Surface contaminants are the most important factor but surface roughness, general composition (particularly the variation in conductivity associated with varying O concentration), and electron beam effects cannot be neglected.  $\delta$  values obtained from three different locations on a single sample of IO on FEP and the variation for two different samples of ITO on borosilicate glass are small. We conclude that the uncertainties in a given measurement of  $\delta$  (and  $\sigma$ ) are approximately  $\pm 0.1$  with variations among samples occasionally outside this range.

The total SEE coefficient for the as-received surface of typical samples of Sheldahl TCC on Kapton and Teflon is not significantly different from the SEE coefficients from the GE as-received surfaces.

A comparison between pulsed beam and short exposure results for the GE samples was made using normalized curves to minimize the effect of variations among different samples of the same material and of possible effects of electron beam dosage as considered later. With the possible exception of IO on FEP Teflon no differences were encountered.

## Magnesium Fluoride Coated Solar Cell Covers

MgF<sub>2</sub> on fused silica required the pulsed beam technique because of the high (essentially infinite) sample resistance. In spite of the charging observed during SEE measurements, AES spectra were obtained without shifts of

---

<sup>†</sup>Bronshtein (ref. 7) using a  $4\pi$  collector geometry, quotes values of 0.38 at 1 kV and 0.41 at 4 kV while our values were 0.25 and 0.27 at these primary energies, with the  $1.5\pi$  solid angle geometry of our apparatus.

the Mg and F peaks, but AES spectra were not obtainable from the other side due to charging. Because of possible identification difficulties in coding of the coated side, both the  $\text{MgF}_2$  and quartz surfaces of the OCLI standard solar cell covers were examined. Figures 6 and 7 present the  $\delta$  and  $\sigma$  data obtained for the  $\text{MgF}_2$  and fused silica surfaces, respectively. All data were obtained by the pulsed beam method in which  $I_+$  and  $I_-$  were directly measured with  $\pm 50$  V potentials on the target. The data for the fused silica side are quite stable when compared to earlier samples, but the  $\text{MgF}_2$  surface appears erratic. These data must be regarded as preliminary as we are not certain of the origin of the variations. As a result we have not listed the yield parameters.

#### Surface Contamination of ITO Coatings

The influence of surface contamination is best illustrated by comparison of SEE coefficients before and after argon ion sputtering. We examine these after presenting the AES evidence for a change in surface composition with sputtering. Auger spectra taken before sputtering of ITO on Kapton and IO on FEP Teflon show the presence of similar contaminants - C, S, Cl - on each of the as-received surfaces. After  $\text{Ar}^+$  sputtering of  $\sim 1$  nm of the nominal 20 nm of ITO on Kapton film, there is little change in concentration except for the expected appearance of Ar and an increase in S. This particular increase correlated with results to be discussed later under electron beam damage. After  $\sim 4$  nm has been sputtered away (on a different sample) ITO on Kapton exhibits a significant clean-up of the surface contaminants. The In/Sn concentration increased but may be an artifact or a depth effect or be sample-dependent. This requires further study, as does our assumption that the 4 nm sputtering produces a "clean" ITO surface. It is, however, consistent with the results of electron beam damage studies discussed later.

Figure 8 shows the large changes in  $\delta$  values as a result of sputtering. The enhancement of the SEE coefficients due to contamination which exists prior to sputtering is evident and merits further study. Normalization of the  $\delta$  curves emphasizes a relative decrease in the high EP values for  $\delta$  with increased sputtering. This difference is unexpected, in the sense that the true SEE coefficients for most materials fit a common normalized yield curve.

#### Electron Beam Effects

Electron beam effects on surface composition have been well documented in the past, particularly in the case of Auger analysis where the measurement process can perturb the results. Such effects have a two-fold relevance to the present study. First, a knowledge of surface composition is essential to the general characterization of the surface for correlation with secondary emission yield. Second, the SEE coefficients (which are measured at a much lower current density than that used for Auger data) depend on electron beam effects. This, in turn, requires a detailed evaluation to predict their applicability to spacecraft charging.

In our preliminary studies of the SEE coefficients of ITO, we discovered that the values were dependent on whether the area under investigation had been previously exposed, as for example, in focussing the primary beam or in

previous Auger studies. After becoming aware of this problem we took data in the short exposure mode as outlined earlier and, when the pulsed beam circuit was available, we used this technique in the majority of cases to minimize dosages. This approach still does not provide a satisfactory answer to the question of the applicability of our results to spacecraft, in view of the extremely low current density in the plasma environment of the craft. To this end, we carried out an investigation of the electron beam dosage dependence of  $\sigma$  and of the Auger measurements of surface composition. This was accomplished by observing the time dependence of the parameter in question at a series of different primary current values, operating in the DC mode.

Measurements of  $\sigma(t)$  at a given current were done at an EP of 3 keV so that they are beyond EP<sub>max</sub>. The primary electron gun was well stabilized before data were taken with the target biased at -50 V relative to ground. The beam size was determined in a position scan across the Faraday cup and typically had a diameter of  $\sim 0.8$  mm. A series of  $\sigma(t)$  values were obtained at each of 6 different values of  $I_p$  ranging from 10 nA to 36  $\mu$ A.  $I_p$  was checked before and after a given series of  $\sigma(t)$  measurements at that current to correct for a slight monotonic drift ( $\sim 2\%$ ) which continued to occur. Results are displayed in figure 9 with data points from 0.1 min to  $\sim 120$  min at each current. The earliest points are not indicated because of the difficulty of displaying the time scale appropriately but all values began at or near a  $\sigma$  of 1.25 to 1.3. Thus, while not shown, rapid drops in  $\sigma$  occurred, particularly at the higher currents. The 55 nA current curve started from a value close to that of the others but dropped abruptly to the "plateau" shown in figure 9. This effect has not been observed at other locations on the sample with other current levels nor has the reproducibility of the 55 nA result been checked. Wherever tested, we note that the effects illustrated here are not reversible with time.

For all  $I_p > 0.6 \mu$ A an obvious discoloration developed with a diameter about equal to the  $e^-$  beam spot area of  $5 \times 10^{-3} \text{ cm}^2$ . At the higher currents (36  $\mu$ A) perforation of the Teflon substrate resulted from the thermal damage. We speculate that contaminants, especially S, are brought to the surface and lead to a decreased secondary yield.

#### Angular Dependence of SEE Yield

It is well known that for metals as well as for semiconductors SEE coefficient  $\sigma$  increases with increasing incident angle  $\phi$  of the primary beam (ref. 7). In accordance with Bruining (ref. 8), primary electrons moving in straight paths penetrate to a smaller depth normal to the surface when the angle is slanting. Thus, secondary electrons are generated on the average at smaller depth and have an increased probability of escape. As a result  $\sigma$  is larger. Simple calculations based on this consideration give the following dependence of  $\sigma$  coefficient on the incident angle,  $\phi$ , relative to the specimen normal.

$$\ln \frac{\sigma(\phi)}{\sigma(0)} \approx x\alpha(1-\cos \phi) \quad (1)$$

where  $x$  is the penetration length measured along the incident path, and  $\alpha$  is



the absorption coefficient. Of course, the constants  $\sigma_0$  and  $\alpha$  should depend upon the primary electron energy. Similar considerations apply to  $\eta$ .

Our aim was to investigate the angular dependence of  $\sigma$  and  $\eta$  coefficients for conducting coatings on Teflon and Kapton substrates. We constructed a new holder with a commutator for in-target current measurements using a Faraday cup with the sample at the focus of the CMA. The specimen rotates such that the incident electron beam varies from 0 to 90 degrees with respect to the specimen normal.

Figures 10 and 11 display experimental data ( $\sigma(\phi)$  and  $\eta(\phi)$ ) for IO on Teflon. Plotted in the form of equation (1), the normalized  $\sigma$  data are linear at EP = 5 keV but fall below the line at small values of  $\cos \phi$  and lower primary energies. The backscatter coefficient shows deviations for the higher energies.

### CONCLUSIONS

Our studies of the electron-induced secondary electron yields for various spacecraft materials may be summarized as follows.

1. Reliable pulsed beam methods have been developed for use with insulating samples.
2. Techniques using low incident electron currents ( $< 10$  na) must be used to avoid  $e^-$  beam damage to plastics coated with ITO. The decreased yields that follow are associated with surface compositional changes.
3. Significant surface contamination is present on as-received materials which results in increased SEE yields. The use of in-situ AES with SEE yield measurements is encouraged.
4. The incident angular dependence of  $\sigma$  and  $\eta$  of thin conducting coatings on plastics is consistent with a simple penetration depth model.

### REFERENCES

1. Katz, K., Cassidy, J. J., Mandell, M. J., Schuelle, G. W., Steen, P. G., and Roche, J. C.: The Capabilities of the NASA Charging Analyzer Program. Spacecraft Charging Technology - 1978, NASA Conf. Publ. 2071, 1979, p. 101.
2. Chase, R. W., Gordon, W. L., and Hoffman, R. W.: Appl. of Surf. Science 4, 271 (1980).
3. Whetten, N. Key,: in Methods of Experimental Physics, edited by L. Marton (Academic Press, New York, 1967), Vol. 4A, Sec. 1.1.4, pp. 69-85.
4. Amore, L. J., and Eagles, A. E.: Materials and Techniques for Spacecraft Static Charge Control, Proceedings of the Spacecraft Charging Technology Conf. - 1976, Pike and Lowell, eds. NASA Tm X-73537, 1978, p.621.

5. Vossen, J.: RCA Review 32, 289 (1971).
6. Eagles, A. E., et al.: Spacecraft Static Charge Control Materials, AFML-TR-77-105 Part II (June 1977).
7. Bronshtein, I. M., and Fraimen, B. S.: Secondary Electron Emission, NAUKA (Science Publishers), Moscow (1969).
8. Bruining, H.: Physica 3, 1046 (1936).

TABLE I

Source	Front Surface Coating Nominal Thickness	Substrate	Back Surface Coating Nominal Thickness
GE (10248 K-2)	ITO <sup>a</sup> 20 nm	Kapton, 3 mil	Al 20 nm
GE (10248 T-1) <sup>b</sup>	ITO <sup>a</sup> 20 nm	FEP Teflon, 5 mil	Ag/Inconel 20 nm
GE	ITO <sup>a</sup> 20 nm	borosilicate glass (Corning 0211 Microsheet)	
GE <sup>c</sup> 4-18-9T1-34	IO 10 nm	FEP Teflon	
Sheldahl <sup>d</sup> G410620	TCC	Kapton 2 mil	Al
G409420	TCC	Teflon 2 mil (probably FEP Teflon)	Ag/Inconel
OCLI <sup>e</sup>	MgF <sub>2</sub>	Fused silica	

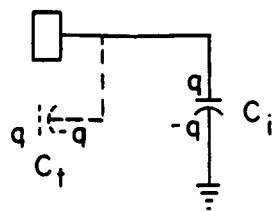
<sup>a</sup>Nominally 90% In<sub>2</sub>O<sub>3</sub> and 10% SnO<sub>2</sub> but uncertain stoichiometry. Prepared by reactive sputtering in an oxygen + argon atmosphere, using magnetron sputtering with in-situ RF activation.

<sup>b</sup>Film showed very high  $\rightarrow \infty$  resistance in two-probe measurement and exhibited serious charging effects in electron beam. ITO layer apparently deteriorated during storage.

<sup>c</sup>Obtained as replacement for original ITO on FEP Teflon film. Non-uniform in that showed large variations in resistance by two-probe measurement.

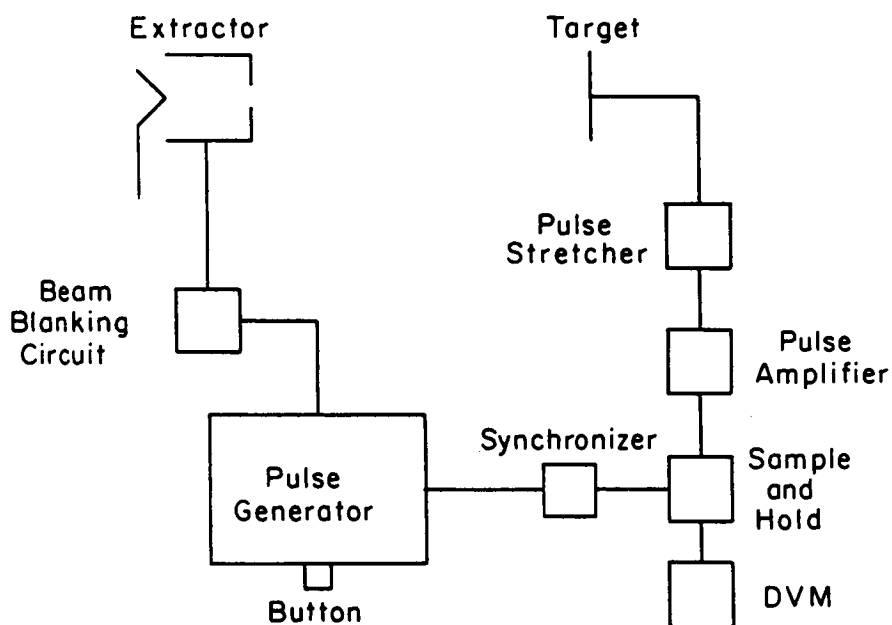
<sup>d</sup>Sheldahl, Northfield, Minnesota 55057. No information supplied on thickness of TCC nor composition. Resistivity given as  $\leq 250 \text{ K}\Omega/\square$ .

<sup>e</sup>Optical Coating Laboratory, Inc., Santa Rosa, California, 95403. No information was supplied.



(a)

Fig. 1(a). The equivalent circuit of the target showing the input capacitor,  $C_i$  and the sample capacitance between the sample surface and carousel,  $C_t$ .



(b)

Fig. 1(b). Block diagram illustrating the circuits used in the pulsed beam mode of operation.

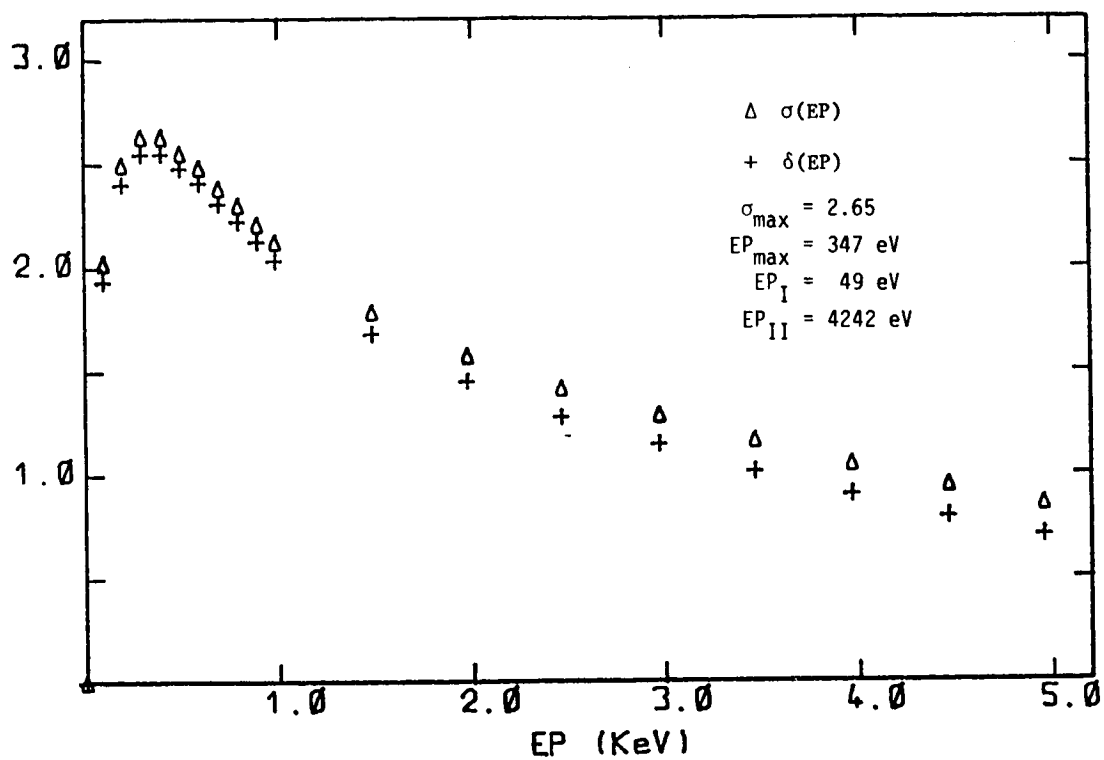


Fig. 2. SEE coefficients  $\delta$  and  $\sigma$  for ITO on Kapton, as-received surface. The short exposure method was used with  $J_p \sim 400 \text{ nA/cm}^2$  and  $I_p = 14 \text{ nA}$ . Sample K-85A.

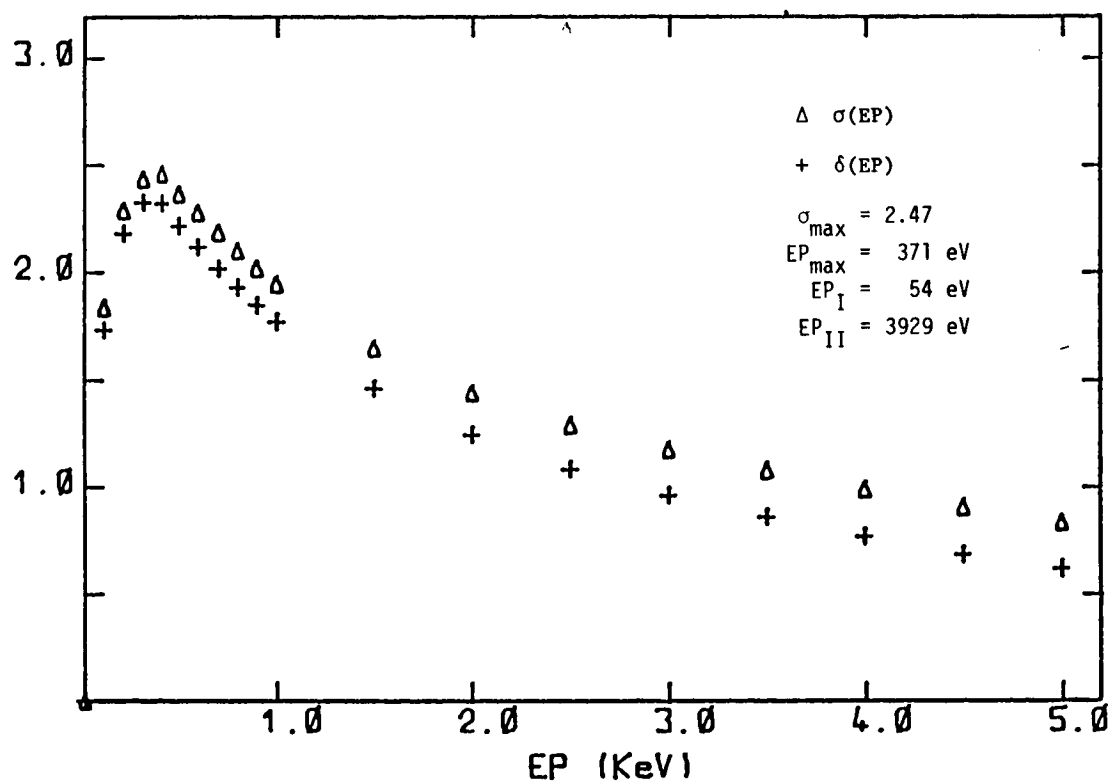


Fig. 3. SEE coefficients  $\delta$  and  $\sigma$  for ITO on borosilicate glass, as-received surface. The short exposure method was used with  $J_p \sim 300 \text{ nA/cm}^2$  and  $I_p = 10 \text{ nA}$ . Sample B-72.

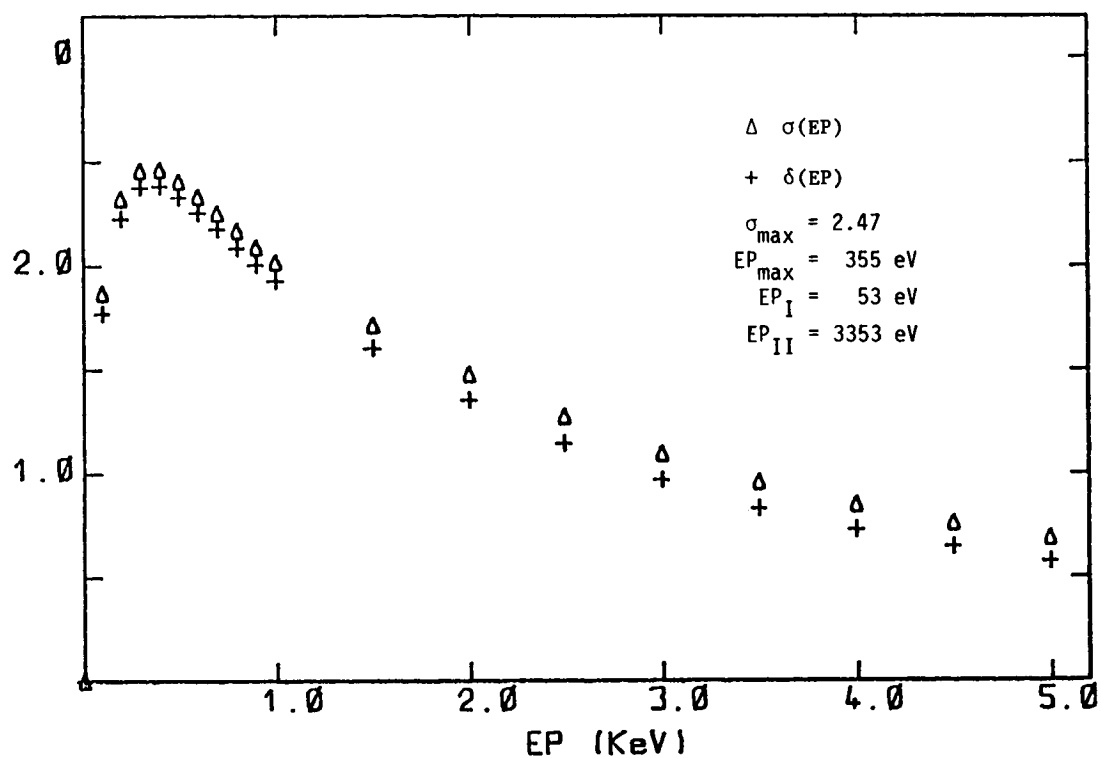


Fig. 4. SEE coefficients  $\delta$  and  $\sigma$  for IO on FEP Teflon, as-received surface. The short exposure method was used with  $J_p \sim 480 \text{ nA/cm}^2$  and  $I_p = 15 \text{ nA}$ . Sample T-86A.

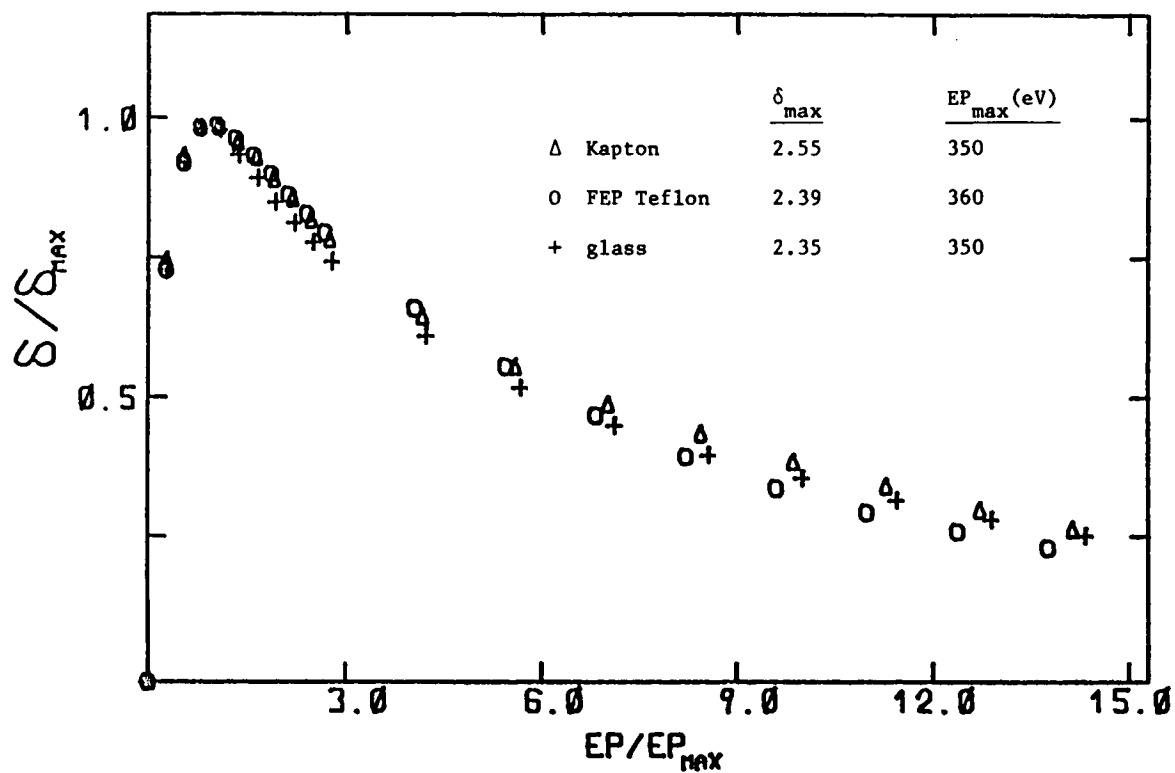


Fig. 5. Normalized  $\delta$  values for the as-received ITO films on Kapton and borosilicate glass and IO film on FEP Teflon. Samples and conditions identical to figures 2, 3, and 4.

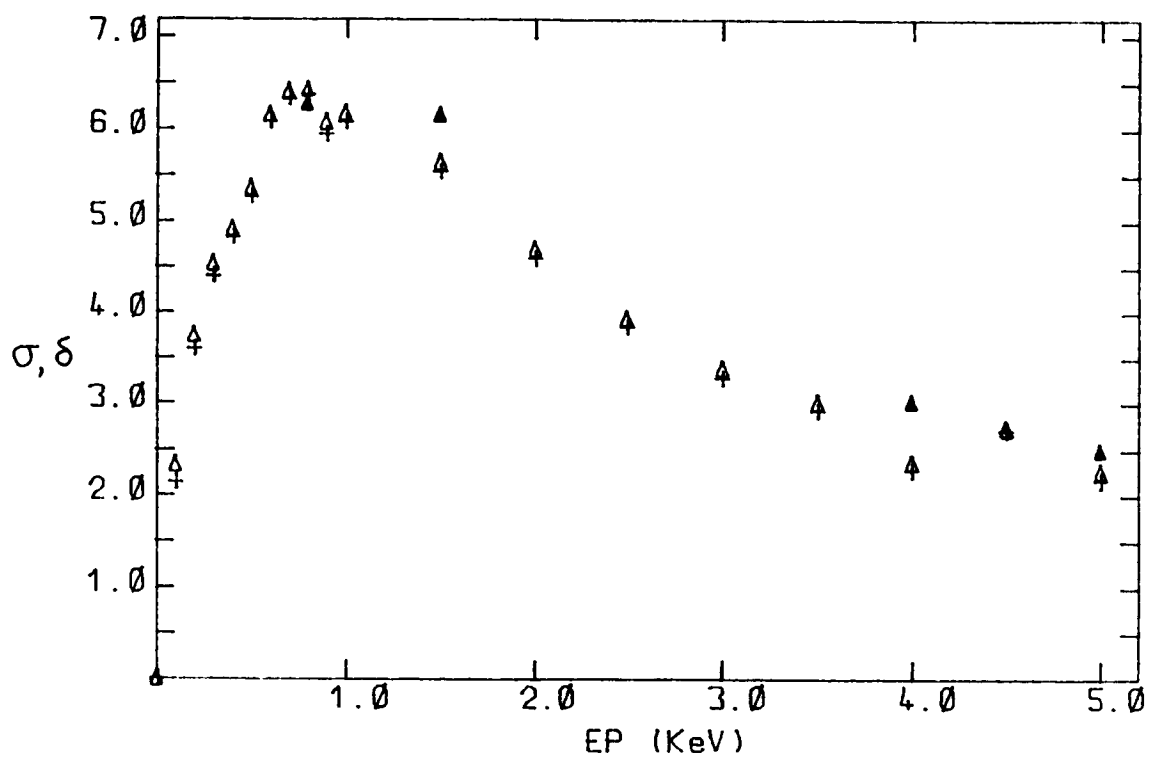


Fig. 6. Preliminary data for SEE coefficient  $\delta$  and  $\sigma$  for MgF<sub>2</sub>, as-received surface. Single pulse method was used with  $I_p = 12$  nA in the pulse.



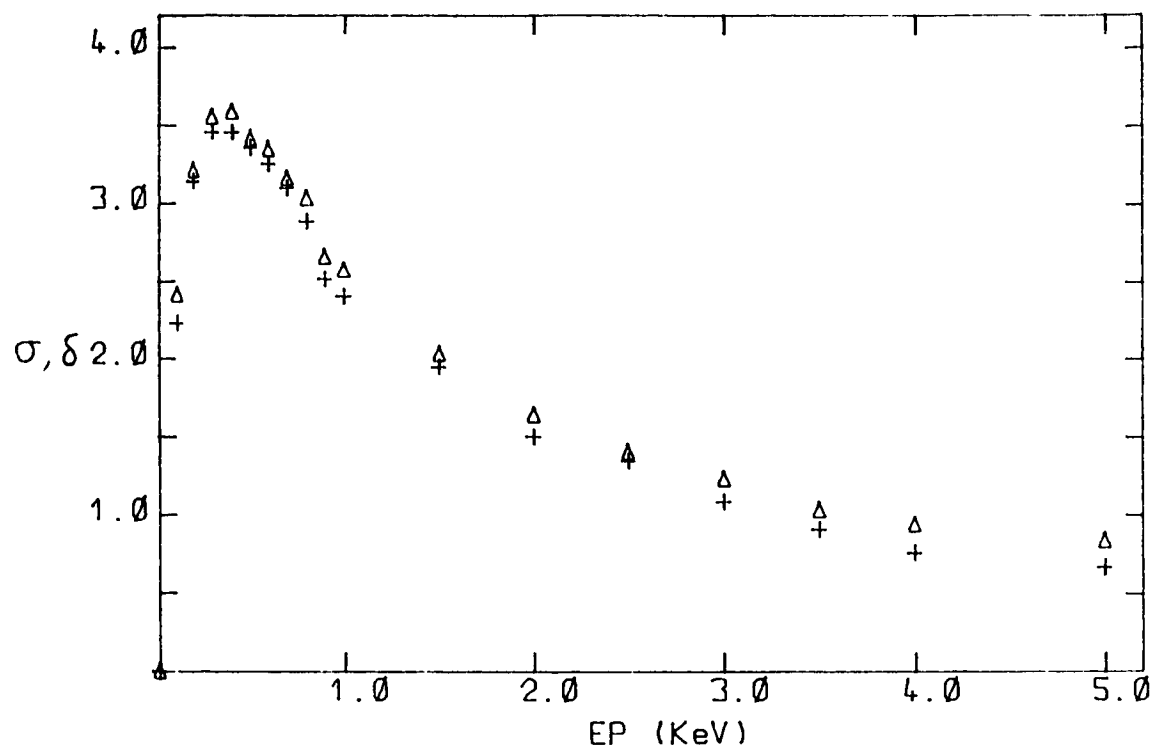


Fig. 7. Preliminary data for SEE coefficient  $\delta$  and  $\sigma$  for fused silica, as-received surface. Single pulse method was used with  $I_p = 12$  nA in the pulse.

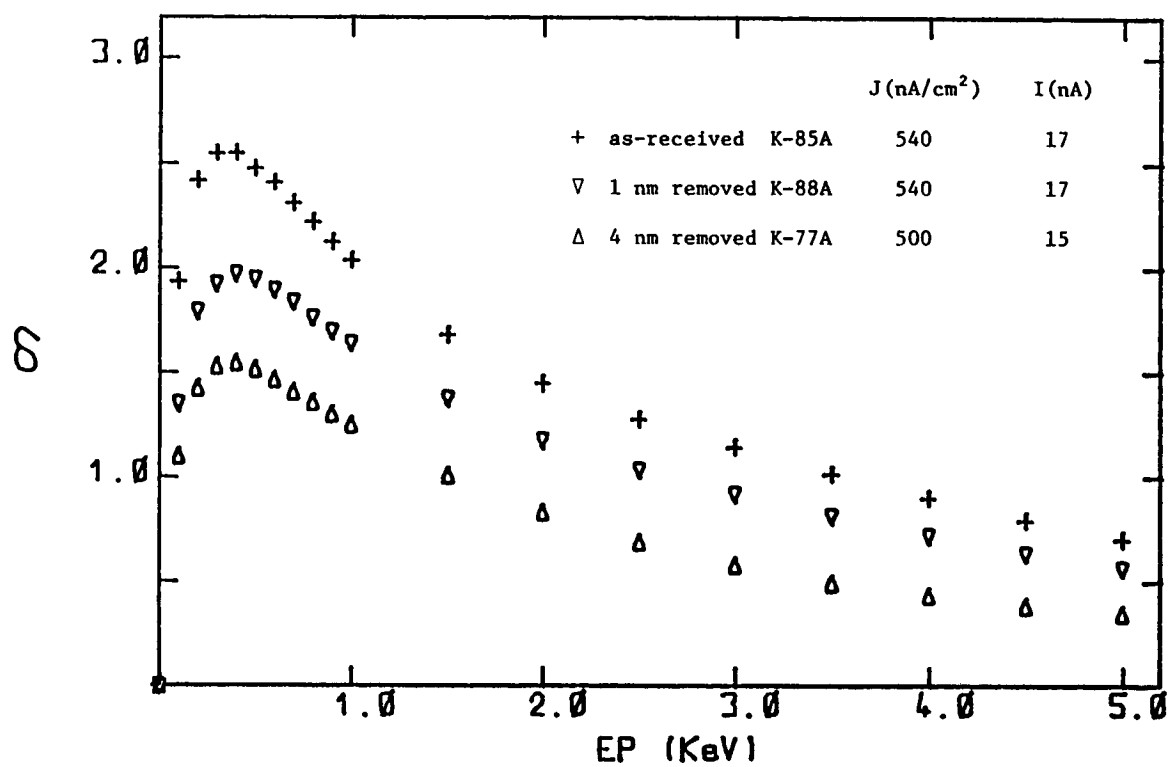


Fig. 8. Comparison of  $\delta(EP)$  for as-received and ion sputtered surfaces of ITO on Kapton. The short exposure method was used.

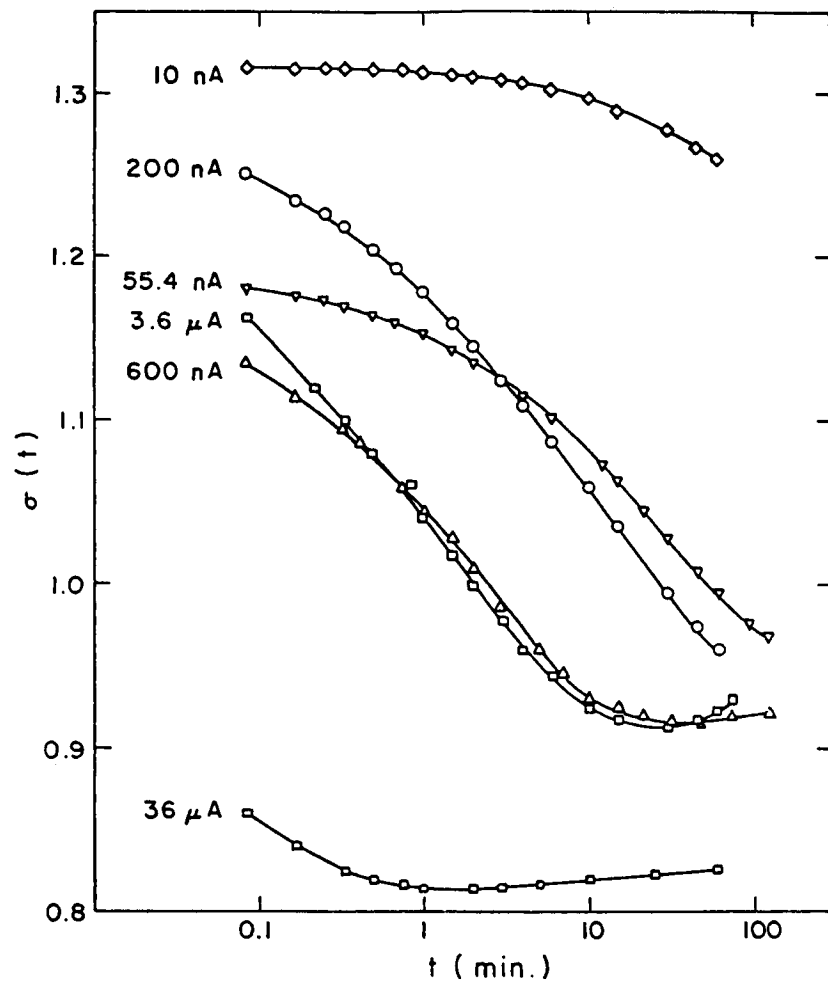


Fig. 9. Total SEE coefficient for ITO on Kapton as a function of time at  $EP = 3$  keV for different electron beam currents,  $I_p$ .

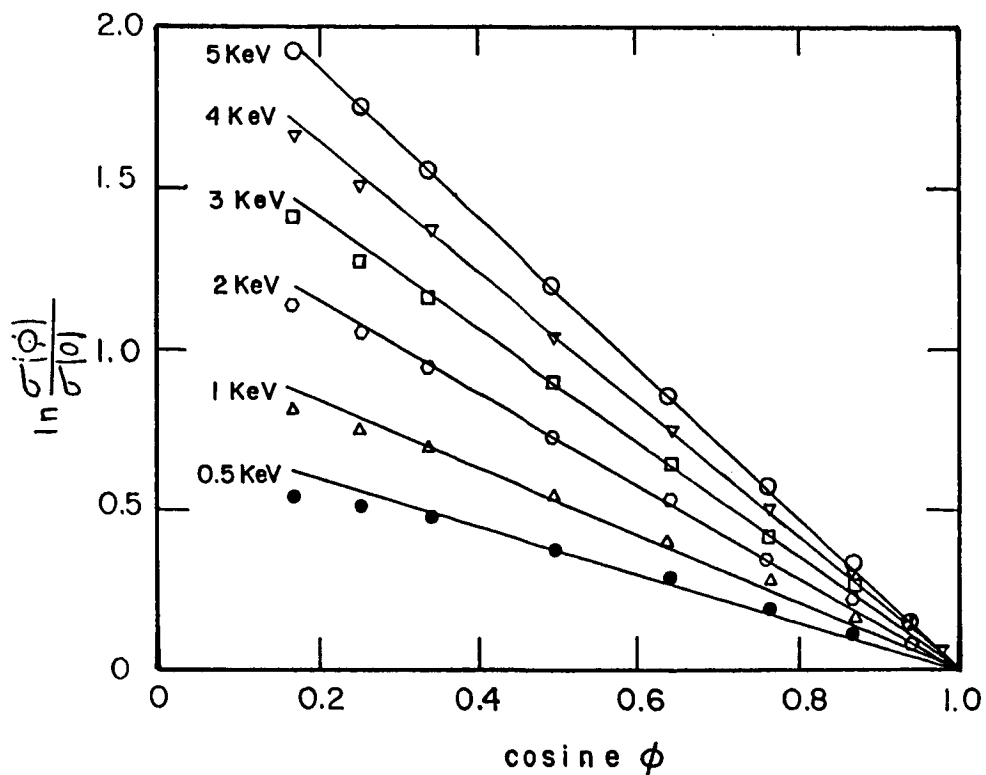


Fig. 10. Angular dependence of normalized SEE coefficient  $\sigma$  of IO on FEP Teflon for several primary beam energies.

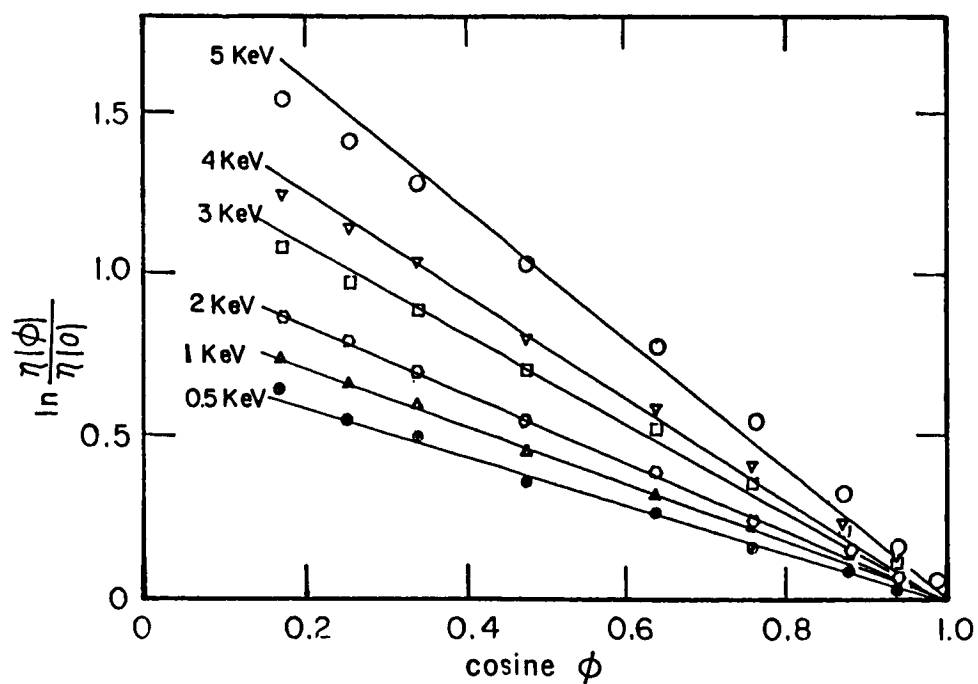


Fig. 11. Angular dependence of normalized SEE coefficient  $\eta$  of IO on FEP Teflon for several primary beam energies.

# OBLIQUE-INCIDENCE SECONDARY EMISSION FROM CHARGED DIELECTRICS\*

James W. Robinson and Paul A. Budd  
The Pennsylvania State University

## SUMMARY

Secondary electron emission coefficients have been measured on FEP-Teflon for normal and oblique incidence in the presence of a normal electric field. Such measurements require knowledge of the electrostatic environment surrounding the specimen, and they require calculation of particle trajectories such that particle impact parameters can be known. A simulation using a conformal mapping, a Green's integral, and a trajectory generator provides the necessary mathematical support for the measurements, which have been made with normal fields of 1.5 and 2.7 kV/mm. When incidence is normal and energy exceeds the critical energy, the coefficient is given by  $(V_0/V)^{.58}$ , and for oblique incidence this expression may be divided by the cosine of the angle. The parameter  $V_0$  is a function of normal field.

## INTRODUCTION

Experimental measurements of secondary electron emission coefficients (SEEC) for FEP-Teflon are reported here. Two features of the work make it unique. Measurements made on a charged specimen are affected by the surface field, and they are made at oblique incidence such that trajectories are influenced by the electric fields. Two activities, experimental measurements and computer simulation, have been combined into a complementary procedure which yields the desired results. The simulations, which have been described in reference 1, are reviewed here briefly, and typical measurements are described.

## Previous Work

Katz et al (ref. 2) have developed a spacecraft charge modelling code NASCAP which uses a functional form for SEEC similar to the straggling theory presented by Lye and Dekker (ref. 3). They also use a functional dependence for angle of incidence similar to that proposed by Jonker (ref. 4). Yet experimental measurements have generally not been available. Quoc-Nguyen (ref. 5) measured SEEC in normal fields for normal incidence, finding that the

---

\*The authors gratefully acknowledge the support of this work by The National Aeronautics and Space Administration under Grant NSG-3166.

critical point for unity emission is a function of surface field. This report is a direct extension of the work initiated by him.

### Procedures

The specimen of 0.12-mm FEP-Teflon is placed on a flat grounded platform which may be rotated in a cylindrical shell as illustrated in figure 1. The specimen is oriented normal to the flux from a mono-energetic flood gun and the cylinder is rotated so that a window is placed above the specimen. After a steady state is reached, the flood gun is turned off and the cylinder is again rotated so that the specimen is enclosed in a well defined electrostatic environment. The specimen holds its charge for long periods of time; decay during an experiment is negligible. Discharging is done by exposing the specimen to the flood gun while the flood gun potential is gradually reduced.

The distribution of charge on the specimen is determined from an assessment of electron trajectories which come near to but do not strike the specimen. The probing beam, which is injected through a slot in the cylinder, has a width less than 0.2 mm and provides highly resolved measurements. When the beam does not strike the specimen, it usually reflects back to the cylinder where it is detected with fine probe wires. Measurements of beam exit positions for various injection points and injection velocities provide a basis for determining the potential distribution on the specimen. The simulations are important in this phase of the work.

Once the distribution of potential is known, impacting trajectories can be simulated for the purpose of calculating impact point, impact angle, and impact velocity. This information is crucial for interpreting the measurements of SEEC. Though SEEC is relatively easy to measure, a measured value is of worth only when the impact parameters are known.

The actual measurements of SEEC are accomplished by directing an electron pulse of known charge (about 1pC) at the specimen and detecting a change of charge induced in the metal substrate behind the specimen. If these charges are designated as  $Q_i$  and  $Q_s$ , then the SEEC is

$$\sigma = 1 - Q_s/Q_i \quad (1)$$

This definition collects backscattering, inelastic scattering, and the low-energy SEEC into a single parameter.

### SIMULATION

The geometry of the experimental system, a half-cylinder, was chosen for several reasons, one being experimental convenience. However the choice was primarily related to the need for simulating the experimental system with a numerically efficient process. The use of a sufficiently long specimen (at least equal to the diameter) allowed calculations to be done in two instead of

three dimensions, and consequently, a technique using conformal mapping could be applied. By this method, the half-cylinder was easily converted to a half-plane where a Green's integral yielded electric potential. Repeated applications of this technique provided the data needed by particle trajectory tracing routines. The methods described here have been developed by Quoc-Nguyen (ref. 5) and Robinson and Tilley (ref. 6), and they have been adapted to this geometry by Robinson (ref. 1).

### Conformal Mapping

If the radius of a semicircle in the upper half plane  $W$  is  $A$  then the mapping

$$Z = 2W / \{1 + (W/A)^2\} \quad (2)$$

converts that semicircle into the upper half plane  $Z$  by opening it at the point  $W=iA$ . The potential of a point is the same in either plane but fields computed in the  $Z$  plane must be transformed according to the equations

$$\begin{aligned} E_u &= S E_x + T E_y \\ E_v &= -T E_x + S E_y \end{aligned} \quad (3)$$

where  $S$  and  $T$  are defined by

$$dZ/dW = S + iT \quad (4)$$

### Green's Integral, Surface Potential, and Fields

In the  $Z$ -plane the potential at some point  $(X,Y)$  is given by an integral over the specimen's surface where potential on the surface is designated  $P'(X)$ . The integral is

$$P(X,Y) = \frac{Y}{\pi} \int_{-B}^B \frac{P'(X') dX'}{(X-X')^2 + Y^2} \quad (5)$$

The surface potential  $P'(X)$  has been expressed for this work as a polynomial in  $X$ , the transformed variable, rather than being expressed in terms of  $U$ . The expression is

$$P'(X) = \sum_{i=0}^m A_i (X/B)^i \quad (6)$$

where  $m$  is finite. It has been assumed that  $P'(-B)=P'(B)=0$  and that, consequently, the sum of even  $A_i$ 's is zero and the sum of odd  $A_i$ 's is zero. It is experimentally convenient that  $A_0$  is the potential at the center of the

specimen. Furthermore all of the odd  $A_i$  values are zero when the potential is symmetric about the origin, a common though not necessary experimental condition.

When the expression for surface potential is substituted into the Green's integral, the resulting expression may be written as

$$P(X,Y) = (Y/\pi) \sum (A_i I_{1i} / B^i) \quad (7)$$

where

$$I_{1i} = \int_L^H \frac{(R+X)^i dR}{(R^2+Y^2)} \quad (8)$$

and where  $L=-B-X$  and  $H=B-X$ . Electric field components are found from the negative gradient of the potential and are

$$\begin{aligned} E_x &= -(2Y/\pi) \sum (A_i I_{2i} / B^i) \\ E_y &= -P/Y + (2Y^2/\pi) \sum (A_i I_{3i} / B^i) \end{aligned} \quad (9)$$

where the integrals are

$$I_{2i} = \int_L^H \frac{R(R+X)^i dR}{(R^2+Y^2)^2} \quad (10)$$

$$I_{3i} = \int_L^H \frac{(R+X)^i dR}{(R^2+Y^2)^2} \quad (11)$$

Typically one specifies the radius  $A$ , the specimen width  $B$  (as measured in the conformed plane), the coefficients  $A_i$ , and some point  $(U,V)$ . Then a direct procedure may be followed to obtain the required results. A conformal mapping yields the point  $Z$  (or  $X,Y$ ) and the three integrals are evaluated. Field components so obtained are then mapped back to the original  $W$  plane.

In the limit as  $Y \rightarrow 0$ , the integrals diverge, but an analytical limiting procedure can be applied to obtain equations for the fields on the surface of the specimen.

#### DeVogelaire's Method

This method, which is used to generate particle trajectories, applies to second order differential equations without explicit first derivatives (ref. 7). It is correct to fourth order and uses a relatively simple stepping procedure. The coordinates and velocity components must be known at some time  $t_1$  and also the coordinates must be known at the time corresponding to a half-step before  $t_1$ . Field components are calculated at these points. Then, for the  $U$ -motion, a new half-step (designated by  $h$ ) is taken with



$$U_h = U_i + V_u T/2 + QT^2((3+F)E_u - FE_{-hu})/24 \quad (12)$$

where T is the time step, U is coordinate, V is velocity, E is field, and Q is the charge/mass ratio. Usually F may be considered to be unity, though it is assigned a different value when a change of time step is implemented. After the half-step, the fields at the new point are evaluated and the whole step is completed with

$$U_{i+1} = U_i + V_u T + QT^2(E_u + 2E_{hu})/6 \quad (13)$$

Equations similar to these are used simultaneously for stepping in the V-direction. After a step has been completed the new velocities are evaluated from the U-equation

$$V_{u,i+1} = V_u + QT(E_u + 4E_{hu} + E_{u,i+1})/6 \quad (14)$$

and from a similar V-equation. The stepping procedure is repeated as many times as needed to trace the complete trajectory.

As the particle approaches the specimen the time increment is reduced by a factor of 4. This is done by defining the factor F to have a value 1/4 for the next step only and by redefining the time step with  $T=FT$ . Likewise for particles leaving the region close to the specimen F is set equal to 4 for one time step only to cause an increase in the size of the time step.

Special procedures are required when the trajectory runs into a boundary. When the particle approaches the plane of the specimen a branch occurs so that the trajectory can be ended precisely on the plane. This is done by calculating the value of time step required for the last step and then by using that time step in the usual formulas. The trajectory may also intersect the circular boundary. In this case the trajectory at the last point inside the boundary is linearly extended until the boundary is crossed.

Two different subroutines have been developed to start two different types of trajectory. In each case the given point which represents injection of a particle is treated as a preceding half step and the reference point is generated by appropriate equations which take an initial half step. One calculation starts from the circular boundary and corresponds to particles injected at that boundary. The other starts on the surface of the specimen and allows the user to specify conditions at that end of the trajectory, which is traced backwards from the specimen to the cylinder.

The trajectory tracing routines have been executed many times for a variety of conditions. Figure 2 shows typical impacting trajectories for which the specimen potential varies as

$$P' = 1-(X/B)^6 \quad (15)$$

and for which the particle energy is 1.56 times the potential at the center of the specimen. Figure 3 shows particles which have energy of 0.85 times the

potential at the center of the specimen.

## EXPERIMENTAL PROCEDURES

The system, shown in figure 1, was placed in a stainless bell jar and evacuated by a turbomolecular pump to a pressure below the gauge limit of  $10^{-6}$  torr. Continuous pumping and operation of filaments for days at a time assured stable and reproducible measurements. Both specimen platform and cylinder were rotated with stepper motors which took 200 steps/revolution. One step corresponded to a motion of 0.8 mm at the periphery of the cylinder. This system could be used in a variety of modes for measuring non-impacting trajectories, specimen surface potentials, and SEEC for impacting trajectories. In an auxiliary series of measurements a small Faraday cup was placed on the platform next to the specimen so that reference measurements of SEEC could be made for the conditions that surface potential was zero and that incidence was normal.

### Probing Beam

The beam was a versatile tool for making the various measurements of interest. It was admitted to the cylinder through a slot cut in the cylinder such that no matter how it rotated, the beam was not blocked. The beam itself was shaped by slits and aperture plates so that it had a cross section of about  $2 \times 0.2$  mm. The longer dimension was oriented parallel to the axis of the cylinder, and the beam was deflected in the direction of the shorter dimension. Sensor wires, mounted at the slot of the cylinder, rotated with the cylinder and detected the beam either where it entered or where it exited, if indeed it did return to the cylinder.

The beam was deflected by applying voltage between deflection plates which were located behind the beam orifice. Either steady state or pulsed voltages could be applied, the steady state being more useful for beams returning to the cylinder and the pulse being useful when the specimen was to be struck briefly with a measurable packet of charge. A typical pulse duration was 1 ms though for some cases much longer pulses were used. Typical beam current was 1 nA and a typical charge packet was 1 pC. By measuring deflection voltage required to move the beam from one sensor wire to another, one could determine the deflection factor and thus correlate simulated and experimental deflections.

The mechanical alignment of the gun was not perfect but that problem was easily resolved by assigning the condition of normal incidence to be that deflection voltage for which a beam returned to its point of origin. This condition was for a charged specimen which was rotated so that it faced the beam.

## Surface Potential

The peak surface potential, which is represented by  $A_0$ , is determined experimentally before computer simulations can be attempted. When the surface has been charged with a flood gun potential of  $V_t$  then the difference,  $V_t - A_0$ , is equal to the critical voltage for which the SEEC is unity. This value is influenced by surface field strength which in turn is related to sample width; it was 6 mm for this work. The surface potential was defined experimentally to be the lowest possible probing beam accelerating potential for which any perturbation in surface charge (or substrate charge) could be noted. Normal incidence at the center of the specimen is required for this measurement. Table 1 shows results of several such measurements and it also shows normal electric field  $E_v$  at the center of the specimen.

When  $A_0$  was determined, then trajectories of the form shown in figure 3 could be compared with experimentally measured trajectories. The end points of the trajectories were the quantities compared. Figure 4 illustrates this comparison for a specimen originally charged with a 10kV flood beam. The various curves correspond to different choices of the exponent  $M$  in the expression

$$P' = A_0 \{1 - (X/B)^M\}, \quad (16)$$

and consequently, for this case  $M$  should be 4 for a best fit. More elaborate functions could be used for  $P'$  but for the study of incidence on the center of the specimen, further refinements were not incorporated.

## SEEC for Uncharged Specimen

The experimental system does not contain provisions for measuring the charge packet delivered by the pulsed probing beam. Consequently several measurements were made with a small Faraday cup inserted above the specimen platform and offset slightly so that the beam could be directed alternately at the specimen and the cup. These measurements were made at normal incidence with the surface of the specimen discharged so that beam trajectories could be assumed to be straight lines. When such measurements had been completed, the SEEC could be computed, and the values so determined could be used for calibrating the beam in the absence of the cup.

For this series only,  $Q_1$  was measured with the cup and  $Q_s$  was the charge induced in the substrate when the beam struck the specimen. Then equation 1 was applied and the SEEC so calculated were represented by

$$\sigma = (V_0/V)^N = (Q_1 - Q_s)/Q_1 \quad (17)$$

where  $V > V_0$ ,  $V_0 = 1.5\text{kV}$ , and  $N$  is approximately constant. Table 2 shows recorded data and the corresponding values of  $N$ . It has been assumed that  $N = 0.58$  for normal incidence on the uncharged specimen, and this value is used in calibrating all other measurements.

## SEEC for Charged Specimen

With no Faraday cup present, the specimen is charged and struck with a charge packet from the probing beam. Thus  $Q_s$  is measured for whatever surface potential and angle of incidence are of interest. Then the surface is discharged and struck again at normal incidence. From this second measurement,  $Q_n$  is determined by using equation 17 and the assumed value of  $N$ . Finally the SEEC is calculated from equation 1.

One requirement is that the injection point and injection velocity be carefully calculated so that the impact parameters will be as desired. The simulation of trajectories provides the necessary data yet an uncertainty does exist as to the value of deflection plate voltage which corresponds to a radial injection of the beam. Ideally this voltage would be zero yet slight misalignment can cause it to be different. Data shown later illustrate this problem which, though not serious, might be alleviated by breaking the metal backing of the specimen into two zones. Then the transition point between zones could be precisely located in terms of deflection plate voltage.

Another requirement is that the charge packet be sufficiently small that the surface potential changes little. If a second response at the same spot is smaller than the first, then the pulse size is too large. Larger pulses could be used when the SEEC was close to unity than otherwise because  $Q_s$  was zero at the unity condition. The challenge of measuring with small charge packets was to establish conditions where drift and noise associated with the electrometer measurement did not obscure the data. One source of noise may be micro-discharges on the surface of the specimen; noise was greater on a charged specimen than on an uncharged specimen. Cleanliness is also important. Drifting generally could be controlled by carefully shielding the critical hardware from the charged particle environment created by the electron beam sources.

## EXPERIMENTAL DATA

Measurements have been made for values of  $V_f$  shown in table 1 of 8 and 12 kV where angles of incidence have ranged as high as 70 degrees. First it is noted that the form of equation 17 is appropriate for normal-incidence data if  $N=0.58$  and  $V_0$  is 1.85 kV for a surface potential of 6.15 kV (or 1.96 kV for 10.04 kV). Figure 5 illustrates the function and shows superimposed data points for the case where surface potential is 6.15 kV. These normal incidence measurements are made in the center of the specimen, yet location of the precise center is not critical as the measured SEEC is insensitive to the point at which the measurement is made. This is because the potential function has a broad maximum in the center and also because slight deviations from normal incidence are inconsequential.

Also shown in figure 5 are curves for angles of incidence  $\theta$  which were obtained by dividing equation 17 by  $\cos(\theta)$  according to the usually assumed

theory (ref. 4). These theoretical curves were used in constructing figure 6 which illustrates measurements at oblique incidence.

All of figure 6 was generated from simulation and the assumed theoretical dependence upon  $\theta$  except for the data points which have been superimposed. Except for an obvious lateral shift of data points, which is related to establishing a reference deflection voltage, the match between theory and data is excellent. The data points themselves are easily located on the figure in terms of the experimental parameters of  $Q_s$ ,  $Q_i$ , and deflection voltage. However some additional explanations are needed<sup>1</sup> for the calculated curves. The experiment was simulated by assuming a form for  $P'$  with an exponent of 6 as shown in equation 15. It was also assumed that the parameters from table 1 for  $V_f=8$  were appropriate. Finally it was assumed that the impacting beam had an energy of 9.5 keV as was the case for the experiment. The injection point for the beam was chosen to cause a 45-degree impact angle at the center of the specimen and then numerous beams were simulated where the deflection angle of the beam was varied, as shown in figure 2. Figure 6 shows the surface potential of the specimen, the impact position for each of several simulated beams, the impact angles of each of those beams, and deflection plate voltages corresponding to each of the simulated beams. Then from figure 5 the secondary emission coefficient was calculated for combinations of surface potential and angle of incidence. The data shown in figure 6 is typical of many measurements which have been made. Its characteristic is that the measured SEEC is much larger off center, where angle of incidence is greater, than in the center where the impact energy is lowest. It should be noted here that the side of the specimen shown is the side opposite from the beam source. The impacts on the near side of the specimen are at lesser angles of incidence and the values of SEEC are corresponding lower. Field strength is of course not constant over the range of data shown but for this case one may assume it to be reasonably constant out to 2 mm where the tangential component becomes significant.

Figure 5 indicates that for angles of 70 degrees or more, the critical point may be as high as 10 kV. This has indeed been demonstrated by measurements with both of the previously specified charging conditions.

#### REFERENCES

1. Robinson, J. W.: Mapping of Electrical Potential Distribution with Charged Particle Beams. NASA Grant NSG-3166, The Pennsylvania State University, September 1980.
2. Katz, I. et al: A Three Dimensional Dynamic Study of Electrostatic Charging in Materials, NASA CR-135256, August 1977.
3. Lye, R. G.; Dekker, A. J.: Theory of Secondary Emission. Phys. Rev. 107,4, pp977-981, August 1957.
4. Jonker, J. L. H.: On the Theory of Secondary Electron Emission. Phillips Research Reports 7, ppl-20, 1952.

5. Quoc-Nguyen, N.: Secondary Electron Emission from a Dielectric Film Subjected to an Electric Field. NASA CR-155213, November 1977.
6. Robinson, J. W.; Tilley, D. G.: Potential Mapping with Charged Particle Beams. Spacecraft Charging Technology-1978, pp 606-620, NASA Conference Publication 2071, 1979.
7. DeVogelaire, R.: A Method for the Integration of Differential Equations of Second Order Without Explicit First Derivatives. J. Res. National Bureau of Standards 54, 119 March 1955.

Table 1: Surface Potential, Critical Voltage, and Normal Field for Various Flood Beam Potentials

$V_f$ (kV)	$A_0$ (kV)	$V_c$ (kV)	$E_v$ (kV/mm)
6.	4.2	1.8	0.98
8.	6.15	1.85	1.50
10.	8.08	1.92	2.09
12.	10.04	1.96	2.73
14.	12.0	2.0	4.08

Table 2: Measurements for the Uncharged Specimen

$V$ (kV)	$Q_s$ (pC)	$Q_i$ (pC)	$\sigma$	$N$
4.0	6.00	12.8	0.53	0.61
5.0	6.25	12.8	0.51	0.55
6.5	3.30	5.75	0.43	0.58
8.0	2.25	3.75	0.40	0.55
10.0	6.50	4.20	0.34	0.57

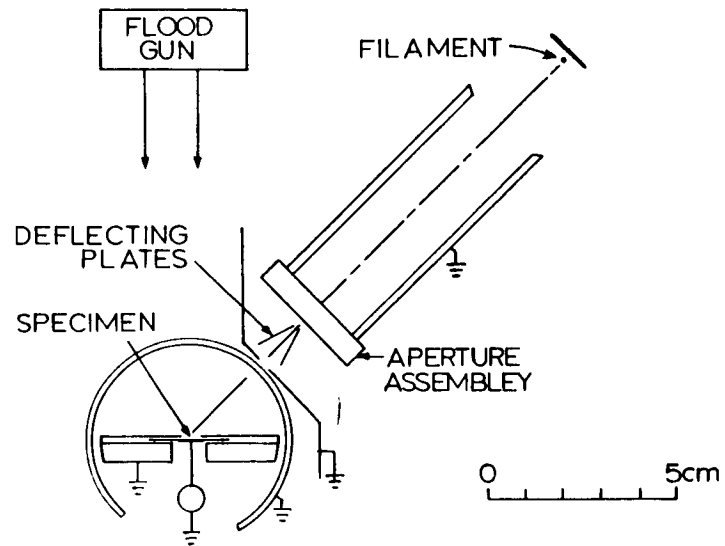


FIGURE 1. EXPERIMENTAL FACILITY

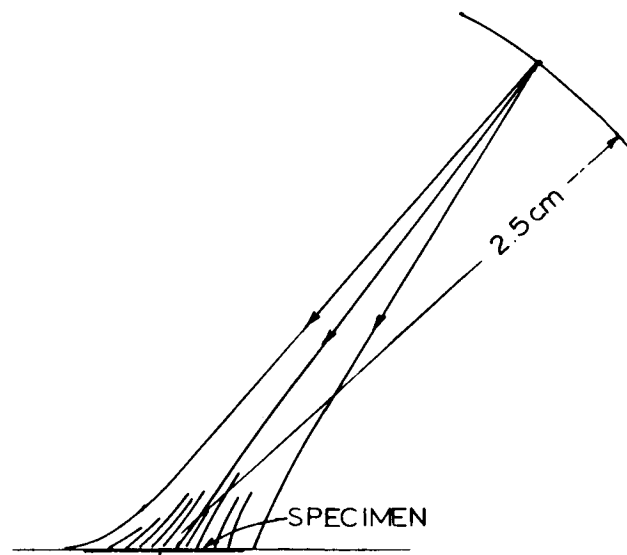


FIGURE 2. SIMULATED IMPACTING TRAJECTORIES

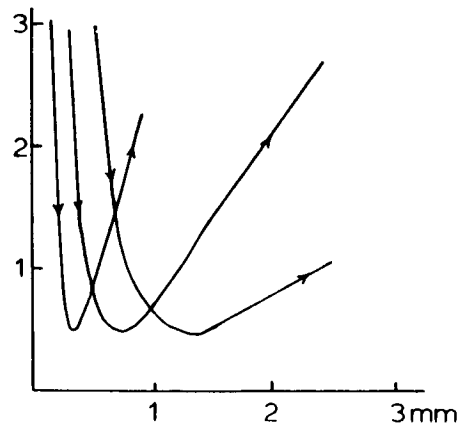


FIGURE 3. SIMULATED REFLECTING TRAJECTORIES

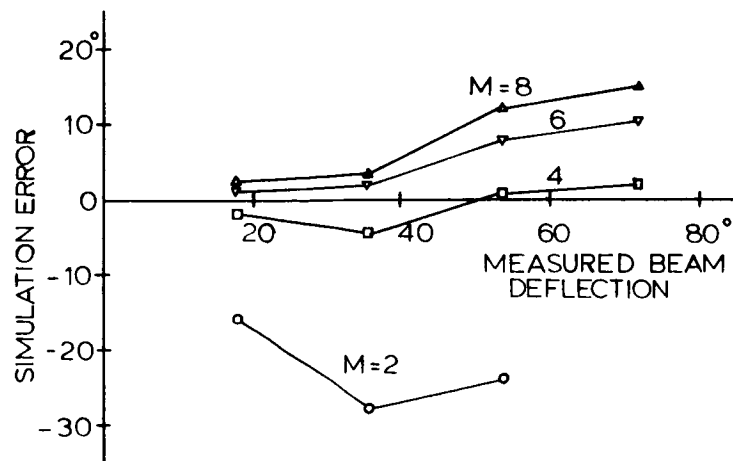


FIGURE 4. COMPARISON OF SIMULATION AND EXPERIMENT FOR DEFLECTED BEAMS



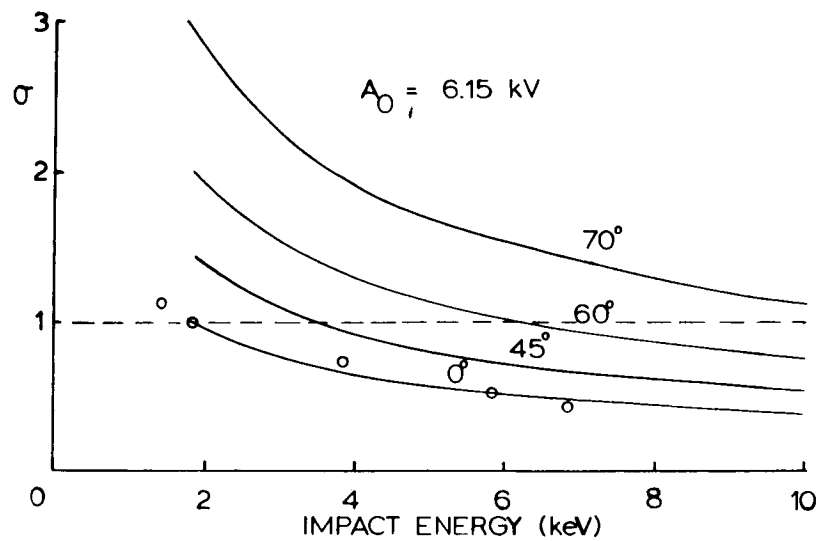


FIGURE 5. THEORETICAL SEEC CURVES BASED UPON NORMAL-INCIDENCE DATA

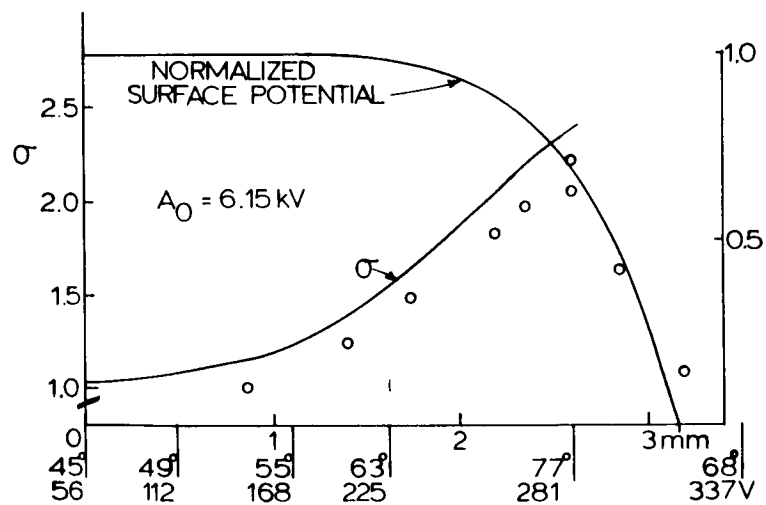


FIGURE 6. COMPARISON OF EXPERIMENTAL DATA WITH THEORY. SIMULATED TRAJECTORY PARAMETERS ARE INDICATED ON THE ABSCISSA.

## **TANK TESTING OF A 2500-cm<sup>2</sup> SOLAR PANEL**

**Renate S. Bever**  
**NASA Goddard Space Flight Center**

**John Staskus**  
**NASA Lewis Research Center**

### **A. INTRODUCTION**

A fairly large, 50cm by 50cm solar panel test patch was investigated for Spacecraft (S/C) charging and arcing effects. This was done in the course of verification testing of a new solar panel design for the Tracking Data Relay Satellites or TDRS System. Thus bombardment with mono-chromatic electrons, whose energy could be varied up to 20 kilovolts, was carried out at the NASA Lewis Research Center, in the 2 m x 2 m tank testing facility.

The objectives of the test were severalfold and somewhat similar to those described by Bogus on the Canadian Technology Satellite type of solar array, reference 1, namely:

- (a) to obtain an estimate at what voltage of electron bombardment arcing would be probable;
- (b) to find whether the energy content within the arcs would be tolerable or damagingly large;
- (c) to repeat and continue an incomplete test on a smaller TDRS solar panel test patch reported upon by Inouye and Sellen, reference 2;
- (d) to try and separate thermal and photoeffects;
- (e) to ascertain whether silver from the interconnects would be sputtered off during arcing;
- (f) to see whether materials used were such as to minimize arcing.

The large electron bombardment facility at Lewis RC is in demand for other projects of higher priority, and thus it was available for TDRS for only a limited time. Despite this, some of our objectives could be accomplished, and this paper reports on several of the observations made.

### **B. DESCRIPTION OF THE SOLAR PANEL TEST PATCH**

The large solar array of the TDRS, being manufactured by TRW Space and Defense Systems for Space Communications Co., consists of two wings, each of 3 panels, each panel measuring 150 inches by 50 inches. These panels are a new design with aluminum honeycomb core and Kapton face sheets. The back face sheet is perforated and painted with graphite-containing epoxy paint of lower than 100,000 ohms/square surface resistivity. The spacing between adjacent solar cells is extremely close with the interconnect stress relief loop protruding above the cover glasses of uncoated ceria-doped glass. See figures 1a) and 1b). In one respect the test patch supplied by TRW Company was different from the flight hardware: the 50cm by 50cm test patch has seven columns (3 strings) of ceria-doped cover glasses and five columns (2 strings) of fused silica cover glasses coated with magnesium fluoride, as shown in figure 2. This panel was one of the Life test

panels. There are diode boards on the panel and bare Kapton borders (the edges are Kapton tape, painted conductively), and thermistors and connectors are at the upper panel edges. The latter were immediately covered with an aluminum shield; also the bare Kapton borders were covered with aluminum foil for some of the data runs, but not all. Thus the test specimen was adequately large and representative of the real design, but it also had considerable complexity.

### C. FACILITY AND INSTRUMENTATION

The 2 m x 2 m NASA-LeRC electron bombardment test facility is shown in figure 3 and also in reference 3. The panel was centered on the vacuum chamber axis 125 cm downstream from five divergent beam electron guns located on the chamber door. Five guns were used in order to improve the uniformity of the electron flux over the large area presented by the test panel. The guns were arranged in a 30 cm square array with one gun in the center to irradiate the corners and center of the test panel respectively. The accelerating potential for all five guns was provided by a single high voltage power supply. The electron flux contributed by each gun could be adjusted by independent filament current and grid voltage controls. The flux at a plane 12 cm in front of the test panel was monitored by a vertical array of five 10 cm<sup>2</sup> discs which could be swept horizontally across the chamber. The center disc traversed a path through the chamber axis. The vertical separation between discs was 15 cm. The currents intercepted by the discs were measured with Keithley 616 digital electrometers whose analog outputs were displayed on one of two eight-channel strip chart recorders. During electron gun adjustment prior to a test, a swinging shield containing an array of current sensors protected the test panel. The test began when the shield was swung to the chamber wall.

The panel surface potential was monitored with two TREK model 340HV electrostatic voltmeters using model 8052E probes. The probes followed curved paths at a distance of two to three millimeters above the surface of the panel. The outputs from the voltmeters were displayed on one of the eight channel strip chart recorders (BRUSH Co.).

A 15 cm diameter loop antenna located to one side of and upstream from the test panel monitored the discharge activity on the panel. The signal from the antenna was fed into three counters with voltage thresholds of 1, 2, and 5 volts. The frequency of the counts indicated the frequency of discharges with energy greater than that required to trip the counter. A still camera located outside one of the windows on the chamber door was also used to record the discharge activity of the panel. Time exposure photos recorded the visible evidence of discharges taking place on the test panel. The camera's field of view covered approximately 40% of the panel area.

A 12 kW, 2 lamp, Xenon arc solar simulator was available to simulate the solar input to the test panel. It was positioned outside the vacuum chamber and the short wavelength cutoff was approximately 2000 Å so little photoemission could be expected from the test panel.

A low energy plasma source producing ionized nitrogen was used between electron bombardment tests to neutralize the negatively charged panel surfaces.

A temperature controllable cylindrical chamber liner was available to investigate thermal effects on the charging and discharging of the test panel. It was capable of operating over a -190°C to +120°C range.

The solar array test panel was mounted on ceramic posts at its corners to provide DC isolation from the chamber. Fifteen leads from the panel were brought through a multipin vacuum bulkhead feedthrough mounted in the center of a 39cm diameter dielectric flange. The dielectric flange provided the necessary DC isolation when it was desired to float the panel or place a multimegohm resistance between it and ground. Ten of the leads came from the five strings of solar cells on the panel. These were then connected to a single common lead external to the vacuum chamber and hence thru an electrometer to ground. Three leads came from two thermistors; one lead from the aluminum honeycomb core and backside conductive paint and hence thru an electrometer to ground; and one lead from the aluminum shield thru an electrometer to ground. Alternatively multimegohm resistor strings could be placed between the various elements and ground. Intercepted or leakage electron currents were measured using Keithley 616 digital electrometers with analog outputs displayed on the 8 channel chart recorders.

#### D. CHARACTERIZATION OF SOLAR PANEL TEST PATCH, WITH METALLIC PARTS GROUNDED

Prior to any electron bombardment, the current-voltage curves of the solar cell strings were obtained at Goddard Space Flight Center. At the LRC facility the electron bombardment was then carried out. For all these experiments, unless otherwise stated, the current flux density in the electron beam, at the sample, was kept at a spatial average of about 3 nanoamperes/cm<sup>2</sup>. It varied somewhat across the cross section of the beam at the sample due to its large size, by about a factor of 2.

An excerpt from a data scroll taken in the test configuration described in part C is seen in figure 4, demonstrating what was continuously and simultaneously recorded: the time in minutes, the current from the aluminum shield in microamperes, the current from the solar cell strings in microamperes, the current from the honeycomb core and backside paint in tenths of microamperes, the surface charge-up voltages as read by the two TREK electrostatic probes, in kilovolts. Below 12kV the current traces were mostly smooth, meaning that no arcing was occurring.

Sustained arcing occurred first at 12keV beam voltage, figure 4. The centers of the ceria-doped glasses are at a lower charge-up voltage  $6 \pm 1$  kV than the fused silica glasses at  $9 \pm 1$  kV, with respect to the grounded interconnects. At a beam voltage of 20kV the arcing events became, of course, extremely numerous. For modest arcing, as in figure 4 at 12keV, the direction of the transient current flow through the solar cell strings was usually an electron flow from ground, but the core and backside paint leads sometimes had an electron flow from ground and sometimes a vastly increased spike over and above leakage current to ground. It must be concluded that for as complex a system as this panel several modes of arcing were possible.

One can summarize an entire data sequence in a graph of electron beam voltage versus coverglass voltage and versus currents to ground, of which the only true leakage current is the honeycomb core current, as in figure 5. The coverglass voltage over the central portion of the glasses is used as the parameter for plotting of the graph here and for discussion because it is easily estimated from the TREK probe tracings. There is a much lower voltage at the edges of the glasses where the arcing really occurs, but this voltage is difficult to ascertain from the tracings. It is obvious that after sustained arcing begins at about 12keV beam voltage the cover glass voltages no longer increase very much with increasing beam voltage. Why arcing from the much less charged ceria

glasses begins at about the same beam voltage as from the more highly charged fused silica glasses is not understood, unless arcing from the latter serves as a triggering mechanism.

Calibrated equipment that permits one to obtain data on the arcing transients as to peak current and time duration is available at LRC. The ground current leads are surrounded by one-turn Pearson model 110S transformers which are connected to Biomation 8100 digital waveform recorders. However, to avoid ringing, the ground lines have to be terminated in 50 ohm impedances which cause a decrease in the amount of charge that would otherwise be removed from the cover glasses during a given discharge. Nevertheless, figure 6 shows a few typical discharge transients:

Beam voltage: 12keV

Time duration: 1 to 2 microseconds

Charge content: 1 to 10 microcoulombs

If from the fused silica glasses charged to 9kV, then Energy content: 0.009 to 0.09 joules

Direction of electron current through solar cell strings: most often from ground.

Two questions now arise:

- (1) If the ground termination resistance were only a few tenths ohms what would the charge and energy contents in the arcs be?
- (2) Are these arcs due to a charge wipe-off from one solar cell, or from a characteristic few, or from the entire panel?

In other words, does the charge and energy content of a given arc depend on the total area of the solar panel? A carefully controlled area experiment, blocking off parts of the panel area with metal masks is needed to settle this question. In the meantime, the fact that our data fits on a charge content versus load resistance graph, figure 7, from a much smaller TDRS type test panel, reference 2, looks somewhat encouraging that only a limited area of cover glasses is involved in a given arc. Moreover, visual observation when beam voltage was 12keV, showed arcs to be associated with a small bright spot surrounded by a bluish glow which, at 12keV only extended over a portion of the field of view, which itself was smaller than the panel.

Time exposure photographs were taken, of which figure 8 is an example showing 20 minutes of arcing in a 20keV electron beam. The arcs occur mostly between the solder strips, interconnects and coverglasses in the same column of cells. Note the very bright arcing between adjacent columns in the upper right-hand corner of this picture. After seeing this picture, it was discovered that a string of 5 cells had inadvertently been left disconnected and floating. This was corrected.

Some other interesting observations were made. Figure 9 shows a charge-up sequence with a 10keV beam. The Kapton border is exposed to the beam this time and charges to its full potential of 7.6kV in a half minute, whereas the coverglasses require five minutes before they become fully charged to 7kV and 4.5kV respectively. Hence differential charging can be most serious during changes in the Space environment-going from sunlight to eclipse and vice versa or beginnings and terminations of geomagnetic substorms.

Measurements were made at 25°C on the volume resistance of the ceria-doped uncoated glasses as compared to the resistance of the fused silica with MgF<sub>2</sub> coated ones:

Fused silica glass resistance in ohms/cm<sup>2</sup> for 0.015 cm thickness, 25°C,

At 250 volts  $R = 3.5 \times 10^{14}$  ohms/cm<sup>2</sup>

1000 volts  $R = 1.9 \times 10^{14}$  ohms/cm<sup>2</sup>

Ceria-doped glass resistance in ohms/cm<sup>2</sup> for 0.015 cm thickness, 25°C,

At 250 volts  $R = 4.2 \times 10^{11}$  ohms/cm<sup>2</sup>

1000 volts  $R = 0.9 \times 10^{11}$  ohms/cm<sup>2</sup>.

Thus ceria doped glass at room temperature has 2000 times the conductivity of fused silica glass, thus permitting charge reduction by leakage current. The delayed reduction of arcing when the solar simulator outside of the vacuum system was turned on and delayed resumption when it was turned off, was probably due to a still further increased conductivity when heated rather than entirely a photoemissive effect. When the lamps were on: the fused silica stayed stubbornly charged at 16kV while the ceria glass came down to 3kV. The ceria glass is therefore a more desirable material from the S/C charging point of view.

#### E. CHARACTERIZATION OF SOLAR PANEL TEST PATCH; METALLIC PARTS SEMI-FLOATING ON 25,000 MEGOHMS TO GROUND

It was decided to characterize the panel with 25,000 Megohms instead of 0 ohms to ground. In this way one simulates two different "grounds":

- (a) The ambient plasma sheath ground = tank walls;
- (b) The spacecraft ground = metallic parts potential.

The effect is seen in figures 10 and 11. At a 10keV electron beam the metallic parts charge to 5000 volts as proved by either the 25,000:1 voltage divider or the high voltage probe readings. When the electron beam voltage is turned off and then the high voltage trace obtained, the negative cover glass voltages with respect to the metallic parts remain, looking like a roof without the house under it and is only between 1 to 2kV. In a 15 keV beam the metallic voltage is -5500 volts, the fused silica is -12,000 volts, the ceria glass is -11,000 volts, the difference still not being quite enough to cause arcing. At 20keV beam voltage, the metallic voltages are at -6250 volts, the silica glass is at -14,000 volts, the ceria glass is at about -12,500 volts; the difference with respect to S/C ground being about 8,000 volts and 6,000 volts respectively, and arcing is sustained as in part D described above. This arrangement with the metallic parts semifloating is probably a better simulation of what happens in Space than to ground the metallic parts. In fact the behavior is very much as in a recent report by Koons, Mizera et al., on SCATHA, reference 5. (There on March 28, 1979, a 20keV substorm caused the S/C to charge to -8,000 volts with respect to the plasma and the materials on the satellite surface potential monitors to various negative potentials in the kV range with respect to the S/C. Two arcing events were recorded as a consequence.) Note that in the dark, even in the 25,000 Megohm to ground arrangement, as in eclipse in Space, the cover glasses are still of negative polarity with respect to the interconnects. Time exposure photographs have verified that under these conditions there is visible arcing. The charge-up voltages and the arcing depend very sensitively on the current density of the beam at a given beam voltage. When the current density was cut from 3 to 1 na/cm<sup>2</sup> at 20kV, arcing stopped from the ceria glasses, but was still happening in a reduced manner from the fused silica glasses.

Work was done with the Solar Simulator on, outside of the vacuum chamber, shining light from the same side as the electron beam: Arcing frequency decreased, but there was a time lag indicative of heat rather than photoeffects. A similar time delayed remission and resumption of arcing occurred when the experiment was repeated by passing hot air through the chamber shroud, thus heating and later cooling the panel against an  $\text{LN}_2$  shroud without any light whatsoever. The ceria-doped glass probably becomes quite conductive with heating, and the effects observed so far are probably thermal rather than photoemissive.

#### F. WORK WITH A BARE KAPTON SUBSTRATE STRIP NEXT TO THE CELLED TEST PATCH

The solar panels on the TDRS System each have a bare substrate portion without solar cells on the front side of area 50 inch by 15 inch. In order to test this situation, a bare piece of substrate 50cm by 15cm, appropriately edged with conductively painted Kapton tape, was butted next to the celled panel. The butt joint was covered with 0.0075cm thick Kapton tape and the honeycomb cores and backside painted coatings were connected together. Electron bombardment with 20keV electrons at the usual  $3\text{ na/cm}^2$  flux was done, with the cores and solar cells grounded through electrometers, or through 50 ohms when transients were measured with the Biomation equipment. Arc counts at about  $-24^\circ$  ( $-10^\circ\text{F}$ ) and  $+46^\circ\text{C}$  ( $+115^\circ\text{F}$ ), as well as time exposure photograph were taken at 30 minute intervals. The total bombardment time accumulated during this part of the experiment was roughly 8 hours with order of magnitude of 10,000 arcs occurring. The results were to some degree surprising:

- (1) The bare Kapton section had puncture arcs through the Kapton tape over the butt joint despite the grounding together of the cores. Thus stubborn arcing occurs at discontinuities.
- (2) Fewer arcs according to the arc counter occurred with the bare Kapton next to the celled panel than without it as seen in table I. However, charge content in most of the arcs is somewhat larger than earlier in the entire investigation. The time exposure photographs, figures 12, and 13 show that at  $47^\circ\text{C}$  ( $115^\circ\text{F}$ ) the appearance of the arcs on the fused silica side is concentrated in a definite pattern whereas at  $-24^\circ\text{C}$  ( $-10^\circ\text{F}$ ) for the silica glass, and at both hot and cold temperatures for the ceria glass the arcing results in more of a diffuse glow. The arc count is less at the higher temperature. At the colder temperature, note the straight line arcing pattern perpendicular to the edge of the solar cells, extending out over the Kapton border for about 2 to 3mm and outlining the underlying honeycomb. This occurs with or without the bare Kapton piece.

#### G. CONTAMINATION AS RESULT OF CHARGING AND ARCING

When the panels were removed from the vacuum chamber, following sequence F above, there appeared on the fused silica glasses, but not on the ceria glasses small discolored contamination areas where the arcing had been hitting the glass as seen in the accompanying photograph, figure 14. Auger spectroscopy revealed this to be mostly silicon, carbon and oxygen with other minor trace elements but decidedly not silver from the interconnects. The origin of these materials could be from the RTV's on the panel or from vacuum chamber sources of contamination. The point here is that interaction of the charging and arcing with whatever matter is present, to the fused silica glasses, but not to the ceria, even when the metallic underlayers are grounded, will produce a deposit of contaminants on the glasses. Effect on the current-voltage curves of strings 4 and 5

that were covered with the fused silica glasses was small, but there was a consistent decrease of output power of 2% as opposed to no change from the ceria glass covered strings.

## H. BACKSIDE BOMBARDMENT WITH ELECTRONS

Abbreviated backside electron bombardment gave results, partly similar to front side work.

- (1) When the metallic portions were grounded, then a very few arcs began to occur with beam voltage at 12kV as recorded by the arc counters. The solar cell leakage current trace became increasingly "noisy" as beam voltage was increased.
- (2) When the metallic portions were on 25,000 Megohms to ground, then the arcs did not begin until beam voltage was 18kV.
- (3) Time exposure photography showed no visual evidence of arcs on the Kapton, indicating that they were induced on the front side and that the conductive painting of the perforated backside Kapton was adequate. However, the unpainted harness insulation appeared as emitting light under electron bombardment.

## I. CONCLUSIONS

Ceria-doped glass is definitely to be preferred to fused silica glass for reducing charge build up.

In sunlight the TDRS solar panel which has ceria glass on the front and conductive paint (100,00 ohms/square) on the backside is probably a good design for reducing charge-up. In a geomagnetic substorm such as simulated here, there will be arcing at the interconnects during eclipse and transitions into and out of eclipse. This is especially true in view of the very cold temperatures that will be reached by this lightweight array, when the ceria glass will not be as conductive as at room temperature.

The Kapton bare patch, although no very large arcs were measured from it, should still be conductively painted. Any discontinuity on it will serve as arcing center.

The differential voltages on the panel determine when arcing first begins, and the electron beam voltages which cause this, vary, depending upon whether the metallic structure is directly grounded or semifloating. This can explain the variety of beam voltages for arcing inception, reported by different experimentors as between 14 kV and 20 kV and obtained by different techniques (reference 5, Table 1-2).

## REFERENCES

1. Bogus, K. P., Investigation of a CTS Solar Cell Test Patch under Simulated Geomagnetic Substorm Conditions. Proceedings of the 1976 Spacecraft Charging Technology Conference; Pike and Lovell Editors, 1977, NASA TMX-73537.
2. Inouye, G. T., and Sellen J. M., TDRSS Solar Array Arc Discharge Tests; Proceedings of the 1978 S/C Charging Technology Conference; NASA Conf. Publ. 2071.



3. Stevens, N. J., et al.; Testing of Typical S/C Materials in a Substorm Environment; Proceedings of the 1976 S/C Charging Technology Conf.; Pike and Lovell Editors, 1977.
4. Koons, H. C., Mizera, P. F., Fennel, J. F., and Hall, D. F.; S/C Charging-Results from the Scatha Satellite; Astronautics and Aeronautics; November 1980, Page 44.
5. Rosen, A., Sanders, N. L., Sellen, J. M., and Inouye, G. T.; Effects of Arcing Due to S/C Charging on S/C Survival; TRW Report No. 33631-6006-RU-00; Nov. 14, 1978.
6. TRW Document No. 29000-412-009; TDRSS Solar Array PDA, January 1978, Chapter 4, Pages 8, 40; Chapter 7, Page 9.
7. TRW Document No. 78-872509-032; TDRSS-78-412-208; Life Test Report, Solar Panels after 920 Cycles in Thermal Vacuum, Sept. 28, 1978, Pages 7, Fig. 2-2.

Table I  
Arc Counts and Currents to Ground, when Bare Kapton Panel is Butted next to Celled Panel

With Bare Kapton Panel next to Fused Silica					
Time Minutes	Arc Count	$i_{\text{shield}}$ x $10^{-6}$ Amp	$i_{\text{cells}}$ x $10^{-4}$ Amp	$ i_{\text{core, min}} $ x $10^{-6}$ Amp	Panel Temp.
0	0,0,0				
30	693,218,12	0.33	0.048	0.8	-23°C
0	0,0,0				
30	320,171,10	0.41	0.057	1.45	+44°C
Without Bare Kapton Panel					
0	0,0,0				
30	922,325,30	0.68	0.054	0.55	-22°C
0	0,0,0				
30	380,189,34	0.47	0.059	0.5	+46°C
With Bare Kapton Panel next to Ceria-Doped Glasses					
0	0,0,0				
30	836,166,21	0.28	0.043	0.75	-23°C
0	0,0,0				
30	424,164,17	0.32	0.0645	1.5	+44°C

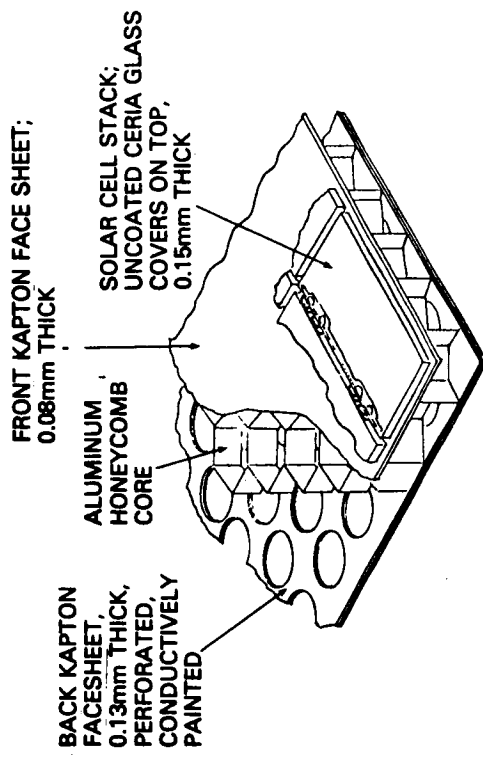


Figure 1a. Cutaway View of Solar Array Cell Stack and Substrate (Reference 6)

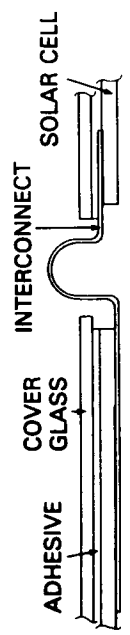


Figure 1b. Cross Section of Solar Cell Stack, Showing Interconnect Stress Relief Loop (Reference 6)

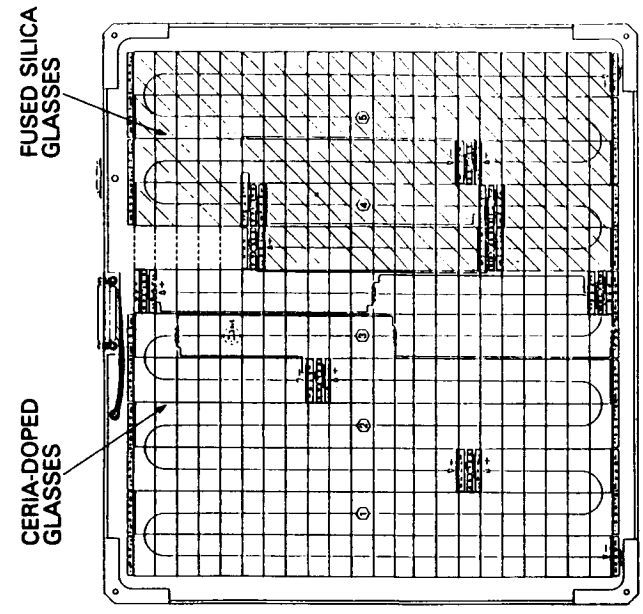


Figure 2. Front Side of Life Test Panel (Reference 7)

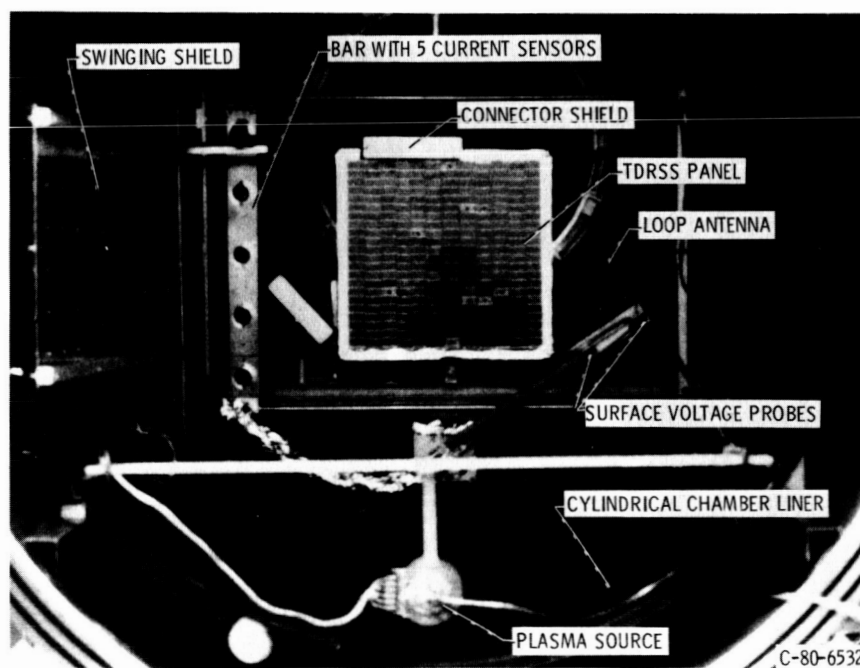


Figure 3. - TDRSS solar test panel in electron bombardment test facility.

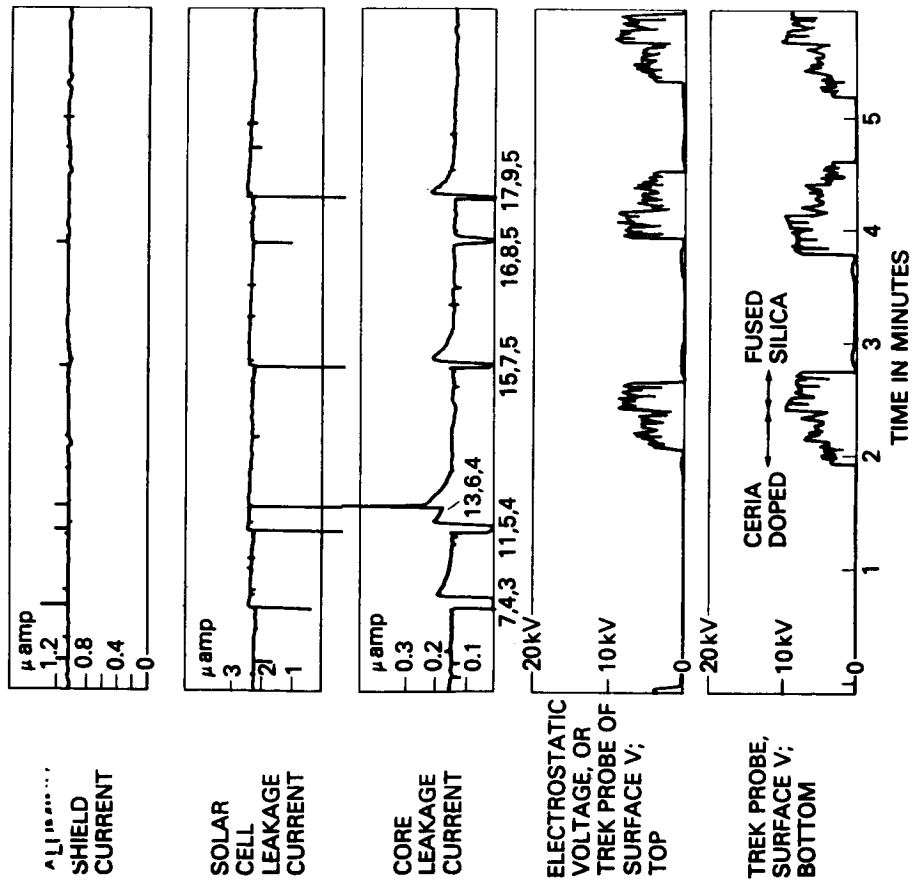


Figure 4. Continuous BRUSH Recording of Currents to Ground, and Surface Voltages, Versus Time; in a 12kV Electron Beam. Kapton Borders Covered with Aluminum.

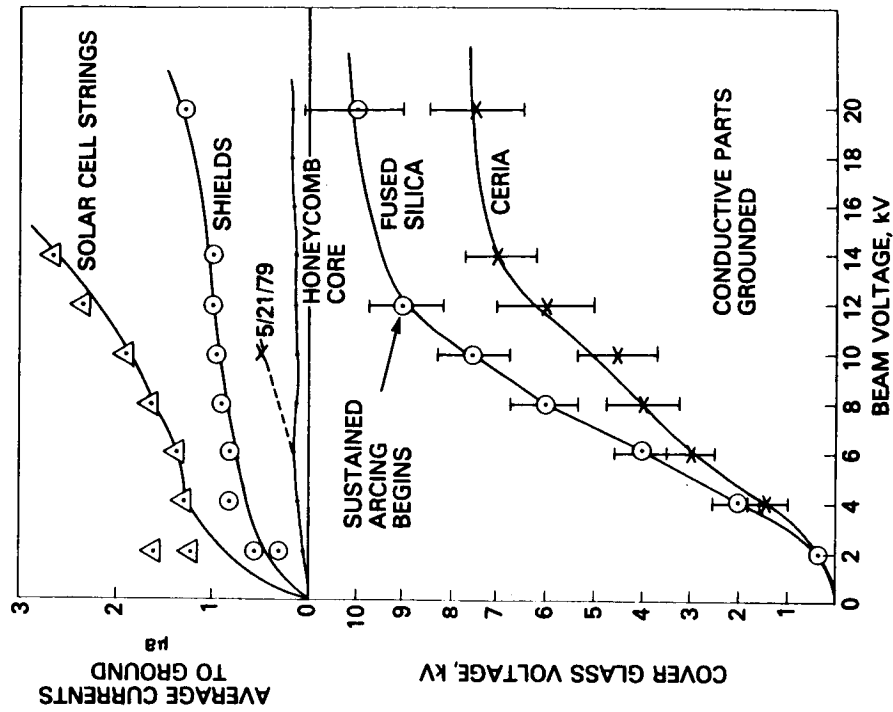


Figure 5. Cover Glass Voltages and Currents to Ground Versus Electron Beam Voltages, 7/11-13/79.

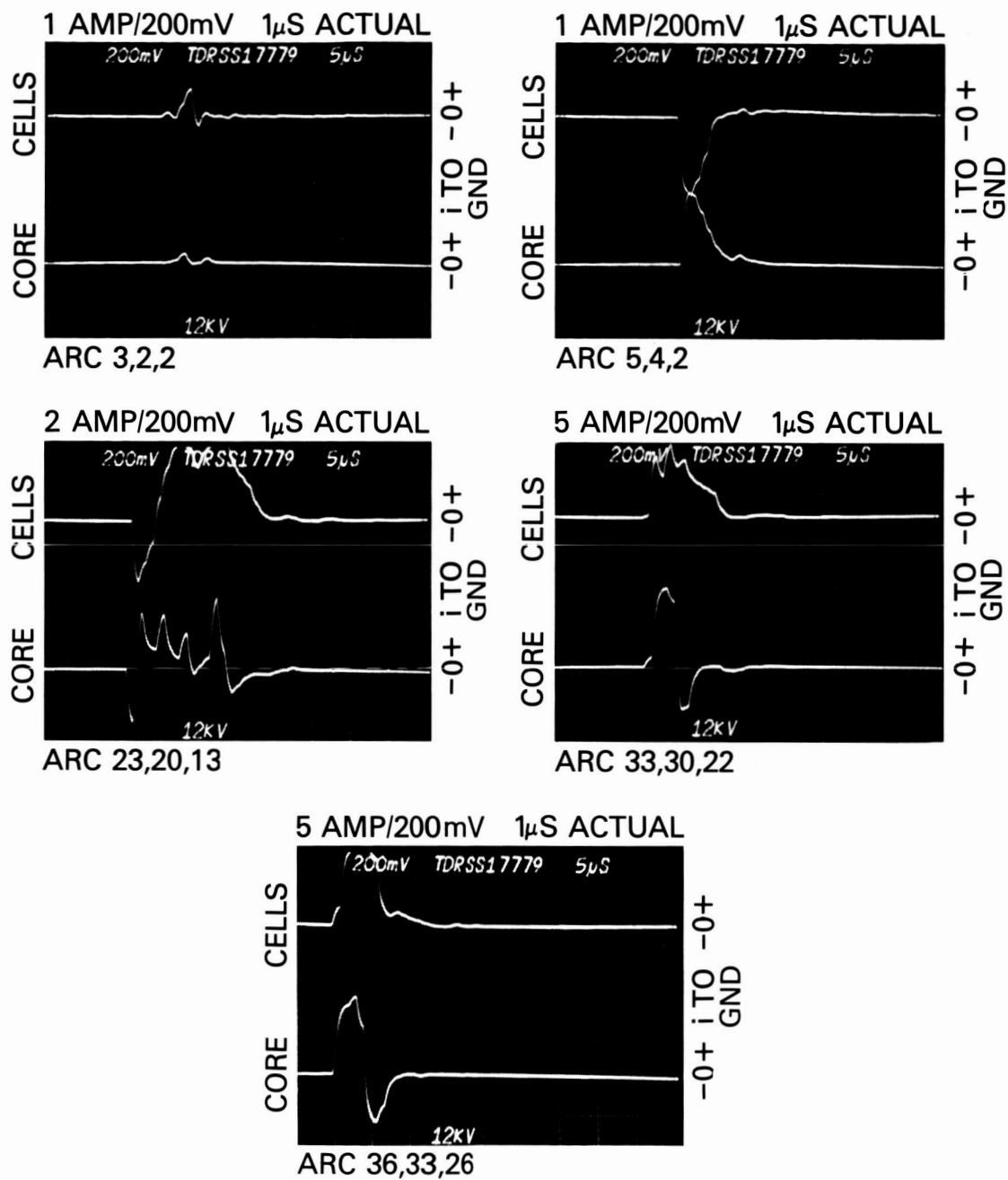


FIGURE 6. Typical Arcing Transients in 12kV Electron Beam, Demonstrating Directional Variety of Current Flows (50 Ohm Resistance to Ground)

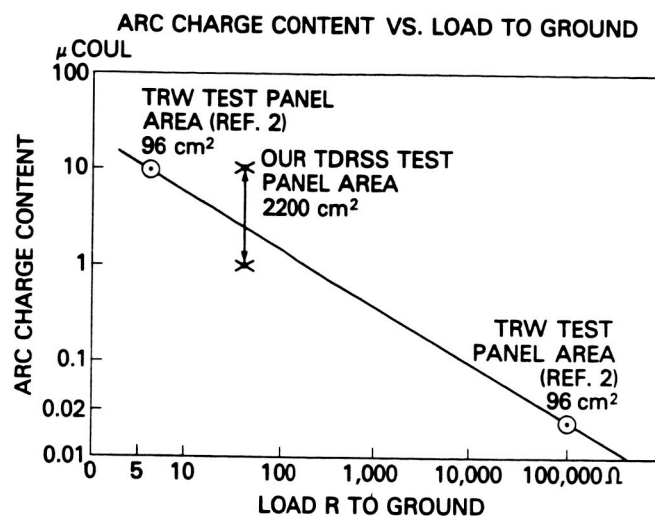
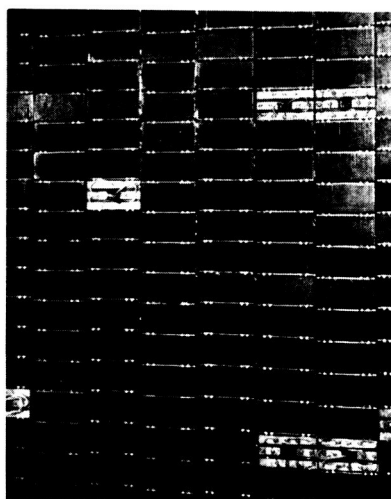


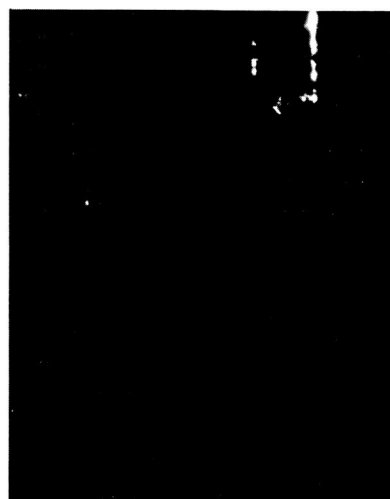
Figure 7. Typical ARC Charge Content  
Versus Load Resistance to Ground

(A) 7/13/79  
PORTRAIT OF PART OF  
PANEL IN ORDINARY  
LIGHT



A

(B) SAME IN 20 MINUTE  
TIME EXPOSURE IN 20  
keV ELECTRON BEAM.  
METALLIC PARTS  
GROUNDED, EXCEPT  
NOTE MUCH BRIGHTER  
ARCS WHERE SEVERAL  
CELLS WERE INADVERT-  
ANTLY NOT GROUNDED.



B

Figure 8. Arcing Shown in 20 keV Electron Beam,  
During 20 Minute Time Exposure

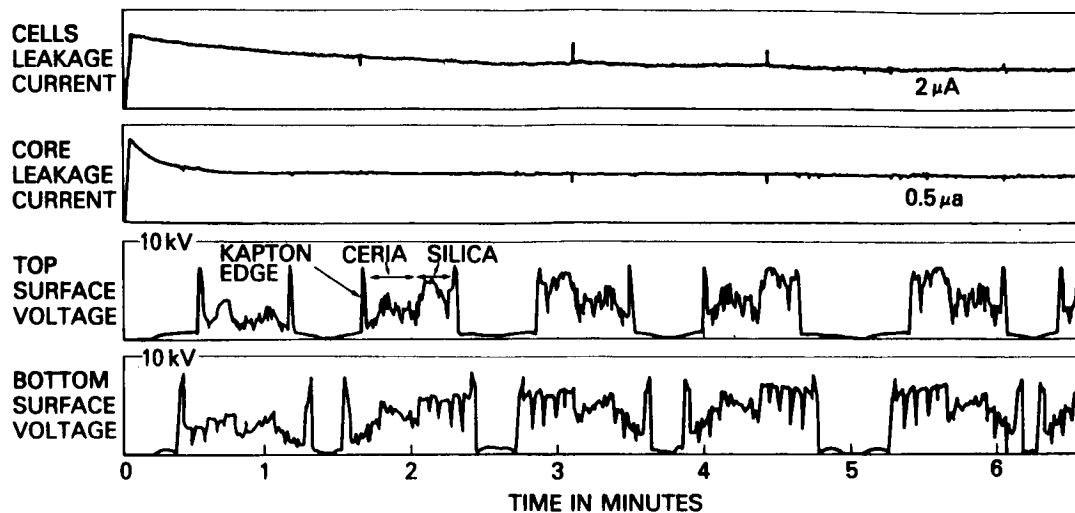


Figure 9. Charging Sequence of Panel Versus Time, Exposed Kapton Edges Charge Up Immediately, Cover Glasses More Slowly. 10 keV Beam.

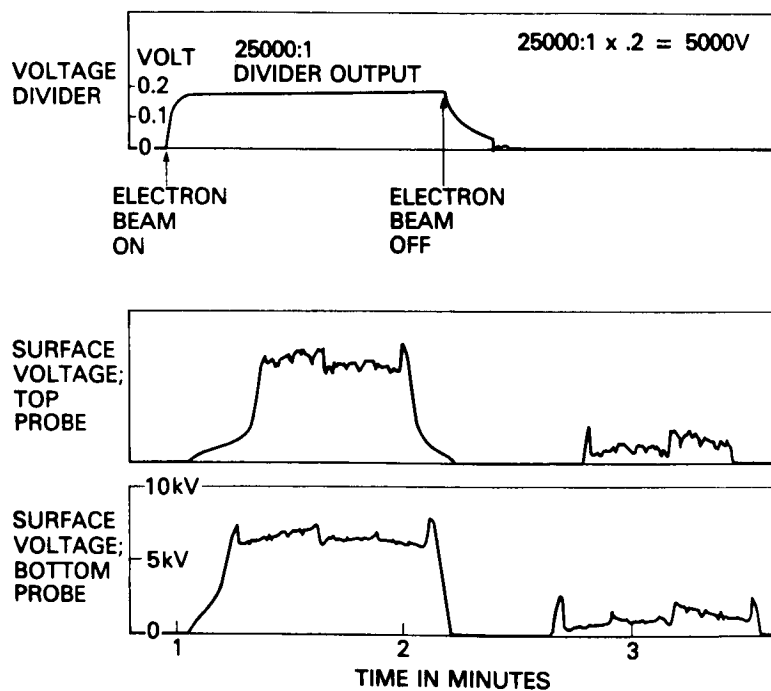


Figure 10. Solar Panel in 10 keV Electron Beam on, then off. 25,000 Megohm from Metallic Parts to Ground, 6/28/79.

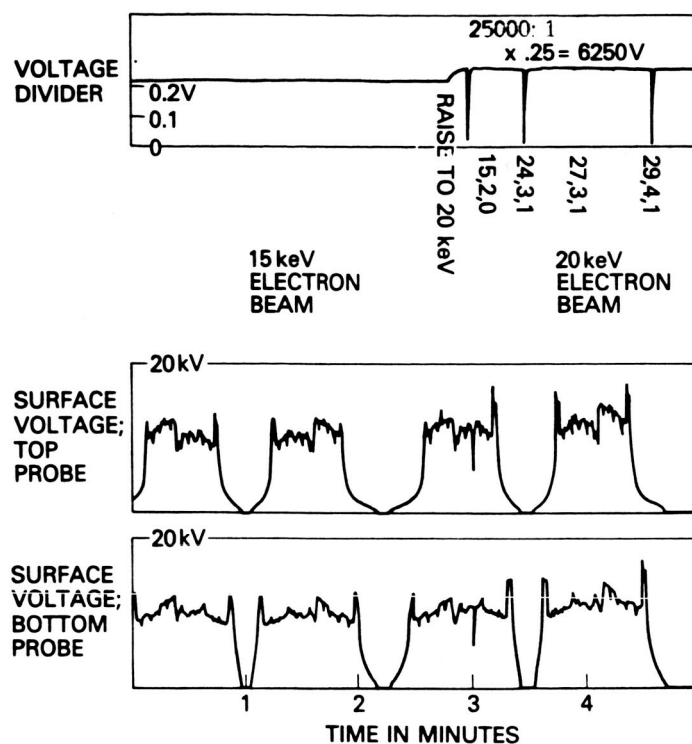


Figure 11. Solar Panel in 15 and in 20 keV Elec-  
tron Beam. 25,000 Megohm from Metallic  
Parts to Ground, 6/28/79.

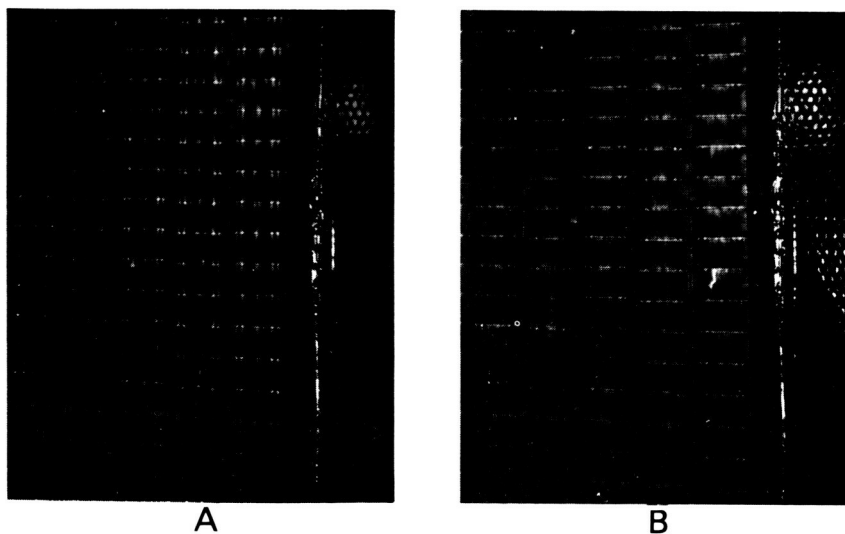


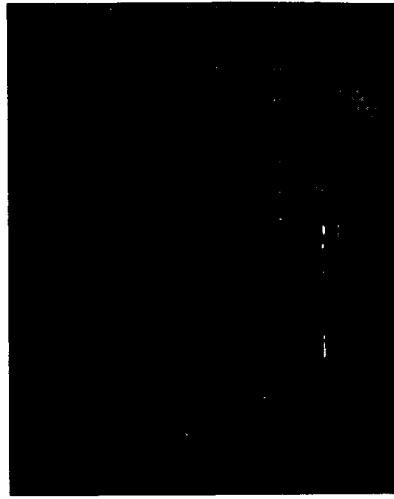
Figure 12. 30 Minute Time Exposure Photographs, Bare  
Kapton Butted Next to Fused Silica - Glassed Portion  
of Celled Panel.

- A. 20 keV Electron Beam, Panel at +46°C
- B. 20 keV Electron Beam, Panel at -24°C





A



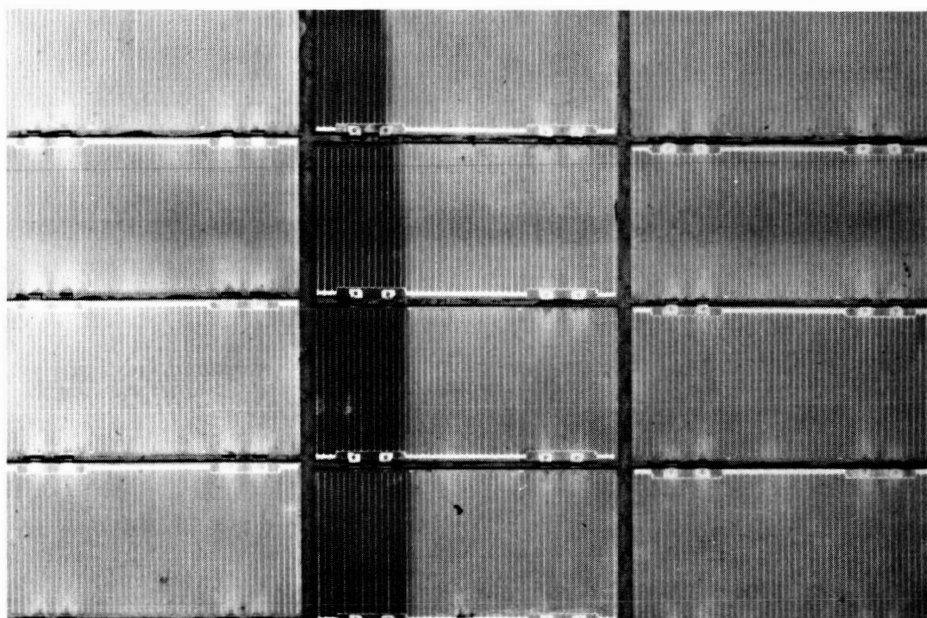
B



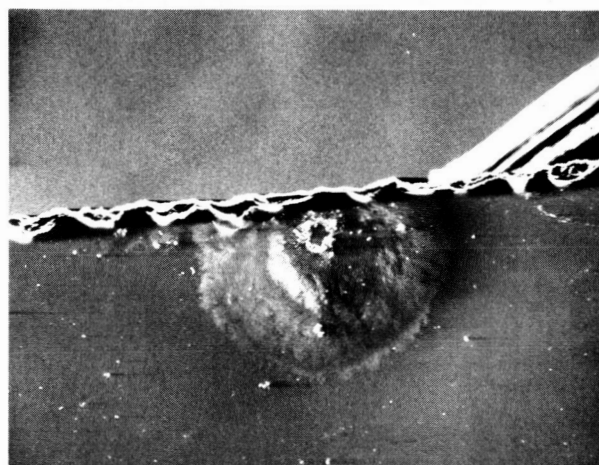
C

- (A) No electron beam,  
tube filaments on,
- (B) 20 keV electron beam,  
panel at  $+47^{\circ}\text{C}$ ,
- (C) 20 keV electron beam,  
panel at  $-25^{\circ}\text{C}$ .

Figure 13. 30 Minute Time Exposure Photographs, bare  
Kapton Portion Butted Next to Ceria - Glassed  
Portion of Celled Panel



A



SEM 320 X  
B

Figure 14. A. Photograph of Contamination Deposit on Silica Glasses After Long-Term Arcing  
B. Scanning Electron Microscope Picture (320X) of Same

## **CHARGING AND DISCHARGING CHARACTERISTICS OF A RIGID SOLAR ARRAY**

**George F. Brady, Jr., David A. Vance, and Stanley A. Greenberg  
Lockheed Missiles & Space Company, Inc.**

### **SUMMARY**

Two rigid solar array panels were subjected to a simulated geosynchronous orbit substorm environment. During the charging sequence, distributions of accumulated surface charge were measured under eclipse and sunlit conditions. Discharge events were characterized with respect to voltage pulse signatures and amplitudes on the solar array bus leads.

Post-exposure analysis of the solar array panels indicated that the electrical characteristics were not degraded in spite of the substantial discharge activity. However, significant cratering and discoloration of the Tedlar dielectric were observed.

### **INTRODUCTION**

Performance characteristics of rigid solar array panels during geomagnetically quiet periods are well documented. However, during substorm conditions, the complex arrangement of dielectric and conductive elements make adequate modeling of the effects of charging and discharging processes on array functional properties very difficult.

Concerns have been raised that solar arrays may suffer degradation as a result of plasma interactions and that anomalies may develop in the spacecraft bus load. Details of the plasma interactions with the materials of construction and how that phenomenology influences solar cell electrical output are not well understood. Under orbital conditions, the surface materials which are directly exposed to the environment include the dielectric panel substrate, cover glasses and anodized aluminum panel rear face. In addition, there are the exposed conductive elements of aluminum honeycomb panel as well as positive and negative terminals and cell interconnects.

This paper describes the low-energy (20 kV) electron irradiation tests which were used as a representative simulated geosynchronous substorm environment for rigid solar array panels and presents the results and analysis of those investigations.

## TEST CONFIGURATIONS

The simulation tests were conducted in the Lockheed Advanced Systems Division's Space Environmental and Research Chamber (SEARCH) located in Palo Alto, California. The vacuum chamber is cylindrical with a diameter and length of 2.4 m (8 ft) and 4.6 m (15 ft),\* and is equipped with a liquid nitrogen shroud. The large chamber dimensions, relative to the test panels, minimize the interactions between the irradiated specimens and the chamber walls. A schematic representation of the test configuration is presented in figure 1. Figure 2 shows the sample mounting and electron gun arrangement on the chamber door prior to test. During test, the chamber pressure was maintained below 1.3 mPa ( $10^{-5}$  torr).

The solar cell panels consisted of eighty-eight 2 cm x 4 cm solar cells connected in series and mounted on a  $2.5 \times 10^{-3}$  cm ( $10^{-3}$  in.) thick white pigmented Tedlar substrate supported by an aluminum honeycomb structure. A resistive load and blocking diode network was provided as a simulation of a spacecraft power bus line (figures 3 and 4).

The electron flux was provided by a Kimball Physics electron flood gun operated at 20 keV. This system provided a nominally uniform circular beam pattern with a diameter of 45 cm (18 in.) at the sample plane. Beam uniformity was determined using a scanning Faraday cup and stationary calibrated Faraday buttons at a series of current densities and electron energies. During the simulation tests, the electron flux was maintained at  $10 \text{ nA/cm}^2$  with 20 kV electrons.

Solar simulation was accomplished with a collimated water-cooled 2 kW mercury-arc lamp mounted externally, the beam being introduced to the chamber through a fused silica window. For this system, 36 percent of the radiant energy lies in the 200 to 400 nm region so that adequate UV radiation for photoemission was available. The total UV intensity was approximately equivalent to one sun. In addition, a 150 W tungsten lamp was used to provide illumination in the solar cell active spectral region so that changes in panel current-voltage characteristics could be monitored in situ.

Solar panel surface potentials were measured by means of a Trek Model 340 HV non-contacting voltmeter probe mounted to an x-y translating table controlled by stepping motors. Coordinates were mapped prior to test in order to index locations and locate limit switches for null adjustment. Locations were repeatable to  $\pm 0.01$  cm. A ground plate was also provided as a voltage probe zero reference.

Discharge voltage pulses across the solar array were recorded by means of a Tektronics 7834 storage oscilloscope and a Micro Instruments 5201B memory voltmeter. The voltage pulses were transmitted through high voltage 100 pF blocking capacitors, as shown schematically in figure 5.

---

\*For the principal measurements and calculations, the International System of units (SI) was actually used.

## TEST PROCEDURE

The test environments and event sequencing are depicted in figure 6. Additional tests were also conducted which simulated eclipse conditions exclusively. Duplicate panels were subjected to the entire testing sequence.

## RESULTS AND DISCUSSION

### Surface Charging Activity

The non-contacting voltmeter indicated significant activity took place on the surface of the solar cells and on the exposed Tedlar dielectric. Solar cell panel surface potentials fluctuated throughout the electron impingement tests during both sunlit and eclipse conditions. In addition, differences in surface potential activity was indiscernible between sunlit and eclipse conditions.

Surface potentials sometimes were greater than 18 kV for short periods before discharging. However, the potentials usually remained between 6 kV and 15 kV. Fluctuations in potential usually consisted of rapid changes as a result of continuous low level discharges (less than 100 V). However, the frequency of major surface flashovers took place on the order of one per minute which resulted in surface potential changes greater than 15 kV.

Flashovers were detected by observations through the chamber view port during eclipse conditions. Time-exposure photographs also recorded discharge activity.

### Bus Voltage Activity

Bus voltage pulses were recorded by photographing the pulse signatures on the oscilloscope screen which were retraced by the oscilloscope memory. Voltage pulses were as great as 1.9 kV across the simulated spacecraft bus load. Typically the pulses had a 10 ns rise time with a duration of 1 ms. The memory volt-meter detected a considerable number of voltage spikes of magnitudes less than 100 V. All voltage pulses were positive. There was not convincing evidence that any negative pulses occurred. A typical pulse is shown in figure 7.

### Panel Material Changes

Discharges from the white pigmented Tedlar film resulted in significant cratering and penetration to the aluminum substrate, as shown in figure 8. Additionally, there appeared to be discharges of opposite direction manifesting themselves as microscopic raised areas with subsurface conical voids terminating at the surface. Areas with significant discharge activity through the Tedlar showed carbonized conductive paths to the substrate. Examination of the Tedlar showed that the discharges caused melting of the aluminum substrate at the base

of the craters. However, the solar cells remained electrically isolated from the honeycomb panel support. Removal of some cells after testing revealed no evidence of discharges under the cells.

Exposure to the electron environment led to a significant darkening of the white Tedlar. In areas of greatest discharge activity, the solar absorptance increased to greater than 0.49 from an initial value of 0.24. Infrared emittance remained unchanged at 0.86.

No evidence of physical or optical property changes was obtained upon examination of the individual solar cells or interconnects.

#### Panel Electrical Output

Comparison of pre-test and post-test electrical characteristics (current-voltage curves) indicated that no significant changes resulted from the simulation tests, despite the extensive charging and discharging activity. During exposure to the simulated substorm environment with illumination, no changes in solar panel electrical output were observed.

#### CONCLUDING REMARKS

Exposure of rigid solar array panels to simulated geosynchronous substorm conditions resulted in no apparent change in their photovoltaic characteristics. However, significant discharge activity into the power bus was observed. Electrical discharges on the Tedlar insulation led to multiple breakdowns with creation of conductive paths to the honeycomb substrate support. From the limited exposure period it is not possible to conclusively determine the probability that cell shorting could result from long-term discharge activity.

In conjunction with the creation of multiple craters in the Tedlar dielectric, the large change in solar absorptance has serious implications. The increased solar absorptance will result in an increase in solar array operating temperature with concomitant reduction in electrical power output.

The high voltage spikes associated with the observed discharges may be propagated into the solar array power conditioning system of a spacecraft via the array buses. These transients may be difficult to filter because of their high energy, high voltage and short duration. In addition, the radiated energy from these pulses can result in significant electromagnetic interference with communications, command and control and logic operations.

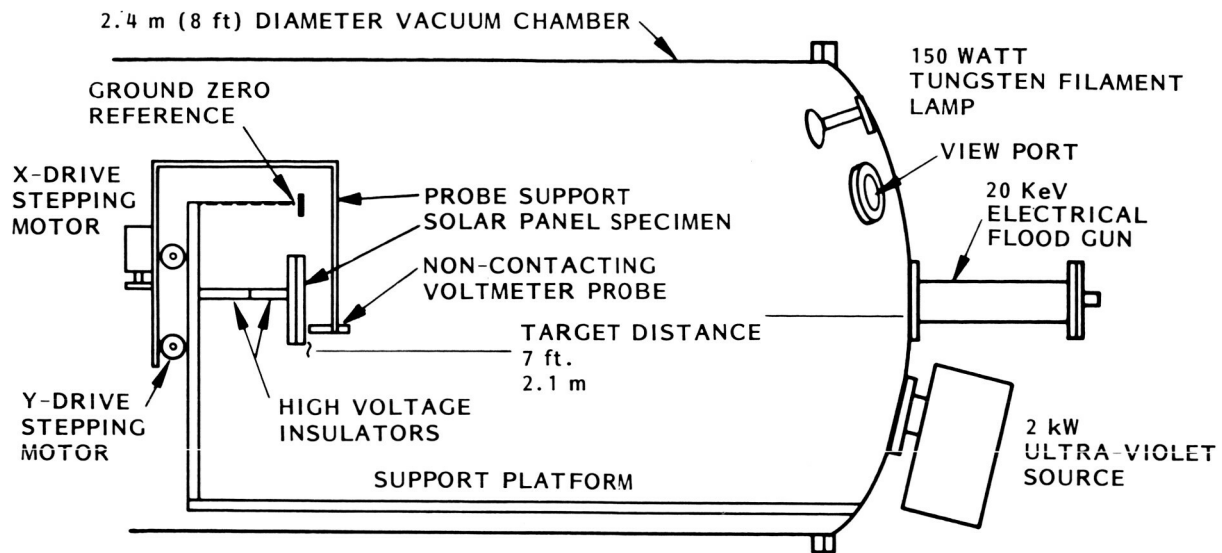


Figure 1 - Schematic Representation of Simulation Facility

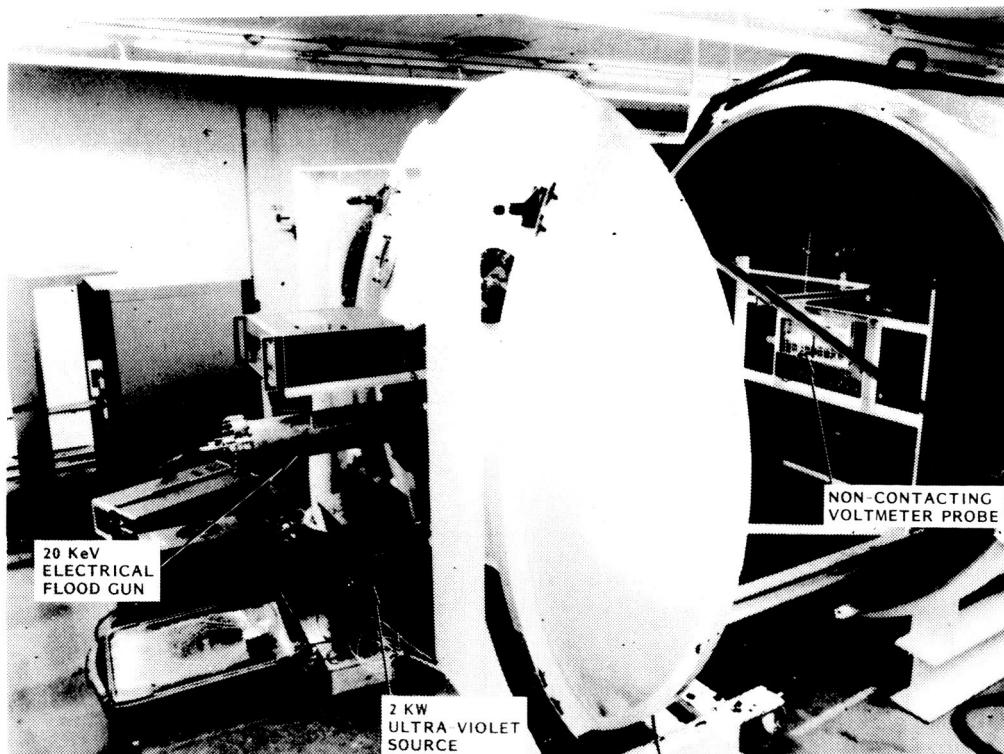


Figure 2 - Solar Panel Mounting and Irradiation Configuration

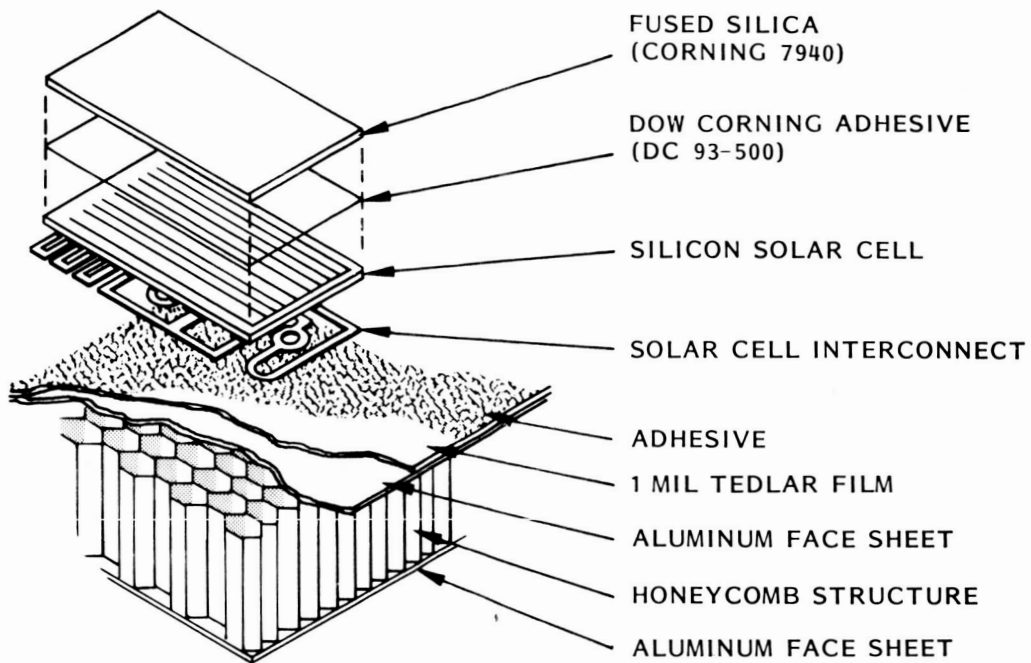


Figure 3 - Solar Cell Panel Construction

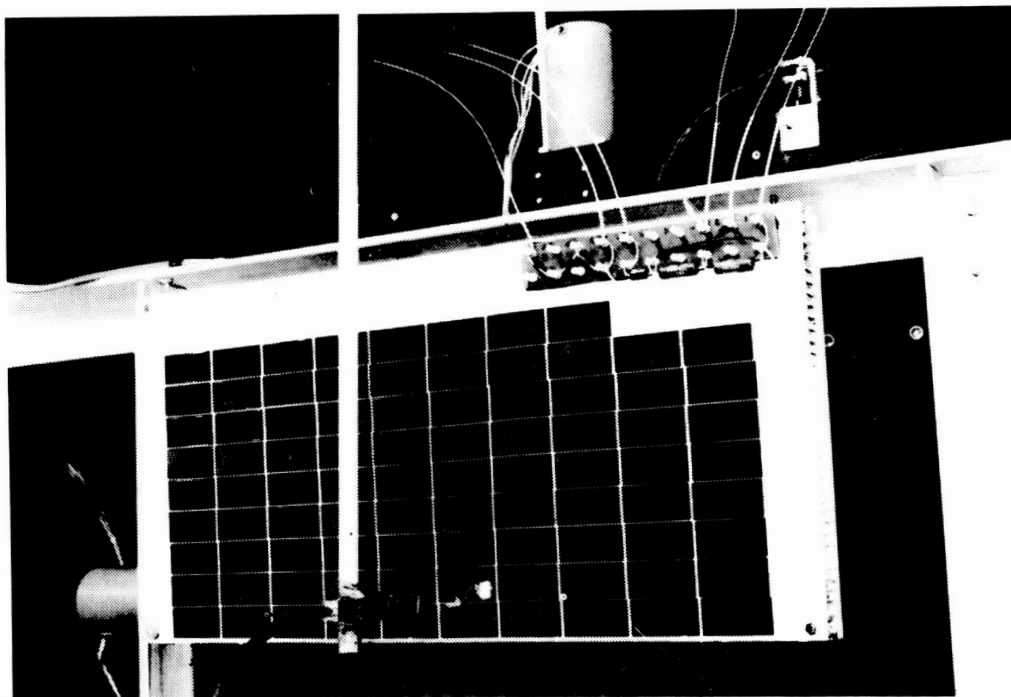


Figure 4 - Solar Panel



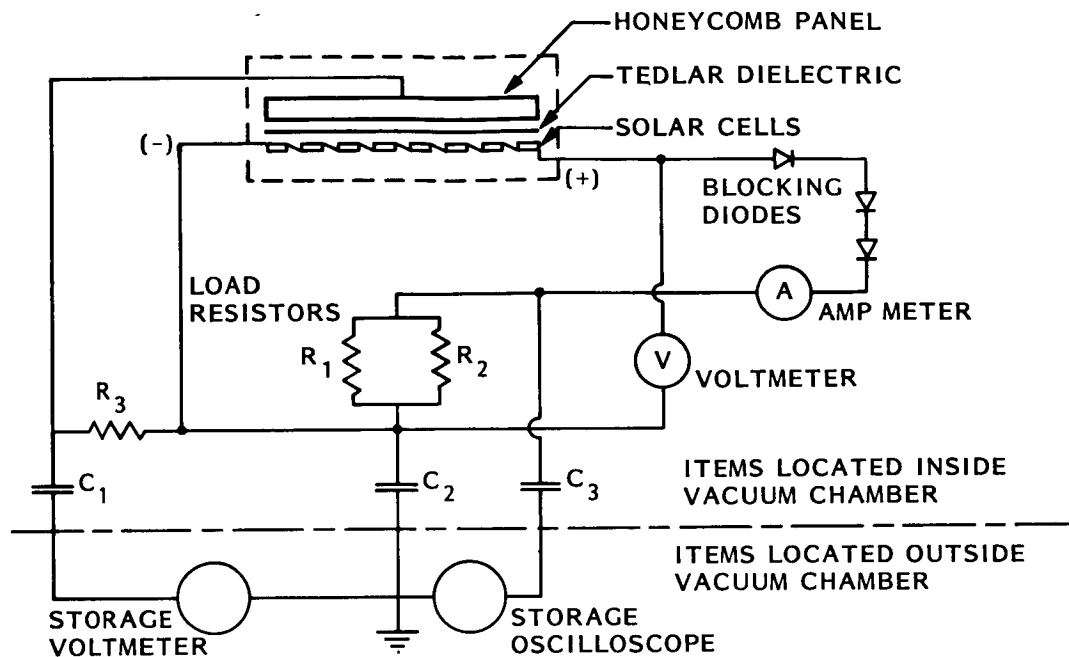


Figure 5 - Electrical Test Network

- I. VACUUM CHAMBER: SET FOR VACUUM CONDITIONS OF LESS THAN  $1 \times 10^{-5}$  TORR
- II. ECLIPSE DURING ELECTRON IMPINGEMENT ACTIVITY
  - A. SUN ON AT  $t_0=0$ . MINUTES  
SUN REMAINS ON UNTIL  $t_{60}$
  - B. ELECTRON GUN ON AT  $t_5$   
ELECTRON GUN REMAINS ON UNTIL  $t_{180}$
  - C. SUN OFF AT  $t_{60}$   
SUN REMAINS OFF UNTIL  $t_{120}$   
TIME EXPOSURE PHOTOGRAPHS TAKEN AT THIS TIME
  - D. SUN ON AT  $t_{120}$   
SUN REMAINS ON UNTIL  $t_{210}$
  - E. ELECTRON GUN OFF AT  $t_{180}$
  - F. SUN OFF AT  $t_{210}$
- III. ELECTRON GUN CAPABILITY: 20 K VOLTS 10 NANOAMPS/cm<sup>2</sup>

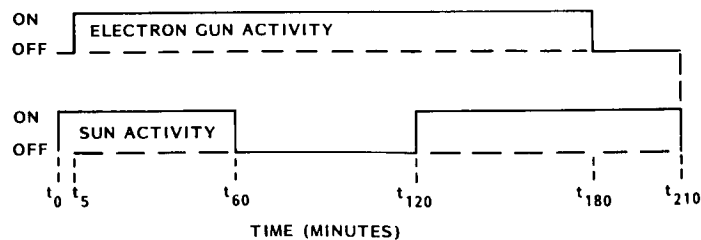


Figure 6 - Simulated Environment Test Sequence

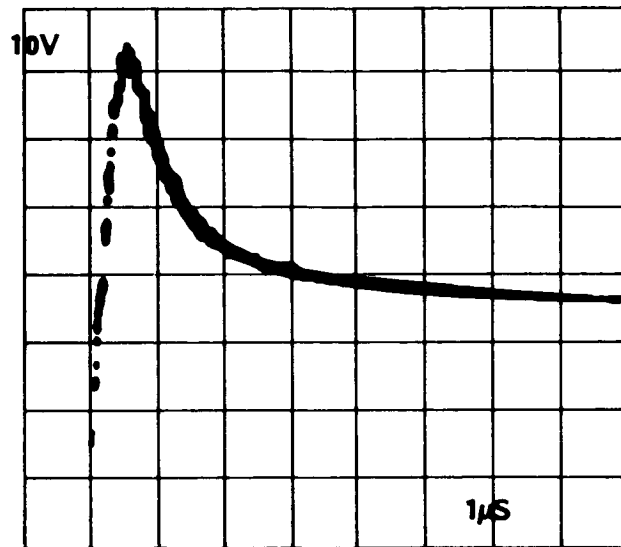
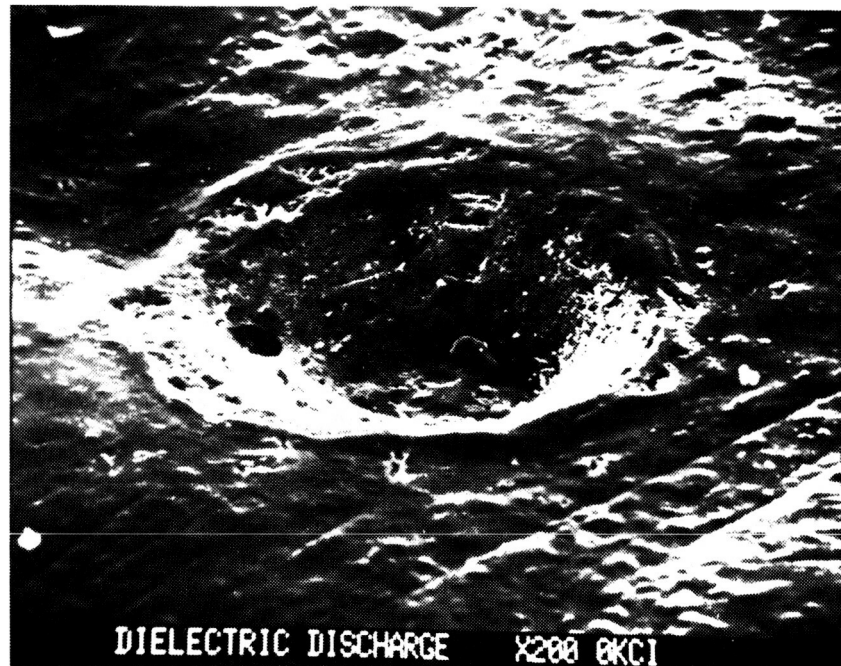
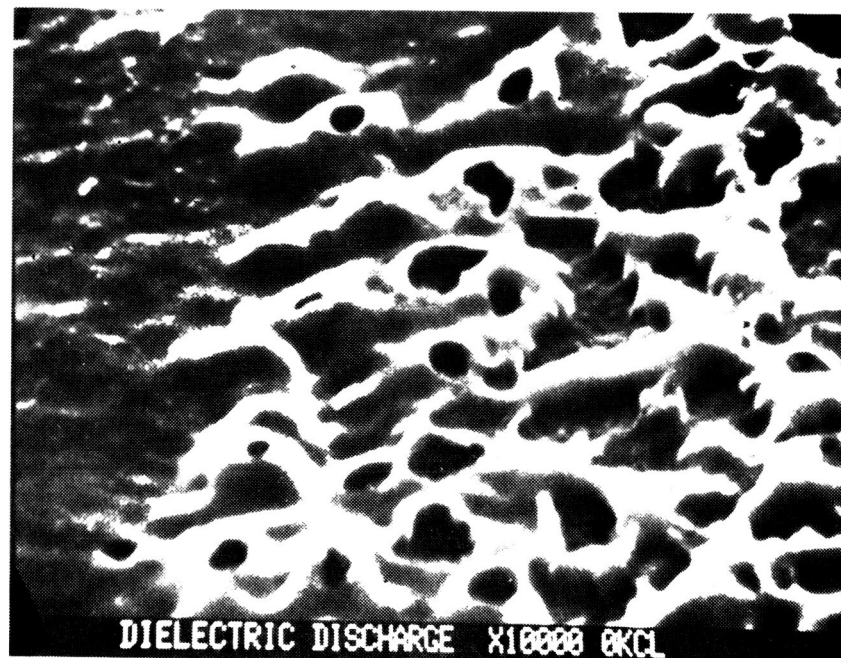


Figure 7 - Typical Discharge Pulse



(a) Crater in Tedlar (200 x SEM Magnification)



(b) Surface Melted Aluminum Substrate at Crater Base  
(10,000 x SEM Magnification)

Figure 8 - Discharge Cratering in Panel Isolation

## **MATERIALS CHARACTERIZATION STUDY OF CONDUCTIVE FLEXIBLE SECOND SURFACE MIRRORS**

**F. Levadou and S. J. Bosma**  
**European Space Research and Technology Centre**

**A. Paillous**  
**Département d'Etudes et de Recherches en**  
**Technologie Spatiale**

### **SUMMARY**

This paper describes the status of prequalification and qualification work being performed at ESTEC Noordwijk and at DERTS Toulouse on conductive flexible second surface mirrors.

The basic material is FEP teflon with either aluminium or silver vacuum deposited reflectors. The top layer has been made conductive by deposition of a layer of Indium oxide. Both materials have been tested in combination with a grounding method developed in the ESTEC Materials Section.

The results of a prequalification programme comprising of decontamination, humidity, thermal cycling, thermal shock and vibration tests are presented. Test parameters are thermo-optical and electrical properties. Furthermore the electrostatic behaviour of the materials under a simulated substorm environment as well as electrical conductivity at low temperatures have been characterised.

The effects of simulated ultra violet and particles irradiation on electrical and thermo-optical properties of the materials are also presented.

## INTRODUCTION

In the frame of studies on electrically conductive thermal control materials, the ESTEC Materials Section has been involved since several years in the development and qualification of conductive flexible second surface mirrors (ref. 1).

The studies presented in this paper have been mainly performed for ISPM and METEOSAT projects as well as in co-operation with DERTS (Toulouse - France) on a DERTS Research Programme for evaluation of conductive thermal control materials and associated grounding techniques under simulated synchronous orbit (ref. 2, 3, 4).

This paper describes the prequalification and qualification status, as they are defined by ESTEC Materials Section, for either conductive flexible second surface mirrors (SSM) commercially available, or for commercial flexible SSM on which a conductive layer has been deposited.

The work performed by ESTEC Materials Section covers the definition and preparation of conductive materials and grounding techniques as well as the prequalification programme.

The technique for grounding conductive layers developed a few years ago by ESTEC Materials Section was utilised for these studies.

The work performed by DERTS was mainly the evaluation of the charging performance and the studies on space stability of the grounded conductive SSM under synchronous space environment.

## MATERIALS PRINCIPLE

Basic materials are flexible second surface mirrors : aluminised or silvered FEP teflon and aluminised Kapton. The front face of the SSM is covered with a conductive transparent layer. The conductive layer must be transparent to avoid changes of the thermo-optical properties (i.e. absorptance and emittance) of the SSM.

The transparent conductive materials can be deposited according to different techniques and are generally Indium-oxide or Indium-Tin oxide (ITO) layers of a few hundred angström thickness.

## PRINCIPLE OF THE GROUNDING CONTACT

ESTEC Materials Section has developed a few years ago a technique which can be used for grounding a conductive surface to a structural part or an intermediate metallic layer (ref. 5). The materials used for the contact joint are silicon rubber RTV 566 produced by General Electric together with conductive powder Cho-bond 1029B from Chomerics.

### Preparation of the conductive adhesive

Hundred parts by weight of RTV 566A are mixed with 250 parts by weight of Cho-bond 1029B. After mixing together, the catalyst RTV 566B is added in 0.15 parts by weight. After further mixing the adhesive is degassed under vacuum.

### Joint formation

Two different kind of joints have been used.

#### Strap joint (fig. 1)

This is an electrical contact between the conductive layer and an aluminium strap. The strap has generally dimensions of 8 mm x 80 mm and a thickness of 30  $\mu$ m. The strap is degassed by being wiped with a Kimwipe soaked in Freon TF. Then the Dow Corning DC 1200 primer is applied at the end of the strap and to the end of the conductive SSM sample. A small amount of the conductive adhesive is applied to the primed area of the conductive sample layer and the primed aluminium foil is placed over it. A special heating tool developed for this purpose by ESTEC Materials Section is applied over the joint. Cure time, temperature of the tool and load pressure are defined. Previous investigation studies have shown that ideal parameters are:

- cure time : 2 minutes
- temperature : 100°C
- load : 200 g

#### Blanket mode (fig. 2)

This is an electrical contact between the top conductive layer and the metallic layer (aluminium or silver/Inconel) on the back side of the SSM.

A hole is punched through the sample. Primer is applied on the edges of both sides of the hole. A small amount of the conductive adhesive is put inside the hole. Two tabs of aluminium, with diameters a bit bigger than the diameter of the hole are applied on both sides of the conductive adhesive after priming. Then the heated tool is applied over the joint with the same parameters as above.

A typical application of a strap joint is at the edge of a sheet, for the interconnection of different sheets or grounding to structural elements. The blanket mode would be applied in the central part of the sheet, e.g. a thermal blanket, to connect the ITO to the metal backside of the SSM.

## TEST SEQUENCE

The test sequence consists of a prequalification programme and a qualification programme as they are defined by ESTEC Materials Section Specifications.

The samples have been submitted to the following prequalification tests:

- chemical spray (also called Decontamination Test)
- humidity test
- thermal cycling test (ref. 6)
- thermal shock test
- vibration test (acoustic)

The test parameters were:

- visual inspection
- electrical contact resistance and total resistance measurements (ref. 7)
- thermo-optical properties measurements (ref. 8)
- adhesion testing (ref. 9)

Table 1 is an example of a typical prequalification programme.

Furthermore, the materials have been submitted to the following qualification tests:

- electrostatic behaviour under a simulated substorm environment
- irradiation test under UV and particles environment.

The test parameters were the same as for the prequalification tests, except that during the electrostatic test the surface potential reached by the sample has been monitored.

In annex I the method developed by ESTEC to measure both electrical contact and total resistances is described.

## TEST MATERIALS

### Aluminised FEP teflon with ITO deposit

- Sheldahl G409520 : 2 mil teflon thickness
- Sheldahl G409550 : 5 mil teflon thickness
- Balzers/Sheldahl : 3 mil teflon thickness with ITO deposit by Balzers.

#### Silver FEP teflon with ITO deposit

- Sheldahl G409420 : 2 mil teflon thickness
- Sheldahl G409450 : 5 mil teflon thickness
- General Electric/Sheldahl : 5 mil teflon thickness with ITO deposit by G.E.

#### Aluminised Kapton with ITO deposit

- General Electric/Sheldahl : 5 mil Kapton thickness with ITO deposit by G.E.
- Sheldahl : 0.5 mil Kapton thickness with Nomex scrim.

Table 2 shows a list of typical values for optical and electrical properties of these materials.

### TEST RESULTS

#### Effects of chemical spray

This test is incorporated in the prequalification programme to simulate the effects of cleaning the conductive materials. Test samples are sprayed for one minute with iso-propyl-alcohol. None of the materials showed a significant variation of electrical conductivity. There is in some cases a slight improvement of solar absorptance due to the cleaning procedure.

#### Effects of humidity exposure

The test materials are submitted to 95% relative humidity and a temperature of 50°C during one week. It appears that humidity has a direct influence on the conductivity of Indium oxyde or Indium-Tin oxyde layers. All test materials show considerable increases in resistivity after exposure; some typical results are:

- 5 mil silver teflon : before humidity  $0.1 \times 10^6$  to  $10 \times 10^6 \Omega$   
after humidity  $10^6$  to  $10^9 \Omega$
- 2 mil aluminised teflon : before humidity  $5 \times 10^6$  to  $20 \times 10^6 \Omega$   
after humidity  $10^8 \Omega$
- 0.5 mil alumin. Kapton : before humidity  $1 \times 10^6$  to  $20 \times 10^6 \Omega$   
after humidity  $10^7$  to  $10^9 \Omega$

After the humidity exposure several test samples were submitted to high vacuum and the electrical resistance monitored in-situ.



The conductivity of each material increased under vacuum conditions, an improvement which continued throughout the exposure to vacuum. An example is shown in fig. 3. These facts support the theory that water absorption has a degrading effect on the conductivity of Indium based layers, but that these effects are not of a permanent nature at least after short term exposure to humid conditions. There is, however, evidence that these layers will not recover after long duration exposure (2 years) to humidity levels of 70% or higher. The optical properties of the conductive SSM are not affected by the humidity test.

#### Effects of thermal cycling

The tests were performed in accordance with specification ESA-PSS-11 (QRM-04T). Some materials were submitted to 100 cycles between +100°C and -150°C, other materials to 100 cycles between +25°C and -150°C. Thermal cycling proved to be detrimental to teflon-based SSM for both sets of temperature limits. The ITO layer on teflon shows numerous microcracks (fig. 4), which are believed to be caused by local stresses originating from the difference in thermal expansion for teflon and ITO. In the case of silver coated teflon, the silver reflector also showed micro-cracking (fig. 5).

On the contrary, ITO layers on Kapton based SSM proved to be stable. No cracking was observed and the conductivity of the ITO layer improved as would be expected due to removal of absorbed water during the vacuum and temperature conditions of the thermal cycling.

Some typical results are:

- 5 mil silver teflon	:	before cycling	$0.1 \times 10^6$ to $10 \times 10^6$ $\Omega$
		after cycling	$10^8$ to $10^{10}$ $\Omega$
- 2 mil aluminised teflon	:	before cycling	$5 \times 10^6$ to $20 \times 10^6$ $\Omega$
		after cycling	$> 10^{10}$ $\Omega$
- 0.5 mil alumin. Kapton	:	before cycling	$1 \times 10^6$ to $20 \times 10^6$ $\Omega$
		after cycling	$1 \times 10^6$ to $10 \times 10^6$ $\Omega$

The 2 mil teflon had a "milky" appearance after cycling, which caused an increase of solar absorptance.

The cracks in the silver reflector of the 5 mil teflon SSM did not cause any measurable variation in optical properties, but are liable to cause losses due to corrosion during long term contact with chemical agents (as existing in an adhesive).

The Kapton SSM also showed no change in optical properties.

## Effects of low temperature

### Test configuration

The surface resistivity measurement is performed with a three electrode arrangement. This method is illustrated in Annex 2.

### Test facility

The test sample with the electrode configuration was mounted to the sample holder of the "BISE" (ref. 10) vacuum facility. This sample holder is a hollow disc through which it is possible to circulate liquid nitrogen.

The temperature of the sample was monitored with three chromel-alumel thermocouples. The electrical leads of the electrode configuration were connected to an electrical vacuum feedthrough to allow for in-situ resistance measurement. A vacuum of more than  $10^{-6}$  torr was achieved with a turbo pump assembly. The liquid nitrogen shroud of the "BISE" chamber was filled before cooling down the sample to avoid excess contamination depositing on the cooled sample surface.

### Electrical measurement method

In-situ measurement: The Voltameter method was applied, as illustrated in the electrical diagram of fig. 6.

The internal resistance of the electrometer is connected in serie with the unknown resistance, to serve as a current limiting element. The current to the test sample was set at  $1 \times 10^{-6}$  A and applied continuously during the test. Voltage and temperature over the test sample were measured and monitored with a chart-recorder during the test run.

Ex-situ measurement: The surface resistivity ( $\rho_s$ ) has been measured with a probe consisting of two 1 cm wide copper electrodes at 1 cm distance of each other, in combination with a Hewlett Packard digital multimeter 3456B. A weight of 200 g was applied to maintain a standard pressure on the probe. Readings are made after one minute electrification time.

### Sample conditioning

The sheet material is stored under a relative humidity of 65% - 70% and a temperature of 18°C - 20°C.

Ex-situ measurements of surface resistivity are performed in the conditions stated above.

In-situ measurements of surface resistivity are performed in the prevailing chamber conditions.

## Test results

Table 3 compiles the last results for the SSM materials. Although the samples do not have similar "absolute" results, they behave identical in various ways:

- Three out of four samples show a sudden decrease in surface resistivity after first exposure to vacuum.
- All samples show a significant drop in surface resistivity after the total test phase, when compared to the initial value under identical conditions.
- All samples show an increase in surface resistivity after air inlet.
- All samples show a drop in surface resistivity when irradiated with UV light and subsequent recovery after interruption of the UV radiation.
- All samples show an increase in surface resistivity with temperature decrease. A nominal value is difficult to determine but it appears that the rate of change is related to the absolute value of surface resistivity of the sample. In terms of the final  $\rho_s$  in vacuum, the  $\Delta\rho_s/\Delta T$  varies between 1% and 10% of  $\rho_s$ .
- Water absorption has a highly negative effect on the conductivity of ITO. The tests demonstrate that the conductivity of the ITO layer improves with vacuum exposure time (fig. 3).

Fig. 7 shows a typical curve for surface resistivity as a function of temperature. The lower two curves are the cooling down and warming-up phases with no correction for the vacuum recovery effects. The upper two curves have been corrected for this phenomenon.

## Effects of electrostatic testing

In order to assess the electrostatic behaviour of ITO coated SSMs, various samples have been tested at DERTS in the CEDRE simulation chamber.

This facility enables to irradiate specimens with electrons in the 4-25 keV range. The irradiation uniformity (better than 10 percent) at the sample is obtained by scattering of the electrons through a thin aluminium foil (1.2  $\mu\text{m}$  thick). Samples are maintained in close contact by their rear side with an aluminium plate which is grounded through a nanoammeter which enables to measure the leakage current  $I$  during irradiation. The current  $I_{\text{sec}}$  collected on a hemicylindrical electrode surrounding the sample allows to evaluate the secondary emission of the irradiated surface. The conductive ITO layer is grounded by means of either a metallic frame in contact with the surface or aluminium straps bonded to the ITO by conductive adhesive, which enables to measure the surface leakage current  $I_{\text{surf}}$ .

The surface potential of the specimens is measured by a contactless method with a potential probe (capacitive sensor) moved by a mechanical scanner. Impulses in the recording of the leakage current indicate the occurrence of discharges if any.

Table 4 shows that the ITO layers deposited by BALZERS and SHELDAHL are equally effective in suppressing potential build up and discharges, when grounded. The surface potentials of non-coated SSMs are also given in table 4 as a comparison. No potential increase has been identified after that both ITO coated samples had been rolled around cylinders (4 mm diameter) in perpendicular directions.

Table 5 gives the results that have been measured under irradiation on two ITO coated aluminised Kapton samples, of which the ITO layer was grounded by means of four interconnects obtained by the conductive adhesive technique; one of these samples has undergone all the prequalification tests. No charge build up has been noticed in the simulated substorm environment. However, the secondary emission as well as the leakage current seem slightly higher in the case of the sample exposed to the prequalification programme. However, its total surface current (collected by the aluminium straps bonded to the ITO) is still very high.

#### Effects of simulated space irradiation

The stability of various conductive SSM has been assessed by irradiation either with UV only or with UV and particles.

Figure 8 gives the results of an irradiation by UV of ITO layers applied by SHELDAHL on silvered FEP 2 and 5 mil thick. The degradation under UV of a 3 mil aluminised FEP from SHELDAHL is also reported in figure 8 together with the degradation of the same aluminised film that has been coated by an ITO layer made by BALZERS. The solar reflectance variations have been obtained at DERTS from in-situ spectral measurements that have been carried out on samples irradiated at 30°C under vacuum by two filtered Xenon short arc sources giving only ultra-violet radiation in the 200-380 nm wavelength range with a sun multiplication factor of 2.

The same UV sources have also been used in conjunction with proton and electron accelerators in order to provide conditions of exposure simulating the geosynchronous orbit environment for a North/South satellite face. The irradiation was sequential with a continuous ultra-violet exposure (2 "suns") and periodic particle bombardment.

In order to simulate one year in space, the following conditions were chosen 1112 UV esh,  $4.29 \times 10^{14}$  protons  $\text{cm}^{-2}$  at 40 keV (normal incidence),  $1.42 \times 10^{13}$  protons  $\text{cm}^{-2}$  at 150 keV (normal incidence),  $8.6 \times 10^{14}$  electrons  $\text{cm}^{-2}$  ( $45^\circ$  incidence). Figure 8 shows the solar reflectance variations that have been measured on a silvered FEP sample (2 mil) and a silvered FEP sample (2 mil thick) with an ITO layer deposited by SHELDAHL. During irradiations the ITO layers were grounded. From the curves in figure 8, it seems that the degradation kinetics of the conductive ITO manufactured by SHELDAHL and irradiated by UV plus particles is nearly identical with the one observed as consequence of an irradiation by UV only. That means that UV radiation is more deleterious than particles in optical degradation of ITO layers. In spite of the short duration of the tests, a tendency towards saturation is noted in the degradation of these conductive layers. On the other hand, the second surface mirrors without conductive overcoating are more severely degraded when irradiated simultaneously by particles and ultra-violet. Of significance might be the less extent of degradation observed in figure 8 with the ITO coatings made by BALZERS and GENERAL ELECTRIC: the preparation method is of prime importance in the colour centre formation under radiation. The behaviour of the ITO layer is the same whether it is grounded during particle irradiation or not.

It has been verified that the total electrical resistance measured in-situ between aluminium straps applied with conductive RTV 566 on the ITO layers (2 mil silvered FEP SHELDAHL) was not modified by exposure to the combined environment described above. (N.B. the samples were not illuminated nor irradiated by particles during measurements).

## DISCUSSION

This research programme has established that conductive layers of Indium-oxide or Indium-tin-oxide do not have a general behaviour pattern, but depend on different application parameters. The performance of the conductive layer will vary with such factors as:

- deposition technique (e.g. vapour deposition or sputtering)
- substrate material
- substrate temperature during deposition
- random conditions during deposition (vacuum, contamination)
- material history (perforation, humidity exposure, handling)

Of the flexible materials tested, Kapton proved to be the best host for an Indium based conductive layer.

Two prequalification programmes on two individual materials from different manufacturers showed that the ITO layer is mechanically stable: no cracks were observed after thermal cycling, neither for a vapour deposited layer nor a sputtered layer. The initial electrical and optical properties did not show major variations after the total prequalification. The conductivity of the ITO layer recovered during thermal cycling from water absorbed during the humidity test. No significant charge build up was observed on the sputtered layer during the electrostatic charging test either on the original material or on a sample which had undergone all prequalification tests.

Teflon based conductive SSM proved to be extremely vulnerable to thermal cycling: both sputtered and vapour deposited ITO layers showed numerous microcracks. In the case of the silver SSM, the metal reflector was also cracked. Thermal cycling caused the 2 mil aluminised teflon to go milky which resulted in a degradation of solar absorptance. The initial resistivity of teflon based conductive SSM tends to be higher than the equivalent Kapton material. The teflon based SSM does not charge during electrostatic charging tests, however, recent results show that a sample which had been submitted to the total prequalification programme did support charge up to several hundred volts.

The degradation of the optical properties of ITO layers under simulated irradiation is very dependant on deposition type and manufacturer. Based on UV and particle irradiation sputtered ITO (GENERAL ELECTRIC) appears to be more stable than vapour deposited ITO (SHELD AHL). The main degrading factor is ultra-violet irradiation, although BALZERS vapour deposit an ITO layer which is very stable under ultra-violet exposure. Unfortunately this material is a one time experimental batch made by BALZERS under ESA contract and is not commercially available. The degradation of the ITO due to UV has a tendency to saturate after exposure periods of more than a year.

Indium based conductive layers are very vulnerable to water absorption. Short term humidity effects will recover during vacuum exposure, however, long term humidity effects cause permanent damage. It is recommended to store conductive SSM in a controlled dry environment and to record batch histories with respect to storage conditions and handling.

The ESA developed grounding technique based on conductively loaded RTV 566 proved to be applicable on both Kapton and teflon SSM and was stable during prequalification and qualification tests.

## CONCLUSIONS

Kapton based SSM with a conductive ITO layer is a very promising solution for electrostatic charging problems. The teflon based SSM with a conductive ITO layer evaluated during this programme will not fulfil strict electrostatic charging requirements. There are still a number of verification tests on-going to determine if the present material, despite the risk of ITO cracking could be used on spacecraft which can tolerate limited charging levels.

Manufacturers are recommended to investigate the possibilities of optimising the ITO layers on teflon with respect to deposition technique, substrate temperature etc. This test programme indicates that initial optical and electrical properties as well as space stability depend heavily on these factors.

Manufacturers must be able to guarantee an ITO layer of standard quality if this type of solution is to be competitive with other types of conductive thermal control coatings in the future.

## REFERENCES

1. Bosma, J. and Levadou F.; Electrostatic Charging and Space Materials. ESA SP-145, October 1979.
2. Paillous, A.; Revêtements Conducteurs Envisagés pour le Satellite METEOSAT. Etude CERT 4108. Contrat ESTEC 4294/80/NL/PP, July 1980.
3. Benisja, A., Levy L., Paillous, A. and Sarraill, D.; Satellite Spacecraft Charging Control Materials. Interim Scientific Report No. 1. Grant Number AFOIR 78-3704B, July 1979.
4. Levy, L., Paillous, A. and Sarraill, D.; Satellite Spacecraft Charging Control Materials. Interim Scientific Report No. 2. Grant Number AFOIR 78-3704B.
5. Bosma, J. and Froggatt, M.; Evaluation of a Conduction Adhesive System for the Grounding of Aluminised Kapton Coated with Indium/Tin oxide, ESA STM-13, August 1980.
6. Screening Test Method for the Selection of Space Materials and Small Assembly by Thermal Cycling under Vacuum. PSS-11/QRM-04T.
7. Electrical Properties Measurements on Conductive Surfaces for Space Use. QRM-38T.
8. Specification for the Measurements of the Thermo-Optical Properties of Thermal Control Materials at ESTEC. PSS-16/QRM-09T, ESA specification.
9. Testing the Peel or Pull-Off strength of Coatings and Finishes by Means of Pressure Sensitive Tape. PSS-18/QRM-13T, ESA specification.
10. Minier, C.F.; Description du Banc d'Irradiations Solaires de l'ESTEC BISE. Internal ESTEC Working Paper No. 986.
11. Paillous, A. and Sarraill, D.; Compte Rendu Final sur Contrat ESTEC 3184/77/NL/HP. Publ. ONERA/CERT/DERTS 4064, February 1979.



## ANNEX 1

### ELECTRICAL RESISTANCE MEASUREMENTS

#### Background

In the case of a grounding point on a highly conductive substrate material, e.g. aluminium, it is sufficient to measure the total resistance of the grounding point and substrate, because a change in the contact resistance from the  $10\Omega$  range to the  $100\Omega$  range will be easily detected, the substrate resistance being a few milliohms only.

In the case of a low-ohmic contact ( $10\Omega$  to  $100\Omega$  range) on a substrate material with a high ohmic resistivity ( $k\Omega$ - $M\Omega$  range), the contact resistance is more difficult to determine. This is the situation for the grounding configuration under evaluation.

The Indium-Tin oxide layer shows variations of hundreds of ohms during a measurement. This is only a few tenths of one percent with respect to the actual resistance of several megohms, but is of the same order of magnitude as the contact resistance of the grounding point.

For this particular grounding configuration, the contact resistance will be defined as the combined resistances of the aluminium strap, the conductive adhesive and the ITO boundary layer at the contact point.

#### Electrical contact resistance

Several methods have been evaluated which appeared capable of determining the contact resistance in a high ohmic chain. Figure 1 shows the sample configuration for the method which proved to be most effective. The three-contact principle is used to obtain the contact resistance of the centre electrode. The three electrodes were formed by aluminium straps bonded with conductive adhesive, as described in section 3. Figure 1 shows the electrical circuit applied.

The power supply and the ammeter are connected to the centre and right electrodes; the right electrode functions only as a current conductor.

The voltmeter is connected between the centre and left electrodes. The left electrode functions as a potential electrode. Owing to the internal resistance of the voltmeter, the current passing through circuit "A" will be approximately a factor 1000 smaller than that passing through circuit "B".

Adjusting the power supply in circuit "B" enables the current through the contact resistance to be fixed. Circuit "A" is used to determine the voltage drop over the contact resistance, from which the contact resistance can be deduced.

On the basis of this method, a jig has been developed which ensures that the samples are measured under similar conditions of electrode pressure and sample positioning.

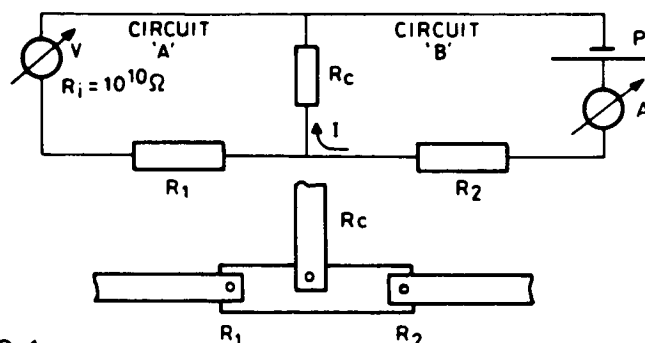


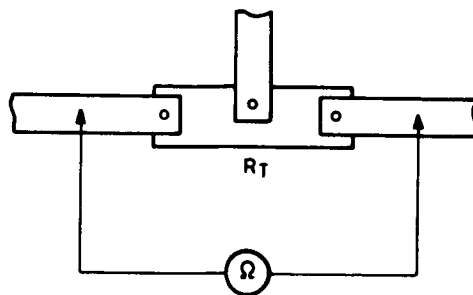
FIG. 1

The symbols used in Figure 1 have the following meanings:

- P = power supply,
- A = Keithly Model 602 electrometer (applied in ammeter mode),
- V = Hewlett Packard multimeter 3465B (applied in voltmeter mode),
- $R_i = 10^{10} \Omega$  = internal resistance of voltmeter =  $10^{10} \Omega$ ,
- $R_1$  = contact resistance of left electrode plus resistance of ITO layer between left and centre electrodes,
- $R_2$  = contact resistance of right electrode plus resistance of ITO layer between right and centre electrodes,
- $R_c$  = contact resistance of centre electrode.

#### Total electrical resistance

After each successive test, the total electrical resistance of each sample was measured with the Hewlett Packard multimeter 3465B applied in ohmmeter mode. The total electrical resistance is defined as the electrical resistance measured between left and right electrodes and includes contact resistance of left and right electrodes as well as the resistance of the intervening ITO layer. Figure 2 illustrates the test method.



$\Omega$  = OHMMETER  
 $R_T$  = TOTAL ELECTRICAL RESISTANCE

FIG. 2

## ANNEX 2

### SURFACE RESISTIVITY MEASUREMENT

We now consider a strip of width  $dx$  which is at a radius  $x$  from the centre of the sample. The resistance of the strip according to the definition of the surface resistivity is:

$$dR = \rho_s \times dx / 2\pi x \quad (1)$$

$\rho_s$  = surface resistivity (Ohm).

The voltage drop  $dV$  over this section will be:

$$dV = I \times dR \quad (2)$$

$I$  = current through sample,

$$\text{or} \quad dV = I \times \rho_s \times dx / 2\pi x \quad (3)$$

The total voltage drop between two electrodes of radius  $R$  and  $R_1$  will be:

$$\int_{V1}^{V2} dV = \rho_s \times I \int_{R1}^{R2} \frac{dx}{2\pi x} \quad (4)$$

$$V2 - V1 = \frac{\rho_s \times I}{2\pi} \ln \frac{R2}{R1} \quad (5)$$

The surface resistivity between two electrodes is given by:

$$\rho_s = 2\pi V / I \times \ln \frac{R2}{R1} \quad (6)$$

For the dimensions of the two inner electrodes as shown in fig. 1 the equation is:

$$\rho_s = 2\pi (V/I) / \ln \frac{67}{50} \quad (7)$$

$$\rho_s = 21.47 \frac{V}{I} \quad (8)$$

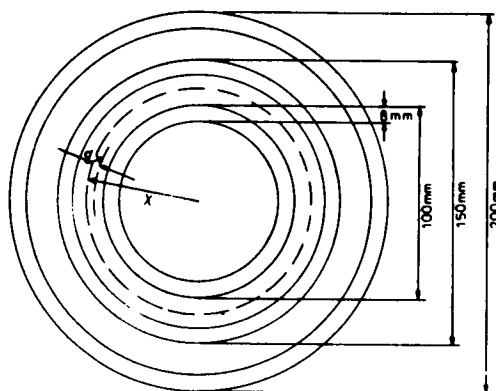


FIG 1 ELECTRODE CONFIGURATION

TABLE I

R	1	2	3	4	5	6	7	8	9	10	11	12	13	14	15	16	17	18	19	20	21	22	23	24	25	26	27	28	29	30	31	32	33	34	35	36	37	38
Sample preparation																																						
visual inspection																																						
in-air resistance																																						
in vacuum resistance																																						
optical and scanning electron microscope																																						
peel testing																																						
long-term storage																																						
Chemical spray (isopropyl alc.)																																						
visual inspection																																						
in-air resistance																																						
peel testing																																						
Heat and humidity (50°C, 95%)																																						
visual inspection																																						
in-air resistance																																						
peel testing																																						
Acoustic (Thor-Delta spec.)																																						
visual inspection																																						
in-air resistance																																						
peel testing																																						
Thermal cycling (-150°C +100°C)																																						
visual inspection																																						
in-air resistance																																						
peel testing																																						

Material	$\alpha_s$	$\epsilon_N$	$\rho_s$
Sheldahl alu teflon 2 mil	0.18	0.64	6-19 M $\Omega$
Sheldahl alu teflon 5 mil	0.20	0.76	9-40 M $\Omega$
Balzers alu teflon 3 mil	0.15-0.17	0.71	0.5-2 K $\Omega$
Sheldahl Ag teflon 2 mil	0.08-0.09	0.64	0.8-2 M $\Omega$
Sheldahl Ag teflon 5 mil	0.10	0.77	1-2 M $\Omega$
G.E. Ag teflon 5 mil	0.12-0.16	0.79-0.80	1-20 M $\Omega$
G.E. alu kapton 5 mil	0.38-0.39	0.77	60-140 K $\Omega$
Sheldahl alu kapton 0.5 mil	0.75-0.73	0.48	50-260 K $\Omega$

Table 2 - Materials Properties

Material	Initial $\rho_s$ in air R.T.	Initial $\rho_s$ in vacuum R.T.	$\Delta\rho_s/\Delta T$	Final $\rho_s$ in vacuum R.T.	$\rho_s$ after UV	Final $\rho_s$ in air R.T.
SHELDAHL FEP/AL 2 mil	22 M $\Omega$	24 M $\Omega$	113-117 K $\Omega$ /°C	6 M $\Omega$	4.6 M $\Omega$	9.4 M $\Omega$
SHELDAHL FEP/Al 5 mil	20 M $\Omega$	7 M $\Omega$	0.60 M $\Omega$ /°C	6 M $\Omega$	3.0 M $\Omega$	11.4 M $\Omega$
SHELDAHL FEP/Ag 5 mil	8 M $\Omega$	7 M $\Omega$	104-118 K $\Omega$ /°C	2 M $\Omega$	0.9 M $\Omega$	1.2 M $\Omega$
BALZERS FEP/Al 3 mil	9.0 K $\Omega$	7.6 K $\Omega$	34-43 $\Omega$ /°C	3.2 K $\Omega$	2.6 K $\Omega$	5.8 K $\Omega$

Table 3

BEAM ENERGY (keV)	INTENSITY (nA cm <sup>-2</sup> )	SURFACE POTENTIAL VOLTS			
		ALUMINIZED FEP 3 mil	ITO (BALZERS) on Aluminised FEP 3 mil	SILVERED FEP 2 mil	ITO (SHELDAHL) on Silvered FEP 2 mil
5	1	1900	< 10	2000	< 10
10	1	5400	< 10	5400	< 10
15	1	10300	< 10	10000	< 10
20	1	15000	< 10	15000	< 10
25	1	discharges	< 10	9800	< 10
10	5	5500	< 10	5400	< 10
15	5	10300	< 10	10000	< 10
20	5	15400	< 10	15400	< 10

Table 4 - Behaviour of ITO coated FEP in a simulated substorm environment. (Not submitted to prequalification test).

		BEAM ENERGY/INTENSITY			
		5 keV 1.25 nA cm <sup>-2</sup>	10 keV 0.7 nA cm <sup>-2</sup>	15 keV 0.5 nA cm <sup>-2</sup>	20 keV 0.5 nA cm <sup>-2</sup>
BEFORE PREQUALIFICATION PROGRAM	V (volts)	< 10	< 10	< 10	< 10
	I (nA)	0.5	0.2	0.08	0.12
	I <sub>surf</sub> (nA)	10.5	11.5	11	10.5
	I <sub>sec</sub> (nA)	12	4	2.5	1.5
	Discharges	no	no	no	no
AFTER PREQUALIFICATION PROGRAM	V (volts)	< 10	< 10	< 10	< 10
	I <sub>C</sub> + I <sub>L</sub> (nA)	1	1.1	1.2	1.2
	I <sub>surf</sub> (nA)	4	5.5	9	8
	I <sub>sec</sub> (nA)	16	8	2.5	1.7
	Discharges	no	no	no	no

TABLE 5 - BEHAVIOUR OF THE ITO-COATED KAPTON GROUNDED WITH A CONDUCTIVE ADHESIVE IN A SIMULATED SUBSTORM ENVIRONMENT

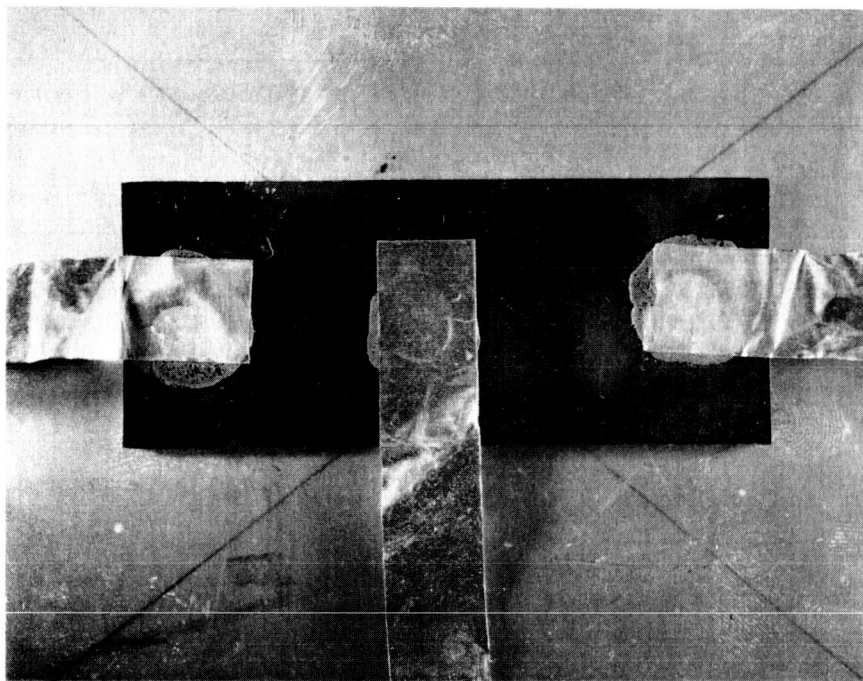


FIG. 1: GROUNDING STRAP CONFIGURATION

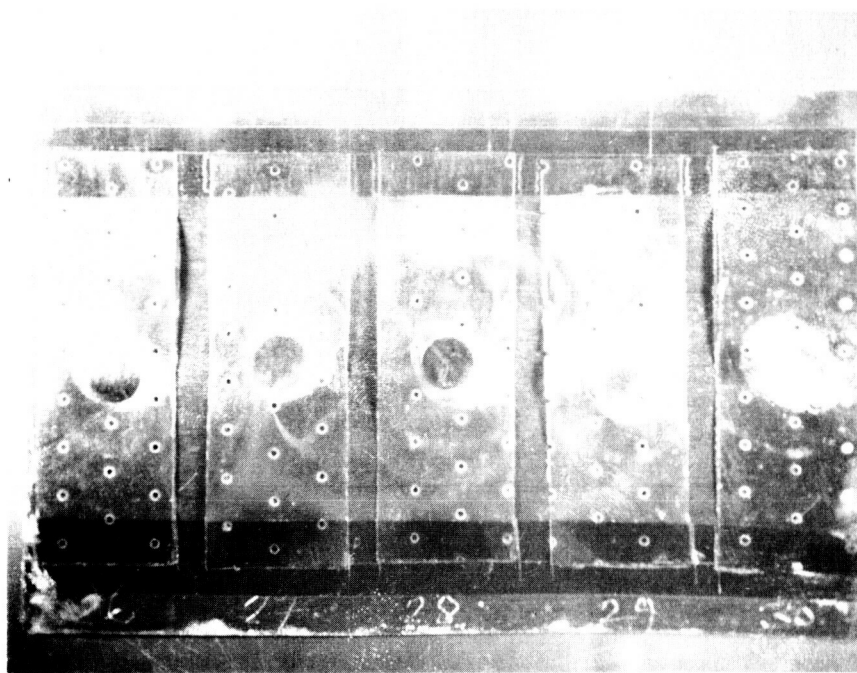


FIG. 2: BLANKET MODE GROUNDING CONFIGURATION

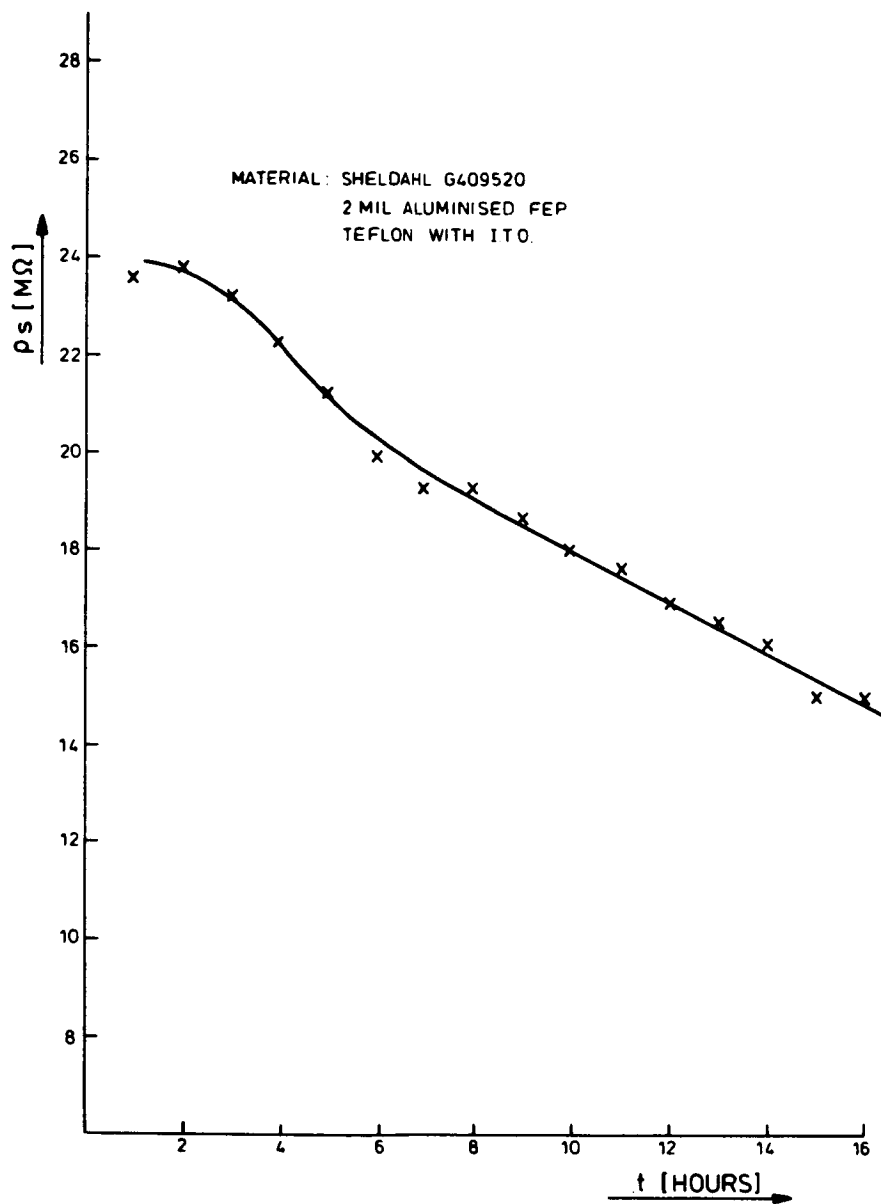


FIG.3 SURFACE RESISTIVITY AS A FUNCTION OF TIME



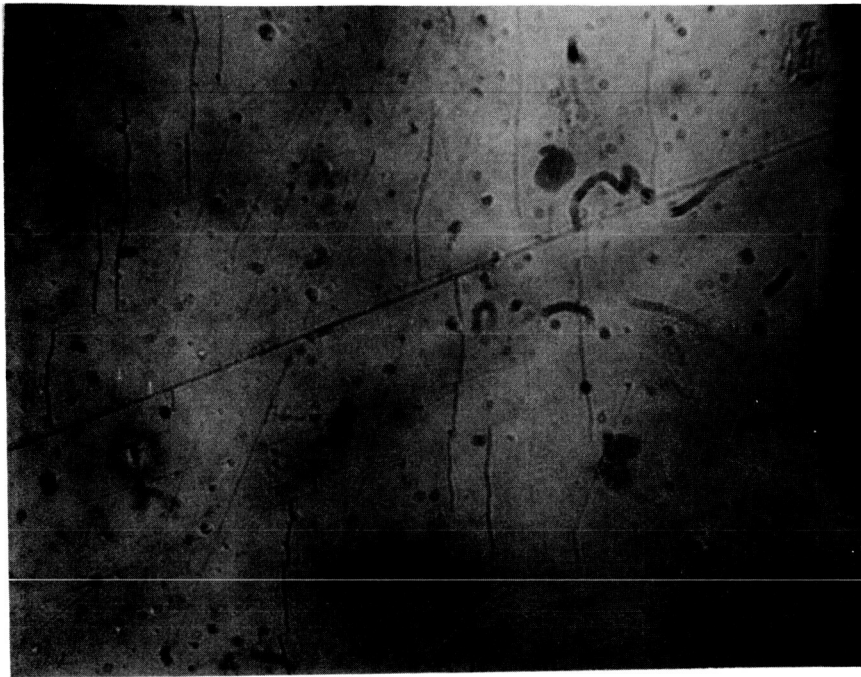


Fig. 4: Micro-cracks in I.T.O.-layer after thermal cycling.

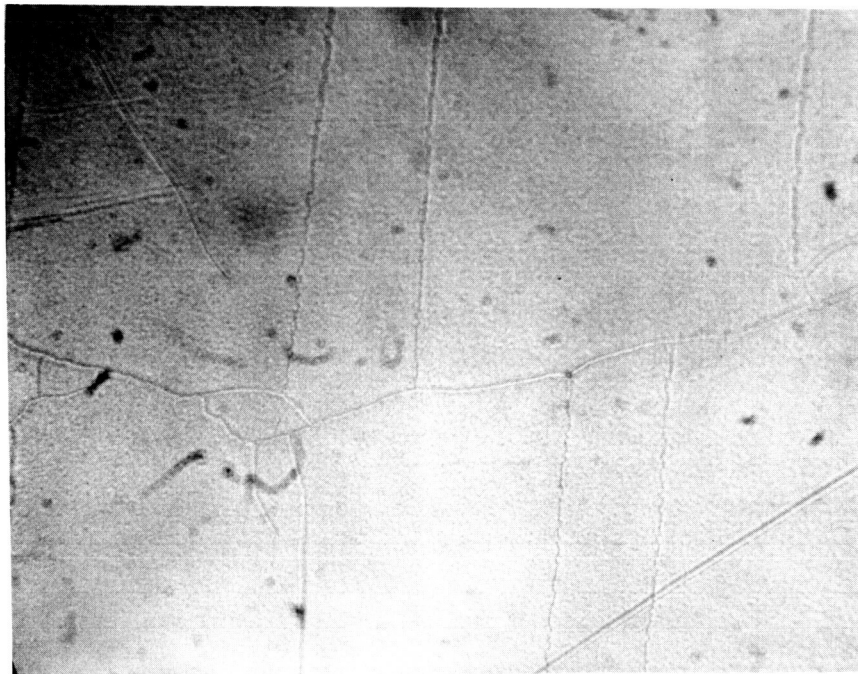


Fig. 5: Micro-cracks in silver layer after thermal cycling.

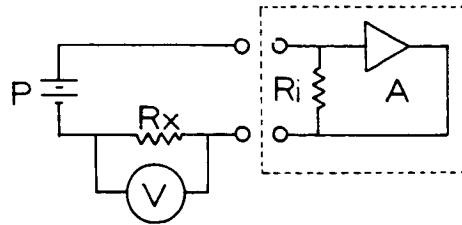


Fig. 6 Electrical measurement diagram.

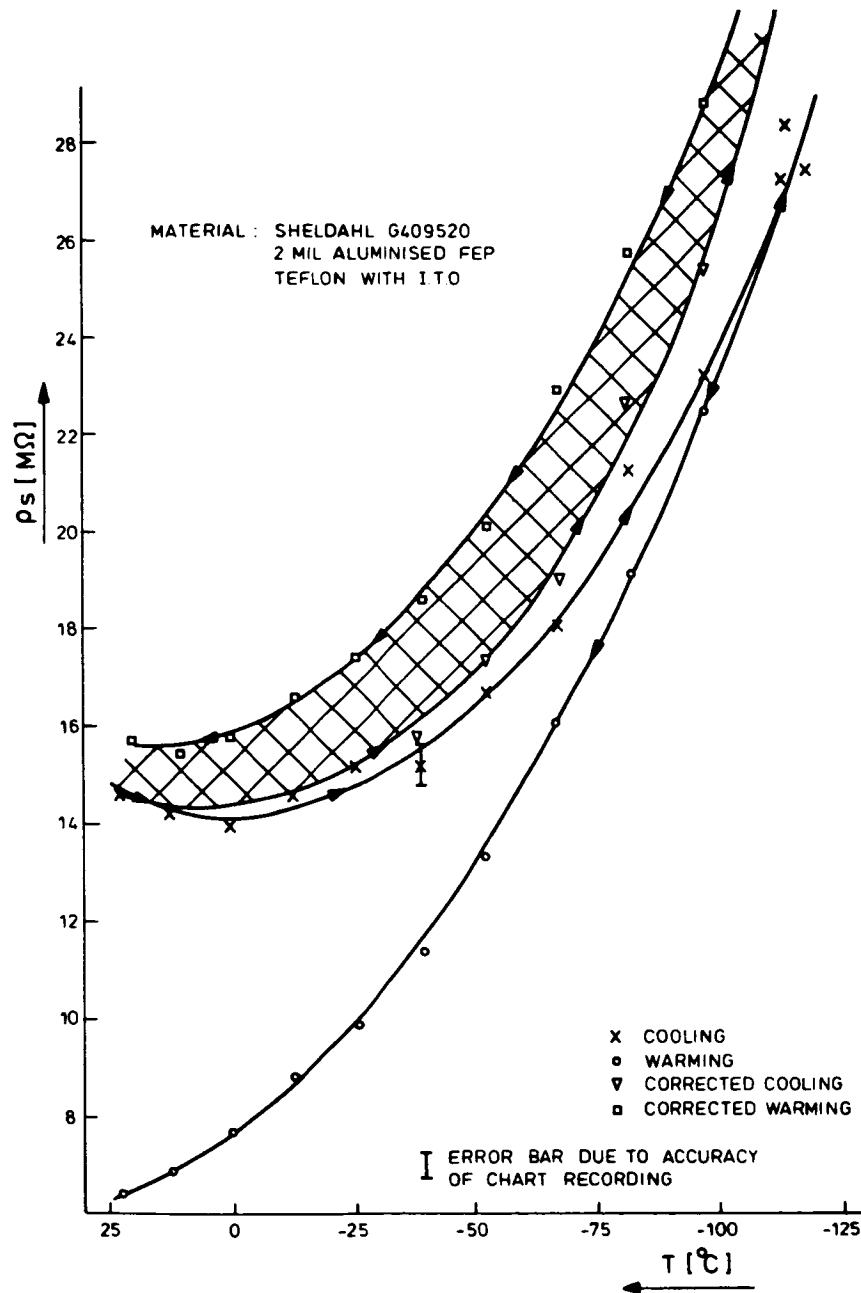


FIG.7 SURFACE RESISTIVITY AS A FUNCTION OF TEMPERATURE

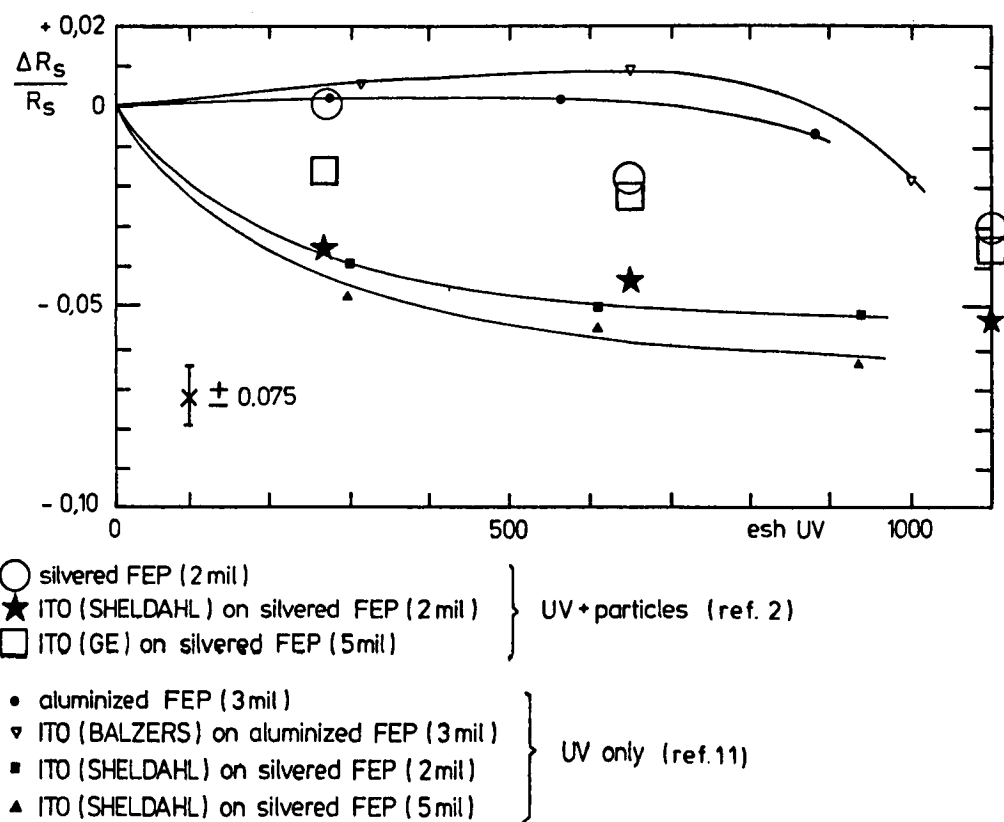


FIG.8

## DESIGN OF AN ARC-FREE THERMAL BLANKET

Christakis N. Fellas  
British Aerospace Public Limited Company  
Space and Communications Division

### SUMMARY

One way of dealing with the problem of spacecraft charging is to provide a thermal control surface which will not charge up to the breakdown level, while retaining its thermal control properties. A thermal blanket configuration meeting these requirements has been designed at British Aerospace (ref. 1).

Arcing is eliminated by limiting the surface potential to well below the threshold level for discharge. This is achieved by enhancing the leakage current which results in conduction of the excess charge to the spacecraft structure. The thermal blanket consists of several layers of thermal control (Space approved) materials, bonded together, with Kapton on the outside, arranged in such a way that when the outer surface is charged by electron irradiation, a strong electric field is set up on the outer Kapton layer resulting in a greatly improved conductivity.

This paper describes how the basic properties of matter were utilised in designing this blanket and how charge removal was achieved together with the optimum thermo-optical properties.

### INTRODUCTION

When a surface is subject to electron bombardment, the important electron parameters are the electron energy and the flux. The electron energy determines the maximum surface voltage that may be attained, provided the target material has a thickness well in excess of the electron range in that material (ref. 1). The flux level, i.e. the current per unit area incident upon the surface determines the rate of charging  $dV/dt$ . This also depends on a number of other factors and is given by the equation

$$\frac{dV}{dt} = \frac{1}{C} (I_{inc} - \sum_j I_j) \quad (1)$$

where  $C$  is the capacity of the surface

$I_{inc}$  is the incident current

$\sum_j I_j$  is the sum of all components of the removal current, given by

$$\sum_j I_j = I_{pr} + I_{ph} + I_{bs} + I_{sec} + I_l \quad (2)$$

where  $I_{pr}$  is the incident proton current

$I_{ph}$  is the photo-electric effect induced current

$I_{bs}$  is the back-scattering current

$I_{sec}$  is the secondary electron current

and  $I_l$  is the leakage current through the dielectric material.

The design of an arc-free thermal blanket involves the enhancing of one of the removal currents, namely the leakage current, so that  $dV/dt$  becomes zero at a surface voltage potential well below that anticipated from the electron energy.

When the equilibrium surface voltage is below the discharge threshold for the entire range of electron energies anticipated, no discharges will occur. Thus an arc-free thermal blanket is obtained.

#### THE LEAKAGE CURRENT

In order to enhance the leakage current the parameters affecting its value are examined and one or more of these are varied accordingly. The leakage current may be considered as the sum of three components. The ohmic current, the internally induced secondary current and the transmission current. Thus we may write

$$I_l = I_{ohmic} + I_{insec} + I_{trans} \quad (3)$$

The ohmic current is the current which flows through the dielectric as a result of the existence of a potential difference across the material. In reference 1 an approximate expression is derived from classical mechanics for this term

$$I_{ohmic} \propto \exp \left( - \frac{\Delta W_j}{KT} \right) \sinh \left( \frac{V}{d} \cdot \frac{ea}{2KT} \right) \quad (4)$$

where  $\Delta W_j$  is the ionization potential of the material

$T$  is the absolute temperature

$K$  is Boltzmann's Constant

$V$  is the surface voltage

$d$  is the material thickness

$e$  is the electronic charge  
and  $a$  is the average distance between atoms in the material.

The internal secondary current, referred to by other authors as "radiation induced conductivity", is the current resulting from the liberation of electrons from the atoms in the material by a process where energy from incoming electrons is transferred to material electrons. Although an analytical expression for this component has not been derived it is believed to be dependent on the electric field, the energy of the incident electrons and the flux of the incoming electrons.

The transmission current is the product of the electron transmission probability and the incoming current. The transmission probability  $P$ , for a simplified square wave potential is given by (ref. 1)

$$P \approx \exp(-2 b' d) \quad (5)$$

where  $d$  is the material thickness  
and  $b'$  is given by

$$b'^2 = \frac{2m_e}{\hbar^2} (V_0 - T_0) \quad (6)$$

where  $m_e$  is the electronic mass  
 $\hbar$  is Planck's Constant (divided by  $2\pi$ )  
 $V_0$  is the max. surface potential  
and  $T_0$  is the kinetic energy of the incoming electrons.

The expressions given by equations (4) and (5) show that the leakage current is dependent exponentially upon the material thickness and consequently a decrease in thickness will lead to a much increased leakage current. In the case of a thin aluminised Kapton sheet, provided the aluminium layer is grounded a decrease in the material thickness will also lead to an increase electric field and this will influence the migration of charges deposited within the material to the aluminium layer. The electric field results from very low energy electrons, with near zero range, depositing their charge on the surface of the material.

As can be seen from equations (4) and (5) when the material thickness is decreased the relative proportion of the constituent currents of  $I_1$  given in equation (3) change, so that for  $d=0$ ,  $I_1 = I_{\text{tran}} = I_{\text{inc}}$  and the surface voltage is zero. When the material thickness has a finite value the ohmic current and the internal secondary current have a non zero value provided there are sufficient low energy electrons to build up a voltage on the surface.

This may lead to a leakage current in excess of the incident current and such currents have been observed experimentally (ref. 1 and 2).

#### THE MULTILAYER THERMAL BLANKET

The thickness of the material determines the thermo-optical properties, so that a decrease in thickness reduces both the absorptivity  $\alpha$  and the emissivity  $\epsilon$  of the material. In general the ratio  $\alpha/\epsilon$ , which is a figure of merit for thermal control materials, increases with decreased thickness. For a 3 mil aluminised Kapton for instance  $\alpha/\epsilon = 0.538$  whilst for a 0.25 mil Kapton this figure becomes 0.688.

Another reason why a super thin dielectric film cannot be used as a thermal blanket is the mechanical properties of such film. The material must be sufficiently strong to withstand the testing environment. Thus for a Kapton film a thickness value of less than 2 mil is not considered practicable.

In order to overcome this problem, a multilayer thermal blanket (\*) has been designed combining good mechanical strength, acceptable thermo-optical properties and the ability to conduct incident charge and keep the surface potential to well below the discharge threshold for the material. The prototype version is shown in figure 1. The outermost layer is a thin aluminised Kapton film. The thickness of 0.25 mil shown here is sufficient to keep the surface potential to below 2.5 KV at room temperature (or below 3.2 KV at  $-170^\circ\text{C}$ ) which is well below the discharge threshold of approximately 9 KV. The maximum potential value is obtained when the incident electrons have a mean range of approximately equal to  $1/3$  of the material thickness. For a 0.25 mil Kapton maximum surface potential is obtained with 7 KeV electrons. At higher energies the surface potential is reduced as the radiation induced conductivity is increased coupled with an enhanced diffusion process in the presence of a strong electric field and a shorter migration distance as the electrons are deposited closer to the charge collector.

The thermo-optical properties of this prototype multilayer thermal blanket are determined by the outermost layer, so for the configuration shown in figure 1  $\alpha/\epsilon$  is 0.688.

The mechanical properties of the blanket are determined by the overall thickness of the blanket. The thicker (2 mil) aluminised Kapton is attached to the thinner aluminised layer by means of a double-sided pressure sensitive adhesive (e.g. Y966 PSA).

The thermo-optical properties of the configuration shown in figure 1 are limited by the thickness of the outermost layer. In order to overcome this the aluminium and the adhesive have been replaced by a single transparent conductive adhesive. This improved version is shown in figure 2.

---

(\*) UK patent application No. 8035523 / USA application No. 204,703

A transparent conductive adhesive does not exist as such but it is possible to dilute a polyurethane based silver or cobalt loaded paint (e.g. Coballoy P212 \*) and use it to attach the two layers of Kapton together. It is possible to spray a layer thin enough to be optically transparent but still retain enough conductivity for the multilayer principle to operate. A resistivity of 2 M $\Omega$  or less is believed to be sufficient.

An alternative to the use of conductive transparent adhesive is to use 0.25 mil Kapton spattered with Indium Tin Oxide and attach it to aluminised Kapton using a clear polyester adhesive. Such an arrangement is shown in figure 3. The advantage of this design is that the materials used are already qualified for Space use and the ITO spattered process on Kapton provides uniform reproducible properties on the inner conductive layer, which are difficult to achieve with a spray.

### EXPERIMENTAL TESTS

The prototype multilayer thermal blanket of figure 1 has been extensively tested at the UKAEA electron Irradiation facility. The test results have been reported elsewhere (ref. 1).

Two samples of approximately 100 cm<sup>2</sup> were irradiated using monoenergetic electrons at 20°C and -170°C. The electron energy was varied from 3 to 30 keV at flux levels varying from 0.4 to 35 nA/cm<sup>2</sup>. No discharges were observed at either temperature during six hour irradiation periods, under several different combinations of flux and energy. The maximum surface voltage recorded was 3.2 kV at -170°C with an incident electron energy of 7 keV and a flux of 24 nA/cm<sup>2</sup>. The surface potential was substantially reduced at higher electron energies. The maximum surface potential at 20°C was 2.4 kV.

The tests described above prove the success of the design in eliminating arcing of a dielectric, while maintaining the good thermo-optical properties. The results obtained from measurements of the leakage current and surface voltage were in accordance with the theory used to design the blanket.

Samples described in figures 2 and 3 are currently being investigated and the results will be the subject of another publication.

### CONCLUSIONS

The success of the multilayer thermal blanket in eliminating arcing indicates the validity of the design principles used. Placing a charge collector at a certain depth in the dielectric sets up a strong electric field, improving charge mobility towards the charge collector and enhancing the leakage current. The increase in the leakage current is sufficient to make  $dV/dt = 0$  at surface voltage level well below the discharge threshold.

\* Available from Graham Magnetics Inc., Texas, USA.



The same principle has been used to design thermo-optically improved versions with optically transparent charge collectors. This design has been applied to second surface mirrors as well and results of the investigations will be published in due course.

#### REFERENCES

1. Fellas C.N. : An Arc-Free Thermal Blanket for Spacecraft Use, IEEE 1980 Annual Conference on Nuclear and Space Radiation Effects, Transactions on Nuclear Science, Vol. NS-27, No. 6, December 1980, p. 1801 - 1809.
2. Staskus J.V. and Berkopce F.D., Proceedings of Spacecraft Charging Technology Conference 1978 (NASA Conference Publication 2071, AFGL-TR-79-0082) U.S. Air Force Academy Colorado Springs, Oct.-Nov. 1978, p. 457-484.

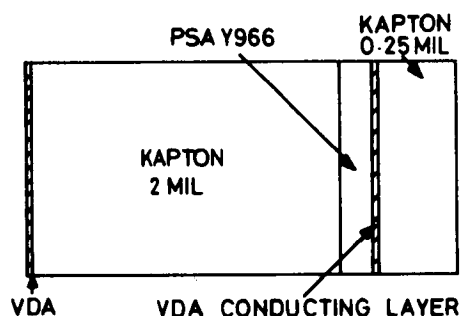


Figure 1. Prototype Version of the Multilayer Thermal Blanket.

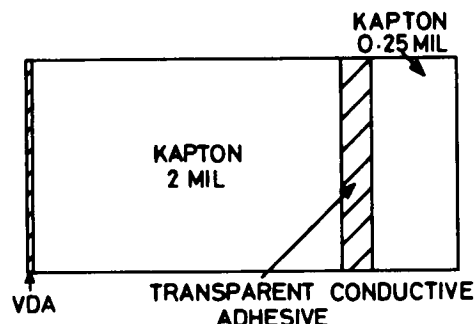


Figure 2. An Example of the Improved Version of the Multilayer Thermal Blanket.

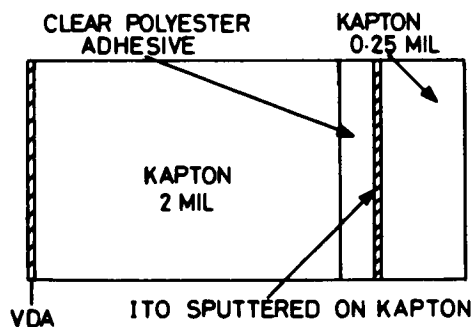


Figure 3. A Further Example of the Improved Version of the Multilayer Thermal Blanket.

## **CHARGING CONTROL TECHNIQUES\***

**R. E. Schmidt**  
**General Electric Company**

### **SUMMARY**

Transparent conductive thin films of indium oxide and indium-tin oxide are evaluated for their properties to control charge buildup on satellite materials. Both oxide coatings are evaluated for their uniformity, stability, reproducibility and characteristics on various substrate materials such as FEP Teflon, Kapton, and glass.

Testing of the coated and uncoated satellite materials have been tested in 30cm square sizes. The materials performance have been characterized in multiple energy electron plasma environment and at low temperatures.

Grounding techniques for application to the coated multi-layer insulation (MLI) blanket designs and OSR arrays have been fabricated in the larger areas and tested under electron irradiation to evaluate their performance.

### **INTRODUCTION**

The application of transparent conductive thin films to external spacecraft dielectric materials has been demonstrated on a small scale and shown to perform satisfactorily in simulated geosynchronous plasma charging environments. (Ref. 1) Several metal oxides have been evaluated using a number of deposition techniques including conventional vapor deposition, and RF and DC sputtering. Thin films of indium tin oxide (ITO) deposited using magnetron sputtering techniques has been found to provide the most stable conductive transparent coatings on spacecraft materials. Developmental work on coatings of indium oxide (IO) have also shown promise but have not been carried as far as the ITO. The work described in this paper represents some of the process development toward the optimization and characterization of these thin semiconductor oxide coatings and the evaluation on larger sizes performed for qualification for use on thermal control satellite materials

### **PROCESS DEVELOPMENT**

The development efforts on the process characterization concentrated on

---

\*This work was supported by the AFWAL, Materials Laboratory under Contract F33615-78-C-5119

determining the allowable variation in the process and coating parameters and still achieve highly transparent and conductive coatings on large sample sizes up to 30cm square. These process development characterizations considered deposition rate, reactive oxygen partial pressure and in situ biasing, coating thickness, uniformity, and a comparison between IO and ITO. This development has been evaluated in terms of the coating's solar absorptivity, surface resistance, stability of its shelf life, stability to tape and rub tests, and charge control performance under simulated substorm environments.

Thin conductive films of indium tin oxide (ITO) and indium oxide (IO) were evaluated on three types of substrates typical of external satellite dielectric materials. The materials considered were silvered and uncoated 125  $\mu\text{m}$  (5 mil) FEP Teflon, aluminized and uncoated 75  $\mu\text{m}$  (3 mil) Kapton and silvered and uncoated glass tiles. These materials represent flexible second surface mirror materials, external multilayer blanket insulation material, optical solar reflectors (OSR) and solar cell coverglasses.

The depositions of the semiconductor oxides onto the substrate materials were made by reactive magnetron sputtering in a Varian 3120H sputtering system using planetary fixture. The reactive deposit is accomplished by sputtering from the indium or indium-tin metal target in a partial pressure oxygen atmosphere. Magnetron sputtering has been found to be a cooler process as compared to conventional vapor deposition techniques. This is an important factor for depositions onto thermally sensitive materials such as Teflon.

#### Deposition Rate, Thickness

Best results were obtained by slowing the deposition rate down to about 1A/sec and using an oxygen/argon gas flow ratio of about 1/3 to 1/4. The combination of the slower deposition and reduced oxygen partial pressure gave highly transparent films which were uniformly conductive across the 30cm square sheets of FEP Teflon and Kapton. The low deposition rate in combination with an in situ RF power applied to the sample holder resulted in an improved coating oxidation. Because of the relatively low melting temperature of the indium-tin target only about one percent of the available magnetron power was used during the deposition. Operation at higher power levels had the tendency to raise the temperature of the target and increase the probability of melting the metal target and electrically shorting the magnetron.

The oxygen/argon ratios were evaluated using a constant value for the oxygen flow rate of about 8cc/min into the chamber which corresponds to a partial pressure of about 53mN/m<sup>2</sup> (0.4m Torr.). Reactively sputtering at 1A/sec, thickness of 200A, 300A, 500A, 800A, 1000A and 5000A were deposited during different runs with the deposition time being the only variable. All of the coatings were done with an in situ RF field of about 250 watts applied to the planetary fixture. 30cm square sheets of FEP Teflon, and Kapton and 12 one inch square tiles of microsheet were mounted onto the planetary during a typical run. Table 1 shows the relative surface resistance and optical properties of the ITO coatings as a function of coating thickness and oxygen/argon relative abundance. There does not appear to be a strong dependence between surface resistance and coating thickness. However, as the partial

pressure of oxygen flowing in the system is reduced, a definite increase in coating conductivity is observed, implying less oxidation and creation of a higher concentration of conduction electrons in the film. Furthermore, while the coating thickness had little effect on coating conductivity, the effect on the optical properties was more pronounced. Figure 1 shows the effect of the coating thickness on the spectral response of the transmittance through the coated microsheet. These values are for the higher resistance coatings in Table 1.

In addition to the SSM applications of the ITO, two coatings were applied to solar cell coverglass to evaluate their effect on cell performance. Figure 2a shows the I-V performance curve of the 2cm by 4cm solar cell before and after deposition of a 300Å coating of indium tin oxide. The curves indicate about a 20% decrease in power at the peak power point. (.109 watt to 0.87 watt) as a result of the coating. The sheet resistance of the conductive coating was measured to be about  $1K\Omega/\square$ . The coverglass was bonded to the cell with Sylgard 182 and tested in a large area Pulsed Solar Simulation (LAPSS) facility.

Figure 2b shows the IV performance curves of a typical 2cm by 4cm solar cell before and after the deposition of a 100Å thick ITO coating. The curves for the 100Å ITO coated coverglass indicates about a 2% decrease in power at the peak point (0.005 watt to 0.113 watts). The transmittance of the 100Å ITO coated coverglass was  $R = 0.120$  and  $T = 0.868$  for an absorptance of 0.01, an increase of less than 1% over the uncoated coverglass. This represents a significant reduction with coating thickness. The effect of the coating observed in both cells was primarily a decrease in the closed circuit current with little to no effect on the open circuit voltage.

### Substrate

A definite dependence of the surface resistance on substrate material is shown in Table 2 with the harder substrates such as Corning 0211 microsheet glass having the highest conductive coatings, while the coatings on the FEP Teflon consistently had a high surface resistance for all of the thicknesses deposited. The amount of variation observed in the surface resistance of the indium tin oxide coatings on glass was found to be highly dependent upon the coating thickness and independent of the oxygen-argon settings. The typical standard deviations decreased from about 50% of the average value of the 100Å coatings to about 10% for the 500Å coatings. In contrast, the standard deviation in the surface resistance of the ITO coatings on the 75  $\mu\text{m}$  (3 mil) Kapton was typically greater than 50% of the average value. Unlike the glass substrate, there was no consistent decrease in the variance with the thicker coatings on the Kapton. The FEP Teflon substrates showed a large variance in surface resistance in relation to the mean value reported in the Table. In all cases, the standard deviation of measurements across the 30cm samples was as large as and in some cases up to two times the average of the measured values.

## IO vs ITO

Initial indium oxide (IO) coatings were deposited by reactive vapor deposition and showed significantly higher surface resistances compared to the ITO coatings deposited by magnetron sputter. They also required post deposition heat treatment to improve the transparency of the deposited films. The increased oxidation during this post deposition treatment resulted in the increased transparency as well as, an increased surface resistance. It also produces the additional undesirable side effect of curling the edges of the polymer substrates, particularly on the FEP Teflon. Since reactive deposition of ITO from an indium-tin target was not attempted using resistive heating techniques, it was not clear whether the magnetron sputtering technique is a preferred technique or that ITO is a superior performance coating. Therefore, a similar process development was undertaken to evaluate indium oxide coatings. The initial coatings were applied in a thickness of 500Å using an RF bias on the sample holder for improved coating oxidation and stability. Transparent conductive coatings were obtained using only slightly different deposition parameters (particularly the O<sub>2</sub>/Ar ratio) than the ITO and required no post deposition heat treatment.

Because of the relative ease of using DC biasing techniques as compared to RF biasing, a DC Power source was used in place of the RF source. The result was that thin conductive transparent indium oxide coatings were deposited on microsheet, Kapton and FEP Teflon substrates with resulting electrical and optical properties as good as was obtained using the RF bias.

Substrates of glass and FEP Teflon were coated with thin coatings of IO and ITO in order to compare the two coatings in their optical and electrical properties in addition to their relative stabilities. The deposition of both oxides were made in thicknesses between 100Å and 300Å according to the quartz crystal monitor (QCM) which was set to their respective densities. Slightly different argon and oxygen flow rates and partial pressures were used to deposit the IO and ITO coatings. Both coatings were deposited using a DC bias on the sample planetary. It was found that in general, a slightly higher oxygen flow rate and partial pressure was necessary to deposit coatings of IO compared to the values required to deposit ITO coatings with similar optical and electrical properties. Table 3 summarizes the coatings which were made and their respective surface resistances which were measured immediately after the deposition.

The surface resistance of IO and ITO coatings from selective runs defined in Table 3 were remeasured after about four weeks. Comparison of measurements on coated samples from run numbers 1, 3, 5, 7, 10, 11, and 13 indicated similar changes in surface resistances for both IO and ITO coatings. In the case of the higher resistance ITO coatings (relative to the other values) deposited during runs number 1 and 3 resistance decreased by factors of 10 and 2 respectively, while for the other IO and ITO coatings the second surface resistance measurements were in general, 2 to 3 times higher. Therefore, both coatings seem to have comparable short term shelf life stability with comparable surface resistances for the same coating thickness.

## QUALIFICATION TESTING

The materials testing discussed in this section cover a wide range of end-user concerns for application of the IO and ITO coated polymers and glass substrates. These include shelf life, humidity, thermal, vacuum, handling, grounding, ionizing radiation in addition to the performance under electron irradiation simulating the geosynchronous plasma environment.

### Stability

Surface resistance and reflectivity measurements were taken on a group of IO and ITO coated samples which had been metalized on the back surface. For both the indium oxide and indium-tin oxide coatings, the surface resistances were in the range of 1 to 10k $\Omega/\square$  with the 300A coatings having the lower samples during the month of close evaluation.

Several large 30cm square samples of indium tin oxide and indium oxide coated Kapton and FEP Teflon which had been prepared early in the program were inspected and remeasured to determine their shelf life surface resistance. The coated samples came from two sets of depositions conducted in October, 1978 (ITO) and April, 1979 (IO). Surface resistance measurements were made across the 930cm<sup>2</sup> area of four sheets of the IO and ITO coated samples and the range of readings reported in Table 4. The values shows very little change in the surface resistance of both the IO and ITO coatings. All the materials had been kept between tissue paper to keep them clean and stored in large envelopes in open laboratory cabinets.

### Humidity and Temperature

Another group of samples containing all six types of substrates and coatings were suspended over a large container which was partially filled with water. The container was then covered and placed in an oven which was maintained at a temperature of about 40°C. The reflectivity of the samples were measured after 3 days and are shown in Table 5. Additional measurements were not possible because of peeling of silvered backing on the glass and FEP samples. Surface resistance measurements on two sets of samples used in the humidity/temperature test are shown in Figure 4. The behavior of the coating surface resistance as a result of the higher temperature and humidity was found to be very dependent upon coating thickness and independent of the substrate. The curves indicate a large increase in the 100A coating compared to a high stability in the 200A and 300A thicknesses. The ITO exhibited larger variations than the IO coatings at the lower thickness. However, the variation in surface resistance during the two to three week exposure of all the coatings remained well within the allowable range for charge control surface properties.

### Handling

A series of handling tests were performed on a 200A thick IO coated aluminized Kapton film. The tests were done to simulate several of the operations which the blanket material might experience during a typical

fabrication operation. A 30cm x 30cm sample was cut up into 2.5cm x 10cm strips for the purpose of this test. The magnetron sputtered coating had a surface resistance of about  $2K\Omega/\square$ . The results are shown in Table 6. The following discussion describes each test.

Crease Test - The strip was bent  $+180^\circ$  with the IO coated side out. The crease was completed by pressing the bend together between the fingertips. The surface resistance was measured before and after the bend. A second strip was then creased in a  $-180^\circ$  bend.

Tape Test - A 1.25cm wide Scotch Brand utility tape from 3M was pressed across the 2.5cm wide coated sample strip and removed. The surface resistance across the area was measured before and after the test. The tape was applied a second time and remeasured.

Rub Test - A 2.5cm wide strip of coated Kapton film was first rubbed with a dry Q-tip for about 10 seconds. A second test was performed with a wet Q-tip soaked in isopropyl alcohol.

Roll Test - A 2.5cm wide strip of coated Kapton was stretched with the coated side facing out over a 0.8cm diameter dowel with 180gm mass attached to the other side for tension. The strip was then slid over the dowel several times and the surface resistance measured periodically.

Thermal Cycle - A 2.5cm wide strip was alternately placed in a dewar of liquid nitrogen and removed and brought back to room temperature. The room temperature resistance of the coating was recorded after each LN<sub>2</sub> cycle.

### Ionizing Radiation

The effect of ionizing radiation on the IO and ITO coatings were evaluated by placing 5cm wide strips of coated Kapton and FEP Teflon in a Gamma Cell model 220. The Cobalt 60 radiation source provided 1.7 and 1.33MeV photons at a flux of about 4.5Krad/min. Because of the ionizing effect of the radiation on air, the test was performed with the samples in a nitrogen gas purged cell. The radiation exposure was performed in 100 hour increments with visual inspection and surface resistance measurements between each increment. The samples were suspended between ends of an 8 inch diameter by 10 inch long cylindrical test cell and removed for each resistance measurement. Since FEP Teflon becomes brittle under this exposure, the surface resistance was measured in situ across the two ends through a piece of 1.25cm wide 3M conductive copper tape bonded to each end. Table 7 summarizes the coating performance after 700 hours of exposure. As seen from the data, the IO and ITO are stable under the ionizing radiation exposure.

### Electron Irradiation

The characteristics of the larger uncoated and coated thermal control materials were tested in GE's large ESD test facility. The primary feature of this 1.3m diameter by 2.1m long vacuum test facility shown in Figure 5, is its dual beam electron flood gun capability. Each gun is capable of simultaneous irradiation of test specimens mounted at the opposite end of the chamber with electron energies from 0.5KeV up to 40KeV and at current densities in excess of  $10nA/cm^2$  or as low as desired. The vacuum test facility uses a combination of cryogenics and turbomolecular pumping to achieve a nominal operating vacuum in the low  $10^{-4}N/m^2$  (high  $10^{-7}$  Torr) range.

The interior of the system is shrouded with a high permeability foil for reduced interference from external magnetic fields. The vacuum is monitored with an ion gauge which is turned off during measurements to prevent photo emission effects from the gauge filament. A viewing port on the side of chamber which is normally covered is used for sample viewing and photographic recording of any ESD phenomenon.

All test samples and diagnostics are mounted on the "swing away" door of the vacuum chamber. The platform for the samples and all diagnostics is a 91cm by 91cm grounded aluminum panel mounted on the inside of the chamber door. This allows for easy access to samples requiring complicated handling techniques. The 91cm square platform allows for simultaneous measurement of the performance of up to four 30cm square samples.

The diagnostics system was assembled to measure the charge control characteristics of flat 30cm square samples of conductively coated polymer films. The 30cm (1 foot) square samples are mounted to aluminum plates which are electrically isolated from the mounting table with Teflon spacers. A square aluminum ring is placed around the perimeter of the sample exposing a 29cm square. This electrode holds the sample in place and is used to measure any surface currents. A schematic of the sample configuration is shown in Figure 6. Keithley 410 picoammeters are connected between the back plate and surface ring and ground to measure displacement and surface currents. The schematic also shows the rotary arm whose axis is at the center of 91cm table. A Faraday cup mounted to a moveable carriage on the arm is used for measuring the current density across the sample. A Trek electrostatic surface voltmeter probe is also mounted on the rotary arm carriage for measuring surface potentials up to 20KV anywhere on the surface.

To provide a data base line for comparison with coated materials two 30cm (12") square uncoated sheets of 5 mil FEP Teflon and 3 mil Kapton were tested simultaneously under electron irradiation. The two samples were tested in an electron beam up to 16KeV at an average current density of about  $2\text{nA/cm}^2$ . Table 8 shows the surface and bulk currents and surface potentials as a function of incident electron energy. Surface discharges became so frequent at this current density above 16KeV that no additional measurements were made.

The surface potential of both materials rises nearly linearly with incident electron energy. The bulk currents of both materials increased significantly with respect to the surface current at the incident energies above 8KeV with the largest increases in the thinner Kapton. The discharge rates were not recorded for these measurements.

Another series of exposures of these two uncoated samples were made using both electron guns to show the charging control influence of the lower energy electrons. Each surface was irradiated for several minutes before steady state current readings and surface potential profiles were recorded. Table 9 summarizes these steady state measurements.

The variation of surface potential with incident electron energy or combination of energies shows the controlling influence of the lower energy



electrons when they are allowed to predominate. Not shown here is the long time constant and relative intensities required of the lower energy electrons to effectively discharge a precharged surface, particularly at the higher voltages.

In contrast to these currents and surface voltages 200Å thick ITO coatings on 30cm squares of 75µm Kapton and 125µm FEP Teflon were tested under similar conditions of energy and density. The surface resistance of both samples were measured before mounting and were in good agreement with the values reported in Table 2. Table 10 summarizes the surface and conduction currents through the ITO coated materials. A change of direction in the bulk current was observed in the thin Kapton between 1 and 2KV due to the materials secondary emission variation over this voltage range. It should be noted that this reversal was not observed in the uncoated materials.

Similar measurements were recorded on 100Å and 200Å IO coatings with similar results. Following stabilization of the currents the Trek probe was swept across the samples while the beam was on. Before and after each sweep the probe calibration was checked over a grounded plate. No significant surface potentials were recorded in any of the measurements on any of the coated materials. Typically surface potentials of the coated polymers were below -10V during radiation and returned to zero when the beam was turned off.

#### GROUNDING

A 30cm X 30cm sheet of IO coated aluminized 50µm thick Kapton was used in the assembly of a conventional multilayer insulation (MLI) blanket to evaluate the utility of conventional blanket grounding techniques. The indium oxide coated Kapton had a surface resistance of about  $2K\Omega/\square$  across the transparent coating. The MLI covered with the transparent conductively coated aluminized Kapton consisted of about 20 layers of alternating doubly aluminized 6µm (0.25 mil) thick mylar and dacron mesh.

The whole assembly was grounded with a Z shaped aluminum foil, which was laid in contact with each aluminized surface, on one edge of the blanket as shown in Figure 7a. The top flap of the Z foil aluminum strip was placed in contact with the indium oxide coating. At the bottom flap of the Z foil a strip of conductive metal velcro was attached. The whole assembly was then sewn together with a dacron thread. The grounding Z foil was about 5cm (2") in width. A similar Z foil was sewn on the same side but opposite corner of the blanket in order to facilitate hanging the blanket for subsequent ESD testing. This second Z foil used a standard cloth type velcro rather than the conductive hook used for ground. The strip of conductive metal velcro was attached to the top of the test sample holder shown in Figure 7b. The velcro was attached to the aluminum plate using Eccobond 57C and the blanket was suspended from the velcro strip. The surface ring with teflon tape on the back side to isolate it from the IO coating was placed over the blanket to prevent irradiation of the exposed blanket edges. The back plate sample holder and masking ring was then connected to ground through Keithley 410A picoammeters. In this configuration the resistance of the IO coating to ground was measured to be within  $50K\Omega$  to  $75K\Omega$  from anywhere on the top of the blanket.

The blanket assembly was then tested in an electron plasma with an average current density of about  $0.5\text{nA/cm}^2$ . The electron energy was varied between 1KeV and 20KeV and the bleed off current from the IO coating to ground was recorded for several minutes at each energy level. The total bleed off current through the ground connection was approximately  $0.5\mu\text{A}$ . The Trek electrostatic voltmeter probe was swept across the center of each sample after about 5 minutes of irradiation at each energy level while the electron plasma was still on. No surface potential above 10 volts was observed.

Two OSR arrays of uncoated and IO coated SSM tiles were tested in a 30cm X 30cm array to evaluate the scaled up grounding technique for the coated tiles.

These coated tiles were bonded to a 30cm square 1mm thick alodined aluminum panel using RTV 566 and 567 loaded with 12% graphite fiber to provide a ground for the IO coating as shown in Figure 8a. A diluted SS 4155 primer was applied to both the aluminum and silvered microsheet OSR surface as is the usual procedure to improve the bonding strength. The average resistance between the top of the coated OSR and the aluminum panel was measured for all 144 tiles to the 44K with a maximum and minimum values of  $410\text{K}\Omega$  and  $140\Omega$ . The tiles were bonded to the aluminum panel using standard vacuum bagging techniques for a uniform pressure application. The 12 by 12 array of IO coated and silvered 0211 glass tiles were mounted in the ESD facility along with a 12 by 12 array of uncoated silvered 0211 glass. The uncoated array was also bonded to an aluminum panel with graphite fiber loaded RTV 566 adhesive. Figure 8b shows the placement of the two OSR panels in the chamber. An aluminum ring insulated on the back was placed over the samples for holding them in contact with the back plate used to measure the ground current. The surface ring was also attached to ground. One row of glass tiles along an edge of the uncoated array was unsilvered in order to evaluate the possible effect of any discharges or current through the glass on the bond with the conductive adhesive.

The samples were irradiated simultaneously by electrons between 1KeV and 16KeV at current densities of about  $1\text{nA/cm}^2$ . Higher energies were not used due to incidence of violent discharge on the uncoated sample. Table 11 summarizes the measured currents and maximum surface potential from the two samples. The measured surface potential on the uncoated array during the 16KeV irradiation is lower than that measured during the 12KeV irradiation, due to the large fluctuations in the surface potentials occurring during the larger discharges. The notation on the uncoated ground currents illustrate the increasing discharges both in magnitude and frequency with increasing electron energy. The surface potential on the array of IO coated OSR's never exceeded 10 volts negative.

## CONCLUSIONS

Highly stable, low resistance, low absorptance thin coatings of indium-tin oxide and indium oxide have been successfully and repeatedly deposited on flexible and glass thermal control spacecraft materials. Reactive magnetron sputtering from a metal alloy target has been shown to provide very repeatable depositions. The results show that optimum transmission and

solar reflectance and performance in a radiation environment can be obtained only by minimizing the coating thickness. The optimal thickness for a particular application must be determined by balancing the deposition capability and handling characteristics with a resistivity and solar absorptivity stability sufficient to achieve charge control.

Storage, handling and environmental testing indicate that 200A coatings can be reproducibly deposited and provide highly stable semi-conducting properties with solar absorptances of less than two percent. The coatings applied to glass, FEP Teflon and Kapton substrates can be tailored to the low kilohm/square range. Because of the nature of the sputtering process, particularly for non-dedicated systems, exact values of the process variables cannot be specified. However, the general dependence between the process variables and coating properties have been established.

All radiation measurements of the coatings under simulated sub-storm conditions have exhibited the characteristics of stable charge control. Measurements of surface potentials during and after irradiation by electrons up to 30KeV and ionizing gamma radiation show an effective stable grounding surface.

#### REFERENCES

- 1 Eagles, A. E., Amore, L.J., Belanger, V.J., Schmidt, R. E.; Spacecraft Static Charge Control Materials; AFML-TR-77-105, Part II, 1978.
- 2 Schmidt, R. E., Charging Control Satellite Materials: AFWAL-TR-80-4017, Part I, 1980.

TABLE 1. COMPARISON OF COATING THICKNESS AND O<sub>2</sub> RELATED PRESSURE

DEPOSITION THICKNESS o (A)	OXYGEN/ARGON FLOW RATE							
	8/24				8/28			
	R	T	A	SURF. RES. (K $\Omega$ )	R	T	A	SURF. RES. (K $\Omega$ )
200	.14	.82	.04	530	.12	.87	.01	9.1
300	.17	.78	.05	1900	.18	.80	.02	6.4
500	.17	.77	.06	127	.17	.76	.07	2.1
800	.17	.77	.06	5600	.15	.76	.09	1.3
1000	.15	.77	.08	735	.15	.77	.08	4.0
5000	.13	.71	.16	70	.14	.71	.15	11.2

Table 2 Average Surface Resistance of ITO Coated Substrates

Thickness o (A)	Oxygen: Argon Flow Ratio = 1:35			Oxygen: Argon Flow Ratio = 1:4		
	Glass	Kapton	PEP Teflon	Glass	Kapton	PEP Teflon
100	331	1330	$207 \times 10^3$	4.7	292	$14.3 \times 10^3$
	59	2960	$10^6$	11.0	65	$8.8 \times 10^3$
200	8.5	532	$13 \times 10^3$	1.1	10	$6.7 \times 10^3$
	6.4	492	$7.8 \times 10^3$	1.5	31	$10.8 \times 10^3$
300	1.22	134	$3.3 \times 10^3$	2.1	340	$12.7 \times 10^3$
	0.84	304	$2.23 \times 10^3$	1.2	26	$3.1 \times 10^3$
500	1.53	633	$4.8 \times 10^3$	1.0	299	$2.9 \times 10^3$
	1.47	88	$6.1 \times 10^3$	0.54	8.0	$5.4 \times 10^3$
				0.72	5.0	$1.5 \times 10^3$

TABLE 3. IO AND ITO COMPARISON

RUN #	SUBSTRATE	SIZE (cm x cm)	THICKNESS (Å)	COATING	SURFACE RESISTANCE ( $\Omega$ )
1	Glass	2.5 x 2.5	100Å	ITO	140 K
	FEP Teflon	2.5 x 5	100Å	ITO	9 Meg
2	FEP Teflon	15 x 15	100Å	ITO	500 K - 5 Meg
3	Glass	2.5 x 2.5	200Å	ITO	20 K - 100 K
	FEP Teflon	2.5 x 5	200Å	ITO	30 K - 40 K
4	FEP Teflon	15 x 15	200Å	ITO	20 K - 80 K
5	Glass	2.5 x 2.5	300Å	ITO	3 - 3.5 K
	FEP Teflon	2.5 x 5	300Å	ITO	5 K
6	FEP Teflon	15 x 15	300Å	ITO	3 - 10 K
7	Glass	2.5 x 2.5	100Å	IO	12 - 18 K
	FEP Teflon	2.5 x 5	100Å	IO	65 - 140 K
8	Glass	2.5 x 2.5	100Å	IO	14 K
	FEP Teflon	2.5 x 5	100Å	IO	80 K
9	FEP Teflon	15 x 15	100Å	IO	35 K - 85 K
10	Glass	2.5 x 2.5	200Å	IO	4 - 6 K
	FEP Teflon	2.5 x 5	200Å	IO	6 - 10 K
	FEP Teflon	15 x 15	200Å	IO	8 - 16 K
11	Glass	2.5 x 2.5	300Å	IO	1.2 K
	FEP Teflon	2.5 x 5	300Å	IO	1.5 K
12	FEP Teflon	15 x 15	300Å	IO	.9 - 1.5 K
13	Glass	2.5 x 2.5	500Å	IO	.5 - .7 K
	FEP Teflon	2.5 x 5	500Å	IO	.4 - .5 K
14	FEP Teflon	2.5 x 5	500Å	IO	.4 - .7 K

TABLE 4. LONG TERM ITO AND IO COATING STABILITY

SUBSTRAT	COATING	THICKNESS (Å)	INITIAL $R_s$ (K $\sim$ )	SHELF LIFE (Months)	SURFACE RESISTANCE (K $\sim$ )
KAPTON	ITO	100	10	22	10-50
		200	20	22	20-490
KAPTON	IO	100	15	16	3-5
		100	8	16	3-8
FEP TEFLON	ITO	100	$1.4 \times 10^4$	23	$3 \times 10^4 - 2 \times 10^6$
		200	$1.2 \times 10^4$	23	$1 - 2 \times 10^6$
FEP TEFLON	IO	100	$2 - 50 \times 10^4$	17	$7 \times 10^4 - 30 \times 10^4$

TABLE 5. COATING STABILITY UNDER HUMIDITY TEST

Coating	Substrate	Coating Thickness (Å)	REFLECTIVITY	
			Initial	3 Days of Humidity
ITO	Glass/Ag	0	0.92	-
		100	0.90	0.88
		200	0.88	-
		300	0.86	0.84
	FEP/Ag	0	0.86	-
		100	0.85	0.85
		200	0.82	-
		300	0.80	0.82
	Kapton/Al	0	0.37	-
		100	0.37	-
		200	-	-
		300	0.35	-
IO	Glass/Ag	0	0.92	-
		100	0.86	0.85
		200	0.84	-
		300	0.81	0.79
	FEP/Ag	0	0.86	-
		100	0.81	0.82
		200	0.78	-
		300	0.76	0.76
	Kapton/Al	0	0.37	-
		100	0.37	-
		200	0.34	-
		300	0.29	-

TABLE 6. IO COATING HANDLING TESTS

TEST	PRE TEST RESISTANCE (KΩ)	POST TEST RESISTANCE (KΩ)
CREASE +180°	3	1.5 x 10 <sup>6</sup>
CREASE -180°	5	330
TAPE 1st	2	4
TAPE 2nd	4	6
RUB-DRY	2	9
RUB 1st WET	3	22
RUB 2nd WET		70
ROLL 3	2.5	3.0
10	--	3.2
20	--	3.8
THERMAL CYCLE 1	3	3
2	--	3
3	--	3

TABLE 7. IONIZING PHOTON<sup>\*</sup> EXPOSURE

EXPOSURE (10 <sup>7</sup> RAD)	IO/KAPTON (K~)	ITO/KAPTON (K~)	ITO/FEP (K~)
0	0.62	5.16	625
2.7	0.53	1.68	340
5.4	0.48	1.47	2400
8.1	0.45	1.18	4500
10.7	0.51	2.22	2100
13.4	0.50	1.32	3200
16.1	0.50	1.18	
18.7	0.47	1.39	

\* Cobalt 60- $\gamma$

TABLE 8 UNCOATED FLEXIBLE SUBSTRATE PERFORMANCE UNDER MONOENERGETIC IRRADIATION

ACCELERATING VOLTAGE (KV)	TEFLON (5 MIL)				KAPTON (3 MIL)			
	PLATE CURRENT (nA)	SURFACE CURRENT (nA)	SURFACE VOLTAGE		PLATE CURRENT (nA)	SURFACE CURRENT nA	SURFACE VOLTAGE	
			MIN (V)	MAX (V)			MIN (V)	MAX (V)
1	43	31	0	-11	23	95	-17	-39
2	68	135	-42	-154	30	244	-775	-998
3	18	88	-900	-1140	28	170	-1450	-192
4	14	92	-1738	-2065	22	157	-2400	-2925
5	15	110	--	-3090	24	175	-3300	-4020
6	14	96	-3550	-4000	26	155	-4200	-4960
7	11	100	-4380	-4870	22	152	-4800	-5730
8	15	99	-4850	-5730	38	152	-5270	-6500
10	28	105	-6570	-7800	80	148	-6950	-8420
12	48	102	-7780	-9240	140	143	-7560	-9390
14	48	105	-9300	-10980	167	145	-8230	-9840
16	59	100	-10970	-12480	200	142	-8790	-10770

TABLE 9 UNCOATED FLEXIBLE SUBSTRATE PERFORMANCE UNDER MULTIPLE ENERGY IRRADIATION

RUN #	GUN	V <sub>ACC</sub> (KV)	I <sub>INC</sub> (nA/cm <sup>2</sup> )	TTP TITAN/Ag			KAPTON/Al		
				I <sub>B</sub> (nA)	I <sub>S</sub> /I <sub>B</sub>	V <sub>S</sub> (V)	I <sub>B</sub> (nA)	I <sub>S</sub> /I <sub>B</sub>	V <sub>S</sub> (V)
1	1	1	0.8	6.0	0.42	-6	24.5	0.15	-27V
2	2	1KV	0.8	7.5	1	-6	48.0	0.17	-7V
2A	2	2KV	0.8	5.2	4.1	-324	17.0	1.1	-914
3	1	2KV	0.8	3.1	4.0	-377	7.2	0.75	-976
4	{	1	1.9	15.8	1.0	-10	88	0.44	-176
		2							
5	{	1	1.9	17.0	1.4	-24	92	0.38	-249
		2							
6	1	3KV	0.8	2.3	5.9	-1486	5.9	1.8	-1950
7	{	1	2.6	28.2	0.9	-1478	45.5	0.38	-1916
		2							
8	1	3KV	0.8	1.95	5.4	-1478	4.8	2.1	-1911
9	{	1	1.5	5.8	6.2	-759	18.5	1.6	-1080
		2							
10	1	1	0.8	3.5	0.6	-6	17.4	0.16	-8
11	2	1	0.8	6.5	0.94	-8	40	0.17	-9
12	1	2	0.8	3.3	4.2	-485	14	0.51	-866
13	{	1	1.4	13.4	0.86	-9	69	0.36	-85
		2							
14	{	1	1.4	15	1.1	-72	79	0.37	-130
		2							
15	{	1	1.5	17.5	1.2	-117	90	0.47	-136
		2							
16	1	4	0.8	3.5	3.9	-2610	41	0.23	-2868
17	1	5	0.8	4.3	3.4	-3521	40	0.23	-3742



TABLE 10 SUMMARY OF CURRENT MEASUREMENT ON ITO COATED KAPTON AND FEP  
TEFLON FLIMS

Beam Voltage (kV)	ITO/Kapton (75 $\mu$ m)		ITO/FEP Teflon (12.5 $\mu$ m)	
	Surface Current (nA)	Bulk Current (nA)	Surface Current (nA)	Bulk Current (nA)
1	720	-75	28	32
2	230	52	36	25
3	270	48	40	18
4	800	37	55	13.5
5	1200	29	84	10
7.5	1500	26	110	7.6
10	1600	25	125	7.3
15	1650	24	150	7.8
20	1700	24.5	170	8.8
30	1800	26	210	10.5

TABLE 11 PERFORMANCE CHARACTERISTICS OF 12" X 12" OSR ARRAY

ACCELERATING POTENTIAL (KV)	INCIDENT FLUX <sub>e</sub> (nA/cm <sup>2</sup> )	UNCOATED		COATED (200A I0)	
		GROUND CURRENT (nA)	SURFACE POTENTIAL (V)	GROUND CURRENT (nA)	SURFACE POTENTIAL (V)
1	1.3	27	-30	89	-15
2	0.9	52	-35	187	-10
3	1.1	355	-280	249	-15
4	1.0	305	-950	240	-10
6	1.3	360	-2425	330	-10
8	1.2	395	-4000	375	-10
10	1.0	335 <sup>+</sup>	-6050	360	-10
12	1.1	370 <sup>++</sup>	-7750	420	-10
16	1.3	560 <sup>+++</sup>	-6500	460	-10

<sup>+</sup>10 DISCHARGES/90 SEC (4:10-40nA; 6: 40-50nA)

<sup>++</sup> 9 DISCHARGES/90 SEC (5:10-50nA; 4: 50-100nA)

<sup>+++</sup>27 DISCHARGES/90 SEC (21: 10-50nA; 5: 50-100nA, 1: 100-200nA)

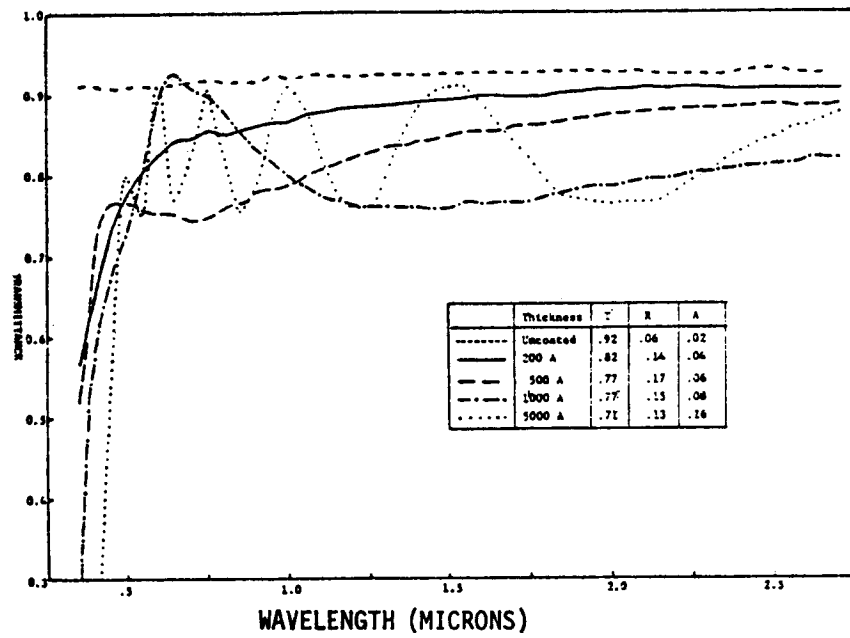


Figure 1. - Transmittance of ITO-coated microsheet.

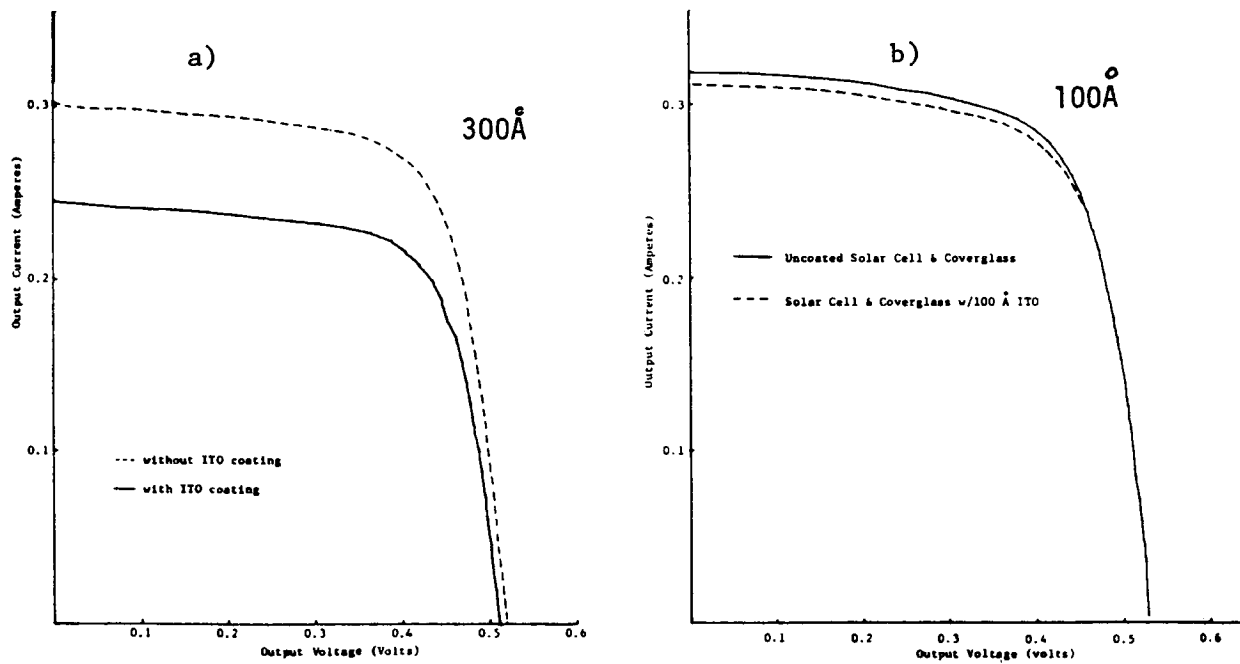


Figure 2. - IV curve of 2-cm x 4-cm solar cell with ITO-coated coverglass.

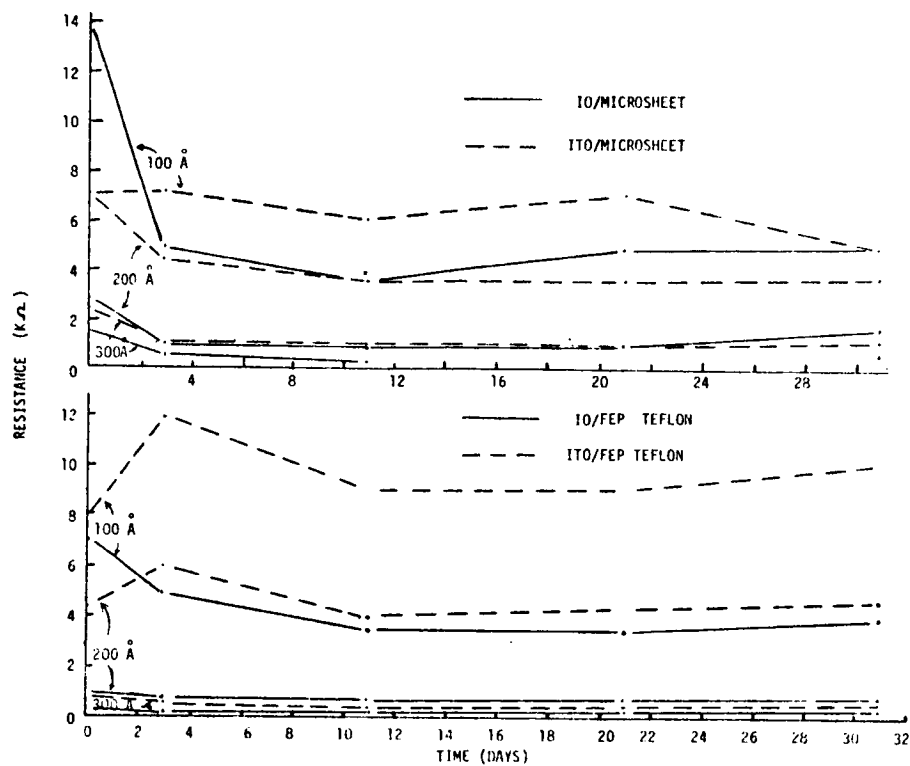


Figure 3. - Surface resistance stability of reference samples.

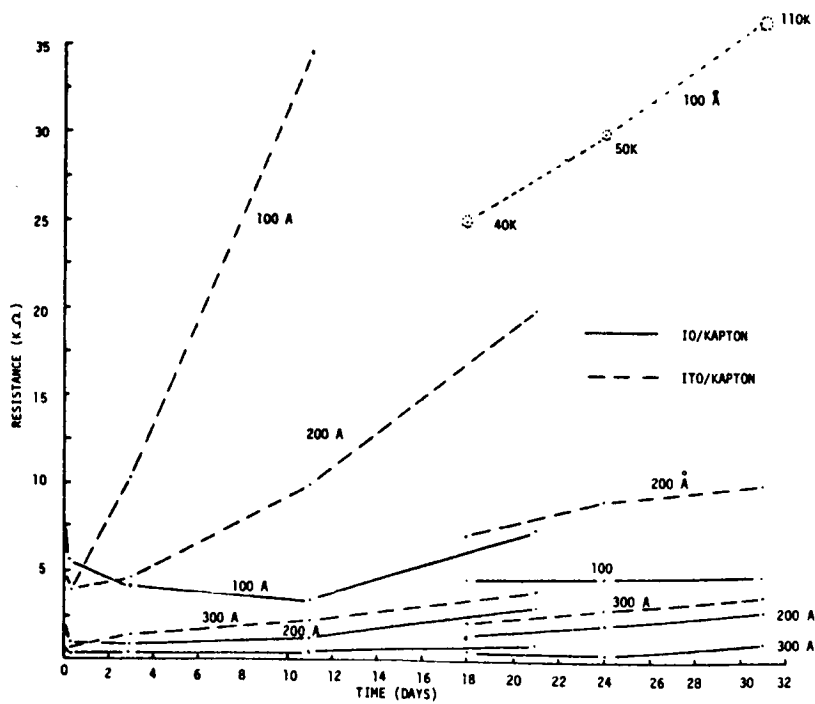


Figure 4. - Typical surface resistance variation during humidity test (Kapton).

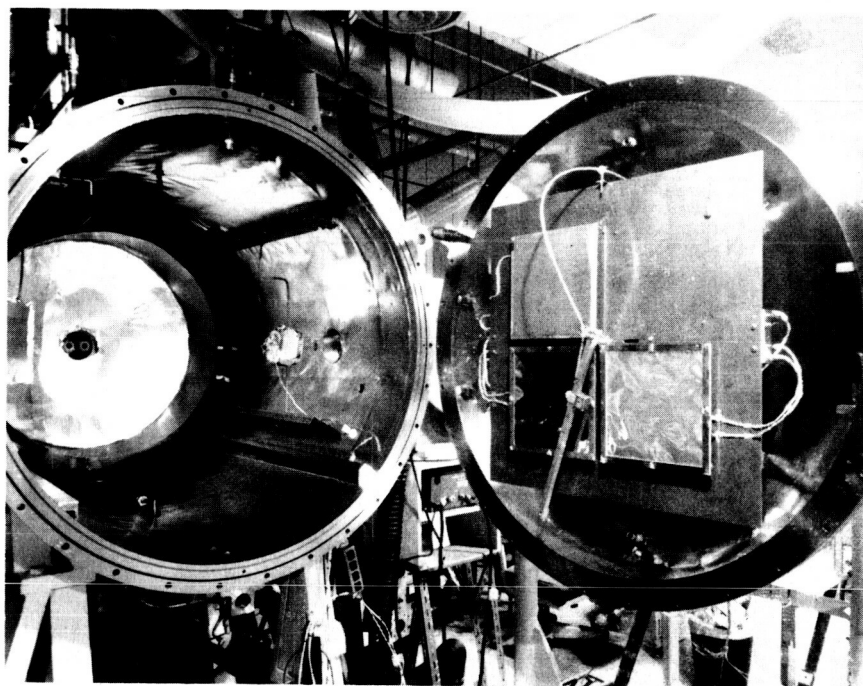


Figure 5. - Sample configuration in test chamber.

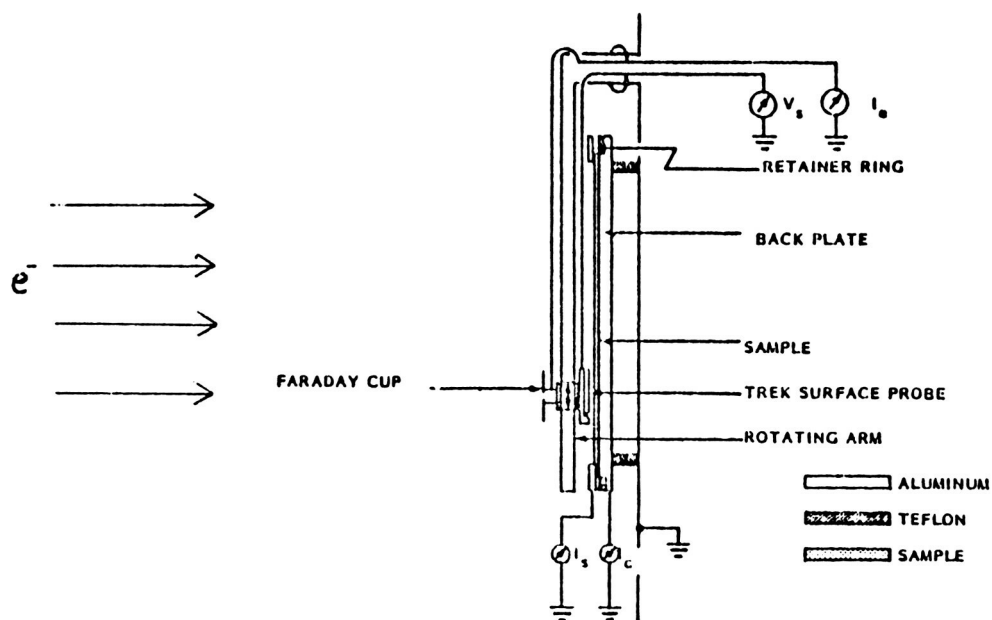


Figure 6. - Sample test configuration.

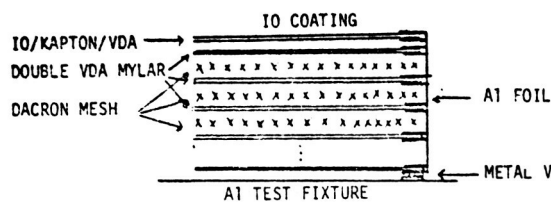


Figure 7a. - MLI blanket grounding.

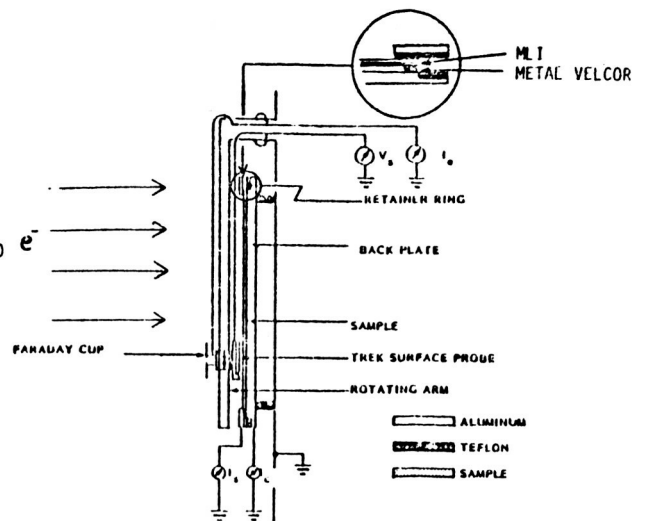


Figure 7b. - Schematic of sample configuration.

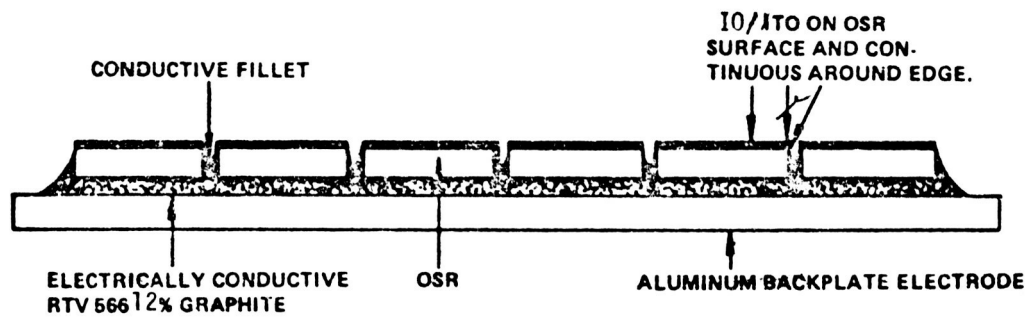


Figure 8a. - Coated OSR array grounding.

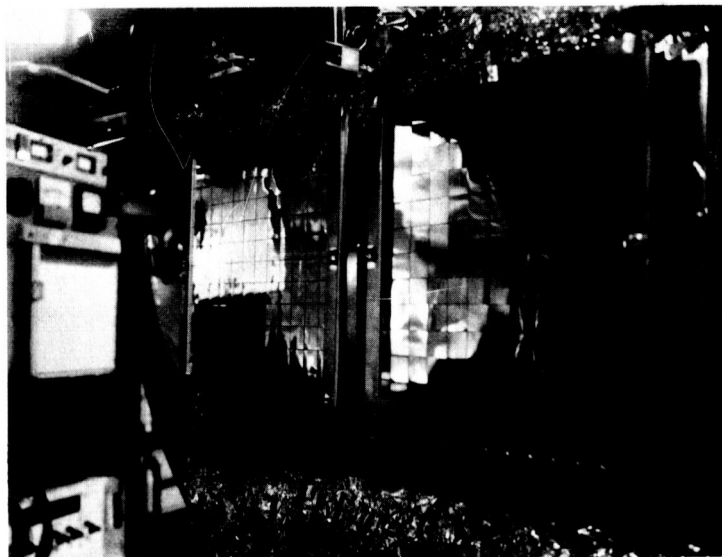


Figure 8b. - Actual OSR test configuration.

## CHARGING CHARACTERISTICS OF SILICA FABRICS\*

Léon Levy and Alain Paillous  
O.N.E.R.A.—Centre d'Etudes et de Recherches de  
Toulouse (France)

### SUMMARY

The charge dissipation mechanism of silica fabrics and FEP/silica fabric/Aluminum composites has been studied by means of various sample configurations that have been tested under mono-energetic electron beams at energies between 5 and 20 keV. Grounding of the aluminum rear face of the composite is necessary in order to ensure a good electrostatic performance. The surface potentials are dependent on the flux rate in the range  $10 \text{ pA cm}^{-2}$  to  $3 \text{ nA cm}^{-2}$ : they are the highest at the lowest flux rate. Strong discharges have been evidenced at 20 keV. They do not occur under 15 keV electrons. A substantial decrease in the surface potential of the sample is observed every time that an irradiation by low energy electrons (2 to 4 keV) is performed simultaneously with the irradiation by medium-energy electrons (10 to 20 keV). Silica fabrics and composites are very sensitive to contamination or contamination-plus-irradiation effects.

### INTRODUCTION

Silica fabrics have been proposed for use as passive thermal control coatings that do not support charge build up under electron bombardment at energies to at least 30 keV with associated current densities in excess of  $30 \text{ nA cm}^{-2}$  (ref. 1).

This excellent behaviour under simulated substorm conditions, has been explained (ref. 2) by a secondary emission conductivity where secondary electrons produced by the primary electron beam are thought to be a cloud of free charges in the voids between the silica fibers within the dielectric material. If that is the case, the charging performance of the quartz fabric ought to be good only if this fabric is directly connected by its back face to a grounded metal plate.

A composite obtained by laminating at  $280^\circ\text{C}$  the quartz fabric with a FEP film and an aluminum foil, has been proposed for use aboard spacecraft, because bonding of the aluminised rear face of

---

\* This work has been supported by the U.S. Air Force Materials Laboratory under grants AFOSR 78-3704 and AFOSR 80-0183.

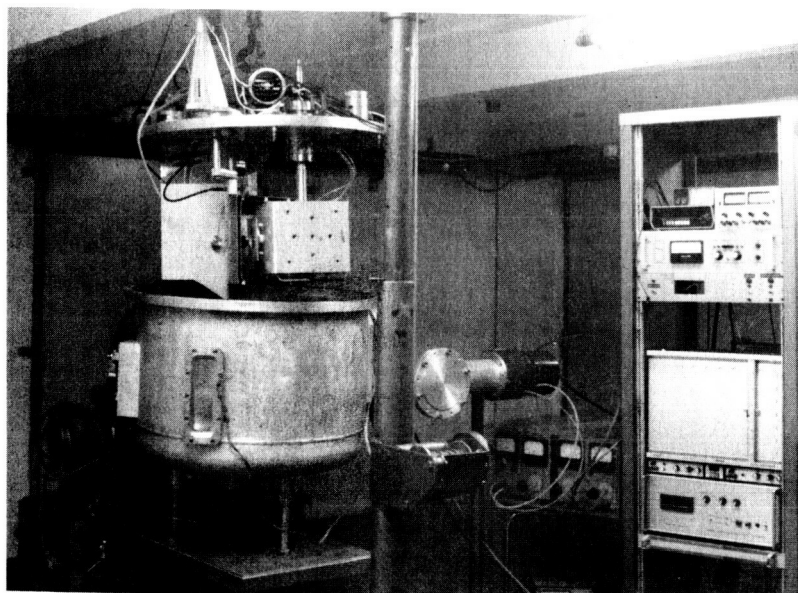
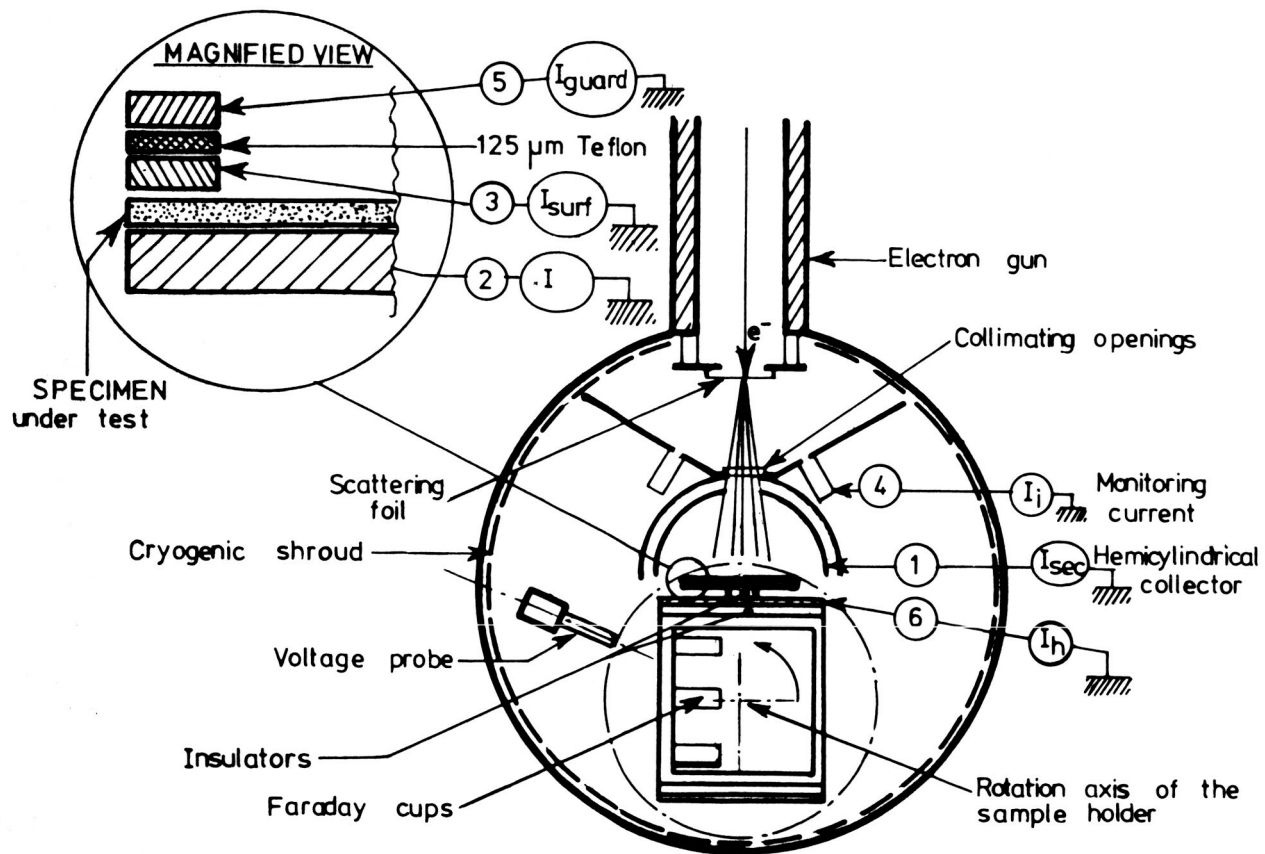


Figure 1 - The "CEDRE" substorm simulation facility

this laminate to the spacecraft structure by means of an adhesive eliminates the problems of adhesive migration and contamination through the fabric (ref. 1).

This composite was said (ref. 3) to have also a good behaviour under electron bombardment (moderate surface potentials, no sudden discharge) in spite of the dielectric nature of the FEP film. It was decided to verify such a behaviour.

Various comparative tests under electron irradiation (in the range of energy 2-20 keV) were performed in order to evaluate the charging performance of diverse configurations all including silica fabrics with or without electrical grounding. Some experiments were also carried out in order to explain the conductivity mechanism of silica fabrics and related composites. Moreover some tests were performed in order to gather data concerning the contamination effect on the charge control performance and a dual electron beam was used so as to assess the experimental validity of results drawn from simulation procedures using a monoenergetic electron beam.

The results of the experiments (that are fully described in ref. 4,5,6) are summarized hereunder.

## MATERIALS

The silica fabric was furnished by AFML/MBE; this material is the 581 Astroquartz lot 98269 heat cleaned at 800°C for 3 hours in air.

The composites were also provided by AFML/MBE: the 581 Astroquartz lot 98369 was heat cleaned in air at 800°C for 3 hours and then laminated at 280°C to an aluminum foil with 1 mil type A FEP Teflon film. Two series of composite specimen that differed by the thickness of the aluminum foil (0.5 mil and 1 mil) were used successively.

## THE FACILITY

Figure 1 is a schematic view of the "CEDRE" (Chambre pour l'Etude des Revêtements sous Electrons) facility used to assess the electrostatic behaviour of dielectric coatings in simulated geosynchronous substorm environment.

Turbomolecular pumping units allow the chamber and the electron gun to be operated at pressure levels less than  $5 \cdot 10^{-5}$  Torr. The main electron accelerator (SAMES manufacturer) works in the range 4 to 25 keV with fluxes up to  $10 \text{ nA cm}^{-2}$  at the sample level. An aluminum foil 1,2  $\mu\text{m}$  thick is used in order to scatter the electrons and to obtain a good irradiation uniformity at the sample.



The sample holder is made up of four plates (200 by 200 mm) each maintained at a constant temperature by a circulating fluid. This holder is sustained by a rotating shaft allowing the presentation of any of the four plates in front of the energetic electron beam. In normal conditions, two faces can receive specimens the two others being used as Faraday cup holder and surface potential measurement calibration system. The irradiated area is restricted at the sample level by use of collimating openings, if it is wished.

The surface potential of specimens is measured by a potential probe (capacitive sensor) moved by a mechanical scanner. A potentiometric system allows the recording on a X-Y plotter of the surface potential profile of the electrically charged coating after that the sample holder has been rotated.

The secondary electrons emitted by the irradiated sample can be measured together with the backscattered electrons by means of a hemicylindrical electrode 1 surrounding the irradiated area and collecting the current  $I_{sec}$  (see Figure 1).

The fixation system of the sample enables to measure the surface leakage current  $I_{surf}$  on a circular ring 3 lying on the sample surface but out of the irradiated area. A circular guard ring 5, electrically insulated from the ring 3 by a 125 micrometer thick FEP film, covers the whole ring 3 and enables to measure the current  $I_L$ . In case of measurements using electrodes 3 and 5, the sample under irradiation is grounded by its periphery; however it is possible to disconnect from the ground the rings 3 and 5 in order to provide a grounding of the sample only by its back face. The specimen is fixed on a metallic plate which is grounded by means of a nanoammeter giving the sum of the volume leakage current plus the capacitor current  $I = I_L + I_C$ . 1, 3 and 5 are also grounded by means of other nanoammeters. All the currents are simultaneously recorded.

Two immovable Faraday cups 4 are used to monitor continuously the electron flux rate during irradiation.

Under certain circumstances, the current ( $I_H$ ) on a metallic plate 6, next the sample but set back from the sample surface, must be measured also.

A second gun enables to irradiate the samples with electrons in the range 2-5 keV. However the implantation of this gun necessitates the removal of the hemicylindrical measurement electrode.

## SECONDARY EMISSION, VOLUME LEAKAGE CURRENT, SURFACE LEAKAGE CURRENT AND POTENTIALS

Secondary emission, volume leakage current and surface

leakage current are the three means by which electrons are likely to escape from a dielectric irradiated by low energy electrons. The knowledge of their relative importance could help to give the best rules of conduct in order to lower the surface potential value and to suppress the arcing risks.

Accordingly, it was decided to evaluate the secondary emission, the volume and surface leakage currents for various sample configurations using silica fabrics and silica fabric/FEP/Aluminum composites.

### Sample configurations

The fixture means and the various electrodes for measurements have been described above. Five samples were used: a) one layer of the quartz fabric in direct contact with the grounded sample holder, b) three layers of the quartz fabric in direct contact with the grounded holder, c) one layer of the quartz fabric insulated from the grounded holder by a FEP film (125  $\mu\text{m}$  thick), d) one layer of the composite (rear aluminum layer in direct contact with the grounded holder), e) one layer of the composite insulated from the grounded holder by a FEP film.

### Procedure

In a first phase, the various samples have been irradiated at one selected beam energy for about 18 minutes with their periphery grounded by the metallic ring as described above. During this period, after fixed times of irradiation (0.5, 1, 2, 5, 10, 18 minutes) the irradiation was stopped and the potential measured. Immediately after this period, without sample discharging, the metallic ring was disconnected from ground for about 10 minutes while the beam conditions were set at the same value. Then an other potential measurement was done.

Four energy levels of the electron beam were used successively: 5, 10, 15, 20 keV with respective intensities 1.25, 0.7, 0.5 and 0.5 nA  $\text{cm}^{-2}$ . At the end of each irradiation stage and before starting the next, the samples were totally discharged by irradiation with low energy electrons (3 to 5 keV).

### Variation with time

a) For a 5 keV electron beam and for all sample types and configurations, the surface potential value is recorded equal (or very near) to zero. All incident electrons are reemitted as secondaries (assuming that the current  $I_g$  collected on the guard ring is in its nature identical with  $I_{\text{sec}}$  collected by the hemicylindrical electrode). The sample-to-holder current  $I$  as well as the leakage current  $I_{\text{surf}}$  are very near to zero.

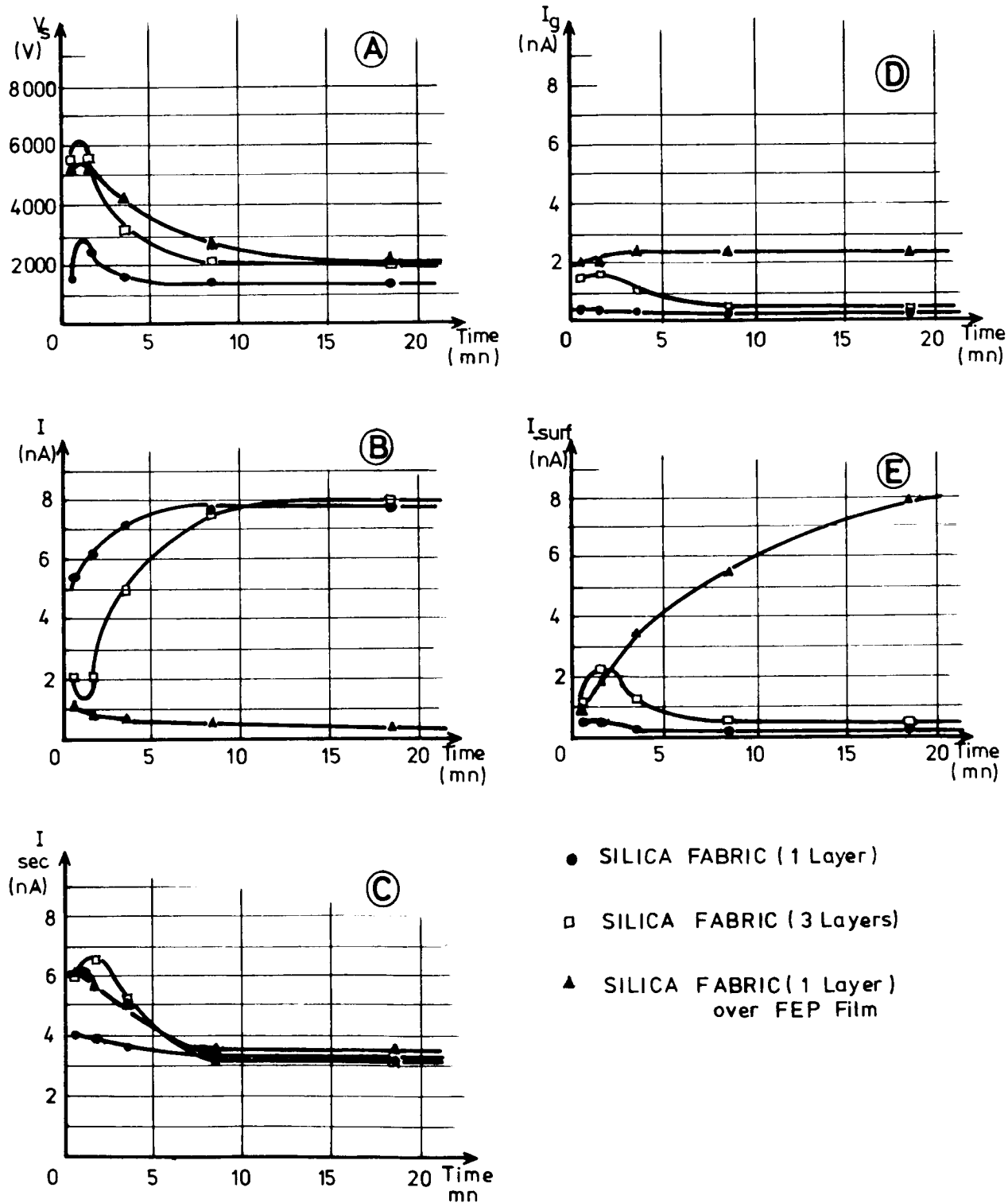


Figure 2: Results of the 15 keV electron irradiation ( $0.5 \text{ nA cm}^{-2}$ )

The electrostatic behaviour here is very independent of the manner the sample is fixed. The interaction of the beam with the quartz fabric seems to take place at the very surface and the direct secondary emission is the only discharging process.

b) At 10, 15 and 20 keV beam energies, two general behaviours can be differentiated. The first one (behaviour "A") corresponds with the usual behaviour of dielectrics under electron beam when their rear face is in contact with a grounded holder. In such a case, an increase in the surface potential with irradiation time is noted simultaneously with a decrease in the sample-to-holder current  $I$ .  $I$  is the sum of the charging current  $I_C$  (related to the dielectric capacity  $C$  by the expression  $I_C = C dV_s/dt$ ), and the leakage current  $I_L$ , through the insulator (whose value increases with the surface potential  $V_s$ ).

The second type ("B") corresponds with a non-monotonic potential variation, increasing for the first few minutes of irradiation, then decreasing to a steady-state, with a leakage current  $I$  generally increasing at the same time.

This behaviour "B" was observed much more generally. Associated with the peak value of the surface potential, a maximum in the secondary electron emission is noted on the  $I_{sec}$  records as well as on the  $I_g$  records. The electric field at the surface is guessed to determine this secondary emission because it is acting as an extracting field.

An increase in the value of the sample-to-holder current  $I$  is generally observed with time. At steady-state, this current is a leakage current. An example of this behaviour is given in figure 2 for the one layer quartz fabric sample not insulated by FEP at 15 keV. In the three layers configuration of the silica fabric in the same beam conditions, it seems that the leakage current is not existing at first and that the behaviour is rather of type "A"; then after a certain threshold of the electric field inside the material has been exceeded, the leakage current arises contributing to discharge the sample. This threshold is not in evidence for all sample configurations : it could happen very soon after beginning of irradiation in the case of a single layer directly grounded (Figure 2) owing to a smaller thickness with regard to the electron penetration depth. This is corroborated by the fact that at 10 keV, the three layers sample of silica fabric shows only the behaviour "A" when the one layer sample shows the behaviour "B" : the rather large thickness in this 3 layers configuration enables to conclude that the back layers of silica fabric are acting as an insulator.

Besides this case, the behaviour A has been noted only at 10 and 15 keV, for the composite insulated by a FEP film.

TABLE 1 - SURFACE POTENTIAL MEASUREMENTS (INVOLTS) AT STEADY-STATE

GROUNDING CONDITIONS	BEAM ENERGY	C O N F I G U R A T I O N S				
		FABRIC 1 LAYER	FABRIC 3 LAYERS	FABRIC OVER FEP	COMPOSITE OVER FEP	COMPOSITE OVER FEP
with grounded peripheric ring at the surface	5 keV	< 10	< 10	< 10	< 10	< 10
	10 keV	260	660	450	480	610
	15 keV	1320	2000	2230 (*)	2210	1485 (*)
	20 keV	5800 (*)	6100 (*)	7425 (*)	5350 (*)	4125 (*)
peripheric ring not grounded	5 keV	< 10	< 10	< 10	< 10	< 10
	10 keV	230	700	770	440	775
	15 keV	1452	1900	2230 (*)	2200	1402 (*)
	20 keV	5500 (*)	6100	7100 (**)	5530 *	4000 (*)

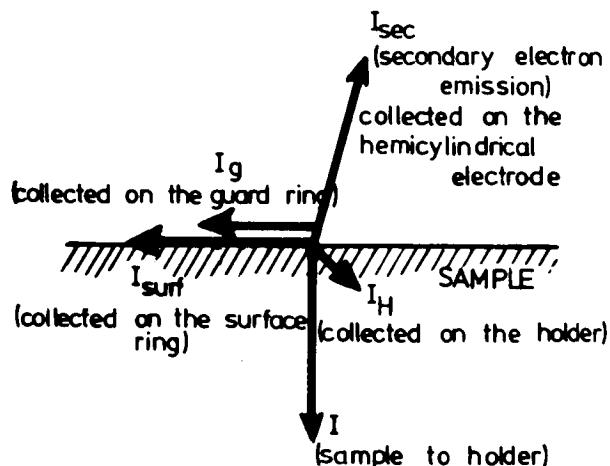
(\*) discharges      (\*\*) not equilibrium conditions  
 Note: the samples had never been irradiated before the experiment starting

The leakage current  $I_L$  observed for the quartz fabric is probably originating from the existence of secondary electrons acting as free charges in the voids between fibers and creating conducting paths through the fabric cross section (ref. 2).

#### Values at steady state

Table 1 reports the surface potential  $V_s$  as a function of the beam energy  $E_p$ . The general trend that is observed is an increase in the potential value when the beam energy is increased. Identical values of  $V_s$  are obtained, in given beam conditions, whether the sample surface is grounded at its periphery or not.

In Figures 4 to 8, the results at steady state are shown in a diagrammatic presentation that allows to visualize the relative importance of the various current components measured as defined earlier. Each current component is represented by a vector the modulus of which is equal to the direct ratio of this current to the sum  $I$  of all the currents.



$$I : I_{sec} + I + I_{surf} + I_g + I_H$$

The  $I_H$  value was not measured for all the configurations. It has been used where available. (\*)

The vector orientation allows to discriminate the various current components as sketched in Fig. 3

Fig. 3 Diagrammatic presentation of measured currents

Secondary emission current ( $I_{sec}$ ), as already said, is the only important discharging mechanism at 5 keV. It decreases when the energy is increased in the 5 to 20 keV range, where the other currents are detected, namely the sample-to-holder current  $I$ , and the surface current,  $I_{surf}$ .

$I_{surf}$  takes a minor importance as a discharge mechanism except in the following cases: silica fabric or composite insulated by FEP, and three fabric layers in contact with the grounded holder. In these three cases, the surface seems to be the less resistive path to ground, compared to the volume. This is noticed

(\*) In figures 4 to 8 a dotted vector denotes that the  $I_H$  component was not measured.

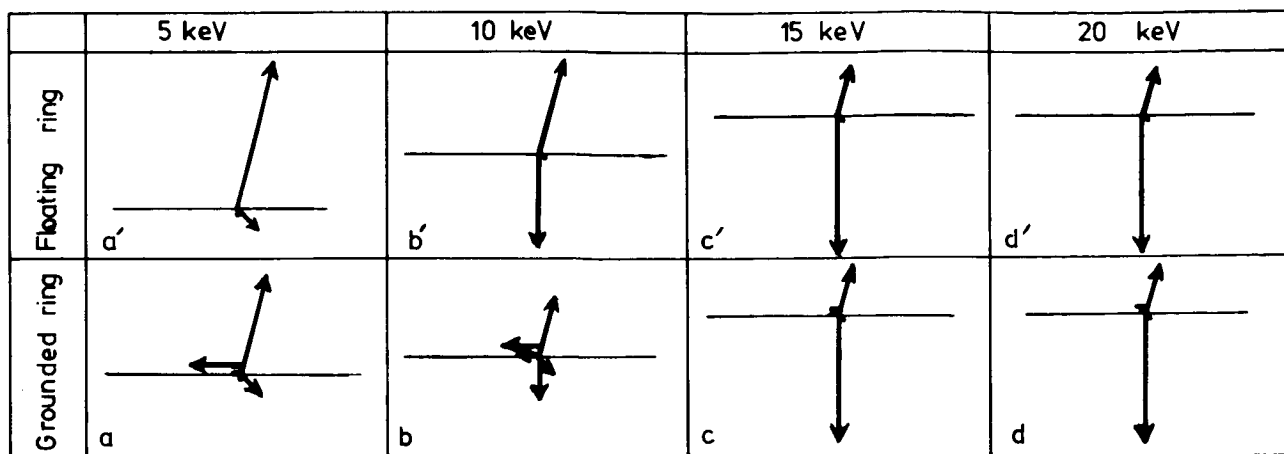


Fig. 4: Current components in the case of one layer of silica fabric

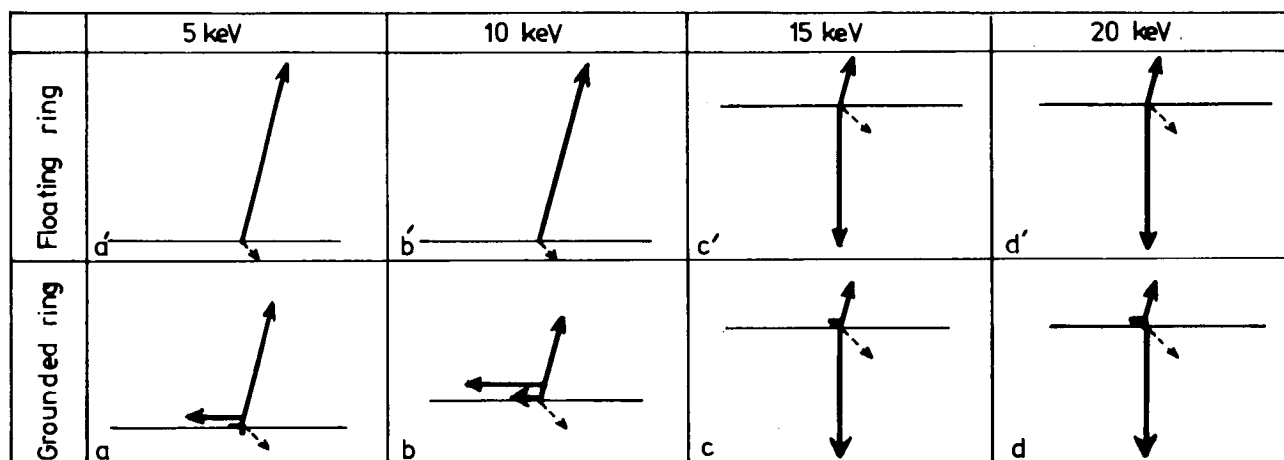


Fig. 5: Current components in the case of three layers of silica fabric

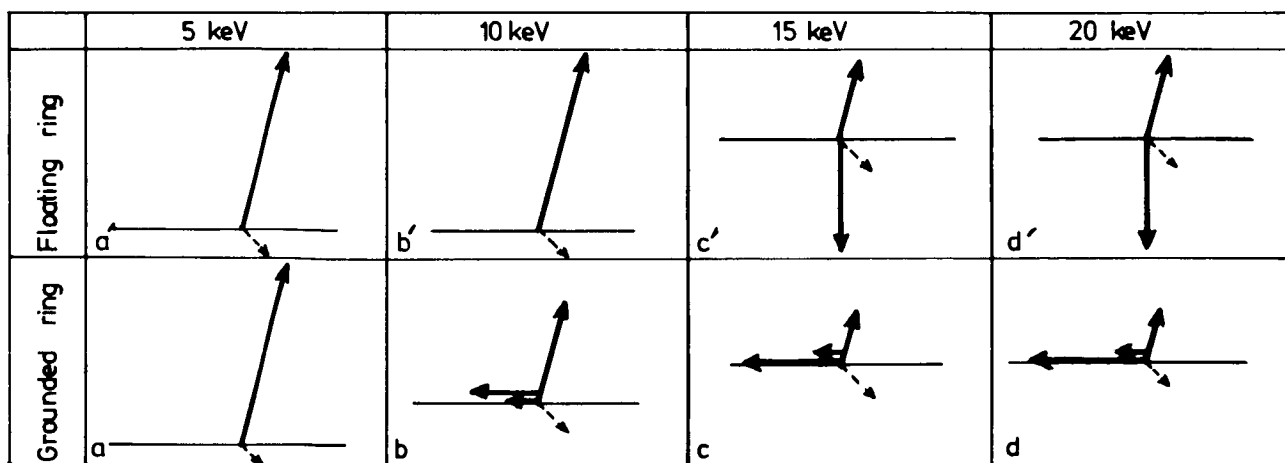


Fig. 6: Current components in the case of one layer silica fabric insulated by FEP

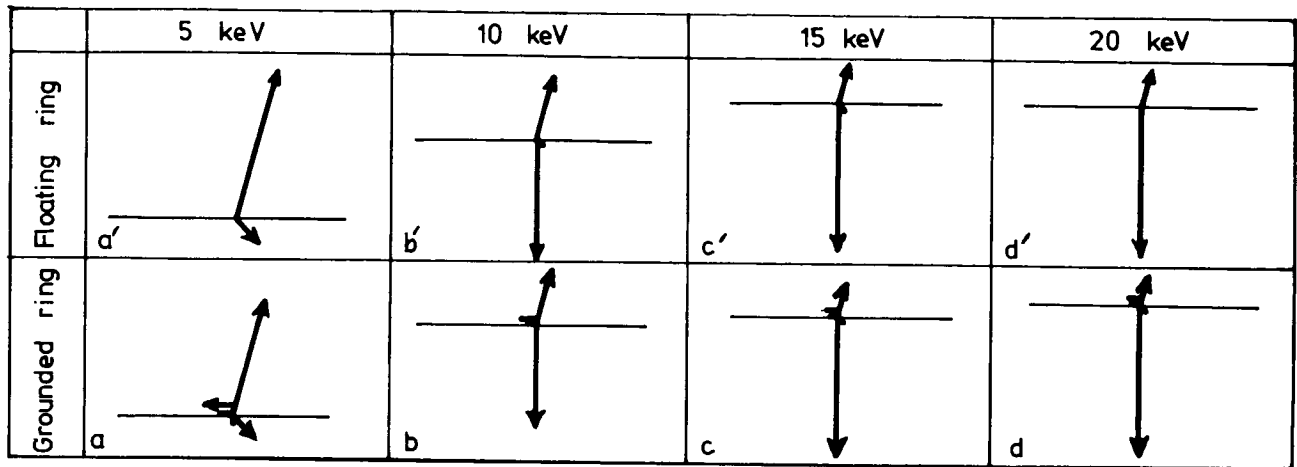


Fig. 7: Current components in the case of composite

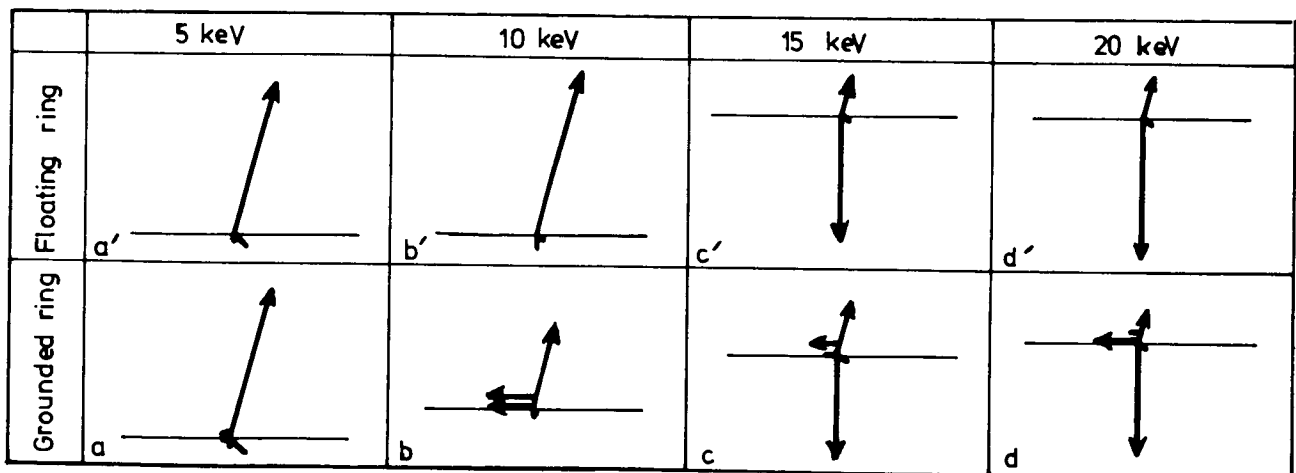


Fig. 8: Current components in the case of composite insulated by FEP



particularly in figure 6 where the grounding of the peripheral ring cancels out the current  $I$ . This is also in evidence in figures 5 and 8 where the same grounding induces only a reduction of  $I$ . In the case of the samples insulated by FEP (figures 6 and 8), care must be taken not to identify the just above mentioned  $I$  current with a leakage current. In the latter case, the  $I$  current that was recorded was probably due to a mechanism different from the secondary emission conductivity: it may be a field emission at the specimen edge as suggested by the very noisy records of  $I$  that were obtained. In all other cases, the  $I$  current can be identified as a leakage current involving a secondary emission conductivity. As such, this leakage current appears to be the most important discharging mechanism at energies greater than 5 keV. This is in evidence in figures 4 and 7 for the 15 keV and 20 keV energy beams.

### Discharges

As a general statement, whenever sudden discharging of the irradiated sample was observed, pulses were recorded on the various currents. A sudden decrease in the sample-to-holder current  $I$  was always correlated to a sudden increase in the  $I_{sec}$  current. This means that electrons emitted from the sample were collected by the hemicylindrical collecting electrode. Other currents showed almost always correlated pulses the polarity of which was not always the same. Their intensity depended on the sample nature as well as the beam conditions. Some very large variations in  $I$  were probably due to the total discharging of the sample surface. Others were probably corresponding to rather small local discharges.

All the sample configurations we tested exhibited a trend towards strong discharges at the 20 keV energy for which very strong pulses occurring at a very high rate were observed with the samples insulated by the FEP film. The samples grounded by their back face (direct contact with the sample holder) showed less pronounced discharges. The grounding of a ring put on the surface did not decrease appreciably the discharge risk.

At 15 keV numerous small current pulses were observed for the composite as well as for the quartz fabric whenever they were insulated by a FEP film. When the rear face of the composite or quartz fabric was in direct contact with the grounded holder, there was neither arcing nor tendency to arcing.

At 10 and 5 keV, discharges did not occur whatever configuration was.

From the various data that were gathered, it seems very difficult to localize the breakdown areas of the various configurations tested. The geometrical disposition of the sample holder, the rings as well as the actual sample configuration could be of first importance in the initiation of discharges. Several

competing mechanisms were obvious for some of the samples we tested.

#### Remarks

The behaviour of the composite under an electron beam simulating the substorm environment seems to be closer to the one of the quartz fabric alone than to the one of the quartz fabric electrically insulated by a FEP film. This observation strongly suggests that the quartz fibers of the composite are in close contact with the back aluminum foil. This fact is corroborated by a study under optical microscope. Therefore the FEP layer does not form a continuous barrier within the laminated composite that we have tested.

The behaviour of the composite is satisfactory only if its aluminum rear face is grounded. The use of a conductive adhesive is therefore strongly recommended for bonding the laminate composite to the metallic spacecraft structure or to the next grounding point.

Strong discharges were observed at 20 keV with the composite material as well as with a silica fabric that was directly grounded by its back face. Previous observations (ref. 2, 3) did not indicate this trend.

#### FIELD-DEPENDENT CONDUCTIVITY OF THE COMPOSITE

The silica fabric behaviour has been attributed (ref. 2) to a secondary emission conductivity. Such a conductivity can explain the decrease in  $V_s$  (or the peak value) in the curve giving the surface potential in terms of time, that has been observed (behaviour "B") at 10, 15 and 20 keV. However this peak value occurred at rather high values of the surface potential (about 1000 Volts). Consequently it appeared useful to evaluate the conductivity in quartz fabrics for similar electrical fields. It was decided to apply to a composite sample such electrical fields corresponding to potentials in the 0-1 kV range and to evaluate the electrical conductivity through the sample under electron beam. The experiments were performed in a facility similar to the one described in reference 2, but with far lower current densities, higher surface potential and higher beam energies.

#### Procedure

Samples were irradiated by an electron beam with a fixed electric field imposed across the cross section of the composite. The composite was mounted with its aluminized back face directly on a grounded sample holder. The outer fabric surface was in intimate contact with a brass grid. The grid potential  $V_0$  with

respect to the sample holder was held below 1500 Volts, which was in the presence of incident electrons, the threshold value for breakdowns to occur. The transmission coefficient of the wire screen was experimentally determined and found to be 50 per cent.

The potential  $V_0$  was fixed at a given level and the three currents  $I_{\text{leakage}}$ ,  $I_{\text{secondary}}$  and  $I_{\text{supply}}$  were simultaneously measured at steady-state. The beam conditions were the following: 5 keV/0.25 nA cm<sup>-2</sup> (at sample level, after grid), 10 keV/1 nA cm<sup>-2</sup>, 15 keV/ 1 nA cm<sup>-2</sup>, 20 keV/ 1 nA cm<sup>-2</sup>.

All experiments have been performed with the sample of the composite.

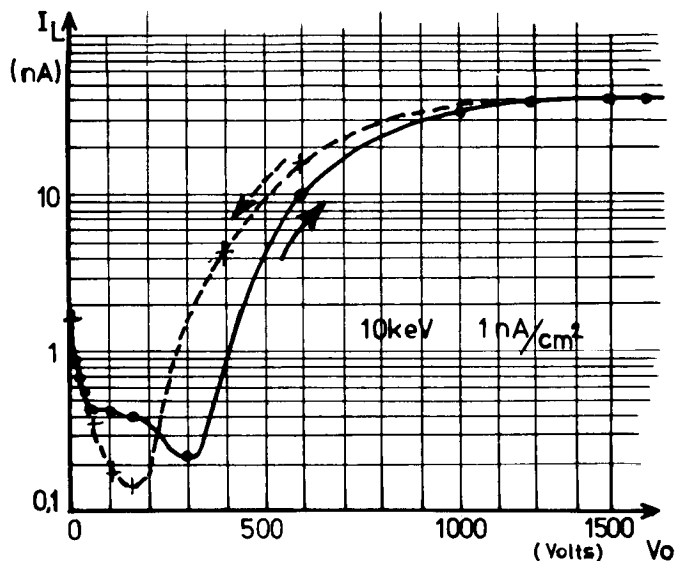


Figure 9A: leakage current versus applied voltage at 10 keV for the composite

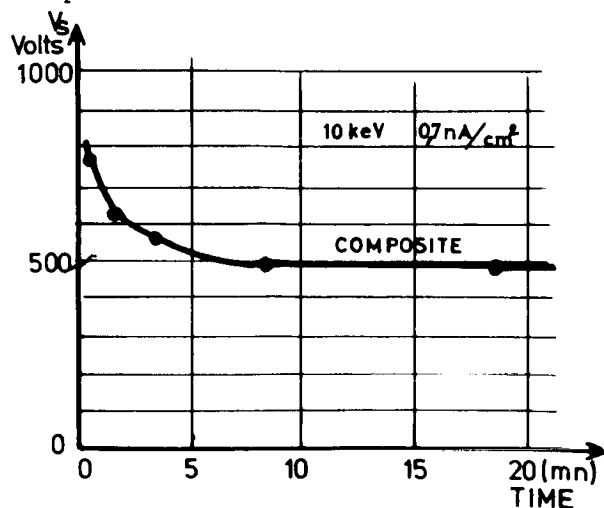


Figure 9B: surface potential versus time at 10 keV for the composite

## RESULTS

There is a very rapid increase in the leakage current with the applied voltage  $V_0$  for  $V_0$  greater than two or three hundred volts. That is to say that the resistance across the cross section of the composite decreases for surface potentials values beyond a certain threshold.

This large dependence of the conductivity on the electric field is shown in Figure 9A for a 10 keV electron irradiation of the sample. In Figure 9B is plotted the surface potential induced by the same electron irradiation in terms of time. Figures 9A and 9B do match together since an increase of conductivity explains quite well the potential decrease after a very short irradiation time. The measured values at 15 keV and 20 keV are equally suggestive of a surface potential in strong correlation with a field-dependent conductivity.

For the lowest electron beam energy (5 keV) the transmitted current  $I_{\text{leakage}}$  is

very low for  $V_0$  less than 1100 Volts; one must remind that the surface potential observed under a 5 keV electron irradiation is zero due to the very high secondary emission that can be evidenced by the current collected on the hemicylindrical electrode.

## INFLUENCE OF THE IRRADIATION DENSITY ON THE CHARGE DISSIPATION PERFORMANCE

### Purpose of study

The secondary emission conductivity mechanism postulates that a free electron population is created inside voids between silica fibers. This suggests a possible irradiation density influence on the charge dissipation performance. Accordingly it was decided to perform several electron irradiations at various beam densities in order to compare their effect.

### Procedure

A first series of tests was run at 10 keV with one specimen of the composite that was irradiated in the following successive conditions:

- (a) 10 pA  $\text{cm}^{-2}$  for 16000 s ; (b) 30 pA  $\text{cm}^{-2}$  for 5300 s ;
- (c) 100 pA  $\text{cm}^{-2}$  for 2800 s ; (d) 300 pA  $\text{cm}^{-2}$  for 1900 s ;
- (e) 1 nA  $\text{cm}^{-2}$  for 1000 s ; (f) 3 nA  $\text{cm}^{-2}$  for 1000 s ;
- (g) 10 pA  $\text{cm}^{-2}$  for 20000 s.;

Between these various irradiations the sample was totally discharged with electrons at 5 keV 1 nA  $\text{cm}^{-2}$ .

The same sample was used for a second series of tests at 15 keV in the following conditions:

- (h) 10 pA  $\text{cm}^{-2}$  for 27000 s ; (i) 30 pA  $\text{cm}^{-2}$  for 13000 s ;
- (j) 100 pA  $\text{cm}^{-2}$  for 4000 s ; (k) 300 pA  $\text{cm}^{-2}$  for 1300 s ;
- (l) 1 nA  $\text{cm}^{-2}$  for 400 s ; (m) 3 nA  $\text{cm}^{-2}$  for 133 s ;
- (n) 10 pA  $\text{cm}^{-2}$  for 27000 s ; (o) 100 pA  $\text{cm}^{-2}$  for 4000 s.

For the irradiations at 15 keV, the sample charge was also removed after each irradiation step with an electron beam at 5 keV 1 nA  $\text{cm}^{-2}$  or 5 keV 10 pA  $\text{cm}^{-2}$ .

The surface potential was measured at several exposure times for each irradiation step.

### Results

Figure 10 gives the surface potential in terms of total incident charge  $Q$  (flux rate by irradiation time) for an electron

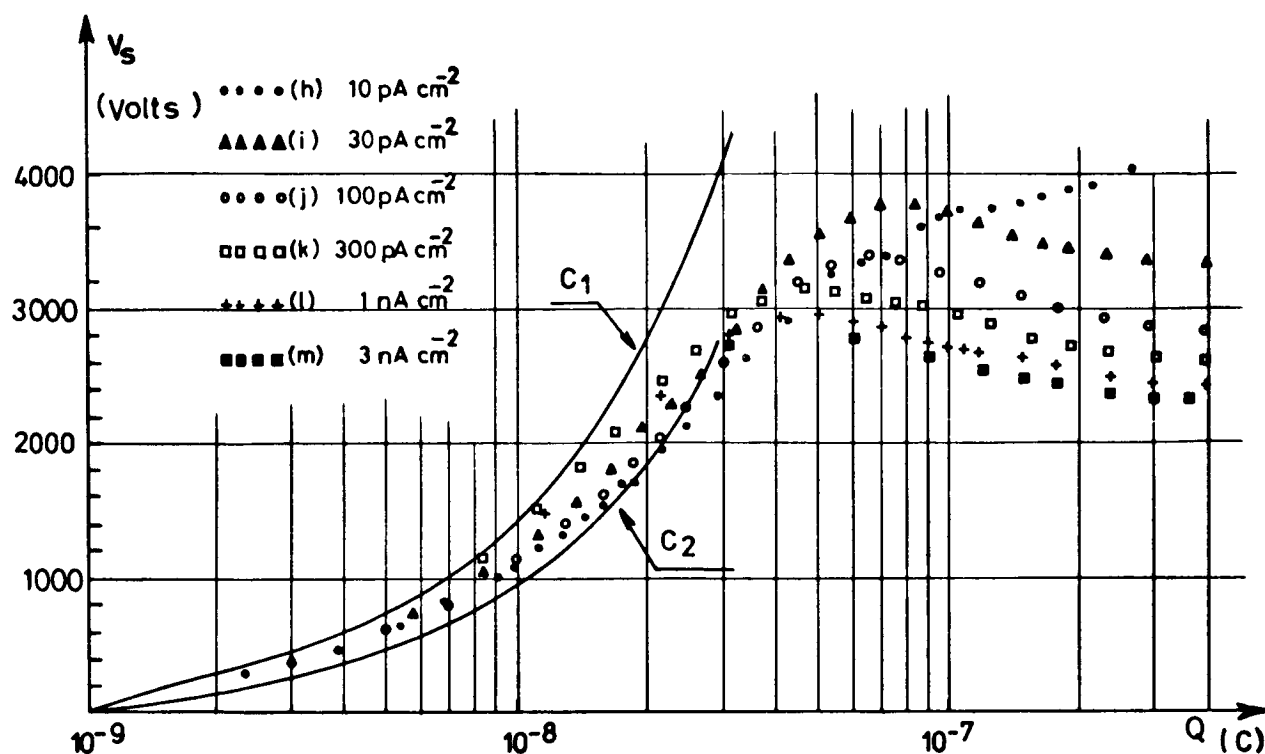


Figure 10: Irradiation density effect at 15 keV

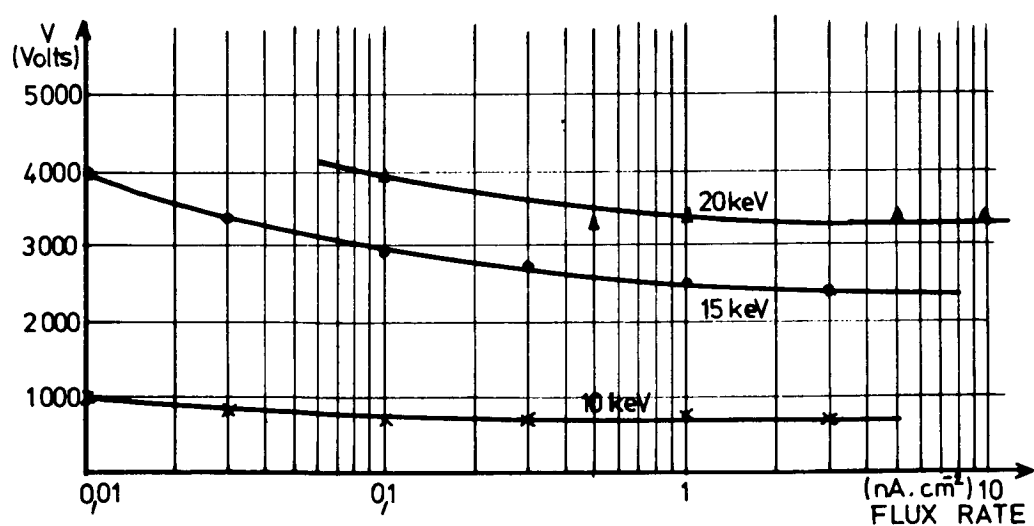


Figure 11: Surface potential (at steady-state) versus flux rate

irradiation at 15 keV. This figure clearly shows that the potential values at steady state depend on flux rate, while the intermediate values (for incident charge lower than  $10^{-8}$  C) depend only on the integrated stored charge. These experimental values of potential can be compared to calculated potential values of pure capacitors submitted to the same irradiation, assuming a secondary emission coefficient equal to 30 per cent. The curves labelled  $C_1$  and  $C_2$  in figure 10 are corresponding respectively with the value 5 and 8 pF cm<sup>-2</sup>. This observation helps to elucidate the electrostatic behaviour of silica fabrics and composites under electron bombardment ; at 15 keV, they behave like a capacitor until a leakage current arises, due to the secondary emission conductivity, for potential values around 1000 Volts.

The flux rate dependency is illustrated in figure 11 where the potential values at steady state are expressed in terms of flux rate. This dependency is particularly obvious at 15 keV between 0.01 and 0.1 nA cm<sup>-2</sup>. At 10 keV the variations of the potential value at steady-state are much less noticeable.

Irradiations at 5 keV and 0.01 nA cm<sup>-2</sup> were also performed in the same sample that had been irradiated with 10 keV and 15 keV electrons. It was checked that no detectable potential appeared in these conditions. Moreover an irradiation at 5 keV and 0.01 nA cm<sup>-2</sup> effectively discharged a sample that had been previously charged at 10 or 15 keV.

It is worth noting that the surface potentials which can be measured for irradiated quartz fabrics and composites are dependent on the sample history : they are increasing with the time of exposure to vacuum and/or irradiations. The irradiation labelled (g) after two days under vacuum and several irradiation steps, corresponded to a potential at steady-state (reported in figure 11) 250 V higher than the one recorded at irradiation (a). However after a certain time a stabilization seems to occur: irradiations (h) and (n), (j) and (o) led exactly to the same potential after respectively four and eight days under vacuum. Nevertheless, one must remind that the results in figures 10 and 11 could be slightly different, depending on the sample history under vacuum (contamination).

#### Forecast consequences

The increase in the surface potential for decreasing flux rates should have no technological consequence, since, for beam conditions that are representative of the geosynchronous environment during substorms (flux rates between 0.1 and 2 nA cm<sup>-2</sup>; ref.7) only very small potential variations are expected for a given energy.

## INFLUENCE OF THE PRESENCE OF LOW ENERGY ELECTRONS (2 to 4 keV) TOGETHER WITH HIGH ENERGY ELECTRONS (10 to 20 keV)

### Purpose

Evidence has been given above that a very high secondary emission can be measured by an hemicylindrical collecting electrode for a 5 keV electron irradiation on silica fabrics with a surface potential equal to zero. When the electron beam energy is increased to 10, 15, 20 keV, the secondary emission is decreased and a leakage current that is due to the secondary emission conductivity can be measured; the surface potential becomes measurable then increases up to reach some thousands volts for a 20 keV beam. However the results that have been reported above for 10 to 20 keV electrons, have been measured only with quasi-monoenergetic electron beams. According to ref. 2, as the beam energy is increased above 5 keV, the incident electrons generate secondary electrons deeper within the material where they are unavailable to act as charge carrier towards the surface. In an actual substorm environment, there is a continuous distribution of electron energies. Accordingly it seems interesting to evaluate the silica fabric behaviour under irradiation either with a wide spectrum of electrons or at least with two simultaneous beams of electrons giving two quasi-monoenergetic beams in two different energy ranges. The second method is easier. It was decided to irradiate the composite with low energy electrons (2 to 4 keV) acting together with medium energy electrons (10 to 20 keV).

### Procedure

The facility was redesigned to allow a simultaneous irradiation by low energy (2 to 4 keV) and medium energy (10 to 20 keV) electrons.

Two samples of the composite have been irradiated with the same procedure. One of them (A) is a specimen that had not been irradiated previously. The second (B) had been irradiated for 32 hours in an earlier test; this latter specimen has therefore a complicated history from both points of view of contamination and irradiation.

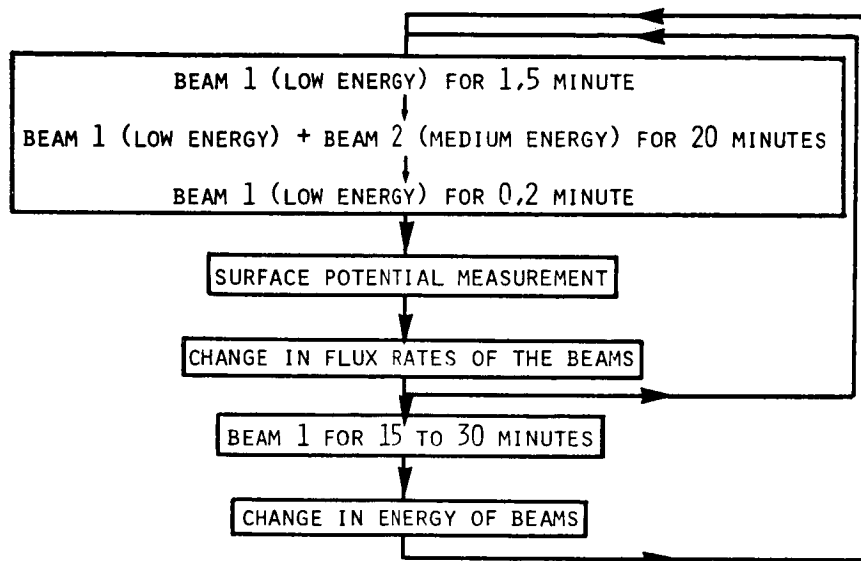
The energy of the low energy beam (beam 1) was set at 2 or 4 keV ; the energy of the medium energy beam (beam 2) was set at 10, 15 or 20 keV.

The following energy pairs have been successively achieved  
(a) 2 keV and 10 keV ; (b) 2 keV and 15 keV ; (c) 4 keV and 15 keV ; (d) 4 keV and 20 keV.

For each energy pair, several ratios of the two beams intensities have been selected. For each of these various ratios, the

sum of the two beam intensities has been kept constant:  $0.7 \text{ nA cm}^{-2}$  for the energy pair (a),  $0.5 \text{ nA cm}^{-2}$  for the next pairs (b), (c), (d).

The procedure and irradiation times are as follows:



The leakage current is the only current that could be recorded during irradiation.

### Results

Table 2 gives the potential values measured for various combinations of energies and beam intensities.

The occurrence of pulses in the leakage current of the samples is also reported in table 2 as number of "arcing events". It is worth noting that four rather small breakdowns have been observed at 15 keV on the contaminated composite (sample B). Many events are noticed at 20 keV for both samples.

### Discussion

A substantial decrease in the surface potential of the sample is observed every time that an irradiation by low energy electrons (2 to 4 keV) is performed simultaneously with the irradiation by medium-energy electrons (10 to 20 keV) : see table 2.

The dependency of surface potentials on the presence of low energy electron is shown to be quite considerable and to make obsolete most previous test results with monoenergetic beams. Moreover,



TABLE 2 - RESULTS OF THE EXPERIMENTS WITH THE DUAL-BEAM

	BEAM 1		BEAM 2		SAMPLE A (*)		SAMPLE B (***)	
	Energy (keV)	Flux rate $nAcm^{-2}$	Energy (keV)	Flux rate $nAcm^{-2}$	Surface potential (V)	Arcing events (**)	Surface potential (V)	Arcing events (**)
1	2	0.7		-	0	-	0	-
2	2	0.6	10	0.1	< 10	-	< 10	-
3	2	0.35	10	0.35	10to20	-	650	-
4	2	0.1	10	0.6	160	-	1260	-
5	-	-	10	0.7	740	-	1460	-
6	2	0.5	-	-	< 10	-	< 10	-
7	2	0.4	15	0.1	10to20	-	300	-
8	2	0.25	15	0.25	400	-	4410	-
9	2	0.1	15	0.4	1180	-	4500	-
10	2	-	15	0.5	1980	-	4500	4
11	4	0.5	-	-	< 10	-	< 10	-
12	4	0.25	15	0.25	1200	-	3960	-
13	4	0.5	-	-	10	no	510	no
14	4	0.4	20	0.1	80	0	720	1
15	4	0.35	20	0.15	360	10	970	1
16	4	0.30	20	0.2	745	9	6600	12
17	4	0.25	20	0.25	1215	14	8190	78
18	4	0.20	20	0.30	1420	12	8100	119
19	4	0.15	20	0.35	3600	12	8200	60
20	4	-	20	0.5	4500	28	8370	150
(*) Experiments 1 to 12 have been successively performed with the same specimen, that was replaced by a new one for the experiments 13 to 20								
(**) For a 20 minutes period of time								
(***) This sample has been previously irradiated and contaminated								

it does confirm the contamination effect to be mainly an alteration of the secondary emission surface properties. The decrease in surface potential is explained by an enhancement of the secondary emission of the silica fabric for primary electrons in the 1 to 5 keV range.

Surprisingly with the medium energy beam fixed at the 20 keV level, arcing events are still observed when the low energy beam is applied. However, the uniformity of the 4 keV beam is rather bad. In its right part, the composite is receiving certainly a far less density of low energy electrons than in its left part. No scan in the horizontal direction could allow to determine whether the surface potential is higher in the right part and whether arcing can originate from this area.

Table 2 shows that the low energy component decreases also the electric charge of the contaminated sample (sample B) under electron beam but it is obvious that its efficiency is far less than with an uncontaminated sample (sample A).

### Consequences

The electrostatic tests that are performed usually on silica fabrics and composites appear to be pessimistic because they are carried out with monoenergetic beams at rather high energies (10 to 20 keV). In space, wide distribution of energies including electrons in the range 1 to 5 keV are always observed. They tend to lessen the surface potentials that could be inferred from the laboratory tests with monoenergetic beams on materials for which the secondary emission conductivity is the principal charge dissipation mechanism.

### REMARKS ABOUT THE EFFECTS OF CONTAMINATION

A systematic increase in surface potentials has been observed as often as successive irradiations under vacuum have been carried out in the same conditions on quartz fabrics and composites - see for instance the examples given above at the section dealing with the effect of flux rate.

This behaviour is probably a consequence of a contamination layer build up in an imperfectly clean vacuum on the quartz fiber surface whose properties, namely secondary emission, are likely modified. Several experiments (that will be reported later on in an other paper) have substantiated this assumption but they have also shown that the contaminant layer as well as its effect depend on the irradiation received by the surface. The results obtained with the dual beam show the great importance of such a phenomenon for the technological use: in space the good electrostatic behaviour

of the quartz fabrics will be probably progressively degraded as a function of the number of orbits with a greater probability of arcing events, if a great care is not exercised in preventing from contamination.

#### CONCLUSION

Owing to a secondary electron conductivity, the silica fabrics support moderate charge build up under electron irradiation simulating the substorm conditions at geosynchronous orbits. The behaviour of the fabric/FEP/Aluminum composite is similar to the one of the silica fabric but its aluminized rear face must be grounded, for instance by use of a conductive adhesive, in order to lessen the discharge risks which could occur between 15 and 20 keV. Silica fabrics and composites are very sensitive to contamination or contamination-plus-irradiation effect: in space, the good electrostatic behaviour of the fabric will be progressively degraded as a function of the number of orbits with a greater probability of arcing events if a great care is not exercised in preventing from contamination.

#### REFERENCES

1. A.E. Eagles et al: Fabric coatings: A New Technique for Spacecraft Passive Temperature Control - AIAA Paper 65-668 AIAA 10th Thermoph. Conf. Denver, Colorado, May 1975
2. V.J. Belanger, A.E. Eagles: Secondary Emission Conductivity of High Purity Silica Fabrics - Proc. Spacecraft Charging Techn. Conf. Colorado Spring, October 1976
3. N.J. Stevens, F.D. Bercopec, J.V. Staskus, R.A. Blech, S.J. Narciso - Testing of Typical Spacecraft Materials in a Simulated Substorm Environment - Proc. 1st Spacecraft Charging Technol. Conf. Colorado Springs (October 1976).
4. B.Benaissa, L. Levy, A. Paillous, D. Sarraïl: Interim Scientific Report - AFOSR Grant 78-3704B for the Period 79 May 01 - 80 Jan 31 (July 1980)
5. L. Levy, A. Paillous, D. Sarraïl - Interim Scientific Report n° 2 on AFOSR Grant 78-3704B for the period 79 May 01 - 80 Jan 31 (March 1980)
6. L. Levy, A. Paillous, D. Sarraïl: Final report on AFOSR Grant 80-0183 (December 1980)

# **ELECTROSTATIC CHARGING CHARACTERISTICS OF THERMAL CONTROL PAINTS AS FUNCTION OF TEMPERATURE\***

**Paul A. Robinson, Jr.\*\*  
Hughes Research Laboratories**

**A. C. Whittlesey  
Jet Propulsion Laboratory  
California Institute of Technology**

## **SUMMARY**

In a study of the charging characteristics of paints for various uses on spacecraft under electron bombardment we have found the following:

There is not a strong temperature dependence of the charging characteristics between  $-155^{\circ}\text{C}$  and  $+30^{\circ}\text{C}$ .

There is a noticeable hysteresis effect as the electron beam energy is varied.

All of the paints tested exhibit large secondary yields at low ( $\sim 1$  keV) bombarding electron energies.

Surfaces can charge either positively or negatively depending on the conditions and the paint.

Paints are not simple; will require more detailed study; and will probably act differently in multiple energy electron tests.

## **INTRODUCTION**

Painted surfaces are common on spacecraft because of their desirable thermal and mechanical properties. The concern of spacecraft designers for the electrical properties of spacecraft surfaces underlines the importance of the charging characteristics of spacecraft paints as well, since in some cases partially conductive paints may be used as substitutes for more traditional materials with high resistivities. Spacecraft design requires that the surface charge build-up be less than the material breakdown voltage. For scientific spacecraft, the absolute potential on the spacecraft surface should be small when compared to the electric fields to be measured or the particle spectra to be sampled.

---

\* The research described in this paper was carried out at the Jet Propulsion Laboratory, California Institute of Technology, under NASA Contract NAS7-100

\*\* Current address: Jet Propulsion Laboratory

Even if the spacecraft has an absolute net charge, the differential charging of surfaces should be limited to avoid further disturbance of nearby electrostatic fields; for the Galileo spacecraft, a maximum 10 volt differential surface potential was desired under all environmental conditions. The electrical properties of spacecraft paints (CTL-15, S13G-low)(1) have been of interest to spacecraft for a long period. Normal paints such as S13G low outgasing do charge to some degree<sup>2</sup>. Nonetheless, they do not charge to the high levels observed for Teflon<sup>R</sup>, and Kapton<sup>R</sup> surfaces. In this report, we will begin by discussing our results on standard spacecraft paint, and then on several conductive paints.

### STANDARD CHEMGLAZE PAINT

The surface potential versus electron beam energy for standard Chemglaze paint is shown in Figure 1. In this experiment, the incident electron flux was kept at about 1 nanoamp/cm<sup>2</sup> and the sample at room temperature. The surface potential builds up almost linearly with the accelerating beam voltage until the beam energy reaches about 10 keV. At that point the surface voltage saturates at just over 400 volts even though the beam energy increases to 20 keV.

After exposure to the 20 keV beam, the beam energy was reduced to 5 keV, and the sample was cooled. The surface voltage did not return to its previous value at 5 keV, but remained at the voltage it had reached in the 20 keV beam. This effect may be important in situations where the environment is changing rapidly.

As the temperature of the sample falls (as seen in Figure 2) the surface potential raises at a rate of approximately 1 volt/degree Kelvin, reaching its highest value near the coldest temperature. These hysteresis effects may be due to the heterogeneous nature of paints. Suppose that part of the paint is a very good insulator, charges to high voltages and has a long decay constant, but that the remainder of the paint is relatively conductive, does not charge to high voltage and tends to bleed charge off rapidly. This material will then behave in a manner similar to that observed. Some electrons will happen to penetrate into regions of high resistance and become trapped. Because these regions have long decay times, varying the incident beam energy will not cause a readjustment of this charge. This will produce the effect seen when the sample was first exposed to a 20 keV beam and then returned to a 5 keV beam without a significant change in the surface voltage.

The second feature of paints observed, namely the increase in surface voltage as the temperature decreases, can be explained by the characteristics of the relatively conductive part of the paint. In most non-metallic materials, the resistance of the material increases as the temperature decreases. In the case of a two-resistivity material, such as the one we have postulated for paints, this means that the ability of the material to bleed charge from the insulating areas is now reduced, and the material will charge to a higher levels as the material is cooled.

Figure 3 shows the increase in surface voltage as the sample is cooled and warmed during exposure to a 20 keV electron beam. The cooling and warming curves are separated by as much as 100 volts. The cooling curve voltage lags while the

warming curve leads the straight line fit to both curves. This could well be due to the difference in temperature between the surface of the paint, and the point of temperature measurement, or it could be due to the fact that all of the surface voltage measurements were made while the temperature of the sample was charging.

### CONDUCTIVE PAINTS

Four paints, 2 black and 2 white, modified to be conductive, have been tested in the experimental facility described in another paper<sup>(3)</sup>. For these tests the paint samples were mounted so as to be in good thermal contact with the liquid nitrogen plate, but electrically isolated from it. The experiment was carried out in the same manner as the tests described above, except that data was taken during both warming and cooling in 1, 5, 10, and 20 keV. The test matrix is shown in Table I. Typical cooling and warming curves are shown in Figures 4 and 5. The rate of cooling (or warming) depends strongly on the rate at which LN<sub>2</sub> (or room temperature air) is pushed into the cooling fixture. These were adjusted by hand to allow the maximum time to be spent at each temperature data point. Table II shows the paint samples tested. The results of extensive testing are shown in the next four figures (6,7,8, and 9). These show the surface potential as measured by a Monroe electrostatic non-contacting voltage probe. The electron beam was removed by closing a mechanical valve between the electron source and the sample during surface voltage measurements. The beam current was adjusted to remain at approximately 1 nanoamp/cm<sup>2</sup>. The temperature was varied using the low temperature fixture described earlier.

These results show there is no strong temperature dependence in the electrical characterization of these paint samples, but the surface potential was in excess of the 10 V differential desired by the Galileo project for science considerations.

One notable result is that there is no apparent temperature dependence to the surface potential, which is at variance with expectations based on resistance measurements. Resistance measurements vs temperature at JPL (not published) show a 10<sup>5</sup> change in resistance over the same temperature range. There is no ready explanation for this apparent discrepancy, but it indicates that conductive paints cannot be analyzed in terms of a simple  $E = IR$  model.

Another of the interesting questions raised by these tests is the apparent non-repeatability of the test results at 1 keV. After exercising the sample in the 5, 10 and 20 keV beams, and throughout the temperature range, the sample was returned to room temperature and exposed to a 1 keV beam. Generally, the results of the last measurement at 1 keV disagreed with the initial data taken at room temperature and 1 keV. This effect could be the same effect we first noticed in testing the regular Chemglaze samples, except that these samples are much more conductive, and so the effect is not as pronounced, however, our experiments with secondary emission described below suggest a more subtle explanation.

The total back current measured in a 1 keV beam is grossly different from the expected beam current even though the surface potential is approximately zero. This is due to high secondary emission at 1 keV. In separate experiments

on selected samples a small bias was applied to the sample to verify that secondary electrons were indeed responsible for the low observed back current. In these experiments the current collected by the wall of the chamber, as well as the current through the sample were measured. The wall current should increase as more secondaries are emitted. The current through the sample with and without a bias applied to the back of the sample were also measured. During these experiments the temperature and electron flux were varied. However, the temperature and flux variations did not have as significant an effect as the time. Figure 10 shows the gradual increase in the secondary emission coefficient as a function of time as measured during these experiments. During this time a cooling and warming cycle took place with little apparent effect. The long time constant observed is apparently due to the nature of secondary emission itself. For this paint, the secondary emission process takes a considerable period of time to become established when exposed to beams which cause high secondary emission. This effect undoubtedly plays a role in the observed discrepancy between samples exposed to 1 keV electrons before and after exposure to other energy electrons.

The most puzzling result of this study is the occasional measured positive surface potentials at high beam energies. Surface contamination causing a very thin insulating surface (perhaps caused by cyro-pumping of outgassed products on the sample) could be responsible, since 20 keV electrons from a thin insulating surface has been suggested as a possible mechanism. Another possibility is the inaccuracy of the voltage probe at such low potentials, or in the presence of the plasma produced by the high energy electron beam.

#### CONCLUSION

Conductive paints are not simple. They will require more detailed study to understand their behavior under electron bombardment. Although they do not charge to any significant degree, they do have very interesting properties.

#### REFERENCES

1. J.E. Gilligan, R.E. Wolf, and C. Ray, "Electrically Conductive Paints for Satellites", p. 593, Proc. of the Spacecraft Charging Technology Conference, 1976, AFGL TR-77-0051, and NASA TMX-73537, C.P. Pike, R.R. Lovell, editors.
2. N. John Stevens, F.D. Berkopec, J.V. Staskus, R.A. Blech, S.J. Narciso, "Testing of Typical Spacecraft Materials in a Simulated Substorm Environment" p. 431 (especially pp 434-435) Proc. of Spacecraft Charging Technology Conference, 1976, AFGL TR-77-0051 or NASA TMX-73537, C P. Pike, and R.R. Lovell, editors.
3. P. Robinson, E. Brown, et al., "Evaluation of Charge Control Techniques on Spacecraft Thermal Surfaces", Paper II 11 Spacecraft Charging Technology Conference, 1980.

TABLE I. TABULAR LISTING OF MEASUREMENT CONDITIONS, TEMPS vs. KeV

	ACCELERATING VOLTAGE, KeV					
	1	2	5	10	15	20
(Room Temp) 23°C	X	X	X	X	X	X
-10	X		X	X		X
-45	X		X	X		X
-88	X		X	X		X
-127	X		X	X		X
-155	X	X	X	X	X	X

TABLE II. ESD-CONDUCTIVE PAINTS TESTED

PAINT	COLOR	METHOD USED TO MAKE CONDUCTIVE
Chemglaze, modified Z004 over 9922 primer with 2% carbon black	Black	Carbon Filler
Bostic Finch 463-14	Black	Carbon Filler
Zinc Orthotitanate	White	Unknown
Goddard NS43C	White	Unknown



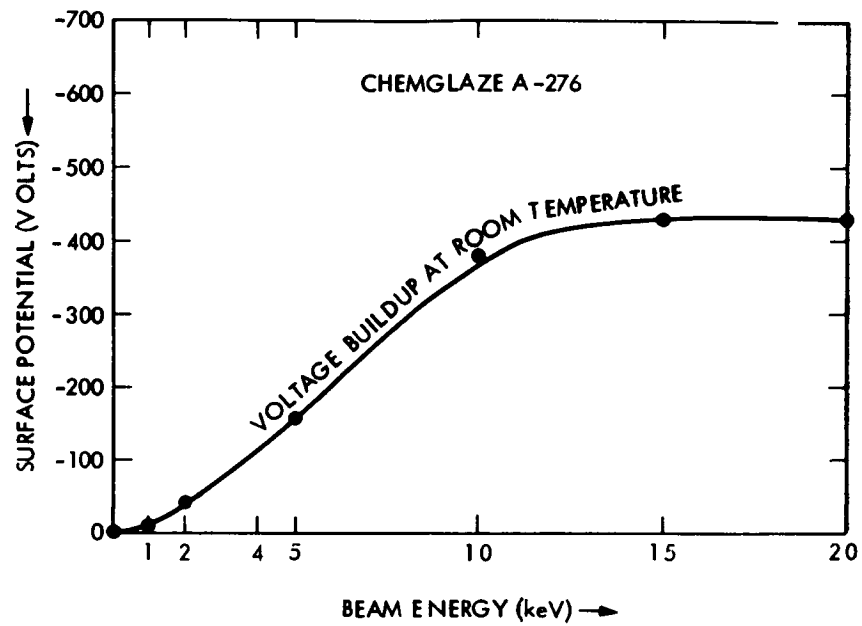


FIGURE 1

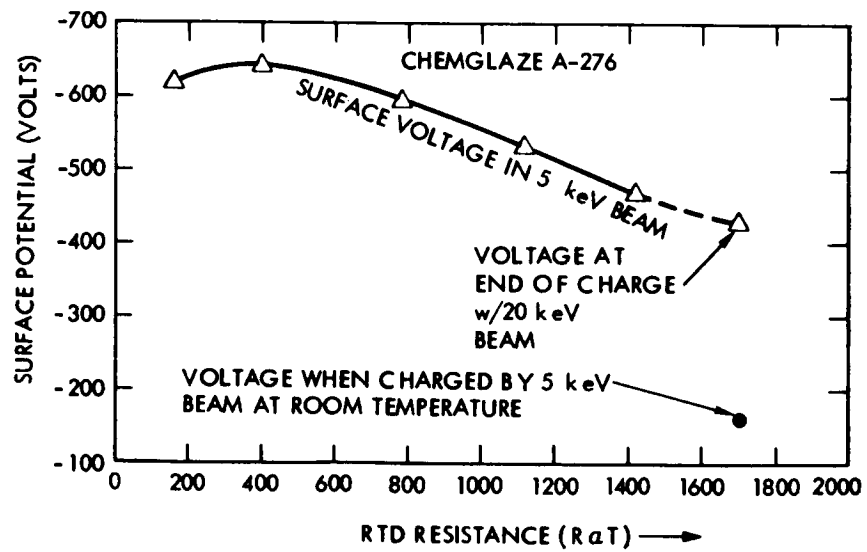


FIGURE 2

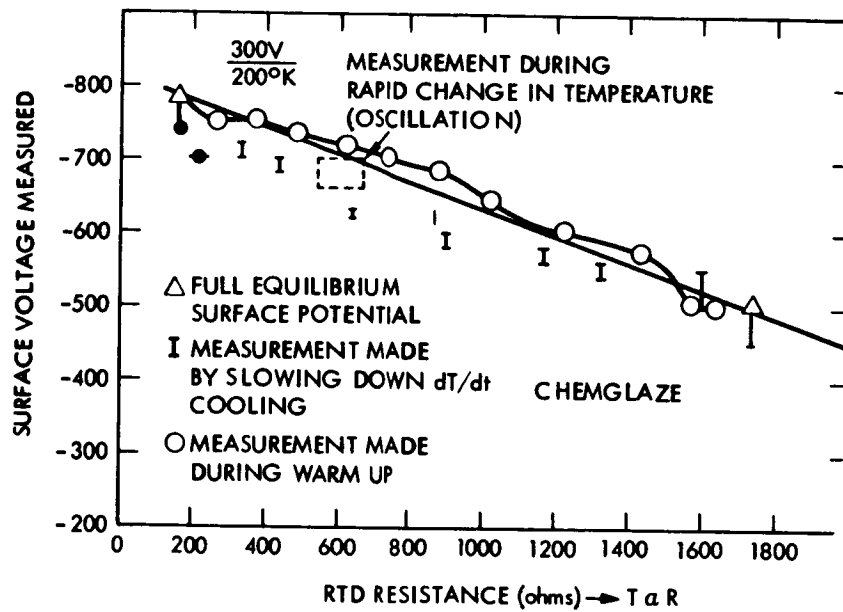


FIGURE 3

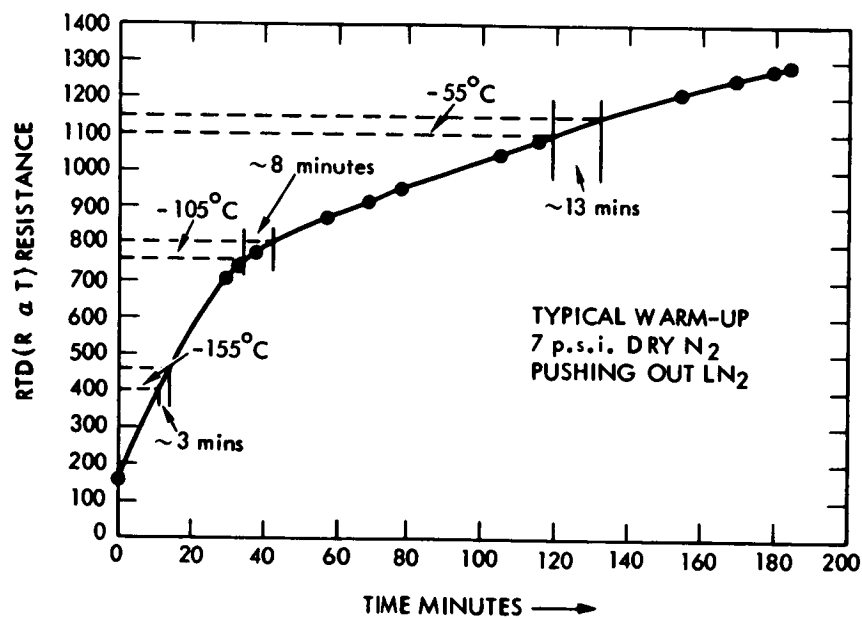


FIGURE 4

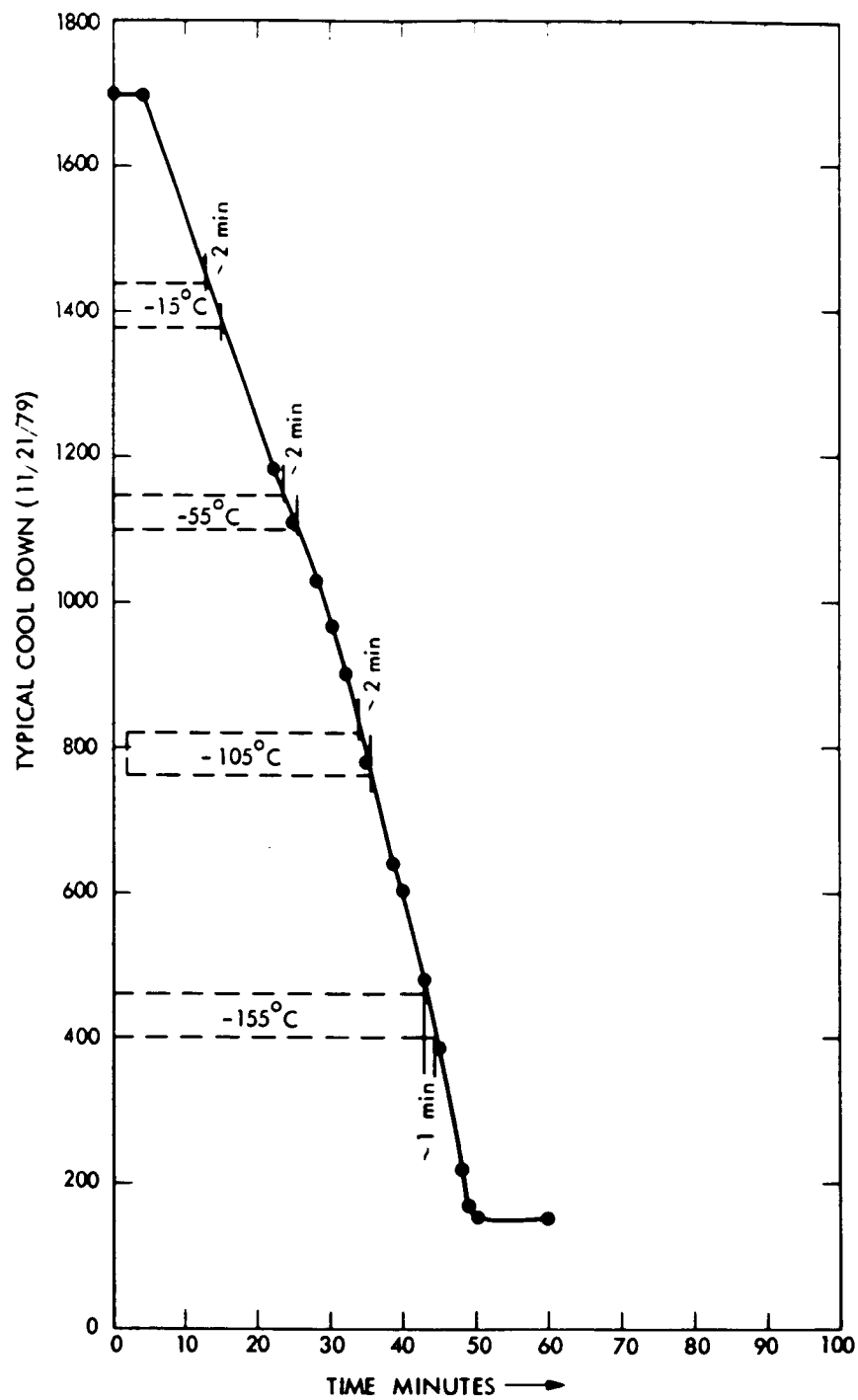


FIGURE 5

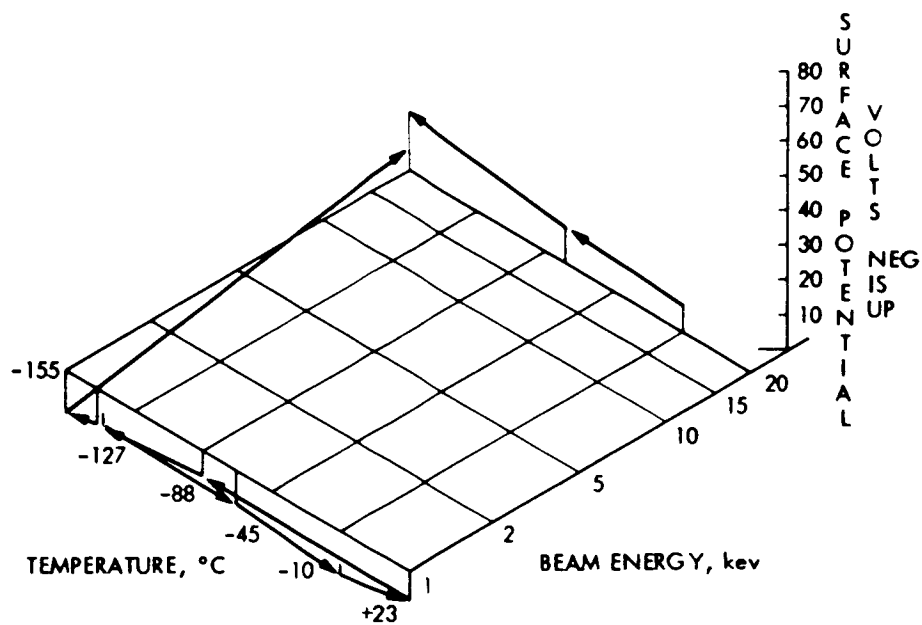


FIGURE 6. SURFACE POTENTIAL CHEMGLAZE BLACK SAMPLE 2-4

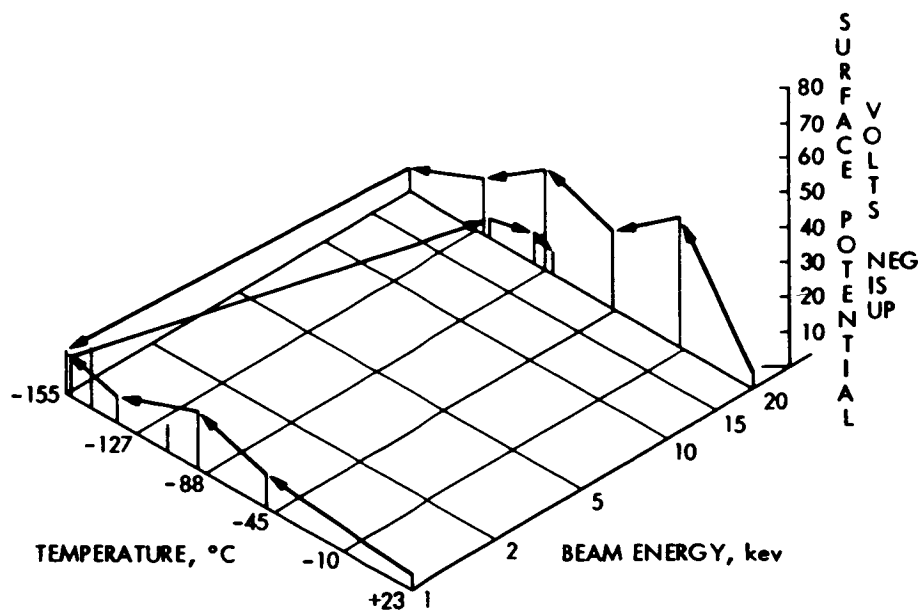


FIGURE 7. SURFACE POTENTIAL BOSTIC-FINCH SAMPLE 3-1

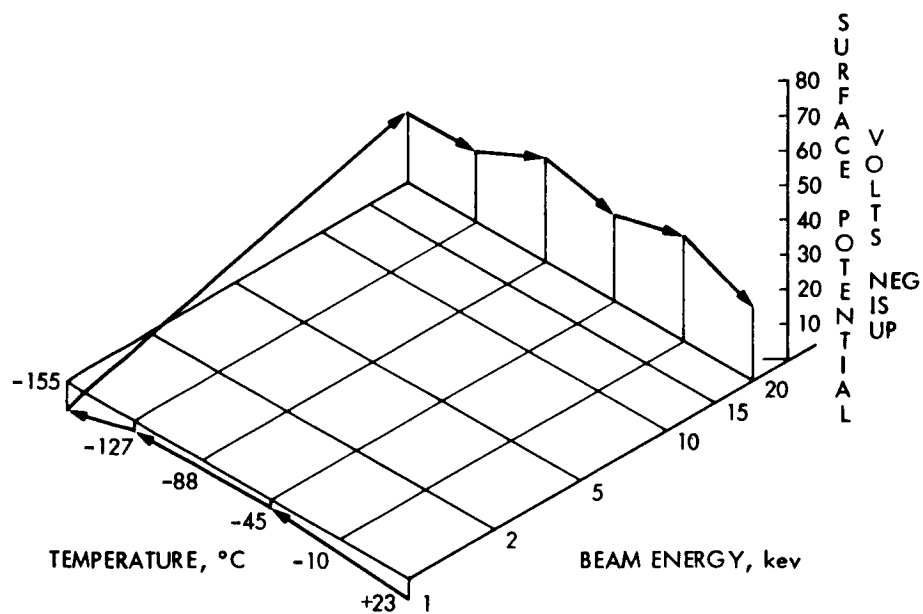


FIGURE 8. SURFACE POTENTIAL ZOT PS7

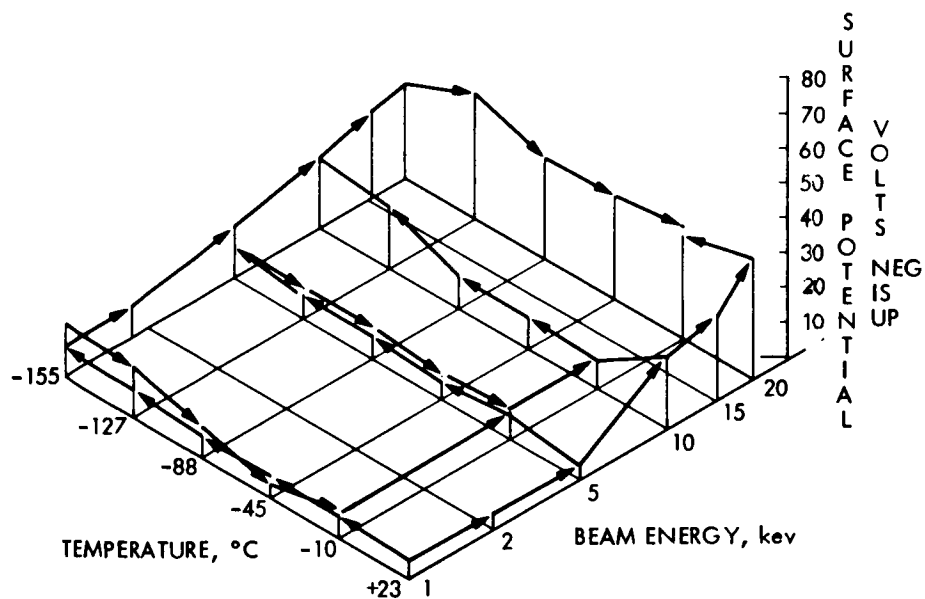


FIGURE 9. SURFACE POTENTIAL GODDARD WHITE NS43C SAMPLE 1-1

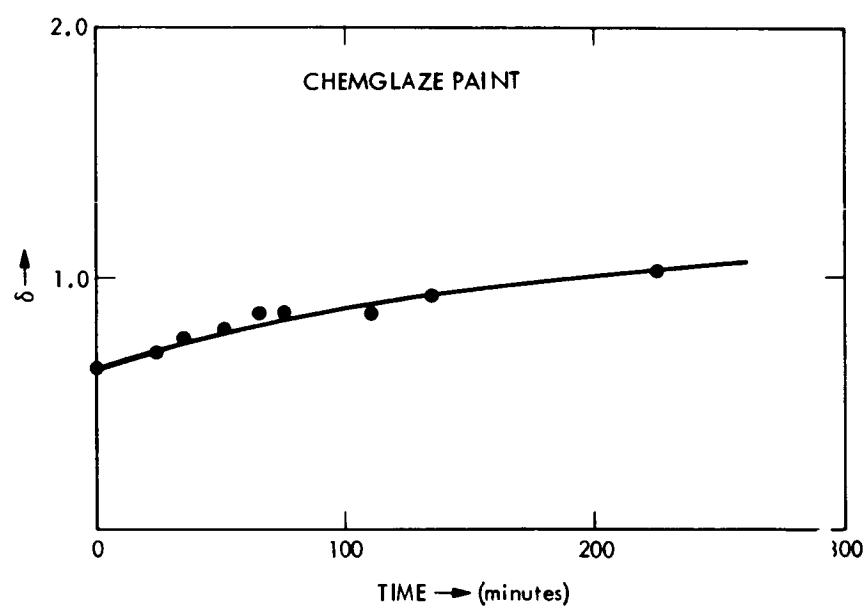


FIGURE 10

## EVALUATION OF CHARGE CONTROL TECHNIQUES ON SPACECRAFT THERMAL SURFACES (ELECTROSTATIC DISCHARGE STUDY)

**\*P. A. Robinson, Jr., E. M. Brown, S. M. Conan, C. R. Dulgeroff,  
W. R. Elkman, G. J. Holm, L. C. Lawton, G. J. Pack, and D. L. Shannon  
Hughes Research Laboratories**

### ABSTRACT

In this study the charging and discharging characteristics of

- Indium tin oxide coatings on Teflon, Kapton, and Quartz,
- CTL-15 white paint,
- Pinyoles at various spacings in Teflon and Kapton, and
- Conductive grids on Teflon and Kapton

were investigated. The test technique, results, and analysis used are presented. The major conclusions are:

- ITD coated Teflon, Kapton, and Quartz do not charge significantly.
- CTL-15 white paint shows no large charge build-up.
- Pinholes in spacecraft dielectrics increase the leakage through the sample and reduce the energy released in an arc.
- Conductive grids reduce the arc energy by two orders of magnitude over untreated samples.
- Extreme low temperatures ( $-195^{\circ}\text{C}$ ) do not significantly increase the arc energy of the gridded sample.

### INTRODUCTION

Under this investigation, many common spacecraft materials were investigated to determine:

- If the sample would arc
- The energy released in an arc.

---

\* Current Address: Jet Propulsion Laboratory

The major conclusions follow:

- Indium tin oxide (ITO) coated teflon, Kapton, and quartz show no significant charge build up.
- CTL-15 paint is at least as good as S13G low-outgassing paint in its ability to drain charge.
- The pinhole charge drainage technique reduces arc energy by an order of magnitude over untreated samples.
- Conducting grids reduce arc energy by two orders of magnitude over untreated samples.
- Extreme low temperature ( $\sim -195^{\circ}\text{C}$ ) does not significantly increase the arc energy for a gridded Kapton sample.

This paper is divided into four parts. The first summarizes the results of tests of various dielectric materials commonly used on spacecraft. The second describes the experimental apparatus, and the third describes the calculations used to analyze the data generated during testing. The final section is a collection of detailed experimental results and speculations.

#### EXPERIMENTAL RESULTS

Table 1 summarizes the results of many experiments on many different materials. Basically, each sample was exposed to a monoenergetic electron beam, and the back current and surface voltage were measured. The exponential decay of the back current with time was then used to calculate the capacitance of the sample. The charge lost during an arc was inferred from the increase in back current following the arc, and the energy in the arc was calculated based on the capacitance and voltage of the sample.

The samples listed in Table 1 are divided into five major classes — Teflon, paint, mirrors, ITO-coated, and Kapton at low temperatures ( $\sim -190^{\circ}\text{C}$ ). Under each major class, the specific samples tested are described. For each specific sample, the second column lists the beam voltage at which arcing was first observed or, if there was no arcing, the highest beam voltage used. The third column indicates whether or not arcing occurred. Because there were so many different samples to be analyzed, each sample was exposed only to (5, 10, 15, and 20 keV) 80, 160, 240, 320 femtojoules. Hence the beam voltage listed in column two is not an accurate discriminator to use in comparing different samples, but it does give an idea of the arcing threshold.

The fourth column, the calculated energy released in an arc for each sample, is a reasonable discriminator between various treatments. All but the mirror samples are (5- by 5 in.) 0.127 by 0.127 meters in size. The mirror samples are made of nine (1- by 1-in.) 0.0254 by 0.0254 meters individual mirrors. In each case, the largest arc observed during the experiment is listed



The fifth column gives a typical surface voltage attained by the sample during the experiment. For the samples that did not arc, this number is especially important since it indicates the amount of charge trapped on the dielectric.

### Teflon

All of the Teflon group of samples arced. (In contrast, a Teflon sample from the ITO-coated group did not arc.) The most energetic arcs came from the plain Teflon sample in a 20-keV beam. The pinhole charge drainage technique improved the situation somewhat, but the aluminum grid produced the most dramatic reduction in arc energy. The aluminum grid on the Teflon sample was made especially for this study. Since the grid was electrically in contact with the vacuum-deposited aluminum (VDA) on the back of the sample, it was impossible to monitor the current to the grid and the back current independently.

### Paints

Both CTL-15 and S13G-Lo are white paints used on thermal control surfaces. Workers at NASA Lewis Research Center have irradiated S13G-Lo with electrons. They observed some charging, and noticed a blue glow in the 20-keV beam. We have repeated their experiments with S13G-Lo, and again noted the glow of the sample. The CTL-15 paint compares well with the S13C-Lo. Neither paint charges significantly. The resistance of the paint samples is on the order of  $10^9 \Omega$ , but each sample is able to bleed off most of the charge in a  $1 \times 10^{-9} \text{ A/cm}^2$  beam. This suggests the possibility of using a paint in a grid pattern on dielectric films as a charge-control technique. This idea, however, was not pursued.

### Mirrors

All of the mirror configurations were made of nine mirrors supported by a honeycomb substrate. Only one configuration (and the ITO-coated mirror) did not arc. The untreated mirrors began arcing in a 15-keV beam. Metal-edged mirrors had not arced in previous experiments, and experiments in a  $1\text{-nA/cm}^2$  beam confirm this result. However, there was a large potential buildup on these samples, which suggests that the metalized edges merely neutralize the most likely arc inception area and do not bleed off all the charge. In later experiments at higher beam current densities, arcing did occur. As shown in Table 1, the energy in those arcs is greater than with an untreated mirror sample. This supports the idea that the lowest breakdown area in the system, but not the charge-buildup mechanism, has been eliminated, the net result being that the system now charges to a higher voltage.

The mirror system with the conductive grout is the most complex system. Carbon fibers are strung along the mirror edges and held in place with a carbon-loaded epoxy. This provides a resistive path from the front surface of the mirrors to ground ( $10^5 \Omega$  from epoxy to ground and  $10^3 \Omega$  from carbon fiber to ground). This sample arced at the same beam energy but with less energy

than the control sample. This may have occurred because the conductive grout limited the

- Number of mirrors involved in the arc
- The electron flow.

#### Low-Temperature Kapton Grid

These experiments were done to determine the effect of extremely low temperatures on the performance of the aluminum grid on Kapton. Since both secondary electron emission and resistivity are temperature dependent, it seemed plausible that the aluminum-on-Kapton technique might not be as effective at cold temperatures. To remove this concern, both plain Kapton and gridded Kapton were run at close to liquid nitrogen temperature. There was no dramatic change in the charging properties of the aluminum grid. Both ambient and low temperature tests show about a two-order-of-magnitude reduction in arc energy for gridded samples. Grids arc at a lower beam energy than does the plain Kapton.

#### ITO-Coated Materials

Coating with ITO holds the promise of neutralizing any charging problems by providing a conducting surface for all thermal materials and dielectrics. All three ITO-coated materials investigated (Teflon, Kapton, and quartz) behaved very well. They did not appear to develop any significant charge in a  $1.0\text{-nA/cm}^2$  beam, as indicated by the absence of arcing and the low surface voltages.

#### EXPERIMENTAL PROCEDURE

All of the electrostatic testing of materials was performed at the Hughes Research Laboratories (HRL) spacecraft charging simulation facility. Samples were typically 0.127 meter (5 in.) square and mounted on stainless-steel plates. There was a 1-cm gap between the edge of the plate and the edge of the sample. The outer 0.5 cm of the metalization on the sample was removed by etching. This was done to prevent arcing around the exposed edges. After being cleaned with alcohol, the sample was mounted in the target chamber (shown in Figure 1). The electron flux at the target, produced by an electron gun (shown in Figure 2), can be varied between 0.1 and  $10\text{ nA/cm}^2$  and the energy between 1 and 20 keV. The pressure in the vacuum chamber was held to about  $2.7 \times 10^{-3}$  Pascals ( $2 \times 10^{-5}$  Torr).

The principal experimental difficulty was in keeping the electron flux accurately calibrated as the filament aged. The electron flux increased several times during the testing even though none of the electron gun controls had been changed. These changes were indicated by the simultaneous increase of

both the wall current and the back current. We have not yet discovered how to eliminate this effect experimentally. It can, however, be accounted for in the analysis.

For the low-temperature tests, it was important to reduce the sample temperature to below  $-100^{\circ}\text{C}$ . To do this, the special mounting fixture shown in Figure 3 was made. Liquid nitrogen (boiling point  $-195.8^{\circ}\text{C}$ ) was used to cool the support that held the sample. Thermocouple readings showed that the sample temperature was at or below about  $-190^{\circ}\text{C}$  when the fixture was full of liquid nitrogen. A heater was used to warm the sample so that it could be removed quickly from the test chamber. In the future, this fixture can be used with other liquids or with temperature-controlled baths to control sample temperature over a wide range.

#### METHOD OF COMPARISON AND ANALYSIS

In the past, dielectrics have been ranked by the energy of the electron beam when arcing began. Since the total energy stored on a dielectric is proportional to the voltage on the sample squared, and the voltage on the sample increases as the electron beam energy increases, this is a good measure of a charge-control technique. However, it ignores some important factors in charge control. In this study, the energy involved in the arc was calculated directly by:

- (1) Fitting the back-current data after an arc
- (2) Using that fit to calculate the total charge lost to the sample
- (3) Estimating the capacitance of the sample from the backcurrent data
- (4) Using the voltage of the sample immediately following the arc to estimate the energy of the arc.

This section deals with the mathematical model used to determine the capacitance and the charge lost during discharging. The development of this model is summarized in Boxes 1, 2, and 3. The results of this analysis are summarized in a later section.

#### Mathematical Details

The text in Box 1 mathematically describes the model of charge buildup on a dielectric surface. The starting point is that the voltage buildup on the front of the dielectric is proportional to the net current to the sample. This equation introduces  $C$ , the capacitance of the sample. The simplest form the various currents can assume is also shown. The current diverted from the beam because the sample is charged is assumed to be a linear function of the surface voltage. The backscattered and secondary-electron currents are related to the net incident electron flux by a single constant  $\beta$ . Leakage through the sample

## BOX 1

## CHARGE-BUILD-UP MODEL

BASIC EQUATION: 
$$\frac{dV}{dt} = \frac{1}{C} \{ i_o - i_D - i_B - i_{SE} - i_L \}$$

(INTRODUCES CAPACITANCE C OF THE SAMPLE)

ASSUMPTIONS:

$i_o$  : ELECTRON CURRENT FROM SOURCE

$i_D$  : CURRENT DIVERTED FROM SAMPLE  $= i_o \frac{V}{E}$

$\left( \text{CURRENT TO SAMPLE IS } i_o \left( 1 - \frac{V}{E} \right) \right)$

$i_B + i_{SE}$  : BACKSCATTER PLUS SECONDARY EMISSION

CURRENTS  $= i_o \left( 1 - \frac{V}{E} \right) \beta$

(INTRODUCES MATERIAL PARAMETER  $\beta$ )

$i_L$  : LEAKAGE THROUGH THE SAMPLE  $= \frac{V}{R}$

(INTRODUCES RESISTANCE OF SAMPLE, R)

E = ENERGY OF THE ELECTRON BEAM

SOLUTION:

VOLTAGE ON SAMPLE

$$V = \frac{i_o \beta E R}{i_o \beta R + E} + \left[ V_o - \frac{i_o \beta E R}{(i_o \beta R + E)} \right] \exp \left[ - \frac{i_o \beta R + E}{E R C} (t - t_o) \right]$$

MEASURED BACK CURRENT

$$C \frac{dV}{dt} + \frac{V}{R} = - \frac{i_o \beta E}{(i_o \beta R + E)} + \left[ i_o \beta + \frac{V_o}{R} - \frac{(V_o i_o \beta R + V_o E)}{E R} - \frac{i_o \beta E}{(i_o \beta R + E)} \right] \exp \left[ - \frac{i_o \beta R + E}{E R C} (t - t_o) \right]$$

is assumed to follow Ohms' law, which introduces the sample's resistivity  $R$ . The next most complicated form would be to assume that the parameter  $\beta$  is itself a linear function of surface voltage. This would result in a solution of exactly the same form as with the first-order theory, but new parameters would have been introduced and the algebra would be more complex. The first-order formulation of the problem can be solved directly for the surface potential as a function of time and initial voltage on the surface. From this, the back current can be inferred.

Box 2 presents a method of fitting a series of data points to an exponential plus a constant. This is the form of the back current in both the first-order model developed in Box 1 and the second-order model. The constant term is approximated by the last current measured; the current which dies away exponentially is then the difference between the initial and final currents. Then the decay constant is calculated based on an intermediate current measurement and is used to correct the original estimate of the constant and exponential currents. These new estimates are used to refine the decay constant calculation and so on. This process is continued until the decay constant stops changing. This method has been satisfactory in estimating the exponential and constant current values for the data collected.

In all the fits presented, the data and the fit have been coplotted as a visual check on the goodness of the fit. Although the form assumed is too simple to fit the back-current data accurately and completely, it is a reasonable approximation to all of the data so far.

The same procedure was used to fit voltage curves. In the case analyzed, the decay constant implied from the voltage data agreed with that implied from the current data. This encouraging result led us to use the simple model in Box 1 and the simple fit in Box 2 to calculate  $R$ ,  $C$ , and  $\beta$  from the fit to the back-current data. Box 3 shows the equations used to calculate  $R$ ,  $C$ , and  $\beta$  from the fit to the back current. These result from equating the results from the model in Box 1 with the corresponding data-determined coefficients in Box 2.

Box 4 shows the equations used to calculate the energy in an arc. The capacitance  $C$  is calculated as in Box 3. The charge lost to the sample is calculated by integrating the exponential part of the current. This underestimates the charge lost slightly. The voltage immediately following the arc is based on direct measurement, or on a correspondence between measured surface voltage and back current.

#### Sensitivity of Calculations to Experimental Parameters

In the current tests, the capacitance values calculated as shown in Box 3 were insensitive to the initial current  $i_0$ . The backscattering-secondary emission parameter  $\beta$  was very sensitive to the initial current  $i_0$ . The resistance may actually vary as a function of beam current and did show some sensitivity to the beam current. This result is to be expected from the form of the back current derived in Box 1. The exponent primarily determines the capacitance, which is not a strong function of  $i_0$ . The resistance depends strongly on the

BOX 2  
FIT TO  $A + Be^{\alpha t}$

INITIAL ESTIMATE:  $A = I(t_{\text{FINAL}})$

$B = I(t_0) - I(t_{\text{FINAL}})$

$\alpha = \frac{1}{t} \ln \left[ \frac{I(t) - A}{B} \right]$

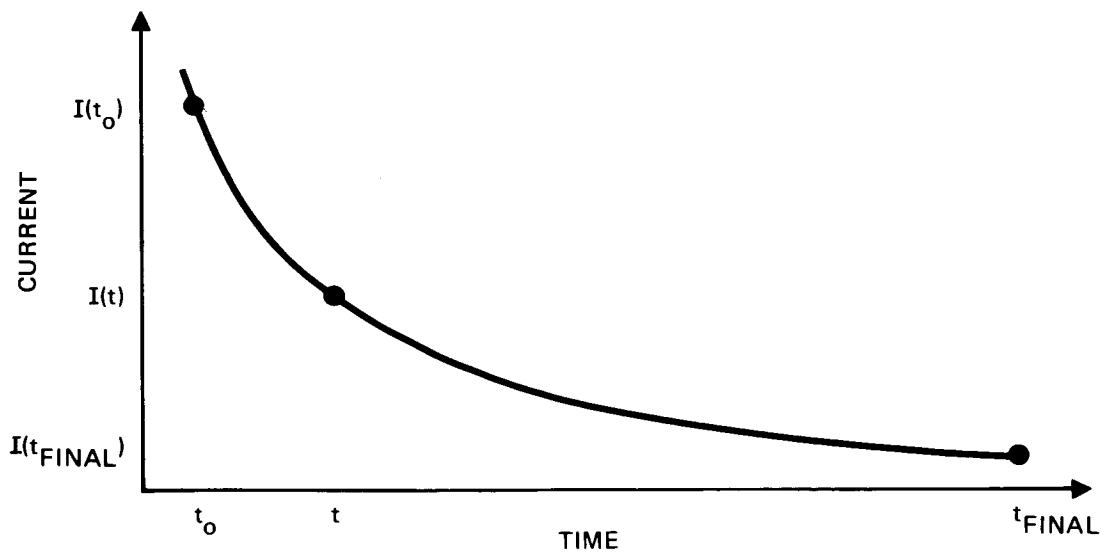
BUT A IS OFF BY  $Be^{\alpha t_{\text{FINAL}}}$

CORRECTION:  $A' = I(t_{\text{FINAL}}) - Be^{\alpha t_{\text{FINAL}}}$

$B' = I(t_0) - I(t_{\text{FINAL}}) + Be^{\alpha t_{\text{FINAL}}}$

RECALCULATE  $\alpha$  AND  $Be^{\alpha t_{\text{FINAL}}}$

REPEAT UNTIL CHANGE IN  $\alpha$  IS SMALL



## BOX 3

CALCULATION OF MATERIAL PARAMETERS R, C, AND  $\beta$  FROM  
FIT TO BACKCURRENT DATA AND INITIAL CONDITIONS

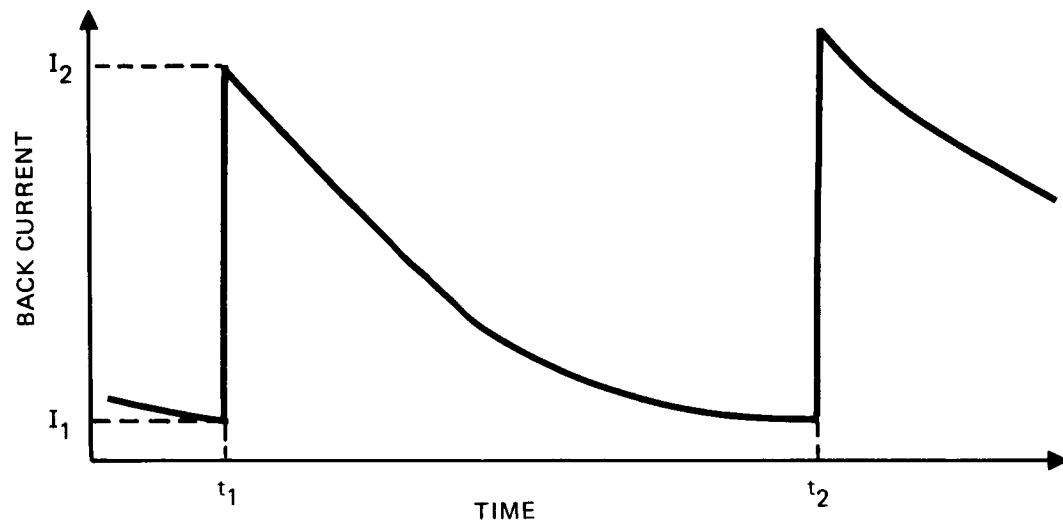
$$R = \frac{E}{A} \left( \frac{B + A \frac{V_o}{E}}{B + A} \right)$$

$$C = \frac{(A + B)^2}{\alpha(E - V_o) \left( B + A \frac{V_o}{E} \right)}$$

$$\beta = \frac{B + A}{i_o \left( 1 - \frac{V_o}{E} \right)}$$

## BOX 4

## CHARGE AND ENERGY RELEASED IN AN ARC



CHARGE RELEASED DURING ARC:

$$\Delta Q \cong \int_{t_1}^{t_2} B e^{\alpha t} dt = \frac{I_1 - I_2}{\alpha}$$

ENERGY RELEASED DURING ARC:

$$\Delta E = \frac{1}{2} C V^2 \bigg|_{V(I_1)}^{V(I_2)} = \frac{\Delta Q^2}{2C} + V(I_2) \Delta Q$$



equilibrium leakage current ( $A$ , in the fit to the back current), which is linearly dependent on  $i_0$ . The backscattering-secondary-emission parameter depends on both  $A$  and  $B$  and is strongly dependent on  $i_0$ . Since  $i_0$  is the most difficult experimental parameter to control, the most uncertain parameter determined is  $\beta$ . It is important to realize that this sensitive exists, since the electron source depends on a tungsten filament. The weld holding the filament in place has on several occasions failed in a manner that increases the electron flux by over an order of magnitude. In that case, if a value of  $\beta$  is known, it can be used to estimate  $i_0$ !

## DETAILED EXPERIMENTAL RESULTS

### Teflon

Tables 2 and 3 give some of the parameters calculated from back-current data for Teflon. Table 2 gives the parameters ( $A$ ,  $B$ , and  $\alpha$ ) that describe the exponential decay of back current with time. Figure 4 shows back-current data for 5-keV electron beams on the 3/8 in. pinhole sample and the fit to it. The other fits shown in Table 2 are similar. Figure 5 shows two arcs for plain Teflon in a 20-keV beam. Table 3 lists the changes in back current observed for typical arcs on Teflon samples.

As with most programs that survey a broad range of parameters, not all of the data is consistent. One particular example is the experiment with Teflon at 10 keV on 26 June. Notice the extremely high values of  $A$ ,  $B$ , and  $\alpha$ . During that experiment, the electron source apparently increased its current density. In later experiments, the values of  $A$ ,  $B$ , and  $\alpha$  were consistent with earlier experiments (28 June). Using the simple model discussed previously and normalizing the current density by assuming that  $\beta$  is the value from other experiments, the decay constant  $\alpha$  can be calculated. This normalized  $\alpha$  agrees with later experiments (28 June). This tends to confirm our high-current-density explanation of the 26 June experiment and the discussion of experimental uncertainties given earlier.

Another interesting result of the fits made to the Teflon data is shown in Table 4. Here the resistances order the samples in the same way the arc energies do.

### Mirrors

All the mirror samples were made from nine individual mirrors and associated adhesives, grouting, etc. This configurational complexity results in a back current that is a complex function of time. Figure 6 shows the back current versus time for the plain quartz sample in a 10-keV beam; the data is very erratic. Modified and plain mirror back-current measurements also show this characteristic. However, the voltage buildup shown in Figure 7 is reasonably smooth and agrees with the initial rates calculated from the back-current data. The surface voltage measurement integrates over a large area compared with the edge of the mirrors and represents the charge buildup on the quartz surface.

The back current, however, responds to currents from any part of the sample. The sputtered edge and plain mirrors have many remarkable similarities even though one arcs and the other does not.

In Figure 6, the best fit to the back-current data of the sputtered edge sample at 10 keV is also plotted. Although it is generally higher than the plain mirror sample, the general trend and order of magnitude is the same.

One difference between the modified and unmodified mirrors is shown in Figure 8, in which the equilibrium leakage current is plotted versus the equilibrium surface potential. The numbers in parentheses are the beam voltages at each point. Although, in the normal quartz configuration, the leakage increases as the voltage increases, the opposite is true for the modified sample. This implies that the conduction mechanism introduced by modifying the mirror's edges becomes less effective as the energy is increased.

### Kapton

During this experimental investigation, the first testing of thin dielectric films at low temperature was performed. Two very interesting effects were noticed. First, the back current of a charged sample with no electron beam increases exponentially and then drops to a low value as the temperature of the sample is increased. This effect may be due to the increased number of states available to trapped electrons as the temperature rises.

Second the back current for the plain Kapton sample behaves strangely when the sample is illuminated by a flashlight. Figure 9 shows the normal back-current decay before and during illumination. The back current increases when the flashlight was turned on the sample. This indicates that the flashlight was discharging the sample. When the light was removed, charging appeared to continue as before. We actually used this effect to delay a sample from arcing.

Before these experiments, only UV light was expected to be able to discharge the sample. During this investigation, filters that remove all UV were used, but the effect persisted. This effect might be used as a radiation detector. The frequency and intensity response will depend on the dielectric materials used, their temperature and thickness, the electron beam, and possibly other factors. We intend to characterize this effect for Kapton and perhaps other materials in the future.

Table 1. Results of Electron-Beam Experiments

Material/Sample	Beam Energy, keV	Did Sample Arc?	Calculated Energy for Largest Arc, mJ	Surface Voltage, kV
TEFLON				
Plain	20	Yes	150	>8.0
Pinholes spaced at 3/8 in.	10	Yes	80	8.5
Pinholes spaced at 1/8 in.	10	Yes	20	4.5
Pattern of +x cut in at 3/8 in. spacing	10	Yes	40	?
Aluminum grid on front surface	10	Yes	2	5.0
PAINT				
CTL-15	20	No	---	0.3
S13G-Lo	20	No	---	0.4
MIRRORS				
Plain	15	Yes	16	4.0
Conductive edge 1.0 mA/cm <sup>2</sup> beam	20	No	---	9.5
Conductive edge 2 nA/cm <sup>2</sup> beam	20	Yes	33	9.5
Conductive grout and carbon fibers	15	Yes	3	4.0
LOW-TEMPERATURE KAPTON				
Plain	20	Yes	160	16.0
Aluminum grid	10	Yes	1	7.0
ITO-COATED MATERIALS				
Mirrors	20	No	---	0.2
Teflon	20	No	---	0.4
Kapton	20	No	---	0.4

Table 2. Teflon Back Current

Description of Teflon Sample	Beam Energy, keV	Date	Back Current		
			Equilibrium Leakage A, nA	Displacement Current B, nA	Decay Constant, min <sup>-1</sup>
Plain	5	5/30	2.83	37.2	-0.1367
Plain; initial voltage = 2.6 kV	10	5/30	4.9	4.3	-0.127
Plain; after charging in 15 keV beam	20	6/14	33.6	44.4	-0.3786
Plain; after arc	20 15	6/14 6/11	22.5 22.8	37.5 15.6	-0.1647 -0.1567
Pinholes spaced at 3/8 in.	5	6/26	11.56	46.44	-0.1605
Pinholes spaced at 3/8 in. (trouble with electron source)	10	6/26	816	4480	-6.06
Pinholes spaced at 3/8 in. (repeat, after repairing electron source)	10 10	6/28 6/28	12.9 10.0	42.1 21.7	-0.1076 -0.1081
Slits 1/8 in. long in + x pattern at 3/8 in. centers	10 10 10	6/5 6/5 6/5	29 40 45.4	40.8 24.0 39.5	-0.1349 -0.1961 -0.1775
Pinholes spaced at 1/8 in.	10	6/4	45.7	32.3	-0.1854
Aluminum grid in hexangle pattern	5	6/15	8.4	49.4	-0.0882

Table 3. Teflon Arcing Parameters (Worst Case)

Sample	$I_1,$ $10^{-8}$ A	$I_2,$ $10^{-8}$ A	$Q,$ $10^{-6}$ C	$E,$ $10^{-3}$ J
Plain 20 keV	2.3	7.8	20.0	146.9
3/8 in. pinholes	1.0	3.4	13.3	36.64
1/8 in. pinholes	5.3	7.9	8.4	21.6
+, x shaped pattern	4.4	8.5	12.5	35.9
Grid	1.74	2.0	0.89	1.55

Table 4. Calculated Resistances for Teflon Samples

Sample	$R, \Omega$
Plain	$1.8 \times 10^{12}$
3/8 in. pinholes	$1.0 \times 10^{12}$
+, x shaped holes	$2.2 \times 10^{11}$
1/8 in. pinholes	$1.8 \times 10^{11}$

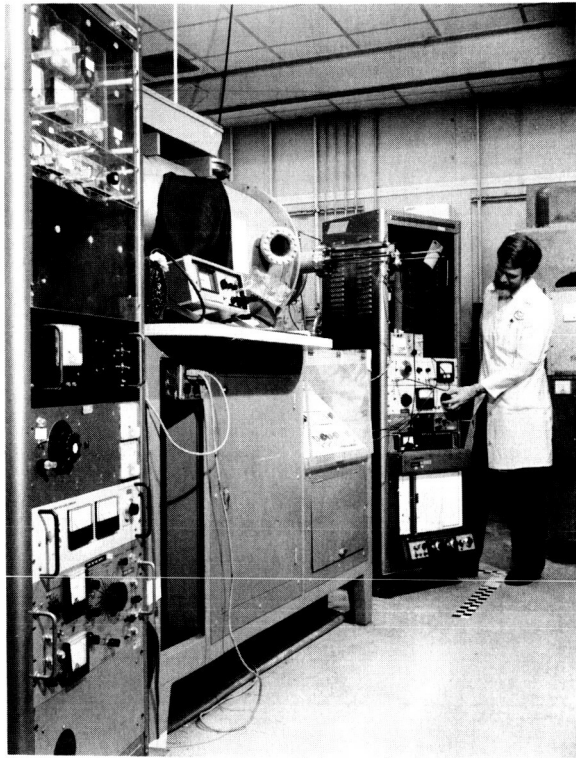


Figure 1. Experimental apparatus.

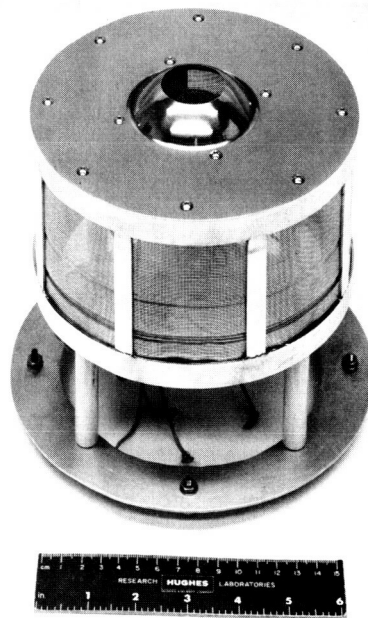


Figure 2. Divergent electron source.

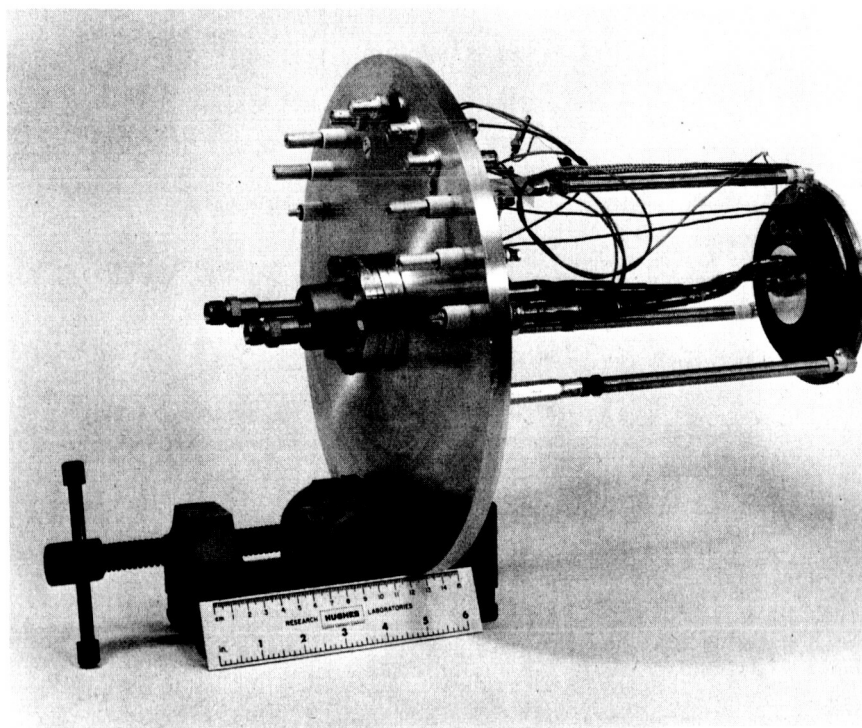
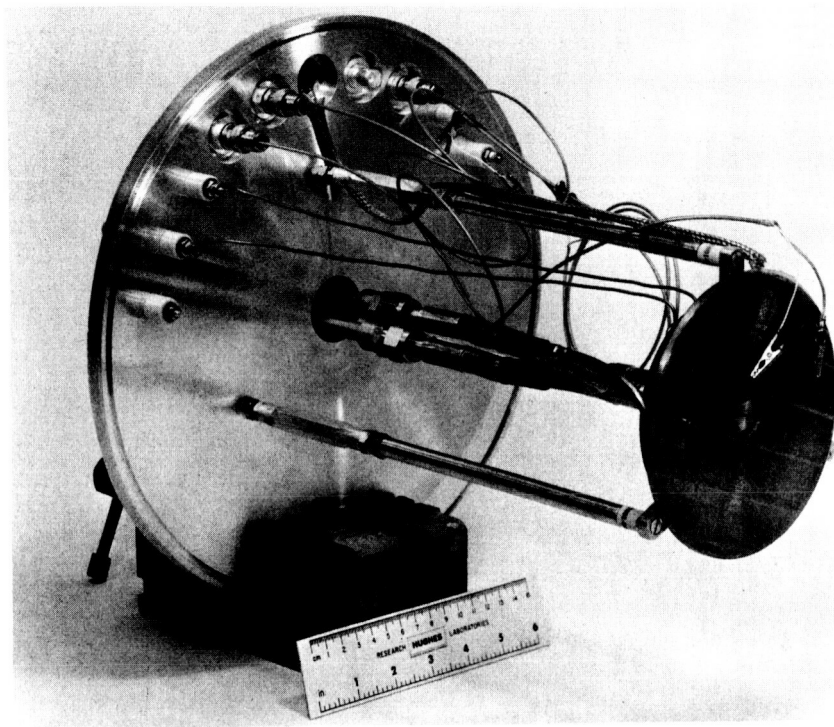


Figure 3. Low temperature fixture.

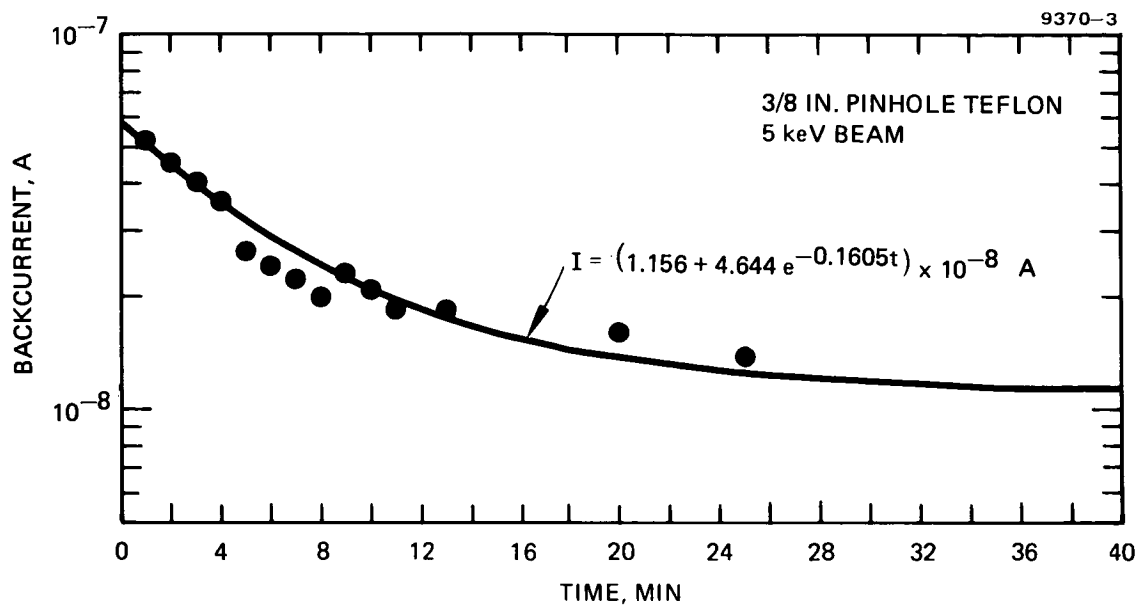


Figure 4. Typical Teflon result.

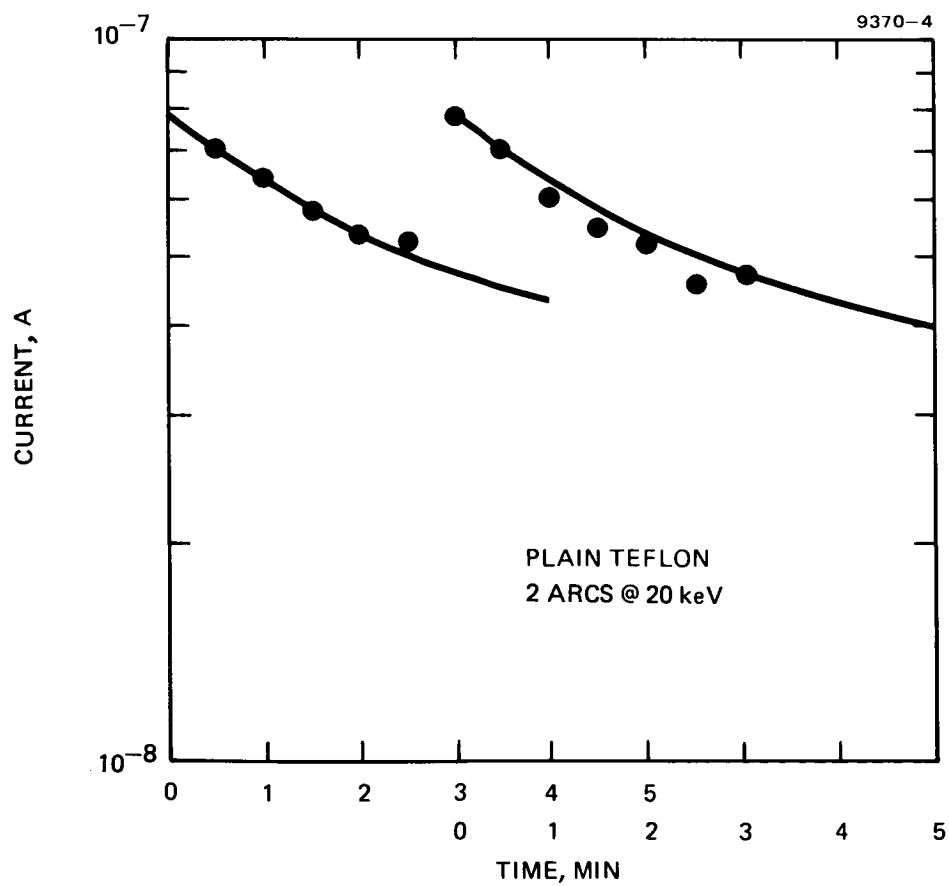


Figure 5. Typical arc data.



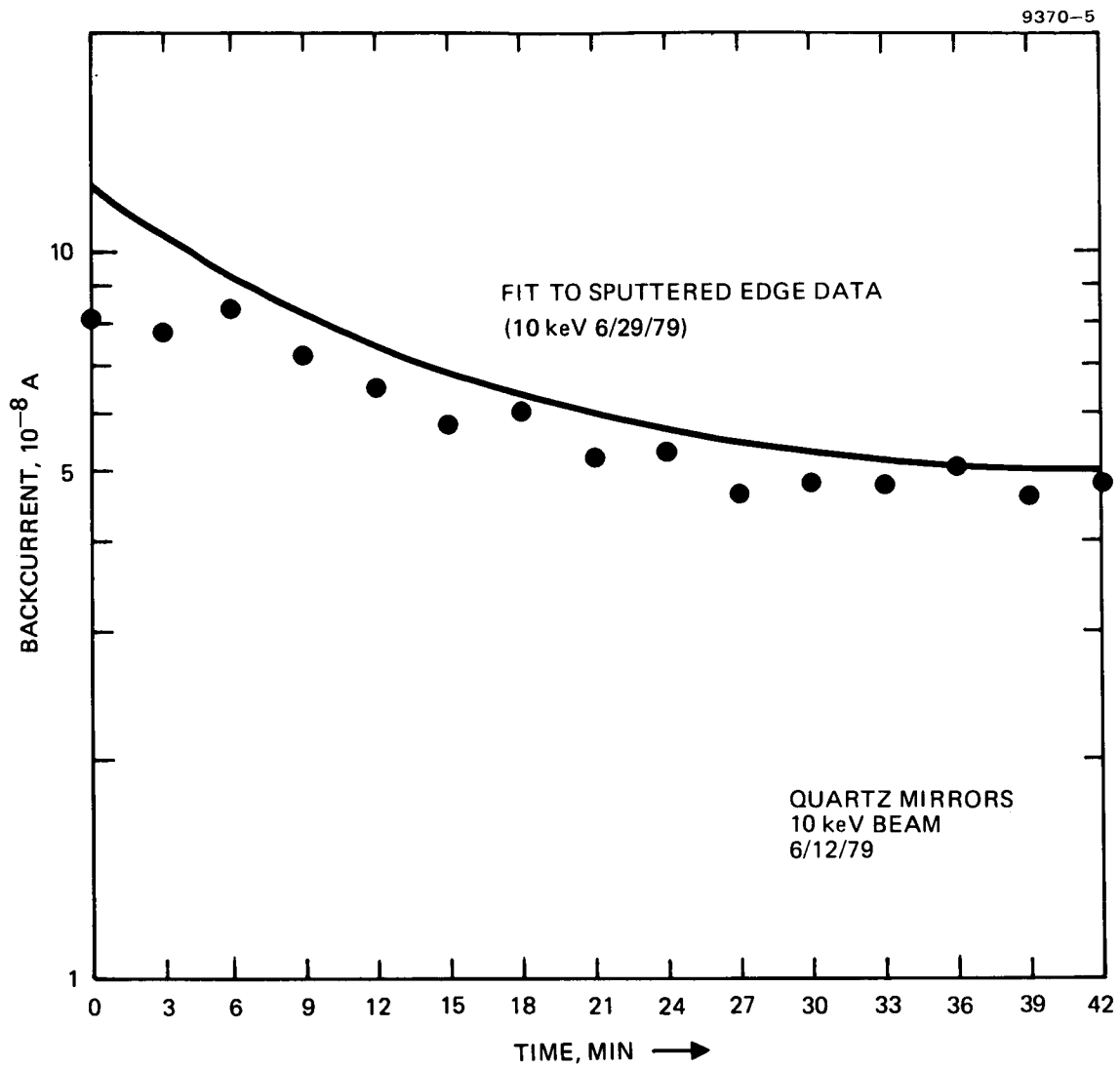


Figure 6. Typical quartz mirror data.

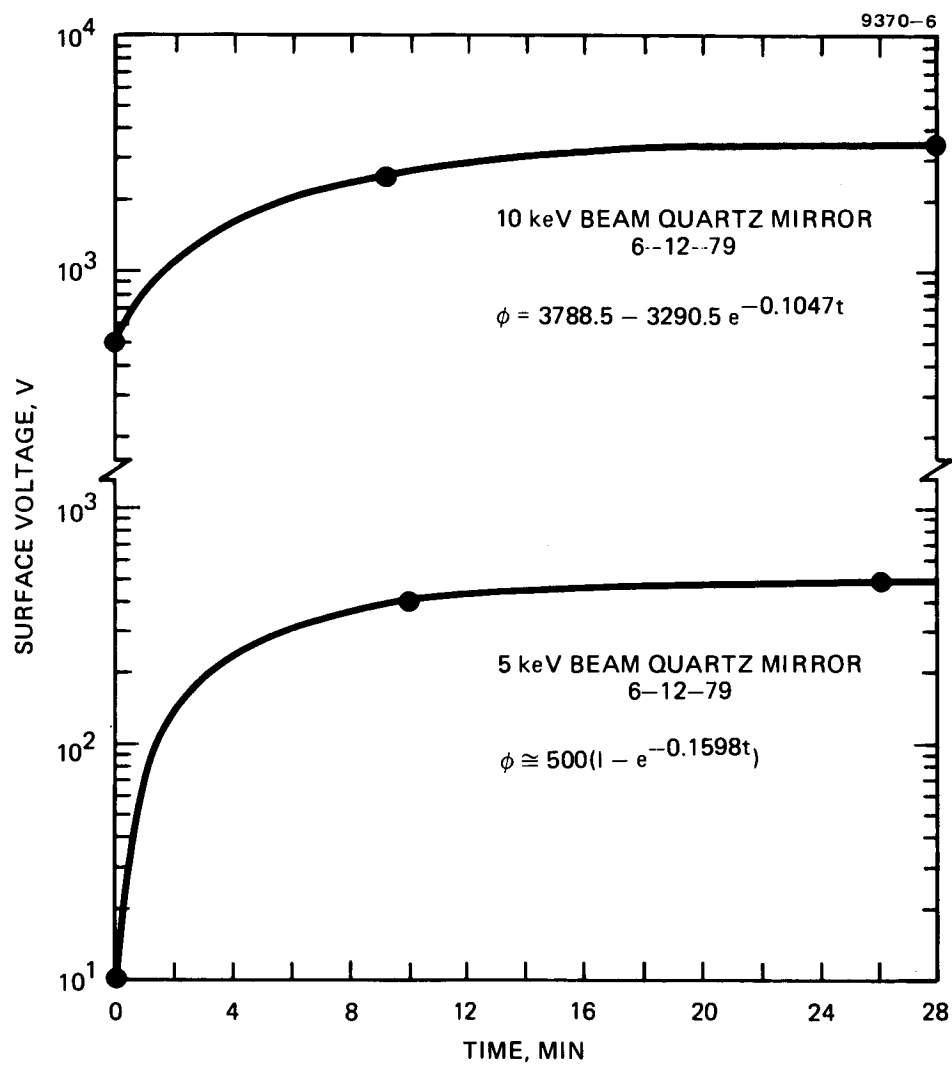


Figure 7. Voltage buildup for quartz.

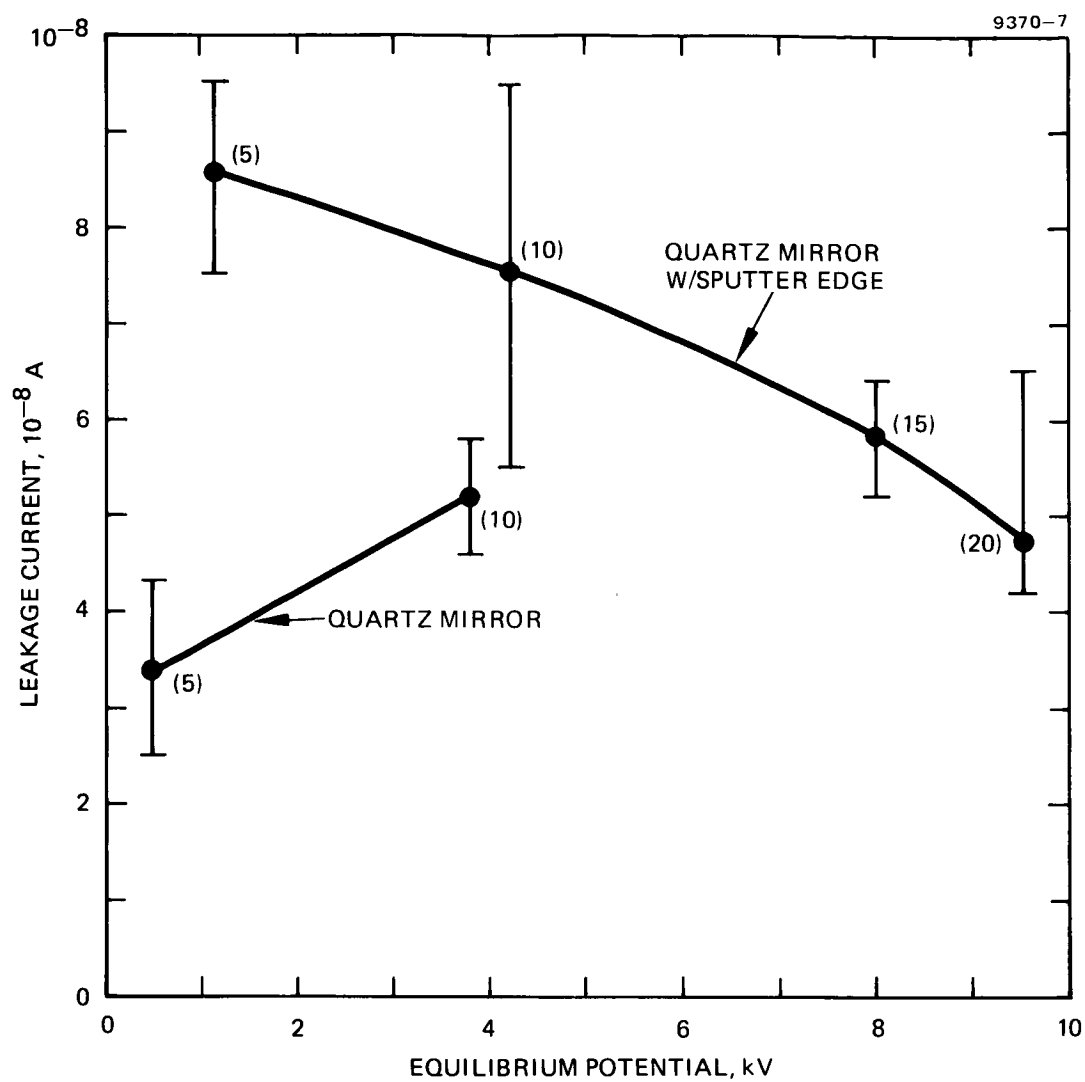


Figure 8. Contrast of standard edge and sputtered edge samples.

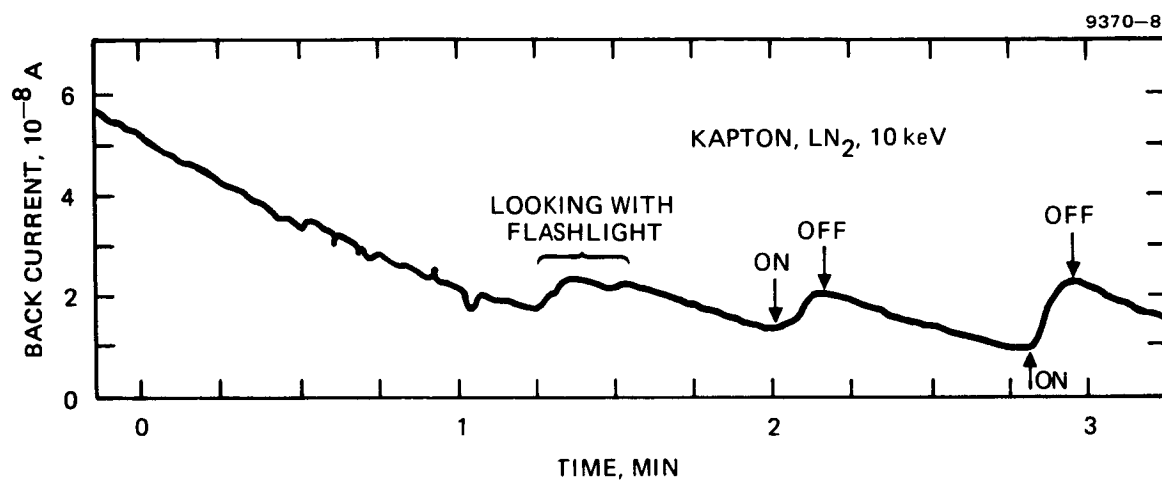


Figure 9. First flashlight effect data.

# CONDUCTION THROUGH PUNCTURES IN METAL-BACKED DIELECTRICS\*

A. Meulenberg  
COMSAT Laboratories

P. A. Robinson, Jr.†  
Jet Propulsion Laboratory  
California Institute of Technology

## SUMMARY

The current conducted through a dielectric, as well as the characteristics of any arcs, are significantly influenced by the presence of punctures through the dielectric. This paper presents a theoretical mechanism to explain the main features of experiments with punctured spacecraft-thermal-blanket materials. The model is based on consideration of the electric fields developed about punctures; the focusing of primary electrons toward the punctures; the generation, migration, and cascade of secondary electrons along the surface; and the radiation induced conductivity characteristics of thin dielectric films. Qualitative predictions of the model agree with experiment results.

## INTRODUCTION

Observation of discharges at defects or edges of thermal blanket materials exposed to an electron beam has led the authors to study pinholes as a means of reducing problems associated with charging of spacecraft dielectrics. Current leakage through punctures in dielectrics to a charged conductor beneath has been a concern for a number of years (ref. 1-7). In 1969 an anomalously high current collection ability of pinholes in dielectrics was first reported by Sellen et al. (ref. 1), who were studying the effects of drainage current through solar cell interconnects in ionospheric (100 to 600 mile altitude) plasma. Pinholes are small, and it would be expected that the trapping of negative charge on the dielectric surface near positively charged pinholes would repel, and therefore reduce, the collection of negative charge (ref. 6).

\*This paper is based in part upon work performed at COMSAT Laboratories under the sponsorship of International Telecommunications Satellite Organization (INTELSAT) and in part upon work performed at Hughes Research Laboratory under Internal Research and Development funds.

†Formerly at Hughes Research Laboratory.

Figures 1 and 2 show some measurements of pinhole current collection for positively biased pinholes, as a function of the area of the dielectric surface and the applied voltage. At low voltages (the conductor beneath the pinhole set below +1000 volts) the pinhole is effectively shielded from the plasma as originally expected. However, as the voltage increases, the current collected on the conductor exceeds that predicted from simple probe theory or simple electrostatic effects (ref. 6). The higher than expected current through the pinhole was tentatively attributed to surface leakage currents near the pinhole. Equally unusual are the effects of the surface area of the specimen (a ring of dielectric concentric about a pinhole). The "effective" area of current collection can be as large as the surface of the sample itself (ref. 2).

## EXPERIMENT

The situation of a positively charged pinhole in a dielectric surrounded by a neutral plasma (as generally assumed in the above references) is somewhat similar to the authors' configuration of a grounded pinhole in a dielectric being irradiated with an electron beam. Experimental results pertaining to pinholes used in this way are shown in figures 3 and 4 and table I. Details of the experiment used to obtain the results presented here are given in Reference 8. In figure 3a, the dielectric surface voltage is plotted versus the electron beam energy for planar Kapton and Kapton with pinholes. At beam energies up to 8 keV, there is no significant difference in equilibrium voltage. Above 10 keV, further charging of the punctured Kapton is prevented by arcs. Similar results below 10 keV for Teflon are shown in figure 3b. The leakage current as a function of the number of pinholes is shown in figure 4. Table I contrasts the arc energies for planar Teflon and pinholed Teflon.

In the discussion that follows, the punctured structure will be compared with an identical planar structure that has not been so altered. The influence on experimental measurements of surface potential and current collected by the metal back will be considered as a function of hole density. The probability and nature of surface discharges will be contrasted for the two structures.

## THEORY

The structure considered is a hole punched through a dielectric sheet (very large compared to the pinhole) from the metal coated side. The conditions include a monoenergetic electron beam normally incident on the dielectric surface with the metal layer grounded. Interaction of the beam with the structure and development of potentials, electric fields, and currents in and around the dielectric adjacent to the hole will be discussed.

## Charging of Planar Samples

An electron beam, incident on a planar dielectric, will generate electron-hole pairs and deposit negative charge up to the electron range in the material. This negative charge will electrostatically drive electrons from the metal backing to ground, leaving a positive charge at the metal-dielectric interface. The electric field generated between the negative front surface volume and the positive back layer will polarize the dielectric and direct the otherwise random motion of thermally generated mobile charge carriers in the bulk and of radiation induced charge carriers in the irradiated volume.

Charging will continue until steady state is established between the incoming electron beam, secondary and backscattered electrons, and carrier migration through the bulk and surface layer of the dielectric. At steady state, since the surface potential will generally be within several kilovolts of the beam energy, the beam will not penetrate as deeply as initially. Therefore, charge redistribution within this surface layer could be considerable; however, most of the charge, prior to steady state, will migrate toward the back surface. Near steady state, the secondary emission coefficient approaches 1, and most of the newly deposited electrons migrate toward the front surface rather than toward the back. (This migration toward the front surface is a consequence of an electric field generated by the positive charge remaining on the front surface when secondary electrons are knocked off by incident electrons, and by the electrons trapped deeper in the dielectric.)

## Charging of Punctured Samples

If the unbounded surface described above is punctured, then a ground point is established on the front surface and steady state conditions are modified significantly in the vicinity of the hole. Initial charging conditions are not much altered until the surface potential begins to approach a high negative steady state value. As the surface potential away from the hole becomes more negative and secondary emission increases, this region contributes less and less to the current being collected at the back surface. The surface in the immediate vicinity of the hole maintains a lower secondary emission because it is still close to ground potential. The near ground potential is maintained by surface conductivity enhanced by tertiary emission (electrons knocked from the surface by secondary electrons) and has several influences:

- a. the beam incident in that area penetrates as deeply as at initiation of charging, and with the much lower secondary emission of the initial conditions;
- b. the incident beam is focused toward the hole by the low potential; and

c. the strong potential gradient on the surface approaching the hole acts as an electron multiplier, thereby transporting a disproportionate number of electrons to the ground plane.

The effect in each case is an increase in the electron current collected on the back plate (figure 4); in fact, the current density collected by the hole and its immediate surface area may be 2 or 3 orders of magnitude higher than that expected from the area of the pinhole alone or than that migrating through an equivalent bulk of the dielectric.

The local potentials are useful in describing the charge and discharge phenomena in the vicinity of a hole. Figure 5 illustrates the potential well in which secondary electrons are trapped and, along with the tertiaries, collected by the ground plane in a hole. This figure also indicates that holes reduce the surface potential in only a small area about the hole; therefore, a very large hole density is required to alter the general surface potential measured only a small distance from the dielectric.

### Discharges in Dielectrics

High energy electrons focused and incident on the area about the hole generate a high density of carriers at a depth greater than that in the planar areas. Since the potential is also much less negative near the hole, transverse surface fields will be much greater and the consequent surface and subsurface current densities will be higher than for nonadjacent regions. If holes in the dielectric are formed by mechanically punching through from the metal layer side, then the metal will probably emerge through the deformed dielectric in such a manner as to intersect the heavily irradiated region (figure 6). The radiation induced conductivity (RIC) would then be field enhanced to propel electrons through the dielectric toward the emergent metal. If such currents happen to find or generate a preferred path, ohmic heating (which will increase conductivity) and thermal runaway could result in an electric discharge across or under the surface near the hole.

Since the discharge mode is for trapped electrons going to ground, a negative pulse is expected. The low energy negative component of this discharge would be confined to the vicinity of the hole (and collected at the ground) except to the extent that the steady state potential is disrupted by the plasma generated by the discharge. However, some electrons would escape and constitute a positive pulse as viewed from the metal back. The positive ions created in the plasma formed by the arc in the hole will be accelerated away from the hole; most will go into space, but many will return to the negatively charged surface away from the hole. Positive ions returning to the surface will generate



secondary electrons, most of which will escape (adding to the tail of the electron pulse), but many of which will find their way to the hole region and contribute to the tertiary electron cascade across the surface toward the ground plane. The resultant current observed on the back metal contact would be a fast, ringing pulse with little energy content.

Two types of discharge are possible in planar dielectrics. The first is a discharge from the stored-charge regions beneath the surface to the metal backing. The energy liberated in the discharge will vaporize material, which often blasts through the front surface as well as the back. If this discharge does not erupt through the front surface, the negative pulse seen in the ground line will be very small since charge redistribution is not great. If, however, the discharge does erupt through the front surface, then a large electron concentration will be accelerated away from the surface and create a strong positive pulse in the ground line. Positive ions (from the plasma caused by the discharge) falling back on the negatively charged surface will generate a large number of secondary electrons which, when also accelerated away, could increase both the intensity and duration of the positive pulse. The presence of a hole in the dielectric will reduce the probability of a discharge to the metal layer in a planar region since a discharge is more likely to occur at the hole. As described above, a discharge near a hole produces a ground pulse which is not very large. Once occurring, it reduces the negative surface potential to some extent over most of the dielectric, as a result of positive ion return and tertiary emission.

The second type of discharge possible in planar dielectrics is a surface discharge resulting from an edge, an anomaly, a bilayer (ref. 9), or some other mechanism. If this discharge creates a plasma on the surface, which is then charge separated by the surface fields, a large pulse will result from the initial flux of electrons (separated from the plasma) driven off and followed by the secondary electrons generated by the returning ions. Again, on a pinhole sample this type of discharge can occur away from a hole, but is less likely to do so because of the lower arcing threshold near a hole.

A major point to be emphasized is that a discharge at or near a pinhole is significantly altered by the presence of this "ground" and its associated electric fields. A large percentage of electrons (particularly the slow ones), that would otherwise escape from the surface and contribute to the positive ground pulse, are collected by the pinhole, and only neutralize their image charge. The current pulses induced by discharges near a hole are therefore much smaller and faster than would be expected from a planar surface. Hence, use of pinholes in dielectrics can lower the impact of surface discharges on a spacecraft by reducing the energy of a discharge (table I), and by reducing the magnitude of the displacement current.

The current collected by the metal back can be dominated by the regions associated with the holes (as described above) and therefore this "back" current should be proportional to the number of holes in the sample. Edge leakage could interfere with this proportionality until the hole currents dominate edge leakage or unless the edges are shielded or "guarded" with a high voltage ring to prevent current flow around the edge to ground. When the pinholes exceed some concentration, the back current will begin to saturate as individual "drainage" patterns begin to overlap.

## CONCLUSIONS

A model describing the charging and discharging of punctured dielectrics exposed to an electron beam has been proposed to explain the experimentally observed reduction in surface potentials and in discharge energies as compared to nonpunctured dielectrics. This model leads to the following predictions for metal coated dielectrics with holes punched through from the metal back:

a. High surface potentials (up to the breakdown level) will still occur over most of the dielectric. A surface potential probe should show dips when it traverses holes only if its sensor is close enough to the surface. Only when the hole density becomes very high will the measured surface potential show significant decrease.

b. Current collected from the back metal layer will be proportional to the hole density over a large range if edge effects are removed and the hole area is not much less than about 0.1 percent of the measured area.

c. Discharges are more likely to initiate at the hole regions, and thereby reduce the probability of discharges occurring elsewhere. The observed discharge image on the "back" current monitor will be faster and much smaller for a discharge near a hole than for a discharge on an unmodified planar sample.

This analysis pertains to a laboratory environment, and must be altered for a dielectric in a "hot" space plasma, where the isotropic energy spectrum will smear out the charge deposition in the surface layer and greatly enhance the space charge beyond the surface. However, the mechanisms for initiating discharges and reducing their impact by the presence of punctures should remain valid and therefore important as a means of charge control in dielectrics.

## REFERENCES

1. Cole, R. K.; Ogawa, H. S.; and Sellen, J. M.: Operation of Solar Cell Arrays in Dilute Streaming Plasmas. 7th Electric Propulsion Conference, Williamsburg, Virginia, March 1969, AIAA Paper 69-262.
2. Knauer, W.; Bayless, J. R.; Todd, G. T.; and Ward, J. W.: High Voltage Solar Array Study. NASA CR-72765, 1970.
3. Grier, N. T. and McKinzie, D. J. Jr.: Current Drainage to a High Voltage Probe in a Dilute Plasma. NASA TMS 67890, 1971.
4. Herron, B. G.; Bayless, J. R.; and Worden, J. D.: High Voltage Solar Array Technology. 9th Electric Propulsion Conference, Bethesda, Maryland, 1972, AIAA Paper 72-443.
5. Kennered, K. L.: High Voltage Solar Array Experiments. NASA CR-121280, 1974.
6. Fralick, G. C.: Calculation of Current Collection in a Dilute Plasma Through a Pinhole in the Insulation Covering a High Voltage Source. NASA TN D7957, June 1975.
7. Stevens, N. John, et al.: Investigation of High Voltage Spacecraft System Interactions with Plasma Environments. NASA TM-78831; 13th Electric Propulsion Conference, San Diego, California, 1978.
8. Robinson, P. A. Jr.: Electrostatic Discharge Study. Research Report No. 532, Hughes Research Laboratories; to be published, Spacecraft Charging Tech. Conf., 1980.
9. Meulenbergh, A.: Evidence for a New Discharge Mechanism for Dielectrics in a Plasma. Progress in Astronautics and Aeronautics, Vol. 47, M.I.T. Press, 1976, pp. 237-246.

Table I. ENERGY REMOVED DURING DISCHARGES IN  
TEFLON AS A FUNCTION OF PINHOLE DENSITY

Sample	Beam Energy (keV)	Arc Energy (mJ)	Surface Voltage (kV)
Plain	20	150	>8.0
Pinholes at 3/8-in. Spacing	10	80	8.5
Pinholes at 1/8-in. Spacing	10	20	4.5

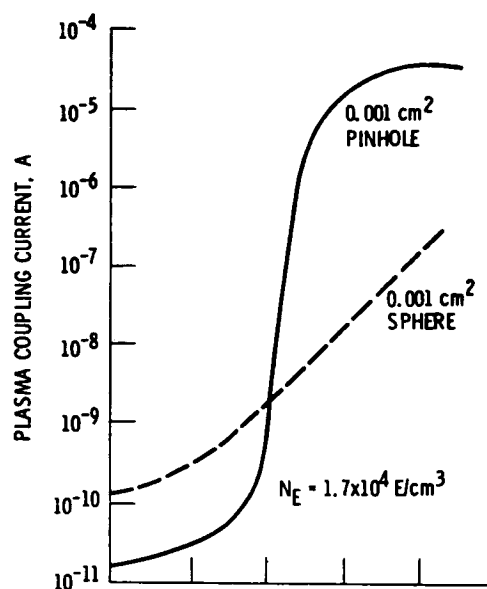


Figure 1. Pinhole Collection Current as a Function of Positive Applied Voltage. Experimental data for a pinhole (solid curve) are compared to simple probe theory for a sphere (dashed curve) (ref. 1)

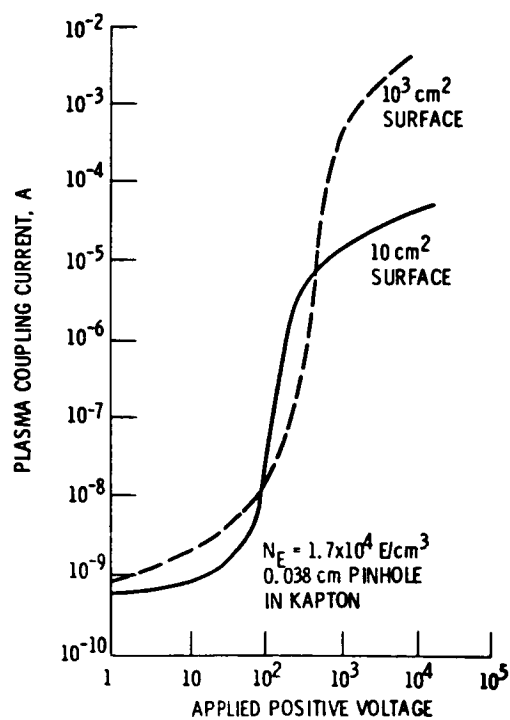
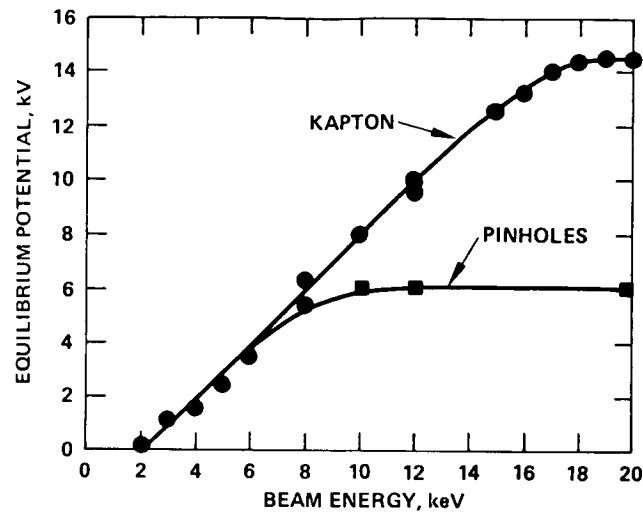
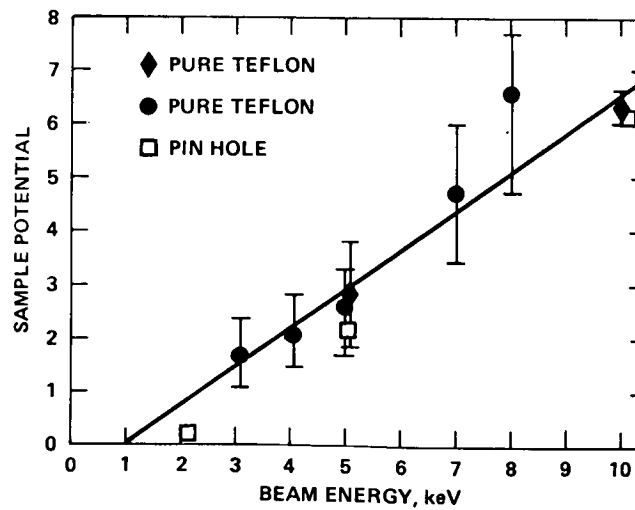


Figure 2. Pinhole Current as a Function of Applied Voltage for Two Dielectric Surface Areas (ref. 1)



A



B

Figure 3. Dielectric Surface Voltage versus Beam Energy for Planar and Punctured Samples of Kapton (A) and Teflon (B)

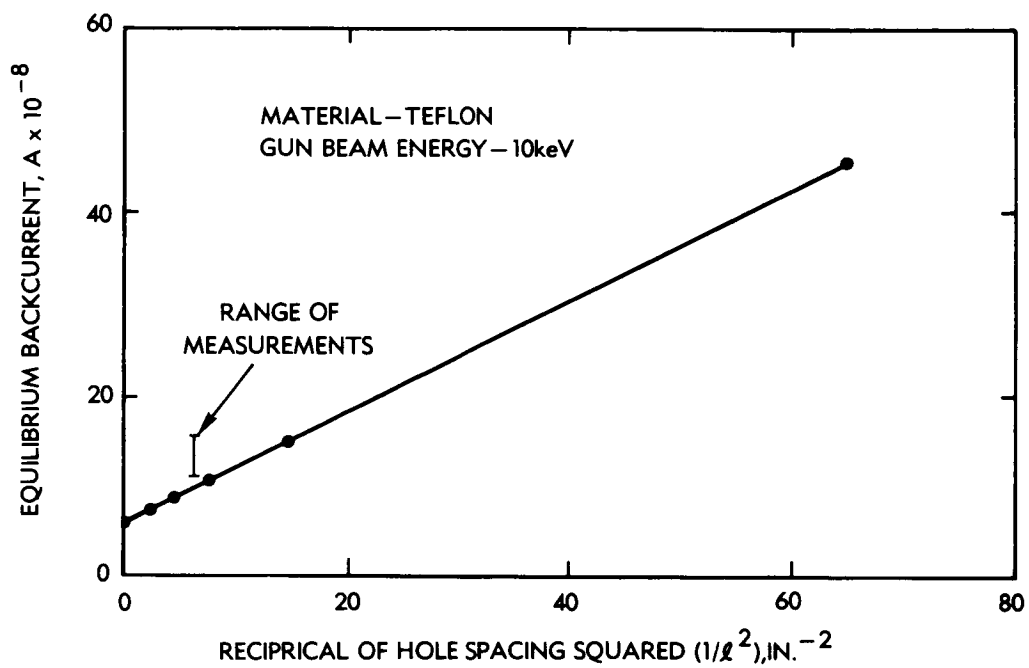


Figure 4. Leakage Current Versus the Reciprocal Pinhole Spacing Squared for a Teflon Sample in a 10-keV Beam

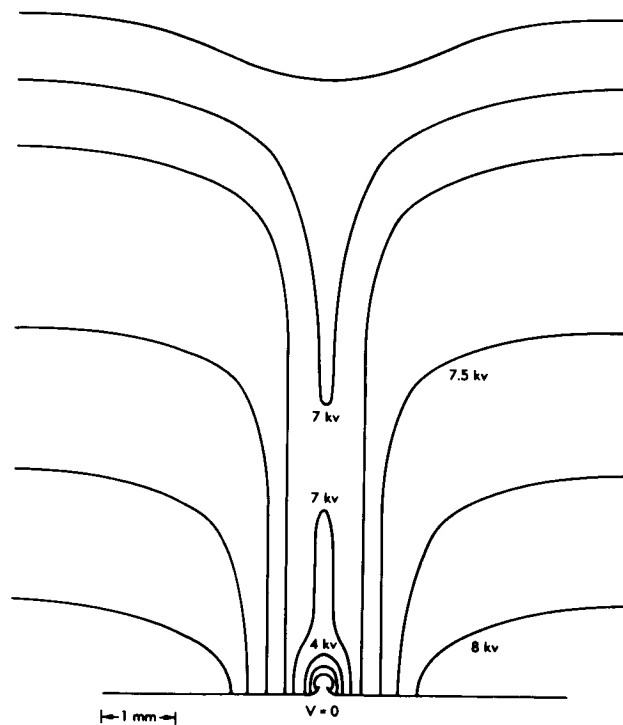


Figure 5. Equipotential Surfaces above a Pinhole through a Metal Backed Dielectric

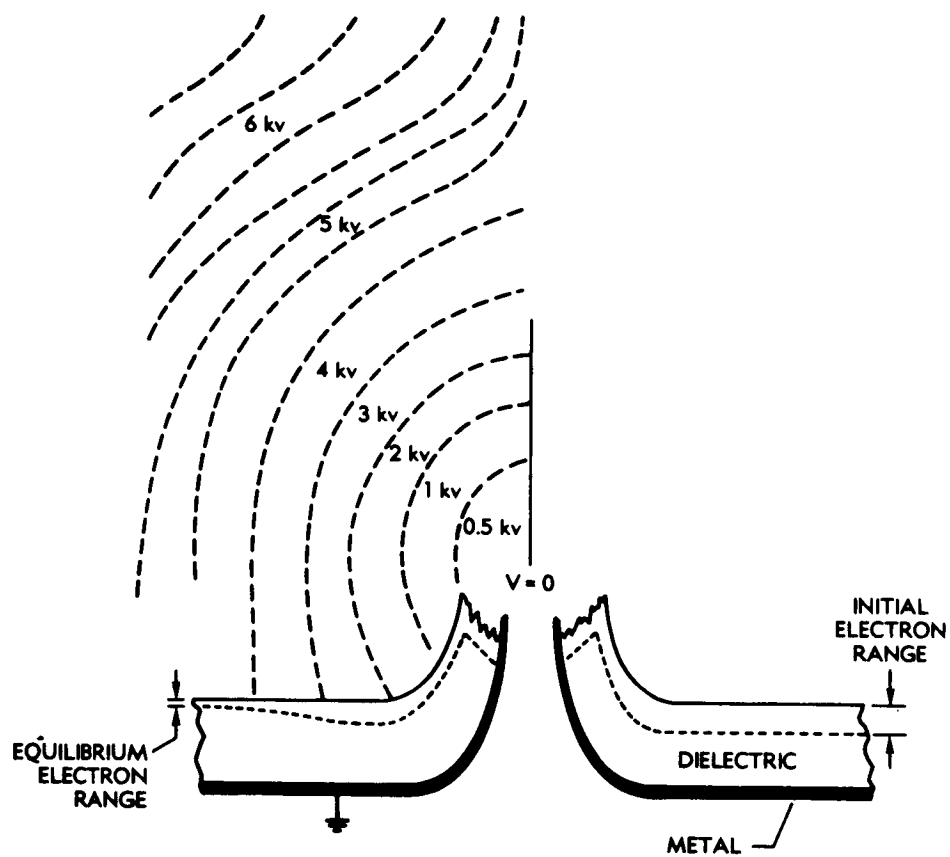


Figure 6. Idealized Structure of a Pinhole Showing the Range of Electrons Prior to Charging and at Equilibrium (left side)

## ACCELERATED ALPHA-S DETERIORATION IN A GEOSTATIONARY ORBIT\*

Otto K. Husmann  
Messerschmitt-Bölkow-Blohm

### SUMMARY

The SSM alpha-s long term stability strongly depends on the charged particle energies encountered in a geostationary orbit. Here the requirement for conductive surfaces leads to accelerated  $\alpha_s$  deterioration, due to lack of retarding potentials.- Dielectric mirrors without conductive coating improve the  $\alpha_s$  long term stability of teflon FEP. Mosaic like fractures within the IF-filter don't affect it. In presence of a conductive layer on top of the IF-filter, however, they lead to the loss of conductivity. A sandwiched in PMMA varnish film for improvement of the substrate tensile strength enhances the  $\alpha_s$  decay. Quartz fiber reinforced teflon FEP as substrate may eliminate the IF-filter tendency to fracture without impairing  $\alpha_s$ .

### INTRODUCTION

Among a limited variety of plastic materials teflon FEP frequently is selected as SSM for satellite thermal protection because of its high transparency over a wide spectral range, the relative stability of its transparency, and because of its applicability also to odd shaped structures.

With the demand for extended satellite life times in a geostationary orbit the teflon FEP alpha-s stability may be insufficient, in contrast to its performance in a near earth orbit (ref.1-5). Here in addition to the electromagnetic radiation, energetic electrons and protons accelerate the SSM  $\alpha_s$  deterioration.

Under charged particle exposure dielectric as well as not grounded conductive surfaces build up electrostatic charges with potentials in the Kvolt range, that may lead to spontaneous discharges (ref.6-8).

In the past, differential charging of satellite dielectric surfaces has led to disturbances and occasionally to the breakdown of the communications system, in conjunction with the destruction of electronic components. To reduce the danger of loss of the satellite through such events, a new requirement was formulated for the lay out of future satellite surfaces. This requirement of an entire outer conductive shell also encompasses the thermal control surfaces. The grounded conductive films

---

\* This work was supported by the BMFT through the DFVLR, W.Germany



eliminate the development of static potentials and differential charging.

In terms of the  $\alpha_s$  stability of SSM, these conductive grounded surfaces are less beneficial, because due to lack of retarding potentials the charged particles impinge on the SSM with their full energies, leading to accelerated alpha-s increases.

Alpha-s changes are related to the generation of F-Centers within the foil. To retard their development, interference filter (IF-filter) were deposited on top of the teflon foil, with their reflection maximum located at 480 nm, according to the extraterrestrial solar radiation intensity maximum. Within its narrow wave length range such dielectric mirror reflects the electromagnetic radiation, before it passes through the SSM. Radiation damage then appears as reduced transparency at increased wave lengths, adjacent to the IF-filter spectral reflectance.

#### SAMPLE SELECTION

Earlier studies showed, that the ZnS/Al<sub>2</sub>O<sub>3</sub> IF-filter on a thin teflon FEP film develop many fine fractures during exposure, which do not affect the alpha-s value (ref.9). However, they severely incapacitate the conductive layer (ITO) conductance. To alleviate this tendency to fracture, a simple remedy was tried. Between the teflon substrate and the IF-filter a two micron thick PMMA varnish layer was sandwiched in. Now the bending radius of the SSM, measured on a cone, decreased from about 13 mm to 6 mm prior to the IF-filter fracture, due to increased tensile strength of its substrate. These samples, and for comparison, samples of the same make, but without PMMA varnish, and without ITO were included in the test. Additionally two teflon FEP samples without the protective IF-filter, one of them with ITO, were tested.

#### SAMPLE FABRICATION

Sample substrate was 125 micron thick teflon FEP, with vapor deposited silver reflector, with a thin Inconel film for corrosion protection. Because both, silver and PMMA varnish do not easily "wet" the teflon foil, prior to their deposition 30 Å thick layer of Al<sub>2</sub>O<sub>3</sub> were placed on both sides of it. Subsequently, PMMA varnish followed on the front side of the SSM and was vacuum dried. For improved adhesion, here again a 30 Å thick Al<sub>2</sub>O<sub>3</sub> film advanced vapor deposition of the seven layer IF-filter, with ZnS its outer components (ref.10,11). To comply with the requirement of a transparent conductive surface, the samples with PMMA varnish finally were coated with 100 Å In<sub>2</sub>O<sub>3</sub> + 10% SnO<sub>2</sub> (ITO). This coating has sufficient hardness to resist wear. It shifts the IF-filter reflection maximum 20 nm upward and increases  $\alpha_s$  by about 0,02.- For contacting,

the short sides of the samples had thin strips of gold coat added, leaving an area of 11 x 11 mm open for the radiation exposure. Both sample sides were ground connected outside the chamber.- With 3M transfer glue 467 they were fixed to their supports.- The majority of the tested samples were fabricated by the R.BOSCH GmbH.

#### TEST EQUIPMENT

For performance evaluation of the teflon FEP SSM under simulated solar radiation conditions, the Messerschmitt-Bölkow-Blohm Combined Effects Chamber was used. The technical capabilities of this chamber are briefly lined out(ref.12). The simulated solar radiation exposures proceeded under clean vacuum conditions, maintained with an ion pump. Pressures ranged around  $2,7 \times 10^{-5}$  Pascal during the UV and electron exposures. With the proton generator on, the pressure was about  $8 \times 10^{-5}$  Pascal.

As UV radiation source a 900 Watt Xenon lamp with Suprasil bulb was employed. To utilize its entire UV output, these lamps are operated in a dry nitrogen atmosphere, in conjunction with a sapphire window toward the vacuum chamber. Their UV spectral intensity distribution repeatedly was measured with a Schoeffel GM-100-3 double monochromator in the wave length range from 180 nm to 450 nm.- There is no flat UV intensity distribution across the sample area. Instead, theoretical studies indicated 33 % decrease from the center samples to the outer ones. The actual intensity distribution varies with the Xenon lamp. It has been measured with a Kendall Mark IV radiometer.

With two Faraday cups, movable across the sample area, scans of the electron and proton current densities were performed. The intensity distributions of both above the samples are flat within + 5 %. However, in presence of targets with dielectric or not grounded conductive surfaces, these charge up and disturb the original current density distribution.- All currents were measured with a Keithley 602 electrometer instrument.

The sample holder temperature was kept at 10°C. Temperatures measured on one sample surface with 50 micron diameter thermocouple wires were close to 27°C, with the UV lamp on. According to the number of solar constants brought onto each of the six samples, maximum sample temperatures were estimated to be close to 40°C.

For in situ alpha-s measurements a Beckman DK - 2A spectrophotometer is mated to the vacuum chamber. Its light spot size on the sample is 4,5 x 7 mm.- 130 reflectance measurements, mostly 10 nm apart, are transferred into a programmed desk calculator,

that prints the  $\alpha$ -s values under consideration of the solar spectral intensities according to ASTM E 490 73a after completion of the scan. The spectrometer is calibrated with an aluminum mirror. The  $\alpha$  measurement error is  $\pm 0,01$ .- For in situ measurement of the surface resistances the vacuum chamber has 52 electrical feed throughs.- Prior to and also after completion of the test, all samples were inspected for fractures, signs of electric discharges, and visible changes of the reflector were checked after exposure. Further, adhesion tape tests provided information concerning adherence of the IF-filter to the substrate.

### TEST PARAMETER

To gain insight into the long term performance of teflon FEP SSM with IF-filter protection, the first test was extended over 11000 equivalent sun hours (ESH), with simultaneous exposure to UV, electrons and protons. During a short supplementary test, electromagnetic and charged particle radiations were alternately applied.

To reduce the time needed for such test, max. UV intensities were 4,5 solar constants. - Electron and proton energies were 20 Kevolt. The charged particle intensities were maintained within the lower  $10^9/\text{cm}^2$  sec range. A total of  $10^{16}/\text{cm}^2$  electrons as well as protons were brought onto the samples.

The electron penetration depth is proportional to  $U^2$ , with U the acceleration potential. For acceleration potentials between 5 Kvolt and 60 Kvolt this penetration depth can be calculated according to the simplified Schonland equation (ref.13,14). The proton penetration is negligible (ref.15).

Pertaining to the small electron and proton current densities in a geostationary orbit, surface resistances in the  $10^8 \Omega$  ohm range are tolerable, if the entire sample surface contributes to the conductance. In contrast, fracture of the conductive coating leads to the development of isolated little islands, that don't contribute to the conductance across the SSM. Here differential charging and increase of the resistance impair the satellite communications.

### TEST RESULTS

Table I presents the data acquired during the 11000 ESH exposure. - The top of table I comprises the accumulated electron and proton radiation doses, followed by the number of ESH and the  $\alpha$ -s. Finally the resistances in  $\Omega$  ohm are compiled. Fig. 1 presents the  $\alpha$  data vs time of UV exposure (ESH). The charged particle and UV irradiations started together.

To study the effect of alternate UV and electron/proton exposures, a second set of similar samples followed the 11000 ESH test. Table II and Fig.2 present their test data.

## DISCUSSION OF RESULTS

### Teflon FEP

Two kinds of alpha-s deterioration have been encountered. The first one, reduction of transparency, predominantly within the visible range, is common to both studied brands. Loss of the Ag - reflector together with its Inconel shield during exposure repeatedly was observed on only one brand of samples.

11000 ESH Exposure : The slow alpha-s growth during the first 600 ESH also of the sample with ITO (fig.1, C & D) is affected by the UV and charged particle fluxes. Within this span of time the spectral reflectance curves reveal not yet damage to the reflector. The  $\Delta\alpha_s$  exceeds that of both other brand samples of the supplementary test, also under consideration of the different charged particle loads. The surface resistance of sample D fluctuates during this time between  $10^4$  and  $2,5 \times 10^5 \Omega$ . Subsequently it moves step by step into the  $10^{11} \Omega$  ohm range (table I).

After 600 ESH and more than  $2 \times 10^{15}$  charged particles/cm<sup>2</sup>  $\alpha_s$  increases at an accelerated pace, up to 0,65 after 11000 ESH. Gradually on both these samples the Ag reflector together with its Inconel shield disappears. This not only is indicated by the accelerated alpha-s increases, but also by the decay of the spectral reflectance, at first between 1 and 1,5 microns, extending later to 2,5 microns wave length.

On one such sample the reflector later was restored, dropping its alpha-s from 0,65 down to 0,33. This leads to a  $\Delta\alpha_s$  of 0,22 due to transparency change of the 125 micron thick foil, in agreement with  $\Delta\alpha_s$  of 0,09 after 11000 ESH, measured earlier on a 50 micron thick different brand teflon FEP sample with no damage to its reflector.-

During the supplementary test, partial loss of the reflector on the first brand of samples was confirmed after 1600 ESH (fig.II, D). Here two samples of the other brand (fig.II, B) show no damage to their reflectors. Over 1800 ESH they reveal only moderate  $\alpha_s$  increases despite grounded ITO. Their surface resistances are fairly high (see table II) and fluctuate between  $10^6$  and  $10^{11} \Omega$  ohm. In particular after the second application of charged particles, accelerated  $\alpha_s$  decay is noticed during the subsequent UV exposure.

### Teflon FEP with IF-Filter

11000 ESH Exposure : During the course of the 11000 ESH exposure alpha-s increases from 0,11 to 0,14 and 0,15 (table I, fig.I, B). Small reflectance losses adjacent to the IF-filter spectral characteristic are the cause. The filter reflectance maximum sagged from 97% down to 90%. - According to J.Stevens

et al. (ref.6) under charged particle exposure on dielectric surfaces retarding potentials develop. Here such potential prevents electrons from penetrating deep into the sample material. It can be estimated, that all electrons are stopped within the IF-filter. Further, the IF-filter reflects within its spectral characteristic the UV radiation, before it can reach the teflon substrate.- After 11000 ESH the only visible changes of these SSM were mosaic like fractures within the filter.

During the supplemental test, two samples (fig.II,A), identical to those of the long term test (fig.I,B) show after the second electron and proton applications only negligible changes of  $\alpha_s$ , less severe than those encountered during the long term test. However, during the long term test first 1800 ESH these samples experienced higher charged particle doses.

#### Teflon FEP with IF-Filter and ITO

After 1500 ESH this sample (fig.II,C) shows a  $\Delta\alpha_s$  of 0,05, with charged particle doses in the  $10^{15}/\text{cm}^2$  range (table II). Its surface resistances are high and fluctuate. It is difficult to assess, how much of its surface contributes to the conductance. Each of the two charged particle administrations leads to accelerated  $\alpha_s$  changes during the following UV exposure. Prior to charged particle application its alpha-s remains unchanged during UV only exposure. The timing of the electron and proton applications is of importance for its alpha-s performance.

#### Teflon FEP with PMMA Varnish, IF-Filter and ITO

Here alpha-s increases fairly steep, and nearly doubles during the first 1200 ESH. It reaches 85 % of its final value after 1800 ESH. Within the first 1800 ESH the surface resistances fluctuate between 3 and  $69 \square \text{K ohm}$ . Later they increase by a few orders of magnitude. How much of the ITO remains ground connected is difficult to assess. Probably the alpha-s changes would have been more severe, if the resistances had not increased.

Microscopic inspection revealed as many mosaic like fractures within the IF-filter, as were encountered on such samples without PMMA varnish and without ITO. Here the spectral reflectance curves imply step by step break down of the IF-filter in the course of the 11000 ESH exposure.

About 3 % shrinkage of the PMMA varnish with fractures of micron size were recorded. Scanning electron beam microscope studies showed partially coagulated  $\text{In}_2\text{O}_3$  in form of tiny droplets.

#### CONCLUDING REMARKS

According to the preceding test results, during extended space missions in a geostationary orbit only those SSM with IF-filter protection yield sufficient alpha-s stability. In

conjunction with an ITO top layer, however, they have two drawbacks : Under the reported test conditions with UV-radiation, and 20 Kevolt electrons and protons they suffer under accelerated alpha-s deterioration. Secondly, IF-filter fracture leads to loss of conductivity .

Comparison of the test results, gained from the SSM with IF-filter protection with those, that carry grounded conductive top layer leads to the conclusion, that the charged particle energies predominantly affect the SSM alpha-s stability(ref.13, 14). According to Holman (ref.16) under "severe" solar substorm conditions the max. electron and proton energies range around 12 Kevolt. During "mild" and also during "moderate" substorm activities , their energies are 3 to 6 Kevolt. Their intensities are similar to those of a "severe" substorm, where the integral particle flux per year amounts to  $10^{16}$  electrons/cm<sup>2</sup> and  $2 \times 10^{14}$  protons/cm<sup>2</sup>. Garrett (ref.17) suggests Maxwell-Boltzmann energy distributions for the charged particles. With such distribution the majority of particles have energies of less than 12 Kevolt. Less energy means less damage. (This also applies to the probability of electrical discharges due to charge build up within the bulk of the SSM (ref.18) ).

Consequently , the presented results may not be identical with the alpha-s deterioration of SSM in a geostationary orbit. For a more realistic damage evaluation, therefore simulation of the actual space environmental radiation conditions is mandatory. Referring to Holman and Garrett , the charged particle energies applied here by far exceed those of the synchronous orbit. Also monoenergetic particles should be replaced by particles with energies , that come close to those of a Maxwell distribution.

To comply with the requirement for conductive surfaces without resistance fluctuations and resistance changes, improved substrates are demanded. To increase its tensile strength, teflon FEP reenforced with quartz fiber may be of advantage for IF-filter deposition. The quartz fiber refractive index nearly matches that of teflon FEP, and quartz fiber is even more resistant to UV radiation, as the plastic is.

Further investigations of this technology, however, only are warranted, if the actual space environment radiation conditions are less severe, than those simulated during the 11000 ESH and the supplementary tests, reported here.

#### REFERENCES

1. Arvesen, J. C. : Spectral Dependence of Ultraviolet Induced Degradation of Coatings for Spacecraft Thermal Control. AIAA Thermophysics Specialist Conference, Paper 67-340, New Orleans, 1967. Published in "Thermophysics for Spacecraft and Planetary Bodies", Progress in Astronautics and Aeronautics, 20., ed. G.B.Heller, Academic Press, 1967.

2. Swofford, D.D. , Johnson, S. W., and Mangold, V. L. : The Effects of the Extreme UV on the Optical Properties of Thermal Control Coatings. Paper 68-783, AIAA 3 rd Thermo-physics Conference, Los Angeles, June 24-26, 1968.
3. Bourrieau, J., and Romero, M. : Dégradation de Matériaux et Composants Optiques par les Particules Ionisantes. Int. Conference, Evaluation of Space Environment on Materials, Toulouse, France, June 17 - 21, 1974.
4. Fogdall, L. B., and Cannaday, S. S. : Radiation Effects on Second Surface Mirrors. Int. Conference , Evaluation of Space Environment on Materials, Toulouse, June 17 - 21, 1974.
5. Fogdall, L. B., and Cannaday, S. S. : Effects of High Energy Simulated Space Radiation on Polymeric Second Surface Mirrors. NASA Rep. CR-132725, 1975.
6. Stevens, N. J., Berkopec, F. D., Staskus, J.V., Blech, R. A., and Narciso, St. J. : Testing of Typical Spacecraft Material in a Simulated Substorm Environment. NASA Rep. TMX-73603, 1976.
7. Davies , D. K. : The Charging and Discharging of Spacecraft Dielectrics. Spacecraft Materials Conference, ESTEC, Noordwijk, October 2 - 5, 1979.
8. Jeffery, J. A., and Maag, C. R. : Contamination Enhanced Electrostatic Discharge Mechanisms. Space Materials Conference, ESTEC, Noordwijk, October 2 - 5, 1979.
9. Husmann, O. K., Kerner, K. , Naegele, J. : Improved Alpha-S Stability of Second Surface Mirrors and Optical Solar Reflectors Protected by thin ZnS Coatings or Selected Interference Filter as Top Layer, and the Conductivity of  $\text{In}_2\text{O}_3$  on SSM. Int. Symposium, Spacecraft Thermal and Environmental Control, Systems, ESA SP-139, 1978.
10. Husmann, O. K., and Kerner, K. : The Alpha-S Stability of Teflon FEP SSM Protected by Vapor Deposited Interference Filter under Accelerated Solar Radiation Test Conditions. Materials Workshop, Toulouse, France, July 4 - 6, 1977.
11. Hass, G. , and Hunter, W. R. : The Use of Evaporated Films for Space Applications, - Extreme Ultraviolet Astronomy and Temperature Control of Satellites. In "Physics of Thin Films" , vol. 10, Hass, G. and Francombe, M.H., eds., Academic Press, Inc., New York, N.Y., 1978.
12. Husmann, O. K. : The MBB Space Radiation Simulation Test Facility : Performance Data and In Situ Evaluation of the Optical Degradation of SSM under UV and Proton Irradiation. Int. Conference, Evaluation of Space Environment on Materials, Toulouse, France, June 17 - 21, 1974.
13. Schonland, in Geiger-Scheel, Handbook of Physics 22/2, Springer, 36, 1933.
14. Bleuler and Zuenti, Helvetia Physica Acta 19. 376. 1946.

15. Baetzner : Ann. Phys. , 25. 233. 1936
16. Holman, A. B. : Spacecraft Charging Specification Baseline, Contract F 04701-76-C-0123, July 1. 1977.
17. Garrett, H. B. : Modeling of the Geosynchronous Plasma Environment. NASA Conference Publication 2071, AFGL-TR-79-0082, Page 11, Nov. 1978.
18. Beers, B. L., Hsing-chow Hwang, Lin, D. L., and Pine, V. W.: Electron Transport Model of Dielectric Charging. NASA Conference Publication 2071, AFGL-TR-79-0082, page 209, Nov. 1978.
19. Balmain, K. G. : Surface Discharge Effects. In "Space Systems and Their Interactions with Earth's Space Environment" , vol. 71, Garrett, H.B. and Pike, Ch.P., eds., Progress in Astronautics and Aeronautics, Academic Press, 1979.

#### APPENDIX

The Schonland equation, used here , is

$$S = 2,1 \times 10^{-12} \times U_{\text{accel}}^2 / \epsilon, \quad \text{cm}$$

with U the acceleration potential in volts, and  $\epsilon$  the density of the sample material in g/cm<sup>3</sup>. S is the electron penetration depth in cm.

This equation may be applied within the energy range from 5 Kevolt to 100 Kevolt (ref. 13, 14).

#### ADDENDUM

Microscopic inspection of the reported samples did not reveal punchthrough electrical discharges . However , damage due to surface discharges on samples without ITO , in particular on those with IF-filter, was noticed (ref. 19).

Fig. 3 presents the exposure dependent alpha-s data of the first 11000 ESH SSM sample test. Here the  $\Delta\alpha_s$  come close to those of the second 11000 ESH exposure. The charged particle energies were maintained at 20 Kevolt, corresponding to those of the second long duration test. - Here ITO were grounded within the vacuum chamber. Therefore no surface resistance data are available. - The substrates of the samples represented by curves A, C, and D are 125  $\mu$  thick teflon FEP ; that of curve B is 50  $\mu$  thick. - All tested SSM have vapor deposited Ag reflector with Inconel corrosion protection.

Sample "curve A" carries a seven layer ZnS/Al<sub>2</sub>O<sub>3</sub> interference filter. Sample C corresponds to that of curve A, but carries in addition a grounded ITO top layer. Sample "curve D" has a PMMA varnish film sandwiched in between the teflon substrate and the IF-filter. A ground connected ITO tops the multilayer SSM. Sample "curve B" is of a different brand. Here the ungrounded ITO has been vapor deposited on teflon.



Table I. 11000 ESH Teflon FEP SSM Exposure  
Alpha-S and Surface Resistance Data

Integral Fluxes								
$e^-/\text{cm}^2$	0	$1 \times 10^{15}$	$2 \times 10^{15}$	$4 \times 10^{15}$	$4 \times 10^{15}$	$6 \times 10^{15}$	$6 \times 10^{15}$	$1 \times 10^{16}$
$p^+/\text{cm}^2$	0	$2 \times 10^{15}$	$3 \times 10^{15}$	$5 \times 10^{15}$	$7 \times 10^{15}$	$1 \times 10^{16}$	$1 \times 10^{16}$	$1 \times 10^{16}$
ESH - UV	0	300	600	1200	1800	3600	7200	11000
Samples	A l p h a - S							
Teflon FEP + PMMA+ IF + ITO	0,13 0,13	0,25 0,21	0,27 0,22	0,29 0,24	0,30 0,24	0,31 0,25	0,32 0,27	0,33 0,28
Teflon FEP + ITO	0,12	0,14	0,15	0,23	0,31	0,55	0,63	0,65
Teflon FEP +IF-Filter	0,11 0,11	0,12 0,12	0,13 0,12	0,13 0,13	0,14 0,13	0,14 0,13	0,14 0,13	0,15 0,14
Teflon FEP	0,11	0,12	0,15	0,26	0,39	0,50	0,57	0,58
S u r f a c e R e s i s t a n c e s, $\square$ Ohm								
Teflon FEP + PMMA+ IF + ITO	$24 \times 10^3$ $3 \times 10^3$	$5 \times 10^3$ $4 \times 10^3$	$7 \times 10^3$ $18 \times 10^3$	$69 \times 10^3$ $19 \times 10^3$	$2 \times 10^3$ $10^4$	$1 \times 10^8$ $5 \times 10^7$	$8 \times 10^7$ $9 \times 10^7$	$7 \times 10^7$ $2 \times 10^{11}$
Teflon FEP + ITO	$10^4$	$17 \times 10^3$	$3 \times 10^5$	$2 \times 10^6$	$1 \times 10^6$	$6 \times 10^6$	$10^8$	$9 \times 10^{10}$

Table II. Alpha-S and Resistance Data of the Alternate  
UV, Electron, and Proton Exposures

Integral Charged Particle Flux							
$e^-/\text{cm}^2$			$5 \times 10^{14}$		$1 \times 10^{15}$		
$p^+/\text{cm}^2$			$9 \times 10^{14}$		$2 \times 10^{15}$		
ESH - UV	0	300		600		1200	1500
SAMPLES	A L P H A - S						
Teflon FEP +IF + ITO	0,132	0,132	0,132	0,139	0,15	0,169	0,185
Teflon FEP + ITO	0,12 0,104	0,12 0,105	0,12 0,107	0,12 0,11	0,124 0,116	0,124 0,117	0,126 0,12
Teflon FEP + IF-Filter	0,1 0,1	0,1 0,1	0,1 0,1	0,1 0,1	0,103 0,103	0,104 0,103	0,104 0,103
Teflon FEP	0,108	0,108	0,114	0,121	0,153	0,183	0,22
S U R F A C E R E S I S T A N C E S, $\square$ Ohm							
Teflon FEP + IF + ITO	$5 \times 10^{10}$	$7 \times 10^{13}$		$5 \times 10^{10}$	$3 \times 10^9$		$3 \times 10^{13}$
Teflon FEP + ITO	$2 \times 10^8$ $10^9$	$5 \times 10^6$ $8 \times 10^9$		$7 \times 10^{10}$ $6 \times 10^{10}$	$10^{11}$ $2 \times 10^{11}$		$4 \times 10^9$ $3 \times 10^{10}$

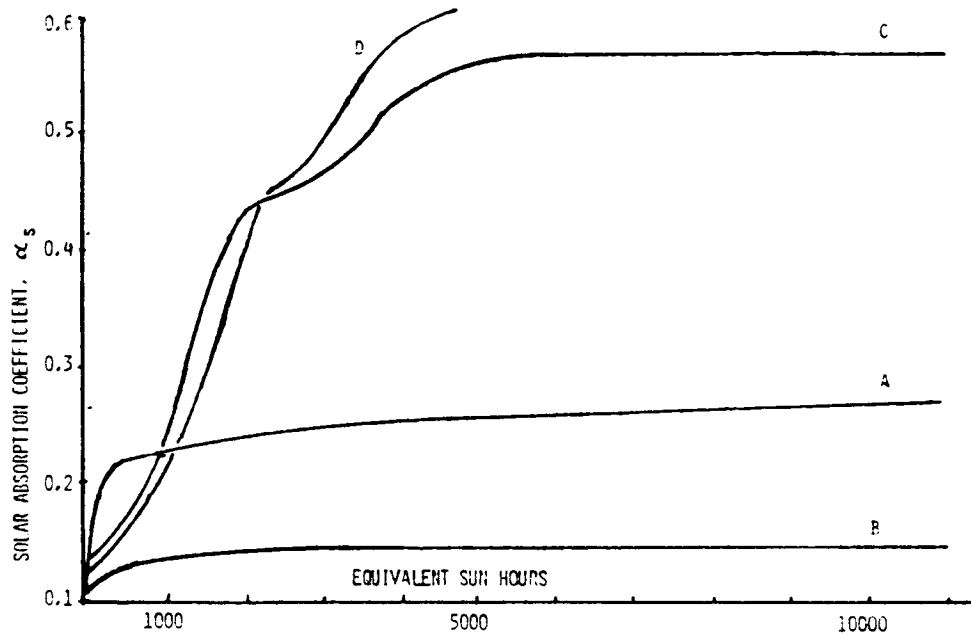


Fig.1. 11000 ESH EXPOSURE OF TEFLON FEP SSM  
 A : + IF-Filter + ITO + PMMA      C : plain Teflon  
 B : + IF-Filter                      D : + ITO

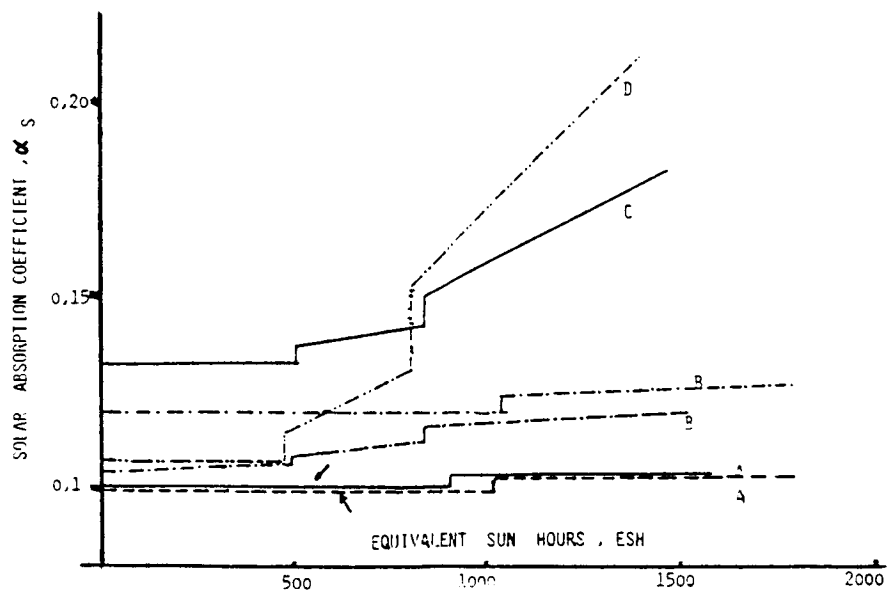


Fig.2. ALTERNATE EXPOSURE TO UV, ELECTRONS, and PROTONS  
 OF TEFLON FEP SSM  
 A : + IF-Filter                      C : + IF-Filter + ITO  
 B : + ITO                            D : plain Teflon

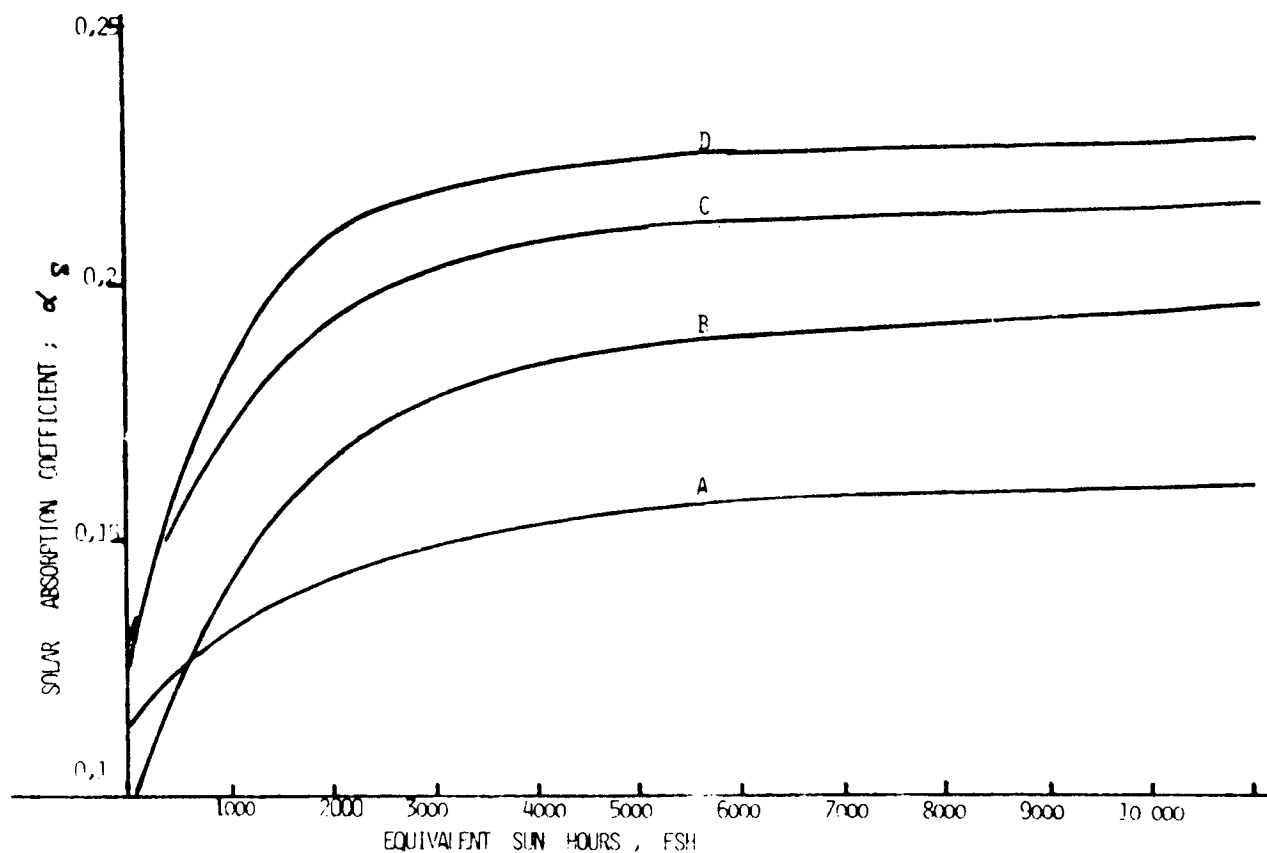


Fig. 3. First 11000 ESH Exposure Test of Teflon FEP SSM

A : + IF-Filter

C : + IF-Filter + ITO

B : + ITO

D : + PMMA + IF-Filter + ITO

A, C, D 125  $\mu$  Teflon FEP

B 50  $\mu$  Teflon FEP

Ag Reflector with Inconel Corrosion Protection

## **OPERATIONAL STATUS OF THE SPACE TEST PROGRAM P78-2 SPACECRAFT AND PAYLOADS**

**1Lt. Richard N. Osgood  
U.S. Air Force Space Division**

### **INTRODUCTION**

The Space Division Space Test Program P78-2 spacecraft is the spaceborne element of the NASA and USAF Charging Investigation. Built by the Martin Marietta Corporation in Denver, the spacecraft provides the on-orbit support for twelve Air Force, Navy, and NASA payloads. These payloads are attempting to measure the buildup and breakdown of charge on various spacecraft components and to characterize the natural environment at synchronous altitudes. The spacecraft and payloads have been on orbit for twenty-one months supporting this investigation. This is a summary of their operations.

### **ORBIT**

On 30 January 1979 at 2203 GMT a NASA McDonnell Douglas Delta 2914 launch vehicle boosted P78-2 into orbit. The booster inserted the spacecraft into a nominal 180 km x 43,240 km orbit from Launch Complex 17, Cape Canaveral AFS, Fla. After the spacecraft separated from the third stage the AF Satellite Control Facility (AFSCF) began its command, control, and communication function. Its first task was to checkout the spacecraft subsystems and prepare the spacecraft for insertion into the final orbit. Seventy-two hours after launch the AFSCF fired the apogee insertion motor (AIM) and placed the vehicle in its near geosynchronous orbit. The final orbit parameters are:

Apogee	43,240 km
Perigee	27,550 km
Inclination	7.9 deg
Drift Rate	5 deg/day easterly

The alignment of this orbit causes two eclipse seasons per year. Each season is approximately forty days long and each eclipse may last up to seventy minutes. Because of the drift and the eccentricity of the orbit, the satellite encounters each eclipse at varying altitudes. A third of the eclipses have been sampled at altitudes above synchronous and the remaining two thirds at altitudes below synchronous altitudes.

## SPACECRAFT

### Configuration

The P78-2 spacecraft has a cylindrical shape 1.70 m in diameter and 1.75 m in length. It is spin stabilized about its axis of symmetry at 1 rpm (fig. 1). Five experiment booms, two to four meters in length, were deployed radially from the center band. This boom configuration isolates sensitive experiments from spacecraft influences and provides a clear field of view. In addition to the rigid booms, a pair of fifty meter electric field antennas extend outward from the base of the vehicle. The solid fueled AIM was ejected from the aft end after final orbit insertion to limit the contamination. All of the booms and antennas deployed successfully, all covers opened, and the AIM was jettisoned without incident. The spin axis is fixed in the orbit plane and is kept broadside to the sun by weekly precession maneuvers.

### Subsystems

All of the spacecraft subsystems checked out properly after launch. Since then only the telemetry subsystem has encountered any problems (table I). After two weeks of use on orbit the signal strength from the vehicle sharply dropped twelve to fourteen decibels. Fortunately the anomalous telemetry string still produced a usable signal. Naturally we were hesitant to select the backup transmitter until the problem with the first was better understood since the second string had to be protected to transmit science data from the first eclipse season. Fortunately the problem disappeared while ground testing of the flight spare was being conducted and it has not reoccurred. Unfortunately the ground tests were inconclusive and although multipaction was the suspected cause, nothing was proven. Operations continued on the first string. Since then, the second string has been selected for its reduced electromagnetic interference. The remainder of the subsystems are operating properly and another three years of operations are possible.

### PAYLOADS

Payload checkouts for SC1 through ML12 were completed by 12 March 1979 despite the difficulties presented by the transmitter anomaly. Only SC6, the AFGL Thermal Plasma Analyzer encountered problems during checkout. On the final step of a stepping operation, SC6 failed due to an excessive power draw in the electron step generator. All attempts to work around the failure and save the ion half of the experiment have also failed. This is a catastrophic failure for SC6.

The next payload problem affected SC7, the NASA/MSFC Light Ion Mass Spectrometer. On 20 Feb 79 the SC7 internal power supply failed after ten days of active data collection. This is a catastrophic failure for SC7. The net effect of losing SC6 and SC7 is the loss of most of the low energy particle data (fig. 2).

No other catastrophic failures have occurred (table II). Lesser failures include the SC2 probe biasing failure, the SC4-1 pulsed mode failure, and the SC4-2 neutralizer failures.

The SC2 boom mounted experiments had the capability of biasing the electrical potential of their spheres. However, during induced charging operations with the SC4-1 electron gun on 30 March 1979, the biasing function of both spheres failed. At the time the electron gun was operating in a continuous mode at -3 KeV. Data obtained from the SC1-8B Pulse Analyzer and the SC1-7 RF Analyzer indicated that discharges were occurring on the vehicle. These discharges were sufficient to disrupt the telemetry signal for thirteen seconds. In addition, both the SC2-1 and SC2-2 probe biasing functions failed coincident with two of the larger pulses. Additional damage was caused because the failures went undetected. Thus the probes remained on with maximum bias and the electrostatic analyzers (ESA's) were inundated with low energy particles. In addition, although the SC4-1 pulsed mode was not being used, it has never operated successfully since then.

The SC4-2 neutralizer elements were used to emit a neutral beam of positive ions and electrons from the ion gun. Both of these elements have failed with time and SC4-2 is now capable of emitting a stream of only positive ions. The magnitude of this loss has been reduced by using the electron gun in coordination with the ion gun.

The most curious anomaly to affect the SCATHA payloads occurs to the SC11 Magnetometer. SC11 incorporates two high pass filters and may select either the 1 Hz or the 5 Hz filter by command from the ground. Its normal configuration uses the 1 Hz filter. However, during some SC4 operations the 5 Hz filter has been switched to without commanding. In addition, SC11 has switched to the 5 Hz filter on one occasion when no SC4 operations were being conducted. This is the only time that it has occurred without SC4 induced charging.

Other than these instances, all experiments are behaving nominally with some degradation to the sensors which have ESA's.

#### SUMMARY

In summary, the P78-2 spacecraft and payloads have operated for twenty one months and have collected data continuously. Four eclipse seasons have been covered in detail. In that time there have been only two failures which might affect the SCATHA mission. These are the SC6 and SC7 failures. Although the mission was only planned for one year, the vehicle has been supported for almost two years and further long term operations with the materials payloads are under consideration.

TABLE I. - P78-2 SPACECRAFT SUBSYSTEMS: OPERATIONAL STATUS

SUBSYSTEM	REMARKS
Telemetry and Command	Signal strength from the vehicle dropped 12-14 dB after two weeks on orbit. Returned to normal after two weeks of reduced operations. No reoccurrence Currently using redundant string (improved EMC)
POWER	NOMINAL (Solar Arrays produce 9 amps, and the nominal load is 8 amps.)
THERMAL	NOMINAL
ATTITUDE CONTROL	NOMINAL (3 year supply of hydrazine remains)

TABLE II. - P78-2 EXPERIMENTS: OPERATIONAL STATUS

#	EXPERIMENT	STATUS
SC1-1,-2,-3	Satellite Surface Potential Monitors	NOMINAL
SC1-7	RF Analyzer	NOMINAL
SC1-8A	VLF Analyzer	NOMINAL
SC1-8B	Pulse Analyzer	NOMINAL
SC2-1,-2	Plasma Potential Sensor	Probe Biasing Failure 3/30/79 and some ESA Degradation
SC2-3E	Electrostatic Analyzer (ESA)	Partial ESA Degradation
SC2-3B	Ion Detector	NOMINAL
SC2-6	Energetic Proton Detector	NOMINAL
SC3	High Energy Particle Spectrometer	NOMINAL
SC4-1	Electron Beam System	Pulsed Mode Failure 3/30/79
SC4-2	Ion Beam System	Neutralizer Failure 10/25/79
SC5	Rapid Scan Particle Detector	Partial ESA Degradation
SC6	Thermal Plasma Analyzer	Failed during checkout 2/10/79
SC7	Light Ion Mass Spectrometer	Failed after 10 days 2/17/79
SC8	Energetic Ion Mass Spectrometer	NOMINAL
SC9	Auroral Particles Experiment	Partial ESA Degradation
SC10	Electric Field Experiment	NOMINAL
SC11	Magnetic Field Monitor	NOMINAL
ML12-3,-4	Thermal Control Coatings	NOMINAL
ML12-6,-7	Temperature Controlled Quartz Crystal	NOMINAL
TPM	Transient Pulse Monitor	NOMINAL

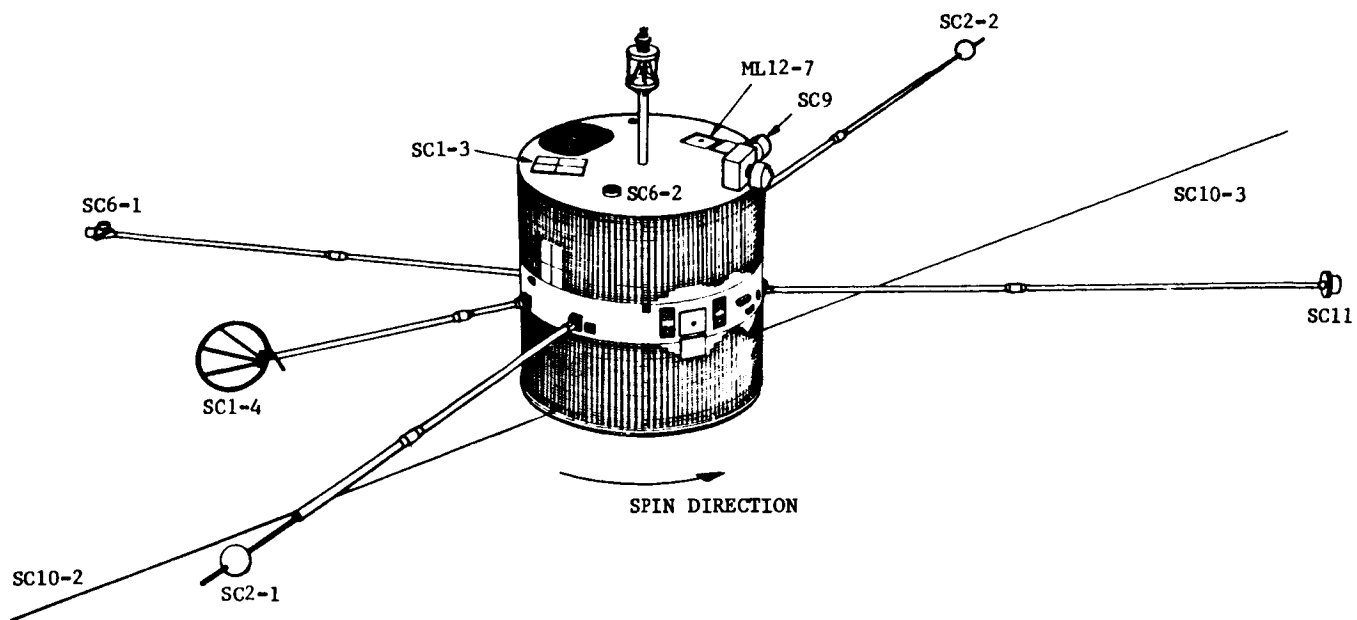


Figure 1. - P78-2 on-orbit configuration.

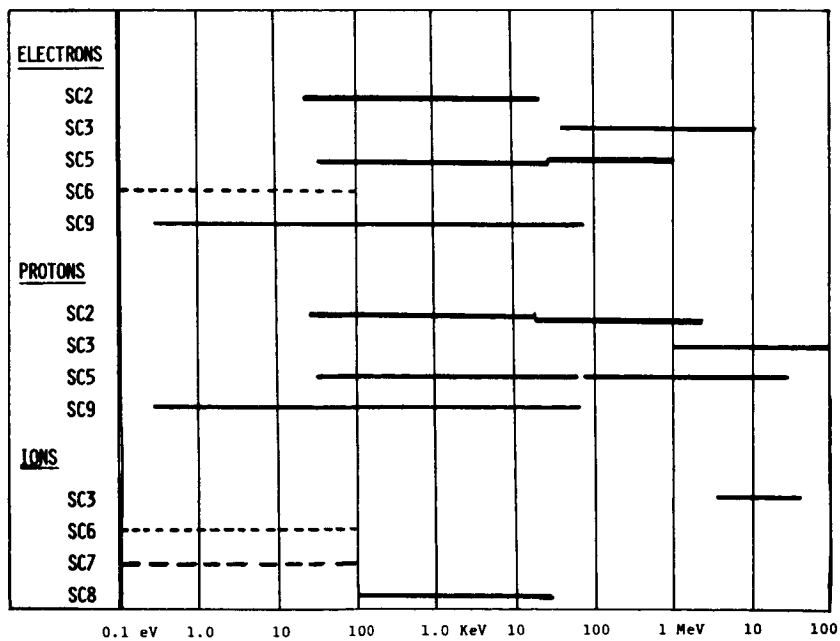


Figure 2. - Particle detector envelope.



## **ELECTRON ANGULAR DISTRIBUTIONS DURING CHARGING EVENTS\***

**J. F. Fennell, D. R. Croley, Jr., P. F. Mizera, and J. D. Richardson  
The Aerospace Corporation**

### **SUMMARY**

The angular distributions of electrons and ions at times of spacecraft charging have been examined for several charging events. Generally it is found that electrons measured perpendicular to the earth's magnetic field are more intense and more energetic than those measured parallel to the magnetic field during charging events. During the substorm charging injection, the electron spectra harden at all angles to the magnetic field as the evolution of the charging spectra is monitored by the P78-2 satellites. An example of the onset of charging and the changes in the electron distributions is examined in detail. The evolution of the electrons from a "soft" plasma sheet distribution to a "hard" charging distribution is compared with the charging of Kapton on the satellite and the spacecraft frame potential. The ions are used to determine the spacecraft potential. Evidence of periodic surface potential variations related to particle anisotropies are presented and discussed.

### **INTRODUCTION**

The evolution of the near synchronous particle environment at the onset of a substorm or injection has been the subject of much investigation over the years. The primary interest has been in trying to understand the physical mechanisms by which the plasma is energized and transported to the near synchronous region. In this report we will not attempt to add to such understanding. Instead, we are going to accept its occurrence as a fact and examine how the plasma changes and the effect the changes have on the satellite itself.

Much has been written on the subject of the plasma's interaction with satellites in space (see ref. 1). We will be emphasizing the charging of spacecraft surfaces and dielectric materials by the energetic plasma that envelopes the spacecraft during substorm injections. We will put special

---

\*This work was supported by the U. S. Air Force Space Division under Contract F04701-80-C-0081.

emphasis on the anisotropies of the plasma and its reflection in final charging of surfaces.

## OBSERVATIONS

The plasma conditions at P78-2 were very benign prior to the onset of the particle injection which caused differential charging of the spacecraft on February 12, 1979. These conditions are shown in figure 1 which is a summary spectrogram showing the first 12 hours of the day. Note the paucity of electrons and ions early in the day. The ions have reasonably high fluxes only above several keV early in the day. The low energy boundary of the ion fluxes is seen to decrease with time indicative of the fact that the satellite is approaching the plasma sheet from inside the plasmasphere. Just as the satellite is crossing into the plasmasheet near 0430-0505 UT a sudden injection of hot plasma occurs. A second injection occurs near 0740 UT.

The first injection is seen in greater detail in figure 2. Figure 2 shows that prior to the first injection near 0503 UT the satellite is immersed in a relatively low energy electron environment (see also figure 3). Prior to injection the majority of electrons are confirmed below 1 keV. At the onset the average energy rapidly changes and the electron intensity increases.

These events are shown in minute detail in figures 3 and 4. Figure 3 shows the electron distribution function ( $f(v)$ ) in velocity space (center), sample spectra (flux vs energy plot, RH panel) and electron angular distributions relative to the local magnetic field (LH panel) observed just prior to the injection. The electron spectra are steep and some anisotropies are present which favor the magnetic field line and the normal to the field line directions at high and low energies respectively (see X and dot points in RH panel). Figure 4 shows the rapid changes which occur in  $f(v)$  and electron spectra in the first  $\sim 4$  minutes of the injection. Each  $f(v)$  diagram starts on the  $-V_{\parallel}$  axis and time increases in the counter clockwise sense on these plots (ref. fig. 4b).

The four panels in figure 4 evidence the change from a relatively cold (i.e., monotonically decreasing flux vs. energy and steep  $f(v)$  versus  $v$ ) electron distribution to a relatively hot (i.e., peaking flux vs. energy profile and slower varying  $f(v)$  versus  $v$ ) distribution. For example, in figure 4b the low energy electron flux (RH panel) has increased and the high energy tail has increased in energy from 2-3 keV at 0502:17 (fig. 4a) to 6-10 keV at 0503:11 UT. This is exemplified by movement of the isodistribution function contours to higher velocities (i.e., along the  $V_{\perp}$  and  $V_{\parallel}$  axes) from fig. 4a to fig. 4b. (Note, the position of the  $f(v) = 10^{-3} \text{ sec}^3 \text{ km}^{-6}$  is marked on each figure and every fourth contour toward  $v=0$  represents one order of magnitude increase in  $f(v)$ .) At end of the interval near 0504:05 UT the electron spectra have formed peaks near 2 keV and the isodistribution function contours are spreading further out in velocity space. By 0504:58 UT the electron spectra are peaked with the peak fluxes occurring at  $\sim 1$  keV for electrons nearly parallel to the magnetic field direction and 3.5-4 keV for

electrons perpendicular to the field. The isodistribution function contours are well spread out in velocity space and are elliptical in shape, extending to higher velocities along the  $V_{\perp}$  axis than the  $V_{\parallel}$  axis. At this time (0504:58 UT) the electron distribution is relatively symmetric in velocity space.

The final distribution (fig. 4d) is obviously much different than the pre-injection distribution as detailed above. The resultant high fluxes at the higher energies ( $> 0.8$  keV) is what causes the charging that was observed to occur. The electron fluxes observed perpendicular to the magnetic field direction,  $J_{\perp}$ , are of higher energy and intensity (especially above 1 keV) than are the parallel fluxes,  $J_{\parallel}$ , and should give rise to a charging asymmetry. The surfaces exposed to the  $J_{\perp}$  fluxes should be more highly charged than those exposed predominantly to the  $J_{\parallel}$  fluxes!

The spacecraft is spinning with its spin axis nearly perpendicular to the magnetic field and perpendicular to the satellite-sun line. The surfaces on the cylindrical sides of the spacecraft are thus oriented at different directions relative to the magnetic field as the satellites rotates. They are roughly perpendicular and parallel (antiparallel) to the magnetic field twice in one satellite revolution. The satellite spin period is about 57 sec. If the charging time of a surface is short compared to a quarter spin period we should see the surface potential fluctuate periodically in phase with the satellite rotation. This is discussed in more detail below.

The spacecraft frame was observed to charge to  $\sim -200$  volts by 0504 UT in response to the injection. The material samples also charged in response to the changing plasma parameters. The charging of one Kapton sample is shown in figure 5. We also show the variation in the intensity of the  $\sim 18$  keV electrons measured by the SC8 experiment on P78-2 (Ref. 2). The field of view of the SC8 experiment and the Kapton sample's surface normal have nearly the same orientation relative to the magnetic field at the same time. As can be seen in figure 5, the peak electron intensity near  $90^{\circ}$  pitch angle (angle between particle velocity vector and magnetic field vector) increased from 18288-18314 sec UT to 18342-18370 sec UT and then decreased by 18896-18422 sec UT. Similarly, the maximum surface charging of the Kapton increased from  $\sim 125$  volts at 18287-18303 sec UT to  $\sim 400$  volts at 18337-18358 sec UT and then decreased to  $\sim 150$  volts at 18373-18410 sec UT. Thus the level of charging tracked the energetic electron intensity.

The Kapton charged only when it was in the satellite shadow. Photo emission discharged the material in sunlight. The correlation is even better than stated above. When one considers the way the Kapton charged on a spin by spin basis, as shown in figure 5, we see that the Kapton sample charged at a different point relative to the start of shadow ( $\sim 180^{\circ}$  pitch angle) on successive spins. If one examines the changes in electron fluxes to the sample, resulting from the electron anisotropy and the satellite rotation, (see fig. 5) then we see a good correlation between the flux and the onset of charging. The more intense electron fluxes caused the material to charge earlier relative to the beginning of the shadow. But in these three satellite rotations we see that the sample did not begin to charge until the surface normal

approached being perpendicular to the magnetic field ( $90^\circ$  pitch angle). The sample potential then decreased as the surface normal rotated further so that it became more nearly parallel to the magnetic field ( $0^\circ$  pitch angle). This decrease occurred prior to exit of the sample from the shadow (vertical arrows in fig. 5).

Since the electrons are known to be more energetic and intense perpendicular to the magnetic field than at other directions (ref. fig. 4) we ascribe the surface potential variation with pitch angle to the electron angular anisotropy. Preliminary calculations of the electron current to the sample as a function of the sample orientation relative to the magnetic field (M. S. Leung, private communication) are in agreement with the above assertion. The current to the sample, which is the charging current, is a maximum when the sample is perpendicular to the magnetic field. Since the sample is closely coupled to the spacecraft the time constant for charging is relatively long and results in a lag between the maximum current and maximum surface potential.

In figure 6 we show another example of the evolution of the electrons during another charging injection. The injection occurred on March 28, 1979 when the satellite was in eclipse. The panels show the changes which occurred in the electrons from prior to the event (Fig. 6a) to injection onset (Fig. 6b), to peak of satellite frame charging (Fig. 6c) to, finally, the late charging time with relatively stable charging late in the eclipse. Figure 6a shows that the preinjection electron fluxes were relatively low energy with the spectral peak near 200 eV. At the onset of the injection the electrons show an increase in flux near 10 keV of about an order of magnitude compared to the preinjection flux (R. H. Panels of figs. 6a and 6b). The peak of the electron fluxes is seen to move to higher energies ( $\sim 0.6$ - $1.0$  keV) also. Figure 6c shows the electron distribution as it begins to stabilize. The peak energy is now  $1.0$ - $3.0$  keV and the 10 keV flux is  $\sim 100$  times what it was prior to the injection.

Figure 6d shows the electron distribution attained during a period when the spacecraft potential was stable for several minutes. The electron peak energy settled at  $2$ - $3$  keV. The stable distribution has a flux asymmetry with the electron flux perpendicular to the magnetic field a factor of  $\sim 3$  greater than that parallel or antiparallel to the field. At the higher energies ( $7$ - $20$  keV) the measured anisotropy still favors the perpendicular fluxes. If one examines the  $> 20$  keV electrons one finds the ratio  $J_\perp/J_\parallel$  ranges from  $1.5$  to  $2.5$  over the energy range  $30 \text{ keV} \leq E_e \leq 260 \text{ keV}$ . Disregarding other aspects, one might expect this to lead to a variation of the potential of a surface which is exposed to this flux anisotropy as the satellite rotates. As we will see below, other effects may be dominant.

Figure 7a shows the spacecraft frame potential estimated from the SC2 ion measurements at  $\sim 14$  second intervals. The frame is negative relative to the plasma and attracts ions. The frame potential is estimated from the ion energy corresponding to the peak in the energy flux spectrum of the accelerated ions. The frame potential is seen to fluctuate quite rapidly in the first few hundred seconds after the injection, which occurred near 59790 sec

UT. During this period there are also rapid variations in the ion and electron fluxes.

Figure 7b shows the response of a spherical conducting probe isolated from the spacecraft frame and mounted on a three meter boom (for details of this experiment see ref. 2). The potential between this Aquadag covered sphere and the spacecraft frame is measured every second. As can be seen, early after the injection onset the probe voltage also changes quite rapidly. The probe voltage is saturated at maximum value near 61150-61490 sec UT. This saturation of the probe is instrumental (ref. 2). Comparison of the sphere voltage and frame potential profiles show that they responded in a similar manner to the changing plasma environment after  $\sim 60050$  sec UT. The sphere is generally positive relative to the spacecraft frame. This may be a result of the electric fields from the charged spacecraft shielding the probe from part of the charging spectrum of electrons or the different surface material properties of the sphere and the exposed conductive spacecraft structure.

Figure 7 does not show the complete charging period. The enhanced plasma conditions lasted well beyond the end of the eclipse period which occurred near 62060 sec UT. The spacecraft charge was mostly neutralized by photoemission once it exited the eclipse. The sphere continued to charge to relatively high levels upon entering the spacecraft shadow and discharge in sunlight until about 63620 sec UT.

Just as the spacecraft frame and sphere experienced charging as a result of the substorm injection, so did the surface material samples on the satellite. The samples are mounted over a grounded frame (see refs. 2-4) and are thus tightly capacitively coupled to the satellite. The potential difference between the sample and the satellite frame is measured once a second.

The early charging of the Kapton samples on the satellite is shown in figure 8. The differential potential between the samples and the satellite frame does not show the rapid changes that the frame potential shows. Instead, the sample potentials reflect the increasing potential difference between the material surface potential and the underlying ground frame with a time constant controlled by the capacitance of the system, conductivity of the material, environmental current, secondary emission and backscatter of electrons and changing electron energies in a manner previously discussed (ref. 3). The unusual feature is the lack of charging of the Kapton #3 which is mounted on the forward end of the satellite as opposed to the Kapton #1 and #2 which are near the center line of the cylindrical sides. This difference in response of the same material on the end and sides of the satellite is not understood at this time.

The difference between samples #1 and #3 and sample #2 in figure 8 is one of sample area. Sample #2 is approximately five times the area of samples #1 and #3. As a result, sample #2 collected a larger total current and charged more easily than the smaller samples. This is evidenced in figure 8 by the fact that sample #2 started charging negatively about 14 sec before sample #1. By the time sample #1 had started charging negatively sample #2 had

charged to  $\sim -150$  volts. By 60,000 sec UT sample #2 was  $\sim -2000$  volts and sample #1 was  $-1500$  volts. While there are some small fluctuations in the Kapton potentials the general trend, from  $\sim 59,780$  to 60,000 sec UT, is a monotonic increase. This is quite different from the trend seen in both the satellite frame and the sphere potentials (see fig. 7).

The small scale fluctuations in the material potential are not easily visible on a logarithmic plot. In figure 9 we show a plot of the estimated spacecraft frame potential (bottom panel) Kapton #2 potential (center panel) and the bulk current through Kapton #2 (top panel) for a limited period during the charging event. The main feature we wish to emphasize here is the fluctuation of the frame and Kapton potentials over a few satellite spins. The fluctuations appear to be spin synchronized. We have marked the midpoints of the decreasing current slopes with the angle between the Kapton sample normal and the direction of the local magnetic field for reference. We have also annotated the angle between the arriving ion velocity vectors and the magnetic field corresponding to the 'peaks' in the estimated satellite frame potential.

The midpoint of the decreasing current slopes occur about 21 degrees after the peak in the Kapton potential. This gives an average for the peaks in the potential of  $12^\circ \pm 3^\circ$  and  $164^\circ \pm 4^\circ$  as the angle between the sample normal and the antiparallel and parallel, respectively to the magnetic field direction. The 'peaks' in the spacecraft frame potential are seen to be roughly at these same angles ( $16.6^\circ \pm 10^\circ$  and  $158^\circ \pm 6^\circ$ ) relative to the magnetic field. By this we mean the ions measured in the peaks have these angles between their velocity vectors and the magnetic field direction. These fluctuations in the potentials are nearly field aligned in which case the electron anisotropy most likely is not the controlling factor.

To examine this in more detail we plot in figure 10 some ion count rates from three different instruments for a range of energies. The energies bracket the spacecraft potential. The three instruments are positioned as shown in the insert. Basically all three instruments show the same effect. The ions with energies near the spacecraft potential show peaks which are biased in one direction relative to the magnetic field in the spin plane of the satellite. They are biased such that the ions are arriving not along the field line direction but at an angle of  $10^\circ$ - $25^\circ$  relative to the field direction. At the higher energies, above the spacecraft potential, the ions arrive at the spacecraft nearly along the field direction.

Such beams of ions are often seen preceeding and during substorm injections (Ref. 5). If these beams have peaked energy spectra (as they often do) prior to experiencing the potential of the spacecraft then they will arrive at the spacecraft with an energy equal to the peak energy of the beam plus the spacecraft potential. The low energy ions will have an energy nearly equal to the spacecraft potential. The addition of the beams, with their high fluxes, can bias the technique used to estimate the satellite potential because it assumes that the peak in the observed spectra is a result of low energy ions being accelerated to the satellite by the potential. Thus the "peaks" in the satellite potential shown in figure 9 are probably artifacts and the true potential is probably represented by the smooth lower bound on which the peaks

are superimposed. This is partially evidenced by the fact that the  $J_{\perp}$  fluxes from SC5 (see fig. 10) show no fluctuations.

No such single simple explanation exists for the fluctuations in the Kapton potential seen in figure 9. The peaks were at the same orientation relative to the magnetic field direction as the low energy component of the ion beams. Thus it would appear that the sample voltage fluctuations are also related to the presence of the beams, but how? As mentioned above, the Kapton voltage peaks occur when the magnitude of the bulk current is decreasing. The ions would be a positive current to the surface and could decrease the magnitude of the current although it is not clear that enough ion current is present to cause the change observed. The electron flux is also minimized in the field line direction (see fig. 6d) and would result in less negative current. The question remains, what causes the potential difference between the satellite ground and the Kapton sample to increase in magnitude at these times? At this point we do not have a good answer other than it is most likely a result of angular asymmetries of the ion and electron fluxes. It will probably require analysis with a complex analytical tool such as the NASCAP program (ref. 6) to proceed further with this problem.

#### SUMMARY

We have been able to show that the electron anisotropy with peak intensity perpendicular to the magnetic field is the most likely cause of the charging of the materials on February 12, 1979. We have also shown the evolution of the charging fluxes during the onset of the substorm for both February 12 and March 28, 1979. In both cases the final state of the charging electron environment is one in which the electron fluxes are higher perpendicular to the magnetic field and the peak energy is generally higher there also.

We have shown that a spherical conducting probe and the spacecraft have similar charging responses during most of the March 28 event. The material samples did not show the rapid potential fluctuations that the probe and spacecraft experienced. This was assumed to be a result of the strong capacitive coupling between the samples and the spacecraft frame ground.

Finally, we have given evidence that the field aligned ions observed during the charging event on March 28 may have some control over the periodic variations in the material potentials observed.

#### REFERENCES

1. Space Systems and their Interactions with Earth's Space Environment, edited by H. B. Garrett and C. P. Pike, Progress in Astronautics and Aeronautics, vol. 71, Am. Institute of Aeronautics and Astronautics, New York, N. Y.

2. Stevens, J. R.; and A. L. Vampola: Description of the Space Test Program P78-2 Spacecraft and Payloads. SAMSO TR-78-24, 1978.
3. Mizera, P. F.; H. C. Koons; E. R. Schnauss; D. R. Croley, Jr.; H. K. Alan Kan; M. S. Leung; N. J. Stevens; F. Berkopec; J. Staskus; W. Lehn; and J. E. Nanawicz: First Results of Material Charging in the Space Environment. Appl. Phys. Letters, 37, p 276, 1980.
4. Koons, H. C.; P. F. Mizera; J. F. Fennell; and D. F. Hall: Spacecraft Charging Results from the SCATHA Satellite. Astronautics and Aeronautics, Nov. 1980.
5. Fennell, J. F.; D. R. Croley, Jr.; and J. D. Richardson: Observations of Field-Aligned Ion Beams at Near Geosynchronous Altitude by P78-2 (SCATHA). EOS Trans. Am. Geophys. Union, 61, Nov. 1980.
6. Katz, I; J. J. Cassidy; M. J. Mandell; E. W. Schnuelle; P. G. Steen; and J. C. Rocha: The Capabilities of the NASA Charging Analyzer Program, in Spacecraft Charging Technology-1978, ed. by R. Finke and C. Pike, NASA Conf. Pub. 2071, 1979.



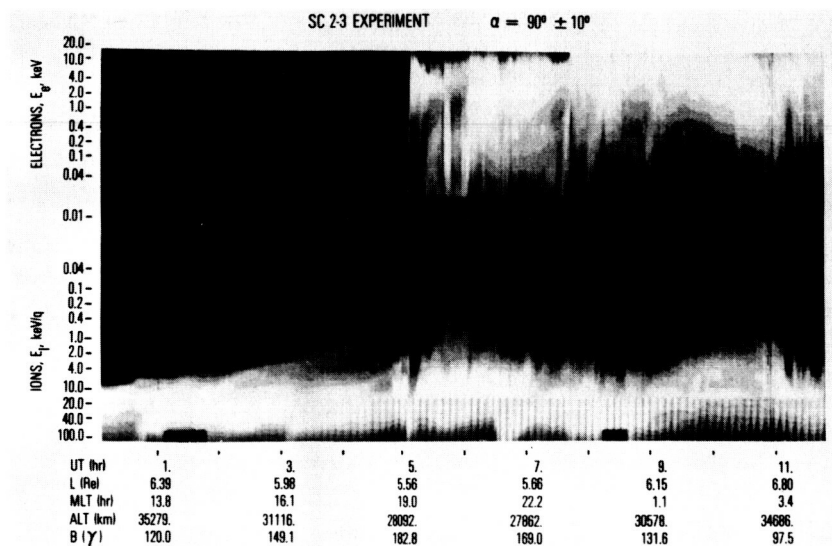


Figure 1. - Spectrogram showing electrons (top panel) and ions (bottom panel) for 0000 to 1200 UT on February 12, 1979. Brightness is proportional to particle energy flux. Increasing energy is upward for electrons, downward for ions.

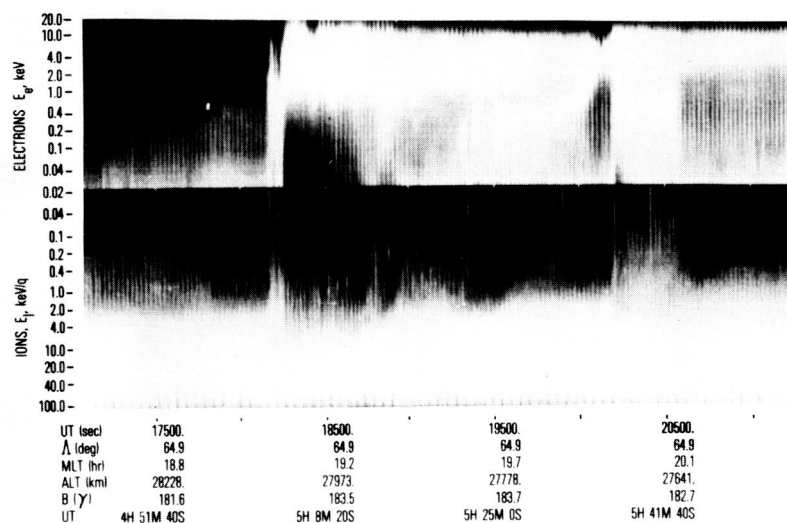


Figure 2. - Spectrogram similar to figure 1 for 0443 to 0556 UT on February 12, 1979.

$L \sim 5.6 R_e$  MLT  $\sim 19.1$  Hr  $B \sim 183 \gamma$

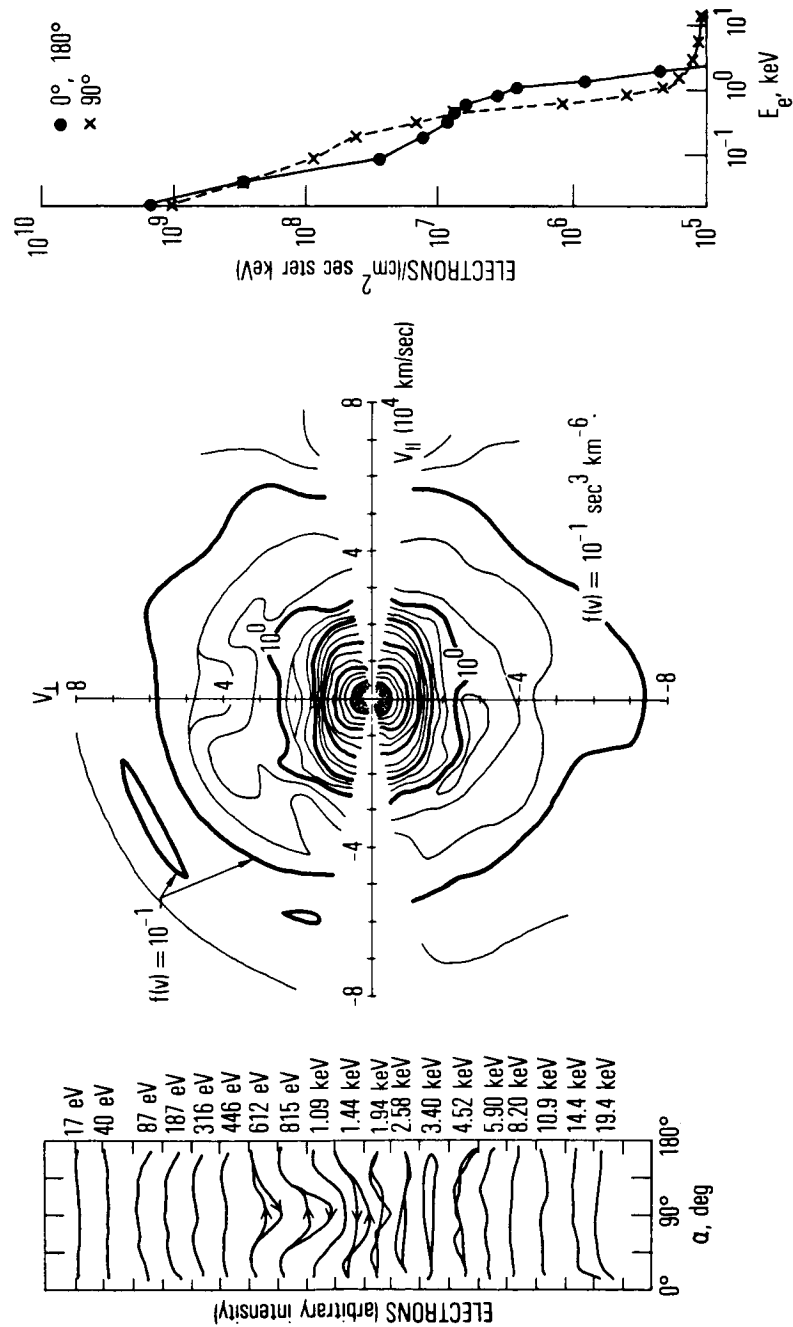


Figure 3. - Electron distributions for 0501 UT on February 12, 1979. Electron angular distributions relative to the magnetic field direction for several energies shown in the left panel ( $\alpha = 0^\circ$  is parallel to the field). Isodistribution function contours in velocity space are shown in the central diagram ( $f(v) \propto J E_e$ ). Electron spectra ( $J$  vs.  $E_e$ ) parallel (dot points) and perpendicular (x points) to the magnetic field direction are shown in the right panel. Data were taken prior to substorm injection.

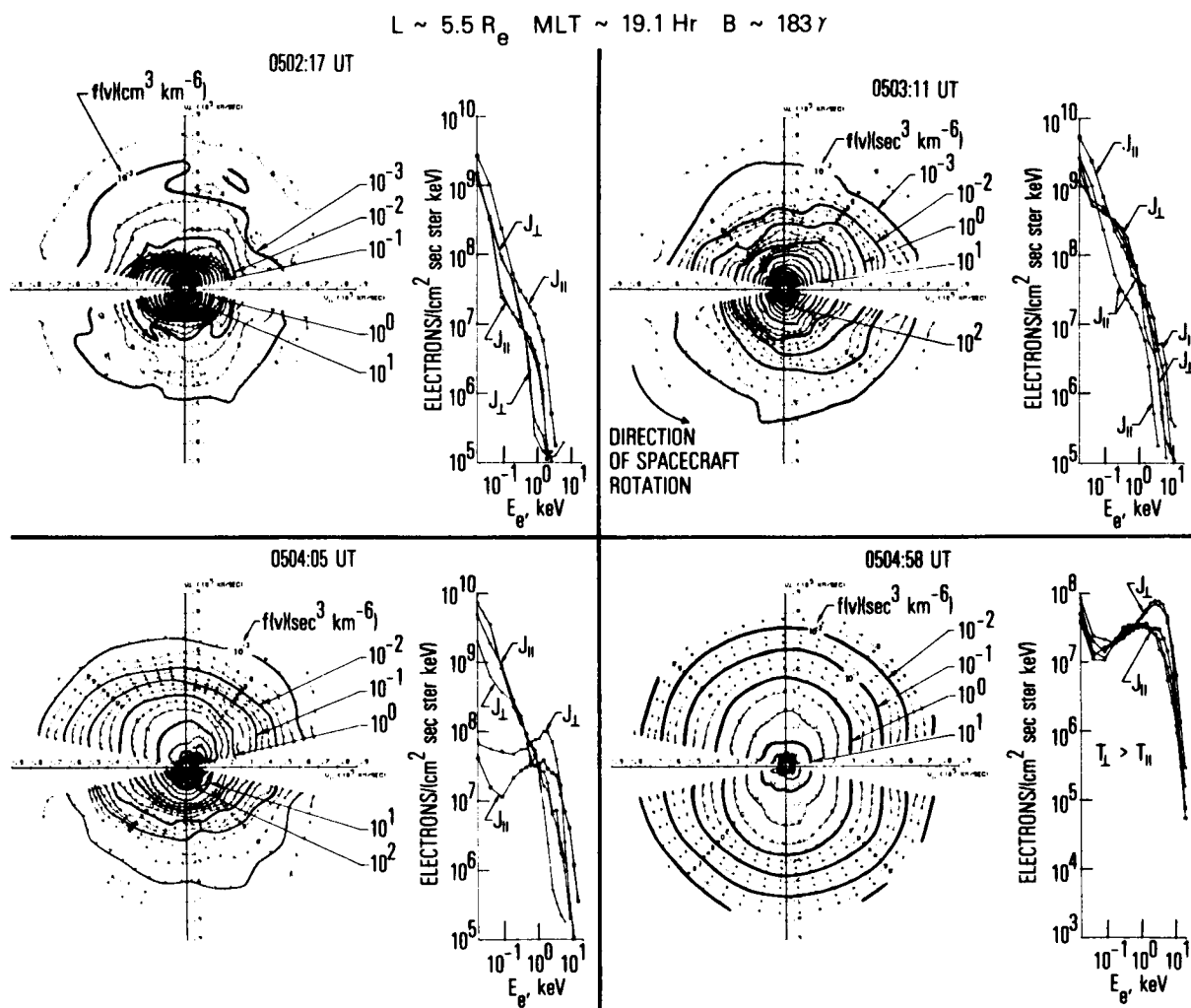


Figure 4. - Electron isodistribution function contours and spectra taken at the start (a) and during the development (b, c) of the injection and after stabilizing (d) to the final charging distribution. Data are from four consecutive satellite rotations.

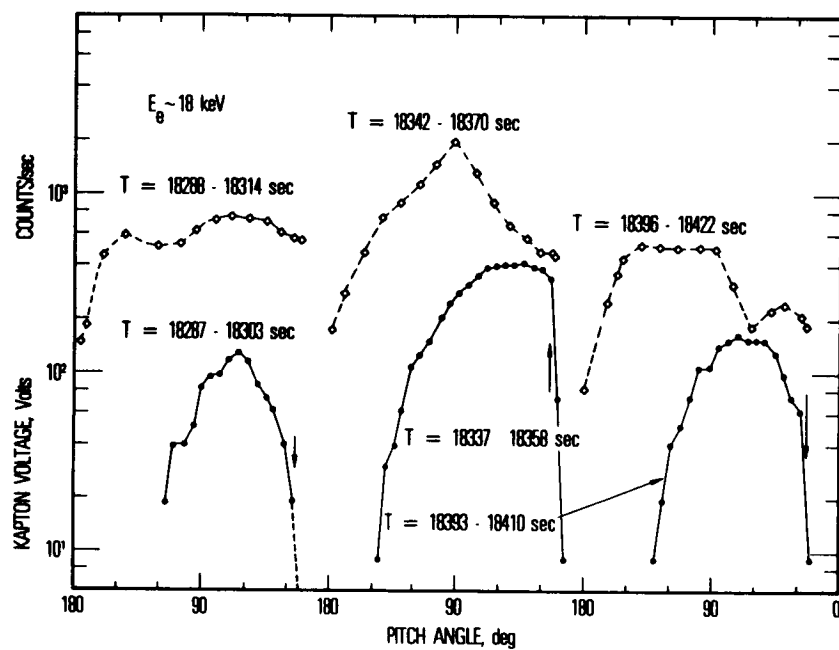


Figure 5. - Angular distribution of energetic electron fluxes ( $E_e \sim 18 \text{ keV}$ ;  $\diamond$  points) and Kapton voltages (dot points) during the February 12, 1979, daylight charging event.

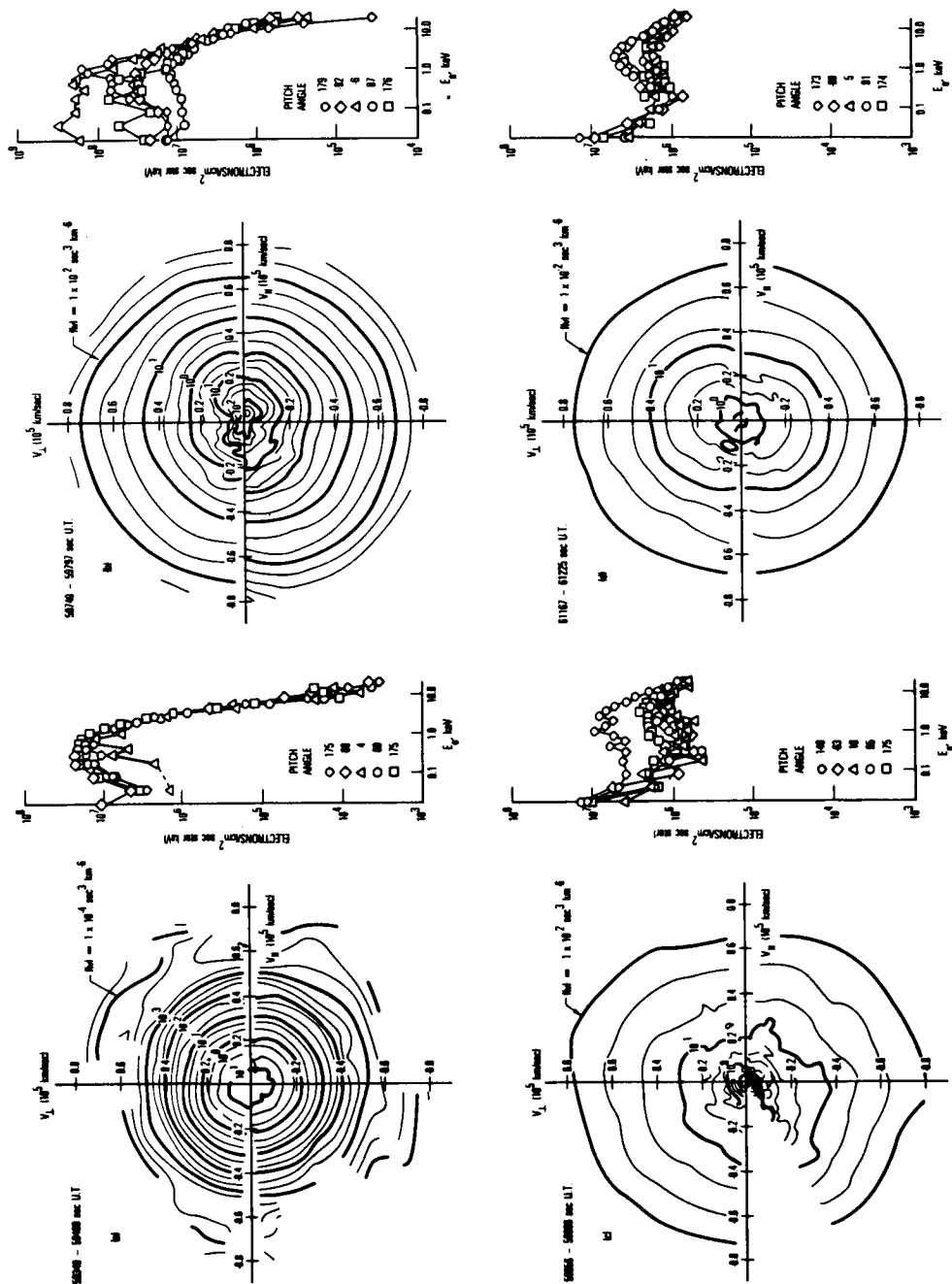
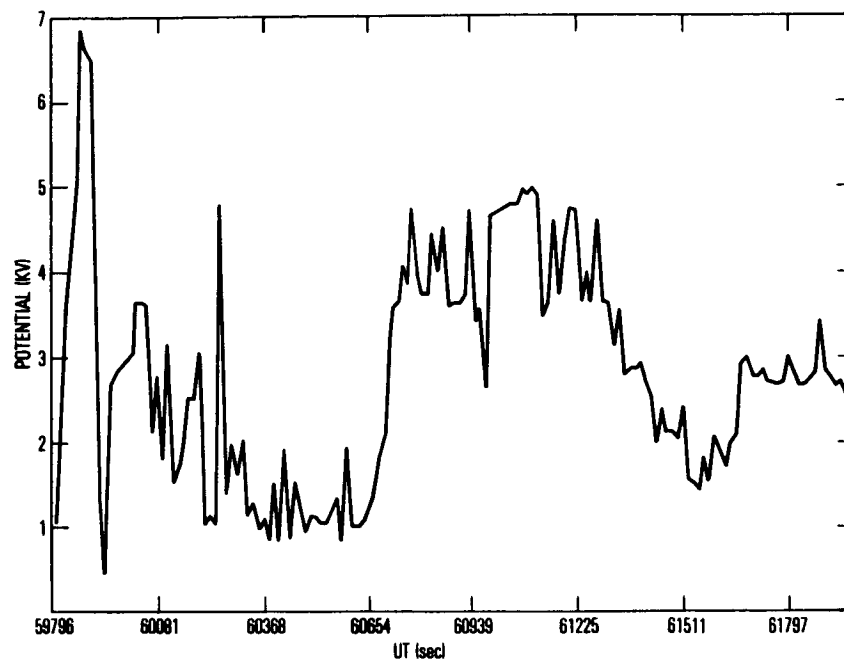
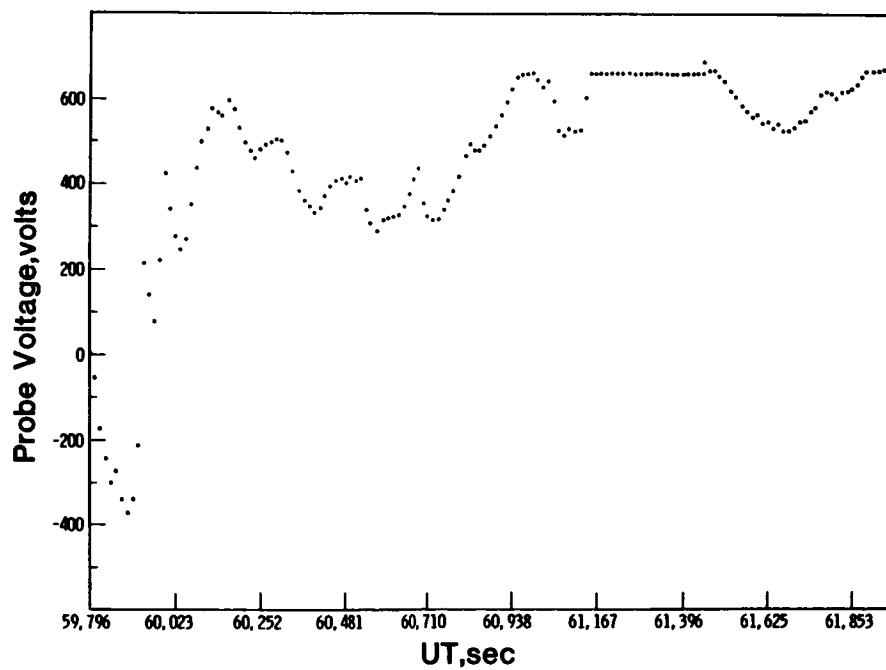


Figure 6. - Electron isodistribution function contours and spectra taken prior to an injection (a), at the beginning of the injection (b), during more complete development (c), and during one equilibrium period (d) of March 28, 1979, charging event.



(a) Spacecraft potential: Potential is estimated from ion distribution function plots using SC2-3 experimental data.



(b) Potential of isolated conducting sphere (relative to spacecraft ground).

Figure 7. - March 28, 1979, charging event.

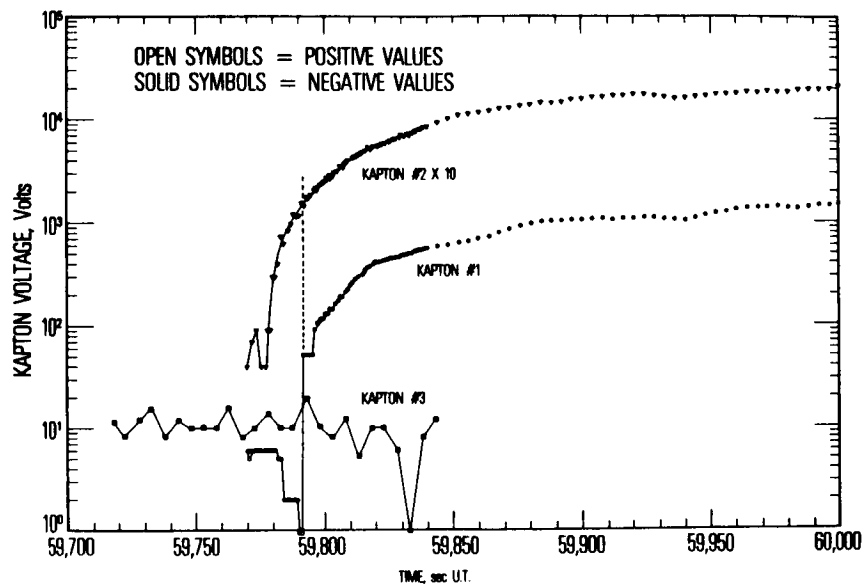


Figure 8. - Voltage history of three Kapton samples during early part of March 28, 1979, charging event.

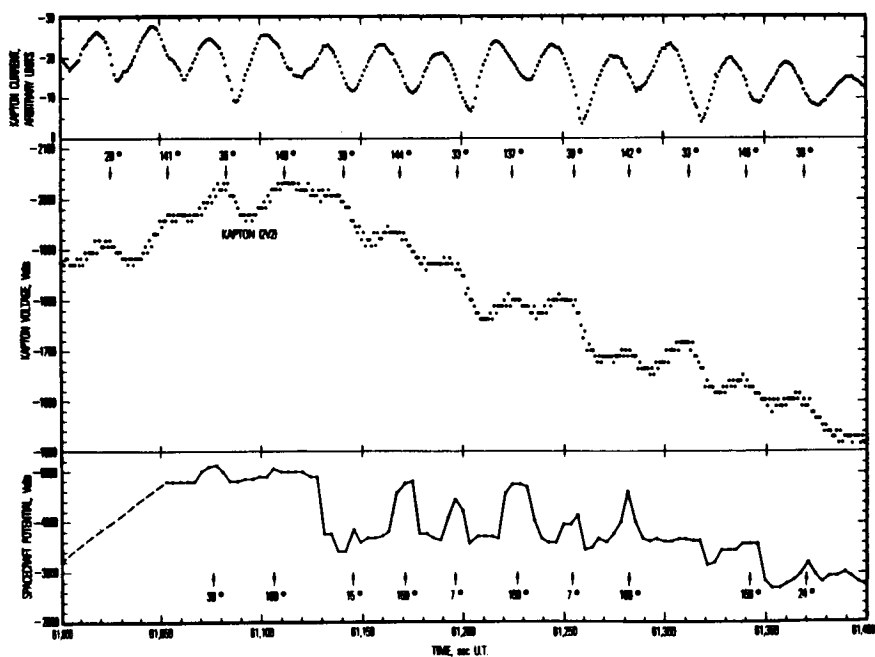


Figure 9. - Kapton current (top panel), Kapton voltage (center panel), and spacecraft potential (bottom panel) expanded to show spin-period-related fluctuations for March 28, 1979, charging event.

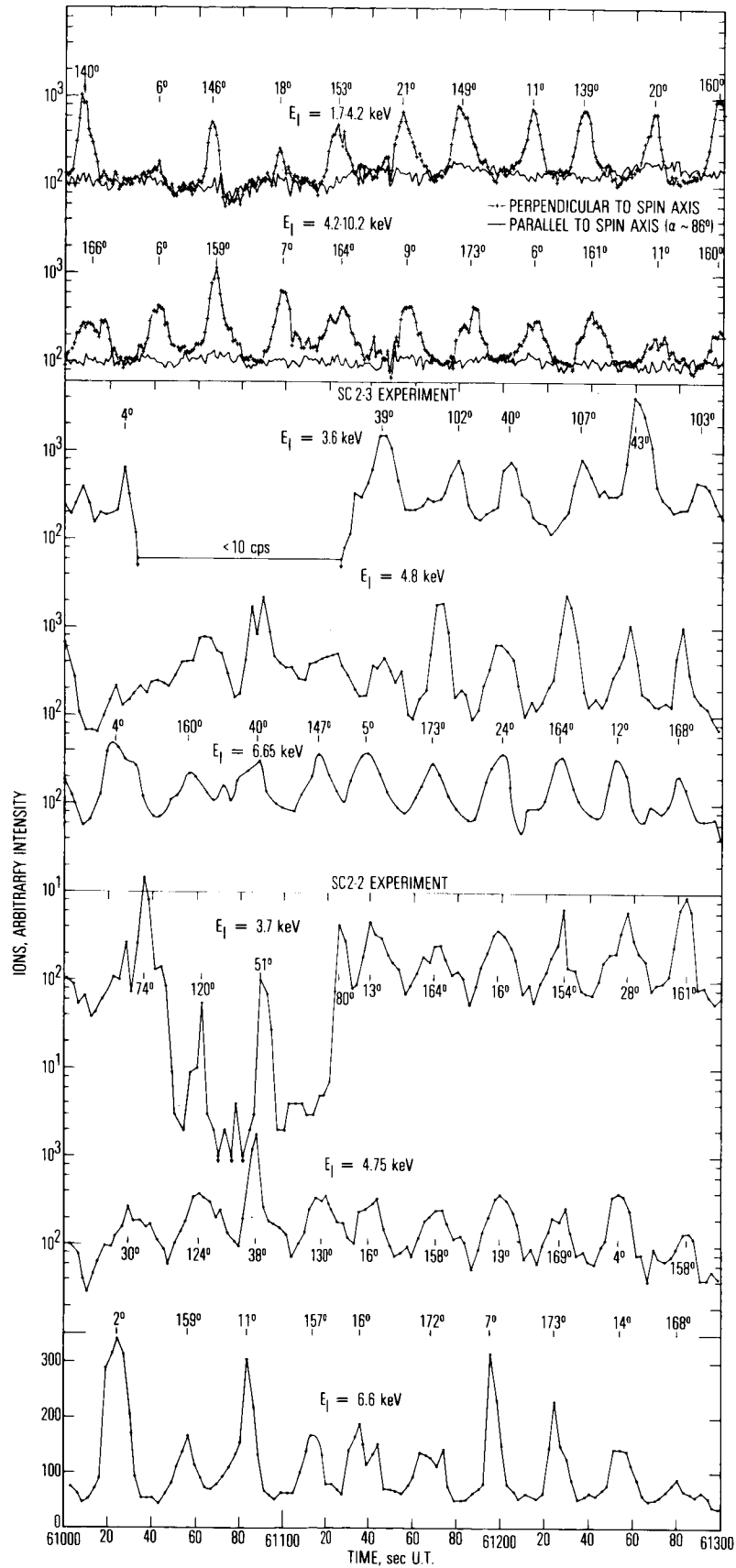


Figure 10. - Ion intensity as a function of time for several channels for March 28, 1979, charging event. The peaks show spin-period-related ion flux anisotropies.



## **OPERATION OF SC5 RAPID SCAN PARTICLE SPECTROMETER ON SCATHA SATELLITE\***

**Frederick A. Hanser and Bach Sellers  
Panametrics, Inc.**

**David A. Hardy and H. A. Cohen  
Air Force Geophysics Laboratory**

**J. Feynman and M. S. Gussenhoven  
Boston College**

### **SUMMARY**

The SC5 Rapid Scan Particle Spectrometer has two identical sets of particle detectors viewing parallel and perpendicular to the SCATHA Satellite's spin axis. A complete spectral measurement is made every second, so 54 complete spectra are measured every satellite rotation (54 seconds). By ground-commanding the instrument into a fixed energy channel, a time resolution of 0.2 second is obtained. The instrument can also be connected to a broad-band FM channel which provides 250  $\mu$ sec time resolution. Each particle detector set consists of two electron/proton ESA's (low energy, 0.05 - 1.7 keV, and high energy, 1.7-60 keV), and a pair of solid state detector spectrometers (30-1000 keV electron, and 100-8000 keV protons).

The normal operation mode of SC5 uses the ESA's in an auto-shutoff mode, in which the SEM bias is turned off while the perpendicular ESA's view the sun. This reduces degradation of the SEM's by solar UV; the large geometric factor and broad energy resolution result in substantial sensitivity to scattered solar UV. The ESA SEM gains are checked a few times a week by a SEM bias level calibration cycle. The normal SEM gain degradation with total accumulated counts was observed to recover partially when the ESA's were turned off, so the ESA's were operated in a mode of on one day and off one day. This has allowed reliable ESA operation for in excess of one year.

---

\* This work was partially supported by the Air Force under contracts F19628-79-C-0099 (Panametrics, Inc.) and F19628-79-C-0031 (Boston College).

The rapid time response of the SC5 instrument has been most useful in conjunction with the electron/ion gun operation. Data from some of the ICE events show that the satellite can take about a second to discharge when the ion beam is turned off. High time resolution FM band data from electron gun operations show that the satellite potential rises in less than 1 msec, with some ESA energy channels indicating that final adjustment of the ambient populations can have a time constant as long as one second. Electron beam turn off results in initial decay of most of the satellite's potential within a few msec, but a low energy (50 - 100 eV) electron component takes closer to 1 second to decay.

## INSTRUMENT DESCRIPTION

A general outline of the SC5 instrument is shown in figure 1 along with the various particle detector apertures. The electrostatic analyzers (ESA's) are dual electron/proton assemblies, two for each view direction to cover the range 0.05-60 keV in a total of eight (8) energy ranges. The solid state spectrometers (SSS's) are two detector telescope configurations used in anti-coincidence for the low energy range and coincidence for the high energy range. The SSS's cover 30-1000 keV for electrons and 100-8000 keV for protons. More detailed descriptions of the SC5 instrument are given in references 1 and 2, while a description of detector calibration is given in reference 3. The ESA detection characteristics are summarized in tables 1 and 2 and are based on the detailed measured responses given in reference 3. The SSS detection characteristics are summarized in tables 3 and 4.

The SC5 instrument is located on the bellyband of the SCATHA satellite as shown in figure 2. The perpendicular detectors look out between the +Y and -Z axes in the spin plane, while the parallel detectors look out the forward end of the satellite, parallel to the spin axis. The electron gun, SC4-1, is located on the bellyband about  $45^{\circ}$  away from SC5, while the ion gun, SC4-2, is located on the aft end of the satellite at  $180^{\circ}$  from the SC5 perpendicular apertures.

The normal mode of operation for SC5 has an energy channel dwell of 0.2 sec, so a complete spectrum is measured once every second. For the 54 second spin period this gives a rotational angular resolution of about  $7^{\circ}$  for the perpendicular detectors. By ground command, the ESA's and/or SSS's can be fixed in any desired energy channel (including the fifth, or background, channel for the ESA's), so 0.2 sec time resolution can be achieved.

The SC5 output can also be connected to a broad-band FM channel which provides 250  $\mu$ sec time resolution. Any single detector can be connected

to the FM channel, as can certain permutations of detectors, by ground command. By fixing to a particular energy channel, the FM data allow continuous measurement of one particle type/energy bin with the 250  $\mu$ sec time resolution.

## IN-ORBIT OPERATION

The SCATHA satellite is oriented with the spin axis in the orbital plane and normal to the earth-sun line, so the perpendicular detectors view the sun once per spin. Since the ESA's have broad energy bins and large geometrical factors, they are moderately sensitive to solar UV, and this contributes to gain degradation of the Spiraltron Electron Multipliers (SEM's) used for particle detection. SEM's generally suffer gain degradation at high total accumulated counts (reference 4), and solar UV adds to the total counts. The ESA's are thus operated in an auto-shutoff mode where a sun-sensing photodiode causes the SEM high voltages to be turned off while the perpendicular ESA's view the sun. Operations with and without this auto-shutoff mode enabled show that it significantly reduces the SEM gain degradation rate.

In-orbit tests also showed that the SEM gains partially recovered when the SEM's were off. The ESA's were thus operated in a cycle of one day on and one day off to reduce the net SEM gain degradation with total counts and thus maximize useful SEM lifetime. With this mode of operation, the ESA's have given useful data for more than a year.

The ESA SEM gains are checked a few times a week by a SEM bias level calibration cycle. By measuring the relative count rates as a function of bias level, the SEM efficiencies for the operating bias level are obtained. These efficiencies vary slowly with time for the normal SC5 operating conditions. Certain operations, such as SC4-1 electron gun operations, result in very high count rates for some of the ESA's and thus may give a significant change in some SEM efficiencies in a short period. Occasionally, intense fluxes of ambient particles, generally electrons in the 1 keV region, are observed for long periods of time, and these too can result in a significant SEM efficiency change for one or two ESA's.

The SC5 solid state spectrometers (SSS's) are on almost continuously since they do not degrade at the rate the SEM's do. The electron SSS's were calibrated with electron beams to about 45 keV, and this calibration was extrapolated to higher energies (reference 3). The two lowest electron SSS bins overlap the two highest ESA bins, and they agree moderately well in this overlap region, with the lowest SSS bin tending to be somewhat low, on the order of 50%. The higher energy SSS bins are in reasonable agreement

with the extrapolated ESA spectra. The proton SSS's appear to be operating properly although a detailed study of the data has not yet been made. More detailed study of both the electron and proton SSS data and comparison with the ESA data will be done in the near future.

## REDUCTION OF ESA SPECTRA

The SC5 ESA's have broad energy bins to allow rapid measurement of 0.05 to 60 keV particles. The typical calibrated energy channel responses are shown in figure 3, which gives the parallel electron ESA  $G(E)$  factors from reference 3. These responses are for saturation SEM efficiencies and must be multiplied by the fractional SEM efficiencies obtained from the SEM bias level calibrations when used with actual data.

The ESA energy channels have about 100% full-width-at-half-maximum (FWHM) energy resolution and a significant high energy tail in  $G(E)$ . The ESA responses are thus dependent on the spectral shape, and adjacent energy channels have significant overlap in response. To obtain the best spectral estimates within the resolution of a given set of ESA's (8 channels for the parallel electron ESA's, etc.), a set of eight central energy bins, corresponding closely to the FWHM energies, is used to define the basic energy detection range. These energies are the same for both electron and for both proton ESA sets, as shown in table 5 which also includes a Low and High bin for corrections in the edge channels. The high energy tail for the LE ESA's is subtracted using the background channel, which has a  $G(E)$  closely matching the high energy tails.

The counts from a given ESA set are used to derive corrected spectra by first calculating a zero order spectrum using the  $G\Delta E$  values in tables 1 and 2. The zero order spectra are then used to calculate spectral power law values ( $dj/dE = j_0 E^{-\gamma}$ , with  $\gamma$  the power law value) which are then used to calculate corrected response values for the central bin and at least one adjacent bin on the low and high energy side for each ESA channel. The resulting response matrix, which is very nearly diagonal, is then easily solved from the ESA counts, obtaining the corrected  $dj/dE$  values (particles/(cm<sup>2</sup>-sec-sr-keV)) for each of the eight Central Bins of table 5. The proton ESA's are done after the electron ESA's and use the corrected electron spectra to subtract the proton ESA response to electrons (see reference 3). The entire procedure is iterated a number of times until the power law exponents ( $\gamma$  values) of the corrected spectra are in close agreement with the input values.

A typical result of the flux correction procedure is shown in figure 4, where the uncorrected and corrected fluxes are plotted for the parallel electron ESA's. The largest correction is for regions of steeply rising or falling spectra. The spectrum in figure 4 is approximately Maxwellian with a temperature near 3 keV. A different type electron spectrum is shown in figure 5, where a two-component power law spectrum is shown. Corrections for a typical proton spectrum are shown in figure 6, where the low energy region ( $< 1$  keV) is below the background-limited threshold for the given electron flux conditions. The data in figures 5 and 6 were taken at the same time, so the electron spectrum in figure 5 was used to correct the electron contribution to the proton spectrum in figure 6.

### ESA DATA SUMMARIES

The SC5 instrument provides enormous quantities of data which must be conveniently summarized to provide an overview from which more detailed studies can be made. Since the most intense fluxes are generally measured by the ESA's, and since the perpendicular detectors generally measure over a large pitch angle range, the perpendicular ESA's are used to provide a daily summary for average energy, energy density, and number density. The measured pitch angle distributions are extrapolated to cover  $0^\circ$  to  $180^\circ$ , and the summaries are given for the full (extrapolated) pitch angle range for electrons and for protons.

Typical summary data plots are shown in figure 7 for electrons and figure 8 for protons. The number density is in particles/cm<sup>3</sup>, the energy density is in eV/cm<sup>3</sup>, and the average energy is in eV. The pitch angle range for the measured data of figures 7 and 8 is shown in figure 9. The narrow double spikes at 0800 and 2030 GMT are from ESA bias level calibrations, while most of the remaining structure is true particle variation. The data in figures 7 and 8 have not had the SEM efficiency divided in as is illustrated by the overshoot in electron number density for the two SEM bias level calibrations. The major structure of the particle flux behavior is, however, still evident and the summary plots are quite useful.

### ESA DATA FROM ION GUN OPERATIONS

The SC5 instrument has provided much data from operations with the ion gun, SC4-2. A typical spectrum during ion gun operation when the satellite was charged to about -400V is shown in figure 10, which shows the corrected and uncorrected parallel proton ESA spectrum for the Induced

Charging Event no. 1 (ICE #1) on day 47 of 1979. The sequence of four consecutive (1 second) spectra during gun turn-off is shown in figure 11, where the spectrum for 0818:24 indicates that beam turn-off/satellite discharge has a time constant on the order of a second, the time resolution of a complete SC5 ESA spectrum.

## ESA DATA FROM ELECTRON GUN OPERATIONS

Some of the most interesting SC5 data have come from operations of the electron gun, SC4-1. A parallel electron ESA spectrum during emission of a 3 keV electron beam, with the satellite charged to +3 keV, is shown in figure 12. Note the large corrections to spectrum channels on each side of the 3 keV peak. The low energy (< 3 keV) part of the corrected spectrum is consistent in shape and intensity with what would be expected from back-scattering of the 3 keV electrons.

High time resolution data from the FM channel were obtained from an electron gun operation on day 297, 1979. With a 500V, 0.1 mA beam the satellite charged to about +100V, and at beam turn-on reached the equilibrium potential within 1 msec as measured by the FM data from the 84 eV channel of the parallel electron ESA shown in figure 13. The beam turn-off data are shown in figure 14. Note the presence of a more intense flux after beam turn-off than before beam turn-on. This is quite frequently observed after electron beam turn-off when the satellite has charged significantly.

Later beam operations with 1.5 keV, 1 mA (nominal, actual was near 0.4 mA) resulted in a satellite potential of about +200V. The potential appears to have risen with about a 2 msec time constant to a slightly higher than equilibrium value and then decayed back to equilibrium with a 0.11 sec time constant. This is illustrated in figure 15, which shows the FM data for the 1.22 keV energy channel of the parallel electron ESA's. When the electron beam was turned off in the 1 mA mode, the satellite potential dropped to 50-100V in a few msec, but then decayed to the normal ambient potential with a 0.7 sec time constant. This is shown in figures 16 and 17, which are the 0.085 eV electron channel FM data for turn-off at 500 eV (figure 16) and 1.5 keV (figure 17). Note that the traces are almost identical since the satellite potential was beam-current limited. The data in figures 15, 16, and 17 are noisier than that in figures 13 and 14 because a higher cut-off frequency was used in playback. These data will all be reprocessed and digitized to yield the actual 250  $\mu$ sec count resolution and thus set more nearly precise values for the electron beam operation rise/fall times. A preliminary summary of some of the day 277 electron beam operation results is given in table 6.

## CONCLUSIONS

The SC5 instrument has operated reliably on the SCATHA satellite for in excess of one year. A large amount of ambient particle data have been obtained. Data from electron/ion gun operations have shown how the satellite potential responds and, in particular, have given some information on the various time constants involved.

## REFERENCES

1. Morel, P.R.; Hanser, F.A.; and Sellers, B.: Design of Instrumentation Suitable for the Investigation of Charge Buildup Phenomena at Synchronous Orbit. AFGL-TR-79-0235, Oct. 1979.
2. Stevens, J.R.; and Vampola, A.L.: Description of the Space Test Program P78-2 Spacecraft and Payloads. SAMSO TR-78-24, Oct. 1978, pp. 39-42.
3. Hanser, F.A.; Hardy, D.A.; and Sellers, B.: Calibration of the Rapid Scan Particle Detector Mounted in the SCATHA Satellite. AFGL-TR-79-0167, July 1979.
4. Klettke, B.D.; Krym, N.D.; and Wolber, W.G.: Long-term Stability Characteristics of Commonly Used Channel Electron Multipliers. IEEE Trans. Nucl. Sci., vol. NS-17, no. 1, Feb. 1970, pp. 72-80.

Table 1

## Summary of Electron ESA Detection Characteristics

ESA /Ch No.	Flat spectrum calculation			From response curves		
	$\bar{E}$ (keV)	$\Delta E(\text{FWHM})$ (keV)	$\bar{G}\Delta E$ (cm <sup>2</sup> -sr-keV)	$E_{\text{peak}}$ (keV)	$\bar{E}(1/2 \text{ ht})$ (keV)	$\Delta E(1/2 \text{ ht})$ (keV)
<b>ESA's</b>						
LE/#1	0.112	0.138	$8.5 \times 10^{-6}$	0.073	0.089	0.077
" /#2	0.27	0.30	$2.8 \times 10^{-5}$	0.18	0.22	0.19
" /#3	0.68	0.87	$7.7 \times 10^{-5}$	0.44	0.53	0.44
" /#4	1.50	1.55	$1.65 \times 10^{-4}$	1.05	1.26	1.08
HE/#1	4.6	6.2	$1.46 \times 10^{-4}$	2.7	3.2	2.7
" /#2	9.0	8.9	$2.4 \times 10^{-4}$	6.3	7.6	7.2
" /#3	23.	25.	$5.4 \times 10^{-4}$	16.	20.	19.
" /#4	53.	53.	$8.3 \times 10^{-4}$	40.	47.	47.
<b>ESA's</b>						
LE/#1	0.110	0.160	$7.0 \times 10^{-6}$	0.070	0.084	0.067
" /#2	0.26	0.33	$2.7 \times 10^{-5}$	0.18	0.21	0.17
" /#3	0.62	0.78	$4.7 \times 10^{-5}$	0.42	0.49	0.38
" /#4	1.57	1.64	$1.52 \times 10^{-4}$	1.10	1.22	1.12
HE/#1	4.4	5.7	$1.06 \times 10^{-4}$	2.7	3.3	3.0
" /#2	9.2	9.1	$2.1 \times 10^{-4}$	6.7	8.0	7.6
" /#3	24.	26.	$4.3 \times 10^{-4}$	17.	20.	19.
" /#4	54.	55.	$7.1 \times 10^{-4}$	49.	47.	46.

Table 2

## Summary of Proton ESA Detection Characteristics

ESA /Ch No.	Flat spectrum calculation			From response curves		
	$\bar{E}$ (keV)	$\Delta E(\text{FWHM})$ (keV)	$\bar{G}\Delta E$ (cm <sup>2</sup> -sr-keV)	$E_{\text{peak}}$ (keV)	$\bar{E}(1/2 \text{ ht})$ (keV)	$\Delta E(1/2 \text{ ht})$ (keV)
<b>ESA's</b>						
LE/#1	0.145	0.134	$2.4 \times 10^{-5}$	0.10	0.125	0.105
" /#2	0.35	0.34	$4.3 \times 10^{-5}$	0.25	0.30	0.27
" /#3	0.78	0.79	$1.38 \times 10^{-4}$	0.55	0.67	0.56
" /#4	1.70	1.57	$3.7 \times 10^{-4}$	1.20	1.44	1.12
HE/#1	4.5	4.3	$8.9 \times 10^{-4}$	3.1	3.8	2.9
" /#2	10.4	8.1	$2.5 \times 10^{-3}$	7.8	9.5	7.3
" /#3	25.	20.	$5.8 \times 10^{-3}$	19.	23.	18.
" /#4	60.	47.	$1.37 \times 10^{-2}$	44.	55.	43.
<b>ESA's</b>						
LE/#1	0.148	0.148	$1.39 \times 10^{-5}$	0.10	0.122	0.101
" /#2	0.34	0.33	$2.6 \times 10^{-5}$	0.24	0.30	0.25
" /#3	0.84	0.86	$8.9 \times 10^{-5}$	0.56	0.68	0.56
" /#4	1.80	1.62	$2.6 \times 10^{-4}$	1.3	1.57	1.31
HE/#1	4.0	3.9	$8.5 \times 10^{-4}$	2.9	3.4	2.6
" /#2	9.7	7.8	$2.3 \times 10^{-4}$	7.3	8.3	6.6
" /#3	23.	19.	$5.0 \times 10^{-3}$	18.	21.	16.
" /#4	55.	45.	$1.16 \times 10^{-2}$	43.	49.	39.



Table 3

## Summary of Electron SSS Properties

Channel No.	Average Energy (keV)	Channel Width (keV)	Effective $\bar{G}\Delta E^*$ (cm <sup>2</sup> -sr-keV)
A0	39	12	$1.21 \times 10^{-2}$
A1	58	24	$5.12 \times 10^{-2}$
A2	96	48	0.144
A3	335	430	1.53
A4	218	95	0.337
C0	>950	-	$3.55 \times 10^{-1}^+$
C1	1040	120	$4.26 \times 10^{-1}$
C2	70-950	-	$3.55 \times 10^{-1}^+$
C3	>950	-	$3.55 \times 10^{-1}^+$
C4	1040	120	$4.26 \times 10^{-1}$

\*Calculated for a flat electron spectrum.

+These values are cm<sup>2</sup>-sr for G(>E), or G(E<sub>1</sub> to E<sub>2</sub>).

Table 4

## Summary of Proton SSS Properties

Channel No.	II Proton SSS			I Proton SSS		
	Av. E(keV)	Width(keV)	$\bar{G}\Delta E$ (cm <sup>2</sup> -sr)*	Av. E(keV)	Width(keV)	$\bar{G}\Delta E$ (cm <sup>2</sup> -sr)*
A0	126	49	0.328	126	49	0.328
A1	188	75	0.502	188	75	0.502
A2	275	100	0.669	275	100	0.669
A3	388	125	0.836	388	125	0.836
A4	499	97	0.644	465	29	0.194
C0	6430	4360	29.1	5020	3460	23.1
C1	3060	2380	15.9	2380	1830	12.2
C2	1410	910	6.07	1100	731	4.89
C3	779	361	2.42	612	242	1.62
C4	573	51	0.341	(485	≈10	≈0.01)

\*Calculated for a flat proton spectrum.

Table 5  
Energy Bins for ESA Response Calculation

<u>Bin Designation</u>	<u>Electron ESA's</u>		<u>Proton ESA's</u>	
	<u>Range (keV)</u>	<u>Center (keV)</u>	<u>Range (keV)</u>	<u>Center (keV)</u>
Low	0.030-0.050	0.040	0.030-0.070	0.050
Center 1	0.050-0.120	0.085	0.070-0.170	0.120
Center 2	0.120-0.300	0.210	0.170-0.400	0.285
Center 3	0.300-0.700	0.500	0.400-0.900	0.650
Center 4	0.700-1.80	1.25	0.900-2.20	1.55
Center 5	1.80 -4.50	3.15	2.20 -5.00	3.60
Center 6	4.50 -11.0	7.75	5.00 -13.0	9.0
Center 7	11.0 -25.0	18.0	13.0 -30.0	21.5
Center 8	25.0 -70.0	47.5	30.0 -70.0	50.0
High	70.0 -150.	110.0	70.0 -150.	110.0

Table 6  
Summary of Electron Beam On/Off Characteristics  
for Some of the Day 297, 1979 Operations

<u>Electron Beam on/off</u>	<u>Beam Voltage (V) (Current=1 mA)</u>	<u>Parallel Electron ESA Energy Channel (E in keV)</u>	<u>Rise/Decay Times (sec)</u>
on	50	1 (0.085)	Rise < 0.001
off	500	1 (0.085)	Rise $\approx$ 0.001/Decay $\approx$ 0.7
on	500	3 (0.500)	Rise $\approx$ 0.001/Decay $\approx$ 0.001
off	1500	4 (1.250)	Decay $\approx$ 0.002
on	1500	4 (1.250)	Rise $\approx$ 0.002/Fall $\approx$ 0.11
off	1500	3 (0.500)	During Channel ID
on	1500	3 (0.500)	Rise < 0.001/Fall $\approx$ 0.001
off	1500	2 (0.210)	Decay $\approx$ 0.005
on	1500	2 (0.210)	Rise < 0.001/Fall $\approx$ 0.001
off	1500	1 (0.085)	Rise $\approx$ 0.001/Decay $\approx$ 0.7
on	1500	1 (0.085)	Rise < 0.001/Fall $\approx$ 0.002

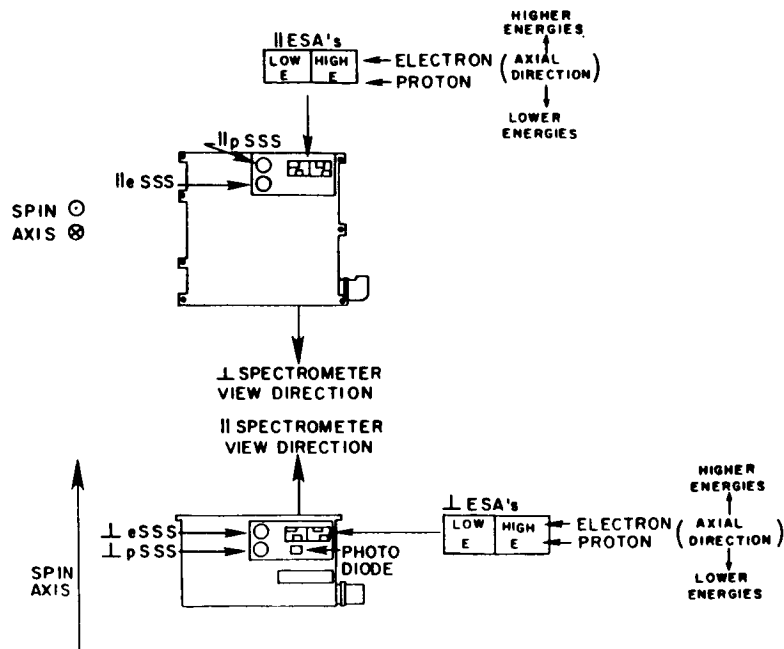


Figure 1. General outline of the SC5 instrument, showing the various particle detection apertures.

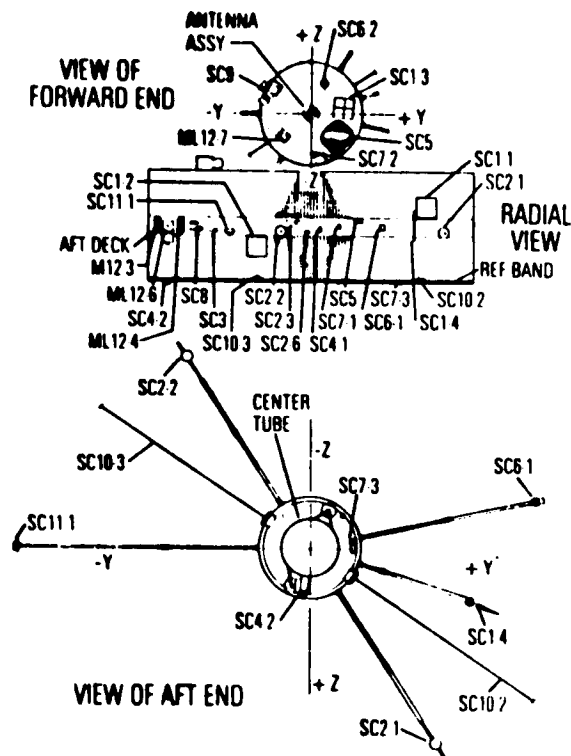


Figure 2. SC5 location on the SCATHA satellite (from reference 2).

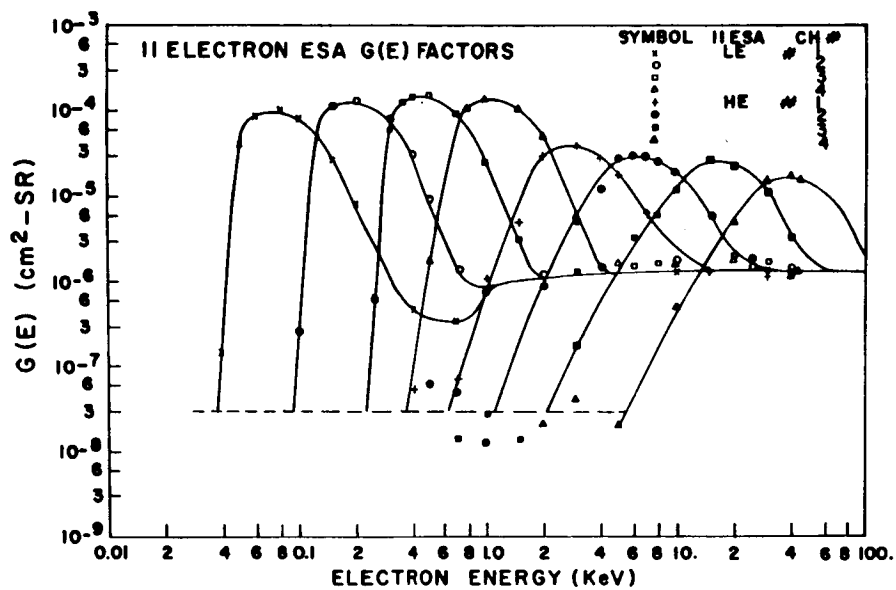


Figure 3. Calibration data and smoothed response curves for the parallel electron ESA's.

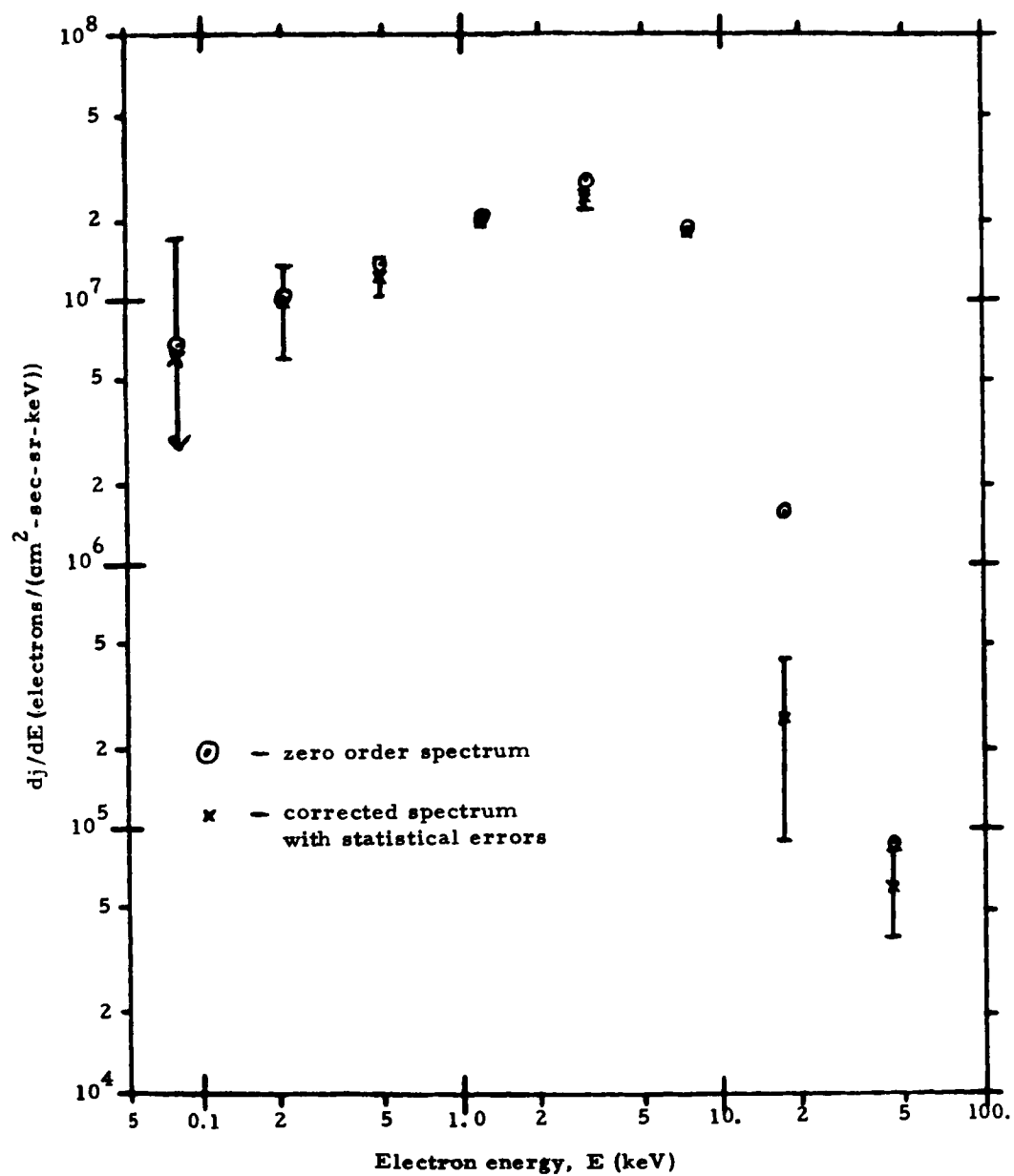


Figure 4. Electron spectrum with an approximately 3 keV temperature.

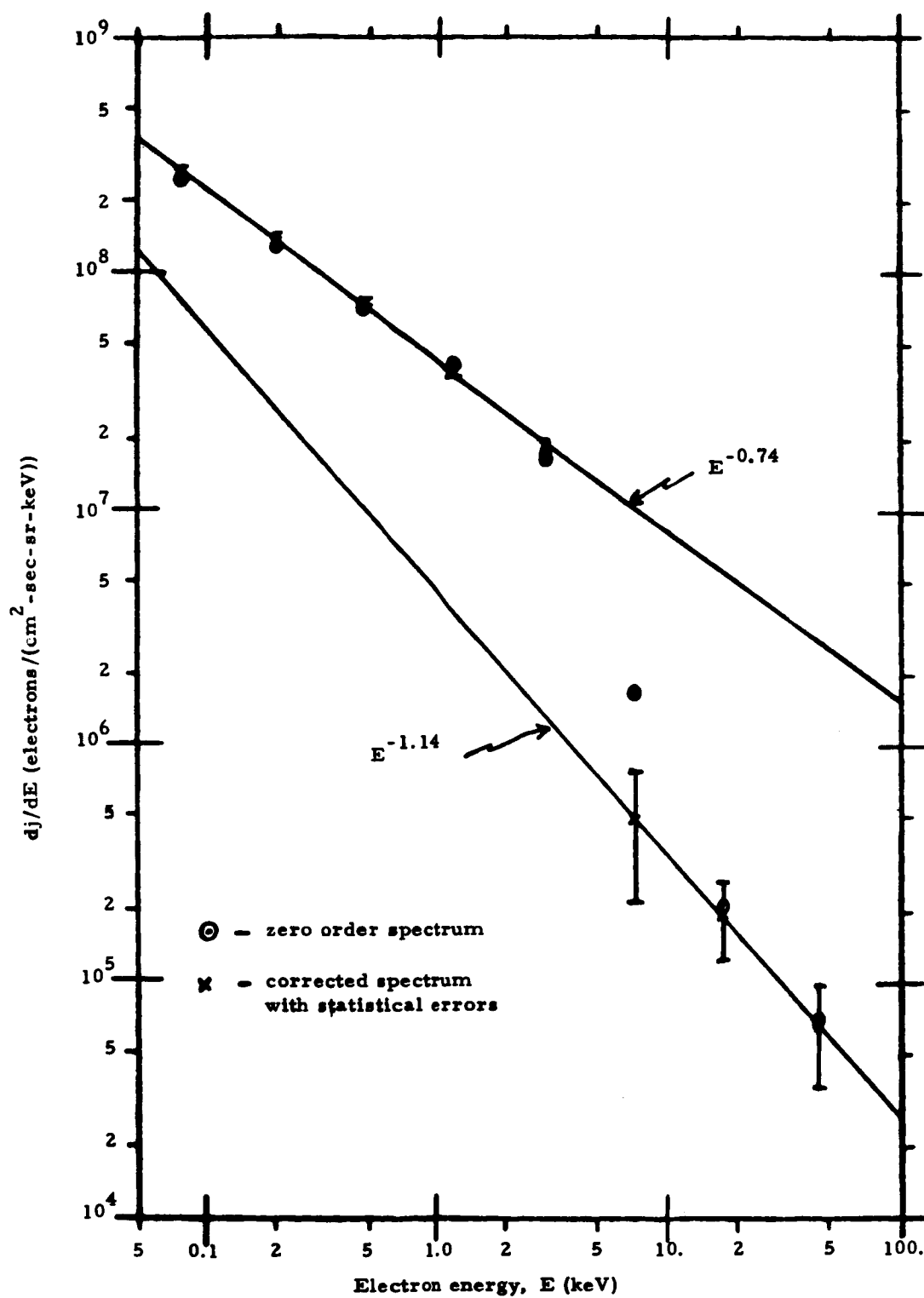


Figure 5. Correction effects on power law electron spectrum.

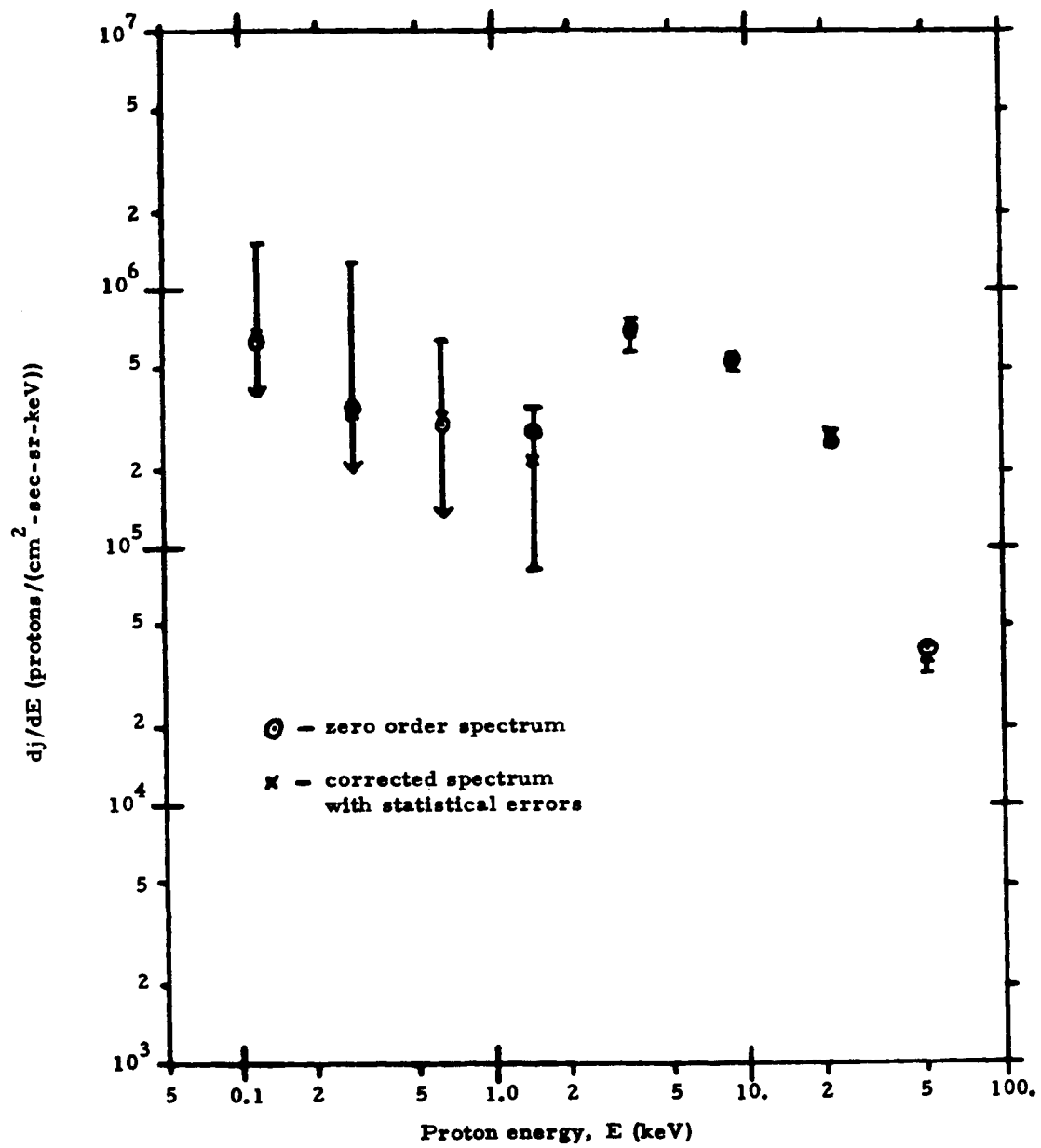


Figure 6. Corrections to a typical proton spectrum.

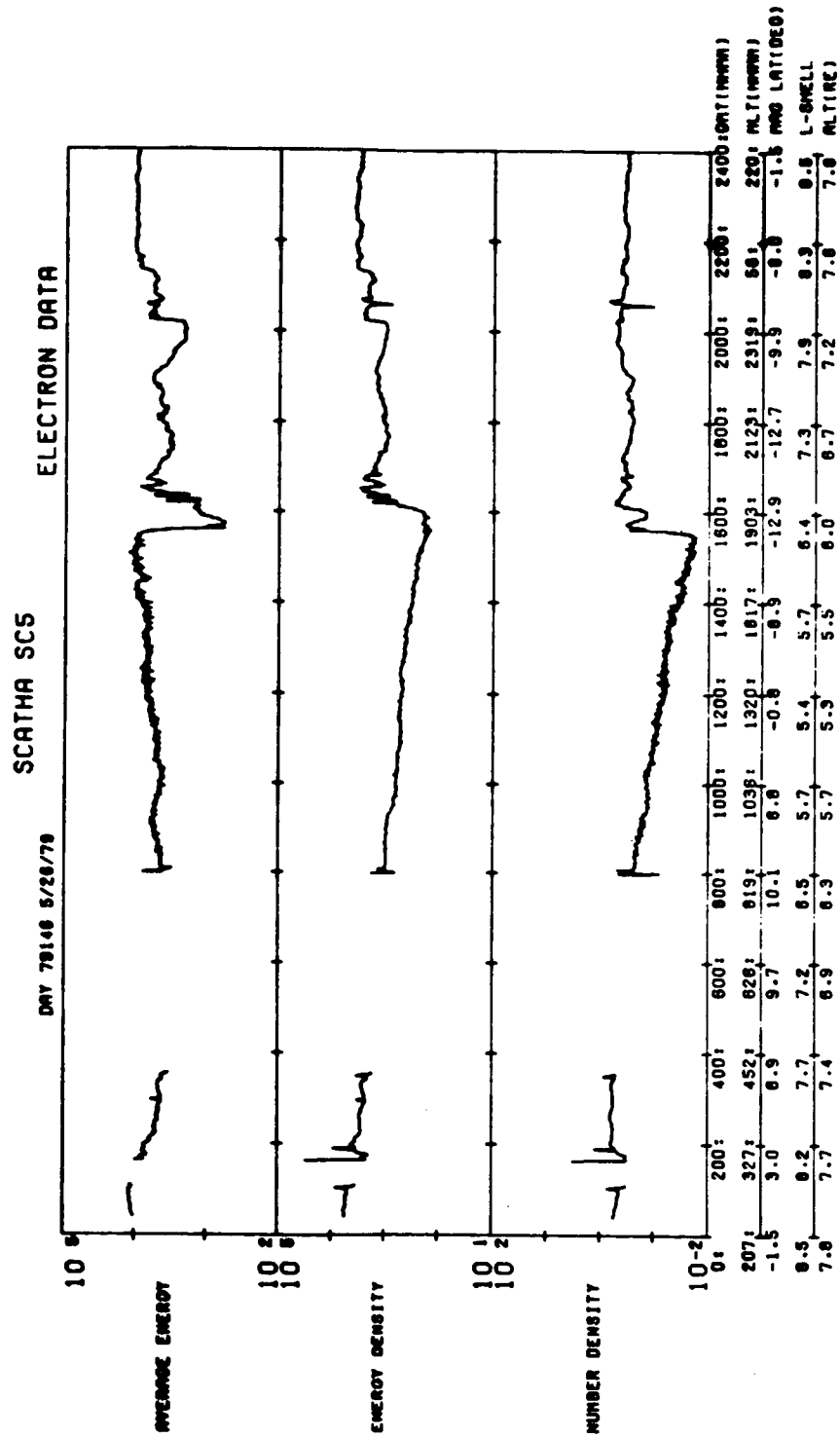


Figure 7. Typical summary plot of SC5 ESA data for electrons.



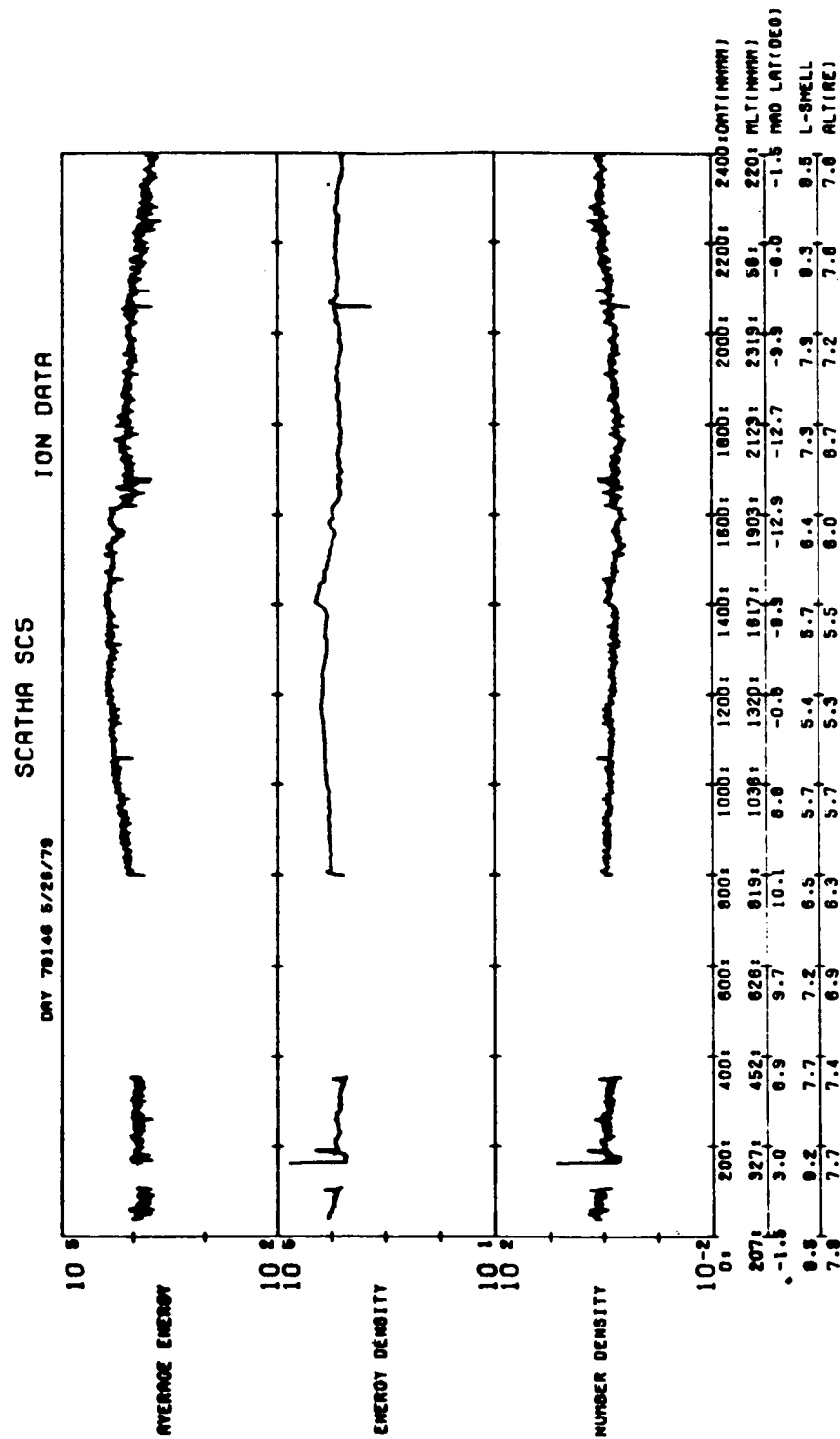


Figure 8. Typical summary plot of SC5 ESA data for protons (ions).



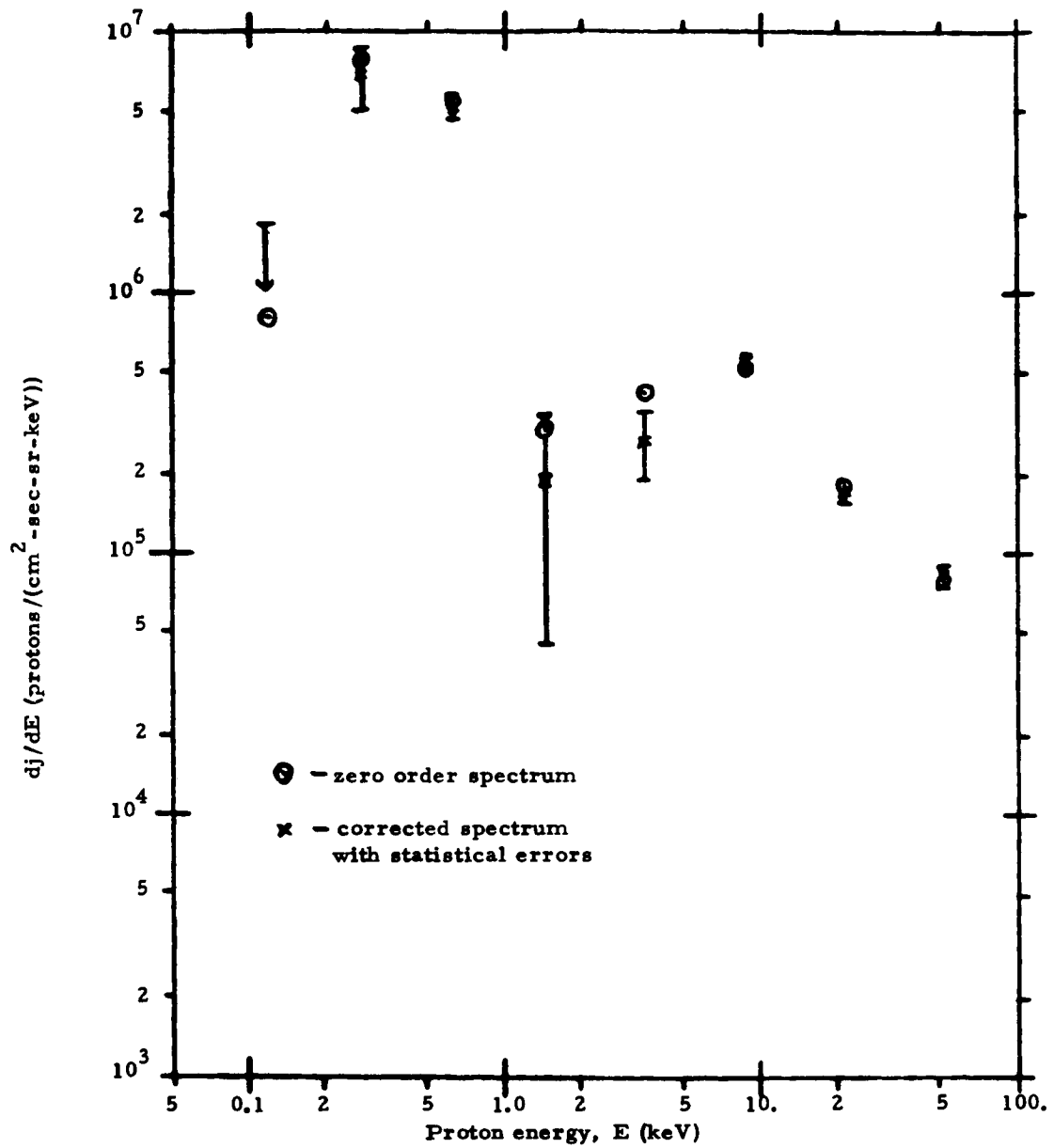


Figure 10. Typical proton spectrum during ion gun operations, corrected and uncorrected.

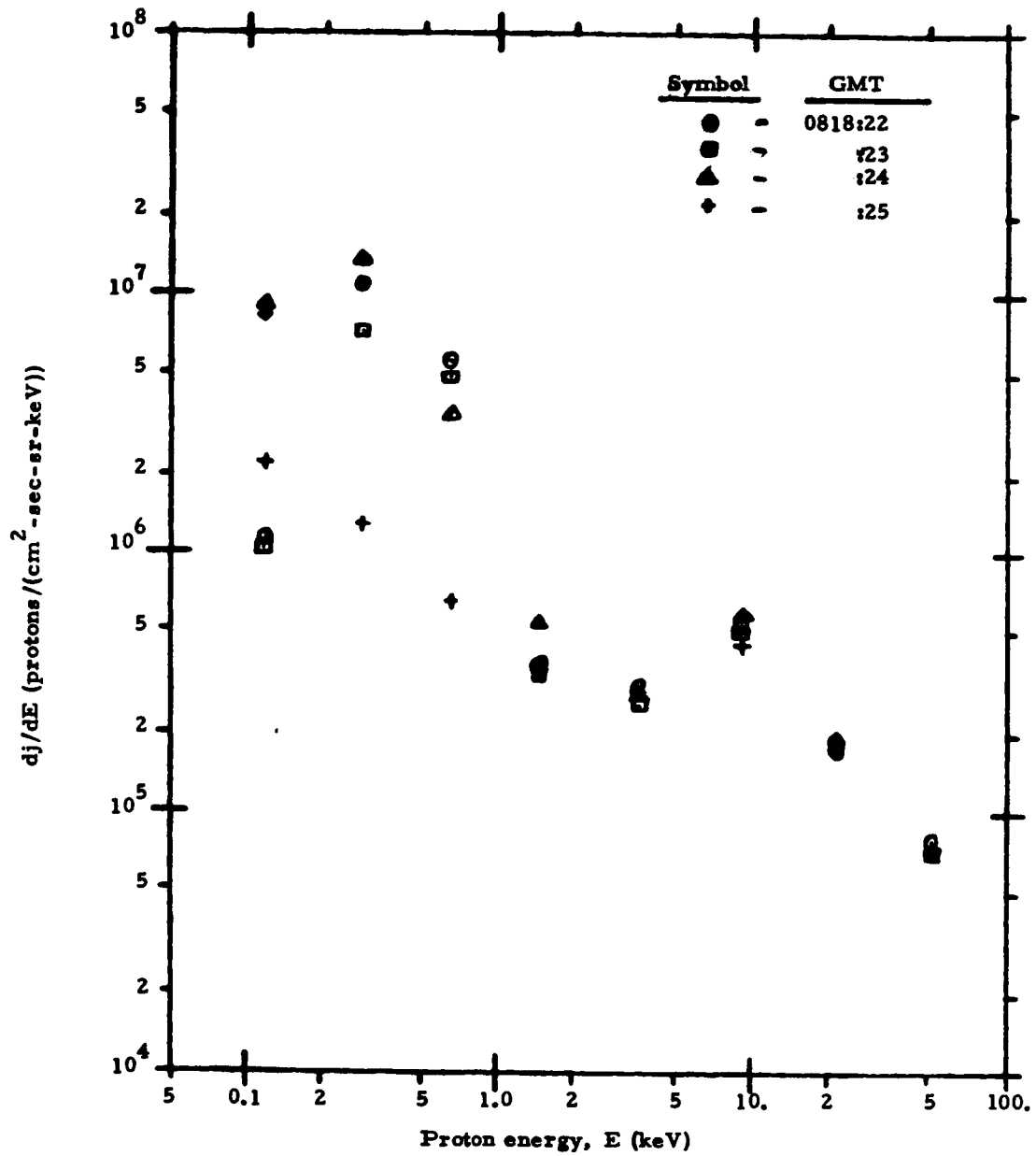


Figure 11. Four consecutive corrected ion spectra during ion beam turn-off in ICE #1 (day 47, 1979).

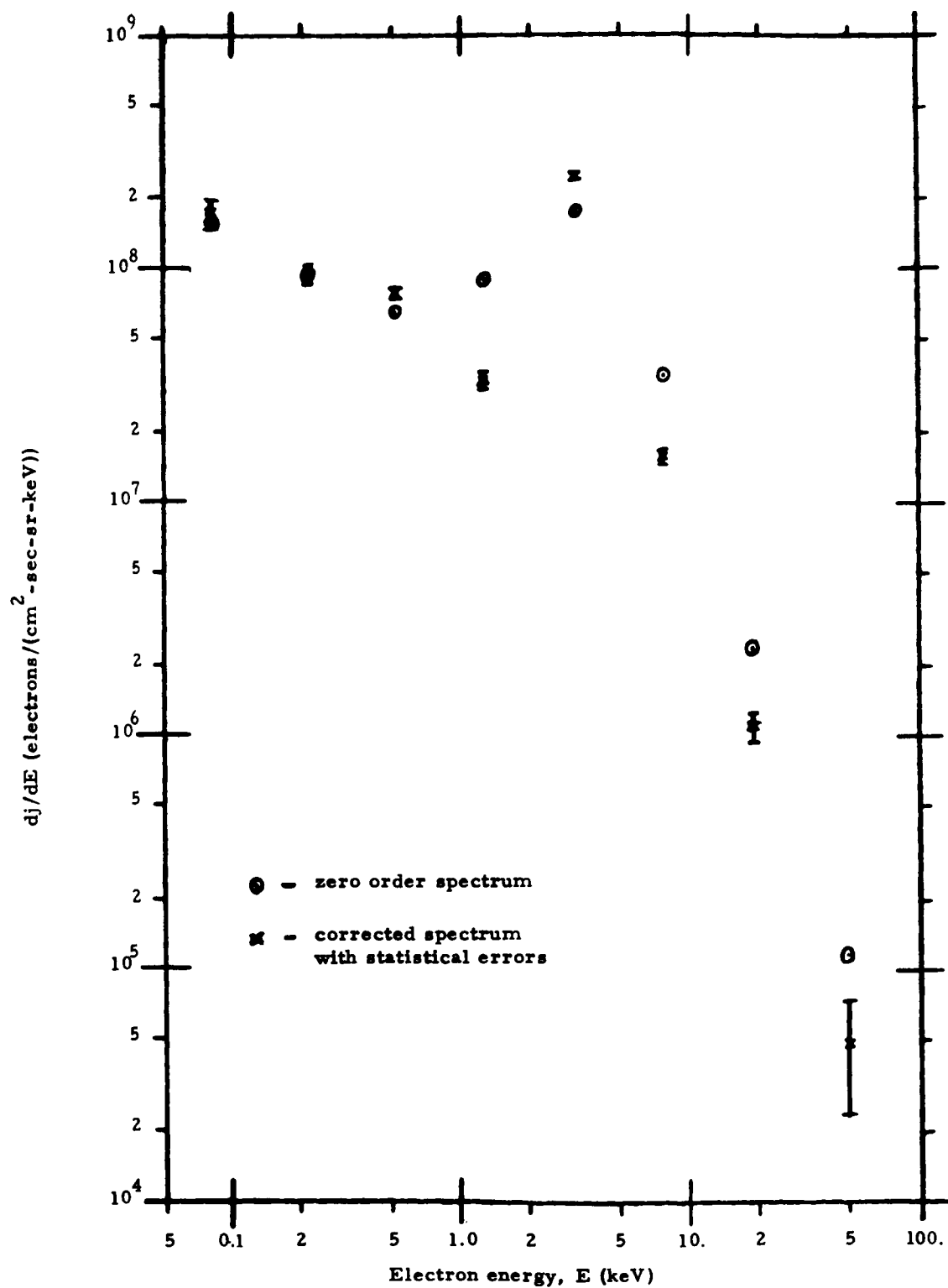


Figure 12. Typical electron spectrum with a strong monoenergetic peak, during electron gun operations.

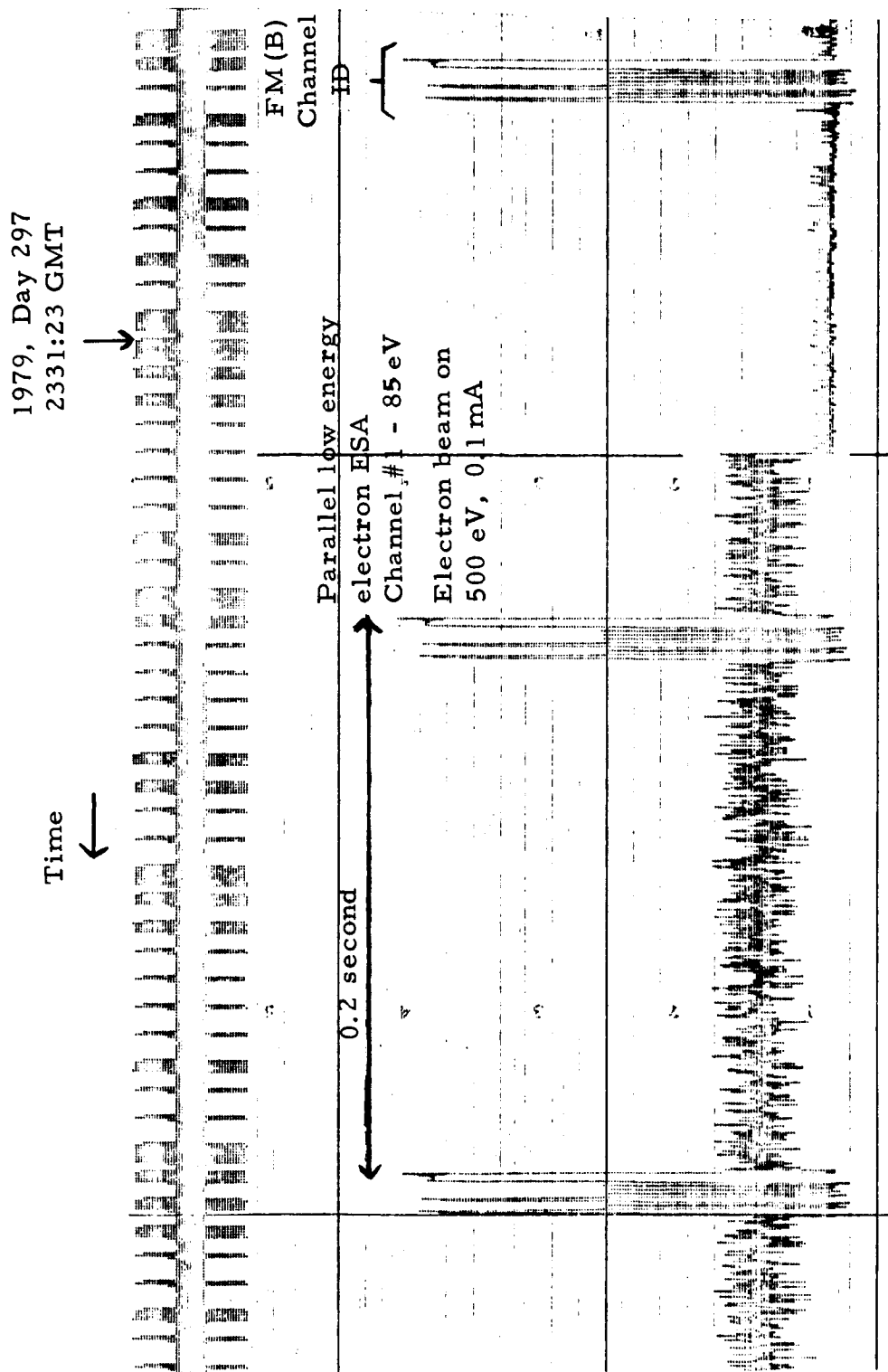


Figure 13. FM data from the low energy parallel electron ESA, in energy channel 1 (85 eV), for electron beam turn-on at 500V, 0.1 mA, on day 297, 1979.

1979, Day 297  
2333:0 GMT

Time  
←

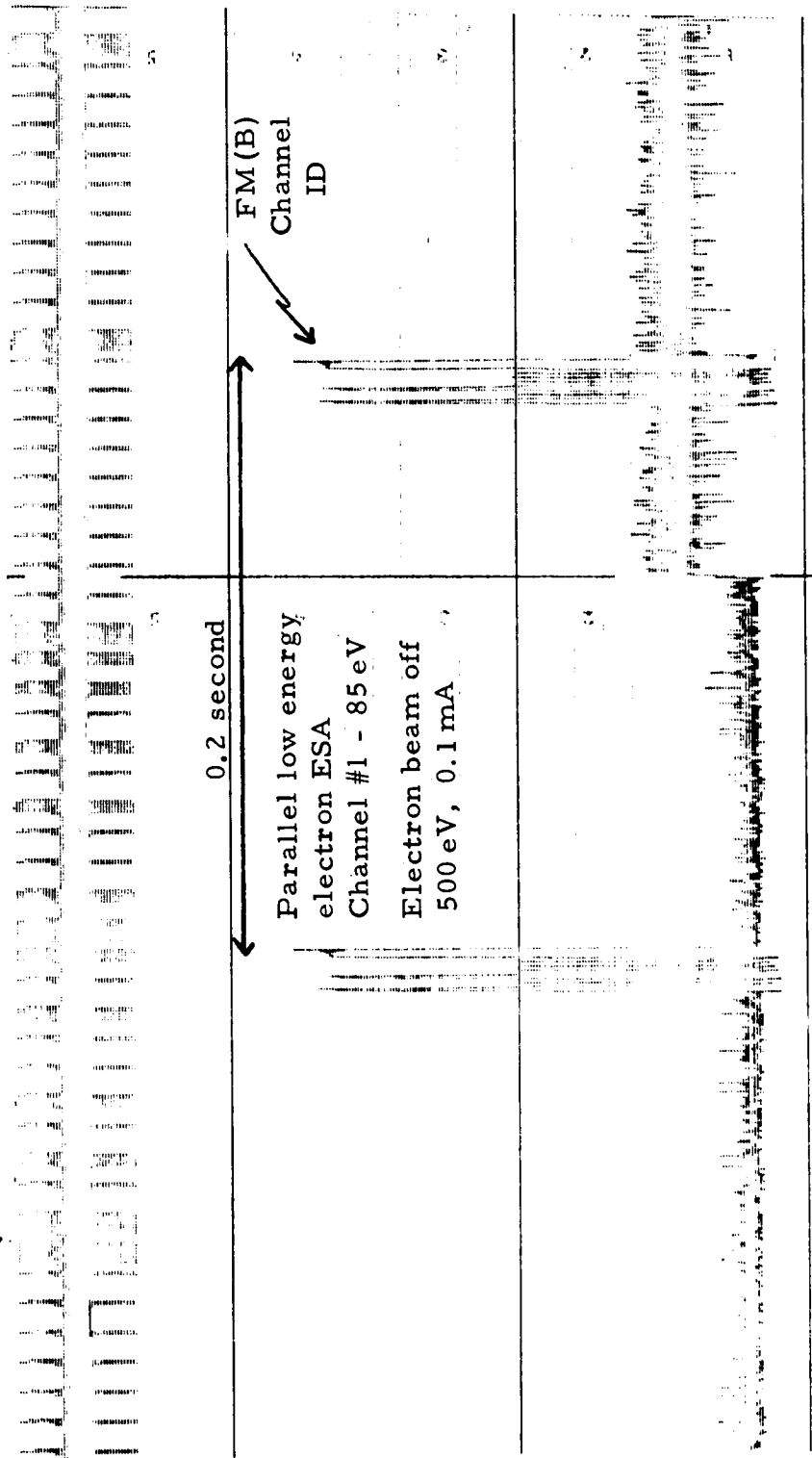


Figure 14. FM data from the low energy parallel electron ESA, in energy channel 1 (85 eV), for electron beam turn-off at 500 V, 0.1 mA, on day 297, 1979.

1979, Day 297  
2348:43.5 GMT

Time  
←

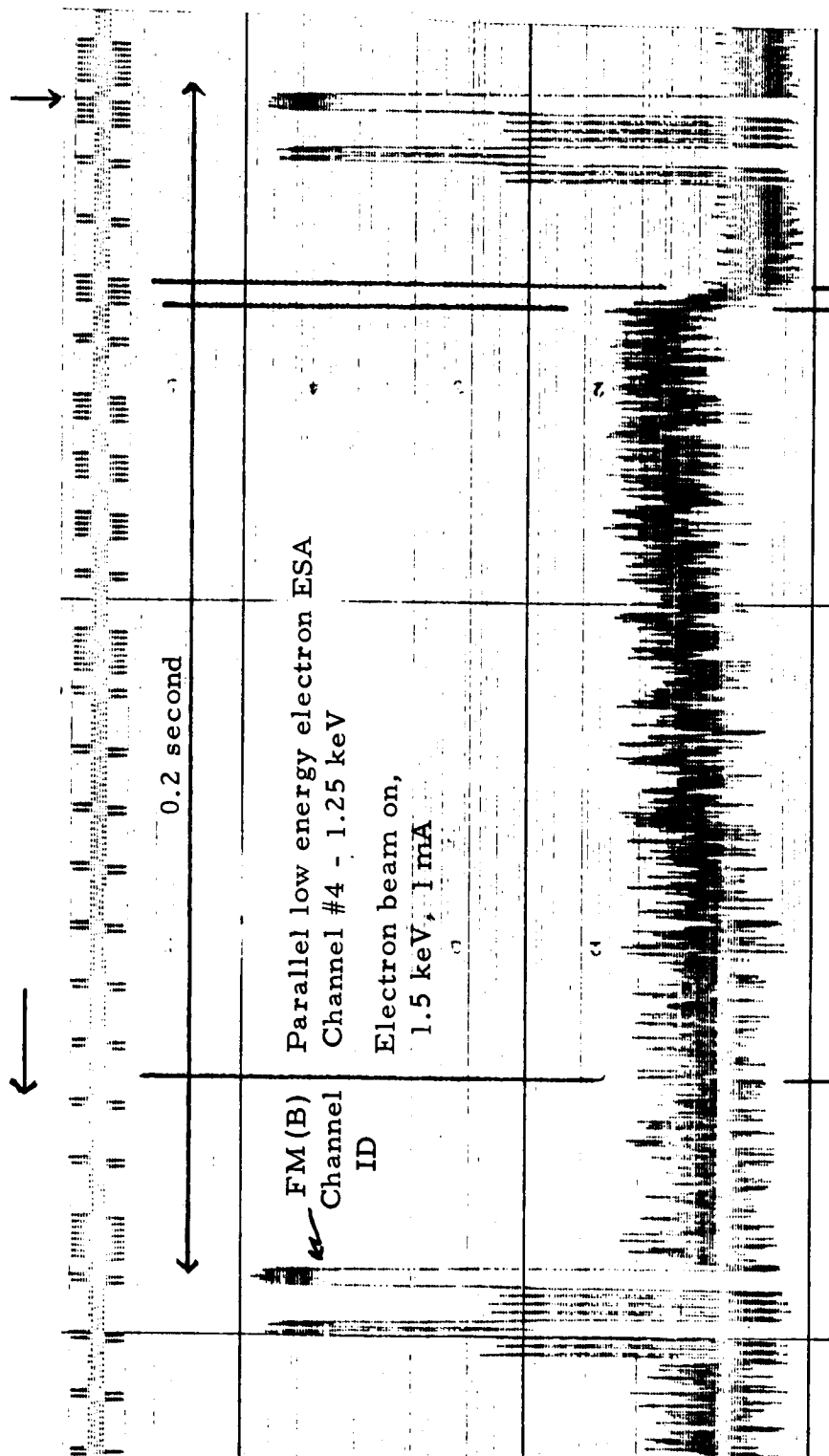


Figure 15. Response of the 1.25 keV parallel electron ESA energy channel to electron beam turn-on at 1.5 keV, 1 mA, on day 297, 1979.



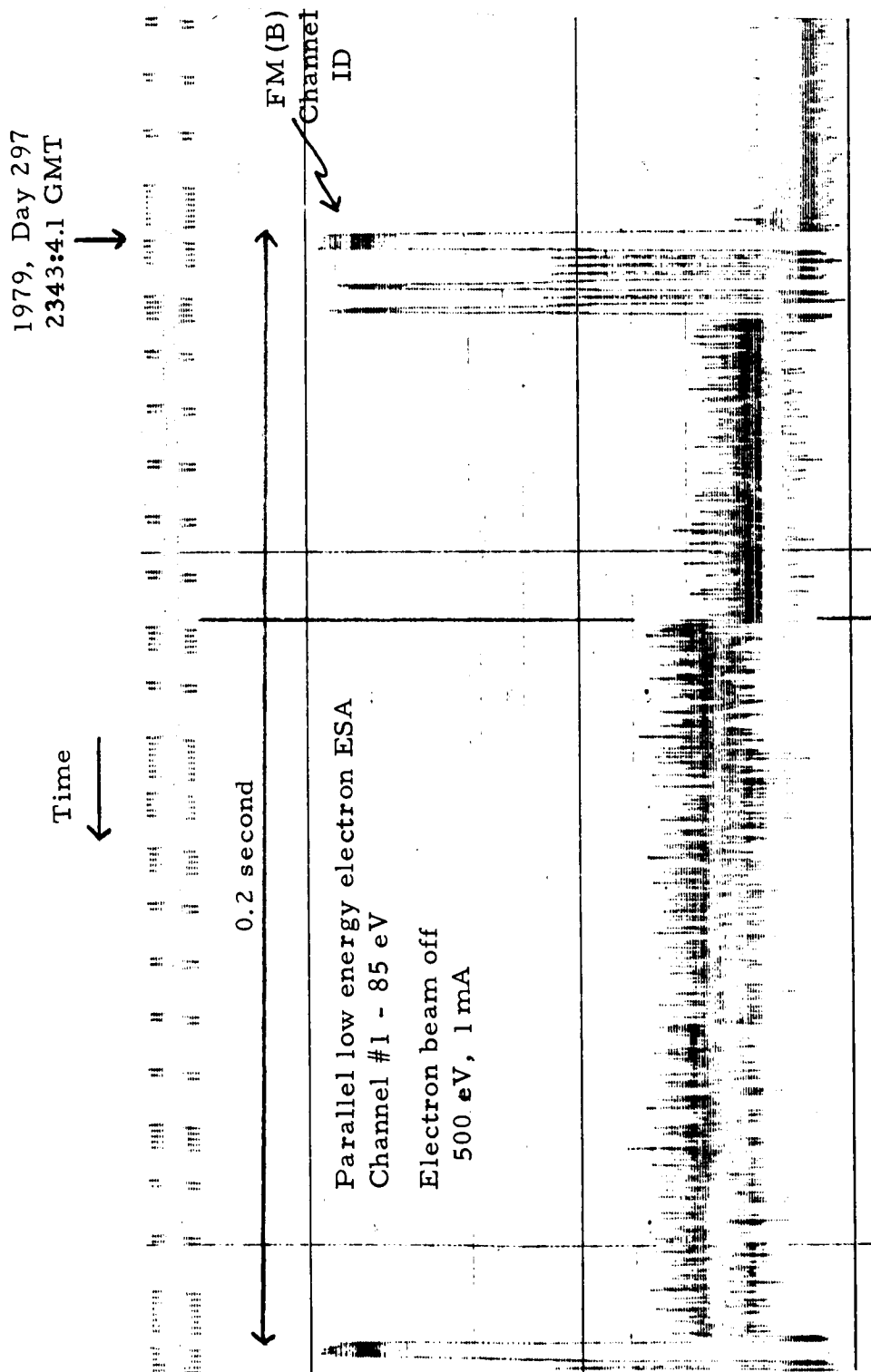


Figure 16. Response of the 85 eV parallel electron ESA energy channel to electron beam turn-off at 500 V, 1 mA, on day 297, 1979.

1979, Day 297  
2354:51.3 GMT

Time  
←

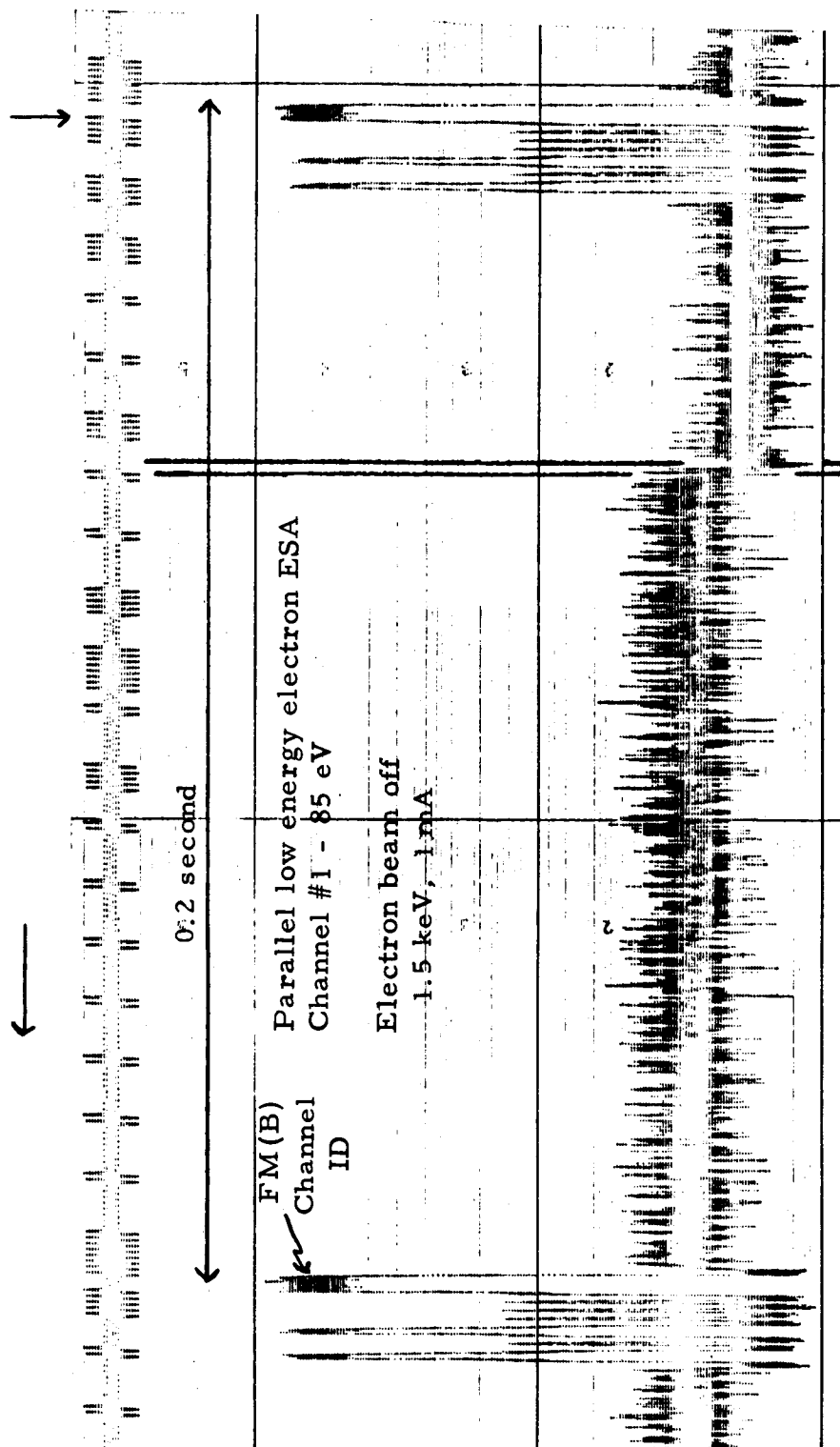


Figure 17. Response of the 85 eV parallel electron ESA energy channel to electron beam turn-off at 1.5 keV, 1 mA, on day 297, 1979.

# REVIEW OF HOT PLASMA COMPOSITION NEAR GEOSYNCHRONOUS ALTITUDE

Richard G. Johnson  
Lockheed Palo Alto Research Laboratory  
and  
University of Bern†

## SUMMARY

The information available on the hot plasma composition at and near the geostationary satellite orbit has increased dramatically during the past four years. At energies below 32 keV, ions of terrestrial origin ( $O^+$  and  $He^+$ ) are frequently observed to be significant contributors to the hot plasma density and energy density, and during geomagnetically disturbed periods,  $O^+$  ions are frequently the dominant ions. During geomagnetically quiet periods  $H^+$  ions are typically the dominant hot plasma ions. Evidence for a solar cycle dependence to the  $O^+$  hot plasma densities at the geostationary orbit has been found. Our understanding of the details of the physical processes involved in the entry, acceleration, transport, and loss of the plasma ions, and thus our ability to model them, is still quite limited.

## INTRODUCTION

As recently as the 1st Spacecraft Charging Technology Conference in 1977, quantitative measurements on the ion composition of the hot (0.1-30 keV) plasmas near the geostationary satellite altitude had not yet been performed (ref. 1). The plasma composition in this region of the magnetosphere was inferred primarily from composition information obtained on similar magnetic L-shells but at much lower altitudes. Such observations led to the conclusion that, at least during geomagnetically disturbed periods, there were significant fluxes of  $O^+$  ions as well as protons in the hot plasmas near the geostationary satellite altitude and that the ionosphere was the origin of the  $O^+$  ions as well as some of the protons (ref. 1).

Prior to the work of Shelley et al. (ref. 2) in 1972, it was generally believed that the energetic ion population in the magnetosphere was always dominated by protons ( $H^+$ ) and that the source of these ions was the solar wind (ref. 3 and 4). This viewpoint was specifically reflected in the summary of the

---

†Most of the unreferenced data presented in this review was reduced and analyzed while I was a Visiting Professor at the University of Bern. I am indebted to Professor J. Geiss and Dr. H. Balsiger for making the visit possible and wish to thank them and other members of the staff at the Physikalisches Institut for making my visit both productive and enjoyable. This research was sponsored by the University of Bern and the Lockheed Palo Alto Research Laboratory.

1965 Conference on Radiation Trapped in the Earth's Magnetic Field (ref. 3) which stated: "The solar wind is the source of all electrons and protons of energy less than 100 MeV by some diffusion and acceleration processes which are currently not understood." This is in contrast to recent observations, discussed herein, which show that near the geostationary satellite orbit the ionospheric component ( $O^+$ ) often dominates the hot plasma density, as well as the energy density, for particle energies up to 32 keV during geomagnetic storms. However, many of the important acceleration and transport processes are still not understood, and the relative contributions of the solar wind and the ionosphere to the hot plasmas and to the more energetic particle populations under the wide variety of geophysical conditions remain to be determined.

Satellite measurements on the mass composition of the hot plasmas did not begin until 11 years after the discovery of the radiation belts. The reason for this delay seems to have been twofold. First, there was no strong theoretical or experimental basis for expecting hot plasma ions with masses greater than hydrogen to play a significant role in the energetics of the magnetospheric processes. Second, the spacecraft resources of payload weight, power, and telemetry bandwidth were quite limited on early spacecraft and this tended to limit the selection of the more complex instrumentation, such as ion mass spectrometers, for the payloads. The number of satellites which have included hot plasma mass spectrometers for magnetospheric measurements are still quite limited and are shown in figure 1. The first three satellites provided composition data only at low ( $<800\text{km}$ ) and intermediate ( $<8000\text{km}$ ) altitudes. In situ observations which extended to high altitudes near the equatorial plane began with the GEOS-1 spacecraft in 1977 (ref. 5), and the first hot plasma composition measurements on a geostationary satellite were obtained with GEOS-2 in 1978 (ref. 6 and 7).

A knowledge of the plasma ion composition as a function of energy and pitch angle is important to spacecraft charging investigations in several ways. The number density of the plasma near a spacecraft during a spacecraft charging event is frequently determined from measurements of the ion fluxes with energies above the spacecraft potential. To correctly calculate the density from ion flux measurements, the composition of the ion fluxes must be known. Also, secondary electron production by plasma ions incident on spacecraft surfaces is typically strongly dependent on the ion mass at a particular energy and angle of incidence. And finally, in a more general way, a more complete understanding of the plasma composition in the magnetosphere under a variety of geophysical conditions is required before a predictive capability for the hot plasma environment in the magnetosphere can be achieved.

This review emphasizes primarily the information available on the composition of the hot plasmas at and near the geostationary satellite altitude. Some discussion of observations at lower and higher altitudes is presented for continuity and for general perspective on the large scale spatial distributions and dynamic characteristics of the hot plasmas. For more general reviews of the origin, entry, acceleration, transport, and loss of the hot plasma and energetic ions in the magnetosphere, the reader is referred to recent review papers by Shelley (ref. 8), Young (ref. 6), Johnson (ref. 9), Spjeldvik (ref. 10) and Cornwall and Schulz (ref. 11).

## OBSERVATIONS AT LOW (<800km) ALTITUDES

Plasma composition observations at low altitudes have made important contributions to our understanding of the hot plasmas in the outer regions of the magnetosphere, but generally in a qualitative way. They have shown that the ionosphere is an important source of hot magnetospheric plasmas, that the ionospheric component is widely distributed in local time and in altitude in the outer magnetosphere, that an acceleration process is operating inside the magnetosphere to produce keV ions from the thermal population, and that the processes are highly dynamic and correlated with geomagnetic activity.

It was discovered by Shelley et al. (ref. 2) in 1972 that large fluxes of energetic  $O^+$  ions were precipitating from the magnetosphere during geomagnetic storms. The observations were made with an ion mass spectrometer aboard the polar orbiting satellite 1971-089A at 800 km altitude and provided the first direct evidence that the ionosphere was an important contributor to the hot magnetospheric plasmas. During geomagnetic storms, it was found that within the instrument energy range of 0.7 to 12 keV the precipitating  $O^+$  fluxes were comparable to and sometimes exceeded the  $H^+$  fluxes. An example of this is seen in figure 2 for data acquired on the precipitating energy fluxes during the 17-18 December 1971 storms. The observed fluxes were widely distributed in geomagnetic latitude (and thus L-values), and the high  $O^+$  fluxes at L-values corresponding to the geostationary satellite altitude ( $L \sim 6.6$ ) led to the earlier prediction (ref. 1) that significant fluxes of ionospheric ions would be found in the hot plasmas near geostationary altitude at least during geomagnetically disturbed periods. However, quantitative information on the ion fluxes in the equatorial regions of the magnetosphere cannot be obtained from measurements at low altitudes because they sample only a small fraction of the equatorial pitch angles.

The precipitating  $O^+$  fluxes observed at low altitudes were found to be correlated with substorms activity (ref. 12), but during magnetically quiet periods, the precipitating fluxes were most often below the sensitivity level of the instrument (about  $2 \times 10^5 (\text{cm}^2 \text{ sec ster})^{-1}$ ).

Although the early low altitude composition measurements indicated an important role for the ionospheric ions in the hot magnetospheric plasmas, they provided little detailed information on the location of the ionospheric source region or on the physical processes responsible for the acceleration, transport, and loss of the ionospheric ions. The need for composition measurements at high altitudes in the equatorial regions and at high latitudes was clearly indicated.

## OBSERVATIONS AT INTERMEDIATE (<8000km) ALTITUDES

Observations at intermediate altitudes have provided the principal basis for understanding the ionospheric source location and the characteristics of the ionospheric ions that are injected into the outer magnetosphere at high

geomagnetic latitudes (ref. 13, 14, 15, and 16). This high latitude region appears to be the principal source of ionospheric ions in the hot plasmas near the geostationary satellite altitude. However, significant contributions to the ion number density and energy density from other ionospheric regions, such as the high altitude plasmasphere, must still remain under consideration (ref. 17).

Hot plasma composition observations at high latitudes were made at altitudes up to 8000km with an ion mass spectrometer aboard the polar orbiting S3-3 spacecraft. Large fluxes of  $O^+$  and  $H^+$  ions and weaker fluxes of  $He^+$  ions were observed flowing upward from the ionosphere with energies in the 0.5 to 16 keV range of the instrument (ref. 13, 14, and 15). The upward flowing ions were also observed without mass discrimination on the same spacecraft with an electrostatic analyzer in the energy range 0.09 to 3.9 keV (ref. 18). The upstreaming ion fluxes are most frequently observed in the 4000 to 8000km altitude range with average energies of a few keV and peak fluxes frequently as high as  $10^8(\text{cm}^2 \text{ sec ster keV})^{-1}$ . From measurements of pitch angle distributions, evidence for both field aligned ion acceleration and acceleration perpendicular to the magnetic field is found. The spatial, energy, and angular distributions and the composition of the upstreaming ions are highly variable.

Ghielmetti et al. (ref. 15) and Gorney et al. (ref. 16) have conducted statistical studies of the latitudinal and local time distributions of the upward flowing ions. The results of Ghielmetti et al. on the occurrence frequency of observation of these ions is shown projected into the equatorial plane in figure 3 (ref. 19). It can be seen that the ionospheric source region is widely distributed and that spacecraft near the geostationary altitude will frequently be on magnetic field lines which connect directly to this source region. Thus, near the geostationary satellite altitude, highly anisotropic ion fluxes with the intensities peaked near or along the magnetic field direction would be an expected consequence of the lower altitude ionospheric source. Such anisotropic ion fluxes were observed initially without mass discrimination on the ATS-6 satellite (ref. 20) and more recently with mass discrimination on the GEOS-1 (ref. 5), GEOS-2 (ref. 6), and SCATHA (ref. 21) satellites.

With the S3-3 satellite data, the composition of the trapped component of the inner ring current during three geomagnetic storms was investigated by Johnson et al. (ref. 22). Although these measurements were not made at equatorial latitudes, they were made at sufficiently high altitudes (5000-8000km) to sample equatorial pitch angles in the range of  $20^\circ$  to  $50^\circ$ . Figure 4 shows examples of the mass and energy spectrums for time periods near the main phase peak of each storm. For these time periods, the  $O^+$  number density within the instrument energy range (0.5-16 keV) exceeded the  $H^+$  number density by factors of 1.5 to 3.0. Since the measurements sampled only a part of the equatorial phase space, extrapolation to the total ring current composition was not possible. However, the large  $O^+$  fluxes up to 16 keV strongly indicated that the ionospheric ions were playing a significant role in the dynamics and energetics of the storm-time ring current and that relatively large fluxes of trapped ionospheric ions would be found in the equatorial latitudes over a wide range of altitudes.

## OBSERVATIONS AT HIGH (>8000km) ALTITUDES

In 1976, McIlwain (ref. 23) reported evidence for ions heavier than protons in the hot plasmas at the ATS-6 geostationary altitude. The instrumentation could not distinguish ion species, but an analysis of data on bouncing clusters of ions in the 0.01 to 1.0 keV energy range showed that the data were best fit if  $\text{He}^+$  or  $\text{O}^+$  ions were assumed. The analysis was applicable only for occasional transient magnetospheric events and thus could not be used to characterize the composition of the more typical hot plasmas (ref. 24).

Ion mass spectrometer measurements on the composition of the hot plasmas in the equatorial regions at high altitudes began with the GEOS-1 spacecraft in May 1977 (ref. 5). This spacecraft was in a highly eccentric orbit at  $27^\circ$  inclination with perigee near 2,000km and apogee near 38,000km. Balsiger et al. (ref. 7) have conducted a survey of the hot (0.9-16 keV) plasma composition during magnetically quiet and storm-time periods using GEOS-1 data from May 1977 to June 1978. An example of the ion mass spectrums obtained with the GEOS-1 spectrometer at the onset of a geomagnetic storm is shown in figure 5. For magnetically quiet periods ( $K_p \leq 4$ ) and for  $L = 6.8$  to  $8.2$ , the average for the ion abundances was about 90%  $\text{H}^+$ , 7%  $\text{O}^+$ , 2%  $\text{He}^+$ , and less than 1% for  $\text{He}^{++}$ . The mean energies for the  $\text{H}^+$  and  $\text{O}^+$  fluxes at quiet times were typically in the 4-8 keV range with  $\text{H}^+$  values typically higher than the  $\text{O}^+$  values.

For 24 days of data acquired near the peak of magnetic storms ( $D_{ST} = -26$  to  $-172\text{nT}$ ) and in the range  $L \approx 5$  to  $8$ , the  $\text{O}^+$  abundances ranged from 1% to 77% with the  $\text{He}^+$  ranging from 0.1% to 19%. It was concluded (ref. 7) that qualitatively about half of the storm-time hot plasmas originated in the ionosphere and half in the solar wind. Mean energies for the  $\text{H}^+$  and  $\text{O}^+$  storm-time fluxes were similar to those found for quiet times.

Radial profiles of the hot plasmas composition during geomagnetic storms were also obtained with GEOS-1 to L-shells as low as  $L = 2.5$  (ref. 5 and 7). Both  $\text{O}^+$  and  $\text{He}^+$  typically increased toward low altitudes and  $\text{O}^+$  often became comparable to or larger than  $\text{H}^+$  at the inner edge of the ring current.

Hot plasma composition measurements in a geostationary orbit began with the GEOS-2 spacecraft in August 1977 (ref. 6 and 7). The mass spectrometer was the same design as the one on GEOS-1 and covered the energy range 0 to 16 keV. A good example of the variability of the hot plasma (0.9-14 keV) composition at the geostationary orbit is shown in figure 6 from Balsiger et al. (ref. 7) for the 10-day period beginning on 24 September 1978. It is seen that prior to the magnetic activity level reading  $K_p = 5$  on 25 September,  $\text{H}^+$  was the dominant ion. During the more disturbed periods ( $K_p \geq 5$ ) of 25-29 September, the  $\text{O}^+$  ions were comparable in density to the  $\text{H}^+$  ions, and on 29 September,  $\text{O}^+$  became by far the dominant ion for about one day. For the period 0600 to 1000 U.T. on 29 September, the magnetopause was compressed inside the GEOS-2 orbit and an enhanced  $\text{He}^{++}$  density, typical of the magnetosheath, is observed. Following the decay of the ring current on 30 September,  $\text{O}^+$  and  $\text{H}^+$  densities are again typical of the magnetically quiet and moderately disturbed periods in which  $\text{H}^+$  ions are dominant.

Young (ref. 25) has conducted a synoptic study of the GEOS-2 composition data during the 11-month period/August 1978 to 20 June 1979. He finds systematic dependences of the ion energy and composition on both local time and magnetic activity. The correlation of the ion densities, when integrated over local time, with the magnetic activity is shown in figure 7 for two energy intervals. A particularly strong dependence of the  $O^+$  density on  $K_p$  is seen in both energy intervals. For the higher energy group the mean energy varied with  $K_p$  from 7.8 to 8.7 keV for  $H^+$ , from 6.1 to 7.1 keV for  $O^+$ , and from 6.1 to 7.6 keV for  $He^+$ .

By combining GEOS-1 and GEOS-2 ion data in the energy range 0.9-14 keV, Young, et al. (ref. 26) have found evidence for a solar activity cycle dependence in the average  $O^+/H^+$  density ratio. The ratio shows a systematic increase over a 3-year period and is well correlated with the increased solar activity as measured by the 10.7cm solar radio flux. Variations of the ion density ratios for selected ions are shown in figure 8 (ref. 26). The increase in the  $O^+/H^+$  ratio with time is quite large whereas the  $O^{++}/O^+$  and  $He^{++}/H^+$  ratios are essentially unchanged.

To emphasize the importance of including the ionospheric portion of the hot plasmas in magnetospheric models, this author has used the data by Young (ref. 25) presented in figure 7, along with different assumptions on the origin of the  $H^+$  ions, to estimate the relative contributions of the solar wind and the ionosphere (terrestrial component) to the observed hot plasmas<sup>†</sup>.  $H^+$  ions are present in high abundance in both the solar wind and the ionosphere. For three separate analyses, three different assumptions were made for the amount of the observed  $H^+$  ions which originated in the ionosphere. The  $He^+$  and  $O^{++}$  have been identified as ionospheric ions and the  $He^{++}$  as solar wind ions by Young (ref. 26) based on a detailed analysis of their temporal, spatial, and energy characteristics. The  $O^+$  ions are identified as ionospheric ions because of their relative high abundance ratio relative to the  $H^+$  ions (ref. 2). For the first case, it was assumed that none of the  $H^+$  ions came from the ionosphere, thus providing a lower limit to the ionospheric contribution. These results for the hot plasma components ( $E = 0.9-16$  keV) are plotted as the bottom curve in figure 9. It is seen that even as a lower limit the ionospheric components are always more than 37% of the solar wind components, and for  $K_p > 3$  the ionospheric components are more than half of the solar wind components. Since the mean energies of the  $O^+$  ions are lower than the  $H^+$  ions by only about 20%, it is evident that the energy density and total energy of the ionospheric components should not be neglected in considerations of the energetics and dynamics of the outer magnetosphere.

For the second case, the  $H^+$  component from the ionosphere is assumed to be 4 times the  $He^+$  component. This is thought to be a conservative assumption because Ghielmetti et al. (ref. 15) found in an 8-month survey of upstreaming ions observed by the S3-3 spacecraft that the  $He^+$  fluxes were typically less than 1% of the  $H^+$  fluxes.  $He^+$  reached 25% of the  $H^+$  fluxes

---

<sup>†</sup>The author is indebted to and thanks Dr. D. T. Young for making his reduced GEOS-2 data available for this analysis while the author was at the University of Bern.



only in very few cases (A. Ghielmetti, private communication). In this case, the middle curve of figure 9 is obtained.

For the third case, the  $H^+$  component from the ionosphere is assumed to be equal to the measured  $O^+$  component for  $K_p < 2$  (i.e., magnetically quiet periods). This is also thought to be a conservative assumption because Collin et al. (ref. 27) find in a survey of upstreaming ions observed during quiet and moderately disturbed periods with the S3-3 spacecraft that  $H^+$  fluxes typically exceed the  $O^+$  fluxes by factors of 2 to 10. For this case the upper curve in figure 9 is obtained. If either of the assumptions in the last two cases is valid, it is seen that for  $K_p \gtrsim 3$  the ionospheric components are comparable to or exceed the solar wind components. The principal point here is that with as little as 15 to 20% of the observed  $H^+$  coming from the ionosphere, the importance of the ionospheric ions in the hot plasmas is particularly emphasized during magnetically disturbed periods and cannot be reasonably ignored in modelling the energetics and dynamics of the hot plasmas under these conditions.

With the launch of the SCATHA satellite in 1979, the hot plasma composition measurements were extended to 32 keV (all previous measurements were below 17 keV) and pitch angle measurements extending to or near the magnetic field directions were routinely obtained. The SCATHA satellite was in a nearly geosynchronous orbit with an inclination of 8 degrees, perigee near 27,000km, and apogee near 43,000km. Johnson et al. (ref. 28) have investigated the hot plasma composition from the first five major ( $D_{ST} > 90$ nT) magnetic storms observed with SCATHA. Near the peak of each storm the  $O^+$  number and energy densities in the 0.1 to 32 keV range are comparable to or larger than the  $H^+$  densities, and even at 32 keV the  $O^+$  number densities (and thus energy densities) are typically comparable to or exceed those of  $H^+$ . Figure 10 shows results from the 3-4 April 1979 storm, which was the largest storm investigated. The general features mentioned above are evident. It is seen that the average energies of the  $H^+$  are generally higher than for  $O^+$  ions and this is also typical of the other storms investigated.

Although a systematic study of the ion composition as a function of pitch angle has not yet been reported for the SCATHA data, specialized studies have shown that  $O^+$  and  $H^+$  fluxes peaked at or near the magnetic field directions are a common feature of the data (ref. 21 and 29).

Hot plasma composition measurements which extend to altitudes much greater than the geostationary satellite altitude are now available for energies up to 17 keV from the ISEE-1 and Prognoz-7 satellites. ISEE-1, with apogee near  $23R_e$  and perigee near  $1.1R_e$ , has provided data near the equatorial plane out to and beyond the boundaries of the magnetosphere on the sunward side and deep into the magnetotail (ref. 30 and 31). The Prognoz-7 satellite with apogee near  $32R_e$  and perigee near  $1.1R_e$  is in a  $65^\circ$  inclination orbit and thus is providing data out to and beyond the boundaries of the magnetosphere at high latitudes (ref. 23). A presentation of detailed results at these higher altitudes is beyond the scope of this review. However, it is noted that ionospheric ( $O^+$ ) ions are commonly observed in the hot plasmas beyond  $8R_e$  at the level of a few to several percent of the  $H^+$  ions during geomagnetically quiet and moderately disturbed periods. During geomagnetic storms,

comparable  $O^+$  and  $H^+$  densities have been observed out to the magnetospheric boundary on the sunward side and to  $15R_E$  in the magnetotail. Ionospheric ions in the keV range are also observed in the high latitude magnetospheric boundary layer (plasma mantle) with the Prognoz-7 satellite (ref. 32).

A preliminary report on coordinated hot plasma composition measurements obtained in 1979 from seven satellites has been presented by Balsiger (ref. 17). These measurements provide simultaneous information on the large scale distributions of the plasmas and assist in separating temporal and spatial variations in the characteristics of the plasmas. Mass spectrometer data were obtained from S3-3, GEOS-1, -2, ISEE-1, -3, Prognoz-7, and SCATHA. Their orbits within the magnetosphere when projected onto the geomagnetic equatorial plane are shown in figure 11 for the 21-22 February 1979 magnetic storms. Universal times are indicated along the orbits beginning on 21 February and the magnetopause locations are shown schematically for low and high solar wind pressures. ISEE-3 was at the sun-earth libration point and provided information on the solar wind composition. Along with geomagnetic indices, the composition data for GEOS-2 and ISEE-1 in the 0.9 to 16 keV range are shown in figure 12 (ref. 17).  $O^+$  ions become dominant during these storms at the GEOS-2 and SCATHA orbits and are more temporally/spatially structured than the  $H^+$  ions. The high  $O^+$  energy densities observed on SCATHA in the 0.1-32 keV range and at 32 keV are seen near the peaks of the storms in figure 13. Enhanced  $O^+/H^+$  ratios are also seen in the ISEE-1 data near the peaks of the storms even when ISEE-1 is relatively deep in the magnetotail. The round, triangular, and square symbols in figure 11 indicate the locations of the satellites at or near the peaks of the storms as indicated by the dotted lines in figure 13. The  $O^+$  densities (not yet published) were also dominant at and near the S3-3 and Prognoz-7 locations indicated by the round circles.  $O^{++}$  ions were also observed as a part of the hot plasma at GEOS-2 during this storm (ref. 17). Preliminary conclusions from the coordinated data are that during geomagnetic storms the ionospheric ion injections occur nearly simultaneously over a wide range of local times and that the ionospheric components of the hot plasmas are distributed over a very large volume of the magnetosphere as opposed to being found just in limited local time and/or spatial regions. Coordinated measurements of this nature hold considerable promise for improving our understanding of the injection, energization, transport and loss of the hot plasmas in the magnetosphere.

#### CONCLUDING REMARKS

Major progress has been made during the past 4 years in understanding the composition and the origins of the hot magnetospheric plasmas near the geostationary satellite altitude. It is now established that during geomagnetically disturbed periods  $O^+$  ions of ionospheric origin are a major and sometimes dominant contributor to the hot plasma number density and energy density in this region of the magnetosphere. With the greatly expanded data bases now available and with new data acquisitions now planned, the phenomenological characterization of the hot plasma populations near the geostationary satellite orbit can be expected to improve substantially in the

next few years. However, our ability to model, and thus to predict, the plasma environment near the geostationary satellite orbit is still in its infancy due to our lack of understanding of the details of the physical processes involved in the entry, energization, transport, and loss of the plasma ions.

#### REFERENCES

1. Johnson, R. G.; Sharp, R. D.; and Shelley, E. G.: Proceedings of the Spacecraft Charging Technology Conference. Edited by C. P. Pike and R. R. Lovell. AFGL-TR-77-0051 and NASA Tmx-73537, 53, 1977.
2. Shelley, E. G.; Johnson, R. G.; and Sharp, R. D.: Satellite Observations of Energetic Heavy Ions During a Geomagnetic Storm. J. Geophys. Res., 77, 6104, 1972.
3. McCormac, B. M.: Summary, Radiation Trapped in the Earth's Magnetic Field. Edited by B. M. McCormac. P. 877, D. Reidel Publ. Co., Dordrecht, Netherlands, 1966.
4. Frank, L. A.: Plasma Entry Into the Earth's Magnetosphere. Proceedings of the Symposium on Critical Problems of Magnetospheric Physics, p. 53. Edited by E. R. Dyer. Published by IUCSTP Secretariat, National Academy of Sciences, Washington, D.C., 1972.
5. Geiss, J. H.; Eberhardt, P. Walker, H. P.; Weber, L. and Young, D. T.: Dynamics of Magnetospheric Ion Composition as Observed by the GEOS Mass Spectrometer. Space Sci. Rv., 22, 537, 1978.
6. Young, D. T.: Ion Composition Measurements in Magnetospheric Modeling. Quantitative Modeling of Magnetospheric Processes. Edited by W. P. Olson. P. 340, American Geophysical Union, Washington, D.C., 1979.
7. Balsiger, H.; Eberhardt, P.; Geiss, J.; and Young, D. T.: Magnetic Storm Injection of 0.9-16 keV/e Solar and Terrestrial Ions Into the High Altitude Magnetosphere. J. Geophys. Res., 85, 1645, 1980.
8. Shelley, E. G.: Heavy Ions in the Magnetosphere. Space Sci. Rev., 23, 465, 1979.
9. Johnson, R. G.: Energetic Ion Composition in the Earth's Magnetosphere. Rev. Geophys. and Space Phys., 17, 696, 1979.
10. Spjeldvik, W. N.: Expected Charge States of Energetic Ions in the Magnetosphere. Space Science Rev., 23, 499, 1979.
11. Cornwall, J. M.; and Schulz, M.: Physics of Heavy Ions in the Magnetosphere. Solar System Plasma Physics, Vol. 3. Edited by C. Kennel, L. Lanzerotti, and E. Parker. North-Holland Pub., Netherlands. p. 165, 1979.

12. Sharp, R. D.; Johnson, R. G.; and Shelley, E. G.: The Morphology of Energetic  $O^+$  Ions During Two Magnetic Storms: Temporal Variations. J. Geophys. Res., 81, 3283, 1976a.
13. Shelley, E. G.; Sharp, R. D.; and Johnson, R. G.: Satellite Observations of an Ionospheric Acceleration Mechanism. Geophys. Res. Lett., 3, 654, 1976.
14. Sharp, R. D.; Johnson, R. G.; and Shelley, E. G.: Observations of an Ionospheric Acceleration Mechanism Producing Energetic (keV) Ions Primarily Normal to the Geomagnetic Field Direction. J. Geophys. Res., 82, 3324, 1977.
15. Ghielmetti, A. G.; Johnson, R. G.; Sharp, R. D.; and Shelley, E. G.: The Latitudinal, Diurnal, and Altitudinal Distributions of Upward Flowing Energetic Ions of Ionospheric Origin. Geophys. Res. Lett., 5, 59, 1978.
16. Gorney, D. J.; Clarke, A.; Croley, D.; Fennel, J.; Luhmann, J.; and Mizera, P.: The Distribution of Ion Beams and Conics Below 8000km. J. Geophys. Res., 86, 83, 1981.
17. Balsiger, H.: Composition of Hot (0.1 to 16 keV/e) as Observed by the GEOS and ISEE Mass Spectrometers and Inferences for the Origin and Circulation of Magnetospheric Plasmas. Adv. Space Res., 1, 289, 1981.
18. Mizera, P. F.; and Fennell, J. F.: Signatures of Electric Fields From High and Low Altitude Particle Distributions. Geophys. Res. Lett., 4, 311, 1977.
19. Lennartsson, W.; Shelley, E. G.; Sharp, R. D.; Johnson, R. G.; and Balsiger, H.: Some Initial ISEE-1 Results on the Ring Current Composition and Dynamics During the Magnetic Storm of December 11, 1977. Geophys. Res. Lett., 6, 483-486, 1979.
20. Mauk, B. H.; and McIlwain, C. E.: (1975) ATS-6 UCSD Auroral Particles Experiment. IEEE Trans. on Aerospace and Electronic Systems, Vol. AES-11, 1125.
21. Kaye, S. M.; Johnson, R. G.; Sharp, R. D.; and Shelley, E. G.: Observations of Transient  $H^+$  and  $O^+$  Bursts in the Equatorial Magnetosphere. J. Geophys. Res., 86, 1335, 1981.
22. Johnson, R. G.; Sharp, R. D.; and Shelley, E. G.: Observations of Ions of Ionospheric Origin in the Storm Time Ring Current. Geophys. Res. Lett., 4, 403, 1977.
23. McIlwain, C. E.: Bouncing Clusters of Ions at Seven Earth Radii. Abstract, EOS, Trans. Am. Geophys. Un., 57, 307, 1976.
24. Quinn, J. M.; and McIlwain, C. E.: Bouncing Ion Clusters in the Earth's Magnetosphere. J. Geophys. Res., 84, 7365, 1979.

25. Young, D. T.: Synoptic Studies of Magnetospheric Composition. Habilitationsschrift, University of Bern, February 1980.
26. Young, D. T.; Balsiger, H.; and Geiss, J.: Observed Increase in the Abundance of Kilovolt  $O^+$  in the Magnetosphere Due to Solar Cycle Effects. Adv. Space Res., 1, in press, 1981.
27. Collin, H. L.; Sharp, R. D.; Shelley, E. G.; and Johnson, R. G.: Some General Characteristics of Upflowing Ion Beams Over the Auroral Zone and Their Relationship to Auroral Electrons. J. Geophys. Res., in press, 1981.
28. Johnson, R. G.; and Kaye, S. M.: Magnetospheric Plasma Composition Observations Up to 32 keV During Geomagnetic Storms. EOS 61, 1080, 1980.
29. Kaye, S. M.; Shelley, E. G.; Sharp, R. D.; and Johnson, R. G.: Ion Composition of Zipper Events. J. Geophys. Res., 86, in press, 1981.
30. Lennartsson, W.; Sharp, R. D.; Shelley, E. G.; Johnson, R. G.; and Balsiger, H.: Ion Composition and Energy Distributions During 10 Magnetic Storms. J. Geophys. Res., in press, 1981.
31. Peterson, W. K.; Sharp, R. D.; Shelley, E. G.; Johnson, R. G.; and Balsiger, H.: Energetic Ion Composition of the Plasma Sheet. J. Geophys. Res., 86, 761, 1981.
32. Lundin, R.; Sandahl, I.; Hultqvist, B.; Galeev, A.; Likhin, O.; Omelchenko, A.; Pissarenko, N.; Vaisberg, O.; and Zacharov, A.: First Observations of the Hot Ion Composition in the High Latitude Magnetospheric Boundary Layer by Means of Prognoz-7. Proceedings of Magnetospheric Boundary Layer Conference, European Space Agency Report SP-148, p. 91, August 1979.

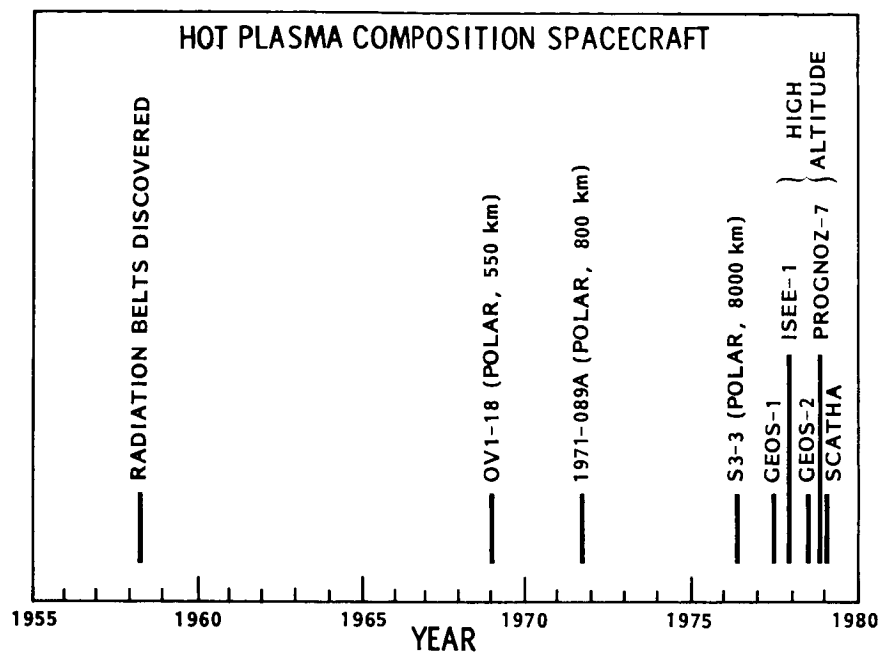


Figure 1. Launch dates and orbit information for spacecraft with hot plasma mass spectrometers.

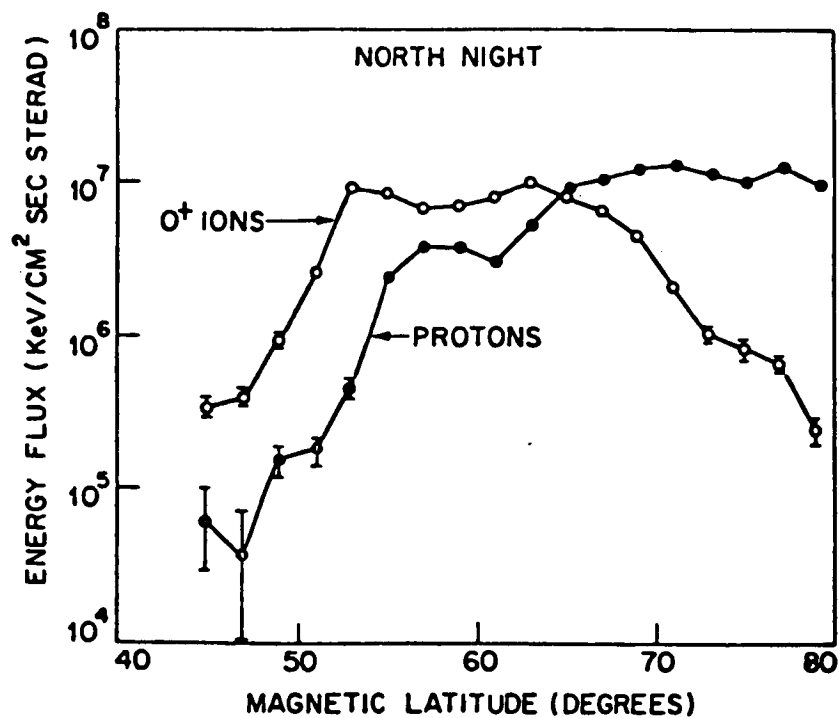


Figure 2. Latitudinal variation of the precipitating energy flux of  $O^+$  and  $H^+$  ion during magnetic storms on 17-18 December 1971 (ref. 9).

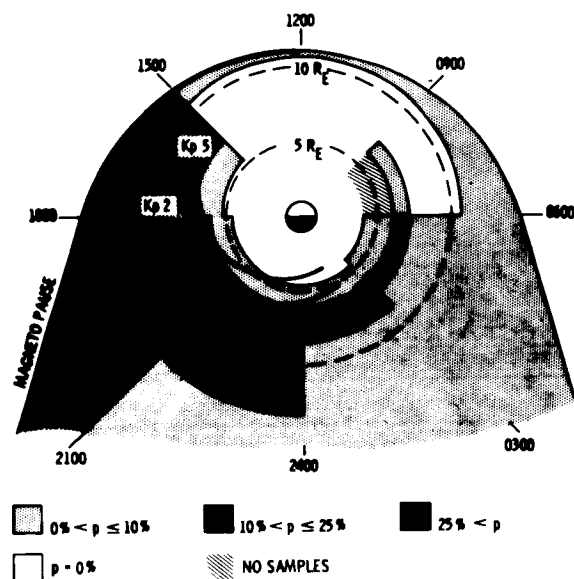


Figure 3. Equatorial projection of occurrence frequencies of upward streaming ions observed below 8000 km with the S3-3 spacecraft (ref. 15 and 19).

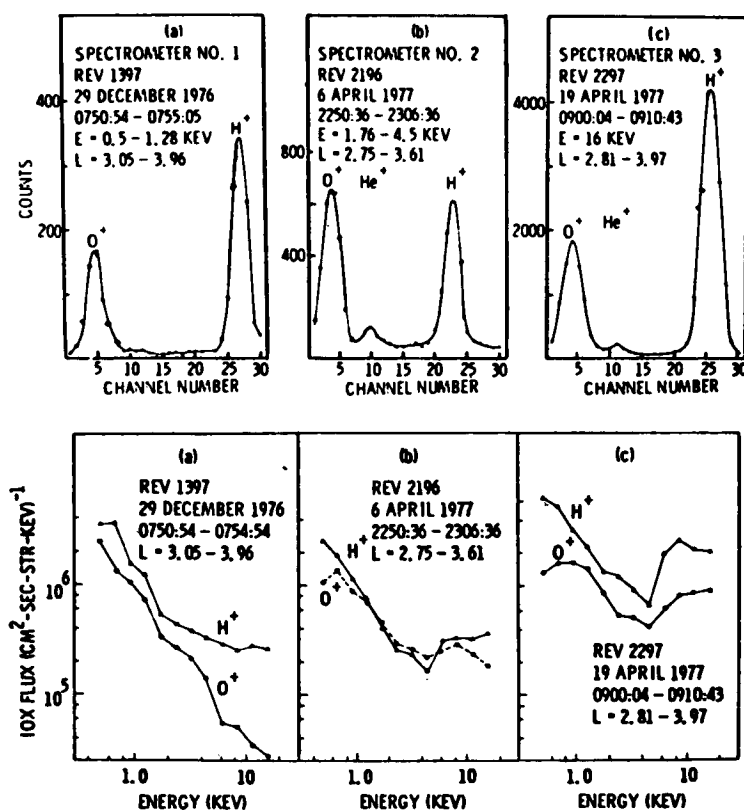


Figure 4. Mass and energy spectra obtained with the S3-3 spacecraft in the inner ring current during three magnetic storms (ref. 22).

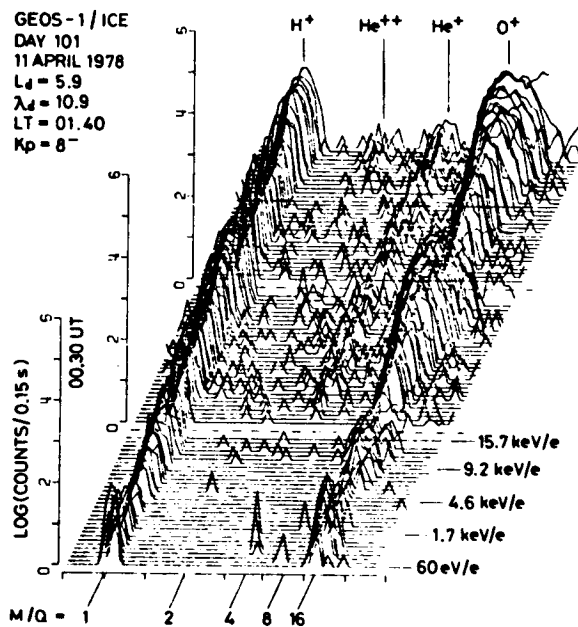


Figure 5. Mass spectrums from GEOS-1, sequentially repeated three times in the energy range noted, demonstrating in an 18-minute sequence the increase in heavy ion fluxes at the onset of a magnetic storm (ref. 7).



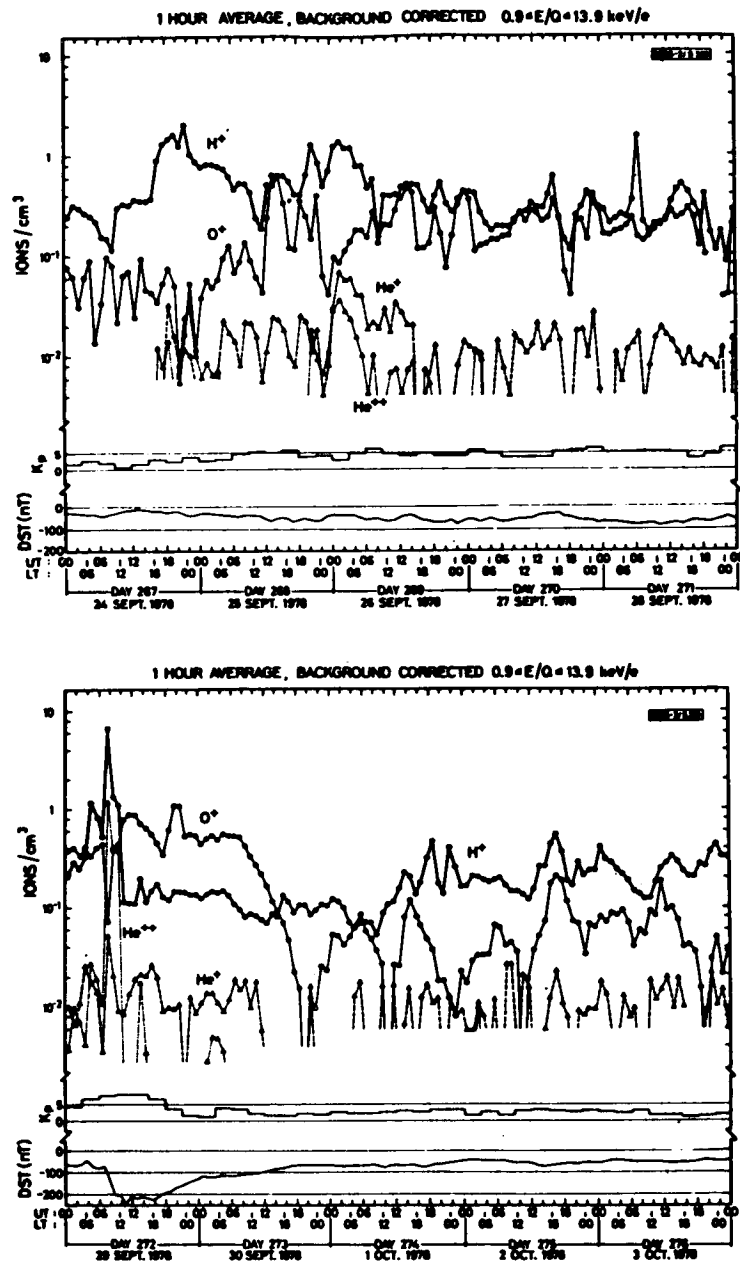


Figure 6. One hour averages of GEOS-2 hot plasma data for a 10-day period demonstrating composition variations for a wide range of geomagnetic activity (ref. 7).

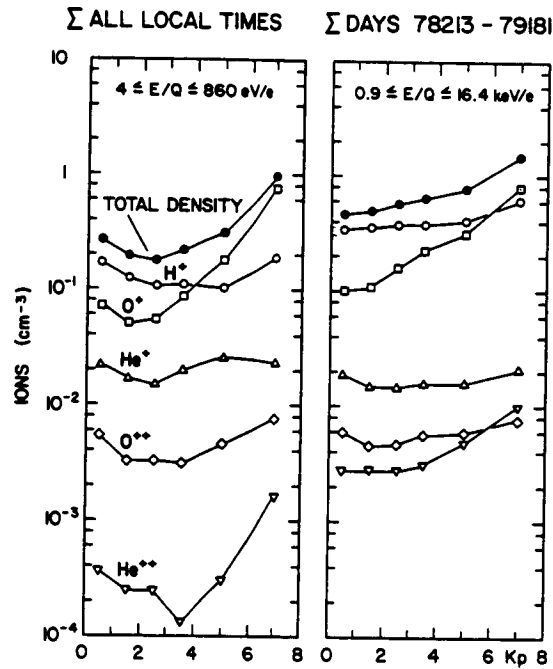


Figure 7. Ion density averaged over all local times using 11 months of GEOS-2 synoptic data (ref. 25).

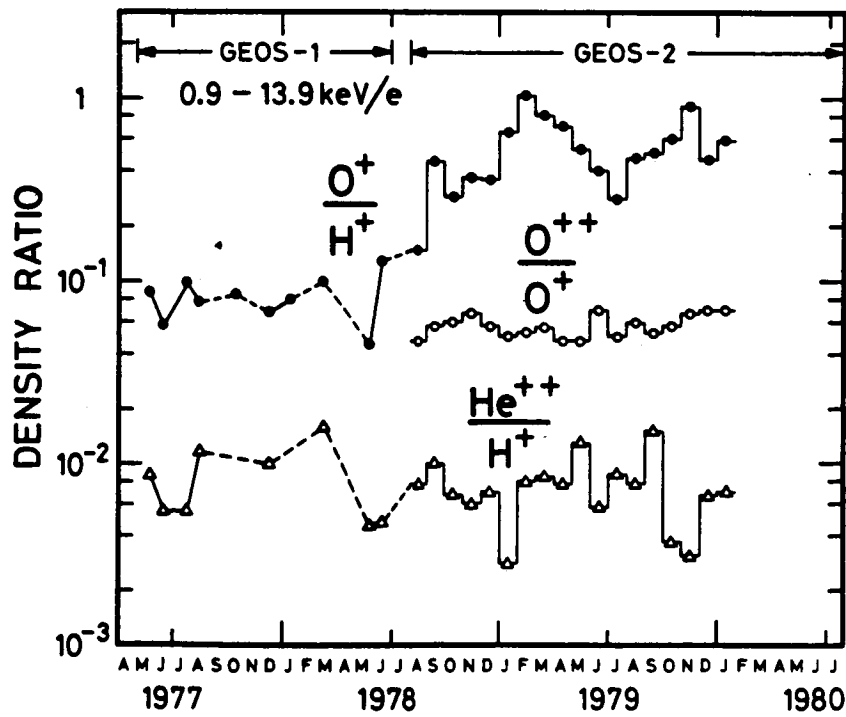


Figure 8. Long term trends in average ion ratios over nearly 3 years of GEOS-1 and GEOS-2 operation (ref. 26).

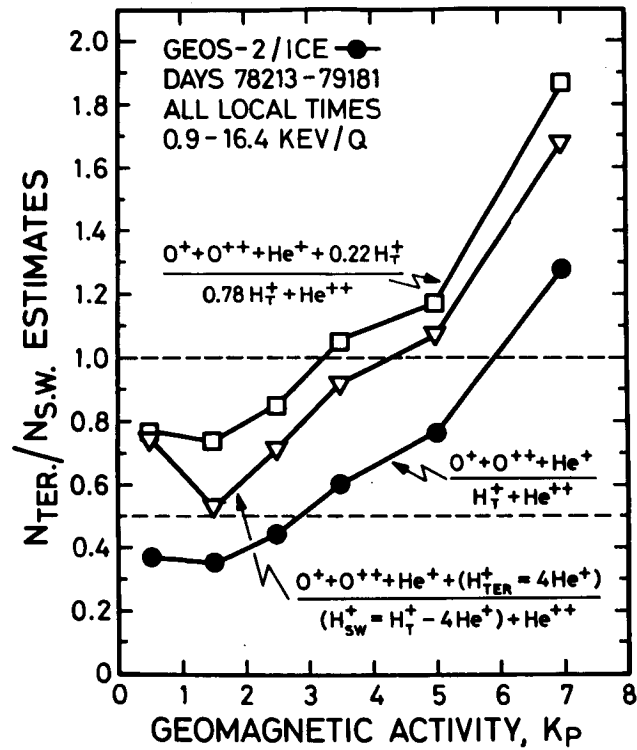


Figure 9. Estimates of the ratio of hot plasma ions of terrestrial origin to those of solar wind origin at the geostationary orbit.  $H_T^+$  is the observed  $H^+$  ions. The bottom curve is directly from the GEOS-2 data presented in Fig. 7 (ref. 25).

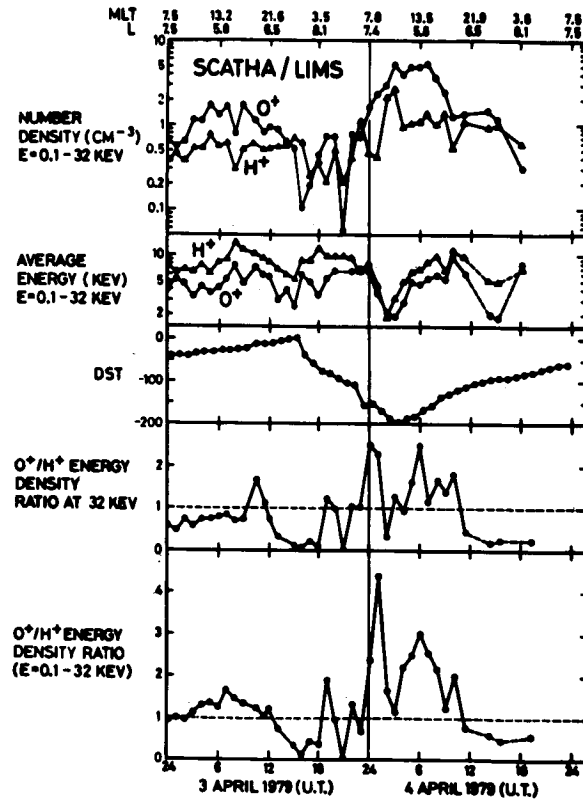


Figure 10. Characteristics of the hot plasma composition during the 3-4 April 1979 magnetic storm.

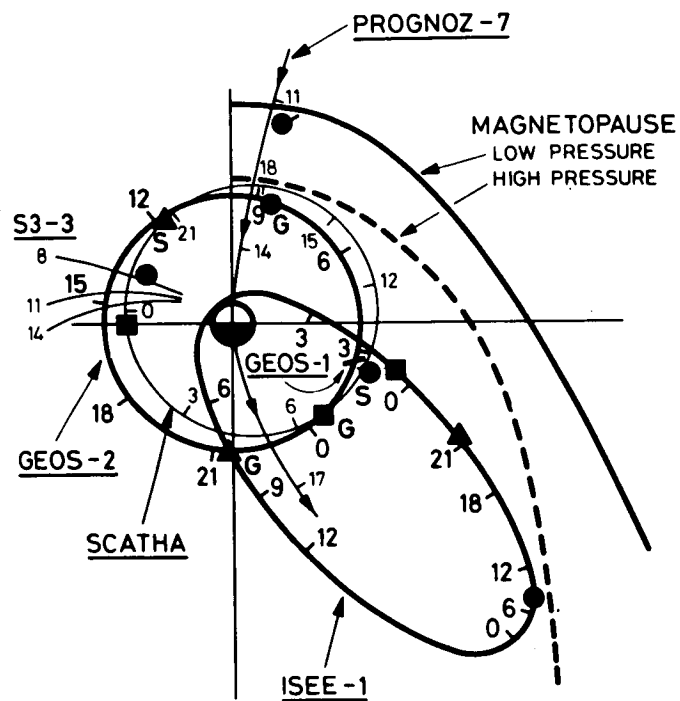


Figure 11. Equatorial projections of satellite orbits during coordinated ion composition measurements of magnetic storms on 21-22 February 1979.

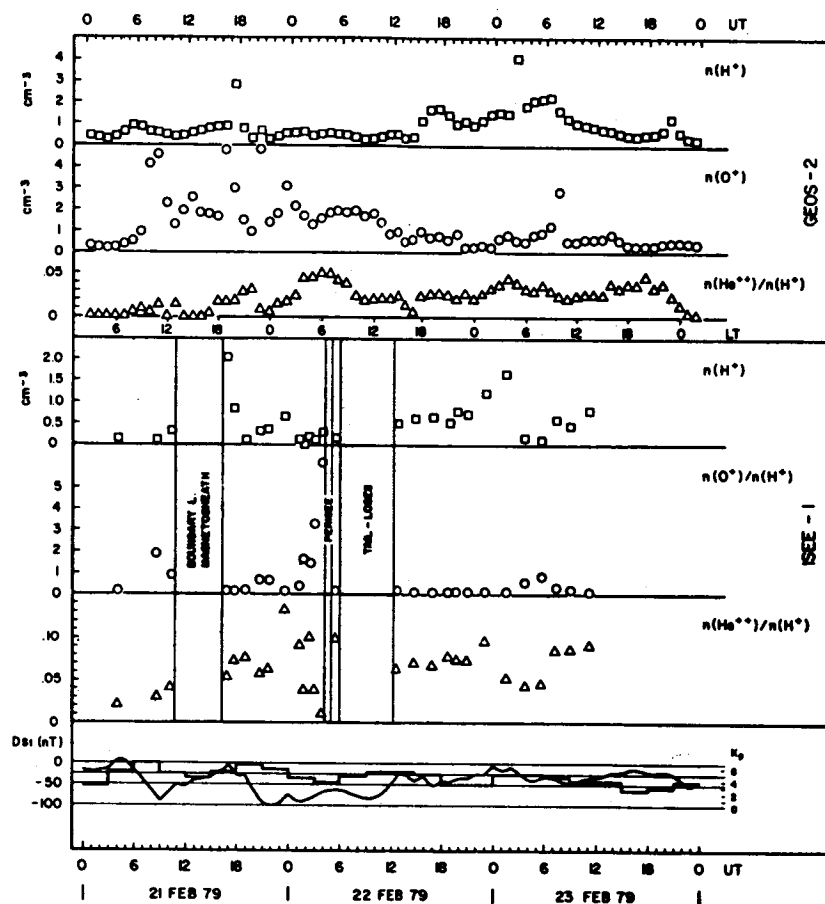


Figure 12. ISEE-1 and GEOS-2 hot plasma composition data during the magnetic storms on 21-22 February 1979 (ref. 17).

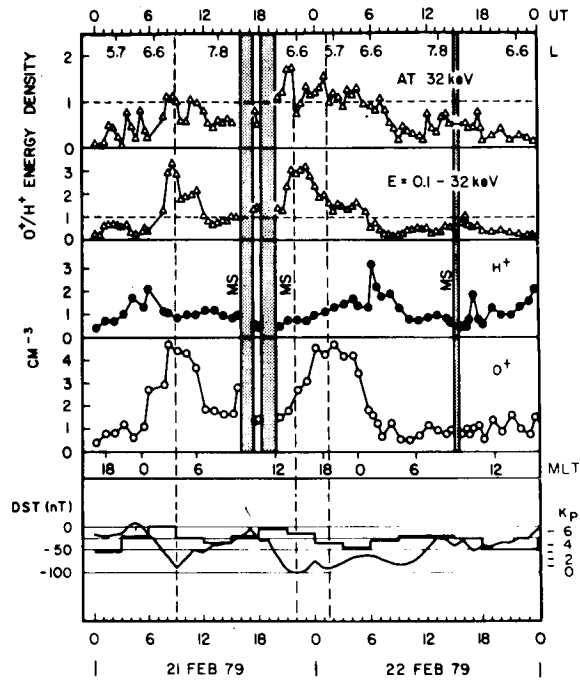


Figure 13. SCATHA hot plasma composition data during the magnetic storms on 21-22 February 1979.

## SCATHA OBSERVATIONS OF SPACE PLASMA COMPOSITION DURING A SPACECRAFT CHARGING EVENT<sup>†</sup>

R. G. Johnson, R. Strangeway, S. Kaye, R. Sharp, and E. Shelley  
Lockheed Palo Alto Research Laboratory

### SUMMARY

During the earth eclipse of the SCATHA spacecraft on 28 March 1979, the spacecraft charged to potentials greater than 1KV for about 30 minutes with extended excursions greater than 4KV. The composition of the hot plasma was obtained in the 0.1 to 32 keV energy range with an ion mass spectrometer aboard the spacecraft. Prior to the onset of the charging event,  $H^+$  was the principal plasma ion, and during the event  $O^+$  was the principal ion. The composition was energy dependent and varied significantly on a time scale of 4 minutes. An assumption that the ion flux was all  $H^+$  would lead to computed number densities that were in error by more than a factor of 2 for several time intervals during the event.

### INTRODUCTION

The number density of the hot plasmas that produces spacecraft charging is frequently determined from on-board measurements of the ion fluxes with energies above the spacecraft potential. To determine ion densities from flux measurements, mass composition of the plasmas must be known or assumed. Also, the secondary electron production by keV ions incident on spacecraft surfaces is often strongly dependent on the ion mass. Prior to 1977 when hot plasma composition measurements at high altitudes in the equatorial regions began, it was generally assumed that  $H^+$  was the dominant hot plasma ion (ref. 1). Measurements extending up to 32 keV have now established that  $O^+$  ions are frequently significant contributors to the plasma density and during times of high geomagnetic activity are often the dominant hot plasma ions (ref. 1, 2, 3).

The SCATHA spacecraft has provided the first opportunity near the geostationary spacecraft altitude to obtain the hot plasma composition during spacecraft charging events that produce potentials above a few hundred volts. (The GEOS spacecraft, which also obtained hot plasma composition measurements (ref. 2), did not charge to high potentials.) This report provides composition information during the charging event on 28 March 1979 with a time resolution of 4 minutes.

---

<sup>†</sup>This research has been sponsored by the Office of Naval Research and the U.S. Air Force under contract N00014-76-C-0444, and by the Lockheed Independent Research Program.



## OBSERVATIONS AND RESULTS

The SCATHA spacecraft is in a nearly geosynchronous orbit with an inclination of 8 degree, perigee near 27,000 km, and apogee near 43,000 km. The spacecraft is spinning at a rate of about one revolution per minute with its spin axis in the orbital plane.

Hot plasma composition measurements are being obtained in the energy range 0.1 to 32 keV with an ion mass spectrometer aboard the SCATHA spacecraft. The ion energy distributions are measured at 24 energies nearly equally spaced on a logarithmic scale of the energy. The instrument view direction is at  $11^\circ$  to the normal to the spacecraft spin axis and thus is providing data on the pitch angle distributions of the ions. A detailed description of the instrument and its operational modes are contained in an earlier report (ref. 4), and a more general discussion of the SCATHA composition results are presented in a separate paper in this conference (ref. 1).

The charging event on 28 March 1979 began while the SCATHA spacecraft was in an earth eclipse and was coincident with a large enhancement of the energetic electron and ion fluxes (ref. 5). The spacecraft potential during most of the event as determined by Fennel, et al<sup>†</sup> (ref. 5) is shown in figure 1. It is seen that the potential is highly structured on a time scale shorter than 4 minutes, which is the temporal resolution thus far used for the ion composition determinations in this event. Measurements are made at a higher sample rate but counting statistics have limited the present analysis to 4-minute intervals.

Prior to and during the charging event,  $H^+$  and  $O^+$  were the principal ions in the hot plasma.  $He^+$  and  $He^{++}$  ions were near or below the instrument background levels during the event and are not included in this analysis. The  $O^+/H^+$  number density ratio averaged over pitch angle during a 15-minute interval prior to the event is shown as a function of ion energy in figure 2. It is seen that  $H^+$  is the dominant ion above 1 keV with  $O^+$  dominant below 1 keV. When integrated over the instrument energy range (0.1-32 keV), the  $O^+/H^+$  density ratio is 0.86 for this time period. After the onset of the charging event,  $O^+$  became the dominant ion except for the first 4-minute interval. The  $O^+/H^+$  density ratios integrated over the instrument energy range and over pitch angle are shown in the top curve in figure 1 and are tabulated for an extended time period in Table I. From these data, it is seen that an assumption that the ion flux contained only  $H^+$  ions would lead to number densities in error by more than a factor of 2 for several of the time intervals.

As seen in figure 1, there are no obvious correlations between the plasma composition and the spacecraft potential. However, it should be emphasized that the 4-minute averaging of the composition data precludes information on the characteristics of the faster temporal structures in the

<sup>†</sup>The authors thank J. F. Fennel, D. R. Croley, P. F. Mizera, and J. D. Richardson for making their data available for our use prior to its publication.

potential as seen in figure 1. In particular, the present analysis does not address the evidence presented by Fennel, et al (ref. 5) that field aligned ions may have some control over the periodic potential variations observed in material samples. The analysis of the plasma composition as a function of pitch angle during charging events is being investigated and will be reported at a later date. However, it is known that for some magnetospheric conditions the composition is strongly dependent on pitch angle (ref. 6 and 7).

The plasma composition is typically energy dependent and it varied significantly during the charging event, even during periods when the change in spacecraft potential was relatively small. This is seen by the data shown in figures 3 and 4 which were adjacent data intervals obtained when the spacecraft was at potentials near 4 KV. The data intervals are labeled A and B in figure 1. An example of the energy dependence when the spacecraft was at lower potential is shown in figure 5 for the time interval labeled C in figure 1. The curves through the data in figures 2 to 4 are least-squared polynomial fits to the points and are included only to indicate the trends in the data.

#### REFERENCES

1. Johnson, R. G.: A Review of the Hot Plasma Composition near Geosynchronous Altitude. Proceedings of the Spacecraft Charging Technology Conference III, this volume.
2. Balsiger, H.; Eberhardt, P.; Geiss, J.; and Young, D. T.: Magnetic Storm Injection of 0.96-16 keV/e Solar and Terrestrial Ions into the High Altitude Magnetosphere. J. Geophys. Res. 85, 1645, 1980.
3. Young, D. T.: Synoptic Studies of Magnetospheric Composition. Habilitationsschrift, University of Bern, February 1980.
4. Stevens, J. R.; and Vampola, A. L.: Description of the Space Test Program P78-2 Spacecraft and Payloads. SAMSO TR-78-24, 1978.
5. Fennel, J. F.; Croley, D. R., Jr.; Mizera, P. F.; and Richardson, J. D.: Electron Angular Distributions during Charging Events. Proceedings of the Spacecraft Charging Technology Conference III, this volume.
6. Kaye, S. M.; Johnson, R. G.; Sharp, R. D.; and Shelley, E. G.: Observations of Transient  $H^+$  and  $O^+$  Bursts in the Equatorial Magnetosphere. J. Geophys. Res. 86, 1335, 1981.
7. Kaye, S. M.; Shelley, E. G.; Sharp, R. D.; and Johnson, R. G.: Ion Composition of Zipper Events. J. Geophys. Res. 86, in press, 1981.

TABLE I

$O^+/H^+$  NUMBER DENSITY RATIOS DURING THE  
SCATHA SPACECRAFT CHARGING EVENT ON 28 MARCH 1979

UT Seconds	Density Ratio $O^+/H^+$	UT Seconds	Density Ratio $O^+/H^+$
59880	0.52	61560	1.55
60120	2.36	61800	1.92
60360	1.17	62040	1.91
60600	1.99	62280	4.67
60840	1.58	62520	4.53
61080	1.33	62760	2.44
61320	2.40	63000	2.41

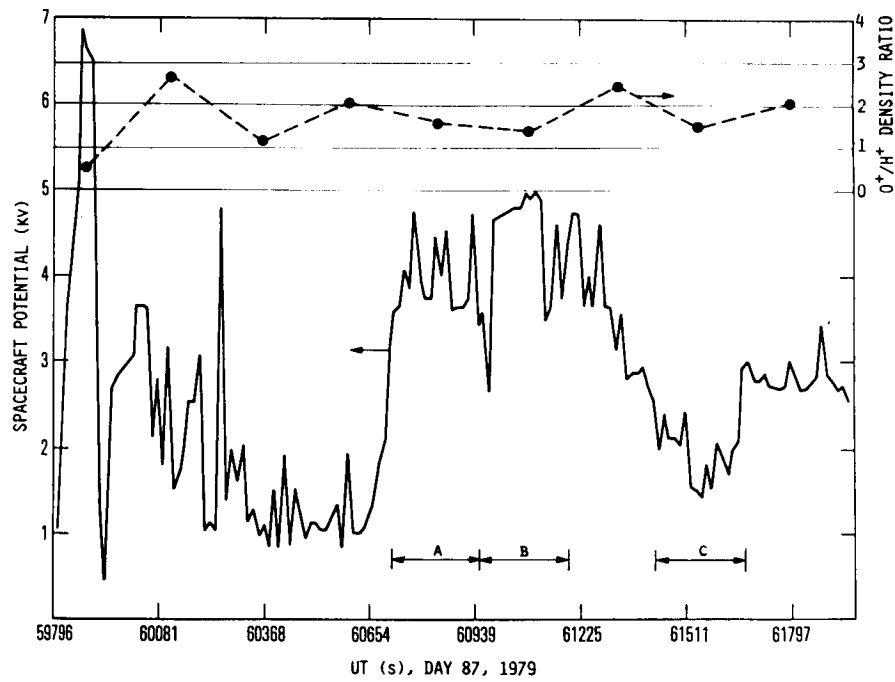


Figure 1. The SCATHA spacecraft potential (ref. 5) and the  $O^+/H^+$  number density ratios of the incident hot plasma ions

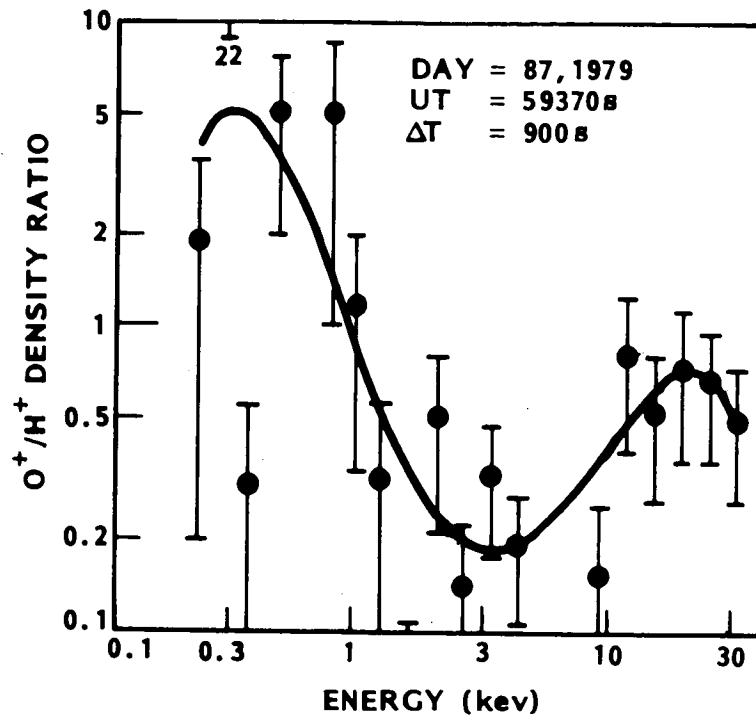


Figure 2.  $O^+/H^+$  number density ratios prior to the SCATHA spacecraft charging event on 28 March 1979.

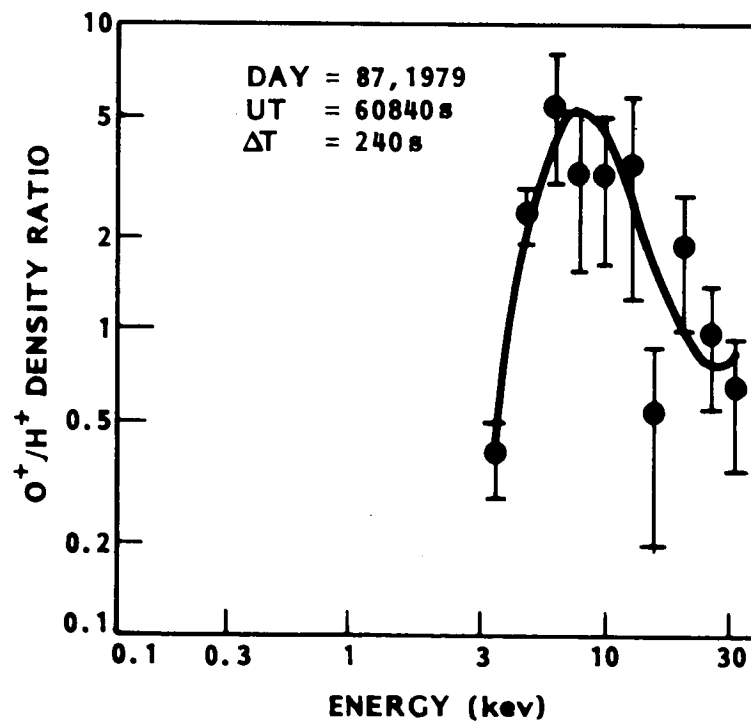


Figure 3.  $O^+/H^+$  number density ratios during the time interval labeled A in figure 1.

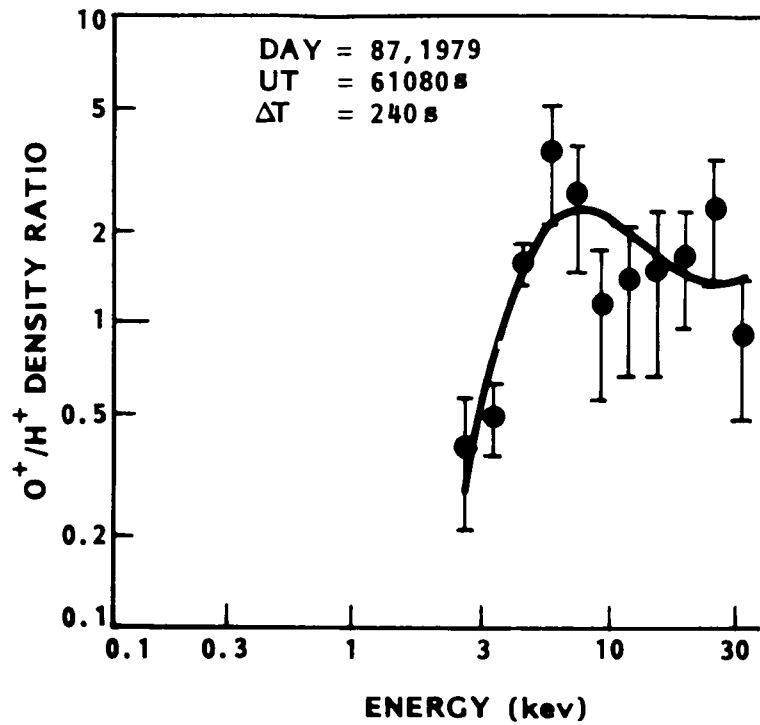


Figure 4.  $O^+/H^+$  number density ratios during the time interval labeled B in figure 1.

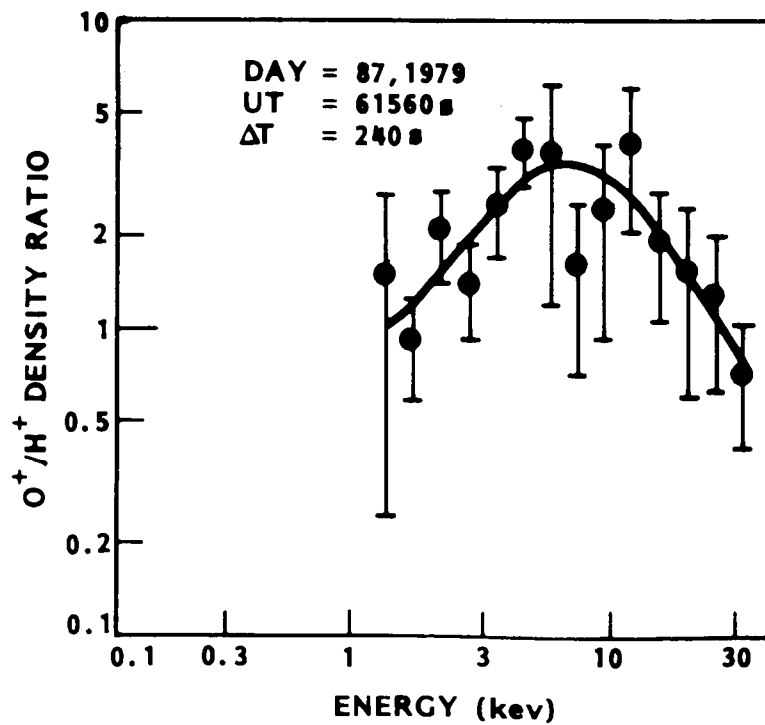


Figure 5.  $O^+/H^+$  number density ratios during the time interval labeled C in figure 1.

## **P78-2 ENGINEERING OVERVIEW\***

**A. L. Vampola  
The Aerospace Corporation**

### **ABSTRACT**

Data from the P78-2 spacecraft are being used in verifying and validating analytical tools being developed for the design of spacecraft, such as NASCAP, for updating Military Standard 1541, for investigation of materials contamination, and for a study of the physics of charging. The analysis of this data has already resulted in changes in laboratory testing procedures, in a better understanding of some properties of materials exposed to the space environment, and in some insight into the EMI caused by discharges on spacecraft in a plasma environment. Some examples of early results from the engineering experiments are presented.

### **INTRODUCTION**

In the original Spacecraft Charging at High Altitude program, the major thrust was directed at laboratory studies and the generation of analytical tools (models) which could describe the charging process, discharges, and EMI coupling into the vehicle and its subsystems. The P78-2 experiment payload, and the data derived therefrom, was relegated to a secondary role; justifiably so, since delays associated with the design and construction of a space payload, the risk involved in a launch, and the possibility of loss of funding at any point could not be allowed to jeopardize the entire program. However, with the successful launch of the P78-2 vehicle and the extremely successful operation of the experiments in orbit, coupled with major progress in the ground-based portions of the program, the data obtained by the P78-2 payload has assumed a much more significant role in the SCATHA program.

Validation and verification of models constructed in earlier phases of the program, such as NASCAP, determination of materials behavior in orbit, characterization of EMI, and measurement of plasma parameters have gained equal importance with or overshadowed the original purpose of the P78-2 engineering experiments: to establish spacecraft charging as a viable mechanism for the production of orbital operation anomalies, to characterize charging, to quantify several parameters associated with it, and to study the properties of the space environment producing it. Figure 1 graphically depicts the interrela-

---

\*This work was supported by the Air Force under Contract No. F04701-80-C-0080.

tionships between the P78-2 data set and the other elements of the SCATHA program. Because the SCATHA program was relatively mature by the time P78-2 orbital data production began, the data are having a major impact only in the validation of ground test procedures, in model verification, in the update of Military Standard 1541, and in anomaly investigations.

Much of the credit for the versatility of the data from P78-2 must go to the balanced complement of instruments incorporated in the mission. The vehicle combined two missions into one payload: SCATHA and PIE. The second, the Plasma Interaction Experiment, provides a considerably more comprehensive description of the plasma environment than would have been available from only the SCATHA mission instruments. In return, the engineering instruments, including the Electron and Ion Beam systems, have provided accessory information of value in interpreting the data from the PIE experiments and have even enabled special experiments to be performed.

In this presentation, we will briefly discuss the engineering experiments and the uses to which their data are being put and then go into some details of the analyses, results, and accessory laboratory data being obtained to assist in the interpretation of the on-orbit data.

#### THE ENGINEERING EXPERIMENTS

The P78-2 spacecraft and payloads have been described earlier (ref. 1). A subset of these payloads, listed in table 1, are considered strictly engineering experiments and as such are the subject of this paper. The other experiments, especially SC3 (Energetic Electrons) and SC11 (Magnetometer) have engineering applications or provide accessory data required for proper interpretation of the engineering experiments data but will not be considered here further. The role of energetic electrons in spacecraft charging has been discussed earlier (ref. 2). SC4 differs from the other engineering experiments in that it is an active experiment. As such, its operations and the resulting interactions between the spacecraft and the plasma are quite complex, with much of the physics of these interactions poorly understood. Its full utility for engineering purposes awaits a more thorough understanding of these physical processes. An analysis of Electron Beam operations on P78-2 will be presented later (ref. 3).

The uses to which the data from the remaining engineering experiments are being put are outlined in table 2. Basically, there are five categories of use: model validation and verification; the Military Standard 1541 update; materials properties and contamination; the physics of the charging process; and anomaly investigation. The latter is aimed at determining whether charging played a part in an anomaly on an operational spacecraft and, if so, whether it was a surface charging event or a deep dielectric charging event. The number of users of data at this stage appears to be large, but the amount of data required by each is quite small for most uses. The primary users are the NASA Lewis Research Center, where a lot of work is being done on validating NASCAP, and Air Force Space Division (including The Aerospace Corporation) where Mil-

tary Standard 1541 is being updated and where materials charging properties, contamination, EMI, and environmental data are utilized for vehicle design evaluation and anomaly investigation. As part of this overview, we shall briefly discuss the engineering instrumentation and present some preliminary results from them.

#### SATELLITE SURFACE POTENTIAL MONITOR

Figure 2 presents schematically the method of measurement of the surface potential of materials which was used in the SCI-1, 2, 3 instruments. A common mounting method was used for all of the sample materials, listed in table 3. The system measures the sample potential which projects through the sample to the electrostatic field sensor, i.e., a back-side measurement of the surface potential. Details of the operation and calibration of this instrument were presented at the 1978 Spacecraft Charging Technology Conference (ref. 4) and will not be repeated here. The ability to measure the potential on the surface while also measuring the current conducted through the sample to the copper collecting surface on the substrate permits direct measurement of the bulk conductivity of the sample while in orbit. Thus, one may observe changes in this important parameter as a result of exposure to the space environment.

Data from the SSPM are being used to validate NASCAP at various facilities: at NASA LeRC, which has the responsibility for developing a charging analysis program; at Systems, Science and Software, Inc. where the NASCAP code was developed; and at the Air Force Geophysics Laboratory, which has the responsibility for developing a sheath model (which is being satisfied by some of the physics embedded in NASCAP). For these evaluations of NASCAP, the P78-2 geometry, with materials properties of those actually used on the vehicle, is input to the program. The environment used in the calculation is an analytic representation of the actual environment measured. The goal of the test run is to calculate potentials similar to those actually measured on test samples and on the vehicle frame. Results of some of those test runs are presented in detail later on in this volume in the section on analytical modeling. In general, the qualitative results appear to be good, especially with respect to prediction of electrical stress points. The quantitative failures which occur are undoubtedly due primarily to an incomplete definition of materials properties. A secondary cause may be an incomplete definition of the plasma environment. Studies incorporating SC2 plasma data and SSPM potential data indicate that the angular distribution of the plasma flux constituents may at times be a crucial factor (ref. 5).

The properties of materials which are probably incompletely defined are the secondary emission coefficients (especially as related to the angle of incidence of the incoming particle) and the bulk conductivity. One of the reasons for this incomplete definition of materials properties is the fact that the properties change upon continued exposure to the space environment. Kapton is a good example. Figure 3 shows the bulk current density as a function of surface voltage for the 1-1 (table 3) sample. The data points labeled "before exposure to radiation" were obtained in the laboratory on a virgin sample,



exposed to an electron beam in the dark. After exposure to simulated solar illumination, the "after exposure" data were obtained at three beam intensities. This was the expected behavior, based on earlier tests of Kapton (ref. 6). In those tests, the samples returned to their low conductivity state after being returned to atmospheric conditions.

Data from an early charging event in orbit, on 28 March 1979, produced bulk conductivity results as would be expected on the basis of exposure to solar illumination in orbit. However, continued exposure to solar UV without restoration of the atmospheric conditions (as occurs in laboratory testing) results in a cumulative effect on the bulk conductivity of Kapton. Figure 3 shows that by June 1980 the 1-1 Kapton sample has become a rather good semiconductor and does not charge above 50 volts even in an extreme charging environment. Incorporation of Kapton properties into a calculation as complex as the NASCAP code becomes very difficult when those properties are changing as radically as this.

In addition to using the SSPM data for validation of the NASCAP model, surveys are being made in an attempt to parameterize the charging environment and the response of different materials on a statistical basis. Figure 4 shows the approach. In this plot, the probability,  $P$ , of the potential of the Kapton 1-1 sample exceeding a voltage  $V$  (with respect to the vehicle frame) is presented for two local time sectors. The data clearly show more charging activity in the post-midnight sector than in the pre-midnight sector, as would be expected. At this stage of the analysis, it is hazardous to draw any quantitative conclusions from this data set, for reasons to be discussed below. The intent of a statistical approach such as this is to furnish the design community with a relative evaluation of the charging behavior of selected materials in the charging environment which will be encountered in orbit.

The shortcomings on the data set used to produce figure 4 deserve discussion since they may be applicable to other data sets obtained either in the lab or in space. First of all, the materials properties of the Kapton sample were changing, due to exposure to solar UV, during the time this data was being acquired. Thus, for a given charging environment, the potential to which the sample charged decreased as a function of time. For this or other materials, it is also possible that penetration by energetic electrons produces permanent changes in bulk conductivity. Finally, exposure to sunlight, deposition of contaminants, erosion, etc., can produce changes in the secondary emission ratio as a function of time. A statistical approach is not completely valid unless the properties remain essentially constant.

A second major problem is the fact that all of the data were obtained over a three month period. To get a good statistical representation of the environment, data should be collected over a major portion of a solar cycle, since the charging environment is ultimately produced by solar activity. Hence, a three month period is unlikely to represent the environment correctly. A third major difficulty is the assumption that all data points can be treated as statistically independent data samples. The data used in this survey was obtained by extracting the maximum potential observed during each one-minute data acquisition period that the vehicle was in the proper local time sector. Obviously,

the correlation time for charging events is much greater than one minute. If a sample shows the potential to be, say, 2000 volts, the preceding and following samples are unlikely to be far different. In order to properly treat data such as this with a statistical approach, one must determine the correlation length (in time) of a charging event. This has not yet been done. Once one knows what the correlation length is, one can assure statistical independence by using that correlation length for the sampling period. However, even definition of correlation length may be difficult for this phenomenon: it may vary for different materials, different vehicles, and different magnetospheric conditions.

The equation given in figure 4 assumes that one can extrapolate the portion of the curve above 500 volts. Again, there is a serious fallacy here if the extrapolation is carried too far: the sample will at some point break down, limiting the potential. Non-linear conductivity effects of a less spectacular nature will also come into play at some point. Because of the complex behavior of some of these materials, a simple approach may be satisfactory for the design engineer: assume the behavior already observed in orbit represents the behavior that will occur in the future for that material. This works only if a compendium of materials behavior is available for various materials and a sufficiently wide range of orbital environments. Lacking that, analyses must be made (again assuming that the analytical models, the environments, and the materials properties used are valid).

Initial analysis of orbital data disclosed significant discrepancies between the behavior observed in the laboratory calibrations of the SSPM and the response in orbit. Figure 5 shows schematically the laboratory test apparatus set up at The Aerospace Corporation to investigate these discrepancies. The notable detail here is the sapphire window used for the solar simulator. Figure 6 presents Kapton data obtained during a charging event in orbit. The upper panel shows the charging profile as the Kapton rotates in and out of sunlight. When it enters shadow, the sample starts charging and then discharges as it reenters sunlight. In the original laboratory tests at LeRC, center panel, the solar simulation was deficient in UV (the window was not made of UV transmitting material) and did not completely discharge the sample when the light was turned on (to simulate rotation into and out of sunlight). As a result, the potential on the Kapton built up to the beam energy (minus the secondary emission crossover potential) in the dark and showed only slight discharging in the light. With the solar simulation used in the Aerospace test, the behavior of the test sample was very similar to that observed in space. For both the LeRC and Aerospace simulations a monoenergetic electron beam was used. Because the photoinduced conductivity does not quench immediately upon removal of the light source, the peak voltage reached by the sample is much less than beam energy.

Another significant deviation between predicted behavior and observed behavior occurred in the quartz cloth sample. Using high energy monoenergetic electron beams, silica and quartz cloth had been charged to kilovolt potentials, but the presence of lower energy electrons (a few kiloelectron volts) limited surface potentials to one or two hundred volts (ref. 7). The difficulty in getting the material to charge to higher voltages in the laboratory

led to its extensive use on DSCS to prevent charge buildup. In orbit, the Astroquartz sample on the SSPM charges to higher potentials than Kapton and over 6000 volt levels have been measured. Measurements of the material in the laboratory disclosed that the material initially charges up to a high potential and then relaxes to a small value. However, as shown in figure 7, the relaxation time constant is a strong function of the input current density (ref. 8). For current densities in the range of those encountered in space, tenths to hundreds of picoamps per  $\text{cm}^2$ , these time constants are long compared to typical charging environment events. In previous laboratory tests, the current densities were in the nanoamp to microamp range. The initial excursion in voltage was treated as an experimental transient and ignored (or missed altogether).

A low-level-of-effort laboratory program is being maintained at Aerospace to continue assisting in resolving discrepancies between the orbital SSPM data and the preconceived response to the environment. The current work is aimed at solving some of the problems in getting NASCAP predictions to agree with orbital data. The approach is to make very careful measurements of the secondary emission ratio of the SSPM materials in order to provide appropriate input constants for NASCAP. The preliminary results of this effort were presented earlier in this volume (ref. 9).

#### SHEATH AND CHARGING PHYSICS

The SC2-1, 2 and 3 sensors are sets of electron and ion detectors which use electrostatic deflection to analyze fluxes of particles in the energy range of about 20 eV to 20 keV. Two sets are mounted in spherical enclosures at the ends of 3-meter booms; the other set is body mounted. The spheres initially were maintained at plasma potential as part of a sheath physics experiment. Arcing induced by electron beam operations disabled portions of the spherical probe circuitry and the enclosures are now maintained at vehicle potential (ref. 3). Measurements of the sheath geometry are made by making simultaneous measurements with the three sets of sensors, all pointing in the same direction but in different portions of the particle trajectory through the sheath. Particles entering one of the sets in a sphere have not traversed the sheath region between the sphere and the vehicle body. Particles entering the body-mounted instrument have had their energy and trajectory modified by the potential between the part of the sheath at which the first sphere is located and the vehicle body. Finally, the detectors in the other sphere are observing particles which have had their trajectories modified by passing near the vehicle body. For a given potential on the body, electrons and ions will show much different behavior for this last set.

The study of the physics of charging requires simultaneous analysis of several sets of data. Figure 8 shows a preliminary step in this analysis. The upper two panels show the electron flux and the ion flux, respectively, measured by the body-mounted sensors. Lighter areas indicate higher flux densities. The data presentation starts in sunlight, as shown by repetitive bright lines in the 20 to 40 keV part of the ion spectrogram (the result of sensitivi-

ty to solar UV by the instrument which measures this part of the ion energy spectrum). Just after going in to the earth's shadow the vehicle is emersed in a hot plasma, as shown by the increase in the energy of the maximum in the electron flux (near 23.7 local time). The Kapton sample responds by charging to about 1500 volts with respect to the vehicle frame, bottom panel. The vehicle frame, too, charges as shown by the change in the ion spectrogram. The cold ambient plasma ions are accelerated by the vehicle potential and are observed at energies in excess of 4000 volts, indicating the vehicle itself has charged to this potential. Note that the Kapton maintains a differential charge with respect to the vehicle. As the vehicle comes back into sunlight, evidenced by the burst of photoelectrons shown at very low energy near the right end of the upper panel, the vehicle potential returns to a low value and the Kapton sample discharges. The pulse analyzer detected discharges during the time when the vehicle was charging up and also when it was discharging, times when maximum electrical stress occurs on the vehicle (bottom panel).

The sheath physics and charging physics task is rather formidable. However, some significant results have already been extracted from the data. One of these, discussed in ref. 5, will probably result in a modification of NASCAP. It appears that differential charging, as distinguished from vehicle charging, is dependent on the angular distribution of the hot plasma particles. The hot plasma particles, unlike the cold background plasma, is frequently asymmetrically distributed.

#### PULSE ANALYSIS

Two experiments contribute to the study of EMI produced by discharges. One experiment, the Charging Electrical Effects Analyzer, consists of three separate instruments, each measuring a different electromagnetic phenomenon. Two of these instruments, the Very Low Frequency Analyzer and the Radio Frequency Analyzer, measure wave frequencies and amplitudes. Preliminary results from these wave analyzers were presented previously (ref. 10). The third instrument, the Pulse Analyzer, is the prime EMI detector/analyzer on P78-2. A complementary experiment, the Transient Pulse Monitor, was added late in the design of the P78-2 to supplement the data obtained by the Pulse Analyzer. The two instruments make different measurements of the same phenomenon, electrostatic discharges, and so the analyses of the two data sets are coordinated. Since virtually nothing was known about the characteristics of discharge pulses in space other than the amplitude distribution observed on cables used as sensors on a couple of previous satellites, the Pulse Analyzer was built with many of its characteristics programmable by ground command. Figure 9 is a simplified block diagram of the Pulse Analyzer. Options which are ground-commandable include: ANTENNA SELECT, which can be set to dwell on one antenna or to cycle through two or four antennae; ATTENUATOR LEVEL, which selects the overall gain through the system; THRESHOLD LEVEL, which selects the trigger level for pulse analysis; and TIME BASE, which selects linear or logarithmic spacing for pulse sampling, and if linear, the time between samples. A more detailed description of the instrument is given in ref. 10.

The great flexibility, which was required to insure having an instrument in orbit which could measure several different parameters in the appropriate ranges, has delayed getting data in the ranges most appropriate for analysis. The relative infrequency of naturally-occurring discharges (an average of about one per fifteen days of data) plus a very long delay in getting the initial orbital data processed (about 9 months between launch and production processing of orbital data) has resulted in only five pulses due to natural discharges having been sampled in the high time resolution mode (15 nanoseconds between samples) required for analytic evaluation. Other data may exist in the data pipeline which will increase this data base.

Figure 10 shows the type of analysis being performed on these high time resolution data. The sixteen pulse samples are fit with a two-frequency damped model. From the fit, the frequencies, damping factors, amplitudes, and phase angle are obtained. The upper waveform in figure 10 is the fit to a natural discharge. It cannot be called a typical discharge, since none of the five discharges analyzed to date are similar to another. The lower waveform is a fit to a pulse observed during an Electron Beam (SC4-1) operation. Most notable is the low damping factor. Details of these pulse analyses are presented elsewhere in this volume (ref. 11). Preliminary indications are that pulses contain a frequency component around 25 MHz, which is probably characteristic of the geometry of the vehicle and its sheath, and a component from a few MHz to a few tens of MHz which is probably characteristic of the discharge path itself. The future emphasis in analysis of the pulse data will be on locating discharge points and characterizing the discharge and coupling into the vehicle. This effort is being augmented by tests on a model of P78-2, SCATSAT.

In addition to the high time resolution data analysis, a larger body of data from the Pulse Analyzer is being used to determine amplitude characteristics of natural pulses. The entire data set from the Pulse Analyzer is useful for this purpose, since only a threshold measurement, not pulse sampling, is required. The TPM provides similar data but with a lower threshold set for pulse analysis. Figure 11 shows a comparison of 19 natural discharges from the Pulse Analyzer data set and about 115 pulses from the TPM. Both sensors have 50 ohm inputs. The pulse distributions from the two instruments are similar, even though the Pulse Analyzer (SC1-8B) distribution appears to be skewed to higher voltages than the TPM. This is an artifact of the data presentation. The data from the Pulse Analyzer were obtained with logarithmically spaced thresholds (only three thresholds are represented in the plot) while the TPM data is obtained with linearly spaced thresholds.

The data from the TPM shown in figure 11 has a companion set obtained from the high impedance antenna on the TPM at the same time. These pulses were all measured simultaneously on both the low and the high impedance antennae. Figure 12 presents the distribution for both of these sensors and also the ratio between the amplitudes measured on the high and low impedance antennae. The ratios vary from less than unity to over 15, with major portions being centered around ratios of five and eleven. Such data is of use in evaluating coupling models. Again, these data are discussed in more detail in following papers (refs. 11, 12).

## CONTAMINATION AND THERMAL CONTROL

In addition to the operational mode changes and electronic subsystem damage which have been blamed on spacecraft charging, degradation effects in thermal control surfaces, optical components and sensors have also been postulated to be enhanced by charging. Figure 13 presents the mechanism schematically. A molecule from the spacecraft, either outgassed or sputtered from the surface of the vehicle, is ionized by a solar photon while still in the vicinity of the vehicle. In the absence of a hot charging plasma, solar-induced photoelectron current from the vehicle normally results in a slight positive potential on the vehicle which would prevent reattraction of such an ion. If the vehicle is charged negatively, the ion can be reattracted to the vehicle if it is still within the sheath region. A thorough discussion of the experiment and some preliminary results are given in ref. 13.

Figure 14 presents some of the preliminary contamination data. The sudden increase at about 120 days is an artifact of the data reduction and analysis. At this preliminary stage of analysis, effects due to temperature changes of the sensor have not been corrected for and the response at 120 days is the result of a temperature command. The primary purpose of displaying this data is to show the requirement for long-term data acquisition on this experiment. The data are plotted on a semi-logarithmic display for ease in determining an extrapolation for long duration missions. If the primary source of contamination is outgassing of vehicle components, one would expect an exponential decay in the rate of accumulation which would result in a straight line on this display. Charging episodes, if they were infrequent and had a significant effect on the deposition rate, would show up as discrete displacements of the curve without a change in slope. If they were frequent, they would change the slope. The data of figure 14 indicate that for the first year the deposition rate was effectively linear. The derivative of this curve, which is presented in ref. 14, indicates that the rate of deposition is actually decreasing with time. It appears that the proper extrapolation of this curve will fall between the light and heavy dashed extrapolations shown on the figure. The Repelling Potential Analyzer, basically an ion trap attached in front of the Thermally-Controlled Quartz Crystal Microbalance, indicates that ions with energies up to 500 eV/charge constitute 25% of the total mass accumulation (ref. 14).

The other portion of this experiment, the Thermal Control Coatings experiment, measures changes in solar absorptivity,  $\alpha_s$ , in a number of typical spacecraft materials. Six of the samples include heaters to provide for desorption cleaning of the sample during flight. A comprehensive description of this experiment, data derived from it, and data analysis techniques are given in ref. 15. Major results to date include measurement of changes in  $\alpha_s$  in several materials, presented in figure 15, and the observation that the use of indium oxide on OSRs and Kapton (in order to control charging) increases the early degradation of their thermal properties. Again, figure 15 is a semi-logarithmic plot in order to easily distinguish between linearly and exponentially decreasing degradation. The time span covered by the data is still too short to determine which is occurring.

The data of figures 14 and 15 show the importance of obtaining very long term data on materials degradation in space. Satellite systems are projected which will require seven to ten year operational capability from the vehicle design. That will be difficult, if not impossible, if materials behavior during long term exposure to the space environment is not known quantitatively. Similar long term data are required for materials response to charging environments.

#### ANOMALY INVESTIGATIONS

Because the P78-2 vehicle makes measurements of a wide range of plasma parameters, from eV to MeV in both electrons and ions, and because it has been providing continuous data coverage, it has assisted in anomaly investigations. In one instance, a new spacecraft experienced the loss of one of a pair of redundant power distribution systems. Evaluation of the geometry of the system and the electrical configuration identified a possible failure mechanism which would be initiated by a momentary short to ground. Such a short to ground could be initiated by a discharge in an exposed cable. Data from the P78-2 vehicle showed that two days previous to the time of the anomaly charging conditions had existed, but were no longer severe at the time of the anomaly. There was an increase in the energetic electron fluxes at the P78-2 orbit.

In June of 1980, a Global Positioning System vehicle experienced an anomaly. The P78-2 data were analyzed to see if they could help in identifying the cause of the anomaly. GPS is in a lower, highly inclined orbit, and as such does not see the same environment as P78-2. However, one can extrapolate the P78-2 data and make good estimates on the GPS environment. The analysis showed that the SSPM, on June 10, had measured the highest potentials recorded since launch, > 10 kV on teflon, > 6 kV on the quartz cloth, and > 2 kV on the Kapton sample on the top (shadowed) instrument. No natural pulses were detected by the SC1-8B Pulse Analyzer. On the 12th, energetic electron fluxes (> 2 MeV) began to increase and, by the 13th, had reached the highest levels measured since launch. On the 13th, the Pulse Analyzer observed two discharges. On the 13, GPS experienced its anomaly. On the 14th, while energetic electron fluxes were still very high (private communication, J. B. Reagan, 1980), another discharge was observed by the Pulse Analyzer and the P78-2 had its first known naturally induced anomaly (a magnetometer mode change). During the period 11 June to 14 June, potentials measured by the SSPM remained much lower than they had been on the 10th. On the basis of the P78-2 data and other considerations, it was concluded that the GPS anomaly was probably due to a thick dielectric charging event caused by energetic electrons. Relatively scant attention has been paid to this portion of the SCATHA program, although some test results are available (refs. 16, 17). It is an area which the P78-2 environmental data set is very qualified to investigate.

## SUMMARY

The engineering experiments on P78-2 are providing new results in three general areas: potentials on materials; EMI; and materials degradation. This data is being used for evaluation of materials and spacecraft design and for validation of several models generated as part of the SCATHA program. Additionally, they are being used to investigate the physics of charging and to assist in the investigation of anomalies on operational spacecraft. The data base that already exists is probably adequate to satisfy the original intent of the program (to establish charging as a mechanism for producing anomalies and to study the physics of the process) and to update the Military Standard 1541. However, continued operation of the P78-2 vehicle would permit obtaining long term data bases on materials degradation and would provide invaluable data for anomaly investigation.

## REFERENCES

1. Description of the Space Test Program P78-2 Spacecraft and Payloads, by Lt. R. N. Osgood, these Proceedings.
2. The Role of Energetic Electrons in the Charging/Discharging of Spacecraft Dielectrics, by J. B. Reagan; R. W. Nightingale; E. E. Gaines; R. E. Meyerott; and W. L. Imhof, these Proceedings.
3. P78-2 Satellite and Payload Responses to Electron Beam Operations on March 30, 1979, by H. A. Cohen et al., these Proceedings.
4. Description and Charging Results from the RSPM, by P. F. Mizera; E. R. Schnauss; R. Vandrey; and E. G. Mullin, Spacecraft Charging Technology - 1978; NASA Conference Publication 2071/AFGL-TR-79-0082, 1979, p. 91.
5. Electron Angular Distributions during Charging Events, by J. F. Fennell; D. R. Croley; and P. F. Mizera, these Proceedings.
6. Effects of Illumination on the Conductivity Properties of Spacecraft Insulating Materials, by R. C. Adamo and J. E. Nanevich, NASA CR-135201, Stanford Research Institute, 1977.
7. Secondary Emission Conductivity of High Purity Silica Fabric, by V. J. Belanger and A. E. Eagles, Proceedings of the Spacecraft Charging Technology Conference, NASA TM-73537 (AFGL-TR-77-0051) 1977, p. 655.
8. Laboratory Study of Charging Spacecraft Materials flown on P78-2 Satellite, by M. S. Leung and H. K. A. Kan, to be published in Journal of Spacecraft and Rockets, 1981.
9. Effects of Secondary Emission on Charging, by M. S. Leung; M. B. Tueling; and E. R. Schnauss, these Proceedings.



10. Characteristics of Electrical Discharges on the P78-2 Satellite (SCATHA), by H. C. Koons, Paper 80-0333, AIAA 18th Aerospace Sciences Meeting, Pasadena, CA, 1980.
11. Aspect Dependence and Frequency Spectrum of Electrical Discharges on the P78-2 (SCATHA) Satellite, by H. C. Koons, this Proceedings.
12. Transient Pulse Monitor (TPM) Data from the SCATHA/P78-2 Spacecraft, by S. A. Damron; R. C. Adamo; and J. E. Nanevich, these Proceedings.
13. Flight Experiment to Measure Contamination Enhancement by Spacecraft Charging, by D. F. Hall, in Proceedings of the Society of Photo-Optical Instrumentation Engineers, Vol. 216, 1980, p. 131.
14. Selected On-Orbit Deposition Rate Variations Detected by the ML12 Quartz Crystal Microbalances Aboard P78-2 (SCATHA), by D. M. Clark and D. F. Hall, these Proceedings.
15.  $\alpha_s/e$  Measurements of Thermal Control Coatings on the P78-2 (SCATHA) Spacecraft, by D. F. Hall and A. A. Fote, Paper 80-1530, AIAA 15th Thermophysics Conference, Snowmass, CO, 1980.
16. High-Energy Electron-Induced Discharges in Printed Circuit Boards, by E. P. Wenaas; M. J. Treadaway; T. M. Flanagan; C. E. Mallon; and R. Denson, IEEE Transactions on Nuclear Science, Vol. NS-26, 1979, p. 5152.
17. High-Energy Electron-Induced Discharges and SGEMP Modification in Cables, Air Force Weapons Laboratory ECEMP Phenomenology Memo No. 29, by C. E. Mallon; M. J. Treadaway; T. M. Flanagan; E. P. Wenaas; and R. Denson, 1979.

TABLE 1. - P78-2 ENGINEERING EXPERIMENTS

<u>STP 78-2 DESIGNATION</u>	<u>TITLE</u>	<u>PRINCIPAL INVESTIGATOR</u>
SC1-1, 2, 3	SATELLITE SURFACE POTENTIAL MONITOR	P. F. MIZERA AEROSPACE CORPORATION
SC1-7 -8A -8B	RF ANALYZER VLF ANALYZER PULSE ANALYZER	H. C. KOONS AEROSPACE CORPORATION
SC2-1, 2, 3	SHEATH ELECTRIC FIELDS	J. F. FENNELL AEROSPACE CORPORATION
SC4-1, 2	ELECTRON AND ION BEAMS SYSTEM	H. A. COHEN AFGL
ML12-3, 4 -6, 7	THERMAL CONTROL COATINGS QUARTZ CRYSTAL MICROBALANCE	D. F. HALL AEROSPACE CORPORATION
TPM	TRANSIENT PULSE MONITOR	R. C. ADAMO SRI, INC

TABLE 2. - USES OF P78-2 ENGINEERING DATA

<u>DATA SET</u>	<u>RECIPIENT</u>	<u>USES</u>
SSPM	AFGL NASA/LeRC S3 AFSD	NASCAP V&V; SC4-1, 2 OPERATIONS ANALYSIS NASCAP V&V NASCAP V&V ANOMALY INVESTIGATIONS; MATERIALS SELECTION
SC1-7, 8A, 8B	SAI JAYCOR IRT SRI	MIL STD 1541 UPDATE TINKSAT TESTS; DISCHARGE MODEL SCATSAT TESTS; COUPLING MODEL TPM ANALYSIS
SC2-1, 2, 3	AFSD AFGL S3 NASA/LeRC	CHARGING PHYSICS (with SSPM) ATLAS; SHEATH MODEL NASCAP V&V (with SC5, SC9) NASCAP V&V (with SC5, SC9)
TPM	SAI AFSD	MIL STD 1541 UPDATE SC1-8B ANALYSIS
ML12	AFML AFSD	MATERIALS PROPERTIES/CONTAMINATION CONTAMINATION

TABLE 3. - SSPM SAMPLE MATERIAL AND LOCATION

SAMPLE POSITION	SCI-1	SCI-2	SCI-3 <sup>(a)</sup>
1	ALUMINIZED KAPTON	ALUMINIZED KAPTON <sup>(b)</sup>	ALUMINIZED KAPTON
2	OSR <sup>(c)</sup>	ALUMINIZED KAPTON	SILVERED TEFLON
3	OSR	REFERENCE BAND	QUARTZ FABRIC
4	GOLD	REFERENCE BAND	GOLD / ALUMINIZED KAPTON

a) On top of spacecraft

b) 125 mil hole through sample

c) Grounded to spacecraft chassis

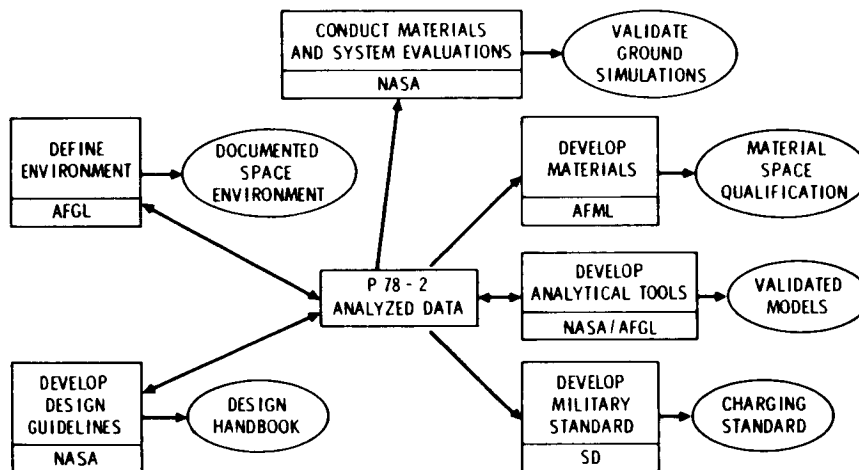


Figure 1. - Interrelationship between P78-2 data and various segments of SCATHA program. The major impact of the P78-2 data is expected to be in model validation and the charging standard.

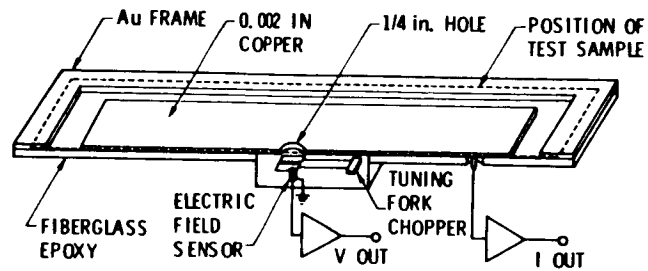


Figure 2. - Method of mounting samples and measuring potential and bulk current on the Satellite Surface Potential Monitor. The potential is measured through the bulk of the sample.

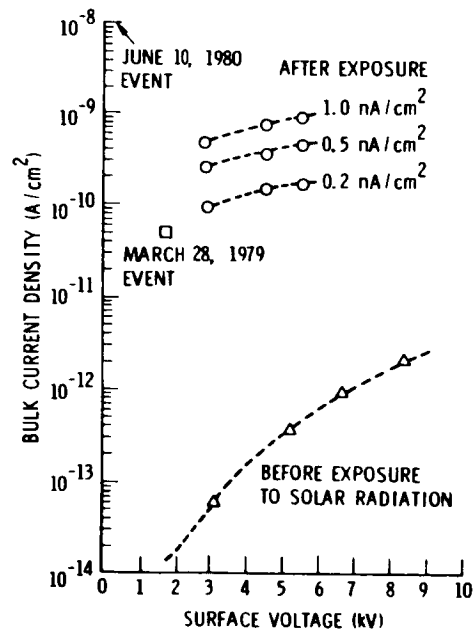


Figure 3. - Bulk current density measured on Kapton 1-1 sample prior to flight and in orbit. By June 10, 1980 the sample would no longer support a large voltage due to cumulative effects in the solar-photoconductivity.

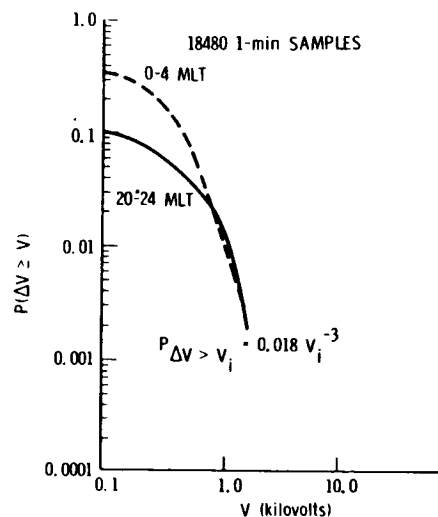


Figure 4. - Probability of seeing a potential greater than a given voltage on Kapton 1-1 sample is plotted for two local time sectors. The equation is valid for these data from 500 to 2000 volts. See cautions in the text regarding extrapolations and interpretations of this figure.

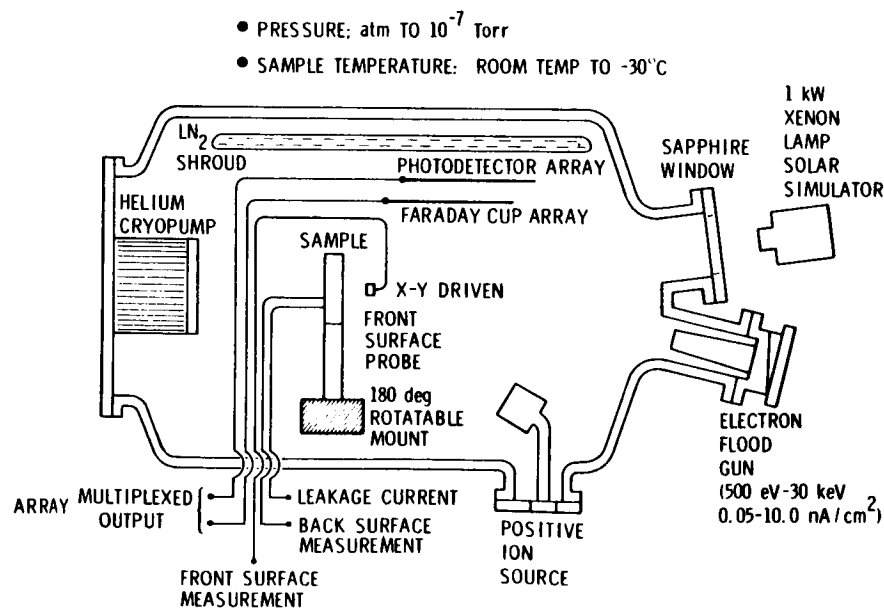


Figure 5. - Schematic diagram of the Aerospace Corporation test chamber being used to reconcile orbital SSPM data to previous measurements of materials properties at other laboratories. This facility has been modified to include a second electron gun for dual-beam energy studies (not shown).

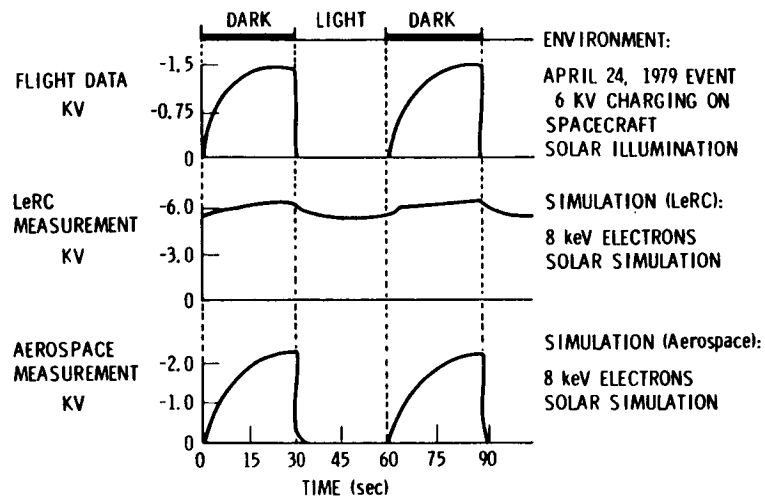


Figure 6. - Comparison of space SSPM data from Kapton 1-1 sample with calibrations prior to flight and with tests in chamber shown in figure 5. Ultraviolet-induced photoconductivity results in complete discharge of the sample in space and in the Aerospace simulation.

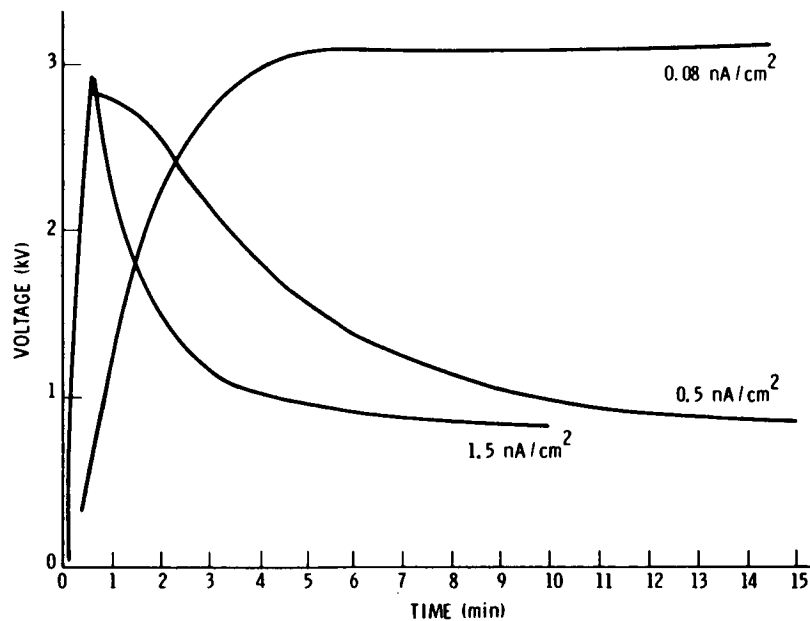


Figure 7. - Effect of current density on relaxation time constant of quartz fabric charged by an electron beam. The 0.08-nA/cm<sup>2</sup> curve is representative of a space charging environment.

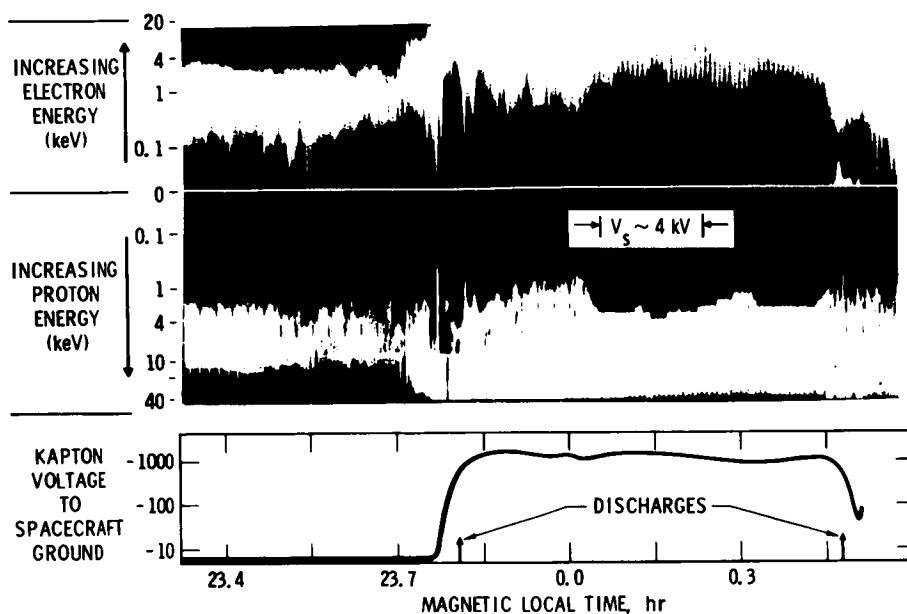


Figure 8. - Natural charging event on P78-2 spacecraft in eclipse. The upper two panels are spectrograms of the electron and ion fluxes. The lowest panel shows the charging profile of a Kapton sample and two natural discharges detected by the Pulse Analyzer. See text for details.

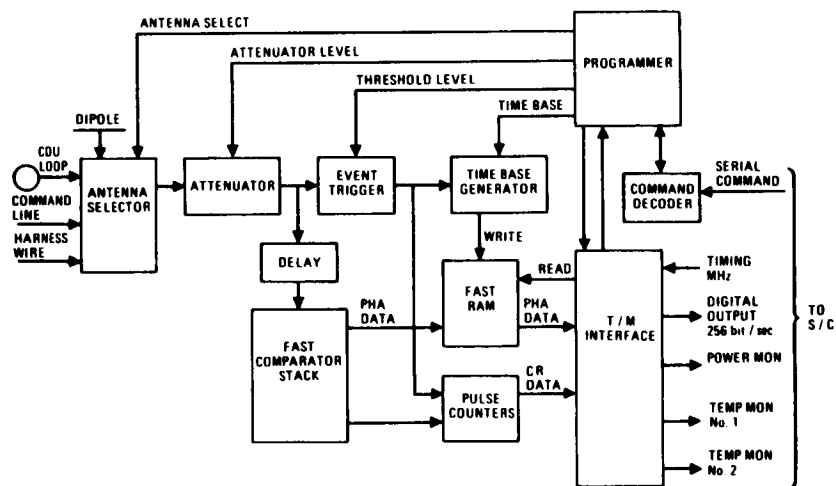


Figure 9. - Simplified block diagram of SC1-8B Pulse Analyzer showing flexibility of operation provided through ground commands. This flexibility was required to insure that the instrument would be able to make measurements of various parameters, each in the proper range, in spite of the fact that virtually nothing was known about the amplitude or frequency components of discharges prior to flight.

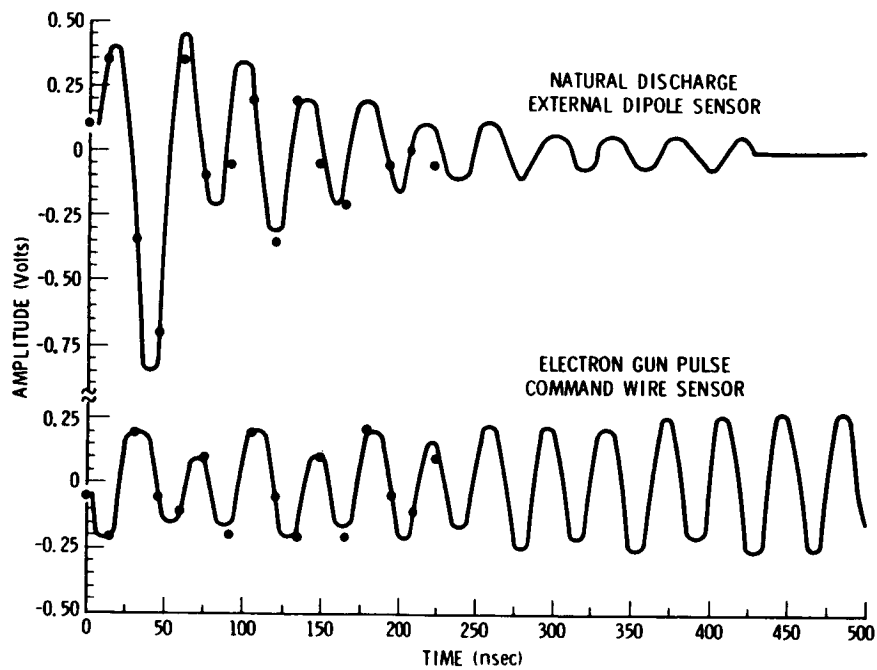


Figure 10. - Plots of results of analysis of data from two discharges observed on P78-2 by SC1-8B Pulse Analyzer. The dots are the data samples at 15-nanosecond intervals. The solid lines are the best fits to the data using two frequency components with arbitrary phase and damping.

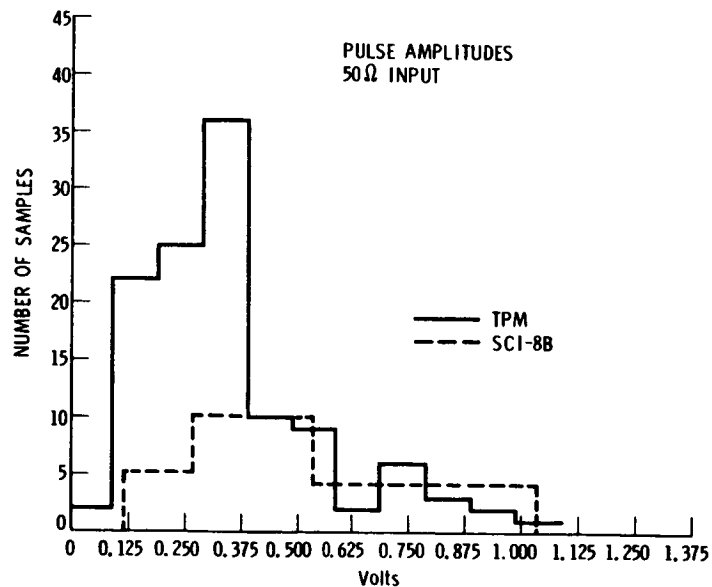


Figure 11. - Comparison of natural pulses detected by TPM and SC1-8B Pulse Analyzer. Distributions are equivalent, though the logarithmically spaced thresholds on the SC1-8B instrument appear to be skewed to higher levels.



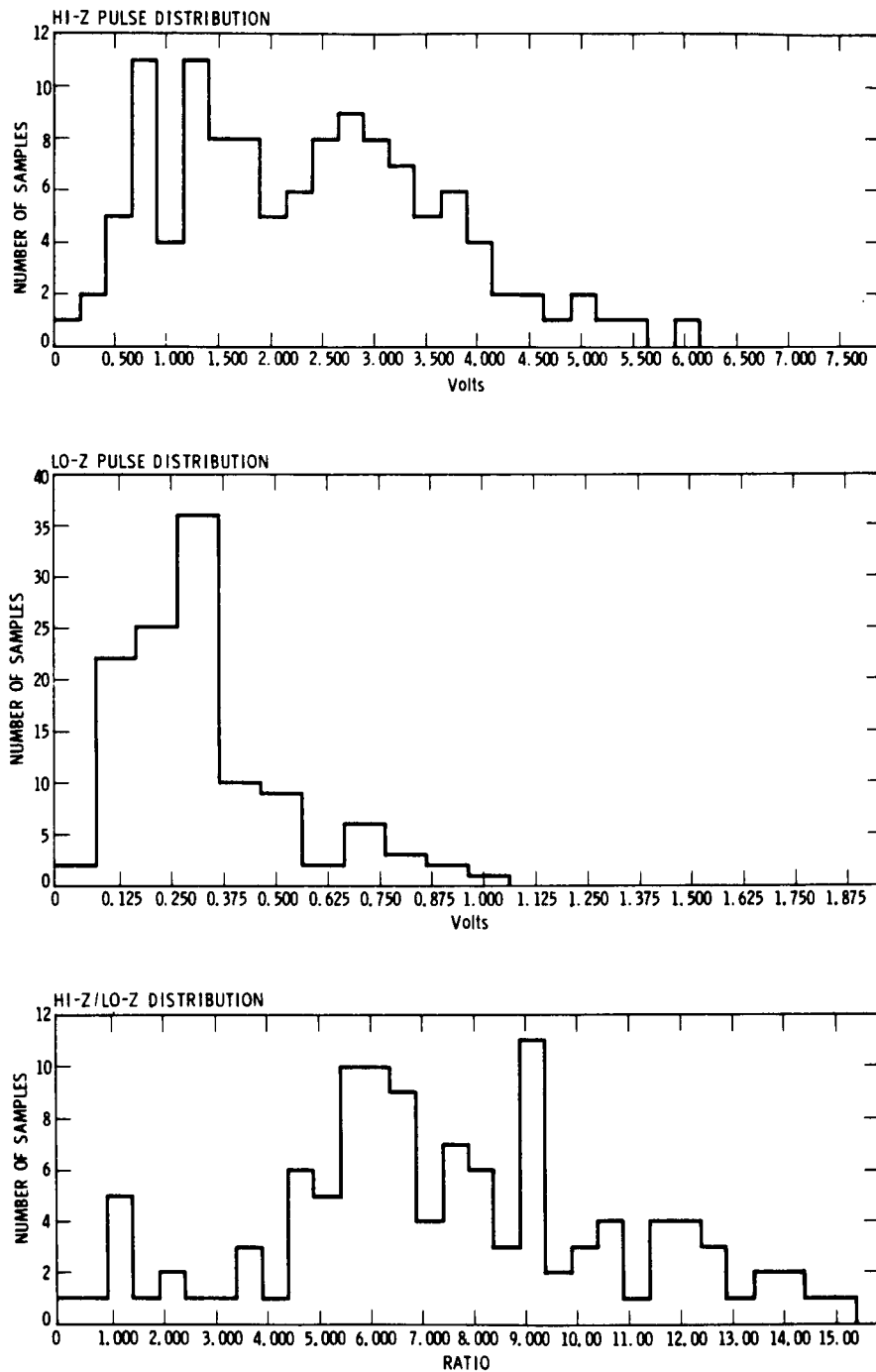


Figure 12 - Distributions of pulse amplitudes observed in TPM high-impedance and low-impedance antennae. The bottom panel presents the ratio of the high-to-low measurement for the same pulse.

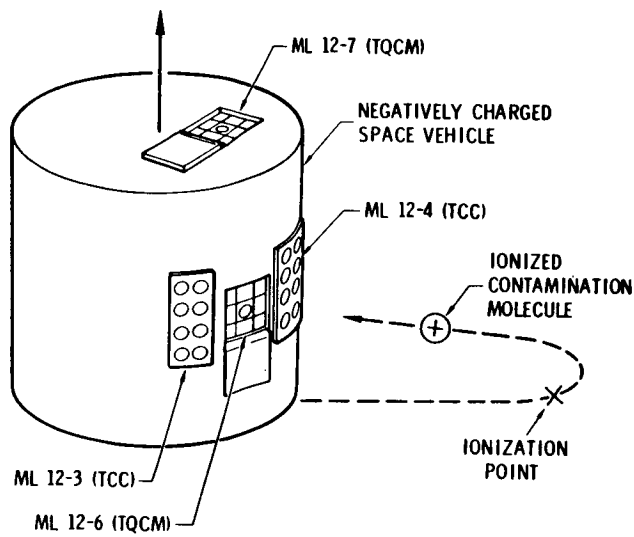


Figure 13. - Schematic diagram of experiment to determine effect of charging on rate of contamination of spacecraft surfaces. A molecule emitted from the surface is ionized by solar radiation while still within the sheath region of the satellite. The ion is then attracted back to the negatively charged vehicle.

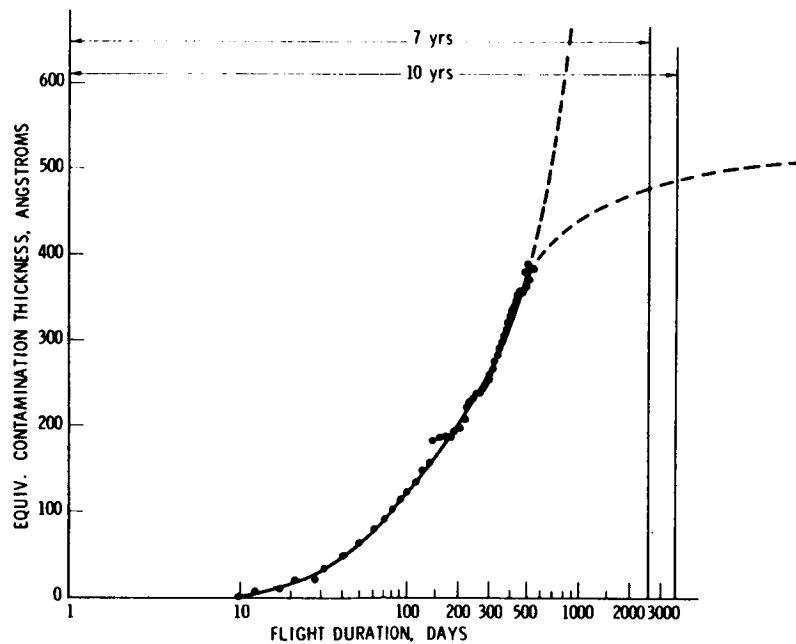


Figure 14. - Preliminary results from Quartz Crystal Microbalance on P78-2 satellite. The data show that a long time base is required in the data set if one wishes to extrapolate contaminant deposition over the design life of satellite systems now being planned.

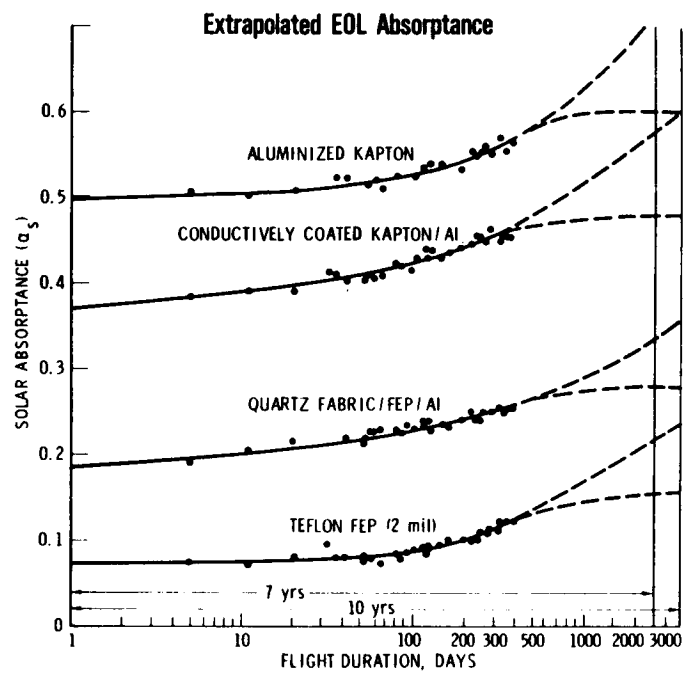


Figure 15. - Data, and conclusions, similar to those of figure 14. These data are from the P78-2 Thermal Control Coatings experiment.

## **SATELLITE SURFACE POTENTIAL SURVEY\***

**Paul F. Mizera<sup>+</sup> and G. M. Boyd**  
**Space Sciences Laboratory**  
**The Aerospace Corporation**

### **SUMMARY**

Results of Kapton differential voltage charging of the SSPM Kapton samples are presented for the first 100 days of P78-2 operations. Daily charging occurrences are plotted in magnetic local time and L-shell (altitude and magnetic latitude) space as a function of magnetic activity. Most of the low level charging occurs well into the dawn local time sector whereas the highest voltage levels occur in the premidnight local time sector. The probabilities of differential charging are extremely dependent on the local time sector, the altitude (or L-shell) and of course, the magnetic activity.

One of the critical engineering experiments flown on the USAF P78-2 satellite was the Satellite Surface Potential Monitor (SSPM). In order to properly characterize spacecraft charging the following observations are necessary: the three dimensional charged particle environment of both high and low energy ions and electrons; the resulting charging profiles of the spacecraft ground and dielectric materials; and electrostatic discharges when material charging levels are sufficiently high relative to adjacent objects. Various models of charging and discharging are currently being developed and used in the laboratory and their predictions must be validated by space data which can only be provided by in situ measurements. To date significant progress has been made in this direction by the SCATHA community using data from the P78-2 experiments. Two charging events, April 24, 1979 (ref. 1,2) and March 28, 1979 (ref. 2) have played a major role in the quantitative understanding of spacecraft differential charging both in sunlight and eclipse.

In addition to individual charging events, a long term statistical survey of spacecraft charging is necessary in order to provide the spacecraft community with information for design guidelines. Material characterization is an integral part of these design criteria. The work presented here is the first part of the SSPM charging survey currently underway at the Space Sciences Laboratory of The Aerospace Corp. To date a little over 100 days of data covering the time interval of Feb. 7 through May 26, 1979 have been processed and results of the differential charging will be discussed.

---

\*Work performed under USAF Contract No. FO4701-79-C-0080

+ On leave at Center for Astrophysics and Space Sciences, University of California, San Diego, La Jolla, CA

Since the inception of the SCATHA program, a back surface measurement was proposed and some results have been presented in references 1 and 2. The best way of judging the validity of the measurements is to analyze the results and interpret them correctly. The following data will show that the SSPM measurements of material charging are a valid technique to describe substorm injection events and the charging of spacecraft materials in space.

Figure 1 shows the response of the back surface potential measurement of the SSPM-2 Kapton sample to the charging environment in the post-dawn local time region on April 21, 1979. The energetic electron environment is primarily responsible for material charging as seen by the integrated flux of electrons with E from 5 KeV up to 80 KeV plotted in Figure 1. These data are averages over the 90° pitch angle spectra provided by the UCSD SC-9 spectrometer (P. Isenberg, personal communication 1980). The SSPM potentials are the maximum value attained in 64 sec time interval which is approximately one satellite rotation into and out of sunlight.

The correlation between the energetic charging current above the secondary electron crossover energy and the maximum SSPM-2 Kapton voltages reached during the same time intervals is remarkably good. The secondary electron crossover occurs below ~ 2 KeV where the secondary yield becomes greater than one. Therefore the results of the SSPM survey using the same measurements should be a valid indicator of substorm injection events and times when differential charging is occurring on the P78-2 satellite due to energetic electrons.

The first 104 days of the SSPM operation are used for these survey results. Since Kapton plays a major role in the SSPM experiment, one of the two Kapton plays a major role in the SSPM experiment, one of the two belly-band samples (SSPM-2) was used to indicate levels and probabilities of occurrence of differential charging of typical spacecraft materials. When levels greater than -50 Volts were observed during any 64 sec time interval of the 104 days survey, the measurements were recorded on an output tape along with all remaining SSPM outputs and selected environmental and geophysical parameters. Each 64 sec intervals was then examined for the maximum voltage attained and binned according to various geophysical parameters including L (drift shell), magnetic local time and magnetic activity as defined by the global index Kp.

Figures 2a, b and c show a polar plot of the occurrence frequency greater than 100 Volts for quiet and disturbed magnetic conditions and greater than 1000 Volts for disturbed conditions respectively. Charging must have occurred at least 5 of the 64 sec intervals in a given 1 hour local time bin for the results to be valid.

The total number of days where this occurred are plotted in Figure 2. Figure 2a shows voltages greater than -100 Volts for quiet conditions defined as  $K_p < 2+$ . The separation at  $2+$  is arbitrary and more or less divides the total sampling intervals equally. Contours are indicated by the cross-hatching and represent levels of 5% and 10% probabilities of charging. [That is 5 days/104  $\approx$  5%]. The results of Figure 2 are not meant to show exactly the probability of charging but to show the spatial regions where charging is most probable. Comparing Figure 2a and Figure 2b, one immediately sees the effect that magnetic activity has on differential charging. Only when  $K_p > 2+$ , does the probability of charging approach 20%. In addition, the maximum occurs in the dawn local time region and at high L shells which is a combination of altitude and magnetic latitude. That is, an L value  $> 7.5$  means the satellite is off the equator and at high altitude.

Figures 2a and 2b show a differential charging threshold greater than -100 Volts, a relatively low level. Figure 2c shows levels greater than -1000 Volts and indicates a few interesting results. That is, highest levels of charging occur near local midnight during eclipse times and high magnetic activity. This is just because no solar UV is present to discharge the materials. There is an additional complication however; the entire spacecraft also charges to high voltages in the shadow and the SSPM measurement is the voltage of material relative to the spacecraft frame. This means the true absolute potential is the sum of the SSPM and the voltage of the spacecraft and is not taken into account here. Another interesting result is that the region of highest potentials reached is not the same as where the maximum probability of occurrence is found. That is, approximately 5% of the time in the 20-24 hours local time interval, greater than -1000 Volts differential charging occurred and almost no charging greater than -1000 Volts was recorded beyond 4-5 hours local time. This is just the opposite of the low level charging as seen in Figure 2b where up to 20% of the time, charging was observed in the 6-7 hours local time region. Another interesting contrast is that very little charging occurs for quiet magnetic conditions in the premidnight versus the postmidnight local time sectors.

The complete results of the Kapton charging survey are better presented in probabilities of occurrence above voltages from -100 volts to greater than -1500 volts. Before these results are discussed, a brief explanation of the satellite coverage is advisable. Table I shows the survey broken into bins of 64 sec intervals and separated into four local time intervals; 0-6, 6-12, 12-18, and 18-24 hours magnetic local time. In order to study the altitude dependence, the data were sorted into low ( $< 6.6R_E$ ) and high ( $> 6.6R_E$ ) L shells:  $6.6R_E$  is of course geosynchronous altitude. The last category used was quiet and disturbed magnetic conditions. ( $K_p = 2+$  was used as the break point.)

One immediately sees from Table I the sampling bias in the data coverage over the the 104 days of the initial survey. Apogee of the P78-2 was

initially in the dawn sector and local time changes only 1 degree or 5 minutes per day. Therefore apogee swings from dawn to dusk over a 1/2 year interval. Of particular importance is the poor coverage of the satellite in the dawn local time sector at L shells below geosynchronous altitude and above  $6.6R_E$  in the dusk sector. This will be discussed later.

Figure 3a shows the percent probability of occurrence,  $P [ > V ]$ , of Kapton charging above a given voltage level from -100 to -1500 Volts in a 64 second sampling interval. This value represents the maximum value reached in that interval. The accumulated results are divided into post-midnight to dawn (0-6 hours) and dusk to pre-midnight (18-24 hours) and disturbed ( $K_p > 2+$ ) and quiet ( $K_p < 2+$ ) magnetic conditions. Figure 3a is for L shells above geosynchronous ( $6.6 R_E$ ) altitude whereas Figure 3b is for  $L < 6.6 R_E$ . The average probability of low charging levels is approximately equal for post-midnight to dawn and dusk to pre-midnight and reaches values of 35-40% for  $K_p < 2+$ . Above -500 Volts, however, the dawn probability decreases significantly while the dusk probability curve remains constant for quiet conditions ( $K_p < 2+$ ) but drops by almost a factor of ten. Only at low voltages does the dawn quiet time charging results. One should note from Figs. 3a and 2a that the dusk probability curve is the result of charging just before local midnight.

The low altitude results in Figure 3b show some additional interesting trends. For disturbed magnetic times, the dusk probability has a similar shape as both the disturbed and quiet, high altitude results with the probability values closer to those at the quiet times. In contrast, the dawn curve in Figure 3b is distinctly different from those in Figure 3a. Perhaps as striking is the null result for the dawn charging at quiet times for  $L < 6.6$ . Referring to Table I, the poorest satellite coverage is in this region of space. Nevertheless, the sampling is sufficient to suggest a very strong decrease in the charging probability near dawn during quiet times and at low altitude. We would estimate an upper limit of 0.1% probability of charging to -100 Volts for the post-midnight to dawn sector in Figure 3b.

#### SUMMARY OF SURVEY RESULTS

Based on the first 100 days of P78-2 operations, the SSPM charging results provided some extremely interesting preliminary results, both engineering and scientific. Using the Kapton voltage measurement as a monitor of the hot charging plasma environment, a number of preliminary conclusions can be reached. For those interested in differential charging in the earth's outer radiation belts, Figures 2a and 2b show some interesting patterns. That is, at a local time near 06 to 07 hrs at  $L > 7.5R_E$ , there is a 20% chance of charging Kapton greater than -100 Volts in magnetically disturbed conditions. The probabilities drop to approximately 10% and are located more toward post midnight as the magnetic conditions become quiet. However the highest charging levels occur in the dusk local time regions.

Figure 3 shows this a little clearer (especially Figure 3a) during disturbed conditions. The dawn local time shows the most variability in charging conditions. This is most likely related to dynamic plasma transport processes at work in this region of the earth's magnetosphere.

The final results should be most applicable to the engineering community interested in overall charging occurrences. If we combined all of the SSPM survey results into two categories, quiet ( $K_p < 2+$ ) and disturbed ( $K_p > 2+$ ) magnetic conditions, the probability of differential charging of Kapton greater than -100 Volts is 8.4% and 19.9% respectively. For levels greater than -1000 Volts, the probabilities drop 0.064% and 0.80% respectively. This means on the average for a spacecraft flying in a high altitude orbit similar to the P78-2 satellite, when the global magnetic 3 hour index  $K_p$  is greater than 2+, there is almost a 20% chance of charging a dielectric similar to kapton to voltages over -100 Volts if that material is shadowed by the spacecraft.

We must caution the reader, however, that most of the satellite coverage for this time period is biased toward high altitude dawn local time samples. There are regions in space and magnetic activity that are not covered by these 104 days and would require at least a year's worth of processed data to begin to provide adequate statistics of spacecraft charging for long term space missions.

#### REFERENCES

1. Mizera, P. F., Koons, H. C., Schnauss, E. R., Croley, D. R., Jr., Kan, H. K. A., Leung, M. S., Stevens, N. John, Berkopce, F., Staskus, J., Lehn, William L., Nanewicz, J. E.: First Results of Material Charging in the Space Environment. Appl. Phys. Lett., 37, 276, 1980.
2. Mizera, P. F., Leung, M. S., Kan, H. K. A.: Laboratory and Space Results from the SSPM Experiment. Accepted for Pub., J. Spacecraft and Rockets, 1980.

TABLE I SSPM SURVEY COVERAGE FOR THE FIRST 104 DAYS  
NUMBER OF SAMPLES (64 SEC)

MLT (hrs)	L < 6.6		L > 6.6		TOTAL
	$K_p < 2+$	$K_p > 2+$	$K_p < 2+$	$K_p > 2+$	
0-6	908	1,202	18,836	22,427	43,373
6-12	2,910	4,512	15,500	18,449	41,371
12-18	9,785	12,816	1,399	2,252	27,252
18-24	9,304	9,695	4,128	5,277	28,404



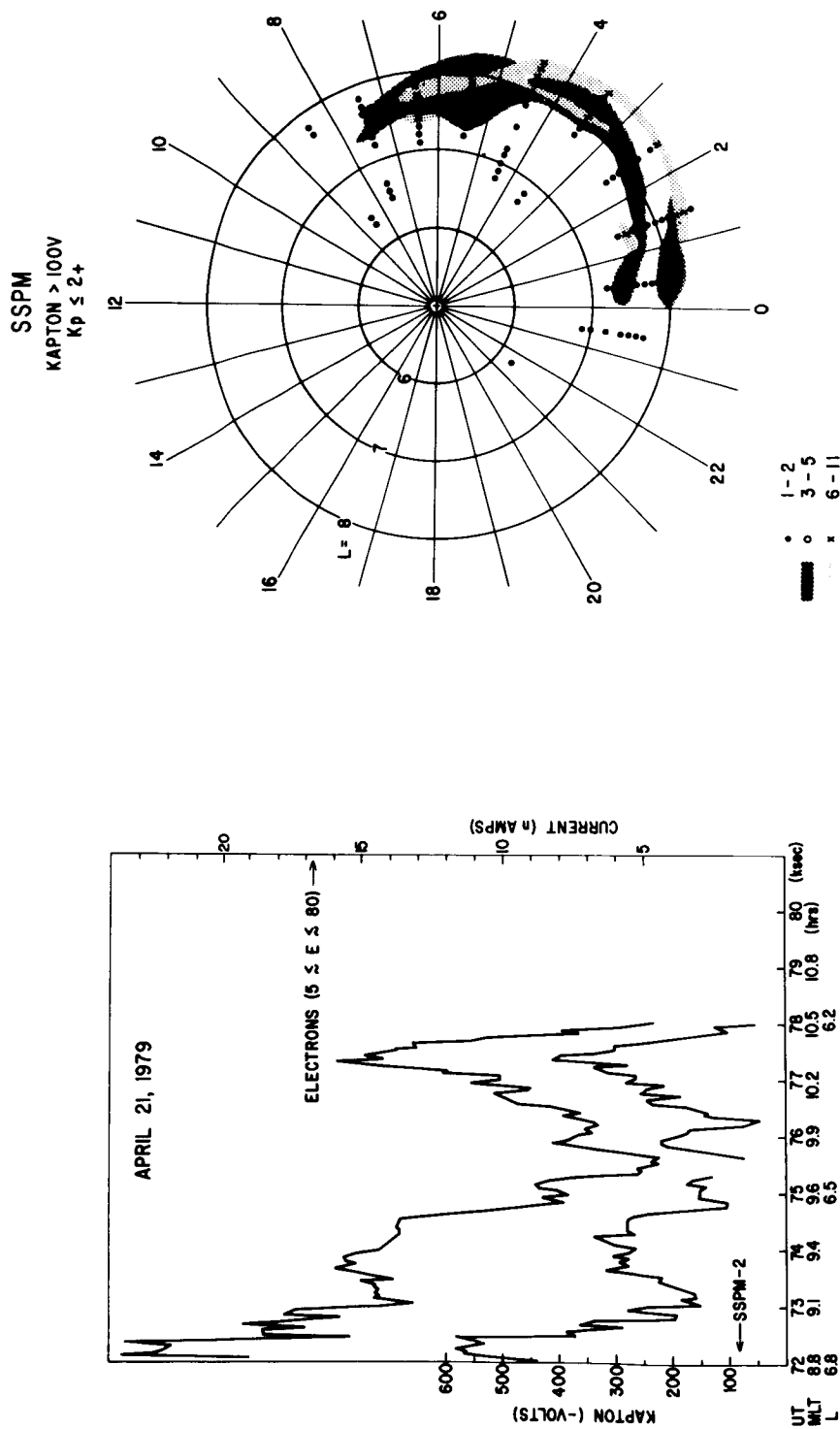


Fig. 1 -- Charging current from electrons with  $5 < E < 80$  KeV and Kapton voltages for a post-dawn pass on April 21, 1979. The electron current is calculated from the average  $90^\circ$  pitch angle spectrum and the SSPM-2 Kapton voltage is the maximum value reached in a 64 sec sampling interval.

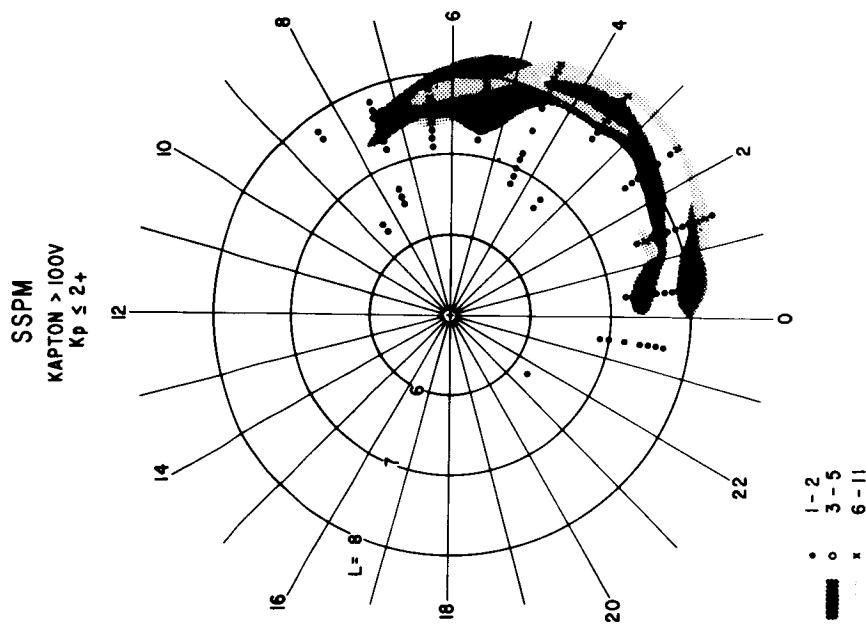


Fig. 2a -- The symbols represent the number of days when the SSPM-2 Kapton sample charged above -100 Volts sorted into 1 hour local time and 0.1 L shell bins. Only events where there was charging at least 5% of the time were considered valid observations. The cross-hatched contours represent approximately a 5% and 10% probability of charging.

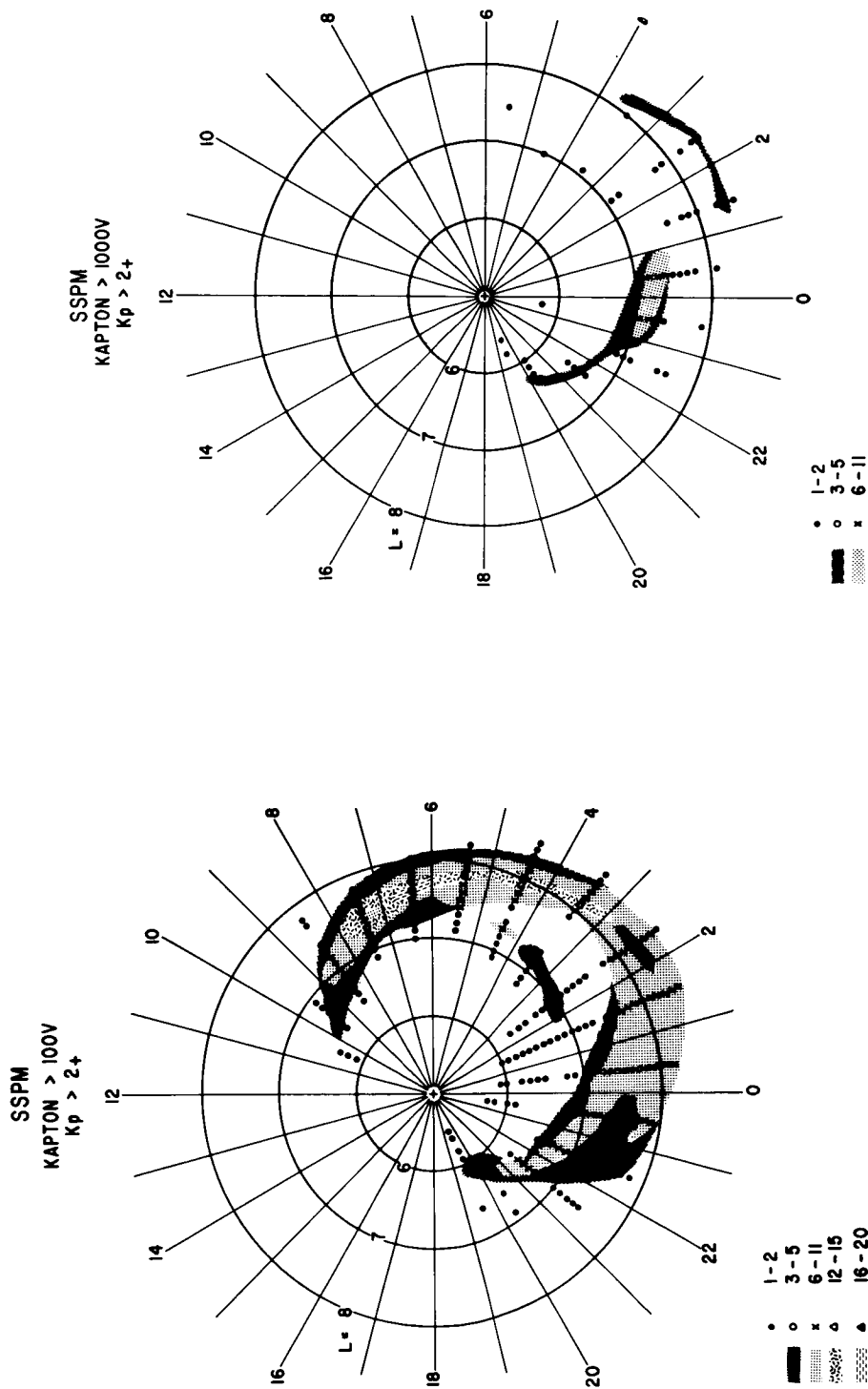


Fig. 2b -- Same as Fig. 2a but for disturbed times defined as  $K_p > 2+$ . The charging probabilities increase to 20% in the 6-7 hr. local time region.

Fig. 2c -- The number of days when the SS PM-2 Kapton charged to greater than -1000 Volts during disturbed magnetic conditions. The maximum occurrence is  $\approx 10\%$  near local midnight and includes eclipse passes.

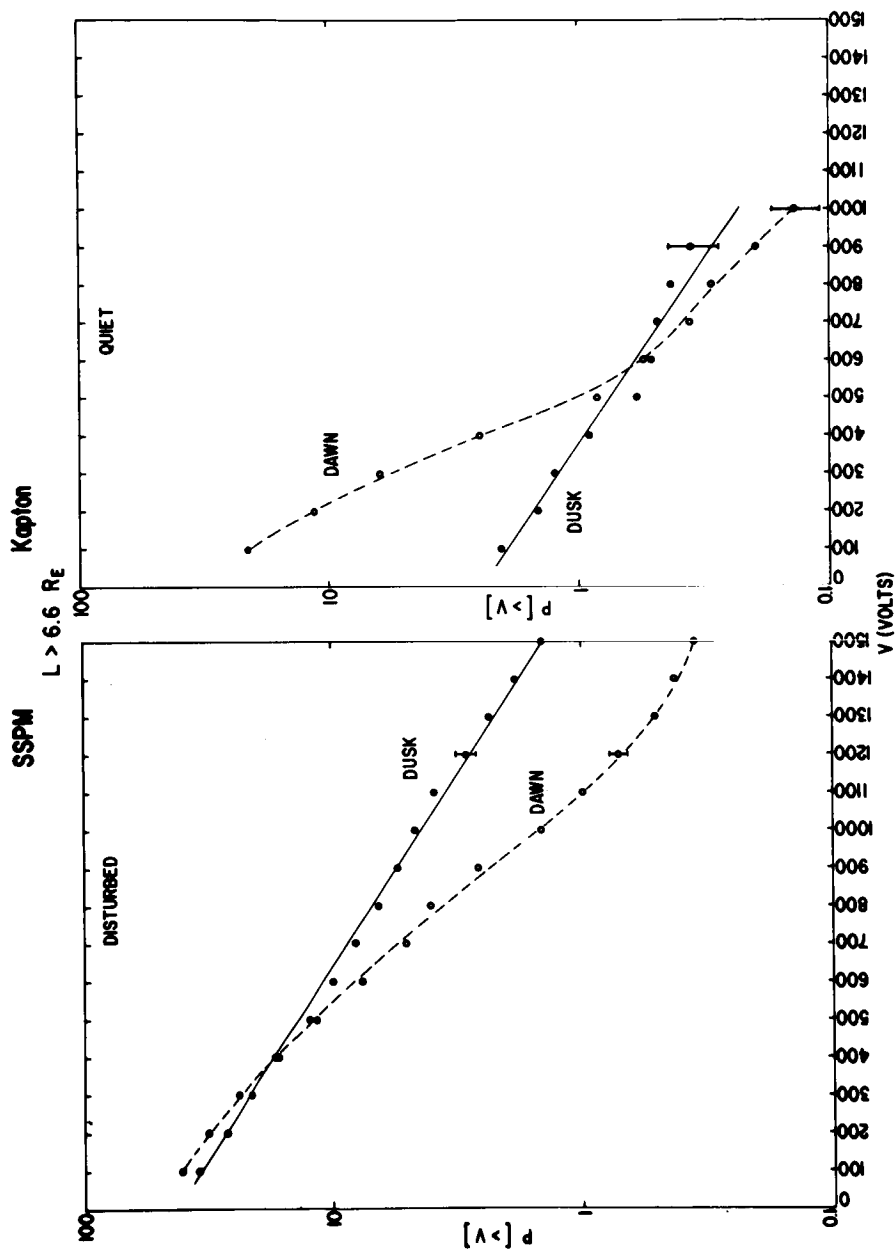


Fig. 3a -- Percentage probability of charging greater than  $V$  for high altitudes ( $>6.6 R_E$ ) sorted into disturbed ( $K_p > 2+$ ) and quiet ( $K_p \leq 2+$ ) magnetic times covering 0-6 hrs postmidnight and 18-24 hrs premidnight local times. The curves are labelled dawn and dusk respectively.

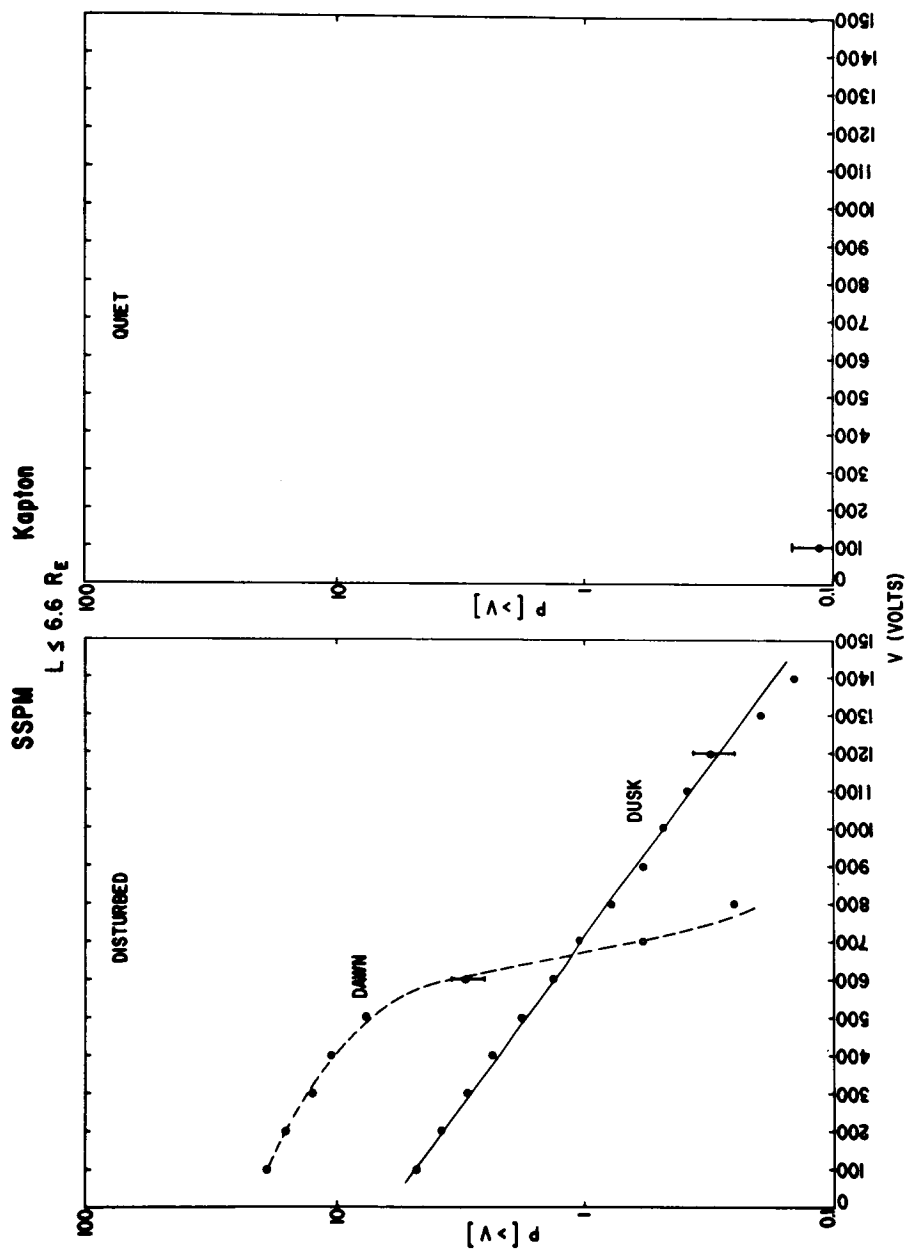


Fig. 3b -- Low altitude ( $\sim 6.6 R_E$ ) charging probabilities for postmidnight and premidnight local times again sorted into disturbed and quiet times and labelled dawn and dusk respectively.

## **PRELIMINARY ANALYSIS OF DATA FROM SRI INTERNATIONAL TRANSIENT PULSE MONITOR ON BOARD P78-2 SCATHA SATELLITE**

**S. A. Damron, R. C. Adamo, and J. E. Nanevich  
SRI International**

To further the understanding of the phenomena associated with electrostatic charging of satellites, the U.S. Air Force and N.A.S.A. have undertaken a joint program called "Satellite Charging at the High Altitudes" (SCATHA). The program addresses a problem of great concern to agencies which operate satellites, the occurrence of electrostatic discharges thought capable of causing various undesirable effects including deleterious transients in electronic circuits on satellites (see Ref. 1). The program's P78-2 satellite carries instruments on a nearly geosynchronous orbit to monitor the high altitude plasma environment and to study the effects of the interaction of this environment with the orbiting satellite. One of these instruments is the SRI Transient Pulse Monitor (TPM) which detects and characterizes the transient electromagnetic signals induced in selected circuits inside the P78-2 (Ref. 2, 3). As a transient detector, the TPM serves several purposes: it records the occurrence of transient signals, it indicates the number of transients observed, and it gives the peak amplitude of the largest transient during each second's interval. In recording the times of transient occurrences, the TPM alerts investigators to periods during which environmental factors

could have caused electrical upsets within the spacecraft. By measuring the intensity and amplitude characteristics of the transients induced in the internal circuitry, the TPM empirically indicates the kinds of electric transients to which spacecraft systems may be subjected.

The TPM detects and characterizes all transients induced in four selected circuits within the P78-2 including transients generated by switching of internal electrical circuits of the spacecraft and by electrostatic discharging on the outside of the craft. In general, most of the early data from the TPM contain pulses associated with internal electrical activity. The data also contain evidence of electrostatic charging on the surface of the P78-2. A very significant finding from analysis of early data is that periods of external discharging do not necessarily coincide with periods in which high potentials are measured on the satellite's surface.

### **TPM OPERATION**

The TPM, described in References 2 and 3, has four sensors which run from various locations inside the satellite to a processing unit. Two sensors measure the transient signals induced in a pair of

specially installed wires which run in an internal Faraday cage containing the command distribution wires. One of these instrumented wires is terminated with a high impedance (High-Z channel), the other with a low impedance (Low-Z channel). The other two sensors measure the signals induced in two selected wires of the regular spacecraft circuitry. The first wire connects the solar array to the power conditioning unit (Array channel). The second wire is the "single point" ground lead from the power conditioning unit (Ground channel) (see Figure 1). The TPM processing unit monitors the four sensors continuously and during each second indicates the negative and positive peak pulse amplitudes of the pulses that occur within that one-second interval. It also indicates the integral of the observed transient signal over the one second interval, and counts the number of times the signal exceeds a preset threshold during the second. For a more detailed description of TPM operation see References 4 and 5.

#### DATA ANALYSIS

In orbit, the TPM records a large number of transient pulses every day. Transients generated by internal electrical operation account for the majority of these pulses. As examples, a clocking pulse produces periodic glitches on the High-Z and Low-Z channels; automatic switching on the power conditioning unit causes random pulses on the Array and Ground channels; and, responses to certain commands issued from ground stations to the satellite cause noise pulses on various monitored channels. In the data analysis so far it has not been possible to devise a scheme for unequivocally identifying and eliminating

all of the random transients that power conditioning activity induces in the Array and Ground sensors.

However, a method has been found to identify and eliminate the internally generated pulses observed on the High-Z and Low-Z sensors (see Ref. 6). Two traits characterize the pulses which remain after this elimination: they appear simultaneously on at least the High-Z and Low-Z peak amplitude sensors, and they are electrically bipolar on these two channels. Since no identifiable internal transients cause pulses of this type, it has been concluded that the pulses result from electrostatic discharges on the spacecraft. The fact that several of these TPM discharge detections have coincided with discharges measured by the SC1-8B transient detector on the exterior of the P78-2 supports the validity of the internal-pulse elimination technique and the claim that the selected pulses do, in fact, result from electrostatic discharges on the exterior of the satellite.

In comparing the TPM results to other transient discharge data, it is interesting to note that the 1973 predecessor to the TPM on another geosynchronous satellite (see Refs. 2 and 7) recorded a diurnal distribution of discharge transients very similar to the distribution seen by the TPM on the P78-2. Figure 2 shows the diurnal distribution of external transient pulse occurrences from about forty days of TPM data. The distribution in both eclipse and non-eclipse orbits demonstrates a tendency for discharges to occur in the night time hours (satellite Local Time), especially after midnight. Although discharges measured on the 1973 satellite were measured on the vehicle's exterior,

they show the same diurnal grouping of pulses in the midnight period. From the data analyzed so far, the TPM senses a daily average of two or three pulses attributable to discharges.

On several days in 1979 there were short periods in which large numbers of discharges occurred. On days 118, 119, and 120 the periods of high discharge activity coincided with or followed shortly after satellite eclipse periods. However, other highly active days, such as days 136, 140, and 146, were after the Spring, 1979 eclipse season. Figure 3 shows the TPM data record of the early part of the first command session of day 146 on which several discharges took place. The Figure shows all five channels of data generated by each of the four sensors the TPM monitors for forty minutes of time. Above the TPM data at the top of the Figure are five rows of ticks indicating issuance of control commands to the satellite and showing unedited SCl-8 transient detector responses; the regular ticks below the TPM data are minute marks in earth time. The very top row of ticks shows the times that commands were issued from a ground station. Each of the other top four rows presents the output of one of the four sensors associated with the SCl-8 transient detector. From top to bottom, these are a sensor on a digital command line, on a harness wire, looped around the command distribution wires (there are no ticks for this row in this particular example), and at the end of a two meter boom (see Ref. 8). A tick on one of these rows corresponds to a non-zero datum at that time for one of the four sensors. As with the

TPM, many of the SCl-8 pulses correspond to internal electrical switching.

Under the five rows of ticks are three lines of data for each TPM sensor (twelve lines total). The top line of each set of three lines indicates the peak amplitude of the largest pulse during each second's interval for both positive and negative signals; the next line down gives the integral value of the positive and the negative pulses over a second's period; and, the bottom line shows the number of times the preset threshold was exceeded during the same second. The scales for each channel are shown on the left. The High-Z and Low-Z sensors measure induced voltages on the internal command wires and the Array and Ground sensors measure the currents induced in loops around the wires they monitor. Hence the peak amplitude scales are in volts and amperes and their integrals are in volt-microseconds and ampere-microseconds, respectively. Beneath the data are minute and ten-minute ticks in earth time, as well as the beginning and ending times of the plot in both Universal Time (UT) and satellite Local Time.

The nine small bipolar pulses labeled one through nine in Figure 3 starting at about 0:42 UT on the High- and Low-Z peak channels indicate external electrostatic discharges occurring late in the first hour of the day. Four of the pulses measured by the TPM on day 146, the second, third, seventh and ninth pulses, occurred simultaneously with pulses recorded by the SCl-8B. The second and seventh pulses occurred when the SCl-8 was monitoring its

outside sensor. These are two of the pulses which both the TPM and the SCl-8 have identified independently as resulting from external discharging. It should be noted that, because the electric coupling from the exterior of the satellite through the frame to the sensors is not known at this time, it is not possible to estimate the amplitude of the discharges these pulses represent. They do give some idea of the magnitudes and rates of occurrence of the electrical transients observed in a well-shielded portion of this particular vehicle during a period of frequent electrostatic discharge. Usually the High-Z sensor measures up to one-half volt and the Low-Z sensor measures up to five volt peaks during discharging activity. Background activity in Figure 3 typifies the conditions observed in periods of normal satellite operation. In spite of the large number of pulses attributed to external discharges on day 146, it is interesting to note that the potentials measured on the spacecraft were only in the few hundred volt range on this day.

On day 43, which was one of the year 1979's quietest days geomagnetically, the TPM recorded two pulses (see Table 1). This Table is a raw data tabulation of the pulse amplitudes observed on each sensor by the TPM and the time when the pulses occurred. In the 1973 satellite data, a strong correlation between geomagnetic activity and the frequency of discharges was observed (Ref. 7), but it was also found that discharges occurred even on undis-

turbed days. The TPM data for day 43 again shows that discharges do occur on "quiet" days.

Day 120, the last day of P78-2's spring eclipse season for 1979, has the longest sustained period of discharges seen by the TPM in the data analyzed so far (see Table 2). The pulses on Day 120 fall into two main clusters. The first cluster occurs just after the penumbral eclipse at midnight Local Time and the other after about three in the morning Local Time. This second cluster seems to correspond with a satellite charging event, but again the charging was only in the several hundred volt range.

In contrast, when the potentials measured on the satellite on day 114 reached the several kilovolts level, the TPM recorded no discharges. On most other days when large potentials were measured, the TPM, with few exceptions, also indicated little activity. One exception was day 113 on which the TPM measured discharges at about the same time the spacecraft was at a potential of one kilovolt. Generally, though, discharge activity is no more likely during periods of high measured satellite frame potentials than it is during periods of low measured potentials.

The relation of transients recorded by the TPM to spacecraft spin orientation has not been established definitely. Some of the data suggest that pulses of like amplitudes might be occurring with a periodicity corresponding approximately to the

---

\* It should be noted that, unlike the TPM, the SCl-8 system does not continuously monitor all of its sensors. Instead the processing electronics is periodically switched from sensor to sensor. Thus the same pulse is never indicated on more than one SCl-8 channel.



one minute spin period of P78-2. If this is true, it would indicate that some of the discharge activity could be associated with specific spacecraft geometries and positions relative to the flux of photons from the sun. A more thorough analysis of the discharges and the spin orientations is needed before this relationship can be validated. Over the span of several active discharge periods, however, no general spin dependency has been observed. This is a departure from the general correlation of spin orientation and discharge occurrence observed by the SRI pulse counting instrument flown in 1973 (see Ref. 7).

#### CONCLUSIONS

On the average, the TPM observes two to three pulses per day which can be attributed to discharges on the exterior of the P78-2 space vehicle. The discharges tend to occur in spurts, with an hour or two of discharging activity followed by several days of quiet. Generally, the pulses occur in the late night and morning periods. So far there has been little correlation between the potentials measured on the satellite frame and discharge activity. This indicates that the charging processes that lead to high frame potentials are not necessarily the ones that lead to the generation of discharges. In addition, TPM data analyzed thus far seems devoid of the general correlation between spin orientation and discharge occurrence which had been observed in 1973 on another high altitude satellite. This suggests that spacecraft discharge activity depends in large part upon the design and construction of each individual craft.

The TPM operating on the P78-2 satellite is adding to the under-

standing of the electrostatic discharge phenomenon on high altitude spacecraft. As a piggyback instrument it represents a cost effective manner of gathering empirical discharge data. From the data analyzed so far, the TPM has shown the times of occurrence and amplitudes of electrical transients caused by electrostatic discharges on the P78-2 satellite, a well shielded space vehicle. The data also appear to indicate that certain characteristics of the discharges may be different from one craft to the next. Generating and analyzing more data of the general kind produced by the TPM on satellites of different geometries and constructions will help to provide spacecraft engineers with the information needed to design satellites to withstand electric system upsets caused by electrostatic discharges.

#### REFERENCES

1. Nanevicz, J. E., and Adamo, R. C., "Occurrence of Arcing and Its Effects on Space Systems," Space Systems and Their Interactions with Earth's Space Environment, H. B. Garrett (ed.), Vol. 71 of Progress in Astronautics and Aeronautics.
2. Nanevicz, J. E., and Adamo, R. C., "Transient Response Measurements on a Satellite System," Proceedings of the Spacecraft Charging Technology Conference, AFGL-TR-77-0051, NASA TMX-73537 (24 February, 1977).
3. Adamo, R. C., and Nanevicz, J. E., "Development of the Transient Pulse Monitor (TPM) for SCATHA/P78-2," Spacecraft Charging Technology, NASA Conference Publication 2071, AFGL-TR-79-0082 (October 31 - November 2, 1978).

4. Hammeren, S. D., and Swanson, S. R., Telemetry Requirements Document -- STP P78-2 SCATHA Satellite, Western Test Range, Space and Missile Test Center, Vandenberg Air Force Base, Programs and Requirements Department, Contract No. F04703-77-C-0111 (April, 1978).

5. Adamo, R. C., TPM Quick-Look Data Interpretation, SRI International, Menlo Park, California (July, 1978).

6. Adamo, R. C., TPM Data Analysis Status Report, Quarterly Report prepared for Science Applications, Inc., Contract No. F04701-80-C-0009, SRI Project 1540, SRI International, Menlo Park, California (March, 1980).

7. Shaw, R. R., Adamo, R. C., and Nanevich, J. E., "Observations of Electrical Discharges Caused by Differential Satellite-Charging," Spacecraft Charging by Magnetospheric Plasmas, Alan Rosen (ed.), American Institute of Aeronautics and Astronautics with The MIT Press, Cambridge, Massachusetts (© 1976).

8. Koons, H. C., Characteristics of Electrical Discharges on the P78-2 Satellite (SCATHA), presented at the AIAA 18th Aerospace Sciences Meeting, Pasadena, California, January, 1980.

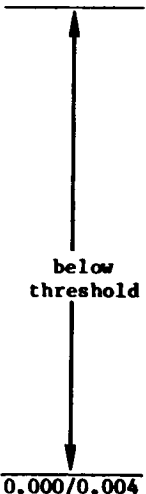
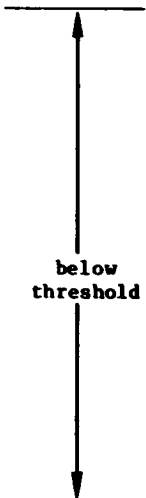
Table 1  
TPM Pulse List

Day 043 1100-1500 UT

Universal Time		Local Time		Peak Amplitude Channels			
Sec	HH.MMSS	Approx.	Dec. Hr.	+LO Z/-LO Z (V)	+HI Z/-HI Z (V)	+ARRAY/-ARRAY (A)	+GRND/-GRND (A)
44425	12.2025	4.432		0.094/0.106	0.792/0.792	below	below
44968	12.2918	4.583		0.186/0.201	2.457/1.622	threshold	threshold

Table 2

Day 120 0500-1100 UT

Universal Time		Local Time		Peak Amplitude		below threshold	below threshold
Sec	HH.MMSS	Approx.	Dec. Hr.	+LO Z/-LO Z (V)	+HI Z/-HI Z (V)		
18184	5.0304	23.427		0.123/0.081	1.293/1.155		
18413	5.0653	23.484		0.811/0.781	5.227/5.637		
20953	5.4913	.118		0.304/0.252	4.168/2.752		
21267	5.5427	.196		0.271/0.225	3.722/2.650		
21405	5.5645	.230		0.084/0.056	1.343/0.921		
21662	6.0102	.293		0.179/0.143	2.194/1.817		
22091	6.0811	.392		0.282/0.160	3.081/1.293		
23025	6.2345	.607		0.304/0.252	4.013/3.081		
23720	6.3520	.766		0.304/0.233	3.865/2.650		
23942	6.3902	.817		0.216/0.216	2.551/1.959		
24448	6.4728	.933		0.396/0.242	3.451/1.749		
24641	6.5041	.978		0.242/0.186	1.886/0.956		
25027	6.5707	1.066		0.304/0.225	2.752/1.343		
25481	7.0441	1.167		0.304/0.235	2.752/1.395		
26838	7.2718	1.458		0.340/0.233	3.081/1.448		
35123	9.4523	3.153		0.282/0.193	2.551/1.245		
35495	9.5135	3.226		0.293/0.186	2.650/1.343		
36246	10.0406	3.374		0.326/0.201	3.081/1.448		
39279	10.5439	3.964		0.143/0.093	1.562/0.887		
40428	11.1348	4.189		0.396/0.206	3.584/1.504		

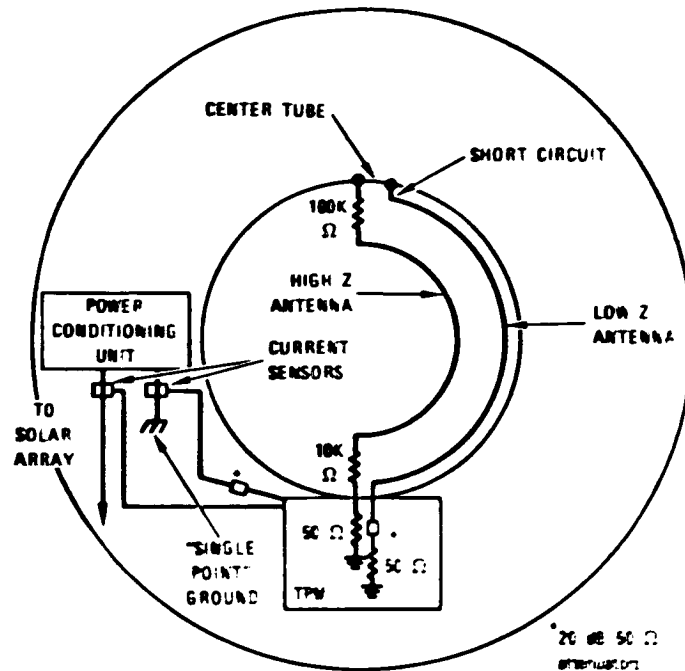


FIGURE 1 TPM SENSOR LOCATIONS ON P78-2

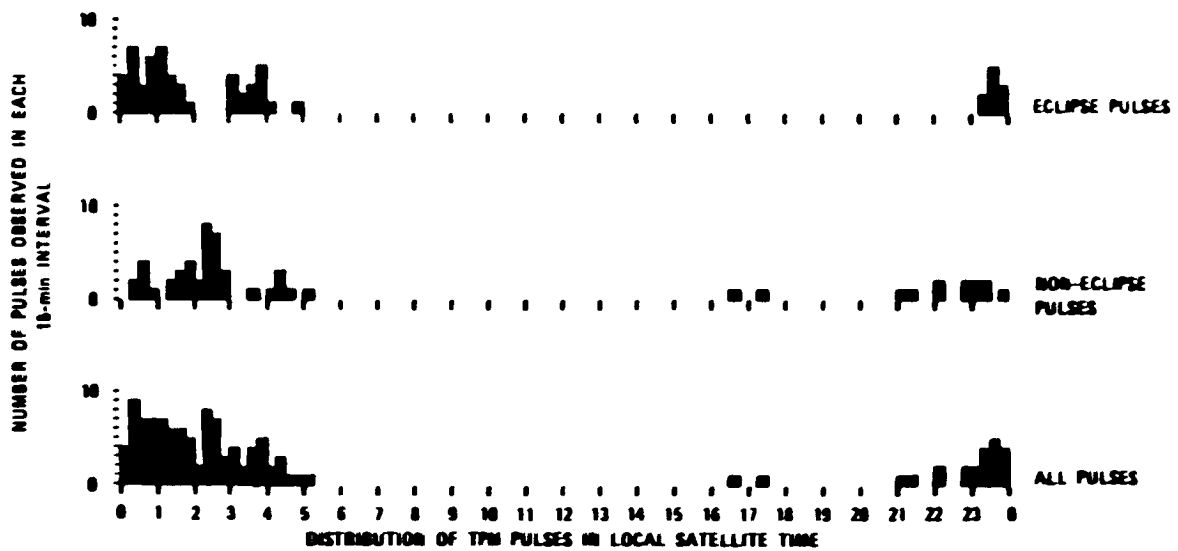


FIGURE 2 DISTRIBUTION OF PULSES OBSERVED BY THE SRI TPM

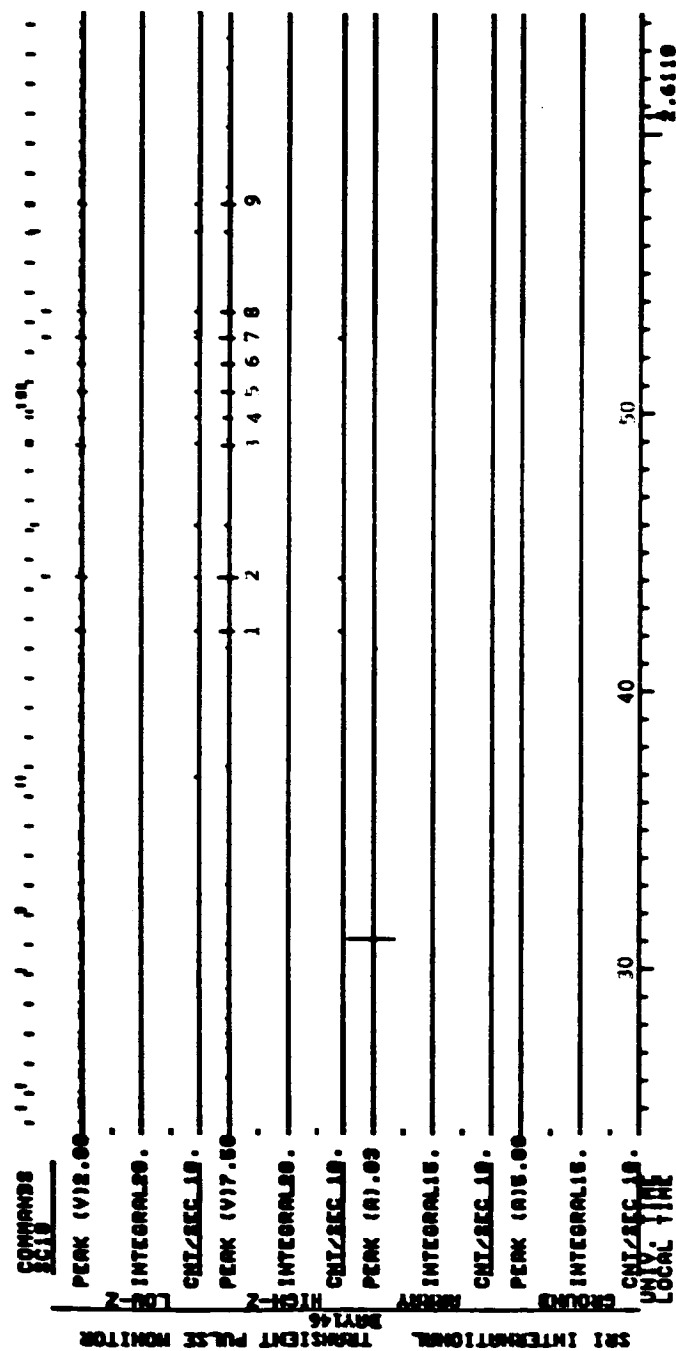


FIGURE 3 TPM DATA (DAY 146, 024:23 1:04:23 UNIVERSAL TIME)

# ASPECT DEPENDENCE AND FREQUENCY SPECTRUM OF ELECTRICAL DISCHARGES ON THE P78-2 (SCATHA) SATELLITE\*

Harry C. Koons  
The Aerospace Corporation

## SUMMARY

The SCATHA (P78-2) satellite payload includes a Charging Electrical Effects Analyzer (CEEA) to measure the characteristics of electrical discharges in both the frequency and time domain. Pulses are detected in response to commands, during electron and ion beam operations and during natural discharge events. The Pulse Analyzer which measures the shape of pulses on four sensors is the primary CEEA diagnostic for the natural discharges. To date 233 days of Pulse Analyzer data have been reduced. Nineteen pulses on ten different days have been related to natural discharges. Many of these related to the solar illumination of the vehicle. Two occurred shortly after the satellite exited the earth's umbra. On May 26, 1979 six pulses were detected in sunlight within a period of 14 minutes. All six occurred at precisely the same spin phase suggesting that a single point on the vehicle was breaking down. Only five discharges have been found in the data at a time when the Pulse Analyzer was in mode with sufficient time resolution to resolve the frequency components in the waveform.

## INTRODUCTION

The Charging Electrical Effects Analyzer (CEEA) was provided for the SCATHA (P78-2) satellite payload to verify that electrical discharges are occurring when other instruments measure large differential potentials between surface materials on the vehicle.

The CEEA consists of three instruments: the Pulse Analyzer, the VLF Analyzer, and the RF Analyzer. The Pulse Analyzer measures the number of pulses, their amplitudes and shapes on four sensors. The VLF Analyzer measures the electric and magnetic field spectra of waves in the frequency range from 100 Hz to 300 kHz. The RF Analyzer measures the electric field intensity on a 1.8-m monopole antenna in the frequency range from 2 to 30 MHz.

In this paper I present results from the Pulse Analyzer from 233 days between 7 February 1979 and 20 June 1980. This period covers quiet and active days, eclipses, and electron and ion beam operations. The instrument is described in the next section. Individual time periods of special interest are described in detail. In the final sections the aspect dependence and frequency spectrum of the natural discharges are described.

---

\*This work was supported by the U.S. Air Force under Contract No. F04701-80-C-0081.

## INSTRUMENT DESCRIPTION

The Pulse Analyzer measures the shape of electromagnetic pulses in the time domain from 7 ns to 3.7 ms. The pulse analyses are made on four sensors: (1) a loop antenna around one of the two redundant space vehicle Command Distribution Units, (2) a wire along the outside of a "typical" space vehicle cable bundle, (3) an external short dipole antenna at the end of a 2-m boom, and (4) a digital command line from the Command Distribution Unit to the Pulse Analyzer.

The signal processor may be switched by command to any of the four sensors. It then steps automatically through the selected sensors monitoring each in turn for 16 sec. The functional block diagram is shown in Figure 1. When a signal exceeds a commandable threshold its amplitude is sampled at 16 points to measure the pulse shape. The 16 samples may be spaced logarithmically or linearly in time. The logarithmic spacing covers the range from 7 ns to 492 s. The linear spacing is commandable with the following options: 0.015, 0.060, 0.24, 1.0, 3.8, 30, and 250 s. The amplitude is measured by a bank of 24 discriminators, 12 positive and 12 negative. The total range of the discriminator bank is 3 mV to 1.8 V. The signal from each sensor can be attenuated by command to place it within this range. There are six attenuation settings that select measurement ranges from 3 mV to 1.84 V at minimum attenuation to 3.46 V to 1910 V at maximum attenuation. The threshold is coupled to the attenuation setting. The attenuation, threshold, and sampling interval can be independently commanded for each sensor. The number of pulses per second above four selectable thresholds is also measured. Three of the thresholds are determined by the attenuation selection, the fourth is the pulse analysis threshold.

The instrument is commanded by a 22-bit serial magnitude command of which only the seven least significant bits are used.

In its normal mode of operation the instrument steps through each of four sensors monitoring each for 16 sec in sequence. The threshold and attenuations for each sensor are determined by experience on orbit.

Initial measurements have been made with the logarithmic sample spacing. Linear spacing (15 ns) have been used since October 1979 because typical pulses prove to be shorter than 200 ns.

Inflight verification of the calibration is accomplished by sending serial magnitude commands from the Command Distribution Unit to the serial magnitude command sensor.

## DATA

The Pulse Analyzer was turned on and successfully checked out on-orbit on February 5, 1979. Initial operations began with the pulse analysis threshold set at 0.651 V and the countrate thresholds set as shown in table 1, column 1. At this setting only two pulses were detected during the 72 hours of data available from February 12-14. Both of these pulses oc-

current during SC4-2 Ion Beam operations on February 14. The pulses had a width at half maximum of 500  $\mu$ s and an amplitude of 0.7 V.

Because it was apparent that very few pulses were being detected the threshold was lowered on February 18 to 0.165 V with the associated count-rate threshold listed in table 1, column 2.

At this threshold the analyzer occasionally responds to pulses generated when commands are sent to the vehicle. Pulses occurring within one second of a command are attributed to a vehicle or payload response to the command and are identified as Command Pulses in table 2.

An interesting variation to this is a pulse that occurs approximately 20 sec after the vehicle transmitter is turned off. These have been identified with the time that the ground station command transmitter ceases sending s-tones to the vehicle. They are identified as Command Pulses in table 2.

A second source of pulses is the antenna switch in the VLF Analyzer. This experiment is housed in the same package as the Pulse Analyzer. When the VLF antenna switches from the magnetic antenna to the electric antenna a pulse is detected on the Pulse Analyzer Command Line Sensor. This pulse occurs once every 64 sec. Since pulses are synchronized to the vehicle clock they can be readily identified and they have been eliminated from the distributions in table 2.

The majority of the remaining pulses listed in table 2 occur during the electron and ion beam operations.

#### NATURAL CHARGING EVENTS

Only 19 of the 2557 pulses cannot be associated with normal vehicle commands or ion and electron beam operations. A summary of these pulses is shown in table 3. Some of these pulses occurred during natural charging events that have been studied in detail.

On 28 March, a natural charging event occurred during eclipse. This event was unusual in that the satellite was in the earth's shadow over 1000 sec before an injection of hot plasma near local midnight charged the vehicle negatively. Figure 2 shows a composite of data from the Satellite Surface Potential Monitors (SSPM), the Pulse Analyzer, and the electron and ion detectors on the Sheath Electric Field Experiment (SEFE). The SSPM and SEFE instruments are described in reference 1. The differential potential between a Kapton sample and the vehicle frame is plotted as a function of time in the bottom panel. At the time the Kapton potential abruptly increases from background to over one kilovolt, the mean electron energy increases from about one kilovolt to greater than 20 kilovolts. About five minutes later a discharge was detected by the Pulse Analyzer. Later a second discharge and a decrease in the average Kapton potential occurred as the satellite crossed the terminator from shadow into sunlight. During this charging event, the vehicle frame increased to  $\sim -8000$  V and maintained a potential near  $-4000$  V until the spacecraft entered the sunlight. The data in fig-

ure 2 confirm that the spacecraft charging induced by energetic electrons produced significant differential potentials and electrical discharges. The low energy limit of the protons in figure 2 represents the potential of the spacecraft frame relative to the plasma environment. This is seen to fluctuate around  $\sim -4$  kV during the charging event. The potential between the Kapton sample and the plasma is found by adding the  $-4$  kV of the spacecraft frame to the Kapton voltage.

On May 26, 1979 a series of six pulses was detected by the Pulse Analyzer while the vehicle was in sunlight. These pulses occurred during the enhancement of the differential potential of a Kapton sample on the SSPM on the end of the vehicle (Fig. 3). At that time the spin axis of the vehicle made an angle of 90 deg with the sun-satellite line. At that angle the Kapton sample is shadowed by the vehicle and is not discharged by sunlight. The data from March 28 and May 26 demonstrate the correlation of eight of the 19 pulses with differential charging on the vehicle. These pulses are assumed to be discharges. These pulses were undersampled in the logarithmic time spacing mode being used at the time. Hence frequency information cannot be obtained from them.

Most of the remaining pulses occurred during time periods when the Kapton samples on the Satellite Surface Potential Monitors were charged. The amplitude distribution of the discharges is shown in figure 4. The location of the satellite at the time these pulses occurred is shown in figure 5 as a function of local time and radial distance. This distribution is certainly consistent with the local time dependence of circuit upsets on DoD and commercial satellites (ref. 2). The data from June 1980 plotted at afternoon local times in figure 5 demonstrate that discharges can also occur on the day side of the earth following moderate substorms.

The Boulder Geomagnetic Substorm Log lists a moderate substorm at 0745 UT on June 11, and a second onset at 2230 UT on June 11 followed by minor magnetic storm conditions throughout the day on June 12 and 13.

#### ASPECT DEPENDENCE

The six discharges detected on May 26 occurred at the time rotational phase of the vehicle. Since the vehicle was in sunlight this suggests that one location on the vehicle was arcing. Presumably this would occur when the potential difference suddenly increased as material on one side of the arc was discharged by photocurrent as it passed into sunlight.

In order to determine if discharges on other dates occurred at the same rotational phase the azimuth and elevation of the sun in spacecraft coordinates was calculated for a number of other discharges. The results are tabulated in table 4 and the direction to the sun for these discharges is shown on a schematic of the vehicle in figure 6. There is a large scatter in the data implying that the location and mechanism described above for the May 26 discharges are not the same for the others. The sun does tend to be 180 deg from the magnetometer boom suggesting that this boom plays a role in a significant number of the discharges. NASCAP models of the SCATHA satellite



show the largest differential potentials occur at the booms (N. John Stevens, private communication, 1980).

#### FREQUENCY SPECTRUM

Five discharge pulses have been detected with the pulse analyzer in a mode of operation with a linear sample spacing of 15 nanoseconds. It can then be used to measure the dominant frequency components in each pulse. A computer fit of the functional form

$$V = V_0 + \sum V_i e^{-k_i t} \cos(2\pi f_i t + \phi_i)$$

was made to the sixteen sample points. The parameters giving the best fit in the least squares sense are shown in table 5. For highly damped waveforms a decaying exponential term was also included in the sum. The data and fits are shown in figures 7 and 8. The pulses are quite different with dominant frequencies from 5 to 32 MHz and peak amplitudes from 0.08 to 0.89 V.

To date too few natural discharge pulses have been found to adequately characterize the discharges for the purpose of validating discharge coupling models and ground-based discharge tests using scale-sized models of the SCATHA satellite.

Pulses are also detected during normal vehicle operations and electron and ion beam operations.

On March 23, 1980, the Pulse Analyzer detected a pulse at 1411:36 UT during electron beam operations at 1.5 kV 1 ma. At 1424:20 UT a pulse due to the automatic antenna switch in the VLF experiment was detected. Both pulses were measured on the command sensor line in the high resolution mode. A computer fit was made to the pulse shapes of these pulses in order to compare them with the discharge related pulses. The parameters giving the best fit are shown in table 6.

For the pulse during electron gun operations that best fit was obtained for two frequencies. One of the two frequencies showed a slight growth rate while the other was slightly damped. The pulse shape is shown in figure 9. I believe that the appropriate conclusion is that the damping is very small and that the data set is too short to determine the damping coefficient.

For the antenna switch pulse the best fit was again obtained for two frequencies. The frequencies differ significantly from those obtained for the electron beam pulse and the natural discharges. The antenna switch pulse is shown in figure 9.

# REFERENCES

1. Stevens, J. R., and Vampola, A. L.: Description of the Space Test Program P78-2 Spacecraft and Payloads, SAMSO TR-78-24, 1978.
2. McPherson, D. A.; Cauffman, D. P.; and Schober, W. R.: Spacecraft Charging at High Altitudes: SCATHA Satellite Program, J. Spacecraft and Rockets, Vol. 12, No. 10, Oct. 1975, pp. 621-626.

Table 1

## PULSE ANALYZER SETTINGS

THRESHOLDS	TIME PERIOD				
	2/ 5/79 - 2/17/79	2/18/79 - 4/26/79	4/27/79 - 10/11/79	10/11/79 - 3/14/80	3/14/80 - date
Pulse Analysis, volts	0.651	0.165	0.327	0.327	0.165
Countrate CR0, volts	0.117	0.030	0.117	0.117	0.030
Countrate CR1, volts	1.85	0.469	1.85	1.85	0.469
Countrate CR2, volts	28.3	7.18	28.3	28.3	7.18
Countrate CR3, volts	0.651	0.165	0.327	0.327	0.165
Pulse Analysis Range, volts	0.05-29.2	0.014-7.43	0.05-29.2	0.05-29.2	0.014-7.43
Time State	Log	Log	Log	Linear(15ns)	Linear(15ns)

Table 2  
DISTRIBUTION OF PULSES DETECTED  
BY THE PULSE ANALYZER

MONTH	DAYS	THRESHOLD VOLTS	TOTAL PULSES	COMMAND PULSES	ELECTRON BEAM PULSES	ION BEAM PULSES	DIS- CHARGE PULSES
79 FEB	10	0.65	15	6	0	9	0
	11	0.17	66	66	-	-	0
MAR	25	0.17	519	249	175	93	2
APR	25	0.17	660	349	10	299	2
	4	0.33	48	47	-	-	1
MAY	30	0.33	238	232	-	-	6
JUN	26	0.33	328	180	148	-	0
JUL	5	0.33	33	28	-	5	0
AUG	9	0.33	46	45	-	-	1
SEP	5	0.33	34	33	-	-	1
OCT	7	0.33	74	41	33	-	0
NOV	22	0.33	134	134	-	-	0
DEC	31	0.33	219	219	-	-	0
80 JAN	17	0.33	101	100	-	-	1
APR	1	0.17	1	0	-	-	1
JUN	6	0.17	41	37	-	-	4
TOTAL	234		2557	1766	366	406	19

Table 3  
SUMMARY OF DISCHARGES

DATE	UT	LOCAL TIME	RADIUS	KAPTON POTENTIAL	COMMENTS
	SECONDS			VOLTS	
28 MAR 79	59851	23.8	6.3	-1725	ELECTRON INJECTION
28 MAR 79	62088	0.4	6.5	-1689	UMBRAL EXIT + 50 SEC
14 APR 79	39940	0.2	6.7	-400	ECLIPSE
18 APR 79	82767	10.8	6.3	NONE	
30 APR 79	25616	1.2	7.4	-840	ONE SAMPLE $\neq 0$ (0.2v)
26 MAY 79	02641	2.6	7.8	-1098	} SAME SPIN PHASE
26 MAY 79	02756	2.7	7.8	-1049	
26 MAY 79	02928	2.7	7.8	-1074	
26 MAY 79	03158	2.7	7.8	-1061	
26 MAY 79	03387	2.8	7.8	-1012	
26 MAY 79	03444	2.8	7.8	-1061	
9 AUG 79	02095	2.3	6.7		
18 SEP 79	35981	1.5	6.2		
24 JAN 80	03082				
16 APR 80	22281	0.5	7.2		UMBRAL EXIT + 92 SEC
13 JUN 80	04322	14.0	5.3		
13 JUN 80	06750	15.0	5.6		
14 JUN 80	09770	16.7	5.6		
20 JUN 80	20132	21.6	7.2		

**Table 4**  
**SOLAR DIRECTION IN SATELLITE COORDINATES**  
**AT TIME OF PULSE**

DATE	UT	ELEVATION	AZIMUTH *
	SECONDS	DEG	DEG
28 MAR 79	59851	90.7	19.4
28 MAR 79	62088	90.7	12.6
14 APR 79	39940	84.7	91.5
18 APR 79	82767	88.7	307.9
30 APR 79	25616	87.2	287.2
26 MAY 79	02641	90.3	265.4
26 MAY 79	02756	90.3	263.8
26 MAY 79	02928	90.3	264.5
26 MAY 79	03158	90.3	261.3
26 MAY 79	03387	90.3	264.3
26 MAY 79	03444	90.3	266.6
9 AUG 79	02095	86.0	51.5

\*Measured counterclockwise from +z axis in spacecraft coordinate system.

Table 5  
NATURAL DISCHARGE FITTING PARAMETERS

Date	UT	Sensor	i	Frequency	Amplitude	Damping	Phase
	Seconds			MHz	volts	$\text{ns}^{-1}$	deg
1/24/80	03082	CMD	0		0.01		
		Line	1	5.0	0.38	$3.4 \times 10^{-4}$	112
			2	25.7	0.13	$1.5 \times 10^{-2}$	-3
4/16/80	22281	Dipole	0		0.00		
			1	11.1	0.89	$2.2 \times 10^{-2}$	29
			2	25.0	0.68	$7.7 \times 10^{-3}$	173
6/13/80	06750	Harness	0		0.08	$9.4 \times 10^{-3}$	
		Wire	1	19.5	0.25	$6.3 \times 10^{-3}$	175
			2	31.8	0.80	$2.1 \times 10^{-2}$	-66
6/14/80	09770	Dipole	0		0.00		
			1	13.3	0.06	$1.6 \times 10^{-2}$	103
			2	26.1	0.08	$2.5 \times 10^{-2}$	79
6/20/80	20132	Dipole	0		0.24	$6.9 \times 10^{-2}$	
			1	21.7	0.12	$5.0 \times 10^{-2}$	21

Table 6  
PULSE FITTING PARAMETERS

DATE	UT	Sensor	i	Frequency	Amplitude	Damping	Phase
	Seconds			MHz	volts	ns <sup>-1</sup>	deg
ELECTRON GUN PULSE							
3/23/80	51096	CMD Line	0		-0.003		
			1	14.1	0.089	+3.57 x 10 <sup>-3</sup>	182.4
			2	26.4	0.140	-1.32 x 10 <sup>-3</sup>	46.9
VLF ANTENNA PULSE							
3/23/80	51860	CMD Line	0		-0.007		
			1	9.0	0.397	3.67 x 10 <sup>-2</sup>	45.6
			2	16.0	0.135	3.95 x 10 <sup>-3</sup>	227.3

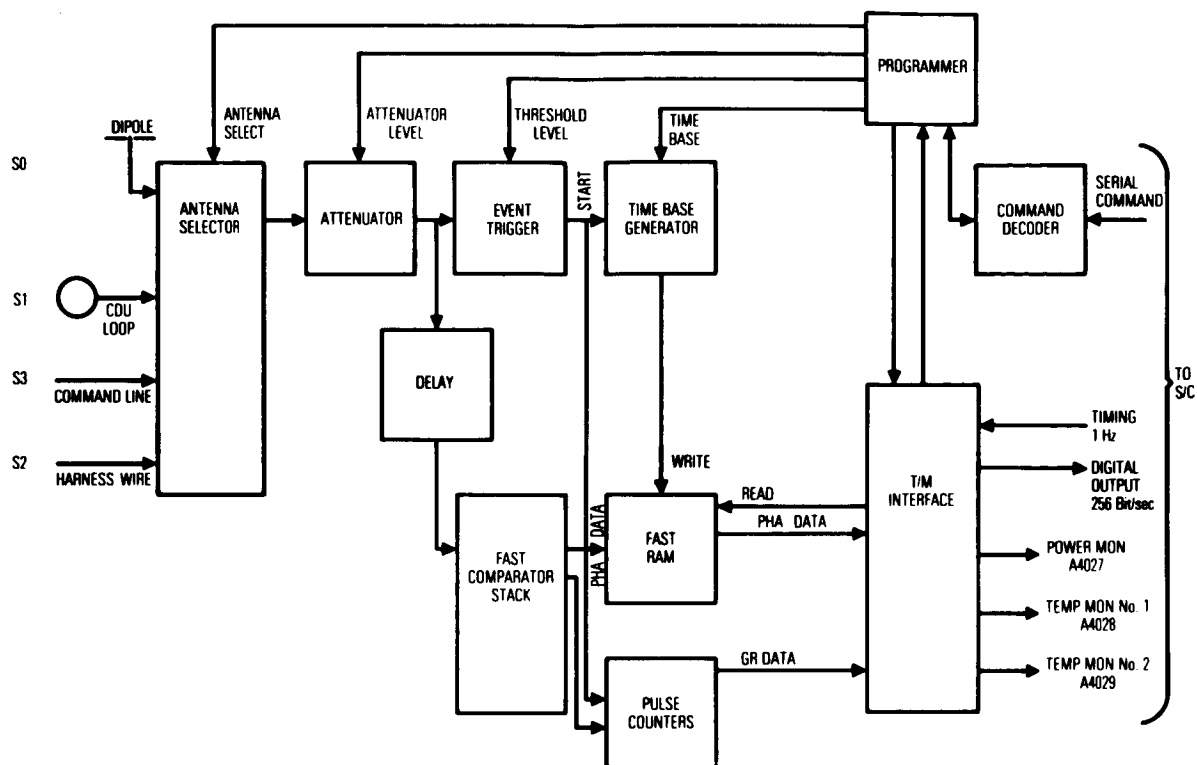


Figure 1

### P78-2 Charging Event in Eclipse

28 MARCH 1979

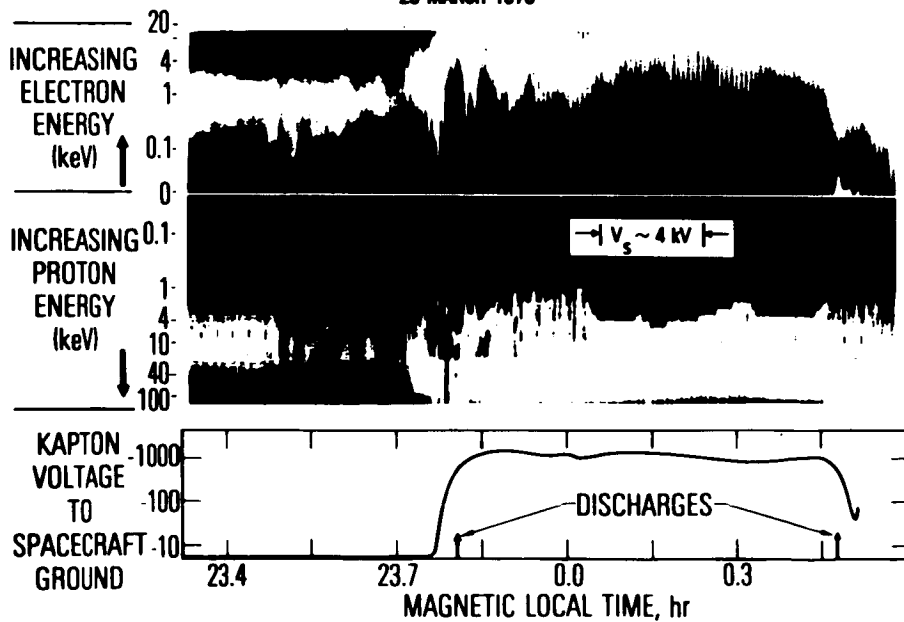


Figure 2

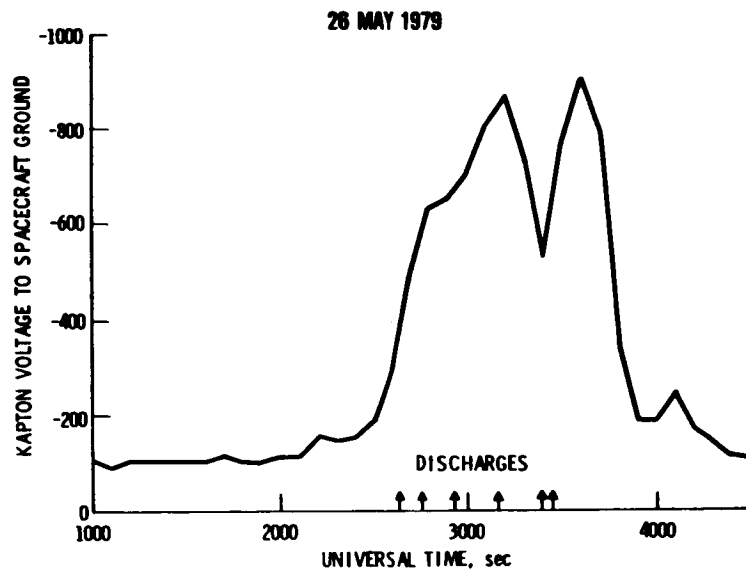


Figure 3

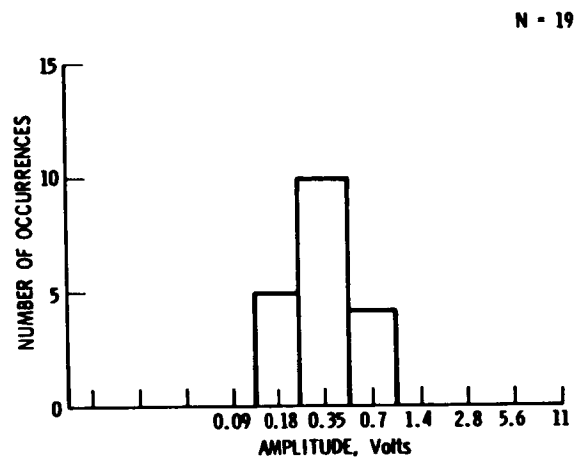


Figure 4



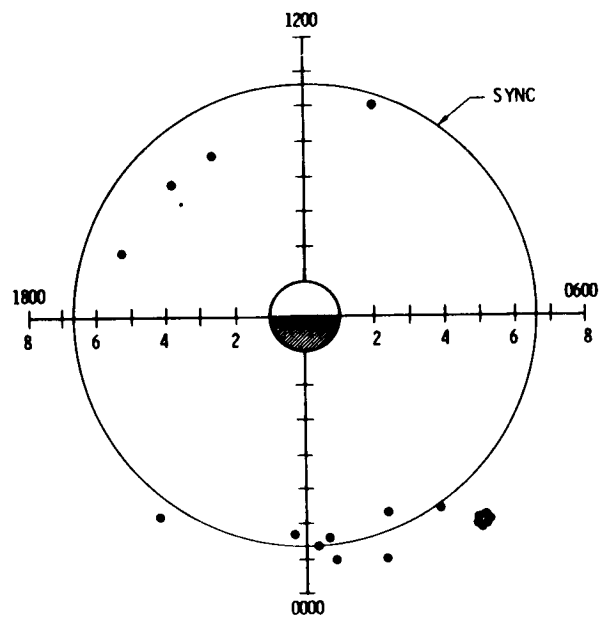


Figure 5

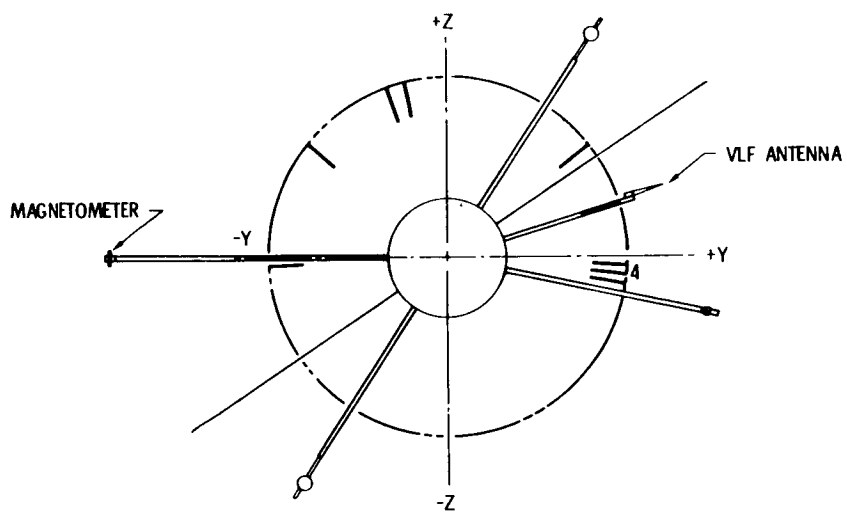


Figure 6

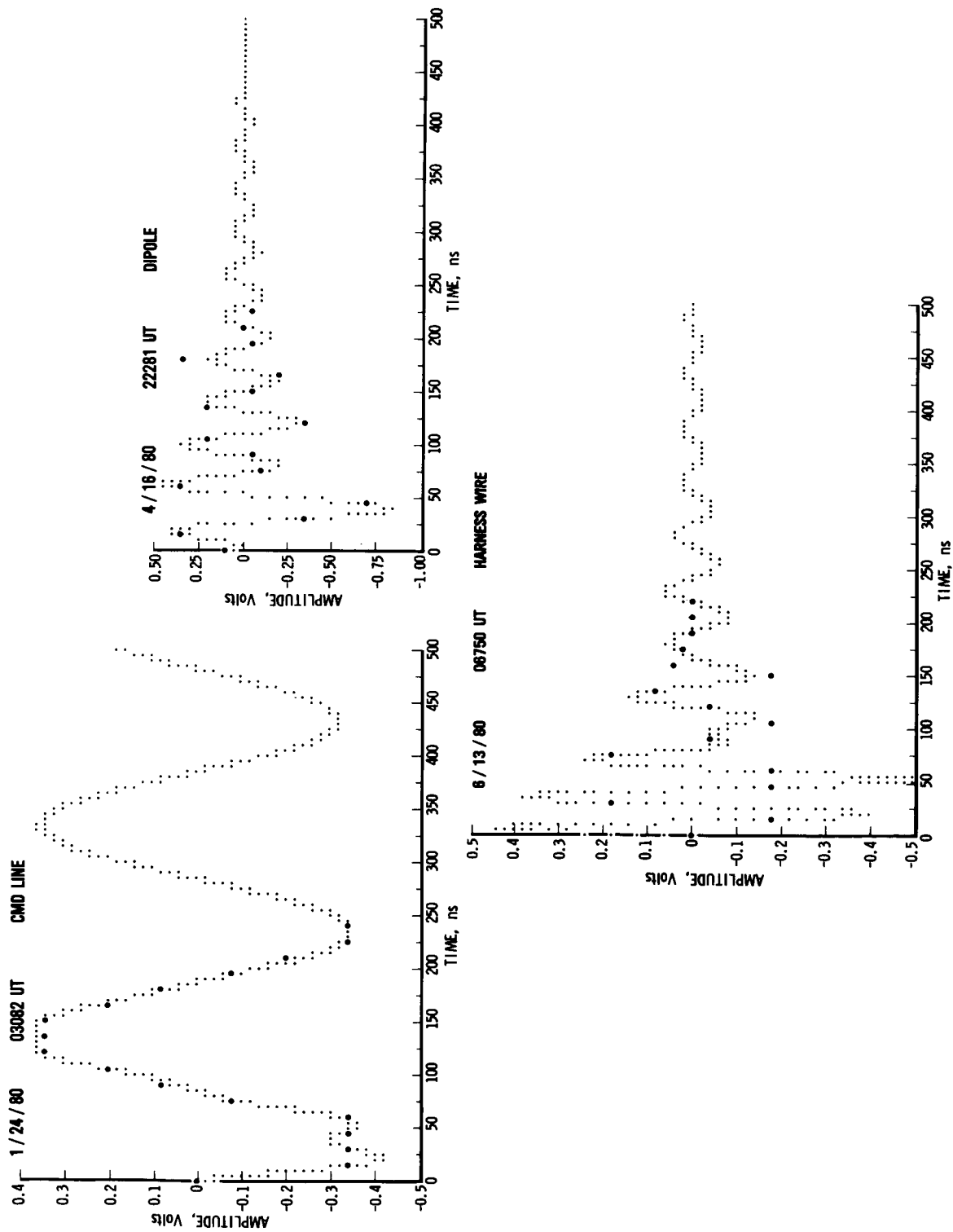


FIGURE 7

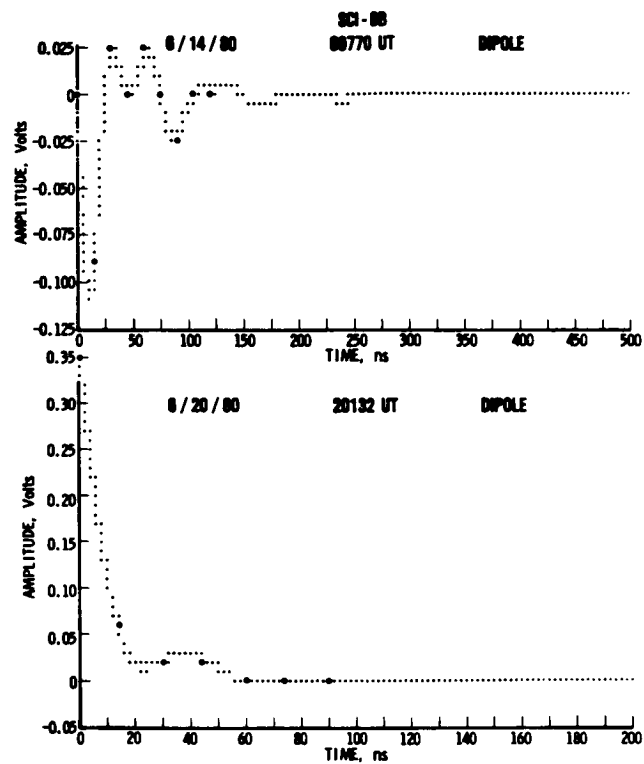


Figure 8

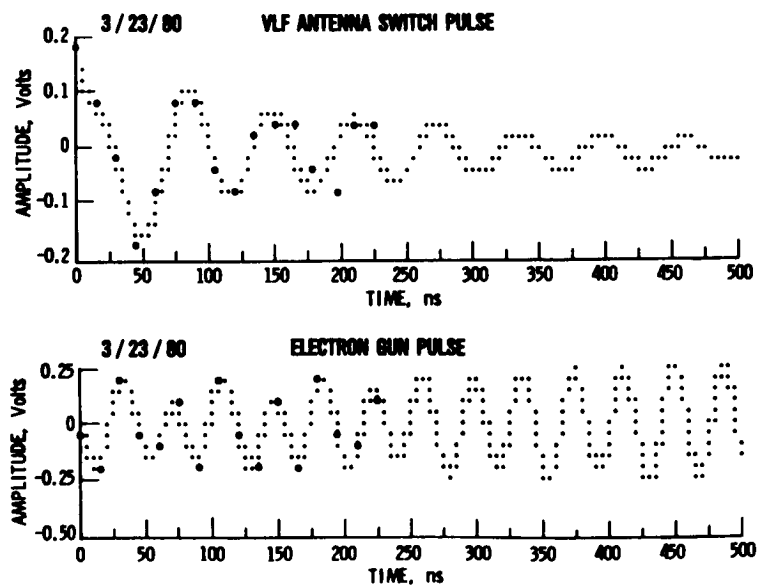


Figure 9

**FLIGHT EVIDENCE OF SPACECRAFT SURFACE CONTAMINATION  
RATE ENHANCEMENT BY SPACECRAFT CHARGING OBTAINED  
WITH A QUARTZ CRYSTAL MICROBALANCE\***

**D. M. Clark and David F. Hall  
The Aerospace Corporation**

**SUMMARY**

A goal of the ML-12 experiment is to determine whether a significant fraction of the mass outgassed by a negatively charged space vehicle is ionized within the vehicle plasma sheath and electrostatically reattracted to the space vehicle. The ML-12 retarding potential analyzer/temperature controlled quartz crystal microbalances (RPA/TQCMs) were designed to distinguish between charged and neutral molecules in order to investigate this contamination mass transport mechanism. In this paper, a preliminary analysis is given of two long-term, quick-look flight data sets, which indicates that on average a significant fraction of mass arriving at one RPA/TQCM was ionized. (Data from the other instrument have been difficult to analyze.) An important assumption is made in the analysis: that vehicle frame charging during these periods was approximately uniformly distributed in degree and frequency. The data are generally consistent with this assumption. These experiments provide evidence that electrostatic reattraction of ionized molecules is an important contamination mechanism at and near geosynchronous altitudes. Some implications of this conclusion for space vehicle design are discussed.

**INTRODUCTION**

It has been proposed that spacecraft charging increases the rate of deposition of contamination on spacecraft surfaces (ref. 1). A major objective of the ML-12 experiment is to determine whether this increase in contamination rate is large enough to significantly shorten the useful life of critical spacecraft subsystems (ref. 2). The proposed mass transport mechanism and the placement of the ML-12 experiment sensors on the P78-2 spacecraft are illustrated in figure 1. The idea is that some of the molecules released from the spacecraft by outgassing, electrical discharges, and thruster operations are ionized by energetic photons or energetic electrons before they reach the boundary of the plasma sheath that surrounds the vehicle when it is negatively charged. Because these ions are positively charged, they would be electrostatically reattracted to the vehicle.

---

\* Work supported by the U.S. Air Force, AFWAL/MLBE WPAFB, and SD, LAAFS, under contract F04701-80-C-0081.

Theoretical estimates of the fraction of released molecules that would be returned by this mechanism vary considerably and require severely simplifying assumptions.

The instrument designed to investigate this phenomenon is a combination of a retarding potential analyzer (RPA) and temperature controlled quartz crystal microbalance (TQCM), as shown in figure 2. Details of this instrument are given in references 2 through 4. Note that the charged particle collector is annular, so that some of the incoming particles reach it and some reach the mass sensor. The potential diagram in figure 3 illustrates the spacecraft frame  $V_{s/c}$  at -100 V with respect to the ambient plasma potential. Three cases of positive RPA grid bias are also shown. A slow molecule ionized at point D could reach the mass or charge collector if the grid were biased as in cases C and B, but not in case A.

Eight different settings of the retarding potential analyzer grid voltage (RPAV) can be commanded: -100, -10, -1, 0, 1, 10, 100, and 500 V. Whenever the vehicle frame potential is less negative than the grid is positive ( $|V_{s/c}| < \text{RPAV}$ ), all the ionized contamination molecules will be reflected. Then only uncharged mass will be collected on the TQCM sensing surface, the potential of which is also  $V_{s/c}$ . Conversely, when the vehicle frame is more negative than the grid is positive ( $|V_{s/c}| > \text{RPAV}$ ), molecules ionized close to the vehicle will be reflected by the grid, whereas those ionized further away but still within the vehicle sheath can be collected. When  $\text{RPAV} < 0$ , ion collection is unaffected, but electron collection is affected.

These ideas are summarized in figure 4, which reveals a qualitative indication of the expected dependence of mass accumulation rate ( $\dot{M}$ ) on RPAV for a case where  $-100 > V_{s/c} > -500$ . When RPAV is 500 V, only un-ionized molecules are measured ( $\dot{M} = \dot{M}^0$ ); when  $\text{RPAV} < 0$ , all ionized molecules with appropriate trajectories are also collected ( $\dot{M} = \dot{M}^0 + \dot{M}^+$ ). In theory, determination of the importance of spacecraft charging on contamination rate, i.e., determination of  $\dot{M}^+/\dot{M}^0$ , is straightforward with this instrument; in practice, it is difficult for the following reasons.

The P78-2 is a relatively clean vehicle with an outgassing rate that is probably significantly less than that of many spacecraft. This results in values of  $\dot{M}$  that must be integrated over hours, if not days, in order to be reliably determined.

The P78-2 also charges to large potentials very infrequently, and then only for relatively short periods of time. (The larger  $V_{s/c}$  is, the greater is the extent of the sheath and the higher the probability of molecular ionization within it.) According to studies conducted by C.K. Purvis with NASA Charging Analyzer Program (NASCAP) (ref. 5), the P78-2 configuration is not as favorable to charging as are configurations typical of three-axis stabilized vehicles. The largest charging events identified have been less than 1 hour in duration and have taken place during eclipses. Enhancement of

$\dot{M}$  has not been detected during these events because thermal effects on the ML12-6 and -7 mass sensors increased detection thresholds by factors of 80 and 4, respectively, and because the main mechanism of molecular ionization, photoionization, is absent during eclipses.

Reliable determination of  $V_{s/c}$  when  $0 > V_{s/c} > -100$  V is sometimes difficult. Because of photoemission from vehicle surfaces, noneclipse charging is usually in this range.

Capabilities to predict or detect spacecraft charging events are meager at present. In fact, it is generally not known until months later whether a moderate event has taken place, because spectrometer data, from which spacecraft charging events are most reliably detected, are generally not available for at least 6 months after the data are collected. Therefore, with the exception of operations during artificial charging events produced by the SC4-2 ion gun, spacecraft charging experiments cannot be planned in advance.

In this paper are reported two experiments that deal with these difficulties statistically. The assumptions made are: (1) charging events are approximately uniformly distributed in time, (2) charging events are large enough, long enough, and frequent enough to make  $\dot{M}^+/\dot{M}^0$  detectable, (3) the rate and composition of mass release from the vehicle are approximately constant over an experimental period, and (4) the adsorption characteristics of mass incident on the mass detector are constant with time. In both experiments, the aperture grid was connected to the spacecraft frame, as shown in figure 2. The coating over the mirrors surrounding the aperture and the skin of the spacecraft out to 25 cm from the aperture are electrically conductive and are also connected to the space vehicle frame. Therefore the electric field in the vicinity of the aperture must be relatively uniform and perpendicular to the aperture plane. The RPA grid voltage was commanded to selected values for periods of 10 or more days, and  $\dot{M}$  values averaged over 5-day segments were compared.

In the first (winter) experiment, a greater than 90 percent confidence was obtained that  $\dot{M}$  is negatively correlated with RPAV, i.e., that some incoming mass is reflected by the grid when it is positively biased. This fraction of the mass must have been positively ionized. The outcome of the recently concluded second (summer) experiment is not as easily assessed. The validity of data from three of the eight experiment segments is questionable and not as yet resolved. Some evidence of negative correlation is obtained when these data points are included in experiment analysis. If the questionable data points are excluded from the summer analysis, however, there is strong evidence of the negative correlation of  $\dot{M}$  with RPAV.

#### EXPERIMENTAL OBSERVATIONS

Analysis of data from these experiments has been complicated by several extraneous effects that affect the TQCM data. These effects are discussed separately for ML12-6 and ML12-7.

### Extraneous ML12-6 Effects

The average ML12-6 TQCM mass accumulation rate has always been significantly greater than that of the ML12-7, except during an unusual period in July and August 1980. This has been ascribed to the fact that ML12-6 receives sunlight while ML12-7 is shadowed (ref. 6). This photochemical effect is "extraneous" because it tends to mask the effect of electrostatic reattraction of ions, but it is not an "instrumental" effect. Two other facets of this effect are discussed here.

The first new observation is that the value of  $\dot{M}_6$  is affected by boom shadowing. This was noticed from study of long-term ML12-6 mass accumulation versus time plots. In general, the time derivative of these plots ( $\dot{M}_6$ ) has minima occurring a few days prior to each maneuver (figure 5). Further investigation of  $\dot{M}_6$  data and vehicle attitude information disclosed a direct relationship between vehicle sun angle (SANG), observed ML12-6 TQCM sensor temperature ( $T_6$ ), and  $\dot{M}_6$ , as shown in figure 6. These relationships are generally consistent with the predictions made with a NASCAP routine of ML12-6 shadowing by booms, as summarized in table I (ref. 7). Thus,  $\dot{M}_6$  is diminished during periods of shadowing compared with periods of normal illumination. The magnitude of this effect was not anticipated, but the effect is consistent with the previous observations and the seasonal effect to be discussed.

Throughout the RPA experiment periods, corrected ML12-6 TQCM sensor temperatures remained between  $-32$  and  $-37^\circ\text{C}$  with the exception of one brief excursion to  $-38^\circ\text{C}$ . Sensor temperature is important not only because it affects the re-evaporation rate of adsorbed mass, but because it also affects the quartz crystal frequency in certain temperature ranges. Changes in crystal frequency are multiplied by a mass sensitivity coefficient to yield changes in adsorbed mass. However, the dependency of ML12-6 frequency on temperature between  $-32$  and  $-38^\circ\text{C}$  is so small that the variation of  $\dot{M}_6$  with SANG cannot be attributed to changes in crystal temperature. The depressed rates of mass accumulation are, therefore, more likely to be related to shadowing of sunlight (i.e., photochemistry) than to the secondary thermal effects of shadowing.

Mass accumulation observations have been restricted to periods of normal illumination to minimize the effects of shadowing. The initial segment of this period is also excluded in order to minimize any short-term effects of the attitude maneuver. As a result, observations have been restricted to those periods where  $86^\circ < \text{SANG} < 91^\circ$ .

The second new observation concerning the effects of sunlight on ML12-6 is that the nearly 7 percent seasonal variation in solar irradiance (ref. 8) appears to modulate  $\dot{M}_6$ . This effect is in addition to the gradual decrease in  $\dot{M}_6$  that results from the decrease in vehicle outgassing rate.

The average ML12-6 TQCM mass accumulation rates during 12 orbital periods are plotted in figure 7. It is seen that assumptions (3) and (4) set forth in the Introduction regarding constancy of mass release and adsorption characteristics are not strictly true. In particular, there has been a gradual, approximately exponential decay in mass accumulation rate versus time with a seasonal modulation superimposed on this general trend. Note that the local maximum in  $\dot{M}_6$  occurs near Day 365 (31 December 1979), or approximately at Earth's perihelion, which occurs on or about Day 2003 (3 January 1980). Similarly, a local minimum in  $\dot{M}_6$  occurs near Day 2185 (3 July 1980), which was near aphelion (around 6 July 1980). The values of  $\dot{M}_6$  to be presented have not been normalized for the modest changes in outgassing and adsorption rates that apparently occurred over the 4- and 3-month experimental periods.

### Extraneous ML12-7 Effects

Random errors that produce small uncertainties in the measurement of  $M_6$  produce much larger uncertainties in the measurement of  $M_7$ . Furthermore, the frequency of the ML12-7 crystal was significantly affected by the variation in temperature during these experiments. (The experiments were conducted with the sensor temperature controller turned off in order to obtain minimum sensor temperatures and, therefore, maximum rates of mass adsorption.) The  $\dot{M}_7$  anomalously occurred during the summer RPA experiment. Because of these factors, ML12-7 data are not included in this paper.

## EXPERIMENTAL RESULTS AND DISCUSSION

### Data Flow and Sources of Random Error

Flight information from the P78-2 vehicle is obtained from two separate but related sources. The first is a detailed and continuous record in the form of digital data tapes, called agency tapes, which are produced for most flight days about 6 months following the date of collection. The second source of information consists of "quick-look" data obtained from the Air Force Satellite Control Facility (AFSCF), Sunnyvale AFS, California. The ML-12 portion of this data is a moderately truncated, approximately 2-min long sampling of instrument output printed about four times per day. In contrast to agency tapes, this material is normally received within a week of its collection. Personnel responsible for P78-2 operations at Mission Control Center F, AFSCF, have provided outstanding service in effectively collecting and promptly shipping ML-12 flight data. Because of this timeliness, a decision was made to utilize AFSCF printer data as source material for preliminary assessment of RPA experiment results, even though processing truncation contributes to random error in the measurement of  $M$ .

Other sources of random error include the 1-Hz resolution of the TQCM frequency counters and any variation in the period of the counter gating pulses supplied by the spacecraft. Another increase in error results from data analysis based upon the change in, rather than the absolute value of  $M_6$  as a function of elapsed time during an experiment period. The estimated



magnitude of the random error in  $\Delta M_6$  is calculated from a model of these truncation errors to be equal to or less than  $\pm 1.2 \text{ ng/cm}^2$  about 68 percent of the time, or  $\pm 4 \text{ ng/cm}^2$  at all times.

### Statistical Analysis of Data Scatter

The scatter of the data from the various segments that comprise the winter and summer experiments was analyzed statistically. A least squares linear regression of  $\Delta M_6$  versus elapsed time that was made of data from each experiment segment yielded a regression coefficient equal to the average mass accumulation rate during that 5-day segment ( $\dot{M}_6$ ), a "standard error of estimate" (ref. 9) of  $\Delta M_6$  on time ( $S_{\Delta M, t}$ ), and a standard error in the determination of  $\dot{M}_6$  ( $S'_1$ ) for the segment. However, because some segments contained a rather small amount of data, and because the sources of random error in the measurement of  $M_6$  are presumably uniformly present for all segments,  $S'_1$ , an improved value for  $S'_1$ , was obtained for each segment as follows. First, the root mean squared standard error of the estimate  $\langle S_{\Delta M, t} \rangle$  was calculated by weighting the  $S_{\Delta M, t}^2$  values from each segment by  $(n-2)$ , where  $n$  is the number of data points comprising each segment. (A value of  $\pm 1.52 \text{ ng/cm}^2$  was obtained for  $\langle S_{\Delta M, t} \rangle$ , and it falls outside the 99.9% confidence random error values calculated from the truncation error model. Therefore, significant sources of random error other than truncation must be present. \*) Finally, this weighted mean standard error of estimate was used to calculate  $S'_1$ , the standard error of each regression coefficient  $\dot{M}_6$ , as follows:

$$S'_1 = \frac{S_1}{S_{\Delta M, t}} \cdot \langle S_{\Delta M, t} \rangle = \frac{\langle S_{\Delta M, t} \rangle}{[\sum t_i^2 - (\sum t_i)^2/n]^{1/2}} \quad (1)$$

The results of these calculations are shown in table II. At no time did  $S'_1$  exceed  $\pm 0.34 \text{ ng/cm}^2\text{-day}$ .

### Results

The results of the RPA winter and summer experiments are tabulated in table II and plotted in figures 8 and 9. Each value of  $\dot{M}_6$  reported represents the average mass accumulation rate over a 5-day period, and the error bars shown are  $\pm S'_1$ . In both experiments, the mass accumulation rate was smaller when RPAV was 500 V than for other values. This is consistent with the idea that reattracted positively ionized contaminants are reflected by the grid. Less easily understood are the values of  $\dot{M}_6$  when RPAV was 100 V, because theory predicts  $\dot{M}_6(100) < \dot{M}_6(\text{RPAV} < 100)$ . One explanation is that vehicle charging might have been more prevalent than normal during these high  $\dot{M}_6$  periods. It is anticipated that the eventual availability of all agency tapes for the

\* Bright, P. B., private communication.

experiment periods will provide further clues to this feature of the data.

To determine the extent to which the  $\dot{M}_6$  values were correlated with RPAV, linear regressions of  $\dot{M}_6$  versus RPAV were calculated separately with data from the winter and summer experiments. In this analysis, a single linear function was fitted to all data from each experiment. As shown in figure 4, theory results in the expectation of a more complicated functional dependence of  $\dot{M}$  on RPAV. However, the size of the data set in this case did not justify fitting a more complex curve to the data. The correlation coefficients associated with these linear regressions of  $\dot{M}_6$  versus RPAV were also calculated. If the data are assumed to be normally distributed, levels of confidence can be assigned to the validity of the hypothesis that  $\dot{M}_6$  is negatively correlated with RPAV, i.e., that contamination is enhanced by spacecraft charging. The results of these analyses are summarized in table III.

The winter experiment results provide a level of confidence of approximately 91 percent in the negative correlation of  $\dot{M}_6$  with RPAV. The sensitivity of  $\dot{M}_6$  to RPAV for the winter experiment is calculated to be

$$\frac{d\dot{M}_6}{dV} = \frac{-0.0028 \text{ ng/cm}^2\text{-day}}{\text{volt}} \quad (2)$$

between limits of  $-100 \text{ V} < \text{RPAV} < 500 \text{ V}$ .

The results from the recently concluded summer experiment are complicated by the fact that data points from three of the eight experiment segments are somewhat questionable, but no unimpeachable grounds were found for excluding them. These are the two smaller  $\dot{M}_6(-100)$  values and the smaller  $\dot{M}_6(100)$  value plotted in figure 9 with triangular symbols. The  $\dot{M}_6(100)$  value is questionable because the  $\dot{M}_6$  versus time data from which it was derived could be better characterized by a "sawtooth" waveform than by a "ramp." Although  $\dot{M}_6$  for the experiment segment as a whole is unusually low, values of  $\dot{M}_6$  for the two individual sawtooth "teeth" in the segment closely approximate other summer values. One of the  $\dot{M}_6(-100)$  values represents a period in which the data set is very small because of a temporary reduction in the number of data transmissions per day. The remaining  $\dot{M}_6(-100)$  value is from the first summer experiment segment, which began 2 days after a TQCM temperature command was issued. Although thermal equilibration time required after such commands is usually only 1 day, it is variable and could influence the data set. Final resolution of TQCM behavior during these three periods will not be possible until appropriate agency tapes are examined.

If the questionable data points are excluded from analysis, the results of the summer experiment provide a 96 percent level of confidence in the negative correlation of  $\dot{M}_6$  with RPAV. The sensitivity in this case is calculated to be

$$\frac{d\dot{M}_6}{dV} = \frac{-0.0019 \text{ ng/cm}^2\text{-day}}{\text{volt}} \quad (3)$$

between the limits of  $-100 \text{ V} < \text{RPAV} < 500 \text{ V}$ . If the questionable data points are included in the analysis, the sensitivity of  $\dot{M}_6$  to RPAV for the summer is calculated to be

$$\frac{d\dot{M}_6}{dV} = \frac{-0.0009 \text{ ng/cm}^2\text{-day}}{\text{volt}} \quad (4)$$

and a 75 percent level of confidence in the negative correlation of  $\dot{M}_6$  with RPAV is obtained.

These linear regressions, which have the form

$$\dot{M}_6(\text{RPAV}) = \dot{M}_6(0) + \text{RPAV} \frac{d\dot{M}_6}{dV} \quad (5)$$

were used to estimate the average percentage of the mass arriving at the detector that was ionized and had kinetic energy of less than 500 eV. This percentage is given by

$$\frac{\dot{M}^+}{\dot{M}^0 + \dot{M}^+} = - \frac{500}{\dot{M}_6(0)} \frac{d\dot{M}_6/dV}{dV} \times 100 \quad (6)$$

and the value ranges from 18 to 31 percent as shown in table III.

As noted in the discussion of extraneous effects, variations in solar irradiance appear to affect the rate of mass accumulation. Data obtained during the RPA experiment support the observation that the presence of sunlight enhances the accumulation of mass on a surface. Specifically, values of  $\dot{M}_6$  during periods of shadowing ( $91^\circ < \text{SANG} < 94^\circ$ ) are as much as 30 percent lower than those observed during nonshadowed periods ( $86^\circ < \text{SANG} < 91^\circ$ ). In addition, values of  $\dot{M}_6$  for periods of lesser average solar irradiance near perihelion are as much as 45 percent lower than those observed during periods near aphelion. During both the winter and summer experiments, accumulation rates for the shadowed ML12-7 TQCM have seldom exceeded  $1 \text{ ng/cm}^2\text{-day}$ , whereas the insulated ML12-6 TQCM rates have ranged from approximately 2 to  $8 \text{ ng/cm}^2\text{-day}$ . It is suspected that this phenomenon is the result of photochemical reactions at or near the adsorbing surface.

#### PRELIMINARY CONCLUSIONS AND IMPLICATIONS

The results of these two long-term experiments provide evidence that spacecraft frame charging significantly affects the rate of contamination of spacecraft surfaces at frame potential. This conclusion is preliminary because it rests on the assumptions set forth in the Introduction. The most important of these, which is uniformity of spacecraft charging over the two long experimental periods, can be validated when a continuous record of P78-2 frame potential is available. The data also indicate that adsorption rate can be a strong function of the average solar illumination of the adsorbing surface.

These results have several implications. Both theory and the results from the Satellite Surface Potential Monitor on P78-2 (ref. 10) demonstrate that dielectric surfaces are much more prone to charging than is the spacecraft frame. Because the exterior materials on most spacecraft are predominately dielectrics (solar cell cover glass, second surface metalized polymers, and second surface fused quartz mirrors), it is likely that high altitude vehicles are more subject to charging enhanced contamination than the approximately 25 percent enhancement measured in this experiment.

Even if the enhancement is only 25 percent, the useful period of on-orbit operation of contamination sensitive systems (such as low temperature radiators) could be extended 25 percent if effective means were employed to ameliorate this effect. Depending on the specifics of the spacecraft design and system requirements, amelioration techniques could include one or more of the following: coating the contamination sensitive dielectric with a transparent conductive film grounded to the vehicle frame, use of a lower resistivity dielectric together with a conductive adhesive mounting system, deployment of biased electrodes in the vicinity of sensitive surfaces such that the resulting electric field would deflect ionized contaminants from the sensitive surfaces, development of dielectrics with more favorable secondary electron emission characteristics to minimize charging, and active control of the spacecraft frame potential with electron emitters. Each of these techniques has disadvantages, but advantages may outweigh disadvantages in particular applications. For instance, indium oxide, the most widely considered conductive coating, is expensive and apparently contributes to the increase in solar absorptance of materials during the first few months on orbit (ref. 11). However, these costs may be acceptable because of increased system life. Furthermore, a technique may be feasible by which management of both ionized and neutral contaminants is combined. In this technique the neutrals would be ionized as they approached a sensitive surface and all low energy ions would be deflected from the surface with electric fields.

#### REFERENCES

1. Cauffman, D. P.: Ionization and Attraction of Neutral Molecules to a Charged Spacecraft, TR-0074 (9260-09)-1, The Aerospace Corp., August 1973.
2. Hall, D. F., et al.: Experiment to Measure Enhancement of Spacecraft Contamination by Spacecraft Charging, NASA SP-379, NTIS, 1975.
3. Hall, D. F., and Fote, A. A.: Preliminary Flight Results from P78-2 (SCATHA) Spacecraft Contamination Experiment, ESA SP-145, Proceedings of an ESA Symposium on Spacecraft Materials, October 1979.
4. Stevens, J. R., and Vampola, A. L., eds.: Description of the Space Test Program P78-2 Spacecraft and Payloads, SAMSO-TR-78-24, NTIS, 1978.
5. Purvis, C. K.: Configuration Effects on Satellite Charging Response, AIAA Paper No. 80-0040, Eighteenth Aerospace Sciences Meeting, Jan 1980.

6. Hall, D. F.: Flight Experiment to Measure Contamination Enhancement by Spacecraft Charging, Proceedings of the Society of Photo-Optical Instrumentation Engineers (SPIE), vol. 216, 1980, pp. 131-138.
7. Steen, P. G.: SCATHA Experiment Shadowing Study, SSS-R-78-3658, Systems, Science and Software, May 1978, pp. 163-166, 380-410.
8. Standard Solar Constant and Air Mass Zero Solar Spectral Irradiance Tables. ASTM Designation: ANSI/ASTM E 490-73a. Part 41 of 1978 Annual Book of ASTM Standards, 1978, pp. 672-675.
9. Hoel, P. G.: Elementary Statistics, Wiley, 1960, p. 149.
10. Mizera, P. F.: Natural and Artificial Charging: Results from the Satellite Surface Potential Monitor Flown on P78-2, AIAA Paper No. 80-0334, Eighteenth Aerospace Sciences Meeting, January 1980.
11. Hall, D. F., and Fote, A. A.:  $\alpha_s/\epsilon$  Measurements of Thermal Control Coatings on the P78-2 (SCATHA) Spacecraft, AIAA Paper No. 80-1530, Fifteenth Thermophysics Conference, July 1980.

TABLE I  
AVERAGE SOLAR INSOLATION ON ML12-6 IN SOLAR CONSTANTS FOR VARIOUS SUN ANGLES

<u>SANG</u> <u>(deg)</u>	<u>Radiator and Sensor Aperture</u>	<u>Aperture Only</u>	<u>Radiator only</u>
80	0.31347	0.31347	0.31347
81	0.31438	0.31438	0.31438
82	0.31520	0.31520	0.31520
83	0.31593	0.31593	0.31593
84	0.31656	0.31656	0.31656
85	0.31709	0.31709	0.31709
86	0.31753	0.31753	0.31753
87	0.31787	0.31787	0.31787
88	0.31811	0.31811	0.31811
89	0.31788	0.31825	0.31780
90	0.31403	0.31645	0.31353
91	0.31058	0.30907	0.31089
92	0.31169	0.30819	0.31241
93	0.31410	0.31472	0.31397
94	0.31598	0.31681	0.31581
95	0.31644	0.31705	0.31631
96	0.31640	0.31656	0.31637
97	0.31592	0.31593	0.31592
98	0.31520	0.31520	0.31520
99	0.31438	0.31438	0.31438
100	0.31347	0.31347	0.31347

TABLE II  
ML12-6 TQCM MASS ACCUMULATION RATES AT  
VARIOUS RPA BIAS SETTINGS  
(Grounded Aperture Grid Condition)

<u>Winter Experiment</u>		
<u>Grid Bias Level (Volts)</u>	<u>Accumulation Rate (ng/cm<sup>2</sup>-day)</u>	<u>Statistical Standard Error (ng/cm<sup>2</sup>-day)</u>
+500	5.662	±0.265
-100	7.483	0.270
-10	6.761	0.308
+10	7.018	0.360
+100	8.069	0.337

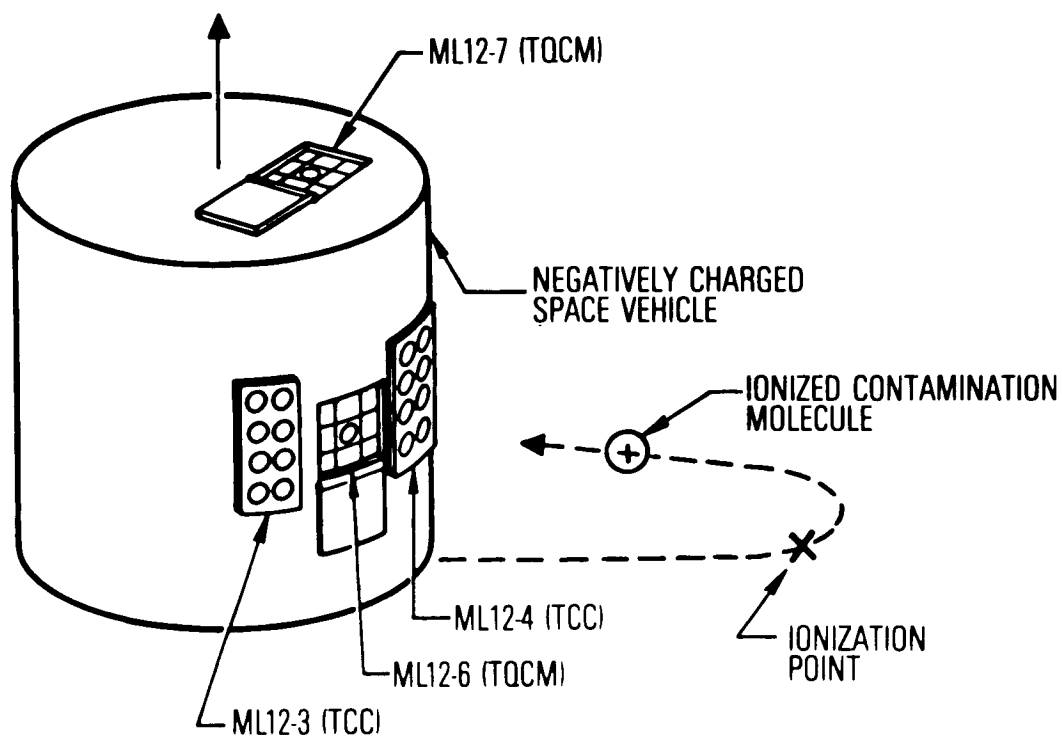
  

<u>Summer Experiment</u>		
-100	1.994	0.288
-100	2.088	0.346
+100	1.044	0.317
+100	3.550	0.314
+500	1.886	0.310
+500	2.172	0.327
-100	3.101	0.311
-100	3.000	0.345

TABLE III  
CORRELATION OF ML12-6 TQCM MASS ACCUMULATION  
RATES WITH RPA BIAS LEVELS

(Grounded Grid Configuration, -100 V < RPAV < 500 V)

<u>Experiment Segment</u>	<u>Regression Coefficient (ng/cm<sup>2</sup>-day)/volt</u>	<u>Correlation Coefficient (r)</u>	<u>Level of Confidence that r &lt; 0</u>	<u>Average Ionized Mass (KE &lt; 500 eV)</u>
Winter	-0.0028	-0.721	~ 91%	19%
Summer (Abbreviated)	-0.0019	-0.828	~ 98%	31%
Summer (All Data)	-0.0009	-0.279	~ 75%	18%



**Figure 1.** Placement of ML12 Sensors and Concept of Contamination Enhancement Mechanism

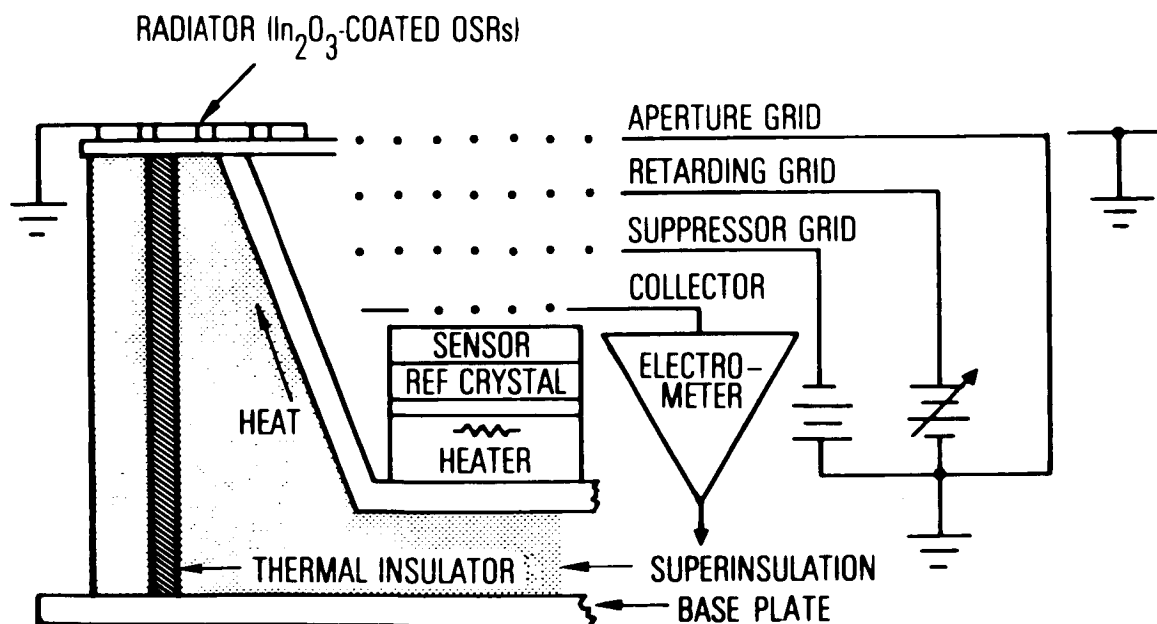


**Figure 2.** Schematic of RPA/TQCM sensors

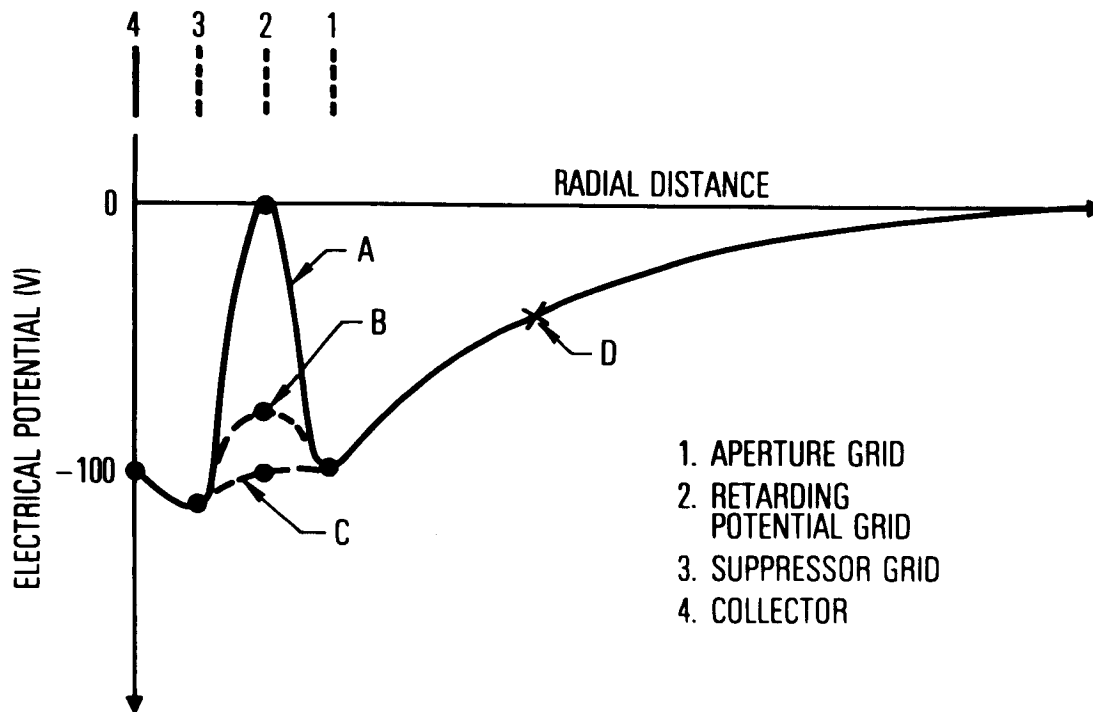


Figure 3. Potential Diagram of RPA on Negatively Charged Spacecraft Showing Three Possible Retarding Potential Grid Biases

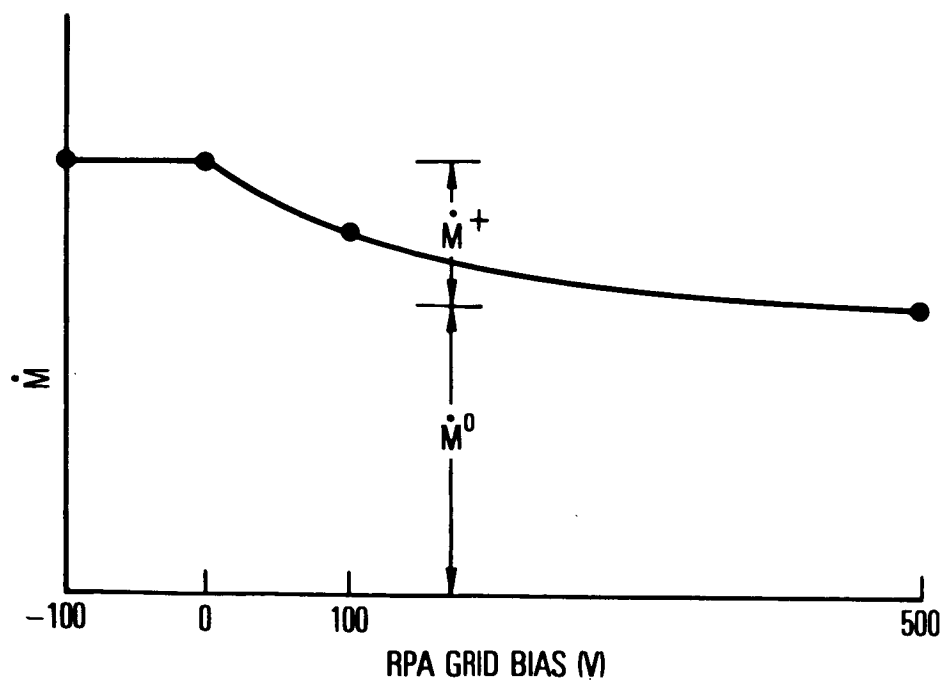


Figure 4. Theoretical Qualitative Dependence of Mass Accumulation Rate on Retarding Potential Grid Bias



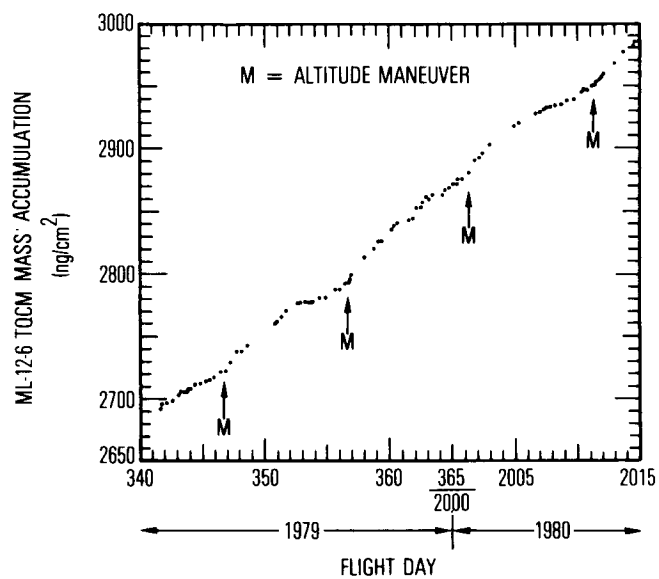


Figure 5. ML12-6 TQCM Mass Accumulation Versus Time, Expressed in Flight Days, for the Period 6 Dec. 1979 to 15 Jan. 1980

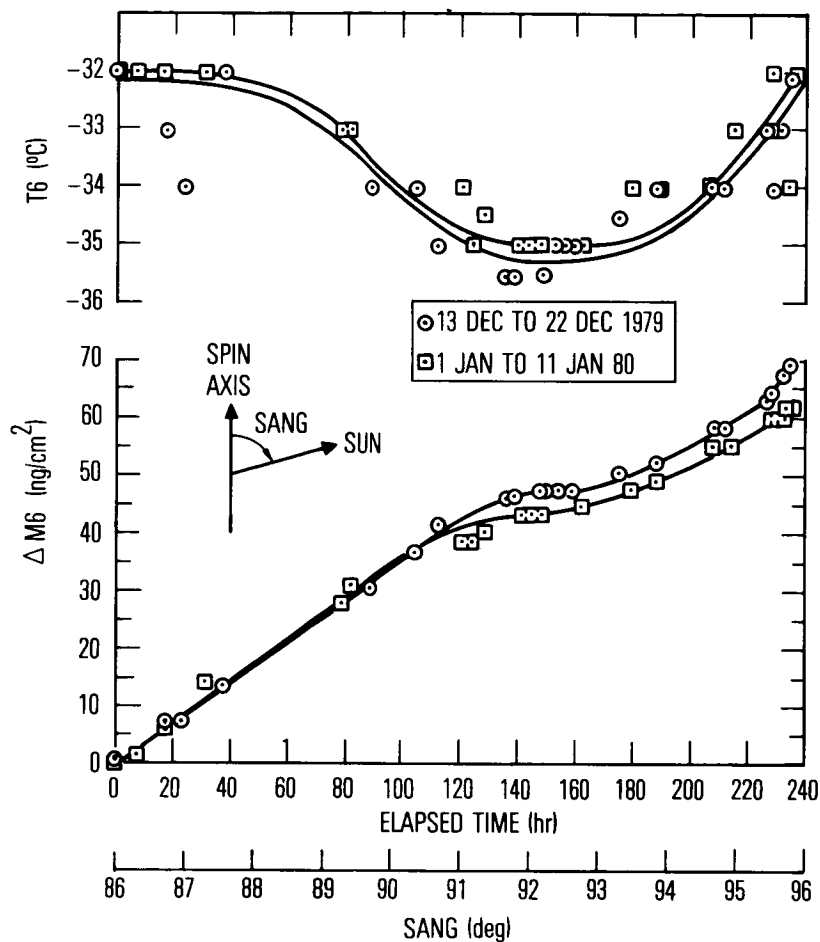


Figure 6. ML12-6 TQCM sensor Temperature ( $T_6$ ) and Change in Mass Accumulation ( $\Delta M_6$ ) Versus Elapsed Time and Vehicle Sun Angle (SANG) for the Period 13 to 22 December 1979 and 1 to 11 January 1980

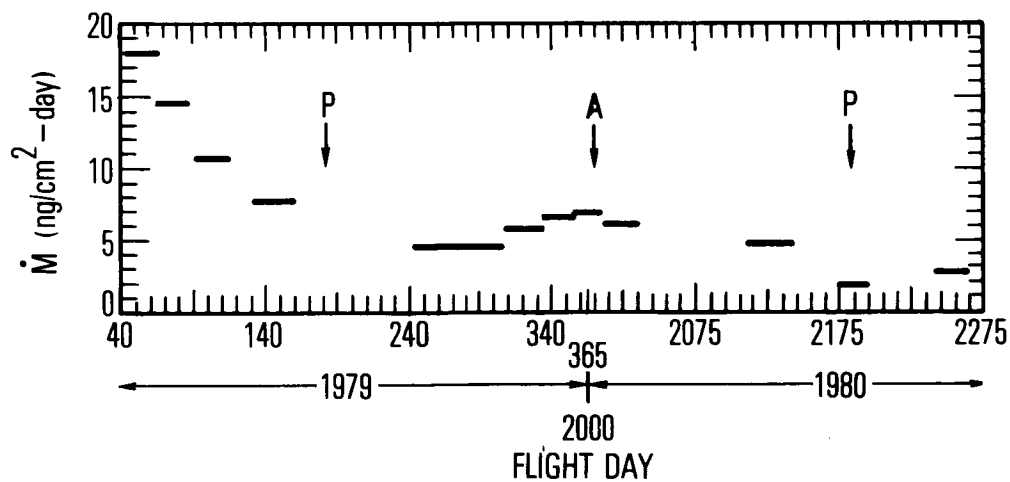


Figure 7. Equilibrium Mass Accumulation Rates of ML12-6 from Early in Flight to 1 October 1980. "P" Denotes Perihelion, "A" Denotes Aphelion

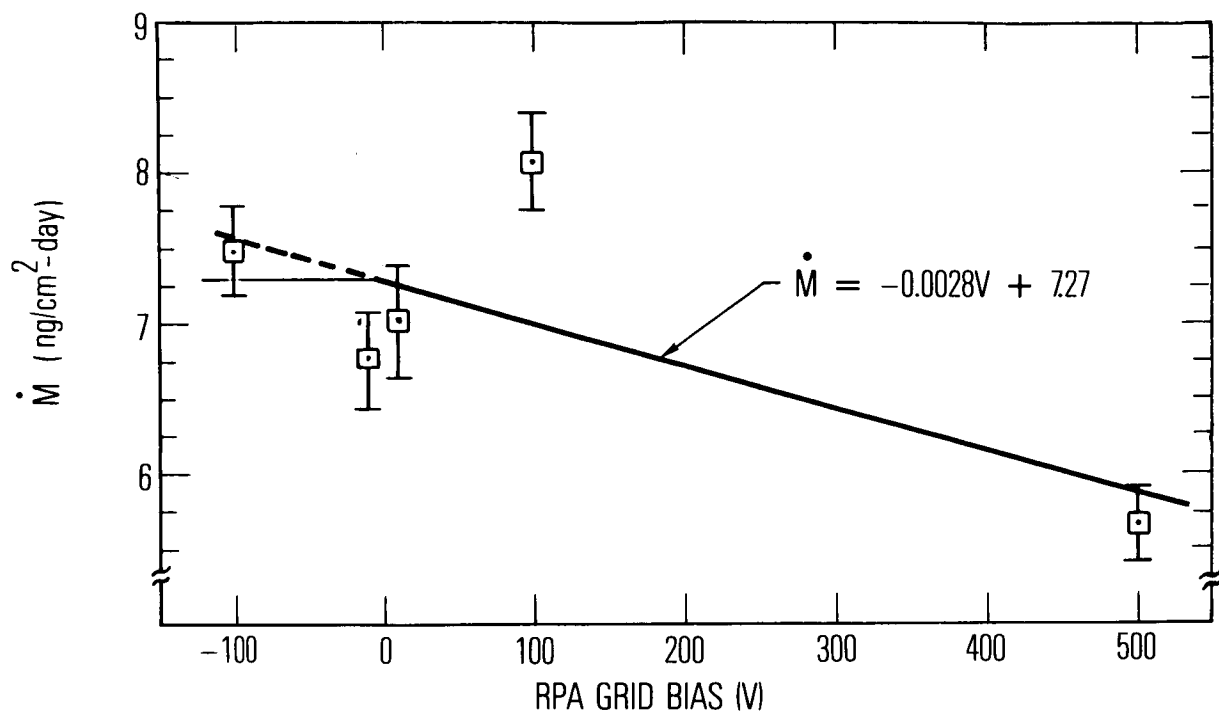


Figure 8. ML12-6 TQCM Mass Accumulation Rates at Various RPA Grid Bias Potentials During Winter Experiment

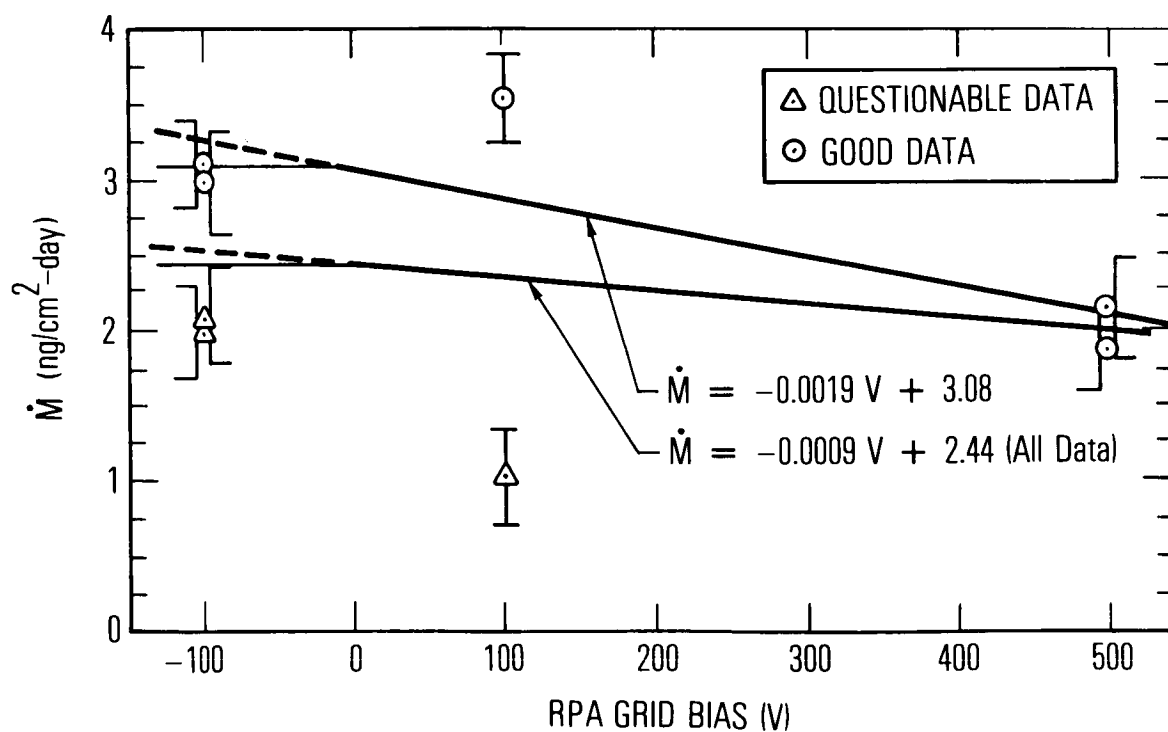


Figure 9. ML12-6 TQCM Mass Accumulation Rates at Various RPA Grid Bias Potentials During Summer Experiment

**P78-2 SATELLITE AND PAYLOAD RESPONSES TO ELECTRON  
BEAM OPERATIONS ON MARCH 30, 1979**

**H. A. Cohen<sup>1</sup>, R. C. Adamo<sup>2</sup>, T. Aggson<sup>3</sup>, A. L. Chesley<sup>1</sup>, D. M. Clark<sup>4</sup>,  
S. A. Damron<sup>2</sup>, D. E. Delorey<sup>5</sup>, J. F. Fennell<sup>4</sup>, M. S. Gussenhoven<sup>5</sup>,  
F. A. Hanser<sup>6</sup>, D. Hall<sup>4</sup>, D. A. Hardy<sup>1</sup>, W. B. Huber<sup>1</sup>, I. Katz<sup>7</sup>,  
H. C. Koons<sup>4</sup>, S. T. Lai<sup>5</sup>, B. Ledley<sup>3</sup>, P. F. Mizera<sup>4</sup>,  
E. G. Mullen<sup>1</sup>, J. E. Nanevich<sup>2</sup>, R. C. Olsen<sup>8</sup>,  
A. G. Rubin<sup>1</sup>, G. W. Schnuelle<sup>7</sup>,  
N. A. Saffekos<sup>5</sup>, M. F. Tautz<sup>9</sup>,  
and E. C. Whipple<sup>8</sup>**

**ABSTRACT**

On March 30, 1979 an electron gun was operated on the P78-2 Satellite. The gun was operated on the satellite before the satellite entered eclipse and during the time of eclipse. The ranges of ejected electron currents and energies were from 0.1 mA to 13 mA, and 0.3 keV to 3 keV. Spacecraft frame, and surfaces on the spacecraft, went positive with respect to points 50 meters from the satellite when the gun was operated. Depending on ejected electron currents and energies, spacecraft frame-to-ambient-plasma potential differences between several volts and 3 kV were generated. Simultaneously, lower potential differences were created between the satellite and a point 3 meters from the satellite. Sample surface potentials were measured during gun operations. When the electron gun was turned off, the vehicle frame swung sharply negative.

Arcing was detected by pulse monitors in several electron beam modes of operation. The ejection of a beam of 6 mA of 3 keV electrons caused three distinct payload failures and created a transient problem in the telemetry system. An attempt has been made to determine the exact time, nature, and cause of these failures; a specific effort has been made to identify which components failed and why they failed. Analytical and modeling techniques have been used to examine possible spacecraft and payload responses to the electron beam ejection which might have contributed to the arcing and payload failures.

- 
- 1 Air Force Geophysics Laboratory
  - 2 SRI International
  - 3 Goddard Space Flight Center, NASA
  - 4 The Aerospace Corporation
  - 5 Boston College
  - 6 Panametrics, Inc.
  - 7 Systems, Science and Software, Inc.
  - 8 University of California, San Diego
  - 9 Radex Laboratory, Inc.

## INTRODUCTION

On March 30, 1979, the SC4-1 payload (electron gun) on the P78-2 satellite was operated for the first time to eject beams of energetic electrons from the spacecraft. A wide dynamic range of electron currents and energies was available and was used to charge the spacecraft frame positive with respect to ambient plasma. The use of SC4-1 caused a number of interesting scientific and engineering results. Some of these results were unexpected and some not only unexpected but quite undesirable. In this latter class are the failure of two instruments and a momentary interruption of the normal telemetry stream caused by the ejection of 6 mA of 3 keV electrons.

The first half of this paper will report on the operating modes of the SC4-1 payload, the resultant charging of spacecraft frame and sample materials on the spacecraft exterior and transient pulses recorded. The second half of this paper will present a detailed engineering analysis of the instrument failures and of the telemetry interruption, and a summary of the investigation into possible causes of these problems. As can be seen by the list of coauthors, this paper is the result of contributions and cooperation by a large number of individuals. This paper reports the results from the initial investigation; further conclusions will be published in later reports.

## INSTRUMENT PLACEMENT

The P78-2 payloads to be discussed and their positions on the spacecraft are listed in tables 1 and 2 and are shown schematically in figures 1 and 2. For a more complete description of the payloads and the P78-2 spacecraft, see reference 1.

Part of the analysis of the events of pass 89.4 requires a knowledge of the directions of the instruments, defined as "look-angles" relative to the Space Vehicle Relative Coordinates (SVRC). The SVRC are defined such that the forward Omni antenna is the +X axis and the SC-11 boom is the -Y axis (figure 1). The "look-angles" are the two rotations necessary to align the +Z axis of the SVRC to the instrument Line-Of-Sight (LOS). The rotations are: Alpha, a rotation about the +X axis (positive angles being a displacement from +Z towards -Y), and Beta, a rotation about the displaced +Y axis (positive angles being a displacement from +Z towards +X). Both "look-angles" are defined relative to the +Z axis. (Note: In table 2, the "look-angle" of a boom is defined by the axis of the boom, not by an instrument on the boom.)

## OPERATIONS SUMMARY

Real time operations for this pass started at Universal Time (UT) 52971 seconds and stopped at UT 57594 seconds. Table 3 and figure 3 outline the operations of SC4-1 for this time period. At the beginning of operations the spacecraft was at 31,000 kilometers altitude, -7.5 degrees latitude, 116 degrees longitude. At the end of operations the spacecraft was at 33,000 kilometers, -7.7 degrees latitude, 119.8 degrees longitude. (A detailed summary of the magnetospheric environment for this pass is included as Appendix 1.) Payload commanding started after the transmitter was turned on and housekeeping instructions were given. A block command was given turning off most of the payloads prior to any SC4 operations. (This is normal safety operating procedure.) The SC2-1 and SC2-2 probes were then turned back on and the 100 kohm shunt which connected the outer surface of the SC2 probe to spacecraft frame was disconnected.

Commands initializing SC4-1 were then sent. These initialization commands set the state for SC4-1 operations but do not turn SC4-1 power on. The power to SC4-1 was turned on and two-and-one-half minutes later the electron beam was turned on. At this time the cap to the electron gun was still in place and no electrons were ejected. The beam inside the closed tube was continuous (0.1 mA of 0.3 keV electrons). SC1, the SC2 probes, SC10, SC11, ML12, and the Transient Pulse Monitor (TPM) were operating, while the power to all the other payloads was kept off. The SC4-1 operating condition with cap closed and beam on was maintained for ten minutes. No changes in the operating conditions of any of the payloads that were on were noted in this time period.

At UT 54082 seconds the command was given to remove the cap from the SC4-1 electron tube. Although the microswitch cap position monitor did not show cap opening, the cap current monitor showed that the cap had been removed. Results from ML12-7, the SC2 probes, and SC10 showed that the cap had been opened and that electrons were being ejected from SC4-1.

The energy of the ejected electrons was then increased from 0.3 keV to 1.5 keV and the beam current was increased from 0.1 mA to 1.0 mA. At 54509 seconds, a command was given to change the electron emission from continuous to pulsed. All of the appropriate monitors indicated that the command was received and a pulsed beam was being ejected from SC4-1. Electrons were ejected in 3.9 mS pulses at a rate of 16 pulses per second. The ejected electron energy was then lowered to 0.5 keV and the command was sent to return the beam to a continuous mode. This command was received and successfully executed. The beam remained continuous from this time until the end of the pass.

The beam current was then increased from 1.0 mA to 6.0 mA. The ejected electron energy was increased to 3.0 keV at UT 54728 seconds. It was during this mode (6.0 mA of 3.0 keV electrons) that identifiable problems of payload and telemetry operation occurred. These problems included: damage to the SC2-1 and SC2-2 probes, interruption of the telemetry, switching the

SC11 wideband telemetry signal line filter from 1 Hertz to 5 Hertz, and the elimination of the SC4-1 pulsed mode.

The SC2-1 probe failed between UT 54728 and UT 54730 seconds and the SC2-2 probe failed between UT 54758 and UT 54759. The telemetry interruption started at UT 54736 and lasted for 14 seconds. A switch in the SC11 filter occurred between UT 54720 and UT 54840 seconds.

SC4-1 was commanded out of this 3.0 keV, 6.0 mA mode at UT 54809, when the energy of the ejected electrons was lowered to 1.5 keV. At UT 54820 the ejected current was increased by command to 13.0 mA.

The SC4-1 pulse mode command was given at 54882. The state monitor indicated that the command had been received but the current remained continuous. Several attempts were made during this pass (and subsequent passes) to put SC4-1 into the pulsed mode: all attempts have been unsuccessful.

There were no other difficulties with SC4-1 during pass 89.4. All commands were received and operated on. There were no signs of poisoning of the SC4-1 cathode. SC4-1 was then commanded through a number of different current and energy modes until it was turned completely off at UT 57109. Real time data acquisition for all the payloads was interrupted during an antenna switch (by command) in the period UT 55728 to UT 55771.

The spacecraft entered penumbral eclipse at UT 56004 (total eclipse at UT 56135) and exited total eclipse at UT 59664 (penumbral eclipse at UT 59832): SC4-1 was operating when P78-2 entered penumbral eclipse and was turned off before P78-2 exited eclipse.

In addition to those payloads turned on prior to the start of SC4-1 operations, the Rapid-Scan Particle Analyzer (SC5) was operated for two short periods during SC4-1 operations. After SC4-1 was turned off (just prior to the end of this pass) all the payloads were turned back on to their normal operating states.

#### VEHICLE POTENTIAL MEASUREMENTS

Prior to pass 89.4, the SC4-2 payload had been used to eject electrons and ions, both separately and together. During these operations a number of instruments had been used to determine the value of the satellite-frame-to-plasma potential difference ( $V_{sc}$ ). These instruments included particle analyzers, (SC5 and SC9), and high impedance differential voltage measurements (SC2-1, SC2-2, and SC10).

Due to the danger of flooding the electrostatic channeltrons with energetic electrons, SC9 was not operated during the SC4-1 operating periods on pass 89.4. SC5 was used for limited time periods during the later stages of this pass. The results and importance of the SC2 measurements (the

difference in potential between spheres three meters from the satellite and spacecraft frame) will be presented in detail in a later section.

For this pass the data from the SC10 measurements were used as the primary source of information concerning the effects of electron ejection on the satellite frame potential,  $V_{sc}$ . The particular SC10 measurement used was the value of the difference in potential ( $V_{10}$ ) between an electrically floating, conducting cylinder and spacecraft frame. The cylinder (20 meters long and 1/4-inch in diameter) is separated from the spacecraft by a kapton-covered 1/4-inch diameter cylinder 30 meters in length. The two cylinders comprise a 50 meter boom (SC10-3). (A similar boom is also extended on the other side of the satellite.) It is assumed that during SC4-1 operations  $V_{sc} = -V_{10}$ . Some corroboration for this assumption is seen in table 4 where the values for  $V_{sc}$  deduced from SC5 and SC10 measurements are compared. It is emphasized that these are two distinctly different types of measurements of spacecraft frame potential.  $V_{10}(t)$ , the measured SC10 value as a function of time for the entire pass 89.4, is shown in figure 4. Values of  $V_{sc}$  for each of the SC4-1 modes are listed in table 4. The values given are the maximum measured voltages for the given time periods. The maximum values show the best correspondence between sunlight values (which show spin modulations) and eclipse values (which do not).

Three aspects of the response of  $V_{sc}$  and  $V_{10}$  to electron beam energy,  $E_b$ , and electron beam current,  $I_b$ , will be singled out for attention:  $V_{sc}(0,0)$ , values of the spacecraft frame potential before and after SC4-1 operations when there was no electron ejection;  $V_{sc}(I_b, E_b)$ , spacecraft frame potential as a function of ejected electron current and energy; and  $V_{10}(I_b, E_b, t)$ , the levels of oscillations of the measured potential difference between the floating SC10 cylinder and spacecraft frame.

Figure 5 shows the period UT 53000 to UT 54080 which covers three different SC4-1 modes:

- (1) SC4-1 had not yet been started;
- (2) The power processor of SC4-1 had been started but no electrons were emitted from the SC4-1 cathode; and
- (3) 0.1 mA of 0.3 keV electrons left the SC4-1 cathode but did not leave the payload because the cap to SC4-1 had not yet been removed.

The character of  $V_{10}(t)$  remains unchanged for these three modes. There is an oscillation of  $V_{10}$  with a peak negative value of -5.8 volts when the SC10 boom solar angle is near zero and 180 degrees. (The boom solar angle is the angle between the boom axis and the sun line, a vector pointing from the satellite to the center of the sun.) When the cap to SC4-1 was removed, at 54082, 0.1 mA of 0.3 keV electrons were ejected and  $V_{sc}$  quickly swung positive to a value exceeding 200 V. After this,  $V_{sc}$  responded quickly to changes in ejected electron currents ( $I_b$ ) and energies ( $E_b$ ).



Table 5 shows that the current required to swing  $V_{sc}$  to a significant fraction of the beam energy lies between 10 and 100  $\mu A$ : more current is required when the satellite is in sunlight than when it is in eclipse.

There is a saturation effect using the 1.5 keV electrons. The maximum vehicle potential is obtained when the ejected current lies between 1 and 6 mA and decreases when the ejected current is increased above 6 mA. The oscillations in  $V_{10}$  values cease when the vehicle is in eclipse as shown in figure 6.

Before electron ejection  $V_{sc}$  was slightly positive, of the order of 6 V. When the electron ejection was stopped (modes 20, 21, and 23)  $V_{sc}$  was first near zero and then slightly negative. When SC4-1 was finally turned off for this pass,  $V_{sc}$  went to minus 360 V and slowly decayed toward zero, as is partially shown in figure 7. This phenomenon of negative vehicle potentials induced by terminating electron ejection has since been repeated.

#### SURFACE POTENTIAL MONITOR MEASUREMENTS

It has been suggested that electron emitters be used on satellites to control spacecraft charging. This pass allowed us the opportunity to study the effects of electron emission on materials typically used on spacecraft. Also, in the attempts to determine the causes of the arcing and instrumentation failures during the operation of SC4-1, conjectures are continuously made about the potentials of the P78-2 surfaces. Actual measured potentials of representative sample surfaces can be used to test various hypotheses. Surface potentials and currents through the samples were measured for various materials during this pass. What will be discussed here are values of the potential ( $iV_j$ ) of the front surface of each sample with respect to spacecraft frame. The back surface voltage of each sample was measured using an electrostatic device and  $iV_j$  was determined on the basis of pre-launch laboratory calibrations.

Values have been determined for the potentials generated by SC4-1 operations as measured on an optical solar reflector (1V3), a floating conducting band (2V4), and samples of aluminized kapton (1V1 and 2V2). The values of  $iV_j$  depended on sample material, size and position on the spacecraft. The floating reference band (2V4) tracked the potential of the spacecraft frame:

$$2V4 \cong V_{sc}^{2/3}$$

for  $V_{sc} > 0.2$  kV. For the other materials,  $iV_j$  remained low until the vehicle became highly positively charged. For the aluminized kapton samples,  $iV_j$  depended on both the position and on the size of the samples. Large values of  $iV_j$  were reached by samples on the equatorial band of the

satellite with the largest values occurring on the largest sample, 2V2 (up to a maximum of -1334 V).

As mentioned previously, SC4-1 ejected 6 mA of 3 keV electrons during mode 11, causing problems for the SC2 payloads and the spacecraft telemetry. Table 6 lists values of the front surface potential of several sample materials during this mode. These values should be used as a guide in assigning values to spacecraft and boom surface potentials in attempts to model particle trajectories or surface behavior during this mode. (Kapton was used on the booms; the potential of the solar cells, which comprise the major areas of the spacecraft, was probably close to that of the sample optical solar reflecting samples; and the floating potential of the conducting reference band is close to the floating potential of the SC2 sphere.) As shown in table 6, the potentials of the samples during this mode, although negative with respect to spacecraft frame, were always positive with respect to the ambient plasma. Figures 8 and 9 show that there were sudden shifts in the current through one sample and also a sudden shift in the front surface potential of another sample, coinciding with the failures of the SC2 spheres and the telemetry interruption. This indicates arcing or a response to arcing at these samples.

With the spacecraft in eclipse, measured values of  $iV_j$  for the aluminized kapton samples showed that the front surfaces of these samples were charged negatively, not only with respect to spacecraft frame, but sometimes even with respect to the ambient plasma.

## PULSES

Two separate payloads were devoted to pulse detection on the P78-2 satellite. A description of sensors, positions, and characteristics measured is given in table 7.

With the exception of changes due to vehicle command related pulses, there was no increase in count rate or amplitude of detected pulses when SC4-1 was first turned on or when a beam was generated but kept in the closed tube. When the cap to SC4-1 was removed and a beam of 0.1 mA at 0.3 keV electrons was ejected, there again was no change in pulse rate or amplitude.

When high energy electrons or high currents were ejected, the rate and amplitude of detected pulses increased significantly. Table 8 shows that there was agreement between the TPM and SC1-8B measurements and that there was a monotonic increase in the pulse rate with current when 3.0 keV electrons were ejected. The 1.5 keV electrons did not lead to a significant increase in pulse rate until a current of 13 mA was used. Even at a large current, the pulse amplitude distribution caused by 13 mA of electrons at 1.5 keV was significantly lower than that caused by the lower current of 6 mA of electrons at 3.0 keV (Figures 10 and 11).

Typical pulse shapes on each of the SC1-8B pulse sensors are shown in

Figures 12-15. The pulses on the same sensor tend to have the same shape. This may suggest that the larger discharges are occurring at the same point on the vehicle. Pulses of differing shapes are seen often enough to rule out an instrumental effect on the shapes. From the results of both the surface potential and pulse measurements, the critical potential on spacecraft frame for the creation of differential charging effects on the P78-2 satellite is between 1.5 and 3.0 kV.

#### SC2-1 AND SC2-2 MEASUREMENTS AND FAILURE

Each SC2 probe consists of a short boom section (2.54 cm diameter, 38 cm long), a 17.8 cm sphere and a shadow stub (2.54 cm diameter, 25 cm long). These three sections are electrically isolated from each other and are all coated with colloidal graphite (Aquadag). As shown in figure 16, each probe is attached to, but electrically isolated from, the end of a 2.52 meter spacecraft boom. The distance between the spacecraft and the center of the sphere is 3 meters.

The difference between the floating potential of each sphere and the spacecraft frame was made by a null measurement. The voltage difference between an internal Faraday cage and the probe surface was sensed and the Faraday cage was driven by a "follower circuit" so that the potential difference was less than 0.01% of the probe voltage relative to the spacecraft frame. The smallest voltage measurable was  $\pm 0.01$  V and the largest was  $\pm 700$  V.

The values of the two probe voltages as a function of time up to mode 11 are shown in Figure 17. The maximum values for each SC4-1 mode are listed in table 9 where they are compared to V10 values. For each SC4-1 mode, the SC2 probe potentials (V2n) are less than the V10 values and the ratio of V2n to V10 decreased monotonically with increasing spacecraft frame potential. Both of these results are consistent with the concept that the SC2 spheres were inside a plasma sheath created by the positively charged satellite.

Up to the time of the start of SC4-1 mode 11, there were no problems with the SC2 probe measurements. Within 1 second of the start of this mode, the SC2-1 probe failed. The SC2-2 probe drifted to an increasingly negative potential for 30 seconds, reaching a maximum negative potential of -550 V and then failed. The time between the two instrument failures is approximately half of the spin period of the satellite.

The positions of the SC2 spheres with respect to the shadow of the satellite, at times of failures, were determined using boom solar angles inferred from the attitude measurements. A summary of these results is shown in figures 18 and 19. For each failure, the instrument in question is approximately 7 degrees from the satellite shadow, going into shadow. Approximately two thirds of the boom was in shadow when each of the failures occurred. The distance from the probe to the closest position

on the boom in shadow was about 1.2 meters. The failure of each of the SC2 probes was nearly coincident with the boom going through a minimum magnetic pitch angle of 13 degrees for SC2-1 and 15 degrees for SC2-2 (figures 20 and 21). (The magnetic pitch angle is the angle between the magnetic vector and the boom axis.)

Table 10 shows tabulations of both sun angle and magnetic pitch angle for SC2, SC4-1 and ML12-7, using the "look-angle" data in table 2. The sun angle data indicates that the X axis of the satellite was between 3.4 and 4 degrees from being normal to the sun line. A three dimensional calculation of the shadowing of the SC2-1 and SC2-2 booms was determined using data on the probe size, boom length, satellite dimensions and tilt. The result shows that neither of the probes had yet reached the shadow of the satellite when they failed. Both, however, were approaching shadow and a significant portion of the boom had been shadowed when failure occurred. The shadowing angles are summarized in table 11.

The data from both the TPM and SC1-8B were compared with the known periods during which the failures and the loss of telemetry sync occurred. The SC2-1 probe returned "good" data at 54727.9 and "bad" data at 54729.9, indicating failure. The data point at 54728.9 was lost, preventing the time of failure from being pinpointed to closer than two seconds from the SC2-1 data alone. The TPM data which was received during second 54730 indicates at least one fairly large pulse and several that exceeded the counting threshold of the high Z (impedance) and low Z detectors. Preliminary analysis of the timing involved in transmitting the TPM data indicates that this data was sampled between 54728.6 and 54729.8. If we assume that the events monitored by the TPM include the SC2-1 failure, this narrows the period of SC2-1 probe failure to about 1 second.

The SC1-8B data is less easy to interpret. This package shows four consecutive seconds of relatively high activity, starting with the data received about 54728.2 (sampled starting at 54727.2). The 3 keV command was given at about 54728.4, indicating that the first second of this period can be disregarded. However, this leaves three seconds of pulses of which none can be specifically identified with the SC2-1 failure.

During both the SC2-1 failure and the loss of telemetry sync, the SC1-8B package was receiving its data from sensor S2 (Harness Wire). During the failure of SC2-2, SC1-8B was sampling sensor S1 (CDU Loop).

The SC2-2 data shows failure between 54757.9 and 54758.9. The only TPM pulse data which appears to span any of this period was received at 54760 and was sampled between 54758.6 and 54759.8. This appears to narrow the region of uncertainty of the time of the SC2-2 failure to the time period between 54758.6 and 54758.9. The SC1-8B package shows a fairly large pulse at 54759.2 (sampled between 54758.2 and 54759.2) which agrees with this time period. Thus it may be said, tentatively, that the SC2-2 failure may have occurred in the 0.3 second period starting at 54758.6, while the SC2-1 failure cannot be isolated to better than 1.2 seconds starting at 54728.6.

## SC2-1 AND SC2-2 PROBE FAILURE ANALYSIS

A partial circuit diagram for the SC2-1 and SC2-2 probes is shown in figure 22. Switches 4 and 5 are open in the floating potential mode which was operational when the probes failed. The high-voltage follower circuit is a high input impedance device when operated within its design dynamic range. The output uses six high voltage transistors to share the high voltage from both the +1 kV and the -1 kV supply. The output follows the input to about  $\pm 700$  V beyond which the output circuit limits. The relatively low output impedance of the follower, when operating within its dynamic range, drives the inner sphere of the probe (Faraday shield) and a dual range voltage-to-frequency converter (which digitally measures this voltage).

The time plot for the SC2-1 and SC2-2 spherical probe outputs shows that both spherical probes had been sitting close to -350 V with respect to spacecraft frame, for a period of 172 seconds prior to failure. At the time of failure the outputs of the followers rose to approximately +700 V (as measured by the voltage-to-frequency monitor circuit). The exact rise time of the output voltage is not known for either probe because of the low PCM sample rate of the follower output monitor (once per second).

In both probes the high voltage follower circuit must have failed such that the string of six transistors from the output to the +1 kV supply is conducting and cannot be shut off. The differential driver circuit is protected in one direction by diode D2 and Zener Z2 and in the other direction by identical diodes connected in the opposite polarity. The resulting failure output level of approximately +700 V is not necessarily the normal positive limit level of the output stage but could be the result of reduced power supply voltage due to the sustained high current load of the failed circuit. (The supplies were designed for a maximum load of about  $\pm 100$   $\mu$ A.)

The failure mechanism was most likely a high negative input current to the outer sphere. This current had to be large enough and from a high enough potential source to drive the follower to its natural output limit level of -700 V at which point the output voltage no longer follows the input. The input-to-output voltage differential increases until diode D2 and Zener Z3 conduct. The output is then essentially shorted to the input within 10 V. The input current can then drive the output circuit to a more negative potential than limit level.

When the diodes conduct, the follower output capacitor of 1000 pF is added in parallel with the equal value capacitor in the input filter. Since the capacitance in the +1 kV supply at the circuit board is 2000 pF, it can provide a current of at least 100  $\mu$ A above the supply design of 100  $\mu$ A for 1 mS and drop only 100 V. Therefore, the output voltage can be dynamically driven by an input current of about 200  $\mu$ A for less than 1 mS to greater negative value than -1 kV, without appreciably pulling down the positive supply potential. At this point, the string of six tran-

sistors from the output to the -1 kV supply is essentially off, due to the relatively low potential across them in either polarity. If the follower output is driven toward -1.4 kV, the voltage across each of the six series field-effect transistors (from the follower output to the +1 kV supply) approaches the avalanche breakdown potential of about 400 V; that is, a total of 2.4 kV appears across the transistor string. (The actual transistors were tested to 350 V at 50  $\mu$ A prior to assembly.)

If the transistor breakdown characteristic has a negative resistance, the junction current can increase while the voltage decreases. When the first transistor breaks down, its voltage decreases, further stressing the remaining transistors and causing them to break down in turn until all six are in avalanche. The total current through the transistors need not be very large at this point. If the current density is high enough at any portion of the transistor junction, catastrophic failure in the conducting mode can take place.

At breakdown the follower input and output are essentially connected together with a total capacitance of 2000 pF relative to ground. The +1 kV supply has a 2000 pF capacitor connected to ground. These capacitances are effectively in series across the six transistor string with approximately 2 kV across them. If the breakdown were to fully discharge this capacitance of about 1000 pF, a total charge of 2  $\mu$ C maximum would be passed through the transistor string. The approximate currents required would be 2 mA in 1 mS to 20 mA in .1 mS.

The following are the requirements for the SC2 failure (table 12):

(1) Sufficient current must have been introduced to the outer sphere to drive the output of the high voltage follower through protective diodes to about -1200 V to -1400 V. Performance tests of the probes using a 13 kV electron gun proved that the probes could shunt 30  $\mu$ A with the follower output limiting to -700 V. Therefore, the input failure current had to be in excess of this value but need only be in the order of 200  $\mu$ A since the design current for the transistors at circuit limit level is approximately 100  $\mu$ A.

(2) The potential of the current source had to be much greater than -1500 V. The electron gun operating potential at the time of failure was 3 kV.

(3) The total charge required to move the 1000 pF capacitors at the follower input and output about 1000 V was 2  $\mu$ C. At 200  $\mu$ A the time to move the voltage on 2000 pF is 10 mS; at 2 mA the time becomes 1 mS. In the extreme case of a 3 kV source with unlimited current capability the maximum current into the input would be limited to less than 250  $\mu$ A by the 10 kohm input resistor. At this current the time to charge the capacitors to 100 V would be of the order of 10  $\mu$ S.

(4) The charge available to destroy the transistors after breakdown is also about 2  $\mu$ C. It is stored in the 2000 pF filter capacitor on

the +1 kV supply line, in series with the 1000 pF capacitor at the follower input and output lines which are charged to approximately -1.4 kV.

The day following the probe failures, switch 5 was closed by ground command connecting a 100 kohm shunt from sphere to spacecraft frame. This caused the probe monitor voltage to drop to about +40 V. The equivalent source at the output is then a +700 V supply with a source impedance of about 1.6 Mohms. This is in agreement with the observation of a 3 to 4 V spin modulation (of the failed probe voltage) when the vehicle is in sunlight. Assuming a probe surface of approximately 1000 cm<sup>2</sup> and a photo-emission of 1 nA/cm<sup>2</sup>, the photo-current modulation as the vehicle spins (rotating the probes in and out of the shadow of the vehicle body) is in the order of 1  $\mu$ A. This should produce a voltage modulation of the order of 1.6 V due to the output impedance of 1.6 Mohms in the failed transistor string.

#### POSSIBLE PROBE FAILURE CAUSES

Either one of two distinctly different processes is thought to be the cause of the SC2 failures during the SC4-1 operations; arcing along the boom to the SC2 sphere, or impact of beam electrons on the SC2 sphere. The attempts to determine the cause of failure have been directed to be consistent with the SC2 failure analysis, including the values listed in table 12. A plausible scenario can be presented for the arcing hypothesis. As expected (and seen from the measurements of the potentials of the sample materials), grounded conductors, floating conductors, and dielectrics did not charge at the same rate during beam operations. These measurements show that there was a large differential charging between surfaces and spacecraft frame when SC4-1 ejected 3 keV electrons. Differential charging should have occurred along the boom during this mode, since the boom was specifically designed to provide alternate sections of conducting and dielectric segments. The differential charging may have been caused or enhanced by beam electrons returning to the spacecraft, and then striking and accumulating on the boom. As the boom went into shadow, the mechanism for removing these electrons (photo-emission) ceased, and could have created higher differential charging between segments of the boom. The recorded pulse rates and amplitudes show that there was significant arcing on the spacecraft exterior. There is, however, no quantitative explanation of the events, or even a localization of the arcs specifically to the booms and the spheres.

One particular mechanism that produces arcing is the breakdown over the surface of a dielectric due to an avalanche of secondary electrons created by the potential gradient along the dielectric (ref. 2). A technique exists for estimating the current,  $I$ , released in this type of arc,

$$I = AC \Delta d,$$

where  $A$  is the area discharged per unit time,  $C$  is the capacitance of the dielectric per unit area and  $\Delta d$  is the decrease in the voltage differential caused by the passage of the discharge wave over the surface of the dielectric.

If the discharge has a width  $W$  and speed  $V$ , then

$$A = WV.$$

Laboratory measurements have shown for some dielectrics that

$$V \cong 10^6 \text{ cm/sec};$$

$$C = 10 \text{ pF/cm}^2$$

(an extreme value of the capacity of boom surface to spacecraft ground);

$$W = \pi d,$$

where  $d = 4.8 \text{ cm}$  (the boom diameter);

$$I = 0.15A$$

is a current sufficient to have caused the failures. Even if the many assumptions made in this calculation were valid, open questions would include the duration of the discharge and the total charge transferred.

The beam electrons returning to the space vehicle were considered more likely to strike the SC2 spheres than the ejected electrons on their outward path. An estimate of the return current of beam electrons,  $I_r$ , can be made from the measurement results (Table 5). Assuming that orbit limited theory can be used (ref. 3) to estimate the return current of plasma electrons of temperature,  $\theta$ ; and that

$$V_{SC} \gg \theta;$$

$$I_r = KV_{SC};$$

where,

$$K = \frac{neA}{(2 \pi m \theta)^{1/2}}$$

( $n$  = plasma electron density,  $m$  = electron mass,  $e$  = electron charge, and  $A$  = spacecraft area).

For two different values of spacecraft potential,  $V_{SC}$  and  $V_{SC}'$ ,

$$I_r' = I_r \frac{V_{SC}'}{V_{SC}}.$$



Using values of  $I_r$ ,  $V_{sc'}$ , and  $V_{sc}$  from table 5 for 3 keV electrons, for mode 11 between 2 and 7% of the return current was due to ambient plasma electrons, and therefore between 93 and 98% of the beam electrons returned to the spacecraft. If a substantial part of this return current struck the SC2 spheres, there would have been sufficient current and energy to destroy the SC2-1 and SC2-2 payloads. However, if the current of  $6 \times 10^{-3} \text{ A}$  was returned uniformly over the entire  $14 \text{ M}^2$  spacecraft area, the current density would have been  $4 \times 10^{-4} \text{ A/M}^2$ , and the current to the  $0.1 \text{ M}^2$  area spheres would have been  $4 \times 10^{-5} \text{ A}$ . This current is far below that required for the damage (see table 11). Theoretical attempts have been made to determine the current density of the returning beam. These procedures have included analytical approximations, numerical, and "particle pushing" models. These attempts have shown that the space charge of the beam electrons is an important factor in the beam dynamics, and that the excursion of the beam for the SC4-1 mode 11 was more than an order of magnitude larger than the size of the satellite. Because of these factors, calculation of the self-consistent charge density, and particle orbits, with sufficient accuracy to predict the current density of the return beam have proven to be intractable by straightforward simulation. A two dimensional model shows that for mode 11 the space charge in the emitted beam spread the beam further than it propagated, implying an isotropic return beam. During mode 11, ML12-7 measured a maximum return current of  $3.6 \times 10^{-8} \text{ A}$ . ML12-7 has a geometric factor of  $4.26 \text{ cm}^2/\text{ster}$ . If an isotropic flux is assumed at ML12-7, the current flux at the instrument is  $5.2 \times 10^{-4} \text{ A/M}^2$ , which is consistent with an isotropic flux over the entire spacecraft.

#### SC4-1 PULSE MODE FAILURE

There are several possible causes of the SC4-1 pulse mode failure. A detailed analysis has eliminated all but one possibility, as the others would have to be random component failures not associated with the 3 kV command execution. A negative transient pulse on the timing gate input line could conceivably damage the input circuit of a TTL 54L14 buffer of the SC4-1. This would have to result in an equivalent short to ground at the input. It is not known how a high voltage transient could be injected onto this line since the timing gate line is double shielded with both shields tied to the connector shell at SC4-1 and grounded at the PCM encoder end. The timing gates from redundant encoders are spliced together within the space vehicle harness wiring. The nature of the splice and shield connections are not known.

#### TELEMETRY ANOMALIES

In addition to the SC2 sphere failures and the SC4-1 pulse mode failure, there was an anomaly in the telemetry bit stream during mode 11 as monitored by the ground receiving station. (See Appendix 2 for a detailed discussion.) The loss of telemetry sync occurred in main frames 25 and 26

at 54736.397 and 54736.522. The TPM shows a fairly small pulse at 54736 which is too soon and a larger pulse at 54738 (sampled between 54736.6 and 54737.8). This appears to be too late but that may be due to an error in the timing analysis. The SC1-8B package shows a few small pulses at 54737.2 which may be considered as the cause of the loss of telemetry sync.

It may be positively stated that the disruption occurred in the PCM encoder accumulator from which the enable gates and shift pulses are generated. It was caused by a gain of counts equivalent to a time period of nine PCM bits, or 1.1 mS. This is equivalent to thirty-six counts at the x4 bit clock input to the encoder from the TDU. This line is the most probable point of noise injection, caused by a discharge, affecting only the accumulator following. This time shift in the encoder accumulator, relative to the time code accumulator, lasted for 106 frames (13.25 seconds) until the master frame sync, on another line from the TDU, resynchronized the encoder accumulator.

At the time of the noise injection, frame sync was lost on the ground due to the shift in time location of the sync pattern at the end of the main frame. Frame sync was also lost at the beginning of the new master frame due to the return shift of the time location of the three-word pattern.

#### PASS 89.4 CONCLUSIONS

The operation of the SC4-1 electron gun on the P78-2 satellite created a positive potential on spacecraft frame. The ejection of 6 mA of 3 keV electrons caused large differential charging of the spacecraft surfaces, arcing, a telemetry interruption, and failure of the SC2-1 and SC2-2 payloads. In addition, there was a failure of the SC4-1 pulse mode operation. An analysis of circuitry has identified the components that were affected and has established a basis for determining the causes of the problems. Theoretical studies and measurement analyses have focused on two hypotheses: arcing along the boom to the SC2 sphere, and impact of beam electrons on the SC2 sphere. These investigations still leave a great uncertainty as to the destructive mechanism.

## APPENDIX 1: THE MAGNETOSPHERIC ENVIRONMENT FOR PASS 89.4 ON MARCH 30, 1979.

### I. Overall Conditions: March 28-30, 1979

On March 30, 1979, the SC4-1 electron beam system on board the P78-2 satellite was operated from ~14:43 to 15:52 UT, while the satellite, in near-geosynchronous orbit, was in the local midnight sector at altitudes of 6.1 to 6.3  $R_E$ . At ~15:30 UT the satellite entered eclipse.

During the time of electron beam operations the magnetosphere was in a stable, quiet period, following two days of intense activity. The activity began with a sudden commencement at 8:27 UT on March 28, and was recorded by all stations in the AFGL mid-latitude magnetometer chain (David Knecht, private communication). The sudden commencement can also be seen in the SC5 particle data and in the SC11 magnetic field data on P78-2.

Following the sudden commencement the magnetosphere became and stayed active for 46 hours, until 07 UT on March 30. Figure 23 shows magnetic indices for the three days. The Auroral Electrojet Index ( $A_E$ ) shows persistent increasing activity from ~150 nT at 08 UT, to >700 nT by 8:30 UT, after which there are impulsive increases in  $A_E$  of up to 1400 nT throughout the active period (7 station  $A_E$  index provided by C.-I. Meng). Mid-latitude magnetic activity, as measured by  $K_p$ , jumped from 4- to 5+ at 09 UT and reached a maximum value of 7- at the end of March 29.  $D_{st}$ , indicating ring current growth, remained at near constant levels (~-40 nT) throughout March 28. On March 29,  $D_{st}$  decreased steadily, reaching -120 nT at the end of the day, and recovering throughout March 30. Within an hour of the sudden commencement the equatorward boundary of the diffuse aurora, measured by the DMSP (F2) polar orbiting satellite, fell to 58° CGL (Corrected Geomagnetic Latitude) at 20 MLT and 55° CGL at 09 MLT, indicating considerable Earthward motion of the plasma sheet.

Auroral electrojet activity abruptly decreased to less than 100 nT on March 30, following a northward turning of the interplanetary magnetic field, measured at the ISEE3 altitude at 6:30 UT (E.J. Smith, private communication). After this,  $K_p$  fell to 1+ and did not exceed 2+ throughout the remainder of the day. For this period  $A_E$  was never greater than 250 nT, typically being considerably less. The evening and the morning diffuse auroral boundaries systematically moved poleward over a 6 hour period to upwards of 65° CGL.

During the electron beam operations (from 14 to 16 UT),  $K_p$  varied from 2+ to 2-,  $A_E$  was less than 170 nT, and  $D_{st}$  ~-54 nT. For this period there were two DMSP (F1) optical images of the south polar region, each covering the dusk half of the oval. For the first image the satellite crossed the pole at 14:30 UT, and for the second at 16:10 UT. Each showed a contracted auroral oval with extended, weak arcs. The later image showed the auroral region in the midnight sector to be thinner by several degrees

and less intense, indicating an uninterrupted quieting process. In all, it can be concluded that the state of the magnetosphere was sufficiently quiet and stable throughout the two hour period to justify extrapolation of plasma parameters into the period of beam operations, since these necessarily interrupt many of the measurements of the ambient plasma. The justification applies to extrapolations in time only. We must also be aware of spatial changes which P78-2 may have encountered during this time.

## II. The Position of the Satellite in the Magnetosphere.

### A. Position with respect to particle populations.

Figure 24 is a schematic diagram of the P78-2 orbit on March 30, in L-shell and in local time (the outer tick marks, with noon at the top of the figure). The tick marks on the orbit itself mark Universal Time. The beginning of March 30 (00 UT) is at dawn. At this time Kp had its highest value for the day, equal to 5. In addition to the satellite orbit, Figure 24 shows boundaries for the two major magnetospheric particle populations: the plasma sheet, a hot, tenuous plasma; and the plasmasphere, a cold, dense plasma. The boundaries are statistically derived, and Kp dependent. The inner edge of the plasma sheet is given by the dashed line, and is taken from a model derived using over 6000 DMSP (F2) auroral oval boundaries (ref. 4). The plasma sheet relaxed outward (away from the Earth) throughout the UT day as activity diminished. (The abrupt changes in the boundary are a result of the 3-hour time intervals of Kp.)

In crossing the plasma sheet an increase in energetic ( $>50$  eV) particles is expected. All increases in energetic particles at near-geosynchronous orbit are, in the literature, somewhat misleadingly referred to as injection events. Plasma sheet crossings are differentiated from other injection events by a clear energy dispersion in the particle flux increases as quasi-stationary Alfvén boundaries for higher energy particles are traversed.

Figure 25 gives the electron number density (in  $\text{cm}^{-3}$ ), energy density (in  $\text{keV}/\text{cm}^3$ ) and average energy (in keV) calculated from the electrostatic analyser data of SC5 for March 30. The energy range is from 50 eV to 60 keV; in order to calculate the moments, the distribution functions obtained at a rate of once per second from the detectors parallel to the spin axis are integrated over pitch angle. The closest approach to the magnetic field varies from  $45^\circ$  at 12 UT to  $4^\circ$  at 16 UT. SC5 did not operate for most of the first half of the day and was turned off for the initial electron beam operations near 15 UT. The large spikes in the data delineate the period of beam operations, ending prior to 16 UT.

The plasma sheet crossing occurred at 13.7 UT, almost precisely at the model prediction. The crossing had a clear signature in the number density (sharp increase) and in the average energy (sharp decrease since the zero energy Alfvén layer was crossed first). After the crossing, the number

density remained fairly constant,  $.35-.5/\text{cm}^3$  for several hours (extrapolating through the data gap and beam operations), while the average energy increased as higher energy Alfvén layers were crossed. The data gap occurred prior to crossing Alfvén layers for particles with energies greater than 10 keV. The temperature, as measured by the average energy ( $3/2kT = \bar{E}$ ), also increased from 260 eV at the plasma sheet crossing to 1.2 keV at 16 UT. Thus, for electrons with energies less than 10 keV, it appears that there were no major spatial changes during the period of beam operations, while there may have been a systematic increase in the mid-range energies (10-60 keV). The solid state detectors on SC5 showed the electron population for energies greater than this (into the MeV range) to be virtually unchanged throughout the period.

Ions do not show a clear signature for plasma sheet crossings. The corresponding values of the moments of the ion distribution, as measured by SC5 in the same energy range, had regular variations over the two hour period of interest. The number density remained relatively constant between  $0.6-0.7/\text{cm}^3$ , and the energy density decreased from  $12 \text{ keV}/\text{cm}^3$  at 14 UT to  $4.8 \text{ keV}/\text{cm}^3$  at 16 UT, while the temperature (determined by average energy) decreased from 11 to 6 keV over the same period.

Of great interest in charging operations is the position of the plasmasphere and the encounter of related, warm plasma populations ( $kT < 30 \text{ eV}$ ). The instruments designed to measure the cold component of the magnetospheric plasma (temperatures less than a few eV) failed early in the P78-2 mission (Experiments SC6 and SC7). SC9 measures particles downward in energy to several eV, and therefore, covers a good portion of the warm plasma component (from 1-30 eV). The higher energy spectrum is well-determined into the MeV energy range for both electrons and ions by the combined measurements of SC2-3, SC-5, SC-3, SC-8, and SC-9. The low energy population greatly affects spacecraft charging and beam operations, and the loss of on-board measurement of this component is debilitating, particularly in modeling efforts. At best we can only set upper limits on densities.

The problem of setting limits on the low energy plasma populations for SCATHA operations can be addressed in two ways: (1) from an overall knowledge of plasmaspheric dynamics; and (2) from near-coincident measurements made by other satellites at geosynchronous altitudes.

In brief, previous studies show that the plasmasphere is a region of high density ( $10-1000/\text{cm}^3$ ) warm plasma that corotates with the Earth and whose source is the ionosphere (ref. 5). The plasmasphere can extend to geosynchronous orbit, most typically after prolonged periods of quiet magnetospheric conditions and for local times in the afternoon sector. During active periods the outer regions of the plasmasphere are depleted and are replaced by the Earthward-moving, low-density, hotter plasmasheet. Subsequent filling of the plasmasphere from the ionosphere after the plasmasheet has receded to quiet time positions is generally slow (on the order of tens of hours). Since the period of beam operations was within 10 hours of a very active period, and since P78-2 was very clearly inside

the plasma sheet at this time, we may safely conclude that P78-2 was not in a region of the highest cold plasma densities ( $100\text{-}1000/\text{cm}^3$ ).

However, intense ( $10\text{-}100/\text{cm}^3$ ) and weak ( $1\text{-}10/\text{cm}^3$ ) warm plasma populations can be encountered outside the plasmasphere at geosynchronous orbit (ref. 6). The former are not found in the midnight sector, and the latter only rarely so during times of low magnetic activity. Geos 2, at geosynchronous orbit, lagged P78-2 by about 5 1/2 hours during March 28-30. The superthermal plasma analyser on board detected cold ion densities ( $T \sim 1$  eV) on March 28, 29 from  $\sim 10\text{-}20$  hours local time (LT) with densities ranging from  $1\text{-}16/\text{cm}^3$ . The peak densities ( $\sim 10/\text{cm}^3$ ) occurred between 13:30 and 15:30 LT. On March 30, this population was not detected at these local times but was encountered beginning at 17 LT, reaching a peak value of  $8/\text{cm}^3$  at 21:30 LT and disappearing by 22:30 LT. Field-aligned cold plasma fluxes (with equivalent densities up to  $10/\text{cm}^3$ ) were encountered from 10 to 21:30 LT (Gordon Wrenn, private communication). Therefore, it can be concluded that the fringes of the plasmaspheric filling process may have been encountered by P78-2 at times near those of beam operations (prior to local midnight). From the Geos 2 data an upper limit to the cold plasma population with temperature  $\sim 1$  eV can be set at  $10/\text{cm}^3$ .

#### B. Position of the satellite in the magnetospheric magnetic field.

Figure 26 is a schematic diagram showing the position of P78-2 with respect to the magnetic field during beam operations on March 30. The projection is in the meridional plane. The satellite is in the southern hemisphere at a magnetic latitude of  $-18.6^\circ$  and a geographic latitude of  $-7.8^\circ$ . The magnetic field, measured by SC11 on SCATHA, is in a tail-like configuration, at an angle of only  $\sim 30^\circ$  to the solar direction.

At the time of the SC2 failure, the total magnetic field was 178 nT, decreasing at a uniform rate of 24 nT/hr. In Earth-Centered Inertial coordinates ( $x$  parallel to the line of equinoxes and in the direction of the autumnal equinox,  $z$  parallel to the polar axis of the Earth's North Pole, and  $y = z \times x$ ) the field components are:  $B_x = -157$  nT,  $B_y = 16$  nT,  $B_z = 82$  nT; that is, the field is nearly meridional, making an angle of  $28^\circ$  with the solar ecliptic. The field remained tail-like throughout the sunlit electron beam operation. At 15:36 UT the field suddenly rotated into a dipolar configuration and remained in this configuration for several minutes. After this the field returned, as suddenly, to a more tail-like configuration (by  $\sim 8^\circ$ ) than prior to the rotation. The field begins a slow recovery toward dipolar-like configuration after 15:50 UT. (Note: further investigation is being conducted to support the existence of the anomalously large rotation at 15:36 UT.)

### III. Distribution Function of the Ambient Plasma Prior to Beam Operations Using SC2-3, SC5, and SC9 Measurements.

Three particle detectors, SC2-3, SC5, and SC9, operated on March 30

to within 12 minutes of the time when the cap on the electron beam was removed. The data from these operations (14:45-14:49 UT) are used to calculate an average isotropic distribution function to represent the ambient plasma. The energy range, position on the satellite, energy pass bands and pitch angles differ for the three instruments and thus they do not lend themselves to easy comparison. A comprehensive intercalibration of the P78-2 instruments is underway. The intercalibration will address the differences cited above, and in addition, differences in calibration methods, degradation in flight, and ion composition. Thus, the distribution function constructed here should be considered preliminary.

Figure 27 is a plot of the distribution functions of electrons and ions for a one minute period in the given 5 minute interval. The breadth in the values for SC2-3 and SC5 result from their pitch angle sampling. The low energy (<10 eV) electrons in one SC9 detector (solid line) and the low energy ions (<10 eV) monitored by SC9 are at background levels.

The ion distribution function is calculated over two energy ranges, <1.5 keV and >1.5 keV. The higher energy range is well-fit up to 188 keV by a Maxwellian distribution with temperature between 14-16 keV, and number density between 0.4-0.6/cm<sup>3</sup>. For the low energy ( ~ .07-1.5 keV) the SC5 counts are at background levels and are omitted from consideration. A Maxwellian distribution is not a particularly good choice for this range, but a reasonable fit is made with temperature and density, 180 eV and .05/cm<sup>3</sup>, respectively. A power law distribution gives a much better fit to the low energy SC9 data down to 10 eV. For a power law:  $f = f_0 E^{-\alpha} \text{ sec}^3/\text{km}^6$ ,  $f_0 = 4.38 \pm .13$ ,  $\alpha = -1.6 \pm .1$ , and the density is .07/cm<sup>3</sup> to within 20%.

The electron distribution functions for the three instruments differ greatly, although the difference is principally in the value of the function, and not the shape. The electron distribution function here, and as is often found to be the case, does not fit a Maxwellian except for small energy intervals. Therefore, we again fit the data to two non-overlapping power law distributions, one in the energy range .050-5 keV, and one >5 keV. In the low energy range  $\alpha = 1.25$ , with  $f_0$  varying between 2.4 and 4.37, giving a density variation from .41 to .75/cm<sup>3</sup>. In the high energy range  $\alpha = 3.2$ ,  $f_0 = 4.95$  and  $n = .008/\text{cm}^3$ . In this last fit, the SC2-3 data was not used. The values are low due to the use of an efficiency factor of unity for all energies. (For the above power laws, E is in keV and  $f_0$  has the same dimensions as f.)

## APPENDIX 2: TELEMETRY ANOMALIES

A detailed analysis of the problem and its probable causes has been made. In order to understand the telemetry data anomalies, a description of the Pulse Code Modulator (PCM) output format follows.

All data inputs to the PCM encoder are sampled at least once in a 16 second interval, the time required for one master frame. The master frame consists of 128 main frames. The time for one main frame is then 0.125 seconds. Each main frame consists of 128 words of 8 bits in length, producing a bit frequency of 8192 bits per second.

Several words of each main frame are dedicated to frame identification, synchronization, and vehicle time. This allows for decommutation of the serial digital data when received on the ground and for time-tagging the encoded data. Table 13 is a listing of the binary values of these dedicated words as decommutated from the data tape.

The first four words of the main frame, words 000 through 003, contain the Vehicle Time Code Word (VTCW). Word 000 contains the 8 most significant bits of the binary time code. Words 001 and 002 contain the next 16 most significant bits, and the first 4 bits of word 003 are the four least significant bits of the time code. The remaining four bits of word 003 are a fixed zero ("A", table 13) and a repeat of the three least significant bits of the time code.

The least significant bit of the time code changes every main frame and therefore has a weight of 0.125 seconds. The capacity of the time code accumulator is  $2^{28} \times 0.125$  seconds or greater than 388 days. This accumulator and the shift register for the vehicle time code (figure 28) are located in the Timing Distribution Unit (TDU).

Word 124 of the main frame is a main frame binary counter readout. It is synchronized to the master frame and is advanced one count each main frame. In normal operation it is identical to the eight least significant bits of the VTCW. It has a capacity of 128 (000 to 127) which is the number of main frames in a master frame. This counter is located in the PCM encoder. It is important to note that although equal to the last eight bits of the time code, the generation of the frame count is accomplished in a different assembly.

The last three words of the main frame (125, 126, and 127) are dedicated to main frame synchronization. These 24 bits have the octal coding 01147537. This sync code resides in a Read-Only-Memory (ROM) located in the PCM encoder.

The PCM encoder (figure 29) generates all enable gates and gated shift pulses for taking data from payloads and the TDU (for the VTCW). Normally these gates are generated using a  $x^4$  bit clock signal (32768 Hz) and a 1/16 Hz master frame synchronizing signal from the TDU.



If the external clock from the TDU fails, there is a crystal controlled clock internal to the PCM encoder which automatically takes over, providing timing gates, enable gates, shift pulses, and special timing gates for experiments SC4, SC9, and SC11, as well as the main frame counter.

During Pass 89.4 of the P78-2 satellite there was a disruption of the digital data stream from the PCM encoder. This occurred 8 seconds after the 3 keV command execution on the electron gun experiment. The first data from AFSCF showed a 14 second data dropout, a loss of about 105 main frames.

After analyzing the data using a program which recognized the start of the master frame and then counted main frames, it was found that the instrument data was not lost nor was it erratic. Successive instrument data samples showed no serious magnitude jumps. The vehicle time code, however, was invalid for these 105 frames.

Since the time code, frame counter, and synchronizing words either remain constant or advance in a predetermined pattern, the main frame words associated with these functions were examined in detail for the data disruption period. A careful examination of table 13 reveals the following:

(1) Up to frame 025 the data was normal. The VTCW and frame counter were incremented by one each main frame. The frame synchronization remained correct and constant.

(2) During frame 025 at UT 54736.397 (assumed to be the time of the start of frame or the time of frame synchronization), the VTCW (PCM words 000, 001, 002, 003) was normal. By the end of the frame, however, the expected bit locations were nine bits early ("B", table 13); word 124, the frame identification word, is a count of main frames in the master frame, and had a count of 9 instead of the expected 25. This count, 00001001, also happens to be the second through ninth bits expected in the frame synchronization pattern (words 125, 126, 127; "C", table 13).

The first 15 bits in the frame synchronization pattern were the same as those expected during normal operation in the tenth through twenty-fourth bits in these three words. This indicates that the PCM encoder was presenting data to the output nine bits early, starting some time after word 003 but before word 124 of frame 025.

(3) During frame 026 at UT 54376.522 the ground decommutation had not yet found the synchronization pattern and was still sampling at the normal rate. Actually, the decommutation and the VTCW were synchronous but the PCM readout was nine bits early. This means that the shift pulses for the first nine bits of the first word occurred as the last nine bits of the last word of frame 025. Since the VTCW shift register was not loaded at the start of the readout, it shifted out nine ones. (The VTCW shift register shifts in all ones into its front end as it shifts out the time code.) The nine ones at the end of frame 025 are then explained.

Assume that the PCM encoder is nine bits ahead of the VTCW shift register

process. Just before the tenth shift pulse, the VTCW accumulator generated a VTCW shift register load signal and loaded the register with the correct time from the accumulator. The next twenty-three shift pulses shifted out the proper time code, most significant bit first, and then the shift pulses from the encoder to the VTCW shift register ceased. The next nine bit slots were all zeros. This apparently was data from SC2 which fits into the eight bits of word 004 and bit one of word 005 of frame 026.

At the end of frame 026 the frame identification and frame synchronization still exhibited the nine bit advance of the PCM encoder but the last sixteen bits were garbled. This is apparently the time during which the ground decommutator corrects for the shift after recognizing the synchronizing pattern.

(4) In frame 027 at UT 54736.646 note first that the UT is 1 mS faster than expected ("D", table 13). Every second frame time-tag ended in a .xx7 or a .xx2. From this frame until the start of a new master frame the time-tags ended in .xx6 and .xx1. This means that the PCM data string was arriving 1 mS (nine serial data bits) earlier than previously.

The first nine bits of the VTCW do not form an identifiable pattern and can probably be explained by the resynchronizing process in the ground decommutator. However, the last twenty-three bits of the VTCW form the exact pattern expected in the first twenty-three bits of the VTCW. This can only occur if the load signal to the VTCW shift register (in the TDU) occurred nine bits later than the beginning of the VTCW shift operation.

It should also be noted in this frame that the frame counter (word 024) and the frame synchronization pattern (words 125, 126, 127) were correct.

(5) In frame 028, at UT 54736.771, all data except the VTCW were correct. The VTCW bit pattern shows that the first nine bits are the same as those expected during normal operation in the last nine bits of the VTCW in the previous frame ("E", table 13). The ground time-tag is 1 mS fast, as compared with time-tags prior to frame 026 and after frame 001 of the next master frame.

This pattern persists until the beginning of the next master frame; that is, the vehicle time code appears to be nine bits late. Frames 035 through 119, although not printed out in this table, did exhibit this pattern.

(6) At UT 54749.271, the beginning of the next master frame, the pattern changed. The PCM encoder circuits were reset by means of a master external sync signal from the TDU. This signal is a 0.0625 Hz square wave, and synchronization occurs on the negative-going edge of this signal. This is always when the last seven bits of the time code (bits 22 through 28 of the VTCW) go to all zeros, indicating frame count decimal 000. However, in frame 000 of the new master frame, the first twenty-eight bits of the first four words are what would be expected with the nine bit VTCW delay.

The frame sync was lost and the ground decommutation process did not pick up frame sync until frame 014.

(7) A second pass of the tape produced data for main frames 002 through 013, and showed that the VTCW neither lost nor gained time relative to the time before the anomaly began. The ground time-tags were all 1 mS earlier than expected during the anomaly ("F", table 13).

(8) All data patterns were normal from UT 54749.522 onward.

A review of the schematics for relevant circuits resulted in the block diagrams for the Vehicle Time Code Generator located in the TDU (figure 28) and the PCM encoder (figure 29). These diagrams reveal the following:

(1) The TDU sends two timing signals to the PCM encoder which are used in normal operation. These are a x4 bit clock square wave at 32768 Hz, and a 0.0625 Hz square wave. The x4 bit clock is used to generate all word enable gates, shift pulses, frame counts, and addresses for the synchronization ROM. Most of these functions are accomplished in the encoder by means of counters and hard-wired logic.

(2) The VTCW is generated in the TDU. The basic clock used for the time code is the same as that used to generate the x4 bit clock signal sent to the PCM encoder. The VTCW shift register is also located in the TDU. Although the shift enable gate and the gated shift pulses for the VTCW shift register are generated in the encoder, the load signal which transfers data from the clock accumulator stages to the shift register (in a parallel fashion) is generated by circuits in the TDU using clock signals from the clock accumulator.

It is therefore possible for the accumulators in the TDU (which generate the VTCW) and the accumulators in the PCM encoder (which generate the enable gates and shift pulses) to be in step but shifted in time if one or the other were to receive spurious signals from some noise source. Realizing this, a re-examination of the VTCW data during this anomalous period results in the following scenario: beginning with frame 028 the VTCW had a nine bit shift; that is, the first nine bits of the code were actually the last nine bits of the code for the previous frame. The remaining bits were the first twenty-three bits of the proper VTCW for that frame.

This is particularly evident in frame 032 where the last bit of the code changed to a one. This is actually bit 23 of the real VTCW. This bit changed in the same frame in which the first five bits were all ones, the last five bits of the real time code belonging in the previous frame. These bits did not change to all zeros until the next frame.

It then becomes obvious that the PCM encoder sent its enable gate and shift pulses nine bits before the TDU generated its parallel load pulse. Under these circumstances, what was left in the VTCW shift register just before the start of the VTCW shift was a string of twenty-three ones

(automatically shifted into the front end of the shift register as the more significant bits were shifted out) and the last nine least significant bits from the previous frame, which were left in the register when the shift pulses ran out.

These nine bits were shifted out at the beginning of the new time code with gated shift pulses from the encoder. At this point the TDU loaded the VTCW register with the new count. What was in the shift register now was the proper time code word, with the most significant bit ready to be shifted out on the next shift pulse. The remaining twenty-three shift pulses from the encoder then shifted out the twenty-three most significant bits, leaving the nine least significant bits in the register, followed by a string of ones, to be shifted out when the next encoder enable gate and shift pulses were received.

The disruption must have been caused by a loss of counts equivalent to nine bits in the VTCW accumulator in the TDU, or a gain of the same number of equivalent counts in the encoder accumulator. One observation points to the latter. During the anomalous condition, the Universal Time tags, placed on the data tapes at the time of reception, are consistently 1 mS ahead of the expected data times. In other words, the PCM stream was shifted ahead by 1 mS during the VTCW disruption, and then shifted back 1 mS at master frame synchronization. The master frame synchronization did not take place until nine bits into main frame 000 of the new master frame.

The frame synchronization was re-established by frame 002 of the new master frame at UT 54749.522, 13.25 seconds after the first disrupted frame. The time code at this point was exactly as it would have been without the PCM disruption.

## REFERENCES

1. Stevens, J.R.; and Vampola, A.L.: Description of the Space Test Program P78-2 Spacecraft and Payloads. SAMSO TR-78-24, Space and Missile Systems Organization, October 31, 1978.
2. Inouye, G.T.; and Sellen, J.M., Jr.: A Proposed Mechanism for the Initiation and Propagation of Dielectric Surface Discharges. Proc. 1978 Symposium on Effects of the Ionosphere on Space and Terrestrial Systems.
3. Langmuir, Irving; and Mott-Smith, Harold, Jr.: Studies of Electric Discharges in Gases at Low Pressures. General Electric Review XXVII, July-Dec. 1924; rpt. in The Collected Works of Irving Langmuir, Vol. 4, ed. C. Guy Suits, Pergamon Press, 1961, p. 31.
4. Chappell, C.R.: Recent Satellite Measurements of the Morphology and Dynamics of the Plasmasphere. Rev. Geophys. Space Phys., 10, 951, 1972, pp. 951-979.
5. Gussenhoven, M.S.; Hardy, D.A.; and Burke, W.J.: DMSF/F2 Electron Observations of Equatorward Auroral Boundaries and Their Relationship to Magnetospheric Electric Fields. J. Geophys. Res., to be published, 1981.
6. Lennartsson, Walter; and Reasoner, David L.: Low Energy Plasma Observations at Synchronous Orbit. J. Geophys. Res., 83, 1978, pp. 2145-2156.

TABLE 1. SELECTED P78-2 INSTRUMENTS

Instrument	Name	Use During Pass 89.4
SC1-1,-2, and -3	Surface Potential Monitors	Measure the charging potentials and currents of various materials.
SC1-7	R.F. Electromagnetic Wave Analyzer	Measures Electromagnetic (EM) emissions from 2 MHz to 30 MHz.
SC1-8A	Very Low Frequency (VLF) Wave Analyzer	Measures EM emission in the ELF, VLF and LF ranges.
SC1-8B	Transient Pulse Shape Analyzer	Measures the shape of EM pulses in the time domain from 7 nsec to 3.7 msec.
SC2-1 and -2 Probes	Sheath Electric Fields	Measure the potential of a conducting sphere 3 meters from the spacecraft.
SC4-1	Satellite Electron Beam System	Eject electrons to charge/discharge the spacecraft frame.
SC4-2*	Satellite Positive Ion Beam System	Eject positive ions and/or electrons to charge/discharge the spacecraft frame.
SC5	Rapid Scan Particle Detector	Measure the charged particle flux incident to the spacecraft.
SC9	UCSD Charged Particle Experiment	Measure the charged particle flux incident to the spacecraft.
SC10-3	Electric Field Detector	Measure the potential of a conducting cylinder at between 30 and 50 meters from the spacecraft.
SC11	Magnetic Field Monitor	Measure the ambient magnetic field at 4 meters from the spacecraft.
MLi2-7	Spacecraft Contamination	Measure electron current to spacecraft.
TPM	Transient Pulse Monitor	Detect and measure electromagnetic pulses.

\* Not used during Pass 89.4.

TABLE 2. INSTRUMENT "LINE-OF-SIGHT" ANGLES

Instrument	Alpha (degrees)	Beta (degrees)
SC1-1	307.5	0
SC1-2	120.	0
SC2-1 Boom	327.2	0
SC2-2 Boom	147.3	0
SC4-1	189.7	0
SC4-2	4.5	304
SC5 Parallel Detector	227.	90
SC5 Perpendicular Detector	227.	0
SC10-2 Boom	304.	0
SC10-3 Boom	124.	0
ML12-7	128.3	90

TABLE 3. SC4-1 MODES

Mode #	Time Start	Time Stop	Eb (keV)	Ib (mA)	Vsc (V)	Notes
1	52971	53745	0	0	5.7	Power off
2	53745	53894	0	0	6.0	Power on
3	53894	54082	0.3	0.1	5.7	
4	54082	54326	0.3	0.1	264.	Cap opened
5	54326	54437	1.5	0.1	1400.	
6	54437	54509	1.5	1.0	1440.	
7	54509	54542	1.5	1.0	-	Pulsed Beam
8	54542	54556	0.5	1.0	-	Pulsed Beam
9	54556	54651	0.5	1.0	480.	
10	54651	54728	0.5	6.0	480.	
11	54728	54809	3.0	6.0	2920.	SC2 damaged; occurrence of telemetry anomaly
12	54809	54820	1.5	6.0	1400.	
13	54820	55058	1.5	13.	1280.	
14	55058	55122	1.5	0.01	80.	
15	55122	55463	3.0	0.01	80.-	
16	55463	55535	0.5	0.01	8.1	
17	55535	55548	3.0	0.01	14.	
18	55548	55658	3.0	0.1	2880.	
19	55658	55707	0.3	0.1	192.	
20	55707	55857	0	0	0	Power off
21	55857	55869	0	0	0	Power on
22	55869	56269	0.3	0.01	268.	
23	56269	56368	0	0	-	Beam off



TABLE 3. SC4-1 MODES (Continued)

Mode #	Time Start	Time Stop	Eb (keV)	Ib (mA)	Vsc (V)	Notes
24	56368	56409	0.3	0.1	270.	
25	56409	56507	0.3	0.01	33.-93.	
26	56507	56519	1.5	0.01	62.	
27	56519	56638	1.5	0.1	1440.	
28	56638	56680	1.5	1.0	1440.	
29	56680	56692	3.0	1.0	2960.	
30	56692	56955	3.0	0.01	400.	
31	56955	56965	0.5	0.01	232.	
32	56965	56974	3.0	0.01	360.	
33	56974	57109	3.0	0.1	2894.	
34	57109	57609	0	0	-320.	Power Off

Table 4. SPACECRAFT FRAME POTENTIALS, SC5 AND SC10

Mode #	Eb (keV)	Ib (mA)	Vsc	
			SC10 (kV)	SC5 (kV)
15	3.0	0.01	0.09 ± 0.01	0.1 ± 0.15
16	0.5	0.01	0.01	0.1 ± 0.05
18	3.0	0.1	2.88	2.4 ± 0.3
19	0.3	0.1	0.19	0.3 ± 0.1
30	3.0	0.01	0.4	0.3 ± 0.1
33	3.0	0.1	2.89	2.7 ± 0.5

TABLE 5. VEHICLE RESPONSE TO ELECTRON BEAM EJECTION ( $V_{sc}/E_b$ )

$I_b$ (mA)	$E_b$ (keV)	3.0 $V_{sc}/E_b$	1.5 $V_{sc}/E_b$	0.5 $V_{sc}/E_b$	0.3 $V_{sc}/E_b$
0.01		*0.03 **0.13	0.004	*0.016 **0.46	0.16
0.1		0.97	0.95	-	*0.64 **0.90
1.0		0.98	0.96	0.96	-
6.0		0.98	0.93	-	-
13.		-	0.85	-	-

\*Sunlight

\*\*Eclipse

TABLE 6. SAMPLE SURFACE POTENTIALS DURING MODE 11

Sample Number	Sample	(V)* Average Volts	(V+ $V_{sc}$ )** Maximum Volts
1V1	Aluminized Kapton	-102	2842
1V3	Optical Solar Reflecting Mirror	-42	2906
2V2	Aluminized Kapton	-1189	1616
2V4	Conducting Reference Band	-258	2649

\*Relative to spacecraft frame

\*\*Relative to ambient plasma

TABLE 7. PULSE SENSORS

Sensor Name	Sensor Position	Measurement Type	Threshold (for 89.4)
TPM Low Z	Vehicle center tube Main vehicle wiring	Voltage	0.12 Volts
TPM High Z	Vehicle Center tube Main vehicle wiring	Voltage	2.40 Volts
TPM Solar	Solar Array to Power Conditioning Unit wire	Current	0.024 Amps
TPM Ground	Power Conditioning to Vehicle Frame wire	Current	0.84 Amps
SC1-8B #0 (Dipole)	External dipole on a 2 meter boom	Voltage	0.30V, 0.165V, 0.469V, 718V
SC1-8B #1 (CDU)	Loop antenna around Vehicle CDU	Voltage	" " " "
SC1-8B #2 (Harness)	Laid along a "typical" cable	Voltage	" " " "
SC1-8B #3 (Command)	Digital Command line from the CDU to SC1-8B	Voltage	" " " "
SC1-7 (RF analyzer)	SC10 dipole antennas 1.8m monopole on boom	RF (2 to 30 MHz)	-110 dBm

TABLE 8. COMPARISON OF PULSES FOR HIGH POWER SC4-1 MODES

Mode#	Eb (keV)	Ib (mA)	Total Pulses		Pulses/Second		Eclipse
			TPM	SC1-8	TPM	SC1-8	
11	3	6	64	71	0.79	0.88	No
13	1.5	13	113	82	0.47	0.34	No
29	3	1	8	0	0.67	0	Yes
33	3	0.1	29	18	0.21	0.13	Yes
18	3	0.1	3	4	0.03	0.04	No

Note: TPM at Pulse Analysis Threshold Level 3  
 SC1-8B at 0.165V Pulse Analysis Threshold

Table 9. A COMPARISON OF SC10 AND SC2 PROBE VOLTAGES

Mode #	Time Start	Time Stop	Eb (keV)	Ib (mA)	-V10 (kV)	-V21 (kV)	-V22 (kV)	V21/V10	V22/V10
4	54082	54326	0.3	0.1	0.264	0.187	0.186	0.71	0.70
5	54326	54437	1.5	0.1	1.400	0.380	0.339	0.27	0.24
6	54437	54509	1.5	1.0	1.440	0.399	0.337	0.28	0.23
9	54556	54651	0.5	1.0	0.480	0.322	0.336	0.67	0.70
10	54651	54728	0.5	6.0	0.480	0.350	0.349	0.72	0.72
11	54728	54809	3.0	6.0	2.96	-	0.550	-	0.18

TABLE 10. MAGNETIC PITCH ANGLE AND SUN ANGLE CALCULATIONS

Period 1 (54728-54730, SC4-1 to 3 keV at 6 mA, SC2-1 probe failure)

Instrument	Time	Pitch Angle Degrees	Sun Angle Degrees
SC2-1 Boom	54728	13.2	146.5
	54729	14.1	152.7
	54730	17.4	158.9
SC2-2 Boom	54728	166.9	33.4
	54729	165.8	27.2
	54730	162.5	21.0
ML12-7	54728	103.1	86.6
	54729	103.1	86.6
	54730	103.1	86.6

Period 2 (54736, loss of telemetry sync)

Instrument	Pitch Angle Degrees	Sun Angle Degrees
SC2-1 Boom	50.3	162.9
SC2-2 Boom	129.6	17.3
SC4-1	88.6	59.4
ML12-7	103.3	86.6

Period 3 (54758-54759, SC2-2 probe failure)

Instrument	Time	Pitch Angle Degrees	Sun Angle Degrees
SC2-1 Boom	54758	164.5	25.4
	54759	160.9	19.2
SC2-2 Boom	54758	15.6	154.8
	54759	19.2	160.9
SC4-1	54758	50.7	162.2
	54759	56.7	156.0
ML12-7	54758	104.0	86.0
	54759	104.1	86.0

TABLE 11. SHADOWING ANGLES

Period 1 (SC2-1 failure)

Shadow entry sun angle =  $165.5^{\circ}$   
 Half-shadow sun angle =  $166.8^{\circ}$   
 Total shadow sun angle =  $168.1^{\circ}$

SC2-1 Boom sun angle =  $146.5^{\circ}$  to  $158.9^{\circ}$

Period 3 (SC2-2 failure)

Shadow entry sun angle =  $165.3^{\circ}$   
 Half-shadow sun angle =  $166.6^{\circ}$   
 Total shadow sun angle =  $167.9^{\circ}$

SC2-2 Boom sun angle =  $154.8^{\circ}$  to  $160.9^{\circ}$

TABLE 12. TABLE OF SC2 FAILURE PARAMETERS

Current away from outer sphere (electrons)	$> 200 \mu A$
Potential of current source (negative)	$\leq 1500 V$
Voltage to which follower output is driven	$-1400 V$
Total input charge required	$2 \mu C$ (max.)
Time required	$10 \text{ mS at } 200 \mu A$ to $100 \mu S \text{ at } 20 \text{ mA}$
Charge available to destroy string	$2 \mu C$

Table No. 13

Pass 89-4 PCM Encoder Output for VTCW, Frame Counter, and Synchronization Words During Anomalous Condition.

Frame	UT (Sec.)	Vehicle Time Code Word (Words 000,001,002,003)	Frame Ctr (Word 124)	Synchronization (Words 125,126,127)
020	54735.772	00100110110110010001000101000100	00010100	000001001100111101011111
021	54735.897	00100110110110010001000101010101	00010101	000001001100111101011111
022	54736.022	00100110110110010001000101100110	00010110	000001001100111101011111
023	54736.147	00100110110110010001000101110111	00010111	000001001100111101011111
024	54736.272	00100110110110010001000110000000	00011000	000001001100111101011111
025	54736.397	00100110110110010001000110010001	00001001	100111101011111111111111
026	54736.522	00100110110110010001000000000000	00001001	100111100000110100000000
027	54736.646	10100010000100110110110010001000	00011011	000001001100111101011111
028	54736.771	1101101100100110110110010001000	00011100	000001001100111101011111
029	54736.896	11100010000100110110110010001000	00011101	000001001100111101011111
030	54737.021	11101010100100110110110010001000	00011110	000001001100111101011111
031	54737.146	11110011000100110110110010001000	00011111	000001001100111101011111
032	54737.271	11111011100100110110110010001001	00100000	000001001100111101011111
033	54737.396	00000000000100110110110010001001	00100001	000001001100111101011111
034	54737.521	00001000100100110110110010001001	00100010	000001001100111101011111
-	-	- - - - -	- - - - -	- - - - -
-	-	- - - - -	- - - - -	- - - - -
-	-	- - - - -	- - - - -	- - - - -
120	54748.271	10111011100100110110110010001011	01111000	000001001100111101011111
121	54748.396	11000000000100110110110010001011	01111001	000001001100111101011111
122	54748.521	11001000100100110110110010001011	01111010	000001001100111101011111
123	54748.646	11010001000100110110110010001011	01111011	000001001100111101011111
124	54748.771	11011001100100110110110010001011	01111100	000001001100111101011111
125	54748.896	11100010000100110110110010001011	01111101	000001001100111101011111
126	54749.021	11101010100100110110110010001011	01111110	000001001100111101011111
127	54749.146	11110011000100110110110010001011	01111111	000001001100111101011111
000	54749.271	11111011100100110110110010000000	00000000	000000000000000100110011
001	54749.396	10101111010000000000000000000000	00000000	110010010000000000000000
002	54749.522	00100110110110010001100000100010	00000010	000001001100111101011111
003	54749.647	00100110110110010001100000110011	00000011	000001001100111101011111
004	54749.772	00100110110110010001100001000100	00000100	000001001100111101011111
005	54740.897	00100110110110010001100001010101	00000101	000001001100111101011111
006	54750.022	00100110110110010001100001100110	00000110	000001001100111101011111
007	54750.147	00100110110110010001100001110111	00000111	000001001100111101011111

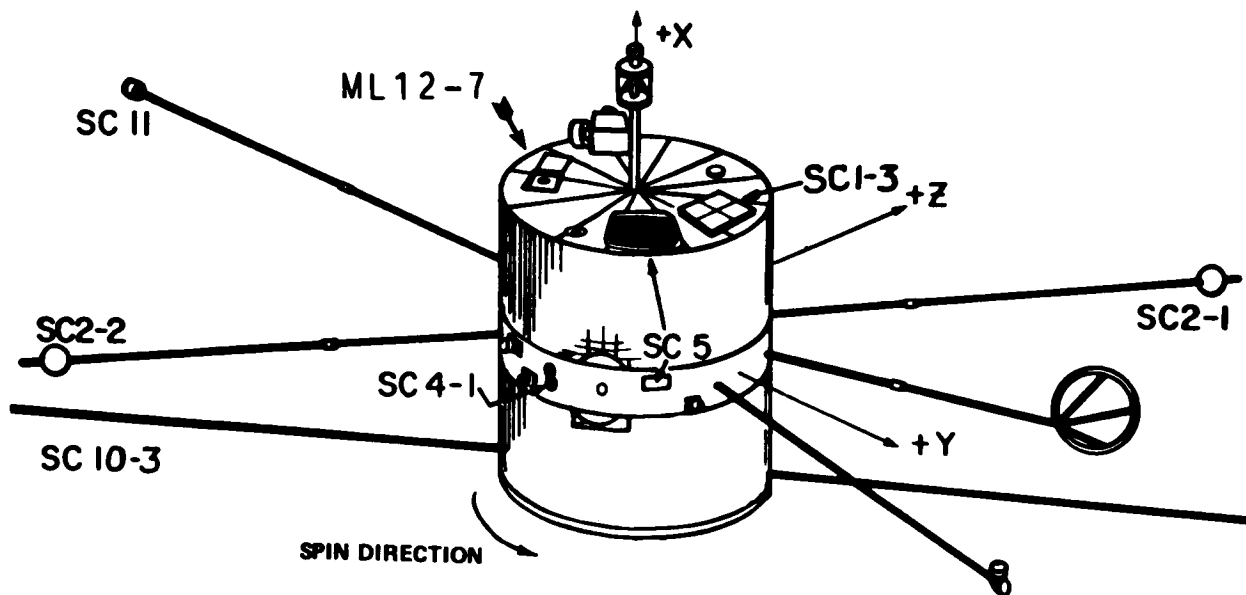


Fig. 1 P78-2

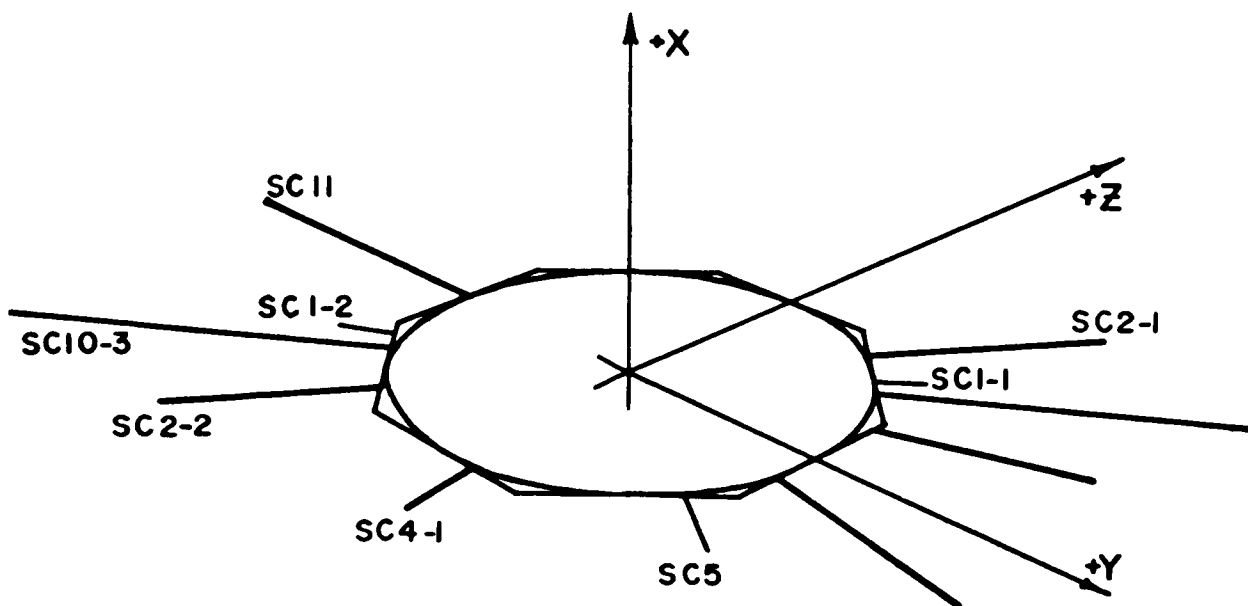


Fig. 2A P78-2 Relative Instrument Angles



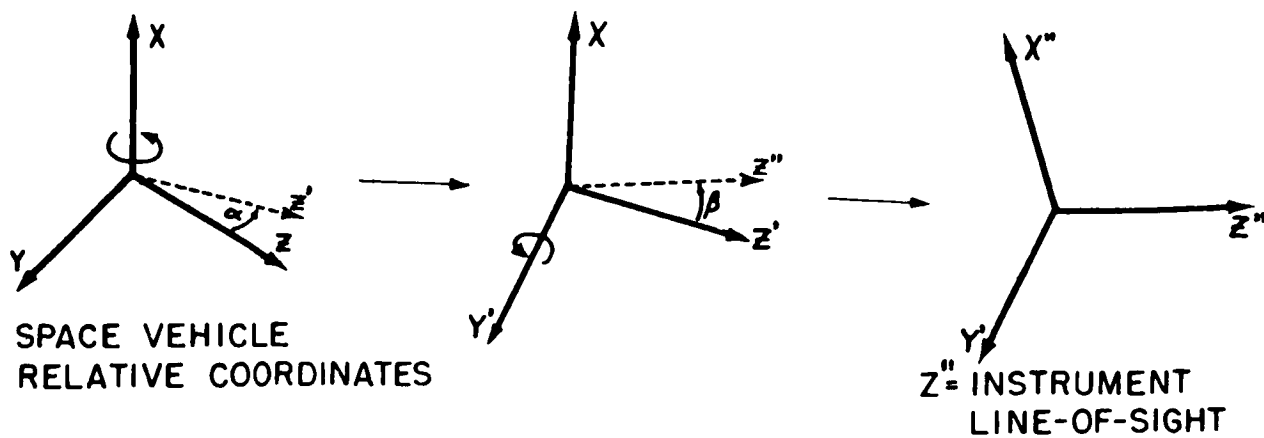


Fig. 2B Space Vehicle Mount Angle Definition

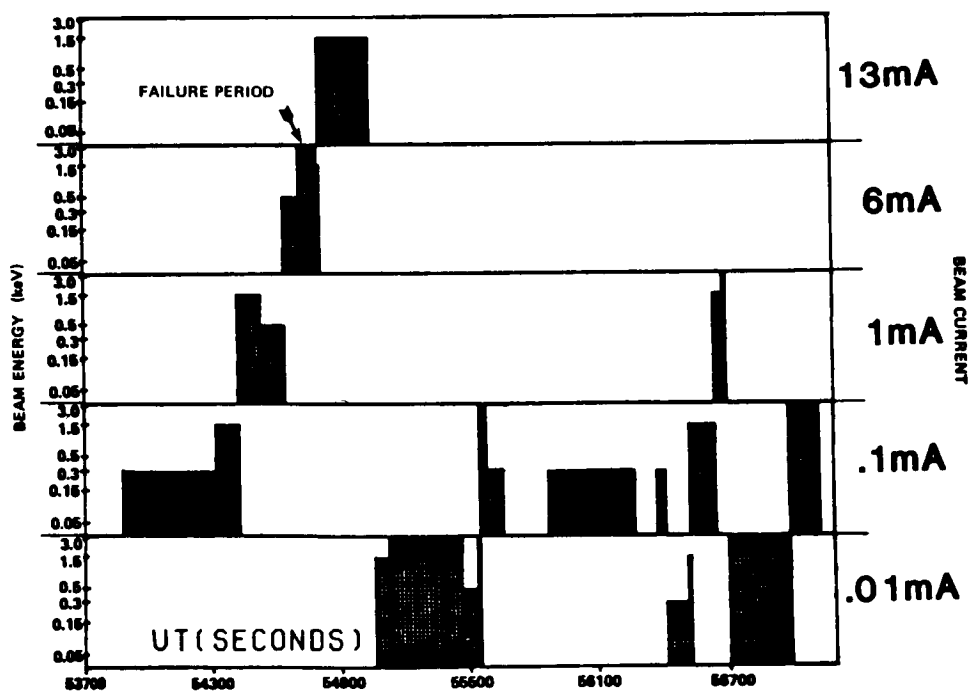


Fig. 3 SC4-1 Operations - Pass 89.4

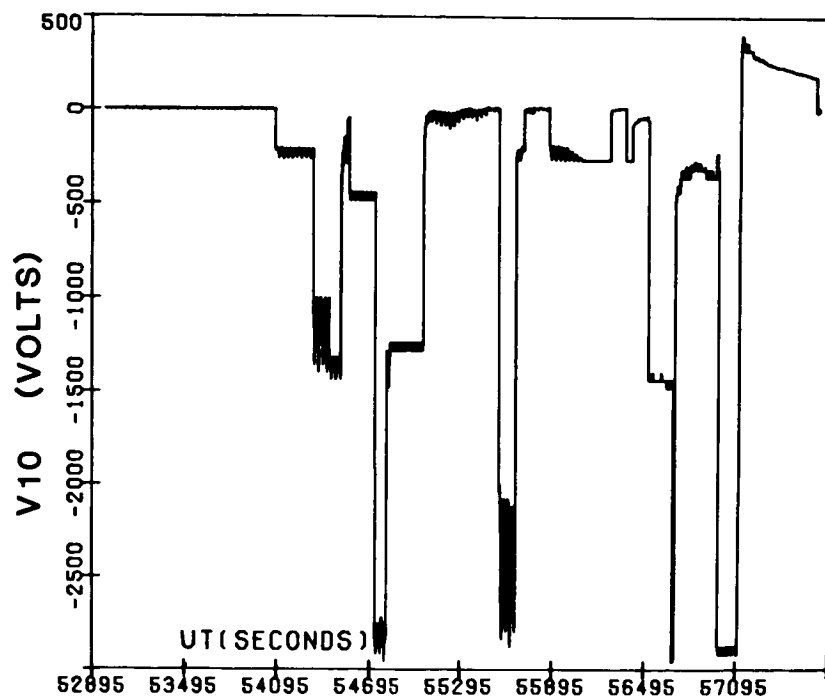


Fig. 4 SC10 Potential - Pass 89.4

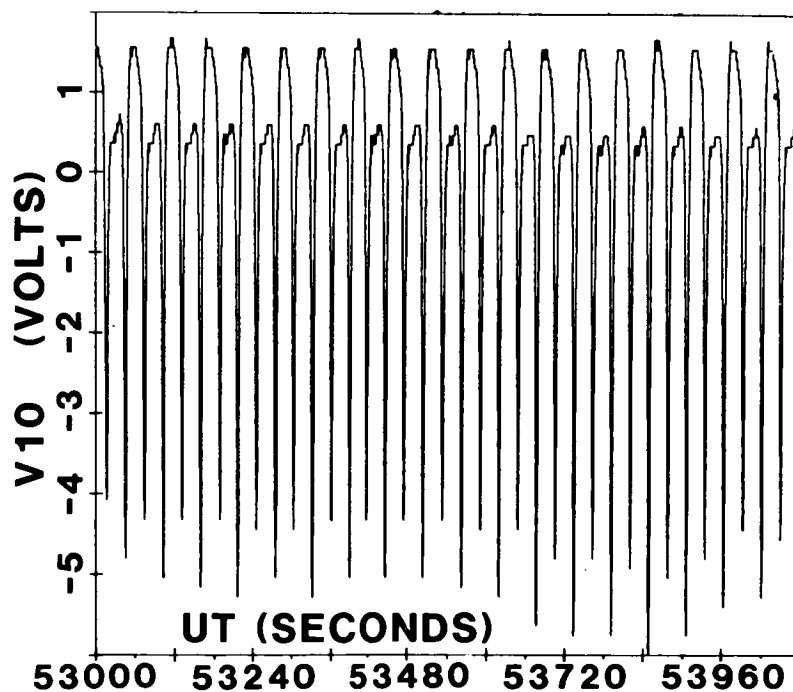


Fig. 5 SC10 Potential During Initial SC4-1 Operation Period

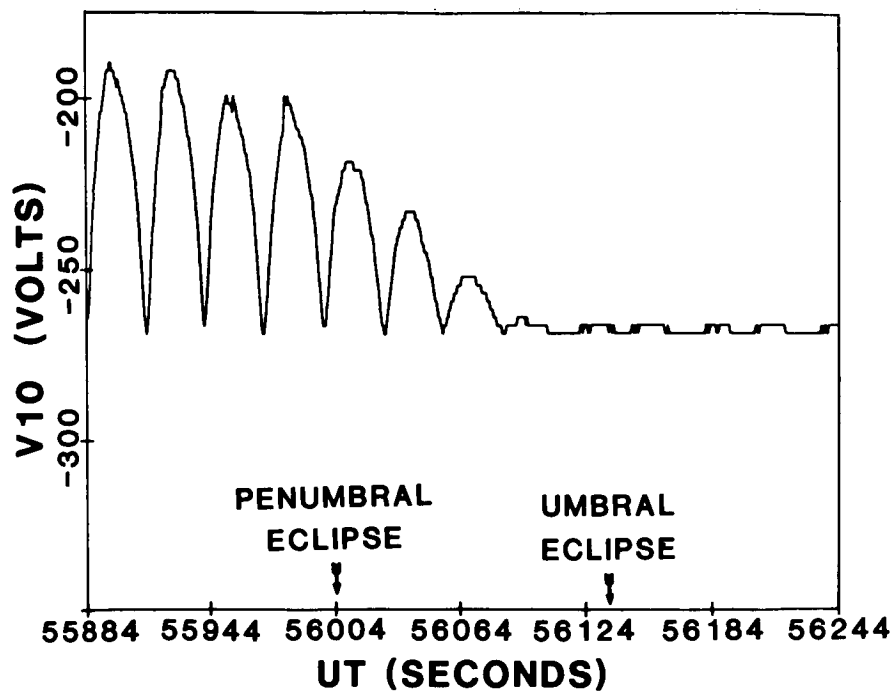


Fig. 6 SC10 Potential Entering Eclipse - Pass 89-4

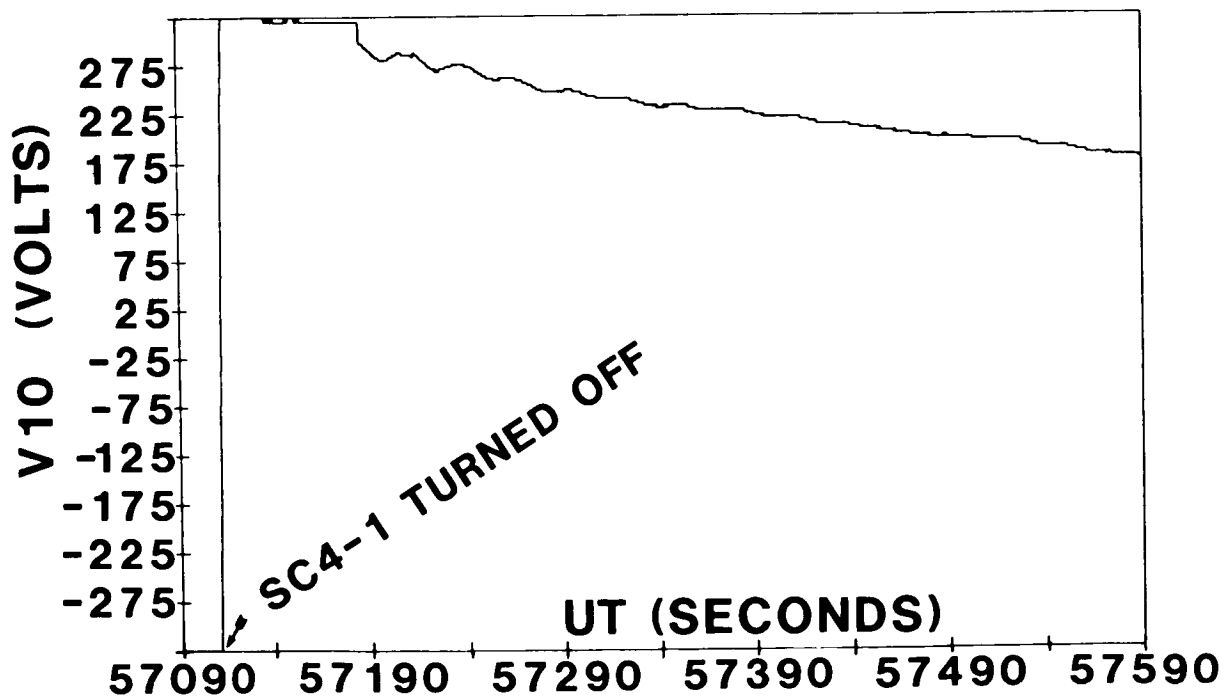


Fig. 7 SC10 Potential at SC4-1 Turn-Off

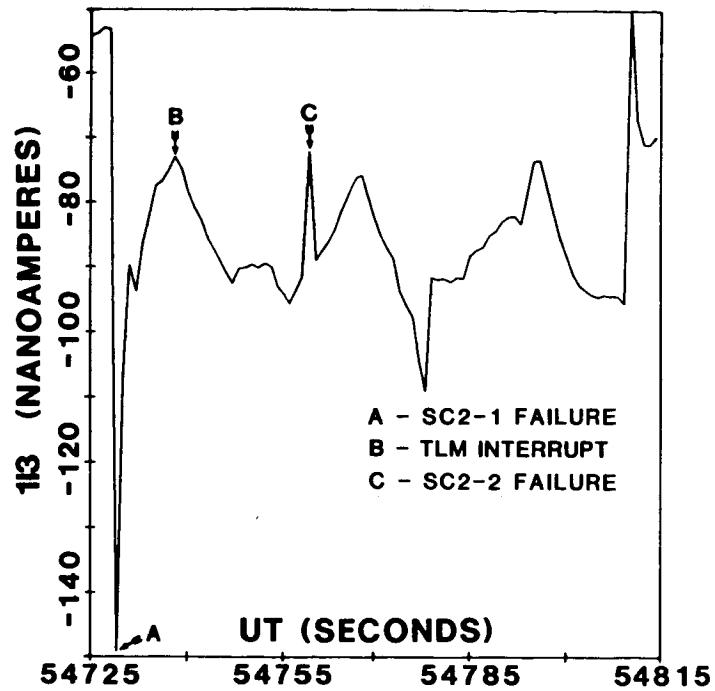


Fig. 8 SPM Current Through Optical Solar Reflector - SC4-1 Mode 11

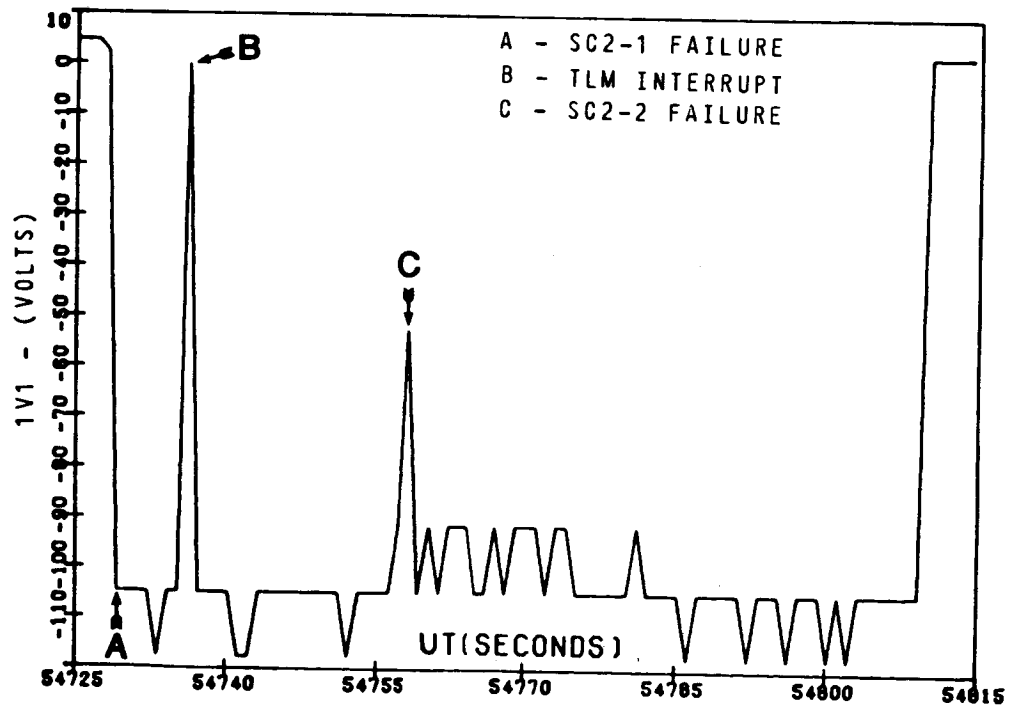


Fig. 9 SPM Front Surface Potential - Kapton Sample - SC4-1 Mode 11

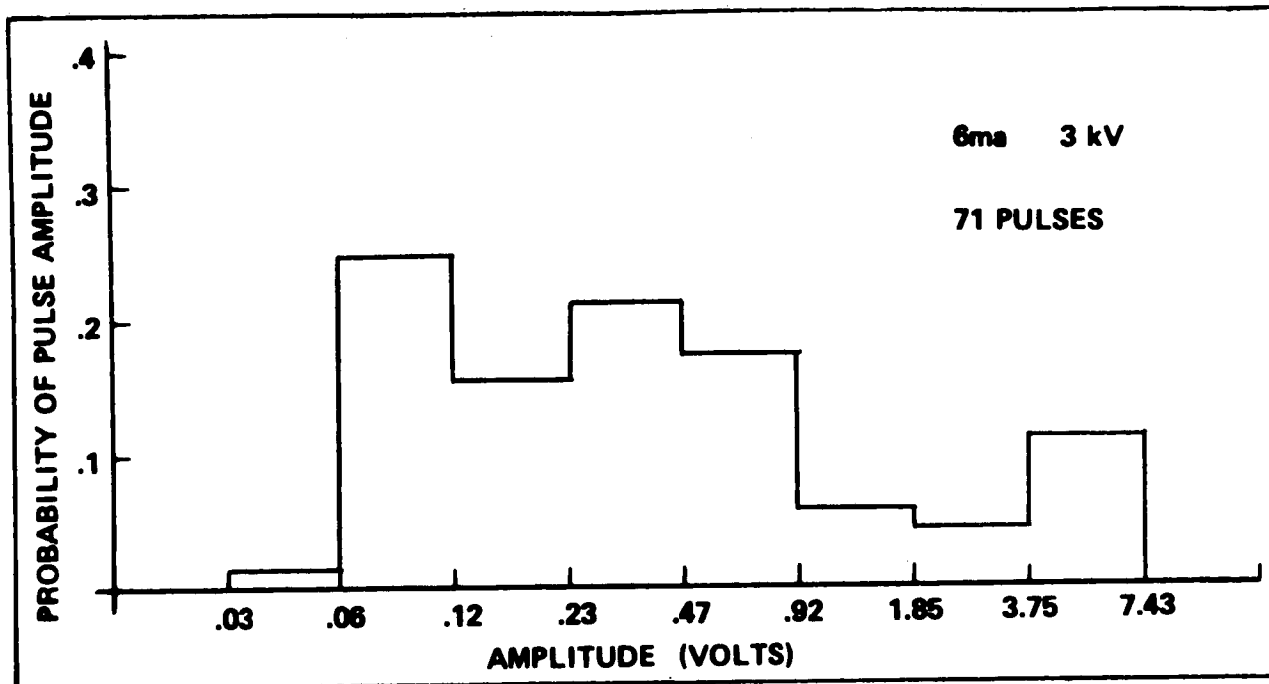


Fig. 10 Amplitude Distribution of SC1-8 Pulses Above Threshold #1

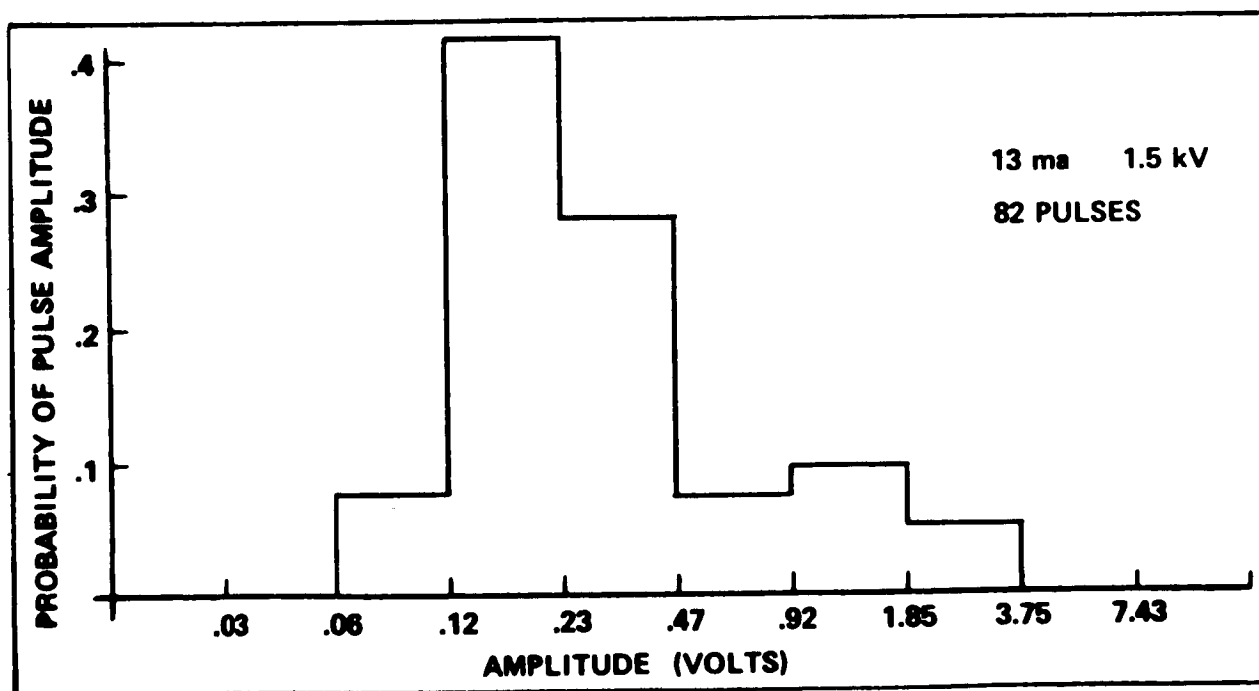


Fig. 11 Amplitude Distribution of SC1-8 Pulses Above Threshold #2

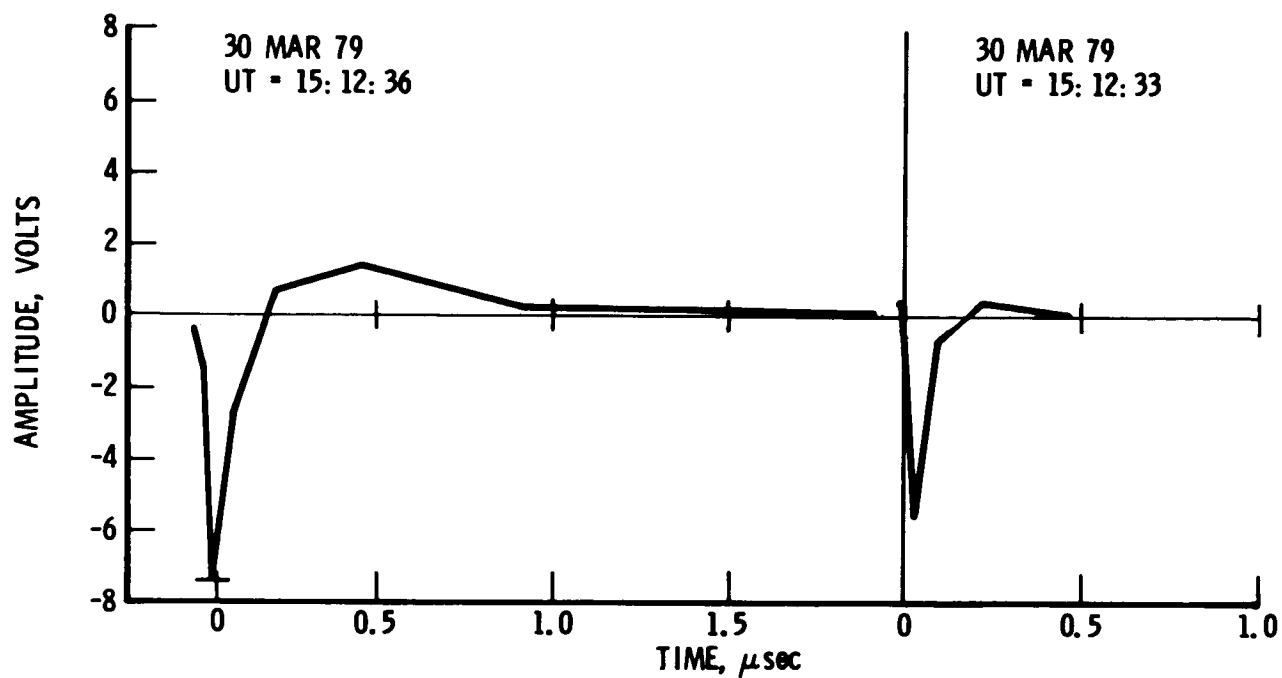


Fig. 12 SC1-8B Pulse Shape - External Dipole

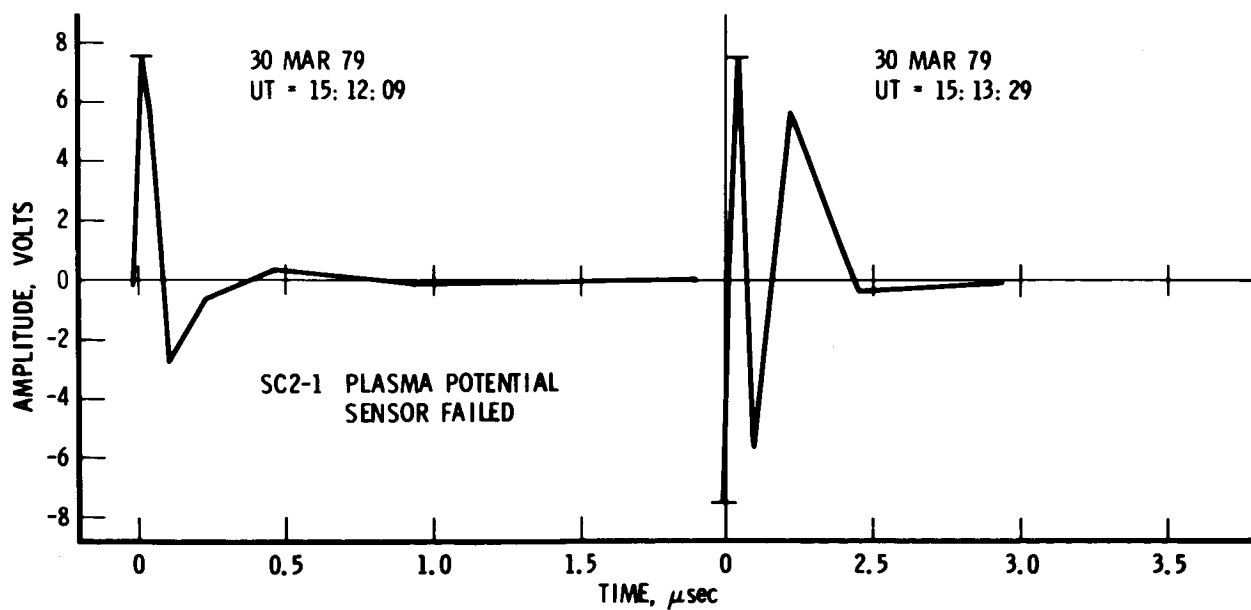


Fig. 13 SC1-8 Pulse Shape - Harness Wire

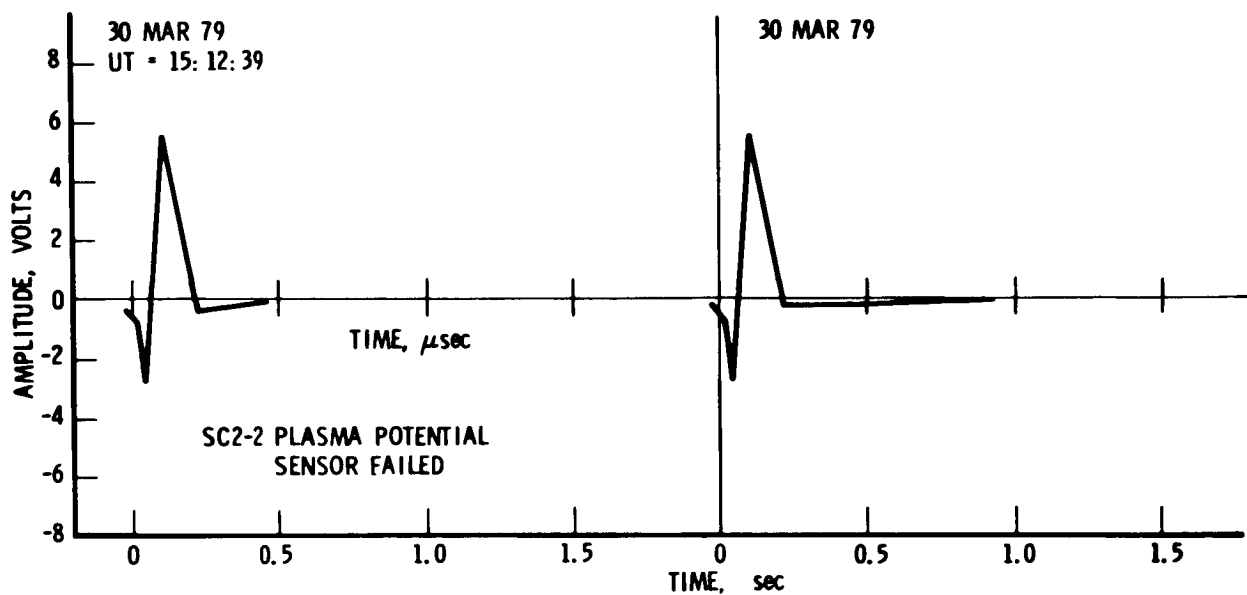


Fig. 14 SC1-8 Pulse Shape - CDU Loop

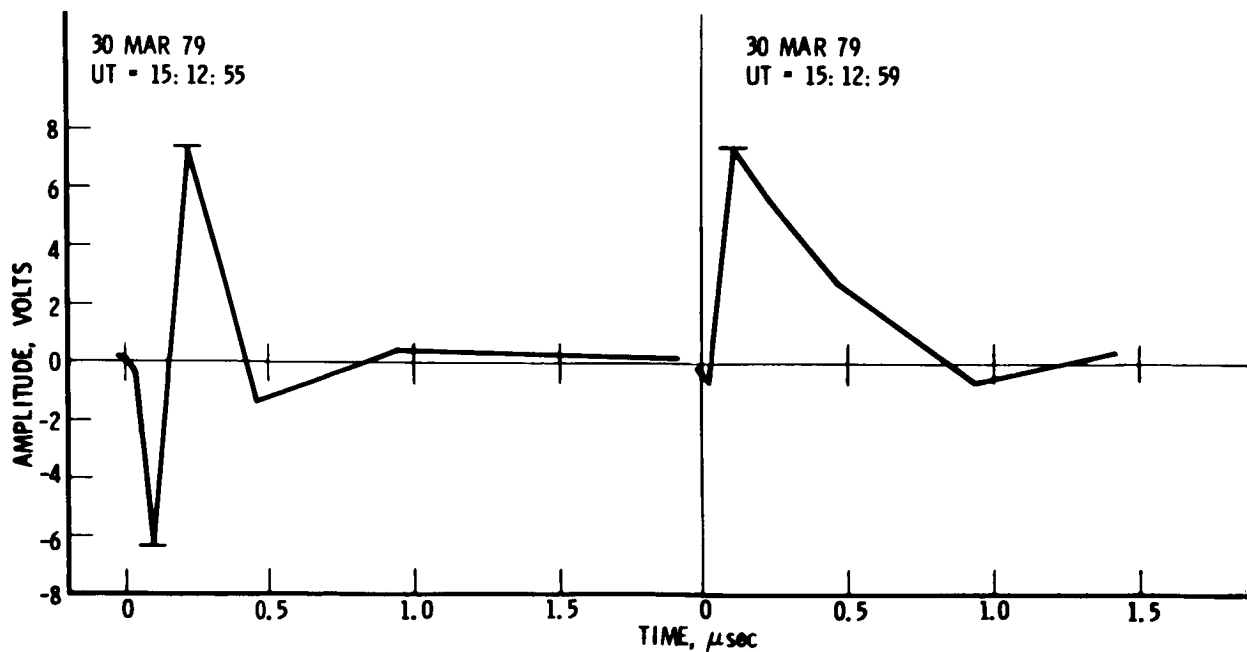
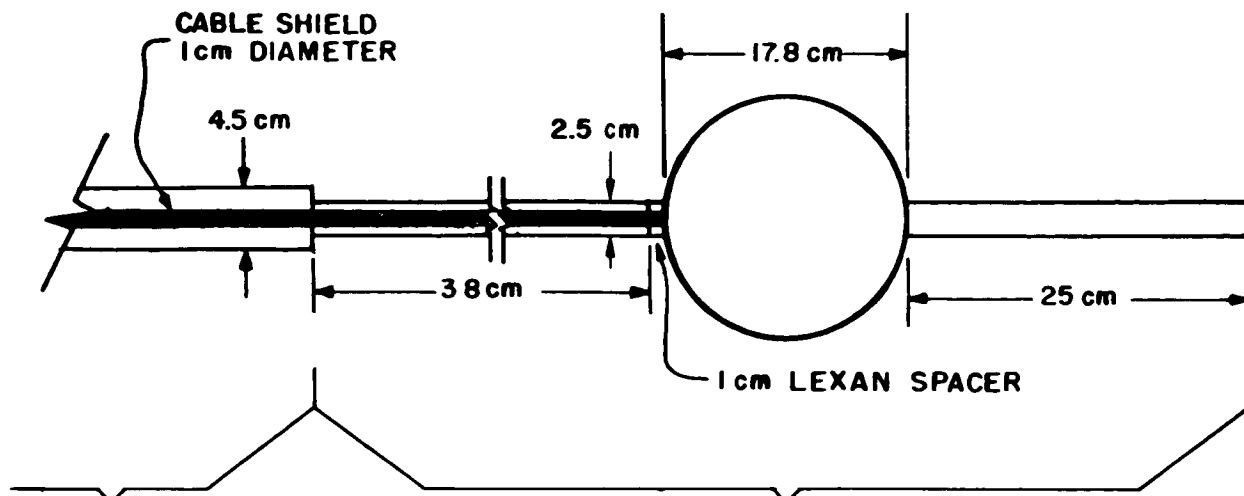


Fig. 15 SC1-8 Pulse Shape - Command Line



SC2 BOOM : 3 m LONG  
KAPTON COVERED WITH  
2.54 cm Pt BANDS,  
0.635 cm SPACINGS

SC2-1, -2 : CONDUCTIVE COATING  
( AQUADAG )

NOTE: CABLE SHIELD REMOVED LAST ~8 cm  
BEFORE LEXAN SPACER

Fig. 16 SC2-1, -2 Experimental Geometry

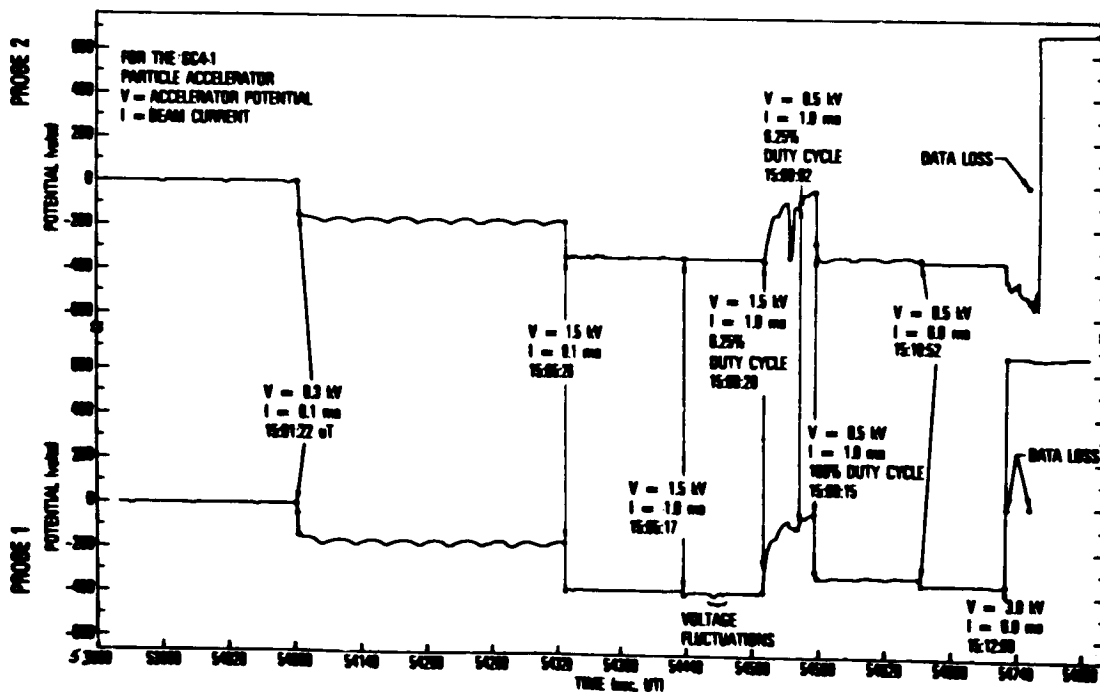


Fig. 17 SC2 Probe Voltages



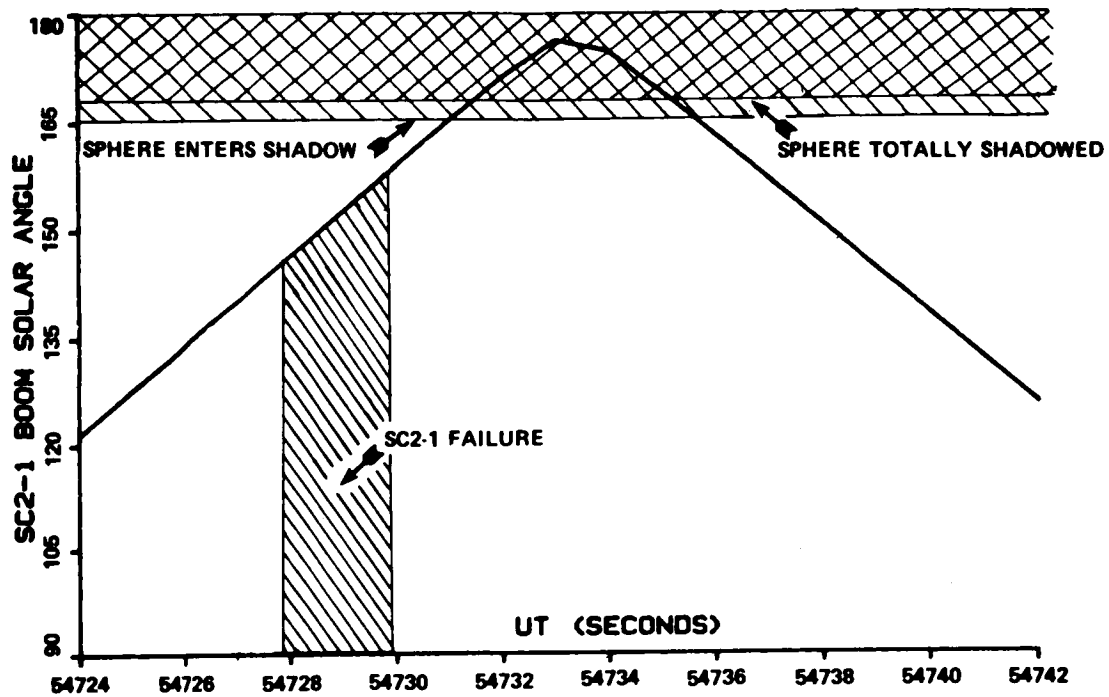


Fig. 18 SC2-1 Boom Solar Angle

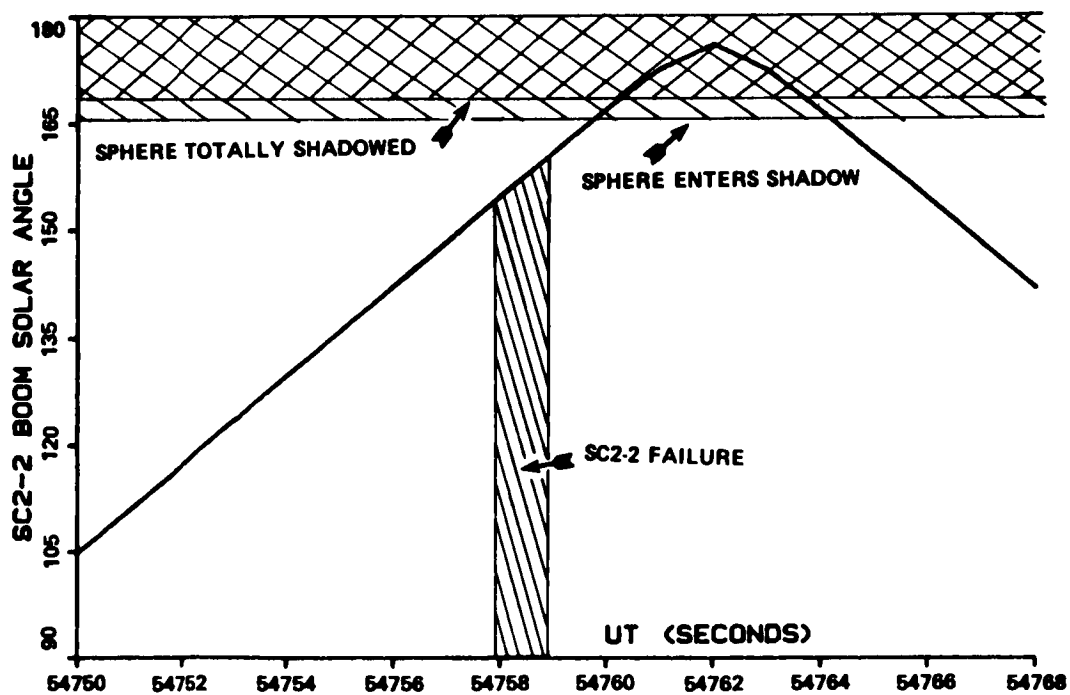


Fig. 19 SC2-2 Boom Solar Angle

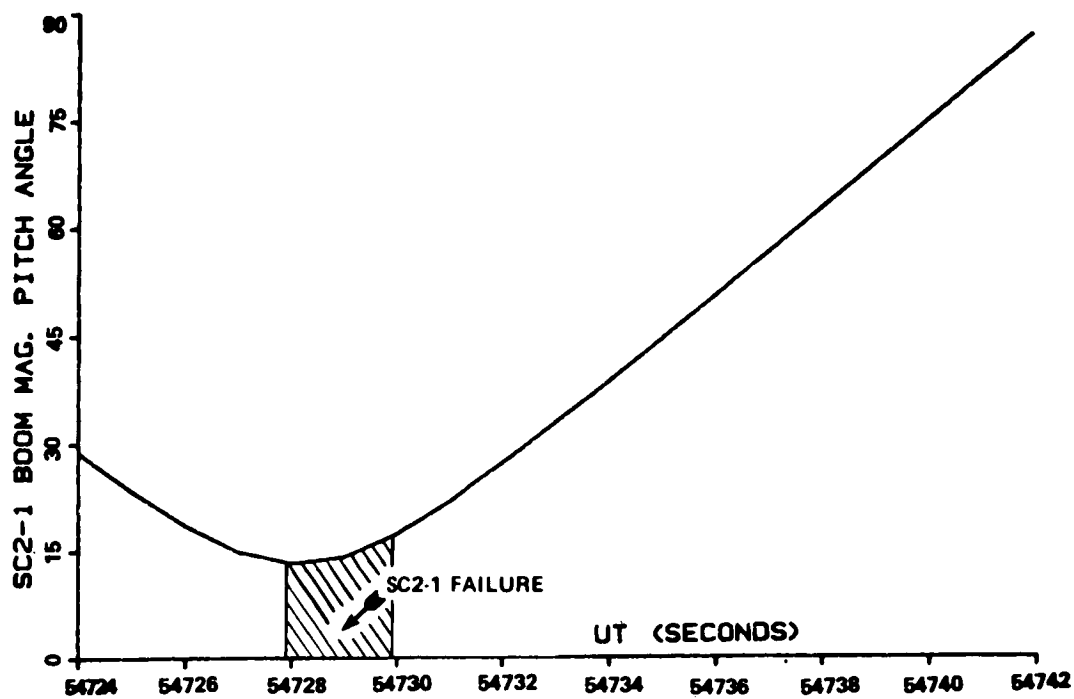


Fig. 20 SC2-1 Boom Magnetic Pitch Angle

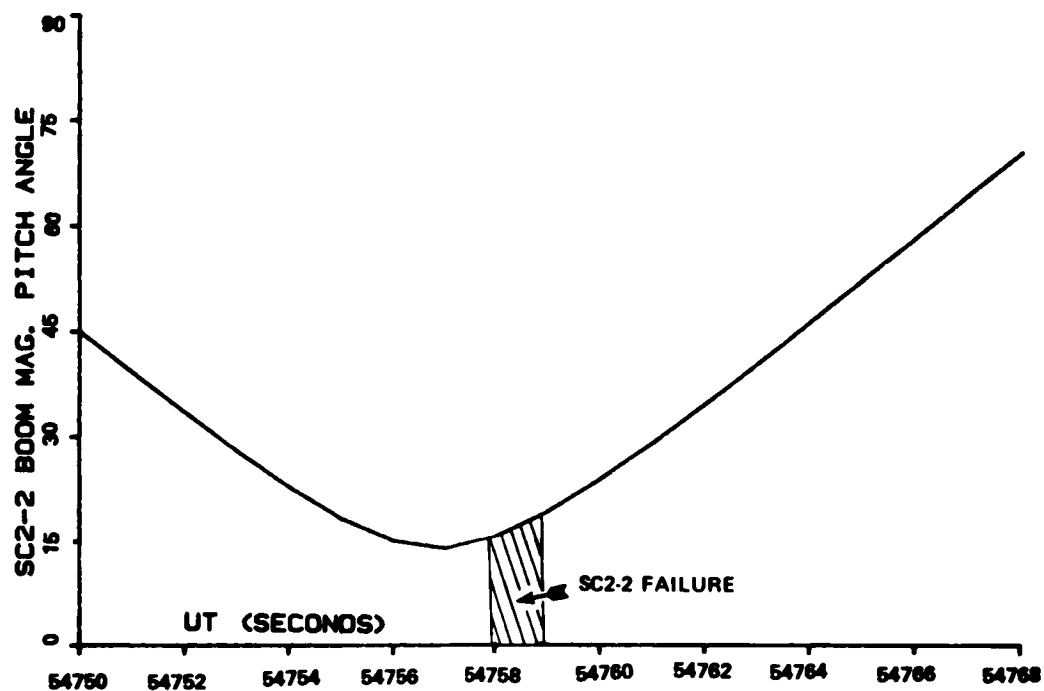


Fig. 21 SC2-2 Boom Magnetic Pitch Angle

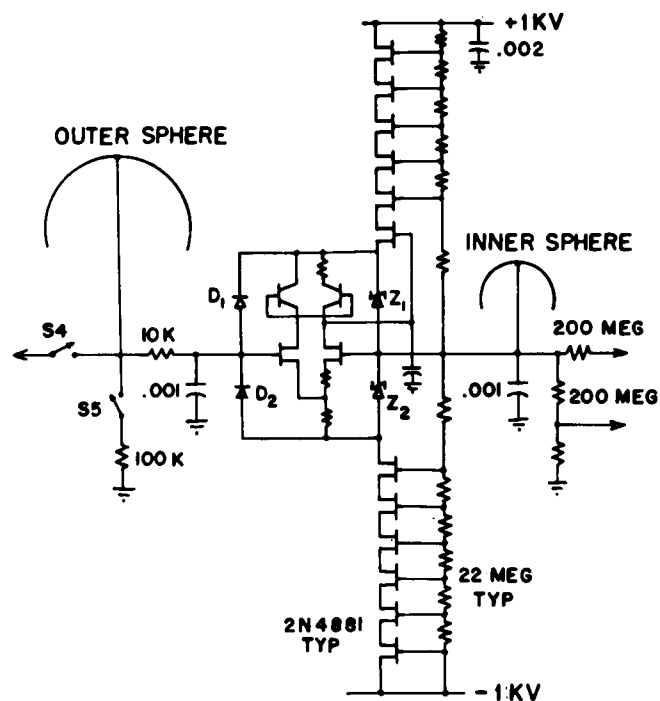


Fig. 22 SC2-1, -2 Voltage Follower Circuit

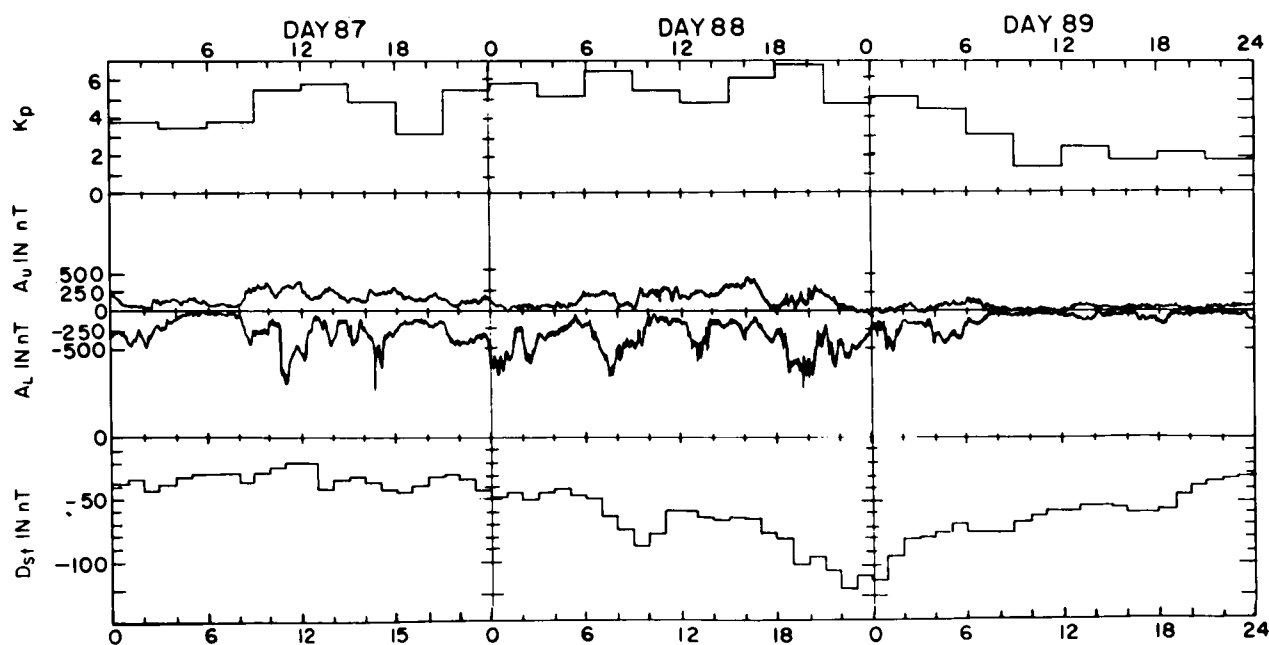


Fig. 23 Magnetic activity indices, March 28-30, 1979

DAY 89

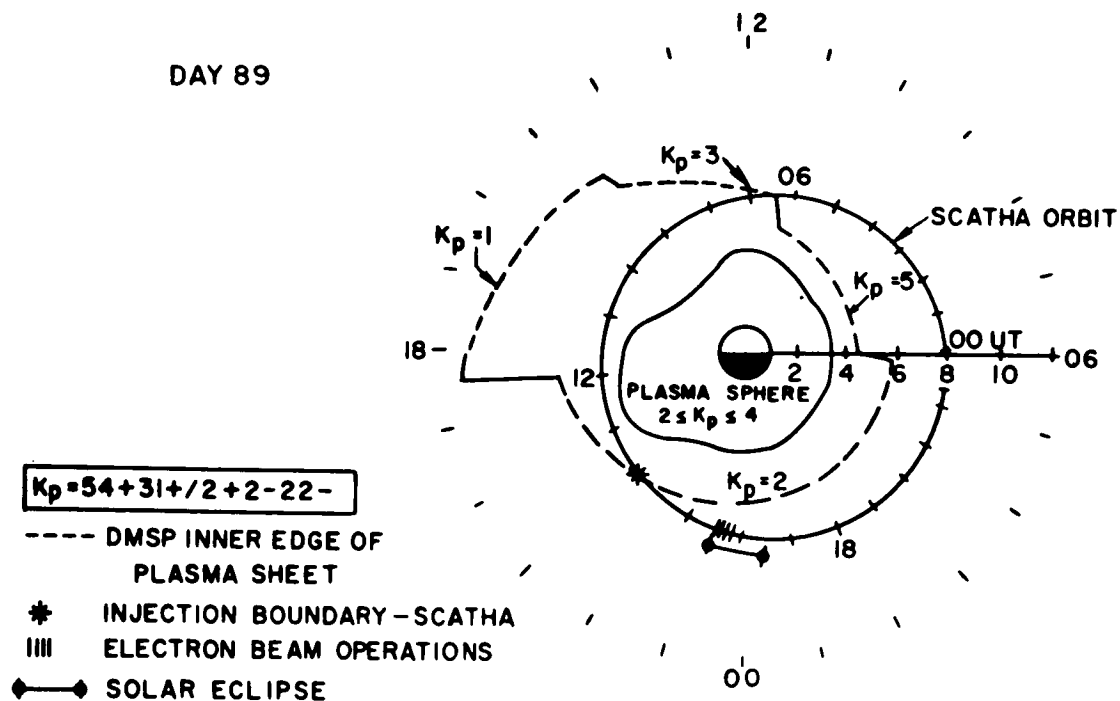


Fig. 24 The SCATHA orbit for March 30, 1979, with plasmasphere and plasma sheet (dashed lines) boundaries.

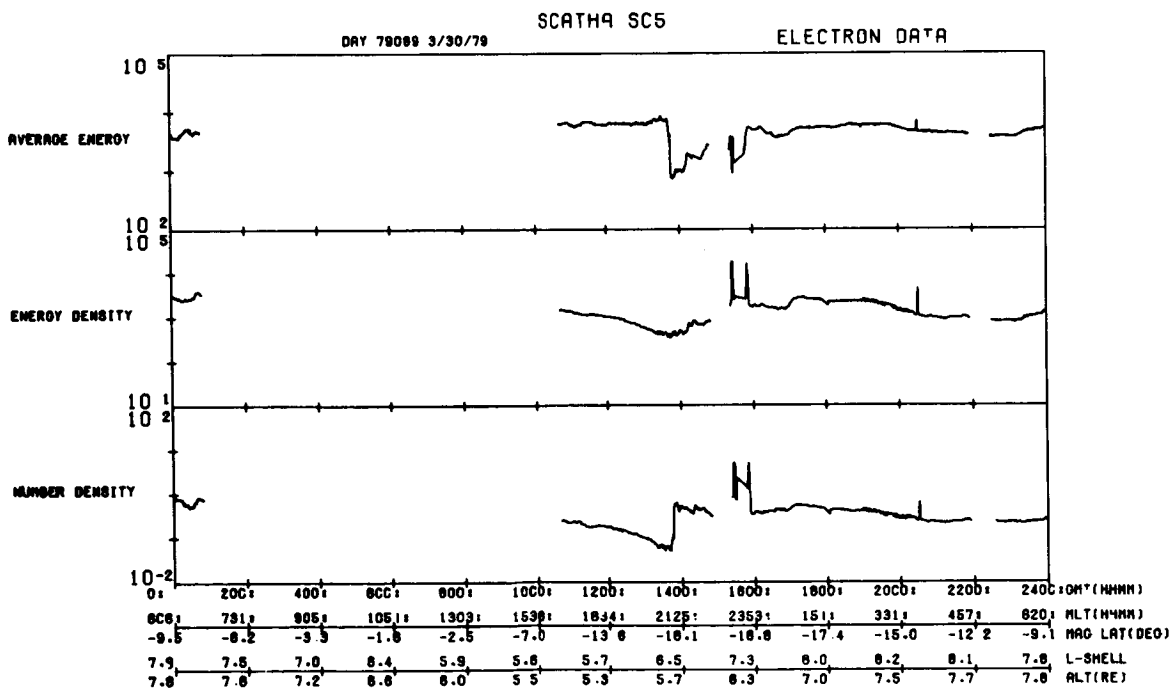


Fig. 25 Electron parameters, measured by SC5, in the energy range .05-60 keV, for March 30, 1979.

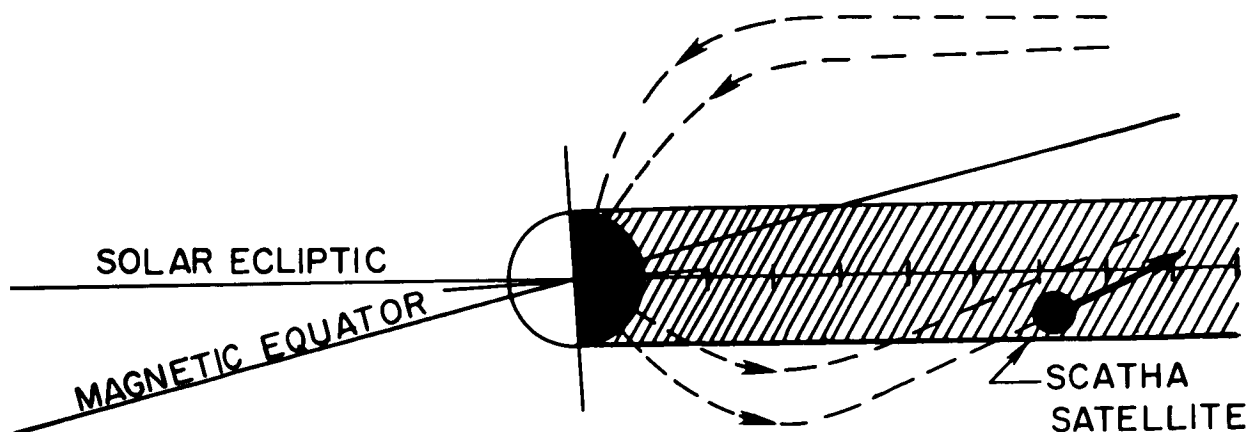


Fig. 26 Schematic diagram of the SCATHA position and the magnetic field direction during pass 89.4.

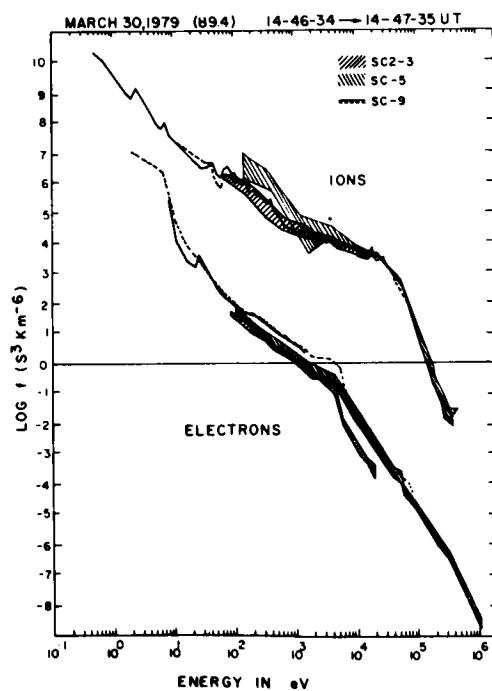


Fig. 27 Distribution functions of electrons and ions measured by SC2-3, SC5 and SC9 on March 30, 1979, at 14:47 UT.

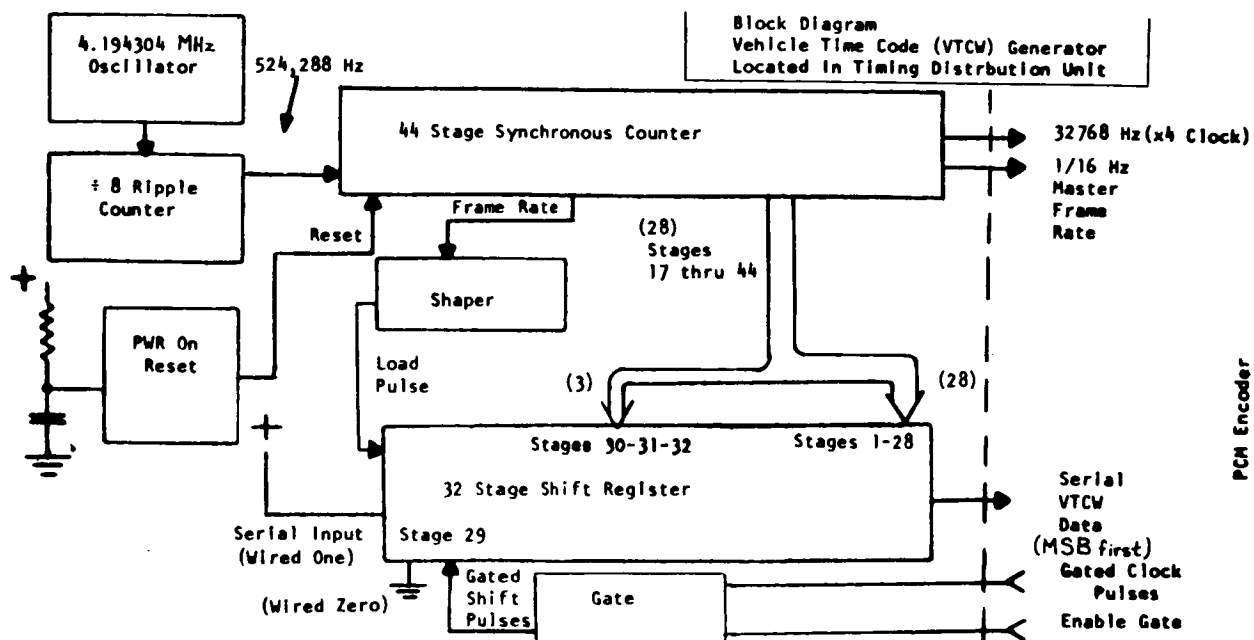


Fig. 28 Vehicle Time Code (VTCW) Generator

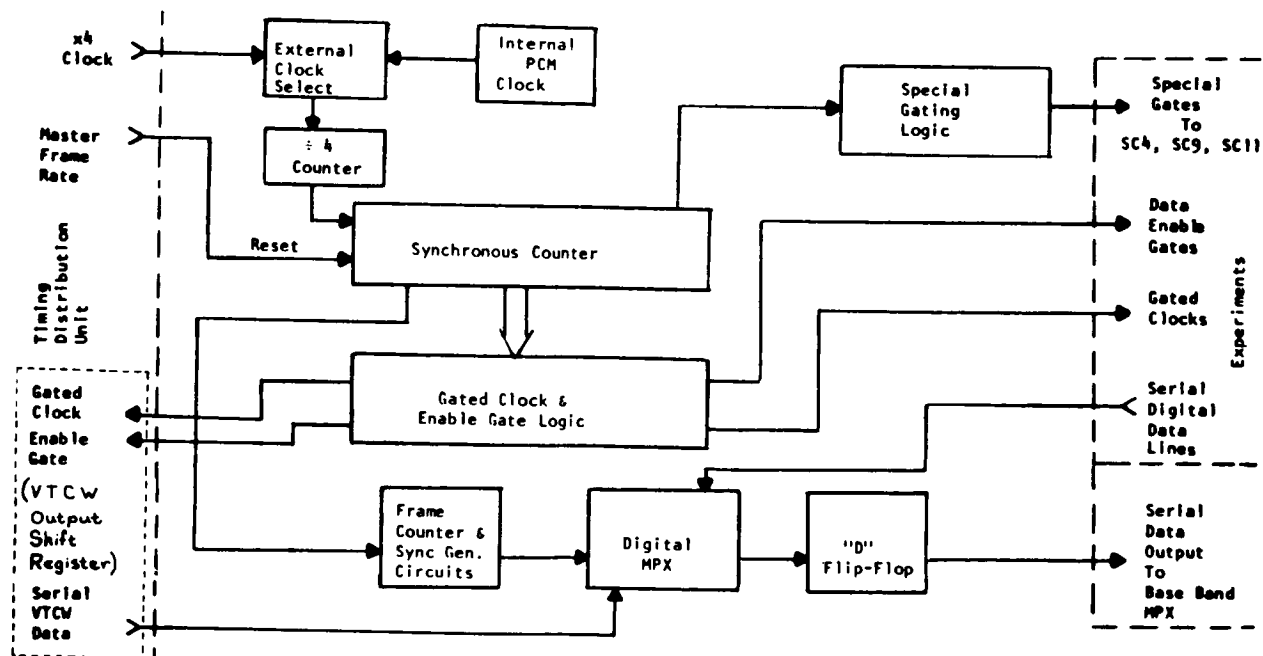


Fig. 29 PCM Encoder - Block Diagram

## **REPRESENTATION AND MATERIAL CHARGING RESPONSE OF GEO PLASMA ENVIRONMENTS\***

**P. R. Stannard, G. W. Schnuelle, I. Katz, and M. J. Mandell**  
**Systems, Science and Software**

### **SUMMARY**

The charging response to measured plasma environments is simulated for solar cell cover slides using the Material Charging Program (MATCHG), associated with the NASA Charging Analyzer Program (NASCAP). The ambient plasma descriptions were obtained from particle detector experiments on the SCATHA vehicle.

The sensitivity of the charging response to the representation of the measured environments, and material properties is discussed. Single and double Maxwellian representations are compared with direct numerical integration of the observed spectra. The effect of anisotropic incident flux distribution is modeled. In addition, the effect of the high energy radiation upon bulk conductivity and hence differential charging is examined and found to be significant in many cases.

### **INTRODUCTION**

The NASA Charging Analyzer Program (NASCAP) is a sophisticated three-dimensional computer code designed to predict the charging response of a complex satellite exposed to space environment (ref. 1). Associated with NASCAP is a simpler code called the Material Charging Program (MATCHG) which calculates the potential of a conducting sphere, covered with a material of interest, exposed to an isotropic plasma. A constant equilibrium potential is reached when the net current flowing to the sphere is zero. The calculation of the net current is made by including contributions from incident electron and ion currents, secondary emission, backscatter, and bulk conductivity. Unlike NASCAP, MATCHG takes no account of surface conductivity of geometrical and field-limiting effects.

---

\* This work supported by the Air Force Geophysics Laboratory, Hanscom Air Force Base, Lexington, MA 01731, and the National Aeronautics and Space Administration, Lewis Research Center, Cleveland, OH 44135 under Contract NAS3-21762.

To better understand the plasma environments encountered in Geosynchronous Earth Orbit (GEO), measurements of the spectral composition of the incident energy flux have been made for both ions and electrons, by detectors on board the SCATHA satellite (refs. 2, 3). From these observations, tabulations of the electron and ion distribution functions have been made in the energy range  $10^2$  -  $10^5$  eV. MATCHG is capable of calculating currents by directly integrating the tabulated spectra, or by integrating analytic representations, such as Maxwellian, and double Maxwellian, forms.

In this paper we examine the sensitivity of the MATCHG predicted equilibrium potential to the way the plasma spectrum is represented. Three environments, observed by SCATHA detectors while the spacecraft was charging rapidly, are singled out for study. These spectra are 16 second averages taken at 16.36.53 (59813 seconds), 16.37.53 (59873 seconds), and 16.57.53 (61073 seconds) on Day 87, 1979, of the mission, following an injection that occurred during eclipse.

#### FITTING THE DATA

Figure 1 shows plots of the raw distribution function data derived from energy flux measurements made at the surface and uncorrected for spacecraft potential. Since the distribution function,  $f$ , is related to the total energy flux,  $\langle Ef \rangle$  collected in a bin of energy,  $E$ , as follows

$$f = \langle Ef \rangle / E$$

noise in the measured energy flux shows up on the distribution function plot as a straight diagonal line. To correct for spacecraft potential, and to find the distribution function at infinity, the Coulombic energy of the particles is added to their energy at the surface. For example, ions arriving at the surface of a spacecraft charged to -2000 volts must have a minimum of 2000 eV in energy. The value of the distribution function,  $f$ , measured for ions with energy equal to 2000 eV at the surface then corresponds to the value for ions with zero energy at infinity.

$$f_{\infty}(E=0) = f_s(E-q\phi)$$

In a similar way, electrons having the energy of zero at the surface correspond to electrons having an energy of +2000 eV at infinity. Since no repelled species having less energy than the spacecraft potential,  $\phi$ , can be observed at the surface, there is no spectral information measured below  $\phi$ . In all three cases studied here the spacecraft is negatively charged and spectral information for the electrons is missing for low energies.



To integrate over the whole distribution at infinity the missing portion must be inferred from the rest. This is done by fitting the remaining data to a functional form. For both species, single and double Maxwellian fits were made to the tabulated distribution functions. The details of the fitting procedure are given in the Appendix. The fits are shown in Tables 1 and 2. Comparisons with real data are shown in Figures 2 and 3. The double Maxwellians are better able to represent the data over the whole energy range, showing that the observed distribution functions are significantly non-Maxwellian. However, the single Maxwellian fits do provide a reasonable "first cut." This is particularly true for the electrons, which consistently show a smoother and more nearly Maxwellian form, than the ions.

### CHARGING RESPONSE

To examine the sensitivity of the charging response to the method of fitting, and compare the fits with directly integrated tabulated data, MATCHG was used to study just one material. The material chosen was "SOLAR", the solar cell cover glass that forms most of the exposed surface area of the SCATHA satellite. The silica cover glass is coated with a non-reflective  $MgF_2$  layer and we assume that it has the same material properties (e.g., secondary emission yield, etc.) as  $MgF_2$ . The MATCHG predicted equilibrium potentials for a sphere covered with "SOLAR" charging under the influence of the three different representations of the environment are compared in Table 3.

Agreement between the two fits and the directly integrated spectra are very good. The direct integration is only possible because a single Maxwellian fit to the known data is used to fill in the part cut out by the spacecraft potential. Furthermore, a much more stable result is obtained when in addition the first 2000 eV of known data for both the ions and electrons is replaced by the Maxwellian fit. The points replaced are highly non-Maxwellian. This could be a real phenomenon or it may be due to the poor signal/noise ratio inherent in measurements of energy flux at low energies. In either case, including it leads to erratic changes in the calculated net current and prediction of more than one equilibrium potential. These additional predicted potentials occur at unphysically low values and are almost certainly false.

Included in Table 3 are the spacecraft ground potentials observed on the SCATHA satellite when the distribution function data was being measured. MATCHG predicts considerably more changing than observed. There are at least three reasons for this:

1. The satellite is not a sphere covered in SOLAR.

2. In space the charging environment is not constant, particularly at the times when our test spectra were measured. MATCHG assumes a steady charging environment.
3. The measured distribution functions are highly non-neutral (see Tables 1 and 2). this is rather unphysical and indicates a systematic deficiency in the measurement in the density of at least one of the species.

Independent measurements (ref. 3) confirm the ion densities and so the electron densities are probably an overestimate. We attempted to correct for this error by adjusting the electron density so that the plasma was neutral. For a plasma made up of only protons and electrons this is accomplished by equating the electron density with the ion density. However, in this case a complication is presented by the observation (ref. 4) that as much as 80 percent of the ions incident at the surface of the SCATHA satellite during the period of interest were  $O^+$  rather than  $H^+$ . The distribution functions for the ions are inferred from the energy flux measurements, assuming that all the ions are protons. This error is cancelled out when MATCHG calculates the net current and does not affect the predicted potentials. It does, however, affect the densities of the reported distribution functions in a way described in Reference [5]. Taking this into account (ref. 5), we obtained the neutral environment for time 59873, shown in Table 1. Only the electron density has been changed. The equilibrium potential predicted with the neutral environment is much closer to the observed satellite potential.

#### THRESHOLD EFFECT

The three environments chosen all charge the SOLAR material to high potentials in all representations. For environments with only a small tendency to charge the material, very small changes in the representation of the plasma can lead to qualitatively very different charging predictions.

Figure 4 shows the effect of varying the electron temperature parameter in the 59873 single Maxwellian representation. There is a definite threshold for charging that occurs at  $T = 6.9$  keV. Below this temperature, no charging is predicted, while only 0.3 keV above it, at  $T = 7.2$  keV, a potential of 4.3 keV\* is forecast. Such small changes in temperature are well within experimental error for measurement and fitting procedures. For "borderline" environments close to

\* The particularly high value of 4.3 keV predicted here is due to the non-neutrality of the plasma.

the charging threshold quite different predictions are possible according to the representation employed.

A similar phenomenon is presented when we examine the effect of changing important material parameters on charging. Figure 5 shows a threshold for charging in the 59873 environment (as given in Table 1), when the maximum secondary electron yield  $\delta_{\max} = 3.1$ . Above this value the net current is positive at zero potential and the spacecraft never negatively charges, while below 3.1 rapid charging to several keV negative is predicted. The usual value used by MATCHG of 2.05 is well into the stable charging range. However, in borderline cases small changes, errors, in material properties can lead to significantly different predicted potentials.

Another factor that can affect charging is the angular distribution of the incident fluxes.

#### ANISOTROPIC FLUX

The SC5 detector on the "belly band" of the SCATHA satellite measures the angular distribution of the energy flux of the surrounding plasma in the plane of satellite rotation (Figure 6a). For an isotropic plasma the flux is constant over a rotation giving a circular radial plot (Figure 6b). For an anisotropic flux (i.e., one having particles aligned preferentially in one direction) the measured plot is distorted. The degree of distortion increases with the degree of anisotropy.

The most extreme case consists of a narrow beam lying the the plane of rotation. As the satellite rotates, the angle of incidence of the beam,  $\theta_0$ , oscillates between 0 and  $\pi/2$ . To investigate the effect of anisotropy on spacecraft charging, we simulated this situation using MATCHG to calculate the potential of an aluminum plate under the influence of a beam with an oscillating angle of incidence  $\theta_0$ .

The secondary emission yields and the backscatter all increase with increasing angle of incidence, and we expect the aluminum to be driven more positive at high angles and more negative at low angles of incidence. Figure 7 shows a plot of potential against time (angle) confirming our expectations.

When the charging response is fast compared to the period of the oscillations, we see the potential of the plate oscillate in time with the angle of incidence of the beam. The faster the charging response (or slower the rotation), the greater the amplitude of the oscillations. For a very fast oscillation, the plate would respond only to an average environment and no oscillations would be seen. The initial oscillations are erratic and more pronounced before settling into a regular pattern. This behavior reflects the two influences on the net

current to the plate; potential and  $\theta_0$ . Initially, these may be out of phase leading to transient potentials that are too high or low.

The mean of the oscillating potential is not the same as that for an isotropic plasma of the same density and temperature. This is because of different incident currents arising out of distributions with the same flux normalization. A directional beam lying in the rotation plane has but one angle of incidence,  $\theta_0$ , so the incident current is proportional to  $\cos\theta$ . The mean incident current is thus the mean of  $\cos$ .

$$\text{Beam: } \bar{I}_B \propto \int_0^{\pi/2} \cos\theta \, d\theta / \int_0^{\pi/2} d\theta = \frac{2}{\pi}$$

For an isotropic distribution an angle of incidence  $\theta_0$  in the rotation plane has associated with it all other angles of incidence due to particles arriving from above and below it. The average of these is  $\sin\theta$ . Thus the current from an isotropic distribution is proportional to  $\cos\theta$  and  $\sin\theta$ , and the mean is the mean of  $\cos\theta\sin\theta$ :

$$\text{Isotropic: } \bar{I}_i \propto \int_0^{\pi/2} \cos\theta \sin\theta \, d\theta / \int_0^{\pi/2} \sin\theta \, d\theta = \frac{1}{2}$$

Thus, the beam current exceeds the isotropic by a factor of  $4/\pi \sim 1.27$ .

This illustrates some importance points regarding the measurement of flux distributions in space:

1. If a detector measures an average flux over a rotation and assumes that it arises from an isotropic plasma, the actual current will be underestimated by an amount that will increase with the increasing directionality of the true angular distribution (reaching a maximum of  $4/\pi$  for a beam).
2. If a detector measures actual average current, then in the same way flux (density) will be overestimated.
3. If a detector measures the angular distribution of the flux, information in both the perpendicular and parallel directions must be known, or implied to infer densities and currents.

4. For a "loss-cone" (negative aligned component) the reverse of 1 and 2 apply.

#### Radiation-Induced Bulk Conductivity

In addition to the electron flux with energy below 100 keV, electrons with energies up to 5000 keV have been observed by detectors on board SCATHA. This high energy radiation makes an insignificant contribution to the total incident electron current but nevertheless can influence differential charging of insulators on a spacecraft.

When high energy radiation, such as a 300 keV electron, passes through an insulator such as Kapton, electrons can be promoted into the normally empty conduction bands and increase the bulk conductivity  $\sigma$ . Frederickson (ref. 6) has represented this by the equation:

$$\sigma = \kappa \dot{D} + \sigma_0$$

where  $\dot{D}$  is the radiation dose rate and  $\kappa$  is the coefficient that depends upon the nature of the material.  $\sigma_0$  is the conductivity in the absence of radiation. As the flux and hence dose rate increases, the radiation-induced conductivity increases. For a sufficiently high flux this could limit the potential differences that can build up between an insulator and the underlying conductor.

To investigate this question we use MATCHG to predict the potential of 0.005 inches ( $1.27 \times 10^{-4}$  m) thick Kapton, subject to the single Maxwellian representation of the 59873 environment, with a range of values for the bulk conductivity. The results are shown in Table 4. The fluxes corresponding to each value of  $\sigma$  can be estimated using an experimental result of Treadaway et al. (Reference 7). He found that a 0.002 inch ( $5.08 \times 10^{-4}$  m) Kapton film subjected to a  $0.05 \text{ pA cm}^{-2}$  beam of 300 keV electrons accompanied by a  $0.2 \text{ nA cm}^{-2}$  beam of 10 keV electrons charged to  $-1600$  ( $\pm 300$ ) V. Simulating this experiment with MATCHG implied a value of  $4.67 \times 10^{-14} \text{ mhos m}^{-1}$  for the bulk conductivity  $\sigma$ . Assuming that  $\sigma_0$  is insignificant we can estimate  $\kappa$ .

$$\sigma = \kappa \dot{D}$$

The dose rate  $\dot{D}$  arises from  $5 \times 10^{-8} \text{ A m}^{-2}$  of 300 keV electrons, i.e., a flux of  $1.67 \times 10^4 \text{ electrons cm}^{-2} \text{ s}^{-1} \text{ sr}^{-1} \text{ keV}^{-1}$ . This is equivalent to a dose rate of  $1.2 \text{ rads s}^{-1}$ .

$$\kappa = 4.0 \times 10^{-14} \text{ mhos m}^{-1} \text{ rad}^{-1} \text{ s}$$

This value is rather higher than Frederickson's estimate of  $10^{-15}$  -  $10^{-16}$  mhos  $\text{m}^{-1} \text{ rad}^{-1} \text{ s}$  (Reference 8).

As we can see from Table 4, as soon as the dose reaches  $\sim 10^2$  electrons  $\text{cm}^{-2} \text{ s}^{-1} \text{ keV}^{-1}$  there is a significant drop in the potential difference that the Kapton film can support. Since a 0.005 inch layer of Kapton is typical of the insulating materials found on satellites, this result suggests that in environments with doses higher than  $10^2$  electrons  $\text{cm}^{-2} \text{ s}^{-1} \text{ sr}^{-1} \text{ keV}^{-1}$ , the radiation induced conductivity may play a significant role in preventing acute differential charging and hence discharges.

Figure 8 shows a plot of the data in Table 4. The vertical lines are drawn to represent the typical values for 200 keV flux on days 146, 87 and 114 (Reference 9). Days 146 and 114 are examples of the lowest and highest extremes documented so far. We see that fluxes in the range where radiation induced conductivity appears to be important are common. It will be interesting to discover, as more data becomes available, if there is any correlation between the high energy flux and discharges on board SCATHA.

### CONCLUSIONS

For the three day 87 cases studied, both single and double Maxwellian fits to observed plasma spectra give similar predictions of equilibrium potential that agree well with the value obtained by direct integration. We expect that for environments with a solid tendency to charge or not to charge, MATCHG and NASCAP predicted potentials will not be overly sensitive to the nature of the representation. In most of such cases a single Maxwellian fit may be quite adequate to obtain a semi-quantitative result. However because of the "threshold effect" described above, charging in "borderline" environments cannot always be predicted with such confidence.

In addition to the spectral composition of the environment, the angular distribution also affects the materials charging. A rotating spacecraft in an anisotropic environment will experience oscillations in ground potential whose amplitude increases with the rate that the spacecraft responds to a charging environment. Implying currents from measured incident fluxes or vice versa requires full knowledge of the three-dimensional angular distribution function.

Finally, it appears that account must be taken of the flux of high energy ( $\sim 300$  keV) electrons, and its effect on the bulk

conductivity of insulators. For fluxes greater than  $10^2$  electrons  $\text{cm}^2 \text{ s}^{-1} \text{ sr}^{-1} \text{ keV}^{-1}$  a significant reduction in differential charging is possible.

#### REFERENCES

1. Katz, I., et al., "A Three Dimensional Dynamic Study of Electrostatic Charging in Materials," NASA CR-135256, August 1977.
2. Olsen, C. and E. C. Whipple, tape of SC9 Data supplied from University of California at San Diego.
3. Nichols, D. and E. C. Whipple, tape of SC9 Data supplied from the University of California at San Diego.
4. Kaye, S., private communication, SC8 Data.
5. Schnuelle, G., et al., "Simulation of the Charging Response of the SCATHA (P78-2) Satellite," to be presented at Spacecraft Charging Technology Conference III, Colorado Springs, CO, 12 - 14 November 1980.
6. Frederickson, A. R., NASA Conference Publication 2071, AFGL-TR-79-0082, 554, 1978.
7. Treadaway, M., results presented at SCATHA meeting, Aerospace Corporation, September 1980.
8. Frederickson, A. R., IEEE Nuc. Sci., NS-24, 2532, 1975.
9. Nightingale, R. W., et al., SC3 Data, Lockheed Research Publication LMSC/D766804.

APPENDIX  
FITTING THE DATA

a. Single Maxwellian Fits

The data was fit to a form

$$f(E) = N \cdot \left( \frac{m}{2\pi T} \right)^{3/2} e^{-E/T}$$

The density  $N$  is given by the zeroth moment  $MO$

$$MO = \frac{4\pi}{m} \left( \frac{2}{m} \right)^{1/2} \int_0^{\infty} E^{1/2} f(E) dE = N \quad (A.1)$$

Equation (A.1) applies when the spacecraft is not charged. For a potential of  $\phi$  on the spacecraft the expression is modified.

$$MO = \frac{4\pi}{m} \left( \frac{2}{m} \right)^{1/2} \int_C^{\infty} E^{1/2} f(E + q\phi) dE$$

where  $C$  is the energy of the lowest energy data points included in the fit (i.e., the cutoff) and  $q$  is the charge on the particle at hand.

$$f(E + q\phi) = e^{-q\phi/T} f(E)$$

$$\therefore MO = \left( \frac{4\pi}{m} \right) \left( \frac{2}{m} \right)^{1/2} N \cdot \left( \frac{m}{2\pi T} \right)^{3/2} e^{-q\phi/T} \int_C^{\infty} E^{1/2} e^{-E/T} dE$$

$$MO = \left( \frac{4\pi}{m} \right) \left( \frac{2}{m} \right)^{1/2} N \cdot \left( \frac{m}{2\pi T} \right)^{3/2} e^{-q\phi/T} \Gamma(3/2, y)$$



It is easy to show that

$$\frac{MO}{N} = e^{-q\phi/T} \frac{\Gamma(3/2, y)}{\Gamma(3/2)} = e^{-q\phi/T} \left[ \text{erfc}(y^{1/2}) + \frac{2}{\sqrt{\pi}} y^{1/2} e^{-y} \right]$$

where  $y = C/T$ .

$$\therefore N = MO e^{q\phi/T} \left[ \text{erfc}(y^{1/2}) + 2 \left( \frac{y}{\pi} \right)^{1/2} e^{-y} \right]^{-1} \quad (\text{A.2})$$

Hence we can estimate the density  $N$  by measuring the moment  $MO$ :

$$MO \approx \sum_{E=C}^{10^6} E^{1/2} f(E) \Delta E \quad (\text{A.3})$$

The second moment,  $M2$ , has the form

$$M2 = \frac{2}{3} \cdot \left( \frac{4\pi}{m} \right) \left( \frac{2}{m} \right)^{1/2} \int_0^{\infty} E^{3/2} f(E) dE = N \cdot T$$

for an uncharged spacecraft. Introducing a cutoff  $C$  and potential  $\phi$  leads to a result similar to that for  $MO$ :

$$T = \frac{\frac{M2}{MO} \left[ \text{erfc}(y^{1/2}) + e^{-y} 2 \cdot \left( \frac{y}{\pi} \right)^{1/2} \right]}{\left[ \text{erfc}(y^{1/2}) + e^{-y} \left( 2 \left( \frac{y}{\pi} \right)^{1/2} + \frac{4}{3} \frac{y^{3/2}}{\pi^{1/2}} \right) \right]} \quad (\text{A.4})$$

Equations (A.2) and (A.4) form two nonlinear simultaneous equations for  $T$  and  $N$ . Solution by iteration leads to values for  $N$  and  $T$  that make up the single Maxwellian fit.

b. Double Maxwellian Fits

The double Maxwellian fits were made by minimizing the relative error (least squares). The desired function has the form:

$$f(E) = N_1 \left( \frac{m}{2\pi T_1} \right)^{3/2} e^{-E/T_1} + N_2 \left( \frac{m}{2\pi T_2} \right)^{3/2} e^{-E/T_2} \quad (A.5)$$

An initial choice of values for  $T_1$  and  $T_2$  were made. The fit was made to agree exactly with the measured data at two points, one from the low and the other from the high energy regime. This determined the values of  $N_1$  and  $N_2$ . and had the effect of weighting the fit around the fixed points and ensuring a good compromise fit over the whole energy range. All possible combinations of choices for  $T_1$  and  $T_2$ , between realistic limits, were tried and the values that gave the minimum error were used as the double Maxwellian fit parameters.

c. Discussion

In all of the fits a cutoff of 1000 eV was used for the repelled species (electrons); i.e., only data above 1000 eV was included in the fits. Using data below this value lead to erratic and often rather unphysical values for the fitting parameters. For the attracted species (ions) the cutoff was taken as 1000 eV or the spacecraft potential, whichever was the greater. In the double Maxwellian fitting procedure the lower limit for the choice of temperature was forced to be one-half of the spacecraft potential for the repelled species. This ensured the absence of low temperature, high density components which were not observable at the surface due to the spacecraft potential.

TABLE 1. SINGLE MAXWELLIAN FITS TO DAY 87 MEASURED DISTRIBUTION FUNCTIONS.

Time (sec)	Species	Density ( $10^6 \text{ m}^{-3}$ )	Temperature (keV)
59813	Electrons	0.79	8.7
59813	Ions	0.086	12.0
59873	Electrons	0.98	12.0
59873	Ions	0.15	9.9
61073	Electrons	0.95	11.0
61073	Ions	0.20	12.0
59873	neutral	Electrons	12.0
59873		Ions	9.9

TABLE 2. DOUBLE MAXWELLIAN FITS TO DAY 87 MEASURED DISTRIBUTION FUNCTIONS.

Time (sec)	Species	Density ( $10^6 \text{ m}^{-3}$ )	Temperature (keV)	Density ( $10^6 \text{ m}^{-3}$ )	Temperature (keV)
59813	Electrons	0.29	5.9	0.48	11.0
59813	Ions	0.020	0.70	0.043	27.0
59873	Electrons	0.062	4.7	0.87	12.0
59873	Ions	0.037	1.0	0.096	14.0
61073	Electrons	0.64	5.1	0.45	16.0
61073	Ions	0.084	2.2	0.11	24.0

TABLE 3. CHARGING RESPONSE (kV) OF SOLAR AS A FUNCTION OF ENVIRONMENT REPRESENTATION

Environment	59813	59873	61073	59873 (Neutral)
Single Maxwellian	-14.5	-22.3	-17.2	-12.1
Double Maxwellian	-17.6	-20.3	-18.9	-
Direct Integration	-16.2	-22.6	-17.9	-
Satellite Potential	-1.9	-7.1	-4.8	-7.1

TABLE 4. THE EFFECT OF RADIATION-INDUCED CONDUCTIVITY ON THE CHARGING OF 0.005 INCH ( $1.27 \times 10^{-4}$  m) KAPTON FILM AS PREDICTED BY MATCHG

300 keV Incident Current pA cm <sup>-2</sup>	Differential Flux (F) electrons cm <sup>-2</sup> s <sup>-1</sup> sr <sup>-1</sup> keV <sup>-1</sup>	Conductivity $\sigma$	Potential* Volts
0	0	0	-15500
0.003	$1.0 \times 10^1$	$2.8 \times 10^{-17}$	-15300
0.03	$1.0 \times 10^2$	$2.8 \times 10^{-16}$	-13700
0.05	$1.67 \times 10^2$	$4.67 \times 10^{-16}$	-12800
0.5	$1.67 \times 10^3$	$4.67 \times 10^{-15}$	- 5600
5.0	$1.67 \times 10^4$	$4.67 \times 10^{-14}$	- 1000
50.0	$1.67 \times 10^5$	$4.67 \times 10^{-13}$	- 100
500.0	$1.67 \times 10^6$	$4.67 \times 10^{-12}$	- 0

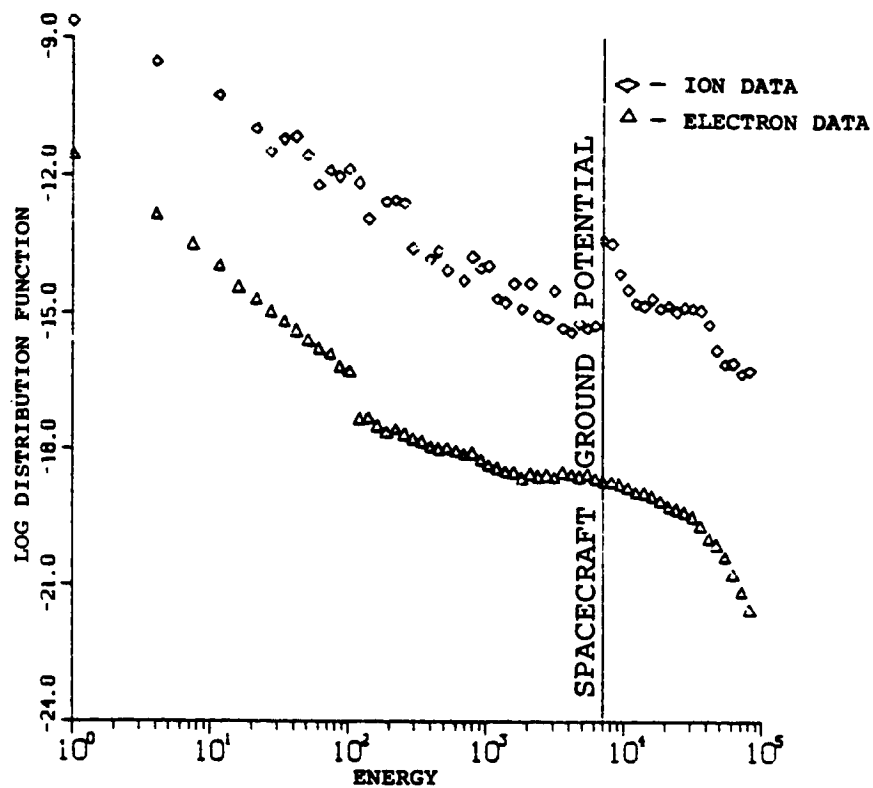
\* Environment at 59873 Day 87 used.

$$n_e = 0.28 \text{ cm}^{-3} \quad T_e = 12 \text{ keV}$$

$$n_i = 0.15 \text{ cm}^{-3} \quad T_i = 9.9 \text{ keV}$$

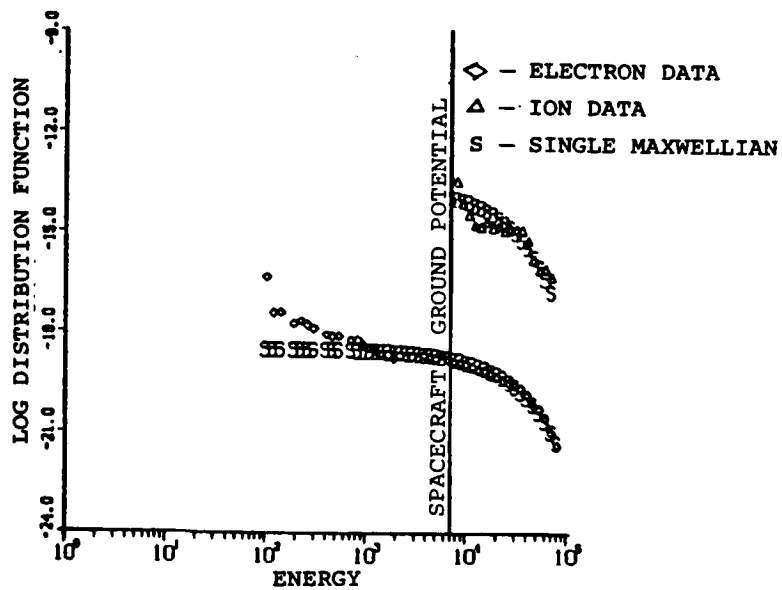
$$\sigma = \kappa F$$

$$\kappa = 2.8 \times 10^{-22} \text{ mhos m electron}^{-1} \text{ s sr keV}$$



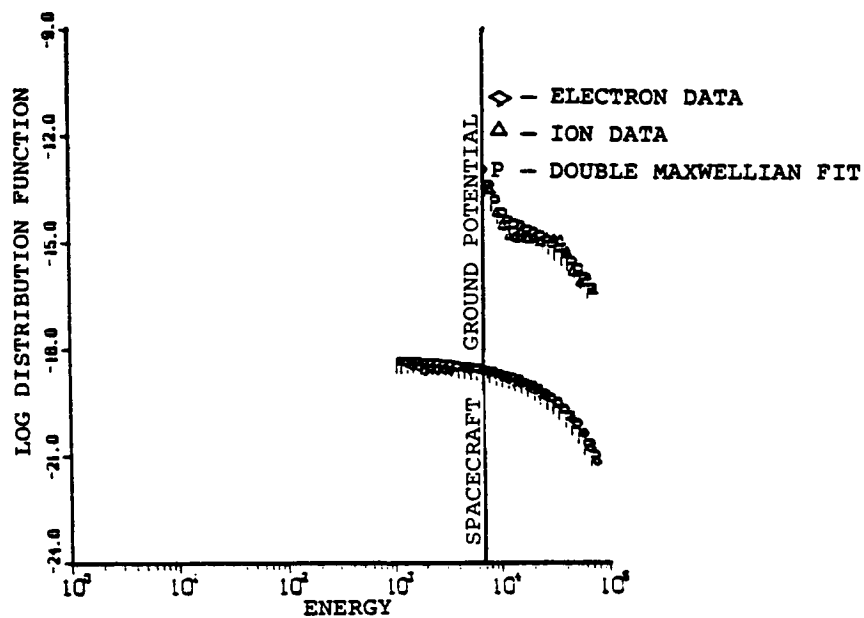
DAY 87, TIME 59873, POT - 7100. VOLTS

Figure 1. - Plot of raw distribution function SC9 SCATHA data.



DAY 87., TIME 59873., POT --7100. VOLTS

Figure 2. - Comparison of single Maxwellian fit (S) with observed ion ( $\Delta$ ) and electron ( $\diamond$ ) distribution functions for SC9 SCATHA data.



DAY 87., TIME 59873., POT --7100. VOLTS

Figure 3. - Comparison of double Maxwellian fit (P) with observed ion ( $\Delta$ ) and electron ( $\diamond$ ) distribution functions for SC9 SCATHA data.

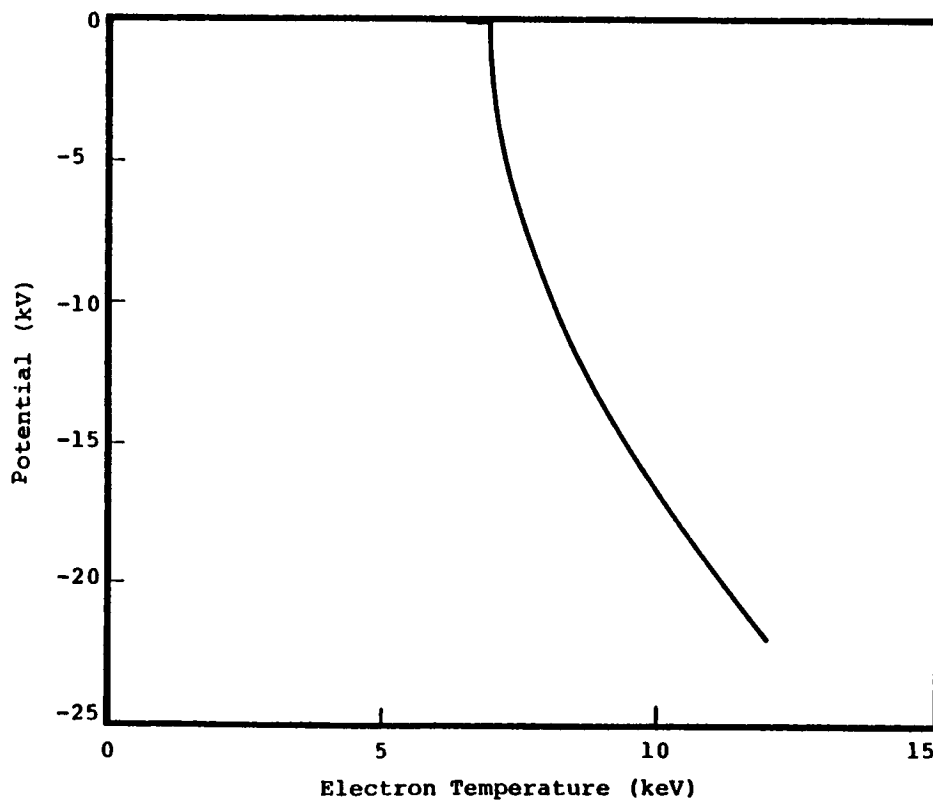


Figure 4. - Charging characteristics of a solar sphere as a function of electron temperature.

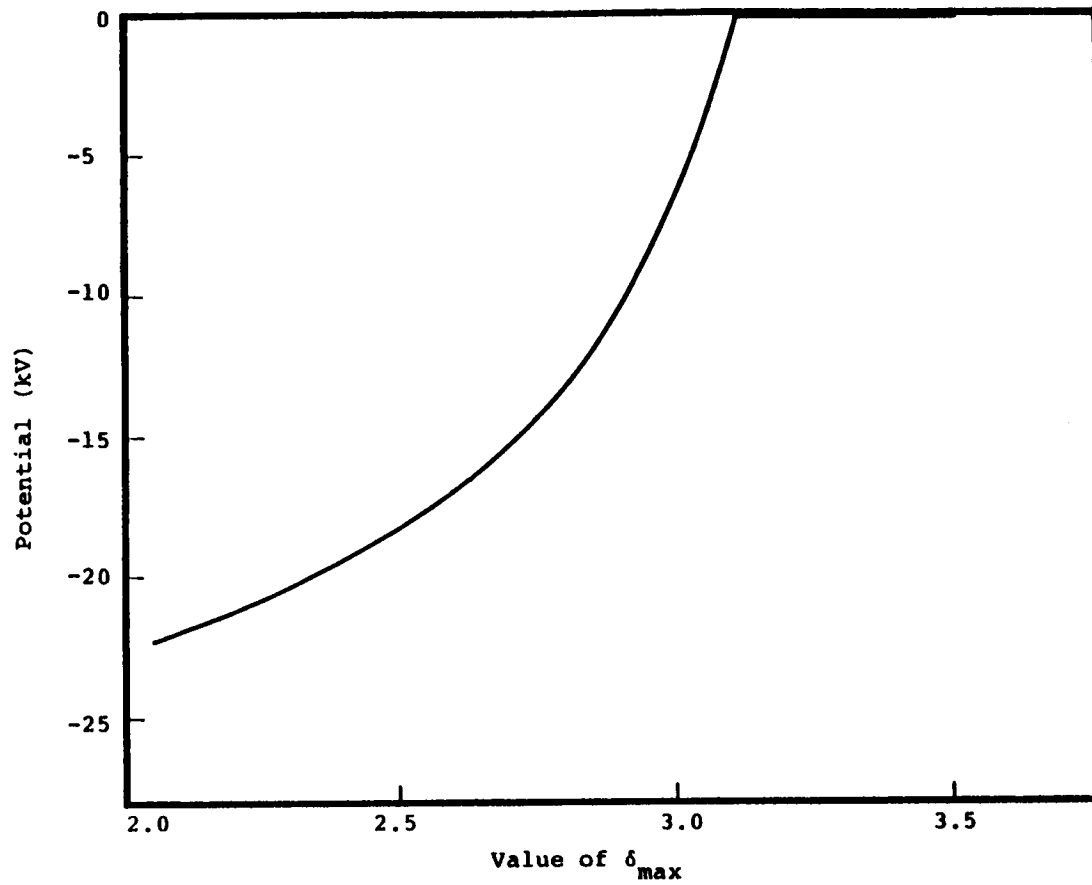


Figure 5. - Charging characteristics of a solar sphere as a function of secondary emission yield ( $\delta_{max}$ ).

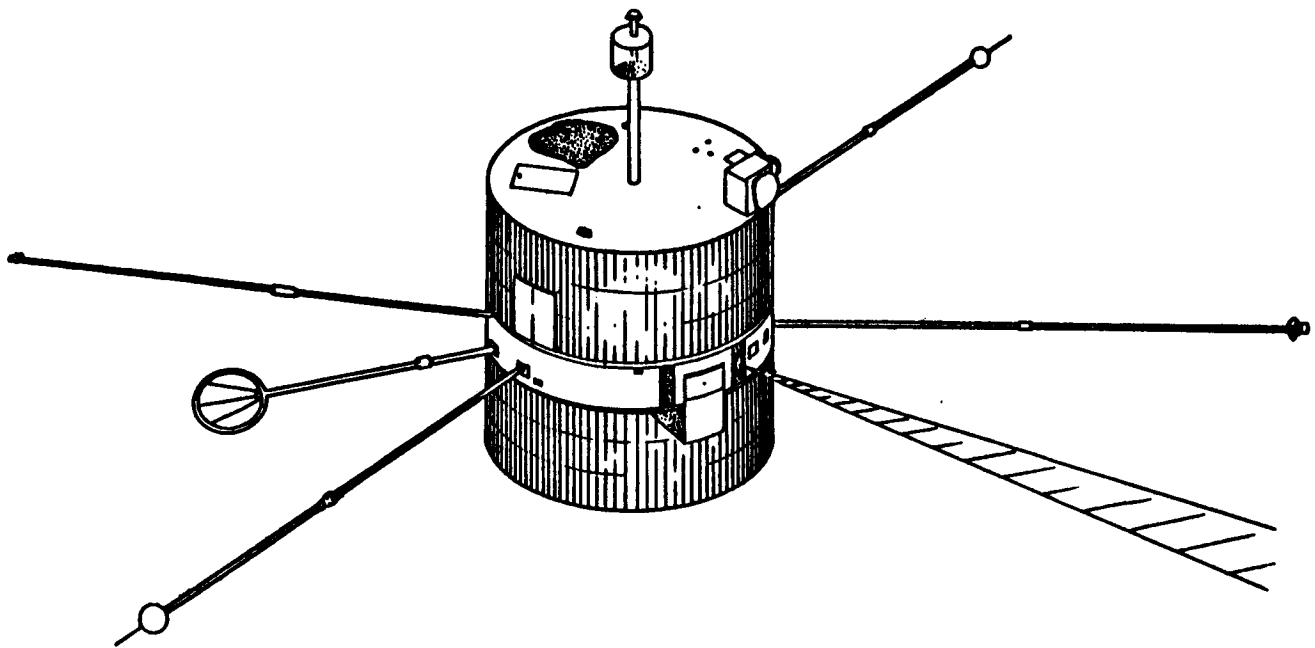


Figure 6a. - SC5 measures angular distribution of flux in plane of rotation of SCATHA satellite.

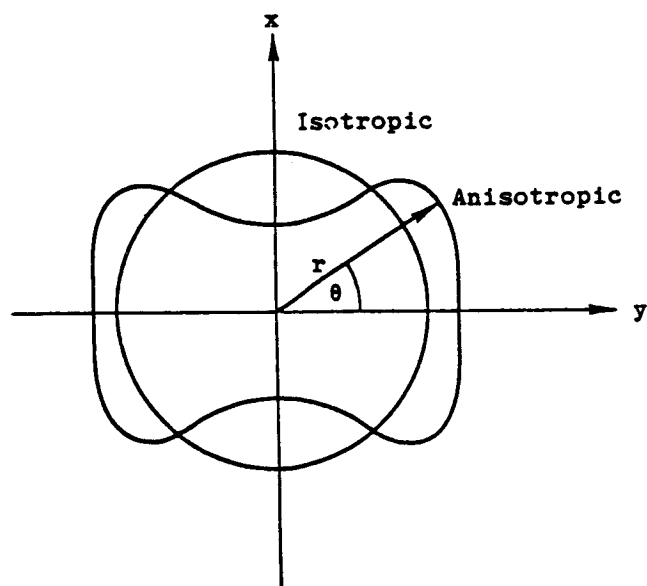


Figure 6b. - Representation of the angular distribution in rotation plane, where  $r$  represents magnitude of flux at angle  $\theta$ .



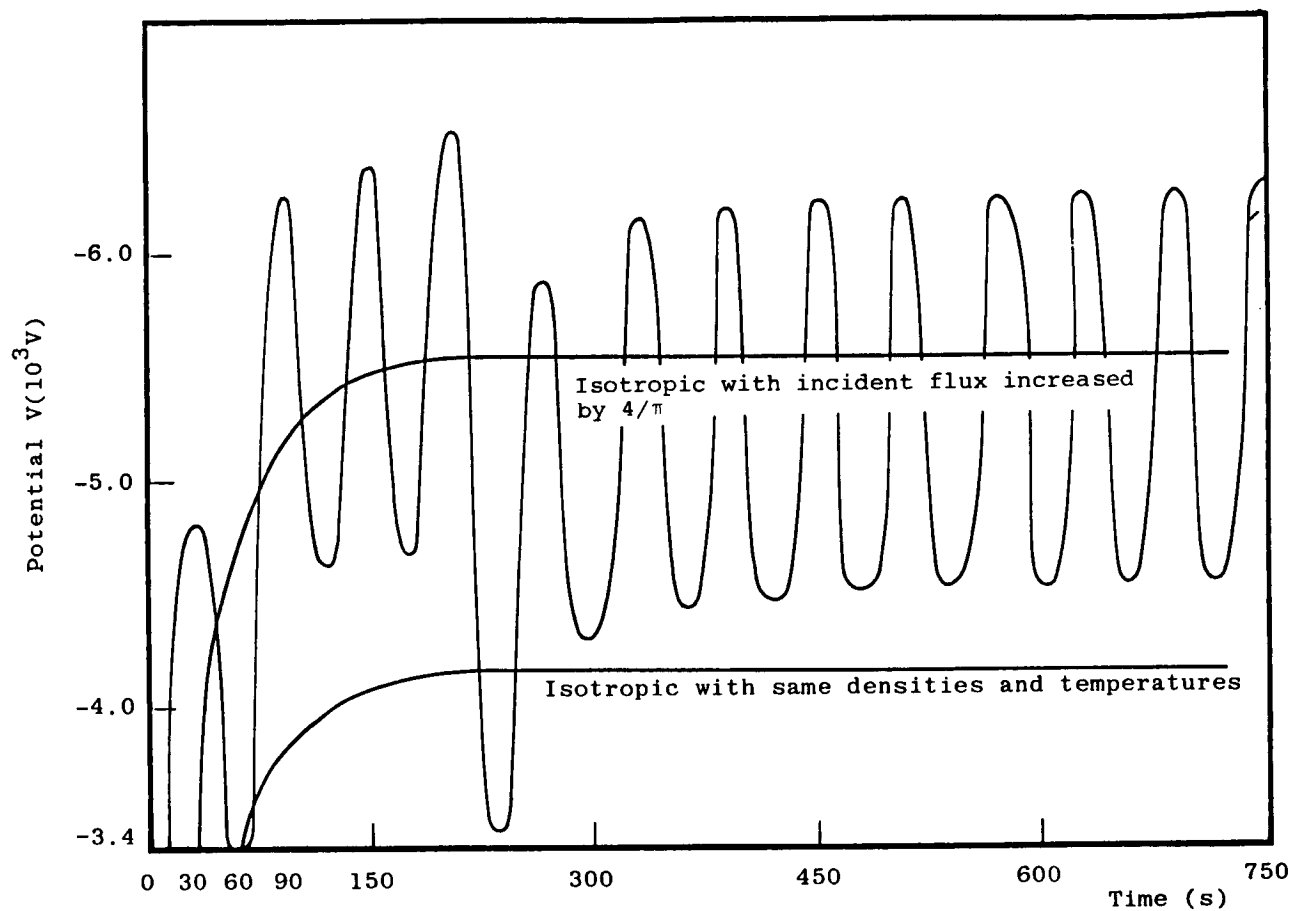


Figure 7. - Plot of aluminum potential as function of time for a beam rotating at 3 deg/sec. Ion density - electron density -  $2 \times 10^6 \text{ m}^{-3}$ ; ion temperature - 1 keV; electron temperature - 5 keV.

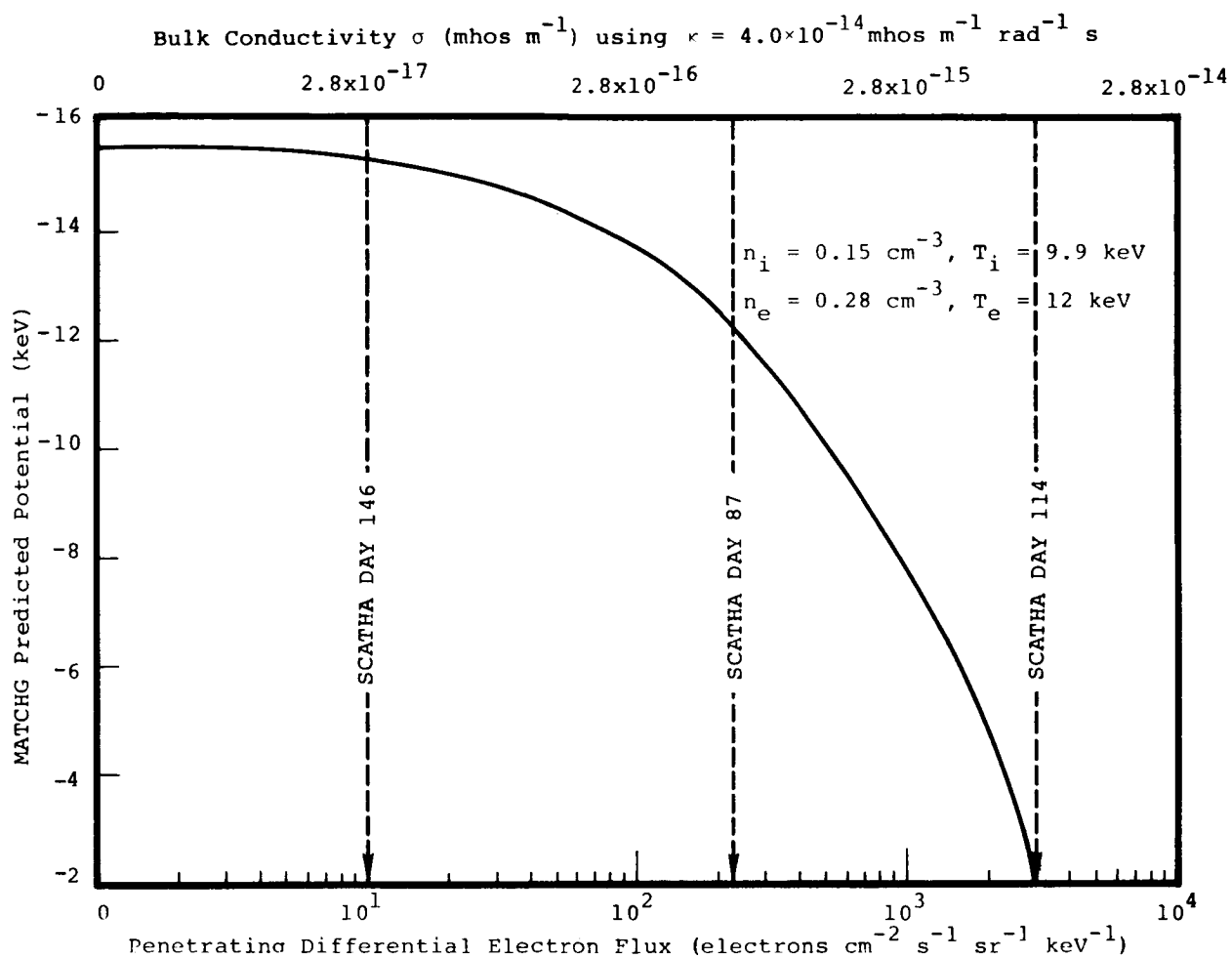


Figure 8. - Equilibrium potential of 5-mil Kapton coating a grounded conductor as function of bulk conductivity.

## **SIMULATION OF CHARGING RESPONSE OF SCATHA (P78-2) SATELLITE\***

**G. W. Schnuelle, P. R. Stannard, I. Katz, and M. J. Mandell**  
**Systems, Science and Software**

### **SUMMARY**

A detailed model of the SCATHA (P78-2) satellite has been used with the NASA Charging Analyzer Program (NASCAP) to simulate the charging response of SCATHA at geosynchronous orbit. The model includes a detailed description of the geometry, currents to exposed surface materials, and electrical connections on the spacecraft. Incident currents are calculated by numerically integrating actual spectra obtained by particle detectors on the SCATHA vehicle.

In this study we have compared the charging response of the vehicle to that predicted by the NASCAP model for the Day 87, 1979 eclipse charging event, in which the spacecraft charged to several kilovolts negative during a magnetospheric substorm. Double Maxwellian representations of the plasma environment reproduce the charging response observed experimentally.

### **INTRODUCTION**

The NASA Charging Analyzer Program (NASCAP) is a three-dimensional, finite element computer code designed to simulate the charging of an object in space. The physical model employed assumes that charge accumulates on a spacecraft due to an imbalance between incoming and outgoing currents to the surface. The sophisticated treatment takes into account incident electron and ion fluxes, secondary emission, backscatter, and surface and bulk conductivities to calculate the net current. NASCAP allows for a detailed three-dimensional geometrical representation of the spacecraft and includes capacitive and direct coupling between different materials when calculating spacecraft potential. The plasma environment can be specified in the form of analytic representations of the particle spectra or directly, as a set of

---

\* This work supported by the Air Force Geophysics Laboratory, Hanscom Air Force Base, Lexington, MA 01731, and the National Aeronautics and Space Administration, Lewis Research Center, Cleveland, OH 44135 under Contract NAS3-21762.

measured data points. A full description of the code and its capabilities appears in References 1 through 3.

We have used NASCAP to simulate the charging of the SCATHA (Spacecraft Charging At High Altitude) (P78-2) satellite. The SCATHA mission was specifically designed to investigate the plasma environment in Geosynchronous Earth Orbit (GEO), and its effects on spacecraft charging. The satellite has a number of particle detectors and emitters attached to the main body, and at the end of long booms. NASCAP can successfully incorporate all of these features into a geometrical model.

The detectors on board SCATHA have transmitted a wealth of information on the plasma environment and corresponding spacecraft potential. Armed with this information, and an accurate representation of the spacecraft, we have been able to make the first direct comparison between the charging behavior predicted by NASCAP, and that actually observed for a real satellite in space. We have also been able to show that physical model upon which NASCAP rests is a sound one.

#### PLASMA ENVIRONMENTS

Measurements made on board SCATHA have provided information about the spectrum of the plasma environment in the form of tabulations of the distribution function, for both electrons and ions, in the energy range  $10^2$  to  $10^5$  eV. This data is based on observations of energy flux, made by the SC9 detector, averaged over a 16-second period, and so has certain associated limitations; i.e.,

a. When the satellite is charged the spacecraft potential affects the energy of charged particles reaching the surface. For example if the spacecraft potential is -2000 V, protons are attracted to it and their energy is increased by 2000 eV at the surface, compared to infinity. In the same way electrons are repelled so that their energy is reduced by 2000 eV at the surface, and those electrons with initially less than 2000 eV of energy do not reach the surface at all.

This distorts the distribution function observed at the surface. While the shape of the distribution function  $f(E)$  is unaffected by spacecraft potential, the energies associated with each value are affected. The particle repelled by the potential  $\phi$  has  $q \times \phi$  less energy at the surface than it did at infinity ( $q$  is the charge on the particle). Hence instead of associating the value of the distribution function  $f_{\infty}(E)$  with energy  $E$ , the value is associated with particles of energy  $E - q\phi$ , i.e.,

$$f_{\infty}(E) = f_s(E - q\phi)$$

Knowing the spacecraft potential, this shift in energies is easily corrected for, providing the repelled species can reach the surface at all. However, those particles with energies at infinity less than  $q\phi$  cannot and so there is no distribution function information measured at these energies.

The lack of information for the repelled species (almost always electrons), below the spacecraft potential, represents a major limitation of the data as measured. This limitation does not apply to the attracted species (ions) since particles of all energies reach the spacecraft.

b. The energy flux is weighted by the energy:

$$\langle \text{Energy Flux} \rangle = \int_0^{\infty} E^2 f(E) dE$$

Measurements at low energies have a lower intensity and poorer signal to noise ratio. Hence the estimates of distribution function derived from these measurements are less reliable at the lowest energies.

The changes in spacecraft potential, following the injection that occurred at ~16.37 on Day 87 of the mission, have been singled out for study. Using the tabulations of electron and ion distribution functions measured at the surface, we have simulated the observed charging events for this period.

NASCAP requires spectral information in the form of a distribution function at infinity. This presents no difficulty for the attracted species but, for reasons discussed above, can lead to complications for the repelled species.

#### DIRECT INTEGRATION

In particular, the absence of spectral information concerning the repelled species for energies below the spacecraft potential has prevented a successful simulation involving direct integration of the observed data points. In principle, the missing data could be replaced by an extrapolation of the known data. This requires some assumption about its functional form and a fit to this form. Two approaches were tried.

1. The whole of the known data was fit to a Maxwellian form.
2. The known data of lowest energy was fit to a Maxwellian form.

The former approach was unsuccessful because the effective temperature of a Maxwellian fit increases with energy (i.e., the known data has a high energy non-Maxwellian "tail"). Thus the fit had a higher temperature than that appropriate for the extrapolated energy range. Figure 1 shows this as Case "C". The higher temperature leads to a lower density than would be expected by smooth extrapolation of the known data (Case "B"), and hence to anomalously low values for the distribution function in the extrapolated region. Such a distribution leads to false multiple equilibrium potentials.

The second approach, fitting only the data at energies close to the spacecraft potential, can lead to unphysically high values for the density and hence anomalously high values of the distribution function in the extrapolated region (Case "A"). This problem arises because the fit is based on an unrepresentatively small sample of points.

Stable predictions were obtained using direct integration of the data when only the high energy points were used, and all of the remainder replaced by a fit to these points. Under these circumstances, it is just as reasonable to replace the whole spectrum with a suitable analytic representation instead.

#### FITTING OF THE DATA

Two types of fit to the data were made.

1. Single Maxwellian - fitted by moments (ref. 4).
2. Double Maxwellian - fitted by least squares analysis.

In general, the double Maxwellian fits were better able to represent the non-Maxwellian character of the data (figures 2 and 3). Even though the fits were good from 100 eV to 100,000 eV, the low energy components of the double Maxwellians were often unphysical with very high densities and low temperatures. This was particularly true for the electrons in cases where the satellite was charged to several thousand volts negative. Under these conditions only the very end of a Maxwellian component with a temperature, say one-tenth the spacecraft potential contributes to the flux at the surface. Such contributions can only be considered as noise.

Increasing the "cutoff," below which data points are ignored, to 1000 eV greatly improves the physical picture provided by the fit. This, coupled with an enforced lowest value of at least half the spacecraft potential for the temperature, leads to a series of double Maxwellian fits that were both physical and accurate in all energy regions (Table 1).

## CHARGE NEUTRALIZATION

While the fits accurately represent both the ion and electron data points as observed, the electron densities tend to be as much as a factor of ten higher than the ion densities at the same time. This implies that the plasma surrounding the spacecraft is highly non-neutral. This unphysical result may be due to a systematic error in the measurement of energy flux for one of the species. Independent measurements indicate that the ion densities are the best choice for the correct value. To neutralize the plasma we renormalize the electron densities so that they are equal to the ion densities. This would be a simple matter if the ions were all protons (as the conversion to distribution function assumes). However, measurements by Kaye, et al. (ref. 5) show that  $O^+$  is often the dominant species. This does not affect the fluxes as calculated by NASCAP because the code also assumes all the ions are protons and so the error is cancelled out. However, a factor of  $(\text{mass})^{-1/2}$  is carried over into the values of the distribution function and hence the estimate of density  $N$ . For a pure  $O^+$  environment an electrically neutral plasma would have  $N^- = (16)^{1/2} N^+$  as calculated assuming that all ions were protons; i.e.,

$$N^+ = 0.25 N^-$$

If only a fraction  $\alpha$  are oxygen

$$N^+ = [0.25\alpha + (1-\alpha)] N^-$$

$$N^- = N^+ / (1 - 0.75\alpha).$$

To correct the values of the density for the electrons the values of  $N_1^-$  and  $N_2^-$  obtained by the fitting procedure were multiplied by the factor  $f$ .

$$f = \frac{(N_1^+ + N_2^+)}{(N_1^- + N_2^-)(1 - 0.75)}$$

Hence we arrived at the final parameters that were used by NASCAP to describe the environment in the simulation of the Day 87 eclipse. (Table 1.)

## CHARGING SIMULATION

The representation of the satellite used in the detailed simulation of the charging response, observed during eclipse between 16:30 and 17:30 on Day 87, 1979, was the so-called "one-grid" model. As its name suggests, this model uses only the innermost NASCAP computational grid. It retains much of the detail included in the so-called "four-grid" model (described extensively in ref. (6)), but requires considerably less computation time to achieve the same result. Even though the resolution is less (zone size is 196 mm versus 115 mm), and the booms are shorter, preliminary studies indicate that the one-grid model gives NASCAP charging predictions similar to those for the four-grid model.

The potential reached by a spacecraft bathed in a plasma environment depends on at least three factors.

1. The nature of the environment (temperature and density).
2. The time it has been exposed to the environment.  
(Charging or discharging is not instantaneous.)
3. The potential of the spacecraft prior to the introduction of the new environment.

To properly simulate the response of the spacecraft to the charging environment, NASCAP takes all of these factors into account. After each cycle, the time elapsed is checked, and the environment parameters used updated to the most recent time for which data was measured. The data points are typically 60 seconds apart.

The results are shown in figure 4. The NASCAP simulation reproduces the two major jumps in potential, but misses the remaining two minor jumps. Quantitative agreement is excellent considering the sensitivity of the NASCAP predictions to the values of the material properties used. The NASCAP simulation is slower to respond to changes in environment than the real satellite, because the environment changes occur in ~60 second steps rather than the continuous adjustment experienced in space.

In addition, the slow discharge rate predicted, following the two charging pulses, would have been faster if shorter computational timesteps had been used.



## CONCLUSIONS

The Day 87 simulation is the first real test of both NASCAP and the physical model on which it is based. The remarkable agreement between the NASCAP predicted potentials and those actually observed on a real satellite in an actual space environment, shown in figure 4, confirms their validity. We can now say with confidence that the physical processes which control spacecraft charging are understood. The accumulation of charge arises because of the collection of currents of charged particles, predominantly with energies below 50 keV, at the spacecraft surface. With NASCAP's accurate representation of these physical processes, we are now in a good position to predict and model spacecraft charging response.

## REFERENCES

1. Katz, I., et al.: A Three Dimensional Dynamic Study of Electrostatic Charging in Materials. NASA CR-135256, August 1977.
2. Cassidy, J. J.: NASCAP User's Manual - 1978. NASA CR-159417, August 1978.
3. Katz, I., et al.: The Capabilities of the NASA Charging Analyzer Program. NASA Conference Publication 2071, AFGL-TR-79-0082, 1978.
4. Stannard, P. R., et al.: Representation and Material Charging Response of GEO Plasma Environments. To be presented at Spacecraft Charging Technology Conference III, Colorado Springs, CO, 12-14 November 1980.
5. Private communication, SC8 data, S. Kaye, et al.
6. Schnuelle, G. W., et al.: Charging Analysis of the SCATHA Satellite. NASA Conference Publication 2071, AFGL-TR-79-0082, 1978.

TABLE 1. NEUTRALIZED FITS TO DAY 87  
ECLIPSE ENVIRONMENTS

ELECTRONS AT 59473. N1=	1.9+05 T1=	800. N2=	6.1+02 T2=	9000.
IONS AT 59473. N1=	5.5+04 T1=	3400. N2=	4.8+04 T2=	43000.
ELECTRONS AT 59673. N1=	4.7+05 T1=	2000. N2=	6.3+03 T2=	7000.
IONS AT 59673. N1=	1.4+05 T1=	2400. N2=	1.5+05 T2=	45000.
ELECTRONS AT 59753. N1=	8.0+05 T1=	4500. N2=	7.4+04 T2=	7000.
IONS AT 59753. N1=	3.5+05 T1=	3500. N2=	1.3+05 T2=	28000.
ELECTRONS AT 59813. N1=	4.3+04 T1=	5850. N2=	7.1+04 T2=	44000.
IONS AT 59813. N1=	2.0+04 T1=	700. N2=	4.3+04 T2=	27000.
ELECTRONS AT 59853. N1=	2.2+04 T1=	5400. N2=	1.2+05 T2=	14000.
IONS AT 59853. N1=	2.1+04 T1=	600. N2=	3.8+04 T2=	46000.
ELECTRONS AT 59873. N1=	2.1+04 T1=	4650. N2=	2.9+05 T2=	12000.
IONS AT 59873. N1=	3.7+04 T1=	1000. N2=	9.6+04 T2=	14000.
ELECTRONS AT 59913. N1=	4.5+05 T1=	4000. N2=	6.6+04 T2=	14000.
IONS AT 59913. N1=	1.2+05 T1=	4900. N2=	9.6+04 T2=	15000.
ELECTRONS AT 59933. N1=	6.7+05 T1=	4840. N2=	3.5+05 T2=	9000.
IONS AT 59933. N1=	1.4+05 T1=	4700. N2=	3.2+05 T2=	10000.
ELECTRONS AT 59973. N1=	1.0+06 T1=	2840. N2=	2.5+05 T2=	9000.
IONS AT 59973. N1=	4.0+03 T1=	400. N2=	5.5+05 T2=	4000.
ELECTRONS AT 60043. N1=	1.5+05 T1=	1600. N2=	2.2+05 T2=	10000.
IONS AT 60043. N1=	7.6+04 T1=	2000. N2=	8.0+04 T2=	29000.
ELECTRONS AT 60053. N1=	2.0+05 T1=	2000. N2=	2.7+05 T2=	9000.
IONS AT 60053. N1=	7.0+04 T1=	1200. N2=	1.3+05 T2=	30000.
ELECTRONS AT 60133. N1=	3.9+05 T1=	1900. N2=	3.4+05 T2=	14000.
IONS AT 60133. N1=	6.8+04 T1=	3400. N2=	2.2+05 T2=	20000.
ELECTRONS AT 60213. N1=	4.2+05 T1=	2000. N2=	2.3+05 T2=	9000.
IONS AT 60213. N1=	1.8+04 T1=	800. N2=	2.4+05 T2=	16000.
ELECTRONS AT 60293. N1=	4.1+05 T1=	3200. N2=	3.6+05 T2=	9000.
IONS AT 60293. N1=	1.2+05 T1=	2200. N2=	1.8+05 T2=	48000.
ELECTRONS AT 60421. N1=	2.1+05 T1=	4550. N2=	2.1+05 T2=	7000.
IONS AT 60421. N1=	9.2+04 T1=	2300. N2=	1.7+05 T2=	45000.
ELECTRONS AT 60493. N1=	1.8+05 T1=	4800. N2=	2.7+05 T2=	7000.
IONS AT 60493. N1=	1.0+05 T1=	4800. N2=	1.9+05 T2=	16000.
ELECTRONS AT 60593. N1=	5.7+05 T1=	2650. N2=	8.4+04 T2=	12000.
IONS AT 60593. N1=	1.0+05 T1=	1000. N2=	2.0+05 T2=	48000.
ELECTRONS AT 60633. N1=	6.4+05 T1=	3450. N2=	1.1+05 T2=	47000.
IONS AT 60633. N1=	1.4+05 T1=	4000. N2=	2.0+05 T2=	45000.
ELECTRONS AT 60653. N1=	5.4+05 T1=	3140. N2=	1.0+05 T2=	20000.
IONS AT 60653. N1=	1.3+05 T1=	4300. N2=	1.6+05 T2=	19000.
ELECTRONS AT 60673. N1=	5.9+05 T1=	3300. N2=	1.3+05 T2=	48000.
IONS AT 60673. N1=	1.5+05 T1=	4400. N2=	1.8+05 T2=	46000.

N1 = density of first component in  $m^{-3}$ .  
T1 = temperature of first component in eV.  
N2 = density of second component in  $m^{-3}$ .  
T2 = temperature of second component in eV.

ELECTRONS AT 60693. N1=	6.9+05 T1= 4050. N2=	1.7+05 T2=19000.	ELECTRONS AT 62093. N1=	5.7+05 T1= 3150. N2=	1.8+05 T2= 8000.
IONS AT 60693. N1=	2.1+05 T1= 1200. N2=	1.8+05 T2=18000.	IONS AT 62093. N1=	2.2+05 T1= 2400. N2=	2.5+05 T2=17000.
ELECTRONS AT 60753. N1=	5.0+05 T1= 3950. N2=	1.3+05 T2=18000.	ELECTRONS AT 62133. N1=	6.3+05 T1= 2000. N2=	1.7+05 T2= 8000.
IONS AT 60753. N1=	1.3+05 T1= 2000. N2=	1.6+05 T2=20000.	IONS AT 62133. N1=	2.9+05 T1= 3500. N2=	2.2+05 T2=21000.
ELECTRONS AT 60833. N1=	3.7+05 T1= 3100. N2=	1.3+05 T2=16000.	ELECTRONS AT 62133. N1=	6.3+05 T1= 2000. N2=	1.7+05 T2= 8000.
IONS AT 60833. N1=	2.0+05 T1= 1600. N2=	1.7+05 T2=19000.	IONS AT 62133. N1=	2.9+05 T1= 3500. N2=	2.2+05 T2=21000.
ELECTRONS AT 60893. N1=	2.3+05 T1= 2700. N2=	1.2+05 T2=13000.	ELECTRONS AT 62233. N1=	4.7+05 T1= 1900. N2=	9.3+04 T2= 8000.
IONS AT 60893. N1=	1.3+05 T1= 1900. N2=	1.3+05 T2=22000.	IONS AT 62233. N1=	1.5+05 T1= 5000. N2=	9.8+04 T2=22000.
ELECTRONS AT 60973. N1=	2.7+05 T1= 3250. N2=	1.5+05 T2=14000.	ELECTRONS AT 62353. N1=	4.7+05 T1= 1500. N2=	1.7+05 T2= 8000.
IONS AT 60973. N1=	1.5+05 T1= 1500. N2=	1.6+05 T2=22000.	IONS AT 62353. N1=	0.0 T1= 0. N2=	2.8+05 T2= 6000.
ELECTRONS AT 61033. N1=	1.8+05 T1= 3900. N2=	1.0+05 T2=15000.	ELECTRONS AT 62393. N1=	7.9+05 T1= 1500. N2=	4.3+05 T2= 8000.
IONS AT 61033. N1=	7.4+04 T1= 4500. N2=	1.0+05 T2=19000.	IONS AT 62393. N1=	3.7+05 T1= 4800. N2=	1.6+05 T2=30000.
ELECTRONS AT 61073. N1=	1.9+05 T1= 5100. N2=	1.3+05 T2=16000.	ELECTRONS AT 62413. N1=	9.0+05 T1= 1900. N2=	4.5+05 T2= 8000.
IONS AT 61073. N1=	8.4+04 T1= 2200. N2=	1.1+05 T2=24000.	IONS AT 62413. N1=	4.2+05 T1= 2500. N2=	1.7+05 T2=22000.
ELECTRONS AT 61133. N1=	4.2+05 T1= 2750. N2=	1.4+05 T2=13000.	ELECTRONS AT 62593. N1=	1.7+05 T1= 1100. N2=	2.3+05 T2= 9000.
IONS AT 61133. N1=	2.1+05 T1= 1100. N2=	1.3+05 T2=24000.	IONS AT 62593. N1=	8.5+04 T1= 1200. N2=	1.1+05 T2=23000.
ELECTRONS AT 61193. N1=	4.3+05 T1= 2600. N2=	2.1+05 T2=12000.	ELECTRONS AT 62693. N1=	3.2+05 T1= 1600. N2=	2.2+05 T2= 9000.
IONS AT 61193. N1=	2.6+05 T1= 1400. N2=	1.5+05 T2=19000.	IONS AT 62693. N1=	1.2+05 T1= 2200. N2=	1.3+05 T2=30000.
ELECTRONS AT 61313. N1=	4.6+05 T1= 2500. N2=	2.1+05 T2=12000.	ELECTRONS AT 62753. N1=	4.4+05 T1= 2000. N2=	1.8+05 T2=12000.
IONS AT 61313. N1=	1.9+05 T1= 1600. N2=	1.0+05 T2=30000.	IONS AT 62753. N1=	1.2+05 T1= 2000. N2=	1.7+05 T2=15000.
ELECTRONS AT 61393. N1=	4.6+05 T1= 1800. N2=	2.6+05 T2=10000.	ELECTRONS AT 62813. N1=	4.8+05 T1= 2100. N2=	9.2+04 T2=13000.
IONS AT 61393. N1=	1.4+05 T1= 2200. N2=	1.7+05 T2=20000.	IONS AT 62813. N1=	4.4+05 T1= 2300. N2=	1.3+05 T2=27000.
ELECTRONS AT 61453. N1=	4.1+05 T1= 1800. N2=	3.0+05 T2= 9000.	ELECTRONS AT 62933. N1=	4.4+05 T1= 2200. N2=	1.2+05 T2=11000.
IONS AT 61453. N1=	1.5+05 T1= 1500. N2=	1.6+05 T2=24000.	IONS AT 62933. N1=	1.8+05 T1= 2900. N2=	8.2+04 T2=30000.
ELECTRONS AT 61513. N1=	4.4+05 T1= 1700. N2=	3.7+05 T2= 9000.	ELECTRONS AT 63053. N1=	3.8+05 T1= 2300. N2=	1.7+05 T2=12000.
IONS AT 61513. N1=	2.0+05 T1= 2200. N2=	1.7+05 T2=23000.	IONS AT 63053. N1=	1.4+05 T1= 2500. N2=	1.2+05 T2=30000.
ELECTRONS AT 61573. N1=	5.6+05 T1= 1550. N2=	3.7+05 T2= 9000.			
IONS AT 61573. N1=	2.3+05 T1= 2200. N2=	1.9+05 T2=23000.			
ELECTRONS AT 61633. N1=	3.2+05 T1= 2650. N2=	3.0+05 T2=10000.			
IONS AT 61633. N1=	1.4+05 T1= 3100. N2=	1.4+05 T2=24000.			
ELECTRONS AT 61653. N1=	2.3+05 T1= 2450. N2=	2.6+05 T2=10000.			
IONS AT 61653. N1=	8.7+04 T1= 2200. N2=	1.4+05 T2=28000.			
ELECTRONS AT 61953. N1=	3.8+05 T1= 3700. N2=	3.0+05 T2= 9000.			
IONS AT 61953. N1=	1.2+05 T1= 3100. N2=	1.7+05 T2=30000.			
ELECTRONS AT 62013. N1=	5.2+05 T1= 4350. N2=	2.6+05 T2= 9000.			
IONS AT 62013. N1=	2.7+05 T1= 2400. N2=	2.2+05 T2=30000.			
ELECTRONS AT 62033. N1=	3.3+05 T1= 3710. N2=	1.5+05 T2= 9000.			
IONS AT 62033. N1=	0.0 T1= 0. N2=	3.0+05 T2= 4000.			
ELECTRONS AT 62073. N1=	4.0+05 T1= 3255. N2=	1.7+05 T2= 8000.			
IONS AT 62073. N1=	1.3+05 T1= 1600. N2=	2.2+05 T2=15000.			

TABLE 1. NEUTRALIZED FITS TO DAY 87  
ECLIPSE ENVIRONMENTS  
(CONTINUED)

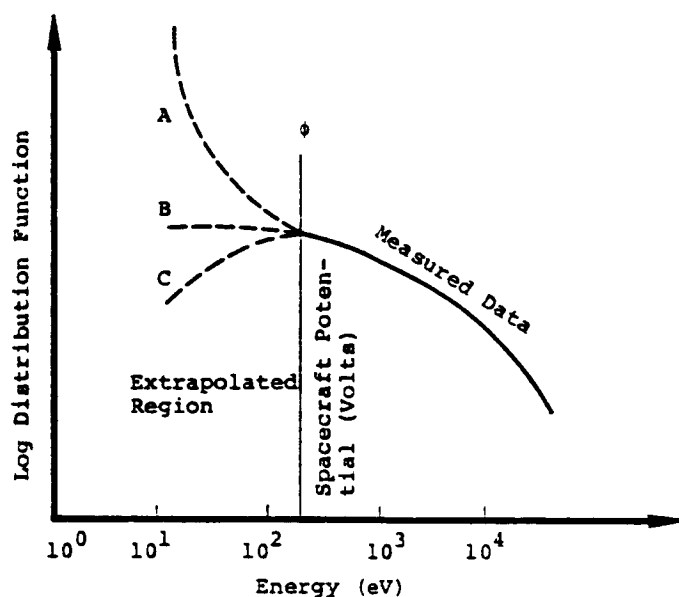


Figure 1. - Extrapolations of measured data beyond the spacecraft potential for the repelled species.

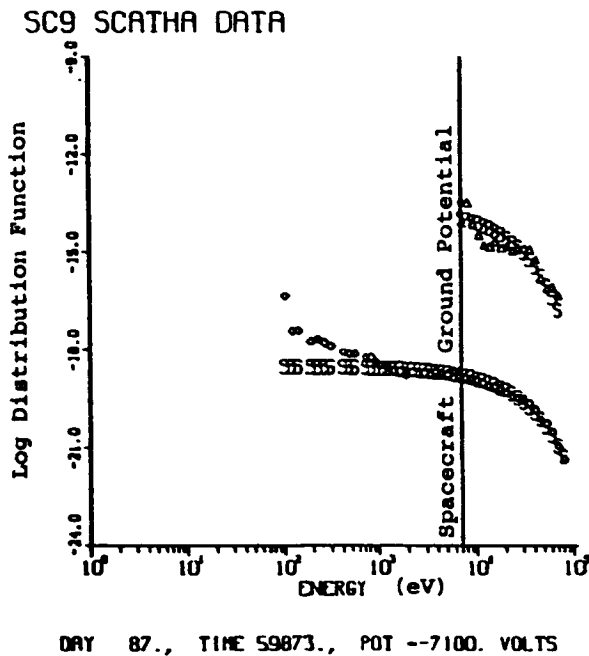


Figure 2. - Comparison of single Maxwellian fit (S) with observed ion ( $\Delta$ ) and electron ( $\diamond$ ) distribution functions.

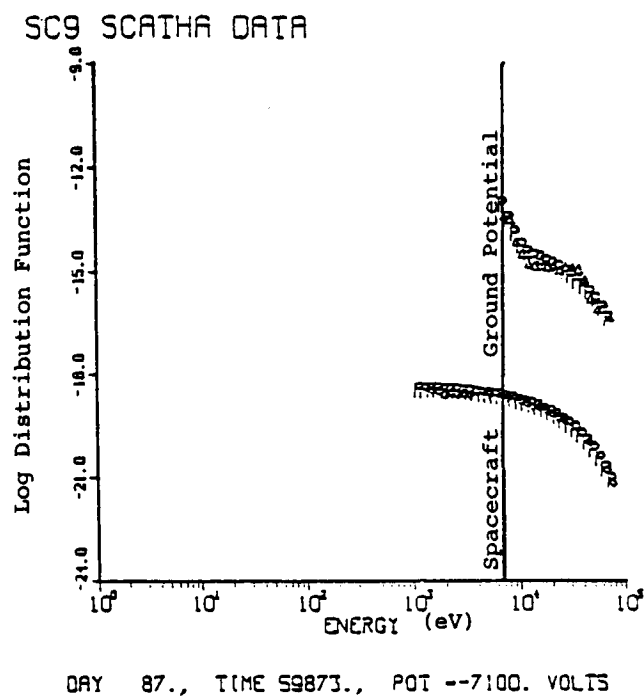


Figure 3. - Comparison of double Maxwellian fit (P) with observed ion ( $\Delta$ ) and electron ( $\diamond$ ) distribution functions.

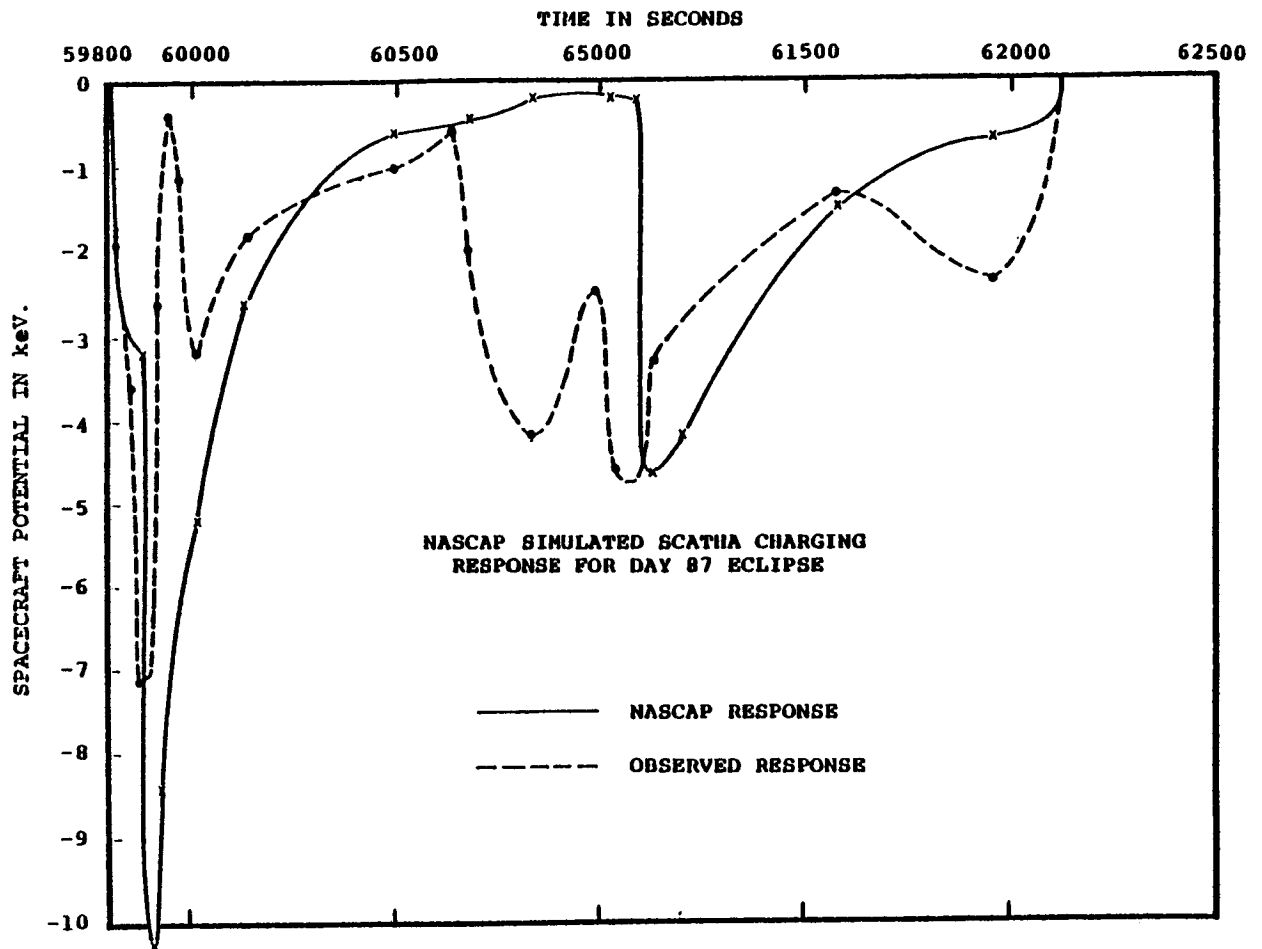


Figure 4. - Comparison of NASCAP simulated SCATHA charging response with observed response.

## **SCATHA SSPM CHARGING RESPONSE: NASCAP PREDICTIONS COMPARED WITH DATA**

**Carolyn K. Purvis and John V. Staskus  
NASA Lewis Research Center**

### **SUMMARY**

The satellite surface potential monitor (SSPM) experiment aboard the SCATHA (Air Force P78-2) spacecraft was designed to investigate the charging response of insulators exposed to the geosynchronous plasma environment. Prior to SCATHA's launch the SSPM flight hardware was calibrated and its charging response examined in electron spraying tests at the NASA Lewis Research Center. This paper reports models for the SSPM units constructed in the NASCAP code and the results of comparing predictions to surface voltage and baseplate current data. Sets of NASCAP material properties that yielded satisfactory agreement are presented. Several peculiarities in the test data are noted. Preliminary results from space simulations of a SCATHA model with environments representative of the day 87, 1979, eclipse injection event are also presented, and their implications for predicting space response are discussed.

### **INTRODUCTION**

The satellite surface potential monitor (SSPM) is one of several engineering experiments flown on the Air Force P78-2 satellite, which is also known as SCATHA (Spacecraft Charging at High Altitudes). The satellite's mission is to examine the geosynchronous environment and the charging response of a spacecraft in that environment (refs. 1 to 3). The SSPM's purpose is to determine the charging responses of selected spacecraft surface materials exposed to the environment. It was designed and built by the Aerospace Corporation in cooperation with the Air Force Materials Laboratory and provides surface voltage and substrate current measurements for each material sample.

Prior to launch the flight hardware was tested in a vacuum facility at NASA's Lewis Research Center to calibrate the flight voltage measurement instrumentation and to provide data for comparison with flight results. Such comparisons must be made with the aid of models because of the differences in environment between the ground and space conditions. Before attempting to predict flight results, it is necessary to develop and exercise the models to predict the response of the samples under ground test conditions. From the viewpoint of physical surroundings and environment, laboratory conditions are better known and simpler than on-orbit conditions. Successful modeling of sample responses under laboratory test conditions thus seems a prerequisite to meaningful modeling of flight response.

This paper presents results of a study in which computer models of the three SSPM units (SC1-1, SC1-2, and SC1-3) were constructed and their charging responses investigated by using the NASCAP code (ref. 4). Model results were compared with ground test data, and selected material property parameters were varied to optimize fit. Sets of material properties were

thus provided that could be used in conjunction with a model of the SCATHA spacecraft to investigate flight responses of the SSPM materials.

An earlier study (ref. 5) used this approach to investigate responses of the SC1-2 Kapton sample. The present effort was focused on the three Kapton samples (one on each unit), the Teflon sample on SC1-3, and the optical solar reflectors (OSR's) on SC1-1. Emphasis was on the ground test comparison. Some rather surprising results from preliminary runs using a SCATHA model and the eclipse environment from day 87 of 1979 are also presented, and their implications are discussed.

### SSPM DESCRIPTION

The SSPM comprises three separate units, each with the exterior dimensions of 33 by 33 by 5 centimeters, identified in the P78-2 experiments list as SC1-1, SC1-2, and SC1-3. The SC1-1 and SC1-3 units contain four test samples apiece, each with an exposed area of 12.4 square centimeters. The SC1-2 unit has a single sample with an exposed area of 28.9 square centimeters. Each test sample is surrounded by a gold frame that is electrically connected to spacecraft ground. Sample surface materials are summarized in table I, and their configurations are illustrated in figure 1. The open circles in the figure indicate the positions at which surface potential measurements are made by a back-side technique. The SC1-2 unit also has a spot at which a "front side" potential measurement is made (solid circle in fig. 1). Here a hole is punched through the Kapton so that surface electric fields can be sensed.

The back-side potential measurement technique, which is the standard for the experiment, is illustrated in figure 2. Insulator samples are mounted, metallized side down, on a copper-clad printed circuit board by using silver-loaded epoxy. At the potential measurement spot there is a hole punched through the printed circuit board where the sample metallization is removed from a 0.64-centimeter-diameter spot. Fields in the cavity formed by this hole are sensed by a Monroe voltmeter. The copper cladding is grounded to the spacecraft structure through an electrometer, which provides the sample current measurement. Each sample has a narrow strip of metallization removed from around its border so that the current reading indicates the bulk leakage current in equilibrium and the sum of bulk leakage and net charging currents during charging but does not include surface currents. Further description of the SSPM can be found in references 1, 5, and 6.

### EXPERIMENTAL INVESTIGATION

Preflight testing of the SSPM units at Lewis has been described previously (ref. 5). Briefly, each SSPM unit was exposed to normally incident electron beams of energies 2.5, 4, 6, and 8 kilovolts at a nominal current density of 1 nanoampere ( $10^{-9}$  A) per square centimeter, at several temperatures, in the dark. During these tests noncontacting surface voltage probes were swept across the sample test surfaces, passing directly over the flight measurement spots. The resulting data were used to calibrate the back-side flight potential measurements.

Because the metallization was removed from the insulator samples at the flight measurement spots, the effective capacitance per unit area of



insulation was smaller at that spot than for the rest of the corresponding sample. In consequence, the surface over the flight measurement spot responded more quickly to the electron beam than did the bulk of the sample. This effect is important to note because the flight surface voltage data represent the response of the measurement spot only, not that of the bulk of the sample. It is the current data that must be used to infer the response of the bulk of the sample.

This difference in charging rates between the flight measurement spot and the rest of a sample is illustrated in figure 3, where data from one test of each of the three Kapton samples are plotted. In this figure the solid symbols represent the measured potential near the measurement spot, and the open symbols represent the spot potential. Clearly, in each case the measurement spot charges much more rapidly than the surrounding insulation, an effect that must be accounted for in the modeling.

Another fact apparent from figure 3 is that, although the base material of the three Kapton samples shows essentially a single charging rate, the measurement spot of the SC1-3 Kapton sample charges significantly more slowly than the spots of the SC1-1 and SC1-2 Kapton samples. That is, the effective spot-to-base capacitances are different. This is not too surprising, given the tolerances in the mounting specifications, but it should be accounted for in modeling and in interpreting flight data.

## MODELING: GROUND TESTS

### Computer Model Description

A computer model for each of the SSPM units was constructed by using the NASCAP code. The appearance of these models, or "objects" as they are called in NASCAP, is illustrated in figure 4, which shows the SC1-3 model. The cell size is 2.54 centimeters (1 in.) on a side. Each unit is modeled by a 14- by 14- by 1-cell object, five of whose surfaces are gold. The remaining surface has patches of surface materials to represent the sample surfaces. Each of the sample surfaces is associated with its own underlying conductor to allow current predictions to be made. Each of the four surface sample areas on the SC1-1 and SC1-3 objects measures 5 cells by 5 cells, representing an area of approximately 161 square centimeters (as compared with  $\sim 154 \text{ cm}^2$  for the actual area). The Kapton surface area on the SC1-2 object is 12 cells by 12 cells or approximately 929 square centimeters (actual Kapton area,  $\sim 836 \text{ cm}^2$ ). The small 1-cell squares at the centers of the individual test surface patches in figure 4 represent the measurement spots.

In the modeling the measurement spots are treated as patches of material having the same properties as their respective base materials except that they are thicker; thus the material designations "THKKAP," etc., are used. This choice for modeling the measurement spots is somewhat arbitrary. The important difference between the charging response of the spot and base materials observed in the test data was in the rate at which these areas charged, or, equivalently, in their effective capacitances per unit area. In the modeling the capacitance of a surface area of insulation depends on the dielectric constant and thickness of the material. Either or both of these parameters could be varied to obtain the observed spot-to-base

charging rates. Thickness was chosen. The spot-to-base thickness ratio simply represents the effective base-to-spot capacitance ratio per unit area.

### Approach

Values of bulk conductivity for the various materials were obtained by averaging the experimentally observed ratios of equilibrium surface potential to leakage current. Bulk sample thicknesses were taken as the nominal values; effective "thick spot" thicknesses were estimated on the basis of experimentally observed initial rise times. Initial values of all other material parameters were taken to be the standard NASCAP values appropriate to the various materials.

NASCAP simulations of charging in a 6-keV, 1-nA/cm<sup>2</sup> beam were made for each of the three objects, and predictions of surface potentials for both spots and base materials were compared with the data. Some of the material properties were then varied to obtain improved fits to the data. The two material properties whose values determined the relative charging rates of the spot and the bulk material were thickness ratio and surface resistivity. Alterations of other parameters were made only when clearly required, and then care was taken to remain within the region of "reasonable values" for these parameters.

Sample current-to-ground predictions were made as follows: The measurement spot cell thickness was set equal to that of the bulk sample, and the surface resistivities were made very large. The reasons for these particular choices were that the measurement spot cell is much larger relative to the sample size than the actual measurement spot (2.54-cm square as compared with a 0.64-cm-diam circle) and that the guard ring geometry of the SSPM eliminates measurement of surface currents but NASCAP includes surface currents as contributing to currents in the underlying conductors. With these two changes, charging simulations were repeated, and the calculated currents were scaled to account for the differences in surface area between the actual and modeled insulations (a factor of 0.90 for SC1-1 and SC1-3 insulators and a factor of 0.95 for SC1-2.)

### Results

Representative comparisons of NASCAP predictions to data for 6-keV conditions are shown in figures 5 (potentials) and 6 (currents). The values of the material property parameters used to obtain these results are listed in table II. In figure 5, the open and solid symbols represent experimental data for the potentials at the measurement spots and the adjacent base materials, respectively. The solid lines represent predicted potentials of the measurement spot cell surface, and the dashed lines represent the potentials on two adjacent cells.

The material properties whose values are listed in table II are those required as inputs to NASCAP (for more detailed descriptions see, e.g., refs. 7 to 9) - with the exception of the spot-to-base thickness ratio, which is specifically for this study. Except as noted in the table, these values are the standard NASCAP material property parameters. Two sets of properties are given for Kapton, one set for SC1-1 and SC1-2, and one for SC1-3. These differ only in the values of surface resistivity and

spot-to-base thickness ratio, two parameters that determine the relative charging behavior of the measurement spot and the base material.

As indicated in the table, a thickness of 0.0076 centimeter (3 mils) was used to obtain the illustrated fits to the Teflon data, rather than the nominal value for this sample of 0.0127 centimeter (5 mils). Predictions using 0.0127 centimeter indicated faster charging than was observed. Comparison of the SC1-3 Teflon data with data taken on other samples of 0.0127-centimeter (5-mil) thick Teflon (e.g., refs. 8, 10, and 11) indicated that the SC1-3 Teflon sample charged more slowly than would have been expected from testing of other samples. Although the reason for this slow charging is not clear, some justification for using the smaller value of thickness is provided. The alternative, which would have been to increase the dielectric constant from 2.0 to about 3.0 or 3.5, seemed much less reasonable, since the dielectric constant of Teflon is reasonably well known.

Table II lists the parameters used to determine secondary electron yield from proton impact, photoelectron current density, and their standard NASCAP values. These values are included for the sake of completeness but have not been verified here because they are not used in the calculations presented.

Figure 6 shows representative comparisons of predicted and observed currents. Open symbols represent data, and horizontal bars indicate the NASCAP time step (60 sec). The currents calculated by NASCAP are essentially averaged over a time step so that no more specific times than the whole time step can be assigned. The predictions generally fit the data quite well, except for the case of SC1-2, for which the data are better fit by one-half of the predicted currents (dashed horizontal bars in fig. 6(c)). This type of fit was obtained for both 6- and 4-keV beam conditions. A review of the data indicated that the measured initial currents for SC1-2 were consistently about twice as large as those for the SC1-1 and SC1-3 Kapton samples. This difference is puzzling since the SC1-2 Kapton sample area is about four times that of the SC1-1 and SC1-3 samples, so that one would expect roughly four times as large a current reading. It is, however, consistent with the fact that half the predicted current fits the data.

The material property parameters listed in table II and a 4-keV beam were used to make another set of NASCAP runs, and the results were compared with laboratory data taken with 4-keV beams. Typical results are illustrated in figure 7(a), where the predictions and data for the SC1-2 Kapton potentials are shown for both the 4- and 6-keV beam cases. The agreement shown in figure 7(a) is typical of that obtained with all the samples studied except the SC1-3 Kapton sample, for which the results are shown in figure 7(b). The 4-keV beam data for the SC1-3 Kapton sample indicate that the base material was charging more slowly and to a lower equilibrium potential than the base material of the SC1-1 and SC1-2 Kapton samples. By contrast, the base material appeared to charge similarly for the three Kapton samples in 6-keV beams. The reason for this behavior is not known. However, the results indicate that caution is needed in comparing SC1-3 Kapton data to Kapton data from the other two units.

## MODELING: SPACE CASE

With sets of material property parameters for the SSPM surface materials in hand, one would like to attempt to model the on-orbit response of these materials. To do so requires a model of the SCATHA spacecraft with suitable SSPM models incorporated, a description of the space environment, and data on the potentials of the spacecraft structure and test surfaces in the specified environment.

### Scatha Model

The SCATHA model used in this study is basically the one developed by Systems, Science and Software and described in reference 12. That model has been modified to incorporate new models of the SSPM units for use in this study (fig. 8). In place of the original SC1-1 and SC1-3 units with one cell each of four different materials, "surface potential test regions" were defined. Each of these has one cell to represent the measurement spot and three to represent the base material. At the original location of SC1-2 and on the top of the spacecraft across from SC1-3, two "current test regions" have been defined, each with its own underlying conductor. The material properties of these patches may be changed easily in a NASCAP runstream so that it is possible to run two different material types in a given simulation run (one potential and current test spot for each material).

### Simulation Results

It was decided to use environment and spacecraft potential data from day 87 of 1979, a day on which SCATHA was charged by a substorm that began during eclipse passage. Since it is not necessary to include the effects of photoemission during eclipse, eclipse conditions present a simpler case than daylight. Even in eclipse, however, one must be aware of the fact that Kapton, in particular, has a resistivity that is very sensitive to exposure to sunlight. The time constant for return to dark conductivity is long, so that even in eclipse the conductivity of Kapton will probably be enhanced for those samples that have been exposed to sunlight.

Two versions of the environment and spacecraft potential history on day 87 of 1979, based on data from the SC9 detector (ref. 3), were obtained from Systems, Science and Software (private communications, with G. Schnuelle). The environments, as received, were in the form of double-Maxwellian fits to the actual spectra. These were converted to single-Maxwellian representations having the same first four moments of the distribution functions.

The initial version of the environment was rather coarse, with approximately the first 120 seconds following the onset of the substorm being represented by only three separate environments with electron temperatures of 7.07, 6.38, and 6.64 keV, in that order. Three simulation runs were made in this environment. First, one SSPM surface potential test patch and one current test patch were given the properties for SC1-3 Kapton (table II), and the other pair of test patches were given SC1-1 and SC1-2 Kapton properties. Second, one pair of test patches was defined to have Teflon's properties and the other SiO<sub>2</sub>'s properties. Finally a run was made in which no thick measurement spots were incorporated, the two surface

potential patches were given the properties of all-thin Teflon and  $\text{SiO}_2$ , and the two current patches were given the properties of Kapton. The reason for the third run was that the results of the first two runs displayed an unexpected and undesirable effect: The choice of material properties for the SSPM test cells had a large effect on the predicted potential of the entire spacecraft structure. Predicted spacecraft structure potentials as a function of time for these three runs, shown in figure 9, illustrate this effect. Clearly, predicted differential potentials (the SSPM measurements are all relative to spacecraft structure) cannot have much meaning when the predicted structure potential is this sensitive to the SSPM test patch material.

There are three possible reasons for the difficulty. Perhaps the "thick measurement spot" modeling technique simply will not work in space eclipse conditions and a new model must be devised. Perhaps a careful choice of "thick spot" materials to use in a given run will at least reduce the difficulty (e.g., one Kapton and one Teflon spot). Or, perhaps the particular environment used represents a near threshold condition (ref. 13), in which case small changes in material properties could cause large changes in predicted potentials.

Because a more detailed environment for this time period had become available, it was decided to pursue the last two possibilities and to develop a "baseline" time history of structure potential by using a model with no thick spots. Following this procedure allows determination of how well NASCAP will predict structure potential (because data on structure potential are available) and of how much influence the addition of thick patches has on predicted structure potential in this more detailed environment.

The electron temperatures used in this simulation, along with measured structure potentials (from SC9 data) and NASCAP results from the simulation, are shown in figure 10. The dashed line indicating NASCAP's predictions represents 125 time steps ranging in length from a few tenths of a second (during periods of rapid change) to 20 seconds during periods of little change in the environment at spacecraft potential. The agreement between data and predictions is believed to be quite good. Since preliminary results of including one thick Kapton and one thick Teflon cell in the model indicate that the predicted structure potential is not greatly affected, that approach is presently being explored.

## SUMMARY OF RESULTS

Generally good agreement was obtained between predicted and measured potentials of flight measurement spots and base materials and between predicted and measured currents for ground test conditions for the Kapton, Teflon, and  $\text{SiO}_2$  test surfaces on the SCATHA SSPM. There were, however, some peculiarities in the data that were identified during this study and that merit further examination.

The SC1-3 Kapton sample data indicate that the sample differs from the other two Kapton samples. The effective capacitance of the SC1-3 measurement spot relative to that of the base material is significantly larger than those of the SC1-1 and SC1-2 Kapton samples. Although in 6-keV beam tests the base material of all three Kapton samples appeared to respond similarly, in 4-keV beam tests the SC1-3 base material charged more slowly

and to lower equilibrium potentials than the other two. The difference in effective capacitance ratios is not surprising, considering sample construction tolerances, and can be dealt with in a straightforward manner in the modeling. The difference in base material response is not understood, however; and at present has not been accounted for in the models.

The SC1-2 current data are about half of what is predicted; they are also about half of what would be expected based on the SC1-1 and SC1-3 current data for Kapton and the relative areas of insulation.

Predictions of potentials and currents for the SC1-3 Teflon sample were quite good when 0.0076 centimeter was used as the material thickness instead of the nominal 0.0127 centimeter. Comparing SC1-3 Teflon data with data on other nominally 0.0127-centimeter-thick Teflon samples indicated that the SC1-3 Teflon sample charged more slowly than previously tested 0.0127-centimeter-thick samples.

Predictions of flight data were found to be complicated by the fact that using the thick cells to represent the SSPM flight measurement spots can have a significant effect on predicted spacecraft structure potential in eclipse. The magnitude of this effect appears to depend on both the environment model employed and the number and properties of thick spots included. A "baseline" run for a model of SCATHA with no thick spots indicated that NASCAP can predict observed spacecraft structure potentials satisfactorily. The investigation of the influence of environment specification and inclusion of thick surface materials is continuing.

#### REFERENCES

1. Mizera, P. F.: Natural and Artificial Charging: Results from the Satellite Surface Potential Monitor Flown on P78-2. AIAA Paper 80-0334, Jan. 1980.
2. McPherson, D. A.; Cauffman, D. P.; and Shrober, W.: Spacecraft Charging at High Altitudes: The SCATHA Satellite Program. Spacecraft Charging by Magnetospheric Plasmas, A. Rosen, ed., Progress in Astronautics and Aeronautics, Vol. 47, American Institute of Aeronautics and Astronautics, Inc., 1976, pp. 15-30.
3. Shane, D. F.: Spacecraft Charging Technology Conference, P78-2 Overview. Proceedings of the Spacecraft Charging Technology Conference, C. P. Pike and R. R. Lovell, eds., NASA TM X-73537, AFGL TR-77-0051, 1977, pp. 25-32.
4. Durrett, J. C.; and Stevens, J. R.: Description of the Space Test Program, P78-2 Spacecraft and Payloads Overview. Spacecraft Charging Technology - 1978, NASA CP-2071, AFGL TR-79-0082, 1979, pp. 4-10.
5. Katz, I., et al.: The Capabilities of the NASA Charging Analyzer Program. Spacecraft Charging Technology - 1978, NASA CP-2071, AFGL TR-79-0082, 1979, pp. 101-122.
6. Stevens, N. J., et al.: Initial Comparisons of SSPM Ground Test Results and Flight Data to NASCAP Simulations. NASA TM-81394, 1980.
7. Katz, I., et al.: A Three Dimensional Dynamic Study of Electrostatic Charging in Materials. (SSS-R-77-3367, Systems, Science and Software; NASA Contract NAS3-20119.) NASA CR-13526, Aug. 1977.
8. Roche, J. C.; and Purvis, C. K.: Comparison of NASCAP Predictions with Experimental Data. Spacecraft Charging Technology - 1978, NASA CP-2071, AFGL TR-79-0082, 1979, pp. 144-157.

9. Purvis, C. K.: Effects of Secondary Yield Parameter Variation on Predicted Equilibrium Potential of an Object in a Charging Environment. NASA TM-79299, 1979.
10. Stevens, N. J., et al.: Testing of Typical Spacecraft Materials in a Simulated Substorm Environment. Proceedings of the Spacecraft Charging Technology Conference, C. P. Pike and R. R. Lovell, eds., NASA TM X-73537, AFGL TR-77-0051, 1977, pp. 431-457.
11. Purvis, C. K.; Stevens, N. J.; and Oglebay, J. C.: Charging Characteristics of Materials: Comparison of Experimental Results with Simple Analytical Models. Proceedings of the Spacecraft Charging Technology Conference, C. P. Pike and R. R. Lovell, eds., NASA TM X-73537, AFGL TR-77-0051, 1977, pp. 459-486.
12. Schnuelle, G. W., et al.: Simulation of the Charging Response of the SCATHA (P78-2) Satellite. Spacecraft Charging Technology - 1980, NASA CP-2182, 1981.
13. Stannard, P. R., et al.: Representation and Material Charging Response of GEO Plasma Environments. Spacecraft Charging Technology - 1980, NASA CP-2182, 1981.

TABLE I. - SSPM SAMPLE MATERIALS SUMMARY

SSPM unit	Materials
SC1-1	Aluminized Kapton (0.0127-cm nominal thickness) Indium-oxide-coated optical solar reflectors (coating grounded) Optical solar reflectors Gold-coated magnesium plate (floating)
SC1-2	Aluminized Kapton (0.0127-cm nominal thickness)
SC1-3	Aluminized Kapton (0.0127-cm nominal thickness) Silver-Inconel-backed FEP Teflon (0.0127-cm nominal thickness) Astroquartz Gold-flashed aluminized Kapton (gold grounded)



TABLE II. - MATERIAL PROPERTY PARAMETERS FROM SSPM GROUND STUDY

Property	SSPM unit			
	SC1-1 and SC1-2	SC1-3		SC1-1
	Material			
	Kapton	Teflon	SiO <sub>2</sub>	
Dielectric constant	a3.0	a3.0	2.0	4.0
Thickness of base material, m	0.000127	0.000127	b0.000076	0.000203
Conductivity, mho/m	c3x10 <sup>-15</sup>	c3x10 <sup>-15</sup>	c1.8x10 <sup>-15</sup>	1x10 <sup>-14</sup>
Atomic number	5	5	7	10
Maximum secondary yield for normally incident primary electrons, $\delta_m$	2.1	2.1	3.0	2.4
Primary energy for maximum secondary yield, E <sub>m</sub>	0.15	0.15	0.30	0.40
$\left. \begin{matrix} r_1 \\ n_1 \\ r_2 \\ n_2 \end{matrix} \right\} (d)$	71.5	71.5	45.4	-1.0
	0.60	0.60	0.40	0
	312.1	312.1	217.6	1.02
	1.77	1.77	1.77	20
Secondary yield for 1-keV incident protons <sup>e</sup> , $\delta_p$	0.455	0.455	0.455	0.455
Primary proton energy for maximum power loss <sup>e</sup> , E <sub>p</sub>	140	140	140	140
Photocurrent <sup>e</sup> , A/m <sup>2</sup>	2x10 <sup>-5</sup>	2x10 <sup>-5</sup>	2x10 <sup>-5</sup>	2x10 <sup>-5</sup>
Surface resistivity, $\Omega$	7.5x10 <sup>12</sup>	2.5x10 <sup>12</sup>	1x10 <sup>13</sup>	1x10 <sup>19</sup>
Spot-to-base thickness ratio <sup>f</sup>	12.5	7.5	3.33	11.0

<sup>a</sup>Standard NASCAP value is 3.5.<sup>b</sup>Nominal value is 0.000127 cm.<sup>c</sup>Based on experimental data from SSPM tests.<sup>d</sup>Electron range is defined by

$$R = r_1 E^{n_1} + r_2 E^{n_2}$$

where E is the energy of the primary electron.

<sup>e</sup>Standard NASCAP properties, not tested for in this study.<sup>f</sup>Not a NASCAP property; represents thickness ratio of measurement spot cell to base material and thus indicates base-to-spot effective capacitance.

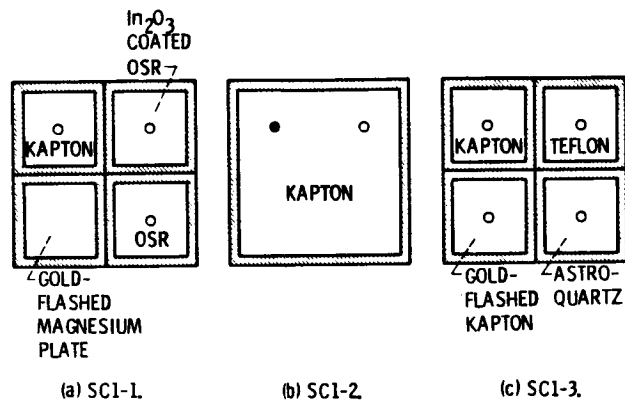


Figure 1. - Satellite surface potential monitor units.

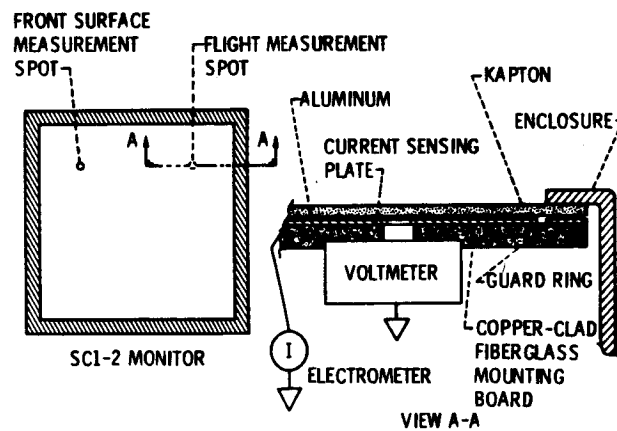


Figure 2. - SSPM flight measurement technique.

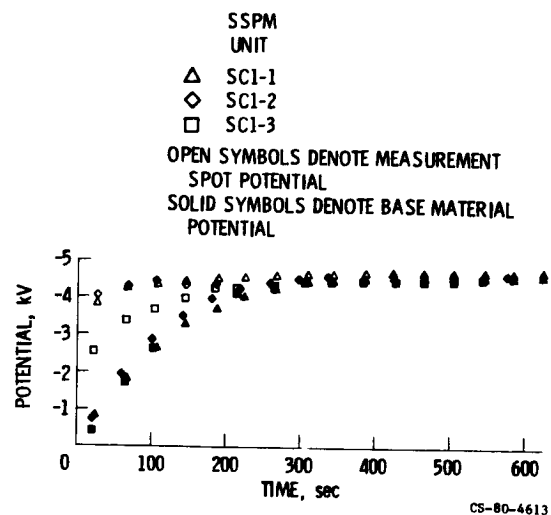


Figure 3. - Response of three Kapton samples - 6-keV beam.

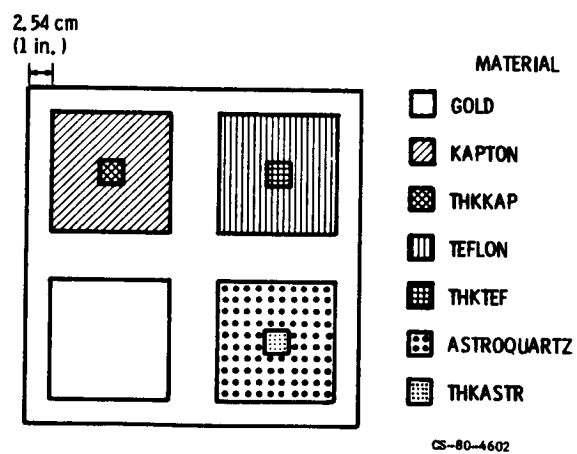


Figure 4. - SC1-3 NASCAP model.

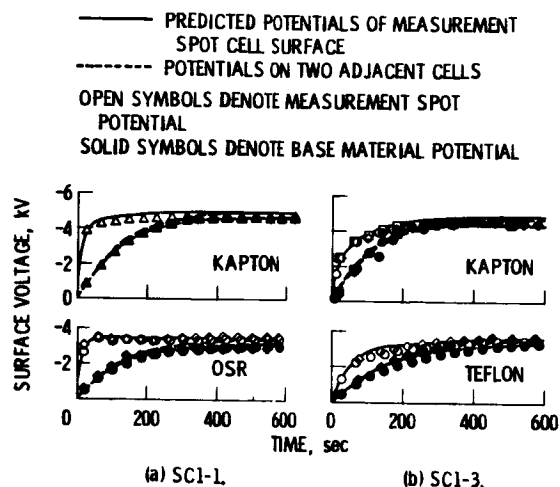


Figure 5. - Comparison of NASCAP predictions with data - surface voltages, 6-keV beam.

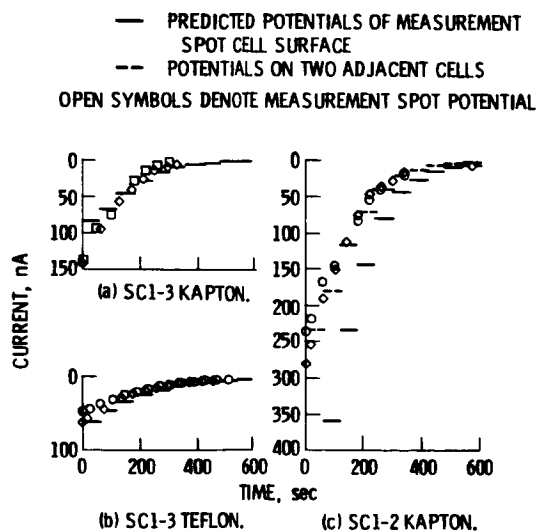


Figure 6. - Comparison of NASCAP predictions with data - current, 6-keV beam.

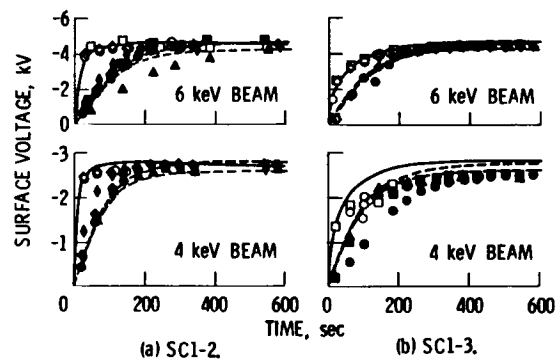


Figure 7. - Comparison of NASCAP predictions with data - surface voltages, Kapton samples.

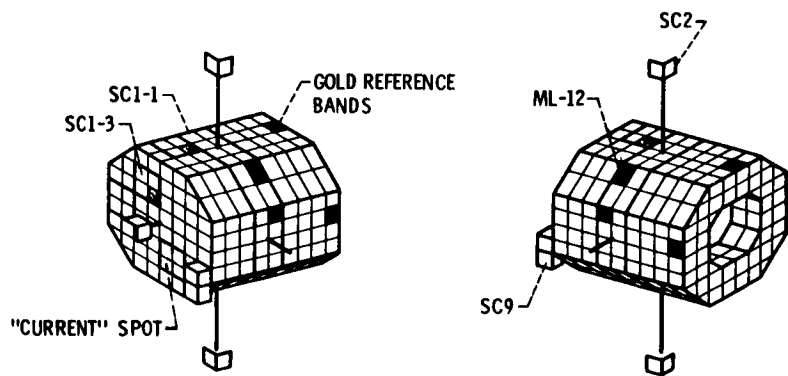


Figure 8. - Revised NASCAP one-grid SCATHA model.

CS-80-4608

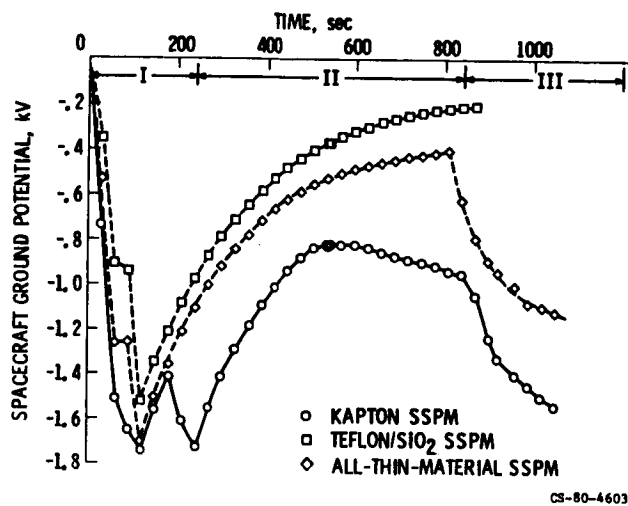


Figure 9. - Effect of SSPM thick cells on predicted ground potential.

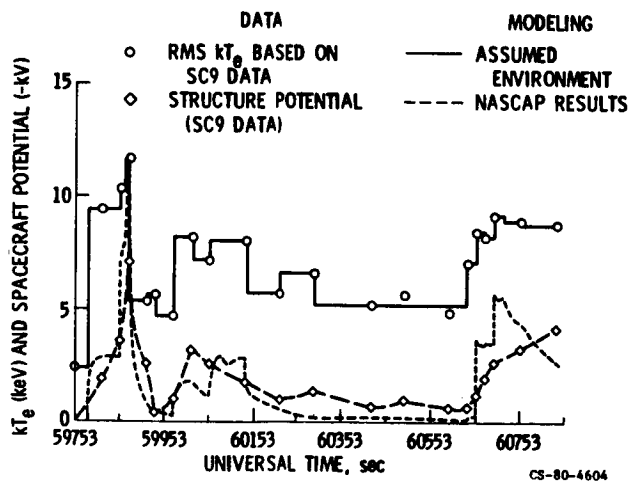


Figure 10. - SCATHA day 87 of 1979 - baseline run.

**THREE-DIMENSIONAL ANALYSIS OF CHARGING EVENTS  
ON DAYS 87 and 114, 1979, FROM SCATHA**

**N. A. Safflekos  
Boston College**

**M. F. Tautz  
Radex Corporation**

**A. G. Rubin and D. A. Hardy  
Air Force Geophysics Laboratory**

**P. F. Mizera  
The Aerospace Corporation**

**J. Feynman  
Boston College**

**SUMMARY**

Detailed observations of angular distributions of ions and electrons from the SCATHA (Spacecraft Charging at High Altitudes) SC-5 experiment were used to investigate the floating potential and the differential charging of the spacecraft as deduced from Liouville's theorem and computed by the NASCAP/AFGL code. The highest resolution data from the SCATHA SSPM experiment were compared to the SC-5 charged particle fluxes and to the NASCAP/AFGL computations. This study led to the following conclusions: a) Short-time charging events on the spacecraft are associated with short-time increases of the intensity of 10 keV to 1 MeV electrons, b) Short time changes of the spacecraft differential potential are associated with simultaneous short-time changes of the spacecraft floating potential, c) Solar U.V. intensities in penumbra, as monitored by the solar panels total current, anticorrelate with the spacecraft floating potentials, d) Based on the measured profiles of U.V intensities, NASCAP predicts correct forms of sun-shade asymmetric surface potentials consistent with the SSPM measurements, e) Certain enhancements of the intensity of energetic ions ( $E_i > 100$  keV) have been observed to diminish the absolute value of the spacecraft surface potential, f) Spacecraft discharging events in times shorter than 20 sec have been observed without obvious changes in the spectrum of the energetic ( $E > 10$  keV) plasma, g) Partial discharging of the spacecraft has occasionally been observed upon entry into a magnetically depleted region, h) Steady state potentials and transient potentials of duration less than 30 seconds have been successfully simulated by the NASCAP code.

## INTRODUCTION

Operational spacecraft (S/C) experience a host of anomalies which vary from nuisance to fatality. It is believed that electrostatic charging events are responsible for some of these anomalies especially at high altitudes and at the popular commercial belt, the geosynchronous orbit. At low altitudes in the absence of intense field-aligned currents (FAC) a high concentration of cold ionospheric plasma keeps the S/C floating potential at a small negative value. The situation however, changes for the worse when FAC's with increased densities strike the surface area of a large structure. Large structures then charge up to kilovolt potential levels which may constitute a serious hazard to such S/C orbiting the earth at lower polar altitudes.

Observed fast discharges can generate large amplitude current pulses on power or S/C ground lines and destroy sensitive solid state devices. To avoid such costly losses, it is highly desirable to enhance our understanding of surface material properties and to develop servomechanisms which will actively control the S/C potential. Perhaps the emission of energetic ion beams together with neutralizing cold electrons is a satisfactory control system. NASA and the USAF, using their experience from the SCATHA (S/C Charging at High Altitudes) satellite, hope to study the charging characteristics important to the design of solar power satellites and other space-based large structures.

The SCATHA spacecraft is an integral part of a mission that interests physicists and engineers alike whose goal is the prevention of spacecraft charging. SCATHA, otherwise designated as satellite P78-2, was launched into a near-geosynchronous orbit on 30 January 1979. By 2 February 1979, the orbit was adjusted to conform to a period of 23.597 hours, a perigee of 27,517 km and apogee of 43,192 km and an inclination of  $7.09^\circ$ . The P78-2 satellite spins at the rate of about 1 rpm with the spin axis pointing along the direction of the vector  $S \times Z$  where  $S$  points towards the sun and  $Z$  along the geographic north axis.

Figure 1 shows the P78-2 S/C payload. Of particular interest to this work are two experiments which measure the S/C potentials with one second resolution. They are designated as SC-1 and SC-5. Both of these instruments are described in full detail in (ref. 1). The SC-1 experiment, otherwise known as SSPM (Spacecraft Surface Potential Monitor), consists of three separate instruments (SSPM-1,-2 and-3) which provide measurements of the surface voltage and the bulk current of S/C insulating and conducting materials frequently used in S/C construction. Redundant measurements of aluminized kapton are made on each of the three instruments (SC1-1, SC1-2, and SC1-3) see Figure 2. The SC1-3 sample is mounted on the top plane of the S/C having its normal parallel to the S/C spin axis. The other two samples, mounted near the equator of the rotating S/C, spend about thirty seconds in darkness and thirty seconds in light during one spin period while not in the earth's shadow. The front surface potential of the samples is derived from the back surface potential using laboratory calibration curves.



The SC-5 instrument scans rapidly through the spectrum of electrons from 50 eV to 1.1 MeV and of protons from 50 eV to 35 MeV. The rapid scan particle detectors measure the differential charged particle flux parallel and perpendicular to the S/C spin axis. From the full pitch angle information in one plane, one derives temperatures, number densities, and bulk flow velocities. From energy dependent pitch angle anisotropies in the distribution, one can infer the occurrence of S/C charging.

In a cooperative effort NASA and the U.S. Air Force have supported the effort of S<sup>3</sup> (Systems, Science and Software, Inc.) which developed a charging analyzer program known by a combination of acronyms as NASCAP/AFGL. This code simulates the electrostatic charging of a three dimensional object at geosynchronous environments. More specifically, an object is introduced into the program by defining the geometrical and electrical properties of the structural materials with considerable complexity. Then the object is allowed to interact with a magnetospheric plasma in darkness or in light. Having at its disposal the object definition and the description of the ambient plasma, the program solves a fully three dimensional problem involving Poisson's equation. The charge distribution on the spacecraft surfaces is calculated from the total current to the spacecraft taking into account proton and electron incidence, backscattering, and secondary emission (electrons only). NASCAP/AFGL has excellent graphics for object representation, external potential contours, and external space charge density contours.

The code obtains these results by following an alternating procedure where in every step it calculates the charge accumulation and the resulting electrostatic potential on each S/C surface. The calculations can be made in the presence of ambient magnetic and electric fields. As an option, the code can do a first order photosheath analysis. More details can be found in (ref. 2) and references therein. In this paper we present some detailed observations and model calculations which lead to the conclusions that the results from SSPM, SC5, and the NASCAP code are internally and logically consistent.

#### CHARGING IN ECLIPSE

On day 87, 1979 SCATHA entered the earth's penumbra at 1615:26 UT (Universal Time) and the earth's umbra at 1618:38 UT. The spacecraft did not show a change of its charging state until 1635:00 UT. In the previous half hour the energetic electrons ( $10 < E_e < 58$  keV) were two to three orders of magnitude lower in counting rate in comparison with the average in the preceding two hours. At 16:36 UT the auroral AE index rose suddenly, reaching a value of 1000 nT ( $1 \text{ nT} = 10^{-5}$  gauss). To within forty seconds of this time, the energetic electron counting rate rose above the preceding dropout levels by about one order of magnitude. For the following five minutes, the charged particle fluxes, the S/C ground potential, and the S/C differential potential all underwent fast (seconds) temporal variations.

Figure 3 shows data from the SC5 and the SC1 experiments on SCATHA.

The top panel shows sun angle and pitch angle for the SC5 electron detector parallel to the S/C spin axis. The middle panel shows the electron fluxes for eight channels identified by their energies and a shift number N in decades needed to separate the traces. The lower panel left scale refers to the SSPM voltage of the samples on top of the satellite. The scale on the right refers to the magnitude of the total real field as measured by the magnetometer SC-11 on SCATHA. The electron measurements were taken at a fixed ( $90^\circ$ ) pitch angle. At about 1636:12 UT we noted a continuous increase in the flux of energy  $E_e < 8.97$  keV while the fluxes of energy  $E_e > 8.97$  keV dropped more abruptly. The more energetic particles reached their peak at 1637 UT whereas the less energetic ones reached their minimum value at about 1638 UT. This flux dependence on energy can be understood in terms of S/C charging where the buildup of negative charge on the S/C inhibits the current flow away from the S/C. It took under two minutes for the S/C ground to reach a negative voltage between -4.57 and -8.97 kV. The average value is -6.8 kV. At 1638 UT, SC9 reported a value of -8.14 kV and SC2 reported the value of -6.9 kV. Our value agrees very well with SC2 and is consistent with the value of SC9.

Later in the plot the lower energy particles recovered during two short UT intervals (1638:40 - 1639:10 and 1639:40 - 1640:00). The 0.1 keV electrons recovered in the first time interval but not in the second. Thus we would place the first S/C ground potential at 0.1 kV and the second at 0.3 kV. The SC9 experiment reported a 0.45 kV and 1.2 kV S/C ground potentials for the two intervals above.

In bottom panel of Figure 3, the 3V3 trace corresponds to the front surface voltage of the quartz fabric sample. A change of its charging state commenced at 1636:40 UT corresponding to the peaking of  $E_e = 23.2$  keV electrons. The 3V2 trace corresponds to silvered teflon sample. It responded five seconds later coinciding with the peaking of  $E_e = 52.7$  keV electron fluxes. Both samples continued to charge linearly in time up until 1638:40 UT. Then both samples partially discharged for thirty seconds keeping in phase with the S/C ground discharging in the same time interval. A similar event was repeated in the interval between 1639:40 and 1640:00 UT. It is interesting to note that the magnetic field strength was significantly reduced during the first S/C discharge. Perhaps the magnetometer sensed a current surge on the S/C surface of the kind that would cause damage to solid state devices. The magnetometer saw a lesser current flow in the second interval (1639:40 - 1640:00) UT.

Figure 4 is similar to Figure 3 except for more energetic electrons. The increase of the fluxes at the onset of differential charging is obvious. The responding SSPM sample 1V1 is aluminized kapton. It began charging at 1636:30, about ten seconds earlier than the commencement of charging in Figure 3, which corresponds to peaking of electron flux in the energy range  $E_e < 23.2$  keV. Kapton also partially discharged during the 1638:40 to 1639:10 UT interval. The minimum differential charging of kapton was about -1750 volts at 1640:20 UT. At that same time interval, silvered teflon of Figure 3 reached about -1500 volts. The other two SSPM samples are: optical solar reflector (1V3) and gold (1V4). Both remained less negative than -200

volts. There is a striking difference in the behavior of the surface potentials between materials placed on top and materials placed near the equator of the spacecraft. The differences cannot be resolved by energy dependent pitch angle anisotropies. Other phenomena causing time dependent behavior of the electrical properties of the materials must be studied more intensively.

In addition to the more accurate representation of the SCATHA object (Figure 2, four grid model) in the NASCAP/AFGL code, the program accepts simpler models roughly approximating the realistic three-dimensional representation of the satellite. In order to study effects of space plasma on the S/C in the absence of sunlight, we selected a test object in the shape of a quasisphere, a figure with 26 sides inscribed in a sphere as shown in Figure 5. All the surfaces are covered with goldpd, a grounded conductor, except for four squares facing the +Y direction covered with silicon dioxide, teflon, gold, and kapton, all allowed to float relative to S/C ground. The four patches are meant to represent the SC1 sample materials. The gold sample is decoupled from the underlying conductor via a large capacitor.

Figure 6 shows the steady state potentials assumed by the S/C ground (goldpd) and the four samples mentioned above using space plasma temperatures and densities derived from the SC5 experiment. We selected those spectra during eclipse when the S/C ground voltage was at a low negative level. We fit the selected spectra with two Maxwellian distributions in the ranges 0.1 to 2 keV and 2 to 60 keV. The resulting temperatures and densities were averaged in the separate energy intervals. The low energy range temperatures and densities for electrons and protons respectively were ( $T_{e1} = 0.338$  keV,  $n_{e1} = 0.12 \text{ cm}^{-3}$ ) and ( $T_{p1} = 0.207$  keV,  $n_{p1} = 0.62 \text{ cm}^{-3}$ ). Similarly the higher energy range parameters were ( $T_{e2} = 9.74$  keV,  $n_{e2} = 0.38 \text{ cm}^{-3}$ ) and ( $T_{p2} = 6.09$  keV,  $n_{p2} = 0.47 \text{ cm}^{-3}$ ). The kapton sample thickness was set at  $1.27 \times 10^{-3} \text{ m}$  and its bulk conductivity at  $\sigma = 1 \times 10^{-14} \text{ mho/m}$ . The decoupling capacitor for gold was set at  $C_{ij} = 5 \times 10^{-9} \text{ F}$  and the grid mesh  $X_{\text{mesh}}$  was set at 0.5m to make the model total volume comparable to that of the real spacecraft. Figure 6 shows that goldpd (S/C ground) charged to -1689 volts. The average S/C ground voltage from 1634:54 to 1715:54 UT was -2771 volts as derived from SC9 ion counting rate data provided by Eldon Whipple of UCSD. In a later time interval from 1703:53 to 1715:54, the average S/C ground potential was -2063 volts differing only by a 17% from the NASCAP/AFGL code calculated value for goldpd. The differential charging for the four samples relative to goldpd were (-2505, -1453, -20, and +65) volts for (kapton, teflon, silicon dioxide (SI02), and gold), respectively. The largest negative values measured by the SSPM experiment were (-1700, -2150, -1100, and -200) volts for (1V1 (kapton), 3V2 (teflon), 3V3 (SI02), and IV4 (gold)), respectively. Except for SI02 which the code predicts, like goldpd, the potentials less than -200 volts are predicted to within a factor of two of the experimental values.

## SPACECRAFT CHARGING DURING ENTRY INTO ECLIPSE

On Day 114, 1979 SCATHA entered the earth's penumbra at 0710:10 UT and was eclipsed totally at 0713:26 UT. During the penumbral transit the solar illumination diminished by atmospheric scattering of sunlight and the S/C photocurrent was decreased in direct proportion. A temporal variation of the S/C photocurrent resulted in a variation of the S/C ground potential. Figure 7 shows the directional differential intensity of ions with energy  $E_p = 9.66$  keV, the directional differential intensity of electrons with energy  $E_e = 4.42$  keV and their respective pitch angle all plotted versus UT. The intensity of the  $90^\circ$  fluxes and the nature of the dependence of flux on pitch angle change drastically around 0713 UT. The electron flux following this time is generally reduced by a factor of 2 whereas the proton flux is generally increased by factors of 4. The electron flux anisotropy becomes deeper after 0713 UT maintaining a ratio of perpendicular to parallel fluxes of about 2 for at least seven minutes. In contrast the proton fluxes anti-correlate with the electron fluxes and they maintain a ratio of parallel to perpendicular number fluxes of about 5. The simultaneity of solar UV decrease with this acceleration of ions and deceleration of electrons argues in favor of a S/C charging event whereby the potential reached about -7 kV capable of affecting the  $E_p = 9.66$  keV and the  $E_e = 4.42$  keV channels. The fact that the ions (electrons) are preferentially accelerated (decelerated) along the  $0^\circ$  and the  $180^\circ$  pitch angles ( $D \cdot B$ ; where,  $D$  and  $B$  are unit vectors with  $D$  being the detector look direction and  $B$  being the direction of the magnetic field) argues against a single localized potential drop parallel to the magnetic field at a latitude other than that of the S/C on the same field lines.

Figure 8 shows distributions from the SC5 rapid scanning particle detectors (RSPD's) parallel to the S/C spin axis during the precharging period at about 0706 UT and during the charging period at about 0717 UT. One readily observes that the electron distribution functions are shifted to lower energies by about 4 keV and the ions to higher energies by about 8 keV. Due to the wide energy windows of the channels  $\Delta E/E \approx 1$ , we cannot specify the S/C potential very accurately using this method. The SC-9 experiment with better energy resolution reported a S/C ground potential of about -5 kV at around 0717 UT. This result is consistent with our inferred S/C ground potential relative to plasma ground. Single Maxwellian fits of the distributions in Figure 8 overestimate the temperatures of lower energy plasma ( $5 < E < 25$  keV). For that reason we chose a plasma about two times colder than that at 0706 UT and assumed it does not change throughout the penumbral transit. The temperatures and densities for electrons and protons, respectively, were ( $T_e = 6.4$  keV,  $n_e = 0.8 \text{ cm}^{-3}$ ) and ( $T_p = 5.8$  keV,  $n_p = 0.5 \text{ cm}^{-3}$ ). This information was then fed into the NASCAP/AFGL code for the quasisphere model. The program was allowed to run until it reached equilibrium surface potentials. Then we turned the solar intensity on as a function of time but now with the time reversed. Figure 9 shows the eight minute calculations of S/C ground (goldpd) potential, insulator (teflon) potential, and insulator (kapton) potential going backwards in time from 0714 UT to 0706 UT. One clearly observes that the transient nature of the potentials resembles the transmitted curve of sunlight through the atmosphere plotted against the

impact parameter. The S/C ground and the insulating materials surface voltages respond to solar UV as soon as the solar illumination level reaches 20%. The spin modulation of the surface potentials of teflon and kapton samples are due to S/C shadowing. During eclipse, teflon and kapton reached -1900 and -4900 volts lower than goldpd. In full sunlight, this computer run showed that teflon discharged almost completely reaching -50 volts in comparison to the +5 volts of goldpd. Kapton maintained a minimum of -800 volts in S/C shadow and a maximum of -80 volts in full sunlight. We did not have measurements of S/C differential charging to compare with these results.

#### SPACECRAFT CHARGING DURING EXIT FROM ECLIPSE

On Day 87, 1979 SCATHA was coming out of total eclipse at 1713:50 UT and left the penumbra at 1716:10 UT. Figure 10, lower panel, shows the solar illumination and four SCATHA SSPM voltages as a function of time. The middle panel shows plots of electron fluxes from the SC5 instrument with field of view perpendicular to the S/C spin axis. The top panel shows the angles between the detector line of sight and the magnetic field and between the detector line of sight and the satellite-sun-line. The relative variation of the solar illumination was measured by the total current of the solar panels. This illumination was also compared to theoretical predictions and was found to be in excellent agreement. Figure 10, middle panel, shows the isotropic electrons  $E_e < 9.16$  keV to increase with the solar illumination following the time 1714:30 UT at which point the solar illumination has approached its 20% value. The rate of recovery of the electrons  $E_e = 4.42$  keV is slow in comparison to the lower energy channels. Thus the S/C potential at the onset of photodischarge was around three thousand volts which is roughly obtained by averaging the 4.42 and 1.57 keV energy channels. We reiterate the wide energy windows of the electron channels  $\Delta E/E \approx 1$  do not allow an accurate estimate of the S/C ground potential relative to plasma ground. The angular resolution of the SC5 experiment, on the other hand, is excellent and Figure 10 upper two panels show that after 1715:50 UT the electron directional differential fluxes for all the presented channels were isotropic in the satellite spin plane. Thus it is believed that all the SSPM samples experienced the same incident electron flux. The SSPM-2 (Figure 10, lower panel) responded to sunlight immediately following 1714:20 UT. The minimum potentials relative to S/C ground that the SSPM's had prior to entering penumbra were (-500, -1650, -200, and -300) volts for (kapton with hole, kapton large sample, reference band, and reference band with high gain) respectively.

In order to simulate the transient behavior of the S/C surface potentials as SCATHA came out of total eclipse, we used the NASCAP/AFGL code with the quasisphere model described in the preceding section. We calculated a two Maxwellian environment from distribution functions in the time interval 1716:00 to 1716:47 UT. The energy spectra were chosen in a fixed pitch angle interval  $80^\circ < \alpha < 90^\circ$ . The spectra were also restricted to ones

corresponding to S/C ground potentials greater than -100 volts so that shifting in energy would not have been a factor. Thus we averaged sixteen electron and ion distribution functions separately and computed temperatures and densities of

$$(T_{e1} = 731 \text{ eV}, n_{e1} = 0.78 \text{ cm}^{-3}, T_{e2} = 6.4 \text{ keV}, n_{e2} = 0.79 \text{ cm}^{-3})$$

$$\text{for electrons and } (T_{p1} = 198 \text{ eV}, n_{p1} = 0.8 \text{ cm}^{-3}, T_{p2} = 5.8 \text{ keV},$$

$$n_{p2} = 0.5 \text{ cm}^{-3}) \text{ for protons.}$$

The Maxwellian fits were made in the energy ranges  $100 < E < 4570 \text{ eV}$  and  $4570 < E < 60000 \text{ eV}$ . The higher energy population was not subtracted from the lower energy population samples. The actual environment used in the NASCAP/AFGL computer run was similarly derived from an average of 55 spectra which yielded

$$(T_{e1} = 338 \text{ eV}, n_{e1} = 0.12 \text{ cm}^{-3}, T_{e2} = 9.74 \text{ keV}, n_{e2} = 0.38 \text{ cm}^{-3})$$

$$\text{for electrons and } (T_{p1} = 207 \text{ eV}, n_{p1} = 0.62 \text{ cm}^{-3}, T_{p2} = 6.09 \text{ keV},$$

$$n_{p2} = 0.47 \text{ cm}^{-3}) \text{ for protons.}$$

Figure 11 shows the temporal variation of the surface potential of the large kapton sample (SC1-2-2) (Ref. 2) together with the surface voltages of teflon and S/C ground (goldpd). The trace light intensity represents the relative solar illumination of SCATHA obtained from the solar panels total current as described in a previous section. The prepenumbral value of the kapton voltage relative to S/C ground was -2527 volts. Clearly as the sun intensity increases, the kapton voltage grows less negative and shows a modulation once per spin period. This again is due to S/C shadowing of the kapton sample. The conductivity and thickness of this material were  $10^{-14} \text{ mho/m}$  and 10 times the nominal thickness, respectively. Comparing the SSPM value of -1650 volts to the NASCAP/AFGL value of -2527 volts, we see that they differ by 35%. The agreement can become better if good knowledge of the S/C ground potential (down to a few volts) is used to correct the distribution functions. Furthermore, measurement of the environment with higher energy resolution may give the temperature and densities more accurately. When very high energy points (hundreds of keV) are included in the distribution functions, the temperatures are overestimated. Figure 12 is included in this study in order to show the effect of high energy protons on S/C charging.

Figure 12, top panel shows pitch angles and sun angles of the SC5 perpendicular protons whose fluxes and energies are given in the figure. The middle panel is similar to the top except for parallel protons. The bottom panel shows the SSPM-1 surface voltages together with the solar illumination versus time. Prior to 1714:10 UT the SSPM sample potentials were flat. At that time a sudden enhancement of the energetic proton flux (up by a factor of 30) appears to have initiated the gradual discharge of the SSPM1-1 (kapton) and the SSPM1-4 (gold). This flux increase did not affect the charging rates of the SSPM1-2 (optical solar reflector, OSR, grounded to

the S/C chassis) and the SSPM1-3, an ungrounded OSR. At 1714:30 UT, twenty seconds later, the parallel protons of the same energy showed a similar flux increase. The delayed arrival of proton enhancements did not affect the charging rates of the SSPM1 on the bellyband. Perhaps it affected the SSPM1-3 on the top of the S/C but that set of data has not been studied yet. The proton flux profiles shown in Figure 12 indicate that the particles peaked in ten seconds and arrived from two different azimuthal directions. The first increase arrived from a direction perpendicular to the satellite-sun vector and the satellite velocity. The second increase arrived from the ram direction. The asymmetry is explainable by a north-south boundary of energetic protons moving eastward. If we assume that the boundary was 1 gyroradius thick (220 km for 126 keV protons), then this boundary was moving with a velocity of 11 km/sec eastward and slightly away from the earth. Such motions may take place during the decay phase of substorms. Ground magnetograms show that the AL index was rapidly decreasing at the time of arrival of the energetic protons. In contrast to the proton weak discharging effect, the SSPM-1 sample responded rapidly to the fast photo-discharging at 1714:40 UT when the solar illumination reached its 20% level.

#### SPACECRAFT CHARGING IN FULL SUNLIGHT

Normally the S/C ground remains at potential levels close to zero or slightly positive when the sun shines on the S/C. This is achieved by the solar UV produced photocurrent. However, occasionally the ambient plasma becomes hard enough to cause charging of shaded insulators to potential levels lower than those of S/C ground. Figure 13 is similar to Figure 10 only in sunlight. The top and middle panels show that the electrons from .11 keV to 53.8 keV are isotropic. Starting with 1316:30 UT, the electrons with energies  $4.42 < E_e < 53.8$  keV increase whereas the electrons with energies  $0.11 < E_e < 4.42$  keV decrease. This is an indication that the S/C entered the plasma sheet region in a period of about 20 seconds. In this case, the absence of low energy electrons does not imply S/C charging. Figure 13, bottom panel, shows that the SSPM1-1 (kapton) responded to differential charging and it reached its extreme value at around 1317:45 UT. A similar S/C charging phenomenon is observed on samples looking in the ram direction. Figure 14, middle panel, shows the energetic electrons from the SC5 parallel to the spin axis detector and bottom panel shows the SSPM-3 samples with normals parallel to the S/C velocity vector. The electron signature of a local acceleration event is similar to that of Figure 13. The SSPM-3-2 (teflon) begins to respond differentially at 1316:50 UT as does the SSPM-3-3 (quartz fabric). The sample of gold (SSPM-3-4) did not show a change in its charge state. The SSPM-3 is not spin modulated as it is constantly in S/C shadow during this orbit. Finally, we would like to include a figure of NASCAP/AFGL calculations which shows quite satisfactorily that the highest spatial resolution model of SCATHA in the code produces results of differential charging in excellent agreement with experimental results.

On Day 114, 1979 (April 24, 1979) from about 0650:40 UT to about 200 seconds later SCATHA was rotating in full sunlight (see Figure 15). Using SC5 data during the pre-eclipse period on this day (see Figure 7), we assumed no charging and fitted the particle phase space densities to single Maxwellians. This fit resulted in temperatures and densities of ( $T_e = 10$  keV,  $n_e = 1 \text{ cm}^{-3}$  for electrons) and ( $T_p = 10$  keV,  $n_p = 0.5 \text{ cm}^{-3}$  for protons). Figure 15 upper panel shows the surface voltage of the SSPM-2-2 samples (large kapton), with thickness 10 times the nominal thickness as calculated by the NASCAP/AFGL code, during three rotations of SCATHA in sunlight. The lower panel shows the spin modulated surface potential of the SSPM-2-2 measurements. The charging rates are in excellent agreement. The discharging rates in each cycle do not match exactly as indicated by the different slopes in the upper and lower panels. This means that the electrical and mechanical properties of the kapton sample need fine tuning. Such an effort should be made after studying S/C charging under many different environments. The theoretical and the experimental results, nevertheless, agree in amplitude and phase in a striking way. We take this agreement to mean that the modeling of SCATHA by the NASCAP/AFGL computer code is valid.

#### CONCLUDING REMARKS

We have presented experimental and theoretical results on S/C charging in full sunlight, during eclipse entry, during total eclipse, and during exit from eclipse. Our principal findings are summarized in the abstract. In order to make further progress in validating the NASCAP/AFGL code, more data are needed from several experiments simultaneously including the ion and electron gun emissions. In addition, the model is in need of better defined materials properties for the monitored samples and for the rest of the materials distributed on the SCATHA surfaces shown in Figure 2.

#### REFERENCES

1. Description of the Space Test Program P78-2 Spacecraft and Payloads. Editors: John R. Stevens and Alfred L. Vampola, 1978.
2. A Three-Dimensional Spacecraft - Charging Computer Code, Allen G. Rubin, Ira Katz, Myron Mandell, Gary Schnuelle, Paul Steen, Don Parks, Jack Cassidy, and James Roche, in Space Systems and Their Interactions with Earth's Space Environment, edited by Henry B. Garrett and Charles P. Pike, Vol. 71 of Progress in Astronautics and Aeronautics.



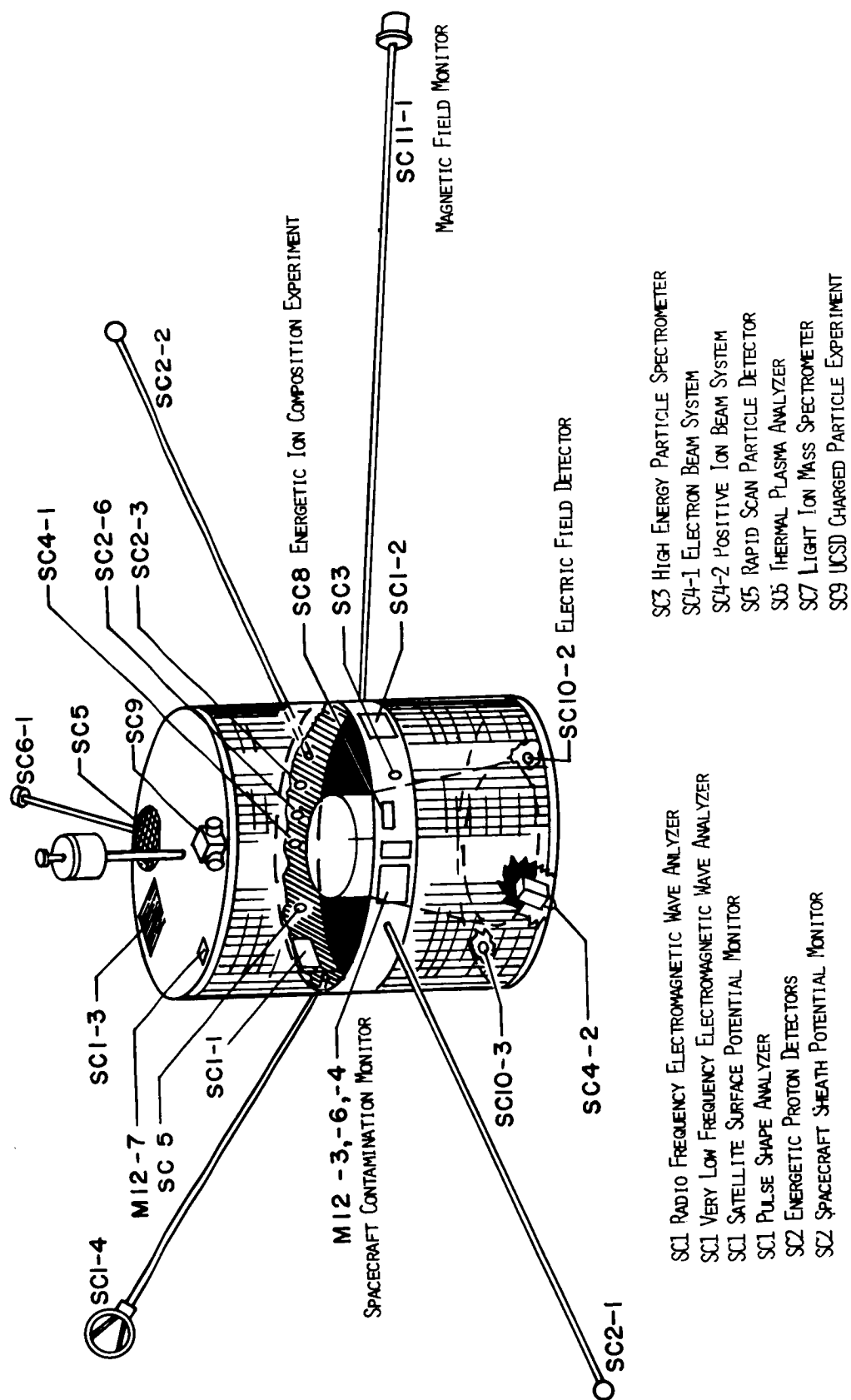


Figure 1. SCATHA spacecraft payload.

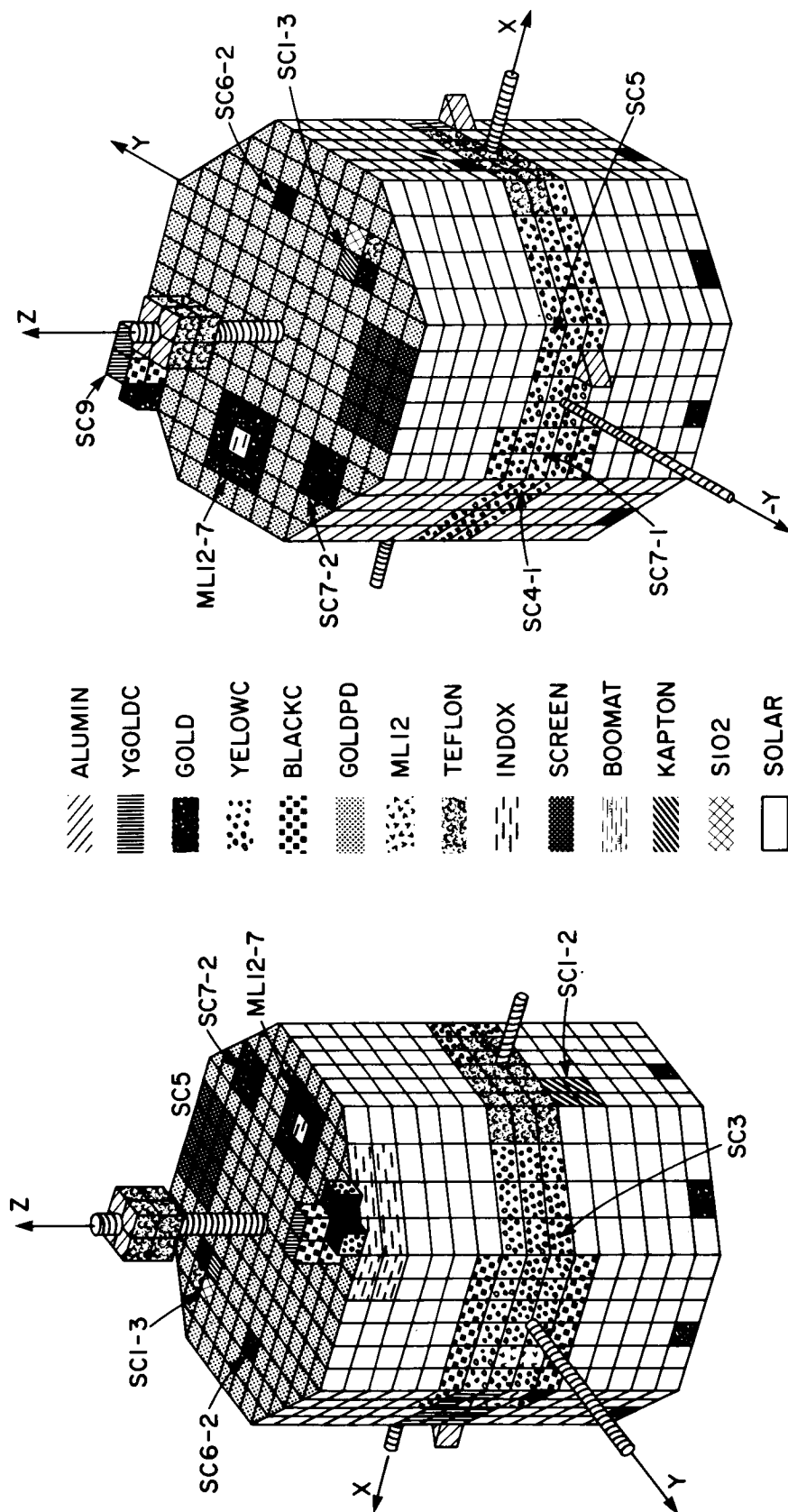


Figure 2. Materials distribution on the surface of the SCATHA satellite.  
 NASCAP graphics generated figures shaded by hand.

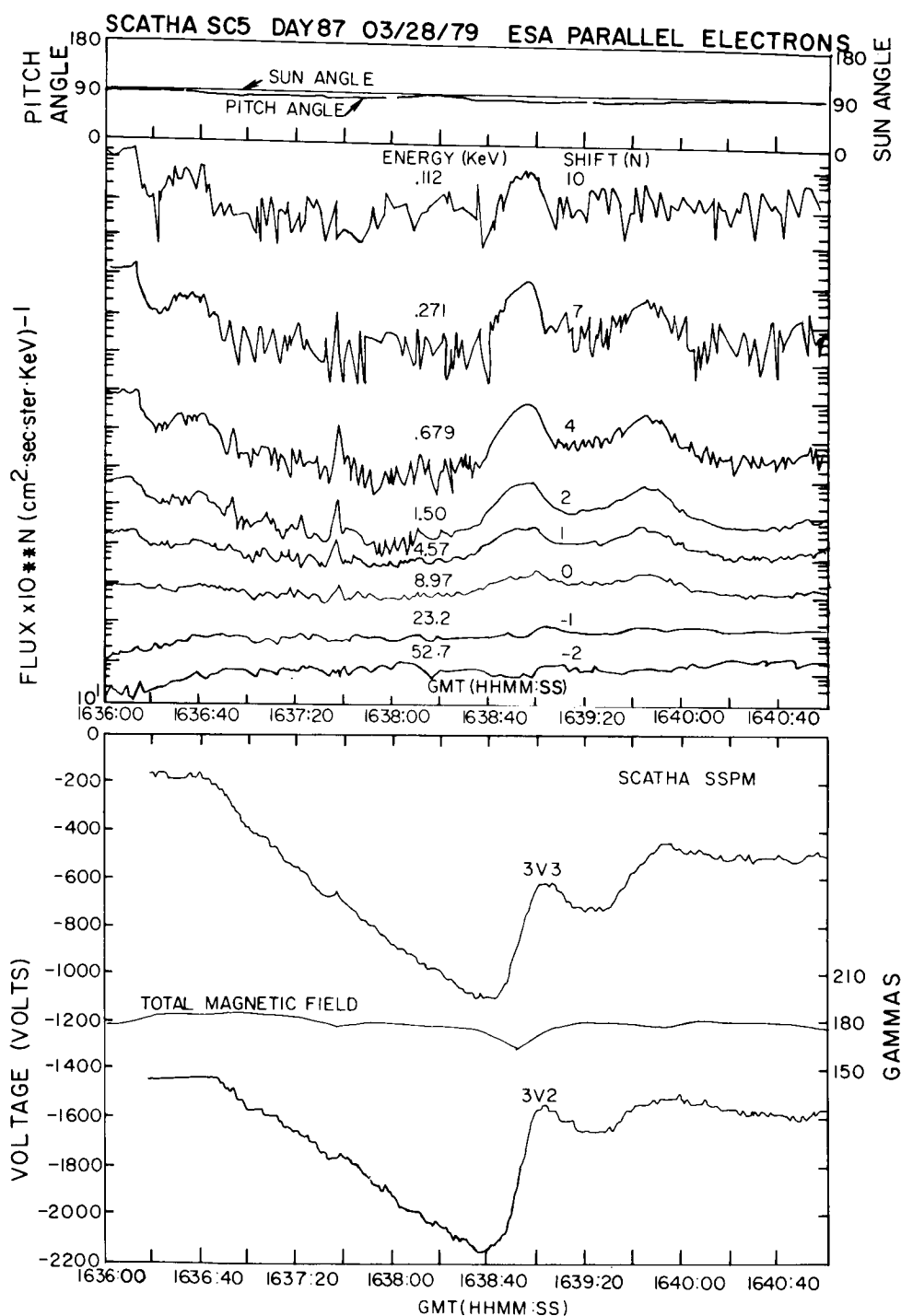


Figure 3. Spacecraft attitude, parallel electron fluxes, surface potentials, and ambient magnetic field plotted versus Greenwich Mean Time (UT).

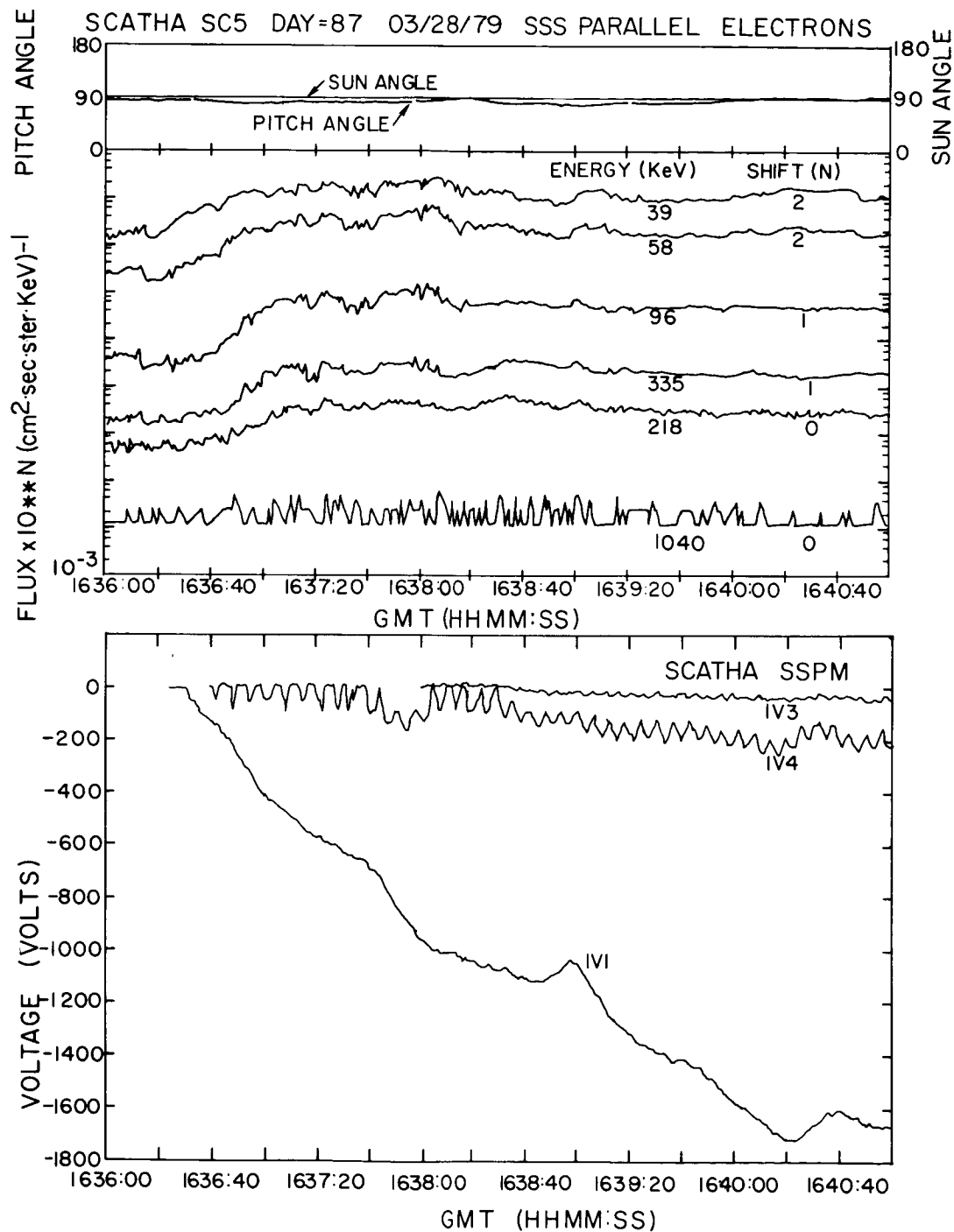


Figure 4. Same as Figure 3 only for more energetic electrons, different surface sample and without magnetic field.

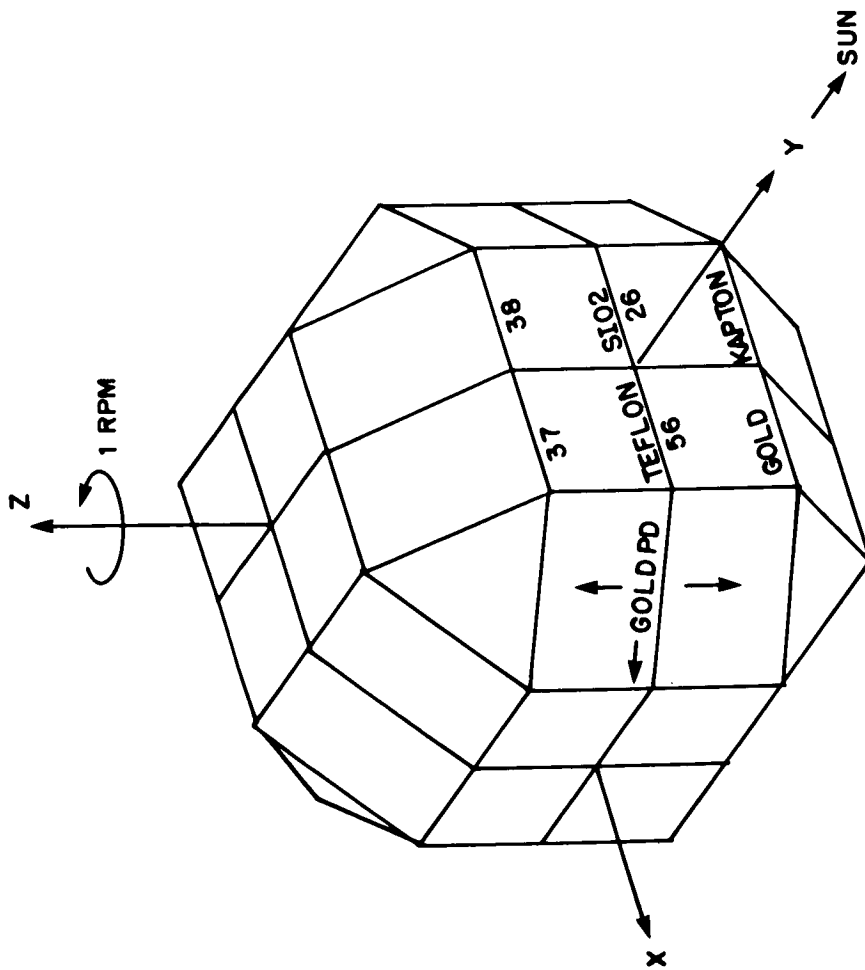


Figure 5. A quasispherical object modeled by the NASCAP/AFGL code.

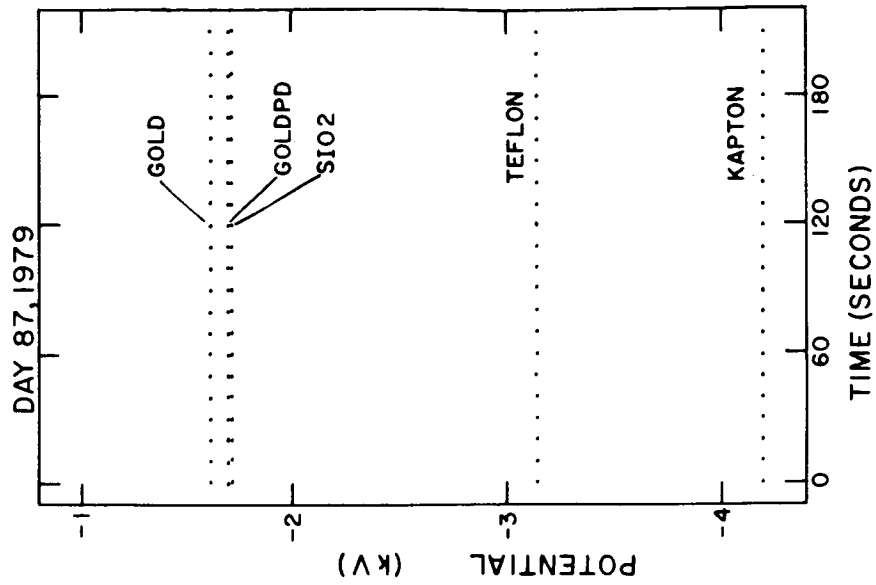


Figure 6. Spacecraft surface potentials simulated by the NASCAP/AFGL computer code.

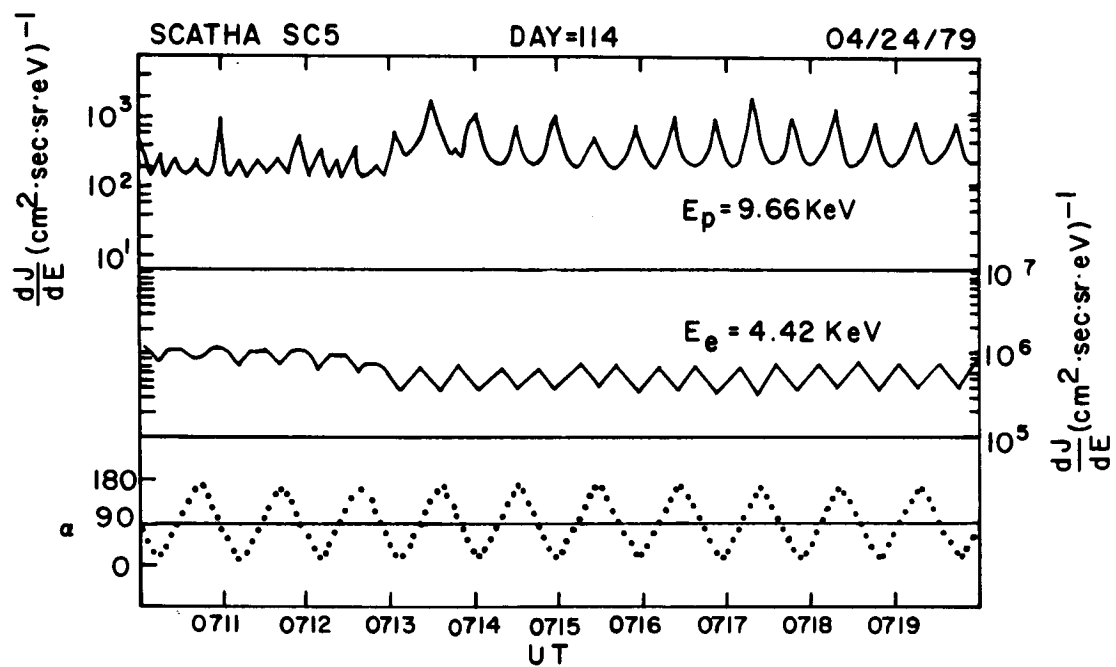


Figure 7. Directional differential intensities for ions ( $E_p = 9.66 \text{ keV}$ ) and electrons ( $E_e = 4.42 \text{ keV}$ ) together with their pitch angles all plotted versus universal time.

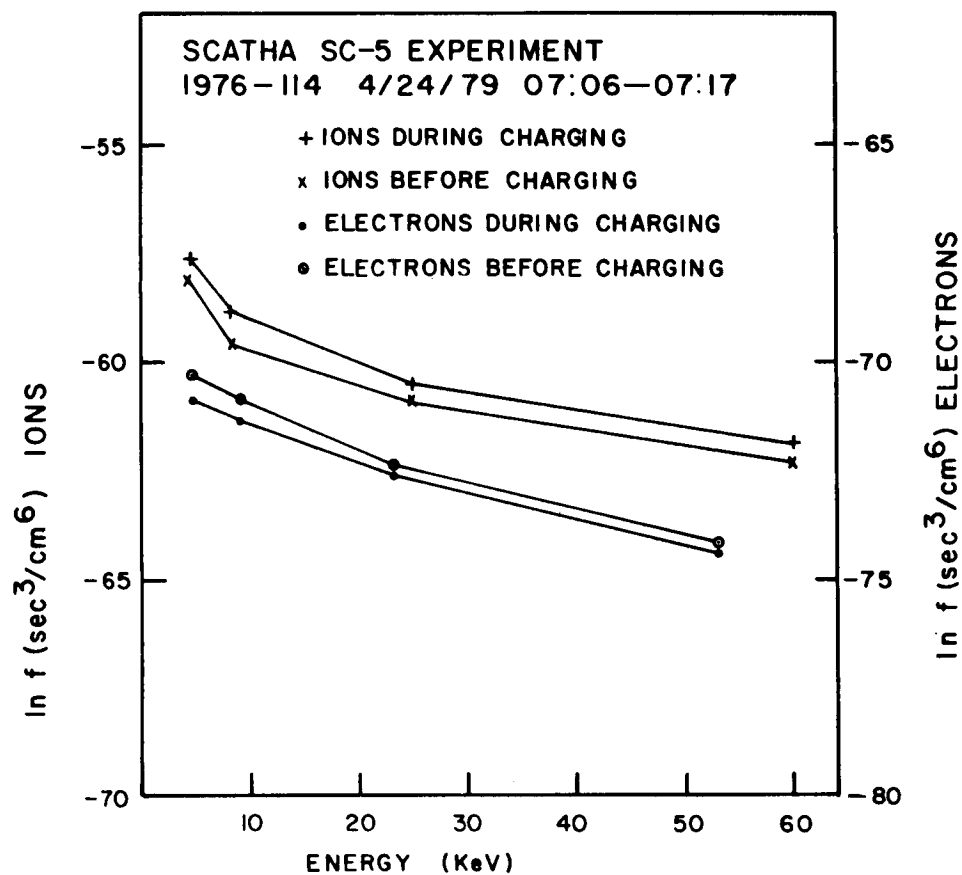


Figure 8. Ion and electron distribution functions versus energy at 0706 and 0717 UT on day 114, 1979 from the SCATHA SC5 experiment.

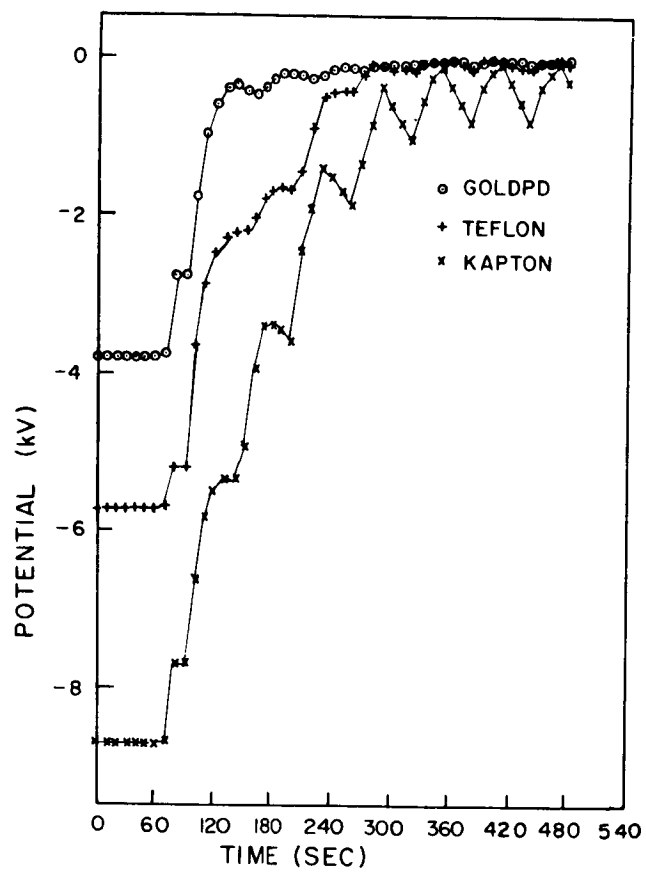


Figure 9. Spacecraft surface potentials simulated by the NASCAP/AFGL computer code.



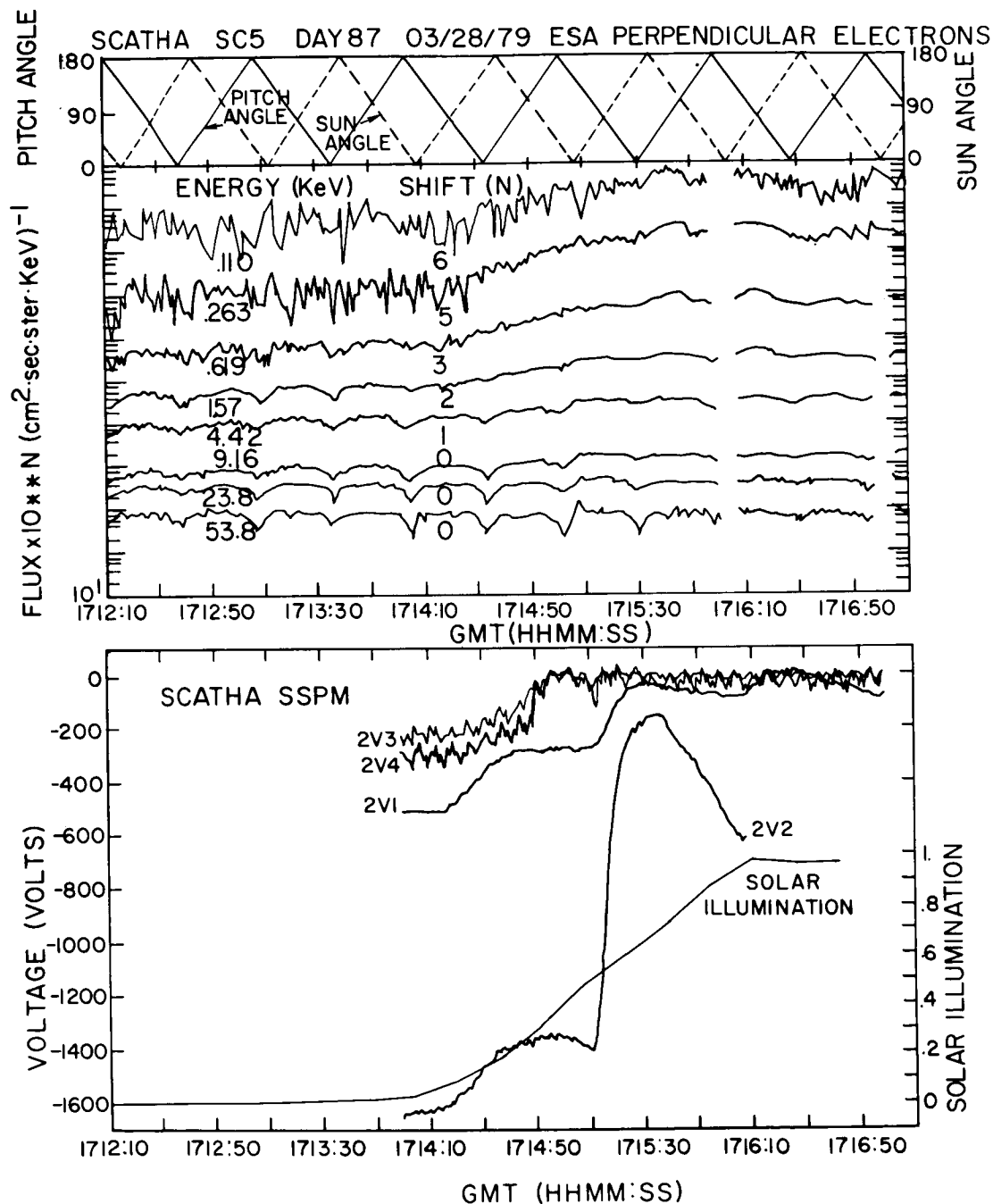


Figure 10. Top panel, pitch angle and sun-angle of SC5 perpendicular detector. Middle panel, directional differential intensities for eight channels each shifted by N decades to resolve the traces. Bottom panel, SCATHA SSPM-2 voltages and solar illumination. All traces plotted versus universal time GMT.

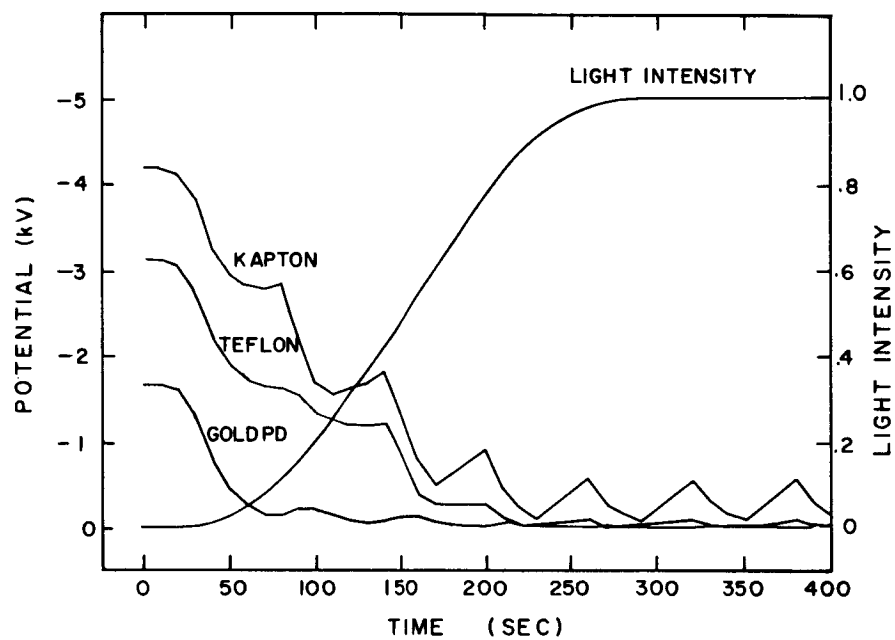


Figure 11. Similar to Figure 9 except for day 87, 1979 during exit from eclipse.

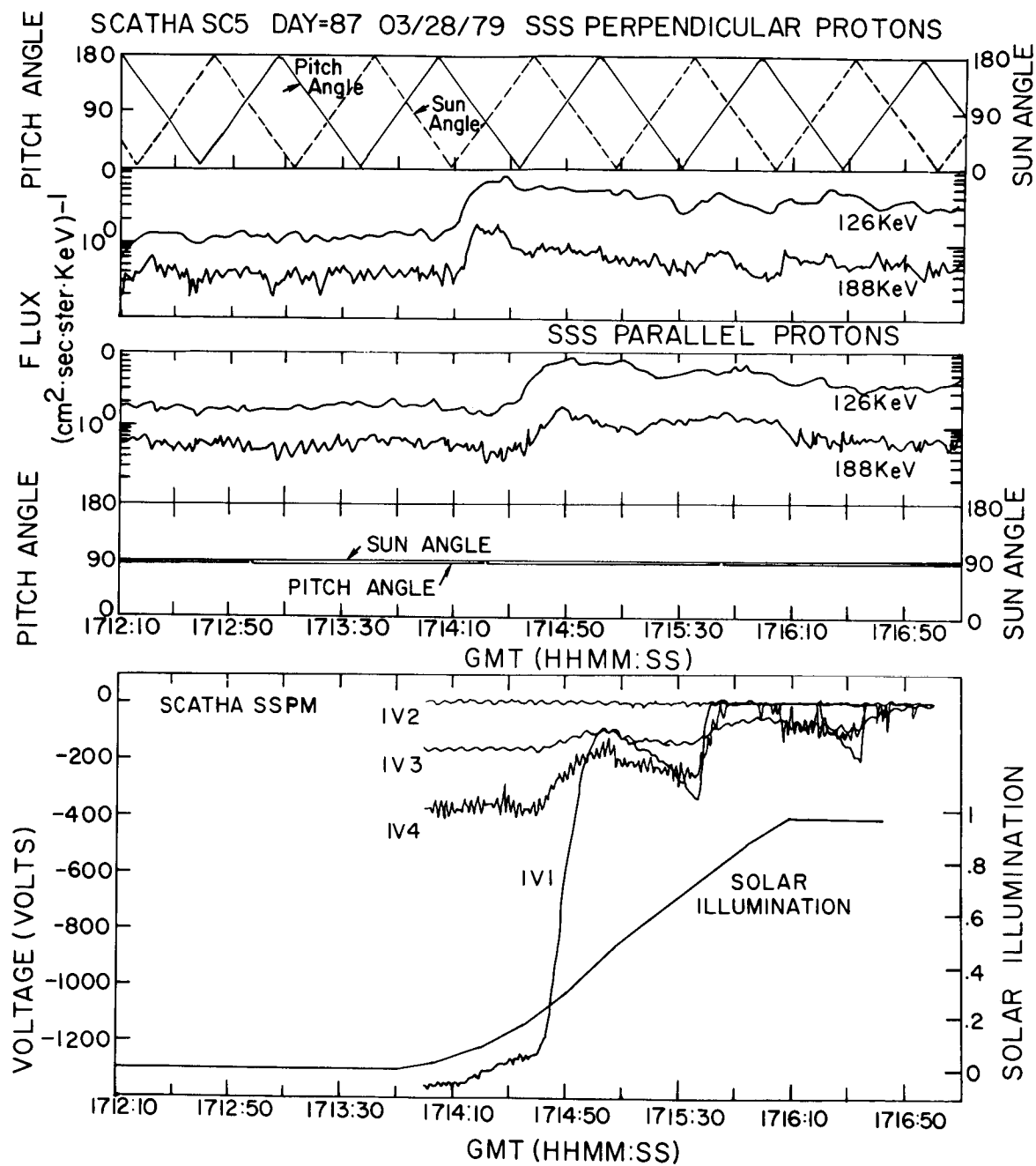


Figure 12. Similar to Figure 10 except for energetic protons and for SSPM-1.

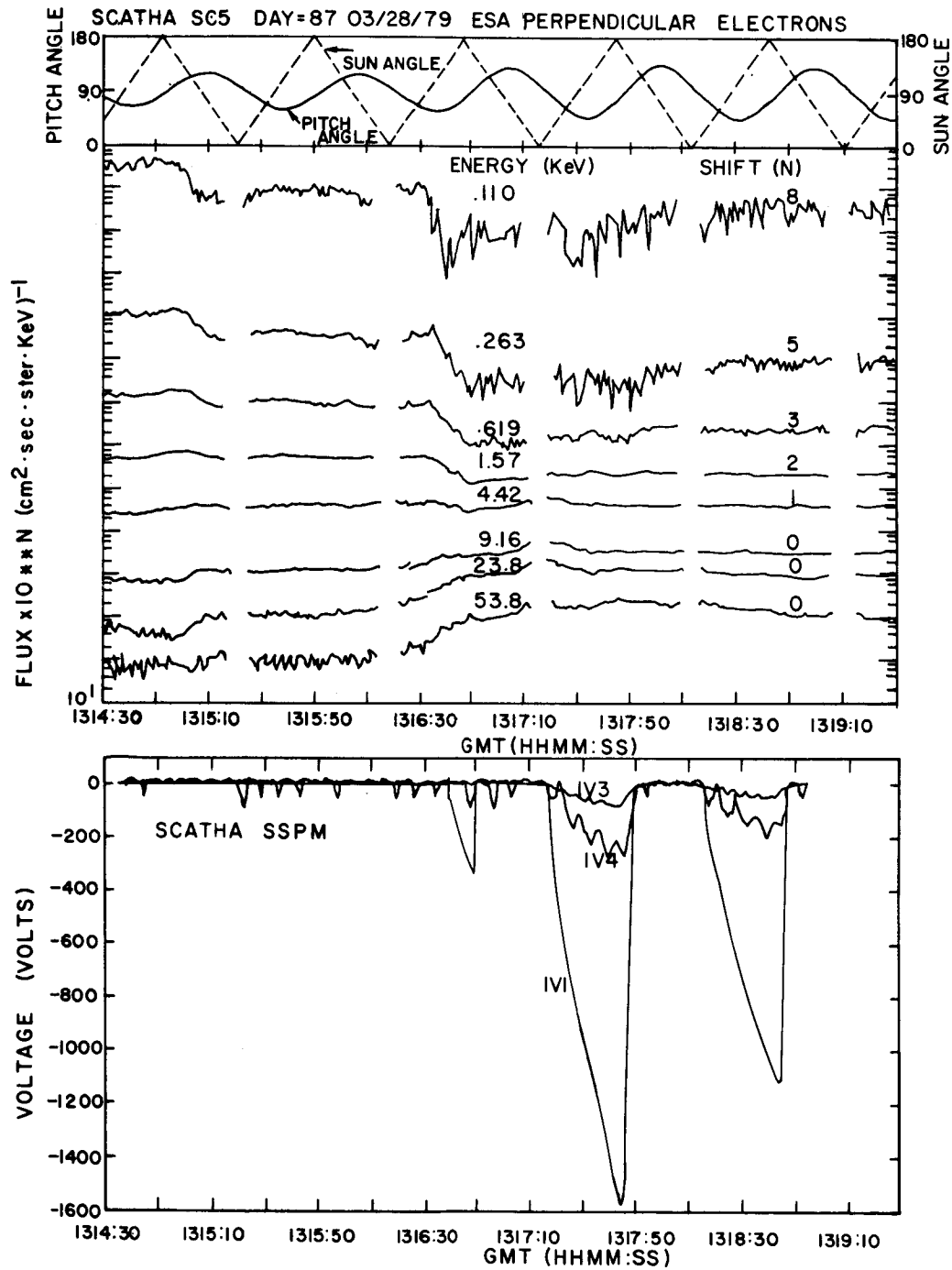


Figure 13. Same as Figure 10 except for energetic ions and for SSPM-1.

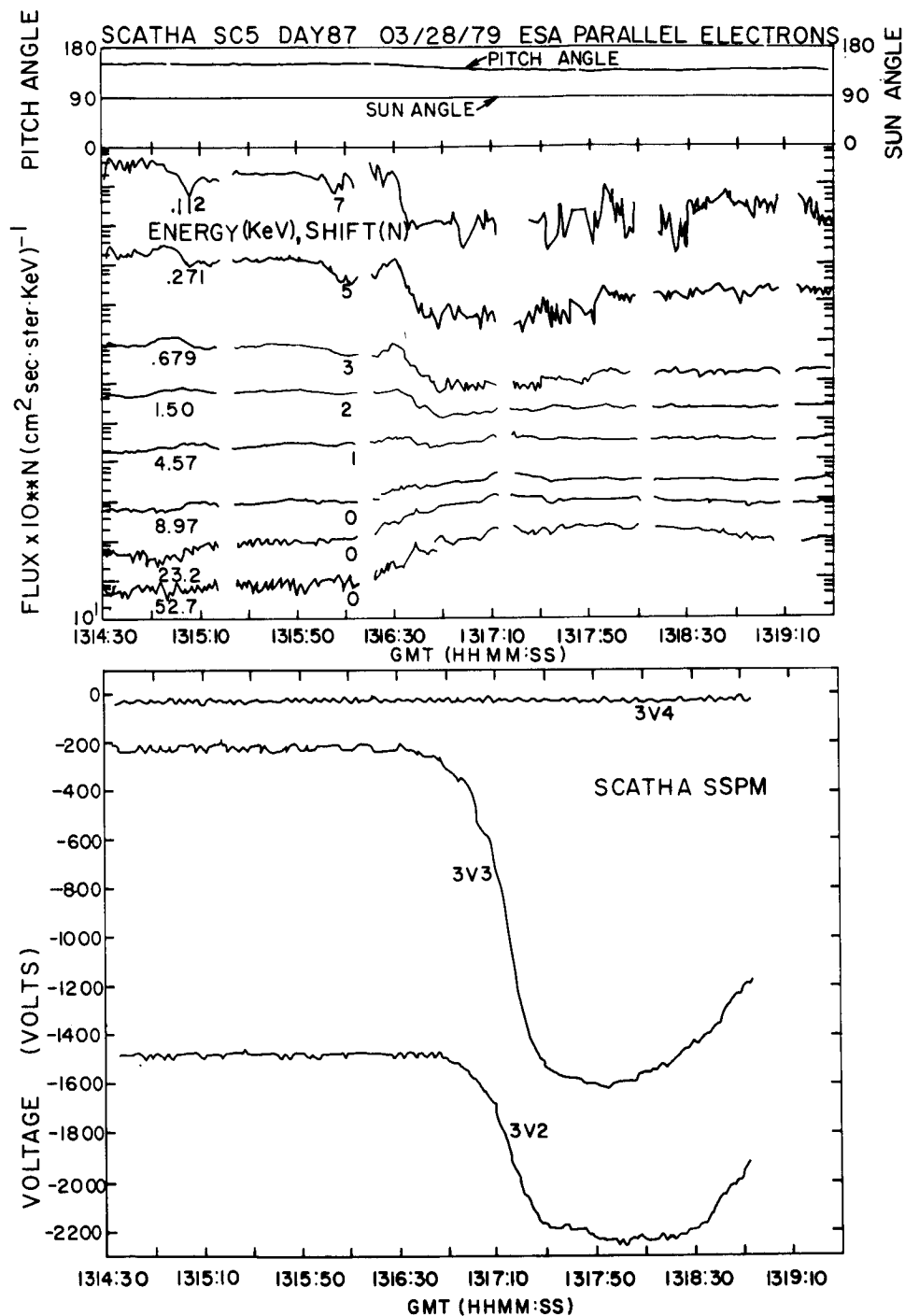


Figure 14. Same as Figure 10 except for parallel electrons and for SSPM-3.

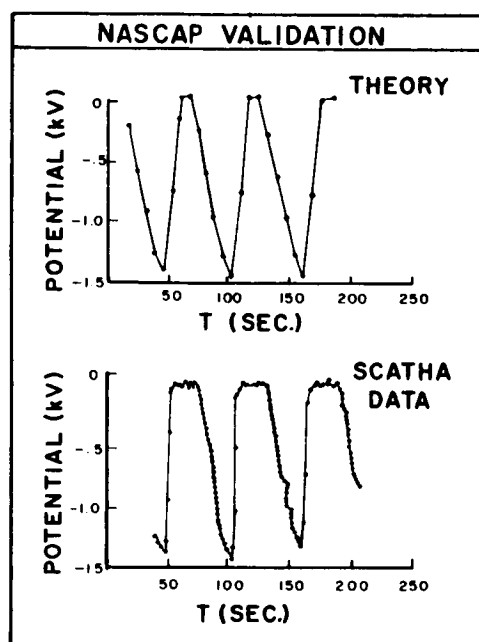


Figure 15. Temporal variation of the kapton sample (SC1-2) potential on the sunlit spinning SCATHA satellite. The upper panel shows the spin modulated potential computed by the NASCAP/AFGL code for the four grid model. The lower panel shows the measured surface potential of kapton in sunlight. The observations were made on day 114, 1979 between 0650:40 and 0653:00 UT.

## **COMPUTER SIMULATION OF SPACECRAFT CHARGING ON SCATHA**

**A. G. Rubin, H. A. Cohen, and D. A. Hardy**  
**Air Force Geophysics Laboratory**

**M. F. Tautz**  
**Radex Corporation**

**N. A. Saffelos**  
**Boston College**

### **SUMMARY**

Computer simulation is used to determine spacecraft charging on P78-2 (SCATHA) during a substorm on March 30, 1979 and for modeling the effects of electron beam emission on the P78-2 ground potential for a variety of beam voltages and currents. Agreement of measured and computed spacecraft potentials is obtained to within several hundred eV. We ascribe the discrepancies to space-charge effects omitted in the code.

### **INTRODUCTION**

Spacecraft in geosynchronous orbit and rarefied plasma regions, like the plasma sheet, are subject to electrical charging to potentials of the order of 10 kilovolts. These potentials lead to differential charging of materials on the spacecraft surface with respect to each other as well as with spacecraft ground. These differential potentials sometimes cause arcs, whose radiation couples into spacecraft and disrupts electronic circuitry. Measurements by instruments on the spacecraft may be affected by surface charging and by the spacecraft sheath field.

One proposal for eliminating spacecraft charging is to emit an electron beam from the vehicle so that the net electrical charge accumulated on the spacecraft surface is balanced by the emitted charge. Space experiments on the emission of electron beams from geosynchronous satellites were carried out on ATS-5 and ATS-6 utilizing low-energy electrons from a heated filament.<sup>1</sup> An electron gun with energies up to 41 eV was employed on ISEE-1 for spacecraft potential control by Gonfalone et al.<sup>2</sup>

The P78-2 (SCATHA) satellite is instrumented for study of spacecraft charging at geosynchronous orbit. Electron guns with energies up to 3 kV and currents up to 13 ma were employed to study how the beam energy and current affect the control of spacecraft potential.

## NASCAP CODE

A 3-dimensional computer code called NASCAP, NASA Charging Analyzer Program, is employed to model the effects of electron beam emission on spacecraft potential. NASCAP provides a finite element geometrical model of P78-2 (SCATHA) as well as modeling the interior electrical connections and materials placement on the surface. Figure 1 shows the SCATHA model.

Given the characteristics of the plasma environment, with NASCAP one may calculate the potential versus time on each surface cell and in the space around the vehicle. Particle emitters are modeled in NASCAP; given the location of the emitter on the spacecraft, as well as the energy and angular width of the beam, particles are tracked in the vehicle sheath field until they escape through a distant boundary or return to a given cell on the vehicle.

In order to follow particle trajectories out to large distances, computations are carried out in a series of nested grids, each successive grid having twice the spacing of the previous grid, the spacecraft being in the innermost grid. A constant magnetic field exterior to the vehicle in which particle orbits are tracked may be employed.

## CHARGE CONTROL

First we give an overview of how the emitter voltage and current affects the vehicle potential. At equilibrium, we would expect physically to have an exact balance between the net current coming to the satellite from the ambient plasma and the net gun current. In Figure 2 we illustrate some typical charging situations which could arise in a gun event. The curve labeled  $I_s$  represents the total current to the satellite, not including the gun, i.e. it would have contributions from the plasma, from secondary interactions and backscatter in the surface materials, from photo currents etc. The vehicle steady state voltage would be determined by the intersection of the line representing the gun current and the  $I_s$  curve. We consider below four possible situations.

1. The trivial case where there is no gun current - here the satellite will charge up to a negative potential  $V(1)$  such that the  $I_s$  curve goes to zero, as shown in Figure 2.

2. The case where the gun current  $I_2$  is less than the ambient current at  $V = 0$ . The vehicle potential will again go negative, but less in magnitude than for case (1).

3. The case where the gun current  $I_3$  is greater than the ambient  $I_s$  at  $V = 0$  but well below the ambient at  $V = E_g$ . Here the vehicle would charge



up positively to some value between 0 and  $E_g$ . No appreciable return current would be expected.

4. The same as case (3) except that now the gun current  $I_4$  is larger i.e. it is of the same order or greater than the ambient at  $V = E_g$ . Here we must allow for the fact that particles with energies less than the vehicle potential will return to the satellite, due to the attraction of the surrounding electric field. Thus, the net escaping gun current  $I_4$  will tend to decrease as  $V$  approaches  $E_g$ . The rate of increase of  $I_4$  would depend on the shape of the emitter energy spectrum. For a monoenergetic beam there would be a sharp drop to zero at  $E_g$ ; for a beam with a significant energy spread, the  $I_4$  decrease would be slower, as indicated in Figure 2.

### RESULTS OF MODELING CALCULATIONS

The results discussed here were obtained using two different spacecraft models in the NASCAP code. Initial runs employed a 2-grid SCATHA model (with foreshortened booms). Later runs employed a quasisphere spacecraft model in order to save computer time. The quasisphere, shown in Figure 3, is the sphere approximation available in the NASCAP code. The quasisphere was taken to be a mixture of conductor material on the flat surfaces and an insulator, Kapton, on the oblique surfaces. This configuration was chosen to give the same initial (gun off) equilibrium state as the larger 2-grid model. The potential is calculated assuming that the spacecraft is spinning sufficiently rapidly that the solar illumination is uniform azimuthally.

The plasma properties employed here are those of a single Maxwellian with  $T_e = 6$  keV,  $T_i = 12$  keV and electron densities of  $0.5 \text{ cm}^{-3}$ .

Table 1 shows results of NASCAP simulation of the effects of electron emitters on SCATHA vehicle potential for electron beam emission operations on March 30, 1979. Comparison of cases 3 to 3' and 4 to 4' show that the 2 grid model and the scaled quasisphere give the same results very closely. The NASCAP potentials obtained in the high current cases ( $>100 \mu\text{A}$ ) are greater than the measured values (see Table 1) and are somewhat higher than the gun energies. This occurs because the beam energy distribution is gaussian and the equilibrium is established by escaping particles from the high energy tail of the distribution. For most of the runs the width of the gaussian beam energy distribution was set at 10% of the gun energy.

In the high current cases, space charge effects cause the measured voltages to fall below the gun energies. To escape, a particle must overcome the vehicle potential and a space charge barrier potential. Therefore, the vehicle potential can be less than the gun energy.

From cases 1 to 3 in Table 1, we observe that the return currents are consistent to a balance with an input current from the ambient plasma of about  $20 \mu\text{A}$ . Thus, these cases would be of type (4) as previously dis-

cussed. For the lower gun current, cases 4 and 4', there is no return current i.e., this is a situation of type (3). For the very large currents, cases 5 and 6, a proper balance was not achieved due to the discrete trajectory model and 100% of the gun current returns. Figure 4 graphically summarizes the comparison of quasisphere and SCATHA model computations with the measured values of charging potential. The agreement is close, considering that space-charge effects have been omitted.

We generate an I,V curve of the type described in Figure 2 by fixing the vehicle potential to some value  $V_c$  and then making a very small time-step (with gun turned off and the potentials freed). The net current calculated by the code will then represent the contributions from all sources except the gun, i.e. it would correspond to  $I_s$  of Figure 2. By stepping  $V_c$  through the values from 0 to  $E_g$ , one can generate the complete  $I_s$  curve. Then, using current balance, one can predict for any given gun current, the expected equilibrium potential. An I,V curve of this type was generated for the scaled-up quasisphere as shown in Figure 5. For a  $10 \mu A$  gun, one would predict an equilibrium voltage of  $\sim 200$  volts. This result is comparable to the results for the quasisphere, starting from zero initial voltage (see case (4)). As a further test, a special run was made using +200 volts as the starting value and then allowing the potentials to float on subsequent steps. The conductor voltage did not deviate much from the starting value.

Some runs have been made with a constant magnetic field of magnitude  $10^{-7}$  webers/M<sup>2</sup>. It is found that the potentials change very little from the pure electric field case. This seems reasonable since a magnetic field only affects the direction of a particle orbit and not its energy. The same number of particles should escape with and without the magnetic field provided the particles are tracked far enough and do not encounter obstacles.

#### EFFECT OF COLD PLASMA COMPONENT ON CHARGING

In this section we survey the effects of a cold plasma on the satellite current-voltage curve when the electron emitter is on. The cold plasma is important in determining the return current to the spacecraft but unfortunately is not well known at the present time. We chose the following cases:

1. The best fit to the hot plasma in the single Maxwellian approximation

$$\begin{array}{ll} N_i = 0.5 \text{ cm}^{-3} & T_e = 6 \text{ keV} \\ N_e = 0.5 \text{ cm}^{-3} & T_i = 12 \text{ keV} \end{array}$$

2. A 2 Maxwellian from 30 March 79 SCATHA data:

$$\begin{array}{ll} N_{e1} = 0.38 \text{ cm}^{-3} & T_{e1} = 6.3 \text{ keV} \\ N_{i1} = 0.24 \text{ cm}^{-3} & T_{i1} = 5.6 \text{ keV} \\ N_{e2} = 7.7 \text{ cm}^{-3} & T_{e2} = 0.114 \text{ keV} \\ N_{i2} = 0.33 \text{ cm}^{-3} & T_{i2} = 0.227 \text{ keV} \end{array}$$

Case (3). An arbitrary cold plasma component is employed with  $n_e = n_i = 0.5 \text{ cm}^{-3}$ ,  $T_e = 0.10 \text{ keV}$ ,  $T_i = 0.20 \text{ keV}$ .

Case (4). An arbitrary cold plasma component is employed whose parameters are  $n_e = n_i = 0.50 \text{ cm}^{-3}$ ,  $T_e = 0.01 \text{ keV}$ ,  $T_i = 0.02 \text{ keV}$ .

Case (5). The measured high-temperature Maxwellian is employed together with the arbitrary low-temperature Maxwellian of Case (3).

Figure 6 show the current-voltage characteristics of SCATHA in the environments described above.

Simulations were run for an electron gun with energy of  $3000 \pm 300 \text{ eV}$  and 100 microamperes current, with the Case (1) high-energy plasma above and with the Case (5) two Maxwellian which consists of the admixture of a low-energy plasma with the Case (1) high-energy plasma.

The effect of adding the cold plasma to the hot plasma is to lower the vehicle potential from +3235 volts to +2785 volts and to decrease the return current from the beam from 80 microamperes to 20 microamperes.

The cold plasmas have a much steeper I,V curve because of the dominance of the Langmuir spherical probe contribution which goes as

$$j \propto 1 + V/kT_e$$

An electron gun case was run with a beam of energy of  $3000 \pm 300 \text{ eV}$  and a current of 6 milliamps. The plasma is the 2 Maxwellian of Case 2 with a high density cold plasma component.

Figure 7 shows the I,V curve for this case. The current scale is milliamperes rather than microamperes as in Figure 6. The return current from the emitter is now 5 ma., a large amount.

The conclusion from this study of the effects of cold plasma is that the cold plasma determines the I,V curve. If a cold plasma component with  $0.5 \text{ cm}^{-3}$  and  $T_e = 100 \text{ eV}$  were present, as in Case (3), the spacecraft potential would be decreased to 2785 volts, somewhat below the observed value of 2880 volts. This means that a denser, colder plasma component is not present.

## CONCLUSIONS

The single-particle trajectory treatment of spacecraft potential control by emission of electron beams predicts the measured SCATHA potential within about 200 volts. This indicates that the basic mechanisms of beam emission, with returning ambient and beam current are correctly treated. The neglect of space-charge leads to some inaccuracy in the computation. Computations, including a cold plasma component, show that for March 30,

1979, Case (1), no appreciable cold plasma is present and good results are obtained employing the observed particle spectra above 100 eV. The results shown here allow reliable computation of the electron beam emission effects on the spacecraft ground potential.

The experiments and simulations show that the spacecraft ground potential can be controlled by emitting an electron beam.

#### REFERENCES

1. Bartlett, Robert O. and Carolyn K. Purvis: Summary of the Two Year NASA Program for Active Control of ATS-5/6 Environmental Charging. Spacecraft Charging Technology - 1978, p. 44, NASA Conference Publication 2071, AFGL-TR-79-0082.
2. Gonfalone, A., A. Pederson, U. V. Fahleson, C.-G. Falthammer, F. S. Mozer and R. B. Tarbert: Spacecraft Potential Control on ISEE-1. *ibid.*, p. 256.

Table 1: Simulation Runs for Day 89 (30 Mar 79)

	Model	Gun Energy	Gun Current	Ground Potential $V_c$	Measured Voltage	Gun Return Current
1)	QS	300+30	100 $\mu$ A	+338	+240	-80 $\mu$ A
2)	QS	1500+150	100 $\mu$ A	+1670	+1360	-80 $\mu$ A
3)	QS	3000+300	100 $\mu$ A	+3235	+2880	-60 $\mu$ A
3')	2G	3000+300	100 $\mu$ A	+3280	+2880	-80 $\mu$ A
4)	QS	3000+300	10 $\mu$ A	+190	+40	0
4')	2G	3000+300	10 $\mu$ A	+303	+40	0
5)	QS	3000+300	6 mA	+3280	Damage	-6 mA
3)''	QS	3000+30	100 $\mu$ A	+3030	+2880	-80 $\mu$ A
6)	QS	1500+150	13 mA	+1938		-13 mA

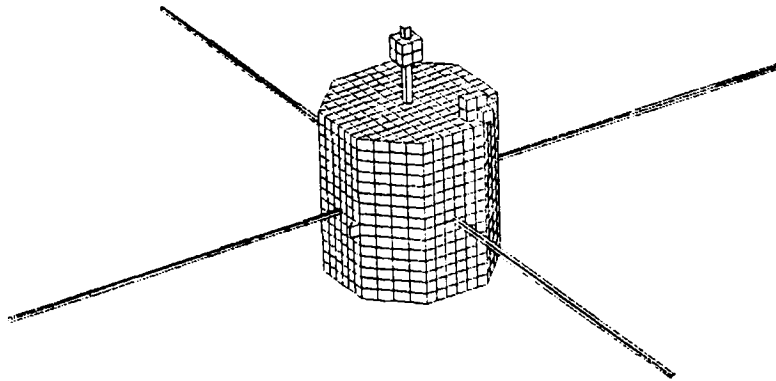


Figure 1. NASCAP P78-2 (SCATHA) model.

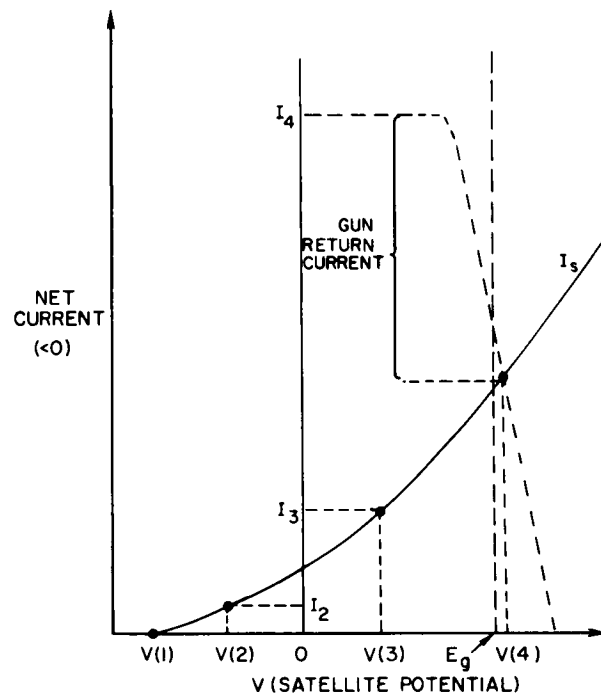


Figure 2. Current balance situations.

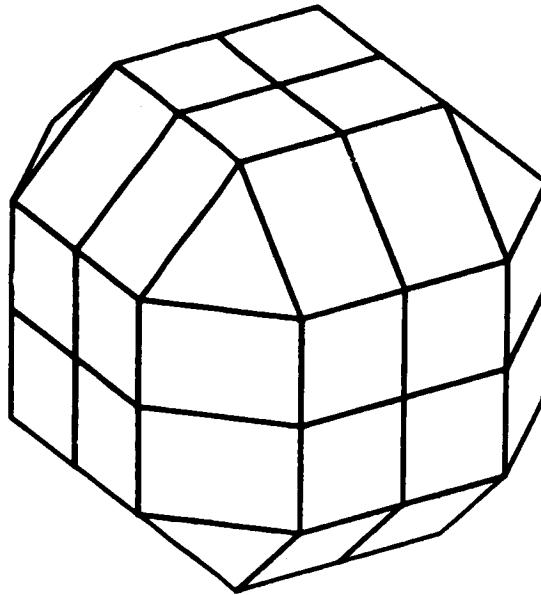


Figure 3. A quasisphere.

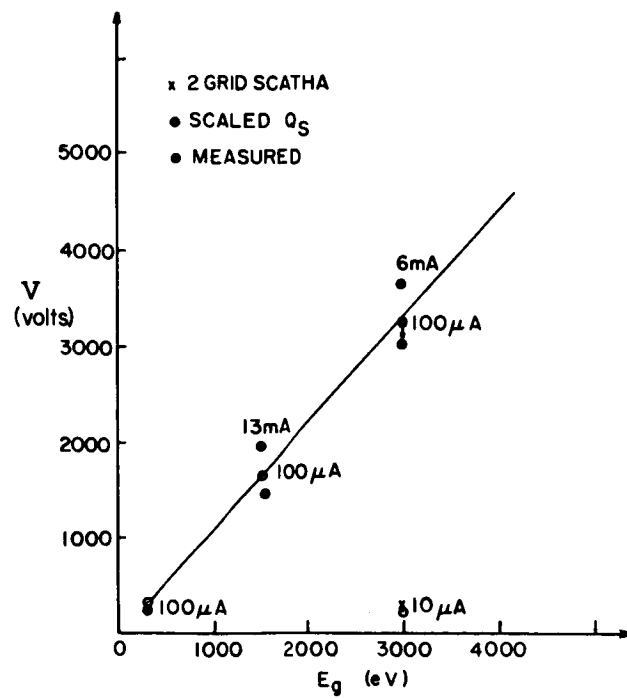


Figure 4. Gun case summary.

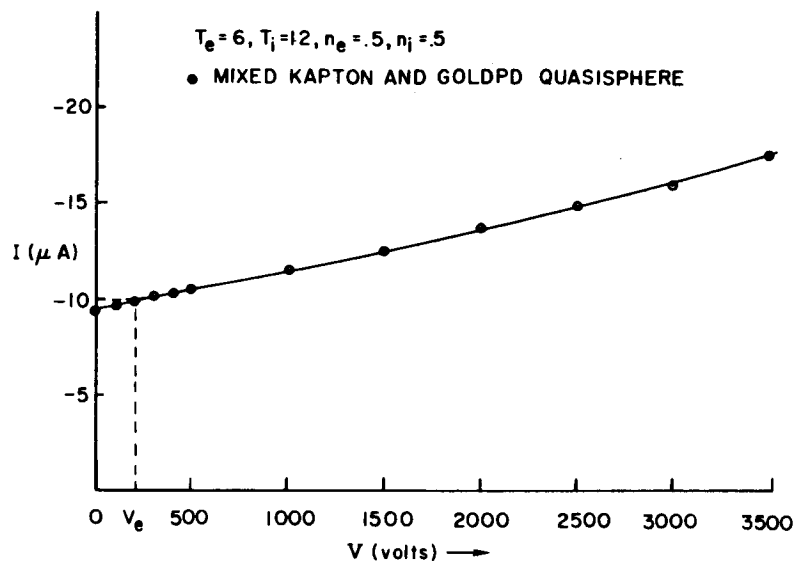


Figure 5. Current-voltage curve for a quasisphere.

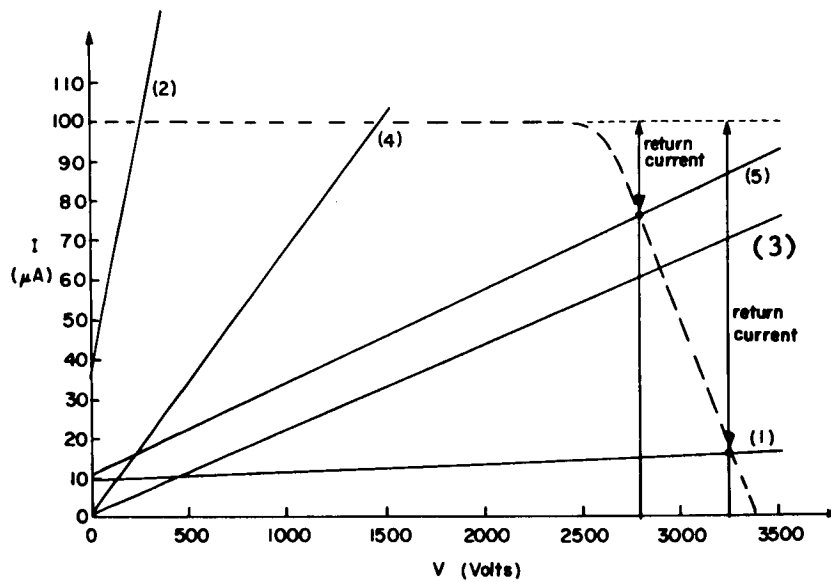


Figure 6. I-V curves for added cold plasma.

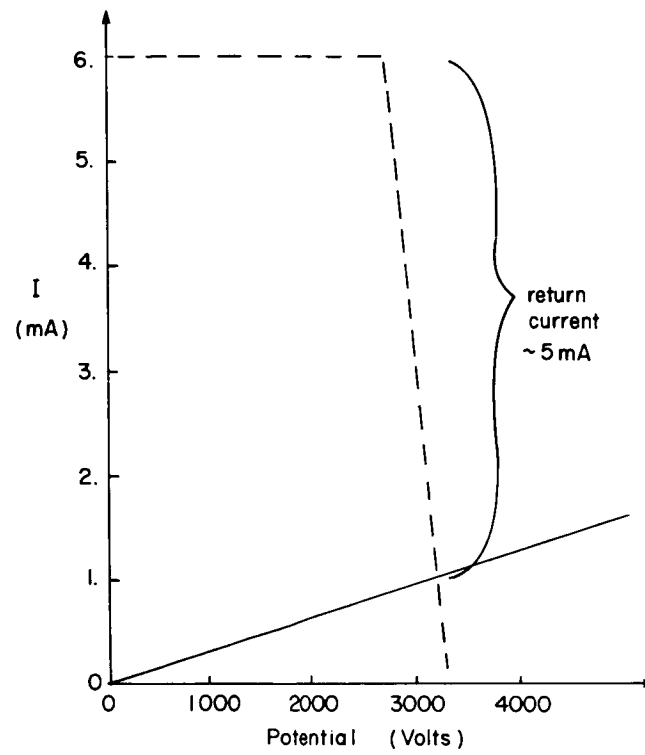


Figure 7. I-V curve for dense cold plasma.



**ANALYSIS OF AMBIENT AND BEAM PARTICLE CHARACTERISTICS DURING  
THE EJECTION OF AN ELECTRON BEAM FROM A SATELLITE IN  
NEAR-GEOSYNCHRONOUS ORBIT ON MARCH 30, 1979**

**M. S. Gussenhoven  
Boston College**

**H. A. Cohen, D. A. Hardy, W. J. Burke, and A. Chesley  
Air Force Geophysics Laboratory**

SUMMARY

On March 30, 1979, with the P78-2 (SCATHA) satellite well-within the plasma sheet, an electron beam system was operated over a wide range of beam currents and energies, for periods both in sunlight and in eclipse. The Rapid Scan Particle Detector, measuring electrons and ions in the energy range  $\sim 0.05$ - $10^3$  keV, both perpendicular and parallel to the spin axis of the satellite, operated when the electron beam current and energy levels were 0.01, 0.10 mA, and 0.3, 0.5 and 3 keV respectively. The shift in the electron distribution function indicates that the satellite became positively charged to a value much less than beam energy for 0.01 mA, and a value approaching beam energy for 0.10 mA. Complex pitch angle modulations of the electron spectra are separately decomposed for each beam operation. When electrons are emitted perpendicular to the magnetic field with an energy of 3 keV and a current of 0.10 mA they return as a coherent beam only to the parallel detector. Throughout the beam operations the pitch angle distributions show electrons with energy less than beam energy streaming along the field line. Analytic expressions for the satellite electric field are constructed and particle trajectories are determined for the observed initial conditions on the electron beam.

INTRODUCTION

Electron beams have been used increasingly in space as a means to probe or control spacecraft environment. A review of the work done in this field has been compiled recently by Winckler (ref 1). By far the greatest number of experiments have been performed with rockets in the ionosphere, however, beams have also been used in deep space at geosynchronous orbit. Very low current, highly focused electron beams were used successfully on the GEOS 2 satellite to measure the magnetospheric electric field (ref 2). Unfocused, low energy electron emission was used on the ATS-5 satellite to control satellite potential (ref 3). In these proceedings Cohen et al. report on the use of the electron beam system onboard the P78-2

(SCATHA) for operations covering a wide range of currents and energies up to 13 mA and 3 keV, respectively (ref 4, 5). Not all beam operations led to anticipated or benign results, a reflection of the need to better understand beam and ambient plasma dynamics in the vicinity of a charged satellite, as well as spacecraft charging effects during current ejection.

Outstanding problems related to the structure of the beam are concerned with the principal forces governing beam expansion and propagation in deep space, and the mechanisms which return the beam to the emitting spacecraft. Problems related to the ejection of charged beams from satellites are: the level of satellite charging for given modes of beam operation; the mechanisms by which current balance to the satellite is achieved; the origin and dynamics of the balancing return electron current.

The SCATHA satellite was designed to study the causes and effects of spacecraft charging. We use SCATHA measurements to study spacecraft charging and to study additional problems associated with the beam. We report here measurements of the plasma made by the SC5 Rapid Scan Particle Detector onboard SCATHA during the first operations of the electron beam on March 30, 1979. These operations took place both in sunlight and in eclipse. For a full discussion of events during this pass and description of the magnetospheric environment, see Cohen et al. (ref 5).

This study presents in detail the incoming particle behavior during operation of a 3 keV electron beam system at two current levels. The lower current ( $10\ \mu\text{A}$ ) leaves the satellite charged to potentials much less than beam energy. The higher current ( $100\ \mu\text{A}$ ) exceeds the current needed to charge the vehicle to beam energy. Both current levels are, in fact, small and beam spreading due to internal forces may be unimportant.

For the two current levels we show that:

- a) The electron beam can achieve large, steady-state changes in the vehicle potential and the returning ambient plasma.
- b) There is no evidence for beam return when the beam current is  $10\ \mu\text{A}$ .
- c) There is strong evidence for considerable beam return when the beam current is  $100\ \mu\text{A}$ .
- d) The plasma measurements show reasonable current balance during beam operations.
- e) There is evidence that the beam follows the classical trajectories of a charged particle in strong electric and weak magnetic fields.

#### INSTRUMENTATION AND BACKGROUND CONDITIONS

The P78-2 satellite (SCATHA) was launched into a nearly geostationary orbit in January, 1979. The apogee, perigee and inclination of the orbit

are  $7.5 R_E$ ,  $5.5 R_E$  and  $7^\circ$ , respectively. The satellite itself is cylindrical in shape with a length and diameter of 1.75 m. It spins about the cylinder axis which lies in the orbital plane, oriented perpendicular to the Sun-Earth line. The period of rotation is 58 seconds. For a more complete description of the satellite and instruments onboard, see ref 6.

The Rapid Scan Particle Spectrometer consists of two sets of particle detectors, one looking parallel, the other perpendicular to the satellite's spin axis. The parallel detector looks out the forward, flat, conducting end of the satellite. The perpendicular detector looks out from a central conducting band, frequently referred to as the belly-band of the satellite. Each spectrometer consists of eight sensors, four electrostatic analyzers and four solid state devices, capable of measuring fluxes of electrons with energies between 50 eV and 1.1 MeV, and ions with energies between 50 eV and 5 MeV. Here we are only concerned with responses from the electrostatic analyzers.

For each particle species, and in each direction there are two electrostatic analyzers, one for particles in the range 0.05 - 1.7 keV (the LE ESAs) and one for particles in the range 1.7 - 60 keV (HI ESAs). A channel set for particles with zero energy (LE ESA 0) is used to estimate the background contribution and is to be subtracted from the other LE ESA channels. Each electrostatic analyzer has four channels whose energy pass bands are very wide,  $\Delta E/E \sim 1$ , but whose accumulation times are short, 200 msec, giving a complete spectrum once every second in the full ESA energy range. Thus, SC5 gives high time resolution, but low energy resolution. In calibrating the ESAs the energy dependent response curves for each energy channel were obtained for isotropic fluxes. Their geometric factors were calculated by integrating the response curves over energy (ref 7). For the purpose of analyzing measurements taken during periods of beam operations, when monoenergetic, highly directed particle fluxes may be anticipated, we use electron count rates and laboratory measured, directional, energy dependent response functions.

The electron beam system, SC4-1, is also mounted on the belly-band of SCATHA, with the beam directed radially outward. The electron beam axis is displaced  $37^\circ$  from the perpendicular ESAs of SC5, lagging SC5 in spin phase by 6 sec. The electron beam system was first operated on March 30, 1979, over a wide variety of beam energies (0.5 - 3 keV) and currents (0.01 - 13 mA), with the satellite both in sunlight and eclipse. At a current level of 6 mA and a beam energy of 3 keV the beam operation disrupted telemetry, caused the permanent malfunction of two onboard instruments and induced multiple surface and electronic circuit arcing (ref 5).

As a precaution during most of the electron beam operations on March 30, the particle detectors on SCATHA were turned off. The exceptions to this were the Retarding Potential Analyzer (ML12), which was on throughout, and the Rapid Scan Particle Detector (SC5), which was operated after the high current beam states, at beam energies of 0.3, 0.5, and 3 keV, and currents of either 0.01 mA or 0.10 mA (referred to in this paper as the low current state and the high current state, respectively). As stated above, we concentrate on SC5 responses during periods of 3 keV beam emissions in

both low and high current states under sunlit and eclipsed conditions.

Before actually considering SC5 data it is useful to summarize conditions in the vicinity of the SCATHA orbit on 30 March. The electron beam operations took place while the satellite was near local midnight, at a radial distance of  $6.2 R_E$  and a magnetic latitude of  $-7.8^\circ$ . SCATHA entered the plasma sheet at 13.7 UT, nearly one hour before the beam operations began. The magnetosphere was in a quiet state ( $K_p = 2$ ), and there is no evidence that any injection event occurred during beam operations (Appendix, ref 5). Plasma parameters calculated for times prior to and after beam operations indicate that for the energy range measured by the SC5 ESAs, the density and temperature of the electron population are  $0.35 - 0.5/\text{cm}^3$ , and 1.2 keV, respectively; and for ions,  $0.6/\text{cm}^3$  and 6 keV. These numbers are obtained by integrating the appropriate moments of particle distribution functions over pitch angle. Throughout this time the ion counts in the energy range 0.05 - 1.7 keV were at background values. During beam operations the magnetic field configuration was more tail-like than dipolar.

## OBSERVATIONS

This section is divided into four subsections. The first contains prefatory remarks on the sequence of beam operations, the format of SC5 data and certain non-physical effects in the data. General features of the SC5 data, discussed in the second subsection are ordered according to the mode of electron beam emissions: i) 3keV, 0.1 mA operations, ii) 0.3 keV, 0.1 mA operations, and iii) 0.01 mA operations. For the sake of comparison sunlight and eclipse responses of SC5 are treated *paripassu*. In the third subsection attention is directed to periods when the 3 keV beam returns to the parallel detector. The final subsection is concerned with the directionality of the electron current to the vehicle.

Format. Modes of electron beam operations, spanning the period when SC5 was turned on, are listed in Table 1. Here and in Figures 1 and 2, the letters A and B are used to designate periods of low (0.01 mA) and high (0.10 mA) currents. During both sunlight and eclipse beam operations, low current states of several minutes duration preceded those of high currents. In the middle of the sunlit, high current operation, the electron beam emission was interrupted for 2 minutes. Data plotted in Figures 1 and 2 give an overview of SC5 electron count rates measured during the sunlit and eclipse beam operations, respectively. Panels proceed, top to bottom, from the highest to lowest energy channels. The second to bottom panel gives the background counts for the four lowest energy channels. The bottom panel gives pitch angles of the parallel and perpendicular detectors. Count rates from both sets of detectors are superposed; those from the perpendicular detector show sun pulses (Figure 1) and loss cone modulations. Due to a high compression and logarithmic scaling of data points many salient differences in the measurements of the parallel and perpendicular detectors are not obvious in Figures 1 and 2. As required, certain periods are shown on an expanded time scale and with counts plotted linearly.

Before discussing the significance of Figures 1 and 2, several non-physical features should be pointed out. 1) When the ESAs are turned on, as they are at the beginning of each Figure (at 55360 and 56782 UT), and after the data gap in Figure 2 at 57180 UT, the ESAs are in the lowest gain state. To correct for channeltron degradation the gain is raised to an appropriate level at some short time interval later (at 55380, 56808, and 57195 UT). Aside from the abrupt changes that result in the counts at these times, all other abrupt changes are a result of beam command changes. 2) The data gap in Figure 1, from 55730 to 55770 UT, resulted from a transmission loss, and occurred while the electron beam was off. Therefore, it is not accompanied by gain changes in SC5. 3) Once per spin the perpendicular ESAs face the sun. Contamination from photoemissions in the channeltrons give the very large, double-peaked pulses in Figure 1. The sun pulses obscure the perpendicular ESA data for 12 seconds. 4) Because of the tail-like magnetic field configuration and the large negative magnetic latitude of SCATHA, the solar directions and the direction anti-parallel to the magnetic field are near one another ( $\sim 30^\circ$ ), a somewhat unusual occurrence. In eclipse, with the absence of the sun pulse, a more complete sampling of pitch angle effects is possible.

General Features of SC5 Measurements. Periods of high current emissions (labelled B in Figures 1 and 2) are characterized in SC5 measurements by greatly enhanced count rates (up to an order of magnitude) in the energy channels close to beam energy. Electron fluxes for the 3 keV, 0.10 mA state (55548 - 55685 UT in Figure 1 and 56974 - 57109 UT in Figure 2) are consistent with a satellite potential of + 3 kV relative to the ambient plasma. The sharp rise of counts in energy channels below 3 keV is attributed to the measurement of backscattered and secondary electrons. Responses in sunlight and eclipse are generally similar. However, the pitch angle variations of the  $\bar{E} = 4.6$  keV channel (closest to satellite potential) show more complexity during eclipse. The parallel detectors show a sharp rise in counts in all energy channels with  $\bar{E} < 9$  keV, followed by a slow decay at 55567 and 55624 UT (Figure 1), and 56996 UT (Figure 2). At these times the electron beam was emitted nearly perpendicular to the magnetic field. These pulses represent direct returns of the beam to the satellite in one gyroperiod. A more detailed presentation of the measurements is given below. An analytical expression for calculating the trajectories of beam electrons in the presence of a magnetic field and a Coulomb-like sheath electric field is derived in the discussion section.

During periods of 0.3 keV, 0.10 mA beam emission (55658 - 55707 UT and 55869 - 55905 UT) the measured fluxes are consistent with a satellite potential of + 0.3 kV. The peak response is in the  $\bar{E} = 0.27$  keV channel. An examination of the response of the perpendicular detector indicates a possible saturation in this energy channel. The perpendicular counts are generally lower than the parallel counts by a factor of 4. More importantly, when the detector look direction is close to the magnetic field, instead of recording increased counts as do all neighboring channels, it records fewer counts. This behavior is consistent with channeltron saturation.

For low current emission periods which coincide with the first several

minutes of Figures 1 and 2 (labelled A) no charging peaks are obvious in the measurements. There are relative shifts of the vehicle potential at these times. Figure 3 shows a plot of four ten second averages of distribution functions measured by the parallel detectors with the 3 keV, 0.01 mA beam on and off, in sunlight and in eclipse. Relative to the 'in-sunlight, beam off' distribution the distribution functions with the beam on in sunlight (eclipse) indicates that the satellite potential is shifted by + 100 (+ 300) volts. The distribution function measured in eclipse with the beam off is depressed relative to all others. Simultaneous measurements by the Electric Field Detector on SCATHA (SC10) indicate that satellite ground was -320 v, below that of the ambient plasma. We do not believe that this measured satellite potential is entirely representative of a natural plasma-satellite equilibrium. It also includes residual effects of previous electron beam operations. Cohen et al. (ref 5) show that after electron beam turn off in eclipse the vehicle potential swings from positive to highly negative, then slowly relaxes to the ambient potential.

Low-energy electrons observed during low-current states were near field-aligned. In sunlight (Figure 1), count rates in the three lowest energy channels ( $\bar{E} = 0.11, 0.27$  and  $0.65$  keV) show a broad increase when the perpendicular detector monitored pitch angles within  $45^\circ$  of the field line. This field-aligned streaming of electrons also may have been present in the high current states, but is obscured by generally high counts when the beam current was increased. We note that the streaming persisted after the high current beam is turned off (55715 UT, Figure 1) extending into the  $\bar{E} = 1.5$  keV channel. In eclipse (Figure 2) the streaming again occurred during low current emissions. Here it appears only in the two energy channels ( $0.27$  and  $0.68$  keV) closest to the satellite potential, and appears to grow with time. During eclipse the peak values did not occur at the closest approach to the field line, but rather at some  $30^\circ$  to the field line, extending from  $6^\circ$   $90^\circ$  and from  $174^\circ$  -  $90^\circ$ . The streaming is not seen when the beam was off in eclipse ( $>57180$  UT), but here the depression in low energy electron counts indicates that the satellite was charged negatively, which would prevent access of the streaming electrons (Figure 3).

Direct return of the 3 keV, 0.1 mA beam to the parallel detectors. Previously we noted pulses in the count rate of the LE ESA channels of the parallel detector at 55567 and 55624 UT (Figure 1) and 56996 UT (Figure 2). These pulses were interpreted as signatures of the 3 keV beam electrons returning coherently to the satellite. In this subsection we support this interpretation by considering the response of various channels as a function of the pitch angle of the emitted beam. That the beam was mono-energetic and highly directed is demonstrated by comparing the pulse shapes with prelaunch calibration curves for SC-5 (ref 7).

Laboratory testing has shown that the background channel as well as channels 1-3 of the electron LE ESA's respond in the same way to 3 keV electrons (Figure 4 of ref 7). In Figures 1 and 2 the pulses are clearly seen in the background channel but are obscured in the other electron LE ESA channels by large numbers of backscattered and secondary electrons

that accompany high current beam operations.

The shape of the pulse can be determined in greater detail by studying the response of the ion LE ESA's. During the period of beam operations, all low energy ion channels were at background levels. Laboratory calibrations show that the ion LE ESA channels respond identically to incident electrons with energies greater than 1 keV that scatter through the detection plates, but are insensitive to incident electrons with energies below 1 keV (Figure 12, ref 7). Because the response of the channels to high energy electrons is the same, the counts can be plotted sequentially in time irrespective of channel. This increases the time resolution from 1 to 0.2 seconds. Figure 4 shows the three pulses as observed by the background and four LE ESA's of the parallel ion detector as functions of time (bottom scale) and pitch angle of the emitted beam (top scale). In all three cases the pulses have identical shapes: a sharp rise in less than one second is followed by a falloff over the next two seconds. In sunlight the pulse peak occurs when the electron beam is emitted perpendicular to the magnetic field; in eclipse it occurs at pitch angles of  $78^\circ$ . The look direction of the parallel detector was  $100^\circ$  (Figure 1) in sunlight and  $96^\circ$  (Figure 2) in eclipse. In the discussion section we show analytically that beam electrons emitted perpendicular to the magnetic field should return to the satellite in the vicinity of the parallel detector if the beam energy and the satellite potential are equal.

The insert to Figure 4 shows the response curves for the  $\bar{E} = 4.6$  keV electron channel to a 3 keV beam as a function of the angles  $\alpha$  (the heavy line) and  $\beta$  (the thin line). The angle  $\alpha$  is measured from the normal to the detector aperture in the plane perpendicular to the plates of the detector. The angle  $\beta$  is measured from the normal to the detector aperture in the plane parallel to the detector plates. The plane containing the angle  $\alpha$  is parallel to the spin axis of the satellite and passes within several inches of it. The response curve for changes in the angle  $\alpha$  closely resemble the shape of the pulses. Since the ion LE ESA is responding to scattered electrons, the similarity in shape could be coincidental. We have, however, compared the pulses as seen in the ion LE ESAs to those seen in the electron LE ESAs, and although the time resolution for a given channel is poorer, the shape is reproduced. The agreement between the pulse shape and the response curve implies that the detector is indeed detecting a monoenergetic, unidirectional beam that is slowly sweeping over the aperture of the detector, while rotating in the  $\alpha$  direction. If the beam were rotating in a combination of the two directions measured by  $\alpha$  and  $\beta$ , the pulse would have a more symmetric shape.

We now wish to calculate the energy of the returning beam and the current it is carrying. For the case of a monoenergetic and monodirectional beam returning to the spacecraft counts will be recorded simultaneously in more than one channel of the detector. This is the result of the very large  $\Delta E/E$  of the instrument. The ratio of the peak counts measured in the different channels will be the same as the ratio of their maximum effective detection areas in those channels at the energy of the beam, i.e.

$$\frac{n_i}{n_j} = \frac{A_{im}(E_B)}{A_{jm}(E_B)} \quad , \quad (1)$$

where  $n_i$ ,  $n_j$  and  $A_{im}$ ,  $A_{jm}$  are the counts and maximum detection areas for channels  $i$  and  $j$  respectively. The effective detection area,  $A(E)$ , is the factor that converts counts to flux for a unidirectional and mono-energetic flux at a specific set of angles  $\alpha$  and  $\beta$ . The maximum effective detection area,  $A_m(E)$ , is the largest value of  $A(E)$  over all angles at a given energy,  $E$ . Values of  $A_m(E)$  for three channels of interest are listed in Table 2.

From the laboratory calibration we know that the ratios of  $A(E)$  for the LE ESA channel 4 and the HI ESA channel 2 at 2, 3, and 4 keV are  $1.12 \times 10^1$ , 2.81, and  $6.61 \times 10^{-2}$  respectively. The channel that shows the peak response to the returning beam is HI ESA channel 1, but it cannot be used in this case since the return flux has saturated the channeltron. The measured ratio of peak count rates for the beam returning for LE ESA channel 4 and HI ESA channel 1 is  $\sim 0.8$ . Interpolating the ratios gives a beam energy of  $\sim 3400$  eV. Considering the uncertainties in the measurements this value is within error of being the beam energy. Taking the beam to have an energy of 3 keV we calculate the current using the count rate seen in the HI ESA 2 and the corresponding value of  $A_m(E)$  listed in table 2. This gives a current of  $\sim 0.1$  nA/cm<sup>2</sup>.

Directionality of Electron Fluxes. Figures 5 and 6 illustrate the directionality and intensity of electron fluxes to SCATHA during low and high beam operations, in sunlight and eclipse. In each case, one full spin of the satellite is represented. Heavy (light) lines represent measurements of the perpendicular (parallel) detector. For convenience in our discussion below, current balance measurements are plotted as directional current densities ( $j^*$ ). These quantities are obtained by numerically integrating differential fluxes over the energy range of the electron ESA's. The pitch angles of the SC5 perpendicular detector and the SC4 beam as functions of time are provided in the bottom panels of the figures. The pitch angle of the SC5 parallel detector was 99-101° in sunlight and 95-96° in eclipse. Data gaps occur during sun pulses.

A comparison of data in the two figures shows that:

- a) The values of  $j^*$  are approximately a factor of ten larger for the high beam current (0.10 mA) than for the low beam current (0.010 mA).
- b) The parallel detectors (thin line) give systematically lower values of  $j^*$  than the perpendicular detectors (heavy line). Except during high current emissions at pitch angles near 90°, discussed above, this is true of all pitch angles.
- c) With the exception of the low current case in sunlight, SC5 shows that there is an enhanced current return at pitch angles near 0° and 180°. The peak return is 10° - 20° from nearest field alignment but in



sunlight occurs on opposite sides of the field than in eclipse. For high currents in sunlight the enhancement near the magnetic field direction accounts for nearly all the pitch angle modulation in the perpendicular detectors. In eclipse, however, there are a variety of additional modulations; one which is as large as the magnetic field-aligned variation occurs for SC5 (SC4-1) pitch angles near 90° (50°, 130°).

## DISCUSSION

Current Balance during Beam Emissions. In an equilibrium situation, the surface potential of a body immersed in a plasma adjusts itself so that there is a zero net current to the body. This is true whether or not the body is an emitter of charged particles. In the case considered here, the satellite emits an electron beam and the current balance equation is:

$$I_B + I_v + I_{2e} + I_i + I_{BS} - I_e = 0, \quad (2)$$

where  $I_B$ ,  $I_v$  and  $I_{2e}$  represent the fraction of the beam, photoelectron and secondary electron currents, respectively, that escape from the satellite;  $I_i$  and  $I_e$  represent the positive ion and electron currents to the satellite from the ambient plasma and  $I_{BS}$  represents the current due to backscattered ambient electrons away from the satellite.

The fraction of the emitted beam that escapes the vehicle and contributes to  $I_B$  is possibly quite different during low and high current beam operations. During low current operations the satellite potential relative to the plasma was a small fraction of the beam energy. In this case, all beam electrons leave the satellite. Only the small fraction of secondary and photoelectrons with energies greater than the satellite potential (+100 - +300V) contribute to  $I_{2e}$  and  $I_v$ . During high current operations the satellite potential approximates the beam energy. Here a substantial fraction of the emitted beam may return to the satellite. The high positive satellite potential completely suppresses  $I_{2e}$  and  $I_v$ . Thus  $I_B + I_i + I_{BS}$  must be balanced by electrons from the ambient plasma,  $I_e$ .

The SC5 measurements can provide empirical indications of the means by which current balance between the satellite and plasma is achieved during electron beam operations. As stated above, the SC5 package consists of two sets of mutually orthogonal, outward looking detectors. The electrostatic analyzers sample incoming electrons and positive ions in approximately 10° by 10° solid angles about appropriate surface-normals in eight rather broadly spaced energy steps. The directional, differential flux ( $J(E_i)$ ) in electrons/(cm<sup>2</sup>-sec-sr-keV) is obtained from the count rate ( $N_i$ ) of the  $i$ th energy channel using the isotropic geometric factor  $G(E_i) \Delta E_i$ :

$$J(E_i) = N_i / (G(E_i) \Delta E_i). \quad (3)$$

The calculation is valid when the incoming plasma is isotropic over the angular width of the detectors, a condition generally met by the ambient plasma even with strong pitch angle modulations found in nature; but not

for the case of a returning beam that is narrow in energy and/or direction. The directional current density to the satellite for the range of the SC5 ESAs is:

$$j^*(A/cm^2sr) = e \sum_{i=1}^8 J(E_i) \Delta E_i, \quad (4)$$

where  $e$  is the charge of an electron ( $1.6 \times 10^{-19}C$ ). Like  $J(E_i)$ ,  $j^*$  has a one second resolution.

The values of  $j^*$  in Figures 5 and 6 represent the total electron current measured by the detectors, but not necessarily the electron current provided by the ambient plasma. That is, electrons which originate on the satellite surface and return to the satellite as a result of the attractive satellite electric field will also be detected if they have energies  $>50$  eV and are directed within  $10^\circ$  perpendicular to the surface. These can include photoelectrons, backscattered and secondary electrons and returning beam electrons. Nevertheless, an initial comparison to the beam current can be made by calculating the total current,  $I$ , to a satellite of area  $A_s$  assuming the particle flux to be isotropic:

$$I = j^* A_s \pi. \quad (5)$$

The area of SCATHA is  $14.2 \text{ m}^2$ . Thus to balance an emitted current of 0.1 (0.01) mA an isotropic directional current density of 0.22 (0.022)  $nA/cm^2sr$  would be required, and is shown as the dashed line in figure 6. In figure 5 the values of  $j^*$  are more than twice the value required for isotropic return.

In view of our anticipatory remarks concerning the effects of the satellite potential ( $\phi_s$ ) on  $I_{2e}$ ,  $I_v$  and the fraction of the beam that escapes, it is not surprising that the naively calculated quantity  $j^* A_s \pi$  exceeds the normally emitted current. To estimate the "contamination" effects of photo, secondary and returning beam electrons on our measurement of  $I_e$  it is useful to define several spin-averaged directional fluxes,  $j^*_T$ ,  $j^*_E$  and  $j^*_{H1}$ .

$$j^*_T \equiv \langle e \sum_{i=1}^8 J(E_i) \Delta E_i \rangle. \quad (6)$$

$$j^*_E \equiv \langle e \sum_{i=k}^8 J(E_i) \Delta E_i \rangle; \quad E_k > |q\phi_s|. \quad (7)$$

$$j^*_{H1} \equiv \langle e J(E_5) \Delta E_5 \rangle. \quad (8)$$

The  $\langle \rangle$  brackets indicate spin-average values. In the averaging process periods are excluded when: (a) the parallel detector was subject to direct beam return, e.g.,  $T = 0 - 30$  sec in Figure 5; and (b) the perpendicular detector is contaminated by sunlight. The averaged quantities in eq 6, 7, and 8 sacrifice the 1 second resolution and pitch angle complexity of  $j^*$ . By excluding electrons with energies less than the satellite potential,

$j^*_E$  eliminates photoelectrons and secondaries whose trajectories begin and end on the satellite from our estimate of  $I_e$ . The quantity,  $j^*_{HI}$ , is the spin-averaged, directional current density to the  $\bar{E} = 4.5$  keV channel. This is the channel closest in energy to 3 keV. It is sensitive to returning beam electrons and to cold, ambient electrons accelerated to a +3 keV satellite.

Equations 6, 7 and 8 can be combined with eq 5 to determine the corresponding spin-averaged total currents:

$$I_T = \pi A_S j^*_T \quad (9)$$

$$I_E = \pi A_S j^*_E \quad (10)$$

$$I_{HI} = \pi A_S j^*_{HI} \quad (11)$$

Values of these quantities in  $\mu A$  during various beam operations are listed in Table 3. The standard notation A, B, S and E are used to describe high and low current and sunlight and eclipse operations, respectively. The column O(S) gives current values when the beam was off in sunlight. Also the averaged currents are listed according to whether the appropriate values of  $j^*$  were calculated using the parallel or perpendicular detector. For zero-order current balance the currents listed in Table 3 should to be compared with the nominal beam currents of 10 and 100  $\mu A$ .

First consider results during low current operations A(S) and A(E):

a) The beam did not return to the satellite.  $I_{HI}$  maintains a value of 6  $\mu A$  with the beam off and on (A(S): 6-7  $\mu A$ ; O(S): 6  $\mu A$ ; A(E): 6  $\mu A$ ).

b) If the value of  $I_e$  in eq 2 is taken to be  $I_E$ , the ambient plasma electrons provide a current to the satellite that is greater by almost a factor of 2 than the current of the beam leaving the satellite (A(S): 16-18  $\mu A$ ; A(E): 19-23  $\mu A$ ; O(S): 16-19  $\mu A$ ). Note that values for A(S), O(S) are nearly the same.

c) For low satellite potentials,  $< +400$  v, ambient keV electrons are little affected by beam operations. Therefore, for low beam current, we divide  $I_E$  into two parts: contributions from  $E < 1.7$  keV, and from  $E > 1.7$  keV. These are shown in Table 3 in parentheses next to the value of  $I_E$ , with the contribution from  $E < 1.7$  keV first. (High current cases contain only contributions to  $I_E$  for  $E > 1.7$  keV, since satellite potential is 3 kV). The high energy contribution ( $> 1.7$  keV) increases between A(S) (11  $\mu A$ ) and O(S) (14  $\mu A$ ); then decreases at the time of A(E) (13-11  $\mu A$ ). The increase between A(S) and O(S) is due to the satellite having crossed a 9 keV Alfvén boundary layer. The decrease between O(S) and A(E) is due to the development of loss cones in the electron pitch angle distribution (cf Figures 1 and 2).

d) Electrons with  $E > 1.7$  keV are responsible for between 11 and 14  $\mu A$  of electron current to the satellite.

e) Beam operations result in an additional electron current to the satellite of between 2 and 7  $\mu\text{A}$ . This current is carried by  $< 1.7$  keV electrons. (Compare A(S): 5-7  $\mu\text{A}$ , and A(E): 6-12  $\mu\text{A}$  low energy currents to O(S): 2-5  $\mu\text{A}$ .)

f) More low energy electrons reach the satellite during eclipse than during sunlight beam operations, (A(S): 5-7  $\mu\text{A}$ ; A(E): 6-12  $\mu\text{A}$ ).

g) While the data has not been explicitly presented, total ion current to the satellite is less than a factor of ten below the total electron current ( $j^* \sim 0.001 \text{ nA/cm}^2\text{sr}$ ) and appears to play little role in current balance.

Consider next the results during high current operations B(S) and B(E):

a) There is evidence that a substantial fraction of the beam returns to the satellite.  $I_{H1}$  ranges between 62 and 105  $\mu\text{A}$  as opposed to 6  $\mu\text{A}$  for the O(S) period, (79  $\parallel$ , 105  $\perp$   $\mu\text{A}$  for B(S) and 62  $\parallel$ , 104  $\perp$   $\mu\text{A}$  for B(E)). As noted above, the channel closest to satellite potential is sensitive both to beam electrons and to accelerated cold plasma. In the last row of Table 3 we have estimated the current that would be provided by cold electrons ( $< 50$  eV) accelerated to satellite potential ( $I_{VS}$ ) assuming a background density of  $1 \text{ cm}^{-3}$ . During high current operations these accelerated electrons could provide up to 72  $\mu\text{A}$ . Note however, that the shifted spectra given in Figure 3 are more consistent with a cold background density of  $< 0.2 \text{ cm}^{-3}$ . We include, as well, the density of the low energy ambient population ( $50 \text{ eV} < E < 1.7 \text{ keV}$ ) which is also accelerated to near beam energy. An upperbound to this density is  $0.5 \text{ cm}^{-3}$  (i.e., the total plasma sheet electron density). Thus, the ambient cold and low energy electrons can make a maximum contribution to  $I_{H1}$  of  $\sim 50 \mu\text{A}$ . The returning beam electron current, then, has lowerbounds to the two detectors between 12 and 55  $\mu\text{A}$ .

b) The current to the 4.5 keV channel is highly pitch angle modulated (Figure 6), with the perpendicular detectors recording 30% to 60% more current than the parallel detectors. (For B(S) compare  $I_{\parallel} = 79 \mu\text{A}$  to  $I_{\perp} = 105 \mu\text{A}$ ; for B(E)  $I_{\parallel} = 62 \mu\text{A}$ ,  $I_{\perp} = 104 \mu\text{A}$ .)

c) The additional current supplied by ambient electrons with  $E > 4.5$  keV to the satellite ( $I_E - I_{H1}$ ) is  $\sim 20 \mu\text{A}$ .

d) The total electron current to the satellite, returning beam plus ambient ( $I_E$ ), is 85-134  $\mu\text{A}$ , or within 30% of beam current.

e) The current to the satellite is greater in sunlight than eclipse; differences between parallel and perpendicular detectors are greater in eclipse.

Beam Particle Trajectories. In this section the dynamics of beam electrons during operations at current levels from 10-100  $\mu\text{A}$  are

described by particle trajectories in electric and magnetic fields, ignoring space charge effects in the beam.

A particle of mass  $m$ , and charge  $q$ , in time-independent electric and magnetic fields,  $\underline{E}(\underline{r})$  and  $\underline{B}(\underline{r})$ , is governed by the equation of motion:

$$m(d\underline{v}/dt) = q\underline{E}(\underline{r}) + q(\underline{v} \times \underline{B}), \quad (12)$$

where  $\underline{r}$  is the position of the particle, and  $\underline{v}$ , its velocity.

The electric field can be written in terms of a scalar potential  $\phi(\underline{r})$ :  $\underline{E} = -\nabla\phi(\underline{r})$ . For the electron beam operations discussed above the beam electrons are in an attractive satellite potential. Writing  $q=-e$ ,  $e\phi$  is a positive quantity. It is assumed that there is spherical symmetry in the electric field potential:  $\phi = \phi(r)$ ; and that  $\underline{B}$  is a constant over the domain of interest.

The coordinate system is chosen such that  $\underline{B} = B_0 \hat{z}$  and the origin of the coordinate system is the center of the satellite. The equations of motion are written in spherical coordinates  $(\hat{r}, \hat{\theta}, \hat{\phi})$ . The initial condition for beam electrons is that at  $t=0$ :  $r=r_0$  ( $r_0$  the satellite radial dimension);  $\theta = \theta_0$  (the pitch angle of the beam); and the electrons leave the satellite radially with kinetic energy,  $E_0$ , and velocity  $v_0 = \left[ \frac{2E_0}{m} \right]^{1/2}$ .

The  $\phi$  and the  $\theta$  components of equation 12, are:

$$\frac{d}{dt} \left[ r^2 \sin^2 \theta \left( \frac{d\phi}{dt} \right) - \frac{\omega}{2} r^2 \sin^2 \theta \right] = 0; \quad (13)$$

$$\frac{d}{dt} \left[ r^2 \left( \frac{d\theta}{dt} \right) \right] = r^2 \sin \theta \cos \theta \left[ \left( \frac{d\phi}{dt} \right)^2 - \omega \frac{d\phi}{dt} \right]. \quad (14)$$

Here  $\omega \equiv \frac{eB_0}{m}$ .

For the equation of motion in  $r$ , we use the lower order (in time derivative) energy conservation equation

$$\frac{1}{2} m \left( \frac{dr}{dt} \right)^2 + \frac{L^2}{2mr^2} - e\phi(r) = E, \quad (15)$$

where  $E$  is the total energy of the particle; and

$$L^2 = m^2 r^4 \left( \frac{d\theta}{dt} \right)^2 + \sin^2 \theta \left( \frac{d\phi}{dt} \right)^2. \quad (16)$$

$\underline{L}$  is the kinetic angular momentum,  $\underline{L} = m\underline{r} \times \underline{v}$ .

Equation 13 can be solved exactly and for the initial condition  $\frac{d\phi}{dt} = 0$  (radially emitted beam), the solution is:

$$\frac{d\phi}{dt} = \frac{\omega}{2} \left[ 1 - \frac{r_0^2 \sin^2 \theta_0}{r^2 \sin^2 \theta} \right]. \quad (17)$$

In the limit  $r_0 \rightarrow 0$ :  $d\phi/dt = \omega/2$ . The electron executes circular motion with frequency  $\omega/2$ , in a coordinate system whose origin is on the path of the particle, (gyromotion of a charged particle in a constant magnetic field). The second term in eq 17 may be considered a small correction resulting from emitting the beam at  $r_0$ , rather than at  $r = 0$ . We will neglect the second term in the following simply to expedite the argument and take:

$$\frac{d\phi}{dt} = \frac{\omega}{2}. \quad (18)$$

Equation 14 has obvious solutions for two values of  $\theta_0$ :  $\theta_0 = 0$ ,

$\pi/2$ , that is, for either  $\sin \theta_0, \cos \theta_0 = 0$ . For both cases,  $r^2 d\theta/dt$  remains zero at  $r = r_0$ . However,  $r$  is generally non-zero, requiring  $d\theta_0/dt = 0$ ,  $\theta = \theta_0$ . We consider only these two cases. For  $\sin \theta_0 = 0$ ,  $L^2 = 0$  and the particle trajectory is along the magnetic field. The equation in  $r$  is:

$$\frac{dr}{dt} = \left[ \frac{2E}{m} + \frac{2e\phi(r)}{m} \right]^{1/2}. \quad (19)$$

For  $\cos \theta_0 = 0$ , (pitch angle of the beam  $\pm 90^\circ$ ),  $L^2 = \frac{m^2 r^4 \omega^2}{4}$ . The

particle motion remains in the plane perpendicular to  $\underline{B}$ , and the equation in  $r$  is:

$$\frac{dr}{dt} = \left[ \frac{2E}{m} + \frac{2e\phi(r)}{m} - \frac{r^2 \omega^2}{4} \right]^{1/2}. \quad (20)$$

Consider two extreme cases. The first is representative of the low current case, in that the satellite potential difference with respect to the plasma,  $e\phi_0$ , is much less than beam energy,  $E_0$ . That is,  $e\phi_0 \ll E_0$ , and  $E \sim E_0$ . Thus, the satellite potential makes only a small perturbation on the motion of an electron with kinetic energy  $E_0$  in the given magnetic field.

The second extreme case represents the maximum potential the satellite can reach; that is, beam energy:  $e\phi_0 = E_0$ . In this case the beam particles leave the satellite with total energy equal to zero. Equations 19 and 20 become:

$$\frac{dr}{dt} = \left[ \frac{2e\phi(r)}{m} \right]^{1/2}, \text{ along the field}; \quad (21)$$

$$\frac{dr}{dt} = \left[ \frac{2e\phi(r)}{m} - \frac{r^2 \omega^2}{4} \right]^{1/2}, \text{ perpendicular to the field}. \quad (22)$$

Solutions to eqs 21 and 22 have turning points for  $r$ , given by  $dr/dt = 0$ . Along the field, the turning point,  $r_t$ , occurs for  $\Phi(r_t) = 0$ . If  $\Phi(r) \rightarrow 0$  at a distance less than infinity, beam particles emitted along the field (or near the field direction) will stream back to the satellite. Perpendicular to the field, the turning point occurs when  $\Phi(r_t) = \frac{m \omega^2 r_t^2}{8e}$ . The value of  $r_t$  is less for perpendicular emission than for parallel emission.

To proceed further we must assume a functional form for  $\Phi(r)$ . The electric potential that results from an excess positive charge on the satellite to lowest order, can be modelled by a Coulomb potential:

$$\Phi = \frac{\Phi_0 r_0}{r} \quad (23)$$

For a Coulomb potential and the given initial conditions the solutions to eqs 21 and 22 are:

$$r = r_0 \left(1 + \frac{3}{2} \Omega t\right)^{2/3}, \text{ along the field; and} \quad (24)$$

$$r = r_0 \left(\frac{2\Omega}{\omega}\right)^{2/3} \sin^{2/3} \left[ \frac{3}{4} \omega t + \frac{\omega}{2\Omega} \right], \quad (25)$$

perpendicular to the field. Here  $\Omega \equiv v_0/r_0$ . To write eq 25 in the form shown, the approximation:  $\sin(\omega/2\Omega) \sim \omega/2\Omega$ , has been used. For a 3 keV beam electron in a 100 nT magnetic field,  $\omega/2\Omega = 3 \cdot 10^{-4}$ .

The time required for the beam electron to return to the satellite can be derived from eq 25. For  $r = 0$ ,

$$\frac{3}{4} \omega t + \frac{\omega}{2\Omega} = n\pi, \text{ } n \text{ an integer.} \quad (26)$$

Choosing  $n = 1$  and neglecting the second term on the left hand side of eq 26,

$$\frac{\omega t}{2} = \Delta\phi = \frac{2\pi}{3}; \quad (27)$$

that is, the beam returns displaced azimuthally by  $120^\circ$ .

The SC5 results indicate that  $\Delta\phi = \pi/2$ . (Recall that the beam emitted perpendicular to the magnetic field on the belly band was detected in the parallel detectors.) Thus, the Coulombic potential is not a good model of the satellite environment. One can anticipate from eq 22 that the addition of a sheath electric field, causing the potential to decrease more rapidly with distance, will give a smaller  $r_t$ . The electron will spend less time in orbit, and  $\omega t$  will be closer to  $\pi/2$ .

We model the sheath field with an infinitesimally thin spherical shell of negative charge at  $r = a$ . The total charge in the shell is taken to be

equal to the excess positive charge on the satellite. Solving Laplace's equation inside and outside the sphere and matching the solutions at  $r = a$ , gives for the sheath potential,  $\phi_s$ :

$$\phi_s = - \frac{\phi_0 r_0}{a} , \text{ for } r < a ; \quad (28)$$

$$\phi_s = - \frac{\phi_0 r_0}{r} , \text{ for } r > a . \quad (29)$$

Combining the sheath potential and the Coulomb potential gives the total potential in the vicinity of the satellite:

$$\phi = \phi_0 r_0 \left( \frac{1}{r} - \frac{1}{a} \right) , \text{ for } r < a ; \quad (30)$$

$$\phi = 0 , \quad \text{for } r > a . \quad (31)$$

Using this potential to determine motion along the field, gives a turning point at  $r_t = a$  (eq 21). Perpendicular to the field,  $r_t$  is less than  $a$  (eq 22). Therefore, for functional analysis we need only use the form for  $\phi$  given by eq 30. Along the field the solution to eq 21 is:

$$r = a \sin^2 \left[ \Omega' t - \frac{1}{3} \left( \frac{r_0}{a} \right)^{1/2} + \left( \frac{r}{a} \right)^{1/2} \left( 1 - \frac{r}{a} \right) \right]^{1/2} . \quad (32)$$

Here  $\Omega' \equiv \left( \frac{r_0}{a} \right)^{1/2} \frac{v_0}{a}$ ; and the form of eq 33 assumes

$$\sin^{-1} \left( \frac{r_0}{a} \right)^{1/2} = \left( \frac{r_0}{a} \right)^{1/2} + \frac{1}{6} \left( \frac{r_0}{a} \right)^{3/2} ;$$

that is, that  $r_0/a \ll 1$ . As before, the beam electron returns to the vehicle ( $r = 0$ ) when the argument of the sine function is  $\pi$ , or for:

$$t = \left[ \pi + \frac{1}{3} \left( \frac{r_0}{a} \right)^{1/2} \right] / \Omega' . \quad (33)$$

To keep the argument tractable, we do not solve eq 22 for the potential of eq 30. But instead we recognize that the time required to return along the magnetic field is always greater than that required to return perpendicular to the field. Using, then, the return time in eq 24 as an upperbound, we calculate the upperbound on the displacement in  $\Delta\phi$ :

$$\Delta\phi = \frac{\omega t}{2} = \frac{\omega}{2\Omega'} \left[ \pi + \frac{1}{3} \left( \frac{r_0}{a} \right)^{1/2} \right] . \quad (34)$$

Neglecting the second term on the right hand side we see that the beam electron can return to the satellite with a displacement of  $\pi/2$  if  $\omega = \Omega'$ ; or if

$$a^{3/2} = \frac{r_0^{1/2} v_0}{\omega} . \quad (35)$$



For a 3 keV electron in a 100 nT magnetic field, eq 36 requires a  $\sim 100$  m. (This value of  $a$  justifies the assumptions concerning the smallness of  $r_0/a$ .)

In this section we have presented simple mathematical models of the satellite potential to show that the electron beam can return to the satellite under the following conditions:

- a. The satellite is charged to beam energy.
- b. The electric potential is Columbic, and the beam is emitted perpendicular to the magnetic field. The beam returns displaced azimuthally by  $120^\circ$ .
- c. The electric potential is a combination of Coulomb and sheath potentials. The beam will have a maximum radial excursion from the satellite, along the field, to the position of  $\Phi = 0$ . Angular momentum effects will turn the beam at a lesser distance when the beam is emitted perpendicular to the field. The functional form of the sheath potential determines the azimuthal displacement, and can reduce it from  $120^\circ$  to  $\sim 90^\circ$ , for a sheath equal to a negatively charged shell at  $\sim 100$  m. It should be noted that such simple potential models give trajectories which reasonably fit the data, because the electrons spend most of their time near the turning point, that is, far from the vehicle where the potential models may be quite good.

Finally, we wish to make a few comments on the low current case. For this case the beam particle trajectories are determined principally by the magnetic field. Motion in a dipole field has been studied thoroughly (ref 8), and we expect the beam electrons to leave the satellite and to gyrate perpendicular to the field, to mirror along the field and to drift eastward. The periods for these motions for a 3 keV electron are:  $4 \cdot 10^{-4}$  sec (gyroradius =  $10^3$  m), 4 sec and  $1.3 \cdot 10^5$  sec. respectively. The volume of space occupied by the beam will approximate a 1 km tube (near the equator) which moves ahead of the satellite (which is also moving eastward) with a relative speed of  $\sim 3$  km/sec. Any interactions between the beam and the plasma will also occupy this volume. When the beam is turned off the satellite will continue to move on field lines which the beam has recently occupied for a time interval on the order of 10 min. The low energy plasma streaming along field lines during the low current operations, and continuing when the beam is turned off, may be an indication of a beam-ambient plasma interaction.

## REFERENCES

1. Winckler, P. R.: The Application of Artificial Electron Beams to Magnetospheric Research. J. Geophys. Res., Vol. 18, No. 3, Aug 1980, pp. 659-682.
2. Melzner, F., G. Metzner and D. Antrack: The GEOS Electron Beam Experiment S329. Sp. Sci. Inst., Vol 4, 1978, pp. 45-55.
3. Goldstein, R., and S. E. DeForest: Active Control of Spacecraft Potentials at Geosynchronous Orbit. Spacecraft Charging by Magnetospheric Plasmas, Progress in Astronautics and Aeronautics, 47, A. Rosen, Ed., 1976.
4. Cohen, H. A., T. Aggson, A. L. Chesley, M. S. Gussenhoven, D. A. Hardy, I. Michael, R. C. Olsen, E. Whipple, and S. T. Lai: A Direct Comparison of Three Techniques of Discharging Satellites. In these Proceedings.
5. Cohen, H. A., R. C. Adamo, T. Aggson, A. L. Chesley, D. Clark, D. R. Croley, S. A. Damron, D. E. Delorey, J. F. Fennel, M. S. Gussenhoven, F. A. Hanser, D. Hall, D. A. Hardy, W. B. Huber, I. Katz, H. C. Koons, S. T. Lai, B. Ledley, P. F. Mizera, E. G. Mullen, J. E. Nanevich, R. C. Olsen, A. G. Rubin, G. W. Schnuelle, N. A. Saflekos, M. F. Tautz, and E. C. Whipple: P78-2 Satellite and Payload Responses to Electron Beam Operations on March 30, 1979. In these Proceedings.
6. Description of the Space Test Program P78-2 Spacecraft and Payloads. J. R. Stevens and A. L. Vampola, Ed. SAMSO TR-78-24, Space and Missiles Systems Organization, Air Force Systems Command, Los Angeles, CA 90009, 1978.
7. Hanser, Frederick A., David A. Hardy, and Bach Sellars: Calibration of the Rapid Scan Particle Detector Mounted in the SCATHA satellite. AFGL-TR-79-0167, Air Force Geophysics Laboratory, Hanscom AFB, MA 01731, 1979.
8. Roederer, J. G.: Dynamics of Geomagnetically Trapped Radiation. Berlin-Heidelberg-New York. Springer Verlag 1970.

TABLE 1  
ELECTRON BEAM OPERATIONS, MARCH 30, 1979

	UT(sec)	Energy (keV)	Current (mA)
In Sunlight			
*	-55058	to 3.0	to 13.
*	55058-55122	1.5	.01
A	55122-55463	3.0	.01
A	55463-55535	0.5	.01
A	55535-55548	3.0	.01
B	55548-55658	3.0	.10
B	55658-55707	0.3	.10
	55707-55869	0	0
B	55869-56269	0.3	.10
In Eclipse			
*	-56692	to 3.0	to 1.
A	56692-56955	3.0	.01
A	56955-56965	0.5	.01
A	56965-56974	3.0	.01
B	56974-57109	3.0	.10

\* SC5 off

A: low current,  $V_s < E_0$

B: high current,  $V_s = E_0$

TABLE 2  
EFFECTIVE DETECTION AREAS

	LE ESA4	HI ESA1	HI ESA2
Energy (KeV)	$A_m(E)(cm^2)$	$A_m(E)(cm^2)$	$A_m(E)(cm^2)$
1.5	7.42(-3)	3.59(-4)	
2.0	4.46(-3)	2.92(-3)	4.00(-5)
2.5		2.67(-3)	
3.0	5.77(-4)	2.57(-3)	1.59(-4)
3.5		2.54(-3)	
4.0	6.33(-5)		9.58(-4)
5.0		1.18(-3)	
6.0			3.10(-3)
7.0		1.01(-3)	3.13(-3)

(-n) =  $10^{-n}$

TABLE 3  
CURRENT TO THE SATELLITE, MEASURED BY SC5

I in $\mu A$		A(S)	B(S)	O(S)	A(E)	B(E)
I <sub>T</sub>		16	124	16	20	103
	⊥	18	157	19	24	155
I <sub>E</sub>		16 (5,11)	105	16 (2,14)	19 (6,13)	85
	⊥	18 (7,11)	134	19 (5,14)	23 (12,11)	130
I <sub>HI</sub>		6	79	6	6	62
	⊥	7	105	6	6	104
I <sub>VS</sub> (n=1)		13	72	--	23	72

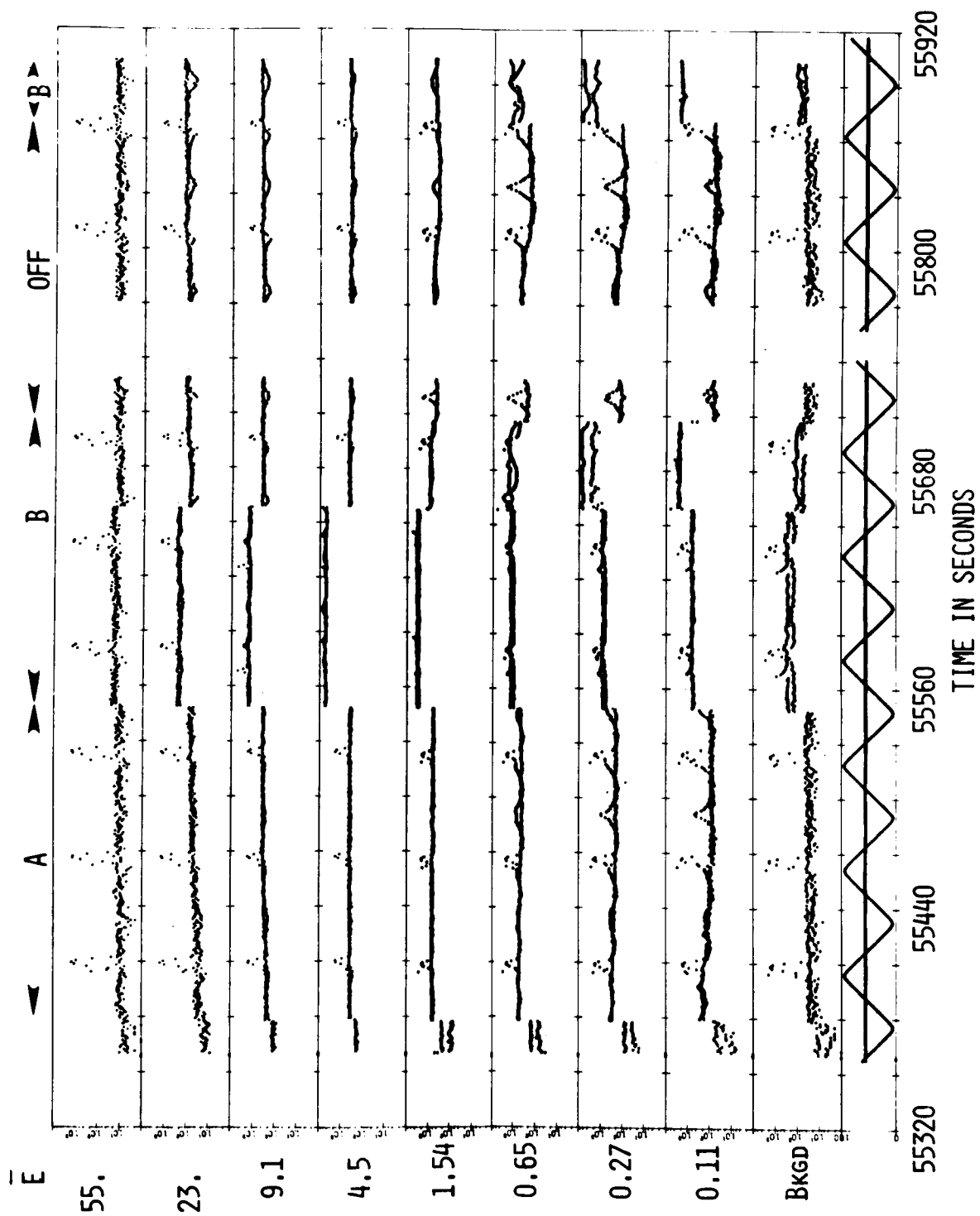


Figure 1 Electron count rates during electron beam operations in sunlight, March 30, 1979.

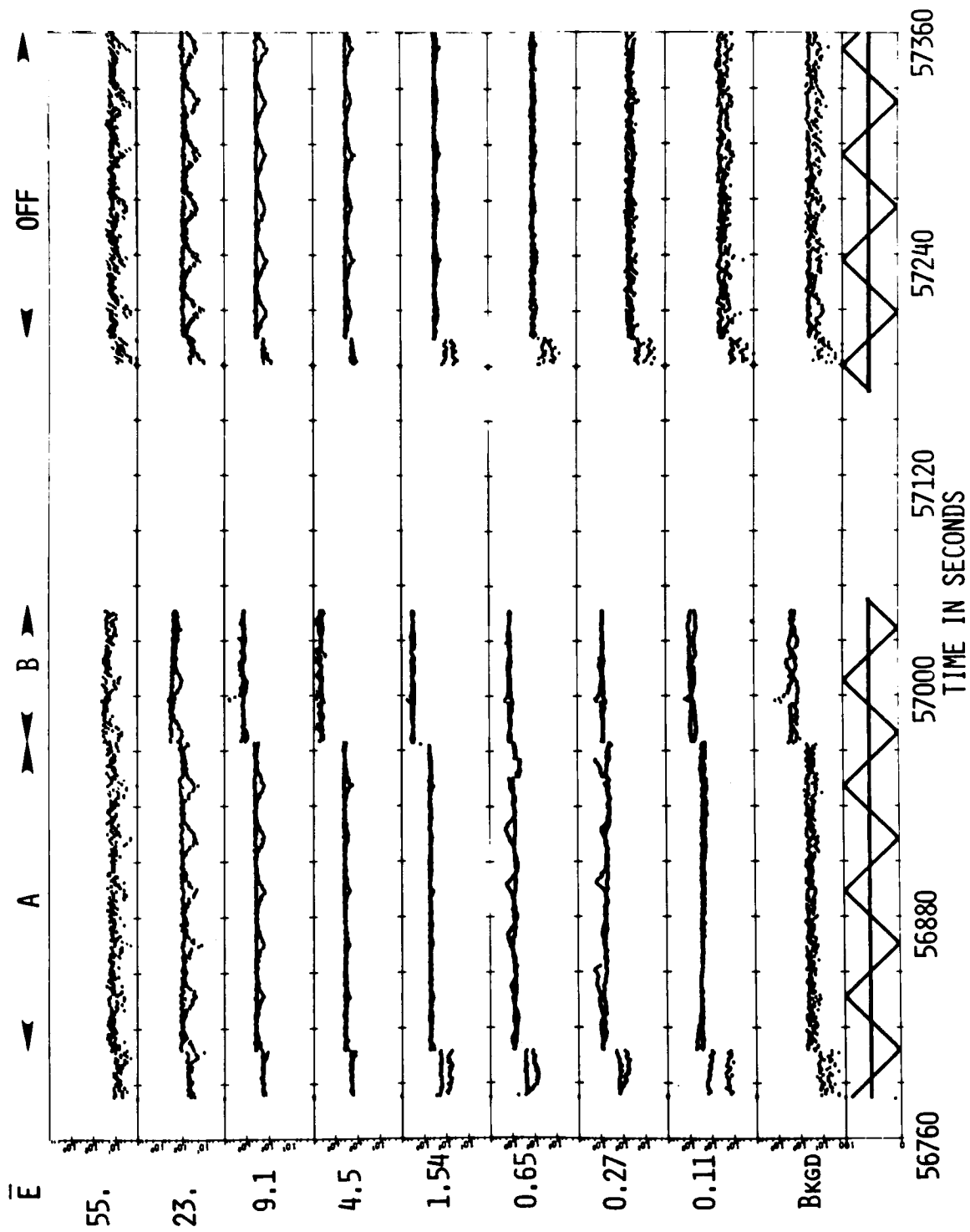


Figure 2 Electron count rates during electron beam operations in eclipse, March 30, 1979.

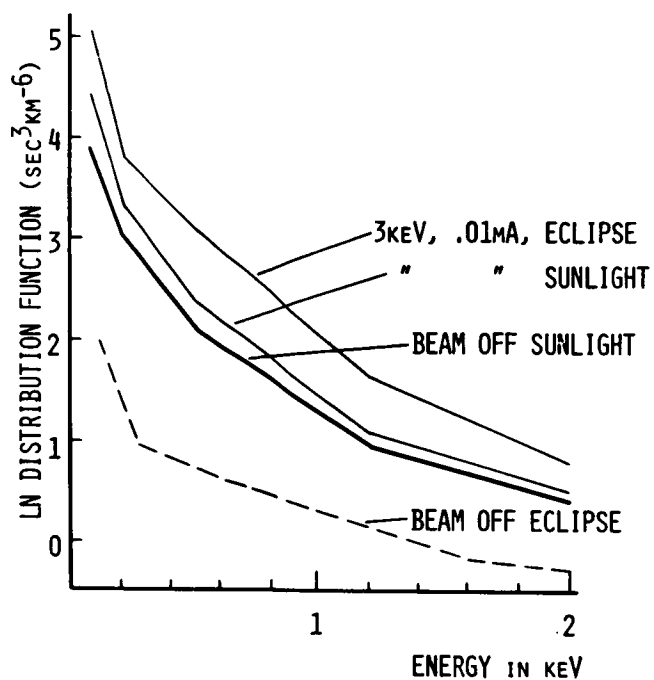


Figure 3 Electron distribution functions for low current electron beam operations on March 30, 1979.

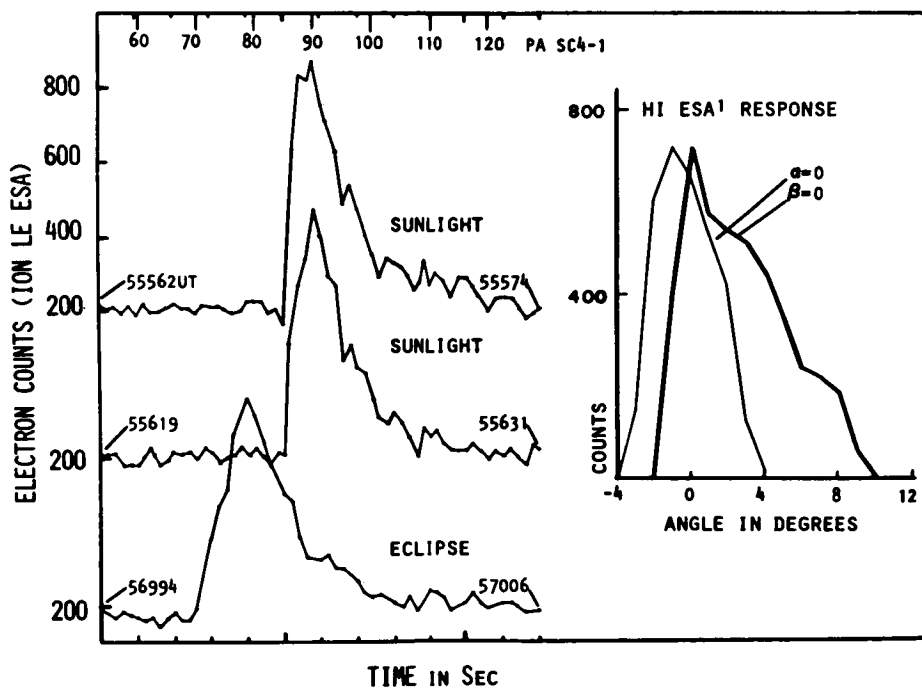


Figure 4 Count rates in the parallel ion detectors for electron beam emission perpendicular to the magnetic field.

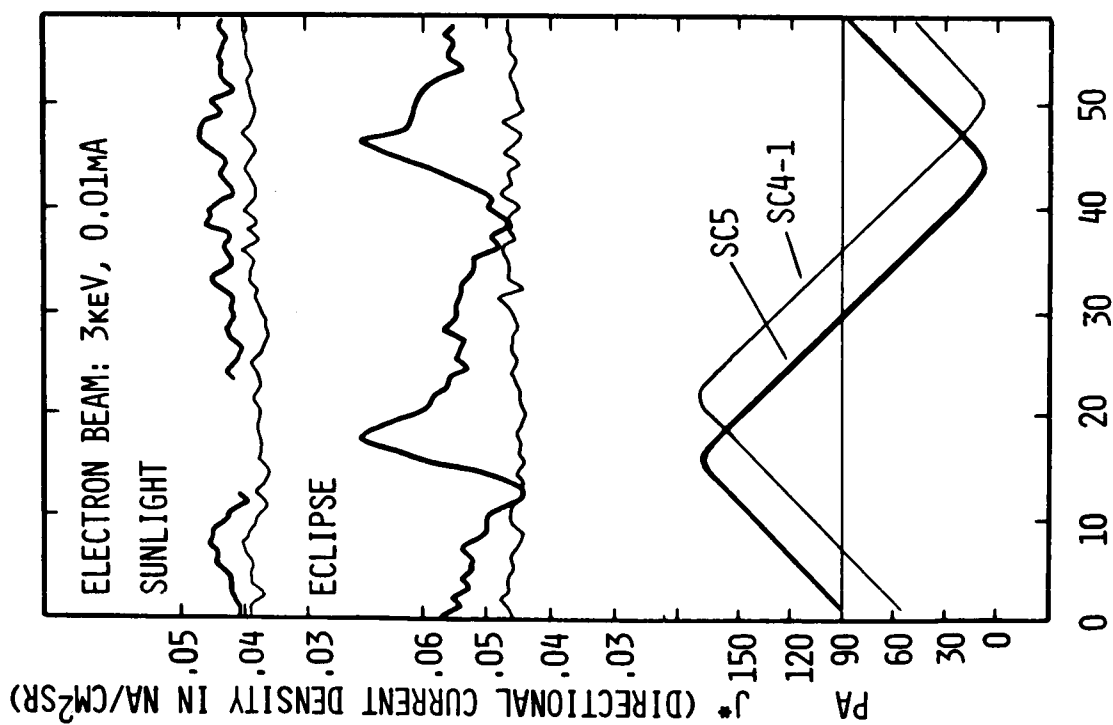


Figure 5 Directional current density for low current electron beam operations.

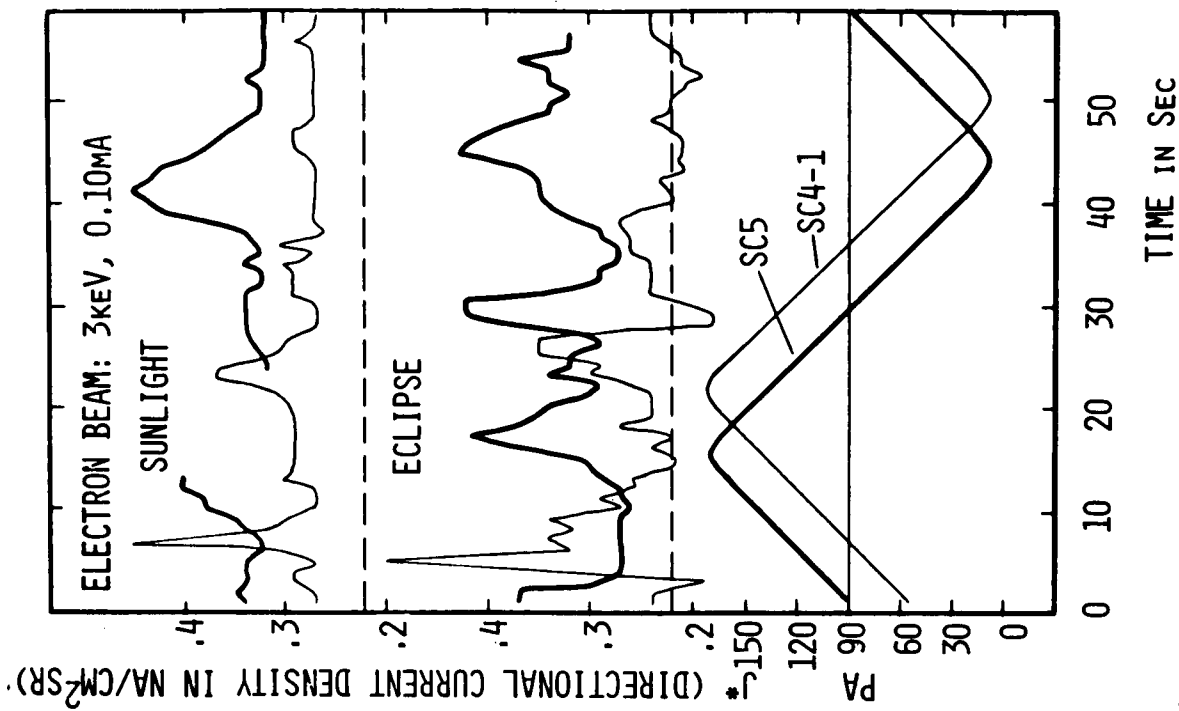


Figure 6 Directional current density for high current electron beam operations.

## COMPARISON OF NASCAP MODELING RESULTS WITH LUMPED-CIRCUIT ANALYSIS

David B. Stang and Carolyn K. Purvis  
NASA Lewis Research Center

### SUMMARY

One of the goals of spacecraft charging studies has been to develop engineering design tools that can be used to predict the development of absolute and differential potentials by "realistic" (i.e., complex in geometry and surface composition) spacecraft under geomagnetic substorm conditions. Two types of analyses are in current use. One is embodied in the NASCAP code, which computes quasi-static charging of geometrically complex objects with multiple surface materials in three dimensions. The second approach is represented by lumped-element equivalent circuit models that have been developed and used by several aerospace corporations for analyses of particular spacecraft. The equivalent circuit models have the advantage of requiring very little computation time. However, they cannot account for effects, such as the formation of potential barriers, that are inherently multidimensional. How much difference does this make in predictions of charging response? The study reported herein provides an answer to this question.

An available charging study for the Defense Satellite Communication System (DSCS-III) spacecraft was used for an equivalent circuit model. This report presents a charging study of this spacecraft made with the NASA Charging Analyzer Program (NASCAP). The spacecraft model is based on the description given in reference 1 and incorporates the material properties given therein. Charging simulation is done in the environment chosen for that study for both equinox and solstice insolation. Steady-state potentials of structure and insulation are compared with those resulting from the equivalent circuit model, and the differences are discussed.

### INTRODUCTION

Various computer models have been developed that attempt to predict surface charging of satellites in geosynchronous orbit. Among these are equivalent circuit models (refs. 1 and 2), one-dimensional Langmuir probe models (refs. 3 and 4), and multidimensional codes (refs. 5 to 7). The multidimensional studies have indicated the formation of potential barriers that cut off low-energy secondary and photoelectron emission, allowing the development of negative potentials on sunlit surfaces. By contrast, the equivalent circuit models generally assume that sunlit surfaces are held near space potential by photoemission. What effect do such simplifying assumptions have on the predicted charging response of a spacecraft? Desire for an answer to this question prompted the study reported herein.

This paper compares the charging predictions of an equivalent circuit model with those of a multidimensional code, NASCAP (ref. 5). The DSCS-III spacecraft was chosen for the comparison because an equivalent circuit study performed on it (ref. 1) also provided sufficient description of the spacecraft to allow development of a NASCAP model. The NASCAP model was



designed to represent the dimensions, geometry, and surface material distribution of DSCS-III as closely as possible. Three different sets of material property parameters were used: standard NASCAP properties, "group A" properties, and "group B" properties. Group A properties consist of the values for dielectric constant, thickness, and bulk conductivity specified in the circuit study and standard NASCAP values for all other material property parameters. Group B properties consist of the specified dielectric constant, thickness, and conductivity values plus a set of secondary electron yield parameters contrived to match as closely as possible the yield fractions used in the circuit study.

Although the equivalent circuit model produced only steady-state potentials, which provide the basis for comparison and are the focus of this report, some transient effects seen in NASCAP simulations are noted.

## SPACECRAFT MODEL

### Geometry

The geometry and dimensions of the DSCS-III satellite and its NASCAP model are illustrated in figures 1 and 2. Areas of various surface materials are listed for both in table I and compared in terms of absolute area and percentage. The NASCAP model is defined in terms of rectangular parallelipeds, octagons, wedges, flat plates, and booms inside a 17x17x33 grid. The length of each grid cell represents a length of 0.3 meter. Each cell on the model's surface is assumed to consist of some material specified in the object's definition. The surfaces and solar arrays are dotted with cells specified to have conducting surfaces representing the exposed metal typically found on spacecraft.

Two models were devised: one for the dawn condition with the solar array wings oriented as shown in figure 2, and one for the eclipse case with the solar arrays rotated 90° so that they face "Earthward." The solar arrays are represented as flat plates, which must be in orthogonal grid planes. The GDA and MBA antennas are modeled as protruding octagons and rectangles because their shadowing effects and relative size can influence the results.

### Materials

The eight materials used for the surfaces of the DSCS-III were modeled in three different ways. First, materials similar to the actual DSCS-III materials were selected from NASCAP's library: "ASTROQUARTZ" for the silica blankets, "SI02" for OSR's, "SOLAR" for the solar arrays, "NPAINT" (nonconducting paint) for Chemglaze, "ITO" for indium tin oxide, and "ALUMINUM" for the exposed metal. Second, the explicitly defined properties of dielectric constant, thickness, and resistivity, as given in reference 1, were inserted for each material, with all other material parameters remaining standard NASCAP. This set of properties is referred to herein as "group A." Third, the materials' secondary electron yield property parameters were also adjusted in order to reproduce as closely as possible the secondary yields specified in the lumped-circuit study. This set is referred to as "group B."

The rationale for using these several sets of material properties was to examine different aspects of the charging response of the model. The first set, standard NASCAP, provides a baseline. The group A parameters represent those likely to be chosen by a spacecraft designer using NASCAP. The group B parameters should allow identification of the magnitude of dimensional effects by eliminating as much as possible those effects due to differences in secondary electron yield formulations between NASCAP and the lumped-circuit model.

Parameters for use in the group B property set were devised by using MATCHG, a simple code that incorporates the NASCAP secondary electron yield formulations. MATCHG does a one-dimensional calculation for charging of a single material surface by using a spherical probe approximation in conjunction with a specified Maxwellian (or double Maxwellian) flux. Two secondary electron yield formulations are available: "NORMAL," which calculates yields assuming normally incident primaries; and "ANGLE," which assumes isotropic primaries.

To calculate secondary electron emission from electron impact, NASCAP uses six material properties: four that determine the shape of the curve displaying normalized yield as a function of primary energy; the maximum yield for normally incident primaries,  $\delta_m$ ; and the primary energy at which  $\delta_m$  occurs,  $E_m$ . Backscattered electron yield is calculated by using the atomic number  $z$ . Calculation of secondary electron yield due to proton impact as a function of incoming proton energy requires two parameters: primary energy for maximum power loss (designated  $E_p$ ), and electron yield for 1-keV protons incident. For more discussion of these parameters see, for example, references 7 and 8.

Massaro and Ling's (ref. 1) secondary electron yield coefficients are simply constant fractions indicating secondary electrons out per primary electron or ion. The values given, 0.75 for all dielectrics and 0.50 for all metals, apply to both electron and ion-generated secondaries. These fractions include backscattered as well as "true" secondary electrons. As part of its charging calculations, MATCHG prints out the various current densities to the surface material being charged at various times. In this work the initial values of the current densities were used. For each material the ratio of electron-induced secondary electron plus backscattered electron current densities to incident electron current density was computed and taken as the "yield fraction." The maximum yield was then varied, and the calculation was repeated until the desired yield fraction was obtained (0.75 for dielectrics, 0.50 for metals). Similarly, the ratio of ion-induced secondary electron current density to incident ion current density was computed, and this fraction was adjusted by varying the yield for 1-keV primaries incident. This procedure was followed for each material, for both secondary emission formulations (ANGLE and NORMAL), and produced two sets of group B parameter values per material, either of which generates the proper initial fractions for the secondary yield coefficients. All of this was done by using the same environment to be used in the later NASCAP calculations. The same environment was used because in the NASCAP formulations the yield fractions depend on the environment as well as on the material properties.

Table II summarizes the material property parameter sets (standard NASCAP, group A, group B (ANGLE), and group B (NORMAL)) used for this study. Included are the initial secondary yield fractions for each set of

secondary yield parameters, labeled  $f_e$  (electrons) and  $f_p$  (protons). Changing the yield fractions can have a significant effect on charging response, as is illustrated in figure 3, where MATCHG's predicted equilibrium potentials are plotted as a function of yield fraction for the optical solar reflector (OSR) properties (see also ref. 8).

### Study Description

The plasma environment chosen for this study is that used by Massaro and Ling (ref. 1) for a "severe substorm." It is a single Maxwellian distribution characterized by  $kT_e = 7$  keV,  $kT_i = 8.8$  keV,  $j_{e0} = 0.5$  nA/cm<sup>2</sup>, and  $j_{i0} = 10$  pA/cm<sup>2</sup>. NASCAP requires number densities rather than current densities as input, so conversion was made by the formula

$$n = \frac{j_0}{e} \left( \frac{kT}{2\pi m} \right)^{-1/2}$$

for each species. Number densities were calculated to be  $n_e = n_i = 2/\text{cm}^3$ . All calculations used this plasma environment definition.

Three different sunlight conditions were investigated: dawn at equinox, dawn at summer solstice, and midnight at equinox. Various combinations of material properties, secondary emission formulation, and insolation were examined; these are summarized in table III. For each case the simulation began with all surfaces at zero potential and was allowed to run for 40 minutes of simulated time to reach equilibrium. By contrast, Massaro and Ling's results (ref. 1) are given as equilibrium potentials hour by hour as the Sun angle changes.

From the standpoint of a hypothetical designer using NASCAP to study charging for this spacecraft, the group A property set seems the logical choice. Given this set of material properties the NORMAL secondary yield formulation represents a "worst case" in a given environment, and the ANGLE formulation represents a "most probable" case. For this study emphasis is on the worst case situation (i.e., NORMAL formulation), but results for the ANGLE case in the dawn equinox condition are also presented for comparison.

## RESULTS

### Dawn at Equinox

As is evident from table III the dawn-at-equinox case was the most thoroughly examined. It is therefore used as a "baseline" case with which to compare results obtained by using the various sets of NASCAP material parameters, as well as for comparing NASCAP and circuit model results. Differences among NASCAP results with the group A (ANGLE), group A (NORMAL), and group B properties should indicate the influence of secondary electron yields on predicted potentials. Differences between group B and circuit model results should indicate the influence of three-dimensional effects such as potential barrier formation.

As can be seen from table II the secondary electron yield fractions for group A properties with the ANGLE formulation are larger than those for group A properties with the NORMAL formulation. The group B properties

yield fraction for incident electrons (0.75) is between the two group A fractions for most of the insulators. This would lead one to expect the group A (NORMAL) properties to result in the most negative absolute potentials, the group A (ANGLE) properties to yield the least negative absolute potentials, and the group B properties to yield intermediate results. That this is the case can be seen from the summary of steady-state potentials for these cases given in table IV. The table also illustrates the sensitivity of the results to the choice of secondary electron yield parameters and formulation. Clearly the magnitude of the absolute potentials is dramatically affected by the choice of yield formulation. The differential potentials ("deltas") are also strongly affected in magnitude and in some cases also in polarity. In this table and subsequent ones, the insulator potentials listed are for the appropriate insulator cell having the largest differential potential.

Results obtained by using the group B properties are similar to those obtained by using group A (NORMAL); that is, they yield more nearly a worst case than does a nominal set of NASCAP predictions. This is particularly interesting when the NASCAP results are compared with those of the circuit study. From table V and figure 4 it is apparent that, with the exception of the OSR's, predicted absolute potentials from the circuit study resemble those from the group A (ANGLE) calculation much more nearly than those from the group A (NORMAL) or group B calculations. The circuit study's predicted OSR potentials alone are similar to the worst-case NASCAP predictions. There are also notable differences in predicted structure potential. The two worst-case NASCAP calculations yield structure potentials in the range -2 to -3 kilovolts. Even the group A (ANGLE) calculation yields a structure potential of -645 volts, more than three times the circuit study's prediction of -200 volts. This is undoubtedly due to the formation of potential barriers that suppress emission of low-energy secondary electrons and photoelectrons, an effect which NASCAP accounts for but for which the circuit code cannot.

For assessing potentially hazardous areas absolute potentials are of less interest than differential potentials across insulation because the latter represents the electric stress on a material. The differential potentials are listed in tables IV and V as "deltas," and illustrated in figure 4 by the cross-hatched areas. They are somewhat easier to see when plotted separately from the structure potentials, as is done in figure 5. Here it is clear that, despite the similarity in absolute potentials of the OSR's for the circuit study and the worst-case NASCAP calculations, the circuit study predicts a much larger stress on this material (-5.2 kV as compared with -2.8 kV for NASCAP).

On the other hand, both the group A (NORMAL) and the group B NASCAP calculations predict relatively large differentials across the silica cloth composite on the MBA antennas, and across the 570 cloth on the Earth coverage horn, which were predicted by the circuit study to have much lower stresses. The NASCAP values quoted are for shaded portions of these materials and indicate that these are potentially hazardous areas from a charging standpoint that were not identified in the circuit study. NASCAP also predicts much larger differentials for the 527 silica cloth on the north and south panels than does the circuit study.

### Dawn: Equinox Compared with Solstice

The circuit study found dramatic differences in the potentials of the south panel's 527 silica cloth and OSR's between equinox and summer solstice conditions of illumination: the south OSR's were at -5.37 kilovolts at equinox and zero volt at solstice, and the 527 cloth was at -0.365 volt at equinox and zero volt at solstice. By contrast, NASCAP predicted only slight differences in the south panel potentials for the two conditions. Table VI summarizes the absolute potentials of the spacecraft and the north and south panel surfaces as computed by NASCAP using group A (NORMAL) and as given by the circuit study. Corresponding differential potentials are illustrated in figure 6. The lack of dramatic change in the south panel potentials between equinox and solstice is evidently a combined consequence of the low Sun angle ( $67^\circ$  to the surface normal) and the formation of local potential barriers.

As was the case for equinox the worst-case NASCAP predictions of differential potentials on shaded OSR's are smaller than those from the circuit study, but the silica cloth is predicted to have larger differential potentials by NASCAP.

### Midnight at Equinox

The final condition examined was passage into eclipse. For this condition the NASCAP simulation was begun with all surfaces at zero potential in sunlight and continued until equilibrium was reached. Then the Sun was "turned off" to simulate eclipse entry, and the computation was continued until steady state was again attained. Steady-state potentials are given in table VII. The values listed as "before eclipse" for the NASCAP computation are those just before eclipse entry. They are compared to values quoted for a time of 2300 in the circuit study. The values listed as "during eclipse" are NASCAP's equilibrium values (at about 20 min after eclipse entry) and the circuit study's values for a time of 2400. For this condition Massaro and Ling (ref. 1) present potentials only for the structure and the OSR material, which had the largest differential potential.

Results from the two computations are strikingly different. The circuit study results indicate a dramatic change in structure potential in eclipse (-14.16 kV as compared with -240 V in sunlight) and a concurrent dramatic reduction in differential potentials (160 V as compared with -5.16 kV on the OSR's in sunlight). The latter implies that all the insulators have potentials within 160 volts of the structure potential according to this model. The NASCAP calculation (group A (NORMAL)) predicts a larger structure potential in sunlight (-3.03 kV) with smaller differential potential across the OSR's, which is consistent with results from the dawn computations, and a much less dramatic shift in structure potential in eclipse (to -6.98 kV). As is indicated in figure 7 for most materials, the differential potentials are predicted to be smaller in eclipse. There is, however, one striking exception: SOLAR, which is the material used to model the solar array cover slips, has a large positive differential of 1.8 kilovolts. This polarity differential has not been investigated extensively in spacecraft charging studies, but work has been done in conjunction with high-voltage power system studies (e.g., ref. 9). The latter have observed arcing on solar array segments biased so that the

cover slips are positive relative to the interconnects in the presence of plasmas. Although 1.8 kilovolts is not expected to be sufficient to cause such arcing in geosynchronous orbit (5 kV is quoted in ref. 9), such large positive differentials have not been examined for potential charging hazards and thus remain suspect.

## TRANSIENT RESPONSE AND SPATIAL VARIATIONS

To this point, all results have been given in terms of steady-state potentials and maximum differential potentials across insulating areas of the spacecraft. In fact, sunlit spacecraft are known to require tens of minutes to attain equilibrium potentials (e.g., ref. 10), and large areas of insulation do not necessarily reach uniform equilibrium potentials. A few interesting temporal and spatial variations that were evident from the NASCAP calculations are discussed in this section.

Figure 8 shows the charging response of several materials and the spacecraft structure for the dawn-at-equinox condition and group A (NORMAL). Here it is clear that the various materials charge at different rates. In a constant environment such as the one used for this calculation, the absolute potentials tend to be monotonic functions of time. However, the differential potentials  $\Delta\phi$  across insulation are not necessarily monotonic, as is illustrated in figure 9, where differential potentials for the figure 8 case are plotted. The OSR shows a monotonic  $\Delta\phi$ , but neither the solar material nor the 570 composite on the MBA antenna does. The differential across the MBA composite early in the simulation is larger than its equilibrium value by about 1 kilovolt. In fact, this was the largest differential potential (-3.8 kV) observed in this study. Thus equilibrium values of differential potential do not necessarily represent a worst case.

Another interesting phenomenon is "overshoot" in absolute potentials of insulating surfaces caused by a sudden change in environment such as entry eclipse. This is illustrated in figure 10, in which the Chemglaze and OSR materials reach absolute potentials more negative than their equilibrium potentials shortly after eclipse entry. In this case differential potentials are maintained at about the pre-eclipse levels during the "overshoot." This type of behavior has been observed in ground-based electron spraying experiments (ref. 11). It is illustrated here to emphasize the point that, even in eclipse, times of the order of tens of minutes may be required for equilibration.

Even in equilibrium, insulating areas are generally not at uniform potentials. The amount of potential variation over an area depends in a complex manner on the geometry, illumination, and material properties of both the insulator in question and the surfaces around it. The complexity of these dependences makes it difficult to generalize. For the worst-case sunlit conditions investigated for this study, typical variations of potential across insulating areas were of the order of 1 kilovolt. Maximum variations, for example, on the MBA composite cloth, were about 2 kilovolts, and minimum variations, on the Chemglaze and OSR's were 100 volts. The 2-kilovolt maximum variations are large enough to suggest the possibility of surface arcing. Figure 11 illustrates the variation in differential potentials with position on the solar array wings for a dawn-at-equinox condition. The solid line (labeled  $x = 0$ ) represents differential potential along the center of the array; the dashed line ( $x = 2$ ) represents

differentials along an edge. The potential variations are clearly nonlinear and are steeper and more negative near the body of the spacecraft.

### CONCLUSIONS

Based on the results of this study it is believed that, although an equivalent circuit analysis may provide a rough estimate of charging effects, an early design check using NASCAP is warranted. For the case of DSCS-III, the NASCAP analysis raised concerns about charging of the silica composites on the MBA antennas and Earth coverage horn that were not identified in the circuit study. The time-dependent calculation performed by NASCAP provides important information because of the long time required for equilibration and the fact that differential potentials may not be maximum at equilibrium (again the MBA composite provides an example).

Finally, it is noteworthy that one of the authors (David B. Stang) who developed the NASCAP model of DSCS-III and ran all the computer calculations, did so entirely within a 12-week student assignment at NASA Lewis as a summer employee. That he was able to accomplish this helps to substantiate the claim that NASCAP is indeed a user-oriented code.

### REFERENCES

1. Massaro, M. J.; and Ling, D.: Spacecraft Charging Results for the DSCS-III Satellite. Spacecraft Charging Technology - 1978, NASA CP-2071, AFGL TR-79-0082, 1979, pp. 158-178.
2. Inouye, G. T.: Spacecraft Potentials in a Substorm Environment. Spacecraft Charging by Magnetospheric Plasmas, A. Rosen, ed., Progress in Astronautics and Aeronautics, Vol. 47, American Institute of Aeronautics and Astronautics, Inc., 1976, pp. 103-120.
3. DeForest, S. E.: Spacecraft Charging at Synchronous Orbit. J. Geophys. Res., vol. 77, Feb. 1, 1972, pp. 651-659.
4. Garrett, H. B.: The Calculation of Spacecraft Potential - Comparison Between Theory and Observation. Spacecraft Charging Technology - 1978, NASA CR-2071, AFGL TR-79-0082, 1979, pp. 239-255.
5. LaFramboise, J. G.; Godard, R.; and Prokopenko, S. M. L.: Numerical Calculations of High-Altitude Differential Charging: Preliminary Results. Spacecraft Charging Technology - 1978, NASA CP-2071, AFGL TR-79-0082, 1979, pp. 188-196.
6. Katz, I.; et al.: The Capabilities of the NASA Charging Analyzer Programs. Spacecraft Charging Technology - 1978, NASA CP-2071, AFGL TR-79-0082, 1979, pp. 101-122.
7. Katz, I.; et al.: A Three Dimensional Dynamic Study of Electrostatic Charging in Materials. (SSS-R-77-3367, Systems, Science and Software; NASA Contract NAS3-20119.) NASA CR-135256, 1977.
8. Purvis, C. K.: Effects of Secondary Yield Parameter Variation on Predicted Equilibrium Potential of an Object in a Charging Environment. NASA TM-79299, 1979.
9. Stevens, N. J.: Interactions Between Spacecraft and the Charged Particle Environment. Spacecraft Charging Technology - 1978, NASA CP-2071, AFGL TR-79-0082, 1979, pp. 268-294.

10. Purvis, C. K.: Configuration Effects on Satellite Charging Response. AIAA Paper 80-0040, Jan. 1980. (Also NASA TM-81397, 1980.)
11. Purvis, C. K.; et al.: Charging Rates of Metal-Dielectric Structures. Spacecraft Charging Technology - 1978, NASA CP-2071, AFGL TR-79-0082, 1979, pp. 507-523.

TABLE I. - AREAS OF SURFACE MATERIALS FOR DSCS-III AND NASCAP MODEL

Spacecraft area	DSCS-III	NASCAP model	Material	DSCS-III	NASCAP model
	Area, m <sup>2</sup>			Area, percent of total	
Earth-facing side	5.28	4.86	527 Silica cloth	35.5	37.0
			570 Silica cloth	12.2	11.1
			Composite silica cloth	44.7	48.2
			Indium tin oxide	.07	1.2
			Exposed metal	7.5	5.6
North panel	4.82	5.13	527 Silica cloth	54.8	61.4
			OSR glass	40.0	35.1
			Exposed metal	5.2	3.5
South panel	5.81	5.13	527 Silica cloth	82.9	73.7
			OSR glass	12.4	12.3
			Exposed metal	4.6	5.3
East panel	3.45	3.51	527 Silica cloth	98.6	97.5
			Exposed metal	3.2	2.5
West panel	3.41	3.51	527 Silica cloth	97.5	97.5
			Exposed metal	2.5	2.5
Back side	5.28	4.86	527 Silica cloth	98.7	98.2
			Exposed metal	1.3	1.0
Solar arrays: Sun side	12.18	10.8	Solar array coverslips	96.0	91.7
			527 Silica cloth	4.0	3.3
			Exposed metal	----	5.0
Back side	12.27	10.8	Chemglaze	100.0	100.0



TABLE II. - MATERIAL PROPERTY PARAMETER SETS

Property	Material							
	527 Silica cloth	570 Silica cloth	Composite silica cloth	OSR glass	Solar array cover-slips	Chem-glaze	Indium tin oxide	Exposed metal (Al)
Dielectric constant: NASCAP Groups A and B	3.8 1.7	3.8 1.9	3.8 1.12	4.0 4.5	3.8 7.0	3.5 2.2	1 2.4	1 1
Thickness, cm: NASCAP Groups A and B	0.028 0.030	0.028 0.068	0.028 0.605	0.013 0.020	0.0179 0.0152	0.005 0.005	----- 0.305	0.10 0.10
Conductivity, mho/cm: NASCAP Groups A and B	2.75x10 <sup>-12</sup> 1x10 <sup>-13</sup>	2.75x10 <sup>-12</sup> 1x10 <sup>-14</sup>	2.75x10 <sup>-12</sup> 1x10 <sup>-14</sup>	1x10 <sup>-14</sup> 1.3x10 <sup>-14</sup>	1x10 <sup>-17</sup> 2.1x10 <sup>-15</sup>	5.9x10 <sup>-14</sup> 3x10 <sup>-14</sup>	----- -----	----- -----
Atomic number	10	10	10	10	10	5	10	13
Mean atomic weight, amu	1.02	1.02	1.02	1.02	3.15	1.05	-----	-----
Photocurrent, mA/cm <sup>2</sup>	0.02	0.02	0.02	0.02	0.02	0.02	0.032	0.04
Surface resistivity, $\Omega$	1x10 <sup>11</sup>	1x10 <sup>11</sup>	1x10 <sup>11</sup>	1x10 <sup>19</sup>	1x10 <sup>19</sup>	1x10 <sup>13</sup>	-----	-----
Standard NASCAP and group A: Maximum secondary energy for normally incident primary electrons, $\delta_m$ Primary energy for maximum secondary yield, $E_m$ Initial secondary yield fraction for electrons, $f_e$ : ANGLE NORMAL	2.4 0.4	2.4 0.4	2.4 0.4	2.4 0.4	4.1 0.41	2.1 0.15	2.205 0.335	0.97 0.3
Secondary yield for 1-keV incident protons, $\delta_p$ Primary proton energy for maximum power loss, $E_p$ Initial secondary yield fraction for protons, $f_p$ : ANGLE NORMAL	0.983 0.663 0.455 140	0.983 0.663 0.455 140	0.983 0.663 0.455 140	0.983 0.663 0.455 140	1.28 0.904 0.244 230	0.824 0.412 0.455 140	1.22 0.781 0.49 123	0.679 0.524 1.5 230
	3.09 1.55	3.09 1.55	3.09 1.55	3.09 1.55	3.10 1.56	3.10 1.56	0.364 0.182	1.19 0.057

TABLE II. - Concluded.

Property	Material							
	527 Silica cloth	570 Silica cloth	Composite silica cloth	OSR glass	Solar array cover-slips	Chem-glaze	Indium tin oxide	Exposed metal (Al)
Group B (ANGLE): Maximum secondary energy for normally incident primary electrons, $\delta_m$ Primary energy for maximum secondary yield, $E_m$ Initial secondary yield fraction for electrons, $f_e$ Secondary yield for 1-keV incident protons, $\delta_p$ Primary proton energy for maximum power loss, $E_p$ Initial secondary yield fraction for protons, $f_p$	1.54	1.54	1.54	1.54	1.51	3.0	0.409	0.415
	0.4	0.4	0.4	0.4	0.41	0.15	0.335	0.3
	0.75	0.75	0.75	0.75	0.75	0.75	0.50	0.50
	0.110	0.110	0.110	0.110	0.110	0.110	0.0753	0.0695
	140	140	140	140	140	140	123	230
	0.75	0.75	0.75	0.75	0.75	0.75	0.50	0.50
Group B (NORMAL): Maximum secondary energy for normally incident primary electrons, $\delta_m$ Primary energy for maximum secondary yield, $E_m$ Initial secondary yield fraction for electrons, $f_e$ Secondary yield for 1-keV incident protons, $\delta_p$ Primary proton energy for maximum power loss, $E_p$ Initial secondary yield fraction for protons, $f_p$	3.04	3.04	3.04	3.04	2.99	6.0	0.819	0.823
	0.4	0.4	0.4	0.4	0.41	0.15	0.335	0.3
	0.75	0.75	0.75	0.75	0.75	0.75	0.50	0.50
	0.220	0.220	0.220	0.220	0.220	0.220	0.151	0.139
	140	140	140	140	140	140	123	230
	0.75	0.75	0.75	0.75	0.75	0.75	0.50	0.50

TABLE III. - CONDITIONS TESTED

Material group	Equinox		Solstice	
	Dawn		Midnight (NORMAL)	Dawn (NORMAL)
	NORMAL	ANGLE		
Standard NASCAP	x	x		
Group A	x	x	x	x
Group B	x	x		x

TABLE IV. - DAWN-AT-EQUINOX STEADY-STATE POTENTIALS

Component	Material group					
	A (NORMAL)		A (ANGLE)		B	
	Dawn-at-equinox steady-state potential, kV					
	Absolute	Delta	Absolute	Delta	Absolute	Delta
Spacecraft structure	-2.69	-----	-0.645	-----	-2.14	-----
North OSR	-5.48	-2.79	-.825	-0.18	-5.05	-2.92
South OSR	-5.44	-2.75	-.825	-.18	-5.05	-2.92
Chemglaze	-3.25	-1.26	-1.47	-.825	-2.94	-.80
Solar array coverslips	-2.39	+.300	-.724	-.079	-1.83	+.31
North panel (527 silica cloth)	-4.17	-1.48	-.821	-.176	-3.55	-1.41
South panel (527 silica cloth)	-3.80	-1.11	-.835	-.190	-3.15	-1.01
East panel	-2.64	+.050	-.514	+.131	-2.22	-.08
West panel	-3.75	-1.06	-.756	-.111	-3.09	-.95
Earth-facing side	-4.49	-1.80	-.561	+.084	-3.93	-1.79
Back side	-3.78	-1.29	-.508	+.137	-3.31	-1.17
MBA (570 silica cloth)	-5.48	-2.79	-.564	+.081	-4.93	-2.79
570 Silica cloth (Earth coverage horn)	-5.54	-2.85	-.502	+.143	-5.06	-2.92

TABLE V. - DAWN-AT-EQUINOX STEADY-STATE POTENTIALS -  
COMPARISON WITH CIRCUIT STUDY

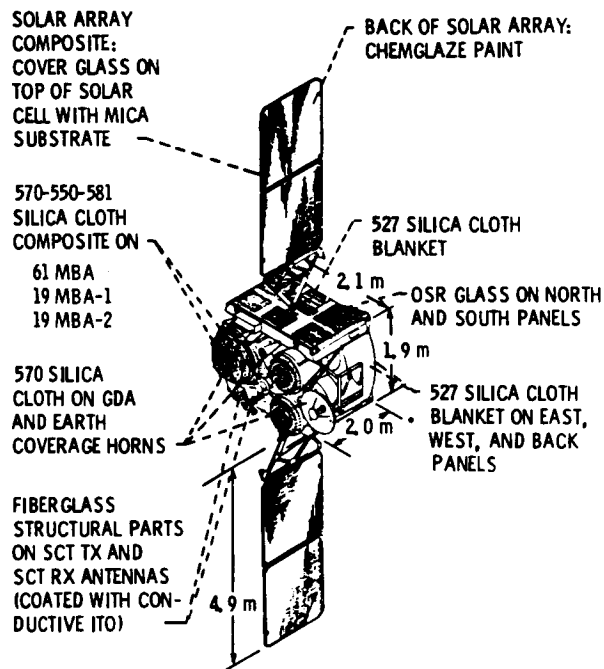
Component	Circuit study		Material group					
			A (ANGLE)		B		Standard NASCAP (ANGLE)	
			Dawn steady-state potential, kV					
	Absolute	Delta	Absolute	Delta	Absolute	Delta	Absolute	Delta
Spacecraft structure	-0.20	-----	-0.645	-----	-2.14	-----	-0.167	-----
North OSR	-5.37	-5.17	-.825	-0.18	-5.05	-2.92	-.219	-.052
South OSR	-5.37	-5.17	-.825	-.18	-5.05	-2.92	-.219	-.052
Chemglaze	-1.56	-1.36	-1.47	-.825	-2.94	-.80	-.382	-.215
Solar array coverslips	0	+2.00	-.724	-.079	-1.83	+3.1	-.20	-.033
North panel (527 silica cloth)	-.365	-.165	-.821	-.176	-3.55	-1.41	-.224	-.057
South panel (527 silica cloth)	-.365	-.165	-.835	-.190	-3.15	-1.01	-.210	-.043
East panel	0	+2.00	-.514	+1.131	-2.22	-.08	-.122	+0.045
West panel	-.365	-.165	-.756	-.111	-3.09	-.95	-.383	-.216
Earth-facing side	-.365	-.165	-.561	+0.084	-3.93	-1.79	-.172	-.005
Back side	0	+2.00	-.508	+1.137	-3.31	-1.17	-.156	+0.011
MBA (570 silica cloth)	-.490	-.29	-.564	+0.081	-4.93	-2.79	-.150	+0.017
570 Silica cloth (Earth coverage horn)	-.420	-.220	-.502	+1.143	-5.06	-2.92	-.146	+0.021
Indium tin oxide	-.198	+0.002	-.645	-----	-2.14	-----	-.167	-----

TABLE VI. - COMPARISON OF DAWN STEADY-STATE POTENTIALS  
FOR EQUINOX AND SOLSTICE

Component	Equinox		Solstice	
	Group A (NORMAL)	Circuit study	Group A (NORMAL)	Circuit study
	Dawn steady-state potential, kV			
Spacecraft structure	-2.69	-0.200	-2.70	-0.176
North OSR	-5.48	-5.37	-5.44	-5.35
South OSR	-5.44	-5.37	-5.39	0
North panel (527 silica cloth)	-4.17	-.365	-4.15	-.340
South panel (527 silica cloth)	-3.80	-.365	-3.56	0

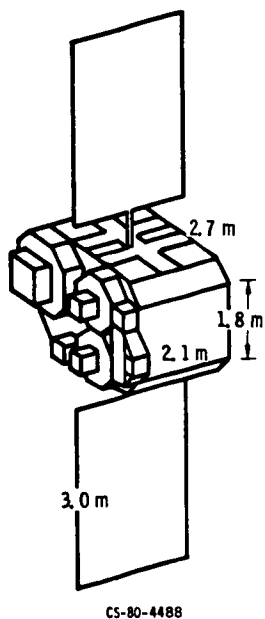
TABLE VII. - MIDNIGHT STEADY-STATE POTENTIALS AT EQUINOX

Component	Before eclipse				During eclipse			
	Group A (NORMAL)		Circuit study		Group A (NORMAL)		Circuit study	
	Midnight steady-state potential, kV							
	Absolute	Delta	Absolute	Delta	Absolute	Delta	Absolute	Delta
Spacecraft structure	-3.03	-----	-0.24	-6.98	-----	-----	-14.16	-----
OSR	-5.65	-2.62	-5.40	-7.91	-0.930	-0.930	-14.0	+0.16
Solar array coverslips	-2.92	+1.10	-----	-5.90	+1.80	+1.80	-----	-----
Chemglaze	-4.21	-1.18	-----	-7.36	-.390	-.390	-----	-----
East panel	-4.20	-1.17	-----	-7.06	-.080	-.080	-----	-----
West panel	-4.25	-1.12	-----	-7.06	-.080	-.080	-----	-----



CS-80-4488

Figure 1. - DSCS-III spacecraft.



CS-80-4488

Figure 2. - NASCAP model of DSCS-III.

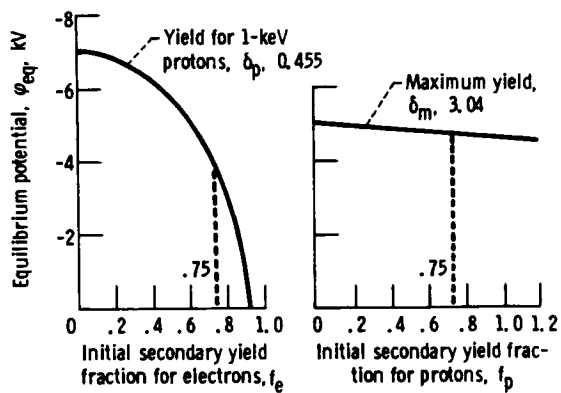


Figure 3. - MATCHG predicted equilibrium potentials as a function of secondary electron yield fraction for optical solar reflectors - NORMAL formulation. Primary energy for maximum secondary yield,  $E_m$ , 0.4 keV; primary proton energy for maximum power loss,  $E_p$ , 140 keV.



Figure 4. - Dawn-at-equinox steady-state potentials.

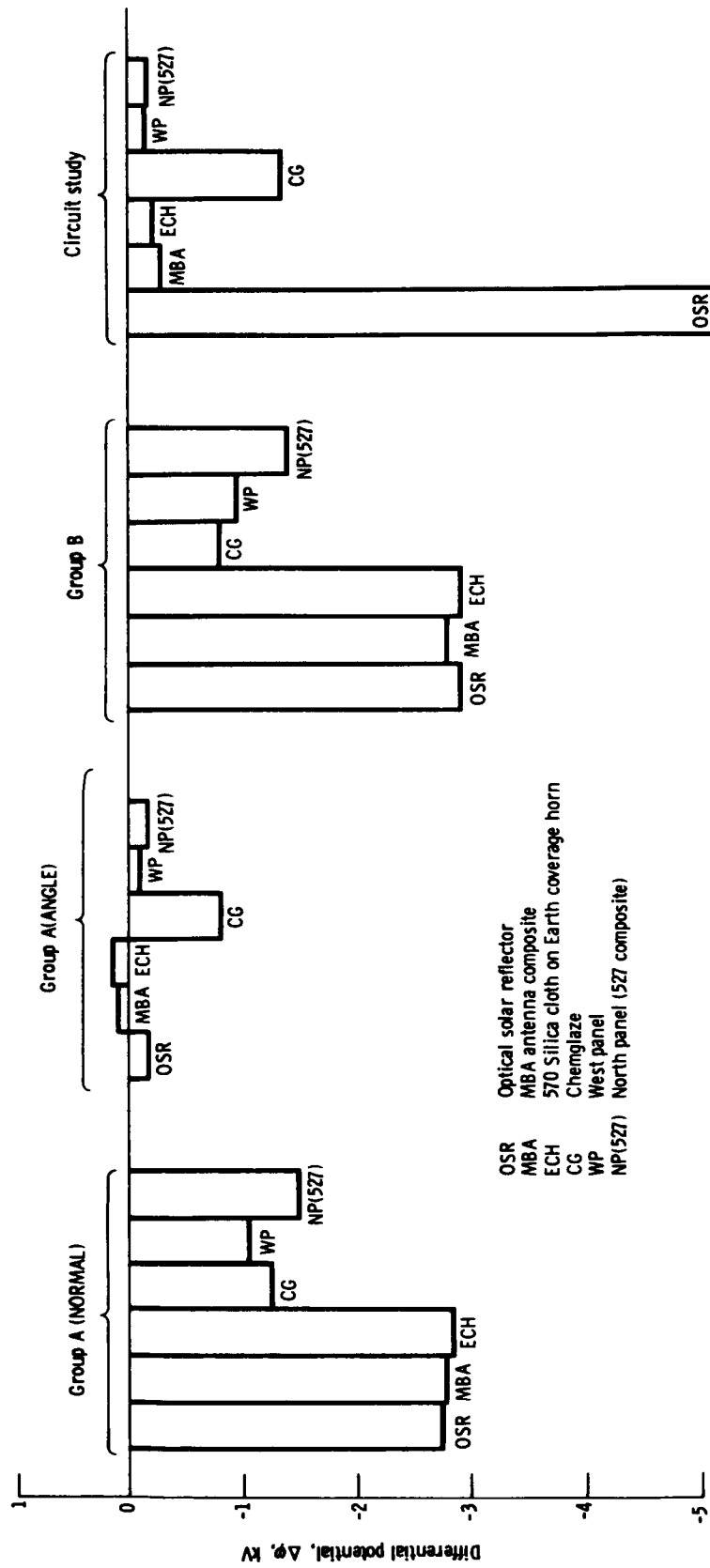


Figure 5. - Dawn-at-equinox differential potentials of selected materials.

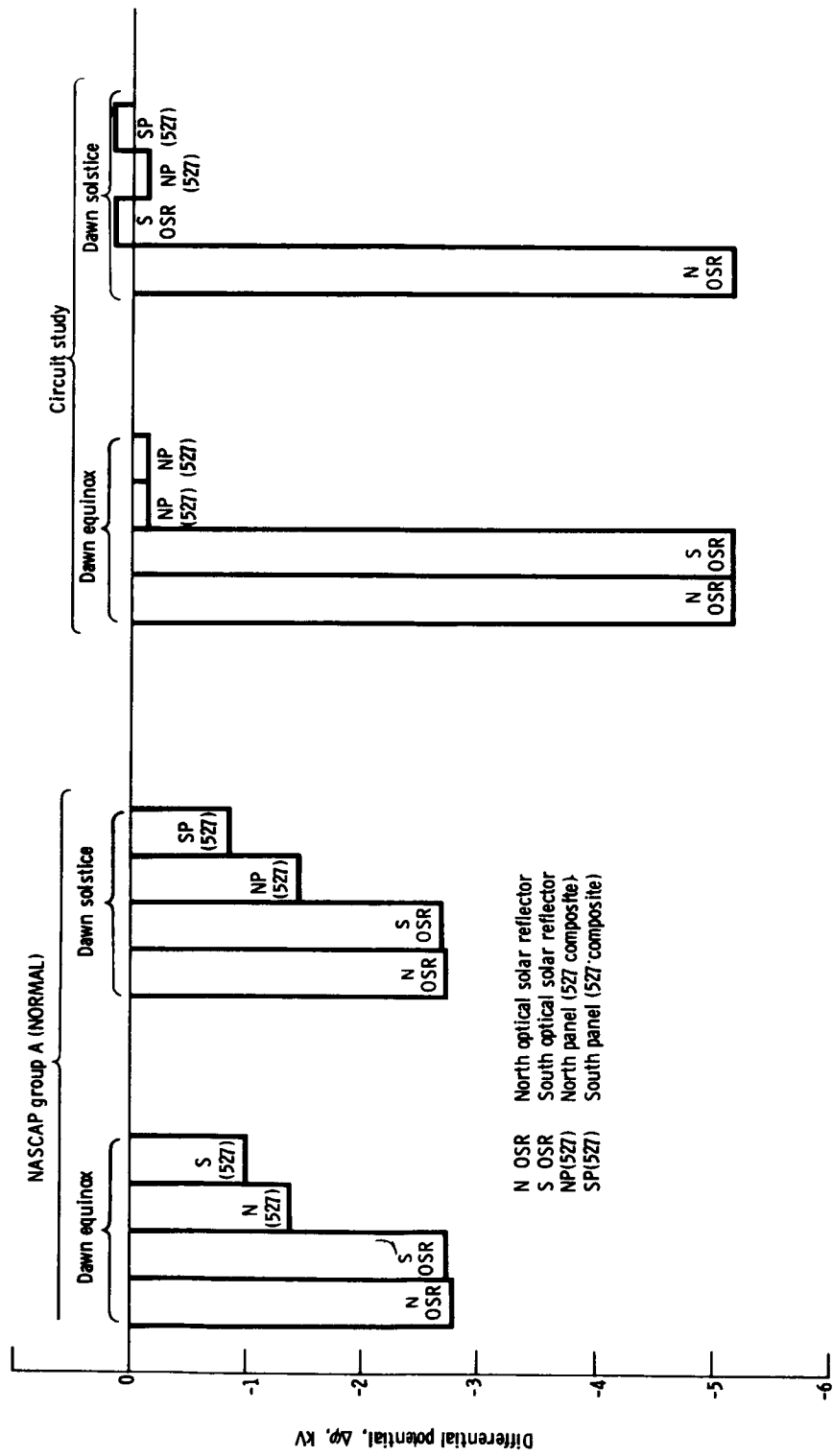


Figure 6. - Dawn differential potentials - comparison at equinox and solstice.



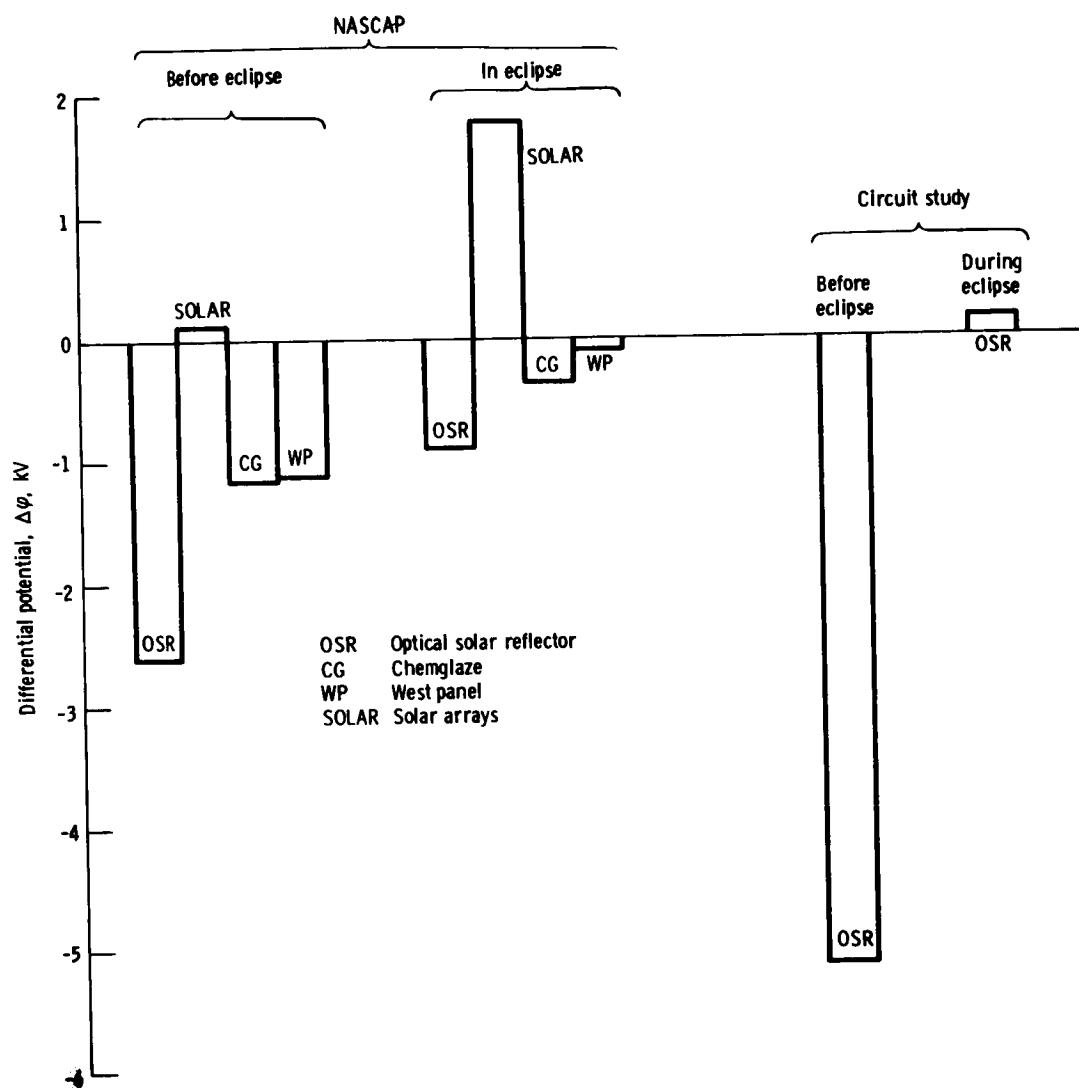


Figure 7. - Midnight-at-equinox steady-state differential potentials before and during eclipse.

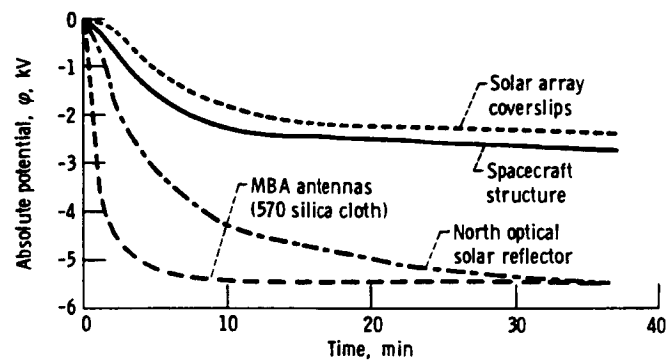


Figure 8. - Dawn-at-equinox absolute potential as function of time for NASCAP group A (NORMAL).

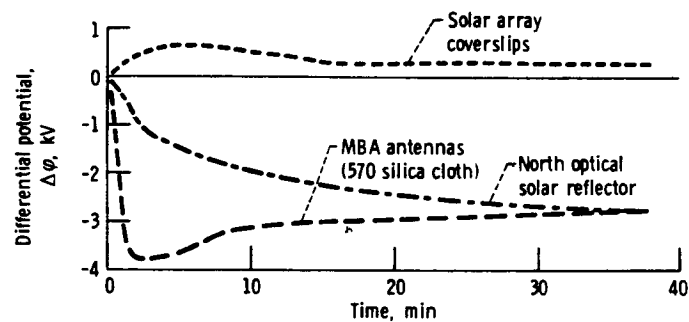


Figure 9. - Dawn-at-equinox differential potential as function of time for NASCAP group A (NORMAL).

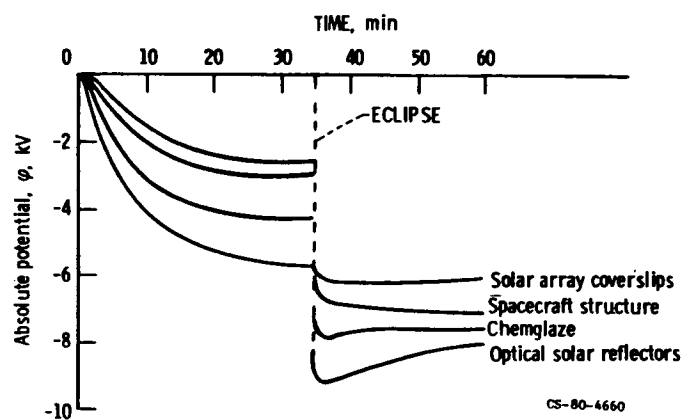


Figure 10. - Midnight-at-equinox potential as function of time for NASCAP group A (NORMAL).

## NASCAP CHARGING CALCULATIONS FOR A SYNCHRONOUS ORBIT SATELLITE

N. L. Sanders and G. T. Inouye  
TRW Defense and Space Systems Group

### INTRODUCTION

The NASA Charging Analyzer Program (NASCAP)<sup>(1)</sup> represents the state of the art in the computation of spacecraft charge up in the energetic plasma environment of geosynchronous orbits. The problem of determining the chargeup potentials of various parts of a real spacecraft in orbit is extremely complex, and the achievement of practical and useable results involves many tradeoffs between the accuracy and self-consistency of the equations solved and the manpower and computer costs. The work discussed in this paper represents the first use of NASCAP by an industrial user and is a part of an effort to eliminate the hazards of spacecraft charging to a satellite in geosynchronous orbit.

#### Satellite Modeling

The modeling of a geometrically complex spacecraft for the purpose of ambient plasma charging analyses was dictated by the capabilities of the NASCAP computer program. The geometrical limitations in defining the spacecraft for NASCAP are

- o The spacecraft must be defined in terms of a limited number of building blocks. These are shown in Figure 1. In addition to the six building blocks shown, thin plates, such as were used to represent the solar array paddles, are included in the repertory.
- o The building blocks must line up with the orthogonal coordinate system. The solar array paddles could not be tilted, for example. This is the reason for the right angle bend in the paddles.
- o The total spacecraft is limited to less than 1200 surface cells.
- o The spacecraft must fit into a volume of 17 x 17 x 33 unit cell dimensions.

Once the spacecraft is defined geometrically, NASCAP provides drawings whereby the definition may be validated visually. Figure 2 is a view showing the building block representation used for the satellite. Figure 3 shows the individual surface cells outlined. Each cell (there are a total of 810) characterized by its material is considered to be an equipotential surface. The unit cell dimension was assumed to be a 1 foot square making the overall dimensions somewhat comparable to the actual spacecraft.

#### Materials Parameters Used in the Charging Analyses

The material properties such as resistivity, photoemission, secondary emission, and backscatter coefficients have a major impact on the charging characteristics and differential potentials obtained when a spacecraft is exposed to the substorm environment. NASCAP has, within its files, 14 typical spacecraft materials characterized in terms of 13 parameters as shown in Table 1.

The 13 parameters or properties are identified in Table 2. For the satellite under study, eight of these were taken without change and a few properties such as thickness and conductivity were changed to values which were more appropriate. These eight materials are listed in Table 3 with reference to the NASCAP material selected to represent it. Also shown are the changes made in the thickness and conductivity values of Table 1. The data in Tables 1 and 2 were taken from Reference 1.

NASCAP provides drawings whereby the specifications of materials may be checked as to the locations on the spacecraft. Figure 3, as an example, shows the bottom view of the satellite model with the materials identified for each surface cell.

### NASCAP Charging Analyses

The spacecraft charging analyses performed by NASCAP are complex and require a very large computer and sophisticated programming. Even with the availability of a large computer, the computations are time consuming and limits, to 1200 surface cells, for example, are required so that computation costs do not become excessive. Additionally, the type of computations performed are simplified to the level where Laplace's equations, rather than Poissons' equations are solved. That is, a particle charge in a given volume in space is assumed to not affect the potential at that location. All potentials in space are therefore defined by surface potentials only.

Figure 5 shows an overview of what NASCAP does. Once the spacecraft and its environment are defined, currents to each surface cell from the environment are defined if its potential is known:

$$I_{\text{external}}(V) = -I_{\text{electron}} + I_{\text{ions}} + I_{\text{photo}} + I_{\text{secondaries}} + I_{\text{backscatter}}$$

The internal currents flowing within the spacecraft are also defined if all of the surface potentials are known:

$$I_{\text{internal}} = (V_i - V_o)/R + C \frac{d}{dt} (V_i - V_o)$$

$$V_i = \text{surface potential}$$

$$V_o = \text{structure potential} \\ \text{(structure assumed} \\ \text{to be conducting)}$$

In this case the currents are functions of the difference between surface and structure potential. A consistent solution is obtained when the sum of all of the currents flowing to structure is zero:

Since all 812 surface cells are involved in this summation, an enormous number of computations are performed in each iteration.

As shown in the lower right-hand box in Figure 5, a Laplace's equation solution is obtained for each iteration of a set of surface potentials. This in itself is a very complicated (actually the most complex part) computation since so many surface cells and an even greater number of spatial volume cells must be included in the computation. The result of this side calculation is used to permit equipotential contours to be drawn in the space surrounding the spacecraft.

An even more important use for the Laplace solution is to indicate situations in which a potential barrier exists at or off the surface of any given surface cell. Since photoelectrons and secondary emission electrons are emitted with only a few electron volts of energy, a potential barrier of a few volts effectively cuts off or prohibits any of these low energy electrons from leaving the surface. NASCAP, then, uses the Laplace solution to cut off the emission of low energy electrons from any given surface cell as soon as a potential barrier is detected for that cell. The net result of this potential barrier effect can be an overwhelming change in the charging characteristics from what would be expected otherwise.

### Environment

The synchronous orbit plasma environment used in the stress analysis uses a two-Maxwellian energy distribution for the electrons as well as the ions so that the differential flux for each species is given by

$$\frac{d\phi}{dE} = \frac{\phi_{01}}{(kT_1)^2} E e^{-\frac{E}{kT_1}} + \frac{\phi_{02}}{(kT_2)^2} E e^{-\frac{E}{kT_2}}$$

By selecting the two temperatures and two fluxes for each particle species the measured environment can be fitted very well. This is demonstrated in Figures 6 and 7. These curves have been generated from ATS-5 data as presented by Garrett.(2)

We see from these figures that whereas a single Maxwellian cannot be made to fit the data throughout the total energy range, the double Maxwellian fits nicely.

We therefore see that the static geosynchronous orbit environment can readily be described by specifying eight quantities:

- a. Two electron temperatures
- b. Two electron number densities

- c. Two ion temperatures
- d. Two ion number densities

Using these parameters, one can determine the fluxes.

The densities and temperatures were taken from Reference 1 with some modifications. In that study the plasma electron and ion densities, temperatures, and fluxes for a double-Maxwellian distribution were computed as a function of  $A_p$  and local time. In those computations the ATS plasma data were fitted to a model which made a linear adjustment of the parameters for the effects of magnetic activity. The flux of electrons and ions was enhanced with increasing  $A_p$ . In the stress analysis performed in the present study two different sets of environmental parameters were used, corresponding to different geomagnetic conditions. These are shown in Table 4.

A "worst" case environment corresponds to an  $A_p$  of 400 and a "severe" case corresponds to an  $A_p$  of 132. The fractional occurrence of  $A_p$  showing the percent occurrence of  $A_p$  from 1932-1975 is given in Figure 8. The  $A_p$  we have used differs from Garretts' by a factor of eight and is the commonly used daily average magnetic amplitude in units of 2 gamma, whereas the Garrett  $A_p$  is the sum of the trihourly  $A_p$ 's and is not normally used in the literature. The densities and temperatures shown in Table 4 were selected to maximize the spacecraft chargeup under the selected conditions. The most severe chargeup does not necessarily occur when the flux of low energy electrons is maximized since these electrons produce secondaries which tend to decrease negative chargeup. Furthermore the large ion fluxes also limit chargeup. For these reasons those parameters which correspond to the largest high energy electron density but to the lowest low energy electron and ion densities were selected from the Garrett model for each  $A_p$ .

#### NASCAP Runs

Several NASCAP runs were performed to determine the location and the magnitude of environmentally induced voltage stresses. Not only were two different environments considered, but also for each environment three solar directions and an eclipse case were analyzed. The cases run are listed in Table 5. The worst case environment is identified by  $A_p = 400$  and the severe environment by  $A_p = 132$ . The NASCAP code permits the direction of the sun relative to the spacecraft to be inserted. The sun can also be turned off to examine eclipse conditions. This was performed in Cases 4 and 8.

A special feature was added to NASCAP for use on this satellite. This feature permitted a spinning spacecraft with sun normal to the spin axis to be simulated by incorporating a spin averaged sun intensity into the program. This feature was used in Cases 3 and 7. The approach is valid since the charging times are long compared to the spacecraft spin period. Since NASCAP is a time dependent code it was necessary to run several cycles for each case, examine the resulting potentials and determine that steady state solution had been reached before changing conditions to the next case.

## Results

The main outputs of the NASCAP program which were used for the stress analysis were the potentials on each of the 810 cells and the differences between each cell potential and the structure (conductor) potential. Tables 6 and 7 show a portion of the 810 cell potential and the conductor/cell potential difference printout. The samples shown are results from Case 7,  $A_0 = 400$ , with the sun direction normal to the spin axis. These data along with a surface cell list, which identify the cells by material, location and orientation, permit one to determine the location and magnitude of the environmentally induced voltage stresses. Table 8 is a sample of the surface cell on the material plots, and the coordinates of the normal give its orientation. All the cells in the sample are identified as ceria doped coverglass on the solar paddles.

We have summarized the large volume of data detailing the potentials and stresses on the surface cells by extracting stresses greater than 1 kilovolt and identifying the materials and location of these large stresses for each of the cases run. When a group of contiguous cells of identical material was found having stresses larger than 1 kilovolt, the largest voltage stress of the group was recorded and located on the spacecraft. The results are shown in Figures 9 through 16. These data are the most significant result of the analysis. The stresses shown in the figures can be assumed to be axially symmetric for the same type of material. The structure potential for each case is also shown in the figures.

The largest potential differences between surface material and structure occur when the sun is normal to the spin axis and a larger fraction of the surface material has kilovolt stresses relative to the structure. For the  $A_0 = 132$  (severe) environment (Figure 11) the potential difference can be as large as 1900 volts. This can occur on the upper teflon portions of the sun shade. In the worst case environment the teflon on the shade can have a potential difference as high as 3720 volts relative to structure. This potential difference is much lower than one would obtain if the "barrier" effect were not included in NASCAP. The low stress predicted by NASCAP in this worst case environment is surprising in view of the numerous reports of arc effects on synchronous orbit spacecraft. Even though the stresses are most severe during side sun conditions, stresses greater than 1 kilovolt are found for all the cases considered. Therefore all the materials and locations identified in Figures 9 through 16 can be the source of an electrostatic discharge if discharges occur at 1 kilovolt.

Another interesting set of outputs generated by NASCAP is the potential contour plots around the spacecraft. Several such plots are made for each case considered. A few samples of the contour plots are shown in Figures 17 through 19 for the worst case environment with the spacecraft in eclipse, sun at  $-Z$  and side sun. The contour lines inside the spacecraft are artifacts of the program and should be considered to close along the surface.

The labels  $Z_{\min}$ ,  $Z_{\max}$  and  $\Delta Z$  on the figures represent the minimum potential contour voltage, the maximum voltage and the voltage between contours. These types of plots can be used to quickly determine the regions

of high potential on the spacecraft, the innermost contours being the largest negative potential (i.e.,  $Z_{\min}$ ). In Figure 17, in the sun -Z case, notice that the regions of highest potential are on the lower portion of the sun shade, the second surfaced mirror area below the shade and the mirrored area above the conical array. On the other hand, the regions of large potential are not regions of large voltage stress as indicated by the smoothness of the contour and its relationship to the spacecraft surface contour. In this case, the largest stresses occur on the solar paddles near  $Z = -5$ . Both Figures 17 and 18 show contours that do not indicate large surface potential changes. In contrast to these, Figure 19, which shows the distortion in the equipotential contours for the side sun case, is indicative of large voltage stresses on the surface.

### Conclusions and Recommendations

The application of NASCAP to a specific satellite to determine its charging characteristics is a reasonably straightforward process for personnel familiar with computer languages and with the field of spacecraft charging. The capabilities associated with NASCAP are continually being upgraded. A few improvements of NASCAP that are suggested have to do with the accessibility of the computational results such as the identification of high stress locations in either tabular or graphical form. The high stress threshold should be entered as a part of the material characterization. One other additional feature which would be useful would be the direct computation of the steady state potentials by elimination of element capacitances. This would circumvent the repetition of runs to examine whether the steady state had been reached.

In regard to the accuracy of NASCAP itself, a few laboratory experiments have been performed<sup>(3)</sup> which verify predictions on small sample measurements. A NASCAP charging analysis of the SCATHA satellite has been performed,<sup>(4)</sup> but correlative data between in-flight performance and the analysis predictions have not yet been published. As noted in the section on the voltage stress analysis results, the very worst case stress of 3720 volts is unexpectedly low as compared to previous stress computations in which the potential barrier effect was not taken into account. In view of laboratory measurements<sup>(5)</sup> which indicate much higher voltage breakdown thresholds (usually 8 kV to 12 kV), one wonders whether the barrier effect is overemphasized in NASCAP, or if some other mechanism must be postulated to account for the numerous reports of in-orbit anomalies due to spacecraft charging. On the other hand, there are many other possible explanations for the apparent discrepancy. For example,

- o Laboratory tests may not reflect true space flight configurations.
- o The observed anomalies in orbit are caused by arcing resulting from differential stresses less than 4 kilovolts.
- o The material properties, e.g., secondary and photoemission, may not be adequately known for the high stress and real in-orbit environment to permit accurate charging/discharging computations.
- o The modeling of the spacecraft for NASCAP may be too coarse to permit the accurate computation of stresses at edges and sharp points.



## REFERENCES

References 1 through 4 were papers presented at the USAF/NASA Spacecraft Charging Technology Conference, 31 Oct. to 2 Nov. 1978, U.S. Air Force Academy, Colorado:

1. I. Katz, J. J. Cassidy, M. J. Mandell, G. W. Schnuelle, P. G. Steen, and J. C. Roche, "The Capabilities of the NASA Charging Analyzer Program."
2. H. B. Garrett, "Modeling of the Geosynchronous Plasma Environment."
3. J. C. Roche and C. K. Purvis, "Comparison of NASCAP Predictions with Experimental Data."
4. D. E. Parks, I. Katz, G. W. Schnuelle, M. J. Mandell, and A. Rubin, "Charging Analysis of the SCATHA Satellite."
5. N. J. Stevens, F. D. Berkopce, J. V. Staskus, R. A. Bleck, and S. J. Narcisco, "Testing of Typical Spacecraft Materials in a Simulated Substorm Environment," Proceedings of the Spacecraft Charging Technology Conference, AFGL-TR-77-0051, NASA TM X-73537, 24 Feb. 1977.

## ACKNOWLEDGEMENTS

The work reported here was sponsored by the Air Force. The cooperation of the S<sup>3</sup> staff, particularly J. Cassidy and I. Katz, was immensely helpful in getting us started and in working out problems. Mrs. B. Benefield's typing and assembling of the manuscript and figures is gratefully acknowledged.

Table 1. Material Properties for Exposed Surfaces

Property <sup>b</sup>	GOLD	SOLAR	WHITEN	SCREEN	BLACKC YELOWC	GOLDDP	KAPTON
1	-	4.00+00	3.50+00	-	3.50+00	-	3.50+00
2	1.00-03	1.79-04	5.00-05	1.00-03	5.00-05	1.00-03	1.25-04
3	-	1.00-14	5.90-14	-	5.00-10	-	1.00-14
4	7.90+01	1.00+01	5.00+00	1.00+00	5.00+00	7.01+01	5.00+00
5	8.80-01	4.10+00	2.10+00	0.00	2.10+00	1.03+00	2.10+00
6	8.00-01	4.10-01	1.50-01	1.00+00	1.50-01	7.20-01	1.50-01
7	8.30+01	-1.00+00	-1.00+00	1.00+01	-1.00+00	8.30+01	-1.00+00
8	1.63+00	0.00	0.00	1.50+00	0.00	1.63+00	0.00
9	3.46+01	2.30+00	1.05+00	0.00	1.05+00	3.46+01	1.42+00
10	7.00-01	2.08+01	9.80+00	1.00+00	9.80+00	7.00-01	9.80+00
11	4.00-01	1.36+00	1.40+00	0.00	1.40+00	4.00-01	1.40+00
12	5.00+01	4.00+01	7.00+01	1.00+00	7.00+01	5.00+01	7.00+01
13	2.90-05	2.00-05	2.00-05	0.00	2.00-05	2.90-05	2.00-05
	SIO2	TEFLON	INDOX	YGOLDC	ALUMIN	BOOMAT <sup>c</sup>	ML12
1	4.00+00	2.00+00	-	-	-	2.00+00	-
2	2.75-04	1.25-04	1.00-03	1.00-03	1.00-03	5.00-03	1.00-03
3	2.75-12	1.00-14	-	-	-	1.00-10	-
4	1.00+01	1.00+01	2.44+01	4.20+01	1.30+01	6.34+01	6.00+00
5	2.40+00	3.00+00	1.40+00	1.49+00	9.70-01	1.86+00	1.00+00
6	4.00-01	3.00-01	8.00-01	4.80-01	3.00-01	5.90-01	3.00-01
7	-1.00+00	-1.00+00	-1.00+00	-1.00+00	2.60+02	8.30+01	-1.00+00
8	0.00	0.00	0.00	0.00	1.30+00	1.63+00	0.00
9	1.02+00	2.00+00	7.18+00	1.02+01	2.40+02	3.46+01	2.00+00
10	2.00+01	1.67+01	5.55+01	4.20+01	1.73+00	7.00-01	1.20+01
11	1.40+00	1.40+00	1.36+00	1.00+00	1.36+00	4.00-01	1.40+00
12	7.00+01	7.00+01	4.00+01	6.00+01	4.00+01	5.00+01	7.00+01
13	2.00-05	2.00-05	3.20-05	2.40-05	4.00-05	2.72-05	2.10-05

Table 2. Material Properties Descriptions

Property 1:	Relative dielectric constant for insulators (dimensionless).
Property 2:	Thickness of dielectric film or vacuum gap (meters).
Property 3:	Electrical conductivity (mho/m). The value = indicates a vacuum gap over a conducting surface.
Property 4:	Atomic number (dimensionless).
Property 5:	Maximum secondary electron yield for electron impact at normal incidence (dimensionless).
Property 6:	Primary electron energy to produce maximum yield at normal incidence (keV).
Property 7-10:	Range for incident electrons. <u>Either</u> :  $\text{Range} = P_7 E^{P_8} + P_9 E^{P_{10}}$ <p>where the range is in angstroms and for the energy in keV or</p> <p><math>P_7 = -1</math>. to indicate use of an empirical range formula</p> <p><math>P_9</math> = density (g/cm<sup>3</sup>)</p> <p><math>P_{10}</math> = mean atomic weight (dimensionless).</p>
Property 11:	Secondary electron yield for normally incident 1 keV protons.
Property 12:	Proton energy to produce maximum secondary electron yield (keV).
Property 13:	Photoelectron yield for normally incident sunlight (A/m <sup>2</sup> ).

Table 3. Satellite Charging Model Materials List

Name	Material Description	Spacecraft Locations	Thickness and Conductivity
1. SSM (SiO2)	10 mil SiO2 (Fused Quartz)	Second Surface Mirrors (SSMs)	10 mils = 254 $\mu$ m, 10 <sup>-16</sup> mho/m
2. SSM (SiO2)	8 mil SiO2 (Fused Quartz)	SSMs	8 mils = 200 $\mu$ m, 10 <sup>-16</sup> mho/m
3. Ceria (SiO2)	6 mil Ceria Glass (may become quartz)	Paddle Solar Cell Covers	6 mils = 150 $\mu$ m, 10 <sup>-16</sup> mho/m
4. Micro (SiO2)	6 mil Microsheet Borosilicate Glass	Cylindrical and Conical Solar Cells Cover-glasses	6 mils = 150 $\mu$ m, 10 <sup>-16</sup> mho/m
5. Whiten	White Paint	Collar Top Bottom of Spacecraft	2 mils = 50 $\mu$ m, 5.10 <sup>-12</sup> mho/m
6. Black C	Black Paint	Top and Parts of Paddle	2 mils = 50 $\mu$ m, 5.10 <sup>-10</sup> mho/m
7. Teflon	Teflon Thermal Blankets	Sunshade Top of RADECs	2 mils = 50 $\mu$ m, 10 <sup>-16</sup> mho/m
8. Aluminum	Aluminum	Structural Parts	---

Table 4. Plasma Parameters used in NASCAP Runs

Case 1. $A_p = 400$ (Worst Case)				
	Low E Maxwellian		High E Maxwellian	
	$N_1(cc^{-1})$	$T_1(eV)$	$N_2(cc^{-1})$	$T_2(eV)$
Electrons	7.6	222	5.7	13,300
Ions	1.6	140	1.8	7,300
Case 2. $A_p = 132$ (Severe)				
Electrons	2.5	234	1.66	11,300
Ions	1.0	270	0.85	10,800

Table 5. Cases Run on NASCAP

Case No.	$A_p$	Sun Direction*
1	132	+Z
2	132	-Z
3	132	$\perp Z$ (Spin)
4	132	(Eclipse)
5	400	+Z
6	400	-Z
7	400	$\perp Z$ (Spin)
8	400	(Eclipse)

\* +Z is parallel to spin axis, toward sensor.

Table 6. Sample of Surface Potentials (Volts) of the 810 Cells

SURFACE POTENTIALS - ALL 810 CELLS						CELL NO.
CELL NO.						
1	-1.0148+04	-1.0148+04	-1.0148+04	-1.0148+04	-1.0148+04	5
6	-1.0148+04	-1.0148+04	-1.0148+04	-1.0148+04	-1.0148+04	10
11	-1.0148+04	-1.0148+04	-1.0148+04	-1.0148+04	-1.0148+04	15
16	-1.0148+04	-1.0148+04	-1.0148+04	-1.0148+04	-1.0148+04	20
21	-1.0148+04	-1.0148+04	-1.0148+04	-1.0148+04	-1.0148+04	25
26	-1.0148+04	-1.0148+04	-1.0148+04	-1.0148+04	-1.0148+04	30
31	-9.0054+03	-8.9576+03	-1.0148+04	-1.0148+04	-9.0513+03	35
36	-9.0497+03	-1.0148+04	-1.0148+04	-1.0089+04	-1.0006+04	40
41	-9.0763+03	-9.0763+03	-8.9352+03	-9.0657+03	-1.0148+04	45
46	-1.0148+04	-8.9503+03	-9.0823+03	-1.0148+04	-1.0148+04	50
51	-8.9118+03	-8.8851+03	-1.0148+04	-1.0148+04	-8.8599+03	55
56	-8.7239+03	-9.4344+03	-8.3359+03	-9.5613+03	-8.5494+03	60
61	-9.0912+03	-7.8520+03	-7.1847+03	-6.7725+03	-6.1758+03	65
66	-6.0580+03	-6.0114+03	-5.9698+03	-5.9927+03	-9.5088+03	70
71	-8.5652+03	-9.0912+03	-7.7536+03	-7.0789+03	-6.5658+03	75
76	-6.2332+03	-6.1118+03	-6.1374+03	-9.0763+03	-6.0066+03	80
81	-9.4398+03	-8.5465+03	-9.0912+03	-7.7424+03	-7.0697+03	85
86	-6.5675+03	-6.2455+03	-6.1513+03	-6.2121+03	-9.0763+03	90
91	-6.5066+03	-6.1981+03	-9.4897+03	-6.2727+03	-6.0529+03	95
96	-9.4994+03	-8.5380+03	-9.0912+03	-7.7243+03	-7.0594+03	100
101	-6.5592+03	-6.2316+03	-6.1111+03	-6.1382+03	-9.0763+03	105
106	-6.0454+03	-6.1138+03	-9.4896+03	-6.0694+03	-6.0018+03	110
111	-9.5447+03	-8.5030+03	-9.0912+03	-7.9126+03	-7.1449+03	115
116	-6.6363+03	-6.2309+03	-6.1465+03	-5.9705+03	-5.9998+03	120
121	-6.0530+03	-9.4149+03	-8.2879+03	-1.0148+04	-1.0148+04	125
126	-1.0148+04	-1.0148+04	-1.0148+04	-1.0148+04	-8.8600+03	130
131	-8.7319+03	-9.4154+03	-8.2915+03	-9.0912+03	-7.7681+03	135
136	-7.4694+03	-6.7305+03	-6.2051+03	-6.1228+03	-5.9569+03	140
141	-5.8423+03	-5.8327+03	-9.0912+03	-5.7910+03	-5.9936+03	145
146	-9.1222+03	-6.8382+03	-9.0932+03	-9.4900+03	-6.3115+03	150
151	-9.1074+03	-9.4900+03	-6.2141+03	-9.0912+03	-5.7692+03	155
156	-6.4738+03	-9.0912+03	-7.7817+03	-7.5047+03	-6.7580+03	160
161	-6.2304+03	-6.0243+03	-5.9289+03	-6.0102+03	-5.9930+03	165
166	-9.4396+03	-8.3471+03	-1.0148+04	-1.0148+04	-9.0054+03	170
171	-8.9578+03	-1.0148+04	-1.0148+04	-1.0148+04	-1.0148+04	175
176	-1.0148+04	-1.0148+04	-1.0148+04	-1.0148+04	-1.0148+04	180
181	-1.0148+04	-8.9292+03	-8.9114+03	-9.5458+03	-8.5065+03	185
186	-9.0912+03	-7.8977+03	-7.1360+03	-6.7072+03	-6.1981+03	190
191	-6.0824+03	-5.9676+03	-5.9752+03	-5.9812+03	-9.0912+03	195
196	-6.0292+03	-5.9945+03	-1.0148+04	-6.2765+03	-6.1019+03	200
201	-5.5923+03	-5.8345+03	-5.2433+03	-5.5727+03	-9.0912+03	205
206	-5.5905+03	-1.0148+04	-6.6947+03	-6.0580+03	-5.6467+03	210
211	-5.4388+03	-5.4568+03	-9.0912+03	-5.5363+03	-1.0148+04	215
216	-7.6603+03	-6.2620+03	-5.7271+03	-5.4801+03	-5.4983+03	220
221	-9.0912+03	-5.5995+03	-1.0148+04	-7.6325+03	-6.2422+03	225
226	-5.7217+03	-5.4742+03	-5.4757+03	-9.0912+03	-5.5452+03	230
231	-1.0148+04	-6.3253+03	-6.4560+03	-5.8424+03	-5.9328+03	235

Table 7. Sample of Potential Differences (Volts) of the 810 Cells

CONDUCTOR I POTENTIAL = -9.0763+03

POTENTIAL DIFFERENCES - ALL 810 CELLS

CELL NO.						CELL NO.
1	-1.0713+03	-1.0713+03	-1.0713+03	-1.0713+03	-1.0713+03	5
6	-1.0713+03	-1.0713+03	-1.0713+03	-1.0713+03	-1.0713+03	10
11	-1.0713+03	-1.0713+03	-1.0713+03	-1.0713+03	-1.0713+03	15
16	-1.0713+03	-1.0713+03	-1.0713+03	-1.0713+03	-1.0713+03	20
21	-1.0713+03	-1.0713+03	-1.0713+03	-1.0713+03	-1.0713+03	25
26	-1.0713+03	-1.0713+03	-1.0713+03	-1.0714+03	-1.0713+03	30
31	7.0922+01	1.1865+02	-1.0714+03	-1.0713+03	2.4974+01	35
36	2.6528+01	-1.0714+03	-1.0713+03	-1.0127+03	-9.2980+02	40
41	0.0000	0.0000	1.4104+02	1.0538+01	-1.0714+03	45
46	-1.0713+03	1.2599+02	-5.9917+00	-1.0714+03	-1.0713+03	50
51	1.6450+02	1.9121+02	-1.0714+03	-1.0713+03	2.1641+02	55
56	3.5239+02	-3.5815+02	7.4038+02	-4.8504+02	5.2689+02	60
61	-1.4916+01	1.2243+03	1.8916+03	2.3038+03	2.9005+03	65
66	3.0183+03	3.0649+03	3.1065+03	3.0835+03	-4.3252+02	70
71	5.1105+02	-1.4916+01	1.3227+03	1.9974+03	2.5105+03	75
76	2.8431+03	2.9645+03	2.9389+03	0.0000	3.0697+03	80
81	-3.6354+02	5.2979+02	-1.4916+01	1.3339+03	2.0066+03	85
86	2.5088+03	2.8307+03	2.9249+03	2.8641+03	0.0000	90
91	2.5697+03	2.8782+03	-4.1341+02	2.8036+03	3.0233+03	95
96	-4.2309+02	5.3826+02	-1.4916+01	1.3520+03	2.0169+03	100
101	2.5171+03	2.8447+03	2.9652+03	2.9381+03	0.0000	105
106	3.0309+03	2.9625+03	-4.1335+02	3.0069+03	3.0744+03	110
111	-4.6846+02	5.7332+02	-1.4916+01	1.1636+03	1.9313+03	115
116	2.4399+03	2.8453+03	2.9298+03	3.1058+03	3.0765+03	120
121	3.0233+03	-3.3858+02	7.6842+02	-1.0713+03	-1.0713+03	125
126	-1.0713+03	-1.0713+03	-1.0714+03	-1.0713+03	2.1633+02	130
131	3.4443+02	-3.3912+02	7.8473+02	-1.4916+01	1.3081+03	135
136	1.6069+03	2.3458+03	2.8712+03	2.9535+03	3.1193+03	140
141	3.2340+03	3.2436+03	-1.4916+01	3.2853+03	3.0827+03	145
146	-4.5953+01	2.2381+03	-1.6921+01	-4.1377+02	2.7648+03	150
151	-3.1096+01	-4.1377+02	2.8622+03	-1.4912+01	3.3071+03	155
156	2.6024+03	-1.4916+01	1.2946+03	1.5716+03	2.3183+03	160
161	2.8459+03	3.0519+03	3.1473+03	3.0661+03	3.0833+03	165
166	-3.6333+02	7.2918+02	-1.0714+03	-1.0713+03	7.0922+01	170
171	1.1846+02	-1.0713+03	-1.0713+03	-1.0713+03	-1.0713+03	175
176	-1.0713+03	-1.0713+03	-1.0713+03	-1.0713+03	-1.0714+03	180
181	-1.0713+03	1.4706+02	1.6483+02	-4.6948+02	5.6978+02	185
186	-1.4916+01	1.1785+03	1.9403+03	2.3691+03	2.8762+03	190
191	2.9939+03	3.1086+03	3.1011+03	3.0951+03	1.4912+01	195

Table 8. Sample of Surface Cell List

SURFACE CELL LIST CELL NO.	CODE	CONDUCTOR	IX	IY	IZ	NORMAL	MATERIAL
1	010206030103	1	2	6	3	C	CERIA
2	010206040303	1	2	6	4	C	CERIA
3	010207030103	1	2	7	3	C	CERIA
4	010207040303	1	2	7	4	C	CERIA
5	010210030103	1	2	8	3	C	CERIA
6	010210040303	1	2	8	4	C	CERIA
7	010211030103	1	2	9	3	C	CERIA
8	010211040303	1	2	9	4	C	CERIA
9	010212030103	1	2	10	3	C	CERIA
10	010212040303	1	2	10	4	C	CERIA
11	010213030103	1	2	11	3	C	CERIA
12	010213040303	1	2	11	4	C	CERIA
13	010214030103	1	2	12	3	C	CERIA
14	010214040303	1	2	12	4	C	CERIA
15	010306030103	1	3	6	3	C	CERIA
16	010306040303	1	3	6	4	C	CERIA
17	010307030103	1	3	7	3	C	CERIA
18	010307040303	1	3	7	4	C	CERIA
19	010310030103	1	3	8	3	C	CERIA
20	010310040303	1	3	8	4	C	CERIA
21	010311030103	1	3	9	3	C	CERIA
22	010311040303	1	3	9	4	C	CERIA
23	010312030103	1	3	10	3	C	CERIA
24	010312040303	1	3	10	4	C	CERIA
25	010313030103	1	3	11	3	C	CERIA
26	010313040303	1	3	11	4	C	CERIA
27	010314030103	1	3	12	3	C	CERIA
28	010314040303	1	3	12	4	C	CERIA
29	010406030103	1	4	6	3	C	CERIA
30	010406040303	1	4	6	4	C	CERIA

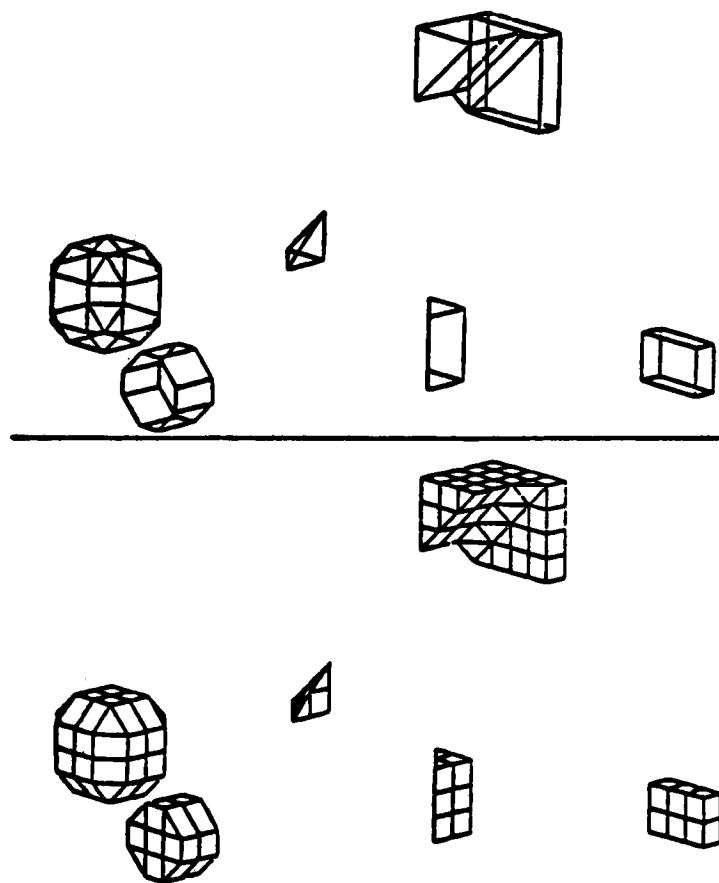


Figure 1. The six building block types are shown here. The uppermost object shows a FIL111 smoothing a corner. Below, from left to right are quasisphere, octagon right cylinder, tetrahedron, wedge, and rectangular parallelepiped.

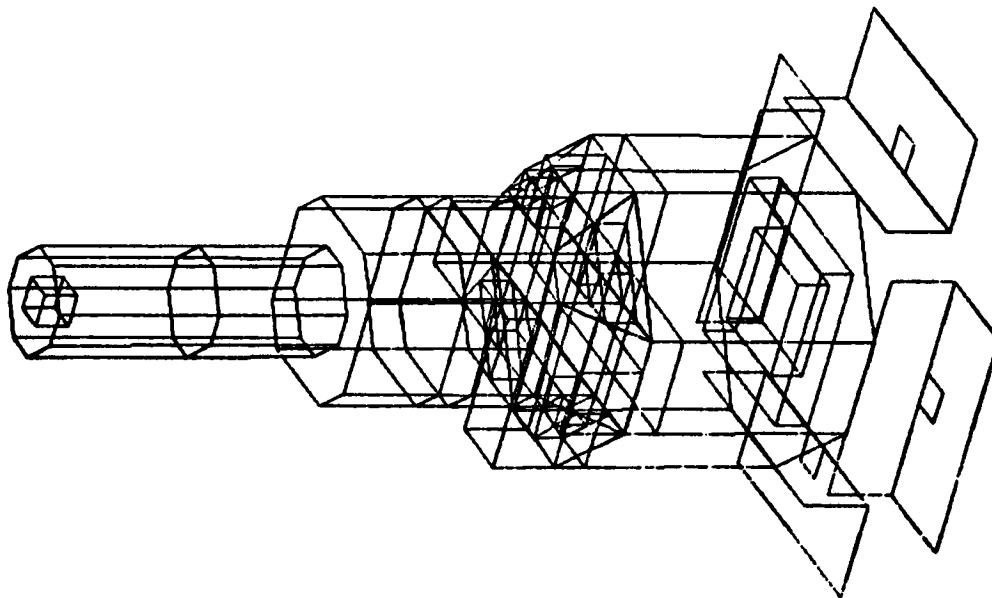


Figure 2. Building blocks used to define the satellite.

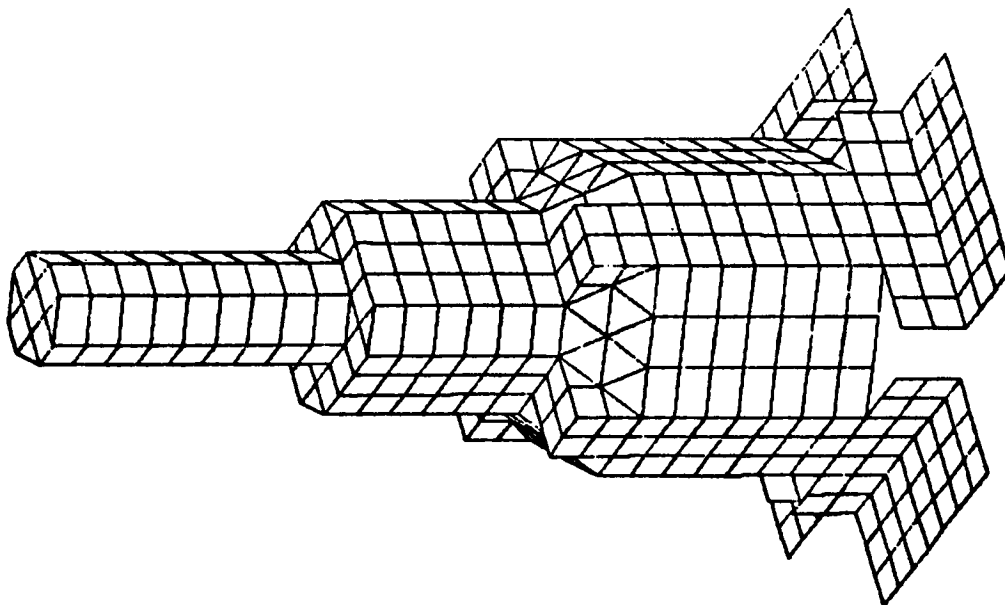


Figure 3. NASCAP drawing of the satellite showing surface cells.



SURFACE CELL MATERIAL COMPOSITION AS VIEWED FROM THE NEGATIVE Z DIRECTION

POP Z VALUES BETWEEN 1 AND 33

MATERIAL LEGEND

3	
CERIA	
5	
SSM	
6	
BLACK	
8	
WHITEN	

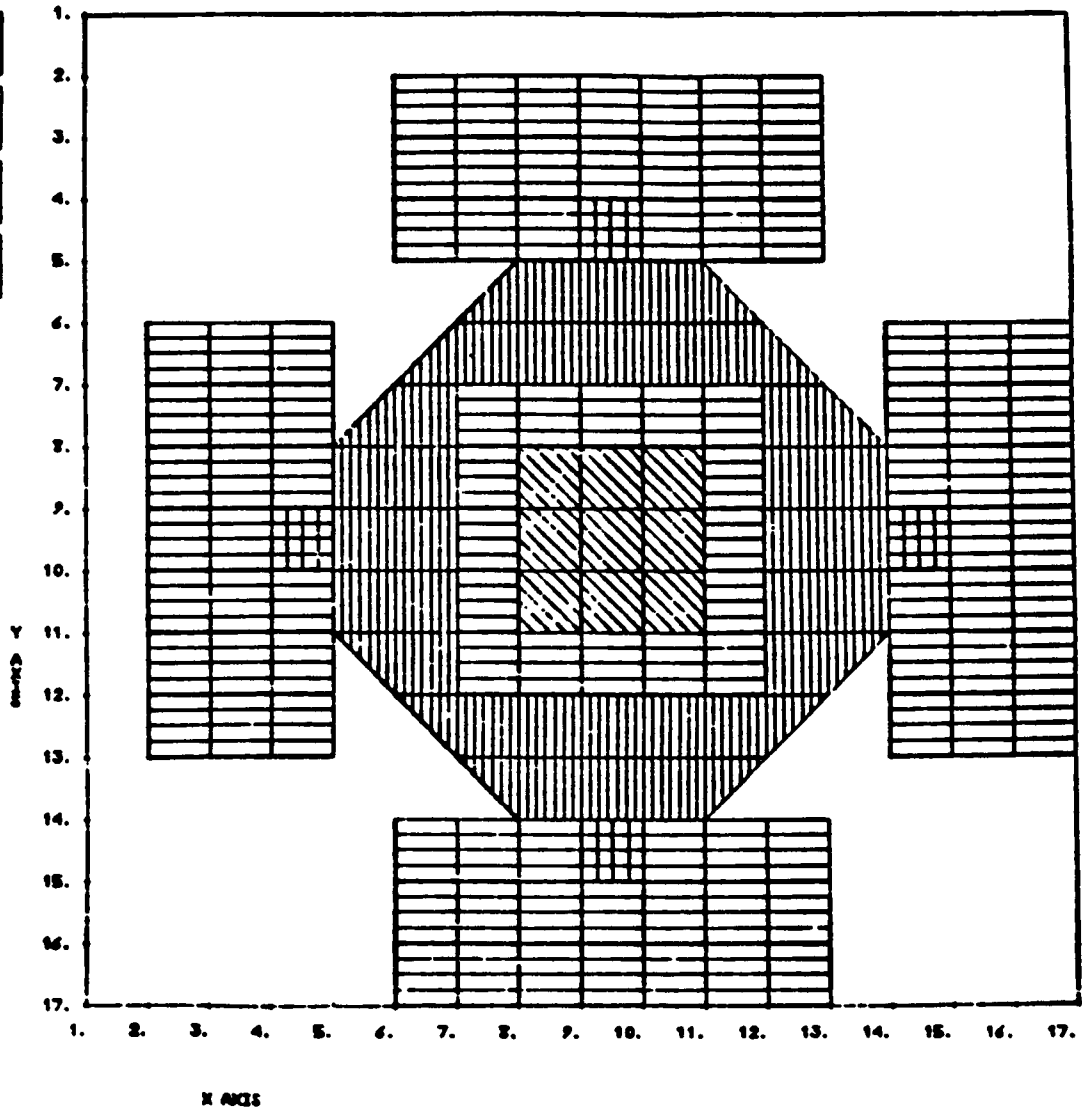


Figure 4. Surface cell material composition as viewed from the negative Z direction for Z values between 1 and 33.



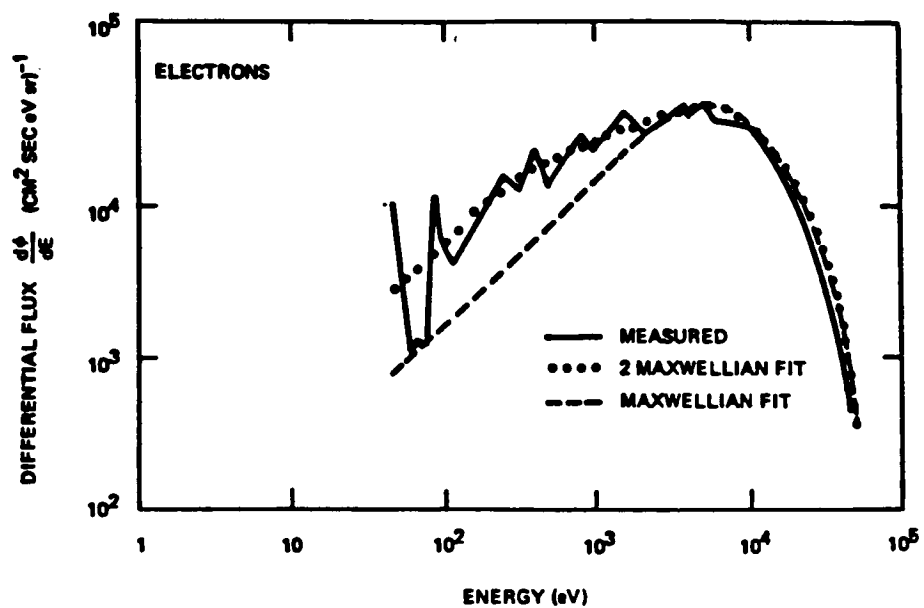


Figure 6. Differential flux of electrons (Sept. 30, 1969, ATS-5).

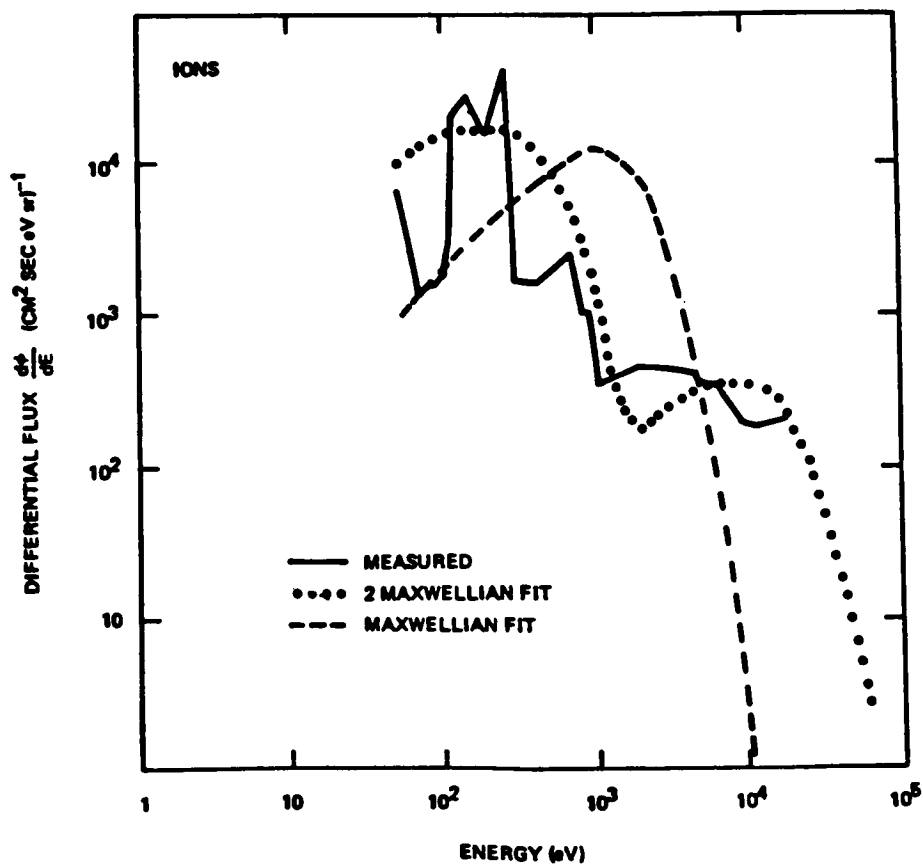


Figure 7. Differential flux of ions (Sept. 30, 1969, ATS-6).

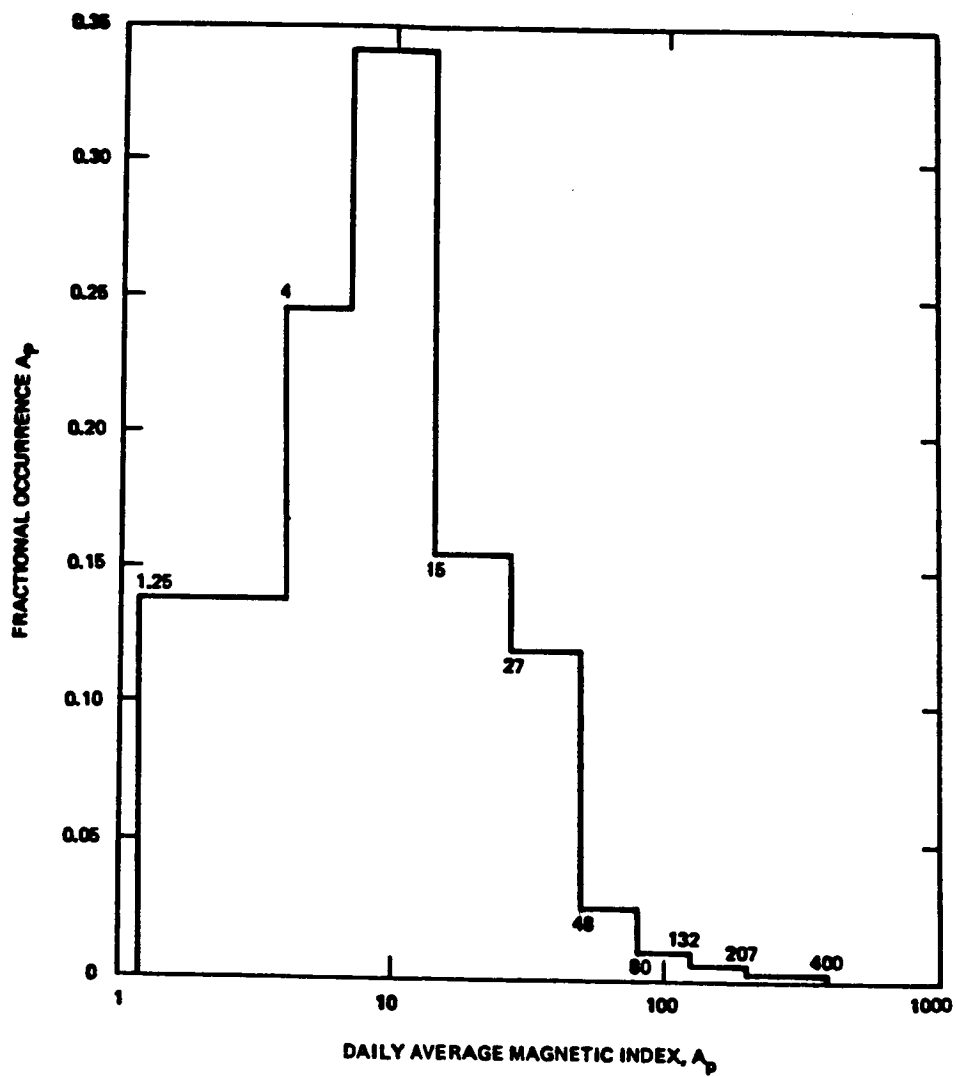


Figure 8. Occurrence of  $A_p$  from 1932-1975.

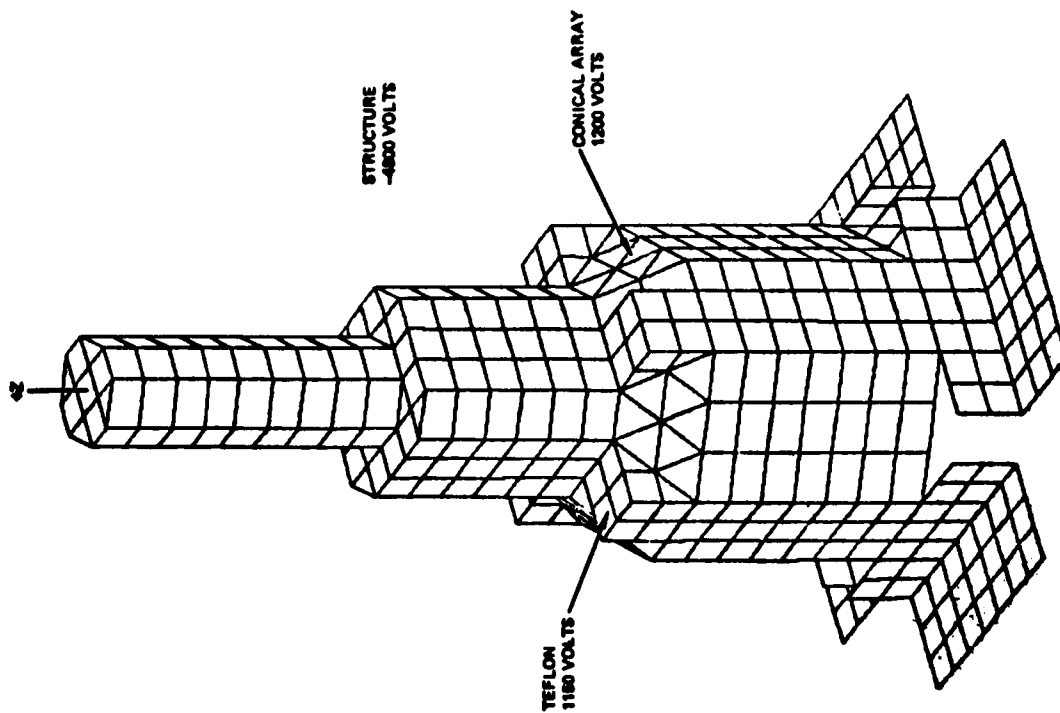


Figure 9. Case 1 - Maximum differential stress (sun +Z) ( $\Delta V > 1000$  V)  $A_p = 132$ .

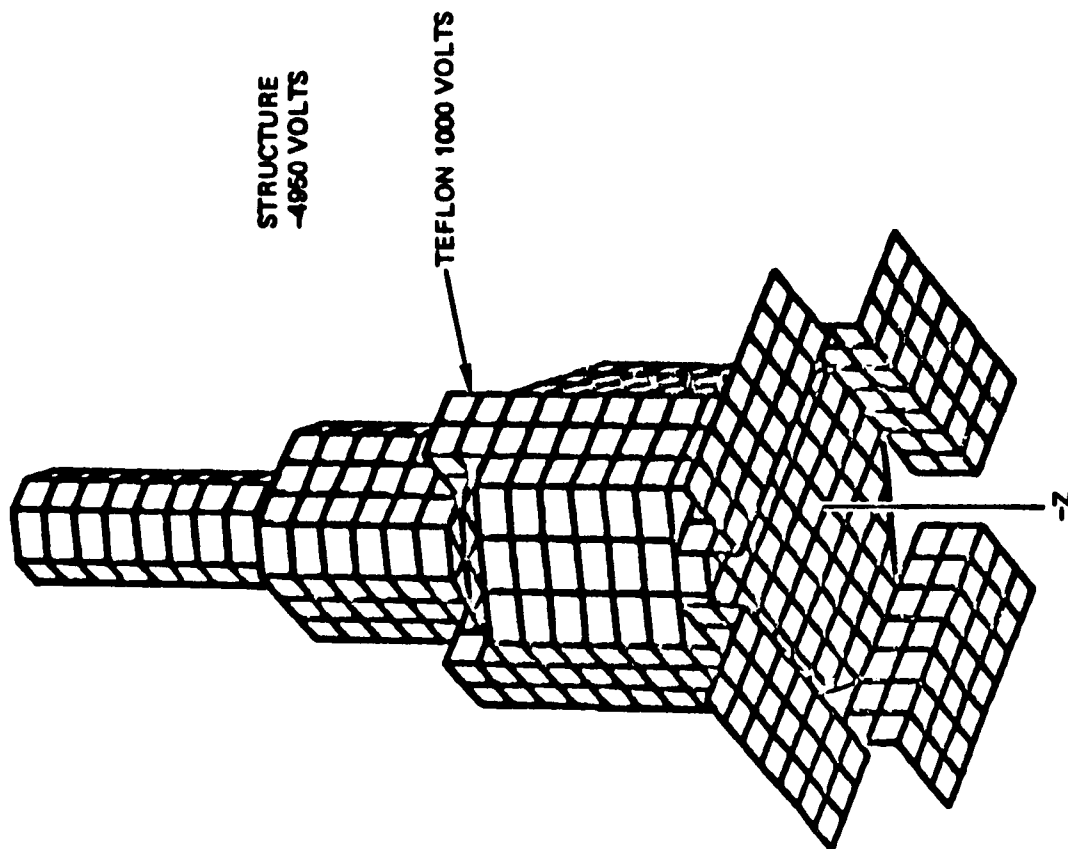


Figure 10. Case 2 - Maximum differential stress (sun -Z) ( $\Delta V > 1000$  V)  $A_p = 132$ .

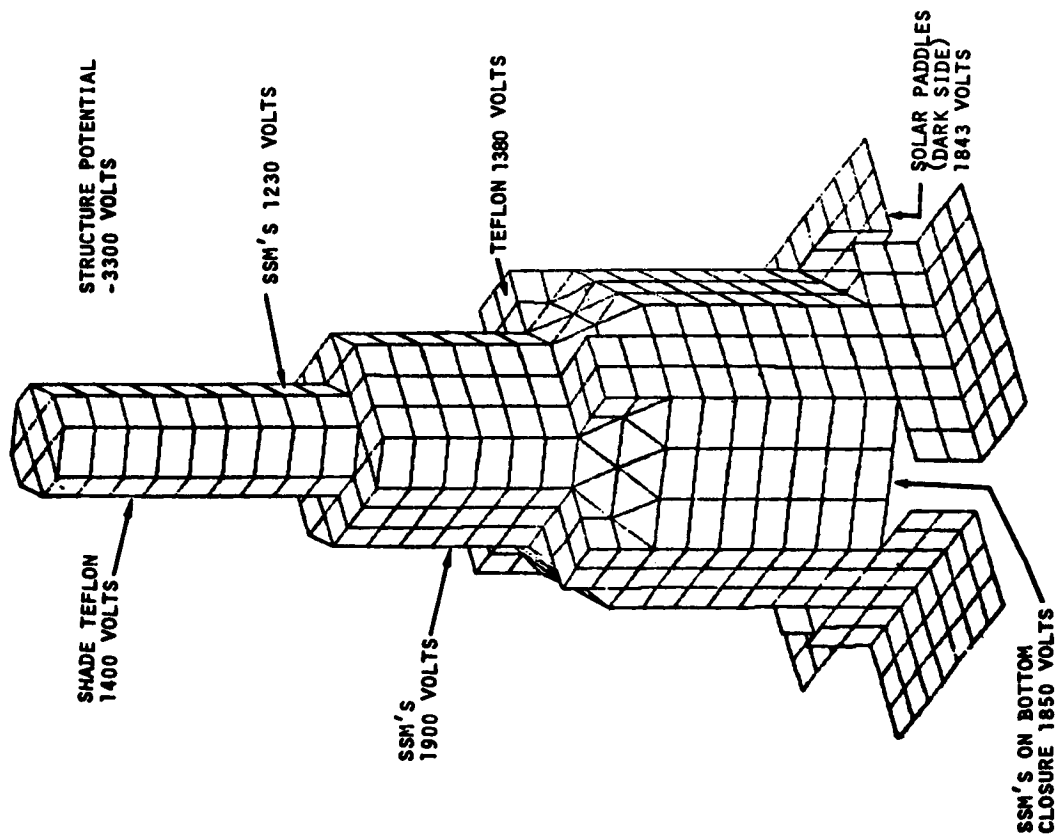


Figure 11. Case 3 - Differential stress (sun LZ, spin,  $A_p = 132$ ) ( $\Delta V > 1000$  V).

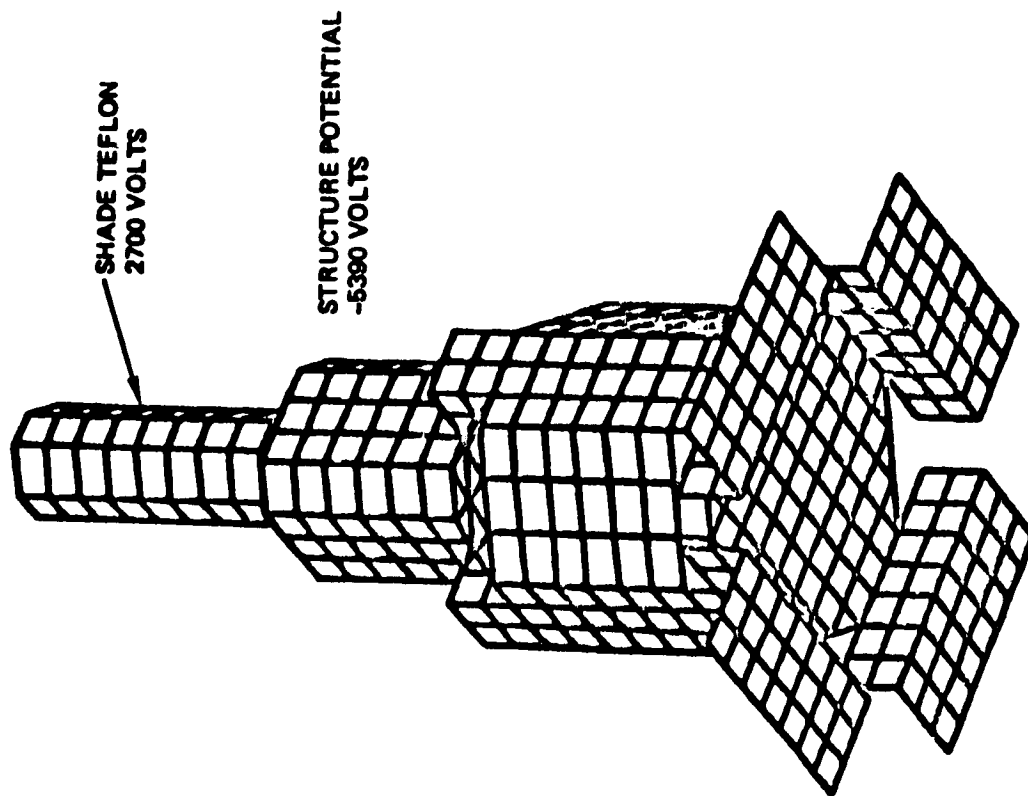


Figure 12. Case 4 - Differential stress (eclipse,  $A_p = 132$ ) ( $\Delta V > 1000$  V).

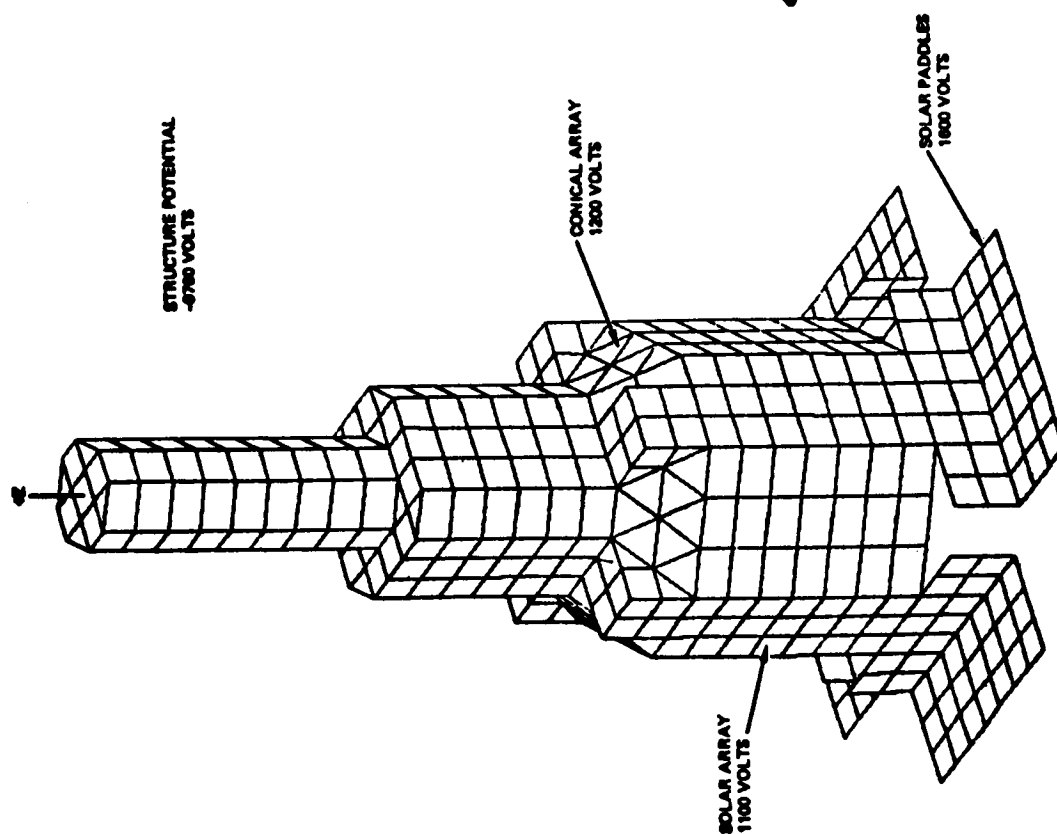
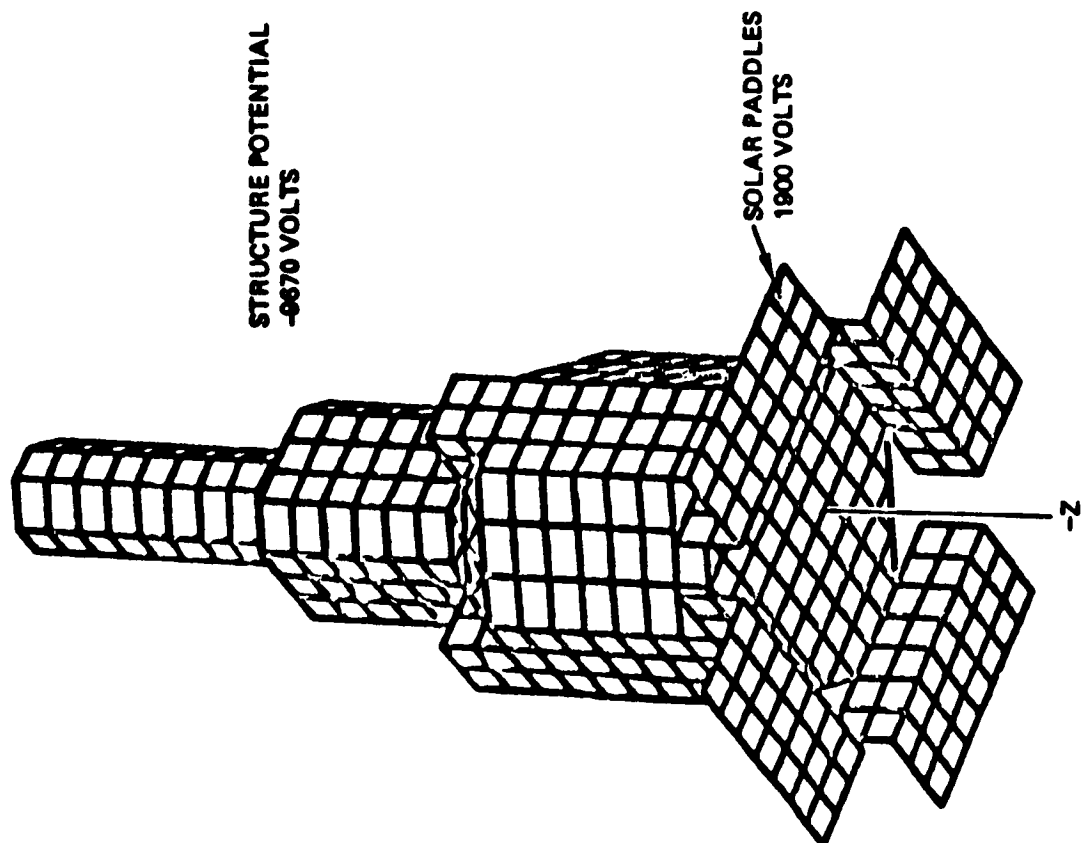


Figure 13. Case 5 - Differential stress (sun +Z,  $A_p = 400$ ) ( $\Delta V > 1000$  V).

Figure 14. Case 6 - Differential stress (sun -Z,  $A_p = 400$ ) ( $\Delta V > 1000$  V).

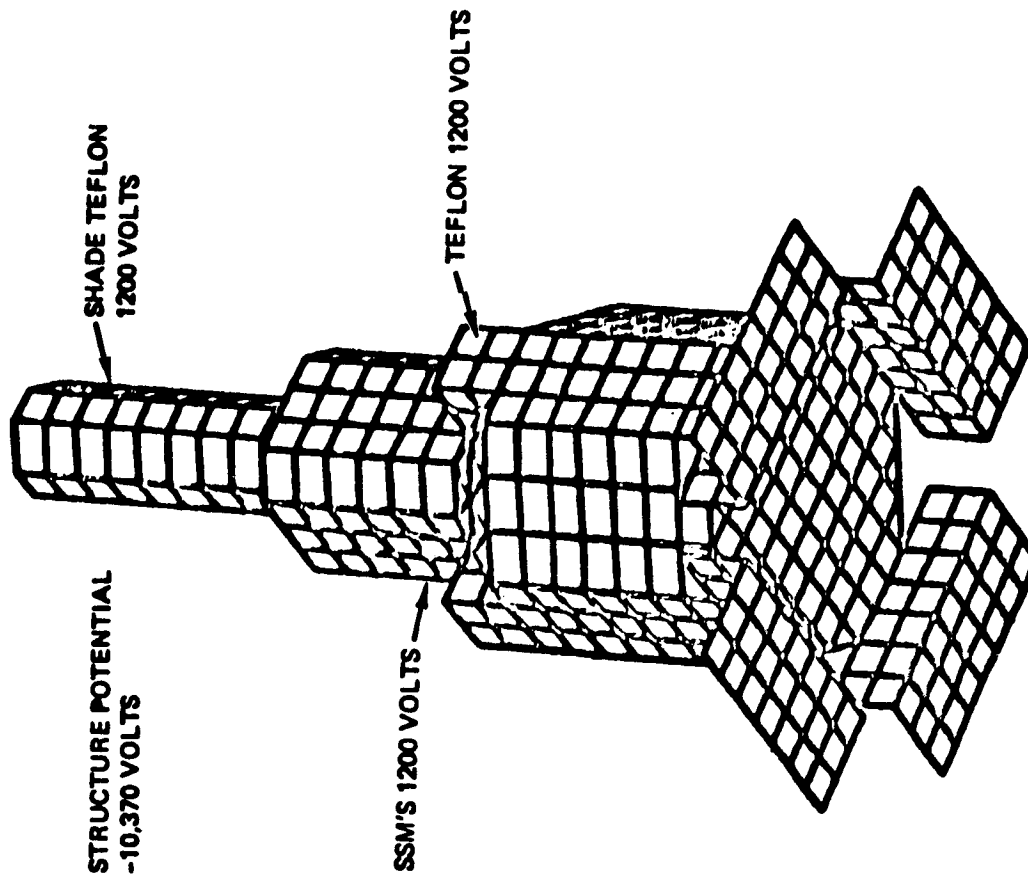


Figure 15. Case 7 - Differential stress  
(sun  $\perp$  Z spin,  $A_p = 400$ )  
( $\Delta V > 1000$  V).

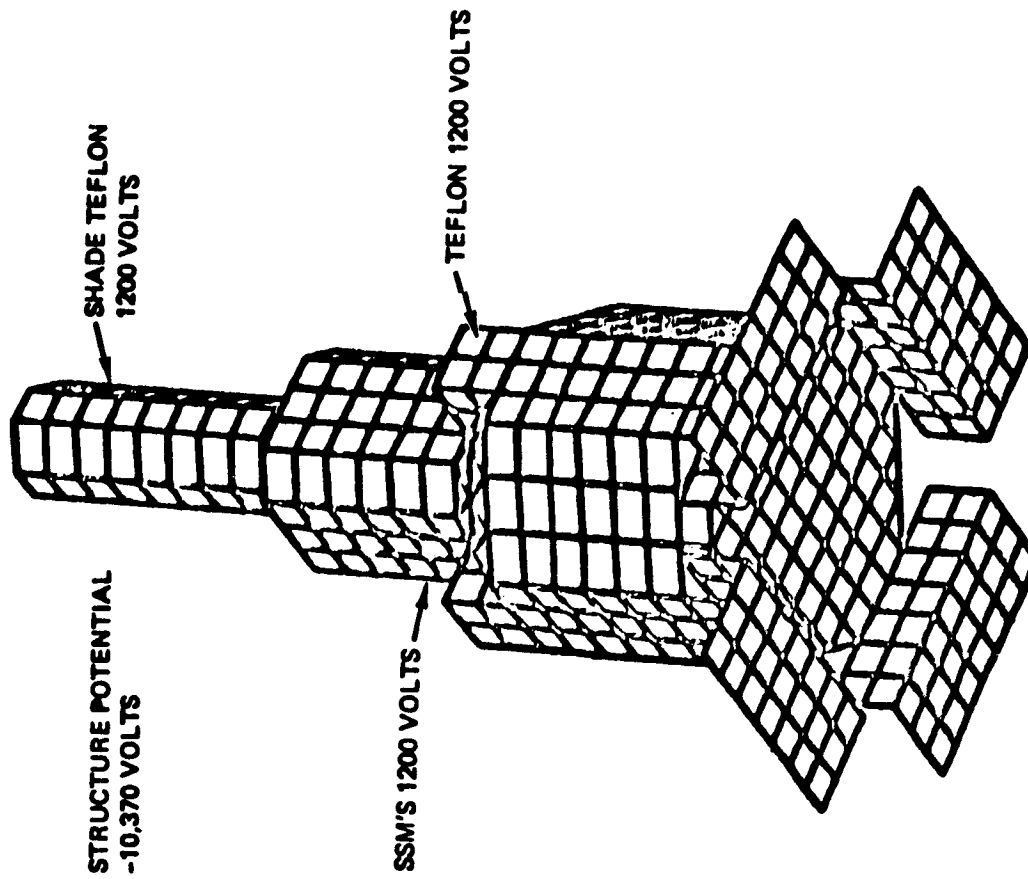


Figure 16. Case 8 - Differential stress (eclipse,  
 $A_p = 400$ ) ( $\Delta V > 1000$  V).



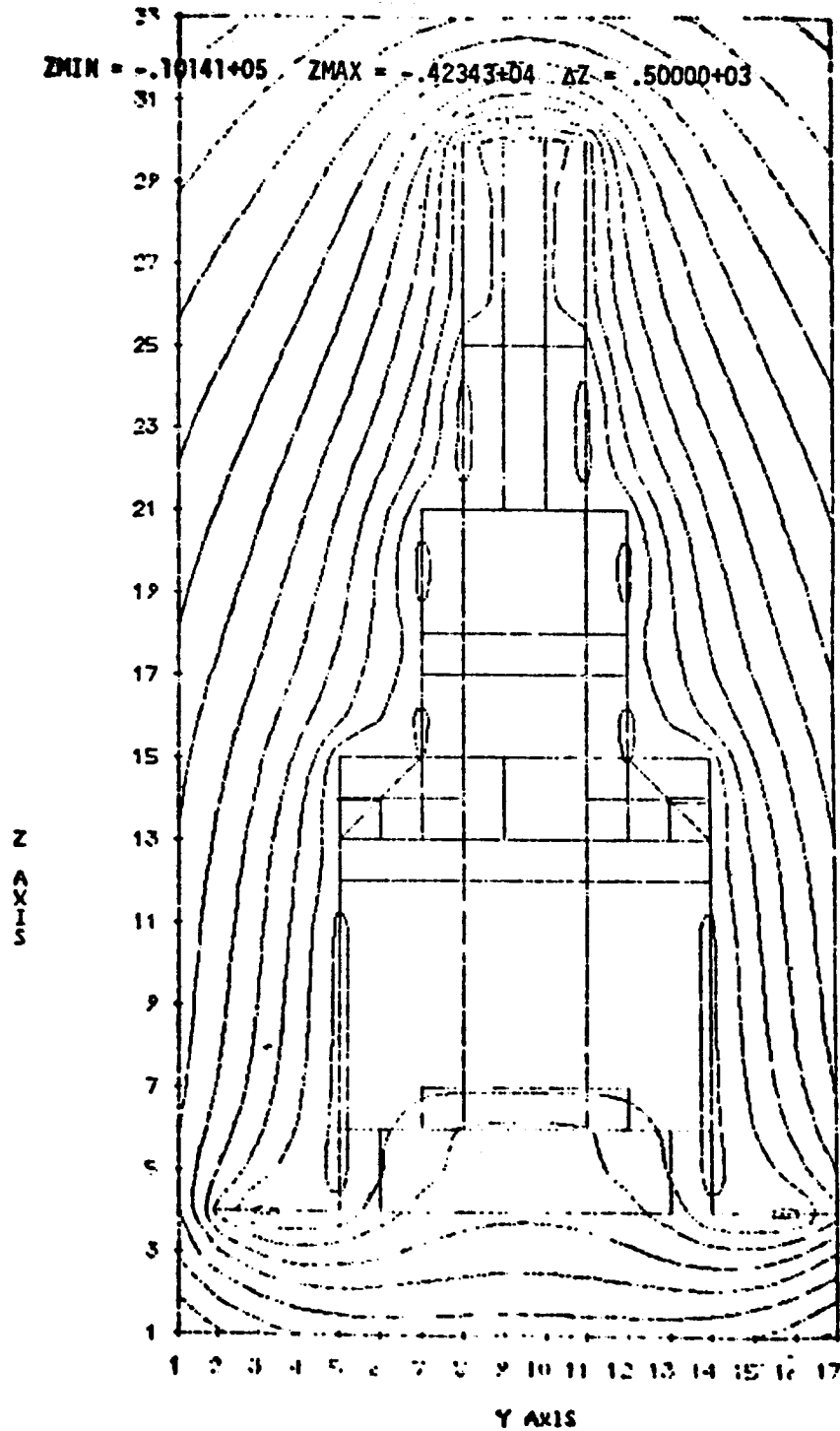


Figure 17. Case 6 (sun -Z,  $A_p = 400$ ) potential contours along the Y-Z plane of  $X = 9$ .

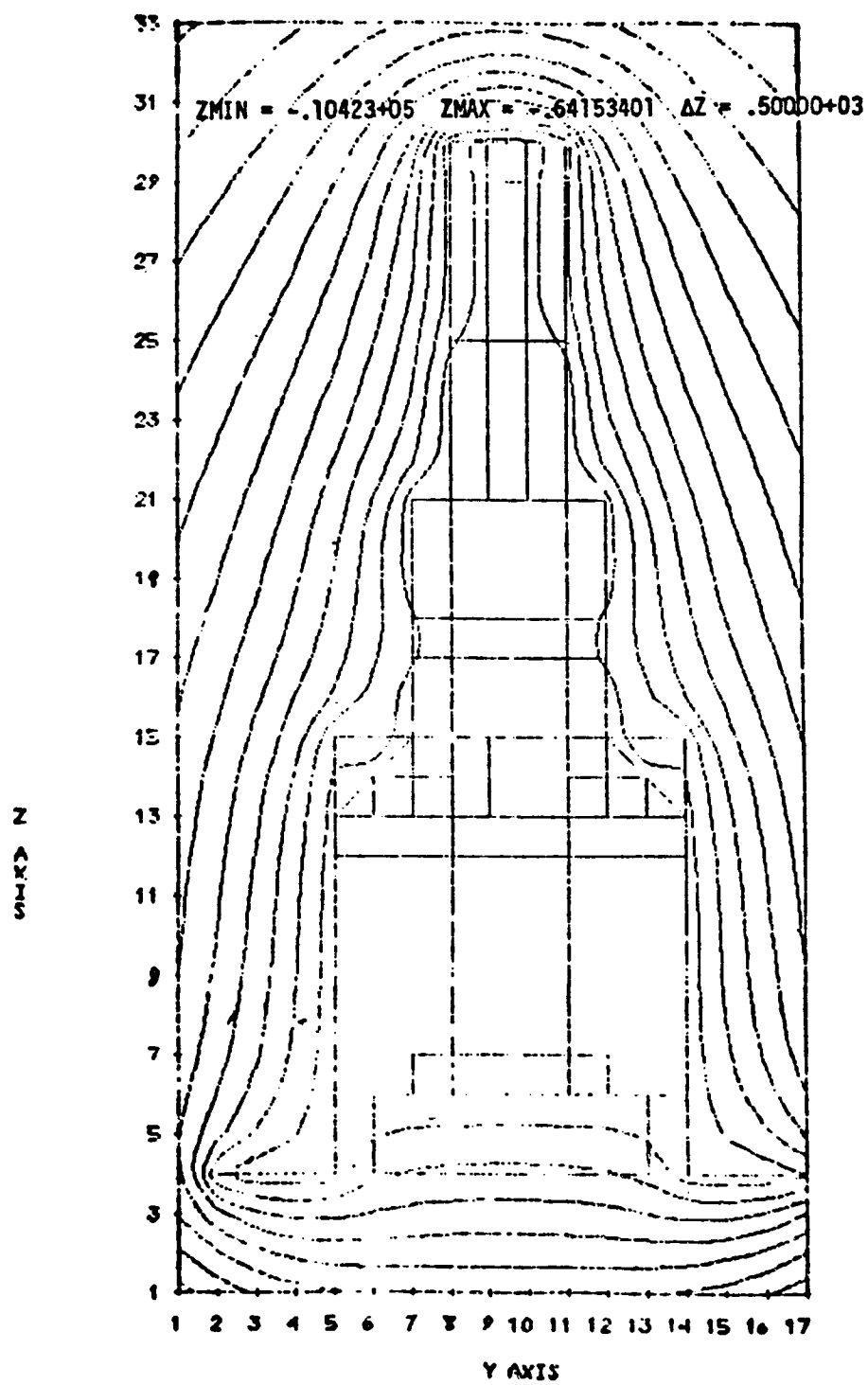


Figure 18. Case 8 (eclipse,  $A_p = 400$ ) potential contours along the Y-Z plane of  $X = 9$ .

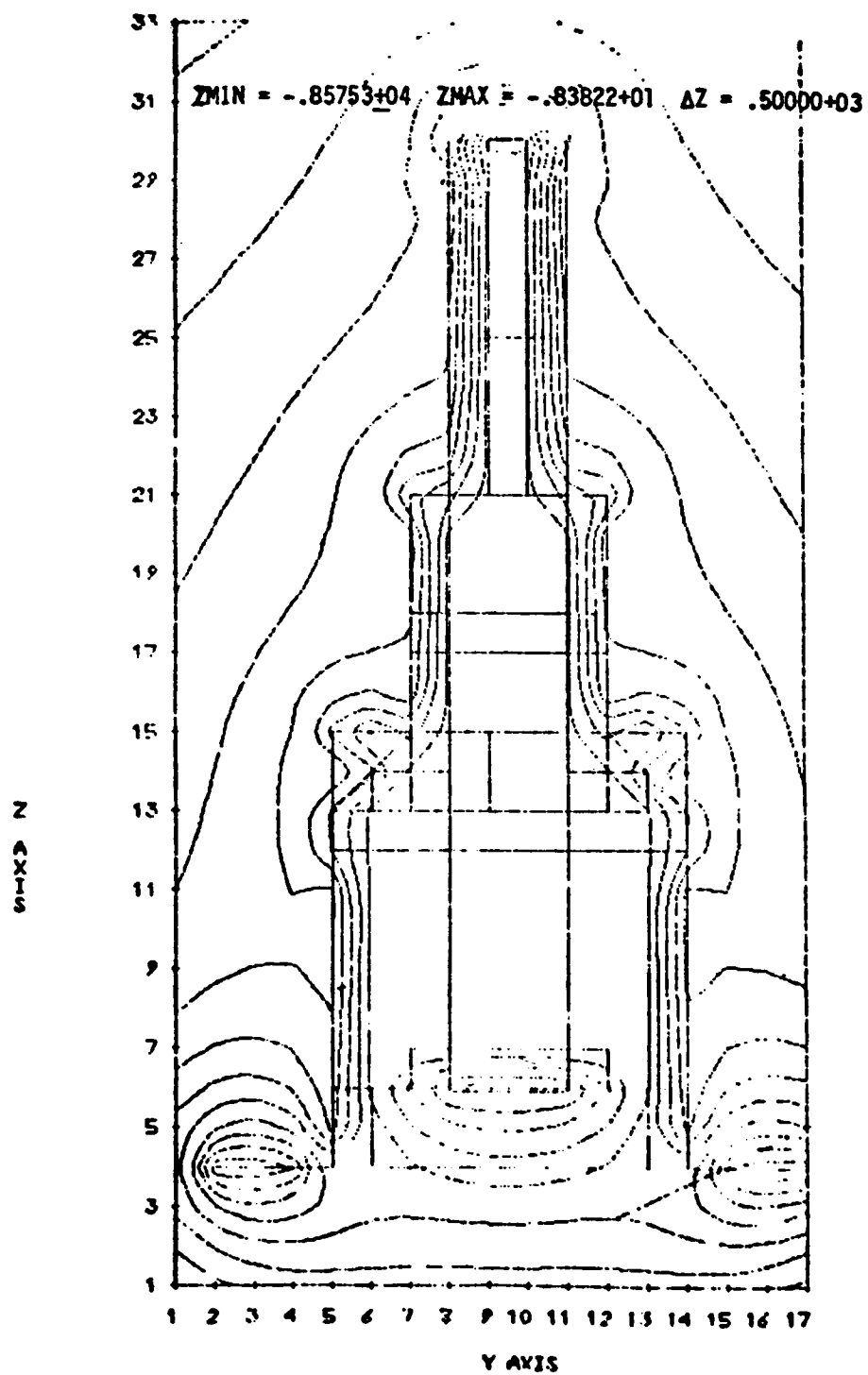


Figure 19. Case 7 (sun  $\perp$  Z,  $A_p = 400$ ) potential contours along the Y-Z plane of  $X = 9$ .

## RESULTS FROM A TWO-DIMENSIONAL SPACECRAFT-CHARGING SIMULATION AND COMPARISON WITH A SURFACE PHOTOCURRENT MODEL\*

J. G. Laframboise, S. M. L. Prokopenko, M. Kamitsuma, and R. Godard  
Physics Department, York University, Toronto, Canada

### ABSTRACT

A two-dimensional spacecraft charging simulation program called CYLVIA, which treats infinite-cylindrical geometries with angle-dependence, has been under development for four years. Two features of this program, its orbit integration and current collection methods, are discussed. A calculation is presented of floating potentials of a spacecraft cross-section which is represented by two conductive sectors, and a comparison is made between the photoemission current distribution obtained therein and another given by an approximate analytic surface photocurrent expression by Laframboise and Whipple.

### 1. INTRODUCTION

A two-dimensional spacecraft-charging simulation program, called CYLVIA (CYLinder Voltages in Ionosphere and Above), has been constructed; descriptions of this program and preliminary results from it have been given previously (Laframboise and Prokopenko, 1977, 1978; Laframboise et al, 1979). Herein, we present (Sec. 2) a more detailed discussion of two of its principal features: the orbit integration and current calculation methods used. We also outline (Sec. 3) an analytic surface photocurrent calculation which is to be described in detail elsewhere (Laframboise and Whipple, to be published), and we compare (Sec. 4) the photoelectron current distribution given by the resulting expression with a corresponding result obtained using CYLVIA.

### 2. ORBIT INTEGRATION AND CURRENT CALCULATION

CYLVIA uses a form of the particle orbit equations in which particle total energy is explicitly conserved. This formulation was adopted because of a difficulty which arose when using more standard methods to integrate photoelectron orbits. Accumulation of numerical errors was occasionally found to change the total energy of an orbit by amounts large compared to the assumed thermal energy of emission (1.5V), especially near points where orbits were "reflected" by a potential barrier; this in turn produced large errors in calculations of photoelectron currents reimpacting spacecraft surfaces.

In order to derive the orbit equations, we consider the motion of a particle in a plane. We let  $(r, \theta)$  and  $(v_r, v_\theta)$  represent its position and

---

\*Work supported by the U.S. Air Force Office of Scientific Research under grant number AFOSR-76-2962.

velocity components in polar coordinates (Fig. 1). We let  $s$  represent arc length along its orbit, and  $\hat{u}$  and  $\hat{n}$  represent unit tangent and unit normal vectors at a point on the orbit, the latter directed toward its local centre of curvature. We let  $\rho$  represent its local radius of curvature. We let  $q, m$ , and  $E$  represent particle charge, mass, and total energy, and  $\varphi(r, \theta)$  represent electric potential. The equation of motion  $m \, d\mathbf{v}/dt = -q\nabla\varphi$  reduces to:

$$v \frac{dv}{ds} \hat{u} + \frac{v^2}{\rho} \hat{n} = \frac{q}{m} \left( -\hat{n} \frac{\partial \varphi}{\partial n} - \hat{u} \frac{\partial \varphi}{\partial s} \right) \quad (1)$$

We equate respective components of Eq. (1), and use the relations  $ds = \rho d(\alpha + \theta)$ ,  $dr = \cos(\alpha) ds$ , and  $r \, d\theta = \sin(\alpha) ds$ . We then obtain the orbit equations in the following form:

$$\begin{aligned} \frac{d\alpha}{ds} &= - \frac{q}{mv^2} \left( \frac{\cos \alpha}{r} \frac{\partial \varphi}{\partial \theta} - \sin \alpha \frac{\partial \varphi}{\partial r} \right) - \frac{\sin \alpha}{r} \\ \frac{dr}{ds} &= \cos \alpha \\ \frac{d\theta}{ds} &= \frac{\sin \alpha}{r} \\ v^2 &= \frac{2}{m} \left[ E - q\varphi(r, \theta) \right] \end{aligned} \quad (2)$$

This system is reduced from fourth to third order because the last equation appears in integrated form. At points where particle reflection from potential barriers produces cusps or near-cusps in an orbit ( $d\alpha/ds$  becomes singular or large), a segment of the orbit is replaced by a parabolic arc.

We illustrate the current calculation method used by CYLVIA by first considering photoelectrons which arrive at a point on the surface whose normal makes an angle  $\theta$  with the sunward direction, each of them having originated at some other surface location  $\theta_0$  (Fig. 2a) and forced to return to the surface by a potential barrier which surrounds the spacecraft. Their current density at the surface location given by  $\theta$  is:

$$J(\theta) = \int_{v=0}^{v=\infty} \int_{\omega=0}^{\omega=\pi} \hat{f}(v, \omega) (v \sin \omega) (v \, dv \, d\omega) \quad (3)$$

where  $v = (v_r^2 + v_\theta^2)^{1/2}$  and  $\omega = \tan^{-1}(v_r/v_\theta)$  are polar coordinates in incident velocity space at the surface location  $\theta$ ,  $\hat{f} \equiv d^2N/dv_r dv_\theta$  is the two-dimensional velocity distribution of photoelectrons, and  $N$  is their number density. By Liouville's theorem,  $\hat{f}$  is constant along a particle orbit. Assuming that photoelectrons are emitted with a Maxwellian distribution corresponding to a temperature  $T$ , their emission flux  $J_{ph}(\theta_0)$  is related to  $\hat{f}$  as follows:

$$\hat{f} = \frac{1}{\sqrt{2\pi}} J_{ph}(\theta_0) \left( \frac{m}{kT} \right)^{3/2} e^{-mv_0^2/2kT} \quad (4)$$

If the sunlit side of the spacecraft has uniform material properties, then

$J_{ph}(\theta_0) = J_{ph}(0) \cos \theta_0$ . We introduce dimensionless variables as follows:

$$\chi = q\phi/kT; \quad u = v(m/2kT)^{1/2} \quad (5)$$

Since  $\frac{1}{2}mv^2 + q\phi = \frac{1}{2}mv_0^2 + q\phi_0$ , (4) and (3) become:

$$\hat{f} = \frac{1}{\sqrt{2\pi}} J_{ph}(\theta_0) \left( \frac{m}{kT} \right)^{3/2} e^{\chi_0 - \chi} e^{-u^2} \quad (6)$$

$$J(\theta) = \frac{2}{\sqrt{\pi}} \int_{u=0}^{u=\infty} du u^2 e^{-u^2} \int_{\omega=0}^{\omega=\pi} d\omega \sin \omega \left[ J_{ph}(\theta_0) e^{\chi_0 - \chi} \right] \quad (7)$$

The factor in square parentheses in (7) is evaluated for each  $u$  and  $\omega$  by integrating the corresponding photoelectron orbit backward to its origin to find  $\theta_0$  and  $\chi_0$ . To do the integrations in (7), we set up a polar-coordinate grid in velocity space at the surface location  $\theta$ , as shown in fig. 2b, where we have defined  $u_n = -u_r$ ,  $u_t = -u_\theta$ . We approximate  $F(u, \omega) \equiv (2/\sqrt{\pi}) J_{ph}(\theta_0) \exp(\chi_0 - \chi)$  in each cell  $u_i \leq u \leq u_{i+1}$ ,  $\omega_j \leq \omega \leq \omega_{j+1}$  by  $(A + Bu)(C + D\omega)$  where  $A, \dots, D$  can be determined if the values of  $F$  at its four corners are found, again by integrating orbits backward. Equation (7) then becomes:

$$J(\theta) = \sum_{i,j} \int_{u_i}^{u_{i+1}} du u^2 e^{-u^2} (A_{ij} + B_{ij}u) \int_{\omega_j}^{\omega_{j+1}} d\omega \sin \omega (C_{ij} + D_{ij}\omega), \quad (8)$$

a form in which all integrals can be evaluated analytically. This method for evaluating  $J(\theta)$  is essentially equivalent to the "inside-out" method of Parker and Whipple (1967). The factor  $\exp(\chi_0 - \chi)$  in  $F(u, \omega)$  may vary strongly within individual cells. The potential barrier which surrounds a spacecraft is always of finite height, permitting some photoelectrons to escape and ambient electrons to reach it. This means that the integration in (8) must be performed over two regions of velocity space, labelled I and II in Fig. 2b, containing photoelectrons (and secondary and backscattered electrons), and ambient electrons, respectively. In general,  $\hat{f}$  will contain a discontinuity at the boundary between I and II (Whipple, 1976) which can produce large errors in the evaluation of  $J(\theta)$ . The integration method used in CYLVIA treats these discontinuities explicitly, using bisection searches to find points such as those circled in Fig. 2b. If the ambient electron velocity distribution is isotropic, then  $F$  in region II will be independent of  $\omega$ .

### 3. SURFACE PHOTOCURRENT EXPRESSION

An analytic expression has been derived (Laframboise and Whipple, to be published) for the surface current density of photoelectron migration along a plane surface  $y=0$ , in the presence of: (a) a uniform normal electric field  $E_y > 0$ , which causes photoelectrons emitted from the surface to reimpact it (b) a uniform tangential electric field  $E_x$  (c) a uniform photoemission current density gradient  $J_{ph}' \equiv dJ_{ph}/dx$ , so that the photoemission current per unit surface area is  $J_{ph}(x) = J_{ph,0} + J_{ph}'x$ . This photoemission gradient, or

"production gradient", would ordinarily be caused by a spatial variation in the illumination of the surface. In the presence of (a) and (b), all photoelectron orbits are parabolas whose axes are parallel to the resultant electric field vector. It is also assumed that photoelectrons are emitted with a Maxwellian velocity distribution corresponding to a temperature  $T_{ph}$ . The surface current  $\Gamma$  in the  $x$  direction, per unit distance  $z$  perpendicular to the  $(x,y)$  plane, can then be found by integrating over position and velocity of emission to find the number of photoelectrons per unit  $z$  and unit time which cross the plane  $x=0$  in the direction of increasing  $x$ , then subtracting the corresponding result for decreasing  $x$ . The net result is:

$$\Gamma = - \frac{4J_{ph,0} kT_{ph} E_x}{eE_y^2} - J_{ph} \left( \frac{kT_{ph}}{eE_y} \right)^2 \left[ 4 + 16 \left( \frac{E_x}{E_y} \right)^2 \right]. \quad (9)$$

where  $e$  is the magnitude of unit electronic charge.

This result contains, respectively, a potential-gradient term, a production-gradient term, and a cross-term. The potential-gradient term is twice that given by Eq. (14) of Pelizzari and Criswell (1978); reasons for this difference are given by Laframboise and Whipple (to be published). It is noteworthy that the production-gradient term is enhanced five-fold if  $(E_x/E_y)^2 = 1$ , in comparison with its value when  $E_x = 0$ ; this is true regardless of the sign of  $E_x$ .

#### 4. RESULTS AND DISCUSSION

Figure 3 shows a CYLVIA calculation of equipotential contours surrounding a cylindrical spacecraft cross-section whose surface consists of two independently floating conductive sectors, the smaller of which is shaded and subtends an angle of  $90^\circ$ . In this calculation the ambient ion and electron velocity distributions are double Maxwellians with the following properties:

$N_{i1} = 1 \text{ cm}^{-3}$	$N_{e1} = 1 \text{ cm}^{-3}$
$T_{i1} = 20 \text{ eV}$	$T_{e1} = 500 \text{ eV}$
$N_{i2} = 1 \text{ cm}^{-3}$	$N_{e2} = 1 \text{ cm}^{-3}$
$T_{i2} = 10^4 \text{ eV}$	$T_{e2} = 5000 \text{ eV}$

The photoelectron charge flux  $eJ_{ph}$  is  $45 \times 10^{-6} \text{ A/m}^2$  at normal sunlight incidence.  $T_{ph} = 1.5 \text{ eV}$ . Secondary and backscattered electron fluxes are assumed zero. Ambient ion and electron and photoelectron currents are calculated using numerical orbit-following as described in Sec. 2. The computation grid in  $(r, \theta)$  contains  $65 \times 48$  intervals. The computation grid in  $(u, \omega)$  contains  $8 \times 16$  intervals for each Maxwellian component of each particle species, apart from bisection searches (Sec. 2) which give finer resolution. Linear space charge is assumed [Laframboise and Prokopenko, 1977, Eq. (3)]. The above-mentioned plasma parameters imply an ambient Debye length of 32.5 meters; spacecraft radius  $r_s$  is 1 meter. The outer boundary of the computation grid is at  $e^5 r_s \approx 148 r_s$ . The most noteworthy feature of figure 3 is a negative saddle-point potential barrier which surrounds the larger sector, and whose height varies from about 2 volts at the sunward point to several hundred volts near the edges of this sector.

The resulting normalized current densities  $j_i$ ,  $j_e$ , and  $j_{ph}$  of ambient ions, ambient electrons, and photoelectrons are shown as functions of surface position in Fig. 4. We have made a separate calculation of  $j_{ph}$  using Eq. (9) with the tangential electric field  $E_x$  set equal to zero since the spacecraft surfaces are conductive. To use (9), we note that the net photoelectron flux out of the surface is equal to the divergence of  $\Gamma$  with respect to surface coordinates. In our geometry, this means that

$$J_{ph,net\ in} \equiv J_{ph,in} - J_{ph,out} = \frac{-1}{r_s} \frac{d\Gamma}{d\theta} = \frac{4}{r_s^2} \frac{d}{d\theta} \left[ \left( \frac{kT_{ph}}{eE_r} \right)^2 \frac{dJ_{ph,out}}{d\theta} \right] \quad (10)$$

where

$$edJ_{ph,out}/d\theta = -45 \times 10^{-6} \sin \theta \text{ A/m}^2 \left( -\frac{1}{2}\pi < \theta < \frac{1}{2}\pi \right),$$

and the radial electric field  $E_r$  is obtained from the numerical solution for  $\varphi(r, \theta)$  used to construct Fig. 3. Net photoelectron currents obtained in this way are shown as dashed curves in Fig. 4. We see that near  $\theta = 0^\circ$ , the net outward photocurrent is badly underestimated by Eq. (10) since the potential barrier for electrons at this location is not much higher than the photoelectron mean thermal energy, so a substantial fraction of photoelectrons escape, and this is not allowed for in Eqs. (9) and (10). However, in the interval  $30^\circ \lesssim \theta \lesssim 90^\circ$ , where photoelectron escape is negligible, agreement between Eq. (10) and the numerical result is much better. The numerical result is about 10% to 20% above that given by (10); the most important reason for this difference is probably the fact that the tangential electric field, although zero at the spacecraft surface, is nonzero outside it, and the form of the cross-term in (9) indicates that the production-gradient current [which is the one calculated in Eq. (10)] is strongly sensitive to such fields. We have shown the photoelectron current as decreasing to zero almost discontinuously beyond  $\theta = 90^\circ$ , because the average angular distance of photoelectron migration in the electric fields at this point ( $E_\theta = 0$ ,  $E_r = 1824 \text{ V/m}$ ) is about  $0.1^\circ$ .

Another noteworthy feature of Fig. 4 is the decrease in the flux of ambient electrons at larger  $\theta$ , caused by the increasing height of the potential barrier as one moves away from the sunward point  $\theta = 0^\circ$

#### REFERENCES

- Laframboise, J.G., Godard, R., and Prokopenko, S.M.L., Numerical Calculations of High-Altitude Differential Charging: Preliminary Results. In: Spacecraft Charging Technology - 1978, NASA Conference Publication 2071, NASA Lewis Research Center, Cleveland, Ohio/AFGL-TR-79-0082, Air Force Geophysics Laboratory, Hanscom AFB, Massachusetts, pp. 188-196 (1979).
- Laframboise, J.G., and Prokopenko, S.M.L., Numerical Simulation of Spacecraft Charging Phenomena. In: Proceedings of the Spacecraft Charging Technology Conference, C.P. Pike and R.R. Lovell, Eds., Report No. AFGL-TR-77-0051, Air Force Geophysics Laboratory, Hanscom AFB, Massachusetts/NASA TMX-73537, Lewis Research Center, Cleveland, Ohio, pp. 309-318 (1977).
- Laframboise, J.G., and Prokopenko, S.M.L., Predictions of High-Voltage Differential Charging on Geostationary Spacecraft. In: Effect of the Ionosphere on Space and Terrestrial Systems, J.M. Goodman, Ed., U.S. Government Printing Office, Washington, D.C., pp. 293-301 (1978).



Parker, L.W., and Whipple, E.C., Jr., Theory of a Satellite Electrostatic Probe. *Ann. Phys.* 44, pp. 126-161 (1967).

Pelizzari, M.A., and Criswell, D.R., Differential Photoelectric Charging of Nonconducting Surfaces in Space. *J. Geophys. Res.* 83, pp. 5233-5244 (1978).

Whipple, E.C., Jr., Observation of Photoelectrons and Secondary Electrons Reflected from a Potential Barrier in the Vicinity of ATS 6. *J. Geophys. Res.* 81, pp. 715-719 (1976).

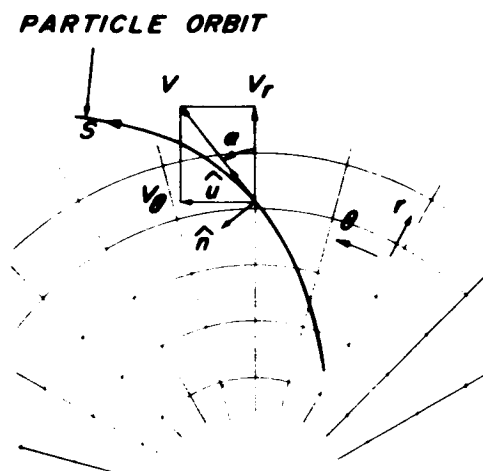


Figure 1. Coordinate system and definitions for particle orbit integration.

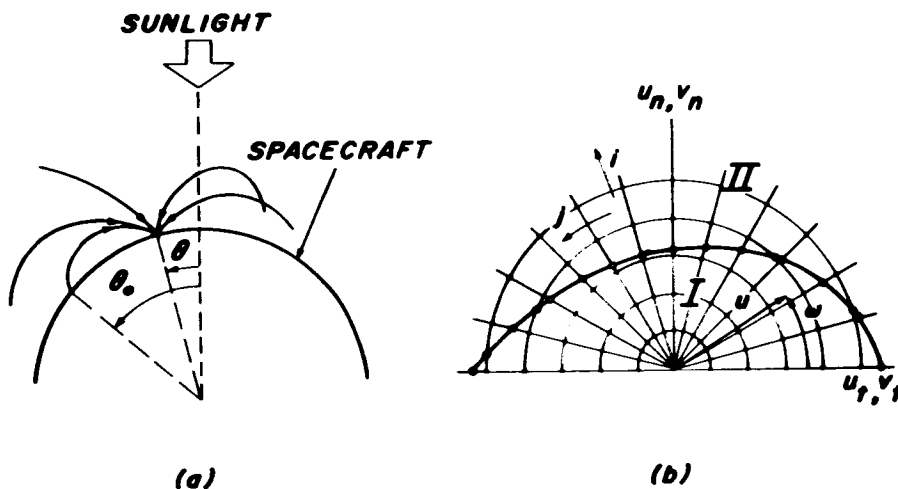


Figure 2. Position-space (a) and velocity-space (b) coordinates for calculation of incident current density at a surface point. Figure 2a shows several particle orbits incident at a surface point  $\theta$ , one of them having originated at the surface point  $\theta_0$ .

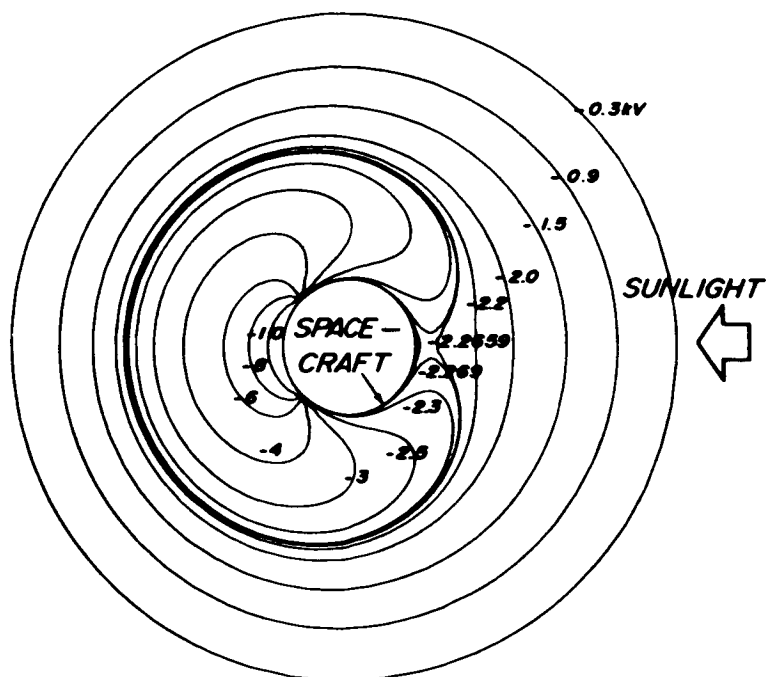


Figure 3. Equipotential contours around a cylindrical spacecraft cross-section with two conductive sectors having angles of  $270^\circ$  and  $90^\circ$ . Sector potentials are -2.265 kV and -11.88 kV, respectively. Other data pertinent to this calculation are given in Sec. 4. The radial coordinate in this figure is  $1 + \ln(r/r_s)$  where  $r_s$  is spacecraft radius.

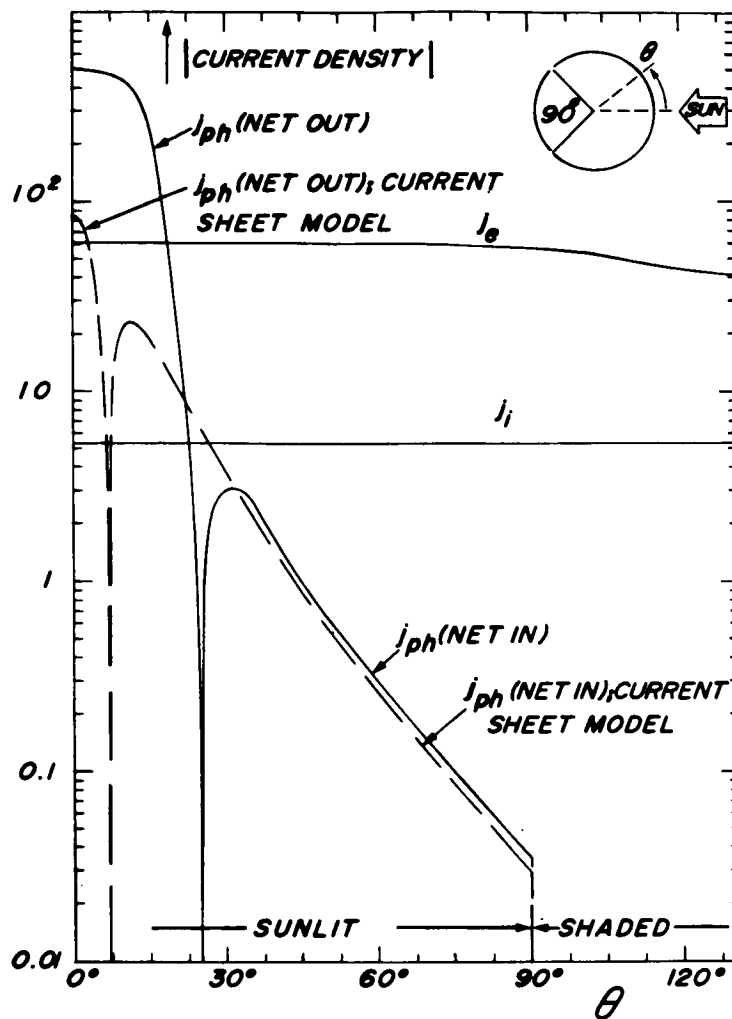


Figure 4. Current densities vs surface position for the situation shown in Fig. 3 and described in Sec. 4. In this figure, normalized current density  $j$  is defined as  $J/J_{\text{ref}}$ , where  $J_{\text{ref}}$  is the random flux of Maxwellian ions having a temperature and density of 1 keV and  $1 \text{ cm}^{-3}$ . Approximate photoelectron currents  $j_{\text{ph}}$  obtained using the approximate surface current ("current sheet") model given by Eqs. (9) and (10) are shown as dashed curves.

# **ANALYTICAL MODELING OF SATELLITES IN GEOSYNCHRONOUS ENVIRONMENT**

**N. John Stevens  
NASA Lewis Research Center**

## **SUMMARY**

Geosynchronous satellites are known to be charged by the geomagnetic substorm environment. Surface charging is often sufficient to result in discharges that can couple transients into satellite electrical harnesses and produce electronic upsets in systems. Ground simulation testing of surface charging has been and is being conducted by using monoenergetic electron beams. Results have shown that massive discharges on dielectric surfaces could occur with sufficiently large differential voltages between the surface and the substrate. With the advent of three-dimensional analytical modeling techniques, however, it has become apparent that the large differential voltages required for these massive laboratory discharges do not occur on satellites in space. The modeling predictions are supported by dielectric charging data from P78-2, SCATHA (Spacecraft Charging at High Altitudes) flight results. Hence other mechanisms leading to discharges on satellite surfaces must be found. Three such mechanisms discussed in this paper are ungrounded insulator areas, buried charge layers (due to mid-energy-range particles), and positive differential voltages (where structure voltages are less negative than surrounding dielectric surface voltages).

## **INTRODUCTION**

In the early 1970's, it was found that the Applications Technology Satellite 5 (ATS-5) spacecraft potential was driven to significant negative voltages when the satellite was in the local midnight region of its orbit (refs. 1 to 4). Values extending to -10 000 volts when the satellite experienced the spring and fall eclipse periods and to -300 volts when the satellite was in sunlight were observed (refs. 2 and 5). The cause of this charging was found to be magnetospheric plasma clouds (substorms) that are periodically generated in this midnight region. The differences in potential between eclipse and sunlight charging events were due to photoemission from sunlit surfaces.

Although this phenomenon was of interest, it was not believed to be serious for system operations since it did not seem to cause problems. When a Defense Satellite Communications System (DSCS) II satellite system failed in 1973, however, the failure review started locating numerous instances of electronic switching anomalies in DSCS II and other geosynchronous satellites (ref. 6). When these anomalous switching events were plotted against local time of occurrence, a peculiar pattern developed (fig. 1). The radial separation of the anomaly distribution in this figure has no significance; it is simply a means of separating the occurrences. The bars indicate the uncertainty in the time of occurrence. From this figure it is apparent that anomalies occurred in the midnight to dawn segment of the orbit, implying substorm charging events.

When the ATS-6 spacecraft was launched in 1974, charging was again observed. Ground potentials on the satellite were driven to -2.2 kilovolts during sunlight charging and to -19 kilovolts during eclipse charging (maximum potentials reported in refs. 4 and 7). Much care was taken to make this satellite immune to external radiation since it had to operate in its own radiofrequency (rf) beam. As a result of this careful design the substorm charging phenomenon did not cause any system upsets (ref. 8). The data from this satellite indicated that spacecraft charging could be related to the absence of low-energy plasmas (fig. 2, ref. 7). Apparently the substorm has the effect of suppressing the natural environment, low-energy plasma.

In 1975, a cooperative Air Force and NASA spacecraft charging investigation was begun to develop means of controlling the absolute and differential charging of geosynchronous satellite surfaces by geomagnetic substorm environments (ref. 9). Although there had been only one catastrophic failure of a satellite system, it was felt that the charging and discharging cycles could have a detrimental effect on future, long-life, unattended-operation missions that were being proposed. Therefore the investigation of this phenomenon and its effect on satellite systems was a logical candidate for a technology program.

The ground technology program concentrated on developing analytical tools and conducting ground simulation experiments in support of the P78-2 (Spacecraft Charging at High Altitudes (SCATHA)) flight program. Both ground technology and flight data were necessary to produce the design guidelines, environmental atlas, and test standards required as the output of the cooperative investigation.

Ground simulation testing was begun first. Monoenergetic electron beams were used to charge typical spacecraft dielectric samples. The responses of the dielectrics were carefully measured and evaluated (ref. 10). When breakdown voltage thresholds were exceeded, discharges occurred and produced spectacular, lightning-like displays (fig. 3). These studies indicated that surface charging could be explained in terms of current balances (ref. 11) and that a differential voltage between the dielectric surface and substrate of 8 to 15 kilovolts was required for discharges.

When discharges did occur, it was found that the energy lost from the sample was large and scaled with the square root of the sample area (refs. 12 and 13). The significant results, characterized in table I, were consistent with the prevailing concepts of spacecraft charging interactions. On the basis of ATS-5/6 data, it was felt that large differential voltages between dielectric surfaces and the subsurface could be developed by substorm encounters.

The development of modeling tools has been proceeding slowly since the start of the joint investigation. The NASA Charging Analyzer Program (NASCAP) has now reached a stage where its predictive capability has been sufficiently cross-checked against ground simulation and flight data (refs. 14 to 17). Computation of satellite behavior in actual space environments indicates that some of the original charging concepts are in error and should be reviewed.

This paper reviews the modeling computations and discusses the effect on discharge processes.

#### SYMBOLS

A	area
C	capacitance
$E_m$	mid-energy-range incident electron
I	current
$n_e$	electron number density
$n_p$	proton number density
P	incident particles (electrons and protons)
$P_o$	photoemitted electrons
s	secondary emitted electrons
$T_e$	electron temperature
$T_p$	proton temperature
$V_L$	voltage at buried charge layer in dielectric
$V_S$	dielectric surface voltage
$V_{S/C}$	spacecraft structure voltage

#### GEOSYNCHRONOUS SATELLITE MODELING

The behavior of geosynchronous satellites in space environments was analyzed by using the NASCAP computer code, a three-dimensional code capable of predicting the response of satellite surfaces to a specified environmental flux as a function of time. The code considers the material properties (e.g., bulk and surface conduction, secondary emission, backscatter, and photoemission) and the influence of fields generated around the satellite by the charged surfaces in computing surface voltages. The code has been described in the literature (refs. 18 to 20).

The satellite model used in NASCAP is shown in figure 4. This model represents a typical three-axis-stabilized satellite as used in the late 1970's. It has two large solar array wings that are assumed to be Sun oriented and capable of generating about a kilowatt of power. It is assumed that the arrays function at 50 volts when generating power. The Sun-facing surface of the array has a silica cover glass that is coated with a magnesium fluoride antireflective coating. The array is assumed to have a 4-mil-thick Kapton substrate. The interconnections are modeled as patches on the array

(to simulate the total interconnection area) and are assumed to be an oxidized aluminum surface. The body of the satellite has Earth-facing antennas and a rear thruster chamber. The body is covered with various dielectrics as shown.

Environmental conditions used in this analysis consist of single Maxwellian temperatures for electrons (with proton temperatures assumed to be twice the electron temperatures), and equal electron and proton densities. Sunlight (with Sun incidence at  $27^\circ$ ) and eclipse conditions were used in this analysis.

The predicted surface potentials (relative to space plasma potential) are shown for selected surfaces, as a function of time, in figure 5. In the first 1000 seconds, when substorm conditions are characterized by 3-keV electron temperatures, no appreciable charging occurs. The concept that a threshold particle temperature must be reached before charging can begin is seen to apply (ref. 21). In the next 1000-second interval, with the satellite still in sunlight but with the substorm intensity increased to 8-keV electron temperatures, both absolute charging and differential charging occur. Differential charging here is defined as the difference between the dielectric surface voltage and the spacecraft structure. Note that the shaded Kapton has become more negative than the spacecraft structure (satellite electrical ground) and that the solar array cover glass is positive with respect to the structure.

When the satellite enters eclipse, there is a rapid change in absolute charging followed by a slower development in differential charging. This is consistent with ground results on charging rates (ref. 22) and has been shown to be true for both 8- and 12-keV substorms. Note that the differential charging of the solar array covers has become more positive with respect to the structure but that the shaded insulators have become more negative. Upon entering the sunlight again, there is another rapid change in absolute values followed by a slower readjustment of differential voltages. Finally, in the last 2000 seconds of this analysis, substorm conditions are allowed to become progressively less intense, and the spacecraft potentials relax accordingly.

This analysis predicts two effects that were not anticipated:

- (1) Low differential voltages across the shaded insulators
- (2) Positive differential voltages on the solar array

The maximum differential voltage across the 4-mil-thick Kapton used in this study is only about 2 kilovolts. Analyses of different satellites under different environmental conditions indicate that, while the absolute voltages can be shifted, the differential voltages remain about the same; that is, the maximum differential voltages across shaded insulators are never predicted to be greater than 4 kilovolts (refs. 23 to 27). This result is due to the suppression of photo- and secondary emission by the three-dimensional electric fields developed on the more negatively charged surfaces (ref. 28). This predicted low level of differential voltage agrees with the P78-2 (SCATHA) surface potential monitor data. Ungrounded spot voltages measured by this monitor indicated differential values reaching -2 kilovolts even though the structure potential reached values to -8 kilovolts relative to the space plasma potential (ref. 29).

The positive differential voltages predicted for solar array cover glasses can range from a few volts to kilovolts depending on the secondary emission characteristics assumed for coatings applied to these covers. For reasonable ranges of values the differential voltage across the cover glass is always positive (refs. 23 to 27). Ground simulation testing is usually conducted by grounding the array electrical circuit and irradiating the cover glass with monoenergetic electrons (ref. 10). Doing so results in a negative differential voltage across the cover glass; that is, cover glass surface voltages are strongly negative with respect to the grounded electrical circuit.

According to the analytical results predicted in this study, discharges similar to those observed in the laboratory should not occur on satellites. The differential voltage across shaded insulators is predicted to be too low to exceed the breakdown threshold derived from ground tests, and the predicted differential voltage across the solar array cover glass is the wrong polarity as compared with the ground test conditions. Yet the fact remains that discharges do occur on satellites (refs. 30 and 31). Therefore it becomes necessary to investigate other possible means of producing discharges in a space environment.

#### DISCHARGE MECHANISMS

From the preceding discussion it is apparent that the mechanisms leading to satellite discharges are not the same as those studied in the laboratory. Three mechanisms leading to discharges are possible:

- (1) Ungrounded insulators
- (2) Buried or trapped charge layers
- (3) Positive differential voltages

These mechanisms are discussed in this section.

#### Ungrounded Insulators

Dielectric areas electrically decoupled from the satellite can charge much more rapidly than areas that remain coupled. Decoupling can occur by breaking electrical grounds to the metallic areas of thermal blankets or optical solar reflectors (OSR). Figure 6 shows a comparison of predicted surface voltages for shaded Kapton and OSR regions in a 8-keV electron temperature substorm. Figure 6(a) shows voltage predictions when these regions are coupled (i.e., metallic areas grounded to structure). Both absolute charging and differential charging are seen to develop slowly. Figure 6(b) shows the voltage predictions with the grounds broken and the insulator regions capacitively coupled to the structure with a capacitance of  $10^{-12}$  farad. Differential charging of these regions occurs rapidly while the structure slowly charges. In this case a large differential voltage can occur in seconds. However, it should be pointed out that the energy storage (for possible discharge pulses) is low because of the small capacitance. The differential voltages for ungrounded insulators could be larger than the 2 kilovolts obtained in this example if different materials and environments were used. Although this type of charging mechanism is always possible, it may develop with time in orbit as a result of the breakup of the thin vapor deposited metal used on these insulators. Hence it is difficult to predict and the only means of protection would be to give careful attention to grounding.



## Buried or Trapped Charge Layers

Ground testing of dielectrics with low-energy, monoenergetic electrons (0 to 20 keV) results in charges being deposited on or near the exposed dielectric surface. These incoming (primary) electrons generate secondary electrons, and eventually an equilibrium is reached. The surface is at a characteristic voltage such that the net current to that surface is zero. However, if the electron energies are higher (100 keV), the incoming particles penetrate the surface and become buried within the dielectric or possibly pass completely through and thus produce different surface voltage characteristics than in the low-energy case. If a test were run in an environment combining a relatively high flux of low-energy electrons (e.g., 5 keV) with a lower flux of mid-energy electrons (e.g., 50 keV), one would expect the dielectric surface to respond to the low-energy flux by developing a characteristic voltage and the mid-energy electrons to penetrate the surface and be buried (fig. 7). A low differential voltage would thus occur between the dielectric surface and the substrate, but very strong voltage gradients would occur within the dielectric because of the buried charges. These gradients could be sufficient to trigger discharges.

In space there is a wide distribution of particle energies. Data on the substorm environment from the P78-2 (SCATHA) instruments (ref. 32) indicate that there is a large constituent of electrons in the mid-energy range (100 keV). In addition, there is a significant ion flux distributed over a wide energy range. Under these conditions it could be possible to duplicate the combined-flux test just described. The low-energy component of the electron flux and the ion flux would interact with the satellite surfaces to produce a relatively low negative surface voltage (the electron flux dominating). If the surface were in sunlight, photoemission from the surface would reduce the negative surface voltage. The mid-energy component of substorm electrons could be buried within the satellite surfaces and generate strong voltage gradients that could trigger discharges. Edges and imperfections in the dielectric can enhance the probability of discharge. NASCAP modeling of satellite behavior does not treat the concept of buried charge, and so would not be able to predict anything other than the surface voltage.

This concept of buried charge was proposed several years ago (ref. 33) and is currently being evaluated analytically (ref. 34) and experimentally (ref. 35). A criterion for breakdown found in the experimental work is a gradient in excess of  $2 \times 10^5$  volts per centimeter. Although this mechanism appears to be a logical means of producing discharges in satellites, additional studies must be conducted.

A phenomenon that might be related to this proposed trapped-charge mechanism is a discharge that is generated in low-energy-electron-beam ground tests. This type of discharge, which occurs infrequently but repeatedly when dielectrics have been differentially charged to a few kilovolts, is usually ignored because of the small resultant pulse and charge loss. In view of the low predicted differential voltages on satellites, however, these low-voltage discharges should be reevaluated.

## Positive Differential Voltages

A positive differential voltage exists when the dielectric surface is at a less negative voltage than the substructure. If there are cracks, edges, or gaps that expose the substructure through the dielectric, a small "electron gun" exists, with the substructure forming a cathode and the dielectric the accelerator plates. Discharges are possible if the differential voltage becomes large enough.

As an example of this mechanism, consider the predicted differential voltages for the solar array on the model used in this study (fig. 8). The coverglass properties include a high-secondary-yield, magnesium fluoride antireflection coating commonly used on space solar arrays. A very strong positive differential voltage exists in the middle and outer areas of this array during the very intense phases of the substorm and is especially large in eclipse (1 kV). Studies of solar array segments with the electrical circuit biased to negative voltages while exposed to plasma environments have shown that breakdowns are possible (ref. 36). Since the laboratory breakdown phenomenon occurred under conditions analogous to those predicted here, it is conceivable that spacecraft discharges could result from this mechanism. Studies conducted with an electrically floating solar array irradiated by monoenergetic electrons have also indicated discharge patterns (ref. 37).

Although only solar arrays have been discussed herein, similar conditions are predicted to exist for dielectric booms on satellites (ref. 27). In either case it is important and necessary to pursue studies of this breakdown mechanism.

## CONCLUDING REMARKS

Reviews of geosynchronous satellite data from ATS-5 to P78-2 (SCATHA) have indicated that satellite surfaces are charged by the geomagnetic environment, that discharges occur, that pulses from discharges can couple into spacecraft harnesses, and that electronic switching anomalies can result. Ground simulation testing has concentrated on discharge phenomena resulting from large differential voltages across dielectrics under the impression that large voltage differences were possible in space conditions. Such testing has resulted in cataloging the characteristics of large differential discharges.

Analytical modeling of satellites in geosynchronous environments with the NASCAP code has matured to a point where predictions agree with observed charging trends. The results of computations based on this modeling indicate that differential voltages on satellites are considerably smaller than those required to trigger discharges in ground tests, an indication that discharges on satellites in space are not the same as those studied in ground simulation tests. Therefore it became necessary to explore other mechanisms that could lead to discharges on satellites.

Three possible mechanisms are suggested in this report. The first is ungrounded insulators, where the dielectric is weakly capacitively coupled to the structure and can charge rapidly. The second is the buried charge layer,

where the mid-energy component of the electron flux in substorms can be buried or trapped within the dielectric, producing strong internal voltage gradients and possibly triggering discharges. The third is positive differential voltages, which can occur when the structure is more negative than the surrounding dielectric.

Each of these proposed mechanisms must be studied to determine if it could be responsible for the spacecraft charging type of discharges. To date, little work has been done on any of them. It is necessary to establish these discharge mechanisms consistent with ground tests, analysis, and space data in order to define a credible discharge criterion for designers to use.

#### REFERENCES

1. DeForest, S. E.; and McIlwain, C. E.: Plasma Clouds in the Magnetosphere. *J. Geophys. Res.*, vol. 76, June 1971, pp. 3587-3611.
2. DeForest, S. E.: Spacecraft Charging at Synchronous Orbit. *J. Geophys. Res.*, vol. 77, no. 2, Feb. 1972, pp. 651-659.
3. Fredericks, R. W.; and Scarf, F. L.: Observations of Spacecraft Charging Effects in Energetic Plasma Regions. *Photon and Particle Interactions with Surfaces in Space*, R. J. L. Garard, ed., Astrophysics and Space Science Library, Vol. 37, D. Reidel Publishing Co., 1973, pp. 277-308.
4. Bartlett, R. O; DeForest, S. E.; and Goldstein, R.: Spacecraft Charging Control Demonstration at Geosynchronous Altitude. *AIAA Paper 75-359*, Mar. 1975.
5. Rubin, A. G.; and Garrett, H. B.: ATS-5 and ATS-6 Potentials During Eclipse. *Spacecraft Charging Technology - 1978*, NASA CP-2071, AFGL TR-79-0082, 1979, pp. 38-43.
6. McPherson, D. A.; Cauffman, D. P.; and Schober, W.: Spacecraft Charging at the High Altitudes: The SCATHA Program. *Spacecraft Charging by Magnetospheric Plasmas*, A. Rosen, ed., Progress in Astronautics and Aeronautics, Vol. 47, American Institute of Aeronautics and Astronautics, Inc., 1976, pp. 15-30.
7. Reasoner, D. L.; Lennartsson, W.; and Chappel, C. R.: Relationship Between ATS-6 Spacecraft Charging Occurrences and Warm Plasma Encounters. *Spacecraft Charging by Magnetospheric Plasmas*, A. Rosen, ed., Progress in Astronautics and Aeronautics, Vol. 47, American Institute of Aeronautics and Astronautics, Inc., 1976, pp. 89-101.
8. Kampinsky, A.; and Keiser, B. E.: ATS-6 Spacecraft: An EMC Challenge," *NASA TM X-70795*, 1974.
9. Lovell, R. R.; et al.: Spacecraft Charging Investigation: A Joint Research and Technology Program. *Spacecraft Charging by Magnetospheric Plasmas*, A. Rosen, ed., Progress in Astronautics and Aeronautics, Vol. 47, American Institute of Aeronautics and Astronautics, Inc., 1976, pp. 3-14.
10. Materials Characterization papers in Proceedings of the Spacecraft Charging Technology Conference, R. P. Pike and R. R. Lovell, eds., AFGL TR-77-0051, NASA TM X-73537, 1977, pp. 431-547. Material Characterization papers in *Spacecraft Charging Technology - 1978*, NASA CP-2071, AFGL TR-79-0082, 1979, pp. 437-756.
11. Purvis, C. K.; Stevens, N. J.; and Oglebay, J. C.: Charging Characteristics of Materials: Comparison of Experimental Results with

- Simple Analytical Models. Proceedings of the Spacecraft Charging Technology Conference, C. P. Pike and R. R. Lovell, eds., AFGL TR-77-0051, NASA TM X-73537, 1977, pp. 459-486.
12. Aron, P. R.; and Staskus, J. V.: Area Scaling Investigations of Charging Phenomena. Spacecraft Charging Technology - 1978, NASA CP-2071, AFGL TR-79-0082, 1979, pp. 485-506.
  13. Balmain, K. G.: Scaling Laws and Edge Effects for Polymer Surface Discharges. Spacecraft Charging Technology - 1978, NASA CP-2071, AFGL TR-79-0082, 1979, pp. 646-656.
  14. Stevens, N. J.; et al.: Initial Comparison of SSPM Ground Test Results and Flight Data to NASCAP Simulations. NASA TM-81394, 1980.
  15. Schneulle, G. W.; et al.: Simulation of the Charging Response of the SCATHA (P78-2) Satellite. Spacecraft Charging Technology - 1980. NASA CP-2182, 1981.
  16. Purvis, C. K.; and Staskus, J.: SSPM Charging Response: Comparison of Ground Test and Flight Data to NASCAP Predictions for Eclipse Conditions. Spacecraft Charging Technology - 1980. NASA CP-2182, 1981.
  17. Saflekos, N. A.; et al.: Three Dimensional Analysis of Charging Events on Days 87 and 114, 1979, from SCATHA. Spacecraft Charging Technology - 1980. NASA CP-2182, 1981.
  18. Katz, I.; et al.: A Three Dimensional Dynamic Study of Electrostatic Charging in Materials. (SSS-R-77-3367, Systems, Science and Software; NASA Contract NAS3-20119.) NASA CR-135256, 1977.
  19. Katz, I.; et al.: Extension Validation and Application of the NASCAP Code. (SSS-R-79-3904, Systems, Science and Software; NASA Contract NAS3-21050.) NASA CR-159595, 1979.
  20. Katz, I.; et al.: Capabilities of the NASA Charging Analyzer Program. Spacecraft Charging Technology - 1978, NASA CP-2071, AFGL TR-79-0082, 1979, pp. 101-122.
  21. Garrett, H. B.; et al.: Comparison Between the 30-80 keV Electron Channels on ATS-6 and 1976-059A During Conjunction and Application to Spacecraft Charging Prediction. J. Geophys. Res., vol. 85, Mar. 1, 1980, pp. 1155-1162.
  22. Purvis, C. K.; et al.: Charging Rates of Metal-Dielectric Structures. Spacecraft Charging Technology - 1978, NASA CP-2071, AFGL TR-79-0082, 1979, pp. 507-523.
  23. Stevens, N. J.; and Roche, J. C.: NASCAP Modelling of Environmental-Charging-Induced Discharges in Satellites. NASA TM-79247, 1979.
  24. Stevens, N. J.: Computed Voltage Distributions Around Solar Electric Propulsion Spacecraft," NASA TM-79286, 1979.
  25. Stevens, N. J.; and Purvis, C. K.: NASCAP Modelling Computations on Large Optics Spacecraft in Geosynchronous Substorm Environments. Optics in Adverse Environments, Vol. 216. M. A. Kahan, ed., Society of Photo-Optical Instrumentation Engineers, 1980, pp. 116-130. (Also NASA TM-81395, 1980.)
  26. Sanders, N. L., and Inouye, G. T.: NASCAP Charging Calculations for a Synchronous Orbit Satellite. Spacecraft Charging Technology - 1980. NASA CP-2182, 1981.
  27. Stevens, N. J.: Utilization of Charging Control Guidelines in Geosynchronous Satellite Design Studies. Spacecraft Charging Technology - 1980. NASA CP-2182, 1981.

28. Mandell, M. J.; et al.: The Decrease in Effective Photocurrents Due to Saddle Points in Electrostatic Potentials Near Differentially Charged Spacecraft. IEEE Trans. Nucl. Sci., vol. NS-25, no. 6, Dec. 1978, pp. 1313-1317.
29. Mizera, P. M.; and Fennell, J. F.: Satellite Surface Potential Survey. Spacecraft Charging Technology - 1980. NASA CP-2182, 1981.
30. Damron, S. A.; Adam, R. C.; and Nanevich, J. E.: Transient Pulse Monitor (TPM) Data from the SCATHA/P78-2 Spacecraft. Spacecraft Charging Technology - 1980. NASA CP-2182, 1981.
31. Koons, H. C.: Aspect Dependence and Frequency Spectrum of Electrical Discharges on the P78-2 (SCATHA) Satellite. Spacecraft Charging Technology - 1980. NASA CP-2182, 1981.
32. Reagan, J. B.; et al.: The Role of Energetic Electrons in Charging/Discharging of Spacecraft Dielectrics. Spacecraft Charging Technology - 1980. NASA CP-2182, 1981.
33. Meulenbergh, A., Jr.: Evidence for a New Discharge Mechanism for Dielectrics in a Plasma. Spacecraft Charging by Magnetospheric Plasmas, A. Rosen ed., Progress in Astronautics and Aeronautics, Vol. 47, American Institute of Aeronautics and Astronautics, Inc., 1976, pp. 237-246.
34. Beers, B. L.; and Pine, V. W.: Electron Beam Charged Dielectrics - Internal Charge Distribution. Spacecraft Charging Technology - 1980. NASA CP-2182, 1981.
35. Frederickson, A. R.: Bulk Charging and Discharging Characteristics of Several Polymers. Spacecraft Charging Technology - 1980. NASA CP-2182, 1981.
36. Stevens, N. J.: Space Environmental Interactions with Biased Spacecraft Surfaces. Space Systems and Their Interactions with Earth's Space Environment, H. B. Garrett and C. P. Pike, eds., Progress in Astronautics and Aeronautics, Vol. 71, American Institute of Aeronautics and Astronautics, Inc., 1980, pp. 455-476.
37. Inouye, G. W.; and Sellen, J. M., Jr.: TDRSS Solar Array Arc Discharge Tests. Spacecraft Charging Technology - 1978, NASA CP-2071, AFGL TR-79-0082, 1979, pp. 834-852.

TABLE I. - TYPICAL DISCHARGE CHARACTERISTICS

[Ground simulation test.]

Breakdown thresholds:

Dielectric punchthrough, V/cm (kV/mil) . . . . .	$3 \times 10^6$ (7)
Edge breakdown, V/cm (kV/mil):	
Teflon and Kapton . . . . .	$\sim 10^6$ (3)
Solar cells . . . . .	$\sim 4 \times 10^5$ (1)

Area scaling for discharges:

Return current amplitude . . . . .	$I \propto A^{1/2}$
Pulse duration . . . . .	$I \propto A^{1/2}$

Discharge propagation velocity, cm/sec . . . . .  $2 \times 10^7$

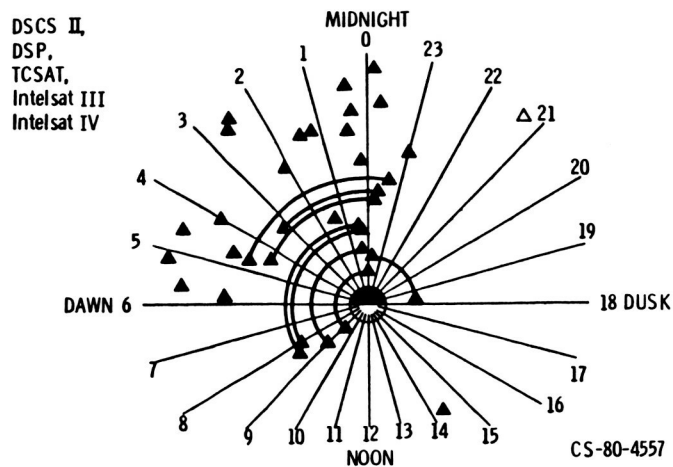


Figure 1. - Occurrence of satellite anomalies in local time.

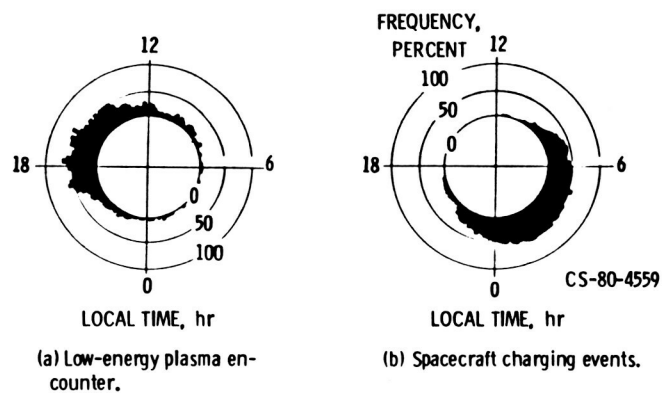


Figure 2. - ATS-6 environment data - local time distributions.



Figure 3. - Discharges in single-sheet silvered Teflon sample.

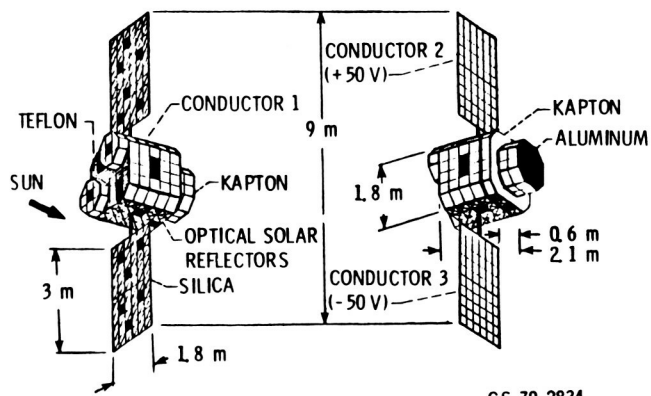


Figure 4. - Typical geosynchronous communications satellite.

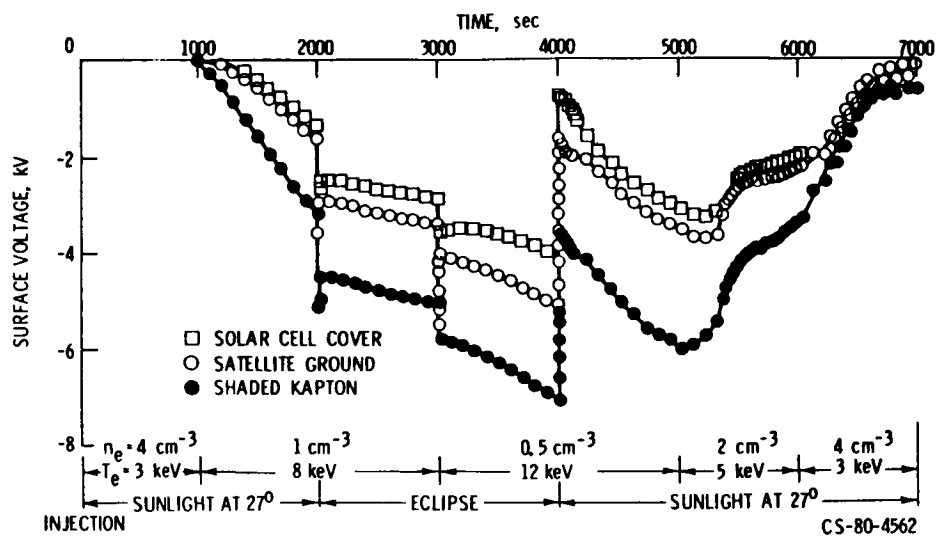


Figure 5. - Predicted potentials for substorm environment - three-axis-stabilized satellite.

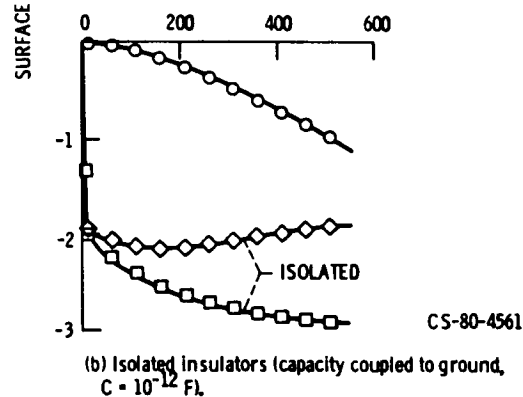
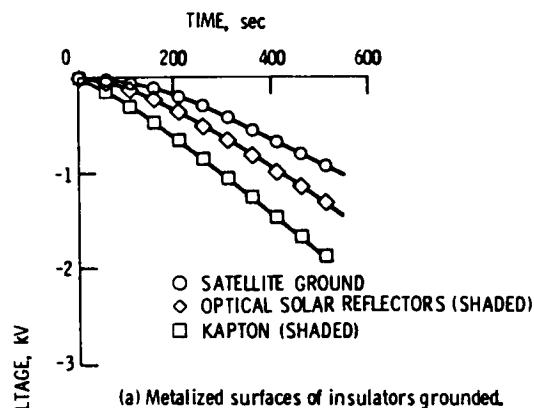


Figure 6. - Comparison of predicted surface voltages for grounded and isolated insulators. Environment:  $T_e = 8$  keV;  $T_p = 16$  keV;  $n_e = n_p = 1$  cm $^{-3}$ ; sunlight at 27° incidence.

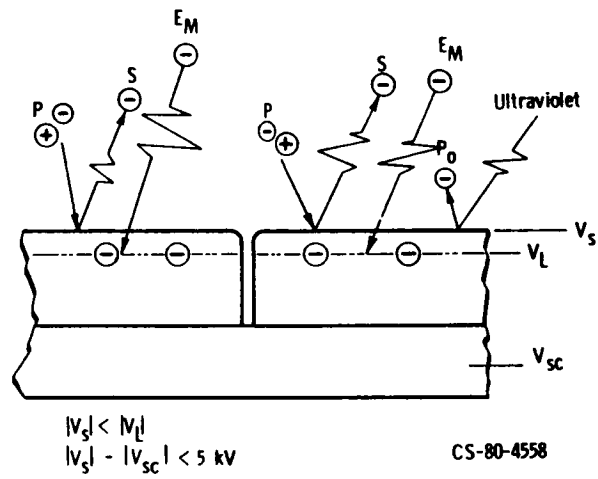


Figure 7. - Buried or trapped charge layers.

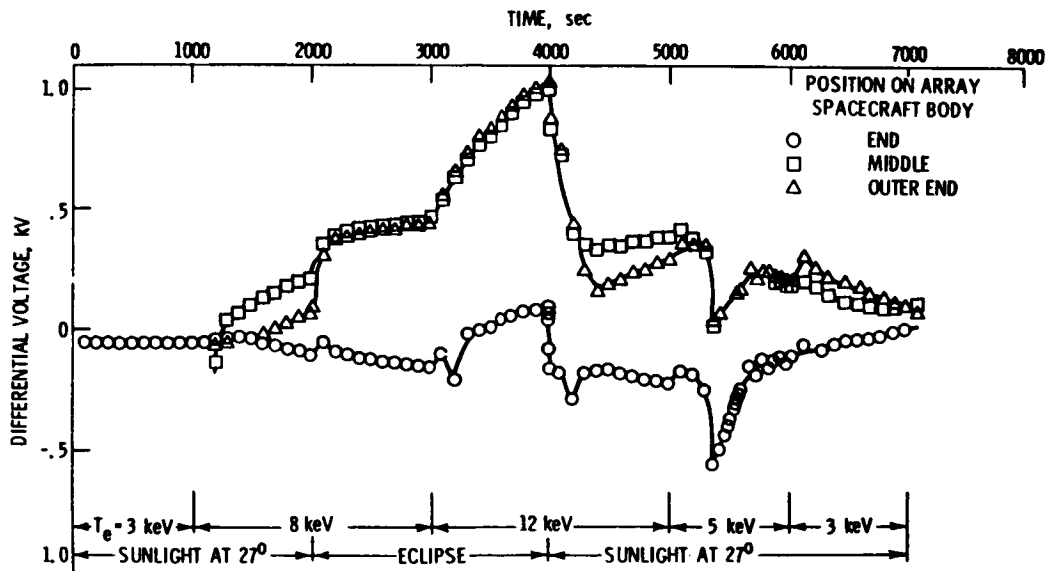


Figure 8. - Predicted differential voltages for positive bias solar array wing.

CS-80-4564



# **CALCULATION OF SURFACE CURRENT RESPONSE TO SURFACE FLASHOVER OF A LARGE SAMPLE UNDER GROUNDED AND FLOATING CONDITIONS\***

**M. J. Mandell, I. Katz, and G. W. Schnuelle**  
Systems, Science and Software

## **SUMMARY**

The authors have presented earlier (reference 1) a theory to explain the magnitude of "blowoff" currents in dielectric surface discharges. Being a purely predictive theory, the computational mechanism allows calculation of the electromagnetic and electrostatic responses with an arbitrary substrate-to-ground impedance.

Here we present results for the electromagnetic response to the discharge of an 80 cm diameter dielectric sample mounted on a 120 cm diameter cylinder. We assume the dielectric to be charged with a known potential profile dropping sharply near the edge, and the substrate initially grounded. During the early part of the discharge ( $\leq 10$  ns) there is little difference between the grounded and floating cases. Beyond  $\sim 10$  ns the grounded experiment is in approximate steady state, continuing to blow off charge until the dielectric is substantially discharged. The floating case, however, shows modestly decreasing emission and response. Eventually, a quasi-steady state is reached in which charge is transported from dielectric to substrate rather than blown off.

## **INTRODUCTION**

Laboratory studies of the blowoff and SGEMP responses to dielectric discharges have been performed by several workers (refs. 2 through 6) using the type of experimental setup shown in Figure 1. We show the equivalent circuit for this measurement in Figure 2. The total circuit current is  $I = V/R + C\dot{V}$ . We have  $C \sim 10^{-10}$  L, where L is the object dimension in meters, and  $R \leq 10\Omega$  in a typical laboratory experiment, giving  $RC \sim 10^{-9}$  seconds for a meter-sized object. The "blowoff current measurement" is, therefore, a measurement of the potential reached by the test object under circumstances where the RC time constant is smaller than any time characterizing the discharge. Experimenters using

\* This work supported by the Defense Nuclear Agency under Contract DNA001-79-C-0079 and DNA001-79-C-0027.

larger resistances (ref. 2) have found substantial changes in their substrate current measurement,  $I_s = V/R$ .

In geosynchronous orbit, however, we have  $R \sim 10^8 - 10^9 \Omega$ , so that  $RC \sim 10^{-2} - 10^{-1}$  seconds. The blowoff current is then given by  $CV$ . For blowoff currents as large as those measured in the laboratory, the entire spacecraft will rise to a potential comparable to the discharge potential in  $10^{-8} - 10^{-7}$  seconds, long before the discharge is complete. The raised spacecraft potential will then prevent blown off electrons from escaping the spacecraft vicinity.

Of great importance in spacecraft charging is the electromagnetic (SGEMP) response of the spacecraft to a discharge. Experiments to measure this response are more elaborate and difficult to interpret than simple blowoff experiments. Nonetheless, such experiments have been performed (refs. 3,4), and long-lasting surface current responses observed.

The SGEMP response is due primarily to the blowoff charge, i.e., to current which travels a long distance. When the blowoff is quenched by an elevated spacecraft potential, there are three possibilities concerning the subsequent SGEMP response: (1) the entire discharge may be quenched; (2) the discharge may proceed in such a way that no electrons travel long distances, thus quenching the SGEMP response; or (3) electrons may continue to travel large distances from one part of the spacecraft to another while the SGEMP response continues. We demonstrate below that, at least for one fully predictive model of the blowoff process, the last alternative holds.

#### DISCHARGE MODEL

Our calculations are based on a discharge model we have presented elsewhere (ref. 1). We neglect the initiation of the discharge and its spread over the sample, and assume the dielectric is emitting electrons in space-charge-limited fashion over its entire surface. By so doing, we achieve material independence at the expense of being able to predict the experimental rise time. Since a sharp potential drop at the sample edge gives an infinite space-charge-limited current, we must make some assumption about the voltage profile. For a circular sample of radius  $R$ , we choose the following form, which has a "healing length"  $\lambda$ :

$$V(r) = V_0 \left[ 1 - e^{-(R-r)/\lambda} \right] / \left[ 1 - e^{-R/\lambda} \right] . \quad (1)$$

For the geometry of figure 3, we find the total emission current (under grounded conditions) to be given by:

$$I = (6.5 \times 10^{-6} + 2.9 \times 10^{-6} R/\lambda) V^{3/2} , \quad (2)$$

where  $I$  is in amperes and  $V$  in volts. Undoubtedly, the constants in equation (2) will display some dependence on experimental design and voltage profile, but we found this expression in good agreement with experimentally measured peak substrate return currents.

For the calculations described here, as well as those performed earlier, we use a hybrid electrostatic/electromagnetic code, in which a non-uniform, high resolution electrostatic grid (needed to resolve thin dielectrics, high potential gradients, and space charge limiting) overlays a uniform electromagnetic grid (needed for conservative, noise free propagation of electromagnetic waves). The trajectories of emitted electrons generate currents and charge densities which couple the solutions on the electrostatic and electromagnetic grids.

The electrostatic portion of the code calculates the electrostatic potential,  $V$ , from

$$\nabla^2 V = -\rho/\epsilon_0 \quad (3)$$

and tracks particles in the electric field  $\tilde{E} = \tilde{E}^T + \tilde{E}^L$  where  $\tilde{E}^L = -\nabla V$ . Separation of the fields into electrostatic ( $\tilde{E}^L$ , longitudinal, curl-free) and electromagnetic ( $\tilde{E}^T$ , transverse, divergence-free) components is a well known technique. For the problems of interest the longitudinal fields are the primary influence on the particle trajectories, while the transverse fields determine the SGEMP response. The electromagnetic code uses the particle information to generate a source current density,  $\tilde{J}$ , and timesteps

$$\epsilon_0 \frac{\partial \tilde{E}^T}{\partial t} = \frac{1}{\mu_0} \nabla \times \tilde{B} - \tilde{J} + \nabla \psi \quad (4)$$

$$\frac{\partial \tilde{B}}{\partial t} = -\nabla \times \tilde{E}^T \quad (5)$$

where  $\psi$  is determined by requiring  $\nabla \cdot \tilde{E}^T = 0$ , or

$$-\nabla^2 \psi = \nabla \cdot \left[ \frac{1}{\mu_0} \nabla \times \tilde{B} - \tilde{J} \right] \quad (6)$$

subject to the same boundary conditions as  $V$ . Knowledge of  $\tilde{B}$  is then equivalent to knowledge of surface currents.

The centering for the electromagnetic code is shown in figure 4. This centering has the advantage that currents and potentials are defined on the object surfaces, while electric fields are defined in space, making it easy to feed electromagnetic fields into the electrostatic code and track particles in the total field. It is essential that the discrete representations of Laplacian, divergence, and gradient form a consistent set, so that  $\nabla \cdot \tilde{E}^T$  vanishes numerically. For this centering, it is not possible to construct a simple operator such that  $\text{div curl } \tilde{B}$  vanishes identically. This problem is solved by inclusion of  $\text{curl } \tilde{B}$  in equation (6).

We wish to follow trajectories of only those electrons which escape the virtual cathode formed immediately above the emitting dielectric surface. The electron emission routine emits that current of zero kinetic energy electrons needed to maintain a non-negative surface normal electric field. This current is given by the Child-Langmuir law:

$$J = (4\epsilon_0/9) (2e/m)^{1/2} |E_z|^{3/2} / (\Delta z)^{1/2} \quad (7)$$

where  $\Delta z$  is the mesh spacing in front of the emitting surface, and  $E_z$  is the mean electric field across  $\Delta z$  (assumed electron repelling).

## RESULTS

For grounded ( $R \rightarrow 0$ ) and floating ( $R \rightarrow \infty$ ) substrate cases, calculations were carried out for an 80 cm diameter dielectric mounted on a 120 cm diameter metal cylinder. The test object was in a grounded 240 cm diameter vacuum tank. The potential  $V_0$  (equation (1)) was -15 kV. In all cases the total emission current dropped from an anomalously high value to a quasi-steady value in  $\sim 10^{-9}$  seconds.

Calculations for grounded substrate configurations were carried out for several values of  $\lambda$ . The SGEMP surface currents were monitored at several places on the cylinder. Some of the data is presented in table I. For small values of  $\lambda$  ( $\lambda/R \lesssim 0.1$ ) the peak surface current is at the sample edge, while for smoother potentials the peak current occurs beneath the sample interior. The front surface current, after a rise time of  $\sim 2$  nsec, has mainly a dc component. The surface current at the rear corner is about an order of magnitude less, and has substantial ringing

imposed on its dc value. The dc components of the response will die out on the time scale for the dielectric to substantially discharge, i.e., 1-10  $\mu$ sec. For small  $\lambda$ , the surface current beneath the sample interior has a negative precursor (figure 5). This can be understood by examining the Maxwell equation

$$\nabla \times \vec{H} = \vec{J} + \epsilon_0 \frac{\partial \vec{E}}{\partial t} . \quad (8)$$

For points far from the sample edge, where  $\vec{J}$  is small, the right-hand side of (8) is initially dominated by the electric field of the large electron currents being emitted near the sample edge.

Simulations for the floating test object were performed for  $\lambda = 0.03, 0.05$ , and  $0.10$ . The results are shown in figures 6 through 10, and in table II. The calculations were carried out for  $\sim 50$  nsec. This is a long enough time to elevate the test object to near its maximum potential, but not enough to discharge the dielectric by more than a few percent. Among the monitored quantities were the emission current  $I$ , the object potential  $V$ , and the sample-edge surface current  $K$ . The test object capacitance was 75 pf.

From figures 6 through 8, three times (designated  $t_1$ ,  $t_2$ , and  $t_3$  in table II) can be identified:

- (1) The rise time of the surface current  $K$ . This is comparable to the time it takes an accelerating electron to travel a distance  $\lambda$ .
- (2) The rise time of the "measured blowoff,"  $\dot{C}\dot{V}$ . This is comparable to the time for an electron of energy  $V_0$  (15 kV) to travel a distance comparable to the sample dimension ( $\sim 1$  m).
- (3) The time for the test object potential to achieve a value comparable to  $V_0$ , at which time the "measured blowoff" exhibits a sharp drop.

Figure 9 shows the evolution of particle trajectories for the  $\lambda = 0.10$  m case. Initially, the electrons travel in nearly straight lines from the neighborhood of the test object to the tank wall, a trip of  $\sim 40$  nsec. As  $t_3$  is passed, the trajectories exhibit substantial curvature. Electrons emitted for  $t \geq t_3$  are seen to turn around and return toward the test object.

It is of interest to compare the time development of the currents  $I$ ,  $K$ , and  $\dot{C}\dot{V}$ . After their initial transients,  $I$  and  $K$  behave similarly, decaying by about  $\sim 30$  percent from  $t_1$  to  $t_3$ . The back corner surface current (figure 10) likewise has a decay

of  $\sim 30$  percent in its dc component over this time, although here the ringing is comparable to the total response. The blowoff current,  $\dot{C}\dot{V}$ , decays more rapidly from its peak at  $t_2$ , as shown by the decrease from  $t_2$  to  $t_3$  of the blowoff fraction,  $\dot{C}\dot{V}/I$ . Table II also indicates the decrease in blowoff fraction as  $\lambda$  becomes small compared with the mask size, i.e., when most of the current is emitted very close to the edge, a substantial fraction hits the mask. This behavior has been seen in the measurements of Balmain (ref. 6).

## CONCLUSIONS

We have simulated the temporal behavior and SGEMP response to a dielectric discharge for a space-charge-limited emission model under grounded or floating conditions. The measured blowoff current,  $\dot{C}\dot{V} + V/R$ , has a rise time comparable to the time it takes an electron to travel a distance comparable to the sample size. Under floating conditions, the test object rises to a potential comparable to the maximum potential across the dielectric. For the geometry considered, this caused a decrease in emission current and SGEMP response of  $\sim 30$  percent. At late times, the electrons formerly blown off to the tank walls or to plasma ground travel large distances around the test object or spacecraft. Thus, on the sample the SGEMP response was decreased only modestly from the grounded case. However, the ground return current was limited to  $V/R$ .

The amount of charge transferred from the discharging surface to the tank walls is substantially reduced when the sample impedance exceeds a few hundred ohms. This agrees well with experimental measurements. The initial blowoff current cuts off on a time scale of less than a hundred nanoseconds for a floating sample as opposed to microseconds when the substrate is grounded.

## REFERENCES

1. Katz, I., M. J. Mandell, D. E. Parks and G. W. Schnuelle: A Theory of Dielectric Surface Discharges. IEEE Trans. Nucl. Sci. NS-27, December 1980.
2. Rosen, A., N. L. Sanders, J. M. Sellen, Jr. and G. T. Inouye: Effects of Arcing Due to Spacecraft Charging on Spacecraft Survival. TRW Report No. 33631-60060RM-00, NASA CR-159593, 1978.

3. Van Lint, V. A. J., B. C. Passenheim, R. Stettner and D. A. Fromme: The Effect of Electron Precharging on the SGEMP Response of Insulators. IEEE Trans. Nucl. Sci. NS-26, 5024, 1979.
4. Treadaway, M. J., A. J. Woods, T. M. Flanagan, R. E. Leadon, R. Grismore, R. Denson and E. P. Wenaas: Experimental Verification for ECEMP Spacecraft Discharge Coupling Model. IEEE Trans. Nucl. Sci. NS-27, December 1980.
5. Balmain, K. G. and G. R. Dubois: Surface Discharges on Teflon, Mylar and Kapton. IEEE Trans. Nucl. Sci. NS-26, 5146, 1979.
6. Balmain, K. G. and W. Hirt: Dielectric Surface Discharges: Dependence on Incident Electron Flux. IEEE Trans. Nucl. Sci. NS-27, December 1980.

TABLE I. SURFACE CURRENT RESPONSE FOR DISCHARGES (GROUNDED SUBSTRATE)						
Voltage Profile ( $V_0 = -15$ kV)	$\lambda = .40$	$\lambda = .20$	$\lambda = .10$	$\lambda = .05$	$\lambda = .04$	$\lambda = .03$
Peak Current (A/m)	8.4	9.3	12.2	18.0	20.7	24.6
Radius of Peak Current (m)	0.24	0.30	0.34	0.40	0.40	0.40
Peak Surface Cur- rent at Rear Corner (A/m)	0.67	0.85	1.3	2.4	2.8	3.4
Negative Precursor (A/m) at $r = 0.20$ m	none	none	none	-1.8	-2.7	-3.8

TABLE II. RESULTS FROM SIMULATIONS OF THE DISCHARGE OF A DIELECTRIC ON A FLOATING TEST OBJECT			
	$\lambda=.03$	$\lambda=.05$	$\lambda=.10$
$t_1$ (nsec)	2.5	2.5	5.0
$t_2$	14	15	18
$t_3$	>25	40	47
Emission Current			
$I(t_1)$ (A)	85	53	31
$I(t_2)$	70	47	27
$I(t_3)$	<62	37	20
Local Ground Potential			
$V(t_1)$ (V)	250	150	350
$V(t_2)$	5500	4700	3700
$V(t_3)$	>12000	14000	11000
Peak Blowoff Current			
$C\dot{V}(t_2)$ (A)	43.5	36.0	24.8
Blowoff/Emission Ratio			
$C\dot{V}(t_2)/I(t_2)$	.62	.77	.92
$C\dot{V}(t_3)/I(t_3)$	<.54	.52	.75
Surface Current			
$K(t_1)$ (A/m)	24	18	11.7
$K(t_3)$	<18	11.5	~8
Emission/Surface Current Ratio			
$I(t_1)/2\pi K(t_1)$ (m)	.57	.47	.42
$I(t_3)/2\pi K(t_3)$	~.55	.51	~.4



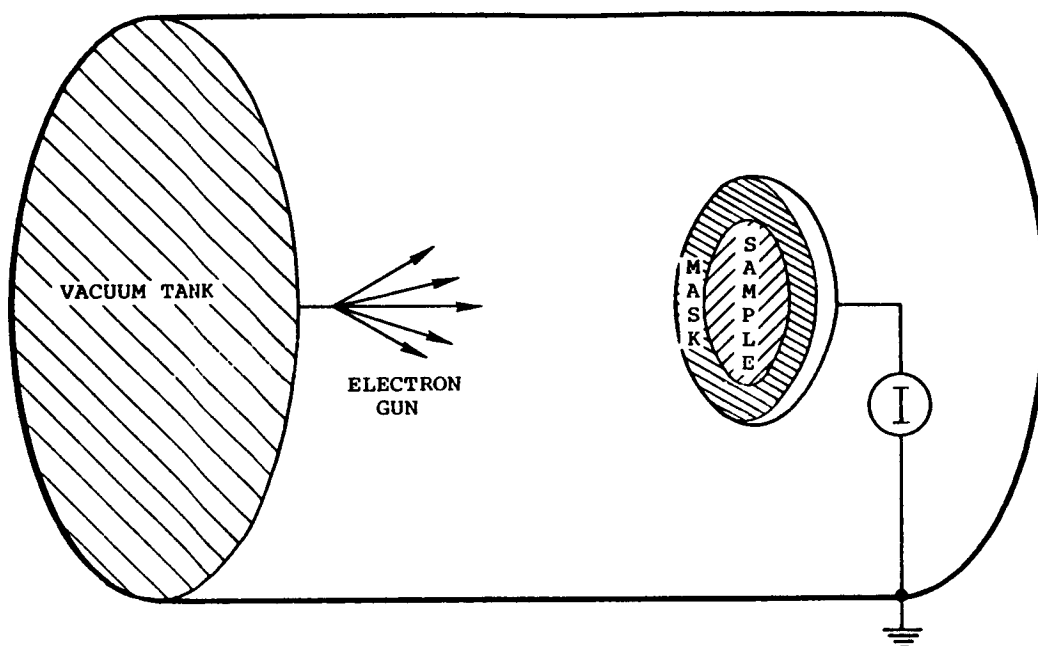


Figure 1. - Typical laboratory setup used for discharge response measurements.

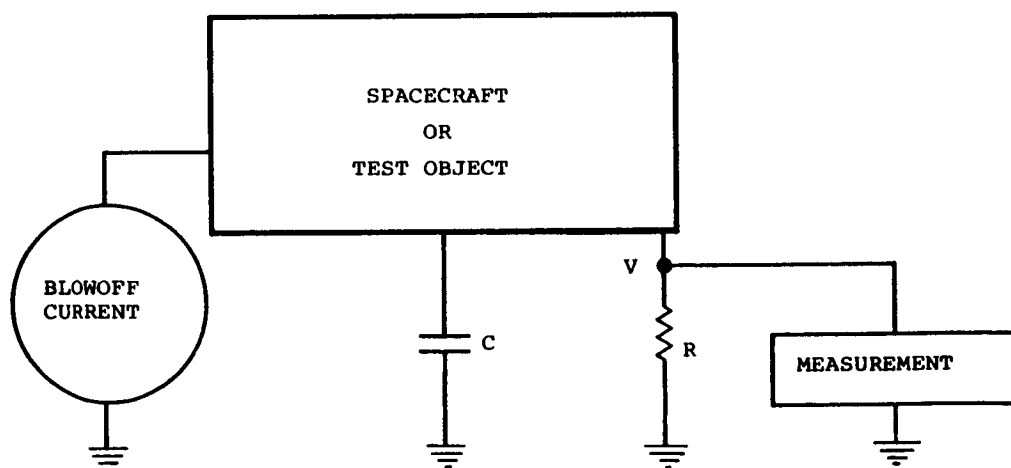


Figure 2. - Equivalent circuit for measurement of blowoff current from a spacecraft or test object undergoing electrostatic discharge.

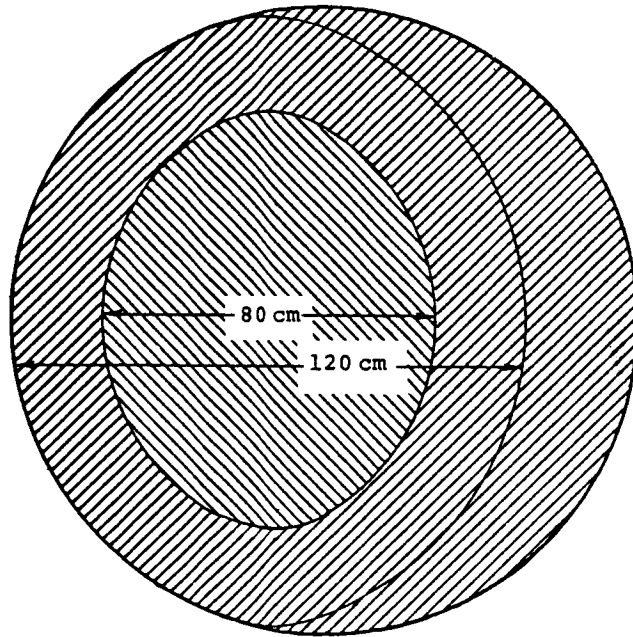


Figure 3. - Dimensions of test object used for these calculations. The electrostatic and particle tracking calculations had 0.2 cm resolution in front of the dielectric, while the electromagnetic calculations had 6.7 cm resolution.

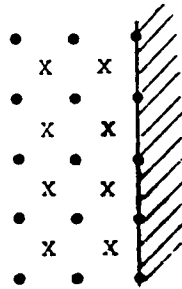


Figure 4. - Centering scheme for transverse electromagnetic code. Scalar quantities (potential  $\psi$ , magnetic field  $B_\phi$ , current divergence  $\nabla \cdot \mathbf{J}$ ) are centered at solid points, while vector quantities (transverse electric field  $\mathbf{E}$ , current density  $\mathbf{J}$ ) are centered at crosses.

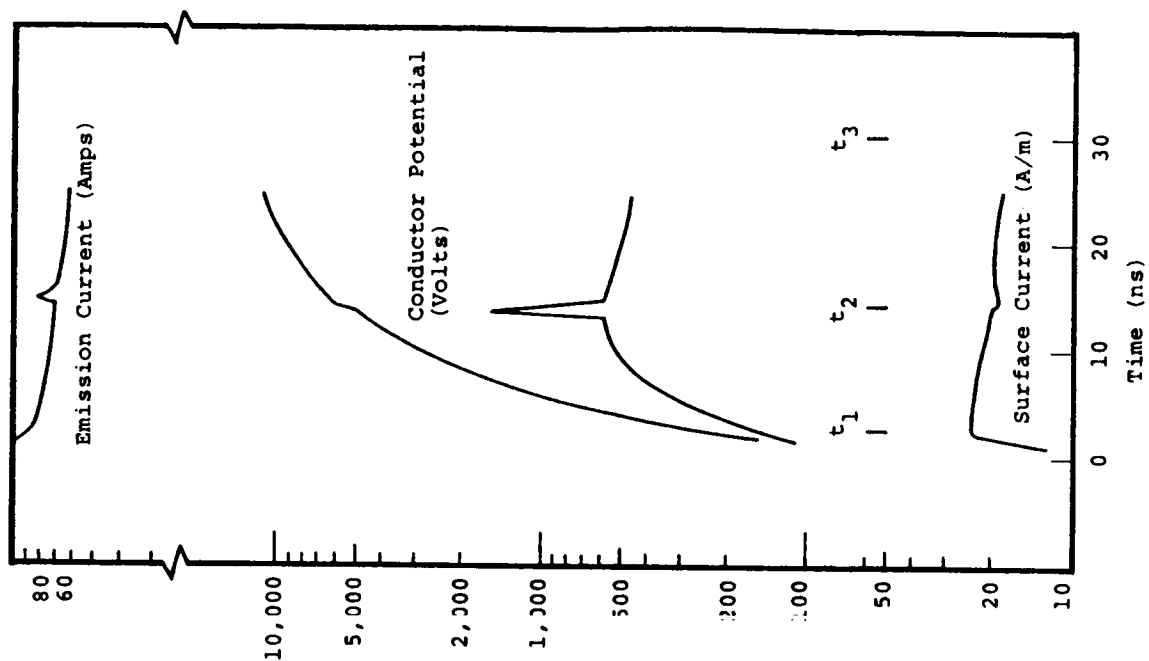


Figure 6. - Emission current, conductor potential and its derivative, and surface current at square edge for  $\lambda = 0.03$  m.

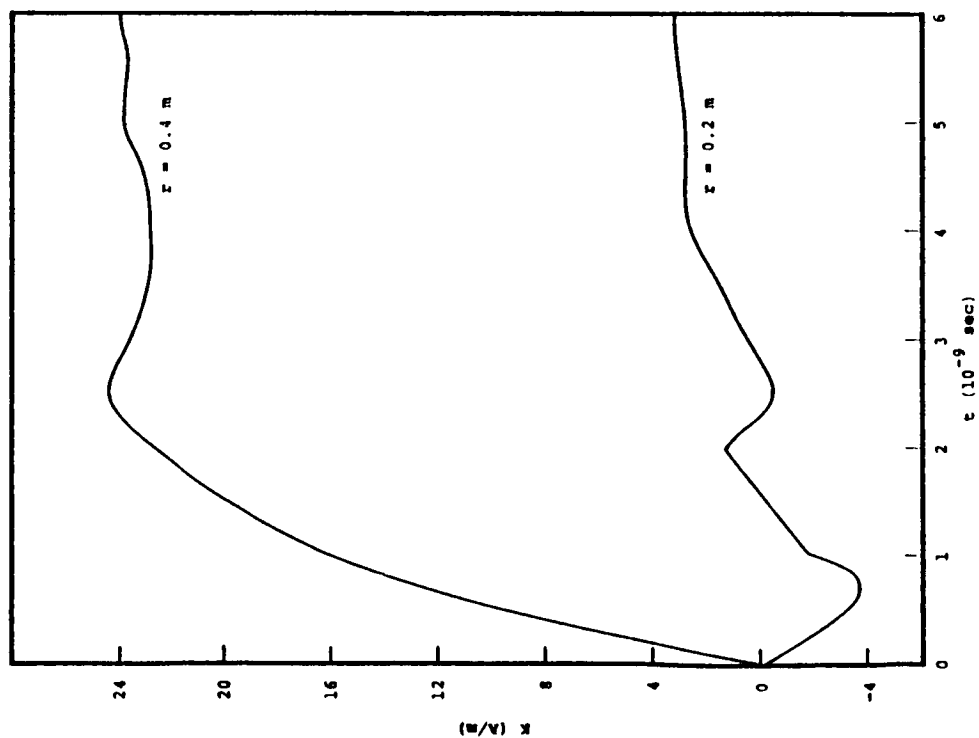


Figure 5. - Surface currents versus time at  $r = 0.4$  m and  $r = 0.2$  m for discharge with  $\lambda = 0.03$  m. Note negative precursor for small  $r$ .

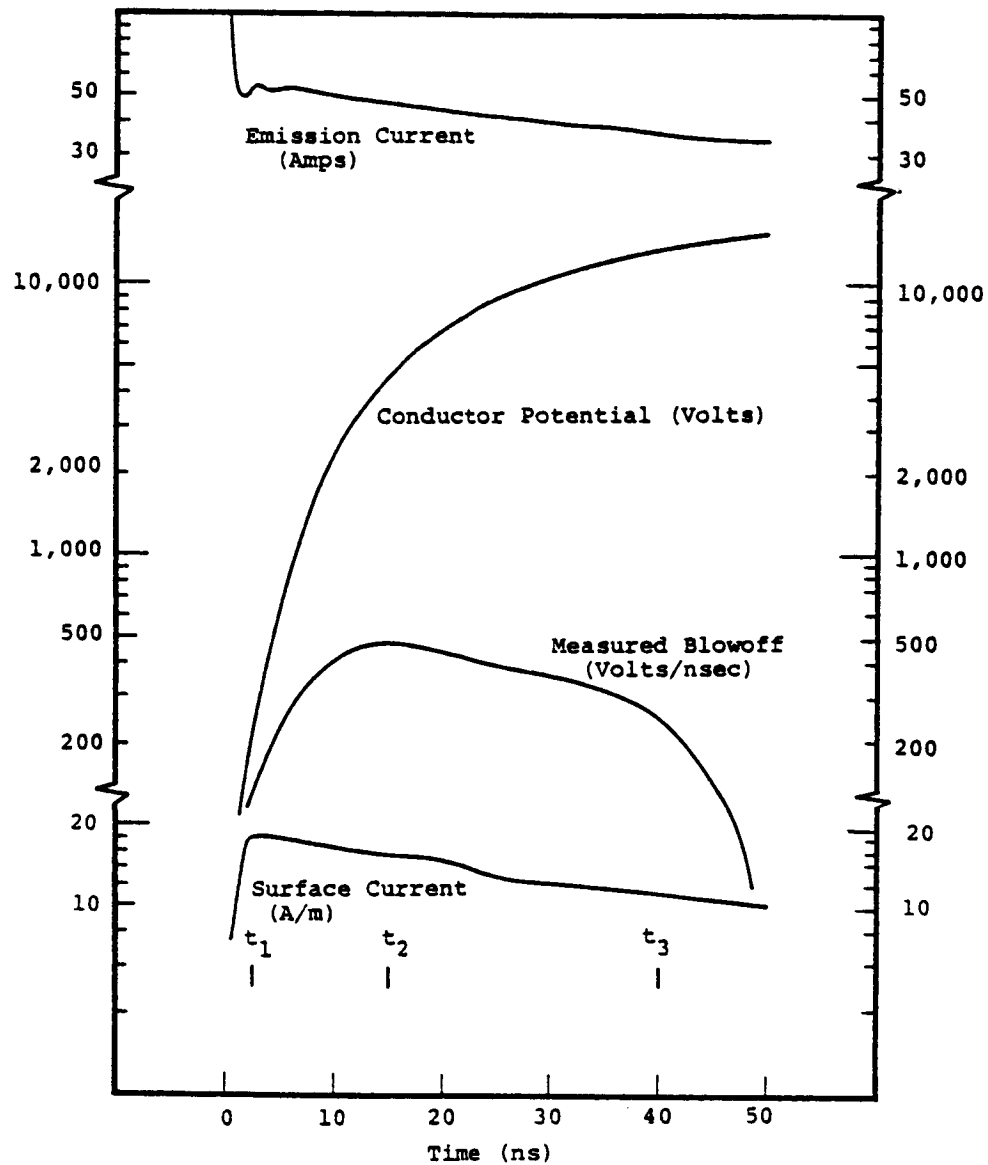


Figure 7. - Emission current, conductor potential and its derivative, and surface current at sample edge for  $\lambda = 0.05$  m.

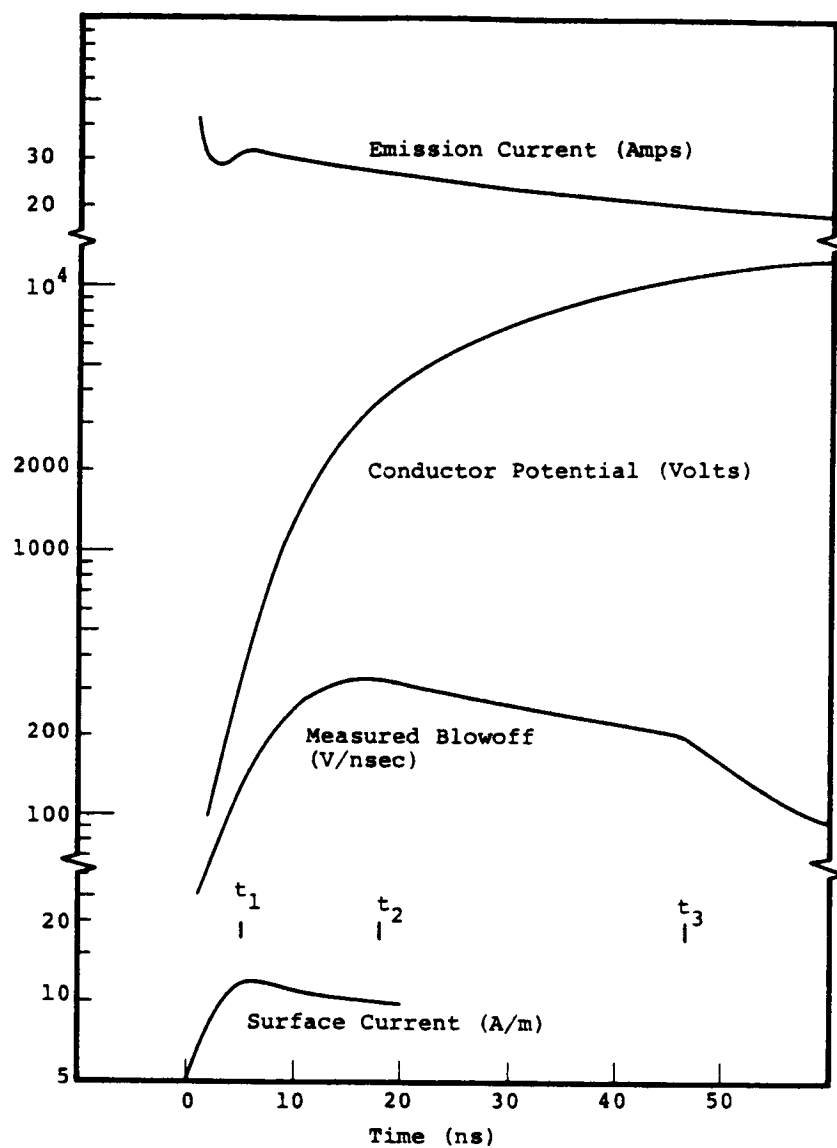


Figure 8. - Emission current, conductor potential and its derivative, and surface current at sample edge for  $\lambda = 0.10$  m.

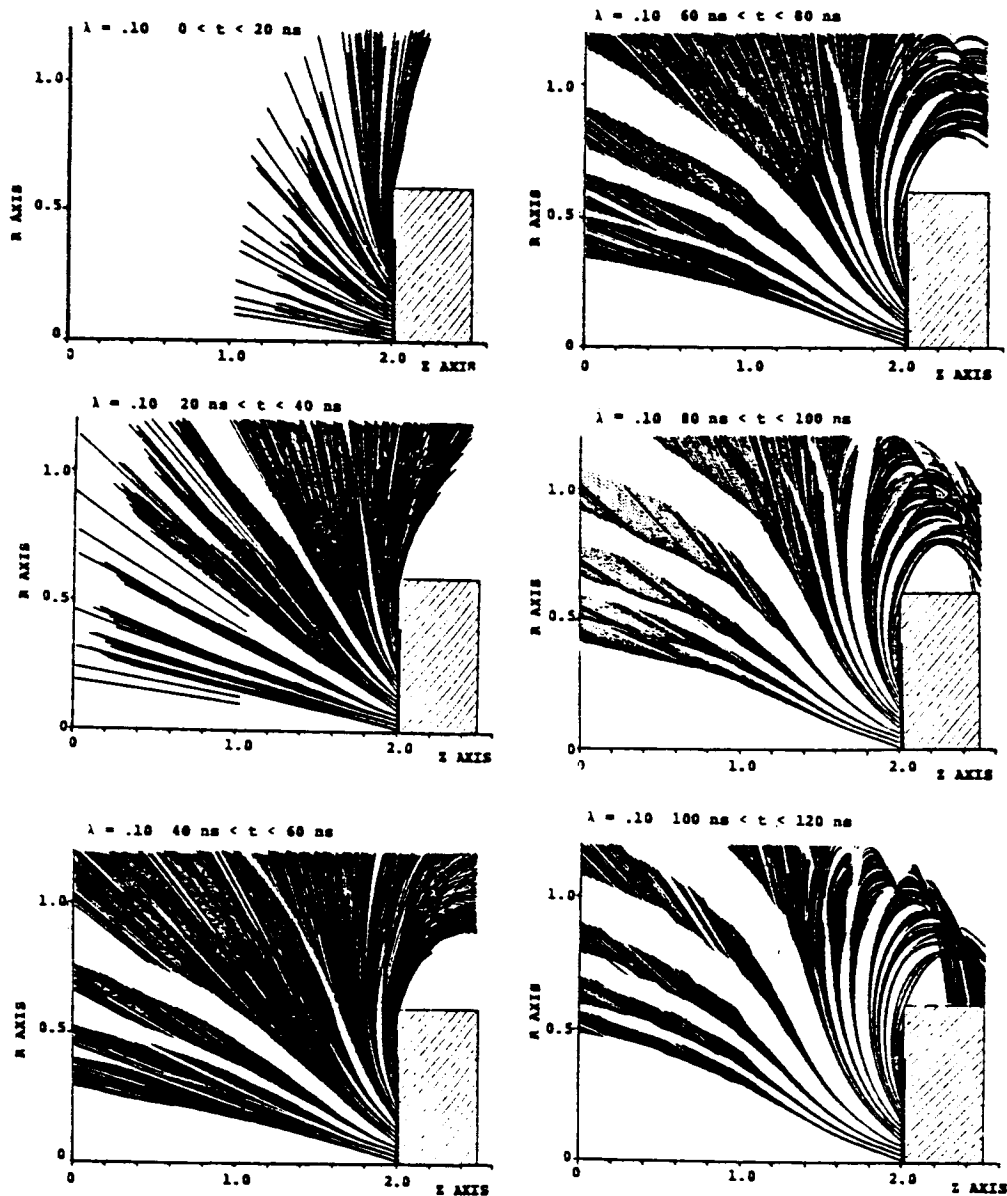


Figure 9. - Time evolution of electron trajectories for  $\lambda = .10$  m, floating test object. Each frame shows all trajectory segments for the specified time period. It is apparent that charge emitted early in time is blown off to the tank wall. Charge emitted beyond about 40 ns, while traveling a comparable distance, is seen to curve back toward the sample can.

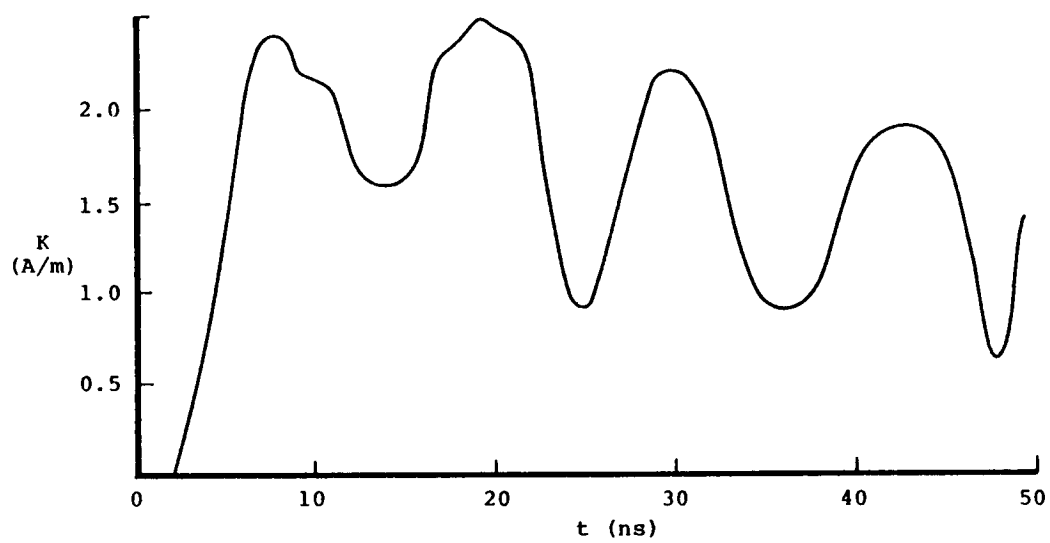


Figure 10. - Surface current at rear corner for  $\lambda = 0.05$  m, floating test object.

## MODEL OF COUPLING OF DISCHARGES INTO SPACECRAFT STRUCTURES\*

A. J. Woods, M. J. Treadaway, R. Grismore,  
R. E. Leadon, T. M. Flanagan, and E. P. Wenaas  
JAYCOR

### INTRODUCTION

A semi-empirical model for electron-caused electromagnetic pulse (ECEMP) from spacecraft dielectrics has been developed and tested experimentally (Ref. 1). That model successfully predicted ECEMP response of moderately complex, 1-m spacecraft structures including reentrant geometries in a simulated space environment. Agreement between experimental data and predictions was substantial, indicating that a general system response predictive tool is well underway to being established and that dielectric breakdown behavior can be further understood through applications of the results.

This paper briefly reviews the calculated results compared to the experimental data for three spacecraft geometries, and then discusses the appropriateness of certain model assumptions which have been employed in the absence of a microscopic theory for dielectric breakdown and associated electron blowoff.

Much of the detail of the model and its experimental verification have been presented elsewhere (Ref. 1), and so is only highlighted here. Results presented in this paper are limited to the exterior response of spacecraft structures, although neither the model nor the experiments were limited to the outside problem. Emphasis here is on providing rationales for model assumptions.

Various efforts have been undertaken to gain theoretical insight into dielectric breakdown processes on a first-principles basis (Ref. 2). At present, however, discharge and blowoff properties are limited to experimentally determined dielectric breakdown parameters. Analytical descriptions of the processes can be incorporated into the predictive capability discussed here as they become available.

### COUPLING MODEL SUMMARY

From the results of previous measurements (Ref. 3), the model was developed on the basis of a limited number of assumptions:

- When a dielectric is charged to a potential,  $V_D$ , a discharge occurs.
- After initiation, the discharge continues until the potential reaches a final potential,  $V_F$ , at which time the discharge ceases.
- During the discharge, a fraction of the stored charge,  $f_B$ , is released as blowoff charge and a fraction,  $f_F$ , as flashover charge.

These assumptions are based on the empirical observations that, although the discharge process is stochastic in nature, the general magnitude of the response of a material can be bounded. The model assumes that coupling of the discharge is dominated by the motion of the blowoff charge; the flashover charge is considered only in that it modifies the surface potential as a function of time.

---

\* Work sponsored by AFWL under Computer Sciences subcontract S-220.



The blowoff electrons are assumed to move in the fields surrounding the object in question. The time history of the charge release is determined by the velocity of propagation of the discharge,  $v$ , and the linear dimension of the dielectric,  $\ell$ . This assumption is based on results of previous measurements performed by JAYCOR as well as those by Balmain (Ref. 4) and others, which show that the discharge pulse width scales as the square root of the area of a dielectric sample. This suggests that the discharge can be described as a propagation phenomenon moving across the linear dimension of a sample. This assumption leads to a triangular shape for total blowoff currents as a function of time. The blowoff electrons are assumed to be released with zero initial energy, where zero simply means some value small compared to the initial dielectric differential potential. Also, the dielectric surface is assumed to reflect electrons specularly, with a reflection coefficient of unity.

Input parameters for discharge coupling calculations ( $V_D$ ,  $V_F$ ,  $f_B$ ,  $f_F$ , and  $v$ ) can be determined from measurements on small-area samples, since previous measurements have shown these quantities to be relatively independent of sample size. The object dimensions enter the calculations as problem-specific input parameters. The input parameters for the present calculations are summarized in Table 1.

Table 1. Discharge Parameters Employed in ECEMP Analyses to Describe Dielectric Geometry and Discharge Due to the Low-Energy ( $\sim 25$  keV) Electron Environment

Material	Second-Surface Mirrors			Solar Panel
	Kapton	(SiO <sub>2</sub> )	Mylar*	
Area (m <sup>2</sup> )	0.79	0.79	0.79	0.09
Thickness (mils)	2	8	3	6
$\epsilon/\epsilon_0$	3.5	4.0	3.5	4.0
Potential at breakdown (kV)	13	6.5	11	7
Pulse rise time, 0 to 100% ( $\mu$ sec)	5	1.5	1.3	0.75
Pulse width, FWHM ( $\mu$ sec)	5	1.5	3	0.75
Blowoff fraction of stored charge	33%	28%	90%	20%
Flashover fraction of stored charge	33%	28%	0	58%
Emission characteristics:				
Initial electron energy (eV)	10	10	10	10
Total current (amp)	400	140	1,150	40
Spatial distribution	Nominally uniform			
Surface properties	Reflection of electrons with charge albedo = 1			

\* Mylar was not included in the previous tests, and all parameters listed here were determined from recent low-impedance discharge characterization measurements.

The nominal model assumes that only electrons are blown off from the samples during discharge. For geometries in which a relatively slow neutral plasma may make a difference in response, it was modeled as a perfect conductor traveling at  $6 \times 10^4$  m/sec, based on the observations of Hazelton (Ref. 5) and on a plasma channel theory by Balmain (Ref. 4) extended to the present configurations.

The dielectric discharge properties are used as inputs for the ABORC SGEMP computer code (Ref. 6). A rotationally symmetric geometry involving an artificial 1.5-cm-thick dielectric sample is employed. The sample capacitance is preserved through use of

an artificially high permittivity. Blowoff electrons move self-consistently in the pre-charge fields and in their own fields, generating replacement currents on the structures.

#### EXPERIMENT SUMMARY

A 1-m-long by 0.67-m-diameter cylindrical test object was constructed with magnetic field time derivative sensors at several locations on the side ( $\dot{H}_\phi$  and  $\dot{H}_z$ ) where  $H$  is the magnetic field and the cylinder axis is also the axis of a  $(z, r, \phi)$  cylindrical coordinate system. Dielectric materials were placed on one end of the cylinder and irradiated with 25-keV electrons in a large vacuum tank (6 m long by 4 m diameter). Data were obtained for low- and high-impedance isolations of the test object, with and without a simulated antenna and solar paddle attached. The antenna and paddle appendages were monitored with current time derivative sensors ( $\dot{I}$ ) on their respective conducting booms, which were connected to the canister ground. The antenna mast length was varied in the tests, and several dielectric materials were examined. Electrical isolation of the canister ground from the tank by a high impedance corresponded to the free-space condition in which a net charge builds up on the body during a breakdown due to the loss of a small fraction of the blowoff electrons to infinity.

The experimental results referenced here are the  $\dot{H}_\phi$  and  $\dot{I}$  signals. The  $\dot{H}_z$  values are defined to be zero by the rotational symmetry of the ABORC code model. This assumes that the discharges and the test object are rotationally symmetric. Neither of the above assumptions is completely true, but differences caused by asymmetries in the experiments were generally small enough that results could be interpreted meaningfully.

#### REVIEW OF MODEL RESULTS COMPARED WITH EXPERIMENTAL DATA

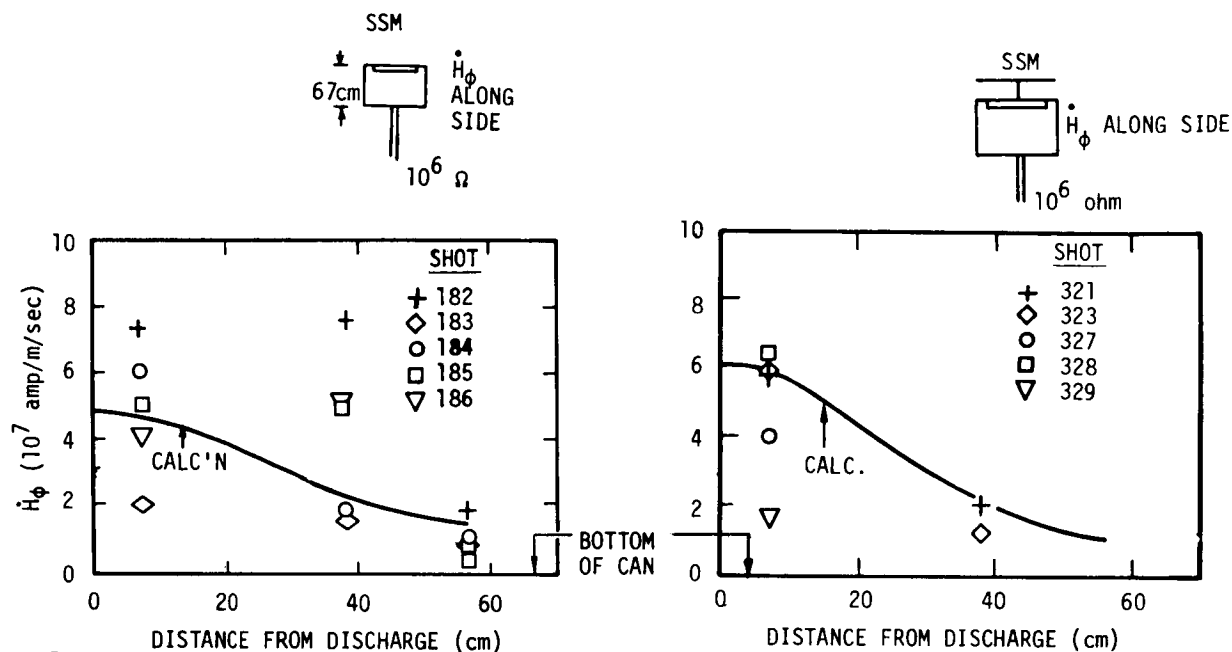
Figure 1 shows calculated and experimentally observed  $\dot{H}_\phi$  signals on the outside of the high-impedance isolated canister as a function of distance down the side, both with and without the antenna present. The experimental data span the calculated curves for both geometries, and the calculated curve shows the trend toward greater falloff away from the discharge with the antenna. Similar quality of agreement between calculated and experimental results was found for Mylar, which emits approximately 10 times as much current as the second-surface mirrors, and it was observed that scaling of responses could be performed from one material to another for which blowoff characteristics are known. Additionally, the model gives an essentially constant  $\dot{H}_\phi$  response as a function of position on the canister for low-impedance grounding. This behavior was both expected and experimentally observed, and is caused by the absence of space-charge limiting. Blowoff charge flows unimpeded to the vacuum tank walls, and is replaced through the grounding cable.

Performance of the model in predicting the current which flowed from the sample to the antenna itself was not good, however, as illustrated in Figure 2. The peak current flowing on the antenna mast was observed to be 420 amps for a 20-cm mast and 120 amps for a 40-cm mast. The pretest computer model without neutral plasma emission predicted only 32 amps for the short mast. That result is plotted on the left-hand graph at the zero initial energy abscissa point for the curve labeled "no plasma," which describes the early assumptions of zero initial energy of blowoff electrons emitted into a perfect vacuum. The obvious failure of the model to reproduce the nearly 90% cleanoff of the dielectric and subsequent mast currents observed led to the specification of a 90% blowoff charge emitted with non-zero energies in the presence of a neutral plasma in the model.

Those results are plotted as a function of emission energy for the 20-cm mast length on the left, and for the 40-cm length on the right. Notice that the observed sensitivity to

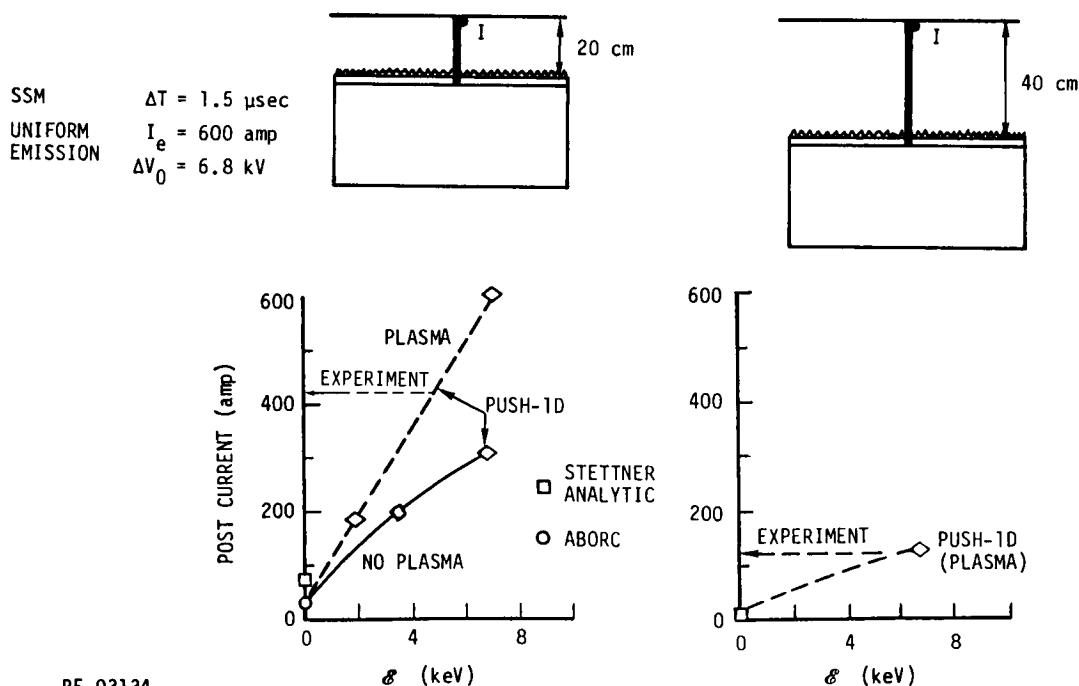
# SIMPLE CANISTER

# CANISTER WITH ANTENNA



RE-03205

Figure 1. Comparison of calculated and experimentally observed peak  $H_\phi$  signals for second-surface mirror discharges; high-impedance canister

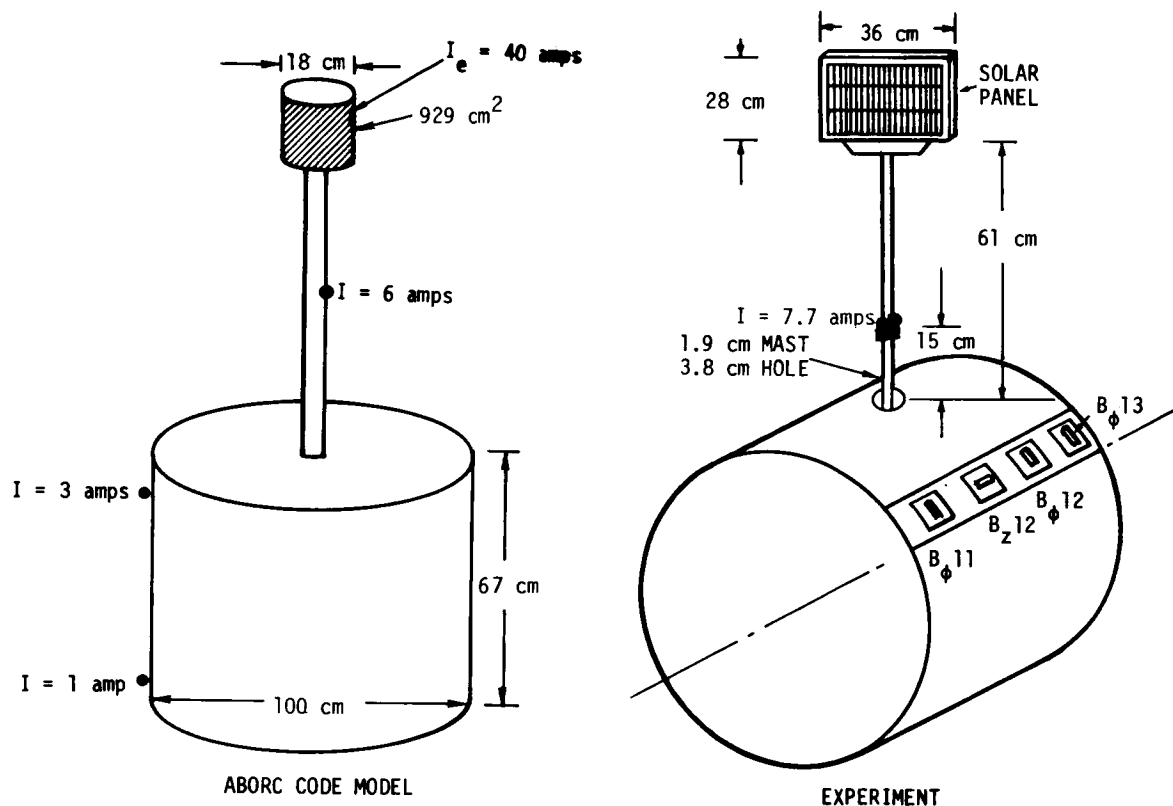


RE-03134

Figure 2. Calculated antenna peak current sensitivity to mast length compared with experimentally observed peak values for high-impedance isolation ( $E$  is the blowoff electron initial energy,  $I_e$  is the peak blowoff current; "plasma" indicates that a neutral plasma emission was modeled in the calculation)

mast length is reproduced by the model only for relatively high-energy electrons. Also notice that the neutral plasma is required even with high-energy emission to reproduce the observed antenna current for the short mast (compare the curves labeled "plasma" and "no plasma").

Performance of the pretest model was much better for the solar panel boom current than for the antenna mast current. Figure 3 shows the experimental geometry and ABORC code representation. Obviously, inaccuracy due to the geometry differences is expected for this highly non-rotational structure, but the code should be able to indicate whether a large or small fraction of the blowoff charge reaches the canister. The currents indicated on the figure show that the boom current is approximately 15% of the blowoff current for both the model and the experiment, which both supports the modeling and suggests that discharges from relatively isolated solar panels may not drive large currents on a satellite center body compared to the total current released.



RE-03116

Figure 3. Computer model for solar panel compared with experimental geometry (calculated peak replacement currents  $I$  also shown for high-impedance isolation)

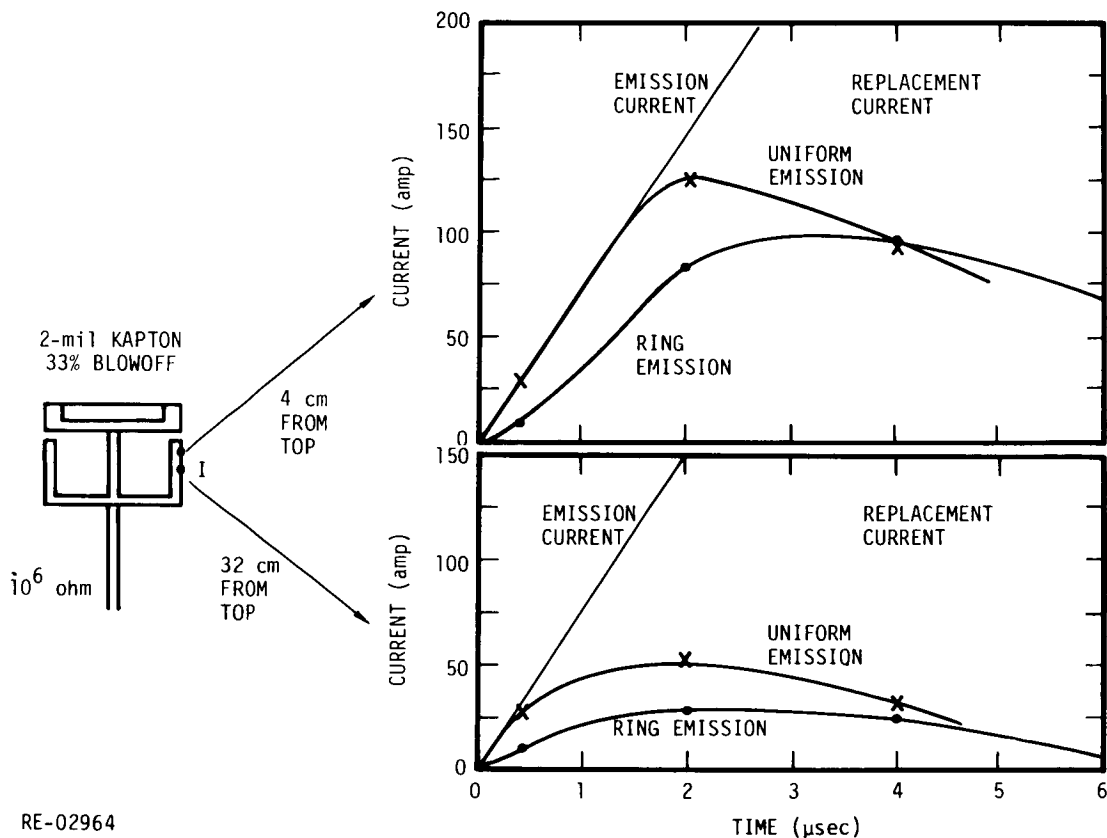
In brief, the performance of the pretest model was found to be excellent for each geometry tested for response locations away from the dielectric surface normal. In general, discharge characteristics were obtained from low-impedance measurements on small samples scaled up to the larger geometries. Difficulties with the modeling were experienced for conductors near the samples in the normal direction, and additional assumptions were required to calculate observed local currents. While the assumptions of energetic electrons and a neutral plasma emission are not totally satisfying, they are supported by recent experimental evidence, and their inclusion leads to the experimentally observed variation with antenna mast length in the antenna configuration.

## DISCUSSION OF MODEL ASSUMPTIONS

This section deals with the most debatable model assumptions of the predictive tool developed in these efforts. The emission current spatial distribution treatment was tested through a parameter variation exercise. Plausibility of the unit albedo assumption is considered in terms of dielectric properties and calculated system behavior. Experimental evidence for the neutral plasma employed in the antenna analysis is cited. Finally, effects of the artificially thick dielectric model are discussed.

The blowoff current emission spatial distribution has been the subject of considerable analysis (Refs. 7-8). A major justification of these efforts is that they may eventually be able to describe anticipated limitations of presently observed area scaling of the blowoff current as dielectrics tend toward larger dimensions. In the meantime, the question is, "How sensitive are the present results to the assumed spatial distribution for 1-m objects?" ABORC code results suggest that the response is only mildly sensitive to the distribution assumed for present-size objects.

The sensitivity of the canister response to the assumed blowoff charge spatial distribution is shown in Figure 4. Calculated replacement currents near the dielectric and half-way down the side of the canister show less than a factor of 2 variation between a uniform spatial discharge and a discharge from a small area at the outer edge. Blowoff charge originated from each area element with equal probability at each time step in the former, but it had to migrate to the outer edge of the dielectric before being ejected in the latter. The emission current and dielectric voltage time histories were the same in each case. We



RE-02964

**Figure 4. Canister response sensitivity to assumed discharge spatial distribution for high-impedance isolation**

conclude that the uniform discharge model is reasonable and, based on these results, we expect no strong sensitivity to a potentially more realistic "traveling discharge."

The calculated insensitivity to the spatial distribution can be better understood with the aid of electron cloud snapshots in time obtained from the computer code. Figure 5 shows the cloud at three different times during discharge of a Kapton sample for both uniform and outer-ring emission assumptions. At very early times, little or no charge returns to the canister because attractive fields are small. The cloud shows a considerable difference in shape, however (see the 200-nsec picture). As the canister begins to attract the cloud strongly due to its net charge, the two emission patterns tend to produce similar space-charge distributions (see the 2- $\mu$ sec picture). Thus, early-time response differences should diminish as limiting increases. This behavior is seen in corresponding currents on the body (Figure 4).

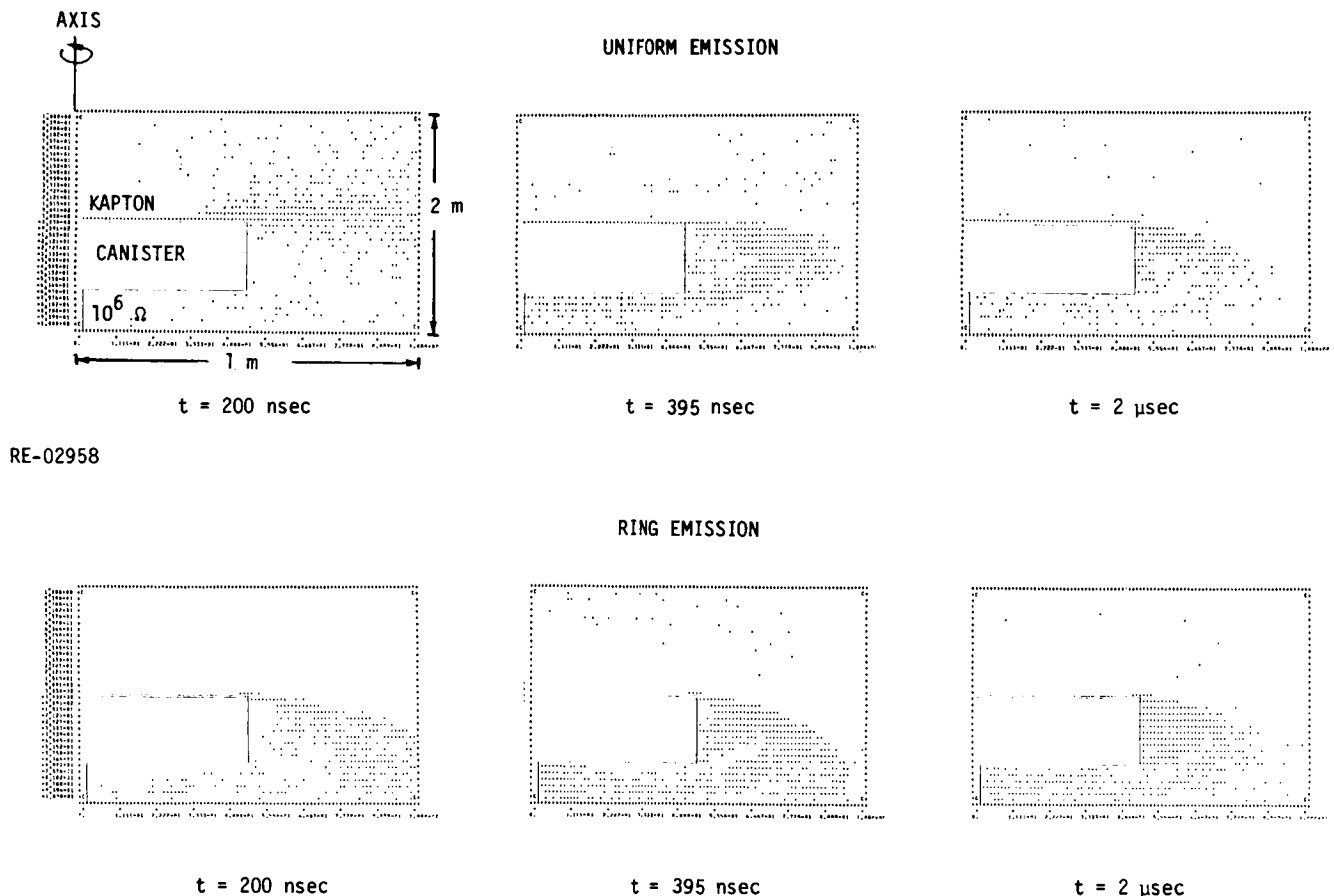


**Figure 5. Time snapshots of the electron cloud for a Kapton dielectric with high-impedance grounding for both uniform and ring spatial emission assumptions**

The snapshots also suggest that the mechanism by which charge travels to the outer edge is not particularly critical, because space-charge limiting keeps the electrons near the top surface in any case.

Whereas the ring emission model treats the propagation of charge to the discharge site as a blackbox, the uniform model requires the additional input of the description of the charge-reflecting properties of the dielectric surface. Without charge albedo, the model would permit only a small fraction of the blowoff charge to escape the surface in the high-impedance isolation case. The upper right-hand snapshot in Figure 5 shows the cloud completely restrained to the surface of the sample, with each particle undergoing numerous reflections before it reaches the edge.

The surface properties of the dielectrics under the intensive fields and breakdown conditions being modeled here are not well known, so a description of albedo can only be approximate. The model presently employs a perfectly reflecting surface in lieu of a more complicated description. This treatment is somewhat justified in view of dielectric properties which are known for weak field conditions (Ref. 9). Electrons striking a surface produce both low- and high-energy reflected components. The energy of the former is approximately 50 eV; the latter are similar to the incident particle in energy. The total yield of the low-energy component can be as high as five times the incident charge for 0.5-keV normally incident electrons on dielectrics, and increasing as much as a factor of 7 between normal and grazing incidences. The high-energy reflected electron yield varies between approximately 10 and 100% of the incident charge between normal and grazing incidence, and is only mildly dependent on the incident particle energy.

Putting the above properties together and assuming that they pertain to the high-field breakdown environment of the Mylar experiments, one obtains a secondary-electron charge albedo of as much as 35 and a primary albedo as high as unity. These values make the present model assumption of unit albedo for all angles and energies appear to be conservative. Also, the distinction between primary and secondary electrons is not critical because zero initial energy of blowoff charge has generally been assumed here anyway.

We conclude that the unit albedo assumption is a conservative treatment for the present series. An investigation which involves a more exact albedo treatment, including effects of strong fields, would be appropriate, especially in an effort to determine scaling to much larger structures.

The plasma emitted from the dielectric has been the subject of some debate in the present computer model for the antenna solution. The major criticism has been that such a plasma is too slow to cause major effects on currents reaching the antenna. Yadlowski (Ref. 10), however, observed essentially equal pulses of positive and negative particles arriving at a Faraday collector 9 cm from a Teflon discharge in less than 1  $\mu$ sec. Assuming that the same plasma could be observed for the second-surface mirrors, it would have traversed almost one-half the distance to the antenna by the time of the peak of the blow-off current pulse. This is sufficient to increase transmission of charge to the antenna by a large amount, and is consistent with the results of the model. Very little is known about the plasma, and its electromagnetic skin depth characteristics are the most relevant properties for these studies. Analytical estimates show a small enough skin depth to close out retarding electric fields for reasonable assumptions of temperature and density (Ref. 1), but more effort is warranted to justify the model. The fact that the plasma arrived at Yadlowski's Faraday cup intact shows that the skin depth was sufficiently small to overcome considerable electric fields.

Finite-difference zone studies were performed in which a Poisson-solver code was used to model actual dielectric material thicknesses and nearby geometry details for comparison with the much coarser grids employed in ABORC (a 2-mil dielectric is typically modeled using two 0.75-cm zones in the code). Comparisons of the calculated precharge fields showed that values were within 10% for grid points at similar positions relative to

the dielectric in both models. Large differences exist over very small dimensions (the fine zones resolve much higher field values than the coarse grid is capable of). These fields occur over a small volume, and are not considered significant enough to impact results presented here. Potential inaccuracies introduced by the thick dielectric assumption should always be reviewed, however, when new physics or geometries are introduced as they were here.

## SUMMARY AND CONCLUSIONS

A semi-empirical model of the coupling of dielectric discharge currents to satellite structures has been developed and tested with considerable success against experimental data. Satellite ECEMP response was predicted within a factor of two for three fundamentally different geometries using different dielectric materials, with discharge characteristics scaled from small-sample measurements. The model reproduced the response of an antenna located near the sample in the normal direction only when additional physics was included post-test. Fundamental model assumptions have been shown to be reasonable and even conservative, based on experimental data comparisons, parameter sensitivity studies, and known material properties. Additional effort in the areas describing the neutral plasma emission and albedo characteristics for high-field conditions appear to be warranted by these studies. The most questionable remaining property of the model behavior discussed here is the high-energy blowoff electron requirement for reproducing the observed antenna mast current. That quantity can probably be relaxed through a more detailed description of the discharge physics and resulting neutral plasma.

Applications of the present model have been made for the low-energy ( $\lesssim 25$  keV) space environment only. Data are also available for combined low- and high-energy-electron-induced discharges, which are typically different from those observed for low-energy exposures (Ref. 11). Straightforward application of the methods described here could also stress the model for such combined environment discharges. It is also significant that the treatments employed here for the external problem could be applied to dielectric discharges induced by high-energy electrons penetrating to internal spacecraft locations.

## REFERENCES

1. M. J. Treadaway et al., "Experimental Verification of an ECEMP Discharge and Coupling Model," JAYCOR report 200-80-231/2176, July 1980 (also presented at 1980 IEEE Conference on Nuclear and Space Radiation Effects).
2. B. L. Beers et al., "Negative Streamer Development in FEP Teflon," IEEE Trans. Nucl. Sci. NS-26, 6, December 1979.
3. T. M. Flanagan et al., IEEE Trans. Nucl. Sci. NS-24, 6, December 1979.
4. K. G. Balmain and G. R. Dubois, "Surface Discharges on Teflon, Mylar, and Kapton," IEEE Trans. Nucl. Sci. NS-26, 6, December 1979.
5. R. C. Hazelton et al., "Measurements of Particle Emission from Discharge Sites in Teflon Irradiated by High-Energy Electron Beams," IEEE Trans. Nucl. Sci. NS-26, 6, December 1979.
6. A. J. Woods and T. N. Delmer, "The Arbitrary Body-of-Revolution Code (ABORC) for SGEMP/IEEMP," DNA-4348T, July 1976.



7. R. Stettner and R. Marks, "Physical Modeling of Spacecraft Discharge Processes and Associated Electron Blowoff," presented at 1980 IEEE Conference on Nuclear and Space Radiation Effects.
8. I. Katz et al., "A Theory of Dielectric Surface Discharges," presented at 1980 IEEE Conference on Nuclear and Space Radiation Effects.
9. J. A. Wall et al., "Results of Literature Search on Dielectric Properties and Electron Interaction Phenomena Related to Spacecraft Charging," Proc. of Spacecraft Charging Technology Conf., AFGL-TR-77-0051, February 1977.
10. E. J. Yadlowski et al., "Characterization of Electrical Discharges on Teflon Dielectrics Used as Spacecraft Thermal Control Surfaces," AFGL-TR-79-0082 (1978).
11. M. J. Treadaway et al., "The Effects of High-Energy Electrons on the Charging of Spacecraft Dielectrics," IEEE Trans. Nucl. Sci. NS-26, 6, December 1979.

**DISAPPEARANCE AND REAPPEARANCE OF PARTICLES OF ENERGIES  $>50$  KEV  
AS SEEN BY P78-2 (SCATHA) AT NEAR GEOSYNCHRONOUS ORBIT\***

**J. Feynman and N. A. Saflekos  
Boston College**

**H. G. Garrett  
Jet Propulsion Laboratory**

**D. A. Hardy and E. G. Mullen  
Air Force Geophysics Laboratory**

**SUMMARY**

The near-geosynchronous orbit of the P78-2 (SCATHA) satellite is ideal for extending studies of processes earlier detected by the series of geosynchronous vehicles. SCATHA's apogee and perigee are 5.5 and 7.7  $R_E$  and the latitudinal drift is  $6^\circ$  per day. This allows SCATHA to sweep through the geosynchronous region and sample the magnetospheric environment over a widened range of latitude and distance from the earth. A survey of the nightside particle environment as observed by the AFGL Rapid Scan Particle Detector frequently shows large, sudden simultaneous changes in the fluxes of electrons and protons with energies above 50 keV which we refer to as dropouts. An interesting feature of SCATHA dropouts is the quasiperiodic behavior of the particle flux amplitudes which often vary with a period of the order of 15 minutes both during the dropout and after the return. A flux return during eclipse caused a major spacecraft charging event of several kilovolts. Our observations are compared with those reported for other geosynchronous satellites. In agreement with ATS-5, we find a marked dependence in the frequency of occurrence due to an effect of the orbit. ATS-5 experienced few dropouts during quiet geomagnetic conditions. However, for an L shell greater than seven, SCATHA particle dropouts occur routinely during quiet conditions. Thus, for SCATHA's orbit, both the orbital position and geomagnetic conditions must be taken into account in evaluating the potential hazard of flux returns.

---

\*This work was supported in part by Air Force Geophysics Laboratory Contract F19628-79-C-0031.

## INTRODUCTION

On the night side of the earth in geosynchronous orbit, there are frequent sudden disappearances and reappearances of fluxes of electrons and ions in the  $E > 50$  keV energy range (Lezniak and Winckler, 1970, Bogott and Mozer, 1973, Walker et al, 1976). These flux changes, called dropouts, are usually ascribed to the satellites exiting and reentering the region of high energy trapped particles that characterize this part of the magnetosphere.

Here we are primarily concerned with the occurrence of these particle dropouts as experienced by P78-2 (SCATHA) in a near-geosynchronous orbit. Transitions between regions of such high and low fluxes of particles represent one of the most dramatic rapid changes of charging environment routinely present in this orbit. For example, on March 28, 1979 (Day 87) SCATHA was already in a dropout region when it entered eclipse. An abrupt return of plasma during the eclipse caused charging of several kilovolts (Saflekos et al., 1980), one of the major charging events seen on SCATHA during the first year of operation. The rapid variations in the fluxes associated with dropouts imply rapid variations in satellite potential. If, in addition, there are high field aligned fluxes at this boundary, as the data suggest, the possibility exists for creating large differential gradients in the spacecraft potential on the satellite surface. As dropouts occur preferentially in the midnight sector (Walker et al., 1976) eclipses of the satellite are likely to occur simultaneously with the dropouts. During the first eclipse season, dropouts were present during a third of the eclipses that lasted more than 45 minutes. Taken together, the the rapid variation in environment, the flux anisotropies, and the possibility of a simultaneously occurring eclipse, cause the region of the magnetosphere in which dropouts occur to pose a severe spacecraft charging threat. The characterization of this region is necessary for a complete understanding of spacecraft charging variations in and near the midnight sector.

For geosynchronous orbit, Lezniak and Winckler (1970) mention such events as seen by ATS-1. Bogott and Mozer (1973) studied an extensive data set from ATS-5 and explained the disappearances as due to the satellite exiting the region of high energy trapped particles because of the distortion of the region towards a more taillike configuration occurring during substorm buildup. This picture is confirmed by a multi-satellite study (Wilken, et al., 1979). The reappearance of the plasma is then due to the relaxation of the nightside magnetosphere during the expansion phase of substorms. Bogott and Mozer (1973) found the events occurred preferentially at higher levels of geomagnetic activity during summer. The seasonal effect was explained as due to the orbit since ATS-5 is at a position closer to the edge of the trapping region in the summer months than in winter. The geomagnetic effect is in agreement with the picture in which the trapped particle region moves earthward during disturbed periods. The relation between sudden flux changes at synchronous orbit and substorms has been studied by Erickson et al. (1979) and Sauvaud and Winckler (1980). It has also been noted that the boundary often undergoes large scale motions which

appear to be due to traveling waves (Kaufman et al., 1972, Su et al., 1976 Wilken et al., 1979) but that effect is outside the scope of this paper. Here we discuss the positions of occurrence and dependence on geomagnetic disturbance of dropouts as seen at SCATHA's near geosynchronous orbit.

## OBSERVATIONS

The data used in this study are from the SCATHA Rapid Scan Particle Detector, SC5, which is sensitive to electrons in the range from 0.05 keV to 1 MeV and positively charged particles from 0.05 keV to 6 MeV. The detectors and their operation are described in detail in the paper by Hanser et al. (1980) presented at this conference. The instrument consists of two sets of detectors, one mounted with the look direction along the spin axis of the vehicle and the other mounted on the belly band with the look direction perpendicular to the spin axis. In this study, data from only the former are used. Each detector set consists of two parts, electrostatic analyzers for electrons and ions of energies below 60 keV and solid state detectors for the higher energy electrons and protons. Complete spectra composed of 14 energy bands for electrons and 18 energy bands for positively charged particles are taken every second. A data format is used in this study in which minute averages of the count rate in each energy range is displayed for the detector with the look direction parallel to the vehicle spin axis.

Dropouts have been identified from the data as shown in Figure 1 which gives the 100 keV electron and 125 keV ion count rate from the solid state detectors for parts of three days. In the top panel, data from March 28, 1979 show the dropout and return during eclipse on the lefthand side of the figure where the electron flux changes by more than three orders of magnitude and the ion flux by two. This dropout occurred at 22:45 local time when  $K_p = 5-$  and SCATHA was at a solar magnetic latitude of  $-19^\circ$  and an L shell of 7. The L shell is calculated using an Olson Pfitzer (1974) magnetic field model for quiet days. For about an hour after the return to high flux levels, the electrons show intensity excursions as large as an order of magnitude. The count rate gradually decreased over the next several hours until it sank below detectable levels at about 02:30 LT when  $K_p = 3$  and the vehicle was at a latitude of  $-15^\circ$  and an L shell of 8.2. A second recovery occurred at about 04:00 LT and was followed by a remarkable set of apparently quasi-periodic variations in both the electron and ion flux.

The dropouts on March 28 are in contrast to the typically featureless behavior of the nightside 100 keV electron and 125 keV positively charged particle count rate shown in the second panel of Figure 1. These data are from the period spanning midnight GMT between July 31 and August 1, 1979. It was a geomagnetically quiet time with  $K_p$ 's of 1 and 2 and at midnight GMT SCATHA was at a latitude of  $8^\circ$  SM and an L shell of 8.3. The third panel of Figure 1 shows an example of a dropout in which both the flux decrease and increase were rapid. The typical quasiperiodic flux variations are seen over a wide energy range of particles both within the dropout region

and following recovery. The latitude at entry was  $10^\circ$  SM, the L shell was 8.6 and Kp 3+. Three other dropouts which occurred during this passage of the nightside are not shown.

The SC5 data for the period between January 20 and August 8, 1979 were examined for dropouts. The 100 keV electron data were scanned for decreases and/or increases of over an order of magnitude in count rate. Then the event was identified as a dropout if the increase or decrease occurred at the same time in all higher electron energies and in all positive particle energies above some threshold. A return from a dropout can be readily distinguished from a dynamic injection seen by SC5 (Moore et al., 1981) by several properties. The dropout return is characterized by a minimum energy above which the increase in flux increases with energy for all energies. The dynamic injection is also characterized by a minimum energy for flux increase but there is a larger energy above which the change in flux decreases with increasing energy. In addition, dropout entry and return occur in both charge species at the same time whereas injections are seen only in one species over a broad energy range.

Comparisons of particle spectra before, during and after a dropout are shown in figures 2 for electrons and 3 for ions. The dropout for which these are taken is shown in the third panel of Figure 1. The relative differential flux is given for the energy range in which the flux is above background during the dropout. Relative flux levels are used in place of absolute flux levels because the efficiency of the instrument determined by in-flight calibration is not yet available for this period. The spectra are determined for 1:30 GMT, well before the dropout, for 3:30 GMT during the dropout and for 4:30 GMT after the positive particle quasiperiodic variations had ceased. The electron spectra in Figure 2 show a dropout spectrum that is depressed by a factor of 2 at 1 keV and a factor of 100 at 40 keV. The electron flux after the dropout is somewhat higher than before the dropout for most of the energy range. Figure 3 shows the ion spectra. The spectrum during dropout is depressed by a factor of 3 at a few keV and by a factor of 20 at 50 keV. The flux at 125 keV is definitely higher than would be expected. Inspection of the data shows the flux level at 125 keV is at a maximum in the quasiperiodic variation in the flux at 3:30 whereas flux levels at lower energies are from minima. The flux minimum at 125 keV is a factor of 10 lower as can be seen in Figure 1. The quasiperiodic structure, then, involves a spectral change, perhaps due to the motion of a dispersed boundary of the high energy trapping region. The positive particle differential flux is almost indistinguishable before and after the dropout and only one line has been drawn in the figure. The stability of the positive particle spectrum is of note when it is recalled that the observations were separated 3 hours in universal time and SCATHA has moved over  $2 R_E$  along its orbit and is half an  $R_E$  further above the equatorial plane during the later measurement.

## MAGNETOSPHERIC POSITION DEPENDENCE OF DROPOUTS

Eight-eight days of SC5 data for the 5 1/2 month period between January 20 and August 8, 1979 were scanned and one or more dropouts identified for 39 of them. The distribution of dropout days in the year is given in two displays in Figure 4. In the bottom panel we show for each 20 day interval the number of dropout days as a percentage of all days for which the data are available. The total number of days with data is given above each 20 day bin. There are three periods during which more than half the days showed dropouts, between days 80 and 100, days 120 and 150 and days 180 and 210. The top panel shows details of the distribution of dropout days. Each day for which the data were available is marked by a line. A short line indicates there was no dropout whereas a long line indicates dropout days. The three dropout rich periods are evident. This clustering into dropout rich and poor periods corresponds to a position dependence in occurrence of dropouts since SCATHA drifts in latitude by  $6^\circ$  a day and has an apogee of 5.5 Re and a perigee of 7.7 Re.

The positions of dropouts are displayed explicitly in Figures 5 and 6. In each of these figures the position of the satellite during the low flux periods is shown as a solid line. The top panels give the L shell and local time whereas the lower panel gives the solar magnetic latitude and local time. Data for flux decreases when  $K_p < 4+$  are shown in Figure 5 and data for  $K_p > 4+$  are in Figure 6. For all dropouts except one, a categorization on the basis of  $K_p$  at flux return would have placed the dropout in the same group as did the categorization on the basis of flux disappearance. The sole exception was a disappearance at  $K_p = 4+$  and a return at  $K_p = 5-$ , and this dropout appears within the clustering apparent in Figure 5. Note that all of the dropouts except one occur between 19:30 LT and 6:30 LT. The dropout beginning at 6:20 LT and continuing to 7:50 shown in Figure 6 occurred when  $K_p$  was 8 and may have been either a dropout or a passage into the magnetosheath. A data gap in our low energy coverage makes it impossible to distinguish between these possibilities. The local time region of dropout appearance shown here agrees with those of ATS-5 and ATS-6, both of which observed dropouts in the region from from 2000 LT to 0830 LT (Bogott and Mozer, 1973; Su et al., 1976). Note that  $L > 7$  for all but 6 dropouts. There is also a region in the vicinity of  $-5^\circ$  SM latitude in which there are no dropouts. The shape of this region is not completely determined, but in this data set it appears to be centered at 1:30 LT and to be about  $10^\circ$  wide. It can be described as oval shaped with a more or less constant width crossing the latitude  $0^\circ$  line at about 05:30 local time and remaining below latitude  $0^\circ$  throughout the evening hours.

Figures 5 and 6 indicate that dropouts are rare during the months of February through August in a region of the magnetosphere bounded by local time 19:30 and 6:30, by L values of about 7 and by the edges of the  $10^\circ$  crescent in solar magnetospheric coordinates discussed above. If this is the case, the orbit of SCATHA during the three dropout poor periods, (before day 80, from day 100 to 120 and from day 150 to 180), should have a relationship to the excluded region of the magnetosphere. In Figure 7 we

show SCATHA's orbit between local times of 19:30 and 6:30 for days 50, 110 and 170. An examination of these orbits show that they lie almost completely within the excluded region. Hence, the division of SCATHA days into dropout rich and poor periods can be understood as a consequence of its orbit and the shape of the region of high energy particle trapping.

#### GEOMAGNETIC DISTURBANCE DEPENDENCE OF DROPOUTS

A very marked dependence of dropout frequency on geomagnetic activity was found for ATS-5 data (Bogott and Mozer, 1973). Walker et al. (1976) observed 75 ATS-6 dropouts for  $K_p < 4+$  in 4.5 months of data and state that this frequency is higher than that seen for ATS-5. They ascribe the frequency difference to ATS-6 being at the higher magnetic latitude but do not discuss the orbital differences in detail.

In the SCATHA data when the satellite was less than  $6.6 R_E$  (not L shell) from the earth, there were only five dropouts for which  $K_p < 4+$  and nine for which  $K_p > 4+$ . Thus, during the first half of 1979 a geosynchronous satellite would have observed few dropouts but would have reported a geomagnetic dependence in occurrence. At the actual SCATHA orbit, the dependence on geomagnetic activity is less pronounced. Figure 4 shows that dropouts were a common occurrence for  $K_p < 4+$ , but they occur at high L shells (and large values of R). A statistical analysis confirms the impression given by Figures 4 and 5, that at SCATHA's orbit, the dropout occurrence probability exhibits a geomagnetic and an orbital dependence which are comparable. In Table 1 the data has been divided into two sets of periods. The one set contains the dropout rich periods, days 81 to 100, 121 to 149 and 181 to 220, whereas the other set contains the dropout poor periods, days 40 to 80, 100 to 120 and 150 to 180. Each set of data is shown separately in the table. Geomagnetic activity as measured by  $A_p$  has been divided into three bins; quiet days with  $A_p$  0 to 9, (daily average three hours  $K_p < 2$ ) moderate days with  $A_p$  10 to 29 ( $2 < K_p < 4$ ) and disturbed days with  $A_p$  greater than 30 ( $K_p > 4$ ). In the dropout poor set, there were a total of 43 days with data of which three had dropouts. In the 45 days of the dropout rich set, 9 had no dropouts. Thus, if a prediction of dropout occurrence were made using only information on whether the day belonged to a dropout poor or rich region, and taking no account of the level of geomagnetic activity, the correct prediction would have been made for about 6 out of 7 days. Conversely, if the prediction had been made based on distinguishing only between quiet ( $A_p < 9$ ) and disturbed ( $A_p > 30$ ) days and taking no account of dropout poor and rich periods, the correct prediction would have been made in 2 out of 3 days. This indicates that at SCATHA's orbit both the details of the orbital position and the geomagnetic conditions must be taken into account in evaluating the probability that the spacecraft will undergo the extreme environmental changes associated with disappearance and return of high energy trapped particle fluxes.

## SUMMARY AND CONCLUSIONS

At SCATHA's orbit on the nightside, the satellite routinely exits and reenters the region of trapped high energy particles. Since these events occur predominantly near midnight and so may be associated with an eclipse, the flux returns pose a serious charging hazard. ATS-5, ATS-6 and SCATHA all report dropouts occurring from 2000 LT to 08:30 LT. SCATHA experiences dropouts predominantly beyond  $L = 7$  and outside of a region about  $10^\circ$  wide in solar magnetic latitude. The probability of SCATHA dropouts occurring during a particular day has a comparable dependence on both its orbital position and on the level of geomagnetic activity.

## REFERENCES

1. Bogott, F.H. and F.S. Mozer: Nightside Energetic and Particle Decreases at the Synchronous Orbit. *J. Geophys. Res.*, 78, 1973, p. 8119.
2. Erickson, K.N.; R.L. Swanson; R.J., Walker; J.R. Winckler: A study of Magnetospheric Dynamics During Auroral Electrojet Events by Observations of Energetic Electron Intensity Changes at Synchronous Orbit. *J. Geophys. Res.* 84, 1979, p. 931.
3. Hanser, F.A.; B. Sellers; D.A. Hardy; H.A. Cohen, J. Feynman and M.S. Gussenhoven: Operation of the SC5 Rapid Scan Particle Spectrometer on the SCATHA Satellite. Presented at the Spacecraft Charging Technology Conference III.
4. Kaufmann, L.R., J.T. Horng, and A. Konradi: Trapping Boundary and Field Line Motion During Geomagnetic Storms. *J. Geophys. Res.*, 77, 1972, p. 2780.
5. Lezniak, T.W. and J.R. Winckler: Experimental Study of Magnetospheric Motions and the Acceleration of Energetic Electrons During Substorms. *J. Geophys. Res.*, 75, 1970, p. 7075.
6. Moore, T.E., R.L. Arnoldy, J. Feynman and D.A. Hardy: Propagating Substorm Injection Fronts, submitted *J. Geophys. Res.*, 1981.
7. Olson, W.P. and K.A. Pfitzer: A Quantitative Model of the Magnetospheric Magnetic Field. *J. Geophys. Res.*, 79, 1974, p. 3739.
8. Saflekos, N.A.; M. F. Tautz; A.G. Rubin; D.A. Hardy; P.F. Mizera and J. Feynman: Three Dimensional Analysis of Charging Events on Days 87 and 114, 1979 from SCATHA. Presented at Spacecraft Charging Technology Conference III, 1980.
9. Su, Shin-Yi,; T.A. Fritz and A. Konradi: Repeated Sharp Flux Dropouts Observed at 6.6 Re During a Geomagnetic Storm: *J. Geophys. Res.* 81, 1976, p. 245.



10. Walker, R.J., K.N. Erickson, R.L. Swanson, and J.R. Winckler: Substorm-Associated Particle Boundary Motion at Synchronous Orbit. J. Geophys. Res. 81, 5541, 1976.
11. Wilken, B., A. Korth, G. Kremser and Th.A. Fritz: Multiple-Satellite Observations of Large Scale Trapping Boundary Motions. Proceedings of Magnetospheric Boundary Layers Conference, Alpbach, 11-15 June, 1979, ESA SP-148, 1979.

TABLE 1  
Periods of few dropouts (days 40-80, 100-120, 150-180)

Range of $A_p$	0-9	10-29	> 30	$\Sigma$
# of dropout days	0	1	2	3
# of no dropout days	17	19	4	40
Total # of days	17	20	6	$\Sigma$ 43

Periods with many dropouts (days 81-100, 121-149, 181-220)

Range of $A_p$	0-9	10-29	> 30	$\Sigma$
# of dropout days	7	20	9	36
# of no dropout days	6	3	0	9
Total # of days	13	23	9	$\Sigma$ 45

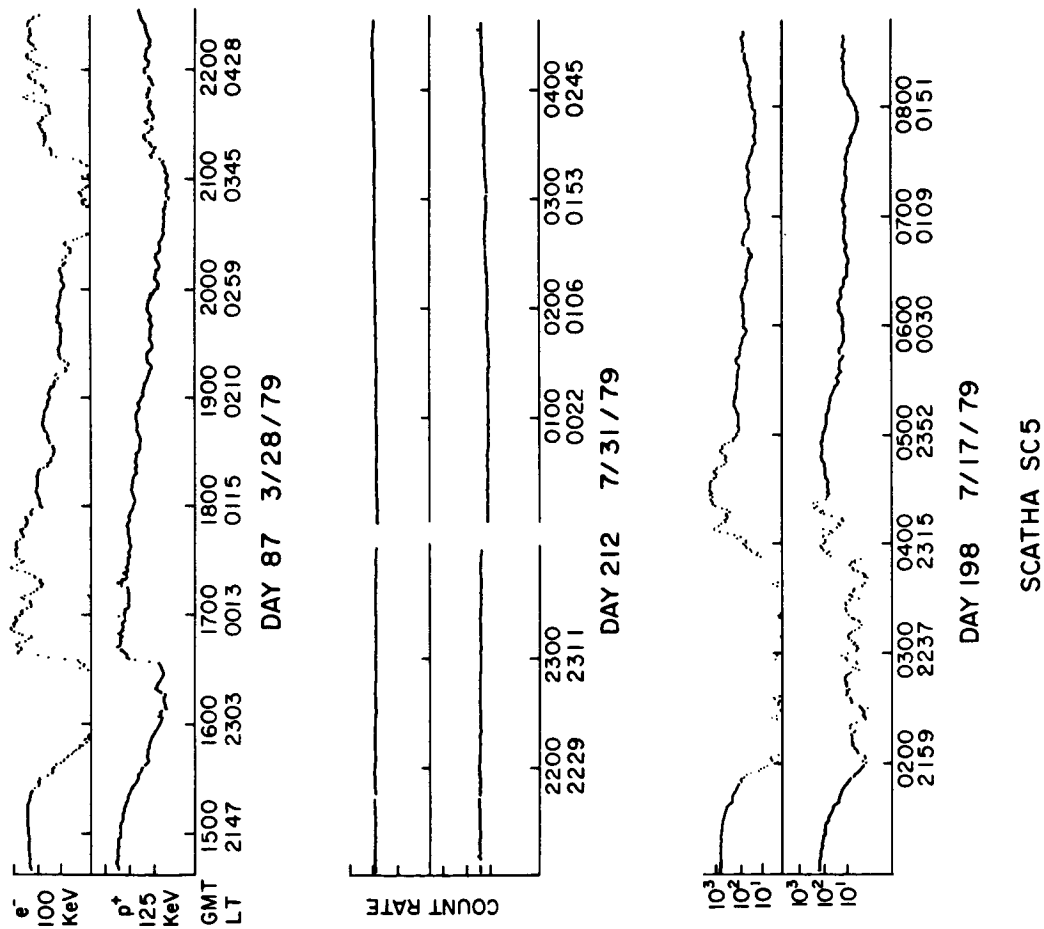


Figure 1. - Dropouts as seen in 100 keV electrons and 125 keV protons by the Rapid Scan Particle Detector, SC5. The first and third panels show dropouts and their characteristic quasisperiodic structures. The center panel contrasts this to a day without dropouts.

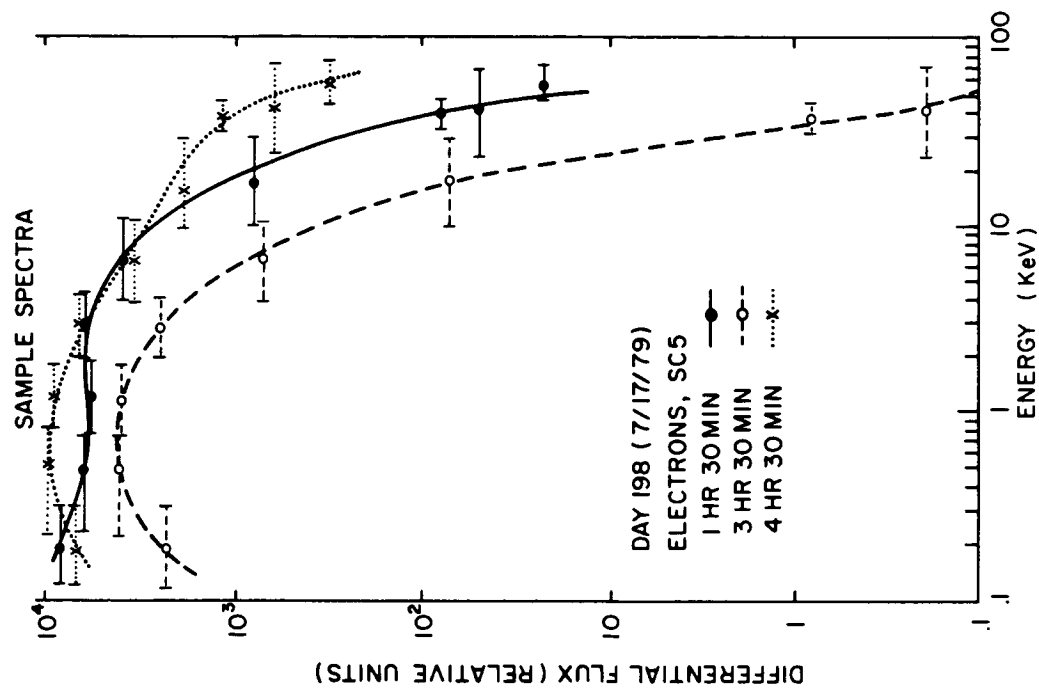


Figure 2. - Electron differential flux before, during and after the dropout shown in the lower panel of Figure 1.

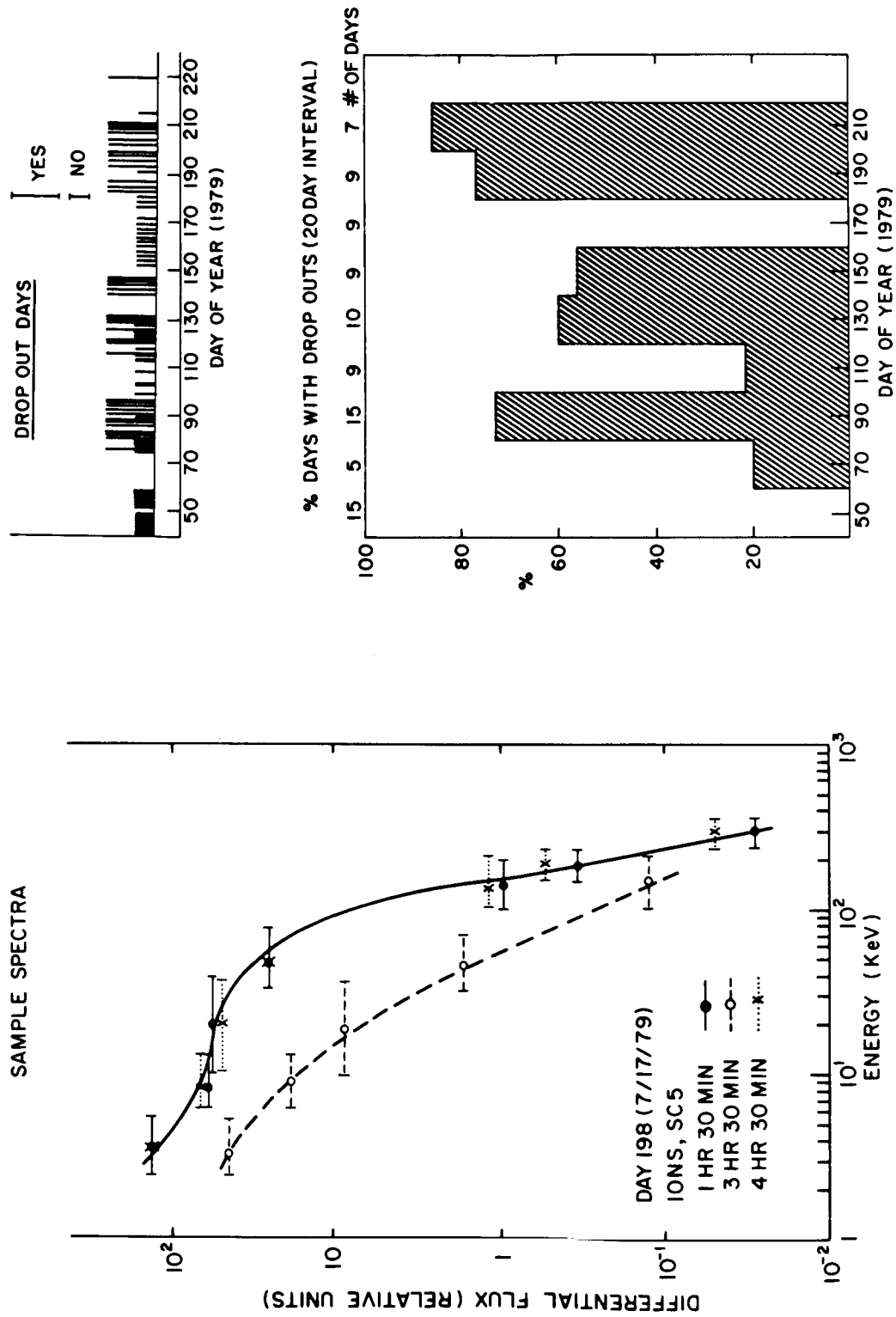


Figure 3. - Ion differential flux before, during and after the dropout shown in the lower panel of Figure 1.

Figure 4. - Dropout occurrence between days 40 and 220, 1979. In the top panel all days for which there are data are labeled according to whether or not dropouts occurred. The percentage of days with dropouts in each 20 day interval is shown in bottom panel.

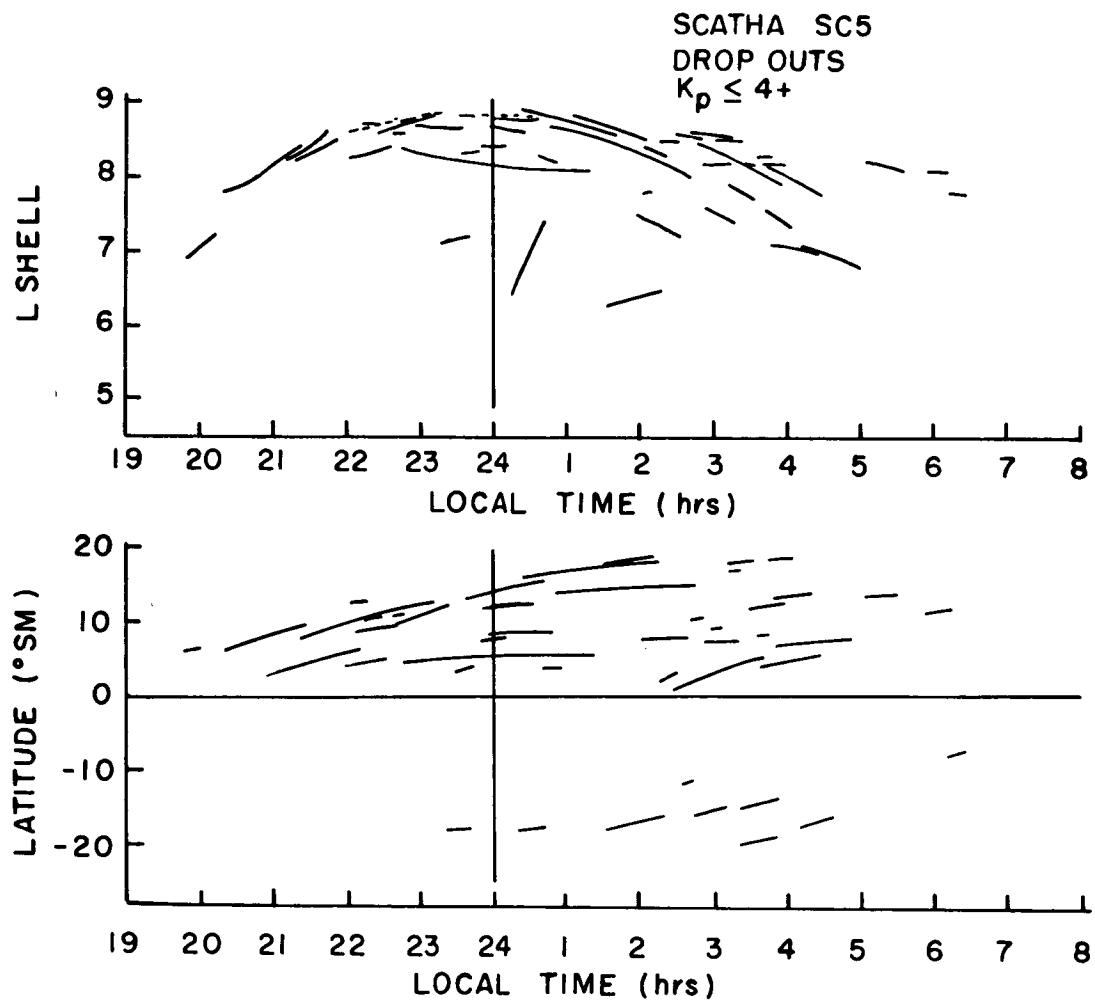


Figure 5. - SCATHA's position during dropouts for geomagnetically quiet days ( $K_p \leq 4+$ ).

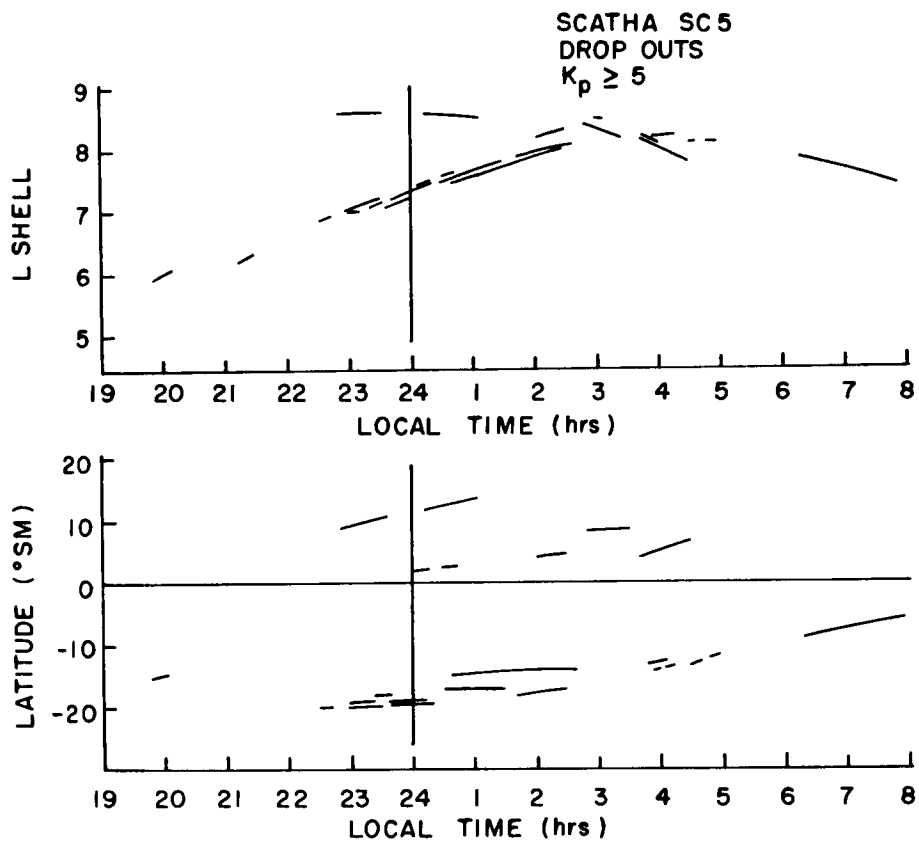


Figure 6. - SCATHA's position during dropouts for geomagnetically disturbed days ( $K_p > 4+$ ).

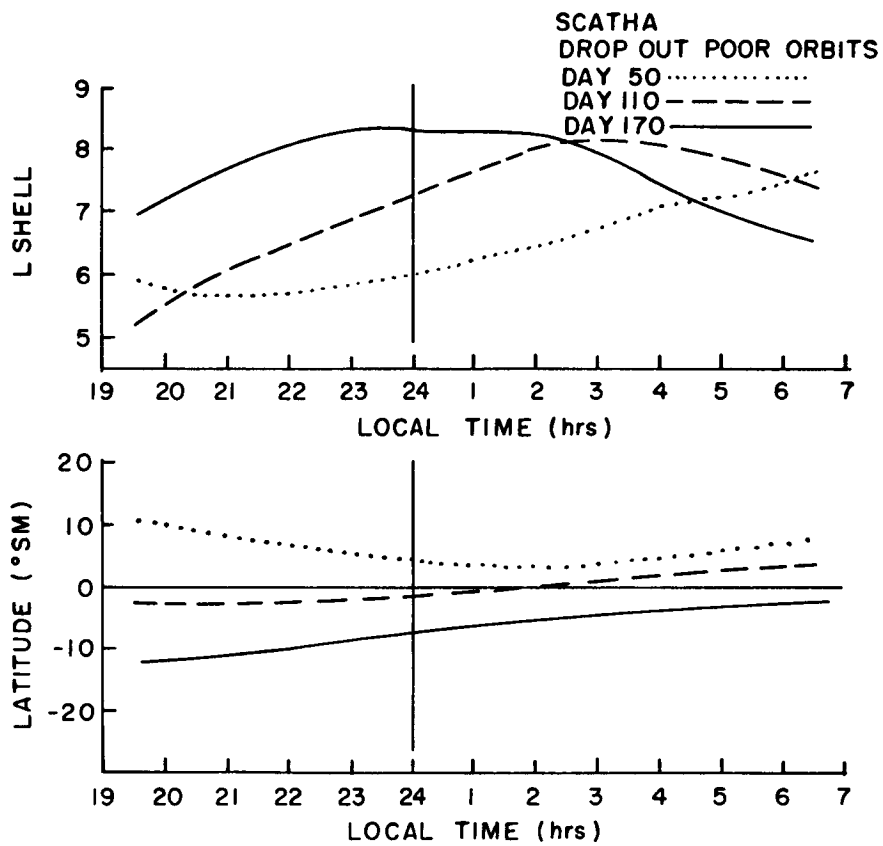


Figure 7. - SCATHA's orbits during the three dropout poor periods evident in Figure 4.

## **MILITARY STANDARDS AND SCATHA PROGRAM UPDATE OF MIL-STD-1541**

**D. T. Frankos  
The Aerospace Corporation**

### **SUMMARY**

MIL-STD-1541 (USAF), Electromagnetic Compatibility Requirements for Space Systems, 15 October 1973, establishes requirements for Electromagnetic compatibility to be met by Industry Contractors for Spacecraft Launch Vehicles and other special space systems. Some technical deficiencies exist in the present issue with respect to spacecraft charge and discharge phenomena in space. The SCATHA Program will produce technical requirements applicable to space systems subjected to space plasma environment(s). The format and subject matter supplied as a result of the SCATHA Program effort must satisfy DOD and AFSD requirements for technical standards as specified in MIL-STD-962, Outline of Forms & Instructions for the Preparation of Military Standards and Handbooks.

### **INTRODUCTION**

The DOD Standardization Program impact on new or revised standards provides for two basic kinds of standards; namely, management and technical standards.

A management standard is contractor task oriented. In simplistic terms "the contractor shall ..." e.g. "the contractor shall generate and submit an EMC Control Plan". Additionally, a Data Item Description (DID) would be supplied to describe the contents and a data submittal requirement in the form of a Contract Data Requirements List (CDRL) line item would be imposed. A technical standard is equipment oriented; again, in simplistic terms "the equipment shall ..." e.g. "the equipment shall comply with the emission and susceptibility limits of MIL-STD-461B for conducted and radiated Electromagnetic Interference (EMI)". Within the established DOD framework, management standards require an extensive approval chain because of their widespread application; whereas, technical standards can be cycled through AFSD for approval because of their limited usage on space systems.

This paper is intended to indicate the technical ramifications for generating a new standard and, in particular, describe how MIL-STD-1541 will be upgraded with requirements supplied as a result of the SCATHA Program effort related to electrical charge and discharge phenomena due to space plasma.

## STRUCTURE OF TECHNICAL STANDARDS

Air Force Space Division Regulation, SD 5-6 (5 Dec 1979) establishes the definition of a technical standard as "Establishes Engineering & Technical Limitations for Items, Materials, Processes, Methods, Designs and Engineering Practices". SD 5-6 also establishes a policy paraphrased as "The format and content of MIL Standards and Space Division Standards will be in accordance with MIL-STD-962". The format and contents of a technical standard per MIL-STD-962 is delineated as follows:

- |            |   |
|------------|---|
| Section 1. | <u>SCOPE</u><br><br>Contains a principal statement: a clear concise delineation of the extent or range of technical content.  |
| Section 2. | <u>REFERENCE DOCUMENTS</u><br><br>Government specifications, standards, drawings and publications may be referenced (do not reference higher tier documents)<br><br>Non-government documents (Industry Organizations and Technical Societies may also be referenced).<br><br><u>NOTE: The number of references should be kept to a minimum so the standard can stand alone as much as possible.</u> |
| Section 3. | <u>DEFINITIONS</u><br><br>Define key terms in detail for clarity. Definitions may be included by reference to documents in Section 2.<br><br>Where standard definitions exist in DOD documents, do not use different definitions.   |
| Section 4. | <u>GENERAL STATEMENTS OF REQUIREMENTS</u><br><br>Requirements include characteristics common to the area covered.   |
| Section 5. | <u>DETAILED STATEMENTS OF REQUIREMENTS</u><br><br>Only state characteristics that can be confirmed by reliable quality criteria or test equipment.  |



## APPENDICES:

Shall be within scope of the standard and not be inconsistent.

Reference the Appendix and the extent of applicability within the standard.

At the beginning of the Appendix, indicate if the contents are mandatory.

Caption and number sections in multiples of 10.

## SCATHA PROGRAM INPUT TO UPDATE MIL-STD-1541

Proper consideration must be given to the technical output of the SCATHA Program effort with respect to its use and usefulness when incorporated into the standard and levied on a Contractor. Not only should the updated standard be technical in nature, but, it must also be presented properly to prevent incorrect interpretation by a contractor. The Contractor must clearly be able to understand the requirements so he can define, schedule and cost work effort to implement the requirements of the standard for bidding in response to an RFP (Request For Proposal).

It is highly desirable to establish both system and equipment level requirements, where applicable, for control of spacecraft charging and to eliminate deleterious effects of discharges, be they performance degradation, malfunction or damage. SCATHA Program data permitting, system and equipment requirements should be specified for design, test and test methods appropriate to controlling charge and eliminating discharge effects. It is recognized that, to date, the information base provided by the SCATHA Program effort is limited and does not include all the subject matter desired for updating MIL-STD-1541. However, what is available will be utilized in the scheduled update of the standard.

To minimize the potential for duplication of effort, the ground rules for the format and content of the SCATHA Program material supplied include 1) generate an Appendix per MIL-STD-962 as discussed earlier, 2) stipulate the applicability of the Appendix and 3) for Section 50 in the Appendix, generate specific system and equipment level requirements for design, test and test methods where the SCATHA Program information base dictates/justifies.

## UPDATING EXISTING OR GENERATING NEW STANDARDS

The process for issuing an updated/upgraded standard or a new one is the same. It is an extensive effort and, in the time domain, is quite lengthy. It incorporates many "checks and balances" including several review cycles via AFSD, Government Agencies and Industry Groups. To better understand how the "system" works, the key milestones for this process are enumerated:

- 1) Rough draft by technical personnel.
- 2) Statement of objective letter to SD/AQ per SD Regulation 5-6.
- 3) Project coordination conference per SD Regulation 5-6.
- 4) Project number assigned when approved.
- 5) Draft in correct format and language.
- 6) "In-House" informal coordination, several cycles.
- 7) Complete draft for review and informal coordination with selected industry and government experts.
- 8) Revise draft based on above; proposed draft printed for formal coordination.
- 9) Coordination request and draft to SD and selected government offices, Industry Groups and Aerospace Corporation.
- 10) Revision per comments received; resolve outstanding serious non-concurrences.
- 11) Final copy prepared (camera ready); approved by SD/AQ.
- 12) Initial printing and distribution by SD.

## **MILITARY STANDARD FOR SPACECRAFT CHARGING STATUS REPORT**

**Alan B. Holman  
Science Applications, Incorporated**

### **SUMMARY**

The Air Force Space Division, with technical support from Science Applications, Inc. and Aerospace Corporation have structured a Military Standard for Spacecraft Charging in the format of an appendix to MIL-STD-1541, Electromagnetic Compatibility Requirements for Space Systems. The document is one of the key products of the Cooperative NASA/AF Spacecraft Charging Investigation. This paper presents the status of the development of the Spacecraft Charging Requirements Appendix and provides an opportunity for a community review of the current document structure and content.

### **INTRODUCTION**

The development of a military standard for spacecraft charging requirements is an essential product of the Cooperative NASA/AF Spacecraft Charging Investigation. Figure 1 presents a timeline of the history of this development over the past 4 years of the NASA/AF program. The current goal is the incorporation of S/C charging requirements into an update of MIL-STD-1541 by the end of Air Force FY82. Over the time period shown, the S/C Charging Standard has evolved from an initial identification of a need for an environmental and test specification, through a potential stand-alone military standard requirements document, to the now planned MIL-STD-1541 revision. The intent is to serve the community of system program offices, NASA labs, and space vehicle contractors with a document which provides a consensus of practical requirements for design, test, and analysis to minimize the effects of the S/C charging phenomena.

The military standard requirements for spacecraft charging will take the structure of an appendix to the MIL-STD-1541 document. Elements within the main body of the current MIL-STD-1541 relating uniquely to S/C charging will be deleted in the formal revision by Aerospace Corporation. The following section of this report provides the Science Applications, Inc. (SAI) recommended inputs for the Spacecraft Charging Requirements Appendix, following a prescribed format. The main sections of the appendix are:

10. SCOPE
20. REFERENCED DOCUMENTS
30. DEFINITIONS
40. GENERAL STATEMENT OF REQUIREMENTS
50. DETAILED STATEMENT OF REQUIREMENTS

This document does not have the formal approval of AF Space Division/Aerospace Corporation at this time. It is a preliminary document intended to undergo a community review. An attempt has been made to quantify as much information as possible based on the current data available. Material with a high degree of uncertainty is flagged or left TBD at this time, with "best available information" in parentheses. The information contained in this version of the Appendix is inclusive of more material than will reside in the final document. Some of the information is more appropriate for a Statement of Work (SOW) than for the MIL-STD Appendix. All of the information, however, has been included here for completeness and for review. Comments from the community will be welcomed.

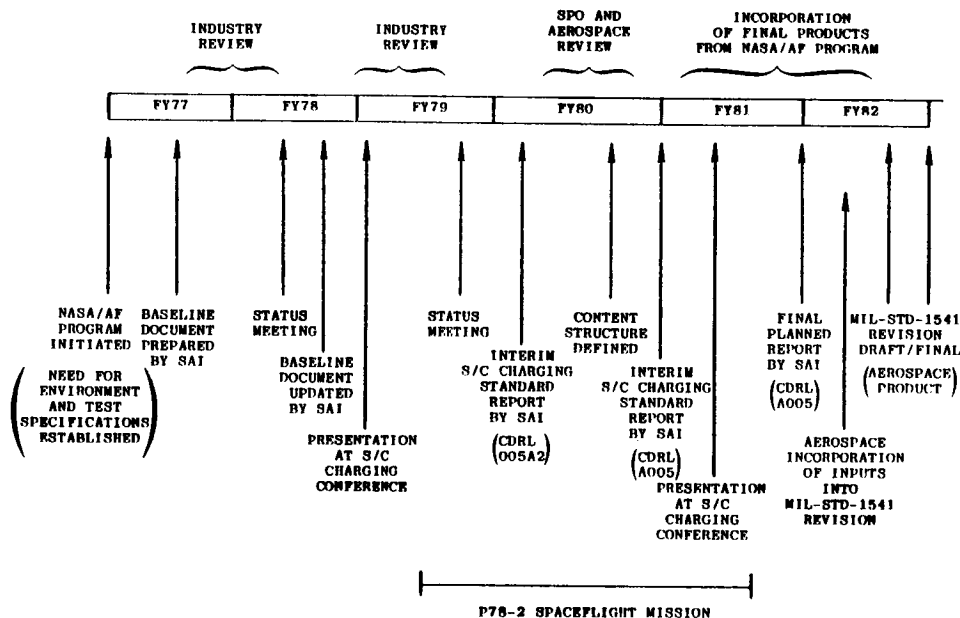


Figure 1. Timeline of S/C Charging Standard Development Activities

## PROPOSED MIL-STD-1541 REVISION

### APPENDIX: SPACECRAFT CHARGING REQUIREMENTS

This appendix includes mandatory material to be considered as part of this standard as prescribed in paragraph TBD of this standard. (Paragraph TBD is an applicability statement within body of MIL-STD-1541).

10. SCOPE

10.1 Scope. This appendix establishes the spacecraft charging (SCC) protection requirements for space vehicles which are to operate in the magnetospheric plasma environment as specified in TBD (AFGL Final Environmental Atlas definition of applicable region of space). This Appendix contains design requirements, analysis requirements, and test requirements and test methods to ensure space vehicle performance will not be degraded below specified levels when subjected to the magnetospheric plasma environment. (Analysis requirements may be transferred to the contractor Statement of Work (SOW)).

10.2 Application. This appendix shall be applicable only to space systems which might enter, during the course of their mission, the region of space containing the plasma environment which can cause spacecraft charging effects. This region is defined in TBD (Final AFGL Atlas). (Regions of space in the vicinity of the earth with L shell values of between 4.0 and 9.0 are representative of the regions of the SCC hazard). This appendix shall apply generally to all space systems exposed to the SCC hazard. Certain requirements may, however, be specifically tailored to individual program specifications with the approval of the procuring agency.

20. REFERENCED DOCUMENTS

20.1 Issues of Documents. The following documents of the issue in effect on the date of invitation for bids or request for proposal, form a part of this Appendix to the extent specified herein:

STANDARDS

Military

MIL-STD-1541 (USAF) - Electromagnetic Compatibility  
Requirements for Space Systems

20.2 Other Publications. The following documents form a part of this appendix to the extent specified herein. Unless otherwise indicated, the issue in effect on the date of invitation for bids or request for proposal shall apply.

NASA TM X-73446 - Provisional Specification For Satellite  
Time in a Geomagnetic Substorm Environment  
(to be updated)

AFML-TR-76-233 - Conductive Coatings for Satellites

AFML-TR-77-174 - Transparent Antistatic Satellite Materials

AFML-TR-77-105 - Spacecraft Static Charge Control Materials

AFML-TR-78-15 - Satellite Contamination

AFGL-TR-77-0288 - Modeling of the Geosynchronous Orbit Plasma Environment - Part I

AFGL-TR-78-0304 - Modeling of the Geosynchronous Orbit Plasma Environment - Part II

AFGL-TR-79-0015 - Modeling of the Geosynchronous Orbit Plasma Environment - Part III

NASA (to be published) - Design Guidelines for Spacecraft Charging Monograph

NASA CR-135259 - NASCAP User's Manual

AFGL (to be published) - Final Environmental Atlas, Preliminary version: P78-2 SCATHA Preliminary Data Atlas

AFWAL-TR-80-4029- Satellite Spacecraft Charging Control Materials

### 30. DEFINITIONS

30.1 Definitions That Apply To This Appendix. The terms used in this appendix are either defined in MIL-STD-1541 (USAF) or listed in the following paragraphs.

30.1.1 Arc Discharge (Vacuum Arc Discharge). A discharge taking place in a vacuum region with initially high potential gradients. The electric field may exist within a dielectric or in the vacuum region surrounding the charge retaining material. In the latter case, the gradients are between the electrode and either the vacuum chamber walls or an equivalent space charge surrounding the electrode. In these cases, the potential gradients must be sufficiently high to ionize and vaporize the charge retaining material. There are different types of important vacuum arc discharges, each classified by the configuration of the electrodes or the characteristics of the current path at the spark gap. These are the dielectric-to-metal discharge and the metal-to-metal discharge, each with a spark gap path that is classified as a punch-through, a flash-over, or a blow-off discharge.

- 3.1.2 Blow-off Discharge (Space Emission Discharge). A vacuum discharge characterized by the ejection of current (blow-off of charge) into space surrounding an electrode. To produce a space emission discharge, the electric field must be sufficiently high to cause ionization and vaporization at the electrode.
- 30.1.3 Backscattering. The deflection of particles by scattering processes in matter such that particles emerge through the same planar surface as they entered.
- 30.1.4 Capacitive Direct Injection (CDI). A method of inducing a space vehicle response that simulates that response to a blow-off discharge. The method involves driving the space vehicle with a current injection into a given point, with charge return accomplished through a drive plate serving as a capacitor.
- 30.1.5 Dielectric-To-Metal Discharge. A discharge between two electrodes, one of which is a dielectric charge retaining material and the other is a conductive (metal) electrode in the vicinity of the dielectric. A dielectric material will typically accumulate charge when irradiated by electrons or ions or under certain conditions when placed in a plasma environment.
- 30.1.6 Differential Charging. The charging of neighboring space vehicle surfaces to differing potentials by the combined effects of space plasma charging, photoemission, secondary emission, and backscatter.
- 30.1.7 Faraday Cage. An electromagnetically shielded enclosure. The term generally refers to a conductive metallic structure, package, or mesh which attenuates external electromagnetic energy to specified levels in the interior.
- 30.1.8 Flash-Over Discharge. A discharge characterized by a current path that travels along a surface of the material (and sometimes around an edge) to close the path between the electrodes.
- 30.1.9 Geomagnetic Substorm Activity. The conditions near geosynchronous altitude during the injection of substorm particles into the earth's magnetic field, including disturbances in the dipole field and increased plasma energies and current densities.
- 3.1.10 Magnetospheric Plasma. The space plasma environment constituent in the magnetosphere. This is an electrically neutral collection of electrons and positive ions (primarily protons) with densities near geosynchronous altitude on the order of one particle/cm<sup>3</sup>.
- 30.1.11 Metal-To-Metal Discharge. A discharge between two conducting electrodes.

- 30.1.12 Photoemission. An effect whereby radiation of sufficiently short wavelength impinging on substances causes electrons to be emitted with an energy that varies with the frequency of the radiation.
- 3.1.13 Punch-Through Discharge. A discharge through the bulk of a dielectric material coupled with a bulk breakdown of the insulating strength of the dielectric separating two electrodes. The current path is through the bulk of the material, with surfaces on opposite sides of the dielectric acting as electrodes. The punch-through discharge may occur in vacuum or in air.
- 3.1.14 Replacement Current. Current that flows to the electrodes in response to a discharge but not as part of the discharge.
- 3.1.15 Secondary Emission. An effect whereby low energy electrons or ions, called secondary electrons or ions, are emitted from a material as a result of the interaction of higher energy electrons or ions with the material. The ratio of secondary particles to primary particles can be greater than unity.
- 30.1.16 Spacecraft Charging (SCC). The phenomenon where space vehicle elements and surfaces can become differentially charged to a level sufficient to cause discharges and resulting EMI. The primary effects of SCC are electrical transients and upsets, material degradation, and enhanced contamination.

30.2 Acronyms Used in This Appendix.

CDI - Capacitive Direct Injection  
EMI - Electromagnetic Interference  
ESD - Electrostatic Discharge  
MLI-- Multi-Layer Insulation  
S/C - Spacecraft  
SCC - Spacecraft Charging

40. GENERAL STATEMENT OF REQUIREMENTS

- 40.1 Spacecraft Charging Protection Program. The contractor's spacecraft charging protection program shall include (a) the preparation and maintenance of an analytical plan and (b) the preparation and maintenance of a test plan. The intent of the program shall be to assure that the space vehicle is capable of operating in the specified space plasma charging environment (Section 40.1.1) without degradation of the specified space vehicle capability and reliability and without changes in operational modes, location, or orientation. This performance must be accomplished without the



benefit of external control such as commands from a ground station. The spacecraft charging protection program, the analytical plan, and the test plan shall be subject to approval by the procuring agency. (The requirements for plans will be transferred to the contractor SOW).

40.1.1 Specified Environment. The space plasma charging environment shall be that as specified in TBD (AFGL Final Environmental Atlas). Other AFGL documents useful to model the plasma environment include: AFGL-TR-77-0288, AFGL-TR-78-0304, and AFGL-TR-79-0015. A "worst case" engineering specification for that environment follows.

A "worst case" substorm is described as a plasma environment composed of electrons (e) and protons (p) with the following temperature and density for the given time intervals (see Figure 2).

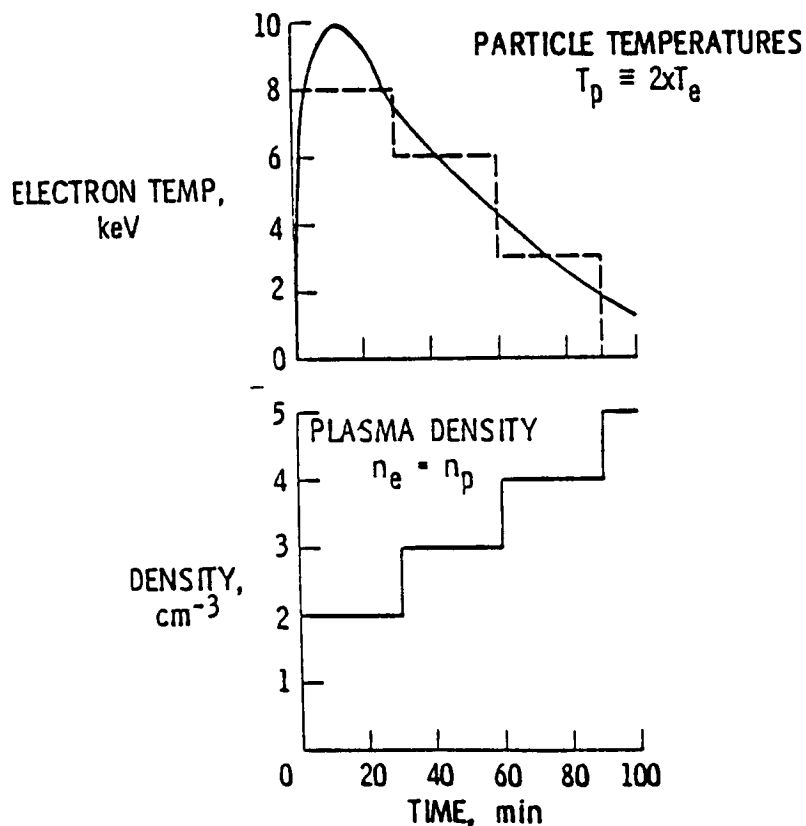


Figure 2. "Worst Case" Substorm Parameters

40.1.2 Performance. Analysis and test shall be used to assure that all space vehicle electrical systems perform to specified capabilities in the specified environment. Specified capabilities and levels of performance shall be established by the procuring agency. (The contractor SOW will call out this requirement).

40.1.3 Design. Protective design measures should be compatible with MIL-STD-1541 (USAF) and TBD (NASA Design Guidelines) to limit the susceptibility of electrical systems and spacecraft materials to the SCC hazard. Materials used in the space vehicle design shall perform to specified capabilities in the specified environment. The space vehicle design shall limit contamination enhanced by electrostatic effects induced by the specified environment to contamination levels that will not reduce the performance of space vehicle surfaces or systems below specified capabilities. Any protective features incorporated in the space vehicle design to reduce the SCC hazard must not reduce space vehicle performance below specified levels.

## 50. DETAILED STATEMENT OF REQUIREMENTS

### 50.1 Performance.

50.1.1 Electrical Subsystems and Systems. Space vehicle electrical subsystem and system outage shall be permissible during an arc discharge if operation and performance returns to specified levels within a telemetry main frame period after onset of the discharge or within some other period as defined by the procuring agency. A command to the space vehicle from an external source such as a ground station is not required to be completed if an arc discharge occurs during transmission of the command, provided that an unintended action does not result and that the space vehicle is capable of receiving and executing subsequent commands and meeting specified performance within a time period as defined by the procuring agency. Space plasma-induced electrical transients shall not affect on-board digital data beyond the specified design limits.

50.1.2 Materials. Thermal control materials and their surfaces, second surface mirrors, solar cells and coverslides, and other critical materials, structures, and components shall not degrade in thermal or optical properties or structural integrity in the specified space plasma environment below the level required to perform to specified capabilities.

50.2 Design. The following design requirements (50.2.1 through 50.2.5) shall be implemented for protection against the SCC hazard. Additionally, the design guidelines in TBD (NASA Design Guidelines Monograph) should be followed wherever reasonable and applicable. Where it is impractical or undesirable to implement the following design requirements, the contractor shall show by analysis or test

that non-concurrence with the requirement will not degrade space vehicle performance below specified capabilities.

50.2.1 Grounding of conducting elements. All space vehicle conducting elements shall be tied by an electrical grounding system so that the DC resistance between any two points is  $\leq 0.1$  ohm. The grounding shall be applicable to all conducting elements with external surfaces exposed directly to the specified plasma environment and for all elements with surface areas  $> 25 \text{ cm}^2$ . DC resistance levels of grounds shall be verified by standard ohm-meter measurements. The grounding does not apply directly to thin ( $< 10\mu$ ) conducting surfaces on dielectric materials. These are treated separately in Section 50.2.2.

50.2.2 Grounding of thin conducting surfaces. All thin ( $< 10\mu$ ) conducting surfaces on dielectric materials shall be electrically grounded to the common space vehicle structural ground so that the DC resistance between the surface and the structure is  $\leq 10$  ohms. DC resistance levels of ground and bonds shall be verified by standard ohm-meter and bond-meter measurements. Thicker surfaces shall be grounded as described in Section 50.2.1. Thin conducting surfaces shall be inclusive of, but not limited to, all metallized surfaces of multi-layer insulation (MLI) thermal blankets, metallized dielectric materials in form of sheets, strips, tapes, or tiles, conductive coatings, conductive paints, conductive adhesives, and metallic grids or meshes. The number of ground points on each conducting surface should follow the following prescription:

Surface Area	Number of Ground Points
$< 1.0 \text{ m}^2$	2 or more
1.0 to $4.0 \text{ m}^2$	3 or more
$> 4.0 \text{ m}^2$	1 per $\text{m}^2$

Additionally, any point on a conducting surface should be within 1 meter of a grounding point.

50.2.3 Shielding of EMI. All electronic cables, circuits, and components shall be provided with EMI shielding to attenuate radiated fields from discharges (100 kHz to 1 GHz) by at least 40 db. Attenuation levels of radiated fields shall be verified by standard measurement techniques or by analysis for representative locations internal to shielding enclosures. The method of verification shall be subject to approval by the procuring agency. The shielding may be provided by the basic space vehicle structure designed as a "Faraday cage" with a minimum of openings or penetrations, by enclosures of electronics boxes, by separate cable shielding, or by combinations of the preceding shields. Electronics units and cables external to the basic space vehicle structure shall have individual shields providing the 40 db attenuation of EMI.

50.2.4 Design against electrical discharges. The spacecraft shall be designed to perform to specified capabilities when subjected to discharges with the following characteristics:

TBD. The preliminary format for the characterization of typical "worst case" SCC associated discharges includes the following parameters:

1. Blow-off and arc current time history (probably monopolar, with rise time of 5 to 100 nanoseconds, dependent on sample linear dimensions; decay times to several  $\mu$ seconds, dependent on RC time constant of the sample; total charge in blow-off or integral of blow-off current is probably proportional to sample area; see Figure 3).
2. Electrical and magnetic fields  
(described as functions of distance and time; dependent on motion of blow-off charge; configuration dependent).
3. Total energy content  
(stored, radiated, and dissipated energies; probably in range of 1 mjoule to 1 joule).
4. Breakdown conditions (extrapolations of ground test data to space conditions)

Additionally, scaling relationships and functional dependencies for the above parameters will be included here or referenced in a supporting document. The discharge characterization is dependent on type of material, sample area, thickness, configuration, charging current density and energy distribution, and irradiation history. Discharges will be described for materials which are commonly used on spacecraft and known to exhibit charging/ discharging effects. Parameters listed above and in the following figure will be quantified as information becomes available.

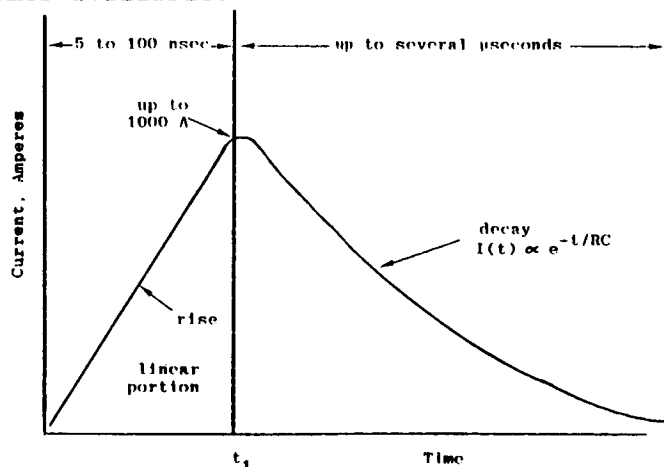


Figure 3. Discharge Current Pulse Shape

50.2.5 Materials selection. Materials used in the space vehicle design shall be selected to minimize differential charging (see Section 50.2.5.1) and discharging (see Section 50.2.4) effects from the specified environment while maintaining specified performance capabilities. All materials used on exposed surfaces should be tested or analyzed to determine their charging and discharging characteristics in the specified environment. The method of test or analysis is subject to the approval of the procuring agency. Surfaces located internal to the outer space vehicle structure should be shielded from the space plasma environment by eliminating openings in the structure. Material selection should additionally be based on minimizing outgassing and other sources of contamination. Exposed surfaces which are susceptible to effects of enhanced contamination due to SCC should be identified and protected where necessary to assure performance to specified capabilities. References useful to spacecraft material selection include AFML reports: AFML-TR-76-233, AFML-TR-77-174, AFML-TR-77-105, and AFML-TR-78-15.

50.2.5.1 SCC associated differential potentials.

TBD. Tables of "worst case" magnitudes of differential potentials and potential gradients expected for selected S/C materials and material configurations on generic S/C designs will be provided. Potentials will be those derived from analysis using the "worst case" substorm environment (Figure 2) and compared to P78-2 data.

To date, representative extreme levels as measured on the P78-2 SC1-3 (shadowed samples) SSPM include:

<u>SAMPLE</u>	<u>POTENTIAL (with respect to S/C ground)</u>
Aluminized Kapton	- 2.0 kV
Silvered Teflon	- 4.0 kV
Astroquartz	- 3.7 kV

50.3 Analysis. As part of the SCC protection program, an analytical plan for SCC shall be prepared and maintained. The SCC analytical plan shall be a detailed plan specifying the SCC analysis program that will be used to achieve conformance with the requirements in this appendix. The plan shall be subject to approval by the procuring agency. The plan shall be implemented to analyze the space vehicle design for susceptibility to SCC. The analysis plan should complement the test plan (see Section 50.4) and the analysis should generate data useful to identify susceptible design areas and locations for testing and to quantify representative test levels. (The requirement for an Analytical Plan will be transferred to the contractor SOW).

50.3.1 Analysis approach. The analysis should be inclusive of a modeling of the charging of the space vehicle by the specified environment

as well as the competing effects of photoemission, backscatter, and secondary emission. Extremes in differential charging levels of the space vehicle and susceptible locations for discharges should be identified. Estimates of discharge characteristics (see Section 50.2.4) should be made for the specific space vehicle design of interest, including the actual materials and mounting configuration used in the design. A coupling analysis should be performed relating the EMI and structural replacement currents resulting from the discharges to electrical transients in internal space vehicle cables. In all cases, estimates should be made of the extremes ("worst case") magnitudes of charging levels, discharges, and electrical transients characteristics for the space vehicle design of interest. The analytical program should be made to complement the test program (see Section 50.4) for SCC effects on the space vehicle. In this manner, test levels and test locations should be an accurate representation of SCC effects on the actual space vehicle design.

50.3.2 Analysis procedure. The following procedure should be followed in analyzing the space vehicle for effects from electrical transients induced by SCC. Any analytical tools or computer codes used shall be described in the analytical plan and subject to approval by the procuring agency.

50.3.2.1 Charging analysis. The specified environment shall be used with space vehicle design features as primary inputs into analytical calculations of the extremes of differential charging for the spacecraft of interest. As a minimum, the analysis should determine:

1. the frequency of occurrence and duration of periods of high charging levels TBD (> 1000 volts)
2. the maximum differential potentials and potential gradients expected
3. the locations of large differential potentials and potential gradients on the space vehicle (candidate spacecraft locations for ESD tests)

(The NASCAP computer code, when validated, will be useful to this analysis).

50.3.2.2 Discharge characterization analysis. The characteristics of discharges caused by SCC are provided in Section 50.2.4 for selected material samples and configurations. These shall be used along with associated analysis of the specific space vehicle design of interest and with the charging analysis (Section 50.3.2.1) to estimate extremes of discharge characteristics expected. As a minimum, the analysis should determine:

1. discharge parameters (amplitudes, pulse shape, frequency content)
2. radiated electric and magnetic fields
3. energy content of discharge pulse
4. potential discharge site locations  
(candidate spacecraft locations for ESD tests)

50.3.2.3 Coupling analysis. The results of the discharge characterization analysis should be used as source terms in an electromagnetic coupling analysis specific to the space vehicle design of interest. Estimates should be made of extremes in magnitude of radiated EMI and structural replacement currents resulting from the expected or specified discharges. The coupling analysis should then determine as a minimum:

1. electromagnetic fields generated interior to the space vehicle due to ESD
2. induced transient pulse characteristics (amplitude, pulse shape, frequency content) for wiring harnesses and sensitive circuits and electronic components
3. identification of susceptible elements in electronic subsystems

Note: The entire section on analysis requirements, approach, and procedures may be compressed and called out in the contractor SOW.

50.4 Testing. As part of the SCC protection program, a test plan for SCC shall be prepared and maintained. The SCC test plan shall be a detailed plan specifying the SCC test program that will be used to achieve conformance with the requirements in this appendix. The plan shall be subject to approval by the procuring agency. The plan shall address the test requirements and test methods for subsystems and systems as presented in the following sections. The test plan should be complementary to the SCC analysis plan (see Section 50.3). The plan shall be implemented to test the space vehicle susceptibility to the effects of SCC. Test procedures as presented in the NASA document, TBD (Design Guidelines Monograph), should be followed where applicable. With the approval of the procuring agency, specific test requirements may be modified to be consistent with the contractor's space vehicle design. Supportive analysis is required to justify the reduction of any test levels below those specified in this appendix. (The requirement for a test plan will be called out in the contractor SOW).

- 50.4.1 Test Requirements. The following SCC test requirements are applicable to prototype and flight model space vehicle subsystems and systems.
- 50.4.1.1 Subsystem Test Requirements. All spacecraft subsystems, components, and their interconnecting cabling shall be subject to the following test requirements.
- 50.4.1.1.1 Direct Injection. All space vehicle subsystems shall be tested for SCC susceptibility by the direct injection of electrical pulses. The test level shall be TBD (amplitude level) or a level 6 dB greater than the threat level as determined by analysis. The test level shall be subject to approval by the procuring agency. Pulse rise times and pulse widths are TBD (10 nsec rise, 2  $\mu$ sec width), and the number of test pulses shall be TBD (30 pulses) at a rate of TBD (one per second) or may be established by analysis and subject to approval by the procuring agency.
- 50.4.1.1.2 Critical Test Points. Injection points may be selected from subsystem box input cables or specific pin locations. The test must drive all subsystem electronic components. Injection test locations shall be subject to approval by the procuring agency.
- 50.4.1.2 System Test Requirements. The space vehicle system shall be subject to the following test requirements.
- 50.4.1.2.1 Capacitive Direct Injection (CDI). The space vehicle system shall be subject to the CDI of electrical pulses to the space vehicle structure. The test level shall be TBD (amplitude level) or a level 6 dB greater than the threat level for a blow-off discharge as determined by analysis and consistent with the specified discharge characterization (Section 50.2.4). The test level shall be subject to approval by the procuring agency. Pulse rise times and pulse widths are TBD (10 nsec rise, 2  $\mu$ sec width) and the number of test pulses shall be TBD (30 pulses) at a rate of TBD (one per second) or may be established by analysis and subject to approval by the procuring agency.
- 50.4.1.2.2 Arc Injection. The space vehicle system shall additionally be subject to the arc injection of electrical pulses to the space vehicle structure. The test level shall be TBD (up to 200 amperes) or a level 6 dB greater than the threat level for a flashover discharge as determined by analysis and consistent with the specified discharge characterization (50.2.4). The test level shall be subject to approval by the procuring agency. Pulse rise times and pulse widths are TBD (10 nsec rise, 200 nsec width), and the number of test pulses shall be TBD (30 pulses) at a rate of TBD (one per second) or may be established by analysis and subject to approval by the procuring agency.



- 50.4.1.2.3 Critical Test Points. CDI test locations and arc injection points shall be selected based on an analysis of the space vehicle design for locations considered the most likely sites for SCC associated discharges. The CDI test must include at least one pulse injection to the S/C common ground structure, and the arc injection must include at least one pulse injection at the solar arrays (if applicable). All test locations must be approved by the procuring agency.
- 50.4.2 Test Methods. The following SCC test methods are applicable to prototype and flight model space vehicle subsystems and systems.
- 50.4.2.1 Subsystem Test Methods. All spacecraft subsystems, components, and their interconnecting cabling shall be tested using the following methods.
- 50.4.2.1.1 Test Setup. Direct injection tests on subsystems shall be accomplished in a bench test. The contractor shall assemble all units and interconnecting cabling of a subsystem as closely as possible to a flight configuration. Each subsystem shall be tested independently..
- 50.4.2.1.2 Test Conditions. Ambient environment testing is adequate. The subsystem should be powered by batteries and operated in representative modes subject to approval by the procuring agency.
- 50.4.2.1.3 Test Equipment. A pulse generator capable of delivering the specified test levels and pulse shape (Section 50.4.1.1.1) shall be utilized for the direct injection tests. The pulse generator shall be approved by the procuring agency. Tests may take the form of single injection or common mode pin tests, or direct drive of box input cables. All subsystem response and circuit monitoring instrumentation and other test equipment shall be subject to approval by the procuring agency.
- 50.4.2.1.4 Test Parameters and Susceptibility Analysis. Crucial subsystem test parameters shall be identified by the contractor as measures of subsystem performance and as measures of susceptibility to the direct injection test. The subsystem shall perform to specified capabilities during and after the test. Test parameters and measures of subsystem performance and measure of susceptibility shall be subject to the approval of the procuring agency.
- 50.4.2.2 System Test Methods. The space vehicle system shall be tested using the following methods.
- 50.4.2.2.1 Test Setup. CDI and arc injection tests on the space vehicle system shall be performed with the system dielectrically isolated from the ground and removed TBD (several) spacecraft diameters from any metallic walls or large metallic structures. Space vehicle telemetry monitoring instrumentation and other test monitoring equipment should be located in an electromagnetic shielded

enclosure. The space vehicle shall be fully assembled and set up as closely as possible to its flight configuration.

50.4.2.2.2 Test Conditions. Ambient environment testing is adequate. The space vehicle system should be powered by batteries and operated in representative modes subject to approval by the procuring agency.

50.4.2.2.3 Test Equipment. Pulse generators capable of delivering the specified test levels and pulse shape (Section 50.4.1.2.1 and 50.4.1.2.2) shall be utilized for the CDI and arc injection tests. The pulse generators shall be subject to approval by the procuring agency. (Figures 4 and 5 represent preliminary schematics for performing the tests.) Test equipment shall be inclusive of system response monitoring instrumentation (all subsystem response monitored via spacecraft telemetry) as well as pulse injection instrumentation. All test equipment shall be subject to approval by the procuring agency.

50.4.2.2.4 Test Parameters and Susceptibility Analysis. Crucial system test parameters shall be identified by the contractor as measures of system performance and as measures of susceptibility to the CDI and arc injection tests. The system shall perform to specified capabilities during and after the test. Test parameters and measures of system performance and susceptibility shall be subject to the approval of the procuring agency.

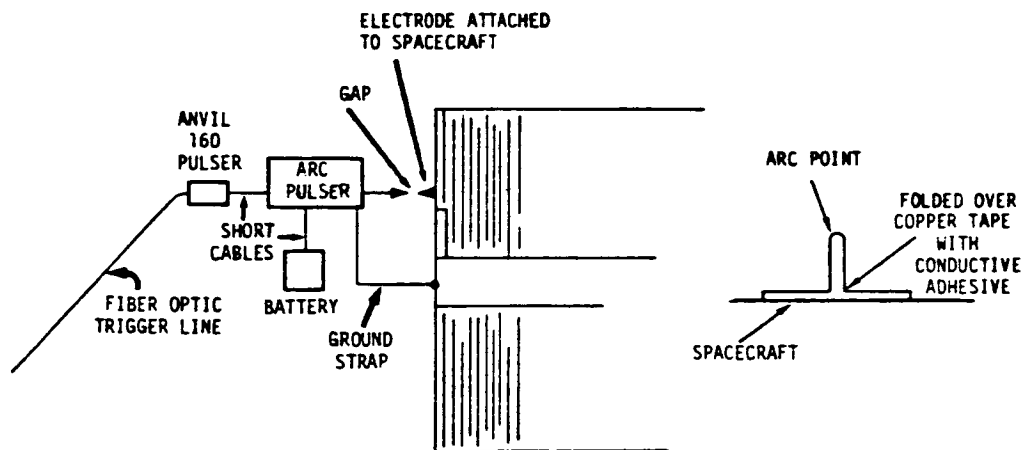


Figure 4. Arc Injection Schematic

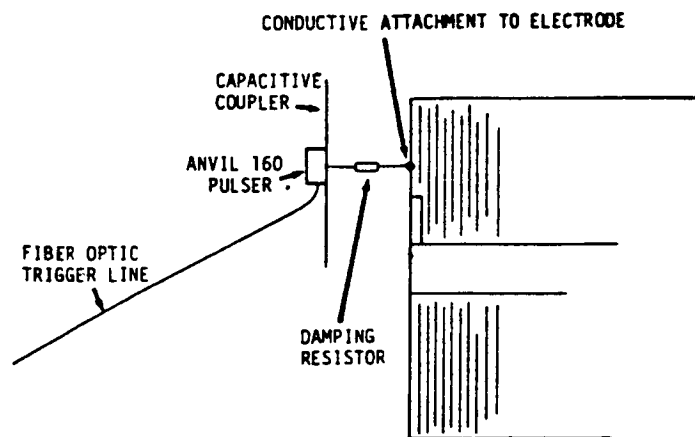


Figure 5. CDI Schematic

# **USE OF CHARGING CONTROL GUIDELINES FOR GEOSYNCHRONOUS SATELLITE DESIGN STUDIES**

**N. John Stevens  
NASA Lewis Research Center**

## **SUMMARY**

The Spacecraft Charging Design Guidelines Handbook has been prepared as a tool to be used in the design of geosynchronous satellites. This handbook compiles the results of prior flight experience with ground technology studies into a series of guidelines that will minimize detrimental effects of interactions with geomagnetic substorm environments. The handbook is organized into two main parts: guidelines to assess charging interactions, and guidelines to minimize charging effects. In this paper several of the principal guidelines are presented with illustrative examples. Although the paper does not cover all guidelines, it does indicate why they should be used and what the designer should be looking for. The handbook does not treat discharge criteria and SCATHA data. Both of these areas are in rapid transition and not ready for inclusion at this time. The handbook will be revised to include these data.

## **INTRODUCTION**

The output of the U.S. Air Force - NASA spacecraft charging technology investigation is to be summarized in three documents (ref. 1): an environmental atlas, a military standard, and a design guidelines handbook. The atlas is to summarize the geomagnetic substorm environments based on Applications Technology Satellites 5/6 (ATS-5/6) and P78-2, SCATHA (Spacecraft Charging at High Altitudes) data (refs. 2 to 4). The military standard is to have the stature of specifications to be imposed on satellite hardware (refs. 5 and 6). The Design Guidelines Handbook is to provide criteria to be used in the design of geosynchronous satellites to minimize spacecraft charging effects (ref. 1). Although all three documents are interrelated, it is the handbook that will compile the available ground technology and flight data into a form usable by designers.

The handbook was first formulated 2 years ago on the basis of reviews with spacecraft contractors and from available data (ref. 7). The handbook was circulated for a limited review and is currently being revised to incorporate the pertinent comments from the review and to update the information prior to a general release.

In its present form the handbook is divided into two main parts: guidelines to assess charging interactions, and guidelines to minimize charging effects. The guidelines to assess charging are based on the use of analytical modeling techniques with a recommended environmental specification. The principal deficiency of the present handbook is the lack of a clear breakdown criterion - a guideline to tell designers when to expect problems. This is caused by the discrepancy between ground test data on

differential voltage thresholds for breakdown and the modeling of predicted differentials (refs. 8 and 9). The document will be updated and reissued when this criterion has been established. Since there is a serious question about breakdown criteria, the section on component susceptibility is equally vague.

The second part of the handbook is subdivided into two additional parts: guidelines for the overall spacecraft, and subsystem guidelines. The spacecraft guidelines refer to such topics as filtering, shielding, materials selection, and incorporation of charge control devices and monitors. The subsystem guidelines are a series of detailed do's and don't's for each of the major spacecraft subsystems.

In this paper several guidelines have been chosen for discussion. These guidelines illustrate how the handbook is to be used. They point out to the designer what to look for and why the guidelines are important to spacecraft system operations in geomagnetic substorm environments. Each of the design guidelines to be discussed herein is given as the title of a major section of this paper. The first two guidelines refer to the assessment of charging interactions; the last three deal with minimization of charging effects. It should be stressed that this paper considers only five of the many guidelines in the handbook.

GUIDELINE - THE GEOMAGNETIC SUBSTORM SPECIFICATION GIVEN HERE  
SHOULD BE USED TO QUALIFY SATELLITE DESIGNS

To assess spacecraft charging interactions, it is necessary to have a specification for the geomagnetic substorm environment in terms that are compatible with available analytical tools. Previous attempts to provide this specification either provided overwhelming data or were based on small data samplings (ref. 10). For this handbook a specification based on an ATS-5/6 statistical summary has been jointly worked out. This specification has been derived to produce the maximum stress within dielectrics specifically for use in design evaluation. It probably does not have the characteristics of a real substorm.

This specification is derived from the previously published 100 days of data on geomagnetic substorm characteristics from ATS-5/6 Auroral Particles Experiments (refs. 11 and 12). When these data were plotted as energy flux against number flux, all the data fell within an envelope (fig. 1(a)). Furthermore it was found that the electron data could be treated by an adiabatic compression relation:

$$kT = A(ND)^{\gamma-1}$$

where

k Boltzmann constant

T temperature

A constant parameter

ND    number density

$\gamma$     ratio of heat capacities (assumed constant)

With  $\gamma = 3$  and  $A$  arbitrarily chosen to be  $10^4$  for severe substorms and 500 for moderate substorms, straight lines could be generated that would fall within the substorm data envelope. Those portions of the envelope associated with the lower number fluxes (i.e., about  $10^7$  eV cm<sup>-2</sup> sec<sup>-1</sup> sr<sup>-1</sup>) represent the quiescent environmental measurements, which do not produce surface charging. From these straight-line relations it is possible to compute electron temperatures and densities. Similar data are available for computing ion temperatures and densities.

Once the temperatures and densities have been obtained, it is necessary to determine how often in a year a satellite could encounter a given intensity substorm. This can be obtained from a probability of occurrence curve (fig. 1(b)). In this curve the percentage of time an energy flux is above a specific value is plotted as a function of that value. The ATS-5 data form the basis for the minimum geomagnetic activity curve, and the ATS-6 data are used for the maximum. The curves are averaged for use in the specification. Hence, there now is a means of computing temperatures and densities as a function of time in orbit (based on 8760 hr/yr).

The resulting specification for satellite time in geomagnetic substorm environments is shown in figure 2. The specification is given in terms of a single Maxwellian temperature for severe and moderate substorms. This temperature description was chosen because previous analysis of satellite surface charging showed that single Maxwellian environments, although not as realistic as the double Maxwellian description, produced more severe charging. The time curve runs out to only 4000 hours since beyond that time particle temperatures drop below levels that produce charging. The ion temperature relations found can be adequately expressed as 10 times the electron density. To account for the ion composition of the substorm environment, which indicates a substantial oxygen ion population in addition to hydrogen ions (ref. 13), the ion density is set to be one-third of the electron density.

From this specification an environment for evaluating satellite designs can be obtained. The recommended environment for this purpose is shown in figure 3 and is based on specification curves for the first 300 hours. Both sunlit and eclipse conditions are considered so that transient conditions are evaluated. It is recommended that sunlight be at some angle of incidence to produce maximum differential charging. This environment starts with a 8-keV, 2.1-electron/cm<sup>3</sup> substorm in sunlight for 15 minutes. Then a simultaneous change to an 11-keV, 1.1-electron/cm<sup>3</sup> substorm in eclipse for 20 minutes is followed by 15 minutes in sunlight at the same intensity. The substorm intensity is reduced to 5 keV, 3.2 electrons/cm<sup>3</sup> for 15 minutes to complete the design environment. The ion parameters are related to the electron as previously described.

GUIDELINE - ALL SATELLITE DESIGNS SHOULD BE EVALUATED BY  
USING ANALYTICAL MODELING TECHNIQUES

The NASA Charging Analyzer Program (NASCAP) computer code is recommended for use in analyzing satellite designs. It has the capability of treating both three-dimensional effects, which are important in accurately predicting surface voltages (ref. 14), and the transient effects required by the design evaluation environment given previously. The code has been adequately described in the literature and is not repeated here (refs. 15 to 17).

As an example, the effect of satellite configuration on surface charging is evaluated by subjecting both a three-axis-stabilized satellite and a spinning satellite to the design environment. A more detailed evaluation of configuration effects is given in reference 18. The NASCAP models of the two configurations are shown in figure 4. The three-axis-stabilized satellite chosen is the NASA Tracking and Data Relay Satellite System (TDRSS) that will replace ground stations. It is a large satellite, 18.9 by 11.7 meters in overall dimensions. It consists principally of two large solar arrays, two main antennas, two smaller antennas, and the spacecraft body. The materials chosen simulate the actual coatings. The two main antennas were modeled as an octagonal rim with a center rectangular feed in order to evaluate the charging of the optical solar reflectors (OSR's) covering the electronic enclosure behind the antenna feed. Since the antenna mesh was transparent, there was the possibility of part being sunlit while the rest was shaded. The backing of the solar arrays was assumed to be plain Kapton. The exposed metal areas were given secondary electron yields of less than 1. The spinning satellite used here is the P78-2 (SCATHA) model similar to the one used in reference 19. It has cylindrical sides covered primarily with solar arrays and uses appropriate dielectrics on the "bellyband" and the top and bottom surfaces.

The design evaluation environment (fig. 3) was used in this study. The Sun incidence for the TDRSS evaluation was offset such that the viewer would be looking at the model from the Sun. For the SCATHA evaluation the Sun was assumed to be normal to the solar array and the satellite to be spinning at 1 rpm.

The results predicted for satellite grounds and shaded Kapton insulation cells are shown in figure 5. In conducting the analysis the voltages for all cells are computed, but for this paper the results presented illustrate the desired effects.

The three-axis-stabilized spacecraft ground is charged more negatively both in sunlight and eclipse than the spinning satellite ground. This is due to the large areas of shaded insulation behind the solar arrays, which charge to high negative values and thus create fields surrounding the satellite and reducing photoemission. The spinning satellite tends to average this shading effect and thus maintain a lower ground potential.

The differential voltage of the shaded Kapton insulation is between 1.5 and 3.0 kilovolts in both cases. These values are too low to produce the

laboratory type of discharge observed (ref. 20). This complicates the problem of telling designers what to look for in evaluating the design. At this point the designer has to watch out for details in construction, for gradients in solar arrays, and for areas decoupled from the structure. An example of such attention to detail is the treatment of the TDRSS antenna to check on the sunlit and shaded OSR's. This was identified as an area of concern, the model was set up to evaluate it, and the results indicated only a small difference in surface voltages. This result was not known beforehand and had to be verified.

It is interesting to compare these results with the actual behavior of the ATS-5 (spinning) and ATS-6 (three-axis stabilized) ground potentials obtained from flight data. The ATS-6 has been charged to a maximum negative ground voltage of -2.2 kilovolts in sunlight (ref. 21) and to -19 kilovolts in eclipse (ref. 22). The model predicts about -3 kilovolts in sunlight and -16 kilovolts in eclipse. The ATS-5 flight data indicate that the maximum potential is about -300 volts in sunlight and about -10 kilovolts in eclipse (ref. 23). The spinning model predicts about -200 volts in sunlight and about -12 kilovolts in eclipse. Therefore the code predicts reasonable trends, and the design environment can be used to evaluate maximum stress.

#### GUIDELINE - SELECTED MATERIALS AND COATINGS SHOULD BE USED TO MINIMIZE CHARGING

It is by the proper choice of available materials that both the absolute and differential charging of satellites can be minimized. At present the only way that satellite potential variations can be eliminated is by making all surfaces conductive and tying them to a common ground. Transparent conductive coatings of indium oxide have been developed for insulators (ref. 24). This technique is expensive and is used only when this uniformity is mandatory for a successful mission (ref. 25).

There are other possible means of reducing surface charging on satellites. Figure 6 shows the effect of using a metal surface that has a high secondary yield on the TDRSS model. Figure 6(a) is the predicted response of the satellite in the design substorm when standard materials are used. Figure 6(b) is the predicted response when the exposed metallic surfaces have been assumed to be coated with an oxide that raises the secondary-electron yield to 2.6. The absolute charging level has been reduced dramatically, and the differential charging of the shaded Kapton has been reduced slightly.

If there is a possibility of using materials with high secondary-electron emission, they should be used. However, changes to specific materials should not be made indiscriminately. Designs with material changes in specified areas should be checked analytically to verify that the change did not introduce problems in other areas of the satellite.



GUIDELINE - ALL CONDUCTING ELEMENTS SHOULD BE  
TIED TO A COMMON ELECTRICAL GROUND

This guideline is one of the earliest ones developed as a means of controlling charging effects (ref. 26). It is still a good guideline. In principle it says that areas on the satellite should not be allowed to float electrically; that is, interstructural capacitances should be controlled. It is believed that lack of control of interstructural capacitance contributed to the power system failure on Defense Satellite Communications System (DSCS II) (ref. 27). The effects of not following this guideline are illustrated by comparing the charging of an ungrounded area (very small capacitance) with the charging of dielectric booms (large capacitance).

The effect of ungrounded or floating areas is shown in figure 7. In figure 7(a) a shaded region of a three-axis-stabilized satellite is considered to be well coupled to the structure. Here the differential charging of the Kapton and OSR's builds up slowly, following the charging curve of the structure. However, if these same materials were allowed to become ungrounded and only weakly coupled to the structure, these insulators would respond very rapidly to the environment, as shown in figure 7(b). The structure charges at essentially the same rate, and this produces a larger differential voltage, which may trigger discharges. Hence, this condition should be eliminated by grounding.

The question of the use of dielectric booms can be evaluated by looking at the boom charging of the spinning satellite (i.e., SCATHA model). The differential charging of one of the boom cells of this model is shown in figure 8. In the first phase of the design substorm environment, the charging is not severe. However, in eclipse the booms charge to large positive surface voltages relative to the satellite. A gap or crack that exposes a metallic surface at structure potential could then act as an electron emitter and trigger discharges. In figure 8 the oscillations of the boom voltage in eclipse are probably a computational artifact and not real. However, the voltage in eclipse is of the order of 1.4 kilovolts positive with respect to the structure. This is sufficient to cause problems. On exit from eclipse the cell potential tends to lag the change in structure potentials rather than follow the structure. Hence one could expect problems entering eclipse in severe substorms and possibly on exit. The SCATHA flight data did indicate discharges during charging in an eclipse in a brief severe substorm surge and also on entering sunlight when still experiencing substorms (ref. 28). Therefore it is probably a good rule not to use dielectric booms on shaded areas of satellites.

GUIDELINE - ELECTRICAL FILTERING SHOULD BE USED TO PROTECT  
CIRCUITS FROM DISCHARGE-INDUCED UPSETS

Satellite surfaces are charged by geomagnetic substorm environments. If these surfaces are charged, there is a finite probability that there will be discharges. In many cases there is no way to prevent them. In figure 9(a) data from sensor monitoring discharges in an OSR array are shown (ref. 29). Even in a quiet time pulses were counted. In figure 9(b) the harness noise count on the Communications Technology Satellite (CTS) for an

active day is shown (ref. 30). As can be seen from these figures, a large number of discharges can occur. Only a relatively small number couple into the harness and probably a smaller number can cause upset. Yet in long missions the probability does exist that upsets can happen. Although it can be argued that the data presented are from two different satellites at different times, it is not logical to assume that this negates the argument. There will be disruptive discharges unless the entire surface is at an absolutely uniform potential.

The usual criterion suggested for filtering is to eliminate noise with less than a specific duration. On CTS, inline transmitters and receivers were used that effectively eliminated noise pulses of less than 5 microseconds (ref. 31). Similar filtering concepts have been proposed for circuits that required protection (ref. 32). Hence filtering is believed to be an effective means of preventing circuit disruption and should be included in system designs.

#### CONCLUDING REMARKS

A design guidelines handbook to provide criteria for minimizing spacecraft charging effects in geosynchronous satellites has been formulated and will be distributed as a design tool. Data used in this handbook have been assembled from interviews with spacecraft manufacturers, from results of ground technology programs, and from available flight results. Since the technology investigation is not complete at this time, the handbook will be revised periodically to incorporate the latest results.

In the present version of the handbook a geomagnetic substorm environment specification for design evaluation is given. This specification is based on available ATS-5/6 data and, when used with the recommended NASA Charging Analyzer Program (NASCAP) computer code, it results in voltage predictions consistent with trends observed on both ATS-5 and ATS-6.

Each satellite design must be analyzed to determine the spacecraft surface voltage profiles. Both absolute and differential voltages are influenced by the satellite configuration and by the choice of spacecraft materials. It has been found that metallic surfaces should be grounded and that dielectric booms should be avoided. Since it is impossible to guarantee absolutely that there will be no discharges, filtering should be incorporated on those circuits where anomalous behavior must be avoided. Testing in accordance with the military standard also must be accomplished to verify that the satellite will be immune from environmental effects.

Though all this sounds like a serious imposition on spacecraft projects, it must be recognized that similar procedures are routinely followed in preparing spacecraft thermal control designs. The handbook procedures are simply to be used in preparing spacecraft electrostatic control designs.

It is recognized that there is a serious deficiency in this handbook: the lack of a criterion for predicting when disruptive discharges can

occur. While several interesting possibilities for establishing this criterion do exist, there is nothing that can now be stated. Therefore the designer is faced with the need of minimizing differential voltages, eliminating edge effects (as much as possible), minimizing positive voltage gradients (structure potential more negative than dielectrics), eliminating capacitive decoupling from the structure, and employing grounding and filtering techniques. When a discharge criterion is established, it will be included in the handbook.

#### REFERENCES

1. Lovell, R. R.; et al.: Spacecraft Charging Investigation: A Joint Research and Technology Program. Spacecraft Charging by Magnetospheric Plasmas, A. Rosen, ed., Progress in Astronautics and Aeronautics, Vol. 47, American Institute of Aeronautics and Astronautics, Inc., 1976, pp. 3-14.
2. Garrett, H. B.; et al.: Modeling of the Geosynchronous Orbit Plasma Environment - Part 2: ATS-5 and ATS-6 Statistical Atlas. AFGL TR-78-0304-Pt-2, 1978. (AD-A067018.)
3. Mullin, E. G.; et al.: P78-2 SCATHA Preliminary Data Atlas. AFGL TR-80-0241, 1980.
4. Mullen, E. G.; et al.: P78-2 SCATHA Environmental Data Atlas. Spacecraft Charging Technology - 1980. NASA CP-2182, 1981.
5. Frankos, D. T.: Updating MIL-STD-1541 in Light of SCATHA Program Revelations. Spacecraft Charging Technology - 1980. NASA CP-2182, 1981.
6. Holman, A. B.: Military Standard for Spacecraft Charging Status Report. Spacecraft Charging Technology - 1980. NASA CP-2182, 1981.
7. Kamen, R. E.; et al.: Design Guidelines for the Control of Spacecraft Charging. Spacecraft Charging Technology - 1978, NASA CP-2071, AFGL TR-79-0082, 1979, pp. 817-818.
8. Sanders, N. L. and Inouye, G. T.: NASCAP Charging Calculations for a Synchronous Orbit Satellite. Spacecraft Charging Technology - 1980. NASA CP-2182, 1981.
9. Stevens, N. J.: Analytical Modeling of Satellites in Geosynchronous Environments. Spacecraft Charging Technology - 1980. NASA CP-2182, 1981.
10. Stevens, N. J.; Lovell, R. R.; and Purvis, C. K.: Provisional Specification for Satellite Time in a Geomagnetic Substorm Environment. Proceedings of the Spacecraft Charging Technology Conference, C. P. Pike and R. R. Lovell, eds., AFGL TR-77-0051, NASA TM X-73537, 1977, pp. 735-744.
11. Garrett, H. B.: Modelling of the Geosynchronous Plasma Environment. Spacecraft Charging Technology - 1978, NASA CP-2071, AFGL TR-79-0082, 1979, pp. 11-22.
12. Garrett, H. B.; Schwank, D. C.; and DeForest, S. E.: A Statistical Analysis of the Low Energy Geosynchronous Plasma Environment. Part I - Electrons; and Part II - Ions. Planet. Space Sci., 1981. To be published.
13. Johnson, R. G.: A Review of the Hot Plasma Composition near Geosynchronous Altitude. Spacecraft Charging Technology - 1980. NASA CP-2182, 1981.

14. Mandell, M. J.; et al.: The Decrease in Effective Photocurrents Due to Saddle Points in Electrostatic Potentials near Differentially Charged Satellites. IEEE Trans. Nucl. Sci., vol. NS-25, no. 6, Dec. 1978, pp. 1313-1317.
15. Katz, I.; et al.: A Three-Dimensional Dynamic Study of Electrostatic Charging in Materials. (SSS-R-77-3367, Systems, Science and Software; NASA Contract NAS3-20119.) NASA CR-135256, 1977.
16. Katz, I.; et al.: Extension, Validation and Application of the NASCAP Code. (SSS-R-79-3904, Systems, Science and Software; NASA Contract NAS3-21050.) NASA Cr-159595, 1979.
17. Katz, I.; et al.: Capabilities of the NASA Charging Analyzer Program. Spacecraft Charging Technology - 1978, NASA CP-2071, AFGL TR-79-0082, 1979, pp. 101-122.
18. Purvis, C. K.: Configuration Effects on Satellite Charging Response. AIAA Paper 80-0040, Jan. 1980.
19. Schneulle, G. W.; et al.: Simulation of the Charging Response of the SCATHA (P78-2) Satellite. Spacecraft Charging Technology - 1980. NASA CP-2182, 1981.
20. Stevens, N. J.; et al.: Testing of Typical Spacecraft Materials in a Simulated Substorm Environment. Proceedings of the Spacecraft Charging Technology Conference, C. P. Pike and R. R. Lovell, eds., AFGL TR-77-0051, NASA TM X-73537, 1977, pp. 431-457.
21. Reasoner, D. L.; Lennartsson, W.; and Chappel, C. R.: Relationship Between ATS-6 Spacecraft Charging Occurrences and Warm Plasma Encounters. Spacecraft Charging by Magnetospheric Plasmas, A. Rosen, ed., Progress in Astronautics and Aeronautics, vol. 47, American Institute of Aeronautics and Astronautics, Inc., 1976, pp. 89-101.
22. Olsen, R. C.; Whipple, E. C.; and Purvis, C. K.: Active Modification of the ATS-5 and ATS-6 Spacecraft Potentials. Effect of the Ionosphere on Space and Terrestrial Systems, J. M. Goodman, ed., Naval Research Lab., Washington, D.C., 1978, pp. 328-336.
23. Purvis, C. K.; and Bartlett, R. O.: Active Control of Spacecraft Charging. Space Systems and Their Interactions with Earth's Space Environment, H. B. Garrett and C. P. Pike, eds., Progress in Astronautics and Aeronautics, vol. 71, American Institute of Aeronautics and Astronautics, Inc., 1980, pp. 299-317.
24. Schmidt, R. E.; and Eagles, A. E.: Materials and Techniques for Spacecraft Static Charge Control II: Spacecraft Charging Technology - 1978, NASA CP-2071, AFGL TR-79-0082, 1979, pp. 524-553.
25. Winkler, W.: Helios Surface Materials, Test-Predictions and Test-Results of Orbit Conditions Compared with Mission Results. Eighth Conference on Space Simulation, NASA SP-379, 1975, pp. 51-62.
26. Keiser, B. E.: ATS-6 Spacecraft Surface Treatment for the Control of Electrical Discharges. IEEE Trans. Electromagn. Compat., vol. EMC-17, Nov. 1975, pp. 226-233.
27. McPherson, D. A.; Cauffman, D. P.; and Schober, W.: Spacecraft Charging at the High Altitudes - The SCATHA Satellite Program. AIAA Paper 75-92, Jan. 1975.
28. Koons, H. C.: Aspect Dependence and Frequency Spectrum of Electrical Discharges on the P78-2 (SCATHA) Satellite. Spacecraft Charging Technology Conference - 1980, NASA CP-2182, 1981.

29. Nanevycz, J. E.; and Adamo, R. C.: Transient Response Measurements on a Satellite System. Proceedings of Spacecraft Charging Technology Conference, C. P. Pike and R. R. Lovell, eds., AFGL TR-77-0051, NASA TM X-73537, 1977, pp. 723-734.
30. Stevens, N. J.; Kline, V. W.; and Gore, J. V.: Summary of CTS Transient Event Counter Data After One Year of Operation. IEEE Trans. Nucl. Sci., vol. NS-24, no. 6, Dec. 1977, pp. 2270-2275.
31. Gore, J. V.: Design, Construction and Testing of the Communications Technology Satellite - Protection Against Spacecraft Charging. Proceedings of Spacecraft Charging Technology Conference, C. P. Pike and R. R. Lovell, eds., AFGL TR-77-0051, NASA TM X-73537, 1977, pp. 773-788.
32. Bower, S. P.: Systems Aspects of Spacecraft Charging. Proceedings of Spacecraft Charging Technology Conference, C. P. Pike and R. R. Lovell, eds., AFGL TR-77-0051, NASA TM X-73537, 1977, pp. 719-721.

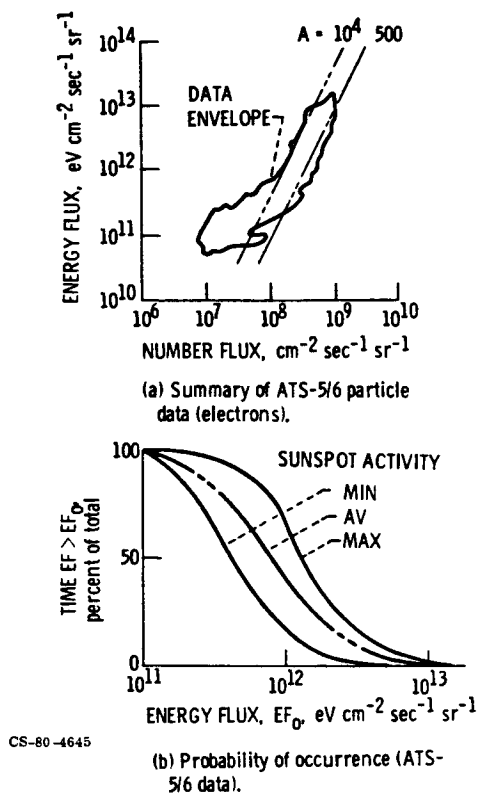


Figure 1. - Flight data used to generate environment specification.

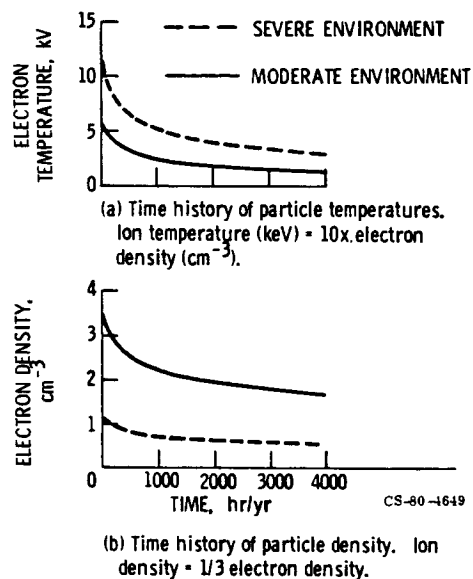


Figure 2. - Specification for satellite time in geomagnetic substorm environments.

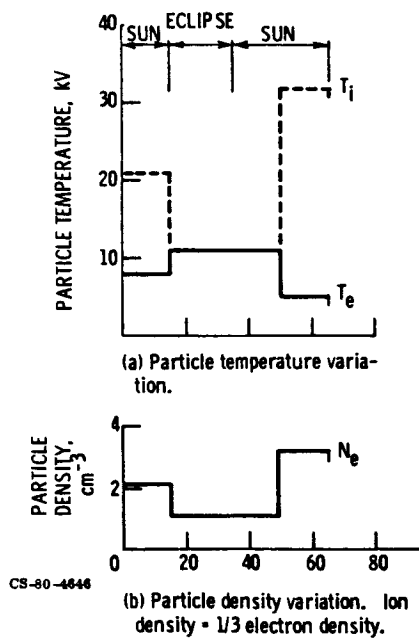


Figure 3. - Substorm environmental conditions for satellite design evaluation.

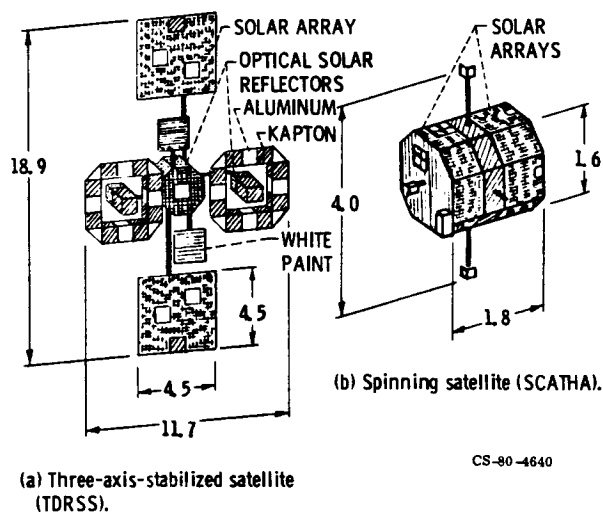


Figure 4. - NASCAP models of geosynchronous satellites. (All dimensions are in meters.)

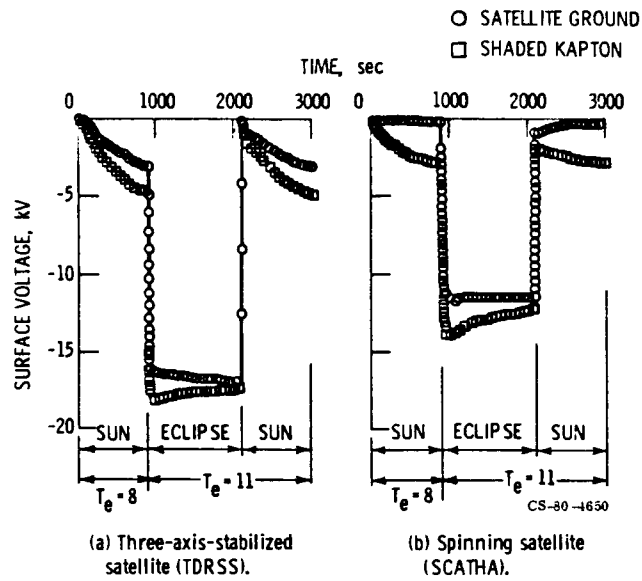


Figure 5. - Predicted behavior in design substorm, showing effect of stabilization.

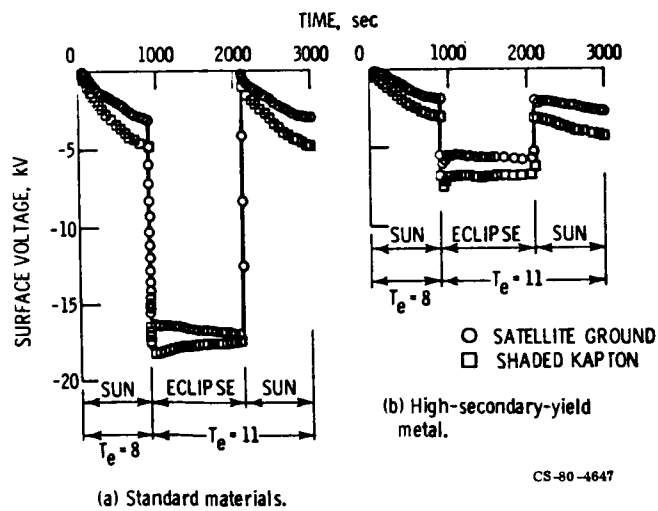


Figure 6. - Predicted behavior in design substorm, showing effect of secondary yield for three-axis-stabilized satellite.

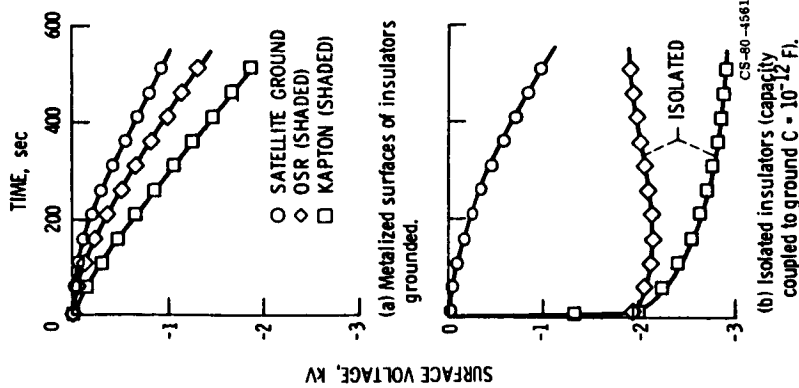


Figure 7. - Comparison of predicted surface voltages for grounded and isolated insulators. Environment  $T_e = 8$  keV;  $T_p = 16$  keV;  $n_e = n_p = 1 \text{ cm}^{-3}$ ; sunlight at  $27^\circ$  incidence.

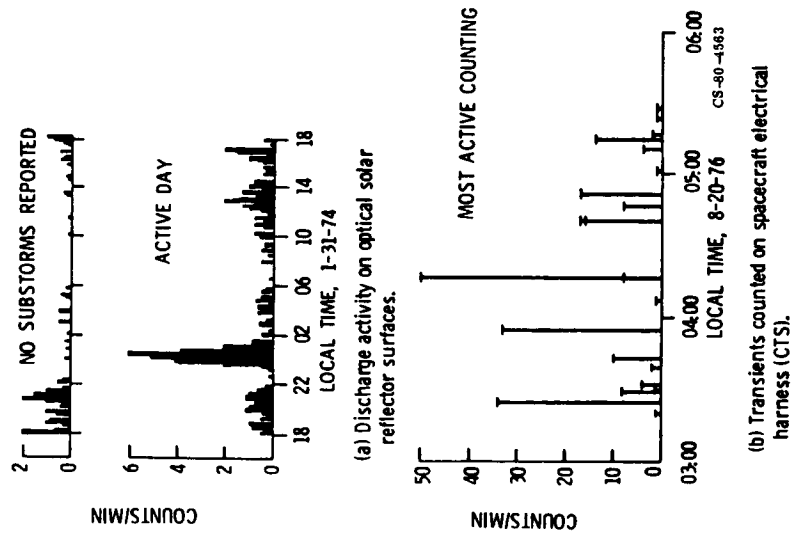


Figure 9. - Discharge activity observed on satellites.

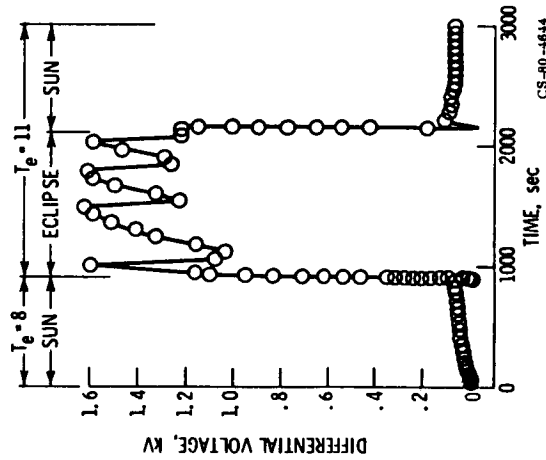


Figure 8. - Predicted behavior of dielectric boom in design substorm, showing spinning satellite differential voltage with respect to satellite ground.



## **P78-2 SCATHA ENVIRONMENTAL DATA ATLAS**

**E. Gary Mullen and David A. Hardy**  
**Air Force Geophysics Laboratory**

**Henry B. Garrett**  
**Jet Propulsion Laboratory**  
**California Institute of Technology**

**Elden C. Whipple**  
**University of California at San Diego**

### **SUMMARY**

A study of the 100 eV to ~1 MeV plasma environment encountered by the P78-2 Spacecraft Charging at High Altitudes (SCATHA) satellite during its initial operation period was conducted. Forty-four days of 10-minute averages of the 4 moments of the electron and ion distribution functions calculated from the SC5 and SC9 energetic particle measurements were analyzed to determine occurrence frequency, local time variation, geomagnetic activity variation, and L-shell variation. The single and double Maxwellian parameters derived from the 4 moments were similarly analyzed. The interrelationships between the moments and derived parameters were computed and the results compared with the ATS-5 and ATS-6 atlas of Garrett et al. (references 4,5). Results of this analysis establish a baseline range for the SCATHA plasma environment.

### **INTRODUCTION**

A preliminary study of the 100 eV to ~1 MeV plasma environment encountered by the P78-2 Spacecraft Charging at High Altitudes (SCATHA) satellite during its initial operation period has been completed. As reported previously (references 1, 2, 3, 4 and 5), a similar analysis was carried out for the ATS-5 and ATS-6 geosynchronous plasma data. The purpose of this paper is to summarize the findings of these studies and to compare the different data bases. The details of the P78-2, ATS-5, and ATS-6 plasma studies are to be found principally in Mullen et al. (reference 6) and Garrett et al. (references 2, 3, 4 and 5).

### **DATA BASE**

Our current understanding of the statistical variations in the geosynchronous and near-geosynchronous plasma environments derives primarily from the University of California (UCSD) plasma experiments on ATS-5 and ATS-6. The recent launch of the P78-2 satellite has allowed an expansion

of this data base as P78-2 flew a UCSD instrument, SC9, identical to those flown on ATS-5 and ATS-6. The diversity of instrumentation on P78-2 has also allowed an intercomparison with a different instrument, SC5, flown by the Air Force Geophysics Laboratory (AFGL). To accomplish this intercomparison, the differential spectra returned by the instruments were integrated to give the 4 moments of the electron and ion distribution functions and estimates of the Maxwellian and 2 Maxwellian temperatures (reference 1). These were combined to give 10 minute averages. These 10 minute averages (approximately 50 days for each instrument) were analyzed statistically in terms of average values, histograms, variations in geomagnetic activity and local time, and interrelationships between parameters. The elliptical orbit of P78-2 also allowed an analysis in terms of radial variations. The instruments will be briefly described below with the variations being discussed in a subsequent section.

The UCSD plasma detectors are described in DeForest and McIlwain (1971)<sup>7</sup> (ATS-5), Mauk and McIlwain (1975)<sup>8</sup> (ATS-6), and Stevens and Vampola (1978)<sup>9</sup> (P78-2). These instruments are similar except for energy range and accumulation time. All 3 instruments consist of pairs of electrostatic analyzers designed to measure the positive ion and electron populations between 51 eV and 51 KeV (ATS-5) or 1 eV and 80 KeV (ATS-6 and P78-2). The ATS-5 detectors measured fluxes parallel and perpendicular to the satellite spin axis whereas ATS-6 and SC9 can scan in the north-south and east-west meridians. ATS-5 returns a complete 64-step spectrum in 20 seconds and ATS-6 and SC9 in 15 seconds.

SC5 (Hanser et al, 1979)<sup>10</sup> is designed to sample the electron and ion fluxes at ~1 second time intervals over a very large energy range (~50 eV - .5 MeV). This energy range necessitates a unique design involving both electrostatic and solid state detectors. The detectors are mounted parallel and perpendicular to the satellite spin axis (only those parallel to the axis were used in this study).

As outlined in Garrett et al. (references 4 and 5) and Mullen et al. (reference 6), there are several constraints on the data base. Summarizing:

- 1) Angular effects - the data have been assumed for the preliminary analysis to be isotropic.
- 2) The ions are assumed to be  $H^+$ .
- 3) Spacecraft charging has not been corrected in the P78-2 data.
- 4) The energy ranges of ATS-6 electrons, SC5 electrons and ions, and SC9 electrons and ions were cut off below 100 eV (ATS-5 was left at 50 eV).
- 5) The high energy cut-offs of ATS-5, ATS-6, and SC9 are considerably lower than SC5. An attempt has been made to correct for this effect by extrapolating the data assuming

Maxwellian distributions but a difference is still noticeable in the data.

- 6) At the time of this paper, the SC5 and SC9 data were still being calibrated (Hardy, private communication) so that the P78-2 data must be considered preliminary.

The above effects, while important, are believed to be acceptable given the order of plasma variations (factors of ~100) and the large statistical samples considered (typically 6000 10-minute averages per instrument). It is intended that the final SCATHA atlas will correct these deficiencies (see Table 5).

#### ATS-5, ATS-6, AND P78-2 INTERCOMPARISONS

Rather than repeat the extensive analysis of the ATS-5, ATS-6, and P78-2 to be found in Garrett (reference 1), Garrett et al. (references 2, 3, 4 and 5), and Mullen et al. (reference 6), this section will present selected examples from that analyses. As the most important parameters for spacecraft charging are the current (J) and Maxwellian temperature, our examples will be confined to these 2 parameters. We have chosen to present the temperature of the high energy 2 Maxwellian component, T<sub>2</sub> (see reference 1). The variations in J are representative of those in the other moments while T<sub>2</sub> is representative of TAVG and TRMS (there are important exceptions, however, and the reports cited above should be consulted).

The basic analysis consisted of calculating the averages of the various moments, the 2 Maxwellian components, and TAVG and TRMS. These averages are listed in Table 1 for the electrons and ions. For completeness, we have also listed the standard deviations (Table 2) but as in most cases the data did not follow a Gaussian distribution, they have limited meaning. Typically the averages of the moments are all in reasonably close agreement with ATS-5 having the lowest values. This is also observed in the temperatures although the differences are much larger (note that T<sub>2</sub><sup>e</sup> is twice the other values for SC5 - we believe this to be an instrumental<sup>e</sup> effect - see later).

Histograms have been prepared of all the variables. Figure 1 is a histogram of the occurrence frequency of K<sub>p</sub> for ATS-5, ATS-6 and P78-2. The P78-2 intervals fall between the ATS-5 and ATS-6 intervals implying that P78-2 saw geomagnetic conditions in between ATS-5 and ATS-6. Likewise, the P78-2 data fall in between ATS-5 and ATS-6 data in the histograms in Figure 2. The major differences in these histograms are between T<sub>2</sub><sup>e</sup> for SC5 and the other instruments and between T<sub>2</sub><sup>i</sup> for ATS-6 and the other instruments. The SC5 variation we believe results from the fact that SC5 can record much higher energy particles than the other instruments.

The ATS-6 difference is consistent with the average increase in geomagnetic activity observed by ATS-6 (Figure 1). In any case, these histograms demonstrate good agreement between the instruments and give the engineer a quantitative measure of the parameter ranges to be expected.

In Figure 3 we have plotted the average variations in local time of  $J$  and  $T_2$ . The local time variations in the current are in excellent agreement between the instruments. For  $T_2$  and to somewhat of a lesser degree for  $T_2^e$ , the SC5 data depart dramatically from the UCSD data. We again attribute this to the difference in instrument energy ranges. Further, the P78-2 data are biased in radial distance - local time (see Table 3). Even so, the data imply a pronounced minimum in the electron current near 16 LT and a weak maximum (except for SC5) in  $T_2$  in the same LT range. As charging is believed to maximize near midnight, these results may imply that it is changes in the electron current that are the primary source of changes in the charging level at geosynchronous orbit.

Also plotted in Figure 3 are the average variations with  $K_p$ . Again the 4 instruments are similar except for  $T_2$  as recorded by SC5 (the trend for  $T_2^e$ , however, is consistent). First, the  $T_2$  parameters show little or no increase with  $K_p$ . Secondly, the largest increase with  $K_p$  is the electron current. There is only a weak increase for the ions. Again this implies that most of the average change at geosynchronous orbit is in the electron current.

The final variation to be discussed is in radial distance or in normalized L-shell coordinates. The SC5 and SC9 variations in L-shell (where  $L=1$  is roughly the radius of the earth) are plotted in Figure 4. Note the non-existent variation in  $J$  and the sharp decrease in  $J_I$  with increasing  $L$  (Note:  $J$  is in  $\text{nA-cm}^{-2}$  and  $J_I$  in  $10^{-2}\text{nA-cm}^{-2}$ ). Both  $T_2^e$  and  $T_2^I$  decrease with increasing  $L$  (again, the difference between SC5 and SC9 is believed to be instrumental). Such variations could not be studied with ATS-5 and ATS-6 and indicate the importance of the P78-2 data in better defining the geosynchronous environment.

## CONCLUSION

The ATS-5, ATS-6, and P78-2 statistical atlas results have been compared in terms of the parameters  $J$  and  $T_2$ . In spite of differences in geomagnetic activity and instrumentation (SC5 versus the UCSD detectors), the different statistical populations are in good agreement. Taken together, they give a strong validation of the current statistical data base established for the geosynchronous plasma.

The justification for studying the P78-2 data is clearly revealed by the comparisons presented here. First, the ATS-5, ATS-6, and SC9 instruments yield consistent results validating our faith in their

reliability overtime. They demonstrate the role of geomagnetic and local time variations and point toward the importance of variations in the current. The differences between the ion temperatures measured by ATS-5, ATS-6, and SC9 also imply long-term variations in the state of the geosynchronous plasma. The SC5 data demonstrate that care must be taken in analyzing a limited energy range - the entire energy spectrum from  $\sim 0$  to 1 MeV may turn out to be important to charging. Future studies should, when possible, include plasma data above 100 KeV. Finally, the P78-2 has allowed an evaluation of radial variations that was impossible with ATS-5 and ATS-6. The data imply strong radial gradients that must be considered in spacecraft charging studies.

In spite of the successes of the preliminary P78-2 atlas, a number of issues remain unresolved. These areas are to be filled in by the final P78-2 atlas. The major areas are listed in Table 5. The preliminary atlas was intended to provide an initial answer to these problems and a baseline for the P78-2. At the same time, it was to provide a confirmation of the validity of the ATS-5 and ATS-6 atlas. These goals, as demonstrated here, have been met.

#### REFERENCES

1. Garrett, H. B.: Modeling of the Geosynchronous Plasma Environment. Spacecraft Charging Technology, 1978. NASA CP-2071/AFGL-TR-79-0082, 1979, pp. 11-22.
2. Garrett, H. B.; Mullen, E.G.; Ziemba, E.; and DeForest, S.E.: Modeling of the Geosynchronous Plasma Environment - Part 2. ATS-5 and ATS-6 Statistical Atlas. AFGL-TR-78-0304, 1978.
3. Garrett, H. B.; McInerney, R.E.; DeForest, S. E.; and Johnson, B.: Modeling of the Geosynchronous Orbit Plasma Environment - Part 3, ATS-5 and ATS-6 Pictorial Data Atlas. AFGL-TR-79-0015, 1979.
4. Garrett, H. B.; Schwank, D. C.; and DeForest, S. E.: A Statistical Analysis of the Low Energy Geosynchronous Plasma Environment. Part I - Electrons. Submitted to Planet. Space Sci., 1980.
5. Garrett, H. B.; Schwank, D. C.; and DeForest, S. E.: A Statistical Analysis of the Low Energy Geosynchronous Plasma Environment. Part II - Ions. Submitted to Planet Space Sci., 1980.
6. Mullen, E. G.; Garrett, H. B.; Hardy, D. A.; and Whipple, E. C.: P78-2 SCATHA Environmental Data Atlas. AFGL-TR-80-0241, 1980.
7. DeForest, S. E.; and McIlwain, C.E.: Plasma Clouds in the Magnetosphere. J. Geophys. Res., 76, 1979, pp. 3587-3611.

8. Mauk, B. H.; and McIlwain, C. E.: ATS-6 Auroral particle experiment. IEEE Trans. Aerospace and Electronics Systems, AEA-11 (No. 6), 1975, pp. 1125-1130.
9. Stevens, J. R.; and A. L. Vampola: Description of the Space Test Program P78-2 Spacecraft and Payloads. SAMSO-TR-78-24, 1978; pp. 49-53.
10. Hanser, F. A.; Hardy, D. A.; and Sellers, B.: Calibration of the Rapid Scan Particle Detector Mounted in the SCATHA Satellite. AFGL-TR-79-0167, 1979.

TABLE 1a. AVERAGES (ELECTRONS)

PARAMETER	ATS-5	ATS-6	SC9	SC5
ND ( $\text{cm}^{-3}$ ) <sub>2</sub>	.80	1.06	1.09	.82
J ( $\text{nA-cm}^{-2}$ ) <sub>3</sub>	.068	.096	.115	.086
ED ( $\text{eV-cm}^{-3}$ )	1970	3590	3710	3240
EF ( $\text{eV-cm}^{-2}\text{-s}^{-1}\text{-sr}^{-1}$ )	$.98 \times 10^{12}$	$2.17 \times 10^{12}$	$1.99 \times 10^{12}$	$2.26 \times 10^{12}$
N1 ( $\text{cm}^{-3}$ )	.578	.751	.780	.654
T1 (KeV)	.277	.460	.550	.725
N2 ( $\text{cm}^{-3}$ )	.215	.273	.310	.169
T2 (KeV)	7.04	9.67	8.68	17.4
TAVG (KeV)	1.85	2.55	2.49	3.20
TRMS (KeV)	3.85	6.25	4.83	8.26

TABLE 1b. AVERAGES (IONS)

PARAMETER	ATS-5	ATS-6	SC9	SC5
ND ( $\text{cm}^{-3}$ ) <sub>2</sub>	1.30	1.20	.58	.69
J ( $\text{pA-cm}^{-2}$ ) <sub>3</sub>	5.1	3.4	3.3	4.1
ED ( $\text{eV-cm}^{-3}$ )	13000	12000	9440	12400
EF ( $\text{eV-cm}^{-2}\text{-s}^{-1}\text{-sr}^{-1}$ )	$2.6 \times 10^{11}$	$3.4 \times 10^{11}$	$2.0 \times 10^{11}$	$2.93 \times 10^{11}$
N1 ( $\text{cm}^{-3}$ )	.75	.93	.19	.33
T1 (KeV)	.30	.27	.80	2.13
N2 ( $\text{cm}^{-3}$ )	.61	.33	.39	.36
T2 (KeV)	14.0	25.0	15.8	21.1
TAVG (KeV)	6.8	12.0	11.2	12.1
TRMS (KeV)	12.0	23.0	14.5	16.8

TABLE 2a. STANDARD DEVIATIONS (ELECTRONS)

PARAMETER	ATS-5	ATS-6	SC9	SC5
ND ( $\text{cm}^{-3}$ )	$\pm 79$	$\pm 1.1$	$\pm 89$	$\pm 75$
J ( $\text{nA-cm}^{-2}$ )	$\pm .088$	$\pm .09$	$\pm .10$	$\pm .08$
ED ( $\text{eV-cm}^{-3}$ )	$\pm 3100$	$\pm 3700$	$\pm 3400$	$\pm 3300$
EF ( $\text{eV-cm}^{-2} \text{ s}^{-1} \text{ sr}^{-1}$ )	$\pm 1.7 \times 10^{12}$	$\pm 2.6 \times 10^{12}$	$\pm 2.0 \times 10^{12}$	$\pm 2.29 \times 10^{12}$
N1 ( $\text{cm}^{-3}$ )	$\pm 55$	$\pm 82$	$\pm 70$	$\pm 60$
T1 (KeV)	$\pm 17$	$\pm 85$	$\pm 32$	$\pm 66$
N2 ( $\text{cm}^{-3}$ )	$\pm 38$	$\pm 34$	$\pm 37$	$\pm 23$
T2 (KeV)	$\pm 2.1$	$\pm 3.6$	$\pm 4.0$	$\pm 11$
TAVG (KeV)	$\pm 2.0$	$\pm 2.0$	$\pm 1.5$	$\pm 2.7$
TRMS (KeV)	$\pm 3.3$	$\pm 3.5$	$\pm 2.9$	$\pm 5.8$

TABLE 2b. STANDARD DEVIATIONS (IONS)

PARAMETER	ATS-5	ATS-6	SC9	SC5
ND ( $\text{cm}^{-3}$ )	$\pm 69$	$\pm 1.7$	$\pm 35$	$\pm 41$
J ( $\text{pA-cm}^{-2}$ )	$\pm 2.7$	$\pm 1.8$	$\pm 2.1$	$\pm 2.6$
ED ( $\text{eV-cm}^{-3}$ )	$\pm 9700$	$\pm 9100$	$\pm 6820$	$\pm 8900$
EF ( $\text{eV-cm}^{-2} \text{ s}^{-1} \text{ sr}^{-1}$ )	$\pm 3.5 \times 10^{11}$	$\pm 3.6 \times 10^{11}$	$\pm 1.7 \times 10^{11}$	$\pm 2.5 \times 10^{11}$
N1 ( $\text{cm}^{-3}$ )	$\pm 54$	$\pm 1.78$	$\pm 16$	$\pm 24$
T1 (KeV)	$\pm 30$	$\pm 88$	$\pm 1.0$	$\pm 1.4$
N2 ( $\text{cm}^{-3}$ )	$\pm 33$	$\pm 16$	$\pm 26$	$\pm 24$
T2 (KeV)	$\pm 5.0$	$\pm 8.5$	$\pm 5.0$	$\pm 8.7$
TAVG (KeV)	$\pm 3.6$	$\pm 8.4$	$\pm 4.6$	$\pm 5.2$
TRMS (KeV)	$\pm 4.8$	$\pm 8.9$	$\pm 5.3$	$\pm 7.1$

TABLE 3

P78-2 10 MINUTE INTERVALS  
IN A GIVEN LOCAL TIME/L SHELL INTERVAL

TOTAL	375	250	454	611	667	352	111	2920
21-24	59	18	6	17	75	94	52	321
18-21	81	16	53	76	42	22	0	290
15-18	38	65	11	0	0	10	10	134
12-15	61	42	85	18	1	0	4	211
9-12	75	46	77	184	59	0	0	441
6-9	56	96	66	109	319	5	0	651
3-6	0	4	109	196	145	70	7	531
0-3	5	63	47	11	26	151	38	341
	5.5	6.0	5.5	7.0	7.5	8.0	8.5	TOTAL
	L SHELL							

TABLE 4  
P78-2 10 MINUTE INTERVALS  
IN A GIVEN Kp/L SHELL INTERVAL

TOTAL	375	250	454	611	667	352	111	2920
5+	10	14	6	17	37	0	4	88
4+	57	31	35	38	96	32	3	292
3+	119	88	83	107	139	81	30	647
2+	100	99	155	205	171	117	41	888
1+	57	69	108	159	121	85	19	618
0+	32	49	67	85	103	37	14	387
	5.5	6.0	6.5	7.0	7.5	8.0	8.5	TOTAL
	L SHELL							

TABLE 5. PROPOSED FINAL ATLAS CONTENTS

Statistical variations of energetic particle fluxes as functions of Kp L-shell and local time.

Average particle distribution functions and ranges of individual distributions to include worst case.

Distribution functions during charging events.

Pitch angle distribution of particles during quiet and charging periods.

Spectrograms.

Ion composition data.

Electric and magnetic fields.

Supplemental data from Geos and other satellites.

Section on plasma dropouts and injection events and their relationship to charging.

Identify regions and conditions for maximum probability of charging.

Determine best fits to particle distribution functions whether physical or empirical for model use.

Simplified "worst case" environment.



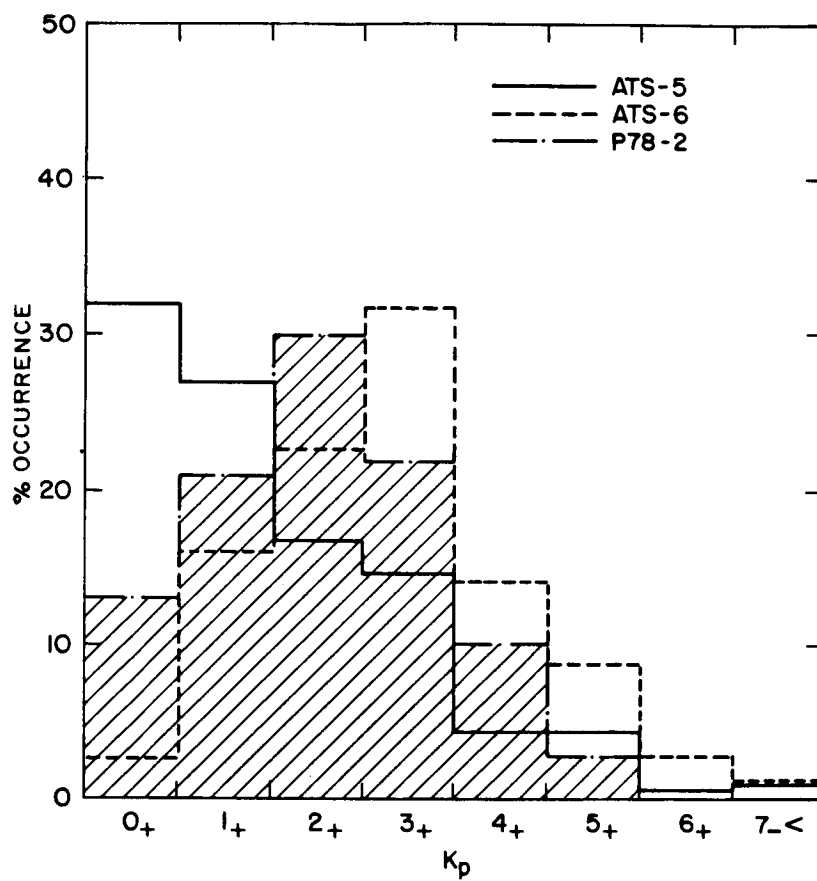


Figure 1. - Occurrence frequency of  $K_p$  for ATS-5, ATS-6, and P78-2 satellites.

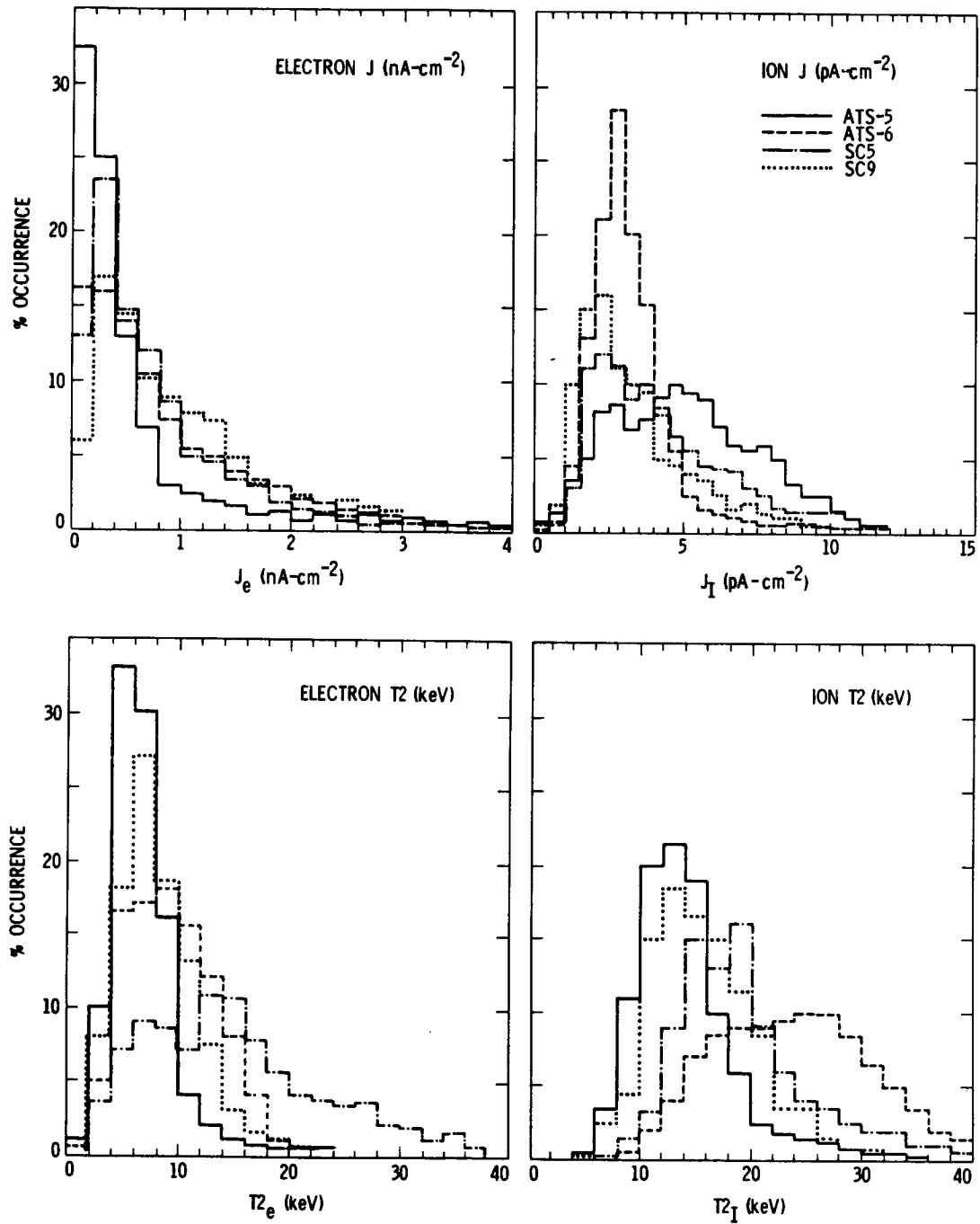


Figure 2. - Histograms of current density  $J$  and 2 Maxwellian temperature  $T_2$  for ATS-5, ATS-6, and P78-2.

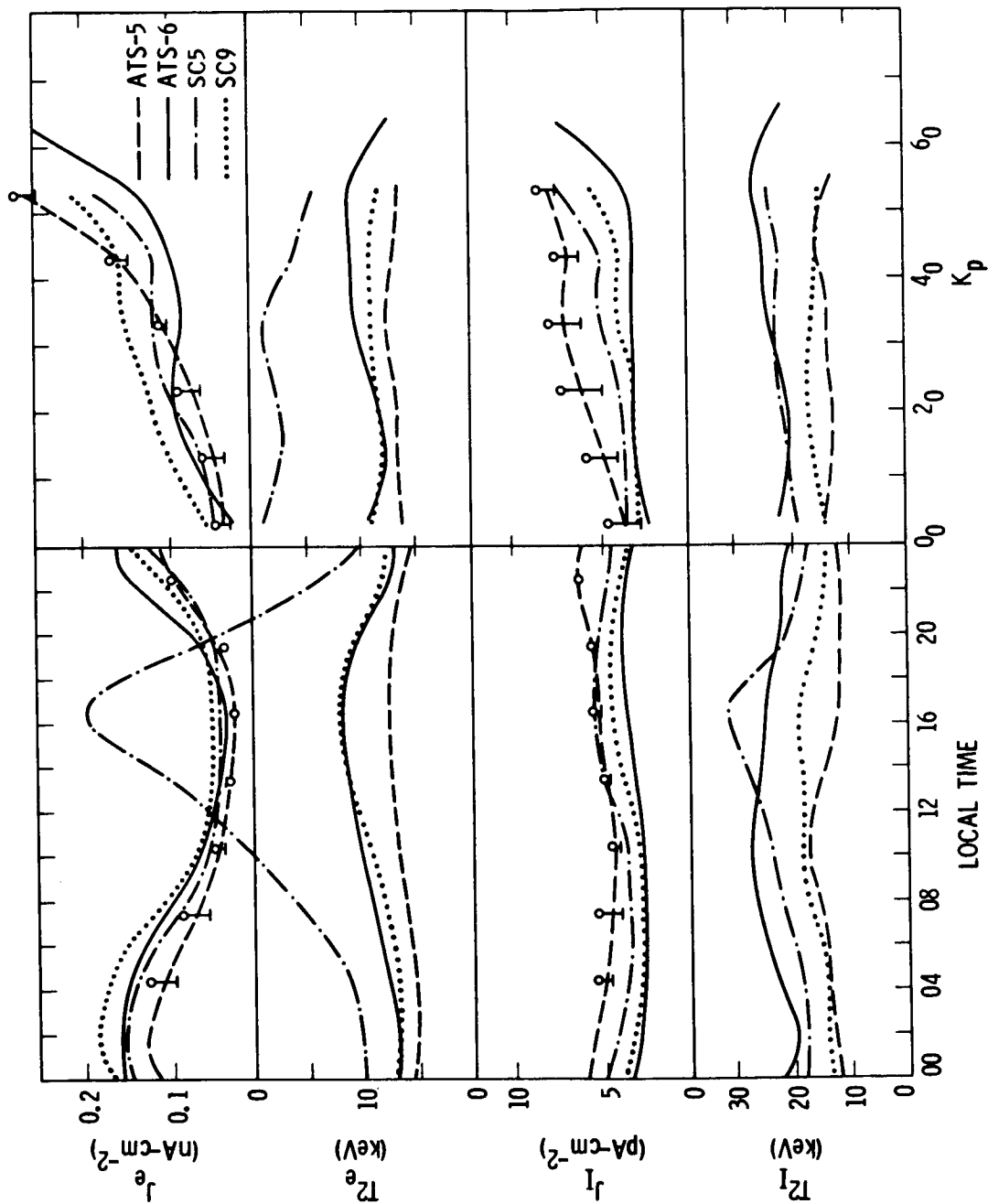


Figure 3. - Plots of average local time and  $K_p$  variations observed by ATS-5, ATS-6, and P78-2. Error bars correspond to average variations of ATS-5 parallel (-) and perpendicular (0) detectors.

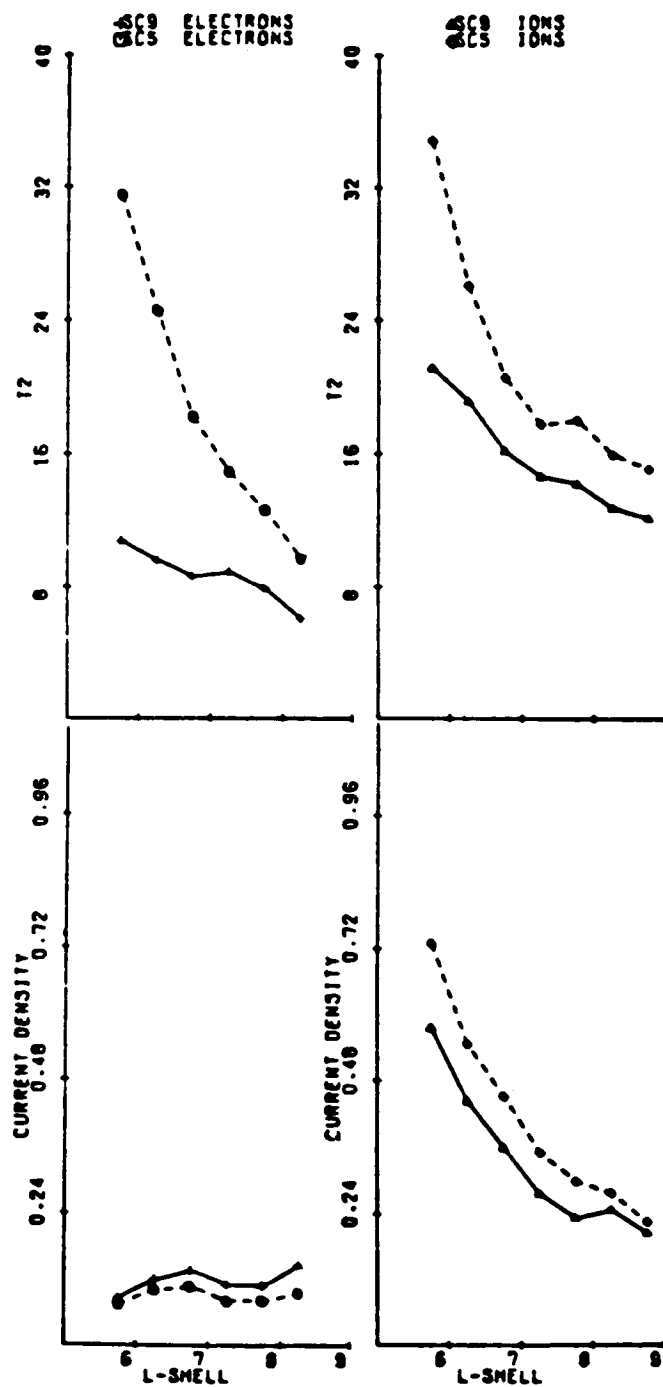


Figure 4. - Plots of variations with L-shell of parameters J (current density) and  $T_2$  (2 Maxwellian temperature component). Current density is in units of  $\text{nA cm}^{-2}$  for electrons and  $10^{-2} \text{ nA cm}^{-2}$  for ions.  $T_2$  is in units for keV.

# METEOSAT SPACECRAFT CHARGING INVESTIGATION

**Dierk G. Hoge**  
**European Space Agency**

## SUMMARY

A number of phenomena observed on the first orbiting METEOSAT satellite have, after analysis, been attributed to spacecraft charging effects. The investigation programme consisted of design analysis, correlation of anomalies with space environmental data, on-ground tests with an engineering model spacecraft, tests on the validity of improvements and, finally, installation of suitable monitors for the second improved flight satellite.

## INTRODUCTION

METEOSAT is a spin-stabilised meteorological satellite in geostationary orbit containing as the main payload a scanning radiometer.

A first satellite (METEOSAT-1) was launched in November 1977 from Cape Kennedy, Florida, U.S.A. The satellite met the mission performance requirements in spite of a number of anomalies, mostly spurious status changes, which have been the subject of investigations for almost three years. However, the low number of such status changes and the type of perturbations caused did not really justify major investigation. It became necessary to investigate these phenomena in detail, however, in view of

- potential irreversible degradation,
- operational impacts,
- improvements for future satellites.

### Spurious Status Changes in Orbit

About 150 status changes have been observed in three years orbiting which could be attributed to spacecraft charging effects. Correlation with local time, sun attitude, eclipses could not be established but correlation with magnetic activity indices of Leirvogur, Lerwick, Friedericksburg and the general planetary index Ap showed good correlations, particularly with magnetic activities occurring two days prior to the anomalous events (Ref. 1).

Certain trends concerning the affected subsystems could be observed over the first two years after which the spacecraft operations were reduced due to

an on-board failure owing to which less anomalies could be detected. Status changes were still observed during the third year in a corresponding proportion.

Finally, one status change (which was equally likely to occur) was only observed once after two and a half years in orbit.

### Satellite Design Features

Following consultations with experts, the satellite design was reviewed with respect to differential charge built up capabilities and the noise immunity protection of interfaces.

#### Outer Surfaces

About 80% of the outer surface of the satellite are not conductive, e.g. solar cell cover glasses, second surface mirrors and black paint. The large metallised surfaces of the thermal shields are not grounded, the main reason being that no cost-effective qualified solution was available for grounding these surfaces.

The main surfaces concerned (Fig. 1) are

- antenna thermal shield, forward thermal shield and afterward thermal shields,
- antenna and shunt second surface mirrors,
- solar panels.

The material (Fig. 2) used for the thermal shields is Kapton of 25 $\mu$ m, aluminised on both sides. The edges of the thermal shields are reinforced. The second surface mirrors have a similar material: FEP Teflon-coated aluminium mirror.

The largest single grounded capacitor is formed by the forward thermal shield sections with about 350 nano farad per section.

#### Command Interfaces

The satellite contains a centralised telecommand decoder which provides individual telecommands to the units. In the case of low power commands, this requires a telecommand amplifier which is characterised by the noise immunity, threshold level and its gain. The decoded telecommands have a duration of 13 ms.

The zero level is  $0 < \text{zero} < 0.7$

The one level is  $2.2 < \text{one} < 5V$ .

There are about 250 telecommands, 80 of which are "low power commands". The performances of the telecommands amplifier of the various equipment show a considerable difference concerning this noise immunity. Status changes could be observed only on those interfaces where low noise immunity amplifiers drive TTL logics rather than relays (Fig. 3). Typical noise immunity figures for the affected circuitry are

5V	330 $\mu$ S	Type 1
5V	10 $\mu$ S	Type 2
5V	1 $\mu$ S	Type 3

In the last case the interface is however not a telecommand interface but an interface to a protection system.

All units passed system level tests.

#### Grounding Concept

As for many other satellites, the grounding system for METEOSAT is a multiple grounding system. The low impedance of the structure interconnects the grounding points with a resistance of less than 10 ohms in most cases. Most of the units which showed status changes were, in fact, double grounded as concerns the command interface.

#### Simplified Analysis

Assuming the status changes were caused by ground currents generated by the arc discharges of the large outer surfaces, one can determine the order of magnitudes for charge voltage, ground current, duration of pulse and, in the case of METEOSAT, arrive at a discrepancy. In the most favourable case, the thermal shield has to charge up to more than 3KV and all discharge current has to pass the interface decoder-telecommand amplifier as a single pulse (Fig. 4). Whereas it appears to be more realistic that the discharge pulse will not be rectangular, only a small fraction of the discharge current will pass the particular interface and the discharge will not be to zero volts.

#### Current Injection Test

Due to the discrepancies in the simplified analysis and to also obtain a better understanding on the real mechanism for the status changes, and finally to test the effectiveness of improvements, it became desirable to

perform a test with an electrical model of the satellite and to simulate the effect of discharges by a high tension capacitor and a spark chamber. The test set-up (Fig. 5) enabled the following test parameters to be varied :

- injection points,
- change voltage (500 - 6000V),
- spark gap (0.1 - 10mm),
- current limiting resistor (0, 1, 10, 100 Ohm),
- polarity,
- shielding of spark chamber (with/without).

The capacitance of the storage capacitor was .47 micro F. The satellite was either "open" (dummy solar panels, dismounted), or "closed".

#### Test Experience

Initial setting up problems was due to the monitoring and sensitivity of test equipment to the discharger and the coupling of the umbilical connector cabling. In the configuration finally used, the spacecraft was completely disconnected from all items of equipment, was operated on its on-board battery and was controlled by the VHF TM/TC system.

#### Test Results

The current injection test reproduced a number of status changes, some of which had already been observed, some not. The most frequent status changes in the radiometer scanning control could not be reproduced. Generally the results were in line with the course analysis, that is the test parameters had to be very favourable (high voltage and current levels, injection points close to the equipment) in order to cause status changes.

The test could also establish that the modifications introduced to increase the noise immunity had no negative effect but failed to establish a real gain. On the whole the test proved that the satellite was quite immune to structural currents - it was felt that the status changes may be caused differently.

A further review of the candidate discharge current sources revealed that the radiometer mirrors were not grounded. The main mirror of the radiometer telescope has a reflector of about 1000cm<sup>2</sup> on a glass structure coated with THF4. The closest structural element has a distance of about 20mm. Simulating a discharge of this surface by current injections into the telescope structure could, in fact, reproduce new status changes.



It was further thought that a real, illuminated solar array might make the satellite more sensitive to arc discharges and the test set-up was changed accordingly. There was no change in the test performance, however.

Finally, a direct charging-up of the thermal shields was tested. Apart from deteriorating the thermal shield, this test did not produce any new results.

### Conclusions

A current injection test is time-consuming and costly. For METEOSAT this test took five weeks to carry out with four operators to control the satellite and perform the testing. The spacecraft, built for currents of maximum 15A, was subjected to transient currents exceeding a hundred times this value without suffering any failure, and only rarely were status changes provoked. This test, if performed as an acceptance test, could have demonstrated the satisfactory immunity of the satellite.

### Sample Irradiation Test

In parallel to the current injection testing, an electron irradiation test programme was initiated in order to establish the charge and discharge characteristics of the satellite surfaces and also to verify the validity of the parameters for the current injection test.

### Thermal Shield

The first sample subjected to an irradiation test was a 20 x 20cm thermal shield in two versions - one with an ungrounded outer surface and the other with a grounded outer surface as foreseen as an improvement for the second flight model. The irradiation was performed with energy levels of 5, 10 and 20KeV and currents of 0.1 to 1.25 (nA/cm<sup>2</sup>). On the first sample discharges were initially observed at low potentials (500V) rising to about 2000V with continuous discharges. The relative low potential seems to be due to edge effects, in particular field emissions. The effect of ultra violet illumination on the charging properties was also investigated. Under test conditions the ultra violet illumination did not prevent the charge build-up and consequent arcing events, but had a reducing effect particularly with low incident angles (Ref. 2). The test set-up enabled the determination of the discharge currents. Typical values were 10A for 500nS which is far below the expected value of about 100A for 500nS and 1KV charging voltage.

## Second Surface Mirrors

The second surface mirrors were irradiated in a similar tests. The SSM showed discharges starting from 15KeV ( $1\text{nA}/\text{cm}^2$ ); typical discharge currents were 15A and 500nS. Again the discharge currents were lower than expected. What was surprising, however, was a strong signal at the pick-up antenna and the fact that discharges seemed to appear in holes rather than at the edges. See Ref. 3 for further detail.

## Radiometer Mirror

A spare scanning mirror, smaller but similar to the primary mirror, was used for this test. As concerns the charging properties, this mirror showed a zener effect on its surface potential at around 5KV (Ref. 4). Discharges could not be discovered. It was further noted that the surface potential was rapidly discharged in the presence of ultra violet illumination.

## Conclusions

The discharge currents of the outer surfaces are far below the values required to produce the levels applied for the current injection test. The simple model for the differential charge build-up and current injection due to arc discharges does not seem to be valid.

## Electron Irradiation Test

The investigations carried out so far have not revealed the real mechanism of the status changes but, on the contrary, have created doubts on simple explanations. Therefore the possibility of performing a full scale space simulation test including electron irradiation was investigated; this test was finally performed. To simplify the test set-up and to reduce the cost, the following restrictions had to be applied :

- passive satellite : to avoid the need to power the spacecraft and to reduce the test team and equipment.
- no sun simulation : to avoid the need for cooling the shrouds and since no valid simulation of ultra violet light was available.
- no thermal control : to simplify the test set-up.

The sole aim was to study the behaviour of the outer surfaces and to attempt not to reproduce anomalies.

The instrumentation to monitor the surface behaviour consisted of

- surface potential probes
- electric field antennae
- photographic equipment.

The spacecraft was in addition equipped with a probe to monitor the primary mirror potential. The test parameters were

- satellite grounding : (free floating or ground resistors).
- motion simulators : zero spin or .5 rpm.
- satellite attitude : (-23 to 23).
- irradiation : acceleration voltage 5 to 30KV  
flux density  $\text{InA/m}^2$   
target disc 3m diameter.

The test set-up (Fig. 6) shows the location of the equipment.

#### Test Results

When irradiated, the surfaces would charge up rapidly and arcing was observed starting at energy levels of about 7KeV on most surfaces. The arcing events were frequent, typically .1 to 1 events per second (Fig. 7). Prior to the test and according to the theory, it was expected that larger surfaces would produce considerably larger discharges. This difference in amplitude could not be observed by the electric field antennae nor by visual observations.

Occasionally cascades of arcs were observed which could, by their combined effect, better explain the status changes. As an interesting detail, the test could clearly identify the rapid arcing of a repaired thermal shield which proves the general suitability of the test.

The test confirmed the basic results of the sample irradiation test which showed already that the larger surfaces did not produce discharges corresponding to their capacity. As a main result, the test demonstrated that under substorm conditions the satellite is virtually covered with arc discharges. This makes it difficult to explain the very low number of actual status changes.

In a last phase, the effectiveness of grounding the outer layer of the thermal shields was tested and improvement foreseen for the second flight model. Figure 8 shows that a general attenuation rather than a reduction in number of discharges takes place based on the electric field measurements. This could mean that the satellite reduces the electric field variation but not necessarily that the arc discharges are less violent. The fact that the number of arc discharges is hardly affected also confirms that the thermal

shields have a minor contribution to the overall arc discharge activities.

### Conclusions

The test did not provide a clear understanding of the mechanism leading to status changes but demonstrated that arcing activities can be very intense even if only small surfaces are involved. Grounding of part of the satellite does not prevent arcing but could reduce it.

### Satellite Design Improvements

Since improvements sometimes make things worse, particularly if the cause of a problem is not fully understood and also due to the advanced state of the hardware, the number of modifications introduced to the second METEOSAT flight spacecraft were limited to

- grounding of the thermal shield,
- improvements of critical interfaces,
- incorporation of charging monitors.

### Grounding of the Thermal Shields

The technology applied uses grounding straps glued to the outer layer with conductive adhesive. So far this design showed only problems during vibration testing due to insufficient stress relief. This was improved in a later version.

### Improvements of Critical Interfaces

Since the sensitive interfaces consisted in all cases of low noise immunity amplifiers and TTL logics modification (Fig. 9) consisted of the use of relays with high immunity amplifiers. Non-critical interfaces have not been modified and can be considered as reference for the orbital behaviour.

### Charging Monitors

The modifications will not exclude arc discharges and possibly status changes in orbit.

To monitor the space environment and the arc discharge activity, the satellite was equipped with two monitors :

- electrostatic analyser :

This instrument is provided by the Emmanuel College, Boston, USA. It was developed for the DMS Programme and is called SSJ/3. It detects and analyses electrons in the energy range of 50eV - 20KeV, by employing a low and a high level channel. The aperture points into space with an inclination of  $45^{\circ}$ . The basic instrument (Fig. 10) consists of

- . instrument aperture
- . deflecting electrostatic field
- . exit aperture
- . channeltron multipliers and counters.

- electrostatic-discharge monitor :

This monitor is designed to detect and analyse the electromagnetic interferences caused by discharges. It provides over one observation period (one telemetry format; 25s) the detection of

- . peak value of highest spike picked up
- . number of events exceeding the background noise and their total duration
- . level of the background noise itself.

The instrument is an in-house development by the Agency's technology centre ESTEC. The block diagram (Fig. 11) shows the automatic setting of the threshold, the event timer and counter and the peak detector. The input to the instrument is provided by a small pickup antenna.

## FINAL CONCLUSIONS

Performance data of the second flight model, in particular in conjunction with the monitor data, may well show that further improvements are required, such as grounding all outer surfaces. Present grounding methods for conductive SSM are under investigation and the overall impact of a requirement for a unipotential outer surface on manufacture is presently being assessed.

It is felt however that a better understanding of the arcing phenomena could lead to more efficient solutions.

## REFERENCES

1. Robbins, A: METEOSAT Spacecraft Charging Investigation. Royal Aircraft Establishment, Farnborough, Hants, England.  
ESA Contract 3561/78/F/CG/sc
2. Levy, L, Sarraill, D: Etude Comparative de Deux Configurations d'Ecran Thermique de METEOSAT en Ambiance d'Orage Géomagnétique. Centre d'Etudes et de Recherches de Toulouse, France.
3. Levy, L, Sarraill, D: Essais de Claquage d'une Portion représentative de SSM de METEOSAT. Centre d'Etudes et de Recherches de Toulouse, France
4. Levy, L, Sarraill, D: Essais d'Irradiation d'un miroir de METEOSAT pour la Détermination de l'Influence de l'Eclairement Solaire sur son Comportement Electrostatique. Centre d'Etudes et de Recherches de Toulouse, France.

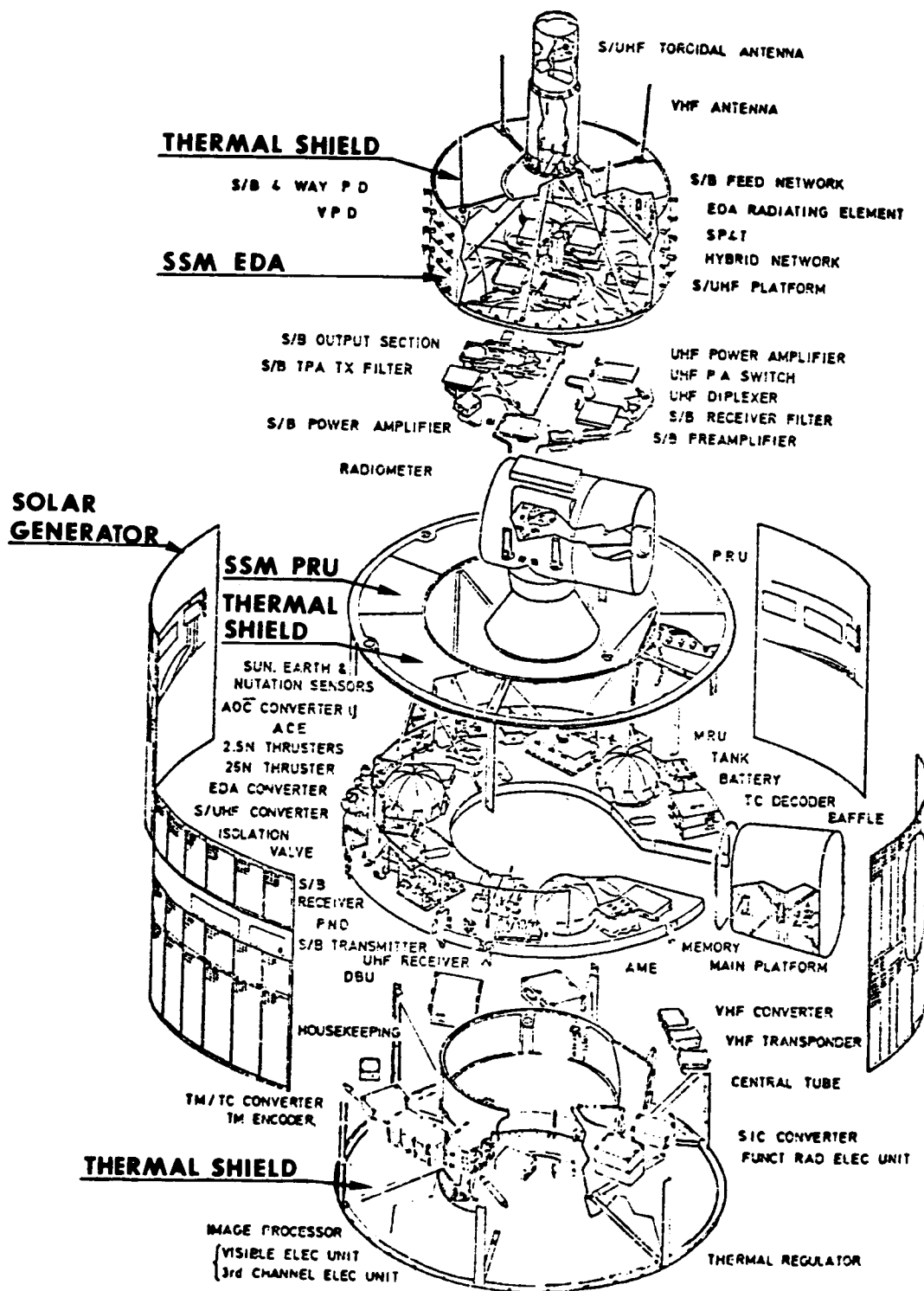
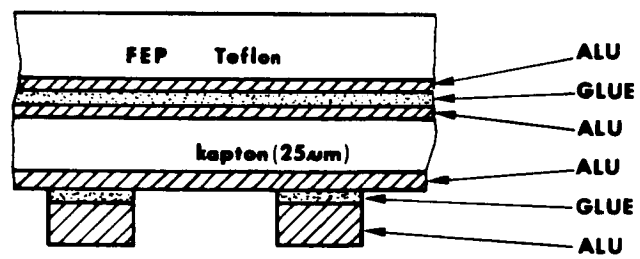


Figure 1. - Satellite configuration and outer surface.

### Second Surface Mirrors



### Thermal Shields

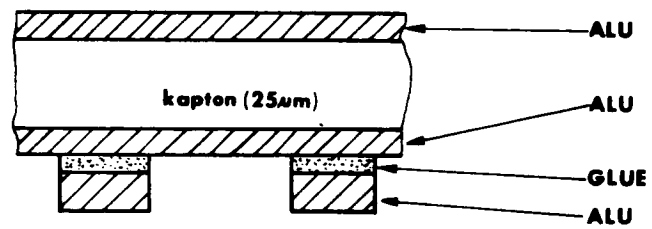


Figure 2. - Thermal shields and second-surface-mirror material.



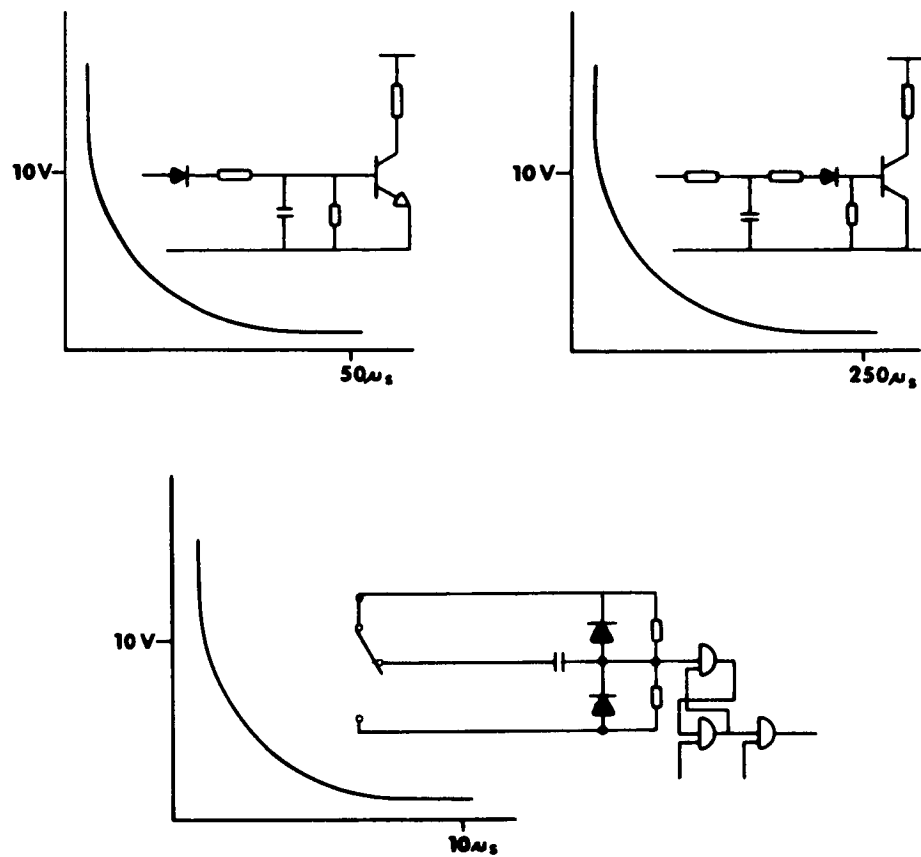
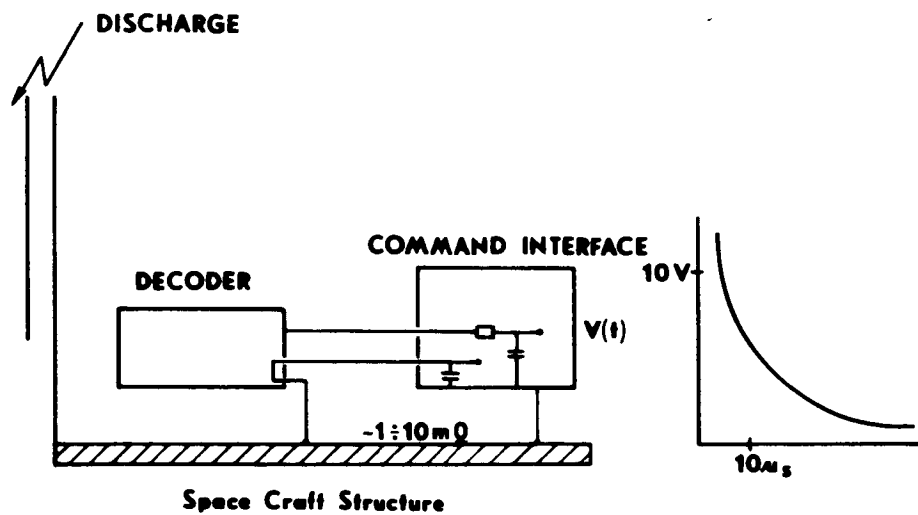


Figure 3. - Command interfaces and noise immunity.



Conditions for Status Change

$V(t) > \text{Volts}, \mu \text{s}$

Discharge: KV, KA,  $\mu \text{s}$ ,  $\mu \text{F}$

Figure 4. - Simplified analysis for status changes.

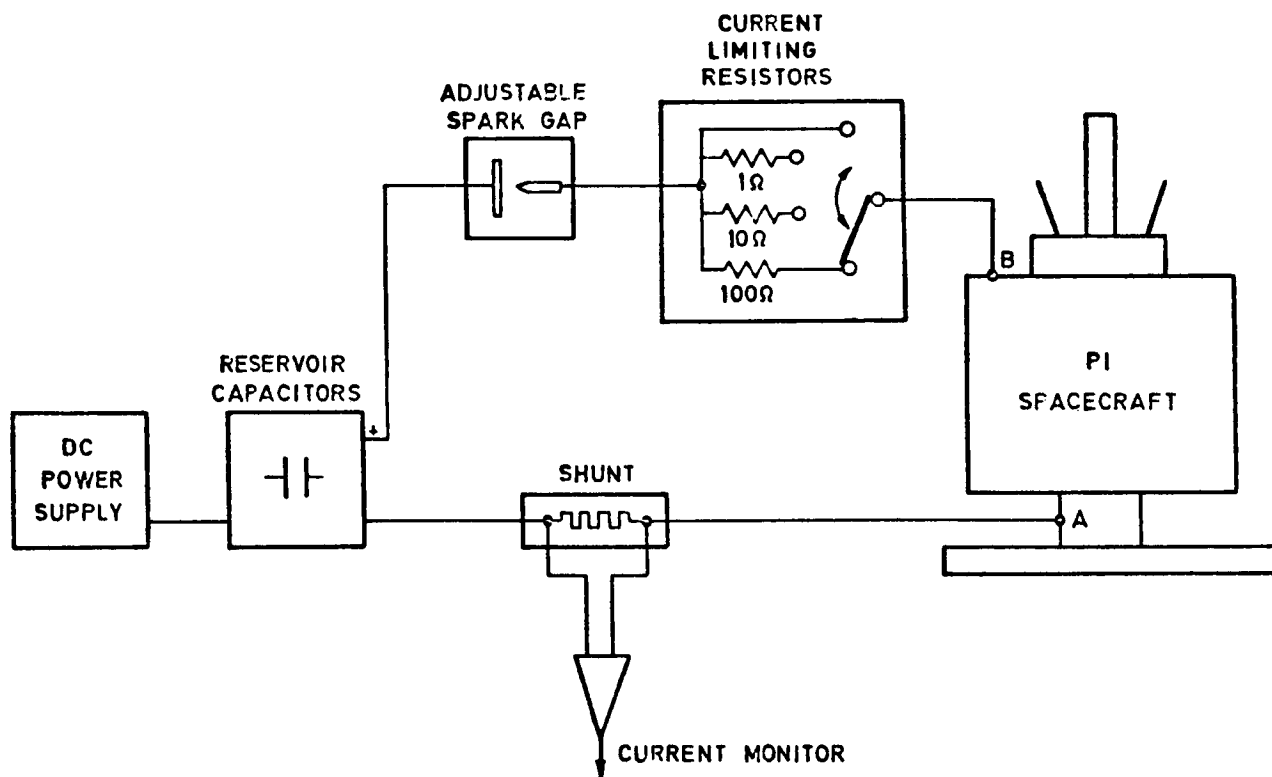


Figure 5. - Current injection test setup.

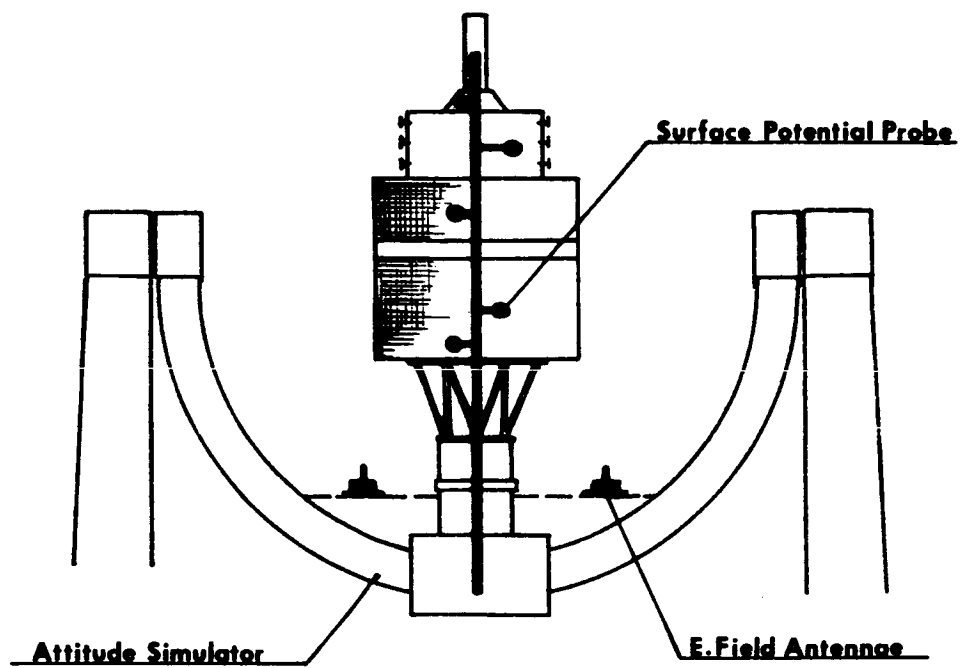


Figure 6. - Electron irradiation test setup.

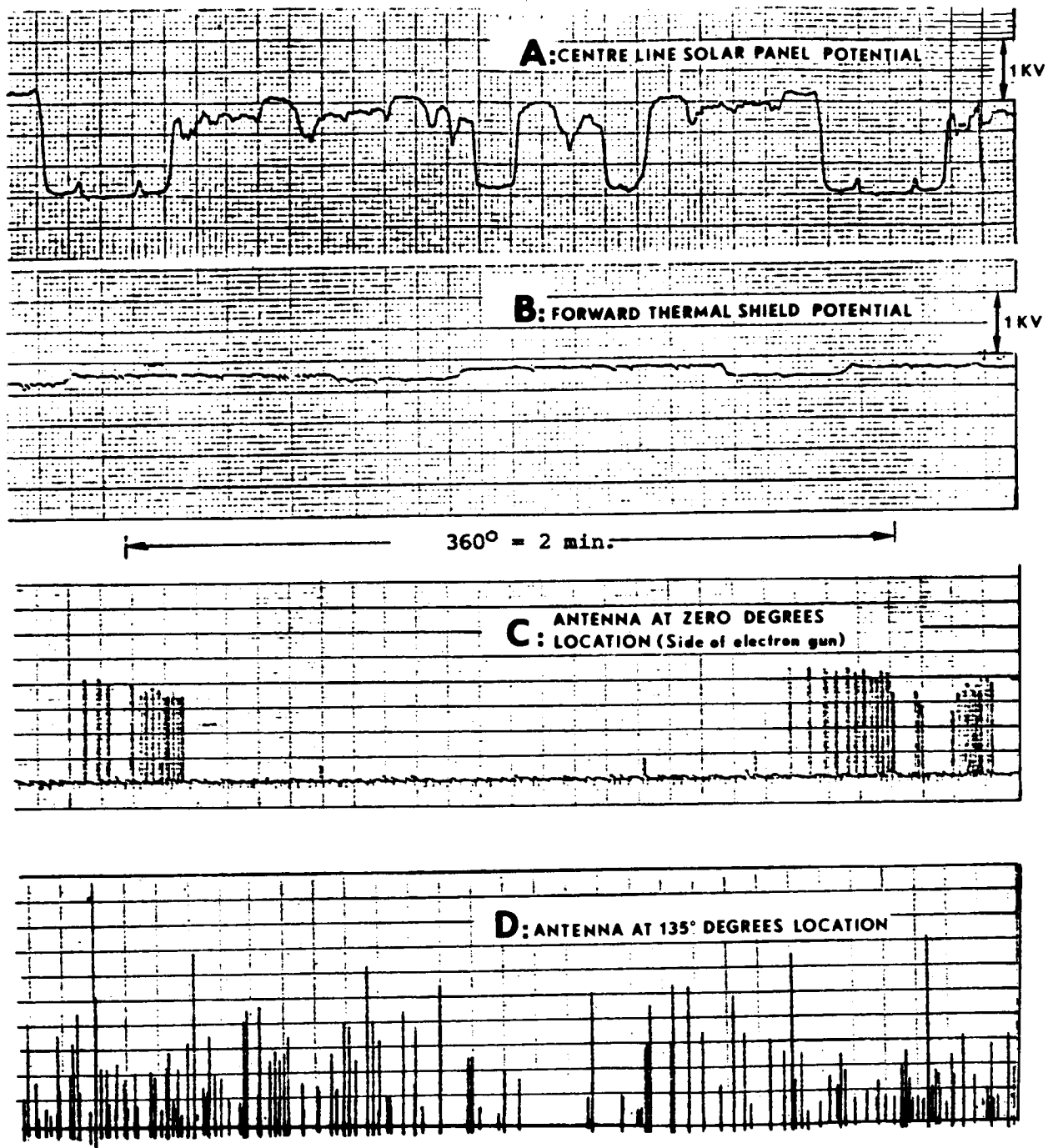
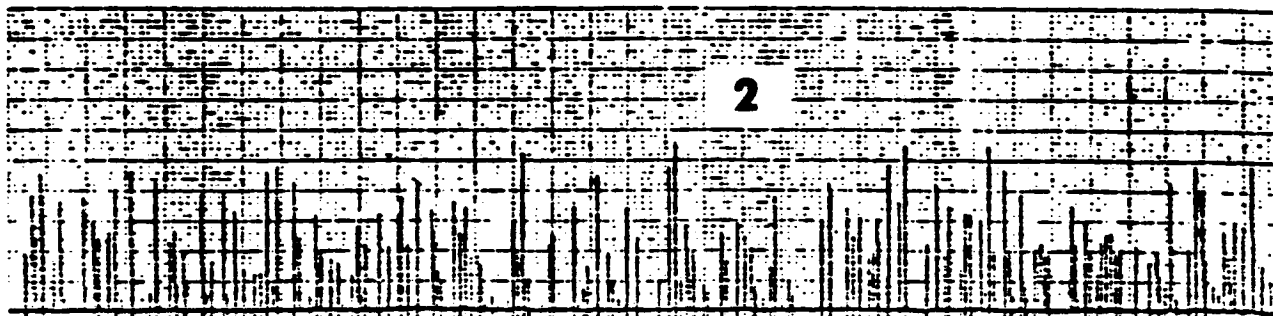
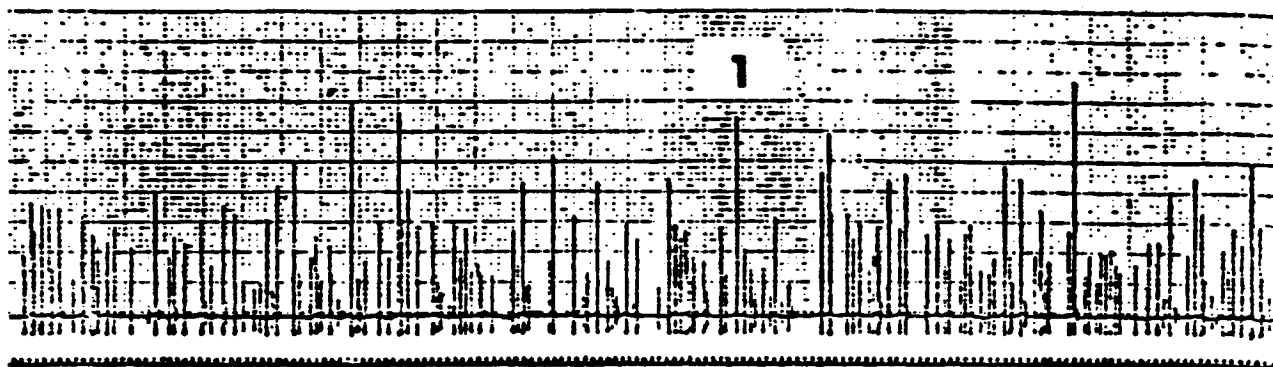
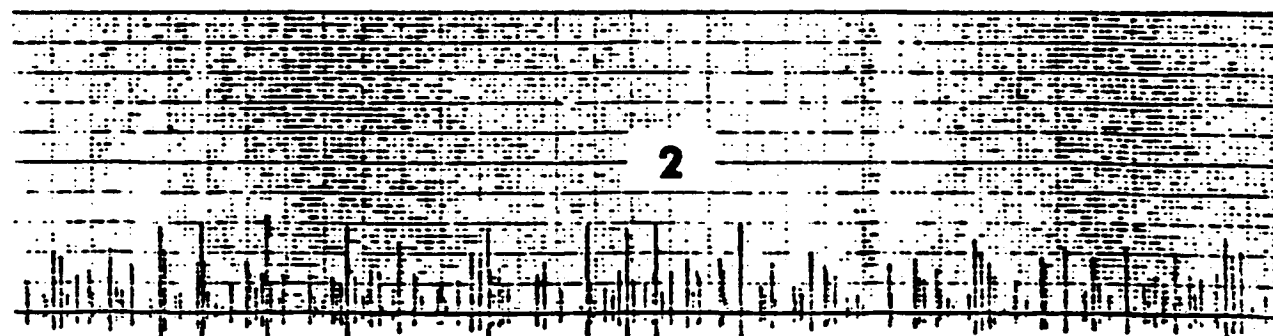
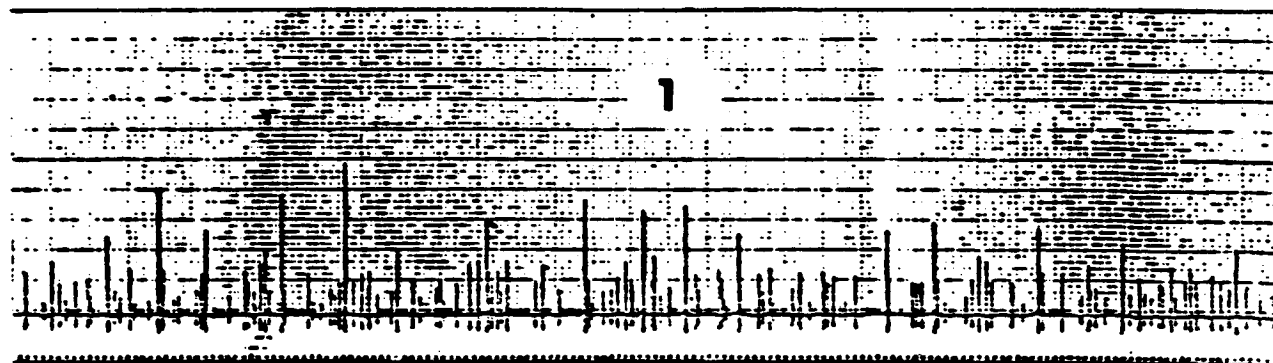


Figure 7. - Typical discharge events under electron irradiation.



BEFORE GROUNDING OF THERMAL SHIELDS



AFTER GROUNDING OF THERMAL SHIELDS

Figure 8. - Effect of grounding thermal shields.

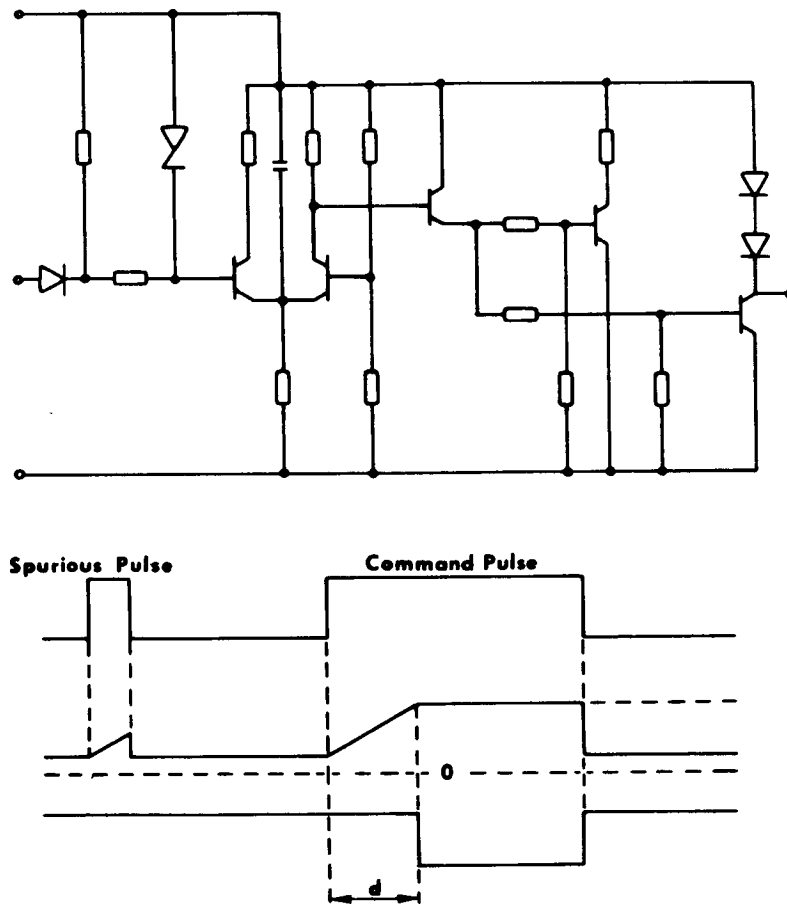


Figure 9. - Improved command interfaces.

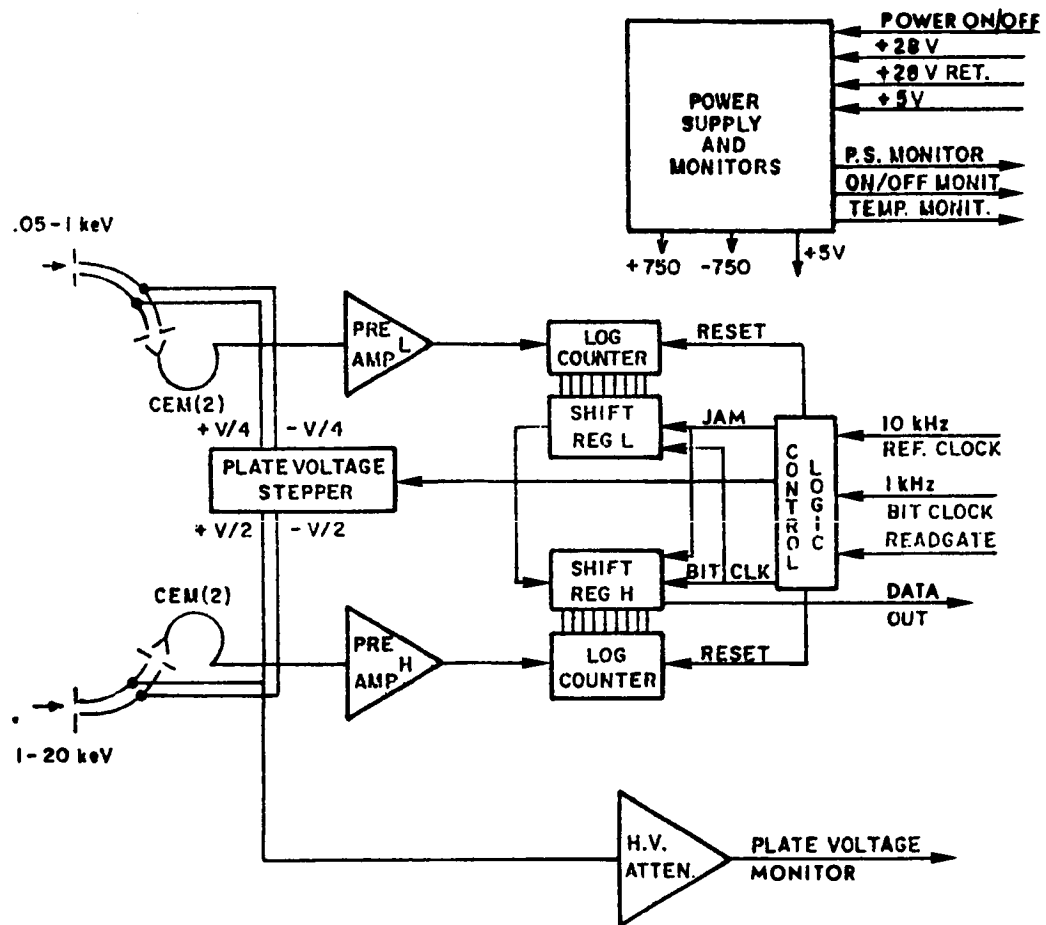


Figure 10. - Electrostatic analyser SSJ/3.



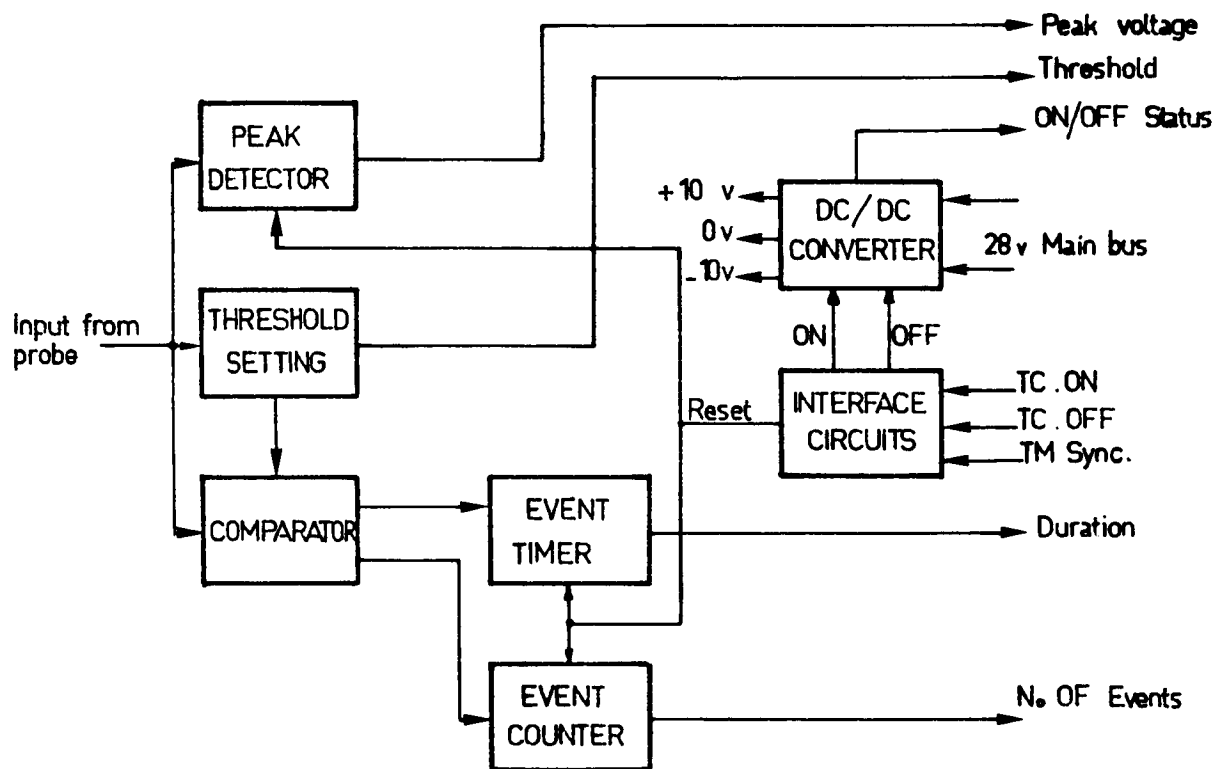


Figure 11. - Electrostatic event monitor.

## **ELECTRON IRRADIATION TESTS ON EUROPEAN METEOROLOGICAL SATELLITE**

**J. Reddy**  
**European Space Agency**

### **SUMMARY**

The observation of in orbit anomalies on **Meteosat** resulted in a test being performed to establish the charging and discharging characteristics of a flight configured engineering model when irradiated with electrons. Surface potentials were measured together with discharge rates and amplitudes.

### **INTRODUCTION**

Following the launch of **Meteosat 1** in 1978, a number of in flight anomalies associated with the radiometer, power and other subsystems were observed (ref. 1). Consideration of the satellite external surface configuration suggested that the most likely cause of the anomalies was the effect on sensitive electronic circuitry of electrostatic discharges. Subsequently a series of discharge tests, using spark gaps, were performed on the electrical model P1, to try to reproduce the effects seen in orbit (ref. 2). At the same time samples of materials i.e. radiometer mirror, thermal shield and SSM were irradiated to establish their charging characteristics (ref. 3).

The results of these studies confirmed the original idea that charging of the satellite due to the electron ( 1-20 keV) environment was responsible for the anomalies. Previously a large scale irradiation facility had been developed by SOPEMEA for ESA suitable for simulating the electron environment in geostationary orbit inside a large vacuum chamber (ref. 4).

It was therefore decided to perform a full scale test on the **Meteosat P1** model, with fully representative external surfaces (i.e. thermal shield, solar panels, etc.) reflecting both the present in flight configuration and the proposed modifications.

**Meteosat 1** has thermal shields and SSM's which are externally aluminized. However the conductive coating is not connected to the satellite ground. It was proposed that **Meteosat 2** should have these surfaces grounded.

## TEST OBJECTIVES

In view of the cost and problems of operating a complete ground station, the test was made on an electrically inert satellite. The test objectives may be summarised as follows:

- a) to measure the induced satellite potentials as a function of incident electron energy
- b) to measure the E-field produced by the discharges
- c) to observe any physical degradation
- d) to observe and locate discharges
- e) to measure the radiometer mirror potential
- f) to observe the variation of charging/discharging characteristics with inclination of the satellite with respect to the incident electron beam
- g) to compare the above measurements for two configurations i.e. satellite external surfaces floating with respect to satellite ground and grounded with respect to satellite ground
- h) finally it was hoped to measure the current discharge by having the possibility of grounding or floating the entire satellite itself

From the above measurements it was hoped to establish whether or not the satellite surface would charge differentially and to define culprit surfaces together with likely amplitudes of discharges.

## TEST CONFIGURATION AND INSTRUMENTATION

### General

A schematic of the test set up is shown in fig. 1. The satellite was mounted on an isolating adaptor ring in the solar simulation facility SIMLES at CNES, Toulouse. The satellite structure was connected to the facility ground by means of a high voltage relay. Switching the relay allowed two satellite configurations to be established i.e. floating and grounded.

Externally the satellite was initially the configuration of F1, with thermal shields isolated from satellite structure and with the F2 flight spare solar panels mounted. Subsequently the satellite was reconfigured to F2 by connecting the external thermal shields to the satellite structure.

The facility instrumentation can be divided into four categories:

- a) Electron source and monitor
- b) Satellite surface potential monitors
- c) Radiometer surface potential monitor
- d) E-field antennas

## Electron source and Monitor

The electron source consists of a conventional electron gun providing a beam of electrons which is diffused by a thin aluminium foil in order to provide an homogeneous beam.

The homogeneity of the beam in the plane of the test object was measured and is shown in figure 2. The electron flux is measured by means of a fixed Faraday cup which is calibrated with respect to given levels in the plane of the test sample. This is monitored continuously during the irradiation.

During the test it was possible to interchange the diffusion foil by means of a simple crank. It should be noted here that after diffusion the electron beam is not monoenergetic. Measurements made at DERTS indicate that the electron energy spectrum will be that shown in figure 3. In this report all electron energy levels are given as the monoenergetic electron energy incident on the diffusion foil.

## Satellite surface potential monitors

To measure the satellite surface potential six TREK potential monitors were installed as shown in figure 4. These probes were mounted on the SIMAT (acronym for the system allowing the satellite to be rotated and tilted simultaneously) and therefore allowed a continuous measurement of the external potential of the satellite as it rotated.

The probes themselves consist of a vibrating fork which samples the electric field and nulls it. Consequently high voltage feed-throughs were required together with intermediate line drivers, in view of the large (14m) separation of the probes from the external equipment.

In principle the separation of the probe from the charged surface is immaterial up to a maximum of 1 cm. However due to the topography of the satellite it was necessary to have a larger separation for which the probes were calibrated (fig. 5).

## Radiometer potential probe

In order to monitor the radiometer mirror surface potential a simple capacitive divider with FET amplifier was used. The instrument, developed by DERTS, was mounted close to the mirror and had a shutter mechanism connected to the satellite ground to provide a reference datum after each measurement.

Data from the sensor was relayed to external monitor using a simple VHF transmitter powered by a battery. Switching of the battery was by means of the solar array.

Because the potential measured is referenced to the satellite ground point the results obtained with this sensor were difficult to interpret and this work is continuing.

### E-field antennas

To monitor the E-fields produced by the discharges six antennas were installed around the satellite. Of these antennas one was calibrated and the resulting E-fields monitored on a BIOMATION 8100 transient recorder.

The other antennas were simple rod antennas mounted on the base of the chamber as shown schematically in figure 6. Four of these antennas were connected to simple detection circuitry to give a count of the number of discharges and to give some idea of the location on the satellite. The fifth antenna was connected to the input of an EMI receiver in an attempt to count only those discharges of high energy i.e. to integrate the pulse height-width product.

### TEST PROCEDURE

The detailed test procedure was defined in ref. 5 and subsequently modified during the test in light of experience gained. Briefly, the test was divided into three phases as follows:

- PHASE A: Satellite vertical and stationary with the radiometer facing the electron gun. After irradiation of duration 1, 2, 4, etc. minutes the satellite was rotated to allow measurement of the potential profile and the radiometer mirror potential. The above performed with the satellite grounded and floating.
- PHASE B: Satellite inclined at  $+ 23^\circ$  and rotating at  $\pm 1$  turn/min. After ten minutes satellite tilted to  $- 23^\circ$ . The objective here was to simulate the inclination of the satellite w.r.t. the sun at soltices. Again the test was performed floating and grounded.
- PHASE C: Satellite inclined at  $+ 23^\circ$  or  $- 23^\circ$  and irradiated for a fixed period and orientations of  $\alpha = 0, 60, 120, 180, 240, 300$  w.r.t. to the electron gun.

For each of the above phases the irradiations were performed with electron energies of 10, 15, and 20 keV.

Phase B and C were performed in both satellite configurations i.e. thermal shields floating and thermal shields grounded to satellite structure.

## PRELIMINARY OBSERVATIONS

Before starting the test a series of tests and controls were made.

A flasher test was performed on each solar panel to ensure each was functioning correctly. This test was repeated after the completion of the whole test and verified that there was no measureable change in the performance of the solar panels. The isolation of the thermal blankets was verified, one was repaired and one correctly isolated after it was found to be arcing at 100v.

No observable degradation was seen as a result of the test. The isolation of the satellite mounting fixture in SIMLES was measured at 500v only and found to be greater than 10 M $\Omega$ . This being the limit of the test equipment.

## TEST RESULTS

The results obtained during the various test phases are summarised in Table 1. Figures 8-10 show the actual surface potential. In view of the fact that the probe separation in the satellite was only measured at intervals of 30° the fine structure of the profile is lost and therefore the original plots are included.

The orientation angle  $\alpha$  is referred with  $\alpha = 0$  as the position where the radiometer mirror is facing the electron gun. Therefore, in view of the position of the probes, i.e. on opposite side of satellite, the plot  $\alpha = 180^\circ$  would correspond to the radiometer facing the probes. (Fig. 7)

Potential plots are only shown for the probe monitoring the satellite circumference. This is due to the fact that considerable difficulty was had in maintaining the correct operation of the probes at all times during the test. During the test some probes became noisy and stopped functioning, other probes started discharging. Unfortunately it was not possible to resolve these problems and the cause of malfunction is being investigated.

It should be pointed out that across the face of the radiometer aperture was placed a metal band connected to satellite structure. Values of  $\alpha = 180^\circ \pm 5^\circ$  correspond to this band.

Clearly evident in these plots are the large potential gradients which can exist together with the relatively low value of satellite structure potential.

The variation of circumferential potential with incident energy is clearly shown in Figure 11.

The discharge activity was assessed quantitatively by the number of counts on the four antenna monitors. With the satellite in the vertical position there is no apparent difference between the antenna readings (Fig. 12). However with the satellite inclined there is clearly a correlation with

antenna position and angle of inclination (figs. 13 and 14).

The measurements of electronic field showed wide differences with a maximum measured field of about 5000 v/m although typical values were between 500 v/m and 1500 v/m. These are shown in figures 15 and 16.

After modifying the external surfaces by grounding them to the satellite the discharge activity was greatly reduced as shown by comparing the antenna readings before and after (fig. 17).

The measurement of generated electric field indicate that the magnitude of the field was reduced by about 20 dB. However, it should be remembered that the grounding of the shields will also improve the r.f. attenuation characteristics should the field be generated inside the satellite structure. This apparent improvement in the generated electric field must be treated with some caution.

#### FINAL OBSERVATIONS

The satellite surfaces were closely inspected before and after the electron bombardment. No visible degradation or effects of any kind were noticeable.

Due to the fact that the satellite was electrically inert it was not possible to see the effects of discharges on the satellite electronics. However, a post check system test verified that no damage was sustained in the electronics during this test.

During the test it was possible to see the discharges occurring over a large part of the satellite. From observations and photos it is clear that the majority of these take place on or around the solar cells with other discharges occurring at the edges of the thermal shield (fig. 18).

#### CONCLUSIONS

It is clear from the foregoing test results that a large number of discharges are possible on the satellite whether or not the external surfaces are grounded.

For the initial measurements we can see that there are very high potential gradients around the satellite which obviously contribute largely to the discharging behaviour.

Results show that the time constant for charging is very small, indicating also that equilibrium conditions are achieved very quickly as the local ambient changes in orbit.

Of particular interest in this test is the comparison between the results obtained with the satellite floating and grounded to the facility.

From a simplistic consideration of the charge-discharge mechanism it would be expected that with the satellite floating no discharges would occur since the satellite should reach equilibrium with the incident electron beam. Where the satellite is grounded a reference plane is obtained which should then propagate discharges.

What has been observed is the opposite. No discharges have been observed when the satellite was grounded and the most intense discharge activity has been obtained with the satellite floating. No explanation of this effect is offered here but the phenomenon will have to be investigated in the future.

There is no indication that the test on P1 with flight solar panels has degraded in any way the optical, thermal, or electrical performance of the satellite. We therefore recommend that this type of test be included as an "acceptance test" for satellites likely to undergo electrostatic charging, to be performed as part of the normal thermal vacuum testing.

In light of experience gained during this test a number of recommendations can be made to improve the quality of data. The most obvious improvement concerns the measurement of surface potential. The inability to measure the potential at all times restricted the scope of the test considerably.

The use of rod antennas to locate the discharges could be extended by employing a matrix of identical antennas.

The auxiliary recording equipment for monitoring the data should be expanded to allow simultaneous records of all parameters to be made. This will allow much better correlation of events during the test.

Finally the addition of on-board satellite monitors will improve the knowledge of coupling mechanisms into the satellite even on an electrically passive model.

#### REFERENCES

1. "METEOSAT Spacecraft Charging Investigation" Final Report ESA Contract 3561/78 F/GG/SC.
2. "Programme d'Essais 'Arcing' METEOSAT P1". Doc 2606/83 TCA May '78 - Aerospatiale/Cannes.
3. "Essais d'Irradiation d'un Miroir de METEOSAT". Etude CERT 4081.



4. "The Qualification of a Large Electron Irradiation Facility for Telecommunications - Satellite - Differential - Charging Simulation". Sérène, Reddy; ESA Journal 1979, Vol. 3.
5. "METEOSAT Irradiation Test Procedure". ESA EOP0 OS/3109-78/DH-JM.

#### TEST SUMMARY

Phase	Satellite configuration	Incident energy	Antenna account	Potentials	E-Field
A1	Floating	10 keV	Few	1 kV	40 v/M
A2	Grounded	10 keV	Nil	1 kV	-
A3	Floating	15 keV	60	3,5 kV	400 v/M
A4	Floating	20 keV	40	6 kV	500 v/M
B1	Floating	15 keV	30	6,5 kV	100 v/M
B2	Floating	20 keV	30	4,5 kV	1200 v/M
C1	Floating	20 keV	20	-	5000 v/M
C2	Floating	20 keV	20	-	5000 v/M
C1.1	Floating	20 keV	Few	4 kV	50 v/M
C2.1	Floating	20 keV	20	4 kV	400 v/M
B1	Floating	20 keV	60	6 kV	150 v/M
EXTERNAL SURFACES MODIFIED					
C1.1	Floating	20 keV	Few L.L	-	40 v/M
C2.1	Floating	20 keV	10	-	400 v/M
B1	Floating	20 keV	Few L.L	-	400 v/M
B2	Grounded	20 keV	Few L.L	-	200 v/M
B3	Floating	15 keV	Few L.L	-	40 v/M
B4	Grounded	15 keV	Few L.L	-	10 v/M
B5	Floating	10 keV	Nil	-	-
B6	Grounded	10 keV	Nil	-	-
B7	Floating	- keV	Nil	-	-
B8	Grounded	- keV	Nil	-	-
C1.2	Floating	20 keV	Nil	-	-
C2.2	Grounded	- keV	Nil	-	-

TABLE 1

TEST SCHEMATIC

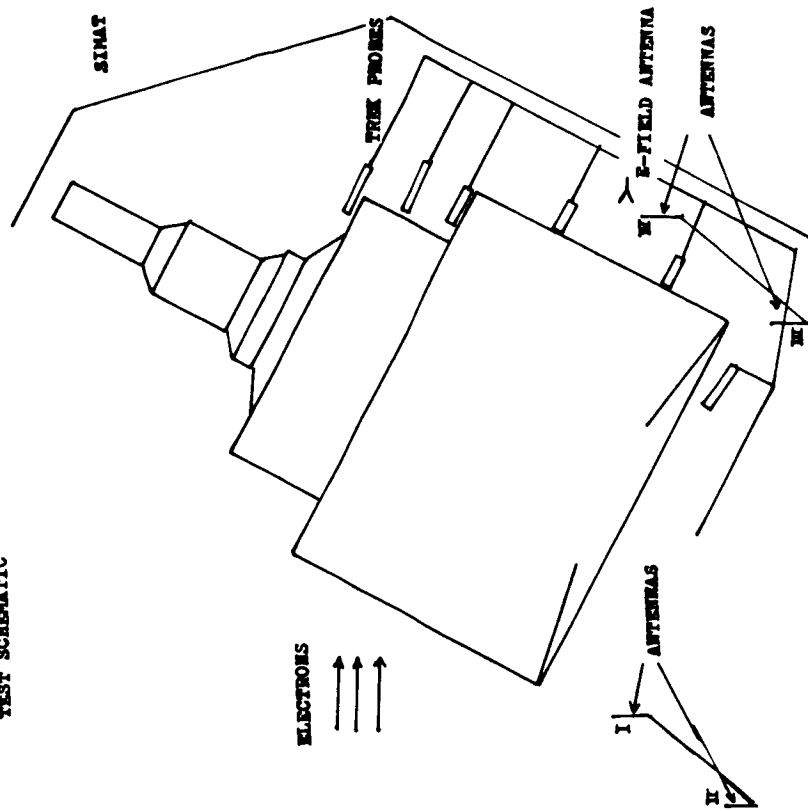
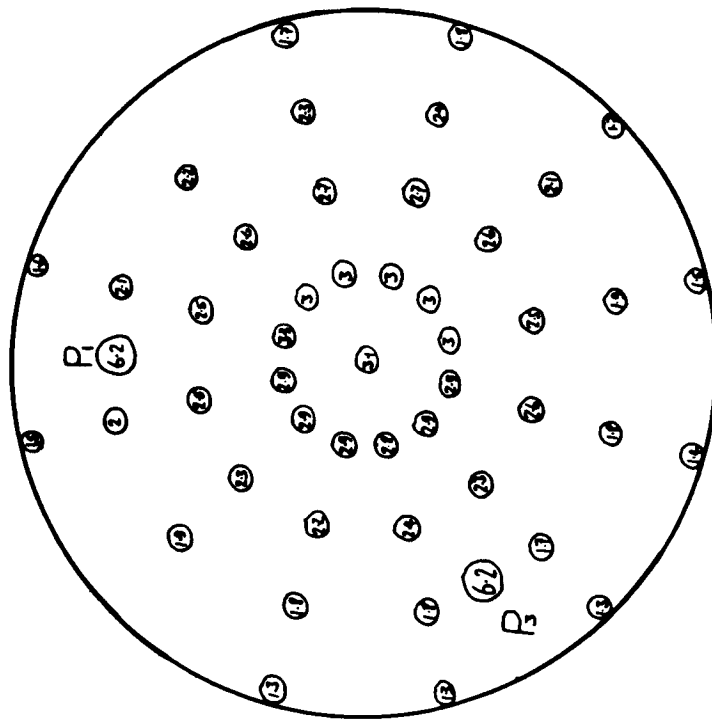


Figure 1



HOMOGENEITY IN PLANE OF SATELLITE ( $\text{nacm}^{-2}$ )  
 $E_1 = 20\text{keV}$   
 $I_1 = 600\mu\text{A}$

Figure 2

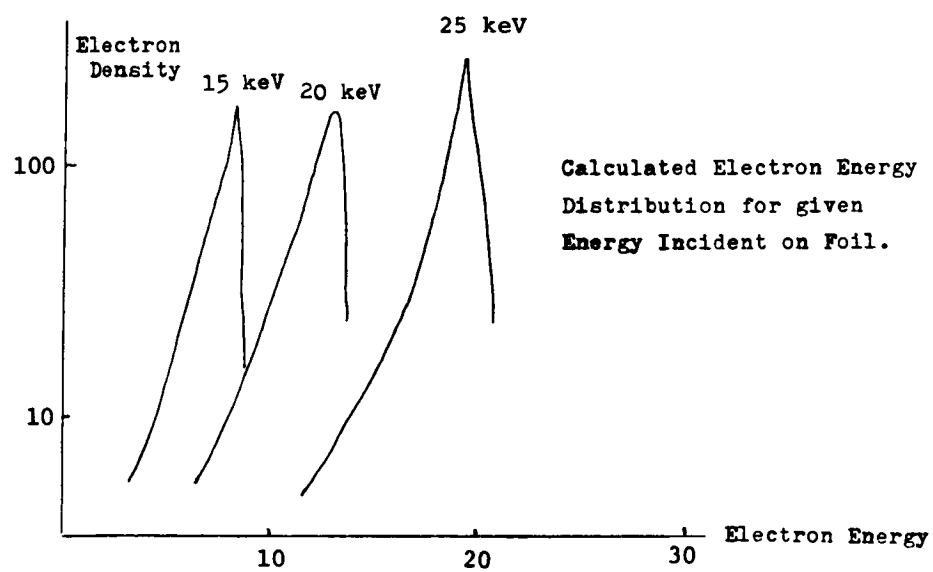
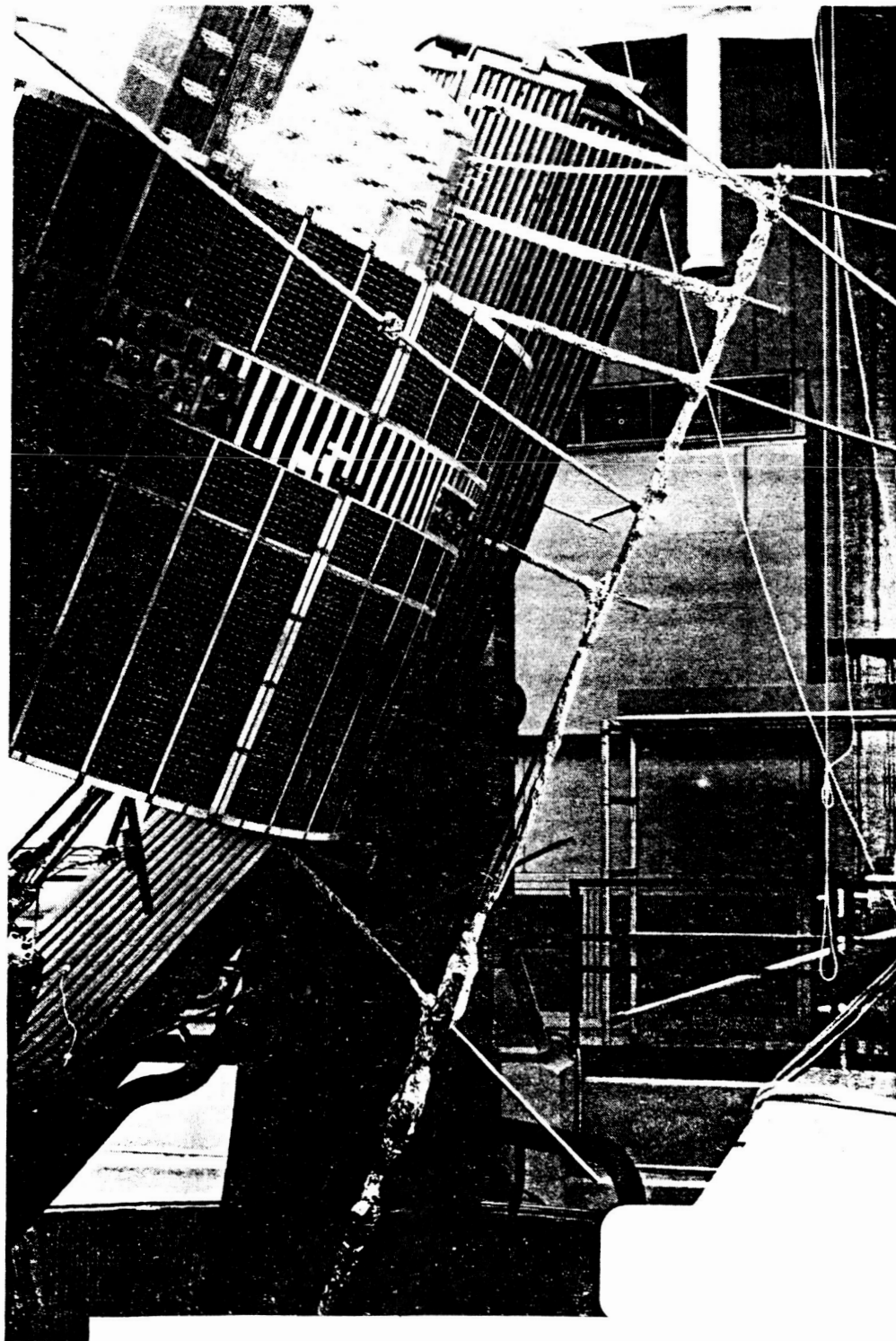


Figure 3



PROBE INSTALLATION RELATIVE TO SATELLITE

Figure 4

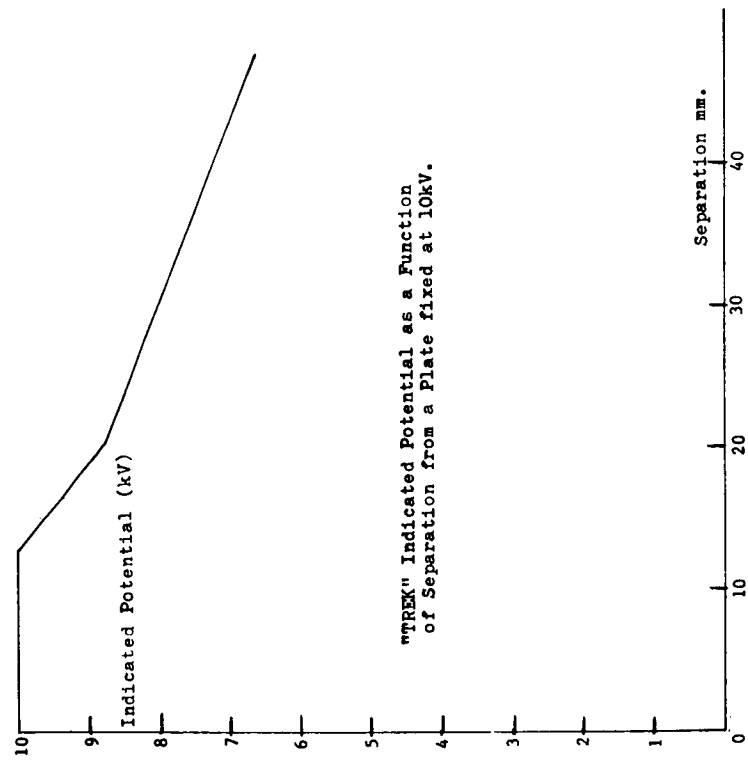


Figure 5

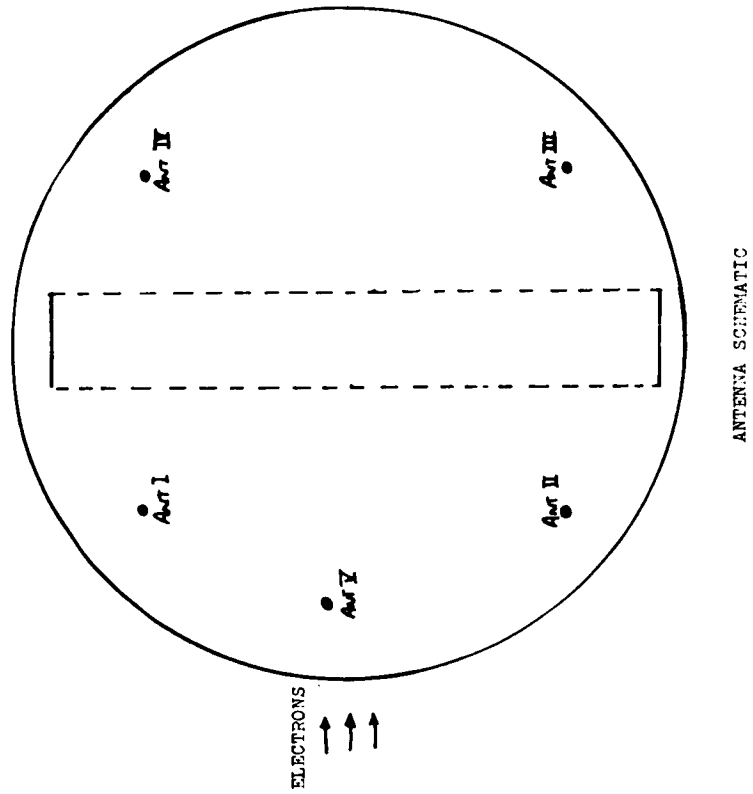


Figure 6

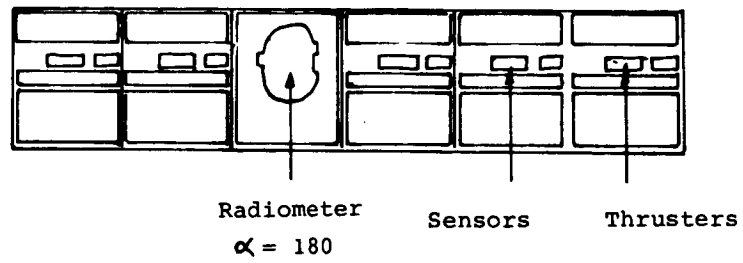


Figure 7

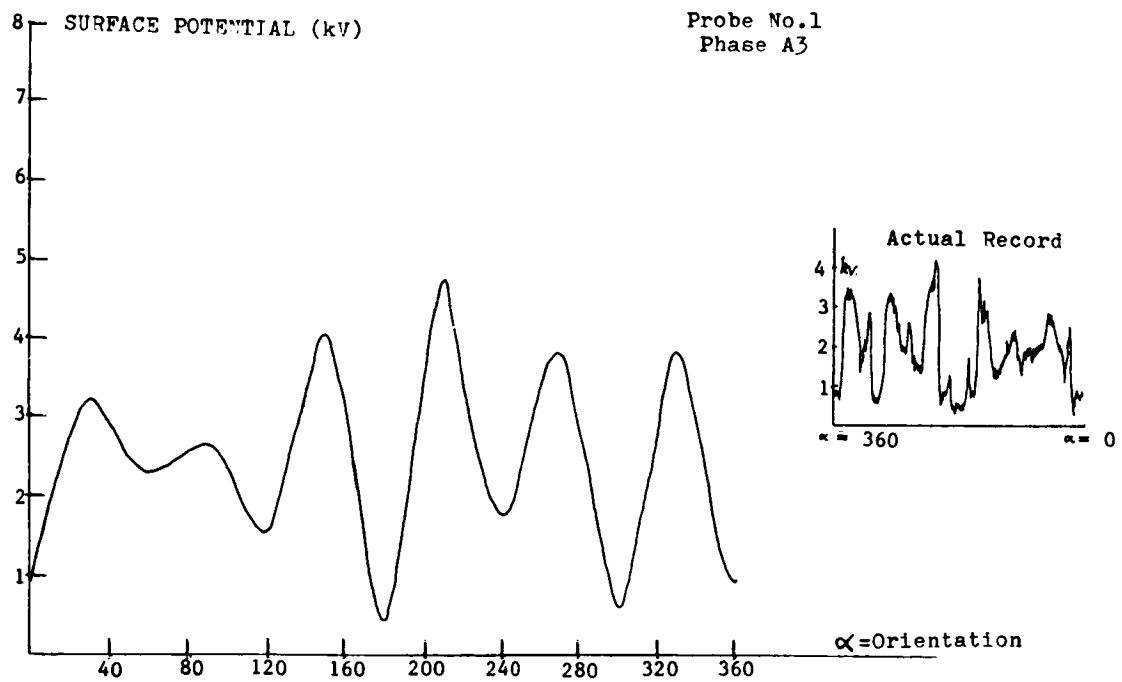


Figure 3

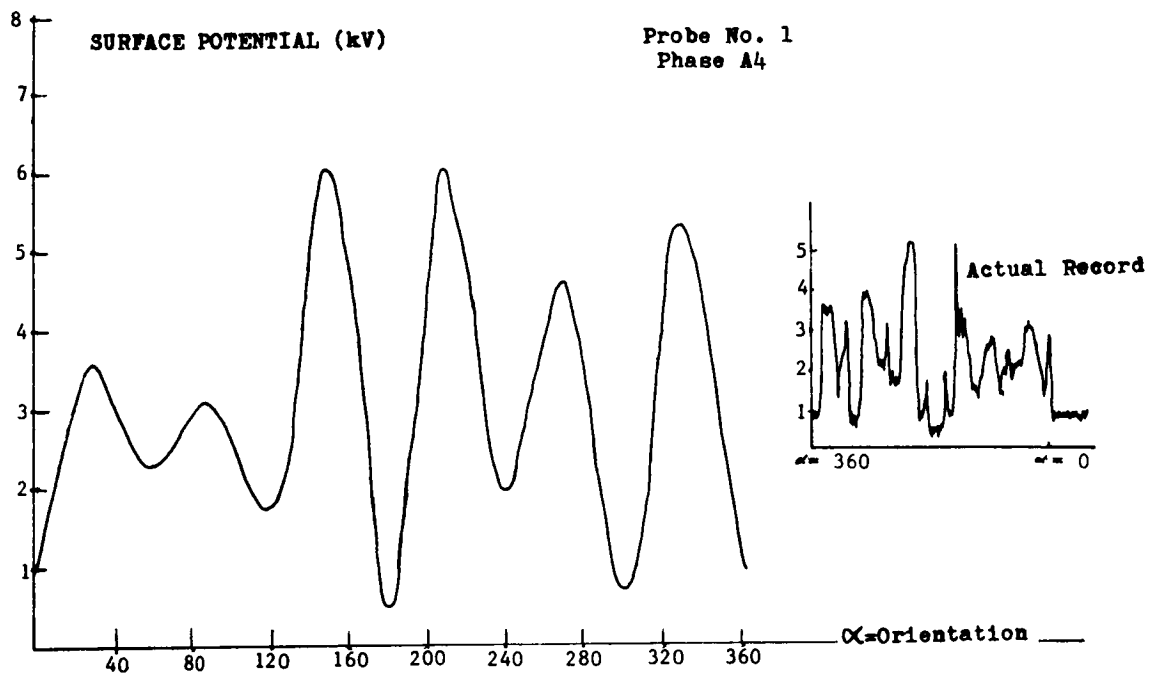


Figure 9

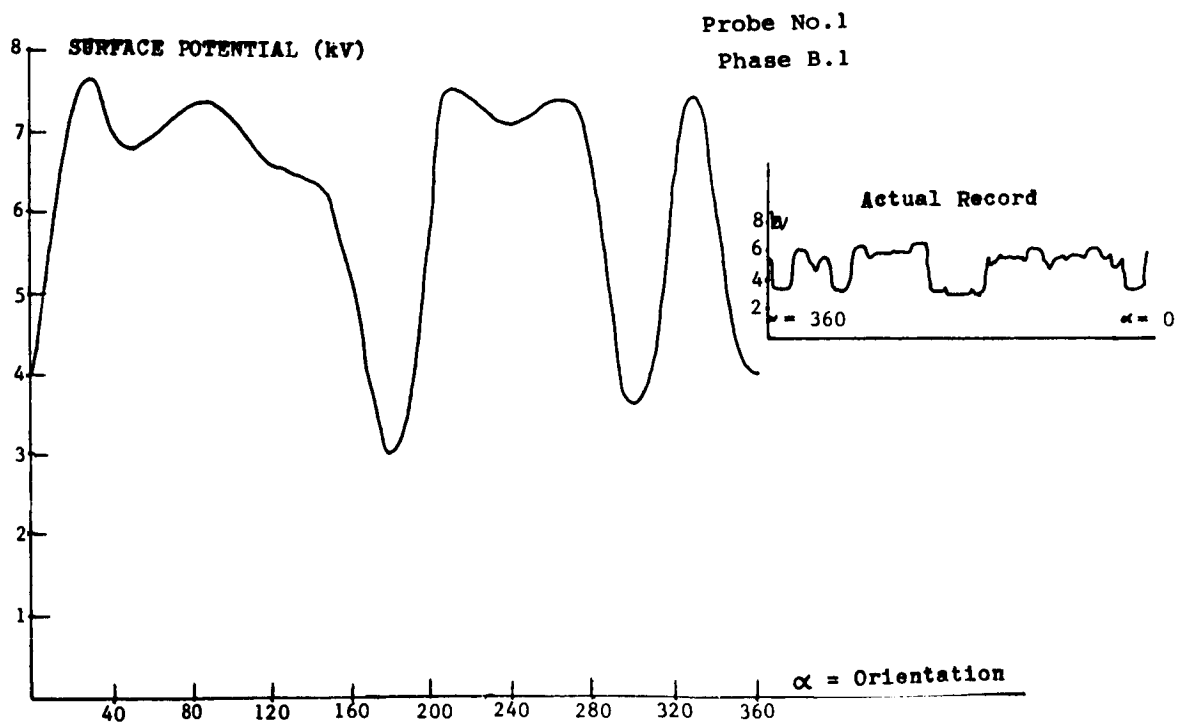


Figure 10

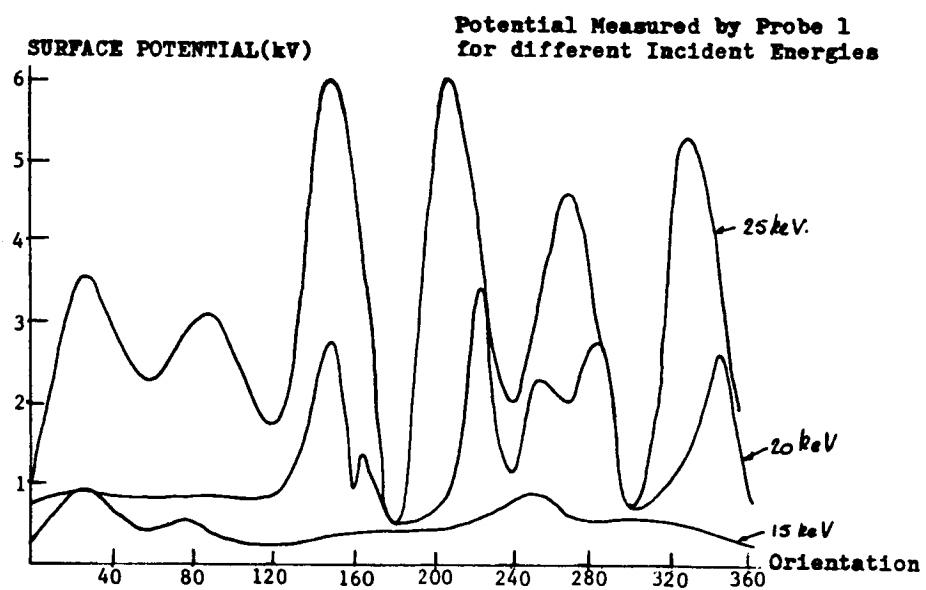
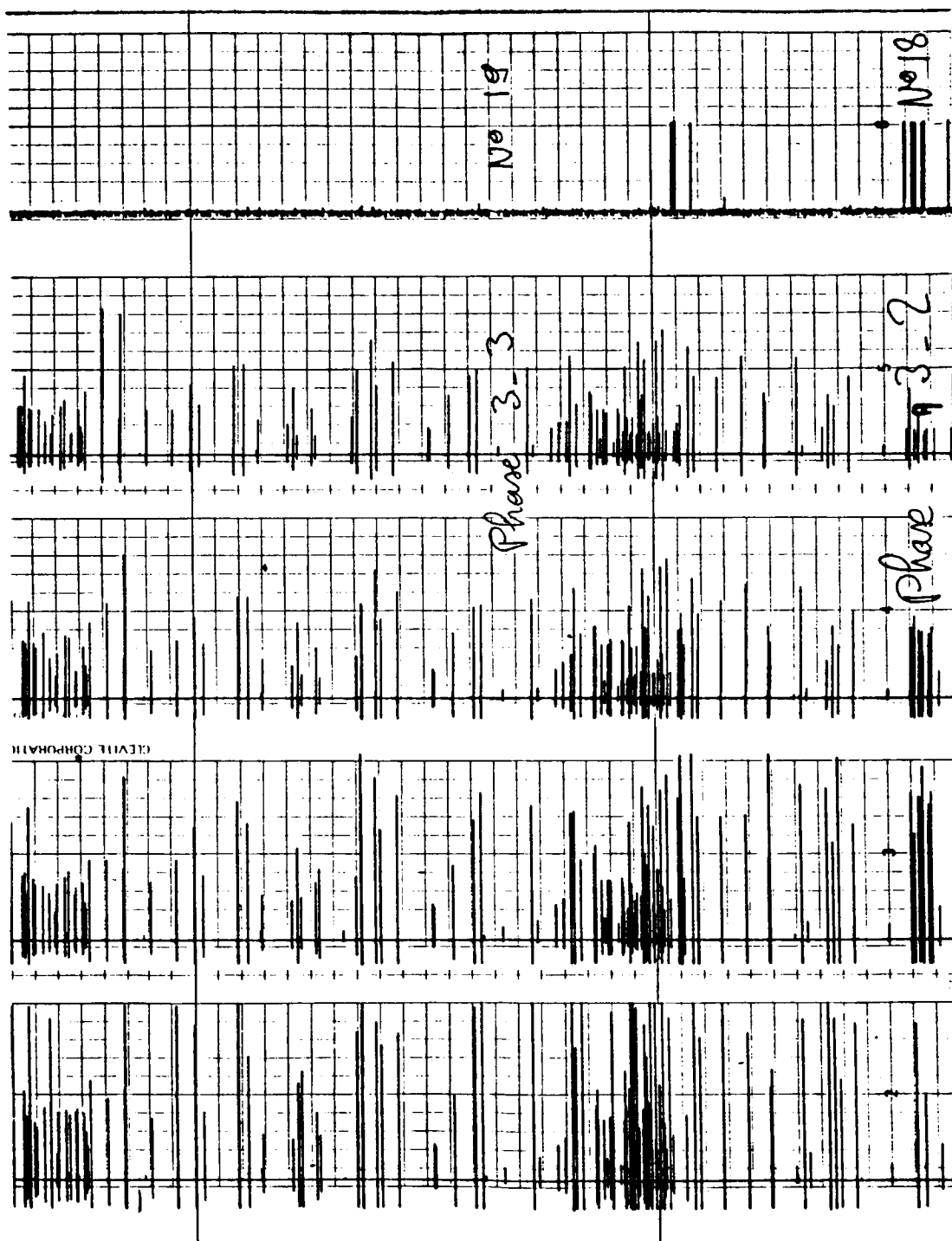


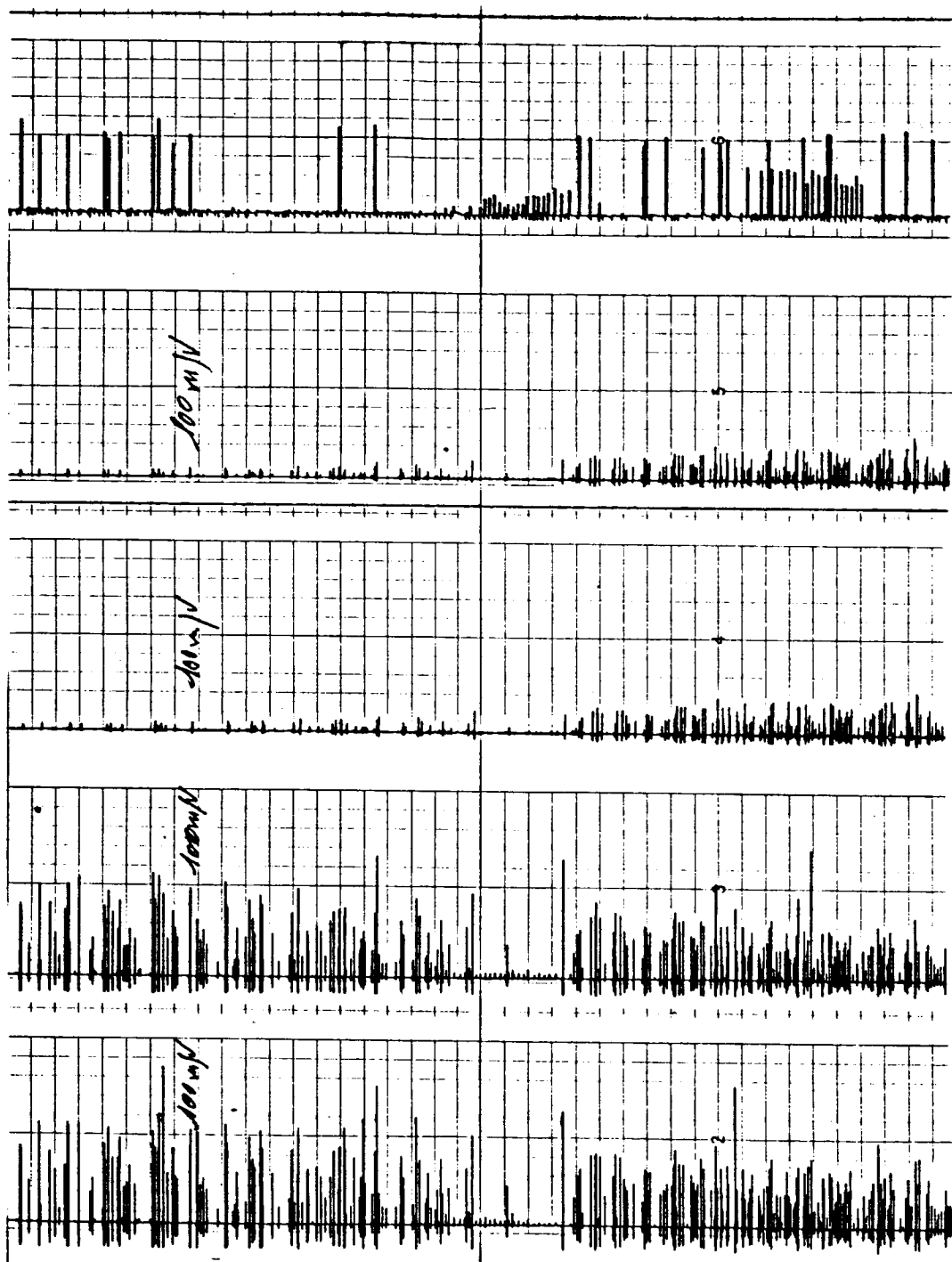
Figure 11





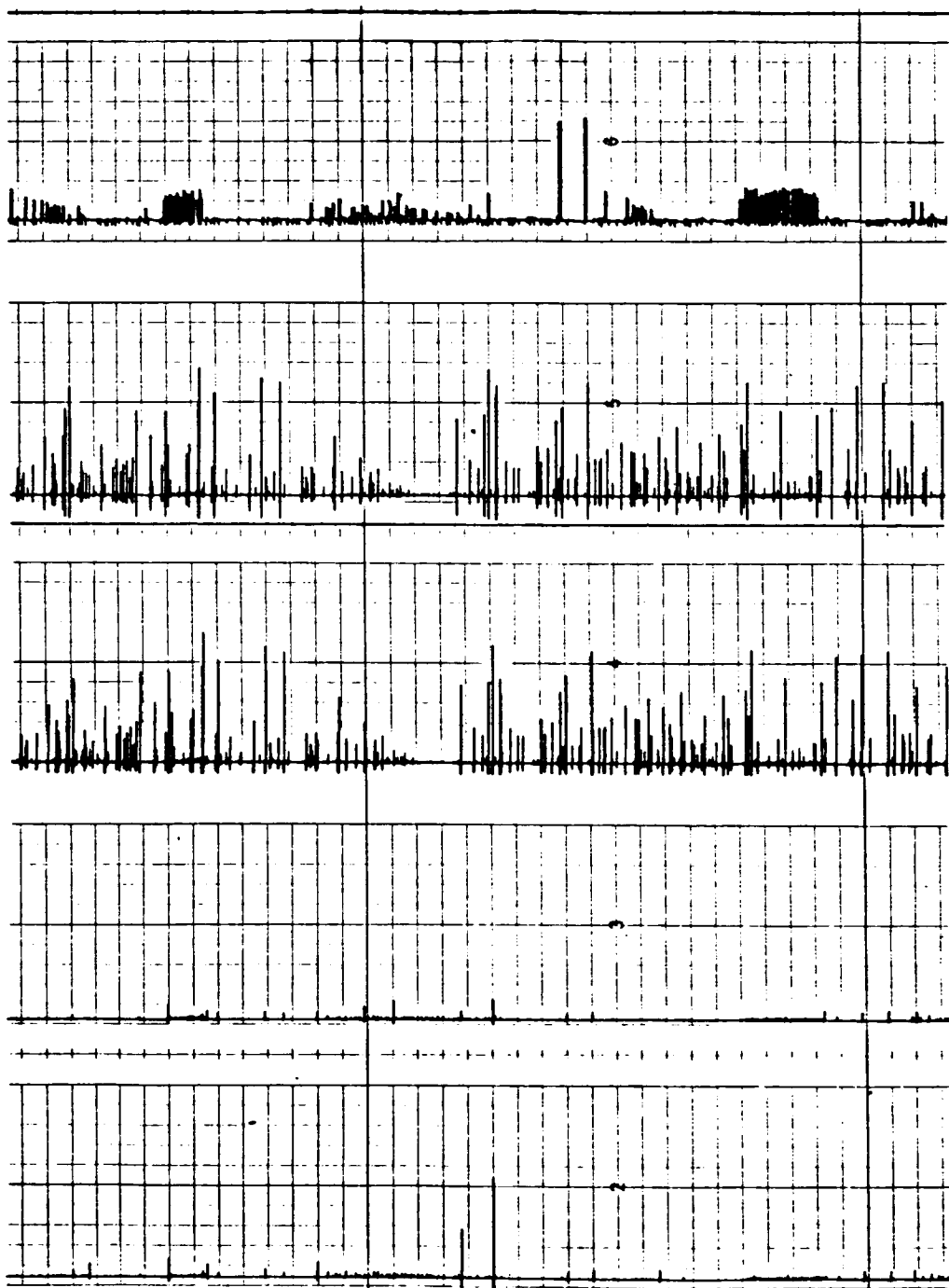
ANTENNA DISCHARGES  
PHASE A3

Figure 12



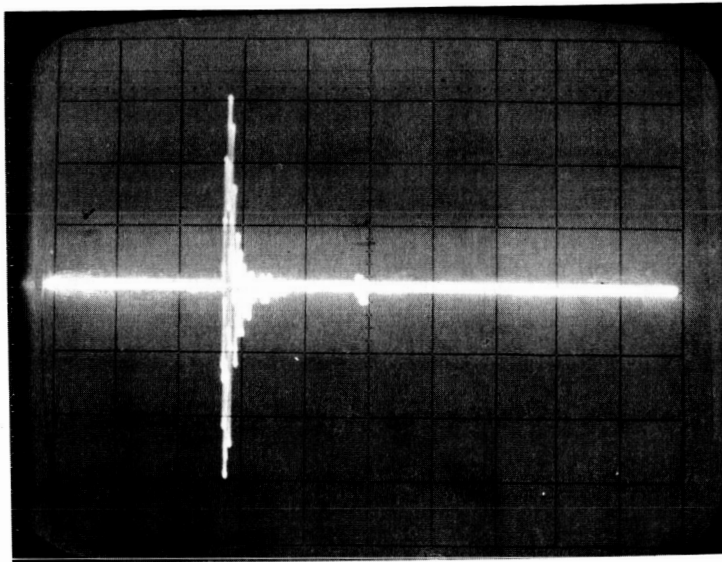
ANTENNA DISCHARGE PATTERN  
 $\beta = +23$

Figure 13



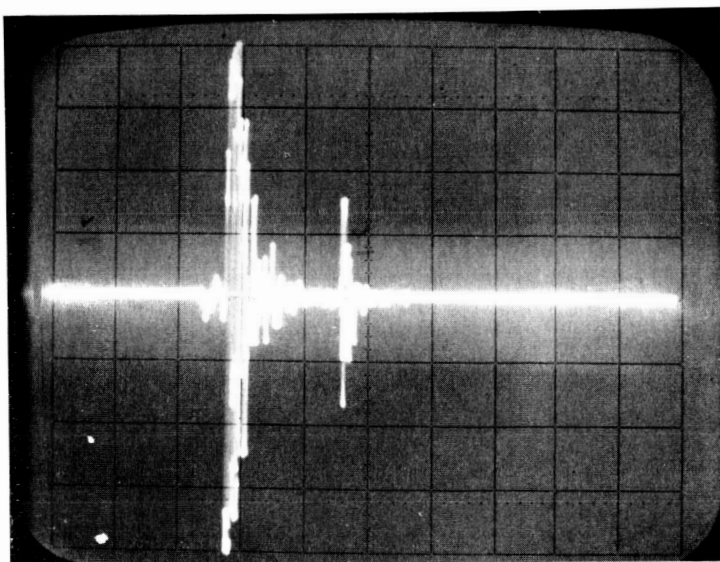
ANTENNA DISCHARGE PATTERN  
 $\beta = -23$

Figure 14



E-Field Discharge  
 500 V/m full scale  
 2 usecs/div  
 Phase B1-4

Figure 15



E-Field Discharge  
 1000 V/m full scale  
 2 usecs/div  
 Phase B2

Figure 16

# TYPICAL DISCHARGE PATTERNS

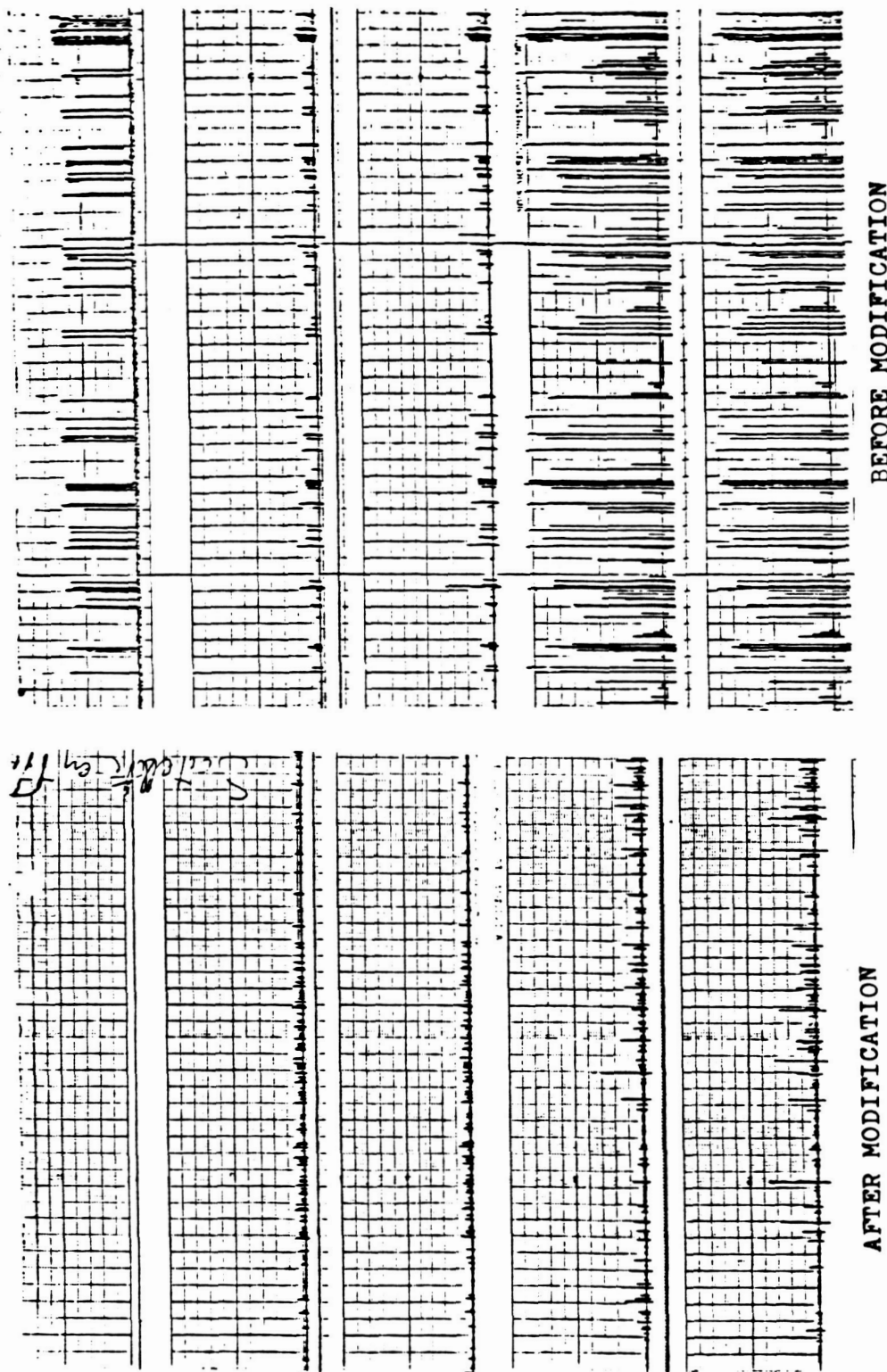


Figure 17

DISCHARGES ON SATELLITE

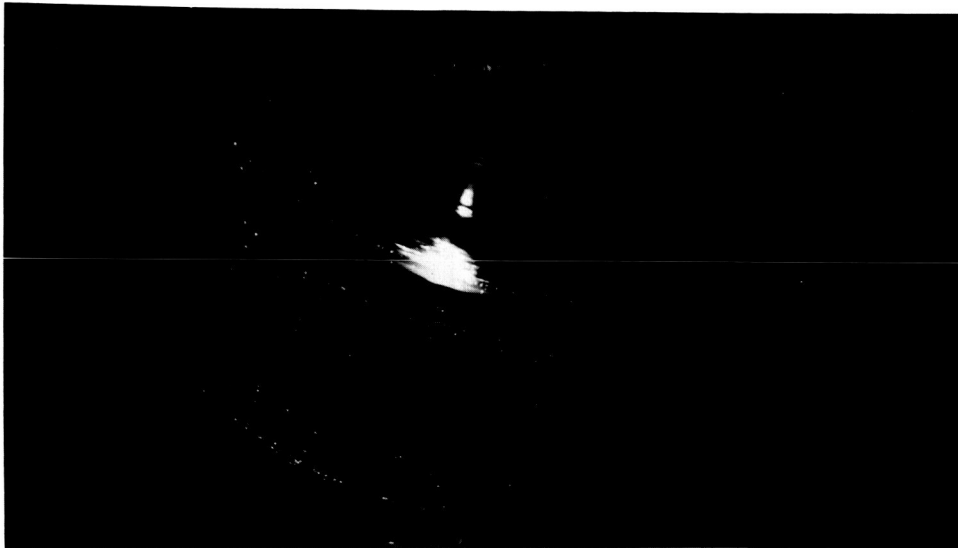


Figure 18

## **SPACECRAFT CHARGING TECHNOLOGY IN THE SATELLITE X-RAY TEST FACILITY**

**Troy J. Sponaugle, Capt., USAF  
Defense Nuclear Agency**

### **SUMMARY**

The Satellite X-Ray Test Facility (SXTF) will be built for studying system-generated electromagnetic pulse (SGEMP) effects on full-scale, operational spacecraft. Pulsed x-ray sources will simulate the environment created by a distant, high-altitude nuclear burst. The facility will be installed in a thermal-vacuum chamber with dimensions greater than 10 m-diameter and 20 m-height and equipped with solar simulators and equipment for simulating the charging environment of space. The spacecraft charging system will consist of several low-energy electron and hydrogen ion sources (5-25 keV), one or two medium-energy electron accelerators (150-300 keV), an array of vacuum-ultraviolet lamps, and geomagnetic field-suppression coils. The facility will be available for testing military, scientific, and commercial spacecraft before launching into the radiation environment of space. Construction of SXTF is scheduled to begin in 1982 and the facility should be available for general use in 1984. Potential users are encouraged to express their needs for specific testing environments in SXTF.

### **INTRODUCTION**

During the 1980's and 1990's, spacecraft will become more and more complicated and vulnerable to threats from the natural radiation environment and from the effects of nuclear weapon detonations in the upper atmosphere and in space. Although there is presently no way to defend a spacecraft from a direct attack, military satellites are designed to withstand the x-ray environment of a distant, line-of-sight nuclear burst. The principal effect of the x-rays is a system-generated electromagnetic pulse (SGEMP) from photoelectrons emitted from the surface of the satellite. Electrostatic charging by space plasmas and photoemission from solar ultraviolet radiation can significantly modify the SGEMP response of a spacecraft under pulsed x-rays.

The Satellite X-Ray Test Facility (SXTF) presently under design by the Defense Nuclear Agency (ref. 1) will be used for SGEMP testing of full-scale, operational satellites in a pulsed x-ray and spacecraft charging environment. The thermal-vacuum chamber will be large enough to accommodate fully-deployed satellites so that testing of a complete system can be performed.

The spacecraft charging technology of SXTF will be useful for environmental testing of military, commercial, and scientific spacecraft which must perform in a plasma and radiation environment. As presently conceived, SXTF will be equipped to simulate visible and vacuum-ultraviolet solar radiation and plasmas with particle energies up to 300 keV in a thermal-vacuum environment.

Construction of SXTF is presently scheduled to begin in 1982 and will be completed in 1984. Potential users of the facility are urged to provide input to DNA on their needs for testing spacecraft in SXTF and information on the specific spacecraft charging environment required.

## SXTF

The Satellite X-Ray Test Facility will be built at one of two existing thermal-vacuum laboratories, either the Mark I Aerospace Environmental Chamber at the USAF Arnold Engineering Development Center (AEDC) near Tullahoma, Tennessee, or Chamber A of the NASA Johnson Space Center, Houston, Texas. The decision between the two locations will be made in the near future.

The Mark I chamber at AEDC is cylindrical with inside working dimensions of 10.4 m in diameter and 20.0 m in height. The chamber is pumped by oil diffusion pumps, liquid nitrogen-cooled coldwalls, and helium-cooled cryopanel to pressures less than  $10^{-7}$  torr. A solar simulator consisting of an array of quartz-iodide lamps can produce up to 110% of a solar constant over the test volume. A planetary albedo and radiance simulator, which is an array of quartz-envelope tungsten filament lamps, is also available. Both the solar and planetary albedo simulator can be adapted for different test vehicle shapes, sizes and requirements. A conceptual diagram of SXTF in the Mark I chamber is shown in figure 1.

Chamber A of the Thermal Vacuum Laboratories at NASA JSC has inside working dimensions of 16.8 m in diameter and 27.4 m in height. The chamber is pumped by oil diffusion pumps, coldwalls and cryopanel to pressures as low as  $10^{-6}$  torr. Xenon and carbon arc lamps simulate the visible and near-UV solar environment. The facility is rated for manned operations inside of the vacuum chamber.

The nuclear weapon simulator will consist of a modular bremsstrahlung source (MBS) and a plasma radiation source (PRS). The MBS is an array of 200 flash x-ray generators; the PRS is an exploding wire or gas-puff source of pulsed soft x-rays. The simulator will deliver  $3-5 \times 10^{-4}$  cal/cm<sup>2</sup> of threat-like x-rays (spectrum, rise time, pulse width) over the surface of large satellites.

The instrumentation (ref. 2) of SXTF, shown schematically in figure 2, will be organized in four data acquisition, monitoring, and control subsystems (DAMCS). The Spacecraft DAMCS will provide power, control, and monitor the status of the satellite under test. The Chamber Environment DAMCS will monitor and control the vacuum system, chamber coldwalls, solar simulators, and the spacecraft charging apparatus. The Photon Sources DAMCS will monitor and control the operation of the MBS and PRS, and the SGEMP and X-Ray DAMCS will use fast transducers and broadband fiber optic links to record the x-ray output of the photon sources and the SGEMP response of the satellite. The operation of the instrumentation subsystems will be supervised at the SXTF Control Console and coordinated by the Master Computer System.



## SPACECRAFT CHARGING TECHNOLOGY

In addition to controlling the vacuum system, chamber cryogenics, solar simulators and planetary albedo simulator, the Chamber Environment DAMCS is responsible for monitoring and controlling the spacecraft charging equipment. This system is presently designed to simulate the charging environment of geomagnetic substorms and medium-energy electrons of natural origin and from plasma injections by distant nuclear bursts. The geomagnetic substorm environment is to be provided by several 5 to 25 keV electron and hydrogen ion floodguns surrounding the test object and an array of vacuum-UV lamps. The medium-energy electrons will be generated by one or two 150 to 300 keV electron accelerators whose beams are rastered over the surface of the spacecraft. A set of magnetic field coils will suppress the vertical component of the earth's magnetic field to assure propagation of low-energy electrons from the guns to the test object.

Table 1 summarizes the preliminary specifications for the spacecraft charging environment. These specifications may change somewhat during the final design of SXTF and can also be altered for special testing programs. The facility is being designed to have considerable flexibility for the spacecraft charging system. Figures 3 and 4 show side views of the reference targets described in Table 1 in the working volumes of the AEDC Mark 1 chamber and NASA JSC Chamber A.

### LOW-ENERGY CHARGING STATIONS

The low-energy electron and hydrogen ion environments will be generated by floodguns on "charging stations" mounted near the wall of the vacuum chamber. The charging stations will be placed in as many as ten locations to provide uniform coverage of the test object. Each station will contain either two conventional electron floodguns operating at different energies, or a "multipactor" electron source which produces a distributed energy spectrum. A duoplasmatron ion gun with a defocused beam will accelerate the hydrogen ions.

Diagnostics will include wall-mounted Faraday cups to monitor the distribution and current density of charged particles which miss the target and beam-probes to monitor the operation of the electron and ion guns.

Figures 5 and 6 show plan views of the reference targets for the low-energy electron and ion floodguns and the proposed locations of the wall-mounted charging stations at the AEDC and the JSC sites.

### MEDIUM-ENERGY CHARGING STATION

The medium-energy electrons (150 to 300 keV) will be provided by one or two electrostatic accelerators mounted on platforms outside of the vacuum chamber near the x-ray source array. The accelerator will produce a  $100\mu\text{A}$  electron beam which enters the chamber through a beam-line isolated from the main vacuum chamber by a gate valve. A magnetic defocusing lens and x-y deflection coils will spread the beam and

raster it over the surface of the target. The rastering driver will be programmed to scan the target's surface as closely as possible to minimize the electron current at the wall of the chamber.

Diagnostics will include the wall-mounted Faraday cups of the low-energy charging stations and probes for direct measurements of the beam divergence and rastering angles at the exit of the deflection system.

## UV SOURCE ARRAY

The ultraviolet source array is designed to partially simulate the hard-UV spectrum of the sun. It is not practical, however, to provide a good spectral reproduction of the sun's emission; for this reason the UV specifications shown in Table 1 are given in terms of photoelectric current density from a reference surface.

The UV source array will be mounted inside of the vacuum chamber near the coldwall and cryopanel. Provisions will be made for mounting the array in several different positions with respect to the satellite under test.

The yield of photoelectrons is a very strong function of the wavelength of the incident radiation, increasing by six decades over a wavelength range of 250 nm to 80 nm for typical spacecraft materials. (ref. 3) The most common sources of vacuum-UV radiation in this wavelength range are discharges in low-pressure noble gases or mercury vapor. Krypton gas, for example, has strong resonance lines at 124 and 117 nm, near the peak of the photoelectric yield of many materials. (ref. 3) Noble gas discharge lamps are used in vacuum-UV monochrometers and are available commercially. Quartz capillary mercury vapor lamps have a strong emission line at 185 nm and, although considerably less efficient in generating photoelectrons, are inexpensive and commercially available in large quantities.

Both noble gas and mercury vapor lamps are being evaluated for the UV source, although an array of low-pressure krypton lamps is presently the preferred design. An array of approximately 100 lamps mounted on a 2 m by 2 m frame would satisfy the UV specifications of Table 1.

## MAGNETIC FIELD SUPPRESSION COILS

The earth's magnetic field in the vacuum chamber is approximately 0.3 gauss, with a dip of about 60° from the horizontal. A magnetic field of this magnitude will severely bend the trajectory of the electrons which must propagate several meters from the low-energy charging stations to the target satellite.

Field coils will be placed around the circumference of the SXTF vacuum chamber to provide a magnetic field to suppress the vertical component of the geomagnetic field. The residual horizontal field of about 0.14 G should not greatly perturb electron beam propagation. The polarity of the magnetic field coils can be reversed to provide a homogeneous magnetic field up to about 1 G for special experiments.

## REFERENCES

1. Anon., "SXTF Description - AEDC and NASA Candidate Sites" (Draft), Defense Nuclear Agency, Washington, DC, August 1980.
2. Sponaugle, T. J., "SXTF Instrumentation System", Report No. 200-81-267/2066, Defense Nuclear Agency, Washington DC, February 1981.
3. Feuerbacher, B. and Fitton, B., "Experimental Investigation of Photoemission from Satellite Surface Materials", J. Appl. Phys. 44, 1563 (1972).

TABLE 1. PRELIMINARY SPECIFICATIONS FOR SXTF  
SPACECRAFT CHARGING TECHNOLOGY

---

### Low-Energy Electrons

Energy: 5 to 25 keV

Flux: 0.05 to 10 nA/cm<sup>2</sup> over a reference cylinder  
4m diam. by 12m high, 7m from x-ray sources

Uniformity:  $\pm 33\%$

### Low-Energy Ions

Energy: 5 to 25 keV

Flux: 1.0 to 250 pA/cm<sup>2</sup> over a reference cylinder  
4m-diam. by 12m-high 7m from x-ray sources

Uniformity:  $\pm 50\%$

Ion Species: Greater than 50% H<sup>+</sup> ions

### Medium-Energy Electrons

Energy: 150 to 300 keV

Flux: 0.1 to 100 pA/cm<sup>2</sup> over reference planes 6m-wide by  
12m-high at 7m, or 6m by 6m at 4m from x-ray sources

Uniformity:  $\pm 33\%$

### Vacuum-Ultraviolet Radiation

Intensity: Sufficient to produce  $0.5^{+0.5}_{-0.3}$  nA/cm<sup>2</sup> of  
photoelectron current density on a tungsten surface  
located anywhere on the reference plane.

Reference Surface: A 6m-wide by 12m-high plane oriented normal  
to centerline of UV source array.

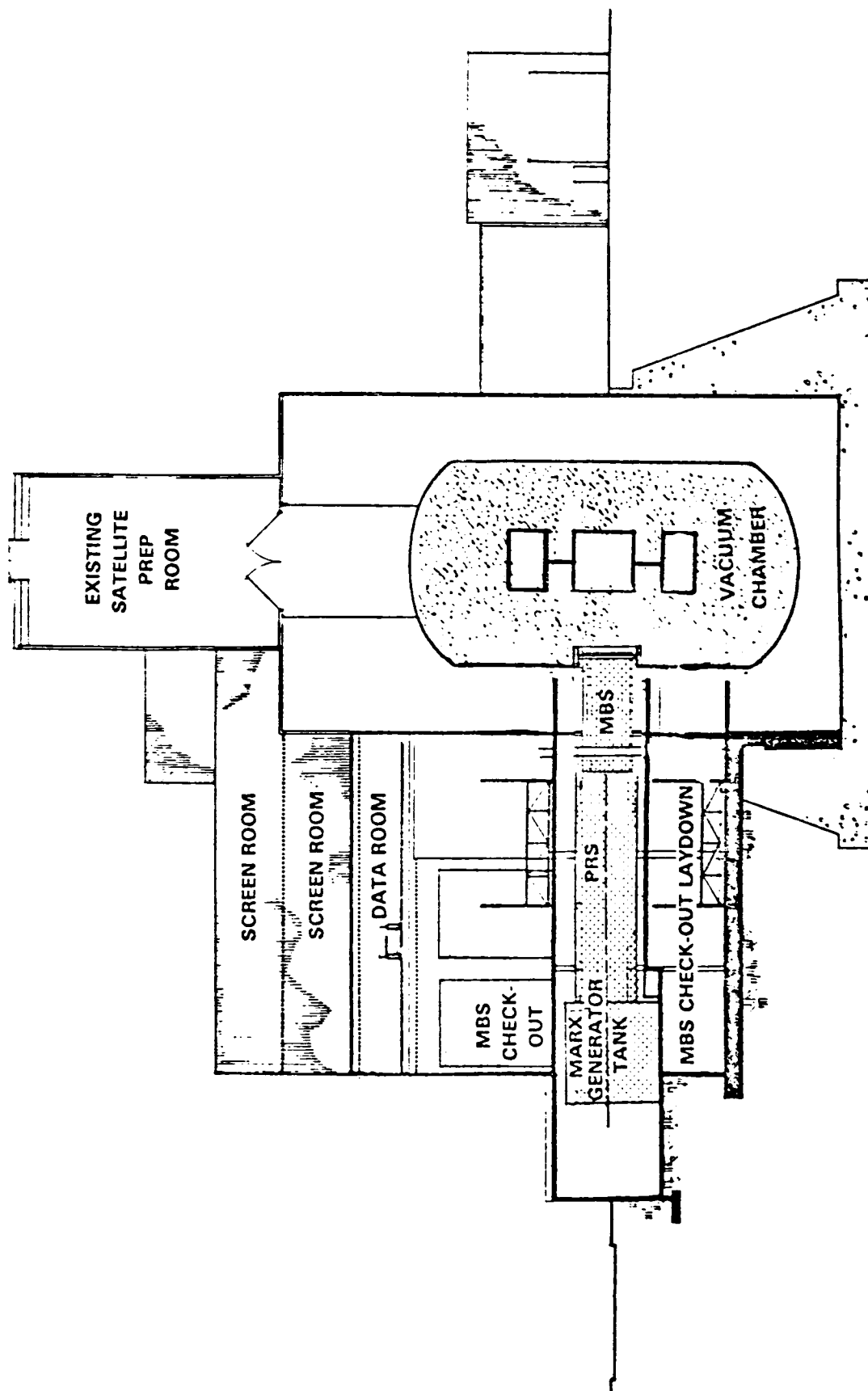


FIGURE 1. CONCEPTUAL DIAGRAM OF SXTF IN AEDC MARK 1 CHAMBER

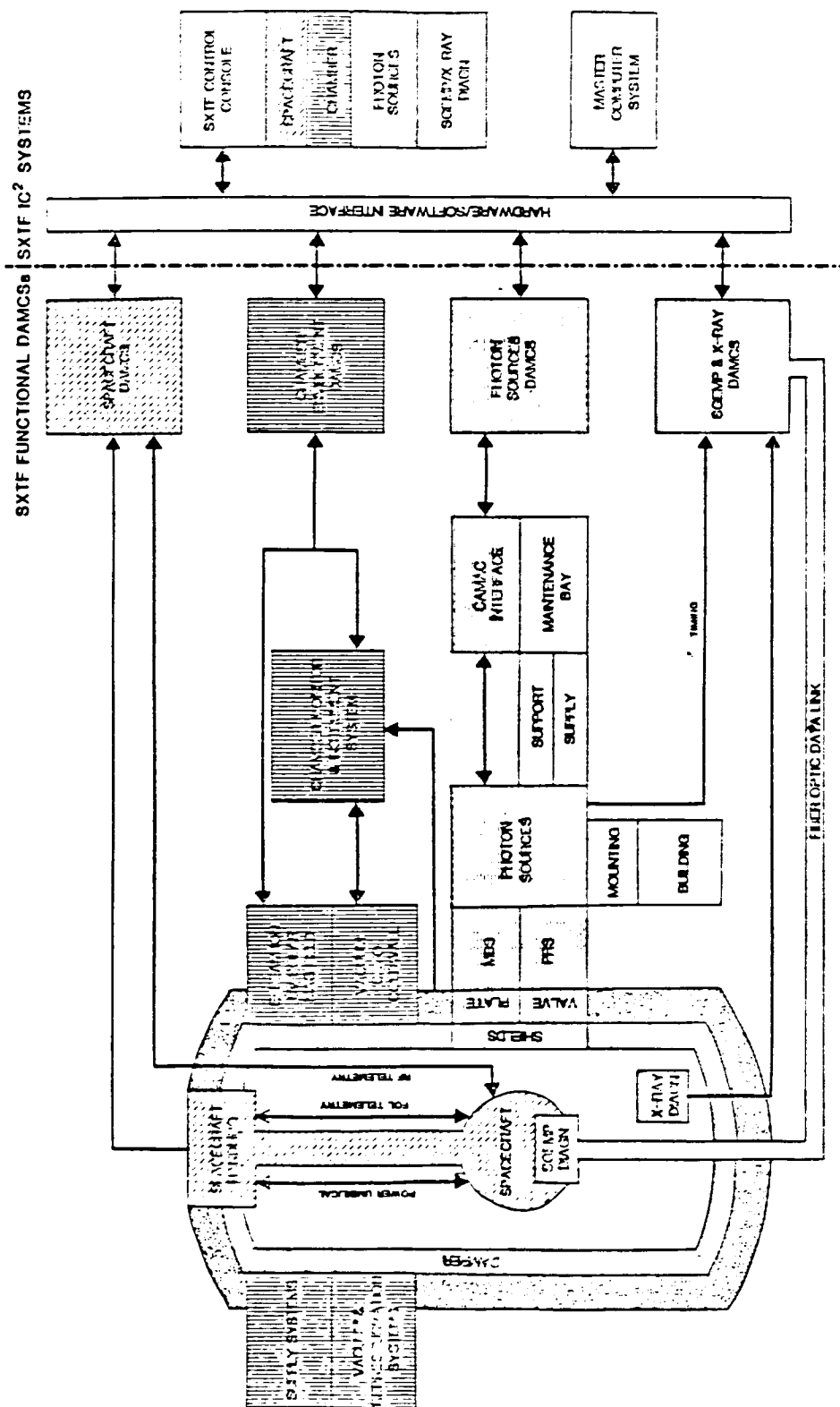


FIGURE 2. SXTF INSTRUMENTATION SYSTEM

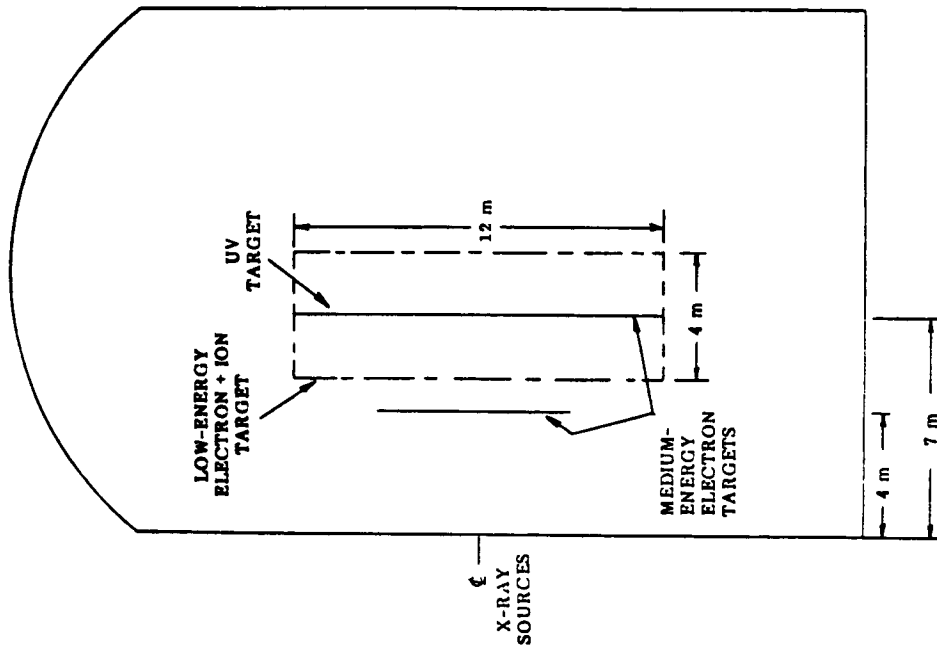


FIGURE 4. REFERENCE TARGETS IN WORKING VOLUME OF JSC CHAMBER A

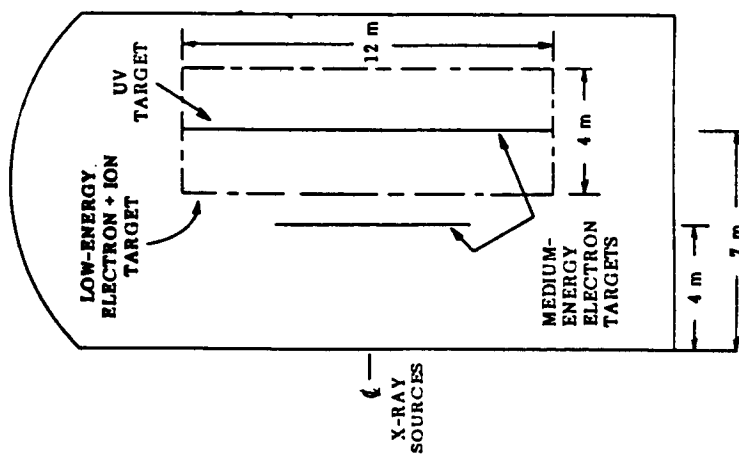
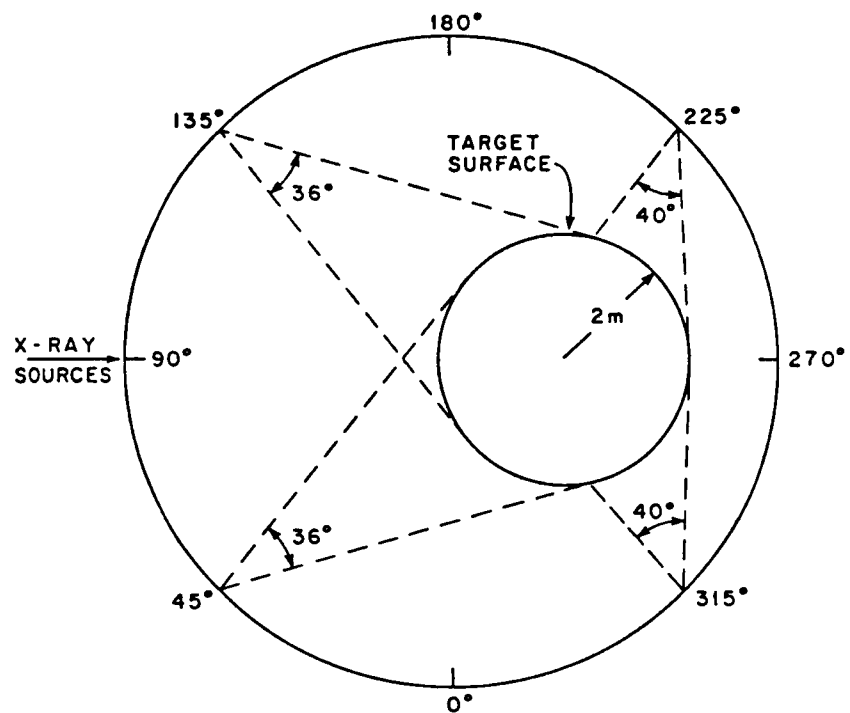
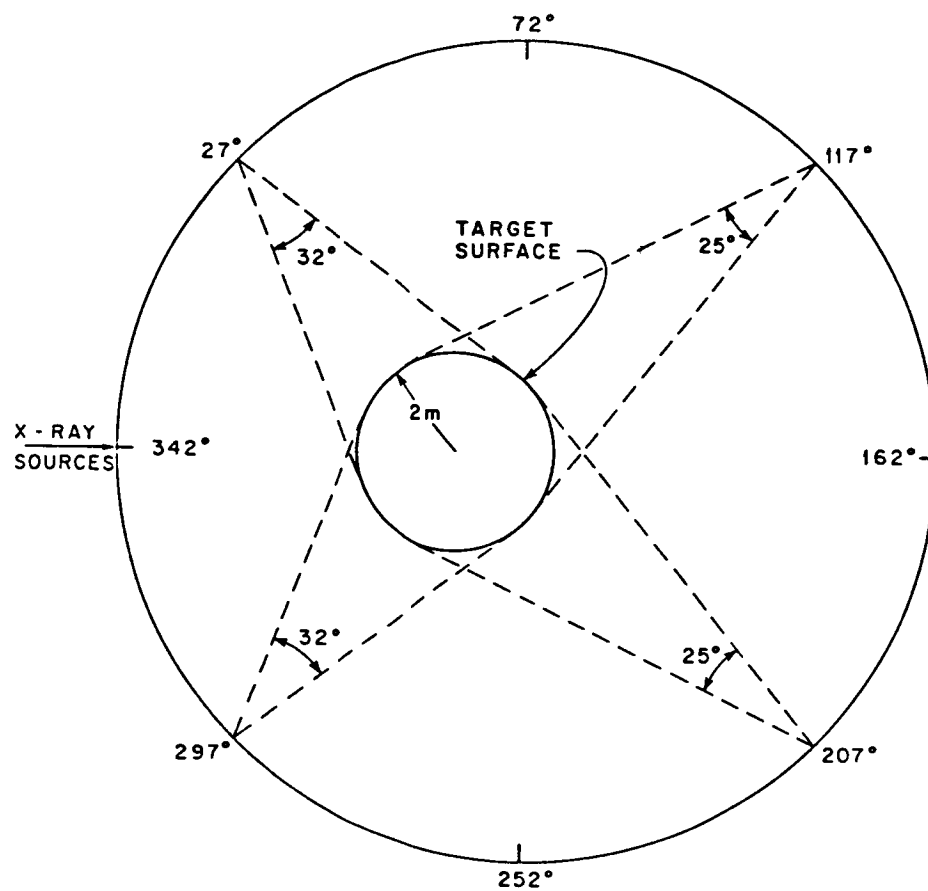


FIGURE 3. REFERENCE TARGETS IN WORKING VOLUME OF AEDC MARK I CHAMBER



**FIGURE 5. PLAN VIEW OF TARGET SURFACE FOR LOW-ENERGY ELECTRONS AND IONS IN MARK I CHAMBER**



**FIGURE 6. PLAN VIEW OF TARGET SURFACE FOR LOW-ENERGY ELECTRONS AND IONS IN CHAMBER A**



# **SIMULATION OF SPACECRAFT CHARGING ENVIRONMENTS BY MONOENERGETIC BEAMS\***

**Ward Halverson  
Spire Corporation**

## **SUMMARY**

We have examined mathematical techniques to choose the energy and current density of monoenergetic beams to simulate the distributed spectra of plasmas in space. In the first approach, the differential current density spectrum of the plasma was divided into a number of energy bands and the beam energy and current were calculated for each band to provide a piecewise reproduction of the distributed spectrum. The second approach was to choose the beam energies and current densities to match the velocity moments of the plasma distribution function. The velocity moments are averages related to physical quantities such as particle density, flux, pressure, and energy flux, and have been used extensively to characterize the measured properties of plasmas in space. Combinations of one, two, and three beams were found to match two to six velocity moments of Maxwellian distributions. The same techniques also can be applied to other spectral shapes, and they were used to examine two-Maxwellian distributions.

A simple computational model was used to compare the charging of a spacecraft by plasmas with distributed spectra and by monoenergetic beams. These calculations were made to gain a qualitative comparison of the approaches for choosing monoenergetic beams to simulate space plasmas. Although a close comparison was not expected when only a few beams were used to simulate the distributed spectrum of a plasma, some combinations of beams gave similar charging rates and equilibrium potentials. The equilibrium potentials found using beams to match velocity moments of a two-Maxwellian plasma generally were within a few kilovolts of charging by the distributed spectrum, but showed more divergence than the simulations of simple Maxwellian plasmas.

## **INTRODUCTION**

Interactions between the plasmas in space and the surface and various subsystems of spacecraft are very complicated and have been the subject of considerable study over the past several years. Electrostatic charging,<sup>(1,2,3)</sup> for example, of a spacecraft's surface can result in discharges which can cause electromagnetic interference,

---

\*Supported by the Air Force Geophysics Laboratory.

degradation of surface materials, and failures of sensitive components. Techniques to influence plasma-spacecraft interactions, such as on-board plasma generators and conductive coatings for dielectrics, are also being actively studied.<sup>(3)</sup>

The plasma environment of space can be partially simulated in the laboratory using low-temperature plasma generators for studies of phenomena in the ionosphere and low-earth-orbit or combinations of electron and ion beams to simulate the conditions in high-altitude orbits. Several small space plasma simulation laboratories<sup>(e.g., 4)</sup> and a few large-scale facilities are in operation<sup>(5)</sup> or being planned.<sup>(6)</sup> Laboratory simulation, however, is necessarily only a partial re-creation of the actual environment to which a spacecraft is subjected.

The selection of the plasma generators or beams to simulate the space environment is now based on intuitive as well as scientific, engineering, and economic grounds. The simulation often represents only the most extreme case expected for a given spacecraft component. There are presently no established techniques for selecting a laboratory plasma environment to simulate the measured or postulated properties of plasmas in space.

The object of this work is to investigate some mathematical techniques which could be used to choose the parameters of monoenergetic beams to simulate space plasmas. The moderate temperature plasmas of geomagnetic substorms serve as examples for simulation, since they are known to cause electrostatic charging on geosynchronous satellites. The multikiloelectronvolt energies and densities of a few particles per cubic centimeter require their simulation by monoenergetic beams rather than by low-energy plasmas with a continuous energy spectrum.

## BEAM SELECTION TECHNIQUES

The plasma environment of space is characterized by a wide variety of particle energies, fluxes, species, and spectral shapes. The particle spectra vary with position in space, time, and solar activity. Models of the environment have been developed in various degrees of complexity, ranging from the definition of average plasma properties such as density and temperature at a given altitude to presentations of detailed spectra of "typical" plasma injection events recorded by instrumented satellites.

In this section we examine techniques which can be used to specify the parameters of multiple monoenergetic charged particle beams which would provide a mathematically correct and physically plausible simulation of a given plasma environment. The techniques are based on the piecewise reproduction of the shape of distributed energy spectra or by matching various averages of the velocity distribution functions by the monoenergetic beams.

In this study we assume that the space plasma to be simulated is of high enough energy and low enough density so that collective effects in the plasma can be neglected. More precisely, the Debye length of the plasma is considerably greater than typical dimensions of a spacecraft. This assumption is justified for the space environment outside the plasmasphere during geomagnetic substorms when strong spacecraft charging events are recorded.

### Piecewise Spectral Reproduction

The simplest and most obvious method to simulate a distributed spectrum is to break the spectrum into several bands and provide monoenergetic beams with appropriate currents and energies to reproduce the distribution in a "piecewise" manner. A very close reproduction of the distributed spectrum can be made in this way, provided there is a sufficient number of available beams.

With a limited number of beams, a problem arises on the choice of the energy boundaries between the parts of the spectrum to be simulated. Possible choices include fractions or multiples of the average energy (temperature) or velocity, or boundaries which divide the particle flux into equal fractions of the total flux. A given spectrum may also be divided to account for particular features, such as a high energy "tail" of the distribution function.

The principles involved in piecewise spectral reproduction can be illustrated by considering a Maxwellian distribution of particle energies. The differential energy spectrum of current density crossing an arbitrary surface is given by

$$\frac{dj}{dE} = j_0 \frac{E}{(kT)^2} \exp\left(-\frac{E}{kT}\right) \quad (1)$$

where

$$j_0 = \frac{qn}{4} \left( \frac{8}{\pi} \frac{kT}{m} \right)^{1/2}$$

is the total current density  $q$  and  $m$  are the charge and mass of the particles.

Integrating Eq. (1) over a range of energy bounded by  $E_1$  and  $E_2$ , we find

$$j(E_1, E_2) = j_0 \left[ \left(1 + \frac{E_1}{kT}\right) e^{-\frac{E_1}{kT}} - \left(1 + \frac{E_2}{kT}\right) e^{-\frac{E_2}{kT}} \right] \quad (2)$$

This current density must be supplied by a monoenergetic beam with an energy between  $E_1$  and  $E_2$  to simulate the corresponding part of the distributed spectrum. The energy of the beam can be chosen in a number of ways; a relatively simple choice is to use the value found by averaging over the differential energy spectrum of the current density.

$$\bar{E}(E_1, E_2) = \frac{\int_{E_1}^{E_2} E \frac{dj}{dE} dE}{j(E_1, E_2)} \quad (3)$$

Integration of Eq. (3) gives,

$$\begin{aligned} \bar{E}(E_1, E_2) = \frac{j_0 T}{j(E_1, E_2)} & \left\{ \left[ \left( 1 + \frac{kT}{E_1} \right)^2 + 1 \right] e^{-\frac{E_1}{kT}} \right. \\ & \left. - \left[ \left( 1 + \frac{kT}{E_2} \right)^2 + 1 \right] e^{-\frac{E_2}{kT}} \right\} \end{aligned} \quad (4)$$

Table 1 gives values for  $j(E_1, E_2)/j_0$  and  $\bar{E}(E_1, E_2)$  for the case of a 10 keV Maxwellian spectrum divided into four ranges of energy with boundaries at 0, 7.5, 15, and 30 keV.

### Velocity Moments

A plasma can be characterized by various averages of the velocity distributions of its constituent particles. In general, the "velocity moments" of a given distribution function,  $f(v)$ , are defined by

$$M_k = 4\pi \int_0^\infty v^k f(v) v^2 dv \quad (5)$$

$k = 0, 1, 2, \dots$

where the  $4\pi v^2 dv$  term represents an infinitesimal element in (isotropic) velocity space.

The velocity moments,  $M_k$ , can be related to physical averages for several values of  $k$ . For example,  $M_0$ ,  $M_1$ ,  $M_2$ , and  $M_3$  are related, respectively, to the average number density  $\langle N \rangle$ , particle flux,  $\langle NF \rangle$ , pressure,  $\langle P \rangle$ , and energy flux,  $\langle EF \rangle$ , of the given particle type in the plasma.

$$\begin{aligned} M_0 &= \langle N \rangle = n \\ M_1 &= 4\pi \langle NF \rangle = n \langle v \rangle = n \left( \frac{8}{\pi} \frac{kT}{m} \right)^{1/2} \end{aligned} \quad (6)$$

$$M_2 = \frac{3}{m} \langle P \rangle = \frac{3\pi}{8} n \left( \frac{8}{\pi} \frac{kT}{m} \right)^1$$

$$M_3 = \frac{8\pi}{m} \langle EF \rangle = \frac{\pi}{2} n \left( \frac{8}{\pi} \frac{kT}{m} \right)^{3/2}$$

$$M_4 = \frac{15}{64} \pi^2 n \left( \frac{8}{\pi} \frac{kT}{m} \right)^2$$

$$M_5 = \frac{3}{8} \pi^2 n \left( \frac{8}{\pi} \frac{kT}{m} \right)^{5/2}$$

The average speed,  $\langle v \rangle$ , in equation (6) is defined by

$$\langle v \rangle = \frac{M_1}{M_0} \quad (7)$$

The expressions on the right-hand side of equation (6) are given for the case of a Maxwellian velocity distribution,

$$f(v) = n \left( \frac{m}{2\pi kT} \right)^{3/2} e^{-\frac{mv^2}{2kT}} \quad (8)$$

where  $n$ ,  $m$ , and  $T$  are respectively the number density, mass, and temperature of the particles and  $k$  is Boltzmann's constant.

A useful method for characterizing a non-Maxwellian plasma is to define effective temperatures which are related to ratios of the velocity moments.<sup>(7)</sup> The average and RMS temperatures are given by

$$T_{AV} = \frac{1}{k} \frac{\langle P \rangle}{\langle N \rangle} = \frac{m}{3k} \frac{M_2}{M_0} \quad (9)$$

$$T_{RMS} = \frac{1}{k} \frac{\langle EF \rangle}{2 \langle NF \rangle} = \frac{m}{4k} \frac{M_3}{M_1} \quad (10)$$

The two temperatures are equal when the velocity distribution is Maxwellian.

#### Monoenergetic Beams to Match Velocity Moments

A technique to simulate a plasma with a distributed velocity distribution is to choose the velocities and particle densities of mononergetic beams so that their velocity moments match those of the plasma. Under these conditions, the average parameters of the beams, such as number density, pressure, or energy flux, are equal to those of the plasma component under simulation.

In general, a single beam can match two moments of the distributed spectrum, so that two beams can match four moments, three beams, six moments, etc. As discussed later, it is also possible to overspecify the problem and use more than the minimum number of beams to match a given number of velocity moments.

A single monoenergetic beam can match two moments according to the simultaneous equations,

$$\begin{aligned} n_b v_b^j &= M_j \\ (j \neq k) \\ n_b v_b^k &= M_k \end{aligned} \quad (11)$$

where  $n_b$  and  $v_b$  are the density and velocity of the beam particles.

For example, when the zeroth (number density) and second (pressure) moments are chosen,

$$\begin{aligned} n_b &= n \\ v_b &= \left( \frac{M_2}{M_0} \right)^{1/2} = \left( \frac{3 k T_{AV}}{m} \right)^{1/2} \end{aligned} \quad (12)$$

or, in terms, of beam energy,  $E_b$ ,

$$E_b = \frac{3}{2} k T_{AV} \quad (13)$$

If the first (number flux) and third (energy flux) moments are used,

$$\begin{aligned} n_b &= \frac{M_1}{v_b} = n \langle v \rangle \left( \frac{m}{4 k T_{RMS}} \right)^{1/2} \\ v_b &= \left( \frac{M_3}{M_1} \right)^{1/2} = \left( \frac{4 k T_{RMS}}{m} \right)^{1/2} \end{aligned} \quad (14)$$

or

$$E_b = 2 k T_{RMS} \quad (15)$$

The densities and velocities of two monoenergetic beams can be found to match the zeroth through third velocity moments of the distributed spectrum by solving four simultaneous equations:

$$\begin{aligned} n_1 + n_2 &= n \\ n_1 v_1 + n_2 v_2 &= n \langle v \rangle \\ n_1 v_1^2 + n_2 v_2^2 &= \frac{3}{m} n T_{AV} \\ n_1 v_1^3 + n_2 v_2^3 &= \frac{4}{m} n \langle v \rangle T_{RMS} \end{aligned} \quad (16)$$

where  $n_1$ ,  $n_2$ ,  $v_1$ , and  $v_2$  are the densities and velocities of the beams, and the velocity moments of the distributed spectrum have been replaced by relations (7), (9), and (10). Boltzmann's constant,  $k$ , has been taken to be unity.

The velocities and densities of the monoenergetic beams can be found analytically,

$$\begin{aligned} v_{1,2} &= \frac{\langle v \rangle}{6 T_{AV} - 2 m \langle v \rangle^2} \cdot \left\{ 4 T_{RMS} - 3 T_{AV} \right. \\ &\quad \left. \pm \left[ 8 T_{RMS} (2 T_{RMS} - 9 T_{AV} + 2 m \langle v \rangle^2) \right. \right. \\ &\quad \left. \left. - 27 T_{AV}^2 \left( 1 - \frac{4 T_{AV}}{m \langle v \rangle^2} \right) \right]^{1/2} \right\} \end{aligned} \quad (17)$$

$$n_1 = n \left( \frac{v_2 - \langle v \rangle}{v_1 - v_2} \right) \quad (18)$$

$$n_2 = n - n_1$$

For a Maxwellian plasma, where  $T_{AV} = T_{RMS} = T$ , equation (17) simplifies somewhat,

$$v_{1,2} = \frac{\pi \langle v \rangle}{6\pi - 16} \left\{ 1 \pm \left( \frac{27}{2} \pi + \frac{128}{\pi} - 83 \right)^{1/2} \right\} \quad (19)$$

The beam densities and energies are then found to be

$$\begin{aligned} n_1 &= 0.382 \, n \\ n_2 &= 0.618 \, n \end{aligned} \quad (20)$$

$$\begin{aligned} E_1 &= 3.007 \, T \\ E_2 &= 0.568 \, T \end{aligned} \quad (21)$$

Six moments of the distributed spectrum can be used to compute the densities and velocities of three monoenergetic beams. No analytical solutions have been found for this case, but iterative techniques can be used to find solutions of the set of six simultaneous, nonlinear equations.

We have used an iterative minimization procedure<sup>(8)</sup> to find the beam velocities and densities in terms of the average speed and density of the plasma particles. For the case of a Maxwellian plasma with temperature,  $T$ , the beam densities and energies are

$$\begin{aligned} n_{1,2,3} &= [0.087, 0.588, 0.325] \, n \\ E_{1,2,3} &= [4.931, 1.657, 0.303] \, T \end{aligned} \quad (22)$$

Different values will be found for other types of velocity distribution functions, but the method used to compute the Maxwellian results is general for all realistic spectral shapes.



## Two-Maxwellian Plasmas

Garrett showed that a two-Maxwellian fit is often a good representation of plasma distribution functions measured during geomagnetic substorms.<sup>(9)</sup> The density and temperature of each Maxwellian component can be found from four velocity moments of the measured spectrum. It is possible, in principle, to find three-Maxwellian fits which match six moments, although the effects of errors in measurement of the plasma spectrum become increasingly exaggerated when computing the high-order moments. It should also be possible to find multiple-Maxwellian least-square fits directly from the measured distribution functions without computing the velocity moments of the data.

A two-Maxwellian distribution has average and RMS temperatures given by

$$T_{AV} = \frac{n_1 T_1 + n_2 T_2}{n_1 + n_2} \quad (23)$$

$$T_{RMS} = \frac{n_1 T_1^{3/2} + n_2 T_2^{3/2}}{n_1 T_1^{1/2} + n_2 T_2^{1/2}} \quad (24)$$

where  $n_1$ ,  $n_2$ ,  $T_1$ , and  $T_2$  are the respective densities and temperatures of the two components of the spectrum.

A single monoenergetic beam can match two velocity moments of the distributed spectrum if its density and energy are chosen according to equations (12)-(15) above. For example, if the beam density is equal to the total plasma density,  $n_1 + n_2$ , and its energy is  $3/2 T_{AV}$ , then the zeroth and second velocity moments of the two-Maxwellian plasma and the monoenergetic beam are equal.

Two methods exist for matching the velocity moments of a two-Maxwellian distribution by two monoenergetic beams. First, the energy and density of each beam can be chosen individually to match two moments of each of the Maxwellian components of the spectrum. In this case, equations (12)-(15) would be employed along with the densities and temperatures of the two-Maxwellian fit.

The second approach is to use the average and RMS temperatures of the two-Maxwellian fit, equations (23) and (24), and to calculate the beam velocities and densities from equations (18) and (18). In both cases, as many as four moments of the two-Maxwellian distribution function can be matched by two monoenergetic beams. In practical situations, physical considerations would be required to make a choice between the two methods of matching velocity moments.

The moments of a two-Maxwellian distribution function can be matched in several different combinations with multiple monoenergetic beams. As in the two-beam case, each Maxwellian component of the plasma can have one or more beams assigned to it which individually match velocity moments. For six-moment matching, three beam energies and densities could be selected using equation (22) for each component, and a total of six beam energies would be required to simulate the two-Maxwellian plasma. As mentioned above, the computed values of the zeroth through fifth moment of the full spectrum can also be used directly to find three beam energies and densities through the iterative minimization procedure.

### Arbitrarily Assigned Beam Energies

The velocity moments of a measured distribution function can also be matched by monoenergetic beams whose velocities are chosen arbitrarily. When the beam velocities are fixed, then it is only a matter of solving a set of linear simultaneous equations for the beam densities. It should be pointed out that not all combinations of beam velocity may be chosen, because negative, and therefore unphysical, solutions for the beam densities can be obtained in some cases. In other cases, the envelope of beam densities is far from being a smooth function of the beam velocity spectrum. The unphysical and intuitively unsatisfying results using arbitrarily assigned beam energies cast doubt on the usefulness of this approach to match velocity moments of distributed spectra.

## SPACECRAFT CHARGING CALCULATIONS

The previous section presented some mathematical techniques to relate the characteristics of undisturbed plasmas to those of one or more monoenergetic beams of charged particles. It was assumed that the plasma or beams produced a flux of particles at a given surface, although no interactions between the particles and the surface were considered.

In this section we shall compare the electrostatic charging produced by plasmas and various combinations of monoenergetic electron and ion beams using a model which accounts for several of the interactions between the incident charged particles and a "typical" spacecraft. The spacecraft charging calculations are, of course, only one of several possible approaches for making a qualitative comparison of the effects of plasmas and combinations of monoenergetic beams. A spacecraft simulation facility, however, will devote a considerable amount of its effort to the study of the effects of electrostatic charging, and this choice for comparison can be justified on these grounds.

## CHARGING MODEL

The spacecraft charging model developed by Garrett<sup>(10)</sup> calculates the equilibrium potential of a surface which receives isotropic fluxes of electrons and ions with arbitrary energy spectra and which loses charge by secondary electron emission, electron backscatter, and photoelectric emission. The model has been rather successful in predicting the potential of high-altitude satellites instrumented to measure the differential energy spectra of electrons and protons in geomagnetic substorm plasmas<sup>(11)</sup>.

The model assumes that the spacecraft can be represented as a spherical Langmuir probe in a plasma whose Debye length is much greater than the dimensions of the probe. The energy spectra of the plasma electrons and ions are divided into 62 energy "bins", and the flux of charged particles to the surface calculated, taking into account the electrostatic potential of the satellite and conservation of mass. Maxwellian, two-Maxwellian, and arbitrary spectra observed from the spacecraft's instrumentation can be loaded into the energy bins.

Secondary electron emission from electron and ion bombardment and electron backscatter are calculated as a function of the incident particle flux and the measured energy dependence of the secondary emission and backscatter coefficients of aluminum. Corrections for the heterogeneous surface of an actual spacecraft are made by small adjustments of these coefficients to bring the calculated potential of the satellite equal to its measured value when the satellite is in "typical" plasma conditions. Charge losses by photoemission are included by an empirical formula.

We have modified the model in two ways. First, the time dependence of charging was included by representing the satellite as an isolated spherical capacitor. The amount of charge gained and lost by the surface is calculated for short increments of time in which the potential is held constant. The net gain of charge is then used to compute the new value of potential to be used during the following time increment. This procedure is repeated until the potential of the model satellite does not vary in succeeding increments of time.

The second modification was used only for potential calculations of the model when irradiated by monoenergetic, initially parallel beams of noninteracting charged particles. It accounts for the electrostatic deflection of the beams in the electric field of the charged body which attracts oppositely charged particles and repels particles of the same sign.

The total current to a surface of arbitrary shape in a parallel beam is simply the product of the current density,  $j$ , and the geometric cross section,  $A$ , in a plane perpendicular to the current density vector. If the initially parallel beam is deflected by a symmetrical potential well, the deflection can be represented as an "effective" cross-sectional area which depends on the strength of the field and the kinetic energy and charge of the particles. The effective area of a spherical conductor of radius  $R$  is,

$$\begin{aligned}
A_{eff} &= \pi R^2 \left( 1 - \frac{q\varphi_s}{|qE|} \right) & (q\varphi_s < |qE|) \\
A_{eff} &= 0 & (q\varphi_s > |qE|)
\end{aligned} \tag{25}$$

where  $\varphi_s$  is the (signed) potential of the sphere, and  $q$  and  $E$  are the (signed) charge and initial kinetic energy of the incident charged particles.

For the charging calculations, the electron and ion current to the model satellite was set equal to the sum of the currents from the monoenergetic beams, each of which was given by  $I_i = j_i A_{eff}$  where  $j_i$  is the unperturbed current density of the  $i^{\text{th}}$  beam with energy  $E_i$ .

The secondary emission current from electron and ion bombardment and the electron backscattering were calculated as a function of the energy of the incident particles by the same subroutines used by Garrett's model for distributed energy spectra. No photoemission was included in the spacecraft charging calculations in order to simplify comparison of the results between monoenergetic beams and distributed spectra.

## Results

The spacecraft charging model was used to calculate the potential of a spherical satellite with a radius of 1 meter and initial potential of zero. The charging by plasmas with several different electron and ion temperatures were compared to charging by beams whose energies and current densities were selected by the methods discussed above. Table 2 presents the parameters of some of the Maxwellian plasmas and beams and for the charging calculations.

Charging by single monoenergetic electron and proton beams and Maxwellian plasma was computed for several beam energies and plasma temperatures. The current densities and energies were selected so that the first (number flux) and third (energy flux) velocity moments of the monoenergetic beams matched those of the Maxwellian plasmas, equations (14) and (15). For this case, the beam energies were twice the corresponding plasma temperature.

$$\begin{aligned}
E_b &= 2 kT \\
j_b &= qn \sqrt{\frac{kT}{2\pi m}}
\end{aligned} \tag{25}$$

where  $n$  and  $T$  are the density and temperature of the Maxwellian plasma component,  $q$  and  $m$  are the charge and mass of the plasma and beam particles (assumed the same species), and  $E_b$  and  $j_b$  are the undisturbed energy and current density of the beam.

Figure 1 shows the charging of the model satellite with a radius of 1 meter under irradiation by single 20 keV electron and proton beams and by a hydrogen plasma in which the electron and ion temperatures are 10 keV. It can be seen that the charging rate and equilibrium potential of the satellite is higher when exposed to the monoenergetic beams, although some differences are to be expected because of the important influence of the secondary electron emission coefficients on the charging process.

The equilibrium potentials found from calculations of charging by Maxwellian plasma and beams with energies and current densities given by equation (25) are compared in figure 2. The correspondence is surprisingly good, considering the crudeness of simulating a Maxwellian velocity distribution by a single monoenergetic beam.

Figure 3 shows calculations of charging by a Maxwellian plasma with an electron temperature of 10 keV and an ion (proton) temperature of 20 keV. Charging by electron beams with an energy of 20 keV and proton beams of 40 keV and current densities for each component given by equation (25) are also shown. In this case, the equilibrium potential in the Maxwellian plasma is somewhat higher than under irradiation by the beams.

The energies and densities required for two beams to match four velocity moments of a Maxwellian plasma are given in equations (20) and (21). We have calculated the charging by two electron and proton beams and in Maxwellian plasmas.

Figure 4 shows the results of the calculations for electron and ion beams with energies of 5.69 keV and 30.1 keV and for a Maxwellian plasma with electron and ion temperatures of 10 keV. The equilibrium potential of the satellite model is more than 2 kV greater for charging by the beams than by the plasma, although the charging rate is about equal for both cases from 0 to 0.05 seconds.

Charging by three monoenergetic electron and three monoenergetic electron and ion beams whose velocity moments match six moments of a Maxwellian plasma was computed using the spacecraft charging model. The beam energies and currents were found from equations (22) to match the velocity moments of a Maxwellian hydrogen plasma with an electron and ion temperature of 10 keV.

The results of the charging calculations are shown in figure 5. There is very close agreement between the charging rates and equilibrium potentials for both the three-beam and Maxwellian plasma cases.

The charging of the satellite model was calculated using beams chosen to simulate the differential energy spectrum of the current density of a Maxwellian plasma. As discussed above, the energy distribution was broken into four parts and the current density and average energy of each part computed, using equations (2) and (4).

Figure 6 shows the charging using the four-beam solution given in Table 1 compared with charging by a Maxwellian plasma with electron and ion temperatures of 10 keV. It is somewhat surprising that the equilibrium potential found with four electron and ion beams chosen to mimic the spectral shape of the Maxwellian plasma is not as close as with other cases with fewer beams.

### Beams and Two-Maxwellian Plasma

The velocity distribution of a non-Maxwellian plasma can be approximated by a two-Maxwellian distribution function, each component of the distribution being characterized by a temperature and a particle density. We have computed the charging of the satellite model in a plasma with a two-Maxwellian electron distribution function and single-Maxwellian ions. The two electron components have temperatures of 10 keV and 30 keV, and densities of  $3.0 \text{ cm}^{-3}$  and  $0.43 \text{ cm}^{-3}$ , respectively. The proton plasma has a temperature of 10 keV and has a number density equal to the total electron density.

We have compared the charging by the two-Maxwellian plasma to that of several combinations of monoenergetic beams. Table 3 shows the beam energies, current densities, and resultant equilibrium potential of the satellite model.

The equilibrium potential found with a single electron beam is presented to show the effect of removing ions from the simulation. Without the ion component, the satellite model charges until the secondary electron emission and backscatter are equal to the incident electron flux. The equilibrium potential is close to that of the electron beam because the secondary electron emission coefficient peaks at an energy of a few hundred electronvolts<sup>(10)</sup> and is small at higher energies.

The single-electron and single-ion beam energies and currents in Table 3 were chosen to match two velocity moments of the two-Maxwellian plasma. The two-electron and single-ion beam energies and currents match the first and third velocity moments (particle and energy flux) of each component of the distribution functions.

The energies and currents of the two-electron and two-ion beam case were found, using equations (17) and (18), to match four velocity moments of the distribution functions, based on the average and RMS temperatures of the plasma particles.

The discrepancies between the calculations of equilibrium potential in the two-Maxwellian plasma and in monoenergetic beams are somewhat greater than those found with a single-Maxwellian plasma. The difference may be caused by the higher temperature component of the electron plasma, which skews the second and third velocity moments of the electron distribution function. The high-energy electron beams required to match these velocity moments apparently have a strong influence on the equilibrium potential of the model.

## DISCUSSION

The calculations give a qualitative idea of the charging which would be observed in a spacecraft testing facility in which monoenergetic beams were used to simulate space plasmas with distributed energy spectra. As expected, the equilibrium potential of the spacecraft under test, and therefore the charge density on its surface, is only a function of the electron and ion beam energies and currents. An important result, however, is the observation that the monoenergetic beams can be chosen to match several velocity moments of a distributed spectrum and, at the same time, produce the same charge density on the spacecraft. Thus, surface phenomena which are influenced, for example, by energy flux as well as charge density can be investigated in a laboratory facility with a reasonable degree of confidence in the simulation fidelity.

It should be made clear that the charging model used here is a very simple one and does not account for the complex geometry or surface details of a real spacecraft. More complicated charging codes exist, however, which could be used to make more detailed comparisons of spacecraft charging by monoenergetic beams and space plasmas. The NASCAP code<sup>(12)</sup>, for example, is probably the most ambitious attempt to represent the geometrical and surface configuration of real satellites in the environment of geosynchronous orbit. Modifications of NASCAP would be required to calculate the charging of a three-dimensional object under irradiation by beams of charged particles, but it is likely that NASCAP would be a useful tool for comparing the conditions of laboratory simulation to those of space.

The author gratefully acknowledges the significant contributions to the work reported here by Betty A. Reid, Stephen N. Bunker and Steven H. Face.

## REFERENCES

1. A. Rosen, editor, Spacecraft Charging by Magnetospheric Plasmas, (M.I.T. Press, Cambridge, Massachusetts, 1975).
2. C.P. Pike and R.R. Lovell, editors, Proc. of the Spacecraft Charging Technology Conference, Report No. AFGL-TR-77-0051, Air Force Geophysics Laboratory, Hanscom AFB, Mass., 1977.
3. R.C. Finke and C.P. Pike, editors, Spacecraft Charging Technology - 1978, NASA Conference Publication 2071, NASA Lewis Research Center, Cleveland, Ohio, 1979.
4. F.D. Berkopce, N. John Stevens, and J.C. Sturman, "The Lewis Research Center Geomagnetic Substorm Simulation Facility", Report No. NASA TM X-73602, NASA Lewis Research Center, Cleveland, Ohio, 1976.
5. O.L. Pearson, "Modification of a Very Large Thermal-Vacuum Test Chamber for Ionosphere and Plasmasphere Simulation", American Institute of Aeronautics and Astronautics, Inc., New York, Paper 78-1625, 1978.

6. W. Halverson, "Modifications of Ionospheric Simulation Capability. Volume 1: Study", Report No. FR-60021, Spire Corporation, Bedford, Massachusetts, 1979.
7. H.B. Garrett, E.G. Mullen, E. Ziemba, and S.E. DeForest, "Modeling of the Geosynchronous Orbit Plasma Environment - Part 2", Report No. AFGL-TR-78-0304, Air Force Geophysics Laboratory, Hanscom AFB, Massachusetts, 1978.
8. P.R. Bevington, Data Reduction and Error Analysis for the Physical Sciences (McGraw-Hill Book Company, New York, 1969), Ch. 11.
9. H.B. Garrett, "Modeling of the Geosynchronous Orbit Plasma Environment - Part 1", Report No. AFGL-TR-77-0288, Air Force Geophysics Laboratory, Hanscom AFB, Massachusetts, 1977.
10. H.B. Garrett, "Spacecraft Potential Calculations - A Model", Report No. AFGL-TR-78-0116, Air Force Geophysics Laboratory, Hanscom AFB, Mass., 1978.
11. H.B. Garrett and S.E. DeForest, J. Geophys. Res. 84, 2083 (1979).
12. I. Katz, J.J. Cassidy, M.J. Mandell, G.W. Schnuell, P.G. Steen, and J.C. Roche, "The Capabilities of the NASA Charging Analyzer Program", Spacecraft Charging Technology - 1978 (see Ref. 3).

TABLE 1.   PIECEWISE REPRODUCTION OF MAXWELLIAN  
SPECTRUM BY FOUR BEAMS

Maxwellian Temperature = 10 keV		
Energy Boundaries $E_1, E_2$ (keV)	Normalized Current Density $j(E_1, E_2)/j_0$	Beam Energy $E(E_1, E_2)$ (keV)
0, 7.5	0.173	4.682
7.5, 15	0.269	11.20
15, 30	0.359	21.49
30,	0.199	42.53



TABLE 2. SPACECRAFT CHARGING BY MAXWELLIAN PLASMAS AND MONOENERGETIC BEAMS

PLASMA		
Electrons:	$T_e = 10 \text{ keV}, j_e = 1.0 \text{ nA/cm}^2$	$\varphi_{eq} = -12.5 \text{ kV}$
Ions:	$T_i = 10 \text{ keV}, j_i = 0.023 \text{ nA/cm}^2$	
Electrons:	$T_e = 10 \text{ keV}, j_e = 1.0 \text{ nA/cm}^2$	$\varphi_{eq} = -14.2 \text{ kV}$
Ions:	$T_i = 20 \text{ keV}, j_i = 0.033 \text{ nA/cm}^2$	
BEAMS		
1 Electron:	$E_e = 20 \text{ keV}$ $j_e = \text{nA/cm}^2$	$\varphi_{eq} = -13.5 \text{ kV}$
1 Ion:	$E_i = 20 \text{ keV}$ $j_i = 0.023 \text{ nA/cm}^2$	
1 Electron:	$E_e = 20 \text{ keV}$ $j_e = 1.0 \text{ nA/cm}^2$	$\varphi_{eq} = -12.9 \text{ kV}$
1 Ion:	$E_i = 40 \text{ keV}$ $j_i = 0.033 \text{ nA/cm}^2$	
2 Electron:	$E_{e1} = 5.69 \text{ keV}$ $j_{e2} = 0.41 \text{ nA/cm}^2$ $E_{e2} = 30.1 \text{ keV}$ $j_{e2} = 0.59 \text{ nA/cm}^2$	$\varphi_{eq} = -15.0 \text{ kV}$
2 Ion:	$E_{i1} = 5.69 \text{ keV}$ $j_{i1} = 0.0096 \text{ nA/cm}^2$ $E_{i2} = 30.1 \text{ keV}$ $j_{i2} = 0.014 \text{ nA/cm}^2$	
3 Electron:	$E_{e1} = 3.03 \text{ keV}$ $j_{e1} = 0.16 \text{ nA/cm}^2$ $E_{e2} = 16.6 \text{ keV}$ $j_{e2} = 0.67 \text{ nA/cm}^2$ $E_{e3} = 49.6 \text{ keV}$ $j_{e3} = 0.17$	
3 Ion:	$E_{i1} = 3.03 \text{ keV}$ $j_{i1} = 0.0037 \text{ nA/cm}^2$ $E_{i2} = 16.6 \text{ keV}$ $j_{i2} = 0.016 \text{ nA/cm}^2$ $E_{i3} = 49.6 \text{ keV}$ $j_{i3} = 0.0040 \text{ nA/cm}^2$	
		$\varphi_{eq} = -11.9 \text{ kV}$

TABLE 3. SPACECRAFT CHARGING BY TWO-MAXWELLIAN PLASMA AND MONOENERGETIC BEAMS

PLASMA		
Electrons:	$T_{e1} = 10 \text{ keV}, j_{e1} = 0.8 \text{ nA/cm}^2$ $T_{e2} = 30 \text{ keV}, j_{e2} = 0.2 \text{ nA/cm}^2$ $(T_e)_{AV} = 12.52 \text{ keV}$ $(T_e)_{RMS} = 14.0 \text{ keV}$	$\phi_{eq} = -14.0 \text{ kV}$
Ions:	$T_i = 10 \text{ keV}, j_i = 0.021 \text{ nA/cm}^2$	
BEAMS		
1 Electron	$E_e = 2(T_e)_{RMS} = 28.0 \text{ keV}$	$\phi_{eq} = -26.8 \text{ kV}$
1 Electron	$E_e = 3/2 (T_e)_{AV} = 18.8 \text{ keV}$ $j_e = 1.1 \text{ nA/cm}^2$	$\phi_{eq} = -12.7 \text{ kV}$
1 Ion	$E_i = 3/2 T_i = 15 \text{ keV}$ $j_i = 0.023 \text{ nA/cm}^2$	
1 Electron	$E_e = 2(T_e)_{RMS} = 28.0 \text{ keV}$ $j_e = 1.0 \text{ nA/cm}^2$	$\phi_{eq} = -19.8 \text{ kV}$
1 Ion	$E_i = 2 T_i = 20 \text{ keV}$ $j_i = 0.021 \text{ nA/cm}^2$	
2 Electron	$E_{e1} = 2 T_{e1} = 20 \text{ keV}$ $j_{e1} = 0.8 \text{ nA/cm}^2$ $E_{e2} = 2 T_{e2} = 60 \text{ keV}$ $j_{e2} = 0.2 \text{ nA/cm}^2$	$\phi_{eq} = -18.2 \text{ kV}$
1 Ion	$E_i = 2 T_i = 20 \text{ keV}$ $j_i = 0.021 \text{ nA/cm}^2$	
2 Electron	$E_{e1} = 7.92 \text{ keV}, j_{e1} = 0.54 \text{ nA/cm}^2$ $E_{e2} = 51.9 \text{ keV}, j_{e2} = 0.46 \text{ nA/cm}^2$	$\phi_{eq} = -19.2 \text{ kV}$
2 Ion	$E_{i1} = 5.69 \text{ keV}, j_{i1} = 0.0096 \text{ nA/cm}^2$ $E_{i2} = 30.07 \text{ keV}, j_{i2} = 0.014 \text{ nA/cm}^2$	

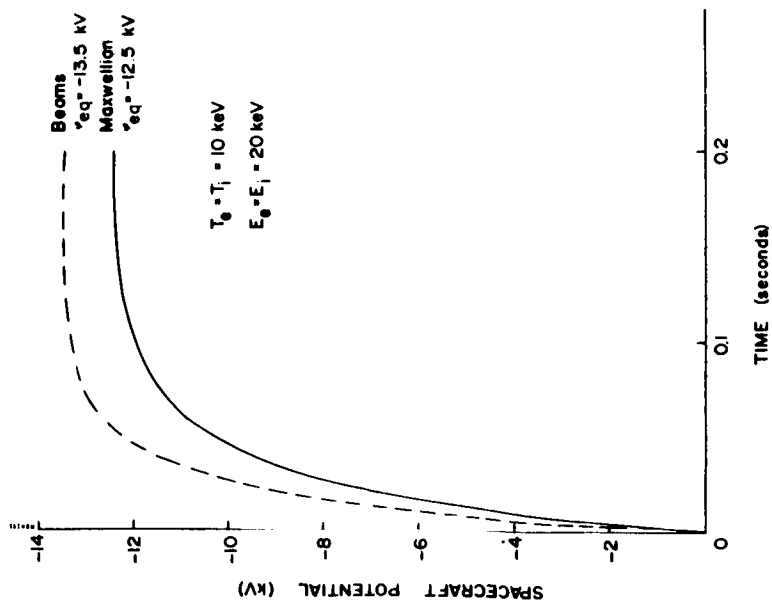


FIGURE 1. SPACECRAFT CHARGING BY 10 keV MAXWELLIAN PLASMA AND 20 keV ELECTRON AND ION BEAMS

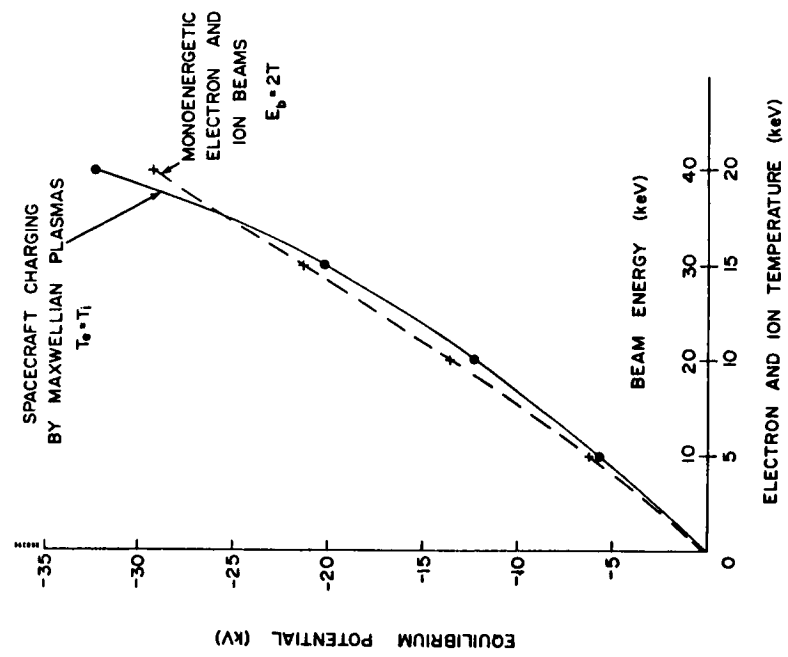


FIGURE 2. EQUILIBRIUM POTENTIAL IN MAXWELLIAN PLASMAS AND SINGLE ELECTRON AND ION BEAMS

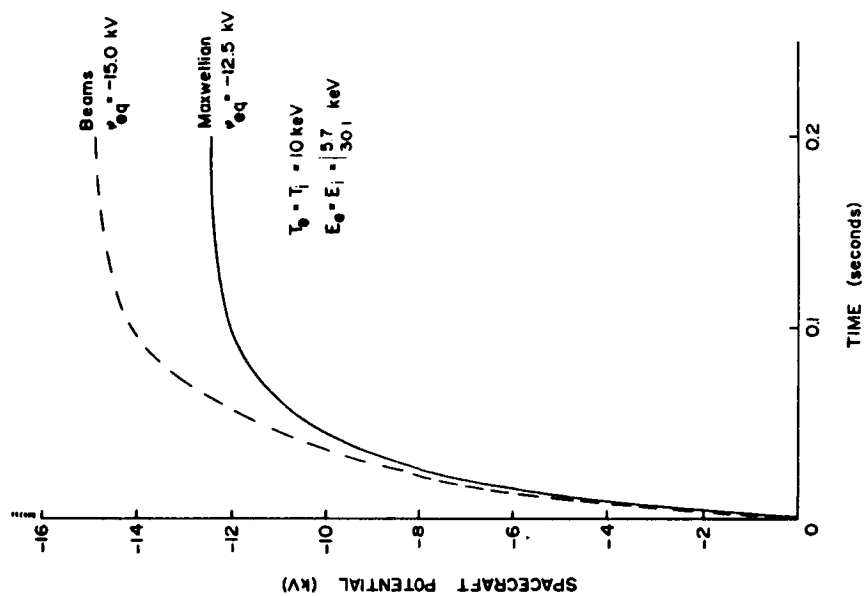


FIGURE 4. CHARGING BY MAXWELLIAN PLASMA AND TWO ELECTRON AND ION BEAMS

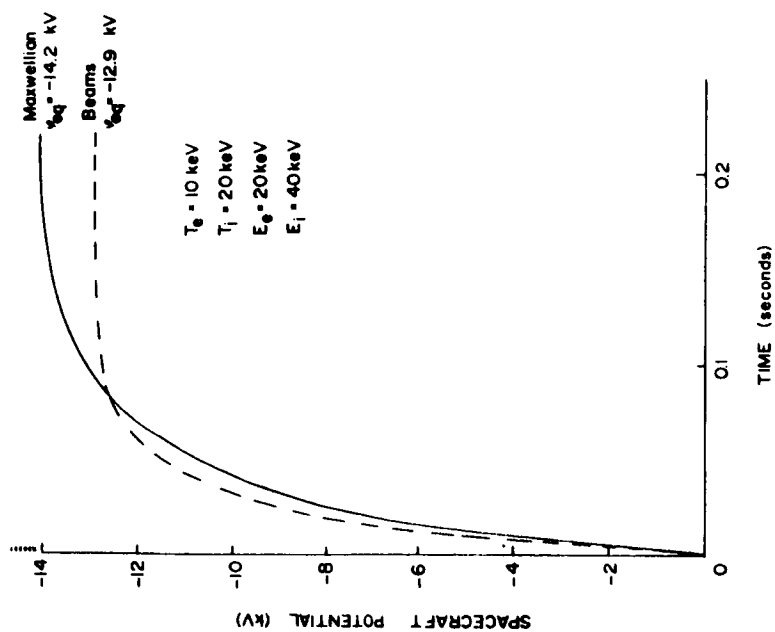


FIGURE 3. CHARGING BY MAXWELLIAN PLASMA ( $T_e = 10$  keV,  $T_i = 20$  keV) AND SINGLE ELECTRON AND ION BEAMS

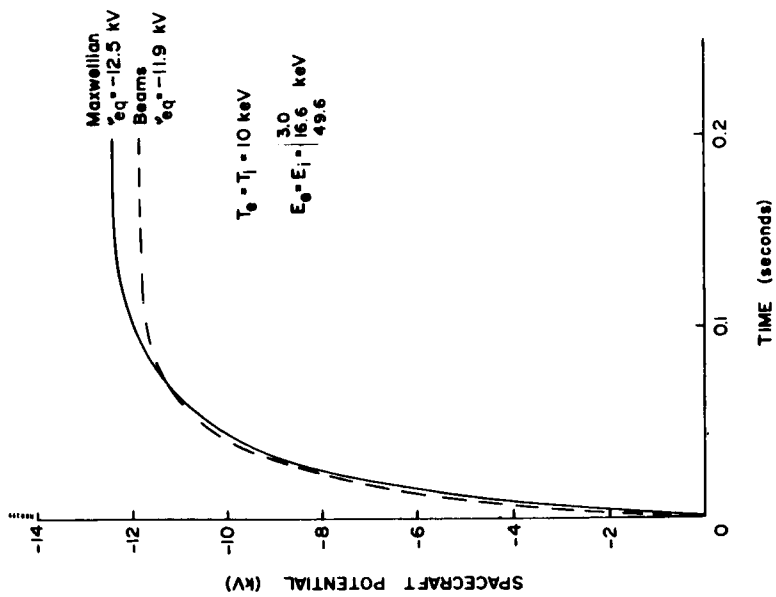


FIGURE 5. CHARGING BY MAXWELLIAN PLASMA AND THREE ELECTRON AND ION BEAMS

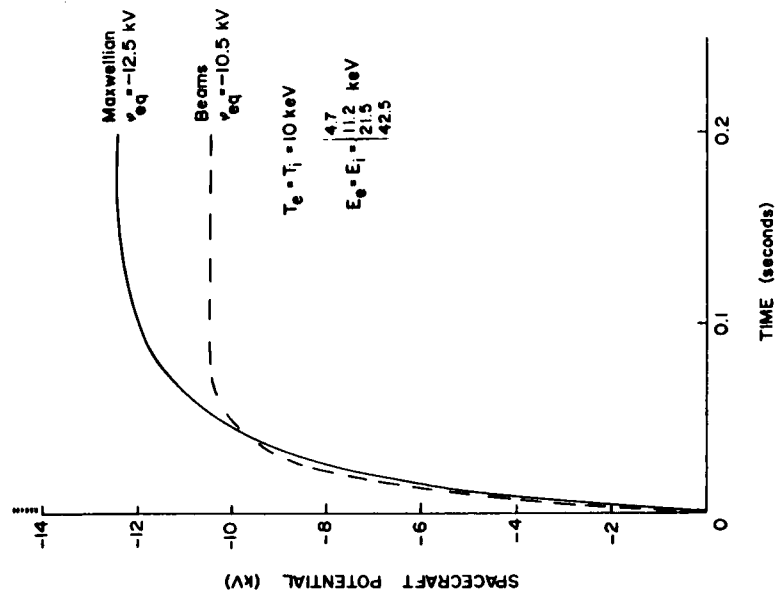


FIGURE 6. CHARGING BY MAXWELLIAN PLASMA AND FOUR ELECTRON AND ION BEAMS

# **IMPORTANCE OF DIFFERENTIAL CHARGING FOR CONTROLLING BOTH NATURAL AND INDUCED VEHICLE POTENTIALS ON ATS-5 AND ATS-6**

**E. C. Whipple and R. C. Olsen  
Center for Astrophysics and Space Science (CASS)  
University of California, San Diego**

## **ABSTRACT**

A review is given of what has been learned about spacecraft charging from the ATS-5 and ATS-6 satellites. The first observation of large (i.e., kilovolt) spacecraft potentials was made on ATS-5. The record potential to date of -19 kV was observed on ATS-6. The connection between spacecraft anomalies and spacecraft charging was inferred from a study of the local time dependence of ATS-6 charging events. The importance of differential potentials in affecting the current balance to a spacecraft was realized through the observations of potential barriers about ATS-6. A large number of active charging experiments have been carried out with the ion thrusters and neutralizers on both ATS-5 and ATS-6. Electron emission alone can only partially discharge a negatively charged spacecraft because of the fact that negatively charged surface dielectrics retain their negative charge. Differential charging can limit the currents from particle emitters, and consequently the time constants involved in charging and discharging a spacecraft can be controlled to a large extent by differential charging. Simultaneous emission of both positive ions and electrons can completely discharge both the spacecraft mainframe and the dielectric surfaces.

## **A COMPARISON OF THREE TECHNIQUES OF DISCHARGING SATELLITES**

**H. A. Cohen and A. L. Chesley**  
**Air Force Geophysics Laboratory**

**T. Aggson**  
**NASA Goddard Space Flight Center**

**M. S. Gussenhoven**  
**Boston College**

**R. C. Olsen and E. Whipple**  
**University of California, San Diego**

### **SUMMARY**

Three techniques of discharging satellites were used on the P78-2 satellite in April, 1979. The three techniques were the ejection of a beam of electrons from an electron gun; the emission of electrons from a heated, biased filament; and the ejection of a plasma containing energetic positive xenon ions and low energy electrons. On April 22, 1979 when the P78-2 satellite ground-to-plasma potential difference reached several hundred volts, each of the three techniques was able to completely discharge the satellite. The comparative effectiveness of the techniques were clearly shown on this day. On April 24, 1979 the satellite charged to -8 kV upon entering eclipse. The electron gun, emitting 1 mA of electrons with 150 eV energy, reduced the difference in potential between satellite ground and the ambient plasma to -1 kV, but could not completely discharge the satellite. The plasma source completely discharged the satellite.

Spacecraft charging at geosynchronous altitude is caused by the accumulation of negative charge due to high energy electrons (ref. 1). Therefore a method of ejecting electrons should be used on satellites in order to discharge the spacecraft. There are several different techniques of ejecting electrons from space vehicles, with comparative advantages and disadvantages for each. The use of the SC4 payloads on the P78-2 satellite presented the opportunity to compare three techniques: a heated wire, an electron gun, and a plasma source.

The heated wire is attractive as an electron emitter because it is simple, can be placed nearly anywhere on the spacecraft, and no high voltages are required. The disadvantage of this type of emission device became evident during its first use on the ATS-5 satellite (ref. 2). That particular unit had not been specifically designed for the purpose of dis-

charging the spacecraft but was used for that purpose on a number of occasions. When heated and allowed to emit electrons, the wire discharged the spacecraft either completely or almost completely. However, this was sometimes a transient phenomenon, and in this case the spacecraft would return to a highly charged state even though the wire was continuously heated. Two possibilities have been proposed for this sequence of events: 1) a local space charge builds up around the wire cutting off electron flow from the wire to the ambient plasma, or 2) a negative potential well exists outside the satellite such that "electrons must be ejected at sufficient energy to overcome the potential barrier surrounding the spacecraft in order to discharge it completely" (ref. 2).

Although the SC4-2 payload on the P78-2 satellite was intended primarily to eject beams of ions or a plasma of ions and electrons, the unit was designed so that the heated wire neutralizer could also be used as an electron emitter. A schematic of the neutralizer circuitry is shown in figure 1. The heater temperature was controlled in order to limit the electron emission to discrete values from  $8 \times 10^{-6}$  A to  $2 \times 10^{-3}$  A which could be commanded from the ground. The bias on the wire could be set to  $\pm 0$ , 10, 25, 100, 500, or 1000 V (with respect to spacecraft frame).

To overcome the local space charge problem created by a bare heated filament, an electron emission system using a triode electron gun was also flown on the P78-2 satellite. Figure 2 is a schematic of this system. This payload, labeled SC4-1, was capable of ejecting electrons in discrete current steps from  $1 \times 10^{-6}$  A to  $1.3 \times 10^{-2}$  A, with energies from 50 V to  $3 \times 10^3$  V. The triode gun was a copy of a proven design which had been used successfully on rocket flights for over a decade (ref. 3).

One of the primary concerns in the initial design of SC4-1 was the economy of power and weight. A great deal of effort was expended in order to produce a small, lightweight package that would use only a small amount of power in generating the required dynamic range of currents and energies. Because of this requirement, the triode gun uses an oxide-coated cathode. This requires little power to heat to thermal emission, but is easily poisoned. In the laboratory it was observed that exposure to oxygen or water vapor (partial pressures of greater than  $2 \times 10^{-6}$  Torr) seriously poisoned the cathode in time periods on the order of minutes.

The gun was therefore sent aloft in a closed container. The container was not opened until the satellite had been in orbit for about a month to allow for outgassing from the satellite. The gun was operated when the container cap was first opened and again four hours later that day. No signs of poisoning were evident in the first days of operating the SC4-1 payload.

One result which had a serious effect on determining operation plans for the period April 22 to 24 was the unanticipated havoc created by the use of the electron gun in emitting 6 mA at 3 keV during March 30, 1979. These results have been reported in a previous paper at this conference ("P78-2 Satellite and Payload Responses to Electron Beam Operations on



March 30, 1979," Cohen et al.) Although it would have been useful to operate the electron gun over the full dynamic range available, due to these effects it was decided to limit the current and energy to a maximum of 1 mA at 0.15 keV.

A plasma source ejects a mixture of positively charged ions, electrons, and neutrals. Such a source had been quite successfully used on the ATS-6 satellite to discharge the spacecraft (ref. 2). Figure 3 is a schematic of the SC4-2 payload configured as a plasma source. In addition to the electron currents previously mentioned for the heater, SC4-2 was designed to eject ion currents of  $3 \times 10^{-4}$  A to  $2 \times 10^{-3}$  A, with energies of 1 and 2 keV. Ion, electron, and net currents flowing from the SC4-2 could be independently varied and measured. The original basis for using the plasma source was that it was expected to act like a low impedance connection from the spacecraft to the plasma, allowing a flow of either electrons or ions, as required. Because the plasma contains almost equal numbers of ions and electrons, it is both impervious to any electrical potential barriers around the spacecraft, and is not limited by space charge restraints in the beam itself.

The different discharge systems were used on the same satellite for the first time in April 1979, when the satellite was charged to an average potential of -380 V during an eclipse period. As shown in table 1, 10  $\mu$ A of electrons emitted at either 50 or 150 eV from SC4-1 reduced the potential to -170 V but did not completely discharge the spacecraft. Raising the ejected current to 100  $\mu$ A completely discharged the spacecraft when 50 eV electrons were used, and even drove the spacecraft slightly positive when the energy of the ejected electrons was increased to 150 eV.

The electron gun (SC4-1) was turned off and the heated wire neutralizer on SC4-2 was started. Currents of 8, 20, 300, and 1000  $\mu$ A were used with a bias of -10 V (with respect to spacecraft frame). As shown in table 2, there was no substantial decrease in spacecraft charging when electrons were ejected with this energy. But when 100 eV electrons were used, the change in spacecraft charging depended monotonically on the current ejected. The plasma source was now turned on, combining the ejected electrons with energetic ions. Previously, 1 mA of 10 eV electrons had little effect on discharging the satellite; however, these electrons, when combined with the 1 mA of 1 keV positive xenon ions, completely discharged the satellite. Reducing both the ion and electron currents to  $3 \times 10^{-4}$  A kept the spacecraft completely discharged during the plasma use.

The vehicle charged to -8 kV during the eclipse period of April 24, 1979. Electrons of 50 eV (ejected from SC4-1) had the effect of reducing the vehicle potential from -8 kV to -3 kV, independent of the current used (10, 100, or 1000  $\mu$ A). Increasing the energy of the electrons to 150 V had the effect of reducing the vehicle charging with higher currents (the vehicle remained near -2 kV with respect to the plasma). Using the plasma source, with electron ejection on the order of 1 mA, completely discharged the spacecraft frame, even with a positive ion ejection as low as 100  $\mu$ A.

What is important here is that the vehicle did not swing significantly positive when this large electron current (combined with a small flow of positive ions) was used.

The conclusion that can be drawn from these operations is that a plasma source represents the best way of discharging spacecraft in geosynchronous orbit.

#### REFERENCES

1. DeForest, S. E., Spacecraft Charging at Synchronous Orbit, J. of Geophys. Res., 77, p. 651, 1972.
2. Goldstein, R., and S.E. DeForest, Active Control of Spacecraft Potentials at Geosynchronous Orbit, Spacecraft Charging by Magnetospheric Plasmas, Progress in Astronautics and Aeronautics, 47, A. Rosen, Ed., 1976.
3. Hess, W. N., M.C. Trichel, T.N. Davis, William C. Beggs, George E. Kraft, E. Stassinopoulos, and E.J. Maier, Artificial Aurora Experiment: Experiment and Principal Results, J. Geophys. Res., 76, 6067, 1971.

TABLE 1

Discharge of Spacecraft Using SC4-1 April 22, 1979

SC4-1 Mode #	Emitted Current Ib (mA)	Electron Energy Eb (volts)	Vehicle Potential V <sub>sc</sub> (10 <sup>2</sup> volts)
1	.01	50	-170 ± 20
2	.01	150	-170 ± 20
3	.1	50	10 < V <sub>sc</sub> < 50
4	.1	150	10 < V <sub>sc</sub> < 150

(Average Spacecraft Potential was 380 volts just before and immediately after SC4-1 operation.)

TABLE 2  
Neutralizer Filament Discharge of P78-2 (April 22, 1979)

$I_F$ (mA)	$-V_{SC}$ ( $10^3$ Volts)	
	Filament Bias $E_{FE} = -10$ V	Filament Bias $E_F = 100$ V
0.008	0.37	0.3
0.02	0.4	0.15
0.3	0.5	0.07
1.	0.3	--

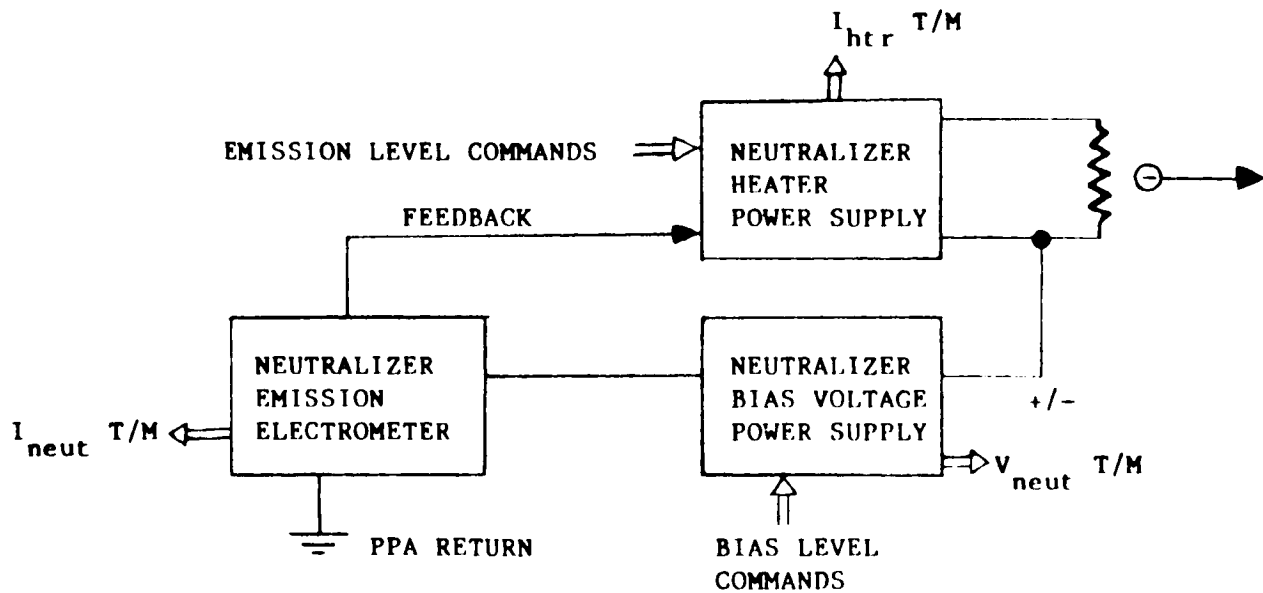


Figure 1 Schematic of Neutralizer Circuitry

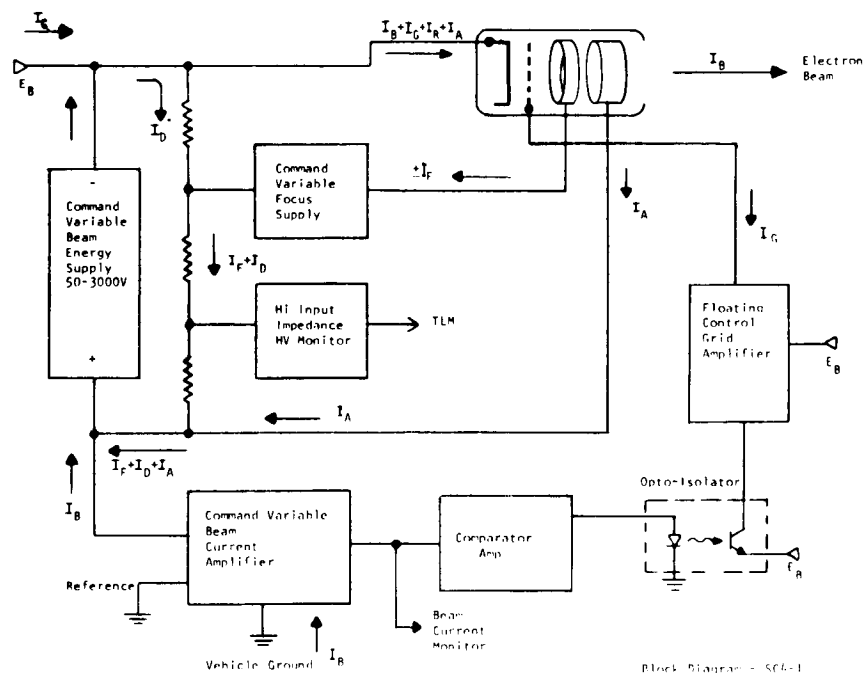


Figure 2 Schematic of Electron Gun

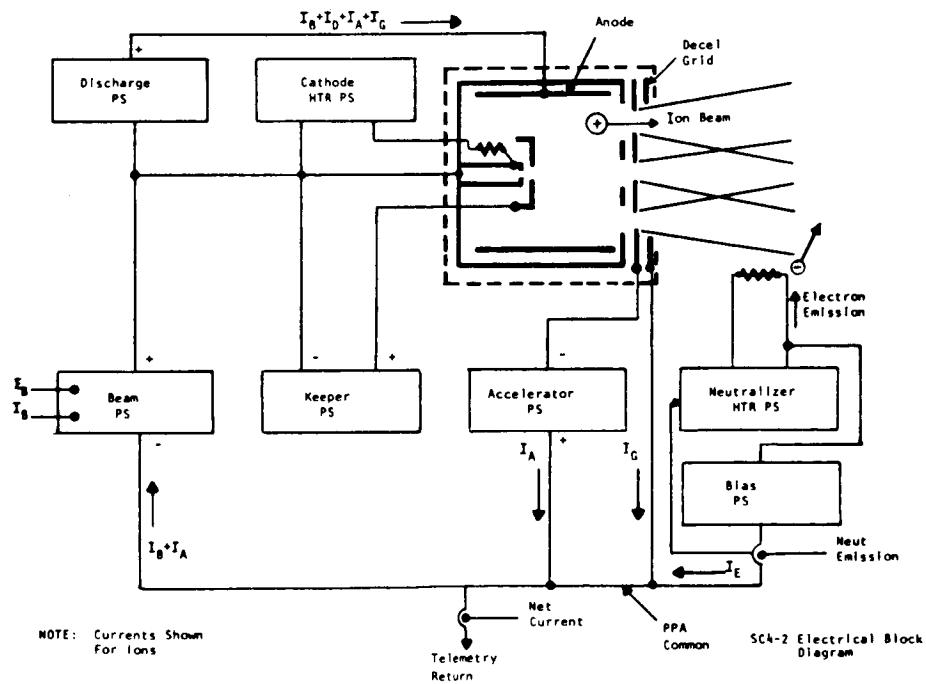


Figure 3 Schematic of Plasma Source

## **ELECTROMAGNETIC FIELDS PRODUCED BY SIMULATED SPACECRAFT DISCHARGES\***

**J. E. Nanevich and R. C. Adamo**  
**SRI International**

**B. L. Beers and T. N. Delmer**  
**Beers Associates, Inc.**

### **BACKGROUND**

This paper presents a description of the results of the initial phase of a broader, more complete program for the characterization of electrical breakdowns on spacecraft insulating materials. This initial phase consisted of the development of a discharge simulator and characterization facility and the performance of a limited number of discharge measurements to verify the operation of the laboratory setup and to provide preliminary discharge transient field data. Some of the early results of this program were presented at the last Spacecraft Charging Symposium.<sup>1</sup>

Another portion of the initial phase of the program was to develop a preliminary model of the electromagnetic characteristics of the discharge. Such a model has been developed. It is based upon the "blow off" current model of discharges, with the underlying assumption of a propagating discharge.

The laboratory test facility and discharge characterization instrumentation were described at the last Symposium and are discussed here only briefly for completeness. The general results of the "quick look" tests will be described here. The results of the "quick look" experiments compare with the preliminary model with reasonable success.

Further tests are planned in the future to carry out the complete program.

### **TEST SETUP**

For the electromagnetic breakdown studies, the test samples were mounted in the middle of a ground plane within an electromagnetically-transparent vacuum chamber in the general manner illustrated in Figure 1. This arrangement simu-

---

\*The work reported here was supported by the U.S. Air Force under contract SAI-77-C-0166. Mr. G. R. Hilbers of SRI was responsible for assembling and debugging the test setup. He and Mr. B. Milligan also at SRI were responsible for generating the test data.

lates a region of charged dielectric mounted on the skin of a satellite. The electron gun is of a special type designed at SRI and uses a multipactor electron source to provide a large-area uniform beam adjustable over a wide range of energies and current densities as discussed at the last Symposium.<sup>2</sup>

This setup produces an electromagnetic environment similar to that existing on a satellite when breakdowns occur. The discharges on the outer surface generate transient electric fields above the skin and transient currents on the skin. The electric fields induce signals in wiring on the exterior of the satellite while both electric fields and skin currents excite apertures in the skin which excite wiring on the interior of the satellite. Measurements of electric field (E) and magnetic field (H) (H is equivalent to skin current) were made using simple antennas located at varying distances from the discharge test panel as suggested in figure 1. The antennas being used were small electric dipoles and half loops. The electric dipole sensors measure E while the loop antennas respond to the H field.

Initially, the glass bell jar, as used in the experiments, had non-conducting surfaces. However, it was found that charge deposited on the inner surface of the bell jar during the charging process was relieved by the discharge process and produced a large artificial dc field change in the measured data. This charging of the bell jar inner surface was eliminated by covering the inner surface with a high-resistance conductive coating. In this way, static charge accumulation is prevented, but the conductivity is low enough that there is little attenuation of the high-frequency signals generated during the discharge.

A large ground plane was used in the test setup to minimize the ringing associated with reflections from the edges of the ground plane. In addition, the region of the ground plane in which the sensors were located was specially treated to minimize edge reflections by the addition of an extension along the six-foot edge. The outboard edge of the extension was rolled over to form a cylinder with a 6-inch radius of curvature. With this arrangement, the high-frequency components in the transient fields propagating along the ground plane surface tend to be radiated as they propagate around the rolled edge and thereby minimize the energy available to form a reflected signal. In general, reflected signals were sufficiently low that they could be ignored in all of the measurements, except those made virtually at the edge of the ground plane where the amplitudes of the measured fields had fallen substantially.

Essentially, with the setup of Figure 1, a controlled environment is created which simulates locally that existing on a satellite when breakdowns occur. In particular, the mean free path in the bell jar is sufficiently great that discharges occur substantially as they would in space. Since the electrons and other discharge products move as they would in space, the electromagnetic source duplicates that on the satellite. Fields propagate over the surface of the ground plane in the same manner as they would propagate on the satellite skin. Thus, the experimental setup is designed to yield results which duplicate the spatial and temporal field variations occurring on satellites under spacecraft-charging conditions.

## EXPERIMENTAL RESULTS

### General

"Quick-Look" measurements were made using three different materials often used as thermal-control surfaces on satellites. The three materials chosen were:

- second-surface quartz optical solar reflectors (OSRs)
- 5-mil silver-coated Teflon tape, and
- 5-mil aluminized Kapton.

The basis for this choice was that, in addition to being widely used, these three materials differ in their physical, optical, and electrical characteristics.

Measurements of the transient electric fields generated by breakdowns on these samples were made at several radial distances from the test samples in order to provide an understanding of the spatial E-field dependence. Both the base current and the ground plane skin current were also measured. Most of these measurements were carried out for all three materials. In the case of Kapton and Teflon, several sample sizes were used, as well, to investigate the dependence of discharge characteristics on the sample dimensions.

Data obtained using the various samples had certain general overall similarities. In all cases, the peak electric field strength for many discharges was greater than 30 kV/m at a distance of 30 cm from the center of the test panels. Electric field pulses of this magnitude are capable of inducing significant transients in nearby wiring and must be considered in designing spacecraft wiring and electronics. The rise time of the transient pulses was between 50 ns and 600 ns, depending on the material and the peak base currents of up to 90 A were measured.

It was found that for both Kapton and Teflon, the peak base current appeared to vary directly with the area of each sample. In addition, the rise times of the pulses and the total charge evolved from the surfaces varied directly with the physical dimensions of the samples.

### Results with Optical Solar Reflectors (OSR)

Figure 2 shows the record of a typical breakdown occurring on the surface of an 8 x 10 inch OSR panel of 10-mil thick, one-inch square second surface quartz mirrors. A positive unipolar pulse was generated in the test sample base return-current circuit, indicating that negative charge was driven away from the sample surface during a breakdown. During the first 370 ns, the current rises to its maximum value of nearly 60 A and then decays monotonically. The positive-going E-field pulse (with inverted displayer convenience) is created by electrons in the breakdown plasma being driven upward. Their increasing dipole moment as they leave the surface generates the electric field pulse.

An additional measurement was made using the OSR panel. A set of four grids was installed above the panel with the first and third shield grids shorted and grounded through a capacitor in the general arrangement described in Reference 3. The signals induced in the second and fourth sensor grids by a discharge were monitored. Charged particles in the vicinity of a sensor grid will induce a corresponding signal in the monitoring oscilloscope channel. Because of the shielding afforded by the two grounded grids, the sensor grids do not respond to charges located beyond the nearest shield. Thus, the induced signals provided an indication of the extent to which charge was expelled from the surface during a discharge. The time of arrival difference between the two grid signals provides information about the velocity of this charge since it is dependent on the transit time between the grids.

The results of the experiments with the four-gridded structure indicated that most of the charge is expelled to, at least, 10 cm from the surface of the OSR panel. A lower bound on the vertical velocity of the expelled charge was also established from this measurement. Since there was no evident time delay in the oscillogram between the signals induced in the two sensing grids, it was argued that the distance between them was traversed faster than can be discriminated from the oscilloscope trace. Using a value of 10 ns as the time limit for discrimination, the charge velocity was calculated to be greater than  $5.8 \times 10^6$  meters/sec. This lower velocity limit is well within reason, since it corresponds to an electron energy of less than 100 eV. At this velocity, electrons would require only 65 ns to travel the 38 cm distance to the grounded electron source above the sample. Thus, it is likely that during the course of a discharge, typically lasting over 400 ns, a column of electrons extending from the test sample to the electron source is established.

One consequence of the high value established for electron velocity is that, were the electron gun not present to intercept the electrons, they would travel much farther than 30 cm before being lost. Thus, the early-time electric fields measured in the laboratory setup most likely constitute lower bounds on what would be found on the surface of spacecraft.

In addition to affecting the amplitude of the transient electromagnetic pulses, the presence of the grounded electron gun alters the time characteristics of the pulses. The grounded portion of the gun acts as a sink for electrons emitted during a discharge. Thus, a plasma of electrons will not readily build up and the accompanying space charge limitations, therefore, do not occur. In space, however, this sink is not present and the amount of charge being blown away from the surface may be limited by the coulomb repulsion of electrons already emitted. This process could change the time span during which electrons are being evolved from the satellite's skin and thereby modify the time structures of the generated transient fields.

To obtain an understanding of how the induced E-field depends on the radial distance from the discharge, an experiment involving two E-field sensors was performed. The referenced sensor was permanently mounted 30 cm from the discharge while a second sensor was moved in increments of 5 cm to locations between 30 cm and 60 cm away from the center of the test samples. Since each discharge varied in amplitude, the peak electric fields actually measured were normalized to correspond with constant discharge amplitudes at the reference



channel. The adjusted data from this experiment are shown in Figure 3 and indicate that the field intensity decreases, at least, as fast as  $1/r^3$ .

A typical record obtained in experiments to study ground plane skin current is shown in Figure 4. The lower trace in the figure shows a record of the skin current, while the upper trace displays the base current to allow comparison with other breakdowns. The skin current waveform closely resembles the base current waveform.

#### Results With Aluminized Kapton

Electromagnetic transient measurements were also made on samples of 5-mil thick, aluminized Kapton material. The results obtained were generally similar to those obtained with the OSR panel. A positive unipolar pulse of base current was generated by electrons being expelled from the sample surface. This, in turn, created a positive-going electric field. Figure 5 shows a typical record generated by a discharge on a 4 x 6 inch sample of Kapton.

While the Kapton record has some features in common with those obtained with the OSR sample of Figure 2, there are several differences in detail. For example, the rise times of the pulses obtained with the Kapton were generally longer than those obtained with OSRs (e.g., 600 ns versus 370 ns). However, the peak current in the Kapton record shown was somewhat less (40 A as opposed to 58 A), so a comparable amount of charge ( $1.2 \times 10^{-5}$ ) coulombs was evolved during the rise time portion of the Kapton discharge.

The electric field generated by discharges from Kapton was measured at three different distances from the sample. As with the OSR panel, the pulse amplitudes were corrected for variations at the reference sensor. These results, shown in Figure 6, indicate an  $r^{-3.7}$  dependence of field roughly as was observed in the OSR tests.

In addition to measurements made on the 4 x 6 inch Kapton samples, similar tests were carried out on a 2 x 3 inch Kapton sample. Although the general characteristics of the breakdowns were similar, two important differences were observed between the results obtained with the two different sized samples. First, the peak current flowing in the base return-current circuit was lower for the smaller sample (200 ns versus 600 ns).

From this it follows that roughly  $2.5 \times 10^{-6}$  coulombs of charge were expelled from the surface of the smaller sample during the pulse rise time, while  $12 \times 10^{-6}$  coulombs of charge left the larger sample during the pulse rise time. The large sample, four times larger than the small one, emitted 4.8 times as much charge. Thus, the amount of charge involved in the breakdowns appears to be proportional to the area of the sample. This indicates that each discharge taps charge which has been deposited on a major portion of the sample surface.

## Results With Silver-Coated Teflon

Measurements of discharge characteristics were also made using 5-mil silvered Teflon tape samples following the general procedures already described for OSR and Kapton panels. Figure 7 shows the base current and E-field generated by a typical discharge from a 4 x 6 inch sample of silver-coated Teflon. Compared to either the OSR or the Kapton material, there are significant differences in the details of this discharge. The peak current of 77 A is almost twice that reached during a discharge on Kapton. Furthermore, the rise time of the transient signal is only 200 ns, about one-half that for the OSRs and one-third of that for Kapton.

As with OSR and Kapton samples, the spatial variation of the E-field was measured. From the plot of peak electric fields as a function of radius in Figure 8, it is seen that it falls off approximately as  $1/r^3$ .

To determine the effects of Teflon sample size, measurements were made with samples of 4 x 1-1/2 inch, 4 x 10 inch, and 1 x 6 inch, in addition to the 4 x 6 inch sample already mentioned. These data show a distinct dependence on sample size of the quantity of charge evolved in a discharge. Both the rise time of the pulse and the peak current increase with increasing sample size. It was also noted that discharges occurred along the length of the tape (perpendicular to all 4-inch dimensions and perpendicular to the 1-inch dimension of the 1 x 6 inch sample) more often than in other directions. This is apparently due to longitudinal scratches which run along the tape. The sample dimensions were chosen to determine whether the charge involved was dependent on this longitudinal dimension only. Although the discharges are probably initiated on the scratches, they apparently tap the entire surface charge since the data indicate that the charge blown away in a discharge appears to be related to the sample length as shown in Figure 9b. Together these observations indicate that the breakdowns, once triggered, propagate along the scratches. Thus, the longer the sample, the more time required to travel the entire length. Perhaps the fact that the measured rise times are less for Teflon than for Kapton samples of equal area indicates that the propagation of the breakdown is facilitated by these scratches. In any event, a discharge from the Teflon sample removes charge from the entire surface since the total charge involved in a discharge is area-dependent as it is with Kapton test samples.

## PRELIMINARY MODEL AND COMPARISON WITH EXPERIMENTS

### Propagating Channel Model

Based on the charging model presented in Reference 4, it is anticipated that electron charging of dielectrics in the normal energy range (5-30KeV) leads to a layer of excess electrons several microns below the surface of the sample. The primary discharge is expected to propagate in this layer of excess charge.<sup>5</sup> A primary discharge channel is formed by the development of a negative propagating streamer of avalanching electrons. The streamer, once formed, is self-sustaining, as it enhances the local field to values substantially larger than the ambient field. The radius of the channel grows by diffusion (square

root of the time), while the length of the channel grows linearly in time. This channel formation process is repeated near the tip of the streamer, giving an effective propagation into the region of large net electron density. The rate at which the channel propagates is governed by the rate at which subsequent channels form. Bifurcation occurs, and subsequent channel formation is viewed as an intrinsically statistical process.

The charge which is released to flow from one end of the channel to the other is controlled by the formation rate of the channel. This process fans out and propagates throughout the entire trapped charge layer, with the current flowing in a tree pattern (all eventually ending in the primary channel). The primary channel delivers the current to a grounding point.

As a consequence of the above picture, the total current reaching a grounding point grows linearly in time. The peak current is proportional to the maximum run length of the discharge. Thus,

$$I = J_{\max} (t/\tau_p) \quad t \leq \tau_p \quad (1)$$

where

$$\tau_p = L/v \quad (2)$$

$L$  is the maximum sample dimension and  $v$  is the velocity of propagation of the discharge. (It is anticipated that the velocity is in the range  $10^7 - 10^8$  cm/s).

The total charge  $Q_T$  released by this process is proportional to the surface area of the sample. Thus

$$Q_T = Q \hat{A} \quad (3)$$

where  $\hat{Q}$  is the charge per unit area involved in the discharge, and  $A$  is the sample area.

The flow of stored charge to the substrate causes the collapse of the associated dipole. The fields associated with this collapse are small compared to the fields due to the space charge current.

## Surface Emission Current

The surface emission current model is very simple. It is assumed that:

- (1) The emission current is dominated by low energy electrons (FleV);
- (2) The total emission current is proportional to the total transverse current; and
- (3) The emission is distributed over the surface of the dielectric in proportion to the subsurface channels.

With the previous information on the transverse current, this information quantifies the surface emission current. (The only parameter requiring specification being the constant of proportionality--it is expected that a substantial amount of the trapped charge is involved in this emission.)

Conceptually, this model of the surface emission can be obtained from the microscopic picture of the development of the transverse discharge tree. The formation of a conducting channel involves the release of a large number of electrons from trapped states to freely mobile states. These electrons diffuse in time away from the central channel. If these mobile electrons are not retrapped, they can diffuse to the surface in a short time. (For buried charge layers a few microns below the surface, and a reasonable diffusion coefficient, this diffusion time is a few nanoseconds.) Reaching the surface (with thermal velocities), these electrons are free to escape the surface. The density of particles reaching the surface is expected to be sufficiently low that short range particle-particle interactions are relatively unimportant. That is, we expect that the electron plasma may be treated as a collisionless plasma. Being non-neutral, this plasma responds to the external macroscopic field, and the long range interelectron Coulomb interaction. These forces are assumed to dominate further motion.

## Satellite Configurations

No attempt is made to model the response of a satellite to the discharge model given here. It should be noticed, however, that the fields and currents which exist on the satellite will be distinctly different than those measured in the laboratory. The important quantity obtained from the laboratory measurements will be the emission current time history (as well as the emission current density). For small enough experimental devices, the time history of the fields is determined by the time history of the emission current. For larger geometries, more complicated solution algorithms are required, and more complicated field histories are expected.

## Zero-Order Space Charge Model

Shown in Figure 1(b) is a drawing showing the dimension of the charging configuration. By inspection, the electric fields near the axis of the chamber

for the charged dielectric will be very similar to one-dimensional fields. For the purposes of a zeroth order model, this is assumed to be the case. Future computations will model the structure more accurately.

Near the sample surface, the electric fields will drive free electrons back toward the multipactor electron gun. Assuming a one-dimensional configuration, this field is given by  $E = V/d$ , where  $V$  is the sample surface potential and  $d$  the sample to multipactor distance of  $15'' \approx 0.38$  m. For a typical surface potential of 10 kV, this corresponds to a field 26 kV/m. An electron released from the surface (with an energy small compared to the surface voltage, so that the initial energy may be neglected.) will transit the gap in a time of about  $\tau_o = 13$  ns, with the velocity at the end of the transit of  $6 \times 10^7$  m/s ( $E = 10$  keV). Compared to the pulses measured in the experiments reported herein, this transit is essentially instantaneous, and just marginally within the resolution of the instrumentation. The lowest order approximation is therefore to neglect the transit time entirely, so that the return current can be interpreted as a direct measure of the emission current. Since, according to the surface emission model, the emission current is directly proportional to the transverse current, the emission current will have the linear rise of Eq. (1).

The total charge in the space above in the experimental setup is given by

$$Q(t) = \tau_o I_{\max} \frac{t}{\tau_p} \quad (4)$$

where  $\tau_p$  is the rise time of the pulse given by Eq. (2) and  $\tau_o$  is the transit time of an electron. The charge density is heavily weighted near the surface and is much more tenuous near the multipactor electron gun. The charge centroid is given by

$$\langle x \rangle = \frac{1}{3} d \quad (5)$$

where  $d$  is the spacing between the test sample and the electron gun. This means that at least 2/3 of the image charge of the space charge shows up on the sample backing plate, and, at most, 1/3 on the multipactor electron gun. It is therefore a reasonable approximation to neglect the image charge on the gun and compute the electric field on the ground plane as due to the space charge only. This gives rise to a quasistatic dipole electric field.

#### Electric Field Model--Temporal Variation

The dipole moment  $p = 2Q\langle x \rangle$  is given by substituting Equations (4) and (5)

$$P = \frac{2}{3} d \frac{\tau_o}{\tau_p} I_{\max} t, \quad (6)$$

which indicates that the base current and electric field pulse will have a linear rise. This result is in good agreement with the measured data in Figures 2, 4, 5, and 7.

#### Electric Field Model--Spatial Variation

The quasistatic electric field on the ground plane due to the dipole is given by:

$$E = \frac{p}{4\pi\epsilon_0} \frac{1}{(r^2 + \langle x \rangle^2)^{3/2}} \quad (7)$$

The closest measurements were performed at  $r = 30$  cm. Even at this distance, the measured distance is three times the charge centroid, so that the dependence on  $\langle x \rangle$  is expected to be weak. This further suggests that higher order moments are relatively important. For large distances, the expected variation of field is  $1/r^3$  precisely as measured. Shown in Figure 10 is a plot of the normalized data from all three samples versus  $1/r^3$  on a log-log plot. The pronounced  $1/r^3$  behavior is apparent.

#### Field and Space Charge Magnitudes

Equation (7) can be solved to yield the dipole moment  $p = 2Q \langle x \rangle$  as follows:

$$P = 2Q\langle x \rangle = 4\pi\epsilon_0 r^3 E_z \text{ (measured)} \quad (8)$$

The results of such calculations using peak electric field data measured on three material samples are shown in the third column of Table 1.

The dipole moment can also be determined from the measured peak base using Eq. (6). Noting that the peak base current occurs when  $t = \tau_p$ , Eq. (6) can be rewritten

$$P_{\max} = \frac{2}{3} d \tau_0 I_{\max} \quad (9)$$

The results of such calculations using peak base current data measured on three material samples are shown in Column 4 of Table 1. In carrying out the calculations using Eq. (9), it has been assumed that the electron transit time  $\tau_0 = 13$  ns.

The value of dipole moment computed from beam current measurements is substantially higher than that obtained from electric field measurements except for the smaller-current case of Kapton. Analysis of additional data not presented here indicates that the results of the two calculations are in good

agreement for discharge pulses less than or equal to about 40 A peak. An interpretation of these results is that space charge limiting effects begin to set in above 40 amps and tend to retard the free flow of charge across the gap. This effectively makes the dipole length shorter.

In view of the simplicity of the space charge model, this agreement is considered to be very satisfactory. It is planned that future work will consider the details of the electron trajectories in greater detail.

No data is available directly from the experiments about the voltage at which the samples broke down. Assuming the breakdown was at roughly 10 kV, then the following quantities of charge were stored at breakdown; OSR's  $0.9 \mu\text{C}/\text{cm}^2$ ; Taflon,  $\sim 1 \mu\text{C}/\text{cm}^2$ ; and Kapton,  $1.6 \mu\text{C}/\text{cm}^2$ . From these estimates, and measured values of the blow off charge, one obtains a rough estimate of the stored charge involved in the flow off; OSR's, 32%; Kapton, 58%; and Taflon, 54%. The major point, of course, is that a substantial fraction of the stored charge is involved in the blow off.

### CONCLUSIONS AND RECOMMENDATIONS

This paper has described the initial phases of a program designed to provide a detailed characterization of the electromagnetic fields produced by electrical discharges on spacecraft-insulating materials. The primary goals of the effort described here were the setup and testing of the material-charging facility and the electromagnetic transient-measurement instrumentation, and the development of a preliminary model of the discharge. This effort has been successfully completed.

In addition, a limited number of "quick-look" transient measurements were performed. The purpose of these measurements was to verify the functioning of the test instrumentation and charging facility and to obtain some preliminary data on the magnitudes and time structures of the transient waveforms for model development purposes.

The results of these measurements indicate that transient electric fields of tens of kilovolts per meter are produced at a distance of 30 cm from discharges on Kapton, Teflon, and OSR samples. These magnitudes of fields are comparable to those produced by nuclear EMP events and by nearby lightning strokes and represent a serious potential threat to electronic systems' operation.

The preliminary model has been compared with the results of these "quick-look" experiments. While many features of the model appear very satisfactory, a number of areas exist where understanding is lacking.

Although the results of the "quick-look" experiments provide useful preliminary inputs to a discharge characterization model, they are based upon a limited number of discharges produced on only a few material sample configurations at a fixed electron-beam energy of 20 keV and current density of  $10 \text{ nA}/\text{cm}^2$ .

As originally planned, the overall discharge characterization program is designed to provide statistically significant data in terms of expected radiated and conducted transient fields for use by the spacecraft EMC community, as well as detailed inputs for the development of a computer discharge characterization model.

## REFERENCES

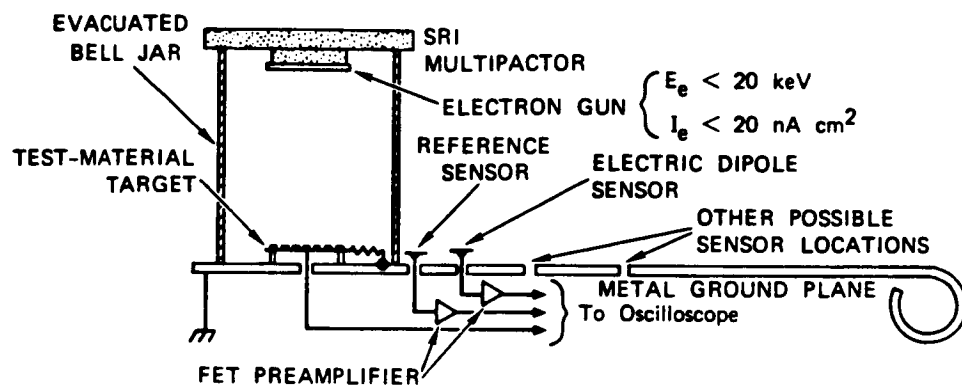
1. Nanevicz, J. E., Adamo, R. C., and Beers, B. L., "Characterization of Electromagnetic Signals Generated by Electrical Breakdown of Spacecraft Insulating Materials," Spacecraft Charging Technology-1978, NASA Conference Publication 2071, AFGL-TR-79-0082.
2. Nanevicz, J. E. and Adamo, R. C., "Further Development of the Multipactor Discharge Electron Source," Spacecraft Charging Technology-1978, NASA Conference Publication 2071, AFGL-TR-79-0082.
3. Nanevicz, J. E. and Adamo, R. C., "Spacecraft Charging Studies of Voltage Breakdown Processes on Spacecraft Thermal Control Mirrors," Spacecraft Charging by Magnetospheric Plasmas, Vol. 47, Progress in Astronautics and Aeronautics, A. Rosen, editor, 1976, p. 225.
4. Beers, B. L., Hwang, H., Ling, D. L., and Pine, V. W., "Electron Transport Model of Dielectric Charging," Spacecraft Charging Technology-1978, NASA Conference Publication 2071, AFGL-TR-79-0082.
5. Beers, B. L., et al., "First Principles Numerical Model of Avalanche-Induced Arc Discharges in Electron Irradiated Dielectrics," SAI Final Report, CR 159560, July 1978.

Table 1

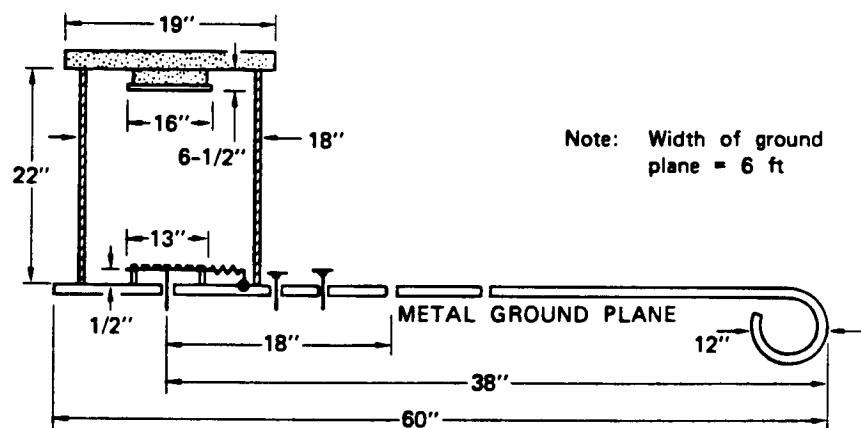
Dipole Moment Estimates from Experimental Data

Material	Experimental Results		Calculated Dipole Moments	
	Peak Field (kV/m)	Peak Current Amps	p( $\mu$ C - cm) Eq. (8)	p( $\mu$ C - cm) Eq. (9)
TEFLON (4" x 6")	43	77	12.9	20
OSR	36	58	10.8	15
KAPTON (4" x 6")	38	40	11.4	10.4





(a) SCHEMATIC ARRANGEMENT



(b) DIMENSIONS

FIGURE 1 EXPERIMENTAL SETUP FOR BREAKDOWN PULSE CHARACTERIZATION

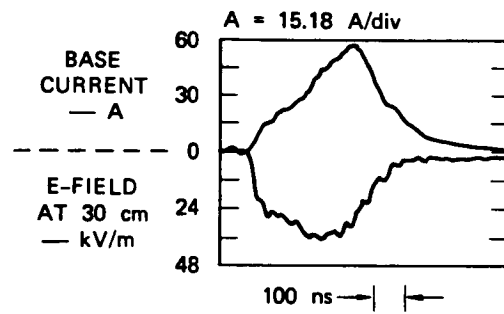


FIGURE 2 TRANSIENT PULSE GENERATED BY OSR PANEL

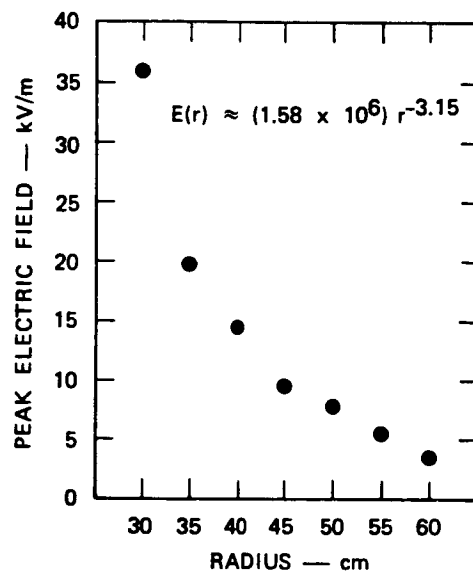


FIGURE 3 SPATIAL VARIATION IN OSR-PRODUCED ELECTRIC FIELD

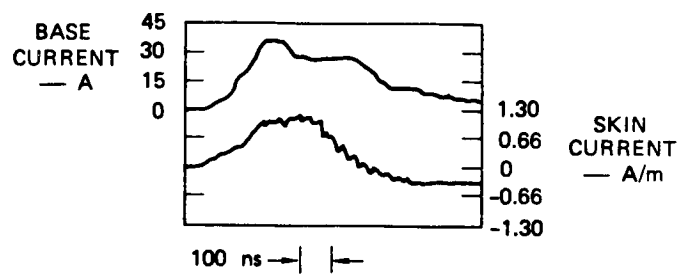


FIGURE 4 CURRENT PULSES GENERATED BY A DISCHARGE ON THE OSR PANEL

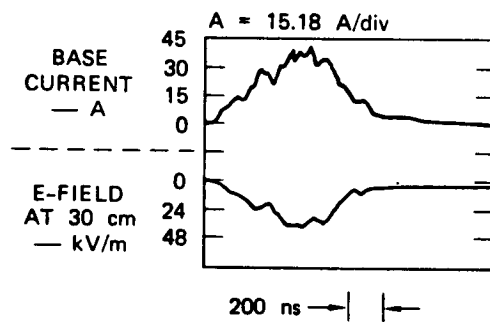


FIGURE 5 DISCHARGE SIGNALS PRODUCED BY A 4 in. by 6 in. KAPTON SAMPLE

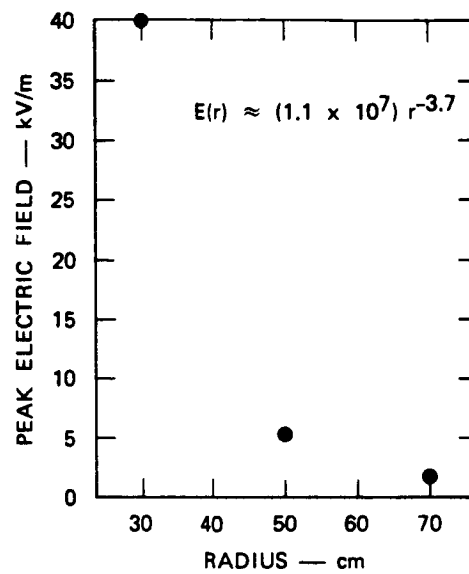


FIGURE 6 SPATIAL VARIATION IN ELECTRIC FIELD PRODUCED BY A 4 in. by 6 in. KAPTON SAMPLE

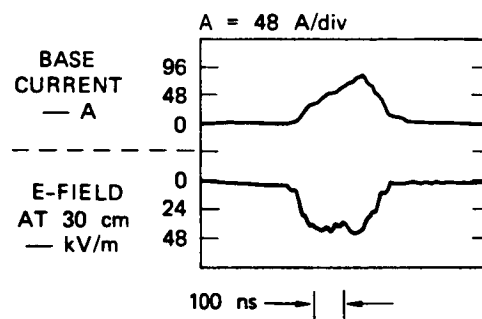


FIGURE 7 TRANSIENT DISCHARGE FROM A 4 in. by 6 in. TEFLON SAMPLE

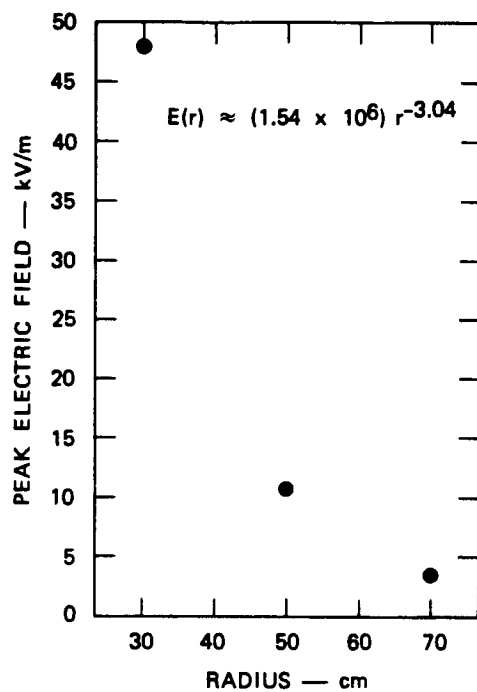


FIGURE 8 SPATIAL DEPENDENCE OF ELECTRIC FIELD GENERATED BY A 4 in. by 6 in. TEFLON SAMPLE

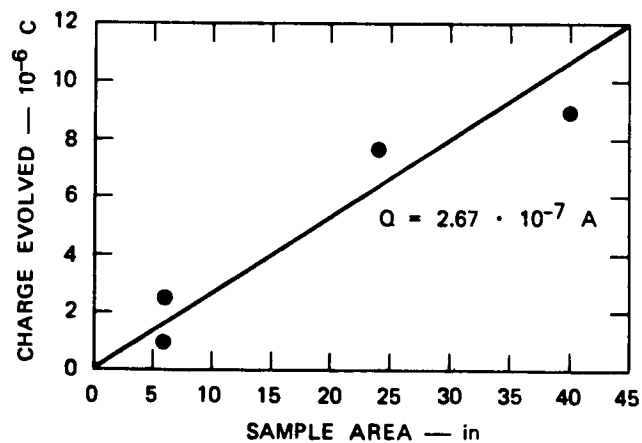


FIGURE 9a RELATIONSHIP BETWEEN SAMPLE AREA AND CHARGE TRANSPORTED DURING PULSE RISE (Teflon)

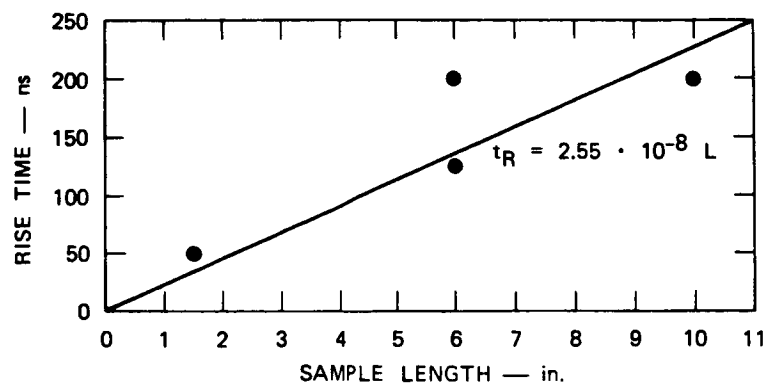


FIGURE 9b RELATIONSHIP BETWEEN SAMPLE LENGTH AND PULSE RISE TIME (Teflon)

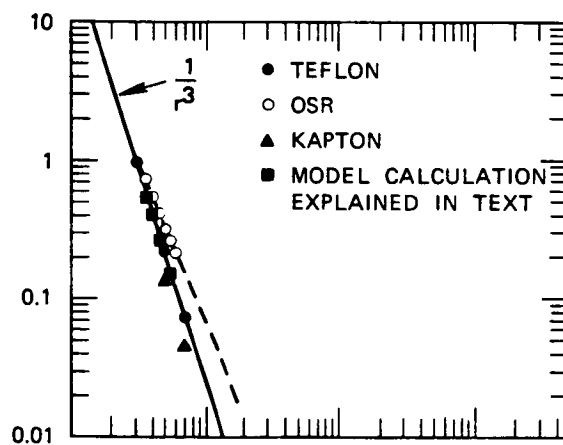


FIGURE 10 SPATIAL VARIATION OF MEASURED ELECTRIC FIELD WITH DISTANCE vs  $1/r^3$  VARIATION

**AGREEMENT FOR NASA/OAST-USAF/AFSC SPACE INTERDEPENDENCY  
ON SPACECRAFT-ENVIRONMENT INTERACTION**

**C. P. Pike  
Air Force Geophysics Laboratory**

**N. J. Stevens  
NASA Lewis Research Center**

**SUMMARY**

The objective of this investigation is to develop technology to control interactions between large spacecraft systems and the charged particle environments of space. This technology will support NASA/DOD operations of the Shuttle/IUS and AFSC Space Division's Space Defense Systems Program concepts, Strategic Satellite system, MSP/Mini-Halo and the DARPA/RADC Space Based Radar technology program.

To achieve this objective, a joint AF/NASA comprehensive research and technology program on spacecraft-environment interactions is being undertaken. This program consists of combined contractual and in-house efforts aimed at understanding spacecraft-environment interaction phenomena and relating ground test results to space conditions. There is a concerted effort to identify project-related environmental interactions of concern. There is a materials investigation to measure the basic properties of materials and develop or modify materials as needed. There is a ground simulation investigation to evaluate basic plasma interaction phenomena and provide inputs to the analytical modeling investigation. Systems performance is evaluated by both ground tests and analysis. There is an environmental impact investigation to determine the effect of future large spacecraft on the charged particle environment. Finally, there will be space flight investigations to verify the results of this technology investigation. The products of this research and technology program are test standards and design guidelines which will summarize the technology, specify test criteria and provide techniques to minimize or eliminate system interactions with the charged particle environment.

**SPACECRAFT-ENVIRONMENT INTERACTION STEERING COMMITTEE**

**Function**

The function of this committee is to coordinate all phases of the investigation, review progress and to direct changes, as required, to satisfy

the need of the AF and NASA. This committee shall meet at least annually to review the program, to resolve pending action items, to receive reports from Working Group Chairmen and to issue required action items. The minutes of these meetings will be issued.

#### Reporting

The committee will report to the NASA (OAST) and AFSC Space Research and Technology Interdependency Working Group.

#### Membership

The Steering Committee consists of the following members:

Cochairmen: Charles P. Pike (AFGL)  
Robert C. Finke (NASA-Lewis Research Center)

Members: Wayne Hudson, NASA HQ  
J. McCoy, JSC  
C. R. Chapell, MSFC  
N. J. Stevens, LeRC  
E. Pawlik, JPL  
W. Lehn, AFWAL  
A. Frederickson, RADC

#### Working Groups

The Steering Committee is advised by Working Groups. These Working Groups have been established to review, plan and coordinate investigations in specific areas, recommend new directions as required and make periodic progress reports to the Steering Committee. The Working Groups will function to keep the various organizations, both those within the formal Spacecraft-Environment Interaction Program and others, coordinated in their various activities.

The Chairman of each Working Group is appointed by the Steering Committee. He has responsibility for the selection of members of the Working Group from the technical experts of government, industrial or university communities.

#### JUSTIFICATION

There is a trend towards missions/programs using very large spacecraft in the mid to late eighties. These missions are initially planned for low Earth (Shuttle) orbits with the possibility of moving to geosynchronous orbit altitudes. Typical examples of these missions include communications platforms and space-based radar. The now-concluding AF/NASA Spacecraft Charging Technology Investigation has shown that the environmental charged particle fluxes can act on spacecraft surfaces and influence system performance. These new,



large spacecraft can have potentially serious interactions at all altitudes and these interactions must be evaluated. The proposed structures have dimensions larger than characteristic plasma lengths and differential surface charging is possible. The motion of such a large structure in the Earth's magnetic field will induce electromagnetic forces on the structure. Since these structures are designed for low density materials, electromagnetically induced stress can impact the mechanical design.

There is also a trend toward high power modules for space applications. Plans have been established for 25 kW modules in the early eighties, expanding to 500 kW modules in the late eighties. At these power levels the operating voltages can be expected to be increased to levels greater than the present range of 30 to 100 volts to increase system efficiency. This elevation of operating voltages means that the probability for interactions between the biased surfaces and the plasma environment can be increased. Laboratory tests on small solar array samples have indicated that possible interactions include the establishment of parasitic current loops through the environment (resulting in power losses), arcing at negative potentials and disproportional current collection through holes in insulation to biased surfaces underneath. These effects can adversely influence the operation of space power modules and must be understood prior to building high powered systems.

As an outgrowth of the AF/NASA Spacecraft Charging Technology Investigation, it is possible to predict the electric fields surrounding the spacecraft due to the surface charging. Using this technique it will be possible to assess the impact of a spacecraft on the measurements provided by spacecraft sensors and instruments; hence, significantly improving confidence in the data.

There is also a growing concern for the influence that the very large structures proposed for future applications can have on the charged particle environment. The tenuous balance established by nature may be upset when these systems are inserted into Earth orbits.

#### SPACECRAFT-ENVIRONMENT INTERACTION TECHNOLOGY INVESTIGATION

The overall objective of this investigation is to develop the technology for controlling spacecraft system interactions with the charged particle environment of space. The technology developed in this investigation will support proposed AF/NASA space mission concepts into the nineties.

The initial emphasis in this investigation will be on low Earth orbit (LEO) conditions. The proposed missions will be catalogued, engineering specifications for the charged particle environment established and possible interactions identified. The ground technology investigation will concentrate on determining and modeling plasma phenomena and then extrapolating these results to system interactions and performance in space. Applicable techniques available to the participants will be utilized.

The environmental interactions for large systems operating in geosynchronous conditions will be evaluated after the low Earth orbit study. The geosynchronous environmental investigation will utilize the LEO study results as well as applicable techniques from the AF/NASA Spacecraft Charging Technology Investigation.

In both the LEO and geosynchronous environmental interactions investigation the effect of large systems on the charged particle environments will be evaluated as well as the effect of the environment on the system performance.

Space flight experiments will be conducted to verify the results of the ground-based technology investigation of the environmental interactions. While these space experiments will be coordinated with the ground-based study, they will be proposed as separate experiments and funded independently.

The output of this investigation will be a series of Test Standards and Design Guideline documents. These will be issued in a preliminary form early in the investigation and upgraded as the study continues. This investigation is planned as a 9-year technology program starting in FY 81 and running through FY 89. The major milestones for this investigation are shown in Figure 1.

#### TECHNICAL APPROACH

In this section the technical approach to accomplish this technology investigation is discussed. For each element of the investigation, the approach will be summarized and the known tasks identified. The agency or agencies responsible for directing and coordinating the work under each task will be given. While the prime responsibility is assigned to one agency, the expertise of other agencies will be utilized.

#### User Requirements

It is necessary to identify those missions or projects that could benefit from the technology that will be developed by this investigation and to incorporate their requirements into this study. This will be accomplished by maintaining close liaison with the government funding sources and project offices. Potential applications of the technology have been identified as: large space structures, large multikilowatt space power systems, large high power communications satellites, large surveillance satellites and scientific spacecraft (charged surface effects on instrument behavior).

The primary interactions to be evaluated have been tentatively identified as:

- a. Large space system interactions. These interactions involve the possible effects due to the motion of a large body in the space environment and due to material reactions to the charged particle fluxes.

b. Biased systems/charged particle interactions. These interactions include spacecraft systems that generate or use high voltages exposed to space. Such spacecraft systems as high voltage space power modules and communications satellites fall into this category.

c. Scientific instruments and sensor interactions. An evaluation of the impact of electric fields surrounding a spacecraft on the behavior of scientific instruments and sensors will be conducted.

d. Large structure interactions on the environment. The presence of the proposed large structures may affect the environment. Such effects must be evaluated.

Other interactions that can be evaluated are:

e. Enhanced particle environment interactions. These interactions involve spacecraft particle sources that can be ionized and increase the charged particle environment around the spacecraft. Close coordination will be maintained with the existing AF/NASA Spacecraft Contamination Investigation.

f. High energy particle interactions. Penetrating radiation effects will be evaluated in this study only insofar as they can influence charging phenomena (e.g., internal spacecraft charging, radiation enhanced conductivity in materials). Close coordination will be maintained with other groups conducting radiation damage evaluations.

The specific tasks and responsible agencies are:

Task 1: Coordination and Overview. The coordination of the users' needs and the incorporation of these needs into the investigation will be the responsibility of the Steering Committee.

Task 2: AF and NASA Contacts. The various agencies will maintain a close relationship with the projects managed within their respective agency to determine user needs for this investigation and report those needs to the Steering Committee for coordination and incorporation into this investigation.

#### Environmental Specifications

Under this element the natural environment will be investigated and engineering specifications generated or updated as appropriate. The impact of large spacecraft on the environment shall also be investigated and evaluated.

The specific tasks and responsible agencies are:

Task 1: Natural Environment Specification. The available data for the low Earth orbit, geosynchronous and solar wind charged particle environments will be reviewed. An engineering specification for these regions will be generated and made available to all parties concerned with environmental inter-

actions. This work will be the responsibility of AFGL.

Task 2: Planetary Environment Specification. The available data for the planetary environments will be reviewed. An engineering specification for these environments will be generated and made available to all parties concerned with environmental interactions. This work will be directed by JPL.

Task 3: Enhanced Spacecraft Environment Specification. The available data on possible outgassing or other sources that can be ionized and enhance the natural charged particle environment will be reviewed. An engineering specification for this enhanced environment will be generated and made available to all parties concerned with spacecraft environmental interactions. Close coordination will be maintained with the AF/NASA Spacecraft Contamination Investigation to avoid duplication. This work will be the responsibility of JPL.

Task 4: Environmental Impact. Using the environmental specifications and the proposed large spacecraft plans, the possible alterations to the natural environment due to the presence of the spacecraft will be investigated and evaluated. This work will be the responsibility of AFGL.

#### Materials Investigation

In this program element the basic properties of typical spacecraft materials, exposed to the space environment, will be determined and new or modified materials will be developed.

The specific tasks and responsible agencies are:

Task 1: Material Property Determination. The classical properties of typical spacecraft materials will be determined as a function of the material parameters and environmental fluxes. The properties to be determined are those which influence the surface potential of the material, e.g., secondary emission, backscattering and photoemission. Electron, proton and photon fluxes as determined by the environmental specifications are to be considered. This work will be the responsibility of JPL.

Task 2: New or Modified Materials Development. In this task materials having selective properties will be developed as a means of controlling detrimental effects of spacecraft environmental interactions. The required properties for these materials, including advanced composite materials, will be defined from the interaction studies. The materials will be developed and tested to show that they will meet the requirements. This task will be the responsibility of AFWAL.

#### Ground Simulation Investigation

Under this technology element existing facilities will be utilized to simulate the space plasma environment and interactions will be studied experimentally.

The specific tasks and responsible agencies are:

Task 1: Basic Interaction Studies. This task will be divided into several subtasks each devoted to the study of a particular aspect of the interaction phenomena.

a. Interactions between the charged particle environment and insulator/biased conductor surfaces will be investigated. Here the interest is in the growth of electric fields on the insulator surfaces as a function of the material properties, charged particle density and voltage. This work will be conducted by the LeRC.

b. Plasma sheath growth phenomena will be investigated. Interactions between large structures moving through the charged particle environment will be investigated. Plasma wake and ram effects and sheath growth will be evaluated. Responsibility for this work will be divided between MSFC for NASA mission requirements and AFGL for unique AF mission requirements.

c. Discharges resulting from environmental interactions will be characterized. Both radiated and conducted characteristics will be determined. This work will be conducted by JPL.

d. Penetrating radiation studies will be conducted to evaluate radiation induced charging interactions. This work will be conducted by RADC.

Task 2: Large High Voltage Power System Studies. In this task the basic interaction study results from Task 1 above will be applied to the design of large power systems for space applications. The interactions will be scaled to the large size of a typical power system, the environmental conditions will be scaled from ground conditions to space, and the effects of the environment on system performance will be evaluated. Means of controlling detrimental interactions will be devised. Wherever possible, experiments will be conducted to demonstrate that the interactions can be controlled. This work will be conducted by JSC for NASA missions and by AFWAL for AF missions.

Task 3: Large Space Structure - Environmental Interaction Experimental Studies.

a. The large structures proposed for future space applications will interact with the environment inducing among other things electrostatic stresses that must be considered in the design of such structures. In this task these interactions will be studied, the effect assessed and control technology developed. This work will be directed by the MSFC.

b. The environmental interactions in large spacecraft can be mitigated by techniques such as active charge control devices. An evaluation of techniques will be conducted to determine the extent that they will alleviate detrimental systems performance. This work will be conducted by AFGL.

## Analytical Investigation

In this technology element models of physical processes and engineering design tools will be developed. Models of individual interactions would be developed to identify critical parameters. These would be incorporated into a general engineering analytical tool (or tools) to aid in designing systems to withstand detrimental environmental interactions.

The specific tasks and agencies are:

Task 1: Basic Plasma Phenomenological Modeling. In this task the basic plasma phenomena necessary to evaluate environmental interactions with spacecraft systems will be modeled. These phenomena will include ram and wake velocity effects, plasma sheath effects and magnetic field effects. Since this modeling will incorporate the capabilities of several AF and NASA centers, the task will be coordinated by the Steering Committee.

Task 2: Discharge Modeling. In this task models of discharge phenomena will be developed. The work will be conducted by JPL.

Task 3: System Level Analytical Models. In this task analytical models will be developed to support design of mission spacecraft for the mid to late eighties. These design tools will incorporate the interaction models developed in Task 1 and will be capable of evaluating the impact of the environmental interactions and of assessing means of minimizing detrimental interactions. The following models will be developed.

a. Large Space Structures. This model will evaluate the interactions between the large space structures and the space environment. It will be developed by AFGL.

b. Large, High Voltage Power Systems. This model will evaluate the interactions that result from the operation of high voltage systems on spacecraft. It will be developed by LeRC.

## Space Flight Experiment Planning and Evaluation

The results of the ground technology program must be verified in the actual space environment. To accomplish this, reasonable space flight experiments must be planned and evaluated. It is anticipated that these experiments will be conducted as Shuttle payload experiments or as secondary payloads on approved missions (such as flight demonstrations of large space structures). Close liaison will be maintained with the NASA Shuttle Project Office and with the AF Space Test Program Office to maintain cognizance of flight opportunities. At this time it is not possible to specify the number and types of experiments that will be required; they will be the logical outgrowth of this technology investigation as it progresses.

All agencies participating in this investigation will assist in the

planning and evaluation of flight experiments. The Steering Committee will coordinate this activity.

#### Design Guidelines and Test Standards

Design Guidelines and Test Standards will be issued and updated as this program develops. These documents will summarize the existing state-of-the-art of the various interactions being studied. Guidelines to be used in designing systems for space applications and test criteria for verifying conformance will be delineated. All participating agencies will submit their contributions for compilation by the Steering Committee. The LeRC will be responsible for issuing the Design Guidelines Document and AFGL will be responsible for issuing the Test Standards.

#### Identified Organizational Responsibilities

- a. Steering Committee: - Overall coordination and planning of the investigation
  - Incorporation of user requirements into the investigation
  - Coordination of basic plasma phenomena modeling
  - Coordination of space flight experiment options
  - Conduct annual meeting and issue minutes
- b. AFGL:
  - AF point of contact
  - Coordination for AF
  - Issue test standards document
  - Natural environment engineering specification
  - Techniques for mitigating systems limiting effects
  - Environmental impact
  - Plasma sheath growth experimental studies
  - Large Space Structures analytical modeling
- c. AFWAL:
  - Development of new or modified materials
  - Large high voltage power system studies
  - Structure concept definition
  - Analytical design tools
- d. RADC:
  - Perform penetrating radiation effects studies on materials
- e. LeRC:
  - NASA point of contact
  - Coordination for NASA
  - Issue design guidelines document
  - Basic interaction experimental studies
  - Enhanced environment - system experimental studies
  - High voltage system analytical model

- f. JPL:
  - Planetary environment specification
  - Material property measurements
  - Evaluation of sensor performance
  - Experimental and analytical discharge studies
- g. JSC:
  - Plasma sheath growth experimental studies
  - Large high voltage system experimental studies
- h. MSFC:
  - Ram and wake and magnetic field experimental studies
  - Large structure experimental studies

#### CONCLUDING REMARK

This Agreement was approved on 15 May 1980 by NASA and Air Force Systems Command.

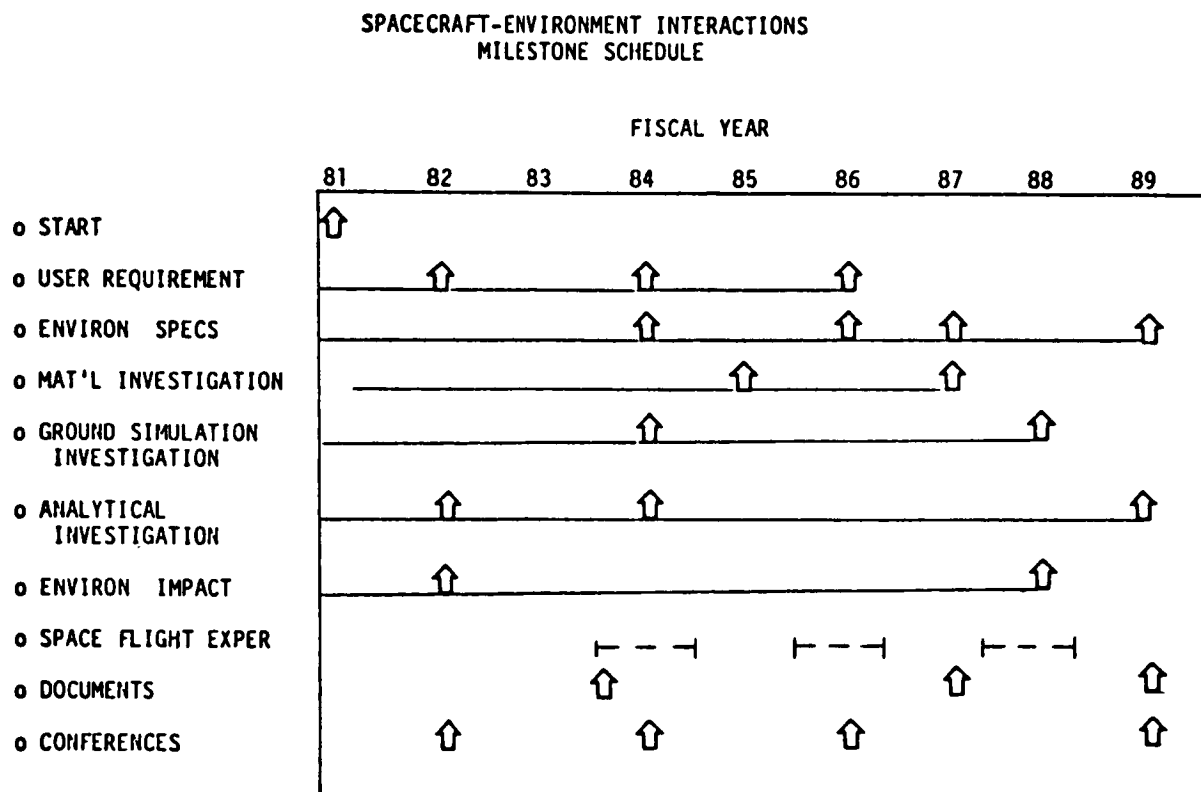


Figure 1



## PLASMA INTERACTIONS WITH SOLAR ARRAYS AT HIGH VOLTAGES

Norman T. Grier, Craig Smith, and Lisa M. Johnson  
NASA Lewis Research Center

### SUMMARY

The problems associated with operating solar arrays at high positive and negative voltages have been investigated at Lewis for several years. These studies have shown that, for arrays biased positively with respect to plasma potential, plasma coupling currents to the array are greatly enhanced by the insulators surrounding current collection points. For arrays biased negatively, arcing occurs at threshold voltages that depend on the plasma densities. This current enhancement and arcing were verified both in ground and space testing for small arrays ( $\sim 100 \text{ cm}^2$ ). Extension of these results to the larger arrays proposed for future missions becomes difficult to verify in ground tests because the sheath generated around a larger surface may extend to the vacuum chamber wall. Scaling laws are therefore required. Scaling from small laboratory-size arrays to large kilowatt and gigawatt power arrays is not reasonable. So the approach taken in this preliminary investigation is to obtain results and devise scaling laws for arrays that can be tested in ground-based space simulation facilities. This report presents preliminary results for tests conducted on solar arrays with areas ranging from approximately 100 to 13 700  $\text{cm}^2$  in a plasma density of roughly  $1 \times 10^4$  electron/ $\text{cm}^3$ . The plasma coupling current for the small array ( $\sim 100 \text{ cm}^2$ ) did not scale linearly to current for the larger arrays.

### INTRODUCTION

The problems associated with operating solar arrays in the kilovolt range have been investigated extensively for several years (refs. 1 to 9). Most of these investigations were carried out on small arrays in relatively small vacuum chambers. Future satellites will require kilowatts to gigawatts of power, necessitating solar arrays of meters to kilometers in length. These arrays will operate at much higher voltages than present arrays. Operating voltages to 45 kilovolts have been proposed (ref. 10). At such high voltage and power levels, large areas of the solar array operating at kilovolts will be exposed to the plasma environment. The interaction of these high-voltage surfaces with the ambient plasma must be understood before these large arrays become operational.

Testing of small arrays in plasma environments has revealed that, if the array is biased positively with respect to the plasma, the electron current coupling the ambient plasma to the array is tens to hundreds of times larger than would be calculated from simple probe theory. If the array is biased negatively with respect to the plasma, blowoff arc discharges cause large current surges in the array harness. Testing for these interaction phenomena on full-scale kilowatt and gigawatt power arrays is impossible in present laboratory plasma simulation facilities. Scaling laws are therefore required.

Scaling from small laboratory-size arrays to large kilowatt and gigawatt power arrays is not reasonable. Thus the approach taken at the Lewis Research Center is to devise scaling laws from arrays that can be tested in ground simulation facilities and then to substantiate these results, where possible, with flight data.

This report presents preliminary results for tests conducted on solar arrays with areas of approximately 100, 400, 800, 1200, 1600, 2000, and 13 700 square centimeters in a plasma density of roughly  $1 \times 10^4$  electrons/cm<sup>3</sup>. The array was externally biased in steps to  $\pm 1$  kilovolt. Four 400-square-centimeter arrays that can be operated independently or in combination to give areas of 400, 800, 1200, or 1600 square centimeters are scheduled to be tested on a flight in mid-1982.

#### EXPERIMENTAL SAMPLES

All the arrays had 2- by 2-centimeter solar cells with 6-mil-thick fused silica glass covering each individual solar cell. The conventional Z-bar interconnections were left uncovered. The interconnections served as the electrodes for collecting charges from the plasma. They represented approximately 5 percent of the total array area. The 100-square-centimeter array consisted of 24 solar cells arranged as a 6- by 4-cell matrix. The 2000-square-centimeter array consisted of 414 solar cells arranged in a 23- by 18-cell matrix. Three columns (18 cells in each column) were removed from another similar 2000-square-centimeter array to form four independent array segments of 400 square centimeters each. The 400-, 800-, 1200-, and 1600-square-centimeter arrays were combinations of these segments. The approximately 13 700-square-centimeter array was formed by arranging seven 1400-square-centimeter solar array panels and two 2000-square-centimeter solar array panels to give one large 3- by 3-matrix solar array panel. This array was tested as a single unit.

#### PROCEDURE

All the solar panels except the 13 700-square-centimeter array were tested in a 2.4-meter-diameter by 3-meter-long vacuum chamber. The 13 700-square-centimeter solar array was tested in the 20-meter-diameter by 27.4-meter-long vacuum chamber at the NASA Johnson Space Flight Center, as well as in a 4.6-meter-diameter by 19.2-meter-long vacuum chamber at the NASA Lewis Research Center. A more detailed description of the 13 700-square-centimeter solar array tests is given in reference 9.

The plasma was generated by bleeding argon gas into a 5-centimeter-diameter by 7-centimeter-long discharge chamber. The argon was ionized by electrons emitted from a hot tungsten filament. The emitted electrons were accelerated through a potential of 50 volts that was applied between the filament and the cylindrical anode. The ionized argon and the electrons formed in the discharge chamber exited through an 1.3-centimeter-diameter orifice at one end of chamber. A sketch of this plasma source is shown in figure 1. These charged particles formed the plasma for the tests. Plasma densities of  $10^2$  to  $10^6$  electrons/cm<sup>3</sup> are possible at the testing location with this source.

In the tests the solar arrays were biased with an external power supply. The small voltage generated by the array had a negligible effect on the plasma coupling current since the vacuum chamber was dark during the tests. The plasma coupling current to the arrays was measured with an electrometer between the power supply and the array while the voltage was slowly increased. A sketch of the test setup is shown in figure 2. Both positive and negative bias were used. The maximum voltages were  $\pm 1$  kilovolt, or less if the sample arced.

## DIAGNOSTICS

The current-voltage (I-V) characteristics of the two spheres (1.9 cm and 1.27 cm diam) were used to determine the plasma parameters. The voltage was varied from -100 volts to 100 volts. Assuming the gas was Maxwellian, the current in the electron repulsion region of the I-V characteristic is given by (ref. 11)

$$I = Aen \left( \frac{kT}{2\pi m} \right)^{1/2} e^{-\left| \frac{eV}{kT} \right|} \quad (1)$$

where  $A$  is the area of the sphere,  $n$  is the electron density,  $k$  is Boltzmann's constant,  $T$  is the temperature,  $m$  is the electron mass,  $e$  is the electronic charge, and  $V$  is the applied voltage. From equation (1) the temperature  $T$  is found to be (ref. 11)

$$T = \frac{k}{e} \frac{V_2 - V_1}{\ln I_1 / I_2}$$

where  $I_1, V_1$  and  $I_2, V_2$  are two current-voltage points in the repulsion region.

The plasma density was found by using the electron saturation region of the I-V characteristic. Assuming the gas was Maxwellian outside the sheath and collisionless within the sheath, the current is (ref. 11)

$$I = \frac{1}{2} neA \left( \frac{2kT}{\pi m} \right)^{1/2} \left( 1 + \frac{eV}{kT} \right)$$

so that after taking the derivative, the equation can be solved for the electron density to give

$$n = \frac{(2\pi mkT)^{1/2}}{e^2 A} \frac{dI}{dV}$$

This equation was used to determine the density of the plasma.

## RESULTS AND DISCUSSION

The plasma coupling current as a function of applied positive voltage for the 100-square-centimeter array is shown in figure 3. The data in this figure show a comparison of flight results with laboratory results. The flight data were obtained from the Plasma Interaction Experiment (PIX) satellite that was launched in March 1978. In addition to the solar array experiment, there were two disk experiments on this flight, a Kapton disk and a plain disk. The Kapton disk consisted of a 1.4-centimeter-diameter gold-coated metal electrode mounted on a 20-centimeter diameter 5-mil-thick sheet of Kapton. The plain disk has the same size gold-coated electrode without the Kapton sheet. More details of the experiments are given in reference 5. In this figure the ground-based data agree well with the flight results.

Figure 4 shows the flight and ground-based results for these same three experiments when they are negatively biased. Again the ground-based data agree well with the flight results. The arc discharges for the solar array are typical for solar arrays negatively biased in a plasma. For this array, arcing occurred at a bias voltage of -700 volts. This is the highest voltage achieved with any of the solar arrays when negatively biased. Figures 3 and 4 show that ground-based facilities can be used to reliably simulate the plasma interaction on small arrays in space.

Figure 5 shows the 13 700-square-centimeter array. This array was formed from nine single panels. The panels were mounted on a aluminum grating structure by using 1.9-centimeter-long ceramic isolators. Each panel could be biased individually or in combination. Figure 5 shows the total plasma current when all panels were biased at the same positive voltage. For comparison the data for a single 2000-square-centimeter panel are also shown in this figure. If the coupling current scaled linearly with area, the nine-panel array current would be approximately seven times larger than the single-panel current. As can be seen from this figure, the nine-panel array current is much higher than this at the low voltages and lower than this at the high voltages. Both panels were tested in the same plasma environment.

Figure 7 shows the results for negative bias on the nine-panel array and the single 2000-square-centimeter panel. As can be seen, the current for negative bias also does not scale linearly with area. However, the inception voltages for arcing on the two arrays are within 200 volts of each other. This agrees with data previously obtained in that the arcing voltage is independent of the size of the array (refs. 6 and 9). Details of the 13 700-square-centimeter solar array results are given in reference 9.

The results for positive bias on the 400- and 1600-square-centimeter arrays are given in figure 8. Above 300 volts the 1600-square-centimeter array current saturated. This indicates that the array was collecting the maximum current possible for this size facility at this plasma density. Below 300 volts the current for the 1600-square-centimeter array was approximately four times that for the 400-square-centimeter array. For these arrays the current does scale approximately linearly with area. This linear scaling was substantiated with preliminary results from the 800- and 1200-square-

centimeter arrays. The currents for these two arrays were two and three times that for the 400-square-centimeter array, respectively.

Also shown in figure 8 are data for the 100-square-centimeter array. The dashed curve shown represents four times the 100-square-centimeter array data. As can be seen, these data fall far below those for the 400-square-centimeter array. One would have expected that the small (100 cm<sup>2</sup>) array current would follow close to spherical theory since end effects are not negligible. Since spheres collect the maximum current, it was expected that the dashed curve would fall above the 400-square-centimeter-array data. Further tests are being performed to investigate this behavior.

The results for negative bias on the 400- and 1600-square-centimeter arrays are shown in figure 9. For voltages above 100 volts for the 1600-square-centimeter array and 200 volts for the 400-square-centimeter array, arc discharges occurred. This 100 volts arc inception voltage is the lowest inception voltage that has been observed for arcing. Before arcing occurred, the current scaled approximately linearly with array area. This was also substantiated with preliminary data for the 800- and 1200-square-centimeter arrays. The current for the 100-square-centimeter array was much too low for negative bias also, as can be seen from the dashed curve in figure 10.

#### CONCLUDING REMARKS

The plasma coupling current as a function of applied voltage has been presented for solar arrays ranging in size from 100 to 13 700 square centimeters. For the 100-square-centimeter array, flight and laboratory data have been presented. The two results were in good agreement. This verified that ground-based facilities can be used to simulate the plasma interaction phenomenon in space for small solar arrays.

One of the objectives of this investigation was to determine whether the plasma coupling current scales linearly with array area. The 100- and 2000-square-centimeter-panel coupling currents did not scale linearly with area to the 13 700-square-centimeter array. However, the coupling current for the 400-square-centimeter panel could be scaled linearly with area to obtain the current for the 800-, 1200-, and 1600-square-centimeter panels. Since these arrays were on the same substrate, this may have contributed to the linear scaling. This result occurred for both positive and negative bias on the arrays. Continued testing is being done to further investigate this effect.

#### REFERENCES

1. Cole, R. K.; Ogawa, H. S.; and Sellen, J. M., Jr.: Operation of Solar Cell Arrays in Dilute Streaming Plasma. (TRW-09357-6006-R000, TRW Systems; NASA Contract NAS3-10612.) NASA CR-72376 1968.
2. Grier, N. T.; and McKinzie, D. J., Jr.: Measured Current Drainage Through Holes in Various Dielectrics up to 2 Kilovolts in a Dilute Plasma. NASA TN D-8663, 1972.
3. Grier, N. T.; and Domitz, S.: Current from a Dilute Plasma Measured Through Holes in Insulators. NASA TN D-8111, 1975.

4. Kennerud, K. L.: High Voltage Solar Array Experiments. (Boeing Aerospace Co.; NASA Contract NAS3-14364.) NASA CR-121280, 1974.
5. Herron, B. G.; Bayless, J. R.; and Worken, J. D.: High Voltage Solar Array Technology, AIAA Paper 72-443, Apr. 1972.
6. Grier, N. T.; and Stevens, N. J.: Plasma Interaction Experiment (PIX) Flight Results. Spacecraft Charging Technology - 1978, NASA CP-2071, AFGL TR-79-0082, 1979, pp. 295-314.
7. Grier, Norman T.: High Voltage Surface - Charged Particle Environment Test Results from Space Flight and Ground Simulation Experiments. NASA TM-79184, 1979.
8. Stevens, N. John: Space Environmental Interactions with Biased Spacecraft Surfaces. Space Systems and Their Interactions with Earth's Space Environment, H. B. Garrett and C. P. Pike, eds., Progress in Astronautics and Aeronautics, Vol. 71, American Institute of Aeronautics and Astronautics, Inc., 1980, pp. 455-476.
9. Grier, Norman T.: Experimental Results on Plasma Interactions with Large Surfaces at High Voltages. NASA TM-81423, 1980.
10. Systems Definition of Space-Based Power Conversion System (D180-20309-1, Boeing Aerospace Co.; NASA Contract NAS8-31628.) NASA CR-150209, 1977.
11. Chen, Francis F.: Electric Probes. Plasma Diagnostic Techniques, R. H. Huddlestone and S. L. Leonard, eds., Academic Press, 1965, Chapt. 4, pp. 113-200.

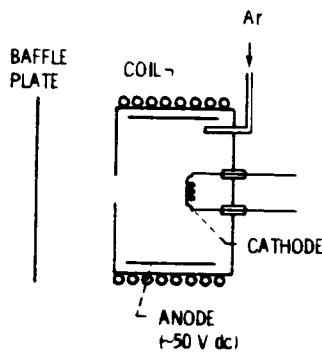


Figure 1. - Plasma-generating source.

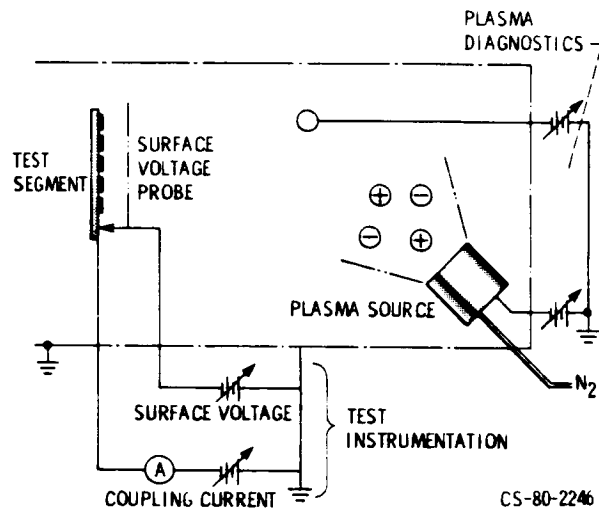


Figure 2. - Schematic diagram of test arrangement.

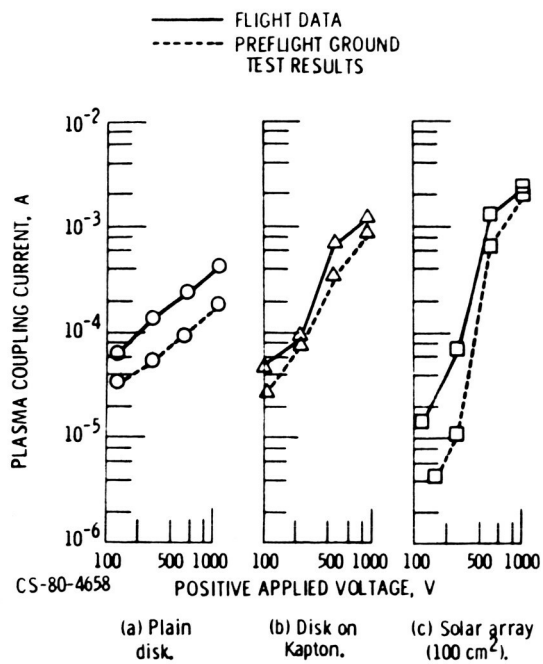


Figure 3. - Adjusted flight current compared with preflight ground current as a function of applied voltage. Plasma density,  $n$ ,  $\sim 2 \times 10^4$  electrons/cm<sup>3</sup>.

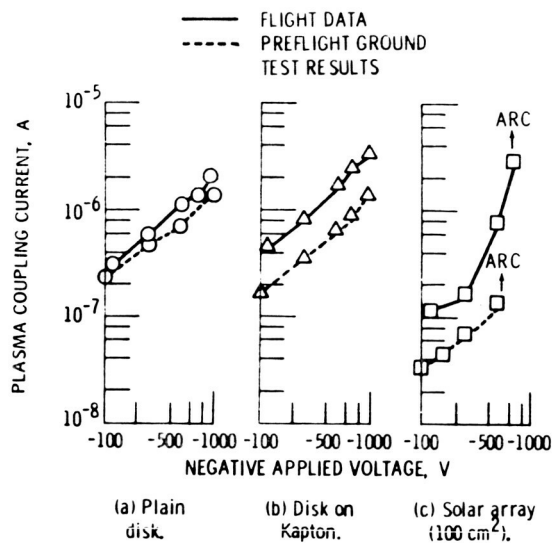


Figure 4. - Flight plasma current compared with preflight ground current as a function of applied voltage. Plasma density,  $n$ ,  $\sim 2 \times 10^4$  electrons/cm<sup>3</sup>.

CS-80-4651

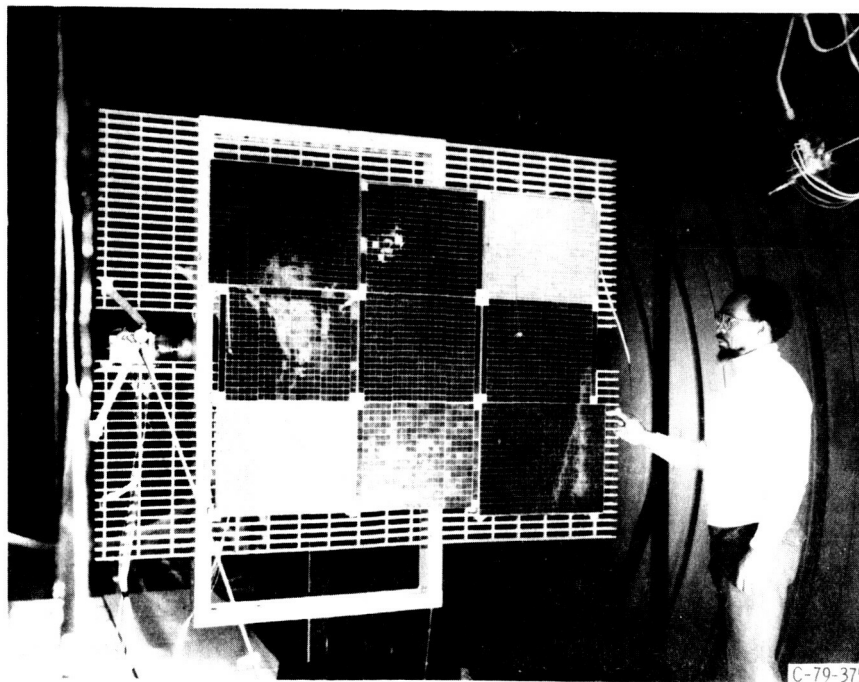


Figure 5. - 13 700-Square-centimeter array.

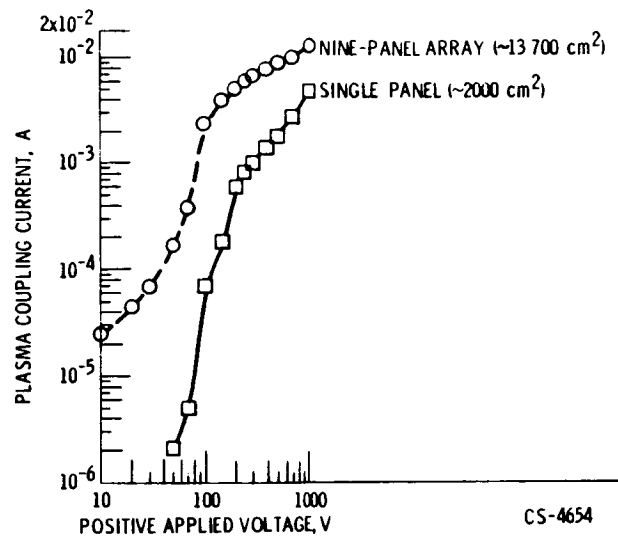


Figure 6. - Plasma coupling current as a function of positive applied voltage for 13 700- and 2000-cm<sup>2</sup> arrays. Plasma density,  $n$ ,  $8 \times 10^3$  electrons/cm<sup>3</sup>.

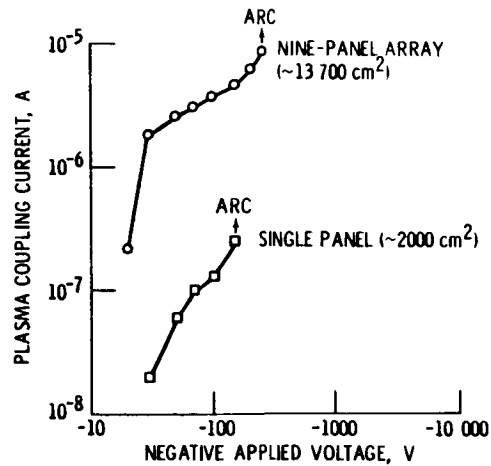


Figure 7. - Plasma coupling current as a function of negative applied voltage for 13 700- and 2000-cm<sup>2</sup> solar arrays. Plasma density,  $n$ ,  $\sim 4 \times 10^4$  electrons/cm<sup>3</sup>.



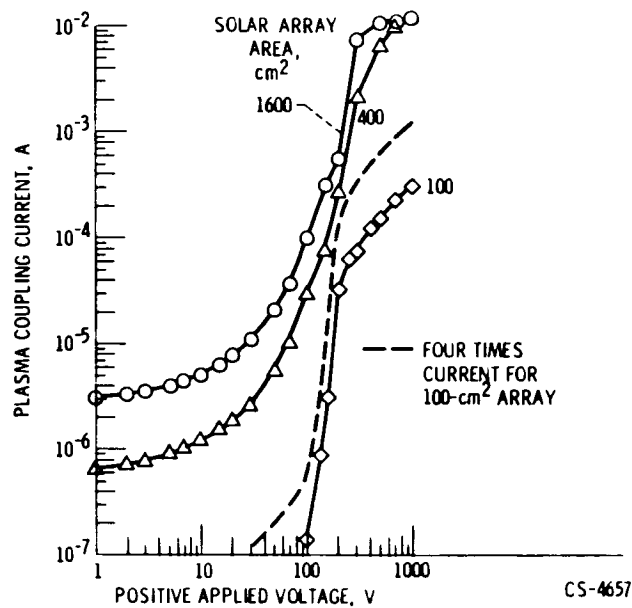


Figure 8. - Plasma coupling current as a function of positive applied voltage for 100-, 400-, and 1600-cm<sup>2</sup> arrays. Plasma density,  $n$ ,  $\sim 9.3 \times 10^3$  electrons/cm<sup>3</sup>.

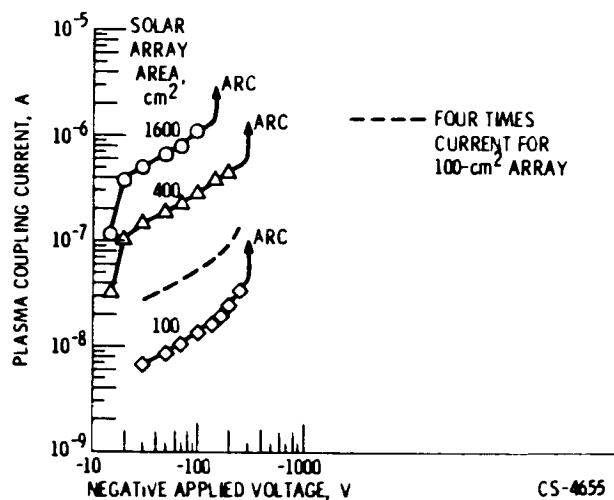


Figure 9. - Plasma coupling current as a function of negative applied voltage for 100-, 400-, and 1600-cm<sup>2</sup> arrays. Plasma density,  $n$ ,  $9.3 \times 10^3$  electrons/cm<sup>3</sup>.

# **EXPERIMENTAL PLASMA LEAKAGE CURRENTS TO INSULATED AND UNINSULATED 10 m<sup>2</sup> HIGH-VOLTAGE PANELS**

**J. E. McCoy and D. T. Martucci**  
**NASA Johnson Space Center**

## **ABSTRACT**

Recent plasma tests in the large chamber at the NASA Johnson Space Center have measured plasma leakage currents to a completely conductive 1-by 10-meter panel biased at voltages up to 3 kV, in an argon plasma at densities from  $10^4$  to  $10^6$  per  $\text{cm}^3$  with  $T_e < 0.2$  eV. The same panel was then insulated by applying Mylar tape to 90-99 percent of its surface and retested in the same plasma conditions. Leakage currents below 40 V were reduced by the insulation but increased rapidly between 50 and 150 V to equal or exceed the currents observed for the uninsulated panel. Plasma current at -200 V to the insulated panel was triple that obtained with no insulation at all. In addition, the insulated panel began to "arc" discharge to the plasma at applied voltages above 200 V. Similar results were obtained with other configurations of conductive, partially conductive, and mostly dielectric panels. Increasing the amounts of surface insulation not only was ineffective in reducing plasma current leakage at voltages above 100 V, but it also reduced the threshold voltage observed for the onset of large transient current increases due to "arcing" to the plasma.

# NUMERICAL SIMULATION OF PLASMA-INSULATOR INTERACTIONS IN SPACE PART I: THE SELF-CONSISTENT CALCULATION\*

J. H. Nonnast, R. C. Chaky, T. P. Armstrong,  
J. Enoch, and G. G. Wiseman  
University of Kansas

## SUMMARY

A computer program is being developed to simulate the interaction of a plasma with a conducting disk partially covered by an insulator. Initial runs consider only charge sticking to the dielectric. Results indicate that the current density drawn by the hole in the dielectric increases approximately linearly with voltage for conductor voltages between 5 Volts and 250 Volts.

## INTRODUCTION

Solar cell arrays which operate at high voltage (kilovolts) are being considered for power generation on satellites. Operating the solar cell arrays in the multikilovolt range provides one means of improving electrical efficiency and reducing weight. However, if the dielectric material insulating the various parts of these solar cells develop holes or cracks at these high voltages, large drainage currents from the ambient plasma will occur, resulting in a degradation of performance. This situation is further complicated by experiments which show that for electron collection the dielectric tends to effectively increase the collecting area of the hole and therefore increase even further the coupling current (refs. 1-3). In this paper we will describe a computer program ESP (for "electrostatic plasma") which is being developed to simulate the interaction of a plasma with a conducting disk partially covered by an insulator and maintained at any desired voltage with respect to the plasma. The simulated system is illustrated in figure 1.

The simulation is written in such a way that various aspects of the plasma-dielectric interaction can be taken into account. In this paper, runs will be described in which the insulator has been treated only as a repository for surface charge. Other computer runs were made which take into account secondary emission from the dielectric (ref. 4). In the future we hope to study edge effects more closely, along with the inclusion of more dielectric properties such as surface currents.

---

\* This work is supported in part by NASA Lewis Research Center, Research Grant #NSG - 3290.

## DESCRIPTION OF THE COMPUTER PROGRAM

The structure of our code ESP is shown in the flowchart in figures 2 and 3. This is a  $2\frac{1}{2}$ -dimensional PIC (particle-in-cell) calculation with several unique features. PIC calculations are described fully elsewhere (refs. 5 and 6).

One unique feature of our program is the use of cylindrical coordinates for our particle mover. For an individual macroparticle, we keep track of a two-dimensional position  $(r,z)$ , the corresponding velocities  $(v_r, v_z)$  and the angular momentum  $\ell$ . The quantities  $r$ ,  $z$ ,  $v_r$  and  $v_z$  change with time;  $\ell$  does not. The particle mover is discussed further in Appendix A.

Another feature of our program is the inclusion of several sources and sinks of particles in our system: there is a current flow to a region of bare conductor on the plate, particles leave the grid region by their inertia, and other particles enter the system as particles from the ambient plasma. The inclusion of these sources and sinks of particles led to another important departure from conventional PIC methods -- the number of particles is allowed to vary with time. In practice, the particle number is limited by the storage we allot at the time of program compilation (presently we allow for up to 3000 macroelectrons and 3000 macroprotons).

There are 6 different regions of our boundary, as shown in figure 4. The  $r$ - $z$  grid represents the cylindrical region we are studying. The three-dimensional cylinder comes from rotating the grid around the  $z$ -axis. We are also assuming that symmetry exists between the top and the bottom of the simulation region. If a particle crosses the  $z$ -axis (into boundary region 1), it is reflected. (This would only happen in the case of zero angular momentum.)

A particle which moves out of the grid because  $r$  or  $z$  is too large (boundary regions 2 and 3) is lost from the grid. Because we have assumed that there is an ambient plasma with a known density and temperature, boundaries 2 and 3 also serve as sources of macroparticles; at every time step, we calculate the number of particles expected to cross into these regions due to thermal movement. We add this number, the velocities of which are chosen from a Maxwellian velocity distribution.

Particles moving across the  $z=0$  plane, outside the disk (boundary region 4), are reflected. In the simplest model, particles which move across the  $z=0$  plane into the region of the dielectric (boundary region 5), contribute to the surface charge density according to their  $r$ -position (i.e., they stick). Particles moving across the  $z=0$  plane in the region of the pinhole (boundary region 6) contribute to the current. It is this current, as a function of plate voltage, that will be used to construct the current-voltage characteristics.

In other respects, our simulation relies on extensively tested PIC methods. At present, the potential is calculated using a relaxation method

(ref. 7). The use of this method for calculating the potential necessitates that the dielectric be coincident with the conductor (i.e., we assume an infinitely thin dielectric). We are presently working on a Green function approach to calculating the potential which we feel will lend greater flexibility in dealing with the dielectric properties. This method will allow the dielectric to be moved off of the grid cell points, thus allowing different dielectric thicknesses.

## RESULTS OF COMPUTER RUNS

In this section we present the results of several runs of the computer code. In these runs, the dielectric acts simply as a medium on which charge will stick. The input parameters for the run are given below:

Temperature of plasma = 10000°K (both species)

Density =  $2.0 \times 10^{10}$  particles/m<sup>3</sup> =  $2.0 \times 10^4$  particles/cm<sup>3</sup> (both species)

Proton mass/electron mass = 1.0

Radius of conductor = 0.50m

Radius of hole = 0.15m

Thickness of dielectric = 0

Size of simulation grid = 20 x 20

Size of grid cell = .05m x .05m

Each simulation run is begun with a uniform Maxwellian plasma occupying our grid area. Enough time steps are then taken so that we reach an equilibrium state. The equilibrium state is looked for by examining several time history plots, three of which are shown for the 50 Volt case in figures 5 through 7.

Figure 5 is a plot of the total amount of charge (esu) on the dielectric vs. time. At the beginning of the run, charge is accumulating very rapidly on the dielectric (since the conductor is being held at +50 Volts, the dielectric accumulates negative charge). Most of the charge has been deposited on the dielectric by time step 200. By time step 700, we appear to have reached an equilibrium. Thus, on the basis of this plot, we are running at an equilibrium state between time steps 700 - 1000.

The cumulative total of macroelectrons collected by the hole as a function of time is shown in figure 6. The current drawn by the hole will be related to the slope of this curve, and the straight line drawn through the points indicates that the current is constant from about time step 500 through time step 1000. For this run of 50 Volts on the conductor, the average electron

current over time steps 500 to 1000 is  $3.735 \times 10^{-4}$  Amperes.

Other quantities which must come to equilibrium is the number of macroelectrons and macroprotons in our simulation system. This is shown in figure 7. (Macroparticles absorbed by the dielectric or conductor are not counted). At the beginning of the run, the numbers of macroparticles of both species are decreased. The macroelectrons are being absorbed by the dielectric and collected by the hole faster than they are being replaced at the boundary (at the outer boundaries, particles are being added at a rate dependent upon their thermal velocity). The number of macroprotons decrease at the beginning of a run because of the unshielded potential on the conductor, forcing them to leave the system at a faster rate than they are being added. The number of both particle species begins to increase as the dielectric begins to build up a significant amount of negative charge. Both the number of macroelectrons and macroprotons remain fairly constant from time step 400 on, indicating an equilibrium has been achieved.

Other plots, such as kinetic energy and drift energy of the macroparticles, the number of macroparticles leaving the system, etc., show that an equilibrium state has been reached for the second half of this simulation run.

The potential in the various grid cells is shown in two different types of plots in figures 8 through 10. The left-hand plot is a three-dimensional representation of the potential. The r- and z-coordinates of the plot represent the spatial coordinates, and the potential is plotted on the y-axis. The dielectric is denoted by "Rd", the hole by "Rh". The right-hand plot shows equipotential contours, with contours plotted for .05 x Voltage, .15 x Voltage, ..., .95 x Voltage.

Figure 8 shows the potentials at the beginning of the 50 Volt run. At this point, no charge has collected on the dielectric, and the potential is uniform over the hole and the dielectric. The potential on the outer grid cells is being forced to zero, which accounts for the departure from oblate spheroids of the outer equipotential contours. The slight variations of the potential contours in the plasma is due to irregularities in the initial loading of the plasma macroparticles.

Figure 9 shows the potential after 500 time steps (each time step is  $1.873 \times 10^{-8}$  sec). By this time, enough charge has collected on the dielectric to cause the potential on the dielectric to be close to zero. An electron sheath has built up around the hole, causing a rapid decrease in potential away from the hole. In the body of the plasma away from the hole and dielectric, the potential is essentially zero. It is this fact which makes the assumption of zero potential on the outer boundary valid. This plot can be compared to figure 10, which is the potential after 2000 time steps for the 200 Volt run. Again, the electron sheath has built up around the hole so that the outer portions of the plasma near the boundary are effectively shielded. The equipotential contours do extend further out into the plasma for this case than they did for the 50 Volt run. This will

eventually place a limit on the voltage which can be put on the conducting disk for our present grid size and plasma parameters.

If there was no hole present, and we had a conductor completely covered by a dielectric, one would expect that at equilibrium the voltage would be zero across the dielectric. (This would be the case for our plasma parameters, i.e. the ratio of proton mass to electron mass equal to one, and the proton temperature and electron temperature equal.) A close examination of the potentials on the dielectric show that a negative potential exists there. This is better illustrated in figure 11, which is a graph of the potentials on the dielectric and the conductor. The potentials indicate that there is an excess of negative charge close to the hole. After the initial charge buildup on the dielectric which occurs in the first part of the simulation run, we have observed that the potentials are always negative on the inner part of the dielectric. As the simulation proceeds, the strong electric fields due to the hole keep protons from this region of the dielectric. Thus, this portion of the dielectric stays negative. One thing which is planned for the future is to start a run with the proper amount of charge on the dielectric so that the potential is zero all the way across the dielectric. It could then be seen if the same equilibrium state is achieved with these initial conditions.

Figure 12 shows the result of our computer runs of ESP. This is a plot of hole current density vs. voltage of the conducting disk. We find that the current density increases approximately linearly with voltage for conductor voltages between 5 Volts and 250 Volts. A factor of 10 increase in voltage increases the current density by a factor of 6. On the same graph is a plot of experimental values obtained for a plain disk resting on a surface held at zero potential (ref. 1-2). The plain disk experiment has similar plasma densities and temperatures as the ESP run. It should also be mentioned that the experimental values compare favorably with theoretical values which have been developed for plain metallic disks as probes on spacecraft surfaces (ref. 8).

The most important difference between the two curves is their differing slopes. At this point, reasons for this difference are pure speculation. One factor which does contribute to the smaller current densities of the simulation is the small negative voltages on the dielectric when equilibrium has been achieved. However, test runs have been made with the potential on the dielectric forced to zero (this should mimic the experiment very closely) and this has resulted in only a 10% increase in current density at 250 Volts.

#### CONCLUDING REMARKS

A computer program is being developed to simulate the interaction of a plasma with a conducting disk partially covered by an insulator. In this report, we considered only charge sticking to the dielectric. Computer runs with this model have been made and results compared with experimental values for a plain conducting disk.

This computer simulation is written so that other dielectric effects can be easily included. Another paper (ref. 4) discusses results obtained when secondary emission from the dielectric was included.

## APPENDIX A

### THE PARTICLE MOVER

The PIC particle mover is the portion of the program which advances the particle positions and velocities ( $r$ ,  $z$ ,  $v_r$ , and  $v_z$ ) each time step.

In cylindrical coordinates, Lagrange's equations for a single particle reduce to:

$$\begin{aligned} m\ddot{r} &= \frac{\ell^2}{mr^3} - \frac{\partial V}{\partial r} \\ m\ddot{z} &= - \frac{\partial V}{\partial z} \end{aligned} \tag{A-1}$$

and  $\ell = mr^2\dot{\theta}$ , where  $\ell$  is a conserved quantity.

We rewrite the first two equations in terms of  $\vec{E}$  and  $\vec{v}$ , and have:

$$\begin{aligned} m \frac{dv_r}{dt} &= \frac{\ell^2}{mr^3} + qE_r \\ m \frac{dv_z}{dt} &= qE_z. \end{aligned} \tag{A-2}$$

In a time  $\Delta t$ , we have, approximately:

$$\begin{aligned} m (v_{r,\text{new}} - v_{r,\text{old}}) &= \Delta t (\ell^2 / mr^3 + qE_r) \\ m (v_{z,\text{new}} - v_{z,\text{old}}) &= \Delta t (qE_z) \end{aligned} \tag{A-3}$$

The equations of (A-3) contain velocities at two different times, and



$E_r$ ,  $E_z$ , and  $r$ , which are function of time. The leap-frog method uses this to advantage by using the velocities preceding and following  $E_r$ ,  $E_z$ , and  $r$  by  $\Delta t/2$ . Thus we have:

$$\begin{aligned} v_{r,t+\Delta t/2} &= v_{r,t-\Delta t/2} + \Delta t \left( \ell^2/m^2 r_t^3 + qE_{r,t}/m \right) \\ v_{z,t+\Delta t/2} &= v_{z,t-\Delta t/2} + \Delta t \left( qE_{z,t}/m \right) \end{aligned} \quad (A-4)$$

In the remainder of this Appendix, the time subscripts will be dropped. The subscripts "old" and "new" will be used only where necessary.

Suppose we were to use (A-4) as it stands using stored values for  $v_{r,old}$ ,  $v_{z,old}$ ,  $r$ ,  $z$ ,  $E_r$ ,  $E_z$ ,  $\ell$ ,  $m$ , and  $q$ . Then to calculate  $v_{r,new}$ ,  $v_{z,new}$ ,  $r_{new}$ , and  $z_{new}$  for one particle at one time step, we would have to do 11 multiplications, 3 divisions, and 5 additions. In our program, we have available the "grid units"  $\Delta r$  and  $\Delta z$ ; these, with  $\Delta t$ , will allow us to rewrite (A-4) in a better form for calculation:

$$\begin{aligned} v_{r,new} \frac{\Delta t}{\Delta r} &= v_{r,old} \frac{\Delta t}{\Delta r} + \frac{\Delta t^2}{\Delta r} \frac{\ell^2}{m^2 \Delta r} \left( \frac{\Delta r^3}{r^3} \right) \\ &\quad + \frac{\Delta t^2}{\Delta r} \frac{q}{m} E_r \\ v_{z,new} \frac{\Delta t}{\Delta z} &= v_{z,old} \frac{\Delta t}{\Delta z} + \frac{\Delta t^2}{\Delta z} \frac{q}{m} E_z \end{aligned} \quad (A-5)$$

$$r_{new}/\Delta r = r_{old}/\Delta r + v_{r,new} (\Delta t/\Delta r)$$

$$z_{new}/\Delta z = z_{old}/\Delta z + v_{z,new} (\Delta t/\Delta z)$$

Letting  $\bar{r} = r/\Delta r$ ,  $\bar{v}_r = v_r (\Delta t/\Delta r)$ , etc., and defining  $a_z = (\Delta t^2/\Delta r) (\ell^2/m^2 \Delta r^3)$ , we can rewrite (A-5).

$$\bar{v}_{r,new} = \bar{v}_{r,old} + a_\ell / \bar{r}^3 + \bar{E}_r$$

$$\bar{v}_{z,new} = \bar{v}_{z,old} + \bar{E}_z$$

(A-6)

$$\bar{r}_{new} = \bar{r}_{old} + \bar{v}_{r,new}$$

$$\bar{z}_{new} = \bar{z}_{old} + \bar{v}_{z,new}$$

Now to calculate  $\bar{v}_{r,new}$ ,  $\bar{v}_{z,new}$ ,  $\bar{r}_{new}$ , and  $\bar{z}_{new}$  from  $\bar{v}_{r,old}$ ,  $\bar{v}_{z,old}$ ,  $a_\ell$ ,  $\bar{r}$ ,  $\bar{z}$ ,  $\bar{E}_r$ , and  $\bar{E}_z$ , we must do 3 multiplications, 1 division, and 5 additions. Equation (A-6) is the basic form of our cylindrical PIC mover.

#### REFERENCES

1. Stevens, N. J.; et al.: Investigation of High Voltage Spacecraft System Interactions with Plasma Environments. AIAA/DGLR 13th International Electric Propulsion Conference Paper 78-672, Apr. 1978.
2. Stevens, N. J.: Interactions Between Spacecraft and the Charged Particle Environment. Spacecraft Charging Technology-1978. NASA CP-2071, 1979.
3. Grier, N. T.; and Stevens, N. J.: Plasma Interaction Experiment (PIX) Flight Results. Spacecraft Charging Technology-1978. NASA CP-2071, 1979.
4. Chaky, R. C.; et al.: Numerical Simulation of Plasma-Insulator Interactions in Space, Part II: Dielectric Effects. Spacecraft Charging Technology-1980.
5. Morse, R. L.: Multidimensional Plasma Simulation by the Particle-in-Cell Method. Methods in Computational Physics, vol. 9, pp. 213-239.
6. Birdsall, C. K.; and Langdon, A. B.: Plasma Physics Via Computer Simulation, 1978.
7. Hockney, R. W.: The Potential Calculation and Some Applications. Methods in Computational Physics, vol. 9, pp. 135-211.
8. Parker, L. W.; and Whipple, E. C., Jr.: Theory of a Satellite Electrostatic Probe. Annals of Physics, vol. 44, pp. 126-161, 1967.

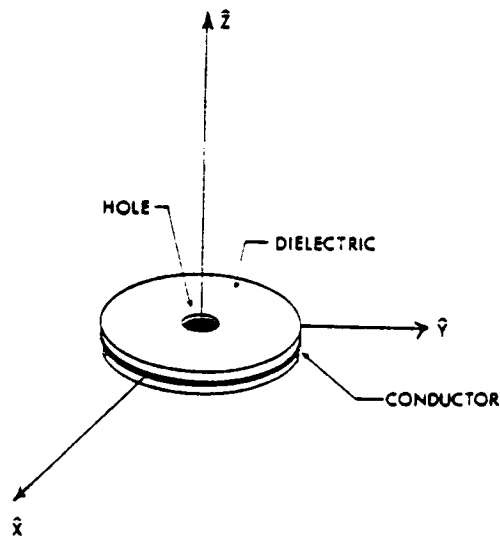


Figure 1 - The system simulated: we have a conducting disk covered with a dielectric. Because we have simplified the system to have up-down symmetry, there are dielectric disks on both sides of the conductor.

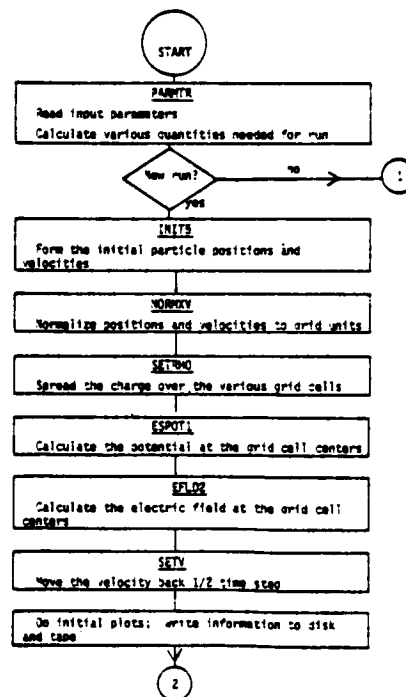


Figure 2 - Flow chart: set up procedure for computer simulation

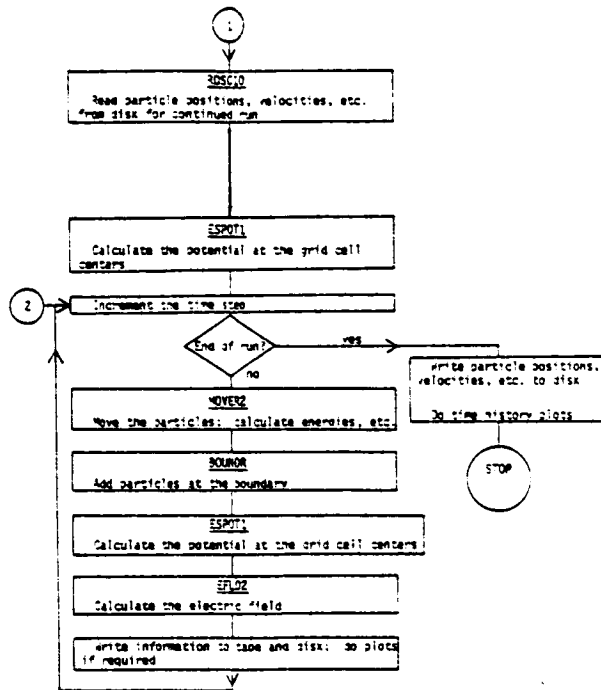


Figure 3 - Flow chart: time step loop for computer simulation.

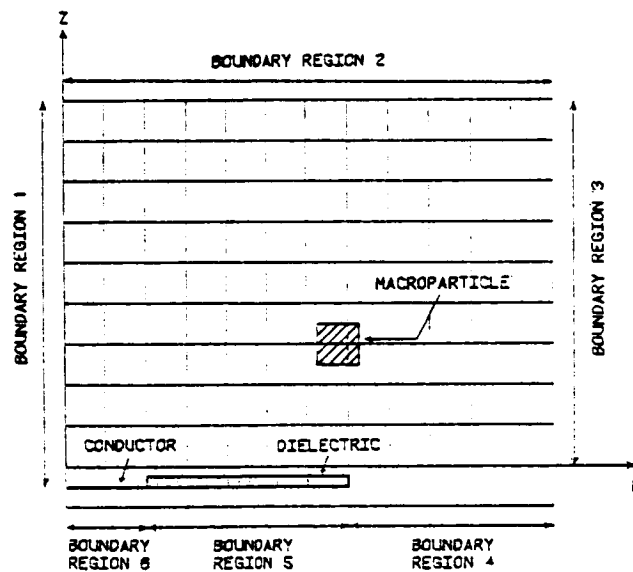


Figure 4 - The calculational grid. One macroparticle is shown on the 20 X 20 grid. The dielectric is divided into 20 sections.

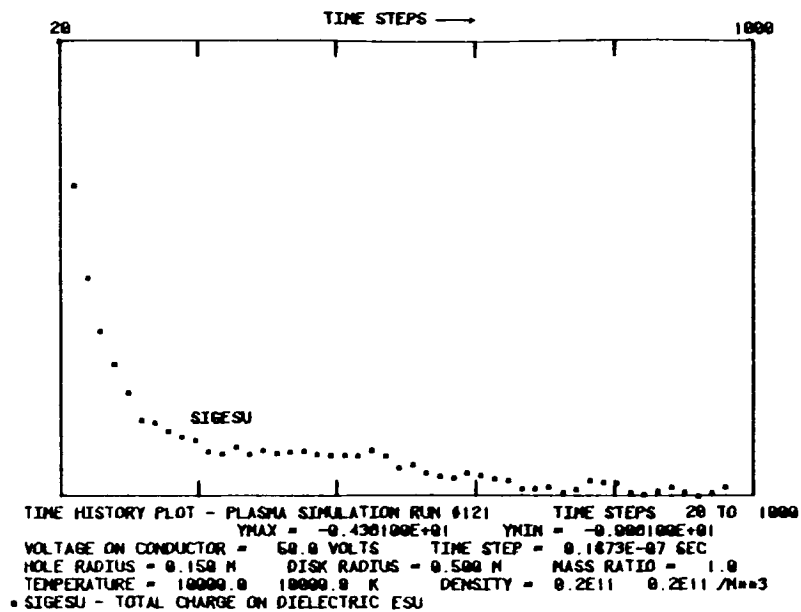


Figure 5 - Plot of total charge accumulated on the dielectric vs. time for a 50 V run.

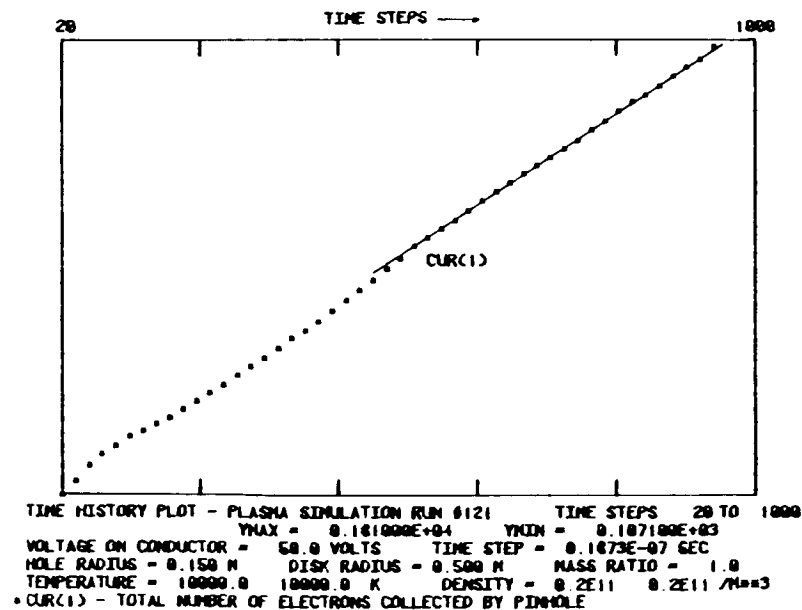


Figure 6 - Plot of the total number of electrons collected by the hole vs. time for a 50 V run

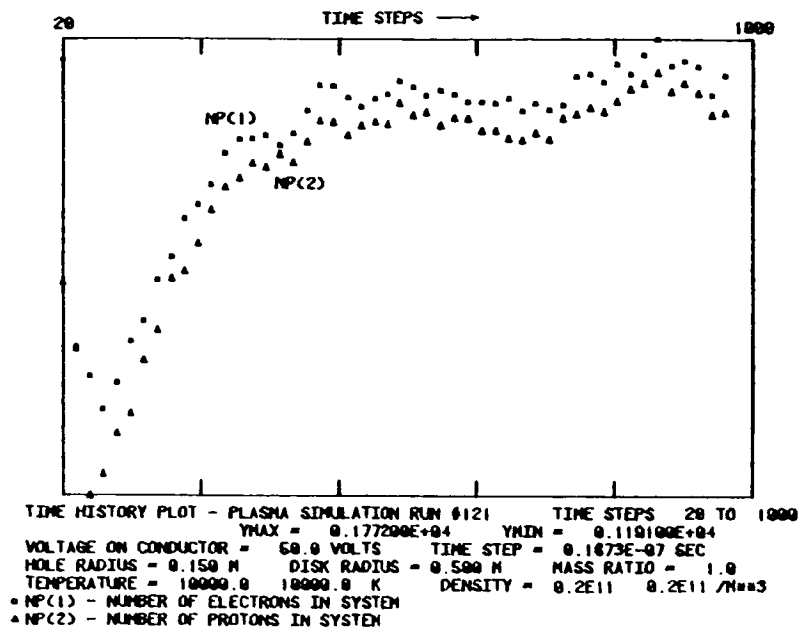


Figure 7 - Plot of the number of macroparticles in the system vs. time for a 50 V run.

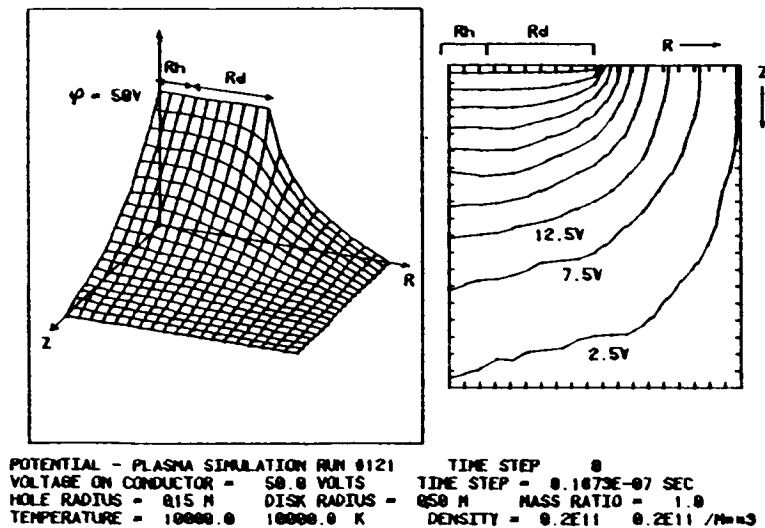


Figure 8 - Potential plots at time step 0 for a 50 V run.

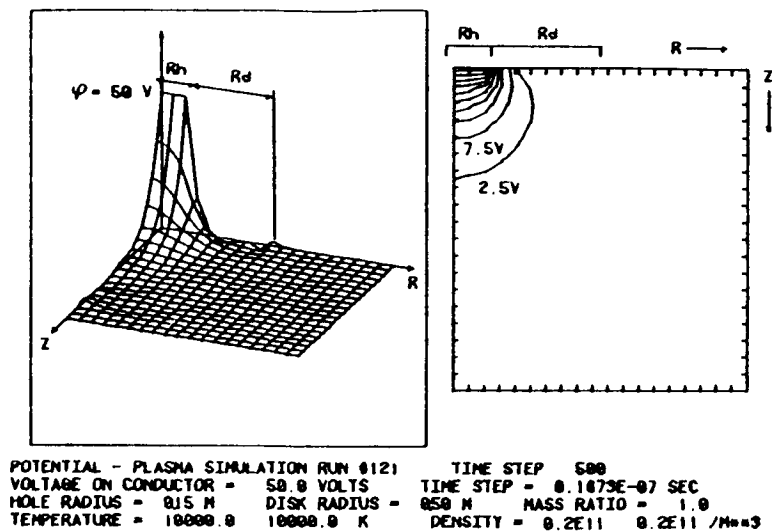


Figure 9 - Potential plots at time step 500 for a 50 V run.

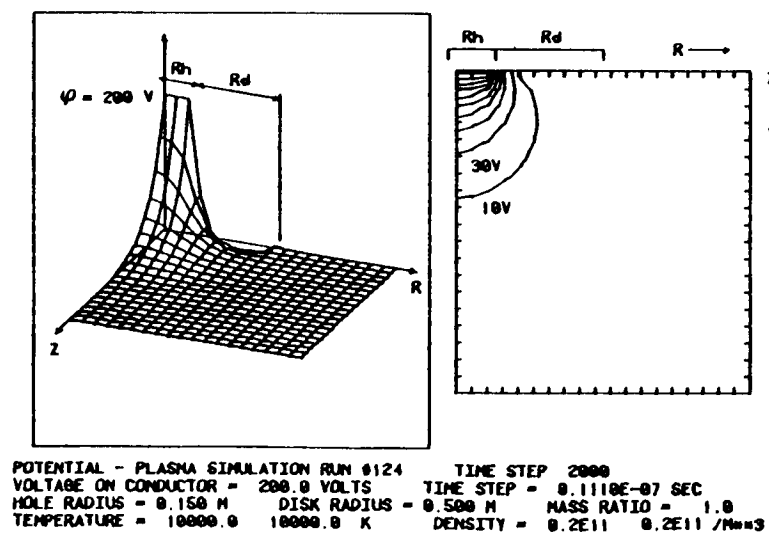


Figure 10 - Potential plots at time step 2000 for a 200 V run.

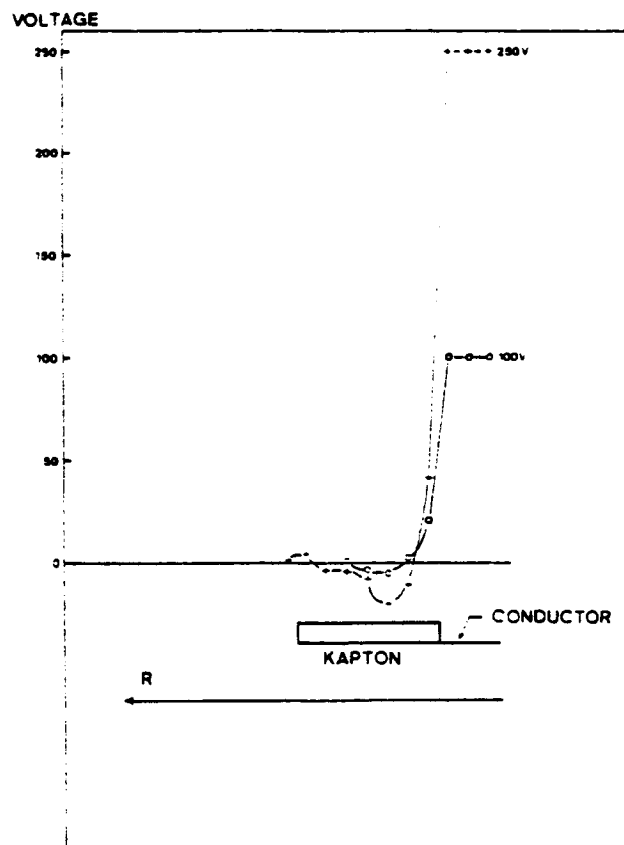


Figure 11 - Surface voltage profiles.

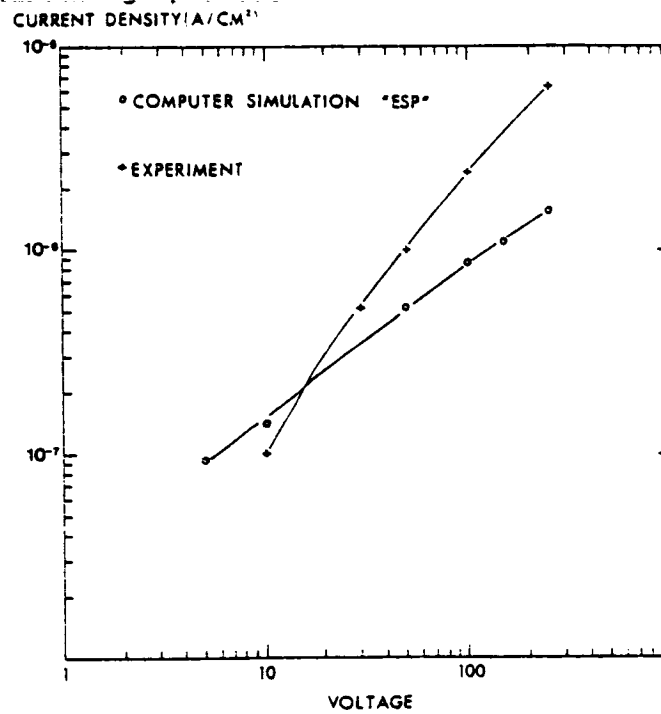


Figure 12 - Plot of current density vs. voltage.



## NUMERICAL SIMULATION OF PLASMA-INSULATOR INTERACTIONS IN SPACE PART II: DIELECTRIC EFFECTS\*

R. C. Chaky, J. H. Nonnast, T. P. Armstrong,  
J. Enoch, and G. G. Wiseman  
University of Kansas

### SUMMARY

In part I of this paper (ref. 1), we explained the overall structure of our computer code for simulating plasma-insulator interactions. In part II we explain how we have begun to model dielectric properties.

The first plasma-dielectric interaction we have included in our code is secondary electron emission (SEE). We present a calculated current density vs. voltage curve, and compare this to an experimental curve.

### INTRODUCTION

Because the PIC method follows particle trajectories, the treatment of the dielectric-particle interaction may be done in close detail. Any process which may be modeled statistically for a single plasma particle may be modeled by PIC; the success of the calculation is then dependent on having a large enough number of particles that the statistical treatment is meaningful. Thus it is possible to include the effects of secondary emission, backscattering, charge sticking and possibly dielectric breakdown, photoemission, and spallation.

Our initial computer runs contained a very naive model of the plasma-dielectric interaction: any particle that struck the dielectric simply stuck to it. We have made the treatment more realistic by including the possibility of SEE, as shown in figure 1: an incoming particle striking the dielectric is capable of giving off secondaries, which may change the amount of current collected by the exposed conductor.

We have retained the geometry used in reference 1. As in reference 1, we are ultimately concerned with producing a current density vs. voltage curve. Each point on the curve requires one computer run, during which the charge density on the dielectric and in space must reach equilibrium.

The balance of this paper will be given to explaining how SEE is included, and showing our results.

---

\* This work is supported in part by NASA Lewis Research Center, Research Grant #NSG - 3290.

## SECONDARY ELECTRON EMISSION -- AN EMPIRICAL TREATMENT

When an incoming electron strikes the dielectric, there is a chance that one or more electrons will be liberated from the surface. The yield of secondary electrons (SE's) depends on the energy and the angle of incidence of the primary.

The dependence of the secondary yield  $\delta$  on the primary energy  $E_0$  is displayed in a yield curve, which is characteristic of a particular target material. The yield curve data comes from normal incidence primaries, and so includes no information on primary angle dependence. An example of a yield curve relation is equation (1), from Haffner (ref. 2):

$$\delta(\alpha_0=0) = K(\exp(-aE_0) - \exp(-bE_0)). \quad (1)$$

$K$ ,  $a$  and  $b$  are characteristic of a given material. The resulting yield curve is shown in figure 2, for Kapton.

Most of the SE's come from a thin layer near the surface. As the angle of primary incidence is slanted from normal incidence toward tangential incidence, more of the primary path is in this upper layer -- hence more electrons are liberated. Wall, Frederickson, and Burke (ref. 3) use the following cosine relation:

$$\delta(\alpha_0) = \delta(\alpha_0=0) \exp(c(1-\cos \alpha_0)) \quad (2)$$

where  $c$  is about 2 for polymers.

Combining equations (1) and (2), we can write the yield as a function of the energy  $E_0$  and angle of incidence  $\alpha_0$  of the primary:

$$\delta(E_0, \alpha_0) = K (\exp(-aE_0) - \exp(-bE_0)) \exp(2(1-\cos \alpha_0)). \quad (3)$$

Equation (3) tells how many outgoing SE's to expect per incoming particle.

To characterize the outgoing particle, we must give its energy  $E$  and the angle it makes with the target surface,  $\alpha$ .

The emission energy distribution spectrum,  $N(E)$  vs.  $E$ , is much more difficult to find in the literature than the yield curve; however, we know the general shape of the curve, shown in figure 3. Figure 3 was drawn from a curve for silver given by Rudberg (ref. 4).

The portion of the emission energy spectrum below about 50 eV is taken to be the "true secondary" region -- the emitted particle is different from the incoming particle. Fortunately for our computer simulation, the shape of this portion of the curve does not depend strongly on the incoming energy.

Figure 3 shows a spike at  $E=E_0$ , which is the backscatter peak. The backscattered particle is the incoming particle, so this peak does not

represent a "true secondary" process.

If the backscatter peak is removed from figure 3 and the area under the curve is calculated, the area must be equal to the yield  $\delta$ ; i.e., letting  $N'(E)$  be the energy distribution function without backscatter,

$$\int N'_{E_0}(E) dE = \delta(E_0). \quad (4)$$

## SECONDARY ELECTRON EMISSION -- THE CALCULATION

The inclusion of SEE into our program begins in a subroutine which is called when a macroparticle crosses the  $z=0$  plane. If the  $r$ -coordinate is such that the macroparticle has hit the dielectric, then the incoming energy,  $E_0$  of the particle and its angle of incidence  $\alpha_0$  are calculated. From  $E_0$  and  $\alpha_0$  we calculate the yield  $\delta$ , using equation (3).

Because we do not know the energy distribution function for polymers, we have used a Maxwellian velocity distribution to calculate the velocities of the SE's. We hope to improve on this, after a more thorough literature search.

The direction of the SE is chosen randomly so that the azimuthal angle is uniformly distributed between 0 and  $\pi/2$ . This is not uniformly distributed in solid angle, but rather gives a preference to normal emission, in keeping with experimental observation (ref. 5).

## A TYPICAL RUN: 200 VOLTS

Figures 4, 5 and 6 are potential plots for a run with 200 Volts on the conductor.

At time step 0 (fig. 4), there is no charge on the dielectric. The dielectric builds up a negative charge with time, so that after 2000 time steps (fig. 5) the potential is zero throughout the simulation region, except very close to the exposed conductor. The potential at time step 4000 (fig. 6) is nearly identical to that at time step 2000, indicating the potential has settled to equilibrium.

A comparison of the equipotential plot of figure 6 with the corresponding plot from reference 1 (fig. 10 of ref. 1) shows the influence of the inclusion of SEE. In the SEE case, the shielding has been reduced, and therefore the equipotentials are pushed farther out into the plasma, away from the plate.

Figure 7 is a time history plot of the number of macroelectrons producing secondaries, and the number of secondaries produced. The numbers plotted are cumulative, so that equilibrium is indicated by the linear form for later time. There is an average of 1.7 outgoing SE's per primary.

Figure 8 is a plot of the same quantities for a 50 Volt run. Here we

have 1.2 secondaries per primary, on the average.

### COMPARISON WITH EXPERIMENT

We compare our calculation results with the experimental results of Stevens, et al. (ref. 6).

The experiment described in reference 6 measured the current to a stainless steel disk (.035 m in diameter and .001 m thick) which rested on a Kapton surface. The conductor disk was held at a given potential, and was allowed to come to equilibrium with the ambient plasma.

We compare our calculated potential in the plane of the dielectric (fig. 9) with the experimentally measured potential (fig. 10). They are qualitatively the same, although the calculated potential drops to zero more slowly than the measured potential, outside of the dielectric region. This difference is due to a grounded plate below the Kapton in the experimental run.

Figure 10 gives some important information about the difference between runs including or neglecting SEE, since the negative voltage case may be compared to a positive voltage case with no secondaries. The case without SEE shows a sharp drop in potential immediately outside the conductor, but the case with SEE shows a gradual drop of potential across the entire extent of the dielectric. This effect showed up in our calculation, as the equipotentials were pushed out further in the SEE case than in the case without SEE. It is also evident in a comparison of figure 9 with the no-SEE case, which is figure 11 of reference 1.

Figure 11 is a current area density vs. voltage plot, showing our calculated results compared to results taken from reference 6. Our results differ by less than an order of magnitude over the range of 10 to 250 Volts.

### DISCUSSION OF RESULTS

The discrepancy between our calculated current density vs. voltage curve and the experimental curve are due to three major causes.

First, the calculated runs and experimental measurements had different conditions. The collector areas were different by a factor of 72. The substrate in the experiment was grounded, while our calculation did not include a grounded substrate.

Second, the SEE treatment needs to be improved. We used a  $100^{\circ}$  K Maxwellian distribution for the SE energy spectrum, which is not realistic.

Third, processes other than SEE may strongly influence our results. In particular, our code does not yet allow for any charge mobility in the dielectric.

## CONCLUDING REMARKS

In this and the preceding paper we have introduced our plasma simulation code, ESP. Because the PIC method follows individual particle trajectories, we may model any process which may be modeled statistically for an individual particle.

We have completed test runs with a statistical model of secondary electron emission (SEE). We have compared our results to experimental data, in terms of the potential directly above the surface, and the current density to a current collector.

## REFERENCES

1. Nonnast, J. H., et al.: Numerical Simulation of Plasma-Insulator Interactions in Space, Part I: The Self-Consistent Calculation. Spacecraft Charging Technology - 1980.
2. Haffner, J. W.: Secondary Electron Effects on Spacecraft Charging. Spacecraft Charging Technology, AFGL-TR-79-0082, 756-68 (1978).
3. Wall, J. W.; Burke, E. A.; and Frederickson, A. R.: Results of Literature Search on Dielectric Properties and Electron Interaction Phenomena Related to Spacecraft Charging. Spacecraft Charging Technology, AFGL-TR-0051, 569 (1977).
4. Rudberg, E.: Inelastic Scattering of Electrons from Solids. Phys. Rev. 50, 138 (1936).
5. Bunney, R. E.: Secondary Electron Emission. NASA CR 54366, December 1964, page 10.
6. Stevens, N. J.; Berkopce, F. D.; Purvis, C. K.; Grier, N.; and Staskus, J.: Investigation of High Voltage Spacecraft System Interactions with Plasma Environments. AIAA/DGLR Electric Propulsion Conference, 78-672, 1978.

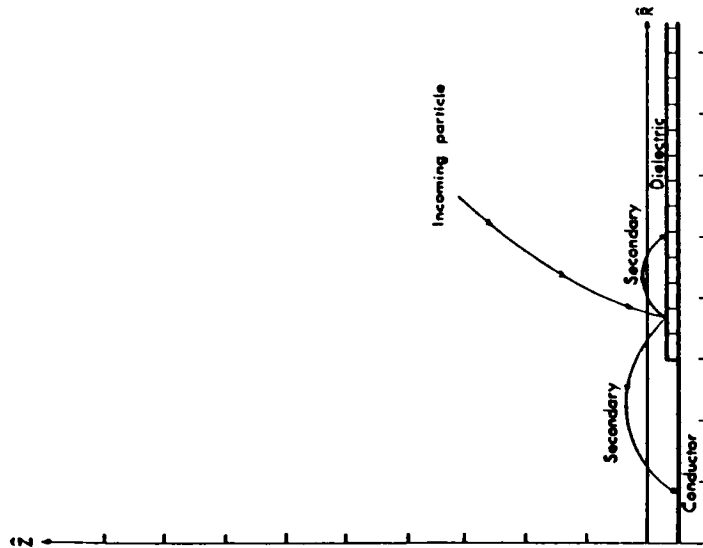


Figure 1. An incoming particle striking the dielectric may give off secondaries, which may affect the current collected by the exposed conductor.

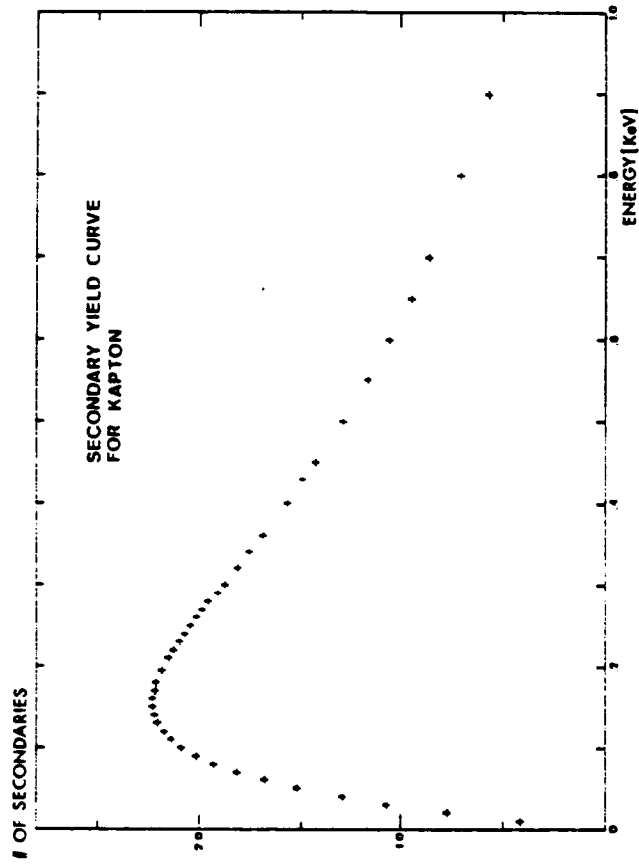


Figure 2. SEE yield curve for Kapton

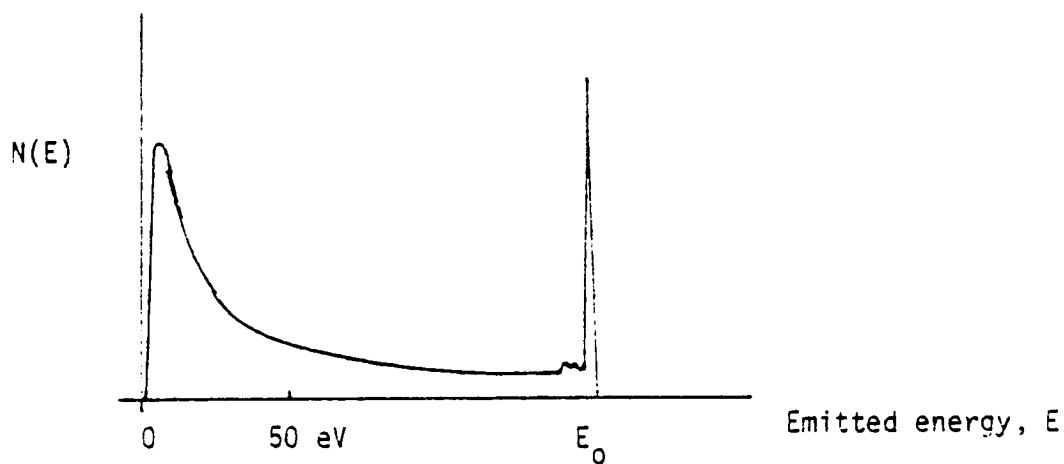


Figure 3. A sketch of the energy spectrum curve for SE's

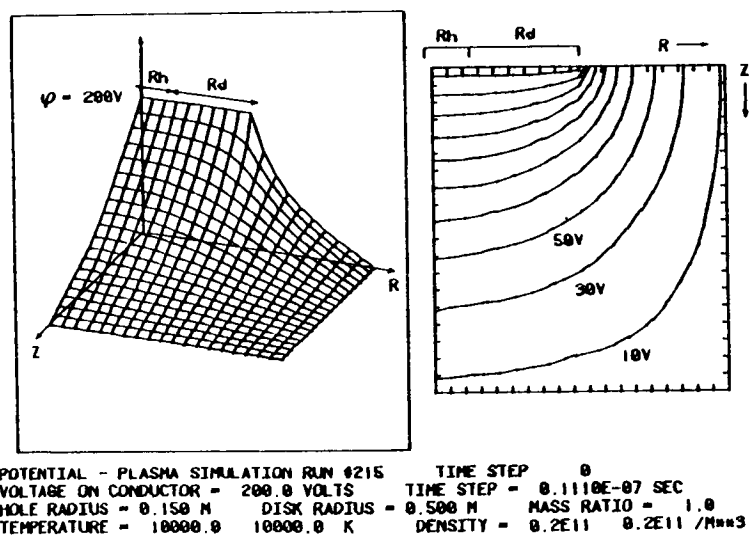


Figure 4. Potential plots at time step 0, with a 200 V potential on the conductor

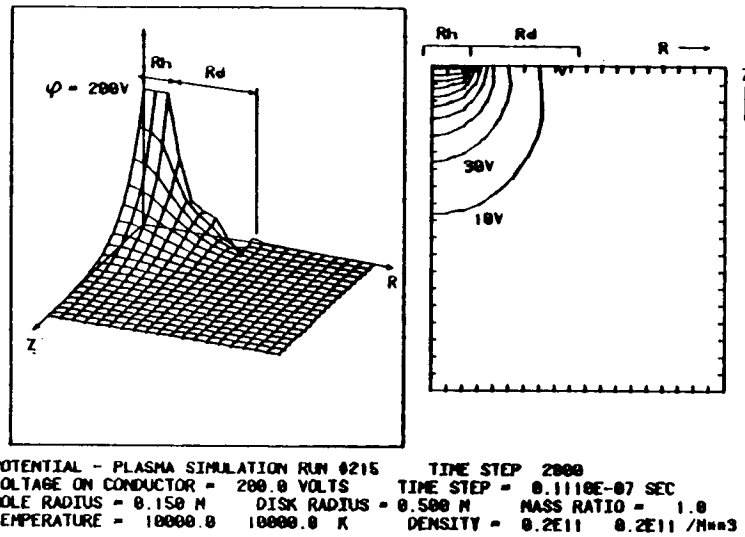


Figure 5. Potential plots at time step 2000, with a 200 V potential on the conductor

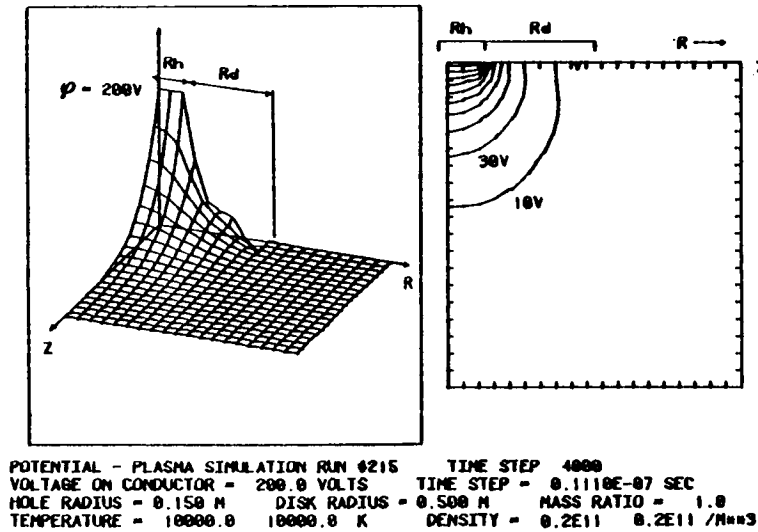


Figure 6. Potential plots at time step 4000, with a 200 V potential on the conductor



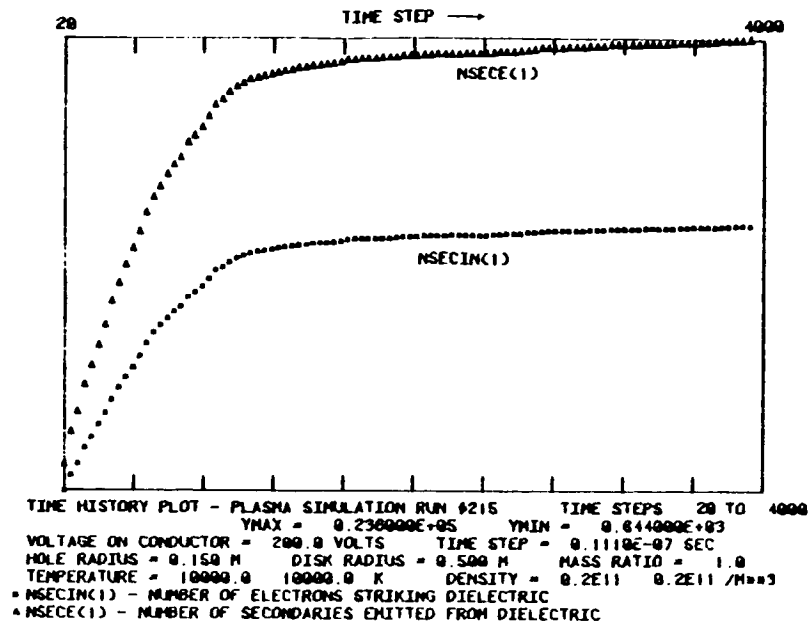


Figure 7. A time plot of the (cumulative) numbers of primaries and secondaries, with 200 Volts on the conductor

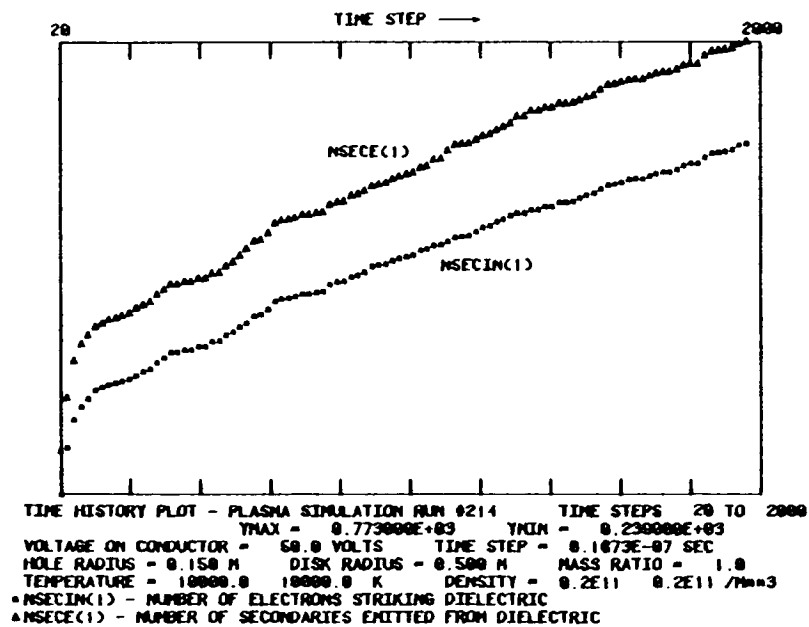


Figure 8. A time plot of the (cumulative) numbers of primaries and secondaries, with 50 Volts on the conductor

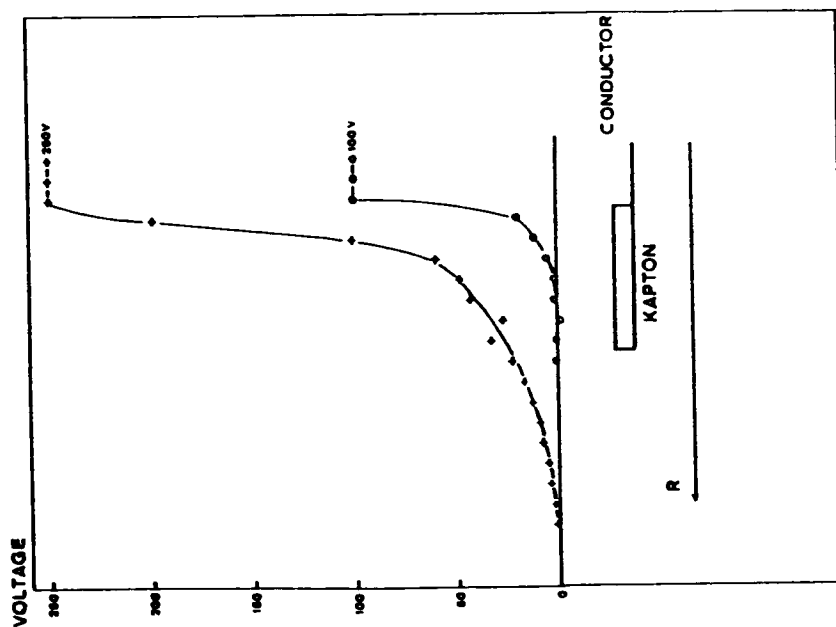


Figure 9. Calculated surface voltage profiles

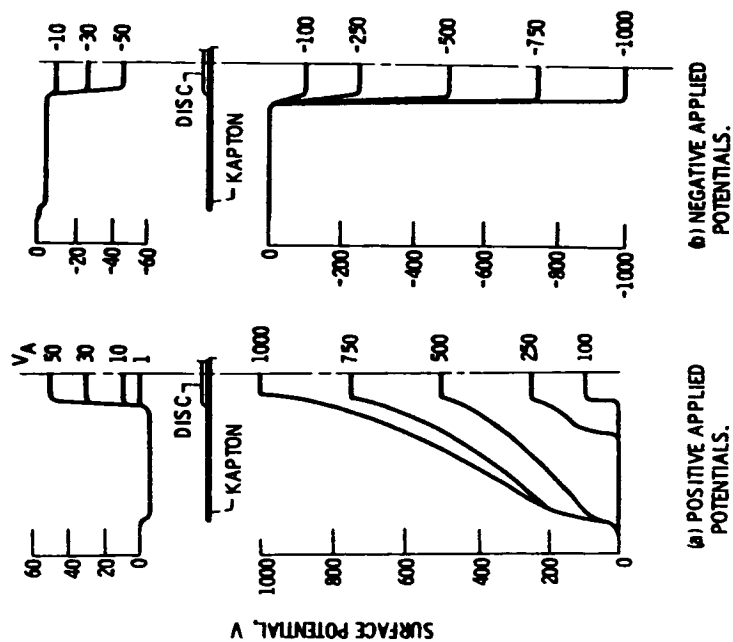


Figure 10. Measured surface voltage profiles, from reference 6; reproduced with permission

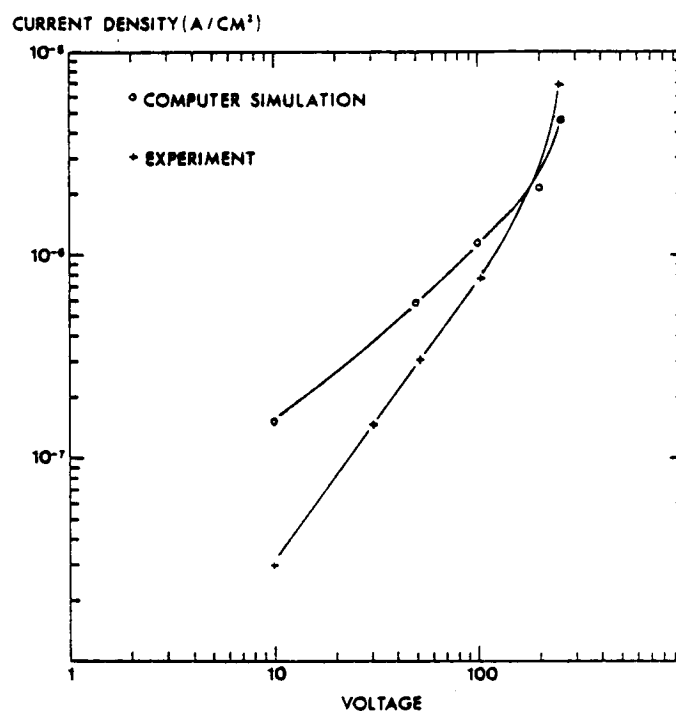


Figure 11. Plot of current area density vs. voltage

# **THREE-DIMENSIONAL SPACE CHARGE MODEL FOR LARGE HIGH-VOLTAGE SATELLITES\***

**David Cooke  
Rice University**

**Lee W. Parker  
Lee W. Parker, Inc.**

**James E. McCoy  
NASA Johnson Space Center**

## **SUMMARY**

High-power solar arrays for satellite power systems are presently being planned with dimensions of kilometers, and with tens of kilovolts distributed over their surface. Such systems will face many plasma interaction problems that must be properly anticipated. Among these are (a) parasitic power leakage due to ambient plasma, ion thruster, and photo-electron currents, (b) particle focusing resulting in enhanced sputtering and erosion, (c) secondary electron emission and cascade, (d) velocity wake effects, (e) differential charging effects, and (f) determination of the equilibrium floating potential which influences all of the above. In most cases, these effects cannot be adequately modeled without detailed knowledge of the plasma-sheath structure and space charge effects. This paper describes two computer programs that have been developed to provide fully self-consistent plasma sheath models in three dimensions. Both programs are a result of recent efforts to model the experimental plasma sheath studies at NASA/JSC. Preliminary results indicate that for the conditions considered, the Child-Langmuir diode theory can provide a useful estimate of the plasma sheath thickness. The limitations of this conclusion are also discussed. Some of the models presented exhibit the strong ion focusing that has been observed in the JSC experiments.

## **INTRODUCTION**

The interaction of a large high voltage solar array with a space or laboratory plasma cannot, in general, be modeled analytically. For this reason we have developed two computer programs, PANEL, and SSB. Both programs

---

\* Work supported in part by NASA grant NAS9-16206.

calculate, self-consistently, potentials, densities, and currents on a three-dimensional grid of points. The method used in PANEL is an extension to three dimensions of the inside-out method developed by Parker (ref. 1), and used by Parker and Whipple (ref. 2) to model two-electrode probes on a satellite. More recently Parker (ref. 3, 4) has used the method to calculate sheath and wake structures about disk and pill-box shaped objects in flowing plasmas. An early version of PANEL, written by Parker (ref. 5) was used by Reiff, Freeman, and Cooke (ref. 6) to model the interaction of a geosynchronous substorm plasma with the NASA/Marshall Space Flight Center baseline design for the solar power satellite. The other program, SSB, is a recent development by Lee Parker, using the outside-in method of calculating densities (ref. 1), and the simplifying assumption of a sharp edge sheath boundary. The purpose for the further development of these programs has been to produce a code capable of augmenting the laboratory studies of a 10 meter solar array in a simulated low Earth orbit plasma being conducted in the large Chamber A vacuum facility at NASA/Johnson Space Center. These studies have identified a number of interesting and unexpected effects such as the strong focusing of attracted particles toward the center of the panel when the panel is biased to kilovolt potentials. Our goal is to develop an accurate model of the plasma sheath surrounding such an array that will identify the parameters affecting sheath structure, help establish the dependence of the experimental results on test conditions, and aid in the extrapolation of these experiments to actual space conditions.

Unless specifically stated otherwise, this report will adhere to the S.I. system of units.

## THE PLASMA SHEATH

Perhaps the best known example of plasma screening is the Debye treatment of the plasma screening of an isolated test charge. A positive test charge,  $\delta Q$ , placed in a plasma of temperature  $T$  and density  $N_0$ , will attract electrons and repel ions so as to develop a surrounding sheath such that the potential at radius  $r$  is given by,

$$V(r) = \frac{\delta Q}{4\pi\epsilon_0 r} \exp(-r/\lambda_D)$$

where  $\lambda_D = (\epsilon_0 kT/N_0 e^2)^{1/2}$  is the Debye length. Implicit in the derivation of this equation (ref. 8) are the assumptions that the charge has negligible cross-section, and that  $V(r) \ll kT/e$  for  $r > \lambda_D$ . For a microscopic body of radius  $R$ , satisfying these assumptions, we can write

$$V(r) = \frac{V_b R}{r} \exp[(R - r)/\lambda_D], \quad r > R \quad (1)$$

where  $V_b$  is the surface potential of the body.

For objects large compared to the plasma Debye length and/or maintained at a high voltage ( $|V| \gg kT/e$ ), the Debye model is no longer adequate. In general, self-consistent treatment of a macroscopic body requires computer modeling. In spite of this difficulty, a better understanding of the shielding process can be gained by studying current limiting by space charge in the

1-D planar electron diode, first treated independently by Child (ref. 9) and Langmuir (ref. 10).

Consider the three electrode system shown in Figure 1. At  $x = -d$ , we have a cathode, with zero potential capable of emitting unlimited quantities of electrons all with zero velocity. At  $x = 0$ , we have a transparent screen at potential  $V_0$ , and at  $x = x_1$ , we have a non-emitting anode at potential  $V_1$ . Poisson's equation in one dimension is

$$\frac{d^2V}{dx^2} = -\rho/\epsilon_0.$$

From the current density,  $J = \rho v$ , we can substitute for the charge density  $\rho$ . Then, from the electron kinetic energy at  $x$ ,  $1/2 m_e v^2 = eV$ , we can substitute for the velocity  $v$ , to get,

$$\frac{d^2V}{dx^2} = -\frac{J}{\epsilon_0} \left(\frac{m_e}{2eV}\right)^{1/2}. \quad (2)$$

This equation may be integrated twice from  $(0, V_0)$  to  $(x_1, V_1)$  to give,

$$x_1 = \frac{b}{\sqrt{J_e}} V_1^{3/4} \left[1 + 2 \left(\frac{V_0}{V_1}\right)^{1/2}\right] \cdot \left[1 - \left(\frac{V_0}{V_1}\right)^{1/2}\right]^{1/2}, \quad (3)$$

where  $b^2 = [4\epsilon_0/9] \cdot [2e/m_e]^{1/2} = 2.336 \times 10^{-6}$  (amps/volts<sup>3/2</sup>), and the boundary condition used at  $x = 0$ , is  $E_x = -(dV/dx)|_0 = 0$ , a common definition of the sheath edge in the spacecraft charging problem. This equation can be applied to region I,  $-d < x < 0$ , where  $V_0 = 0$  (zero initial velocity) to recover the Child-Langmuir (C-L) result

$$d^2 = 2.336 \times 10^{-6} V^{3/2}/J_e, \quad (4)$$

where  $d^2$  and  $J_e$  must have the same unit of area. If  $d$  and  $V$  are fixed, equation (4) gives the maximum conducted current despite an unlimited supply of electrons. If  $d$ ,  $V$ , and  $J_e$  are all considered independent, the sheath edge electric field becomes the dependent variable and cannot be set to zero.

Another variation of this problem is given by Birdsall (ref. 11). The conditions are illustrated in the lower portion of Figure 1, with the grids at  $x = 0$  and  $x_1$  both at the same positive potential  $V_1$ , and the separation distance  $x_1$  considered fixed. The negative space charge of the electrons in the gap between zero and  $x_1$  will depress the potential in the gap and give rise to current limitation if the potential drops to zero. This variant is more suited for comparison to PANEL, since the geometry is fixed and only voltages and charge densities vary. The potential distribution in the gap is determined by subdividing region II into regions A and B whose boundary at  $x_m$  is the point of minimum potential where we have the condition of zero electric field. The potential as a function of  $x$  is then determined separately in regions A and B with exactly the same approach that led to equation (3). Since the details of this analysis are somewhat involved and given in Birdsall's book (ref. 11), it will not be reproduced here. We have labeled this variant on the classical diode the "gap" problem. The solutions to this problem have been very useful in the development and verification of PANEL.

PANEL's predictions for the gap problem are presented in figure 2, and will be discussed shortly.

If we assume that under appropriate conditions the plasma sheath can form a "sharp-edge" outer boundary, we can consider a Child-Langmuir sharp-edge sheath (CL-SES) model for the satellite-plasma sheath, with equation (4) giving the sheath thickness for a planar satellite surface and sheath. This model should be limited to the following conditions:

1. Satellite dimensions should be larger than estimates of sheath thickness, such that a planar approximation is justified.
2. The surface potential is greater than the plasma temperature, so the initial velocities of particles entering the sheath can be neglected, and so the repelled particles will not penetrate significantly into the sheath since the C-L treatment considers only attracted particles.
3. The current is assumed to be the random thermal current ( $J_0 = N_0 e \sqrt{kT/2\pi m}$ ) of attracted particles falling on the sheath edge.

We can relax condition 2 somewhat by using equation (3) for the sheath thickness. To apply equation (3) to a planar spacecraft surface at potential  $V$ , we identify  $x_1$  with the spacecraft surface, and  $x = 0$  with the sheath edge where  $E \approx 0$ . Region I is now identified with the undisturbed plasma where  $V_0$  represents the average thermal energy of the electrons, and region II is the plasma (electron) sheath with thickness  $x_1$ . Equation (3) was derived for a beam-like monoenergetic electron source, and will not be accurate for an isotropic thermal plasma, but it nevertheless shows that a non-zero plasma temperature will increase the sheath thickness.

For diode geometries other than planar, Langmuir (ref. 10) has shown that the space charge limited current will always be proportional to  $V^{3/2}$ , however, the distribution of potential in space does depend on geometry. The problems of current flow between concentric spheres and cylinders has been addressed by Langmuir and Blodgett (ref. 12). Their solutions take the form of equation (4) with  $d$  replaced by various series expansions in terms of the ratios of the electrodes' radii, with the results presented in tabular form. Parker (ref. 13) has adapted these results to estimate sheath thickness for charged spherical satellites, and provides a convenient fit to those results. In the following equations  $a$  = sheath radius,  $r_0$  = body radius, and  $d$  is the C-L screening distance given by equation (4).

$$\begin{aligned}
 \frac{1}{2} + \left[ \frac{1}{4} + \frac{d}{r_0} \right]^{1/2} & \quad ; \frac{d}{r_0} < .2 \\
 \frac{a}{r_0} = \frac{1}{2} + \left[ \frac{1}{4} + \frac{d}{r_0} \right]^{1/2} + 0.052 \frac{d}{r_0} & \quad ; .2 < \frac{d}{r_0} < 19 \quad (5) \\
 \left[ 1 + \left( \frac{d}{r_0} \right)^{.753} \right]^{.7524} \approx \left( \frac{d}{r_0} \right)^{.567} & \quad ; \frac{d}{r_0} > 19
 \end{aligned}$$

Restriction 1 can be removed and the CL-SES model extended to spheres with equations (5), and to cylinders with the expansions given by Langmuir and Blodgett. As an analytic approximation to the satellite plasma sheath, the CL-SES model does not provide much detailed information about the sheath and it is limited to very simple geometries; and therefore does not eliminate the need for numerical modeling. The SES model is attractive because it offers the possibility of predicting sheath effects without performing time consuming rigorous calculations. The computer model SSB described in this report takes advantage of this idea. A sharp sheath edge, however, is a potentially questionable approximation. Parker (ref. 13) has suggested that the highly perturbed sheath region will connect with the undisturbed plasma through a presheath region characterized by weak electric fields and potentials less than  $kT/e$ . The influence that this presheath region might have on various aspects of the plasma-spacecraft interaction has not been fully determined. We anticipate that quantifying this presheath influence, or at least evaluating the sharp-edge sheath model, will be a major result of the intercomparison of rigorous PANEL, SSB, and experimental results.

#### PANEL (THE INSIDE-OUT METHOD)

The classical theory of electrodynamics states that the scalar electrostatic potential  $V(\vec{x})$  and the charge density  $\rho(V(\vec{x}))$  will satisfy Poisson's equation

$$\nabla^2 V(\vec{x}) = -\rho(V(\vec{x}))/\epsilon_0. \quad (6)$$

In problems where the charge density does not depend upon the potential, equation (6) becomes an inhomogeneous linear elliptic partial differential equation. For such equations, the theory of partial differential equations (ref. 8), will guarantee a unique solution interior to a closed boundary  $S$ , on which is specified either (but not both) the potential  $V(\vec{x}_s)$  (Dirichlet boundary conditions), or the normal derivative  $\partial V(\vec{x}_s)/\partial n_s$  (Neuman boundary conditions). Unique solutions may also be obtained for problems with mixed boundary conditions with Dirichlet conditions on part of the boundary, and Neuman for the rest. For the general non-linear problem where the charge density depends on the distribution of potential, there are no uniqueness or existence guarantees for solutions to equation (6). Experience, however, leads us to believe that the physically real problems that we encounter in the study of plasma-spacecraft interactions do have at least one self-consistent solution for  $V$  and  $\rho$ . It is this experience that leads us to pursue solutions to such problems.

The inside-out method adopts an iterative approach to solving plasma sheath problems on a grid of points at which  $\rho(\vec{x})$  and  $V(\vec{x})$  are defined. The best estimate for  $\rho(\vec{x})$  is used in equation (6) to obtain a new estimate for  $V(\vec{x})$  using an over-relaxation technique. Next, new estimates for  $\rho(\vec{x})$  are obtained via solutions of the Vlasov equation using the latest values of  $V(\vec{x})$ . This process is repeated until the problem has converged. This process can become unstable if the problem space spans more than a few Debye lengths. This problem is overcome by mixing at each point the appropriate fraction of



the potential from the most recent iteration with the potential from the previous iteration. The calculation of  $\rho(\vec{x})$  has been labeled the "Vlasov problem" and the problem of finding solutions to (6) is called the "Poisson problem."

PANEL has the feature of being able to operate in both a two-dimensional and a three-dimensional mode. The three-dimensional version is presented here.

**The Poisson Problem:** With  $\rho(\vec{x})$  temporarily considered known and independent of  $V(\vec{x})$ , equation (6) becomes linear, thus a well posed boundary value problem will have a unique solution. PANEL uses a standard finite-difference method to solve Poisson's equation (ref. 14). The approach is to discretize the space to be modeled by constructing a three-dimensional grid of points  $P_{i,j,k}$ . The standard approach is to let the  $x$ ,  $y$ , and  $z$  spacings all be a constant  $h$  so that there is a cube of volume  $h^3$  associated with each interior point. But, in modeling many objects it is convenient to use variable spacing to achieve greater economy by allowing a higher density of points where a need is anticipated. With variable spacing, the volume associated with a point  $P$  becomes a rectangular parallelepiped with faces located at the midpoints between  $P$  and its neighbors. The notation, E, W, N, S, U, D is used for the positive and negative  $x$ ,  $y$ , and  $z$  directions, respectively. Variable spacing does, however, reduce the accuracy of the finite difference method, so its use must be carefully considered to minimize errors.

To develop a differenced form of Poisson's equation, we first throw it into partially dimensionless form by dividing by  $kT/e$ , so with  $\phi = Ve/kT$  and  $\lambda_D^2 = \epsilon_0 kT/N_0 e^2$  we get

$$\nabla^2 \phi(\vec{x}) = \lambda_D^{-2} (n_e - n_i) = R, \quad (7)$$

where  $n_e$  and  $n_i$  are the electron and ion densities in units of the ambient density  $N_0$ . Integrate now (7) over the cell volume associated with point  $P$ , and apply the divergence theorem to the left hand side;

$$\iiint \nabla^2 \phi d^3x = \oint_s \frac{\partial \phi}{\partial n} ds = \iiint R d^3x = Q, \quad (8)$$

where  $\partial \phi / \partial n$  is the outward normal derivative at the surface of the cell.  $Q$  can be identified as the net charge within the cell, however, this identification is not implicit in the formal development. We next approximate the surface integral in (8) by the sum:

$$\sum_F A_F \left( \frac{\partial \phi}{\partial n} \right)_F \equiv Q, \quad (9)$$

where  $F = N, S, E, W, U, D$ , and  $A_F$  is the area on each of these faces. These areas are given by,

$$\begin{aligned}
A_N &= A_S = \frac{1}{4}(x_{i+1} - x_{i-1})(z_{k+1} - z_{k-1}) \\
A_E &= A_W = \frac{1}{4}(y_{j+1} - y_{j-1})(z_{k+1} - z_{k-1}) \\
A_U &= A_D = \frac{1}{4}(x_{i+1} - x_{i-1})(y_{j+1} - y_{j-1}).
\end{aligned} \tag{10}$$

The partials  $(\frac{\partial \Phi}{\partial n})_F$  are approximated by the difference quotients:

$$\left(\frac{\partial \Phi}{\partial n}\right)_N = \frac{\Phi_N - \Phi}{y_{j+1} - y_j}, \quad \left(\frac{\partial \Phi}{\partial n}\right)_S = \frac{\Phi_S - \Phi}{y_j - y_{j-1}}, \tag{11}$$

and similarly for the E, W, U, and D directions, where  $\Phi$  is the potential at the point P, and  $\Phi_N, \Phi_S$ , etc. are the neighboring potentials. Thus substituting equations (10) and (11) into (9) we obtain the algebraic expression,

$$C_N \Phi_N + C_S \Phi_S + C_E \Phi_E + C_W \Phi_W + C_U \Phi_U + C_D \Phi_D - C\Phi = Q, \tag{12}$$

where

$$C_N = \frac{(x_{i+1} - x_{i-1})(z_{k+1} - z_{k-1})}{4(y_{j+1} - y_j)},$$

and likewise for  $C_S$  through  $C_D$ ;  $C = \sum_F C_F$ .

Equation (12) can be applied to each interior point in the model, but exterior or boundary points require a modified treatment so as to include the required boundary conditions. The types of boundary conditions (B.C.) used in PANEL are:

1. Floating, where the outward normal derivative on the cell and model boundary is linearly related to the potential on the boundary<sup>†</sup>.

---

<sup>†</sup>In the theory of boundary value problems, independent specification of the normal derivative and potential is an over specification of the boundary conditions and there will be no solution unless the solution was already known and used to specify the B.C. Here we are specifying only a relation between the two conditions, but even this implies a knowledge of the Green function for the problem. For the case where the boundary is far enough away from the "object" for the object to look like a point charge or at least a uniformly charged sphere, we can assume a Green function of  $1/r$ , so we have the relations:

$$\frac{\partial \Phi}{\partial n} = \hat{n} \cdot \vec{\nabla} \Phi = \frac{-\hat{n} \cdot \vec{r}}{r^2} \Phi.$$

For a closer boundary, the possibility exists for finding the appropriate Green function, but we have not yet pursued that possibility.

2. Neuman, where the inward normal component of the electric field is specified.

3. Dirichlet, where the boundary potential is specified.

4. Extended Dirichlet, where a boundary potential of zero is assumed to exist one interval beyond the usual model boundary.

5. Reflection, where like condition 4, an extended boundary is assumed, but with a potential equal to the nearest interior neighbor.

When a boundary is assumed to represent "infinity", i.e. a source of undisturbed plasma at zero potential, the boundary should be far enough away from the "object" that all boundary conditions give the same results. It is frequently impractical to make grids that large so it becomes necessary to choose the B.C. which best approximates "infinity" on a limited grid. Parker and Sullivan (ref. 15) have addressed this problem, and it will not be discussed here except to state that we have found B.C. 4 and 5 to be the most useful for problems with planar geometry. All of these boundary conditions are effected by treating a boundary point as an interior point, and adding the appropriate "off-grid" potential.

With the appropriate consideration of exterior points, we can now apply equation (12) to all grid points giving a system of linear equations that is solved by the method of over-relaxation (O.R.) (ref. 16). Faster and more sophisticated methods are discussed by Hockney (ref. 17), but O.R. has been chosen for its programming simplicity and versatility. This iterative procedure should not be confused with the overall iteration process used in the inside-out method.

The Vlasov Problem: In kinetic theory, the density and current of species  $s$  at a point  $\vec{x}'$  are given by the 0th and 1st velocity moment of the single particle distribution function,  $f_s$ ;

$$N_x(\vec{x}') = \int f'_s(\vec{x}', \vec{v}') d^3\vec{v}' \quad (13)$$

$$\vec{J}_s(\vec{x}') = q_s \int f'_s(\vec{x}', \vec{v}') \vec{v}' d^3\vec{v}', \quad (14)$$

The distribution function is the density of particles in six-dimensional phase space (three position and three velocity coordinates). Further progress now requires finding  $f'$  at  $\vec{x}'$ . Application of Liouville's theorem<sup>†</sup> to a collisionless plasma leads to the collisionless Boltzmann or Vlasov<sup>†</sup> equation (ref. 18).

---

<sup>†</sup>The Vlasov equation represents the zeroth order terms in a cluster expansion of the Liouville equation, with smallness parameter  $g = (n_0 \lambda_d^3)^{-1}$ , the inverse of the number of particles in a Debye sphere. For GEO under substorm conditions  $n_e \approx 1/\text{cc}$  and  $kT_e \approx 10 \text{ kev}$ ,  $g \approx 10^{-15}$ , and in the F region with  $n = 10^6/\text{cc}$  and  $kT_e \approx 0.2 \text{ ev}$ ,  $g \approx 10^{-5}$ . So, in both cases the collisionless approximation is justified.

$$\frac{Df_s}{Dt} = \frac{\partial f_s}{\partial t} + \vec{v} \cdot \nabla \vec{f}_s + \frac{q_s}{m_s} (\vec{E} + \vec{v} \times \vec{B}) \cdot \nabla_{\vec{v}} \vec{f}_s = 0. \quad (15)$$

In words,  $f_s$  is constant along a particle's path in six-dimensional phase space, which can be characterized by the constants of the motion. For a time-independent electrostatic field such a constant is the total particle energy, defined by

$$H_s(\vec{x}, \vec{v}) = \frac{1}{2} m_s \vec{v}^2 + q_s V(\vec{x})$$

where  $q_s V(\vec{x})$  is the potential energy of the particle at  $\vec{x}$ . The six-dimension phase space path projected onto the three space coordinates is just the usual particle trajectory.

Consider the trajectory connecting  $(\vec{x}', \vec{v}')$  with  $(\vec{x}, \vec{v})$  for a given electrostatic field where at  $\vec{x}$ , the distribution of particles of specie  $s$  is known to be  $f_s(\vec{x}, \vec{v})$ . The constancy of  $f$  gives us

$$f_s(H(\vec{x}, \vec{v})) = f'_s(H(\vec{x}', \vec{v}')). \quad (16)$$

Note that some different value of  $\vec{v}'$  will map to a different point  $(\vec{x}_2, \vec{v}_2)$  where we know the distribution function to be different (or zero). Thus, in evaluating the integrals in equations (13) and (14), equation (16) must be used to develop a composite expression for  $f'$ . For example, consider the problem of a non-emitting body immersed in a Maxwellian plasma. If at infinity, the distribution function in three-dimensions for specie  $s$  is assumed to be,

$$f_s(\vec{\infty}, \vec{v}) = N_s \left( \frac{m_s}{2\pi kT_s} \right)^{3/2} \exp \left[ -\frac{H(\vec{v})}{kT_s} \right]. \quad (17)$$

Then, at some point  $\vec{x}'$  near the body, the distribution function will be,

$$f'_s(\vec{x}', \vec{v}') = N_s \left( \frac{m_s}{2\pi kT_s} \right)^{3/2} \exp \left[ -\left( \frac{1}{2} m_s \vec{v}'^2 + q_s V(\vec{x}') \right) / kT_s \right] \times G_s(\vec{x}', \vec{v}'), \quad (18)$$

where  $G_s$  is a function with a value of either zero or one depending on whether or not  $(\vec{x}', \vec{v}')$  maps the source at infinity. In other formulations, the  $G$  function is effectively replaced by reconstructing the limits of integration in equations (13) and (14).

In practice, the integrals in (13) and (14) are approximated by summations over a discrete set of velocities where each value of  $\vec{v}'$  represents a trajectory that must be followed to evaluate  $G(\vec{x}', \vec{v}')$ . We now have the choice of either starting trajectories at "infinity" and following them in; or because of the assumed time-independence, we could start at  $\vec{x}'$  and follow trajectories backwards in time to "infinity". The first technique has been dubbed the "Outside-in Method" by Parker (ref. 1) and is used in the program, SSB. It has the advantage of having all trajectories successfully connecting to a source and of supplying useful trajectory information to all points along

the trajectory. Its chief disadvantage lies in the difficulty of getting adequate trajectory probing of some regions of the problem. The Inside-out Method derives its name from the alternate approach of following trajectories backwards in time. This allows one to evaluate  $G(\vec{x}', \vec{v}')$  at all points with equal accuracy, but can lead to large numbers of trajectories to be retraced with each iteration. This last difficulty has been recently diminished by recording the fate of each trajectory so that in subsequent iterations, that information can be used to trace only those trajectories that lie on the velocity space boundary between null and escaping trajectories. This "boundary tracking" innovation can greatly increase storage requirements, but the reduction in time requirements make it essential. PANEL traces trajectories on the same grid that is used for the Poisson calculation. Each grid point has an associated cell. Trajectories are traced from cell to cell, using a uniform electric field within each cell. These cells are subdivided for greater trajectory accuracy in regions where subcell electric fields would differ greatly from the average whole-cell electric field.

For problems where the panel potential is much greater than the plasma potential, the number of trajectories to be traced is further reduced by assuming a monoenergetic distribution for the attracted particles.

#### PANEL RESULTS

So far, most of the models that have been produced with PANEL have been developmental, and we have only recently begun to model in 3-D the Chamber A experiments at the Johnson Space Center. The models presented here are two-dimensional.

Figure 2 shows PANEL's predictions for the previously discussed gap problem. In this model, electrons are accelerated from a cold cathode ( $T = 0$ ) at  $x = -d$  to the potential  $V_1$  (see the lower portion of figure 1) at  $x = 0$ , to produce a beam current  $J$ . PANEL models this experiment by assuming that there is an undisturbed Maxwellian plasma at  $x < -d$ , so that the current  $J$  is the random thermal current ( $J_0 = N_0 e \sqrt{kT/2\pi m}$ ) crossing the grid at  $x = -d$ . This current is normalized by the CL current given by equation (4) with  $d = x_1$  and  $V = V_1$ , so that the space charge in the gap ( $0 < x < x_1$ ) is characterized by the current ratio,

$$\beta = J/J_{CL}.$$

In the models Gap 06 and Gap 07, the transmitted electrons travel from right to left across a gap of one meter. This is modeled by 24 grid points; 12  $z$  and 2  $x$  coordinates. At  $z = 0$  electrons are absorbed; at  $z = 11$  (not shown), they are generated; and they are reflected at both  $x$  boundaries. (Since this is a one-dimension problem, PANEL could have been fitted with a one-dimension option, but unlike the two-dimension option, a one-dimension option would have only limited applications.) In both plots, the potentials predicted by the classical theory are labeled as curve A, and the results of PANEL are labeled P. For these two problems, the model parameters are:

Gap 06;  $\beta = 10$ ,  $J = 2.373 \times 10^{-2} \text{ A/m}^2$ ,  $T_e = 10 \text{ eV}$ ,  $V_1 = 100 \text{ V}$ , and  $N_0 = 2.8 \times 10^5 \text{ cm}^{-3}$ .

Gap 07;  $\beta = 10$ ,  $J = 2.373 \times 10^{-2} \text{ A/m}^2$ ,  $T_e = 1 \text{ eV}$ ,  $V_1 = 100 \text{ V}$ , and  $N_0 = 8.9 \times 10^5 \text{ cm}^{-3}$ .

The density integrations were performed using 8 energy intervals each with 64 angles for a total of 512 trajectories at each point per iteration; however, because of PANEL's phase space boundary tracking feature, only a fraction of the total number of possible trajectories were actually traced with each iteration. The error bar in Gap 07 indicates the degree of convergence at the point of maximum uncertainty; the convergence is better at other points. We consider these models to be a positive test of PANEL, in spite of the deviations from the classical predictions, since the classical theory considers a source of electrons with no thermal spread. By comparing Gap 06 with Gap 07 we can see that as the source plasma cools from a temperature of 10 eV to 1 eV, the potentials approach the classical value.

Figure 3 shows a simple but important test of PANEL. This is a comparison of PANEL with the Child-Langmuir law, equation (4). Due to the close agreement, a curve has been drawn only through the PANEL points. At selected points, PANEL and C-L potentials are given for comparison. The C-L potentials are given in parentheses and C-L densities are plotted with crosses. Here 32 points ( $2 \times 16$ ) are used to model a diode with a 16.51 meter plate separation, and a 100 volt potential difference. The model parameters are:

Pan 21;  $T_e = 1 \text{ eV}$ ,  $N = 3.2 \times 10^2 \text{ cm}^{-3}$ ,  $\lambda_d = 0.4 \text{ m}$ , and  $J = 8.58 \times 10^{-6} \text{ A/m}^2$ .

The greatest disagreement between PAN 21 and the C-L theory occurs at  $z = 14$ , where the PANEL prediction is 22% high, with improved agreement at lower  $z$  values. At  $z = 8$ , the disagreement is only 1%. The larger deviations should be expected in the low voltage region near the cathode due to the non-zero injection velocity of the electrons in the PANEL model.

Pan 36 is a two-dimensional model of a cross-section of an infinitely long, one meter wide panel held at a potential of 100 volts in a hydrogen plasma with equal ion and electron temperatures of 10 eV. The chosen plasma temperature of 10 eV is higher than the usual temperatures encountered in LEO or in the JSC Chamber A experiments which are frequently less than 1 eV. Models with a plasma temperature of 1 eV and panel potentials greater than 100 V are being processed, but under these conditions the convergence is significantly less stable. To achieve stability thus requires a smaller mixing parameter, more iterations and more computing time; so for these first models, a higher but not unreasonable temperature was chosen.

Due to the symmetry of the problem, it was possible to model the entire cross-section by calculating potentials and densities in one quadrant only by using the reflection boundary condition on the DOWN and WEST boundaries. Both the UP and EAST boundary conditions are  $V = 0$ . This model used 90 grid points and the following plasma parameters:

$$T_i = 10 \text{ eV}, T_e = 10 \text{ eV}, N_o = 1.9 \times 10^4 \text{ cm}^{-3}, \lambda_D = .17\text{m}, \text{ and } J_{oe} = 1.61 \times 10^{-3} \text{ A/m}^2,$$

The density and current integrations were performed with 8 energy and 64 angular intervals. Pan 36 results are shown in figures 4, 5, and 6. Figure 4 shows equipotential contours in one quadrant, with one half of the panel represented by the 100 V line. The points in the figure are interpolation points and not grid points. The electron currents collected from above the panel are indicated by the arrows below the panel in figure 4 and have been normalized by the random thermal current,  $J_o$ . In PAN 36 we begin to see a slight reduction in current collection near the edge. The strong central focusing (greater than an order of magnitude difference between central and edge currents) observed by McCoy (ref. 19) in the solar panel tests at JSC is not indicated in this model. This focusing, however, generally occurs at a higher panel voltage than that considered here and may be due to a band of dielectric along the edges of that test panel.

For PAN 36, the C-L screening distance, given by equation (4) is  $D_{CL} = 1.2 \text{ m}$ , and the corrected screening distance, from equation (3) is  $D_s = 1.73 \text{ m}$ . These points are indicated in Figures 4, 5, and 6, and the uncorrected C-L contour is marked with crosses in Figure 5. Figures 4 and 6 show that potentials have been reduced to less than  $1/2 \text{ kT/e}$  ( $= 5 \text{ V}$ ) within either estimate. There is some "compression" of the contours caused by the closeness of the  $V = 0$  boundaries, as is evidenced by the most distant points in Figure 6 where the electron density unrealistically drops below the proton density due to the artificially high electric field between the outermost two points. Although the PAN 36 boundaries are too close to allow a complete presheath and undisturbed plasma region to develop, figure 6 shows the beginning of a presheath region beyond the  $D_{CL}$  point with electron and proton densities nearly equal but reduced from the ambient values.

#### THE SHARP SHEATH BOUNDARY MODEL

We have discussed the General Space Charge (GSC) model, i.e. PANEL, that treats general boundary conditions and particle velocity distributions, under relatively few simplifying assumptions. The sheath structure is obtained automatically, requiring only sufficient numbers of grid points and that the computational boundary be sufficiently far out to represent the solution reasonably accurately.

An alternative computer model is the Sharp-Sheath-Boundary (SSB) model. In similarity with the GSC model, the alternate SSB version solves the non-linear Poisson equation by computing rigorous space charge densities that require the following of particle trajectories on the computer, and by obtaining self-consistent solutions by iteration. (Both SSB and GSC models are based on approaches innovated by Lee W. Parker, Inc.) However, the SSB model is an attractive alternative because it is computationally inexpensive compared with the GSC model. The simplifying approximation is made that in three-dimensions a sharp sheath boundary surface exists (in three-dimensions) generalized from those of the (one-dimensional) Child-Langmuir diode models in

planar/cylindrical/ spherical symmetry. On this boundary surface the potential is zero, and from it attracted particles are emitted which fall inward (while creating space charge) toward the panel surface, starting with zero energy. The self-consistent solution includes finding the shape of the SSB surface such that the electric field also vanishes at all points of the surface. This approximation seems justifiable because the panel voltages of interest are large compared with  $kT/e$ , and the panel dimensions are large compared with the plasma Debye length. Ultimately, however, its accuracy (and cost effectiveness) can be assessed by comparisons with experiment as well as with solutions obtained with the more rigorous GSC model. The method uses a flexible "dynamic mesh" with sliding grid points such that the bounding surface can expand or contract, acquiring whatever shape is required for the given body shape and body surface potential distribution. To achieve flexibility in sheath shape and body shape, a triangularized finite-element method is used. Figure 7 illustrates the nature of the grid employed.

In Fig. 7 a coarse grid is used (two-dimensional cross-section) to obtain a sample solution for a conducting panel 1 m wide, with 500 V on the panel and plasma parameters  $n_0 = 10^6/\text{cm}^3$  and  $kT = 0.4$  eV. Both the initial (assumed) sheath shape and final sheath shape are shown, where the final "converged" shape has been obtained by iteration. The dimensions shown are in units of the panel width. The final sheath thickness at the center is about 1.2 m, essentially equal to the value given by the planar Child-Langmuir formula. Some ion trajectories are shown in the upper half of the mesh.

Since ion-focusing effects are of concern, a series of focusing runs have been made as preliminary solutions obtained by the SSB model. For a panel (1.22 m) 48", with 6" insulated borders, and with plasma parameters  $n_0 = 10^6/\text{cm}^3$  and  $kT = 0.4$  eV, the following sample results are obtained, on a two-dimensional cross-section (Fig. 8):

The ion focus occurs at the panel center for a voltage of about 3000 V. For lower voltages the focal position appears to be behind the panel, with high surface current densities on either side of the panel center (at about 0.4 m and 0.24 m from the center at 500 V and 1000 V, respectively; the 500-V case is not shown in the figure). For the lower voltages, the sheath shape is "boxy" with a "flattish" top and vertical sides. The sheath thickness at the panel center is about 1.6 m at the "focal voltage" of about 3000 V, and the sheath shape is oval with larger vertical than horizontal dimension, but nearly circular. At higher voltages (e.g. 5000 V) the focus occurs above the panel center, and the sheath is oval-shaped.

## DISCUSSION

The results of both the PANEL and SSB models indicate that at least for the range of parameters and geometry considered, the Child Langmuir diode model provides a useful estimate of the plasma sheath thickness. This conclusion is also indicated by the Chamber A solar panel experiments (ref. 19). We do not claim that this result will hold true under all conditions, nor are we presenting these results as a confirmation of a C-L sharp edge sheath model.



Furthermore, it should be pointed out that an earlier study (ref. 13) found that a CL diode model could not adequately predict the current/voltage behavior of a sphere with radius equal to 100 Debye lengths. Such confirmation must await further analysis of the CL-SES model and the use of such a model to make definite predictions. Also, we plan a thorough analysis of the sharp edge sheath concept, independent of a C-L diode space charge model, because of its potential usefulness in simplifying plasma sheath calculations.

In their present forms, both programs appear capable of producing results that will be quite valuable in interpreting the Chamber A experiments and in increasing the general understanding of the plasma screening process. However, as we consider increasingly complex models, computer time limitations will require a "smarter" type of program. Such a program might include a marriage of both outside-in and inside-out methods of rigorously calculating particle densities and currents, with program "intelligence" used to choose which method would be the most efficient and effective for each grid point.

#### REFERENCES

1. Parker, L. W., "Numerical Methods for Computing the Density of a Rarefied Gas about a Moving Object," AFGL-64-193, Allied Res. Assoc., Inc., Concord, Mass., 1964.
2. Parker, L. W., and E. C. Whipple, "Theory of spacecraft sheath structure, potential, and velocity effects on ion measurements by traps and mass spectrometers," J. Geophys. Res., 75, 4720, 1970.
3. Parker, L. W., "Computation of collisionless steady-state plasma flow past a charged disk," NASA CR-144159, Lee W. Parker, Inc., Concord, Mass., 1976.
4. Parker, L. W., "Calculation of sheath and wake structure about a pill-box shaped spacecraft in a flowing plasma," in Proceedings of the Spacecraft Charging Technology Conference, ed. by C. P. Pike and R. R. Lovell, AFGL-TR-77-0051, 331, 1977.
5. Parker, L. W., Power loss calculation for high-voltage solar arrays, final report for NASA Contract NAS3-2085, Lee W. Parker, Inc. Report, 1977.
6. Reiff, P. H., J. W. Freeman, and D. L. Cooke, "Environmental protection of the solar power satellite," in Space systems and Their Interactions with Earth's Space Environment, ed. by H. B. Garrett and C. P. Pike; Progress in Astronautics and Aeronautics, 71; by Am. Inst. of Aeronautics and Astronautics, 1980.
7. McCoy, J. E., and A. Konradi, "Sheath effects observed on a 10 meter high voltage panel in simulated low earth orbit plasma," Spacecraft Charging Technology-1978, ed. by R. C. Finke and C. P. Pike, AFGL-TR-79-0082, p. 315, 1978.

8. Jackson, J. D., Classical Electrodynamics, Wiley and Sons, Inc., p. 341, 1962.
9. Child, C. D., "Discharge from hot CaO," Phys. Rev., 32, 492, 1911.
10. Langmuir, I., "The effect of space charge and residual gases on thermionic currents in high vacuum," Phys. Rev., 2, 450, 1913.
11. Birdsall, C. K., and W. B. Bridges, Electron Dynamics of Diode Regions, Academic Press, New York, N. Y., 1966.
12. Langmuir, I., and K. B. Blodgett, "Currents limited by space charge between concentric spheres," Phys. Rev., 24, 49, 1924.
13. Parker, L. W., "Plasma-photosheath theory for large high-voltage structures," in Space Systems and Their Interactions with the Earth's Space Environment, ed. by H. B. Garrett and C. P. Pike; Progress in Astronautics and Aeronautics, 71, American Inst. of Aeronautics and Astronautics, 1980.
14. Collatz, L., The Numerical Treatment of Differential Equations, Springer-Verlag, 1960.
15. Parker, L. W., and E. C. Sullivan, "Boundary conditions and iterative procedures for plasma sheath problems," in Sixth Int'l Symposium on Rarefied Gas Dynamics, II, 1969.
16. Stiefel, E. L., An Introduction to Numerical Mathematics, Academic Press, p. 199, 1963.
17. Hockney, R. W., "Solution of Poisson's equation using Fourier Analysis," J. Assoc. Computing Mach., 12, 95, 1965.
18. Montgomery, D. C., and D. A. Tidman, Plasma Kinetic Theory, p. 51, McGraw-Hill, 1964.
19. McCoy, J. E., "High voltage space plasma interactions", in Proceedings of the Solar Power Satellite Program Review, DOE/NASA, avail. from NTIS, S285 Port Royal Road, Springfield, Virginia 22161, 1980.

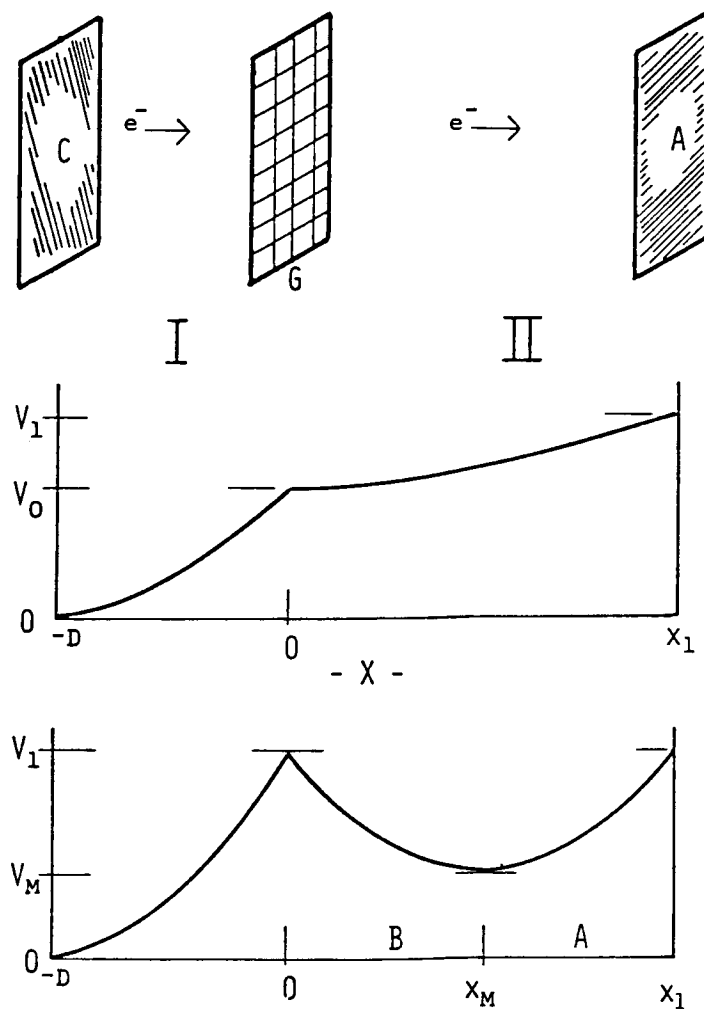


FIG.1

Schematic representation of a planar electron diode, showing the effect of the electron space charge on the interelectrode potential for two different arrangements of the electrode potentials.

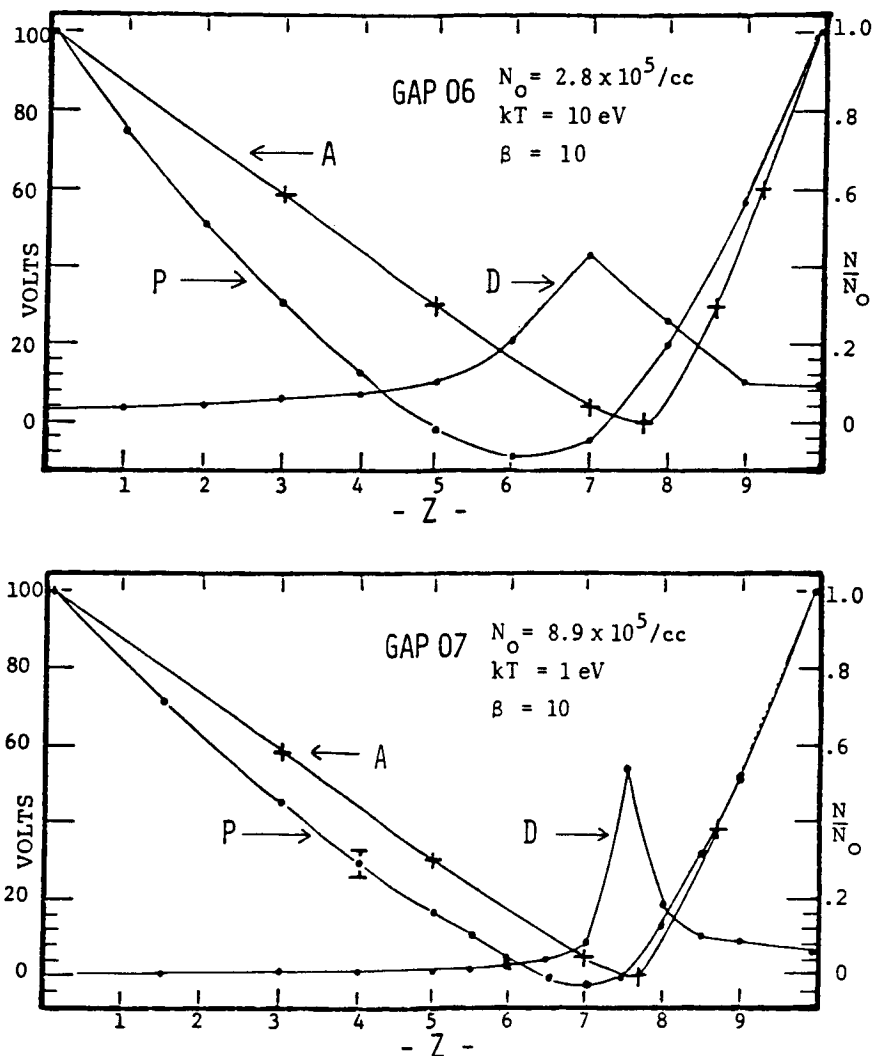


FIG. 2: In both graphs, curve P is PANEL's prediction for the inter-electrode potentials, curve A is the classical prediction, and curve D is PANEL's prediction for the electron density. The  $Z$  distance unit is 0.1 meter.  $\beta$  is the normalized current density.

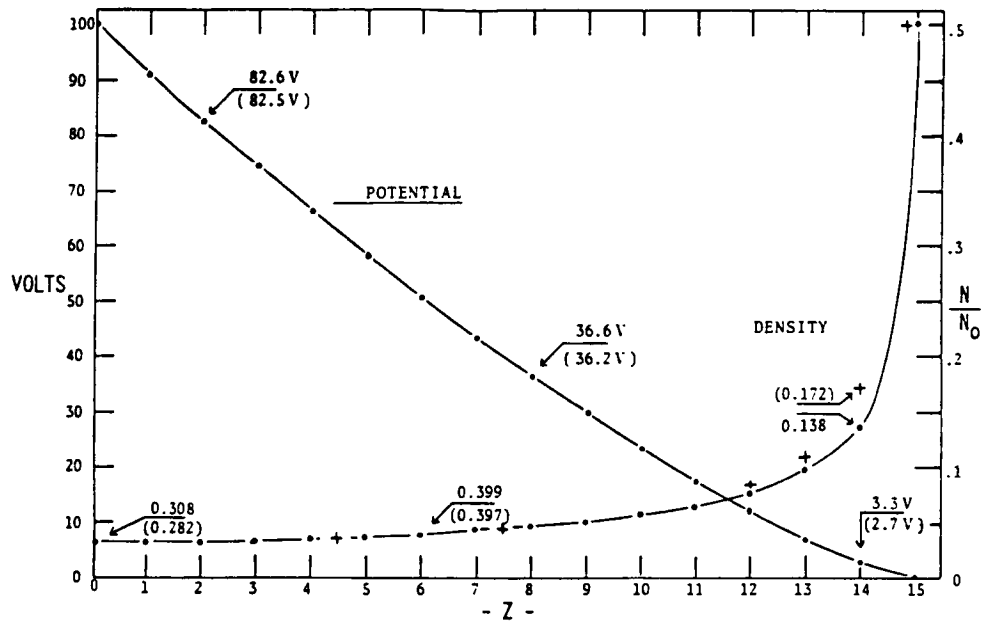


FIG. 3: PANEL's predictions for the Child-Langmuir electron diode are plotted with the connected dots, and selected values of potential and density are presented. The classical C-L density predictions are plotted by the unconnected crosses, and for comparison, selected values of the C-L potential and density are given in parenthesis. For this model,  $N_0 = 320/\text{cc}$ ,  $J_e = 8.6 \times 10^{-6} \text{ A/m}^2$ , and the total diode separation is 16.51 meter.

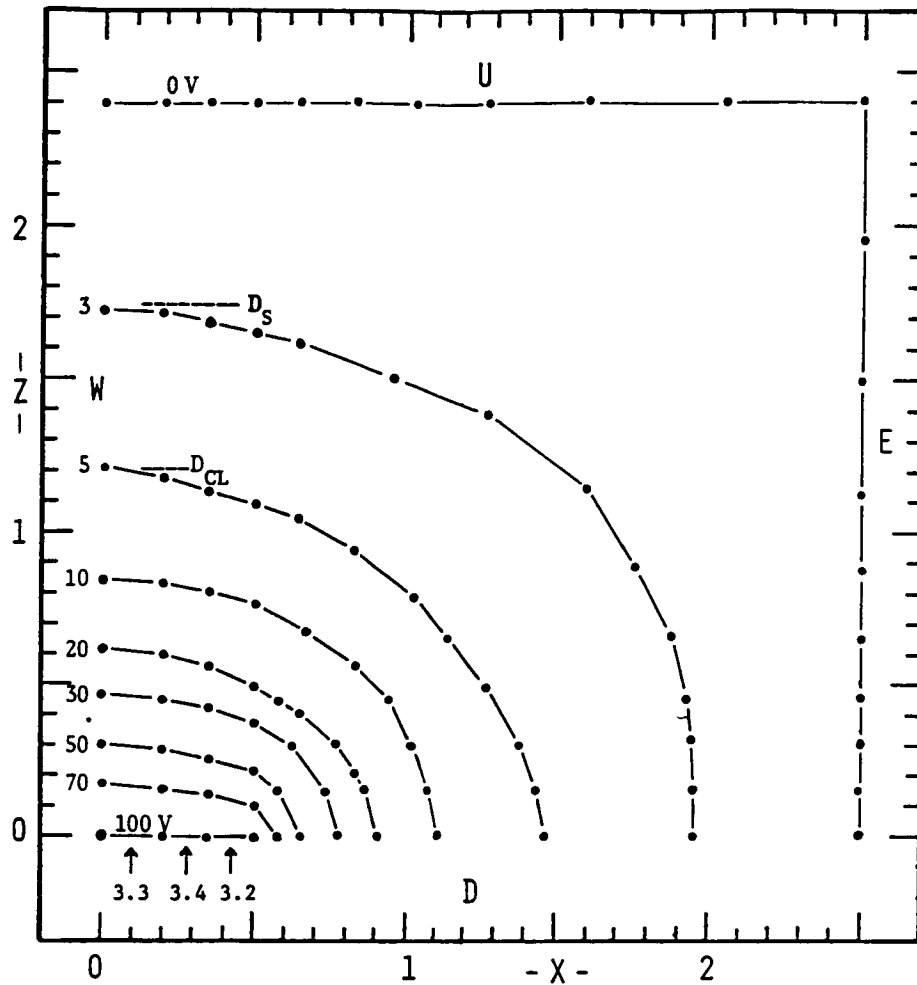


FIG. 4, Model Pan36: The same panel and plasma of model Pan29 are modeled here with 90 grid points (not shown), and with a  $V = 0$  boundary condition on both the UP and EAST boundaries. The distance unit is 1.0 meter.

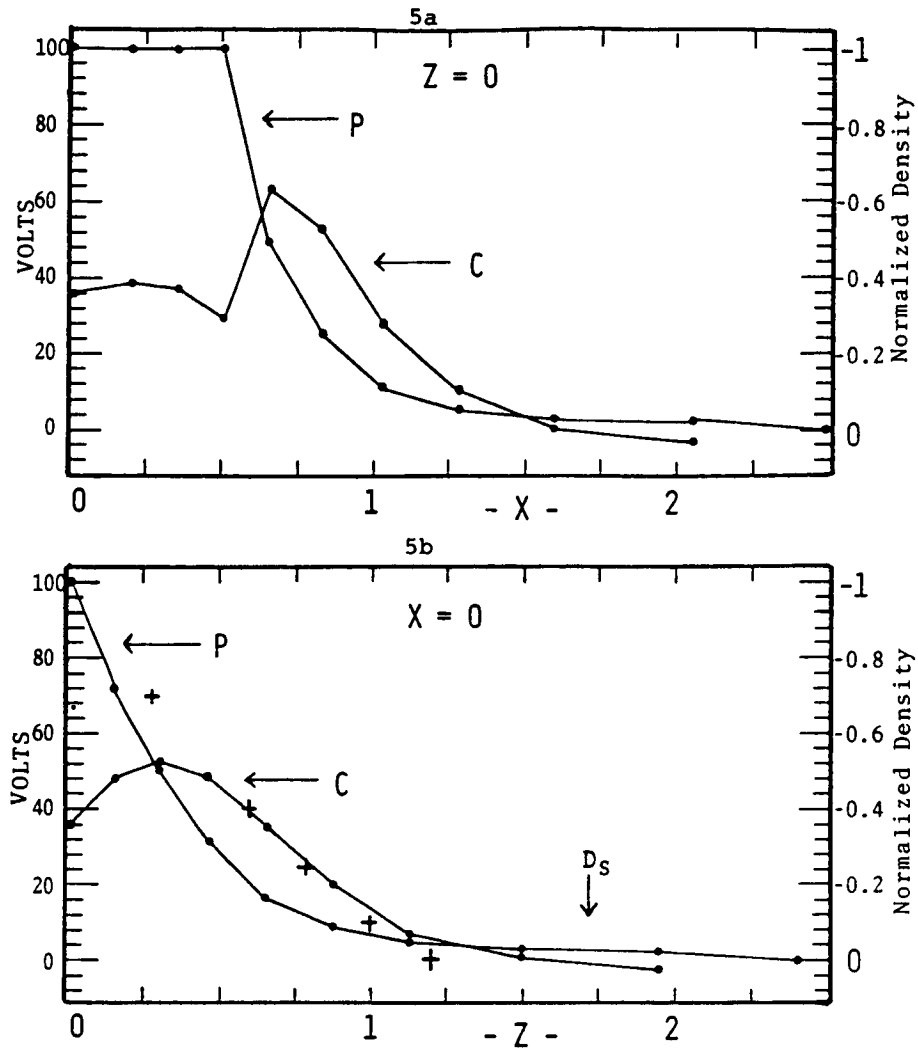


FIG. 5 : Potential (curve P) and charge density (curve C) profiles along the DOWN ( 5a ) and WEST ( 5b ) boundaries for the model Pan36. The density scale on the right is normalized to the ambient density,  $N_0 = 1.9 \times 10^4/\text{cc}$ . In 5b , the Child-Langmuir potential profile is indicated by the unconnected crosses, and the initial velocity corrected C-L screening distance,  $D_s$ , is indicated by the arrow. The distance unit is 1.0 meter.

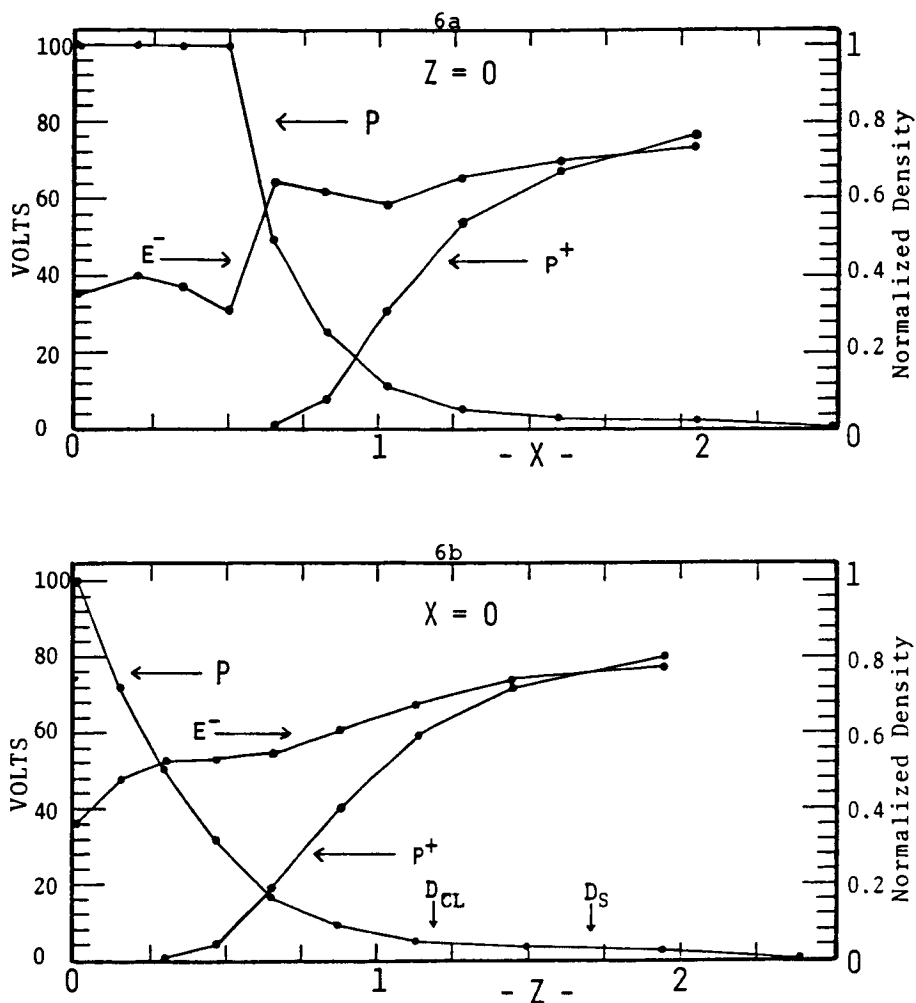


FIG. 6: Potential (curve P), and electron and proton density profiles along the DOWN (6a) and WEST (6b) boundaries for the model Pan36. The corrected and uncorrected Child-Langmuir screening length estimates  $D_S$  and  $D_{CL}$  are indicated in 6b. The distance unit is 1.0 meter.



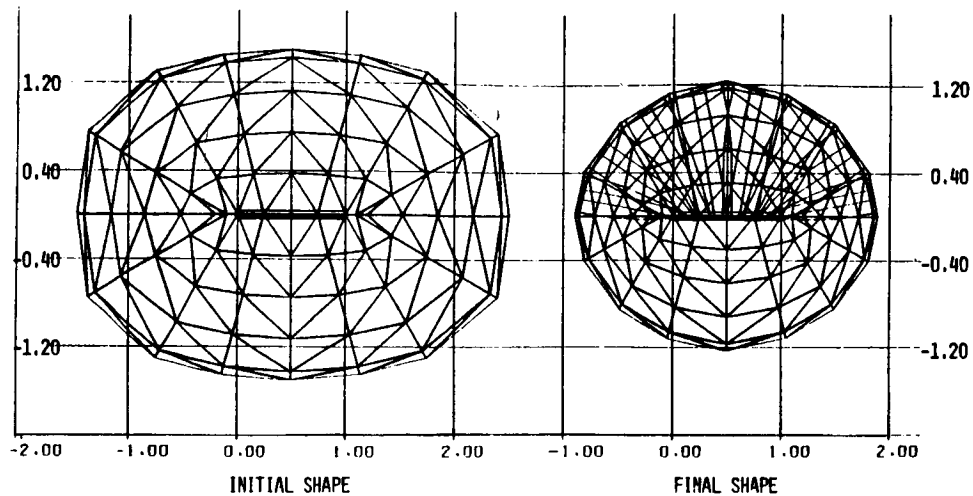


FIG. 7 . CONDUCTING PANEL SHEATH (SSB Model)

(Dimensions in units of panel width)

Self-adjusting finite-element grid. Boundary position adjusts to satisfy boundary conditions  $V = \partial V / \partial n = 0$ .

Panel width = 1.0 m. Panel voltage = 500 V.

Plasma density and temperature =  $10^6/\text{cm}^3$  and 0.4 eV.

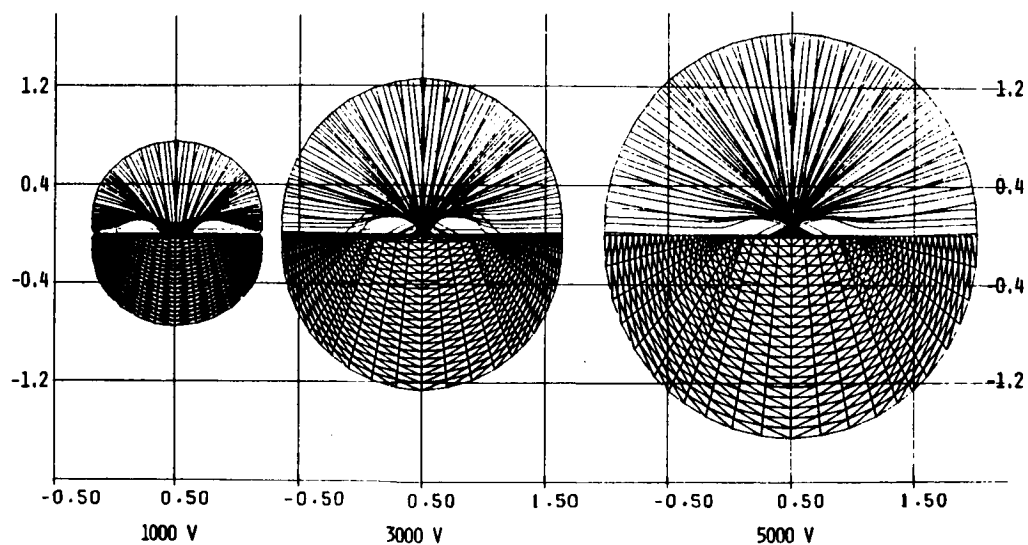


FIG. 8 ION FOCUSING ON PANEL WITH INSULATED ( $V=0$ ) BORDERS (SSB Model)

(Dimensions in units of panel width)

Self-adjusting finite-element grid. Voltage variable.

Panel width = 48" (1.22 m), Border width = 6"

Plasma density and temperature =  $10^6/\text{cm}^3$  and 0.4 eV.

## CHARGING OF A LARGE OBJECT IN LOW POLAR EARTH ORBIT\*

D. E. Parks and I. Katz  
Systems, Science and Software

### SUMMARY

We have investigated the charging of a large sphere subject to the environment encountered by the shuttle orbiter as it passes through the auroral regions in its low polar earth orbit. The environment consists of a low temperature dense plasma and a relatively intense ( $200 \mu\text{A}/\text{m}^2$ ) field aligned flux of energetic electrons ( $\sim 5$  to  $10 \text{ keV}$ ).

The potential on a sphere in eclipse is presented as a function of the ratio  $\kappa$  of the charging rate produced by precipitating electrons to the discharging rate produced by ram ions. We find that a 5 meter conducting sphere charges to potentials of order 1 kilovolt for  $\kappa \sim 2$ , even though a 0.5 meter sphere charges to less than 100 volts.

It is concluded that the natural charging environment can induce large potentials ( $\sim 1$  kilovolt) on the shuttle orbiter.

### INTRODUCTION

The shuttle orbiter, passing through the ionosphere at altitudes of a few hundred kilometers, develops electrical potentials through accretion of charge from the natural environment. Under normal ambient conditions the particle energies viewed from the satellite range from a few tenths of an electron volt to a few volts. Thus, the magnitude of vehicle potentials are at most a few volts. However, while passing through polar latitudes the vehicle may be subjected to a substantial flux of energetic electrons moving through the auroral zone following their injection in the magnetosphere. This may cause charging to high potentials.

Most experimental studies of spacecraft charging in low earth orbit have concerned small objects ( $\sim 1 \text{ m}$ ) moving through the ionosphere. In the absence of energetic precipitating electrons,

---

\* This work supported by Air Force Geophysics Laboratory, Hanscom Air Force Base, Lexington, MA 01731, and the National Aeronautics and Space Administration, Lewis Research Center, Cleveland, OH 44135, under Contract NAS3-21762.

the magnitude of the observed electric potentials on the INJUN 5 satellite were less than a few volts, in accordance with theoretical expectations (ref. 1). Even during impulsive precipitation events, observed potentials did not exceed -40 volts negative.

More recently, theoretical studies have focused on charging of large objects. Parker has presented a method for computing sheath structures of large spherical bodies with high-voltage surfaces and with photoelectric/secondary emission (ref. 2). McCoy et al. have considered problems associated with the operation of large, high-voltage solar arrays in the ionosphere (ref. 3). Liemohn has considered the electrical charging of the shuttle orbiter in the absence of fluxes of energetic precipitating electrons (ref. 4). Inouye et al. (ref. 4) investigated the charging of a space based radar system having an antenna with a diameter of about 70 meters (ref. 5). Their calculation of electrical potentials in the presence of energetic particles are based on the application of orbit limited theory of Langmuir and Mott-Smith to determine the currents of attracted species (ref. 6).

The investigations of charging presented below are for the regime where body dimensions are large compared to the relevant Debye length. In this regime the currents of attracted species are estimated by adapting the large spherical probe theories of Langmuir and Blodgett (ref. 7) and Al'pert et al. (ref. 8). We examine the charging of a conducting sphere subjected to intense fluxes of energetic electrons. Factors relevant to a more thorough analysis of complex objects with dielectric surfaces are summarized. Conclusions are given in the final section of the paper.

## ANALYSIS

The purpose of the following analysis is to estimate the magnitudes of potential that develop on objects in low earth orbit (200 to 400 km) when subjected to high fluxes ( $\sim 200 \mu\text{A}/\text{m}^2$ ) of hot (5 to 10 keV) precipitating magnetospheric electrons. Nominal values of the satellite and environmental parameters relevant to the analysis are summarized in Table 1.

We are concerned primarily with the possibly large negative potentials that may be produced by the currents of hot electrons incident from the magnetosphere. Questions related to the satellite wake and its structure are not considered; we consider the ram ion current density  $\text{NeV}_0 \sim 10^{-8} \text{ amp}/\text{cm}^2$  apparent to a co-moving observer as the only relevant attribute of the satellite motion. Thus, for example, it is anticipated that the  $\text{V}_0 \times \text{B}$  inductive electric fields are small relative to the electrostatic fields produced by charging.

To proceed further, let us first neglect the magnetic field. The effects of a magnetic field will be discussed later. The flux of hot electrons to the satellite is assumed unidirectional. Since the ram ion energy ( $E_o \approx 5$  eV) is much larger than the ion temperature, the ram ion flux will also be considered unidirectional. In the absence of electric potential the precipitating electron and ram ion currents to the satellite will be  $j_p \pi R_o^2$  and  $j_r \pi R_o^2$ , respectively.

For negative potentials electrons are repelled and the current of precipitating electrons at the satellite is approximately  $j_p \pi R_o^2 \exp\{e\phi/\theta_p\}$ . This is an accurate approximation if the effective collection radius  $R_c$  is not much greater than  $R_o$ , that is, if the thickness  $R_c - R_o$  of the non-neutral space charge region around the object is less than the satellite radius. For all practical purposes in the cases of interest,  $-e\phi \gg \theta_e$ . Thus the cold plasma electrons do not enter the sheath region.

The effect of space charge upon current collection in low earth orbit by large high voltage objects is well-known, having been studied both theoretically and with laboratory experiments. Space charge effects dramatically reduce the current collected per unit area compared to those predicted by orbit limited theory. The I-V characteristics of a spherical probe with a ratio of radius to Debye length of 10 is shown in figure 1. The current collected per unit area at large voltages is substantially less than the very large Debye length orbit limited theory would predict. However, the auroral electron fluxes in polar earth orbit are incident currents which may be substantially larger than the ram ion currents. We are then interested in the inverse function, that is, the V-I characteristic (figure 2). Note how dramatically the probe voltage must rise to increase the current collected per unit area. It is this steep V-I characteristic which forms the basis of the following analysis.

The theory of the sheath surrounding a large spherical probe with radius  $R_o \gg \lambda_D$  at high potential  $|e\phi| \gg \theta_e$ ,  $\theta_i$  in an isotropic plasma is given in Langmuir and Blodgett (ref. 7) and Al'pert et al. (ref. 8). The effective collection radius  $R_c$  for the case of ion attraction can be expressed as

$$\frac{R_c}{R_o} = F \left( \frac{e\phi}{\theta} \left( \frac{\lambda}{R_o} \right)^{4/3} \right) \quad (1)$$

where  $\theta$  is the temperature of the attracted species and  $\lambda$  the

Debye length.  $F$  is an increasing function of its argument and hence of the satellite potential.

In order to adapt the Langmuir-Blodgett theory as an approximation to the case of streaming ions, we relate the temperature  $\theta$  to the kinetic energy  $E_o$  of ions relative to the satellite by requiring that current entering the sheath in the isotropic and streaming cases be the same,

$$N V_o^2 \pi R_c^2 = 4 \pi R_c^2 N (8\theta/\pi M)^{1/2} \quad (2)$$

giving

$$\theta = \frac{\pi M V_o^2}{8} = \frac{\pi E_o}{4} \quad (3)$$

where  $M$  is the ionic mass. The equivalent Debye length is

$$\lambda = 743 (N/\theta)^{1/2} \text{ cm} \quad (4)$$

Table 2 gives values of  $R_c/R_o$  as a function of  $z \equiv (e\phi/\theta)(\lambda/R_o)^{4/3}$ . For values of  $R_c/R_o \leq 1.05$ , the collection radius and potential are related by the plane electrode Child-Langmuir law

$$\frac{R_c}{R_o} = 1 + \frac{2\sqrt{2}}{3} z^{3/4} \quad (5)$$

with an accuracy better than 3 percent.

The potential on the sphere is determined by balance of currents,

$$\pi R_o^2 j_p (1-s_p) e^{e\phi/\theta} = \pi R_c^2 j_r (1+s_i) + I_v \quad (6)$$

where  $s_p(s_i)$  is the total secondary yield from electron (ion) impact and  $I_v$  is the total photoemission current.

Defining

$$\bar{j}_p = j_p (1-s_p)$$

$$\bar{j}_r = j_r (1+s_i)$$

as effective electron and ion current densities corrected for secondary emission, equation (6) becomes

$$\kappa = \bar{j}_p / \bar{j}_r = \left( \frac{R_c}{R_o} \right)^2 \exp |e\phi / \theta_p| + \frac{I_v}{\bar{j}_r \pi R_o^2} \quad (7)$$

Figure 3 shows the dark potential on spheres of 0.5 and 5 m radius as a function of ratio of precipitating electron to ram ion current densities in a plasma with ambient density  $10^5 \text{ cm}^{-3}$ . For a given current ratio the potential on the sphere scales roughly as the radius. More precisely, the potential scales with radius as  $(R_o/\lambda)^{4/3}$  for  $|e\phi| \ll \theta_p$ , but somewhat more slowly with  $R_o/\lambda$  as  $|e\phi|$  increases. Observe that the potential is an extremely sensitive function of  $\bar{j}_p/\bar{j}_r$  for values of this ratio near unity, especially for the larger sphere.

The theory predicts that the 5 m sphere will charge to about the 1 kilovolt level for electron to ram ion current density ratios of only about two. This is to be contrasted with the result predicted by orbit limited ion collection. The approximate dark current balance

$$\frac{j_p}{j_r} \approx \left( 1 + \frac{|e\phi|}{\theta} \right) e^{|e\phi|/\theta_p}$$

for orbit limited collection predicts, for example, that  $j_p/j_r \approx 300$  would be required to sustain a 1 kilovolt potential on the sphere.

## DISCUSSION

Several effects have been neglected in determining that hot electrons precipitating from the magnetosphere can charge a large object to kilovolt potentials. We shall now argue that accounting for these effects will not alter the conclusion that such high potentials should be expected for the assumed charging environment.

Consider first the effect of a magnetic field on the ram ions entering the sheath surrounding the satellite. A component of magnetic field perpendicular to the satellite velocity will tend to insulate the surface from the ram ion currents, leading to larger negative potential of the satellite. For cases of interest however, the effect is negligible. A measure of the size of this effect is given by

$$\alpha = \frac{\frac{1}{2} M \omega_{ci}^2 d^2}{|e\phi|} \approx \omega_{ci}^2 \tau^2$$

where  $M$  is the ion mass,  $\omega_{ci}$  its gyrofrequency,  $d$  the thickness of the sheath, and  $\tau$  the flight time of an ion across the sheath. For the cases represented in figure 1,  $d \lesssim R$ , so that

$$\alpha \lesssim 0.2/|e\phi \text{ (volts)}|$$

which is negligibly small except at very low levels of satellite potential.

The hot electrons responsible for charging the satellite were considered to approach the space charge sheath unidirectionally, as pertains in the limit of strong magnetic fields where the Larmor radius is small compared with the radius of the satellite. More probably, the electrons, because of their pitch angle distribution, would enter the repulsive sheath with a more nearly isotropic distribution of directions. Assuming that the one sided thermal plasma current densities are the same in the unidirectional and isotropic limits, the effective electron current toward one hemisphere of the satellite in the isotropic limit is twice that which pertains in the unidirectional case. In the absence of no other effect associated with the magnetic field, the result would be greater charging.

The charging current given by equation (6) for the case of repelled electrons incident unidirectionally from infinity applies in the limit of zero gyroradius. In the opposite limit of vanishing magnetic fields, again assuming that electrons enter the sheath unidirectionally, fewer electrons reach the satellite because of the deflection by the repulsive electric field. The reduction in current is small however, and the charging current accurately represented by equation (6) provided that the repulsive potential on the satellite satisfies  $(e\phi/\theta_p)^2 \ll 1$ . This requirement, which is satisfied in the case of figure 1 for potentials less than about 2 kV, follows from the conservation laws of energy and angular momentum which permit one to express the current to the satellite as

$$I = N_0 (m/2\pi\theta_p)^{1/2} \pi R_0^2 \int_{\left(\frac{2e\phi}{m}\right)^{1/2}}^{\infty} dv \, v e^{-mv^2/2\theta_p} \left\{ 1 - \frac{2e\phi}{mv^2} \right\}$$

Essentially, the electron current crossing the sheath is not substantially modified by the magnetic field, a circumstance we expect to pertain is long as

$$(\omega_{ce}\tau)^2 \ll \frac{1}{2} m \omega_{ce}^2 d^2 / \theta_p \ll 1$$

This condition is well satisfied for potentials in figure 3 at the kilovolt level.

In applying the Langmuir-Blodgett probe theory, we have neglected the contribution of electrons to the space charge in the sheath. This is a valid approximation because the velocity of electrons in the sheath is large compared with ion velocities, except perhaps for the contribution of secondary and photoelectrons near the surface. Near the surface, however, the electric fields are dominated by surface charge and little affected by space charge.

Secondary and photoelectrons move through the sheath with smaller energies than the precipitating magnetospheric electrons and are therefore more strongly affected by the magnetic field. The potential developed by the satellite is affected however only if the emitted electrons return to the surface, leading to higher potentials than if the electrons escape.

In all previous considerations, we have supposed that the satellite is a conducting sphere. The shuttle orbiter is actually a geometrically complex object whose surface is coated with dielectric materials, and both ion and electron fluxes are apt to be strongly heterogeneous functions over the satellite's surface. The degree of heterogeneity will be affected by the geometry of the satellite, its motion through the ionosphere, the variation of surface properties, such as secondary yield, and by the magnetic field. Undoubtedly the sheath surrounding the orbiter will have a complicated geometrical structure not easily represented by simple spherical probe models. Multidimensional computer models will be required to determine the strong differential voltages which are expected to develop on the vehicle.

## CONCLUSIONS

Ambient currents of hot electrons (5-10 keV) of  $200 \mu\text{A}/\text{m}^2$  will charge a 5 meter sphere in low polar earth orbit to kilovolt potentials in eclipse. Such potentials are about 1 order of magnitude larger than occur for smaller satellites ( $\sim R_0 \sim 0.5 \text{ m}$ ) in a similar orbit. On this basis, one should expect negative potentials of around 1 kilovolt to develop on the shuttle orbiter. Because of the dielectric coating on the orbiter, and the non-uniform



character of the charged particle fluxes expected at the vehicle's surface, differential surface potentials of the order of one kilovolt should also occur.

#### REFERENCES

1. Sagalyn, R. C. and W. J. Burke: INJUN 5 Observations of Vehicle Potential Fluctuations at 2500 km. Proceedings of the Spacecraft Charging Technology Conference, AFGL-TR-77-0051, NASA TMX-73537, February 1977.
2. Parker, L. W.: Plasmasheath-Photosheath Theory for Large High-Voltage Space Structures. Space Systems and Their Interaction with Earth's Space Environment, Progress in Astronautics and Aeronautics, 71, 477, 1980.
3. McCoy, J. E., A. Konradi and O. K. Garriott, *ibid*, p. 523.
4. Liemohn, H. B.: Electrical Charging of Shuttle Orbiter. Battelle, Pacific Northwest Laboratories Report BN 5A 518, June 1976.
5. Inouye, G. T., R. L. Wax, A. Rosen and N. L. Sanders: Study of Space Environment Physical Processes and Coupling Mechanisms. AFGL-TR-79-0206, September 1979.
6. Mott-Smith, H. M. and I. Langmuir, *Phys. Rev.*, 28, 727, 1926.
7. Langmuir, I. and K. Blodgett, *Phys. Rev.*, 22, 347, 1923; 24, 99, 1924.
8. Al'pert, Ya. L., A. V. Gurevich and L. P. Pitaevskii: Space Physics With Artificial Satellites. Consultants Bureau, New York, 1965, pp. 186-210.

TABLE 1. - NOMINAL VALUES OF PARAMETERS WHICH INFLUENCE ELECTRICAL CHARGING IN LOW EARTH ORBIT

Sphere Diameter	1000 cm
Satellite Velocity $V_o$	$8 \times 10^5$ cm/sec
Ambient Ion Temperature $\theta_i$	.1 - .5 ev
Ambient Electron Temperature $\theta_e$	.1 - .5 ev
Precipitating (Hot) Electron Temperature $\theta_p$	5 - 10 kev
Neutral Atom Density (0)	$10^{10}$ cm <sup>-3</sup>
Ion Density ( $0^+$ )	$10^4 - 10^6$ cm <sup>-3</sup>
Ambient Debye Length	<1 cm
Thermal Electron Larmor Radius	2 cm
Hot Electron Larmor Radius	400 cm
Ion Larmor Radius	300 cm
Current Density (amp/cm <sup>2</sup> )	
Thermal Electron $j_e$	$10^{-7}$
Thermal Ion ( $0^+$ ) $j_i$	$10^{-10}$
Photoelectron $j_v$	$10^{-9}$
Precipitating (Hot) Electron $j_p$	$2 \times 10^{-8}$
Ram Ion $j_r$	$10^{-8}$

TABLE 2. - EFFECTIVE COLLECTION RADIUS AS FUNCTION OF  $z \equiv e\phi/(\lambda/R_o)^{4/3}$

$R_c/R_o$	$z$
1.005	.001
1.018	.005
1.030	.010
1.050	.019
1.100	.052
1.150	.094
1.200	.143
1.250	.199
1.300	.264
1.340	.337
1.400	.421
1.450	.510
1.500	.610
1.600	.833
1.700	1.092
1.800	1.384
1.900	1.711
2.000	2.074
2.100	2.479
2.200	2.919
2.300	3.400
2.400	3.920
2.500	4.479
2.600	5.113
2.700	5.752
2.800	6.472
2.900	7.196

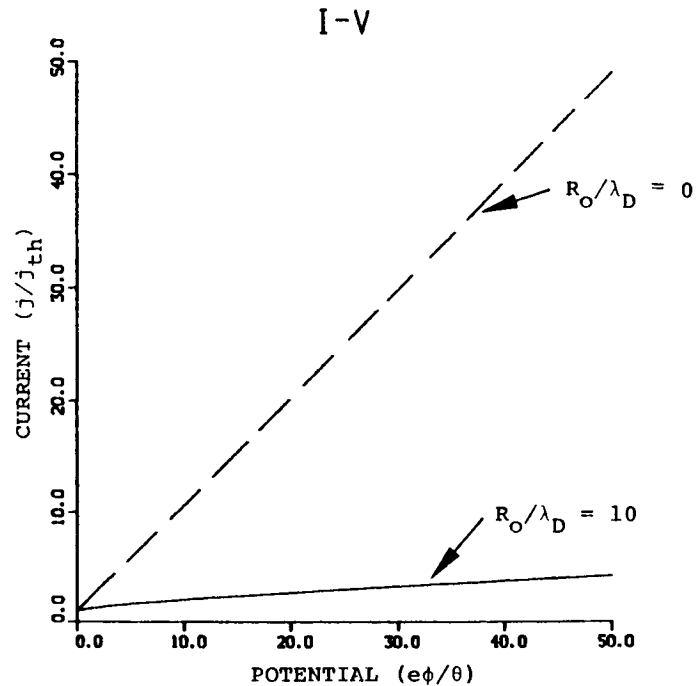


Figure 1. - The I-V characteristic for a spherical probe in a small Debye length plasma. Note how even at large potentials the probe collects just a few times the plasma thermal current. The dashed line is for long Debye length orbit limited collection. It is not applicable to large objects in low earth orbit.

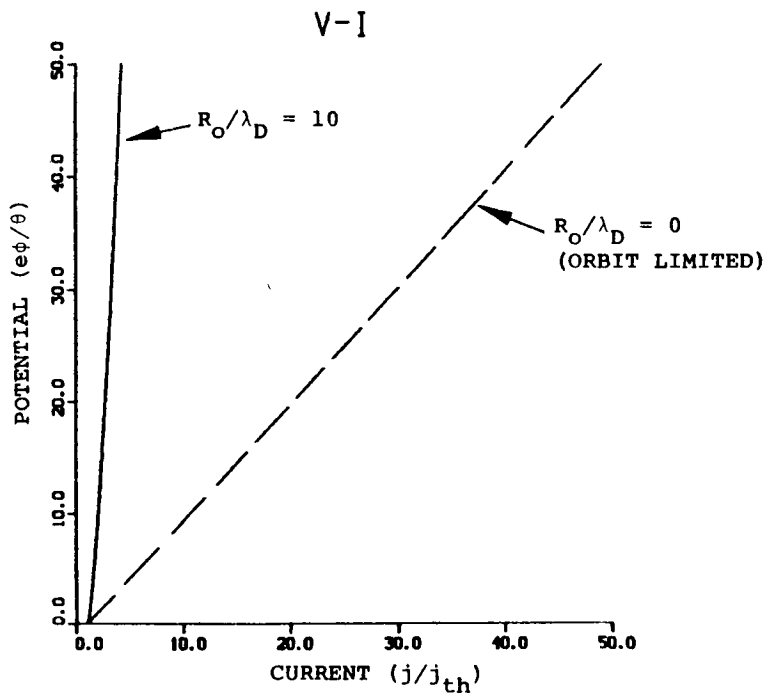


Figure 2. - The V-I characteristic for a spherical probe in a small Debye length plasma. Note how even a small increase in probe current causes a very large change in the potential of the sphere. The dashed line is for long Debye length, orbit limited collection.

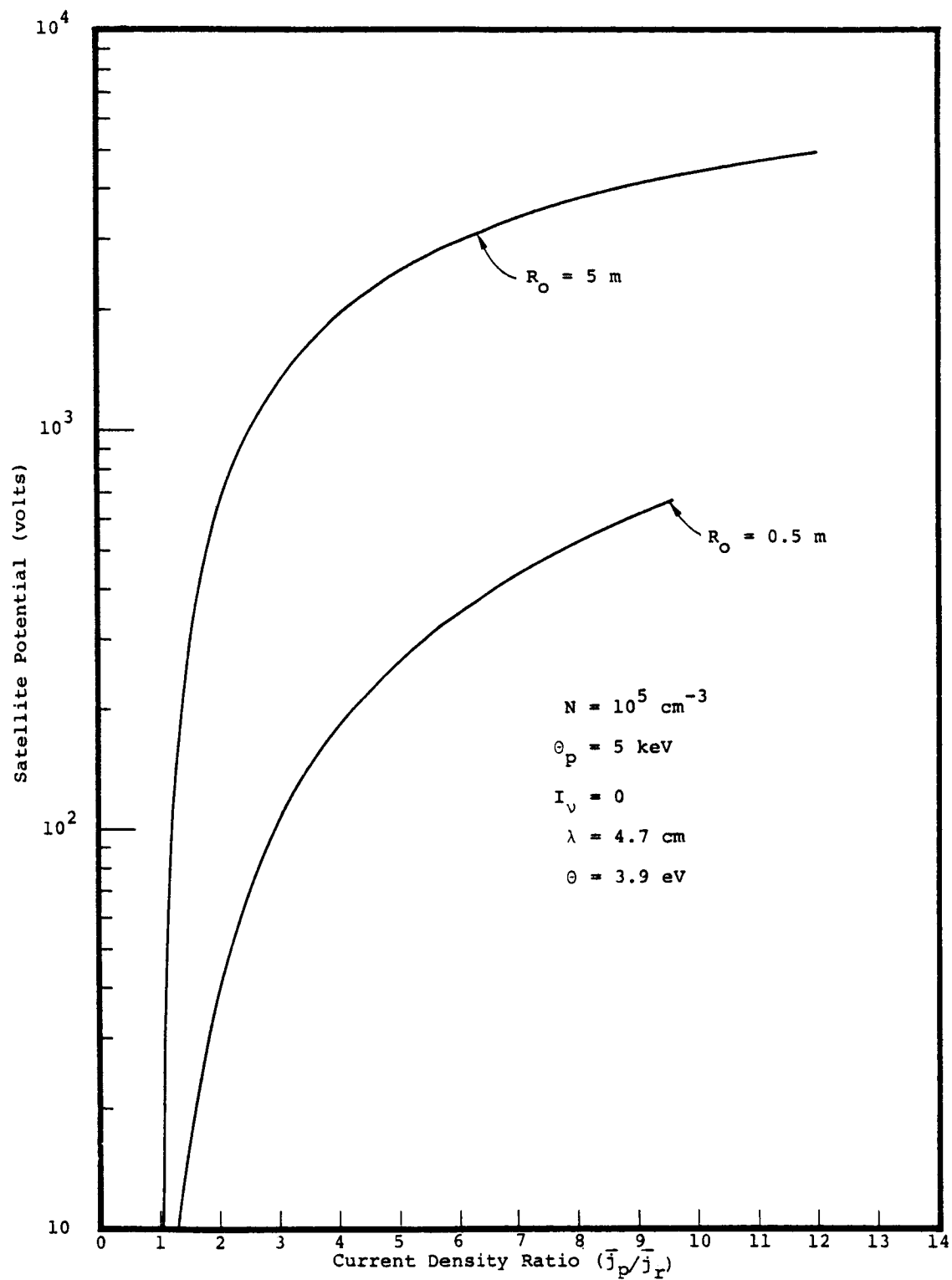


Figure 3. - Satellite potential as function of current density ratio.

## PANEL DISCUSSION

A panel discussion on the update of Military Standard 1541 was chaired by Major Jack Roberts from the U.S. Air Force Space Division (AFSD), the SCATHA program manager and also the Air Force point of contact for the spacecraft charging technology investigation. Panel members included Alan Holman, the program manager for the Science Applications, Inc. (SAI) effort to develop a draft version of the standard for AFSD; James Frankos, from the Aerospace Corporation's Electrical Systems Department; George Brady, a reliability engineer in the Space Systems Division of Lockheed; Paul Robinson, with the Jet Propulsion Laboratory as Group Supervisor of the Engineering Requirements Section; Ronald Schmidt, a materials physicist at General Electric and a member of the survivability group; and John Reddy, from ESTEC, Test Facilities Division.

Major Roberts: The spacecraft charging military standard is a Space Division requirement as outlined in the joint NASA/U.S. Air Force Spacecraft Charging Technology program. Our approach to filling our commitments under that interagency program is to update the current version of Military Standard 1541, which is the electromagnetic compatibility (EMC) requirements for spacecraft with spacecraft charging requirements. Our goal is to have that updated version published by the end of 1982. SAI has been contracted to pull together the detailed technical elements and write a fairly complete draft version of this document. They should have that done by the end of 1981. Then the Aerospace Corporation will take over exclusively, obtain the system program office and industry reviews, incorporate the comments, and have the document ready for publication by the end of 1982. The Air Force places a great deal of emphasis on military standards. As the name implies, they are standardization documents that are very useful, in our opinion, especially in letting requests for proposal. They give the contractor some definite guidance in judging the scope of the work and enable him to submit a better-thought-through bid. By the same token, they help the Government to evaluate better the bids received from the contractors and, once a contractor is selected, to evaluate his performance in the design and test phases. Of course the overlying benefit here is the elimination of gross under- and overdesigns and the costs that can be associated with them. Therefore military standards are a very useful tool for both the system program offices and industry if they are written properly.

The key to a military standard, in particular this one, is its contents. The inputs must be of high quality; that is, we have to have faith in what we put in there; it has to be well thought out and based on a good data base; the utility has to be clear; the credibility has to be there and therefore all these things blend into the acceptability of the document. In other words, for a military standard to be effective the system program offices and the contractors have to accept it.

The major theme of this panel discussion then is how to achieve the acceptability of Military Standard 1541. For instance, if the system program offices do not have faith in a standard, they may not use it, or they may eliminate sections. Therefore all our efforts will reap no benefit. By the same token, industry and the contractors will protest

mainly by increased costs, if they perceive the standard to be unreasonable, too restrictive, or too vague. The military standard, in a way, is really a document that must be accepted by everybody; really it is a group effort wherein everybody has to put their efforts together to accomplish a successful product.

There is an obvious trade-off in the contents of a military standard. Simplistically speaking, there are two approaches that can be taken. One is to try to spell everything out in detail as a requirement, "The equipment shall" sort of thing, but perhaps in some cases this is too restrictive and requires a high degree of confidence. The other approach is to give merely information or guidelines. These guidelines are subject to interpretation in many different ways and by many different people. It can be very vague. So do you use one approach or the other or an approach somewhere in between to develop a military standard with the greatest usefulness? There are many elements to be considered: Analytical models, tools, coupling models, test levels, test requirements - should they be stated as requirements or guidelines? The panel members will discuss the approach to Military Standard 1541, the contents, the test requirements, and the acceptability of the document.

Dr. Holman: To strengthen the point Major Roberts just made, about the importance of making this a salable document acceptable by the system program offices and the contractor community, it must still represent the actual spacecraft charging hazard. Any design analysis or test that is called for must be able to be addressed in a practical way by the contractors.

I want to remind you of the need for an applicability statement within this document. And I would like, when we open this up to the floor, some comments on how that applicability statement should be addressed. Should it be addressed as the definition of a region in space that is important to spacecraft charging concern, or should it be addressed in some other way? There is certainly useful information coming from the P78-2 vehicle, but that information has to be supplemented by all the inputs that are coming from the community. SAI and Aerospace are the focal points for collecting that information and including anything of technical merit that is applicable to the military standard appendix.

It is still vague how we can call out analytical requirements within the format and structure that are currently prescribed for the military standard appendix. That issue should be discussed. Analysis is very important, especially for determining test levels. For example, a spacecraft with multilayer insulation surfaces could be subjected to fairly large discharges, and we would probably come up with some maximum and extreme worst-case level of the discharge and from that define a test level. But as Drew Muhlenberg and Paul Robinson mentioned, the method of puncturing the thermal blankets with pinholes results in many small "earthquakes" instead of one large earthquake. And, if the test level should then be dependent on the smaller discharges that are generated off these kinds of blankets, it will be a less severe environment than the maximum worst-case environment. You really need some analysis of your specific spacecraft design before a representative test level for your design can be determined. I want to remind you of the importance of the high-energy electron charging of dielectrics within the spacecraft. This

might very well drive subsystem design requirements, and I want you to give some more thought to that so that we can discuss these issues later in more detail - always keeping under consideration the salability, acceptability, and practicality of the technical information to be included in the military standard.

Mr. Frankos: I have been one of the "working troops" in the electromagnetic compatibility field, and there has always been a problem between management and the working troops, especially in electromagnetic compatibility. I am concerned that the military standard, when it is updated, really spells things out clearly for management so that the working troops do not have to spend time trying to explain to management what it means and what the company has to do to satisfy the requirement. It has to be practical from the standpoint of the contractor: He has to be able to do whatever it is. As Major Roberts said, it has to be useful - we don't want money going down the drain. My area of responsibility is supporting the program offices and the Air Force and checking the contractors' technical work. If a document is clear and straightforward and spells out the things to be done, it makes my job easier and it makes the contractor's job easier so that everybody benefits.

Mr. Brady: As one of the working troops in reliability I have viewed Military Standard 1541 as it affects testing of spacecraft, space platforms, and subsystems. I am not sure that all these changes should be incorporated into 1541 through an appendix. Although there are some changes that should be incorporated, 1541 actually does cover some discharge space plasma events and perhaps just a beefing up of that area would be appropriate. Some definitions, such as dielectric discharges, should be incorporated as well as - for large space platforms - Debye lengths and plasma sheaths. In addition, there could be a pitfall in trying to design a document around one particular day of one particular space vehicle, in this case for the SCATHA vehicle on day 87. It is only a preliminary analysis, yet this has been called a worst case. However, the ATS vehicles, particularly ATS-6, have experienced some charging activity much greater than that experienced by the SCATHA vehicle. So the environment is yet to be determined.

There seems to be some problem in defining the tests to be incorporated for any system or subsystem. There is a great variety in testing capabilities and procedure, such as using monoenergetic electrons or two electron guns or ions and electrons at the same time - quite a variety. There is also some difference of opinion on the need for incorporating ultraviolet sources. Military Standards 461 and 462 probably should be changed to incorporate additional testing procedures rather than incorporating these procedures in the appendix to 1541.

The analysis is a good idea also, but there could be a problem trying to get NASCAP to agree with what we have seen on the SCATHA vehicle. And NASCAP could be used to analyze test articles in a chamber. For instance, in a test at Lockheed, some charge was inexplicably lost. Perhaps the NASCAP program could tell us where it went.

Regarding the procedures for eliminating differential charging - we know that with conductive paths we get a return current that is much higher than the current from a semiconductor path. And, in fact, 1541 says we should use no materials on the spacecraft surface with a resistivity greater

than  $10^9$  ohm/cm, and this appears to be adequate from other experiments and from analysis. Perhaps a bleed path with that magnitude would be adequate. In summary, we need a lot more analysis from the SCATHA vehicle for defining the worst case. For instance, the worst case is probably going to come up in 1983, and we need some more test results and some more information on how to combine test results with the analytical approach. All the viewpoints expressed here are my own and not necessarily the viewpoints of Lockheed.

Mr. Robinson: Speaking for myself also, I agree with the general tenor of standard 1541. I think there must be a top level specification that includes spacecraft charging, and as has already been well pointed out it must be realistic, because you do not want to require that the disturbances from spacecraft charging be smaller than the ones from the spacecraft's operating equipment. Also, the standard should allow for as many innovative solutions as it can. For example, the plasma source that Herb Cohen and Chris Olsen and others have suggested as a way to control the spacecraft potential ought to be allowed for because it does provide a nice framework to work in. We need, of course, as Hank Garrett pointed out, to get a clearly defined worst-case environment. We need that modeling effort. We need to provide a procedure for determining material parameters. If you have a novel way of doing your thermal control surfaces, you need a way to verify that and to provide better understanding of the physics involved. This kind of specification should lead to a test program. If you think the spacecraft will not charge up because you have been very clever with the surface or with the materials chosen, you ought to be able to prove it. And if you think your subsystems are good enough that they are immune whether the spacecraft charges or not, you ought to be able to prove that as well. In short, it is a real problem if we ignore it, but otherwise it is well within our capabilities.

This testing may require some upgrading of the ground support equipment as well as the spacecraft itself. The "box" may survive the test fine, but the thing you were monitoring the box with may not. And so you have to look at the whole procedure. We do not know the whole story on how dielectrics charge and discharge. John Stevens, Robb Frederickson, and practically all of us have pointed out details where our models did not seem to hold correctly - they did not predict what we wanted. Perhaps the threshold effect that some people talked about is a real effect. Maybe we do have the right parameters in there and maybe it's a delicate difference between one environment and the next. At this time there is no theory of dielectrics that predicts all the effects that we see.

The same holds for radiation-induced conductivity. We do not as far as I know really come up to that from basic principles. We can put in some coefficients that we think handle it, but we do not have a fundamental understanding of it or of how the arc itself is formed.

Mr. Schmidt: My outlook on the proposed revision is primarily from what has been done on the DSCS-III program. However, I do not speak for General Electric on any of these points, primarily because I joined GE after most of their work on spacecraft charging and design efforts was completed or well under way. Many of the approaches that were used on the DSCS program are very similar to what is spelled out in the proposed revision - the use of



the Faraday cage, conductive materials, and charge modeling with the SCAP program that was presented at the previous charging conference. The program modeled structural currents due to worst-case discharges and used materials testing to determine the needed material properties. These are all very similar and I agree with a lot of the revisions that are proposed, although I do not know why the radiated-fields aspect, which was included in the 1541 treatment of spacecraft charging, has been omitted from the revision. That aspect has a meaningful role in either the analysis or the testing. My biggest concern is the use in the revision of analytical methods primarily in the coupling and discharging areas, which are not really well understood yet. There has been a lot of work in that area, and much needs to be done before it can be used to generate threat level requirements on possible flight-qualified vehicles. This has to be mixed very heavily with an empirical program to give a firm feeling of what is going to happen during the test on a flight-qualified vehicle. SCATHA's primary role in the development of the proposed revisions could be in defining the environment, which is the missing element in the definition of what and how to test. What information SCATHA can bring to the definition of how to develop coupling models is yet to be determined.

Mr. Reddy: I would like to address the approach to including SCATHA data into a standard and the contents of the data. Two types of data are needed: data to support data scientific analysis of the sort that would be done by NASCAP, and more importantly engineering data. Here I agree with most of the panel members. I think it is all well and good talking about electron temperatures and the like, but the technician operating his voltmeter in his laboratory does not relate to electron temperatures very easily. He needs some sort of engineering format. Therefore this document should include two types of test requirements. There are two options when you build a satellite: You can build it to charge and discharge, or you can build it not to charge. Military Standard 1541, if it is going to be revised, should address both of these options. Furthermore the test requirements should be at the system and unit level, rather than at the subsystem level. Subsystem tests have yet to give any meaningful data.

It is a bit peculiar that a strong requirement is given as an appendix to a military standard. And what's more, this appendix quotes 1541 as an applicable document. That's a little bit chicken-and-egg.

On the last point, as to whether or not we should produce a requirement that is acceptable to industry, two years ago at this conference there was a panel session that related to the credibility gap between studies by the SCATHA group and those by the electrostatic charging groups and the difficulty of convincing management that there was in fact a problem. If two years later we still cannot convince management that there is a problem, we might as well throw this thing out the door now. If we believe there is a problem, if we can identify this problem, if we can produce numbers to the problem, then whether industry finds it acceptable or not is by-and-large immaterial - satellites still have to survive in this environment.

Major Roberts: Obviously, our intent when we set up this panel was not to speak with one unified voice because it is early enough in developing this military standard that we need to have some healthy and diverse dialogue

over what we are doing and our approach to it. So I have encouraged that and I encourage it from the audience. Some good points have been brought up by the panel to jog your thought processes and memories.

Question: I have a question for Al Holman. Al, I noticed in the military standard that most of our efforts have been concentrated on the geosynchronous environment. Will we be flying satellites in other environments, and if so, will the standard address these environments or is that something to be added later?

Dr. Holman: Well, you are certainly referring to flying more of your JPL payloads around Jupiter and Saturn. Currently, 1541 is an Air Force military standard meant to address requirements for Air Force programs. Most Air Force programs involve satellites still flying around the Earth, in the general vicinity of synchronous. There has got to be a better definition of where the region of spacecraft charging exists. And that, no doubt, is the way it is going to be called out in the applicability statement within the military standard. Now that does not mean 1541 cannot be picked up by a program office supporting the development of a Jupiter probe, for example, and still called out in their statement of work as an applicable document. But presently we do not have a good enough definition of the region of space that should be of concern. We are looking for a better definition to come out of the Environmental Atlas.

Panel member: To add a little more to what Al has responded, the update of Military Standard 1541 is based on the SCATHA program effort. If there is a concern for the near-Earth environment, or even farther out than geosynchronous, the SCATHA program cannot provide the basic information. If future programs can provide it, there will be another update.

Mr. Garret: Would you feel then that there is a need for a follow-on program to define other regions of the near-Earth environment?

Major Roberts: Yes, there is under assessment right now a program plan to update Military Standard 1541 additionally around 1986 based on information from the Environmental Interactions Technology program.

1. Report No. <b>NASA CP-2182</b> <b>AFGL-TR-81-0270</b>		2. Government Accession No.		3. Recipient's Catalog No.	
4. Title and Subtitle  <b>SPACECRAFT CHARGING TECHNOLOGY 1980</b>				5. Report Date <b>October 1981</b>	
				6. Performing Organization Code	
7. Author(s)				8. Performing Organization Report No.	
9. Performing Organization Name and Address  <b>National Aeronautics and Space Administration</b> <b>Lewis Research Center</b> <b>Cleveland, Ohio 44135</b>				10. Work Unit No. <b>76610803</b>	
				11. Contract or Grant No.	
12. Sponsoring Agency Name and Address <b>National Aeronautics and Space Administration</b> <b>Washington, D.C. 20546 and</b> <b>U.S. Air Force Geophysics Laboratory (PHK)</b> <b>Hanscom Air Force Base, Massachusetts 01731</b>				13. Type of Report and Period Covered  <b>Conference Publication</b>	
				14. Sponsoring Agency Code	
15. Supplementary Notes <b>Cochairmen: N. John Stevens, NASA Lewis Research Center, Cleveland, Ohio, and Charles P. Pike, U.S. Air Force Geophysics Laboratory (PHK), Hanscom Air Force Base, Massachusetts</b>					
16. Abstract  <b>The third Spacecraft Charging Technology Conference, sponsored by the National Aeronautics and Space Administration and the U.S. Air Force, was held at the Air Force Academy from November 12 to 14, 1980. The proceedings contains 66 papers, dealing with the geosynchronous plasma environment, spacecraft modeling, charged-particle environment interactions with spacecraft, spacecraft materials characterization, and satellite design and testing. The proceedings is a compilation of the state of the art of spacecraft charging and environmental interaction phenomena.</b>					
17. Key Words (Suggested by Author(s))  <b>Spacecraft charging; Environmental interactions; Space environment; Satellite modeling; Satellite design; Satellite test; Satellite materials characterization</b>				18. Distribution Statement  <b>Unclassified - unlimited</b> <b>STAR Category 18</b>	
19. Security Classif. (of this report)  <b>Unclassified</b>		20. Security Classif. (of this page)  <b>Unclassified</b>		21. No. of Pages  <b>1005</b>	
				22. Price*  <b>A99</b>	

\* For sale by the National Technical Information Service, Springfield, Virginia 22161